Luis Rueda
Domingo Mery
Josef Kittler (Eds.)

Progress in Pattern Recognition, Image Analysis and Applications

**12th Iberoamerican Congress
on Pattern Recognition, CIARP 2007
Viña del Mar-Valparaiso, Chile, November 2007, Proceedings**

IAPR

Springer

Lecture Notes in Computer Science 4756

Luis Rueda   Domingo Mery   Josef Kittler (Eds.)

Progress in Pattern Recognition, Image Analysis and Applications

12th Iberoamerican Congress
on Pattern Recognition, CIARP 2007
Viña del Mar-Valparaiso, Chile, November 13-16, 2007
Proceedings

Springer

Volume Editors

Luis Rueda
Universidad de Concepción, Chile
Department of Computer Science
E-mail: lrueda@udec.cl

Domingo Mery
Pontificia Universidad Católica de Chile
Department of Computer Science, Santiago 22, Chile
E-mail: dmery@ing.puc.cl

Josef Kittler
University of Surrey
Department of Electronic Engineering
Guildford GU2 7XH, UK
E-mail: J.Kittler@surrey.ac.uk

Preface

These proceedings offer a written account of the scientific contributions presented at the 12th Iberoamerican Congress on Pattern Recognition (CIARP 2007), held in Viña del Mar-Valparaíso, Chile. The aim of the congress was to promote and disseminate ongoing research and mathematical methods for pattern recognition, image analysis, and applications in such diverse areas as computer vision, bioinformatics, robotics and remote sensing, industry, health, space exploration, data mining, document analysis, natural language processing and speech recognition, among others. The volume is a manifestation of the ongoing success of the Iberoamerican Congress on Pattern Recognition (CIARP) that has featured in the landscape of international scientific conferences on pattern recognition and computer vision in the past few years. It provides evidence of the growing stature of the Iberoamerican scientific community in this subject area and of the interest its scientific contributions generate worldwide. As in the previous years, CIARP 2007 hosted participants from all over the world.

CIARP 2007 was organized by the Department of Informatics Engineering of the University of Santiago de Chile (USACH) and the Department of Informatics of the Technical University Federico Santa María (USM). The event was sponsored by the Advanced Technologies Application Center of Cuba (CENATAV), the Mexican Association for Computer Vision, Neurocomputing and Robotics (MACVNR), the Cuban Association for Pattern Recognition (ACRP), the Portuguese Association for Pattern Recognition (APRP), the Spanish Association for Pattern Recognition and Image Analysis (AERFAI), the Special Interest Group on Pattern Recognition of the Brazilian Computer Society (SIGPR-SBC), the Chilean Society for Computer Science by means of its technical committee, the Chilean Association for Pattern Recognition (AChiRP), the International Institute for Innovation and Entrepreneurship (3IE) and the Southeastern Pacific Research Institute for Advanced Technologies (SEPARI). CIARP 2007 was endorsed by the International Association for Pattern Recognition (IAPR).

CIARP 2007 received contributions from 36 countries, registering a total of 200 papers submitted, out of which 97 were accepted for publication in these proceedings and for presentation at the conference. The review process was carried out by the Scientific Committee composed of internationally recognized scientists, all experts in their respective fields. Each paper was subject to a double-blind review, carried out by at least two reviewers. We are especially indebted to the reviewers for their effort, ensuring the quality of the papers selected for the proceedings.

The conference program was augmented by invited keynote papers, presented by internationally renowned scientists. The talks addressed an interesting mix of topics in theory and applications of pattern recognition and were given by:

- Prof. Anil Jain, Department of Computer Science and Engineering, Michigan State University, USA.
- Prof. Horst Bunke, Institute of Computer Science and Applied Mathematics, University of Bern, Switzerland.
- Prof. Maria Petrou, Department of Electrical and Electronic Engineering, Imperial College, UK.
- Prof. Sorin Draghici, Department of Computer Science, Wayne State University, USA.

We would like to express our thanks to the members of the Organizing Committee for their contribution to the success of the conference and to these proceedings. We would also like to convey our special thanks to the members of the Local Committees for their help in the submission and reviewing process, as well as in editing these proceedings. Finally, we would like to express our gratitude to the members of the Steering Committee for their support and help in bringing this congress to Chile for the first time.

<div align="right">

Luis Rueda
Domingo Mery
Josef Kittler

</div>

Organization

CIARP 2007 was organized by the Department of Informatics Engineering of the University of Santiago de Chile (USACH) and the Department of Informatics of the Technical University Federico Santa María (USM)

General Conference Co-chairs

Max Chacón — Department of Informatics Engineering, Universidad de Santiago de Chile, Chile

Héctor Allende — Department of Informatics, Universidad Técnica Federico Santa María, Chile

Program Committee Co-chairs

Luis Rueda — Department of Computer Science, Universidad de Concepción, Chile

Domingo Mery — Department of Computer Science, Pontificia Universidad Católica, Chile

Josef Kittler — Department of Electrical Engineering, Surrey University, UK

Steering Committee

José Ruiz Shulcloper — ACRP, Cuba
Alberto Sanfeliu — AERFAI, Spain
Aurélio Campilho — APRP, Portugal
Eduardo Bayro-Corrochano — MACVNR, Mexico
Héctor Allende — AChiRP, Chile
Herman Martin Gomes — SIGPR-SBC, Brazil

Local Committee

Cesar San Martín — Department of Electrical Engineering, Universidad de La Frontera, Chile

Local Arrangements Committee

Claudia Arancibia — Department of Informatics, Universidad Técnica Federico Santa María, Chile

Scientific Committee

Ablameyko S.V.	The National Academy of Sciences of Belarus, Republic of Belarus
Acuña G.	Universidad de Santiago de Chile, Chile
Aggarwal J.K.	University of Texas at Austin, USA
Alquezar-Mancho R.	Universidad Politécnica de Cataluña, Spain
Altamirano-Robles A.	Instituto Nacional de Astronomía, Óptica y Electrónica, Mexico
Araujo H.	Universidade de Coimbra, Portugal
Atkinson J.	Universidad de Concepción, Chile
Bayro-Corrochano E.	Centro de Investigación y de Estudios Avanzados del Instituto Politécnico Nacional, Mexico
Bertalmío M.	Universitat Pompeu Fabra, Spain
Bezdek J.	University of West Florida, USA
Bioucas-Dias J.	Instituto Superior Técnico, Portugal
Bloch I.	Escuela Nacional Superior de Telecomunicaciones, France
Borges D.	Universidade do Brasilia, Brazil
Bunke H.	University of Bern, Switzerland
Campilho A.	Universidade do Porto, Portugal
Cano S.	Universidad de Oriente, Cuba
Carrasco-Ochoa J. A.	Instituto Nacional de Astronomía, Óptica y Electrónica, Mexico
Chacón M.	Universidad de Santiago de Chile, Chile
Colmenares G.	Universidad de los Andes, Venezuela
Corchado E.	Universidad de Burgos, Spain
d'Avila-Mascarenhas N.	Universidade Federal de Sao Carlos, Brazil
Desachy J.	Université des Antilles et de la Guyane, France
Diday E.	Universite Paris Dauphine, France
Facon J.	Pontificia Universidade Catolica de Parana, Brazil
Figueiredo M.	Instituto de Telecomunicaciones, Portugal
Fred A.	Instituto de Telecomunicaciones, Portugal
Gelbukh A.	Instituto Nacional Politécnico, Mexico
Gibert K.	Universidad Politécnica de Cataluña, Spain
Gomes H.M.	Universidade Federal de Campina, Brazil
Gomez-Gil M.	Universidad de las Américas - Puebla, Mexico
Gomez-Ramirez E.	Universidad La Salle, Mexico
Gordillo J.L.	Center for IS, Tecnológico de Monterrey, Mexico
Graña M.	Universidad del País Vasco, Spain
Grau A.	Universidad Politécnica de Cataluña, Spain

Haindl M.	Czech Academy of Sciences, Czech Republic
Hancock E.	University of York, UK
Hernando J.	Universidad Politécnica de Cataluña, Spain
Jain A.	Michigan State University, USA
Kamel M.	Univeristy of Waterloo, Canada
Kasturi R.	University of South Florida, USA
Kittler J.	University of Surrey, UK
Koschan A.	Universidad de Tennessee, USA
Kropatsch W.G.	Vienna University of Technology, Austria
Kuncheva L.I.	University of Wales, UK
Lazo-Cortés M.	Instituto de Cibernética, Matemáticas y Física, Cuba
Levachkine S.	Instituto Politécnico Nacional, Mexico
Lopez de Ipiña K.	Universidad del País Vasco, Spain
Lopez-Lopez A.	Instituto Nacional de Astronomía, Óptica y Electrónica, Mexico
Lorenzo-Ginori J.V.	Universidad Central "Marta Abreu" de Las Villa, Cuba
Marques J. S.	Universidade Técnica de Lisboa, Portugal
Martinez-Trinidad J.F.	Instituto Nacional de Astronomía, Óptica y Electrónica, Mexico
Medioni G.	University of Soutern California, USA
Mery D.	Pontificia Universidad Católica de Chile, Chile
Moctezuma-Flores M.	Universidad Nacional Autónoma de México, Mexico
Morales E.	Instituto Nacional de Astronomía, Óptica y Electrónica, Mexico
Nascimento J.	Universidade Técnica de Lisboa, Portugal
Ngom A.	University of Windsor, Canada
Novovicova J.	Czech Academy of Sciences, Czech Republic
Padilha A. J.	Universidade do Porto, Portugal
Peña M.	Universidad Nacional Autónoma de México, Mexico
Perales F.	Universidad de las Islas Baleares, Spain
Pereira F.	Instituto de Telecomunicacçõnes, Portugal
Perez de la Blanca N.	Universidad de Granada, Spain
Petrou M.	Imperial College, UK
Pham Tuan	James Cook University, Australia
Pina P.	Instituto Superior Técnico, Portugal
Pinho A.	Universidade de Aveiro, Portugal
Pinto C.	Universidade Técnica de Lisboa, Portugal
Pla F.	Universitat Jaume I, Spain
Randall G.	Universidad de la República, Uruguay

Rannou F.	Universidad de Santiago de Chile, Chile
Reyes-García C.A.	Instituto Nacional de Astronomía, Óptica y Electrónica, Mexico
Riazanov V.	Russian Academic of Science, Russia
Rodríguez R.	Instituto de Cibernética, Matemáticas y Física, Cuba
Roman-Osorio R.	Universidad Nacional Autónoma de México, Mexico
Ross A.	West Virginia University, USA
Rueda L.	Universidad de Concepción, Chile
Ruiz del Solar J.	Universidad de Chile, Chile
Ruiz-Shulcloper J.	Centro de Aplicaciones de Tecnología de Avanzada, Cuba
Sanfeliu A.	Universidad Politécnica de Cataluña, Spain
Sang-Woon Kim	Myongji University, South Korea
Sanniti di Baja G.	National Research Council, Italy
Sansone C.	Universita' di Napoli "Federico II", Italy
Sbarbaro D.	Universidad de Concepción, Chile
Shirai Y.	Ritsumeikan University, Japan
Sossa-Azuela J.H.	Instituto Politécnico Nacional, Mexico
Soto A.	Pontificia Universidad Católica de Chile, Chile
Sucar E.	Instituto Nacional de Astronomía, Óptica y Electrónica, Mexico
Taboada-Crispi A.	Universidad Central "Marta Abreu" de Las Villa, Cuba
Torres M.I.	Universidad del País Vasco, Spain
Trucco E.	Heriot Watt University, UK
Valev V.	Saint Louis University, USA
Verri A.	Universita degli Studi di Genova, Italy
Vidal E.	Universidad Politécnica de Valencia, Spain
Villanueva J.J.	Universidad Autónoma de Barcelona, Spain
Wang S.	University of Sherbrooke, Canada
Zegers P.	Universidad de los Andes, Chile
Zhang D.	Hong Kong Polytechnic University, Hong Kong

Sponsoring Institutions

University of Santiago de Chile USACH
Technical University Federico Santa María USM
The International Institute for Innovation and Entrepreneurship (3IE)
The Southeastern Pacific Research Institute for Advanced Technologies SEPARI
Chilean Association for Pattern Recognition AChiRP

The International Association for Pattern Recognition IARP
Cuban Association for Pattern Recognition ACRP
Mexican Association for Computer Vision, Neural Computing and Robotics
    MACVNR
Special Interest Group of the Brazilian Computer Society SIGPR-SBC
Spanish Association for Pattern Recognition and Image Analysis AERFAI
Portuguese Association for Pattern Recognition (APRP)

Table of Contents

Image Coding, Processing and Analysis

Shape and Texture Analysis

Computer Vision

Pattern Recognition Principles

Artificial Intelligence Techniques and Recognition

Logical Combinatorial Pattern Recognition

Neural Networks

Kernel Machines

Bioinformatics

Data Mining

Natural Language Processing and Recognition

Industrial and Medical Applications of Pattern Recognition

Robotics and Remote Sensing Applications of Pattern Recognition

Document Processing and Recognition

Fuzzy and Hybrid Techniques in Pattern Recognition

Learning in Computer Vision: Some Thoughts

Maria Petrou

Communications and Signal Processing Group,
Electrical and Electronic Engineering Department,
Imperial College,
London SW7 2AZ, UK

Abstract. It is argued that the ability to generalise is the most important characteristic of learning and that generalisation may be achieved only if pattern recognition systems learn the rules of meta-knowledge rather than the labels of objects. A structure, called "tower of knowledge", according to which knowledge may be organised, is proposed. A scheme of interpreting scenes using the tower of knowledge and aspects of utility theory is also proposed. Finally, it is argued that globally consistent solutions of labellings are neither possible, nor desirable for an artificial cognitive system.

1 Introduction

The word "learning" has many interpretations among the pattern recognition community in general, and the computer vision community in particular. It has been used to loosely mean anything between the identification of the best value of a parameter from training data, to learning how to recognise visual structures. So, perhaps we should try to distinguish the interpretation of the word as it appears in the mathematical formulation of problems, from its interpretation as it appears in cognition related tasks. In the sections that follow, we shall try to understand the significance of learning in the context of computer vision and identify a possible relationship between these two interpretations of the word.

2 The Main Characteristic of Learning

Some of the first learning algorithms in relation to cognitive tasks, that have been proposed in the past, are the various types of neural network. Proponents of neural networks often comment on the generalisation capabilities of the networks they develop. Generalisation is one of the characteristics of learning. Indeed, we, humans, teach our children often with fairy tales and parables, assuming that they have the ability to generalise to real situations. It is preposterous to expect that we shall have to teach our children about all individual possible situations they may encounter in life, in order to make sure that we have taught them well. We may safely conclude, therefore, that

This implies that classical pattern recognition methods, that use training examples to span the feature space, are not really learning methods in the cognitive sense of the word. Even neural network based methods, in order to generalise well, rely heavily on the availability of enough training samples to populate adequately the feature space. The training patterns are used by the neural networks to approximate the class boundaries in the feature space with piece-wise linear segments. When an unknown pattern arrives, it can be associated with the class that has been identified to populate the part of the feature space where the pattern appears. Some old [3] and some more recently developed methods [1], that can work with fewer training patterns than straightforward methods, do so by selecting the patterns that matter most in defining the class boundaries, rather than by using some higher level generalisation abilities of the classifier [23]. So, neural networks and pattern classification methods are not learning methods in the cognitive sense of the word.

The question then that arises is: is learning, as understood by cognitive scientists and psychologists, algorithmic, or is it something beyond the current grasp of mathematical formalism? Evidence against learning being algorithmic is the ability of humans to learn even from single examples. A counter-argument is that humans take a lot of time to learn, and it is possible that what we witness as super-fast learning is simply a manifestation of the application of some meta-knowledge, some generic rules that have been slowly and painfully learnt subconsciously. I would like to clarify that "learning" here does not refer to getting a University degree. This is indeed a very long process and it takes almost one third of the life span of a person. Learning here refers to survival skills, to skills needed to operate in everyday life. Given that a human becomes reproductive roughly between the ages of 12–15, we may assume that nature considers the human child becoming ready for life at that stage. So, we may say that humans "learn" what they have to learn, to be ready for life as independent entities, over a period of 12–15 years, which is still a significant fraction of their life span. Therefore, humans seem to be slow learners after all. They take a lot of time to work out the rules of meta-knowledge. It is these rules, that have possibly been learnt in an algorithmic way, that allow then the human to learn in the super-fast, almost magical, way that we often witness. We may conclude from the above arguments that:

– generalisation is an important characteristic of learning;
– generalisation in algorithmic learning may only be achieved by having enough training examples to populate all parts of the class space, or at least the parts that form the borders between classes;
– we have true generalisation capabilities, only when what is learnt by training examples are rules on how to extract the identity of objects and not the classes of objects directly. If such learning has taken place, totally unknown objects may be interpreted correctly, even in the absence of any previously seen examples.

This conclusion implies that what we have to teach the computer, in order to construct a cognitive system, are relations rather than facts. For example, memorising

the dictionary of a language, does not teach a person the language. The person has to learn the relations between words in order to master the language. This is in agreement with Winstone's pioneering experiments on teaching the computer to recognise arches. He did not show to the computer all possible types of arch it may encounter. He showed it examples and counter examples of arches and taught it to recognise relations between components, such as "supports" or "is supported by" [26].

3   Knowledge and Meta-knowledge

There are at least 50 theories of learning developed by cognitive scientists [28]. In computer science, we tend to distinguish two forms of learning: learning by experimentation and learning by demonstration. Inductive learning is also used by computer scientists, but we shall not deal with that here, because it implies that the learner has already learnt the rules of logic. So, inductive learning may be thought of as a way of applying the already learnt rules of meta-knowledge [22].

Learning by experimentation implies the ability to try, reason about the results and draw conclusions. In its simplest form, this is what fully automatic programs do. A fully automatic segmentation algorithm, for example, will work as follows: perform segmentation, assess the quality of the result, adjust the parameters and try again. The immediate conclusion is that learning by experimentation requires the presence of a feed-back loop. It also requires the availability of a criterion that says how well the system has performed each time. It is important for this criterion to be independent of the knowledge or information used to perform the segmentation in the first place, otherwise the result will be a self-fulfilling prophecy. In semi-automatic systems, the criterion is provided by the human. The reported results in the literature then include a statement of the type: "the best threshold was found by trial and error." This method is a perfectly legitimate method of learning. It comes under the umbrella of supervised learning and it corresponds to human learning with the help of a teacher.

Proceeding to fully automated methods is equivalent to assuming that the computer has somehow passed that stage of learning the meta-knowledge, necessary to construct rules, and now learning proceeds very fast, making use of these meta-rules. For example, if we know that agricultural fields tend to have straight borders, we may judge the output of a segmenter of an image, captured by an airborne sensor, as good or bad, according to whether it produced regions with straight borders or not. The knowledge that fields have straight boundaries is a meta-knowledge. The segmenter might have operated using only texture and edge information. The straightness of the inferred borders may be used as a criterion to drive the system to use its feed-back loop to work out a better segmentation. The question then is: how did the system acquire this meta-knowledge? As argued earlier, it must be the meta-knowledge that had to be learnt by the human child (or the computer learner) painfully slowly by seeing lots of examples of agricultural fields. And although no method has been found yet to transplant this meta-knowledge to the brain of the human child

from the brain of the teacher, computers have an advantage here: the teacher, i.e. the human, may insert the meta-knowledge into the system while developing the criterion of self assessment of the algorithm. From this line of argument, we conclude that:

- meta-knowledge may take the form not only of relations, but also of generic characteristics that categories of objects have;
- in interactive systems, meta-knowledge is inserted into the computer learner by the human teacher manually;
- in automatic systems, meta-knowledge is supplied to the computer learner by the human teacher in the form of a criterion of performance assessment.

Two questions then arise:

- what connects the knowledge with the meta-knowledge?
- how is meta-knowledge learnt in the first place?

4   Learning by Demonstration

To answer the above questions, we get a clue from the second type of learning we mentioned earlier, namely learning by demonstration. The demonstrator here is the teacher. The next is a story I heard from my grandmother. Remember that the traditional way of teaching children has always been through stories and parables. This story offers the clue we are searching for.

'Once upon a time there was a potter who got an apprentice who wanted to learn the art of pottery. The potter made his clay pots and put them in the oven. After two hours, he turned the fire off, and sat down to rest and smoke, as he was an old man. Then he took the pots out of the oven. They were perfect. The apprentice later decided to do his own pots. He made them out of clay and put them in the oven. After two hours, he took them out. The pots broke. He repeated the task and he had the same results. He went back to the potter: "You did not teach me well. Such and such happened." "Did you stop to smoke after you switched off the fire?" "No, I am not a smoker." "So, you got the pots out of the oven too soon."'

I am sure the story was related to me in order to teach me to pay attention to the detail. Indeed, if the apprentice had seen the potter performing the act dozens of times with slight variation each time, but always with the pause before the pots were taken out of the oven, he might have worked out that that pose was crucial to the process. On the other hand, the teacher might have been a better teacher if he had made that information explicit.

So, this story tells us that we learn fast, from very few examples, only when somebody explains to us ᵧₓₓ things are done the way they are done. A child asks lots of "why"s and that is how a child learns. This tells me that ᵧ ₓₓₓₓ

ᵧ ₓₓₓₓ   One may consider the following exchange between a teacher and a learner:

"What is this?"
"This is a window."
"Why?"
"Because it lets the light in and allows the people to look out."
"How?"
"By having an opening at eye level."
"Does it really?"

This sequence of learning is shown in Fig. 1. This figure proposes that knowledge in our brain is represented by a series of networks, forming a complex structure that I call the "tower of knowledge". The network of nouns is a network of object names, labels, e.g. "window", "chimney", "door", etc. The network of verbs or actions, is a network of functionalities, e.g. "to look out", "to enter", "to exit", etc. The network of appearances is a network of basic shapes necessary for a functionality to be fulfilled, e.g. "it is an opening of human size at floor level". So, the flow of knowledge goes like the fragment of conversation given above. The loop closes when we confirm that the object we are looking at has the right characteristics for its functional purpose to be fulfilled.

The task, therefore, for the artificial vision scientist, is to model these layers of networks and their inter-connections. We have various tools at our disposal: Markov Random Fields [8], grammars [19], inference rules [24], Bayesian networks [16], Fuzzy inference [27], etc. I would exclude from the beginning any deterministic crisp approaches, either because things are genuinely random in nature (or at least have a significant random component), or because our models and our knowledge is far too gross and imperfect for creating crisp rules and dogmatic decisions.

5 Markov Random Fields

Some recent work [17] showed evidence that the network of nouns (better described in psychophysical terms as network of "ideas") is topologically a random network, while the network of relations, made up from pairs of ideas, is topologically scale-free. For example, pairs like "fork-knife", "door-window" come up much more frequently in trains of thought than "door" alone, or "window" alone. This indicates that the connections in these networks are of varied strength, and actually are not always symmetric. For example, the idea "door" may trigger the idea "window" more frequently than the idea "window" triggers the idea "door". This asymmetry in the interactions is a manifestation that Markov Random Fields (MRFs) are not applicable here in their usual form in which they are applied in image processing. An example of the interactions in a neighbourhood of an MRF, defined on a grid, is shown in Fig. 2b. This MRF, and the weights it gives for neighbouring interactions, cannot be expressed by a Gibbs joint probability density function. For example, the cell at the centre is influenced by its top left neighbour with weight -1, but itself, being the bottom right neighbour of the cell at the top left, influences it with weight $+1$. This asymmetry leads to

instability when one tries to relax such a random field, because local patterns created are not globally consistent (and therefore not expressible by global Gibbs distributions) [18]. According to Li [9,10,11], relaxations of such MRFs do not converge, but . .,, . between several possible states. (Optimisations of Gibbs distributions either converge to the right interpretation, but more often than not, they . .,, . . . , i.e. they settle on wrong interpretations.)

So, one could model the network at each level of the tower of knowledge shown in Fig. 1, using a non-Gibbsian MRF [5]. The interdependences between layers might also be modelled by such networks, but perhaps it is more appropriate to use Bayesian models, as the inter-layer dependencies are causal or diagnostic, rather than peer-to-peer.

The question that arises then is: "where are we going to get the knowledge to construct these networks?" Where does the mother that teaches her child get it from? There is no "ground truth" or universal knowledge the mother transfers to her child: she sees something and talks about it to the child, then she remembers something else, according to her own network of related ideas that invoke each other and are prompted by her own sensory input, talks again to the child, and so on. So, all the mother (the teacher) does is to transfer to the child her own connections between ideas and concepts. If the mother tells the child "This is a pencil and that is a rubber. The pencil helps us write and the rubber helps us erase what we wrote.", the child will make the same connections as the mother had in her own brain. Pencil-rubber will have a strong mutual recall in the child's network of nouns, as well as write-erase in the child's network of verbs. So, one thing we can do is to model our own mental connections between ideas and functionalities. Then let the child (the computer) ask the right questions. For every answer, the strength of the corresponding connection is increased. We may turn these strengths into probabilities. Then a totally new scene may be shown to the computer. The child/computer must be able to use the connections it has learnt to interpret this new scene.

In practice, this is done by using manually annotated images. Heesch and Petrou [5] did exactly this to interpret outdoor scenes of buildings: they used hundreds of annotated images to learn the Markov dependencies of region configurations, defining the neighbourhood of a region to be the six regions that fulfil one of the following geometric constraints: it is above, below, to the left, to the right, it is contained by, or contains the region under consideration. An unknown scene was then labelled using a preliminary labelling performed on the basis of individual measurements made on each region, and relaxing the MRF defined on the segmented regions, using graph colourings and drawing labels for each region according to the local conditional probability of labels, conditioned on the current labels of the neighbours. No global consistency is guaranteed that way, but no global consistency exists, when the interdependencies between labels are asymmetric. We may intuitively understand this, as in an outdoor environment the long range interactions between objects are probably too weak to have a significant effect on the identity of a region. For example, if this region that belongs to this house here is a door, that region that is at the other end of the
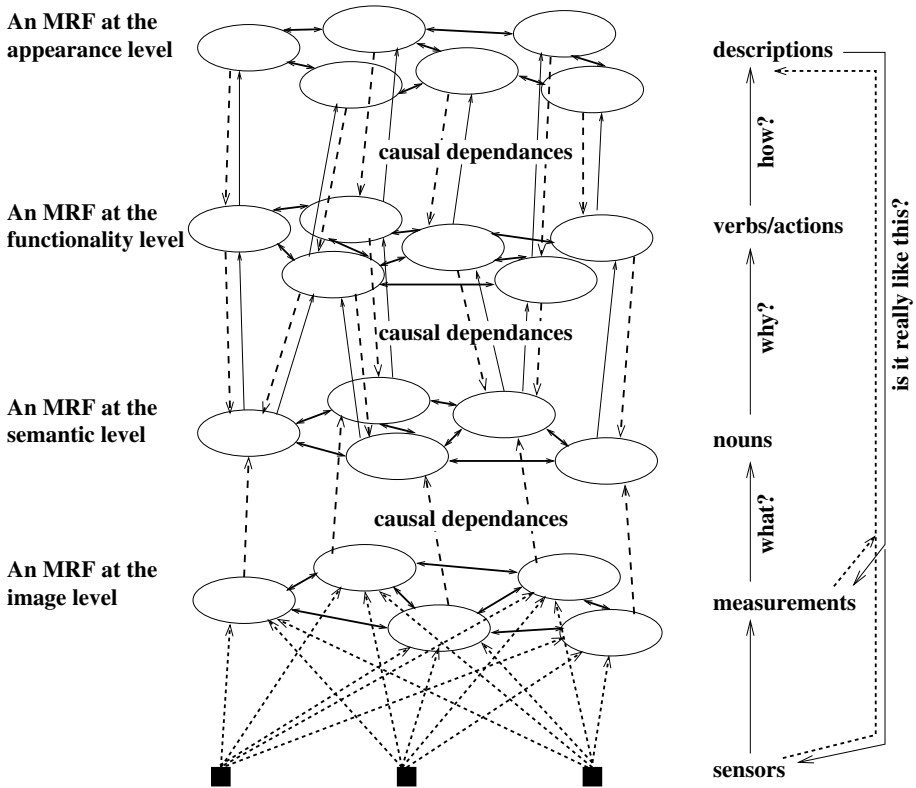
Fig. 1. The tower of knowledge: how knowledge may be organised. The double-headed arrows represent contextual interactions. The thin continuous arrows represent queries. The dashed arrows represent answers, i.e. transfer of information. The level of interest in a cognitive vision task is the level of nouns, where we wish to assign labels to objects. Examples of nodes with contextual connotations in the network of nouns are "door", "window", "balcony". Examples of nodes with contextual connotations in the network of functionality are "lets air in", "lets light in", "allows a person to enter". Examples of nodes with contextual connotations in the network of descriptions are "has a glass pane", "is at eye-level", "has a handle to open it".

field of view may be a car, a bush, a window, a house, or a tree. The differentiation of such options in terms of probabilities must be very small: the correlation function between labels, referring to objects beyond a certain distance apart, flattens out and provides no useful information. So, no global model is expected to be relevant or useful.

6 Bayesian Inference

Bayesian approaches have been used so far in two ways: either in the form of probabilistic relaxation (PR) [7] or in the form of Pearl-Bayes networks of

inference [16]. Probabilistic relaxation has its origins in the seminal work on constraint propagation by Waltz [25], who used crisp constraints and solved once and for all the problem of globally inconsistent labellings that led to impossible objects [6]. Probabilistic relaxation updates the probabilities of various labels of individual objects by taking into consideration contextual information [7]. As this contextual information is in effect peer-to-peer, probabilistic relaxation is **not** an appropriate tool for modelling causal relationships. It is rather an alternative tool to MRFs discussed in the previous section for modelling influences at the same layer. Probabilistic relaxation, just like MRF relaxation, is not guaranteed to converge to a unique global solution, unless special conditions are obeyed [21]. We discussed earlier that this is not an issue in reality: labellings of scenes do not have to be globally consistent, but only locally consistent. This statement seems to be in contradiction with a previous statement, saying that probabilistic relaxation is the generalisation of Waltz's algorithm which solved the problem of inconsistent labellings in the 60s. This contradiction, however, is only superficial. The problem of inconsistent labellings of the 60s was referring to the labellings of single solid objects, by labelling their sub-parts [4] and not the labellings of scenes that contain many different objects, where constraints between objects are far weaker than constraints within the subparts of the same solid object.

The second form of Bayesian approach is that of Pearl-Bayes networks of inference. Here the relations may be causal, and so these networks are appropriate for inter-layer inference. Bayesian approaches depend on conditional probabilities. How to choose these conditional probabilities has always been a problem for such methods. Conditional probabilities may have to be learnt painfully slowly from hundreds of examples. Stassopoulou et al. [20] solved the problem of learning the conditional probabilities, by mapping the class boundaries expressed by such a network, to a neural network, which was subsequently trained to learn these conditional probabilities. Alternatively, conditional probabilities may be transferred ready from another already trained network: the network of the teacher. This transference is equivalent to choosing them to have some parametric form (e.g. Gaussian) with parameters chosen "arbitrarily". The arbitrary choice of form and parameters usually leads to the criticism of the approach being ad-hoc or unjustified. It is not, if the teacher simply transfers their own hard gained knowledge to the pupil (the computer). Such an approach leads us to new theories, like for example the so called "utility theory" [12].

Utility theory is a decision theory. Assigning labels to objects depicted in an image is a decision. In the Bayesian framework we make this decision by maximising the likelihood of a label given all the information we have. In utility theory, this likelihood has to be ameliorated with a function called "utility function", that expresses subjective preferences or possible consequences of each label we may assign. The utility function multiplied with the Bayesian probability of each label and summed over all possibilities leads in one pass only to the final label. So, this approach avoids the iterations used by MRFs and PR. The utility function may be identified with the innate meta-knowledge somebody has acquired about the world. It is that knowledge, that might have been learnt algorithmically and

from many examples, but which now is expressed in the form of conditions and prejudices that cannot be fully justified by the measurements we make. It is the knowledge that tells us to be cautious when we want to buy a car from a man that postponed the appointment we made several times, that did not produce immediately the maintenance record of the car we requested, and so on. Such ideas have been around for some time, without people using the term "utility function". For example, psychologists in the mid-nineties were talking about the so called p-maps and m-maps. The p-maps were meant to be the prior knowledge we have about various possible patterns that we may encounter in life. A p-map guides us to sample a scene more or less carefully at places where it matters or it does not matter, respectively, producing the m-map that is specific to the present situation. One may identify here the p-maps as being the utility functions of today and the m-maps the Bayesian part of labels conditioned on the measurements we have made[1].

In the computer vision context, utility theory has been used by Marengoni [13] to select the features and operators that should be utilised to label aerial images. Further, one may interpret the work of Miller et al. [14] as using a utility function that penalises the unusual transformations that will have to be adopted to transform what is observed to what the computer thinks it is. The authors effectively choose labels by maximising the joint likelihood of the probability density function of the observed transforms and the probability density function of the labels and observations, assuming that transforms and labels/measurements are independent.

7   Modelling the "Why" and the "How" in Order to Answer the "What"

Let us consider the tower of knowledge presented in Fig. 1. We shall formulate here the problem of learning to recognise objects in a scene, using this hierarchical representation of knowledge and utility theory.

Let us assume that we use maximum likelihood to assign labels to a scene. In the conventional way of doing so, object o_i will be assigned label l_j with probability p_{ij}, given by:

$$p_{ij} = p(l_j|m_i)p(m_i) = p(m_i|l_j)p(l_j) \tag{1}$$

where m_i represents all the measurements we have made on object o_i, and $p(m_i)$ and $p(l_j)$ are the prior probabilities of measurements and labels, respectively. Probabilistic relaxation will update these probabilities according to the contextual information received from neighbouring regions. We do not follow that route here. Instead, we shall use the information coming from the other layers of knowledge to moderate this formula. Let us identify the units in the "verbs"

---

[1] The ideas of p-maps and m-maps first came to my knowledge by Robin Shirley of the Psychology Department of Surrey University, who passed away before he had the chance to make them more concrete and publish them.

level of Fig. 1 by f_k, and the units at the descriptor level of Fig. 1 by d_l. Then we may choose label l_j for object o_i as follows:

$$j_i = \arg \max_j \underbrace{\sum_k u_{jk} \sum_l v_{kl} c_{il} \, p_{ij}}_{\text{utility\_function}(i,j)} \qquad (2)$$

where u_{jk} indicates how important is for an object with label l_j to fulfil functionality f_k; v_{kl} indicates how important characteristic d_l is for an object to have the possibility to fulfil functionality f_k, and c_{ik} is the confidence we have that descriptor d_l applies to object o_i.

Note that the value of the utility function expresses the evidence we have that region o_i has the necessary characteristics to fulfil its role as object l_j. For example, if the label we consider of assigning to object o_i is "balcony", the utility function must express whether this object has dimensions big enough to allow a human to stand on it, whether it is attached on a wall, and whether there is a door leading to it. All these are conditions that will allow an object to play the role of a balcony. A learning scheme must be able to learn the values of u_{jk} and v_{kl} either directly from examples (slowly and painfully), or by trusting its teacher, who having learnt those values himself, slowly and painfully over many years of human life experiences, directly inserts them to the computer learner. The computer learner then must have a tool box of processors of sensory inputs that will allow it to work out the values of c_{il}.

−1	−1	−1
1		1
−1	−1	−1

−1	−1	1
−1		1
−1	1	1

(a)   **(b)**

Fig. 2. (a) A local neighbourhood at the pixel level with globally consistent Markov parameters: if this field is relaxed it will lead to horizontal strips of similar labels which will be distinct from the labels above and below. In image processing it will lead to a texture pattern with strong horizontal directionality. (b) A local neighbourhood at the pixel level with globally inconsistent Markov parameters: the top left pixel tells the central pixel to be different from it; the central pixel, seen as the bottom right neighbour of the top left pixel, tells it to be similar to it.

8   Conclusions

I have argued here that learning is characterised by the ability to generalise, and that this can only be achieved if what is learnt is not the labels of the objects viewed, but the rules according to which these labels are assigned. I have also argued that this meta-knowledge may be transferred to the learner (the computer)

directly by the teacher (the human developer), in the form of rules, or in the simplest way, by the human using the parameters of the algorithms according to their personal experience and intuition. This puts me at odds with the majority of the community of reviewers who tend to reject papers on the grounds that the parameters have been chosen ad hoc with no proper explanation: these are the cases of the teacher transplanting to the learner their painstakingly acquired knowledge. The alternative is for the learner each time to acquire this knowledge painfully slowly from thousands of examples.

I have also argued that we do not need globally consistent labellings of scenes. Global consistency will never allow us to label correctly the scene painted by Magritte of a train storming out of a fire place, because trains do not come out from fire places! It will never allow the computer to recognise green horses with 5 legs, but we, humans, do. So, what we need is fragments of reality and knowledge.

In computer vision, the idea of abandoning globally consistent solutions has now matured. This is not in isolation from other sciences. Strategy analysts talk about "fragments of learnt actions", and even mathematicians have long ago abandoned the idea of a globally self-consistent mathematical science: Bertrand Russell had to abandon the idea of globally consistent mathematics based on a small number of axioms, when Gödel's proof was published [15]. Natural systems are not globally consistent: they oscillate between states, and we, humans, manage to survive through this constantly dynamic, globally inconsistent and ambiguous world. A robotic system must be able to do the same and perhaps the only way to succeed in doing that is to be constructed so that it is content with a collection of fragments of understanding.

References

1. Cortes, C., Vapnik, V.N.: Support-Vector Networks. Machine Learning Journal 20, 273–297 (1995)
2. Christmas, W.J., Kittler, J., Petrou, M.: Structural matching in Computer Vision using Probabilistic Relaxation. IEEE Transactions on Pattern Analysis and Machine Intelligence 17, 749–764 (1995)
3. Devijver, P.A., Kittler, J.: On the edited nearest neighbour rule. In: Proc. 5th Int. Conf. on Pattern Recognition, pp. 72–80 (1980)
4. Guzman, A.: Computer Recognition of three-dimensional objects in a visual scene. Tech. Rep. MAC-TR-59, AI Laboratory, MIT (1968)
5. Heesch, D., Petrou, M.: Non-Gibbsian Markov Random Fields for object recognition. The British Machine Vision Conference (submitted, 2007)
6. Huffman, D.A.: Impossible Objects as Nonsense Sentences. Machine Intelligence 6, 295–323 (1971)
7. Hummel, R.A., Zucker, S.W.: One the foundations of relaxation labelling process. IEEE Transactions PAMI 5, 267–287 (1983)
8. Kindermann, R., Snell, J.L.: Markov Random Fields and their Applications. First book of the AMS soft-cover series in Contemporary Mathematics, American Mathematical Society (1980)

9. Li, Z.: A neural model of contour integration in the primary visual cortex. Neural Computation 10, 903–940 (1998)
10. Li, Z.: Visual segmentation by contextual influences via intra-cortical interactions in the primary visual cortex. Networks:Computation in Neural Systems 10, 187–212
11. Li, Z.: Computational design and nonlinear dynamics of a recurrent network model of the primary visual cortex. Neural Computation 13, 1749–1780 (2001)
12. Lindley, D.V.: Making Decisions. John Wiley, Chichester (1985)
13. Marengoni, M.: Bayesian Networks and Utility Theory for the management of uncertainty and control of algorithms in vision systems. PhD thesis, University of Massachusetts (2002)
14. Miller, E.G., Matsakis, N.E., Viola, P.A.: Learning from one example through shared densities on transforms. In: CVPR (2000)
15. Nagel, E., Newman, J.R.: Gödel's Proof. Routledge and Kegan Paul (1959) ISBN: 0710070780
16. Pearl, J.: Probabilistic reasoning in intelligent systems: Networks of plausible inference. Morgan Kaufmann Publishers Inc., San Francisco (1988)
17. Petrou, M., Tabacchi, M., Piroddi, R.: Networks of ideas and concepts. IEEE Transactions of Man Machine and Cybernetics (submitted, 2007)
18. Petrou, M., Garcia Sevilla, P.: Image Processing, Dealing with Texture. Wiley, Chichester (2006)
19. Schlesinger, B.D., Hlavac, V.: Ten lectures on Statistical and Structural Pattern Recognition, ch. 10. Kluwer Academic Publishers, Dordrecht, The Netherlands (2002)
20. Stassopoulou, A., Petrou, M.: Obtaining the correspondence between Bayesian and Neural Networks. International Journal of Pattern Recognition and Artificial Intelligence 12, 901–920 (1998)
21. Stoddart, A.J., Petrou, M., Kittler, J.: On the foundations of Probabilistic Relaxation with product support. Journal of Mathematical Imaging and Vision 9, 29–48 (1998)
22. Tenenbaum, J.B., Griffiths, T.L., Kemp, C.: Theory-based Bayesian models of inductive learning and reasoning. Trends in Cognitive Sciences 10, 309–318 (2006)
23. Tong, S., Koller, D.: Support Vector Machine active learning with applications to text classification. Journal of Machine Learning Research 2, 45–66 (2001)
24. Walker, T.C., Miller, R.K.: Expert Systems Handbook: An Assessment of Technology and Applications. Prentice-Hall, Englewood Cliffs (1990)
25. Waltz, D.: Understanding line drawings of scenes with shadows. In: Winstone, P. (ed.) The Psychology of Computer Vision, pp. 19–91. McGraw-Hill, New York (1975), http://www.rci.rutgers.edu/~cfs/305_html/Gestalt/Waltz2.html
26. Winston, P.H.: Learning structural descriptions from examples. The psychology of computer vision, 157–209 (1975)
27. Zadeh, L.H.: A fuzzy algorithmic approach to the definition of complex or imprecise concepts. Int. J. Man-Machine Studies 8, 249–291 (1976)
28. http://www.emtech.net/learning_theories.htm

Biometric Recognition: Overview and Recent Advances

Anil K. Jain

Department of Computer Science and Engineering
Michigan State University, East Lansing, MI 48824, USA
jain@cse.msu.edu
http://biometrics.cse.msu.edu

Abstract. The emerging requirements of reliable and highly accurate personal identification in a number of government and commercial applications (e.g., international border crossings, access to buildings, laptops and mobile phones) have served as an impetus for a tremendous growth in biometric recognition technology. Biometrics refers to the automatic recognition of an individual by using anatomical or behavioral traits associated with that person. By using biometrics, it is possible to recognize a person based on who you are, rather than by what you possess (e.g., an ID card) or what you remember (e.g., a password). Besides bolstering security, biometric systems also enhance user convenience by alleviating the need to design and remember multiple complex passwords. In spite of the fact that the first automatic biometric recognition system based on fingerprints, called AFIS, was installed by law enforcement agencies over 40 years back, biometric recognition continues to remain a very difficult pattern recognition problem. A biometric system has to contend with problems related to non-universality of biometric (failure to enroll rate), limited degrees of freedom (finite error rate), large intra-class variability, and spoof attacks (system security). This paper presents an overview of biometrics, its advantages and limitations, state-of-the-art error rates and current research in representation, fusion and security issues.

1 Introduction

A reliable identity management system is a critical component in several applications that render services to only legitimately enrolled users. Examples of such applications include sharing networked computer resources, granting access to nuclear facilities, performing remote financial transactions or boarding a commercial flight. The proliferation of web-based services (e.g., online banking) and the deployment of decentralized customer service centers (e.g., credit cards) have further enhanced the need for reliable identity management systems. The overarching task in an identity management system is the determination (or verification) of an individual's identity (or claimed identity). Traditional methods of establishing a person's identity include knowledge-based (e.g., passwords) and token-based (e.g., ID cards) mechanisms, but these surrogate representations of the identity can easily be lost, shared, manipulated or stolen thereby

undermining the intended security. Biometrics offers a natural and reliable solution to certain aspects of identity management by utilizing automated schemes to recognize individuals based on their inherent anatomical and/or behavioral characteristics [1]. By using biometrics it is possible to establish an identity based on *who you are*, rather than by *what you possess*, such as an ID card, or *what you remember*, such as a password.

Although biometrics emerged from its extensive use in law enforcement to identify criminals, i.e., forensics, it is being increasingly used today to carry out person recognition in a large number of civilian applications (e.g., national ID card, e-passport and smart cards) [1], [2] (see Figure 1). Most of the emerging applications can be attributed to increased security threats as well as fraud associated with various financial transactions (e.g., credit cards).

What physical measurements qualify to be useful in a biometric system? Any human anatomical or behavioral characteristic can be used as a biometric characteristic as long as it satisfies the following requirements:

- Universality: each person should have the characteristic;
- Distinctiveness: any two persons should be sufficiently different in terms of the characteristic;
- Permanence: the characteristic should be sufficiently invariant (with respect to the matching criterion) over a period of time;
- Collectability: the characteristic can be measured quantitatively.

However, in a practical biometric system (i.e., a system that employs biometrics for person recognition), there are a number of other issues that should be considered, including:

- Performance, which refers to the achievable recognition accuracy and speed, the resources required to achieve the desired performance, as well as the operational and environmental factors that affect the performance;
- Acceptability, which indicates the extent to which people are willing to accept the use of a particular biometric identifier (characteristic) in their daily lives;
- Circumvention, which reflects how easily the system can be fooled using fraudulent methods.

A practical biometric system should meet the specified recognition accuracy, speed, and resource requirements, be harmless to the users, be accepted by the intended population, be easy to use and be sufficiently robust to various fraudulent methods and attacks on the system. Among the various biometric measurements in use, systems based on fingerprints [3], face [4] and iris [5] have received the most attention in recent years. A biometric system is essentially a pattern recognition system that operates by acquiring biometric data from an individual, extracting a feature set from the acquired data, and comparing this feature set against the enrolled template set in the system database. Depending on the application context, a biometric system may operate either in a verification mode or an identification mode [6] (see Figure 2). A biometric system is designed using the following four main modules: (i) sensor module, (ii) feature extraction module, (iii) matcher module, and (iv) system database module.

(a)   (b)

(c)   (d)
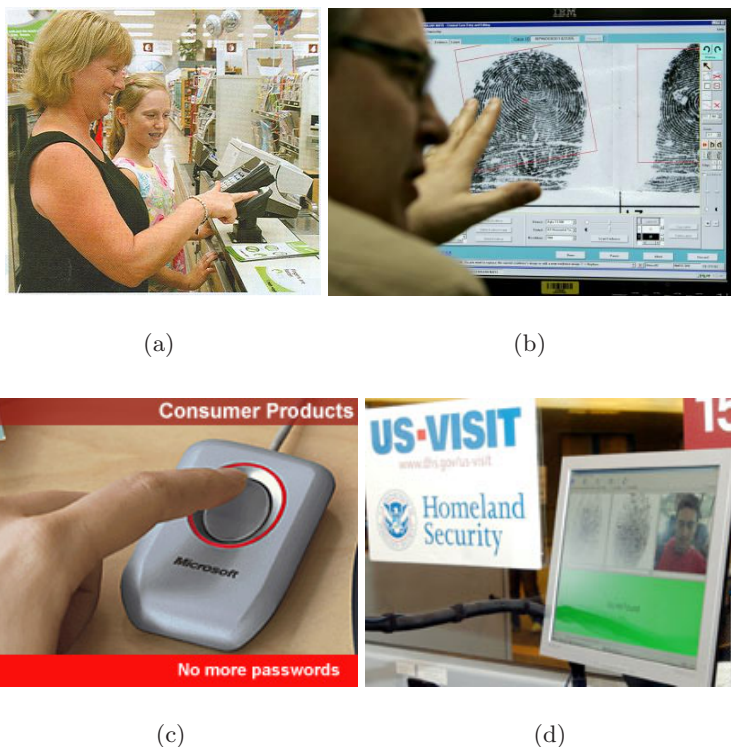
Fig. 1. Biometric systems are being deployed in various applications. (a) A Pay-by-Touch system (www.paybytouch.com) at a grocery store where customers pay by finger-prints; (b) An Interpol fingerprint expert identifies a tsunami victim using the victim's fingerprint at a laboratory in Phuket, Thailand; (c) A fingerprint verification system used for computer and network log-on and (d) The US-VISIT program currently em-ploys two-print information to validate the travel documents of visitors to the United States (www.dhs.gov).

2   Issues and Research Directions in Biometrics

Two samples of the same biometric characteristic from the same person (e.g., two impressions of a user's right index finger) are not exactly the same due to imperfect imaging conditions (e.g., sensor noise), changes in the user's physical or behavioral characteristics (e.g., cuts and bruises on the finger), ambient con-ditions (e.g., temperature and humidity) and user's interaction with the sensor (e.g., finger placement). In other words, biometric signals have a large *intra-class variability*. Therefore, the response of a biometric matching system is a match score that quantifies the similarity between the input and the database template representation. A higher score indicates that the system is more certain that the two biometric measurements come from the same person. The system deci-sion is regulated by the threshold: pairs of biometric samples generating scores
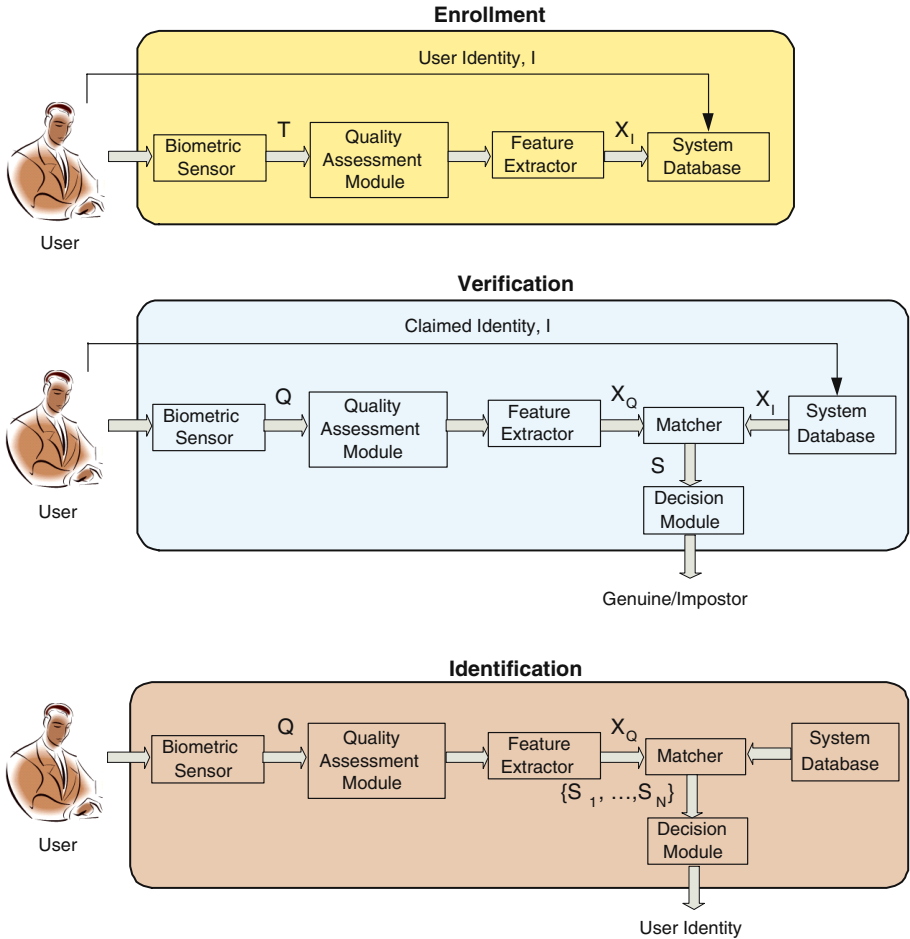
Fig. 2. Block diagrams of enrollment, verification, and identification tasks. Enrollment creates an association between an identity and its biometric characteristics. In a verification task, an enrolled user claims an identity and the system verifies the authenticity of the claim based on her biometric feature. An identification system identifies an enrolled user based on her biometric characteristics without the user having to claim an identity. Here, T represents the biometric sample obtained during enrollment, Q is the query biometric sample obtained during recognition, X_I and X_Q are the template and query feature sets, respectively, S represents the match score and N is the number of users enrolled in the database.

higher than or equal to the threshold are inferred as mate pairs (i.e., belonging to the same person); pairs of biometric samples generating scores lower than the threshold are inferred as non-mate pairs (i.e., belonging to different persons). A biometric verification system makes two types of errors: (i) mistaking biometric measurements from two different persons to be from the same person (called *false match*), and (ii) mistaking two biometric measurements from the same person

to be from two different persons (called *false non-match*). These two types of errors are often termed as *false accept* and *false reject*, respectively.

Deployment of biometric systems in various civilian applications does not imply that biometric recognition is a fully solved problem. Table 1 presents the state-of-the-art error rates of four popular biometric traits. It is clear that there is a plenty of scope for improvement in the performance of biometric systems. We not only need to address issues related to reducing the error rates, but we also need to look at ways to enhance the usability of biometric systems and address the *return on investment* issue.

Table 1. False reject and false accept rates associated with state-of-the-art fingerprint, face, voice and iris verification systems. Note that the accuracy estimates of biometric systems are dependent on a number of test conditions (e.g., population characteristics and specific sensors used).

Biometric Trait	Test	Test Conditions	False Reject Rate	False Accept Rate
Fingerprint	FVC 2006 [7]	Heterogeneous population including manual workers and elderly people	2.2%	2.2%
	FpVTE 2003 [8]	U.S. government operational data	0.1%	1%
Face	FRVT 2006 [9]	Controlled illumination, high resolution	0.8%-1.6%	0.1%
Voice	NIST 2004 [10]	Text independent, multi-lingual	5-10%	2-5%
Iris	ICE 2006 [9]	Controlled illumination, broad quality range	1.1%-1.4%	0.1%

Biometric systems that operate using any single biometric characteristic have the following limitations: (i) noise in sensed data, (ii) intra-class variations, (iii) lack of distinctiveness [11], (iv) non-universality, and (v) spoof attacks. Some of the limitations imposed by unibiometric systems can be overcome by using multiple biometric modalities (such as face and fingerprint of a person or multiple fingers of a person). Such systems, known as multibiometric systems, are expected to be more reliable due to the presence of multiple, independent pieces of evidence [12]. These systems are also able to meet the stringent performance requirements imposed by various applications [13]. Multibiometric systems address the problem of non-universality, since multiple traits ensure sufficient population coverage. Further, multibiometric systems provide anti-spoofing measures by making it difficult for an intruder to simultaneously spoof the multiple biometric traits of a legitimate user. By asking the user to present a random subset of biometric traits (e.g., right index finger followed by right middle finger), the system ensures that a "live" user is indeed present at the point of data acquisition. Thus, a challenge-response type of authentication can be facilitated by

using multibiometric systems. Of course, multibiometric systems involve additional cost and increase the enrollment and verification times.

With the widespread deployment of biometric systems in various applications, there are increasing concerns about the security and privacy of biometric technology [14]. Public confidence and acceptance of the biometrics technology will depend on the ability of system designers to demonstrate that these systems are robust, have low error rates and are tamper proof. To avert any potential security crisis, vulnerabilities of a biometric system must be identified and addressed systematically. A number of studies have analyzed potential security breaches in a biometric system and proposed methods to counter those breaches e.g. [15], [16]. In particular, biometric template security is an important issue because unlike passwords and tokens, compromised biometric templates cannot be revoked and reissued. Due to intra-user variability in the acquired biometric traits, ensuring the security of the template without deteriorating the recognition performance is a challenging task. Although a number of biometric template protection schemes have been proposed [17,18,19,20,21], a comprehensive template protection mechanism with provable security guarantees and high recognition performance has thus far remained elusive and the development of such a mechanism is crucial when biometric systems proliferate into the core physical and information infrastructure in the near future.

3   Summary

Reliable personal recognition is critical to many government and business processes. The conventional knowledge-based and token-based methods do not really provide positive person recognition because they rely on surrogate representations of the person's identity (e.g., exclusive knowledge or possession). It is, thus, imperative that any system assuring reliable person recognition would involve a biometric component. This is not, however, to state that biometrics alone can deliver error-free person recognition. In fact, a sound system design will often entail incorporation of many biometric and non-biometric components (building blocks) to provide reliable person recognition. As biometric technology matures, there will be an increasing interaction among the market, technology, and the applications. This interaction will be influenced by the added value of the technology, user acceptance, and the credibility of the service provider. It is too early to predict where and how biometric technology would evolve and get embedded in which applications. But it is certain that biometric-based recognition will have a profound influence on the way we conduct our daily business.

References

1. Jain, A.K., Ross, A., Prabhakar, S.: An Introduction to Biometric Recognition. IEEE Transactions on Circuits and Systems for Video Technology, Special Issue on Image- and Video-Based Biometrics 14, 4–20 (2004)
2. Wayman, J.L., Jain, A.K., Maltoni, D., Maio, D. (eds.): Biometric Systems, Technology, Design and Performance Evaluation. Springer, Heidelberg (2005)

3. Maltoni, D., Maio, D., Jain, A.K., Prabhakar, S.: Handbook of Fingerprint Recognition. Springer, Heidelberg (2003)
4. Li, S., Jain, A.K. (eds.): Handbook of Face Recognition. Springer, Heidelberg (2005)
5. Daugman, J.: Recognizing Persons by their Iris Patterns. In: Jain, A.K., Bolle, R., Pankanti, S. (eds.) Biometrics: Personal Identification in Networked Society, pp. 103–122. Kluwer Academic Publishers, London, UK (1999)
6. Jain, A.K., Bolle, R., Pankanti, S. (eds.): Biometrics: Personal Identification in Networked Security. Kluwer Academic Publishers, Dordrecht (1999)
7. Biometric System Laboratory - University of Bologna: FVC 2006: The Fourth International Fingerprint Verification Competition Available at http://bias.csr.unibo.it/fvc2006/default.asp
8. Wilson, C., Hicklin, A.R., Bone, M., Korves, H., Grother, P., Ulery, B., Micheals, R., Zoepfl, M., Otto, S., Watson, C.: Fingerprint Vendor Technology Evaluation 2003: Summary of Results and Analysis Report. Technical Report NISTIR 7123, NIST (2004)
9. Phillips, P.J., Scruggs, W.T., OToole, A.J., Flynn, P.J., Bowyer, K.W., Schott, C.L., Sharpe, M.: FRVT 2006 and ICE 2006 Large-Scale Results. Technical Report NISTIR 7408, NIST (2007)
10. Przybocki, M., Martin, A.: NIST Speaker Recognition Evaluation Chronicles. In: Odyssey: The Speaker and Language Recognition Workshop, Toledo, Spain, pp. 12–22 (2004)
11. Pankanti, S., Prabhakar, S., Jain, A.K.: On the Individuality of Fingerprints. IEEE Transactions on Pattern Analysis and Machine Intelligence 24, 1010–1025 (2002)
12. Ross, A., Nandakumar, D., Jain, A.K.: Handbook of Multibiometrics. Springer, Heidelberg (2006)
13. Hong, L., Jain, A.K.: Integrating Faces and Fingerprints for Personal Identification. IEEE Transactions on Pattern Analysis and Machine Intelligence 20, 1295–1307 (1998)
14. Prabhakar, S., Pankanti, S., Jain, A.K.: Biometric Recognition: Security and Privacy Concerns. IEEE Security and Privacy Magazine 1(2), 33–42 (2003)
15. Jain, A.K., Ross, A., Pankanti, S.: Biometrics: A Tool for Information Security. IEEE Transactions on Information Forensics and Security 1(2), 125–143 (2006)
16. Buhan, I., Hartel, P.: The State of the Art in Abuse of Biometrics. Technical Report TR-CTIT-05-41, Centre for Telematics and Information Technology, University of Twente (2005)
17. Teoh, A.B.J., Goh, A., Ngo, D.C.L.: Random Multispace Quantization as an Analytic Mechanism for BioHashing of Biometric and Random Identity Inputs. IEEE Transactions on Pattern Analysis and Machine Intelligence 28(12), 1892–1901 (2006)
18. Ratha, N.K., Chikkerur, S., Connell, J.H., Bolle, R.M.: Generating Cancelable Fingerprint Templates. IEEE Transactions on Pattern Analysis and Machine Intelligence 29(4), 561–572 (2007)
19. Juels, A., Sudan, M.: A Fuzzy Vault Scheme. In: Proceedings of IEEE International Symposium on Information Theory, Lausanne, Switzerland, p. 408 (2002)
20. Nandakumar, K., Nagar, A., Jain, A.K.: Hardening Fingerprint Fuzzy Vault Using Password. In: Proceedings of Second International Conference on Biometrics, Seoul, South Korea, pp. 927–937 (2007)
21. Dodis, Y., Ostrovsky, R., Reyzin, L., Smith, A.: Fuzzy Extractors: How to Generate Strong Keys from Biometrics and Other Noisy Data. Technical Report 235, Cryptology ePrint Archive (2006)

A Family of Novel Graph Kernels for Structural Pattern Recognition

Horst Bunke and Kaspar Riesen

Institute of Computer Science and Applied Mathematics, University of Bern,
Neubrückstrasse 10, CH-3012 Bern, Switzerland
{bunke,riesen}@iam.unibe.ch

Abstract. Recently, an emerging trend of representing objects by
graphs can be observed. As a matter of fact, graphs offer a versatile al-
ternative to feature vectors in pattern recognition, machine learning and
data mining. However, the space of graphs contains almost no mathe-
matical structure, and consequently, there is a lack of suitable methods
for graph classification. Graph kernels, a novel class of algorithms for
pattern analysis, offer an elegant solution to this problem. Graph ker-
nels aim at bridging the gap between statistical and symbolic object
representations. In the present paper we propose a general approach to
transforming graphs into n-dimensional real vector spaces by means of
graph edit distance. As a matter of fact, this approach results in a novel
family of graph kernels making a wide range of kernel machines applica-
ble for graphs. With several experimental results we prove the robustness
and flexibility of our new method and show that our approach outper-
forms a standard graph classification method on several graph data sets
of diverse nature.

1 Introduction

The field of pattern recognition can be divided into two sub-fields, namely the
statistical and the structural approach. In statistical pattern recognition, pat-
terns are represented by feature vectors $(x_1, \ldots, x_n) \in \mathbb{R}^n$. The recognition pro-
cess is based on the assumption that patterns of the same class are located in a
compact region of $\mathbb{R}^n$. In recent years a huge amount of methods for the clas-
sification of patterns represented by feature vectors have been proposed, such
as Bayes classifier, neural network, support vector machine, and many more.
Object representations given in terms of feature vectors have a number of useful
properties [1]. For example, object similarity, or distance, can easily be com-
puted by means of Euclidean distance. Computing the sum or weighted sum of
two objects represented by vectors is straightforward, too. Yet graph-based rep-
resentations, which are used in the field of structural pattern recognition, have a
number of advantages over feature vectors. Graphs are much more powerful and
flexible than vectors, as feature vectors provide no direct possibility to describe
structural relations in the patterns under consideration. Furthermore, while the
size of a graph can be adjusted to the size and complexity of the underlying pat-
tern, vectors are constrained to a predefined length, which has to be preserved

for all patterns encountered in a particular application. On the other hand, a major drawback of graph representations is their lack of suitable methods for classification. This is mainly due to the fact that some of the basic operations needed in classification are not available for graphs.

It turns out that the lack of operations needed for the implementation of classification algorithms in the graph domain can be overcome by means of kernel methods [2,3]. Although some mathematical foundations of kernel methods have been developed long ago [4], the practical usefulness of kernel methods for the fields of pattern recognition, machine learning and data mining has been recognised only recently [5]. During the past ten years kernel methods have become one of the most rapidly emerging sub-fields in intelligent information processing. The vast majority of work in kernel methods is concerned with transforming a given feature space into a higher-dimensional space without computing the transformation explicitly for each individual feature vector. However, more recently the existence of kernels for symbolic data structures, especially for graphs, has been shown [6]. By means of suitable kernel functions, graphs can be mapped into vector spaces in an explicit or implicit fashion. Hence, rather than computing the Euclidean distance, a weighted sum, the average of a set of graphs, and similar quantities in the domain of graphs – which is actually not possible in general –, the corresponding operations are carried out in the target space of the kernel function, i.e. in a vector space. Consequently, a large class of classification algorithms, originally developed for feature vectors, become applicable to graphs. Hence, by means of kernel functions one can benefit from both the high representational power of graphs and the large repository of algorithmic tools available for feature vector representations of objects.

In the rest of this paper, we give a general introduction to graph kernels in Section 2. Then, in Section 3, a new family of graph kernels developed recently is introduced [7,8,9]. In Section 4, an experimental evaluation of these kernels is described. Finally, conclusions are drawn in Section 5.

2   Graph Kernels

For a general introduction to kernel methods we refer to [2,3]. While the bulk of work on kernel methods has been concerned with mapping vectors from a low- to a high-dimensional space, recently also kernels on symbolic data structures have been proposed. In this section we give a brief survey on graph kernels. For an earlier survey see [6].

A well-known class of graph kernels is based on the analysis of random walks in graphs. These kernels measure the similarity of two graphs by the number of random walks in both graphs that have all or some labels in common [10,11]. In [10] an important result is reported. It is shown that the number of matching walks in two graphs can be computed by means of the product graph of two graphs, without the need to explicitly enumerate the walks. In order to handle continuous labels the random walk kernel has been extended in [11]. This extension allows one to also take non-identically labelled walks into account. The

problem of tottering, is addressed in [12]. Tottering is the phenomenon that, in a walk, a node may be revisited immediately after it has been left. In order to prevent tottering, the random walk transition probability model is appropriately modified in [12].

Another class of graph kernels is given by diffusion kernels (e.g. in [13]). The kernels of this class are defined with respect to a base similarity measure which is used to construct a valid kernel matrix. This base similarity measure only needs to satisfy the condition of symmetry and can be defined for any kind of objects.

An important contribution to graph kernels is the work on convolution kernels, which provides a general framework for dealing with complex objects that consist of simpler parts [14]. Convolution kernels infer the similarity of complex objects from the similarity of their parts. The ANOVA kernel [15], for instance, is a particular convolution kernel, which uses a subset of the components of a composite object for comparison.

A number of additional kernels are discussed in [16,17,18]. In [16] support vector machines are applied to attributed graphs where the kernel matrices are based on approximations of the Schur-Hadamard inner product. The idea underlying the kernels in [17,18] is to find identical substructures in two graphs, such as common subgraphs, subtrees, and cycles.

In a recent PhD thesis [19] graph kernels derived from graph edit distance are introduced. These kernels can cope with any type of graph and are applicable to a wide spectrum of different applications.

3   Novel Graph Kernels Using Vector Space Embedding Based on Edit Distance

The present paper introduces a new class of graph kernels which are based on vector space embeddings of graphs by means of prototype selection and graph edit distance computation. In contrast to some other kernel methods, the approach proposed in this paper results in an explicit embedding of the considered graphs in a vector space. Hence, not only scalar products, but individual graph maps are available in the target space. We observe that this approach is more powerful than some other graph kernels for a number of reasons. First, as the map of each graph in the target vector space is explicitly computed, not only kernel machines, but also other non-kernelizable algorithms can be applied to the resulting vector representation. Secondly, there are almost no restrictions on the type of graphs the proposed method can deal with. It can be applied to directed or undirected graphs, and to graphs without or with labels on their nodes and/or edges. In case there are labels on the nodes and/or edges, these labels can be of any nature, for example, they can be elements from a finite or infinite set of discrete symbols, the set of integer numbers, real numbers, or real vectors. Thirdly, the method is versatile, i.e. it is possible to integrate domain specific knowledge about object similarity when defining the costs of the elementary edit operations. Hence the kernel can be made more discriminative by tuning graph similarity to the specific application area.

3.1   Graph Edit Distance

Similarly to [19], the new graph kernels proposed in this paper make use of the edit distance of graphs. Therefore, we give a brief introduction to this graph distance measure in this section.

Graph edit distance is one of the most flexible graph distance measures that is available [20,21]. The key idea of graph edit distance is to define the dissimilarity, or distance, of graphs by the amount of distortion that is needed to transform one graph into another. These distortions are given by insertions, deletions, and substitutions of nodes and edges. Given two graphs – the source graph g_1 and the target graph g_2 – the idea is to delete some nodes and edges from g_1, relabel some of the remaining nodes and edges (substitutions) and possibly insert some nodes and edges, such that g_1 is finally transformed into g_2. A sequence of edit operations that transform g_1 into g_2 is called an *edit path* between g_1 and g_2. One can introduce cost functions for each edit operation measuring the strength of the given distortion. The idea of such cost functions is that one can define whether an edit operation represents a strong modification of the graph or not. Hence, between two structurally similar graphs, there exists an inexpensive edit path, representing low cost operations, while for structurally different graphs an edit path with high costs is needed. Consequently, the *edit distance* of two graphs is defined by the minimum cost edit path between two graphs. The edit distance can be computed by a tree search algorithm [20], or by a faster, suboptimal method [22,23].

3.2   Basic Embedding Approach

The novel graph kernels described in this paper are based on the idea of embedding a population of graphs in an m-dimensional real vector space. Such an embedding is motivated by the lack of suitable classification algorithms in the graph domain. Another approach to graph embedding has been proposed in [24]. This method is based on algebraic graph theory and utilizes spectral matrix decomposition. Applying an error-tolerant string matching algorithm to the eigensystem of graphs to infer distances of graphs is proposed in [25]. These distances are then used to embed the graphs into a vector space by multidimensional scaling. In [26] features derived from the eigendecompostion of graphs are studied. In fact, such feature extraction defines an embedding of graphs into vector spaces, too. In our approach we will explicitly make use of graph edit distance. Hence, we can easily deal with various kinds of graphs (labelled, unlabelled, directed, undirected, etc.) and utilize domains specific knowledge in defining the dissimilarity of nodes and edges through edit costs. Thus a high degree of robustness against various graph distortions can be achieved. The idea underlying our method was originally developed for the problem of embedding sets of feature vectors in a dissimilarity space [27]. In this paper we introduce a new version of this method for the domain of graphs.

Assume we have a labelled set of training graphs, $T = \{g_1, \ldots, g_n\}$. Let $d(g_i, g_j)$ be the edit distance between graph g_i and g_j. After having selected

a set $P = \{p_1, \ldots, p_m\}$ of $m \leq n$ prototypes from T, we compute the edit distance of a graph $g \in T$ to each prototype $p \in P$. This leads to m dissimilarities, $d_1 = d(g, p_1), \ldots, d_m = d(g, p_m)$, which can be interpreted as an m-dimensional vector $(d_1, \ldots, d_m)$. In this way we can transform any graph from the training set, as well as any other graph from a validation or testing set, into a vector of real numbers. Formally, if $T = \{g_1, \ldots, g_n\}$ is a training set of graphs and $P = \{p_1, \ldots, p_m\} \subseteq T$ is a set of prototypes, the mapping $t_m^P : T \to \mathbb{R}^m$ is defined as a function $t_m^P(g) \mapsto (d(g, p_1), \ldots, d(g, p_m))$ where $d(g, p_i)$ is the graph edit distance between the graph g and the i-th prototype.

3.3   Prototype Selection

The method described in Section 3.2 crucially depends on the prototypes. Therefore, an important problem to be solved is an appropriate choice of the prototype set $P = \{p_1, \ldots, p_m\}$. A good selection of m prototypes seems to be crucial to succeed with the classification algorithm in the feature vector space. The prototypes should avoid redundancies in terms of selection of similar graphs, and prototypes should include as much information as possible. In this section we discuss five different algorithms for the task of prototype selection[1]. Note that all of the proposed prototype selection methods can be applied class-wise and class-independent, i.e. the selection can be executed over the whole training set, or the selection can be performed individually for each of the classes.

CENTERS. The CENTERS prototype selector selects prototypes situated in the center of the graph set T. This is achieved by iteratively taking the set median graph out of the set T. The set median graph is the graph whose sum of distances to all other graphs in this set is minimal.

RANDOM. A random selection of m prototypes from T is performed.

SPANNING. A set of prototypes, P, is selected by the SPANNING prototype selector by means of the following iterative procedure. The first prototype selected is the set median graph. Each additional prototype selected by the spanning prototype selector is the graph the furthest away from the already selected prototype graphs.

k-CENTERS. The k-CENTERS prototype selector tries to adapt to the graph distrubution of set T and selects graphs that are in the center of densely populated areas. First a k-means clustering procedure is applied to set T. The number of clusters to be found is equal to the number of prototypes to be selected. Once the clusters have been established, the median of each cluster is selected as a prototype.

TARGETSPHERE. The TARGETSPHERE prototype selector first selects a graph g_c situated in the center of T. After finding the center graph, the graph $g_f \in T$ whose distance to g_c is maximum is located. Both graphs g_c and g_f are selected as prototypes. The distance $d_{max} = d(g_c, g_f)$ is then divided in $m - 1$ partitions with $interval = \frac{d}{m-1}$. The $m - 2$ graphs that are located the nearest to the interval borders are selected as prototypes.

---

[1] For a detailed review of the applied prototype selection method we refer to [28].

Of course, one can imagine other techniques and strategies for prototype selection, for example, mixing some of the strategies described above with each other. The intention of all methods remains the same – finding a good selection of m prototypes that lead to a good performance of the resulting classifier in the vector space.

3.4   Dimensionality Reduction

In Section 3.3 a number of prototype selectors have been introduced. Typically, these prototype selectors are tested on a validation set and the one that leads to the best classification performance is finally chosen. A similar procedure can be applied in order to find the optimal number of prototypes. That is, the number of prototypes is varied over a certain range and the number that results in the highest classification rate is adopted for the final system.

In the current section we describe an alternative approach where we use all available elements from the training set as prototypes, i.e. $P = T$ and subsequently apply dimensionality reduction methods. This process is more principled and allows us to completely avoid the problem of finding the optimal prototype selection strategy. For dimensionality reduction, we make use of the well known Principal Component Analysis (PCA) and Fisher's Linear Discriminant Analysis (LDA) [1,29].

The Principal Component Analysis (PCA) [1,29] is a linear transformation. It seeks the projection which best represents the data. PCA is an unsupervised method which does not take any class label information into consideration. We first normalize the data by shifting the mean to the origin of the coordinate system and making the variance of each feature equal to one. Then we calculate the covariance matrix of the normalized data and determine the eigenvectors $\mathbf{e}_i$ and the eigenvalues λ_i of the covariance matrix. The eigenvectors are ordered according to decreasing magnitude of the corresponding eigenvalues, i.e. $\lambda_1 \geq \lambda_2 \geq \ldots \geq \lambda_n \geq 0$. The data is then represented in a new coordinate system defined by the eigenvectors. For reducing the dimensionality of the transformed data we retain only the $m < n$ eigenvectors with the m highest eigenvalues.

Fisher's Linear Discriminant Analysis (LDA) [1,29] is a linear transformation as well. In contrast with PCA, LDA takes class label information into account. In its original form, LDA can be applied to two-class problems only. However, we make use of a generalization, called Multiple Discriminant Analysis (MDA), which can cope with more than two classes. In MDA, we are seeking the projection of the data which best separates the classes from each other. For all further details, we refer to [1,29]. Note that under this transformation the maximal dimensionality of the transformed feature space is $c - 1$, where c is the number of classes.

3.5   Multiple Classifier System

Recently, the field of multiple classifier systems has become a very active area of research. The fundamental observation that motivates the combination of

classifiers is that the sets of patterns misclassified by different classifiers do not necessarily heavily overlap. Hence, errors of a single classifier can be compensated by the other classifiers of an ensemble [30]. In the case of statistical patterns, that is, patterns represented by feature vectors, a large number of methods for the creation and combination of classifiers have been developed over the past years [31,32,33].

Regarding the family of graph kernels proposed in this paper, if we repeat the process of random prototype selection a number of times, we can derive different graph subsets that can be used to map a given population of graphs to various vector spaces. As a result, one can create a statistical classifier ensemble for structural input data.

In Algorithm 1 the random prototype selection strategy is described. This procedure selects n times a subset of size m out of the training set. Once a graph has been selected it becomes temporarily unavailable until all training patterns have been selected. This is achieved by a tabu list, which contains all patterns that are already selected (line 11). The randomized prototype selection is performed on the subset $T \setminus TABU$ only (line 9). Whenever the tabu list contains all patterns of T, a reset is done such that all training elements become available again (line 6 and 7).

Algorithm 1. Generating n prototype sets out of one graph set.

Input: Training graphs $T = \{g_1, \ldots, g_t\}$, number of required prototype sets n,
           and dimensionality of the resulting feature vectors m
Output: Set $PROTO$ consisting of n different prototype sets of size m each

```
 1: initialize TABU to the empty list {}
 2: initialize PROTO to the empty list {}
 3: for i = {1, ..., n} do
 4:     P_i = {}
 5:     for j = {1, ..., m} do
 6:         if |TABU| == t then
 7:             reset TABU to the empty set {}
 8:         else
 9:             select p randomly out of T \ TABU
10:             P_i = P_i ∪ {p}
11:             TABU = TABU ∪ {p}
12:         end if
13:     end for
14:     PROTO = PROTO ∪ {P_i}
15: end for
16: return  PROTO
```

To generate a classifier ensemble, we apply a methodology which is known as *overproduce-and-select* [30]. The idea is to produce a pool of classifiers, followed by a selection procedure that picks the classifiers that are most diverse and accurate. We make use of the accuracy of the resulting ensembles to control the selection of a subset out of the classifier pool. To create a good performing ensemble a sequential floating search selection [34] is applied. For the combination of the individual ensemble member outputs, plurality voting, Borda count and linear score combination have been applied, depending on the type of output delivered by the individual classifier.

4   Experimental Results

In this section we provide the results of an experimental evaluation of the proposed embedding kernels. We aim at empirically confirming that the method of graph embedding and subsequent classification in real vector spaces is applicable to different graph classification problems and matches, or even surpasses, the performance of a k-nearest neighbor classifier (k-NN) in the original graph domain. Note that k-NN classifiers are the only classifiers that can be directly applied in the original graph domain. The classifier used in the vector space is the SVM [5]. Of course, any other classifier could be used for this purpose as well. However, we feel that the SVM is particularly suitable because of its theoretical advantages and its superior performance that has been empirically confirmed in many practical classification problems.

For further results achieved with the novel family of graph kernels, especially for comparisons with other reference systems, we refer to [7,8,9,28].

4.1   Experimental Setup

In each of our experiments we make use of three disjoint graph sets, viz. *validation set*, *test set* and *training set*. The validation set is used to determine optimal parameter values for graph embedding, ensemble generation, and classification. The embedding parameters consist of the number of prototypes, i.e. the dimensionality of the resulting vector space, and the best performing embedding method[2]. The parameters for ensemble generation consist of the optimal dimensionality of the random prototype sets and the optimal members of the classifier ensemble. Finally, the parameters for classification consist of parameter k for the nearest neighbor classifier and the different parameters for the SVM. The RBF-kernel SVM used in this paper has parameters C and γ, where C corresponds to the weighting factor for misclassification penalty and γ is used in our kernel function $K(\mathbf{u}, \mathbf{v}) = exp(-\gamma \cdot ||\mathbf{u} - \mathbf{v}||^2)$. The parameter values, the embedding method, the classifier ensemble, and the dimensionality that result in the lowest classification error on the validation set are then applied to the independent test set.

4.2   Databases

For our experimental evaluation, four data sets with quite different characteristics are used. The datasets vary with respect to graph size, edge density, type of labels for the nodes and edges, and meaning of the underlying objects.

The first database used in the experiments consists of graphs representing distorted letter drawings. In this experiment we consider the 15 capital letters of the Roman alphabet that consist of straight lines only (*A, E, F, ...*). For each class, a prototype line drawing is manually constructed. To obtain aribtrarily large sample sets of drawings with arbitrarily strong distortions, distortion operators are applied to the prototype line drawings. This results in randomly translated, removed,

---

[2] Note that with dimensionality reduction algorithms (PCA and LDA) only the dimensionality has to be validated.

and added lines. These drawings are then converted into graphs by representing lines by edges and ending points of lines by nodes. Each node is labelled with a two-dimensional attribute giving its position. The graph database used in our experiments is composed of a training set, a validation set, and a test set, each of size 750.

For a more thorough evaluation of the proposed methods we additonally use three real world data sets. First we apply the proposed method to the problem of image classification. Images are converted into graphs by segmenting them into regions, eliminating regions that are irrelevant for classification, and representing the remaining regions by nodes and the adjacency of regions by edges [35]. The image database consists of five classes (*city, countryside, people, snowy, streets*) and is split into a training set, a validation set and a test set of size 54 each.

The second real world dataset is given by the NIST-4 fingerprint database [36]. We construct graphs from fingerprint images by extracting characteristic regions in fingerprints and converting the results into attributed graphs [37]. We use a validation set of size 300 and a test and training set of size 500 each. In this experiment we address the 4-class problem (*arch, left-loop, right-loop, whorl*).

Finally, we apply our novel graph kernels to the problem of molecule classification. To this end, we construct graphs from the AIDS Antiviral Screen Database of Active Compounds [38]. Our molecule database consists of two classes (*active, inactive*), which represent molecules with activity against HIV or not. We use a validation set of size 250, a test set of size 1500 and training set of size 250. Thus, there are 2000 elements in total (1600 inactive elements and 400 active elements). The molecules are converted into graphs by representing atoms as nodes and the covalent bonds as edges. Nodes are labelled with the number of the corresponding chemical symbol and edges by the valence of the linkage.

4.3   Results and Discussion

In Table 1 we provide the classification accuracy on all described datasets achieved with all of the proposed methods. In the first row of the embedding kernel classifiers the classification results achieved with an SVM based on prototype selection and graph embedding are given. Note that this kernel outperforms the reference system on all datasets, in four out of six cases with statistical significance. Similar results can be observed with the SVM based on the PCA reduced vectors where three out of six improvements are statistically significant. The SVM based on LDA reduced vectors perform poorly on the fingerprint and molecule data. Note that with LDA reduction the maximal dimensionality of the transformed feature space is $c - 1$, where c is the number of classes, i.e. on the fingerprint graphs three dimensions are used and on the molecule graphs only one dimension is used for classification. Nevertheless, on the remaining databases three out of four improvements over the reference system are statistically significant. The last column of Table 1 provides results achieved with a multiple classifier system based on plurality voting. Compared to the reference system in the graph domain four out of six improvements are statistically significant. Note that this system achieves three times the overall best result among all proposed methods (Letter high, Fingerprints, and Molecules).

Table 1. Classification accuracy in the original graph domain and in the embedded vector space

	Ref. System	Embedding Kernel Classifiers			
Database	k-NN (graph)	Prototype-SVM	PCA-SVM	LDA-SVM	Plurality Voting
Letter (low)	98.3	98.5	98.5	99.1	98.3
Letter (med)	94.0	96.9 ∘	97.2 ∘	96.5 ∘	97.1 ∘
Letter (high)	90.1	92.9 ∘	93.7 ∘	94.0 ∘	94.3 ∘
Image	57.4	64.8	61.1	68.5 ∘	61.1
NIST-4	82.6	85.0 ∘	84.6	66.6 ●	85.2 ∘
Molecules	97.1	98.1 ∘	98.2 ∘	95.3 ●	98.3 ∘

∘ Statistically significantly better than the reference system (= 0.05)
● Statistically significantly worse than the reference system (= 0.05)

5   Conclusions

Although graphs have a higher representational power than feature vectors, there is a lack of methods for pattern classification using graph representations. By contrast, a large number of methods for classification have been proposed for object representations given in terms of feature vectors. The present paper introduces a novel family of graph kernels in order to bridge the gap between structural and statistical pattern recognition. These graph kernels make explicit use of graph edit distance and can therefore deal with various kinds of graphs (labelled, unlabelled, directed, undirected, etc.). The basic idea of the embedding kernel is to describe a graph by means of m dissimilarities to a predefined set of graphs termed prototypes. That is, a graph g is mapped explicitly to the m-dimensional real space $\mathbb{R}^m$ by arranging the edit distances of g to all of the m prototypes as a vector. We show that the embedding process can be controlled by different prototype selectors or by well-known dimensionality reduction algorithms. By means of this procedure one obtains not only pairwise scalar products in an implicit kernel feature space but also the maps of the individual graphs. Furthermore, the proposed family of graph kernels lends itself to a method for the automatic generation of classifier ensembles. From the results of our experiments, one can conclude that the classification accuracy can be statistically significantly enhanced by all embedding methods but LDA on all considered databases.

Acknowledgements

References

1. Duda, R., Hart, P., Stork, D.: Pattern Classification, 2nd edn. Wiley-Interscience, Chichester (2000)
2. Schölkopf, B., Smola, A.: Learning with Kernels. MIT Press, Cambridge (2002)

3. Shawe-Taylor, J., Cristianini, N.: Kernel Methods for Pattern Analysis. Cambridge University Press, Cambridge (2004)
4. Vapnik, V., Chervonenkis, A.: On the uniform convergence of relative frequencies of events to their probabilities. Theory of Probability and its Applications 16(2), 264–280 (1971)
5. Vapnik, V.: Statistical Learning Theory. John Wiley, Chichester (1998)
6. Gärtner, T.: A survey of kernels for structured data. SIGKDD Explorations 5(1), 49–58 (2003)
7. Riesen, K., Neuhaus, M., Bunke, H.: Graph embedding in vector spaces by means of prototype selection. In: Accepted for the 6th Int. Workshop on Graph-Based Representations in Pattern Recognition (2007)
8. Riesen, K., Kilchherr, V., Bunke, H.: Reducing the dimensionality of vector space embeddings of graphs. In: Accepted for the International Conference on Machine Learning and Data Mining MLDM (2007)
9. Riesen, K., Bunke, H.: Classifier ensembles for vector space embedding of graphs. In: Accepted for the 7th Int. Workshop on Multiple Classifier Systems (2007)
10. Gärtner, T., Flach, P., Wrobel, S.: On graph kernels: Hardness results and efficient alternatives. In: Schölkopf, B., Warmuth, M., eds.: Proc. 16th Annual Conf. on Learning Theory, pp. 129–143 (2003)
11. Borgwardt, K., Ong, C., Schönauer, S., Vishwanathan, S., Smola, A., Kriegel, H.P.: Protein function prediction via graph kernels. Bioinformatics 21(1), 47–56 (2005)
12. Mahé, P., Ueda, N., Akutsu, T.: Graph kernels for molecular structures – activity relationship analysis with support vector machines. Journal of Chemical Information and Modeling 45(4), 939–951 (2005)
13. Lafferty, J., Lebanon, G.: Diffusion kernels on statistical manifolds. Journal of Machine Learning Research 6, 129–163 (2005)
14. Haussler, D.: Convolution kernels on discrete structures. Technical Report UCSC-CRL-99-10, University of California, Santa Cruz (1999)
15. Watkins, C.: Kernels from matching operations. Technical Report CSD-TR-98-07, Royal Holloway College (1999)
16. Jain, B., Geibel, P., Wysotzki, F.: SVM learning with the Schur-Hadamard inner product for graphs. Neurocomputing 64, 93–105 (2005)
17. Ramon, J., Gärtner, T.: Expressivity versus efficiency of graph kernels. In: Proc. First International Workshop on Mining Graphs, Trees and Sequences, 65–74 (2003)
18. Horvath, T., Gärtner, T., Wrobel, S.: Cyclic pattern kernels for predictive graph mining. In: Proc. International Conference on Knowledge Discovery and Data Mining, pp. 65–74. ACM Press, New York (2004)
19. Neuhaus, M.: Bridging the Gap Between Graph Edit Distance and Kernel Machines. World Scientific (to appear, 2007)
20. Bunke, H., Allermann, G.: Inexact graph matching for structural pattern recognition. Pattern Recognition Letters 1, 245–253 (1983)
21. Sanfeliu, A., Fu, K.: A distance measure between attributed relational graphs for pattern recognition. IEEE Transactions on Systems, Man, and Cybernetics (Part B) 13(3), 353–363 (1983)
22. Riesen, K., Neuhaus, M., Bunke, H.: Bipartite graph matching for computing the edit distance of graphs. In: Accepted for the 6th Int. Workshop on Graph-Based Representations in Pattern Recognition (2007)
23. Neuhaus, M., Riesen, K., Bunke, H.: Fast suboptimal algorithms for the computation of graph edit distance. In: Ribeiro, C.C., Martins, S.L. (eds.) WEA 2004. LNCS, vol. 3059, pp. 163–172. Springer, Heidelberg (2004)

24. Wilson, R., Hancock, E., Luo, B.: Pattern vectors from algebraic graph theory. IEEE Trans. on Pattern Analysis ans Machine Intelligence 27(7), 1112–1124 (2005)
25. Wilson, R., Hancock, E.: Levenshtein distance for graph spectral features. In: Proc. 17th Int. Conf. on Pattern Recognition, vol. 2, pp. 489–492 (2004)
26. Luo, B., Wilson, R., Hancock, E.: Spectral embedding of graphs. Pattern Recognition 36(10), 2213–2223 (2003)
27. Duin, R., Pekalska, E.: The Dissimilarity Representations for Pattern Recognition: Foundations and Applications. World Scientific (2005)
28. Riesen, K., Bunke, H.: A graph kernel based on vector space embedding (Submitted)
29. Bishop, C.: Neural Networks for Pattern Recognition. Oxford University Press, Oxford (1996)
30. Kuncheva, L.: Combining Pattern Classifiers: Methods and Algorithms. John Wiley, Chichester (2004)
31. Breiman, L.: Bagging predictors. Machine Learning 24, 123–140 (1996)
32. Ho, T.: The random subspace method for constructing decision forests. IEEE Trans. on Pattern Analysis ans Machine Intelligence 20(8), 832–844 (1998)
33. Freund, Y., Shapire, R.: A decision theoretic generalization of online learning and application to boosting. Journal of Computer and Systems Sciences 55, 119–139 (1997)
34. Pudil, P., Novovicova, J., Kittler, J.: Floating search methods in feature-selection. Pattern Recognition Letters 15(11), 1119–1125 (1994)
35. Le Saux, B., Bunke, H.: Feature selection for graph-based image classifiers. In: Marques, J.S., Pérez de la Blanca, N., Pina, P. (eds.) IbPRIA 2005. LNCS, vol. 3523, pp. 147–154. Springer, Heidelberg (2005)
36. Watson, C., Wilson, C.: NIST special database 4, fingerprint database. National Institute of Standards and Technology (1992)
37. Neuhaus, M., Bunke, H.: A graph matching based approach to fingerprint classification using directional variance. In: Kanade, T., Jain, A., Ratha, N.K. (eds.) AVBPA 2005. LNCS, vol. 3546, pp. 191–200. Springer, Heidelberg (2005)
38. DTP, D.T.P.: Aids antiviral screen (2004), http://dtp.nci.nih.gov/docs/aids/aids_data.html

A System Biology Approach for the Steady-State Analysis of Gene Signaling Networks

Purvesh Khatri[1], Sorin Draghici[1,*], Adi L. Tarca[1,2], Sonia S. Hassan[2], and Roberto Romero[2]

[1] Department of Computer Science, Wayne State University
[2] Perinatology Research Branch, NIH/NICHD, Detroit, MI 48201
purvesh@cs.wayne.edu, sorin@wayne.edu,
atarca@med.wayne.edu, shassan@med.wayne.edu,
prbchiefstaff@med.wayne.edu

Abstract. The existing approaches used to identify the relevant pathways in a given condition do not consider a number of important biological factors such as magnitude of each gene's expression change, their position and interactions in the given pathways, etc. Recently, an impact analysis approach was proposed that considers these crucial biological factors to analyze regulatory pathways at systems biology level. This approach calculates perturbations induced by each gene in a pathway, and propagates them through the entire pathway to compute an impact factor for the given pathway. Here we propose an alternative approach that uses a linear system to compute the impact factor. Our proposed approach eliminates the possible stability problems when the perturbations are propagated through a pathway that contains positive feedback loops. Additionally, the proposed approach is able to consider the type of genes when calculating the impact factors.

1 Introduction

While high-throughput life science technologies have enabled the collection of large amount of data, they have also posed challenges related to the extraction of knowledge from these data. For instance, the typical result of a microarray experiment is a list of differentially expressed (DE) genes that quantitatively reflect the changes in gene activity in response to a particular treatment, or in a given condition. The challenge common to all experiments is to translate such lists of DE genes into a better understanding of the underlying phenomenon. An automated Gene Ontology (GO) based approach has been proposed in order to help in this process [1,2]. This approach uses an over-representation analysis (ORA) of the list of DE genes in order to identify the GO categories that are significantly over- or under-represented in a given condition. This type of analysis has been very successful to the point of becoming a *de facto* standard in the analysis of microarray data [3]. A more recent approach considers the distribution

---

* To whom the correspondence should be addressed.

of the pathway genes in the entire list of genes and performs a functional class scoring (FCS) which also allows adjustments for gene correlations [4,5,6,7,8].

Both ORA and FCS techniques currently used are limited by the fact that each functional category is analyzed independently without a unifying analysis at a pathway or system level [8]. This approach is not well suited for a systems biology approach that aims to account for system level dependencies and interactions, as well as identify perturbations and modifications at the pathway or organism level [9]. In particular, all existing ORA and FCS approaches ignore a number of important biological factors including the amount of change in gene expression, the interactions between genes and their positions on a given pathway [10].

Recently, an impact analysis method was proposed that combines these important biological factors with the classical statistical analysis in order to identify the most perturbed signaling pathways in a given condition [10]. An *impact factor* (IF) is calculated for each pathway incorporating parameters such as the normalized fold change of the differentially expressed genes, the statistical significance of the set of pathway genes, and the topology of the pathway.

In this paper, we propose using a different approach to calculate the impact factors. Rather than propagating the perturbation through the pathway in a neural network-like fashion, here we propose to calculate the stable-state values of the perturbations by using a system of simultaneous equations. The main differences occur when pathways includes loops, which is true for most of the known gene signaling pathways. In such cases, in the previously described impact analysis the computation of the gene perturbation factors (PFs) was done through an iterative process. Problems are created by the fact that in the graph that describes the given pathway, multiple paths of different length are usually available to propagate the signal from any one source node to any one destination node. In order to address this, the previous version of the impact analysis approximates the PFs by going around each loop only once. No such approximation is necessary when the pathways are described by a system of simultaneous equations in which the PF of each gene is a function of the PFs of all other genes on the pathway. The previous approach of approximating the PFs by propagating the perturbations from node to node is still used when the system does not have an exact algebraic solution.

2   Impact Analysis

The aim of this approach is to establish a model that accounts for both the statistical significance of the set of genes and the perturbations of the individual genes on each pathway. A variety of models can be proposed here, but Occam's razor suggests to start with the simplest possible model and increase its complexity only if this model fails to capture the complexity of the phenomenon studied. One of the simplest possible models is a linear additive model in which the *impact factor* (IF) of a pathway P_i can be calculated as the sum between a probabilistic term and a perturbation term:

$$IF(P_i) = log\left(\frac{1}{p_i}\right) + \frac{\left|\sum_{g \in P} PF(g)\right|}{|\Delta E| \cdot N_{de}(P_i)} \tag{1}$$

The first term captures the significance of the given pathway P_i as provided by the classical statistical approaches, where p_i corresponds to the probability of obtaining a value of the statistic used at least as extreme as the one observed when the null hypothesis is true. We would like the IF to be large for severely impacted pathways (small p-values) so the first term uses $1/p_i$ rather than p_i. The log function is necessary to map the exponential scale of the p-values to a linear scale compatible with our intended linear model. The p_i value can be calculated using either an ORA (e.g., z-test [11], contingency tables [12,13], etc.), a FCS approach (e.g., GSEA [6,7]) or other more recent approaches [8,14,15].

The second term in (1) is a functional term that depends on the specific genes that are differentially expressed as well as on the interactions described by the pathway (i.e., its topology). In essence, this term sums up the values of the *perturbation factors* (PF) for all genes g on the given pathway P_i. The perturbation factor of a gene g_i is calculated as follows:

$$PF(g_i) = \alpha(g_i) \cdot \Delta E(g_i) + \sum_{j=1}^{n} \beta_{ji} \cdot \frac{PF(g_j)}{N_{ds}(g_j)} \tag{2}$$

In (2), the first term captures the quantitative information from the gene expression experiment. The factor $\Delta E(g_i)$ represents the signed normalized measured expression change of the gene g_i. The factor $\alpha(g_i)$ is a weight that captures the potential for systemic changes associated with the type of gene g_i. For most genes, α will be 1. However, if the gene is a transcription factor or similar, α can take a larger value set by the user. Thus, the user can divide the genes into various categories and associate different weights to various categories depending on the target organism.

The second term is a sum of the perturbation factors of all the genes g_j on the pathway P_i, normalized by the number of downstream genes of each such gene $N_{ds}(g_j)$, and weighted by a factor β_{ji}, whose absolute value quantifies the strength of the interaction between g_j and g_i. The sign of β reflects the type of interaction: +1 for induction, -1 for repression. Note that β will have non-zero value only for the genes that directly interact with the gene g_i. The second term here is similar to the PageRank index used by Google [16,17,18] only that we weight the downstream instead of the upstream connections (a web page is important if other pages point to it whereas a gene is important if it influences other genes).

Under the null hypothesis which assumes that the list of differentially expressed genes only contains random genes, the likelihood that a pathway has a large impact factor is proportional to the number of such "differentially expressed" genes that fall on the pathway, which in turn is proportional to the size of the pathway. Thus, we need to normalize with respect to the size of the pathway by dividing the total perturbation by the number of differentially expressed genes on the given pathway, $N_{de}(P_i)$. Furthermore, various technologies

can yield systematically different estimates of the fold changes. For instance, the fold changes reported by microarrays tend to be compressed with respect to those reported by RT-PCR [19,20]. In order to make the impact factors as independent as possible from the technology, and also comparable between problems, we also divide the second term in (1) by the mean absolute fold change $\overline{|\Delta E|}$, calculated across all differentially expressed genes. Assuming that there are at least some differentially expressed genes anywhere in the data set[1], both $\overline{|\Delta E|}$ and $N_{de}(P_i)$ are different from zero so the second term is properly defined.

Note that (2) essentially describes the perturbation factor PF for a gene g_i as a linear function of the perturbation factors of all genes in a given pathway. In the stable state of the system, all relationships must hold, so the set of all equations defining the impact factors for all genes form a system of simultaneous equations. Equation 2 can be re-written as:

$$PF(g_i) = \alpha(g_i) \cdot \Delta E(g_i) + \beta_{1i} \cdot \frac{PF(g_1)}{N_{ds}(g_1)} + \beta_{2i} \cdot \frac{PF(g_2)}{N_{ds}(g_2)} + \cdots + \beta_{ni} \cdot \frac{PF(g_n)}{N_{ds}(g_n)} \quad (3)$$

Rearranging (3) gives

$$PF(g_i) - \beta_{1i} \cdot \frac{PF(g_1)}{N_{ds}(g_1)} - \beta_{2i} \cdot \frac{PF(g_2)}{N_{ds}(g_2)} - \cdots - \beta_{ni} \cdot \frac{PF(g_n)}{N_{ds}(g_n)} = \alpha(g_i) \cdot \Delta E(g_i) \quad (4)$$

Using (4), a pathway P_i composed of n genes can be described as follows:

$$\begin{pmatrix} 1 - \frac{\beta_{11}}{N_{(1)}} & -\frac{\beta_{21}}{N_{(2)}} & \cdots & -\frac{\beta_{1}}{N_{(\ )}} \\ -\frac{\beta_{12}}{N_{(1)}} & 1 - \frac{\beta_{22}}{N_{(2)}} & \cdots & -\frac{\beta_{2}}{N_{(\ )}} \\ \cdots & \cdots & \cdots & \cdots \\ -\frac{\beta_{1}}{N_{(1)}} & -\frac{\beta_{2}}{N_{(2)}} & \cdots & 1 - \frac{\beta}{N_{(\ )}} \end{pmatrix} \begin{pmatrix} PF(g_1) \\ PF(g_2) \\ \cdots \\ PF(g_n) \end{pmatrix} = \begin{pmatrix} \alpha(g_1) \cdot \Delta E(g_1) \\ \alpha(g_2) \cdot \Delta E(g_2) \\ \cdots \\ \alpha(g_n) \cdot \Delta E(g_n) \end{pmatrix}$$

$$\begin{pmatrix} PF(g_1) \\ PF(g_2) \\ \cdots \\ PF(g_n) \end{pmatrix} = \begin{pmatrix} 1 - \frac{\beta_{11}}{N_{(1)}} & -\frac{\beta_{21}}{N_{(2)}} & \cdots & -\frac{\beta_{1}}{N_{(\ )}} \\ -\frac{\beta_{12}}{N_{(1)}} & 1 - \frac{\beta_{22}}{N_{(2)}} & \cdots & -\frac{\beta_{2}}{N_{(\ )}} \\ \cdots & \cdots & \cdots & \cdots \\ -\frac{\beta_{1}}{N_{(1)}} & -\frac{\beta_{2}}{N_{(2)}} & \cdots & 1 - \frac{\beta}{N_{(\ )}} \end{pmatrix}^{-1} \begin{pmatrix} \alpha(g_1) \cdot \Delta E(g_1) \\ \alpha(g_2) \cdot \Delta E(g_2) \\ \cdots \\ \alpha(g_n) \cdot \Delta E(g_n) \end{pmatrix}$$

Since the perturbations of the genes are obtained as the solution of a linear system, this approach aims to characterize the steady state of the system rather than rapidly transient states before an equilibrium has been established. Once the perturbation factors of all genes in a given pathway are calculated, (1) is used to calculate the impact factor of each pathway. The impact factor of each pathway is then used as a score to assess the impact of a given gene expression data set on all pathways (the higher the impact factor the more significant the pathway).

For some pathways, the matrix describing the interactions between the genes may be singular. In such cases, the perturbation factors as approximating by propagating the perturbations as previously described [10].

---

[1] If there are no differentially expressed genes anywhere, the problem of finding the impact on various pathways is meaningless.
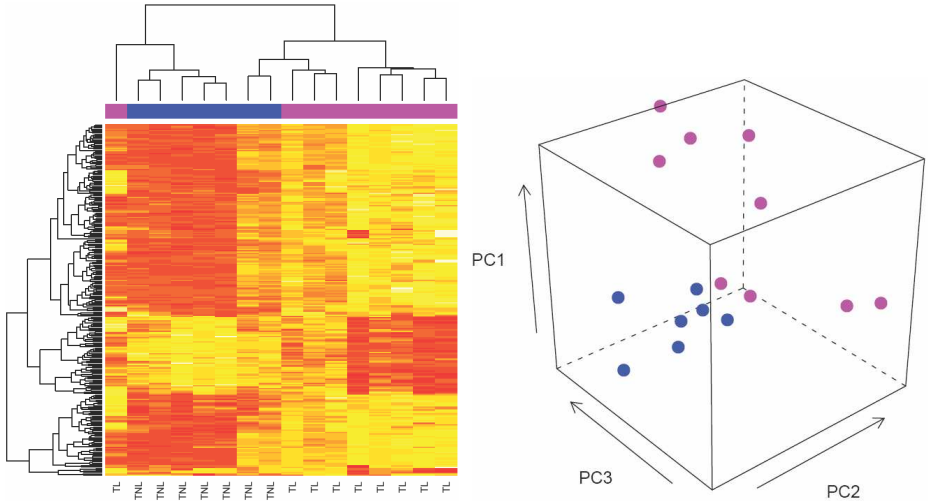
Fig. 1. Cervix data quality assessment. Unsupervised bi-clustering (left panel) of the cervix data using the 263 genes with the largest variability irrespective of the group identifies the two groups, term labor (TL) and term not labor (TNL), in the dataset. Visualization of the 16 samples using PCA (right panel) also shows that the samples are linearly separable using the first 3 principal components.

3   Results and Discussion

We used the proposed pathway impact analysis approach to analyze the differences between cervix tissue in women after term labor ($n = 9$) and those who reached the term without the on-set of labor ($n = 7$). The results obtained from the impact analysis were compared with the results obtained using ORA (hypergeometric p-value) and GSEA. The cervical transcriptome was profiled with Affymetrix HG-U133 Plus 2.0 microarrays. The details of this study and its biological significance are described elsewhere [21,22].

The microarray data was pre-processed using Robust Multi-array Average (RMA) [23]. In order to assess the quality of the microarray data, we used two unsupervised methods. First, we used a bi-clustering procedure [24] that hierarchically partitions the genes and the samples simultaneously. We used 263 genes for clustering that exhibit the largest variability among all 16 samples irrespective of the group they belong to. This approach is unsupervised since it does not use group information. The result of the bi-clustering is shown in Fig. 1. As shown in the Fig. 1, the clustering retrieves the two groups of the samples. Next, we applied the principal component analysis (PCA) [24] using all probesets on the HG-U133 plus 2.0 microarray. The results of PCA are shown in Fig. 1. As shown in Fig. 1, the two groups of samples can be separated in the space of the first 3 principal components with a hyperplane. Both types of results indicate that the data is meaningful in terms of differences between classes.

Pathway name	ORA (hypergeometric)	
	p-value	FDR
Cytokine-cytokine receptor interaction	6.78E-12	3.87E-10
Complement and coagulation cascades	4.78E-06	1.36E-04
Leukocyte transendothelial migration	1.12E-03	2.12E-02
ECM-receptor interaction	5.12E-03	5.83E-02
Jak-STAT signaling pathway	5.09E-03	5.83E-02
Focal adhesion	1.43E-02	1.36E-01
Toll-like receptor signaling pathway	2.22E-02	1.81E-01
Renal cell carcinoma	2.60E-02	1.85E-01
Cell adhesion molecules (CAMs)	4.32E-02	2.46E-01
Phosphatidylinositol signaling system	4.14E-02	2.46E-01
mTOR signaling pathway	5.43E-02	2.81E-01
Chronic myeloid leukemia	9.62E-02	4.26E-01
Wnt signaling pathway	1.02E-01	4.26E-01
Type II diabetes mellitus	1.09E-01	4.26E-01
Apoptosis	1.12E-01	4.26E-01

(A)

Enriched in term labor (TL)

Pathway Name	NOM p-val	FDR q-val	FWER p-val
Cytokine-cytokine receptor interaction	0.022	0.683	0.340
Complement and coagulation cascades	0.062	0.634	0.617
Toll-like receptor signaling pathway	0.075	0.560	0.664
Jak-STAT signaling pathway	0.077	0.821	0.583
Apoptosis	0.135	0.505	0.765
ECM-receptor interaction	0.136	0.504	0.714
Maturity onset diabetes of the young	0.138	0.485	0.807
Cell adhesion molecules	0.156	0.472	0.880
Adipocytokine signaling pathway	0.157	0.437	0.838
Focal adhesion	0.171	0.451	0.820
Regulation of actin cytoskeleton	0.201	0.498	0.947
MAPK signaling pathway	0.205	0.531	0.942
Type I diabetes mellitus	0.220	0.494	0.919
Leukocyte transendothelial migration	0.237	0.483	0.950
Type_II_diabetes_mellitus	0.240	0.459	0.952

(B)

Enriched in term not labor (TNL)

Pathway Name	NOM p-val	FDR q-val	FWER p-val
Ubiquitin_mediated_proteolysis	0.063	0.794	0.545
Notch_signaling_pathway	0.087	0.763	0.744
...	...	...	...

Pathway name	Impact Factor		
	IF	p-value	FDR
Cytokine-cytokine receptor interaction	27.75	2.55E-11	1.45E-09
VEGF signaling pathway	15.08	4.55E-06	1.30E-04
Circadian rhythm	14.49	7.92E-06	1.46E-04
Complement and coagulation cascades	14.21	1.02E-05	1.46E-04
Toll-like receptor signaling pathway	12.05	7.60E-05	8.66E-04
Long-term potentiation	9.19	1.04E-03	9.92E-03
Leukocyte transendothelial migration	8.84	1.42E-03	1.16E-02
Olfactory transduction	7.74	3.82E-03	2.72E-02
ECM-receptor interaction	7.05	6.99E-03	4.42E-02
Epithelial cell signaling in Helicobacter	6.79	8.75E-03	4.99E-02
Jak-STAT signaling pathway	6.49	1.13E-02	5.48E-02
Antigen processing and presentation	6.46	1.17E-02	5.48E-02
Cell adhesion molecules (CAMs)	6.38	1.25E-02	5.48E-02
Focal adhesion	6.24	1.41E-02	5.74E-02
Adipocytokine signaling pathway	5.88	1.93E-02	6.94E-02

(C)

Fig. 2. A comparison between the results of the classical approaches (A - hypergeometric, B - GSEA) and the results of the pathway impact analysis (C) for a set of differentially expressed genes in term labor. The pathways marked in red are well supported by the existing literature. After correcting for multiple comparisons, GSEA does not identify any pathway as significantly impacted in this condition at any of the usual significance levels (1%, 5% or 10%). The hypergeometric model identifies *cytokine-cytokine receptor interaction*, *complement and coagulation cascades* and *leukocyte transendothelial migration* as significantly impacted pathways at 5%, and *ECM-receptor interaction* and *Jak-STAT signaling* at 10% after correction for multiple comparisons. In contrast, in addition to the 3 pathways identified by the hypergeometric at 5% significance, the impact analysis also identifies *VEGF signaling*, *toll-like receptor signaling* and *ECM-receptor interaction*. Furthermore, at 10%, the impact analysis identifies *Jak-STAT signaling*, *antigen processing and presentation*, *cell adhesion molecules* and *focal adhesion* as significantly impacted pathways.

Next, we applied a moderated t-test [25] to select a list of DE genes. The p-values obtained from the moderated t-test were corrected using the False Discovery Rate method [23]. We selected 960 genes with corrected p-value less than 0.05 and fold change greater than 2 as DE genes that are both meaningful and verifiable. These 960 genes were used as the input to the ORA analysis using hypergeometric distribution and the impact analysis. GSEA was applied on the normalized expression matrix of all 19,886 unique genes on the array.

Figure 2 shows the comparison between the two classical approaches (hypergeometric and GSEA) and the pathway impact analysis. Note that the figure only shows the top 15 pathways as identified by each approach. For the rest of this section we will discuss the significance of a pathway as indicated by the FDR corrected p-values unless noted otherwise.

When considering the nominal p-value, GSEA finds the *cytokine-cytokine receptor interaction* pathway significant at 5%. However, when the correction for multiple comparisons is applied, GSEA does not find any significantly impacted pathways at any of the usual (1%, 5% or 10%) significance levels.

The hypergeometric model yields 3 pathways significant at the 5% significance level: *cytokine-cytokine receptor interaction*, *complement and coagulation cascades* and *leukocyte transendotheial migration*. These pathways are compatible with our current understanding of the phenomena involved in labor. The *cytokine-cytokine receptor interaction* and *leukocyte transendothelial migration* pathways are both associated with the innate immune system. The involvement of the innate immune system in cervical dilation and remodeling is well established in the literature [26,27]. Also, the *complement and coagulation cascades* include a part of the PLAU signaling and plasmin signaling pathways. There are several studies suggesting the involvement of plasminogen in cervical dilation and remodeling after term labor [28,29]. In particular, the plasminogen activation cascade plays an integral role in the remodeling of extracellular matrices during pregnancy and parturition [28]. In essence, the top 3 pathways identified by the classical ORA approach appear to be relevant.

At the same significance level, the impact analysis agrees on these pathways, but also identifies 7 additional pathways. Among these, *VEGF signaling*, *toll-like receptor signaling* and *ECM-receptor interaction* also appear to be very relevant. In fact, 2 of these 3 pathways point in the same direction: *toll-like receptor signaling* is another pathway associated with the innate immune system while *ECM-receptor interaction* describes the interactions between trans-membrane proteins and the extra-cellular matrix, already known to be heavily remodeled during pregnancy [30,31]. The remaining pathway, VEGF contains a number of genes previously shown to be differentially expressed between labor and non-labor (see Fig. 3) [21]. Finally, if the significance level were to be relaxed to 10%, the impact analysis also identifies *antigen processing and presentation* pathway, which is again part of the immune system.

It is important to point out that neither the hypergeometric model nor GSEA manage to identify any adhesion-related pathway at the usual 1% or 5% levels. Similarly, in spite of the differential expression of a number of genes related to
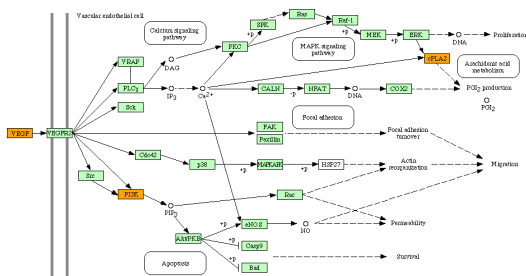
Fig. 3. The VEGF signaling pathway is one of the pathways identified by impact analysis. The genes found to be differentially expressed between labor and non-labor are highlighted in red. A more complete discussion about this pathway and its role in parturition is available elsewhere [21].

the VEGF-signaling, neither GSEA nor the classical ORA approach indicate that this pathway may be meaningful.

4   Conclusion

The classical statistical approaches used to identify significantly impacted pathways in a given condition only consider the number of differentially expressed genes and completely ignore other important biological factors. The impact analysis method uses a systems biology approach to extend the classical approach by incorporating important biological factors such as the magnitude of the expression changes, the topology and the type of signaling interactions between the genes on the pathway, and position of the differentially expressed genes on the pathway. The previously described impact analysis approach first computes the perturbations introduced by the differentially expressed genes in a pathway, and then propagates these perturbations throughout the pathway in order to calculate its impact factor. The perturbation propagation approach yields only an approximation of the gene perturbations when the pathways include loops. Here, we describe a modified impact analysis approach that addresses these stability issues. The results obtained on a human uterine cervix data set suggest that: i) the modified impact analysis approach has a higher statistical power and ii) it can identify several additional pathways that are likely to be involved in cervical dilation and re-modeling.

Acknowledgements

expressed in this material are those of the author(s) and do not necessarily reflect the views of the NSF, NIH, DOD or any other of the funding agencies.

References

1. Khatri, P., Drăghici, S., Ostermeier, G.C., Krawetz, S.A.: Profiling gene expression using Onto-Express. Genomics 79(2), 266–270 (2002)
2. Drăghici, S., Khatri, P., Martins, R.P., Ostermeier, G.C., Krawetz, S.A.: Global functional profiling of gene expression. Genomics 81(2), 98–104 (2003)
3. Khatri, P., Draghici, S.: Ontological analysis of gene expression data: current tools, limitations, and open problems. Bioinformatics 21(18), 3587–3595 (2005)
4. Pavlidis, P., Qin, J., Arango, V., Mann, J.J., Sibille, E.: Using the gene ontology for microarray data mining: A comparison of methods and application to age effects in human prefrontal cortex. Neurochemical Research 29(6), 1213–1222 (2004)
5. Goeman, J.J., van de Geer, S.A., de Kort, F., van Houwelingen, H.C.: A global test for groups of genes: testing association with a clinical outcome. Bioinformatics 20(1), 93–99 (2004)
6. Mootha, V.K., Lindgren, C.M., Eriksson, K.F., Subramanian, A., Sihag, S., Lehar, J., Puigserver, P., Carlsson, E., Ridderstråle, M., Laurila, E., Houstis, N., Daly, M.J., Patterson, N., Mesirov, J.P., Golub, T.R., Tamayo, P., Spiegelman, B., Lander, E.S., Hirschhorn, J.N., Altshuler, D., Groop, L.C.: Pgc-1α-responsive genes involved in oxidative phosphorylation are coordinately downregulated in human diabetes. Nature genetics 34(3), 267–273 (2003)
7. Subramanian, A., Tamayo, P., Mootha, V.K., Mukherjee, S., Ebert, B.L., Gillette, M.A., Paulovich, A., Pomeroy, S.L., Golub, T.R., Lander, E.S., Mesirov, J.P.: Gene set enrichment analysis: A knowledge-based approach for interpreting genome-wide expression profiles. Proceeding of The National Academy of Sciences of the USA 102(43), 15545–15550 (2005)
8. Tian, L., Greenberg, S.A., Kong, S.W., Altschuler, J., Kohane, I.S., Park, P.J.: Discovering statistically significant pathways in expression profiling studies. Proceeding of The National Academy of Sciences of the USA 102(38), 13544–13549 (2005)
9. Stelling, J.: Mathematical models in microbial systems biology. Current opinion in microbiology 7(5), 513–518 (2004)
10. Draghici, S., Khatri, P., Tarca, A.L., Amin, K., Done, A., Voichita, C., Georgescu, C., Romero, R.: A systems biology approach for pathway level analysis. Genome Research 17 (2007)
11. Doniger, S.W., Salomonis, N., Dahlquist, K.D., Vranizan, K., Lawlor, S.C., Conklin, B.R.: MAPPFinder: using Gene Ontology and GenMAPP to create a global gene expression profile from microarray data. Genome biology 4(1), R7 (2003)
12. Pan, D., Sun, N., Cheung, K.H., Guan, Z., Ma, L., Holford, M., Deng, X., Zhao, H.: PathMAPA: a tool for displaying gene expression and performing statistical tests on metabolic pathways at multiple levels for Arbidopsis. BMC Bioinformatics 4(1), 56 (2003)
13. Pandey, R., Guru, R.K., Mount, D.W.: Pathway Miner: extracting gene association networks from molecular pathways for predicting the biological significance of gene expression microarray data. Bioinformatics 20(13), 2156–2158 (2004)
14. Breslin, T., Krogh, M., Peterson, C., Troein, C.: Signal transduction pathway profiling of individual tumor samples. BMC Bioinformatics 6, 1471–2105 (2005)

15. Robinson, P.N., Wollstein, A., Bohme, U., Beattie, B.: Ontologizing gene-expression microarray data: characterizing clusters with gene ontology. Bioinformatics 20(6), 979–981 (2004)
16. Brin, S., Page, L.: The anatomy of a large-scale hypertextual Web search engine. Computer Networks and ISDN Systems 30(1–7), 107–117 (1998)
17. Haveliwala, T.: Efficient computation of PageRank. Technical Report 1999-31, Database Group, Computer Science Department, Stanford University (February 1999)
18. Page, L., Brin, S., Motwani, R., Winograd, T.: The pagerank citation ranking: Bringing order to the web. Technical report (1998)
19. Canales, R.D., Luo, Y., Willey, J.C., Austermiller, B., Barbacioru, C.C., Boysen, C., Hunkapiller, K., Jensen, R.V., Knight, C.R., Lee, K.Y., Ma, Y., Maqsodi, B., Papallo, A., Peters, E.H., Poulter, K., Ruppel, P.L., Samaha, R.R., Shi, L., Yang, W., Zhang, L., Goodsaid, F.M.: Evaluation of dna microarray results with quantitative gene expression platforms. Nat. Biotechnol. 24(9), 1115–1122 (2006)
20. Draghici, S., Khatri, P., Eklund, A.C., Szallasi, Z.: Reliability and reproducibility issues in DNA microarray measurements. Trends Genet. 22(2), 101–109 (2006)
21. Hassan, S.S., Romero, R., Haddad, R., Hendler, I., Khalek, N., Tromp, G., Diamond, M.P., Sorokin, Y., Malone, J.J.: The transcriptome of the uterine cervix before and after spontaneous term parturition. Am. J. Obstet. Gynecol. 195(3), 778–786 (2006)
22. Hassan, S.S., Romero, R., Tarca, A.L., et al.: Signature pathways identified from gene expression profiles in the human uterine cervix before and after spontaneous term parturition. Am. J. Obstet. Gynecol. 197(3), 250.e1–250.e7 (2007)
23. Irizarry, R.A., Hobbs, B., Collin, F., Beazer-Barclay, Y.D., Antonellis, K.J., Scherf, U., Speed, T.P.: Exploration, normalization, and summaries of high density oligonucleotide array probe level data. Biostatistics 4(2), 249–264 (2003)
24. Tarca, A.L., Carey, V.J., Chen, X.W., Romero, R., Draghici, S.: Machine learning and its applications to biology. PLoS Comput. Biol. 3(6), e116 (2007)
25. Smyth, G.K.: In: Limma: linear models for microarray data, pp. 397–420. Springer, New York (2005)
26. Saito, S., Shima, T., Nakashima, A., Shiozaki, A., Ito, M., Sasaki, Y.: What is the role of regulatory t cells in the success of implantation and early pregnancy? J. Assist Reprod. Genet. Epub. ahead of print (August 2007)
27. King, A., Kelly, R., Sallenave, J., Bocking, A., Challis, J.: Innate immune defences in the human uterus during pregnancy. Placenta Epub ahead of print (July 2007)
28. Tsatas, D., Baker, M.S., Rice, G.E.: Differential expression of proteases in human gestational tissues before, during and after spontaneous-onset labour at term. J. Reprod. Fertil. 116(1), 43–49 (1999)
29. Koelbl, H., Kirchheimer, J., Tatra, G.: Influence of delivery on plasminogen activator inhibitor activity. J. Perinat. Med. 17(2), 107–111 (1989)
30. Turpeenniemi-Hujanen, T., Feinberg, R.F., Kauppila, A., Puistola, U.: Extracellular matrix interactions in early human embryos: implications for normal implantation events. Fertil Steril 64(1), 132–138 (1995)
31. Xu, P., Wang, Y.L., Zhu, S.J., Luo, S.Y., Piao, Y.S., Zhuang, L.Z.: Expression of matrix metalloproteinase-2, -9, and -14, tissue inhibitors of metalloproteinase-1, and matrix proteins in human placenta during the first trimester. Biol. Reprod. 62(4), 988–994 (2000)

Σ-Δ Background Subtraction and the Zipf Law

Antoine Manzanera

ENSTA - Elec. and Comp. Sc. lab
32 Bd Victor, 75015 Paris, France
antoine.manzanera@ensta.fr
http://www.ensta.fr/~manzaner

Abstract. The Σ-Δ background estimation is a simple non linear method of background subtraction based on comparison and elementary increment/decrement. We propose here some elements of justification of this method with respect to statistical estimation, compared to other recursive methods: exponential smoothing, Gaussian estimation. We point out the relation between the Σ-Δ estimation and a probabilistic model: the Zipf law. A new algorithm is proposed for computing the background/foreground classification as the pixel-level part of a motion detection algorithm. Comparative results and computational advantages of the method are commented.

Keywords: Image processing, Motion detection, Background subtraction, Σ-Δ modulation, Vector data parallelism.

1 Introduction

Background subtraction is a very popular class of methods for detecting moving objects in a scene observed by a stationary camera [1] [2] [3] [4] [5]. In every pixel p of the image, the observed data is a time series $I_t(p)$, corresponding to the values taken by p in the video I, as a function of time t. As only temporal processing will be considered in this paper, the argument p will be discarded. The principle of background subtraction methods is to discriminate the pixels of moving objects (the foreground) from those of the static scene (the background), by detecting samples which are significantly deviating from the statistical behaviour of the time series. To do this, one needs to estimate the graylevel distribution with respect to time, i.e. $f_t(x) = P(I_t = x)$. As the conditions of the static scene are subject to changes (lighting conditions typically), f_t is not stationary, and must be constantly re-estimated. For the sake of computational efficiency, which is particularly critical for video processing, it is desirable that f_t should be represented by a small number of estimates which can be computed recursively. In this paper, we focus on recursive estimation of mono-modal distributions, which means that we assume that the time series corresponding to the different values possibly taken by the background along time, presents one single mode. This may not be a valid assumption for every pixel, but it does not affect the interest of the principle since the technique presented can be extended to multi-modal background estimation.

The Σ-Δ background estimation [6] [7] [8] is a simple and powerful non linear background subtraction technique, which consists in incrementing (resp. decrementing) the current estimate by an constant value if it is smaller (resp greater) than the current sample. Our objective is to discuss the foundations of this method, with regards to statistical estimation. We show the relation between the Σ-Δ estimation and the probabilistic model of Zipf-Mandelbrot, and compare it with two other recursive methods: exponential smoothing and Gaussian estimation. Section 2 presents the general framework of recursive estimation. Section 3 presents the particular case of Σ-Δ estimation, and provides the full numerical algorithm to compute it in the mono-modal case. Section 4 shows some results and discuss the computational advantages of Σ-Δ background subtraction, proposing in particular a complete vector data parallel implementation adapted to the SIMD-within-register framework. Section 5 concludes and presents the possible extension of the primitive algorithm.

2 Recursive Estimation

If one should represent f_t by one single scalar estimate, one of the most natural would be the average M_t of the time series I_t. The naive recursive computation: $M_t = \frac{1}{t}I_t + \frac{t-1}{t}M_{t-1}$ can be used as initialisation for the small values of t, but is not numerically realisable for long series. So one common solution is to use a constant weight (or learning rate) $\alpha \in]0,1[$ for the current sample: $M_t = \alpha I_t + (1-\alpha)M_{t-1}$. This is sometimes referred to as running average, and corresponds to the recursive implementation of exponential smoothing.

One way of generalising this is to write the updating equation in an incremental form: $M_t = M_{t-1} + \delta_t(I_t)$, where δ_t is the increment function, depending on the current sample I_t. In the case of exponential smoothing, δ_t is the affine function $\alpha(I_t - M_{t-1})$ (Fig. 1(1)). This linear dependence is not satisfying, since, in most cases, a sample which is far from the average is out of the background model and should have little effect on the estimate updating. This problem can still be addressed in the exponential smoothing framework, by using two distinct constants α_1 and α_2 such that $\alpha_1 > \alpha_2$, and by defining $\delta_t(I_t) = \alpha_1(I_t - M_{t-1})$ if I_t is in the background model, and $\delta_t(I_t) = \alpha_2(I_t - M_{t-1})$ if I_t is foreground. This results in a discontinuous increment function δ_t, as shown in Fig. 1(2), where the decision background/foreground is done by simply thresholding the absolute difference: The pixel is foreground if $|I_t - M_{t-1}| > Th$. It appears however, that the discontinuity of δ_t makes the choice of Th critical.

To get a more continuous behaviour, we shall follow [9], who suggests that the weight α attached to the current sample I_t should depend on its probability $f_t(I_t)$. But, as noted by [10], the mere product $\delta_t(I_t) = f_t(I_t) \times \alpha(I_t - M_{t-1})$ suggested by [9] is not usable in practise because of increments too small in general to be numerically operative. A proper way to achieve this, if α_{max} is the maximal desired weight, and as M_{t-1} is the mode of the current distribution f_t, is to use:

$$\delta_t = \frac{\alpha_{max} f_t(I_t)}{f_t(M_{t-1})} \times (I_t - M_{t-1}). \tag{1}$$

If we use a Gaussian distribution as density model like in [9], we get the following increment function:

$$\delta_t = \alpha_{max} \times \exp(\frac{-(I_t - M_{t-1})^2}{2V_{t-1}}) \times (I_t - M_{t-1}). \tag{2}$$

The model needs the temporal variance V_t. In [9], it is computed as the Gaussian estimation of the series $(I_t - M_t)^2$. But this leads to a double auto-reference in the definitions of M_t and V_t, which is prejudicial to the adaptation capability of the algorithm. We recommend rather to compute V_t as the exponential smoothing of $(I_t - M_t)^2$, using a fixed learning rate α_V.

One of the interest of computing V_t is that it provides a natural criterion of decision background/foreground through the condition $|I_t - M_t| > N \times \sqrt{V_t}$, with N typically between 2 and 4. Note that the increment function (Fig. 1(3)) is very different from the previous ones, and has a derivative-of-Gaussian shape.

This Gaussian estimation provides some attractive features compared to the exponential smoothing: the update of the estimates depends on the probability of the current sample, and the increment values are globally higher when the background density is more dispersed. Nevertheless, it is less used than exponential smoothing because of the computational load much higher. Now, what does the increment function look like if we take the Zipf law as the probabilistic model ?

3   Zipfian Background Estimation

Originally the Zipf law is an empirical principle [11] at the crossroads of linguistic and information theory, stating that, in any sense-making text, the probability of occurrence of the nth most frequent word is $1/n$ the probability of occurrence of the (first) most frequent word. So the Zipf distribution is a hyperbolic decreasing function. Recently, it has been used in several applications of image processing [12], in particular as a model for the distribution of local spatial features. We use it here as a model for (pixel-wise) temporal distribution.

Because of the divergence of the sum $1/n$, the Zipf density function includes a power factor: $1/n^s$, with $s > 1$. The general expression of the continuous symmetric Zipf-Mandelbrot distribution can be written:

$$Z_{(\mu,k,s)}(x) = \frac{(s-1)k^{s-1}}{2(|x - \mu| + k)^s}. \tag{3}$$

In this expression, the parameter μ represents the mode of the distribution, and k determines its dispersion. The remarkable property of Z, taken as the density model f_t of the time series I_t (and then, replacing eq. 3 in eq. 1), is the shape of the increment function δ_t (Fig. 1(3)), which is close to the Heaviside shaped function: $H_{(\mu,\kappa)}(x) = -\kappa$ if $x < \mu$, $+\kappa$ if $x > \mu$, with $\kappa = \alpha_{max}k^s$. Thus it is naturally related to the Σ-Δ modulation, classically used in Analog to Digital Conversion:

(1)

(2)

(3)

(4)
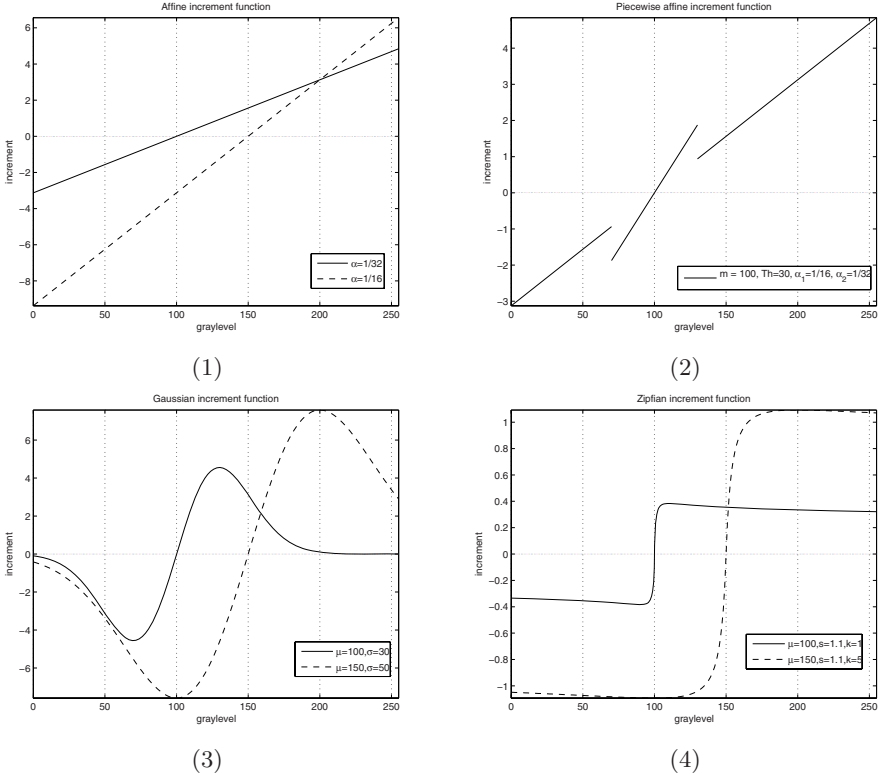
Fig. 1. The different increment functions δ_t associated to the different distribution models: (X axis: graylevel I_t, Y axis: increment value $\delta_t(I_t)$). (1) Exponential smoothing (plain: $\alpha = 1/32$; dashed: $\alpha = 1/16$) (1) Bi-level exponential smoothing ($m = 100$, $Th = 30$, $\alpha_1 = 1/16$, $\alpha_2 = 1/32$) (3) Gaussian laws, $\alpha_{max} = 1/4$ (plain: $\mu = 100$, $\sigma = 30$; dashed: $\mu = 150$, $\sigma = 50$) (4) Zipf laws, $\alpha_{max} = 1/4$ (plain: $\mu = 100$, $k = 1$, $s = 1.1$; dashed: $\mu = 150$, $k = 5$, $s = 1.1$).

For every time step Δt:

If $M_{t-\Delta t} > I_t$ then $M_t = M_{t-\Delta t} - \varepsilon$;

If $M_{t-\Delta t} < I_t$ then $M_t = M_{t-\Delta t} + \varepsilon$;

Here, the average increment per time unit is $\kappa = \frac{\varepsilon}{\Delta t}$. Digitally, the elementary increment ε is the least significant bit of the representation, i.e. 1 if the values are integer-coded. Adaptation to the dispersion of the model can then be done by tuning the updating period Δt: the greater the variance, the smaller Δt should be. The following algorithm reproduces such behaviour. The principle is to attach to every pixel, in addition to the mode estimator M_t, a dispersion estimator V_t. Suppose that $V_t \in]0, 2^m - 1[$, which means that it is coded on m bits:

For every frame t: {

      rank = t % 2^m ; pow2 = 1 ;

      do { pow2 = 2× pow2 ; } while((rank % pow2 == 0) && (pow2 < 2^m))

If $(V_{t-1} > \frac{2}{pow2})$ {
         If $M_{t-1} > I_t$ then $M_t = M_{t-1} - 1$;
         If $M_{t-1} < I_t$ then $M_t = M_{t-1} + 1$;
         }
$D_t = |I_t - M_t|$;
If $(t \% T_V == 0)$ {
         If $V_{t-1} > \max(V_{min}, N \times D_t)$ then $V_t = V_{t-1} - 1$;
         If $V_{t-1} < \min(V_{max}, N \times D_t)$ then $V_t = V_{t-1} + 1$;
         }
}

Here $x \% y$ is x modulo y. The purpose of the two first lines of the algorithm (which are computed once for all the pixels at every frame) is to find the greatest power of two (pow2) that divides the time index modulo 2^m (rank). Once this has been determined, it is used to compute the minimal value of V_{t-1} for which the Σ-Δ estimate M_t will be updated. Thus the (log-)period of update of M_t is inversely proportional to the (log-)dispersion: if $V_t > 2^{m-1}$, M_t will be updated every frame, if $2^{m-2} \leq V_t < 2^{m-1}$, M_t will be updated every 2 frames, and so on.

The dispersion factor V_t is computed here as the Σ-Δ estimation of the absolute differences D_t, amplified by a parameter N. Like in Gaussian estimation, we avoid double auto-reference by updating V_t at a fixed period T_V. V_t can be used as a foreground criterion directly: the sample I_t is considered foreground if $D_t > V_t$. V_{min} and V_{max} are simply used to control the overflows ; 2 and $2^m - 1$ are their typical values.

Note that the time constants, which represent the period response of the background estimation algorithm, are related here to the dynamics (the number of significant bits) of V_t, and to its updating period T_V. For the other methods, the time constants were associated to the inverse of the learning rates: $1/\alpha_i$ for the exponential smoothing and $1/\alpha_{max}$ and $1/\alpha_V$ for Gaussian estimation.

4   Results

Figure 2 shows the background estimation for all the time indexes, and one particular pixel. This is a difficult case for pixel-level motion detection: an outdoor scene where the background signal (high grass meadow with wind) is corrupted by the passage of two foreground objects. The Boolean condition "$D_t > V_t$" is used as foreground classification.

Figure 3 shows the result for all the pixels, at 4 different time indexes of the classical *Hall* sequence, in which two people are moving in radial motion, i.e. in the direction of the optical axis. This is a difficult case too, since the values in the centre of the moving objects do not change much (aperture problem). For reference, the last row of Figure 3 displays the hand drawn ground truth for the 4 frames.
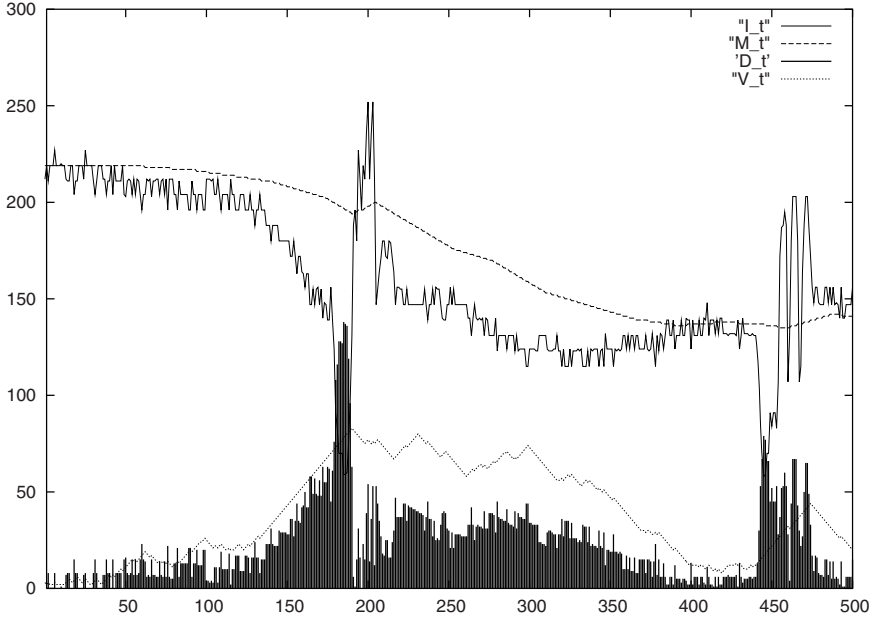
Fig. 2. Σ-Δ background estimation running on a given pixel. (X axis: time index, Y axis: graylevel). All values are 8-bit coded. Amplification factor N is 2. Variance updating period T_V is 1. Plain line: I_t, Dotted line: M_t, Impulses: D_t, Dashed line: V_t.

This ground truth is used for the quantitative evaluation (detection and false alarm rates are averaged on these 4 key frames) shown on Table 1, for different values of the amplification constant N, and of the updating period T_V. Those results are resumed on Figure 4, where the 9 Σ-Δ algorithms are compared with 6 different Gaussian algorithms. Note that these figures relate to pixel-level methods, and should not be interpreted in absolute, since a simple spatial regularisation appreciably improves the two measures, in all cases.

Table 1. (Detection, False alarm) rates for 9 Σ-Δ background subtraction algorithms. Measures are averaged on the 4 key frames of the *Hall* sequence.

	N=1	N=2	N=4
$T_V = 1$	(0.74,0.25)	(0.62,0.10)	(0.53,0.02)
$T_V = 8$	(0.91,0.38)	(0.87,0.23)	(0.85,0.12)
$T_V = 32$	(0.95,0.45)	(0.94,0.38)	(0.94,0.33)

The relevance and power of the Σ-Δ estimation, as a pixel-level temporal filter, is comparable to that of the Gaussian estimation, whereas its computational cost is even inferior to that of exponential smoothing. Indeed, the algorithm proposed in Section 3 is straightforward to compute in any fixed-point
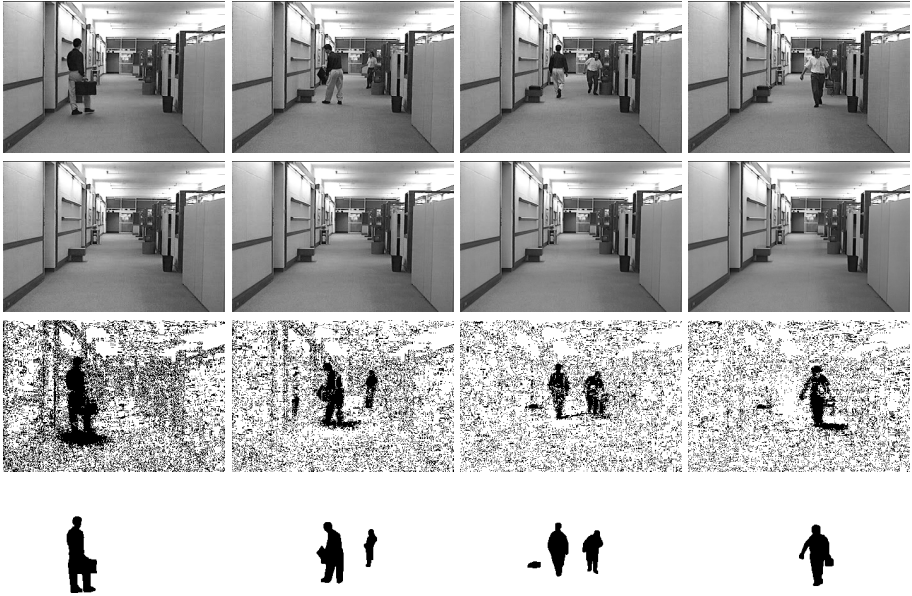
Fig. 3. Background subtraction shown at different frames of the *Hall* image sequence. Row 1: Original sequence, frames 38, 90, 170 and 250. Rows 2 and 3: Σ-Δ Background and foreground, with N=2, and $T_V = 8$. Row 4: (Fore)ground truth.

arithmetic, using an instruction set limited to: absolute difference, comparison, increment/decrement. Thus, it is well adapted to real-time implementation using dedicated or programmable hardware.

Another important computational property of Σ-Δ background subtraction, is that, once chosen the number of bits used to represent the estimates M_t and V_t, every computation can be made at full precision without increasing the data width. This allows in particular to make the most of the data parallelism provided by the SIMD-WAR (Single Instruction Multiple Data Within A Register) paradigm, which consists in concatenating many short operands in one single very long variable, and then applying scalar operations on the long variables. This implementation is available on most personal computers, using for example the SSE-2 (Streaming SIMD Extensions 2) instructions of the Intel®C++ compiler [13]. We provide hereunder the vectorised pseudo-code of the Σ-Δ background subtraction. Here, a 16-times acceleration is achieved by performing the operations on a 128-bit register made of 16 8-bit data.

```
vmin = 2; vmax = 255; logN = 1; Tv = 4;// Scalar constants definition
// Vector constants definition: creates 128-bit constants
// by concatenating 16 8-bit constants
VMIN = vector16_define(vmin);
VMAX = vector16_define(vmax);
// Sigma-Delta initializations
for(i=0; i<height; i++) {
```
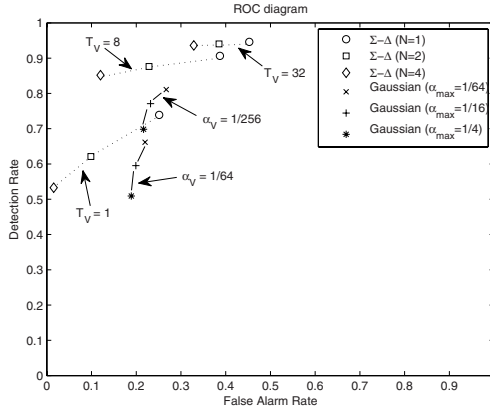
Fig. 4. Detection / false alarm rates diagram, for 9 Σ-Δ and 6 Gaussian background subtraction algorithms. Measures are averaged on the 4 key frames of the *Hall* sequence.

```
|  for(j=0; j<width/16; j++) {
|  |  I = I(0);// I(0): first image
|  |  M = I; // M(0) = I(0)
|  |  V = VMIN; // V(0) = vmin
|  }
}
for(t=1; t<=tstop; t+=1) {// Time loop*******************************
|  // Computation of the update threshold according to the time index
|  rank = (t%256); pow2 = 1; thres = 256;
|  do { pow2 = pow2*2; thres = thres/2;
|     } while (((rank%pow2)==0)&&(thres>1));
|  TH = vector16_define(thres);// vector variable
|  for(i=0; i<height; i++) {// Space loop----------------------------
|  |  for(j=0; j<width/16; j++) {
|  |  |  // (1) Update of Background M(t)
|  |  |  I = I(t);//loading I(t)
|  |  |  UPDATE = vector16_compare_greater(V,TH);// Comparison (>)
|  |  |  //if V(t-1)>th, update= FF (-1), else update = 0
|  |  |  C1 = vector16_compare_greater(I,M);
|  |  |  //if I(t)>M(t-1), c1= FF (-1), else c1 = 0
|  |  |  C2 = vector16_compare_less(I,M);// Comparison (<)
|  |  |  //if M(t-1)>I(t), c2= FF (-1), else c2 = 0
|  |  |  C1 = vector128_and(C1,UPDATE);// Bit-wise logical AND: Update is
|  |  |  C2 = vector128_and(C2,UPDATE);// effective only if V(t-1) > th
|  |  |  M = vector16_sub(M,C1);//M(t) = M(t-1) - c1
|  |  |  M = vector16_add(M,C2);//M(t) = M(t-1) + c2
|  |  |  // (2) Computation of absolute difference D(t)
|  |  |  MAX = vector16_max(I,M); // max(I(t),M(t))
|  |  |  MIN = vector16_min(I,M); // min(I(t),M(t))
|  |  |  D = vector16_sub(MAX,MIN); // d = |I(t) - M(t)|
|  |  |  // (3) Update of variance V(t): one over Tv frames
```

```
| | | if (t % Tv == 0) {
| | | | ND = D;  // Difference amplification (Saturated addition)
| | | | for (k=1;k<=logN;k++) ND = vector16_add_sat(ND,ND);
| | | | BDEC = vector16_max(ND,VMIN);// Variance is bounded
| | | | BINC = vector16_min(ND,VMAX);// between Vmin and Vmax
| | | | C1 = vector16_compare_greater(V,BDEC);
| | | | //if V(t-1)>max(D(t),Vmin) c1= FF (-1), else c1 = 0
| | | | C2 = vector16_compare_less(V,BINC);
| | | | //if V(t-1)<min(D(t),Vmax) c2= FF (-1), else c2 = 0
| | | | V = vector16_add(V,C1);//V(t) = V(t-1) + c1
| | | | V = vector16_sub(V,C2);//V(t) = V(t-1) - c2
| | | }
| | | // (4) Computation of Foreground label L(t)
| | | L = vector16_compare_greater(D,V);
| | | //if D(t)>V(t) L(t)= FF, else L(t) = 0
| | }
| }// end of space loop----------------------------------------
}// end of time loop********************************************
```

5   Conclusion and Extensions

We have proposed a justification of using the Σ-Δ estimation as a background subtraction method, based on the use of the Zipf law as a density model. We have proposed an algorithm implementing this method and allowing to adapt the background updating to the temporal dispersion. We have shown the computational advantages of the Σ-Δ estimation, illustrated by the vector SIMD implementation.

The limitations of this algorithm - used "as is" in a motion detection system - are inherent to its mono-modal nature: first, one single mode in the density model can be inefficient to discriminate moving objects over a complicated background, and second, one single dispersion estimate, related to one time constant, may not be sufficient for certain kind of motion such as remote objects with radial velocity w.r.t. the optical centre. Nevertheless the basic model can be enriched, either by using a multi-modal Zipfian distribution like it is done in [9] for Gaussian estimation, or by using several time magnitudes, as shown in [8].

References

1. Karmann, K.P., von Brandt, A.: Moving Object Recognition Using an Adaptive Background Memory. In: Time-Varying Image Processing and Moving Object Recognition, Elsevier, Amsterdam (1990)
2. Toyoma, K., Krumm, J., Brumitt, B., Meyers, B.: Wallflower: Principles and Practice of Background Maintenance. In: Proc. IEEE ICCV, Kerkyra - Greece, pp. 255–261 (1999)
3. Elgammal, A., Harwood, D., Davis, L.: Non-parametric Model for Background Subtraction. In: Proc. IEEE ECCV, Dublin - Ireland (2000)

 4. Piccardi, M.: Background subtraction techniques: a review. In: Proc. of IEEE SMC/ICSMC (October 2004)
 5. Cheung, S.C., Kamath, C.: Robust techniques for background subtraction in urban traffic video. In: Proc. SPIE Video Com. and Image Proc. San Jose - CA (2004)
 6. McFarlane, N., Schofield, C.: Segmentation and tracking of piglets in images. Machine Vision and Applications 8, 187–193 (1995)
 7. Manzanera, A., Richefeu, J.: A robust and computationally efficient motion detection algorithm based on Σ-Δ background estimation. In: Proc. ICVGIP 2004, pp. 46–51 (December 2004)
 8. Manzanera, A., Richefeu, J.: A new motion detection algorithm based on Σ-Δ background estimation. Pattern Recognition Letters 28, 320–328 (2007)
 9. Stauffer, C., Grimson, E.: Learning patterns of activity using real-time tracking. IEEE Trans. on PAMI 22(8), 747–757 (2000)
10. Power, P., Schoonees, J.: Understanding background mixture models for foreground segmentation. In: Imaging and Vision Computing New Zealand, Auckland, NZ (2002)
11. Zipf, G.: Human behavior and the principle of least-effort. Addison-Wesley, New-York (1949)
12. Caron, Y., Makris, P., Vincent, N.: A method for detecting artificial objects in natural environments. In: Int. Conf. in Pattern Recognition, pp. 600–603 (2002)
13. Intel, C.: Intel®C++ Compiler for Linux Systems - User's Guide (1996-2003) Document number 253254-014

Model-Based Correlation Measure for Nonuniformity Gain and Offset Parameters of Infrared Focal-Plane-Array Sensors⋆

César San Martin[1,2] and Sergio N. Torres[1]

[1]Department of Electrical Engineering, University of Concepción.
Casilla 160-C, Concepción, Chile
`cesanmartin@udec.cl, sertorre@udec.cl`
[2]Department of Electrical Engineering, University of La Frontera.
Casilla 54-D, Temuco, Chile
`csmarti@ufro.cl`

Abstract. In this paper, we proposed a model based correlation measure between gain and offset nonuniformity for infrared focal plane array (FPA) imaging systems. Actually, several nonuniformity correction methods perform correction of nonuniformities by means of gain and offset estimation in a detector-by-detector basis using several approach such as laboratory calibration methods, registration-based algorithm, and algebraic and statistical scene-based algorithm. Some statistical algorithms model the slow and random drift in time that the gain and offset present in many practical FPA applications by means of Gauss-Markov model, assuming that the gain and offset are uncorrelated. Due to this, in this work we present a study and model of such correlation by means of a generalized Gauss-Markov model. The gain and offset model-based correlation is validate using several infrared video sequences.

Keywords: Gauss-Markov Model, Image Sequence Processing, Infrared FPA, Signal Processing.

1 Introduction

Infrared (IR) cameras use an IR sensor to digitize the information, and due to its high performance, the most employed integrated technology in IR sensors is the Focal Plane Array (FPA). An IR-FPA is a die composed of a group of photodetectors placed in a focal plane forming a matrix of $X \times Y$ pixels, which gives the sensor the ability to collect the IR radiation.

Nonuniformity noise in IR imaging sensors, which is due to pixel-to-pixel variation in the detectors' responses, can considerably degrade the quality of IR

images since it results in a fixed-pattern-noise (FPN) that is superimposed on the true image. Further, what makes matter worse is that the nonuniformity slowly varies over time, and depending on the FPA technology, this drift can take from minutes to hours. In order to solve this problem, several scene-based nonuniformity correction (NUC) techniques have been developed [1,2,3,4]. Scene-based techniques perform the NUC using only the video sequences that are being imaged, not requiring any kind of laboratory calibration technique. Our group has been active in the development of novel scene-based algorithms for NUC based on statistical estimation theory. In [5,6] we have developed a Gauss-Markov model to capture the slow variation in the FPN and have utilized the model to adaptively estimate the nonuniformity in blocks of infrared video sequences using a Kalman Filter. In such work the gain and offset are assumed uncorrelated.

The principal contribution of this works is a study and model the detector gain and offset correlation. The model, called generalized Gauss-Markov model, is based in a measure of the correlation between gain and offset nonuniformity of infrared detectors. To study this correlation, we employ the detector parameters estimated from three published nonuniformity correction method: a neural network approach, a non-linear filtering method and statistical algorithm. With those method the correlation function is estimated and the Gauss-Markov model is then generalized. To validate the proposed model we tested with several infrared video sequences captured by an infrared camera.

This paper is organized as follows. In Sections 2 the IR-FPA model and the Gauss-Markov model are presented. In Section 3 the generalized Gauss-Markov model is developed. In Section 4 the correlation between gain and offset is measure and validate with sequence of real infrared data. In Section 5 the conclusions of the paper are summarized.

2   Gauss-Markov Model for the Nonuniformity Detector Parameters

In this paper, we model the pixel-to-pixel variation in the detectors' responses (nonuniformity) using the commonly used linear model for each pixel on the IR FPA. For the $(ij)^{\text{th}}$ detector, the measured readout signal $Y_{ij}(n)$ at a given time n is represented by the approximate linear relation

$$Y_{ij}(n) = X_{ij}^{(1)}(n)T_{ij}(n) + X_{ij}^{(2)}(n) + V_{ij}(n),$$

where $X_{ij}^{(1)}(n)$ and $X_{ij}^{(2)}(n)$ are the gain and the offset of the ij^{th} detector respectively and $T_{ij}(n)$ is the real incident infrared photon flux collected by the detector. The term $V_{ij}(n)$ represents the read-out noise associate with the ij^{th} detector at time n. the subscript ij is omitted with the understanding that all operations are performed on a pixel by pixel basis.

In practice, vectors of observations are captured over which the gain and offset are approximately constants. This is an acceptable assumption in applications where the observation vector is short. At a later time, other vectors of observation

are captured for which these parameters may have drifted. This slow random variation of the gain and offset between consecutive vectors of observation is modeled by a Gauss-Markov process. It is also considered that the gain and offset at kth vector-time are uncorrelated. The driver noise for the gain and offset are assumed gaussian individually and mutually uncorrelated among them. Mathematically, the Gauss-Markov state equation is given by

$$\boldsymbol{X}_{k+1} = \boldsymbol{\Phi}_k \boldsymbol{X}_k + \boldsymbol{G}_k \boldsymbol{W}_k, \tag{1}$$

where $\boldsymbol{X}_{k+1} = \begin{bmatrix} X_k^{(1)} \\ X_k^{(2)} \end{bmatrix}$ is the state vector at kth vector time. $\boldsymbol{\Phi} = \begin{bmatrix} \alpha_k & 0 \\ 0 & \beta_k \end{bmatrix}$ is called the state transition matrix between the states at kth and $k+1$th time vector. α_k and β_k represent the level of drift in the gain and offset between consecutive vectors of observation, respectively. The parameter α_k (β_k) is chosen according to the magnitude of the drift between the gain (offset) at state k and the state $k+1$. $\boldsymbol{G}_k = \begin{bmatrix} 1 & 0 \\ 0 & 1 \end{bmatrix}$ is a identity matrix that randomly relates the driving noise vector $\boldsymbol{W}_k$ to the state vector $\boldsymbol{X}_k$. $\boldsymbol{W}_k = \begin{bmatrix} W_k^{(1)} \\ W_k^{(2)} \end{bmatrix}$, $W_k^{(1)}$ and $W_k^{(2)}$ are the driving noise for the gain and offset process, respectively.

Finally, to complete the Gauss-Markov model, the observation model for the detector response is given by

$$\boldsymbol{Y}_k = \boldsymbol{H}_k \boldsymbol{X}_k + \boldsymbol{V}_k, \tag{2}$$

where $\boldsymbol{Y}$ is the observation vector at kth block, and the length of observation vector is l_k. $\boldsymbol{H}_k = \begin{bmatrix} T(1) & 1 \\ . & . \\ . & . \\ . & . \\ T(l_k) & 1 \end{bmatrix}$ is the irradiance at kth block. $\boldsymbol{V}_k$ is the vector of independent, additive temporal noise elements in the kth block. The main assumption in the observation model is that the input irradiance $T(n)$ is a uniformly distributed random variable in the range $[T_k^{min}, T_k^{max}]$ constituting the range common to all detectors of possible irradiance levels prior to saturation. For a complete development for the gain and offset estimation of each detector in the FPA using an optimized recursion algorithm such that Kalman filter, see [5].

3   Generalized Gauss-Markov Model

In this paper, we propose generalize the model given at equation (1) by the next equation

$$\boldsymbol{X}_{k+1} = \boldsymbol{\Phi}_k \boldsymbol{X}_k + \boldsymbol{G}_k \boldsymbol{W}_k, \tag{3}$$

where the transition matrix between the states at kth and $k+1$th time vector is modified to $\boldsymbol{\Phi} = \begin{bmatrix} \alpha_k & \rho_k \\ \delta_k & \beta_k \end{bmatrix}$ where ρ_k and δ_k represent the cross correlation

between the gain and offset in consecutive vectors of observation, respectively. The stability of the system of (3) is given by $|\lambda_i(\Phi_k)| < 1$, i.e., the product of the eigenvalues must be lower than 1. Note that if we multiplied (3) by $\boldsymbol{X}_{k+1-l}$ and applying the expectation value we obtain

$$E\left[\boldsymbol{X}_{k+1}\boldsymbol{X}_{k+1-l}^T\right] = \boldsymbol{\Phi}_k E\left[\boldsymbol{X}_k\boldsymbol{X}_{k+1-l}^T\right] + G_k E\left[\boldsymbol{W}_k\boldsymbol{W}_{k-l}^T\right] G_k^T, \qquad (4)$$

where $l = 0, 1, ...$ For a complete knowledge of the generalized Gauss-Markov model we need to determine the $\boldsymbol{G}_k$ and $\boldsymbol{\Phi}_k$ matrices. Now, in the next sections we present the development of the (4) on two cases: when $l = 0$ and when $l > 0$. The first case permits found the matrix $\boldsymbol{G}_k$ and the second case, permit found an expression for the transition matrix $\boldsymbol{\Phi}_k$.

3.1   Solution for G_k: Case Where $l = 0$

In this case, setting $l = 0$, using (3) for $\boldsymbol{X}_{k+1}$, and replacing on (4) we obtain

$$E\left[\boldsymbol{X}_{k+1}\boldsymbol{X}_{k+1}^T\right] = \boldsymbol{\Phi}_k E\left[\boldsymbol{X}_k\boldsymbol{X}_k^T\right] \boldsymbol{\Phi}_k^T + G_k E\left[\boldsymbol{W}_k\boldsymbol{W}_k^T\right] G_k^T, \qquad (5)$$

and solve (5) for $E\left[\boldsymbol{W}_k\boldsymbol{W}_k^T\right]$ we obtain that

$$E\left[\boldsymbol{W}_k\boldsymbol{W}_k^T\right] = G_k^{-1}\left\{E\left[\boldsymbol{X}_{k+1}\boldsymbol{X}_{k+1}^T\right] - \boldsymbol{\Phi}_k E\left[\boldsymbol{X}_k\boldsymbol{X}_k^T\right] \boldsymbol{\Phi}_k^T\right\} G_k^{-1}{}^T, \qquad (6)$$

and assuming that X_k is a stationary random variable

$$E\left[\boldsymbol{X}_{k+1}\boldsymbol{X}_{k+1}^T\right] = E\left[\boldsymbol{X}_k\boldsymbol{X}_k^T\right] = \begin{bmatrix} \sigma_a^2 & \sigma_{ab} \\ \sigma_{ab} & \sigma_b^2 \end{bmatrix}$$

and

$$E\left[\boldsymbol{X}_{k+1}\boldsymbol{X}_{k+1}^T\right] - \boldsymbol{\Phi}_k E\left[\boldsymbol{X}_k\boldsymbol{X}_k^T\right] \boldsymbol{\Phi}_k^T = \begin{bmatrix} \sigma_1^2 & \sigma_0^2 \\ \sigma_0^2 & \sigma_2^2 \end{bmatrix}$$

where $\sigma_0^2 = (1 - \alpha\beta - \delta\rho)\sigma_{ab} - \alpha\beta\sigma_a^2 - \rho\beta\sigma_b^2$, $\sigma_1^2 = (1 - \alpha^2)\sigma_a^2 - 2\alpha\rho\sigma_a b - \rho^2\sigma_b^2$ and $\sigma_2^2 = (1 - \beta^2)\sigma_b^2 - 2\beta\delta\sigma_a b - \delta^2\sigma_a^2$, and considering $\boldsymbol{G}_k = \begin{bmatrix} 1 & g_{12} \\ g_{21} & 1 \end{bmatrix}$ we found that

$$E\left[\boldsymbol{W}_k\boldsymbol{W}_k^T\right] = \begin{bmatrix} \sigma_{wa}^2 & 0 \\ 0 & \sigma_{wb}^2 \end{bmatrix}$$

i.e., $\boldsymbol{W}_k$ is uncorrelated only if g_{12} and g_{21} satisfies that

$$g_{12} - \frac{g_{21}\sigma_1^2 - \sigma_0^2}{g_{21}\sigma_0^2 - \sigma_2^2} = 0,$$

with $\sigma_{wa}^2 = \sigma_1^2 - 2g_{12}\sigma_0^2 + g_{12}\sigma_2^2$ and $\sigma_{wb}^2 = \sigma_2^2 - 2g_{21}\sigma_0^2 + g_{21}\sigma_1^2$. For example, if $g_{21} = 0$ then $g_{12} = \frac{\sigma_0^2}{\sigma_2^2}$ and

$$G_k = \begin{bmatrix} 1 & \frac{\sigma_0^2}{\sigma_2^2} \\ 0 & 1 \end{bmatrix}, \tag{7}$$

which implies that the W_k is uncorrelated. Similarly, the expectation of W_k can be obtained from (3) by means

$$E[W_k] = G_k^{-1}[I - \Phi_k]E[X_k] = G_k^{-1}[I - \Phi_k]E[X_0].$$

3.2   Solution for Φ_k: Case Where $l > 0$

In this case, replacing $l > 0$ on (4) we obtain

$$E\left[X_{k+1}X_{k+1-l}^T\right] = \Phi_k E\left[X_k X_{k+1-l}^T\right], \tag{8}$$

and expanding (8) on each elements of X, using correlation function notation and solve for Φ_k we obtain

$$\Phi_k = \begin{bmatrix} R_{X^{(1)}X^{(1)}}(l) & R_{X^{(1)}X^{(2)}}(l) \\ R_{X^{(2)}X^{(1)}}(l) & R_{X^{(2)}X^{(2)}}(l) \end{bmatrix} \begin{bmatrix} R_{X^{(1)}X^{(1)}}(l-1) & R_{X^{(1)}X^{(2)}}(l-1) \\ R_{X^{(2)}X^{(1)}}(l-1) & R_{X^{(2)}X^{(2)}}(l-1) \end{bmatrix}^{-1}, \tag{9}$$

or

$$\Phi_k = R_X(l)R_X^{-1}(l-1). \tag{10}$$

Note that in [5] they assume that gain and offset are uncorrelated, $\alpha_0 = \alpha_1 = ... = \alpha_k = \alpha$ and $\beta_0 = \beta_1 = ... = \beta_k = \beta$. Replacing this assumption on (9) results

$$\Phi_k = \begin{bmatrix} \frac{R_{(1)(1)}(l)}{R_{(1)(1)}(l-1)} & 0 \\ 0 & \frac{R_{(2)(2)}(l)}{R_{(2)(2)}(l-1)} \end{bmatrix} = \begin{bmatrix} \alpha & 0 \\ 0 & \beta \end{bmatrix}, \tag{11}$$

this mean that the gain and offset are signals with exponential correlation function, i.e., following a Gauss-Markov model given in (1). Note that (11) correspond a particular case of (9), called the generalized transition matrix. In the next section we present the methodology to obtain an estimation of Φ using (10), i.e., based on estimate the correlation functions $R_X(l)$ and $R_X(l-1)$ obtained using some NUC published method.

4   Estimation and Validation of the Generalized Model

In this section we obtain an estimation of Φ_k from (10) using three NUC published method: the neural networks approach [1,2,3,4], nonlinear filtering [7,8]

and statistical algorithm [9]. Briefly, the neural networks approach use a hidden layer like a two-point NUC neurons that models the gain and offset of each detectors. This NUC technique is derived using and adaptive least-square (LMS) approach, making it a comparison between neighboring pixels as new frames of data are input (the retina-like processing). The second NUC method, nonlinear filtering, is used to obtain an individual estimation of gain and offset with recursive least-square (RLS) based on minimizing the error between a preliminary true scene estimation and the corresponding frame corrected for each pixel. This preliminary estimation of true irradiance is performed by a spatial nonuniformity filtering of readout data reducing the spatial signal resolution that is restored by the RLS algorithm. Both NUC methods, LMS and RLS based, perform the detector parameters estimation in a frame by frame basis. On the other hand, the statistical algorithm assumes that the irradiance at each detector is a uniformly distributed random variable and that the gain and offset are temporally constant within certain blocks of time. This mean that the gain and offset estimation is performed in a block of frame basis, i.e., when a new block of raw data arrives, the method perform the NU correction by a finite-impulse response filter and then, the temporal filter is adapted to the changes in the detector parameters and the gain and offset are updated to the next arrivals of raw data.

Now, to obtain an estimation for the gain and offset $(X^{(1)}, X^{(2)})$ we use real infrared data captured by the 128×128 InSb FPA cooled camera (Amber Model AE-4128) operating in $3 - 5\mu m$ range. The sequences were collected at 1 PM with 3000 frames collected at a rate of 30 frames/s and each pixel was quantized in 16 bit integers. Using this raw data, we able to estimate for each method the detector parameters correlation function $\boldsymbol{R_X}(1)$ and $\boldsymbol{R_X}(0)$ to obtain a suitable estimation of $\boldsymbol{\Phi}_k$. Additionally, in this work we assume that $\boldsymbol{\Phi}_0 = \boldsymbol{\Phi}_1 = ... = \boldsymbol{\Phi}_k = \boldsymbol{\Phi}$. Now, the correlation function between X^i and X^j with $i = 1, 2$ and $j = 1, 2$, can be estimated by [10]

$$\hat{R}^n_{X^{(\ )}X^{(\ )}}(l') = \frac{1}{n} \sum_{k=0}^{n-1} X^{(i)}(k)X^{(j)}(k+l') \tag{12}$$

where $\hat{R}^n_{X^{(\ )}X^{(\ )}}(l')$ is the estimation for $R_{X^{(\ )}X^{(\ )}}(1)$ and $R_{X^{(\ )}X^{(\ )}}(0)$ when $i = 1, 2$, $j = 1, 2$ and $l' = 0, 1$. In (12) the knowledge of $X^{(1)}$ and $X^{(2)}$ at each time k is required. Since from the three NUC method we have an estimation of the gain and offset we can express (12) by the following recursive algorithm

$$\hat{R}^n_{X^{(\ )}X^{(\ )}}(l') = \frac{n-1}{n} \hat{R}^{n-1}_{X^{(\ )}X^{(\ )}}(l') + \frac{1}{n} X^{(i)}(n-1)X^{(j)}(n-1+l'), \tag{13}$$

and then, using (9) we finally obtain the estimated $\boldsymbol{\Phi}$ for each method.

In summary, to obtain an estimation for $\boldsymbol{\Phi}$ we needed to make the following steps: i) using real infrared sequence captured by Amber camera, estimate the gain and offset by three NUC methods, ii) estimate the correlation function for $\boldsymbol{R_X}(1)$ and $\boldsymbol{R_X}(0)$ using (13) and finally, iii) obtain the estimated $\boldsymbol{\Phi}$ for each method using (10).

To validate the parameters of each model, we considered two aspect: the NUC performance and the estimation error. For study the NUC capability of each model we use the roughness parameters defined by

$$\rho(f) = \frac{||h * f||_1 + ||h^T * f||_1}{||f||_1}, \tag{14}$$

where h is a horizontal mask, $||f||_1$ is the L_1 norm of frame f and $*$ represents discrete convolution. In the other hand, to validate the model we use equation (2) in order to calculate the mean-square error (MSE) between the raw data $\mathbf{Y}_k$ and the estimation $\hat{\mathbf{Y}}_k(\mathbf{\Phi}^j)$ for each model, given by [11]

$$MSE = \frac{1}{N} \sum_{k=0}^{N-1} \left[\mathbf{Y}_k - \hat{\mathbf{Y}}_k(\mathbf{\Phi}^j)\right]^T \left[\mathbf{Y}_k - \hat{\mathbf{Y}}_k(\mathbf{\Phi}^j)\right], \tag{15}$$

where $\hat{\mathbf{Y}}_k(\mathbf{\Phi}^j) = \mathbf{HX}_k = \mathbf{H\Phi X}_{k-1}$ is the *a priori* estimate of $\hat{\mathbf{Y}}_k$ based on the model $\mathbf{\Phi}^j$ for $j = 1, 2, 3$.

Table 1. Result on Validation for different models

Model	$|\lambda_i(\phi^j)|$	$\rho(f)$	MSE
$\mathbf{\Phi}^1$	7.59×10^{-9}	2.2425	0.8844
$\mathbf{\Phi}^2$	0.2353	2.2127	0.8591
$\mathbf{\Phi}^3$	0.0244	2.1313	0.1909

Following the previous procedure we obtain three generalized models corresponding to each NUC algorithm given by:

$$\mathbf{\Phi}^1 = \begin{bmatrix} 0.5026 & -0.5026 \\ -0.5026 & 0.5026 \end{bmatrix} \tag{16}$$

$$\mathbf{\Phi}^2 = \begin{bmatrix} 0.8834 & -0.7384 \\ -0.7384 & 0.8835 \end{bmatrix} \tag{17}$$

$$\mathbf{\Phi}^3 = \begin{bmatrix} 0.6031 & -0.5505 \\ -0.1252 & 0.1548 \end{bmatrix} \tag{18}$$

where $\mathbf{\Phi}^1, \mathbf{\Phi}^2$ and $\mathbf{\Phi}^3$ correspond to the model obtained with neural network approach, nonlinear filtering and statistical algorithm respectively. Note that all NUC methods presented are stable (see Table 1) and shows that $X^{(1)}$ and $X^{(2)}$ are correlated. This mean that the assumption that the gain and offset in consecutive vector of observation are uncorrelated is not valid. Even more, whereas LMS and RLS algorithm exhibit a large correlation, the statistical algorithm shows that the gain strongly is influenced by the gain and offset of the previous state, i.e., we can assume that the offset indirectly is estimate from gain. It is very important conclusion because we need the knowledge only of one state to reduce NU.
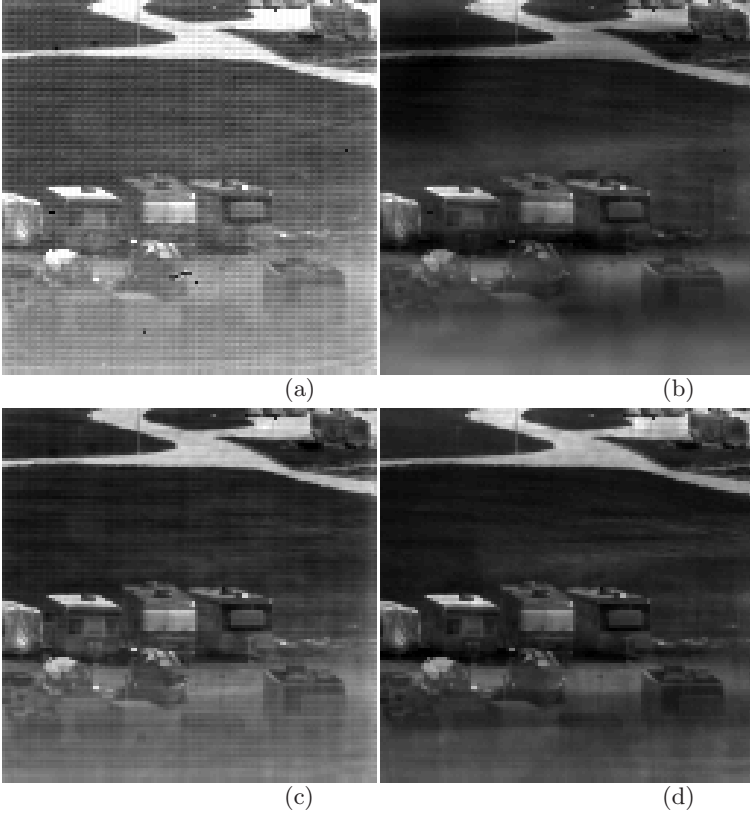
Fig. 1. The $2220 - th$ frame form 1 PM sequence captured with Amber infrared camera: a) the corrupted raw frame, corrected frame with b) neural network approach, c) nonlinear filtering, and d) statistical algorithm. It can be seen by using only the naked eyes that a good NUC is obtained from the three NUC methods.

In Table 1, the $|\lambda_i(\varPhi^j)|$ for each model, spatial average of ρ and MSE parameters are presented. We can observe that the best performance is obtained for statistical algorithm ($\varPhi^3$). Additionally, from equations (16),(17) and (18) we can observe that as the magnitude of the drift between the gain (offset) at state k and state $k+1$ is more different (i.e., the correlation between gain and offset is considered), the NU correction and the model estimation are improved. This in addition confirms the assumption of the gain and offset are temporally constant in a block of time. Finally, for illustration proposed, the LMS-based, RLS-based and statistical algorithm were applied to the 2220-frame image sequence, and the results is shown in Figure 1. In this figure, Fig. 1(a) correspond to the corrupted frames, Fig. 1(b), Fig. 1(c) and Fig. 1(d) shows the corrected frames with neural network approach, nonlinear filtering, and statistical algorithm respectively. This figure clearly shows that the statistical method present a good reduction of FPN.

5   Conclusions

In this paper a study of correlation between gain and offset is present. It was shown experimentally using real IR data that the assumption of gain and offset is uncorrelated is not valid on some NUC scene-based method. Indeed, when the asymmetry is more notable in the generalized transition matrix, i.e., the magnitude of the drift between the gain (offset) at consecutive block of frames is more different, the method has shown an improved in reduction of nonuniformity and in estimation error. This allows to conclude that the gain and offset are temporally constant in a block of time and the gain and offset are correlated. From this assumption, we can reformulate the model present on [5]. Future work consider a generalized Gauss-Markov model by obtain an adaptive estimation of nonuniformity using a Kalman filter and an evaluation to compare with uncorrelated Gauss-Markov model.

References

1. Scribner, D., Sarkady, K., Kruer, M.: Adaptive Nonuniformity Correction for Infrared Focal Plane Arrays using Neural Networks. Proceeding of SPIE. 1541, 100–109 (1991)
2. Scribner, D., Sarkady, K., Kruer, M.: Adaptive Retina-like Preprocessing for Imaging Detector Arrays. Proceeding of the IEEE International Conference on Neural Networks. 3, 1955–1960 (1993)
3. Torres, S., Vera, E., Reeves, R., Sobarzo, S.: Adaptive Scene-Based Nonuniformity Correction Method for Infrared Focal Plane Arrays. Proceeding of SPIE. 5076, 130–139 (2003)
4. Vera, E., Torres, S.: Fast Adaptive Nonuniformity Correction for Infrared Focal Plane Arrays. Journal on Applied Signal Processing EURASIP (2005)
5. Torres, S., Hayat, M.: Kalman Filtering for Adaptive Nonuniformity Correction in Infrared Focal Plane Arrays. The JOSA-A Opt. Soc. of America. 20, 470–480 (2003)
6. Torres, S., Pezoa, J., Hayat, M.: Scene-based Nonuniformity Correction for Focal Plane Arrays Using the Method of the Inverse Covariance Form. OSA App. Opt. Inf. Proc. 42, 5872–5881 (2003)
7. Torres, F., Torres, S., Martn, C.S.: A Recursive Least Square Adaptive Filter for Nonuniformity Correction of Infrared Image Sequences. In: Sanfeliu, A., Cortés, M.L. (eds.) CIARP 2005. LNCS, vol. 3773, pp. 540–546. Springer, Heidelberg (2005)
8. Torres, F., Martin, C.S., Torres, S.: A RLS Filter for Nonuniformity and Ghosting Correction of Infrared Image Sequences. Sequences. In: Martínez-Trinidad, J.F., Carrasco Ochoa, J.A., Kittler, J. (eds.) CIARP 2006. LNCS, vol. 4225, pp. 464–473. Springer, Heidelberg (2006)
9. Hayat, M., Torres, S., Amstrong, E., Cain, S., Yasuda, B.: Statistical Algorithm fo Nonuniformity Correction in Focal Plane Arrays. Applied Optics 38, 773–780 (1999)
10. Therrien, C.W.: Discrete Random Signal and Statistical Signal Processing. Prentice Hall Press, USA (1992)
11. Pezoa, J., Hayat, M., Torres, S., Rahman, M.: Multimodel Kalman Filtering for Adaptive Nonuniformity Correction in Infrared Sensors. JOSA A 23, 1282–1291 (2006)

A Cyclostationary Analysis Applied to Detection and Diagnosis of Faults in Helicopter Gearboxes[*]

Edgar Estupiñan[1], Paul White[2], and César San Martin[3,4]

[1] Department of Mechanical Engineering, Universidad de Tarapacá
Casilla 6-D, Arica, Chile
eestupin@uta.cl
[2] Institute of Sound and Vibration,University of Southampton
SO17-1BJ, Southampton - U.K.
prw@isvr.soton.ac.uk
[3]Department of Electrical Engineering, Universidad de Concepción
Casilla 160-C, Concepción, Chile
cesanmartin@udec.cl
[4]Department of Electrical Engineering, Universidad de La Frontera
Casilla 54-D, Temuco, Chile
csmarti@ufro.cl

Abstract. In several cases the vibration signals generated by rotating machines can be modeled as cyclostationary processes. A cyclostationary process is defined as a non-stationary process which has a periodic time variation in some of its statistics, and which can be characterized in terms of its order of periodicity. This study is focused on the use of cyclic spectral analysis, as a tool to analyze second-order periodicity signals (SOP), such as, those who are generated by either localized or distributed defects in bearings. Cyclic spectral analysis mainly consists of the estimation of the random aspects as well as the periodic behavior of a vibration signal, based on estimation of the spectral correlation density. The usefulness of cyclic spectral analysis for the condition monitoring of bearings, is demonstrated in this paper, through the analysis of several sections of vibration data collected during an endurance test of one of the two main gearbox transmissions of a helicopter.

Keywords: Signal Processing, condition monitoring, vibration analysis, cyclostationarity.

1 Introduction

A cyclostationary process is a non-stationary process which has a periodic time variation in some of its statistics. The framework of cyclostationarity provides

a powerful framework for modeling vibration signals from rotating machines. Such signals can be characterized by the different order of cyclostationarity they exhibit. In rotating machines, imbalances and misalignments can lead to vibrations that are examples of first-order periodicity processes (FOP). Whereas modulations generated by wear, friction forces or impact forces generate vibration signals that are second-order periodic (SOP) processes. To analyze FOP signals, different techniques such as the classical spectral analysis combined with time synchronous averaging can be employed. These methods provide powerful analysis tools suitable for many applications.

This study aims to consider the early detection faults in gearboxes, using vibration analysis, and exploiting the SOP structure of signals, through the use of cyclic spectral analysis. Cyclic spectral analysis involves the estimation of the random aspects of a signal as well as its periodic behavior. In this work the estimation of the spectral correlation density is computed using the averaged cyclic periodogram estimator [1,2]. The use of cyclostationarity for the detection and diagnosis of faults of bearings is demonstrated in this paper, through the analysis of vibration data registers from one of the two main gearboxes of an UH-60 Black Hawk helicopter.

This paper is organized as follows. In section 2 the cyclostationary analysis is presented. Section 3 presents the application of the cyclic spectral analysis to faults detection based on vibration signals processing. In section 4 we validate the proposed method using real vibration data register from gearboxes of an UH-60 Black Haw helicopter. In Section 5 the conclusions of the paper are summarized.

2 Cyclostationary Analysis

A cyclostationary process is considered as a stochastic process that exhibits some hidden periodicities, also called *periodically correlated* processes [3]. Non-stationary signals are considered cyclostationary when some of its statistics are periodic

$$f_x(x,t) = f_x(x, t+T), \tag{1}$$

where $f_x(x,t)$ denotes some appropriate, time varying, statistic of the signal. Some typical examples of cyclostationary signals are obtained through the periodic amplitude or frequency modulation of stationary processes.

A signal $x(t)$ is said to be n^{th} order cyclostationary with period T if its nth order moments exist and are periodic with period T. A signal with first-order periodicity is defined as one which has a finite-amplitude additive periodic component, and which consequently exhibits lines (Dirac delta functions) in its power spectral density. The FOP components can be separated from a signal through synchronous averaging. A pure FOP signal can be considered as being non-stationary in the sense that its mean is time-varying. Examples of FOP vibration signals that can be generated by rotating machines are imbalances, misalignments, anisotropic rotors, flexible coupling, etc. Some of the most common tools used to analyze (FOP) signals are: synchronous average, comb-filters, blind filters and adaptive comb-filters [4].

A signal with second-order periodicity (SOP) is defined as one which can be converted into a signal with FOP by a quadratic time invariant transformation [5]. These types of signals do not have a time-varying mean but do have a time-variant auto-correlation function. Stochastic processes with either amplitude or frequency modulation are typical examples of SOP signals. Faulty gearboxes may exhibit vibration signals that are amplitude modulated, leading to SOP, if, for example, the load being driven by the gearbox varies randomly.

Second order tools are based on the autocorrelation function. The instantaneous auto-correlation, the Wigner-Ville spectrum and the spectral correlation are second order tools, obtained from linear transformations of the autocorrelation function. For a cyclostationary signal $x(t)$, the auto-correlation function (ACF) is defined by

$$R_{xx}(t, \tau) = E\left\{x(t + \bar{\beta}\tau)x(t - \beta\tau)^*\right\}, \tag{2}$$

where $\bar{\beta} + \beta = 1$. If $x(t)$ is cyclostationary with cycle (or period) T, then the ACF is also a cyclic function of time, i.e.,

$$R_{xx}(t, \tau) = R_{xx}(t + T, \tau), \tag{3}$$

and it can be expanded into their Fourier series and the Fourier coefficients of the ACF correspond to the cyclic ACF (CACF) given by

$$R_{xx}(\tau, \alpha) = \int R(t, \tau)e^{-j2\pi\alpha t}dt, \tag{4}$$

where α correspond to the cyclic frequencies. The CACF gives an indication of how much energy in the signal is due to cyclostationarity at each frequency α. Note that for $\alpha = 0$, the CACF yields the conventional auto-correlation function. The Fourier transform of the CACF is known as the cyclic power spectrum given by

$$S_{xx}^{\alpha}(\alpha, f) = \int R_{xx}(\tau, \alpha)e^{-j2\pi f\tau}d\tau, \tag{5}$$

and we can note that the spectral correlation is a continuous function in frequency f and a discrete function in terms of the cyclic frequency α. For the case $\alpha = 0$, the cyclic spectrum reduces to the classical power spectrum or spectral density function (through the Wiener-Khinchin relation) [3].

In the next section we introduce the cyclostationary analysis applied to the gearboxes and bearings, showing the potential of this analysis tools of detection and diagnosis of fault using vibration signals.

3   Cyclic Spectral Analysis Applied to Faults Detections

In several cases the vibration signals generated by rotating machines can be modeled as cyclostationary processes. For instance, cyclic spectral analysis results in appropriate tool to provide a statistical description of the random aspects of a

cyclostationary vibration signal, as well as a description of the periodic behavior. In this work, we focused on vibrational signals measured from two rotating machines: gearbox and rolling bearings.

The vibration signals measured from a gearbox typically exhibit cyclostationarity of second and higher-orders. However, usually these components normally have a negligible energy when compared to the strong periodic signal generated by the meshing of the teeth. For this reason, it is important to subtract the synchronous average of the signal (FOP components) before analyzing the SOP cyclostationarity [4]. Vibrations generated by gears are typically polycyclostationary, since many different periodicities and periodic modulations associated with several rotating parts may be present in the raw signal.

For the rolling bearings signals, they usually exhibit a second order cyclostationary behavior, with the presence of localized as well as distributed defects [6]. In the case of localized defects in rolling bearings, a series of impacts are produced whose rate of repetition depends on their location. However, these impacts are not precisely periodic due to random slippage on each rotation; to reflect this effect the process is more correctly referred to as quasi-cyclostationary [7]. Further, the amplitude of the impacts can be modulated by the rotations of the inner race, outer race or the cage.

In practice, digital signal processing algorithms are required to estimate the cyclic-statistics of a cyclostationary process. In this paper we use the *Averaged Cyclic Periodogram* (ACP), which is one of the most common estimators used to estimate the spectral correlation function, because of its high computational efficiency [1,2]. In the cyclic spectrum, the cyclic frequencies α, are multiples of the reciprocal of the period of the cyclostationarity. The ACP is defined by the expression

$$S_{xx}(f,\alpha) = \frac{1}{K\Delta_t} \sum_{K}^{k=1} X_N^{(k)}\left(f + \bar{\beta}\alpha\right) X_N^{(k)}\left(f + \beta\alpha\right)^*, \tag{6}$$

where $X_N^{(k)}$ is the discrete time Fourier transform of the *kth* sequence. In order to mitigate the effect of cyclic leakage, an overlap between adjacent segments of the signal should be incorporated. When a Hanning or Hamming data window is used, the overlap should be $\geq 67\%$, in order to minimize the presence of cyclic leakage [1].

The cyclic coherence function is a useful tool for analysis of cyclostationary signals, to determine the strength of the correlation between spectral components spaced apart by cyclic frequencies. The cyclic coherence function is normalized between 0 and 1, similarly to the spectral coherence. The cyclic coherence function for a single signal can be calculated from:

$$\Gamma_{xx}(f,\alpha) = \frac{S_{xx}(f,\alpha)}{\left[S_x^0(f + \bar{\beta}\alpha)S_x^0(f - \bar{\beta}\alpha)\right]^{1/2}}. \tag{7}$$

4 Detection Faults in Helicopter Gearbox Using Cyclic Spectral Analysis

In this section, sixty two vibration data registers of one of the two main gearboxes of an UH-60 Black Hawk helicopter have been analyzed using second order tools to identify the presence of cyclostationarity. The UH-60 Black Hawk main gearbox transmission is a complex system, composed of different gear transmissions, as it is shown in figure 1. This study is focus on the analysis of a fault detected in the inboard roller bearing SB-2205, which supports the combining bevel pinion in one of the input modules (see figure 2a). A fault in this bearing is particularly challenging since it is located deep inside the gearbox and the background noise may hidden the spectral components produced by the presence of a fault. Besides, the vibratory signal is also affected by the periodical components produced by the gear transmissions.
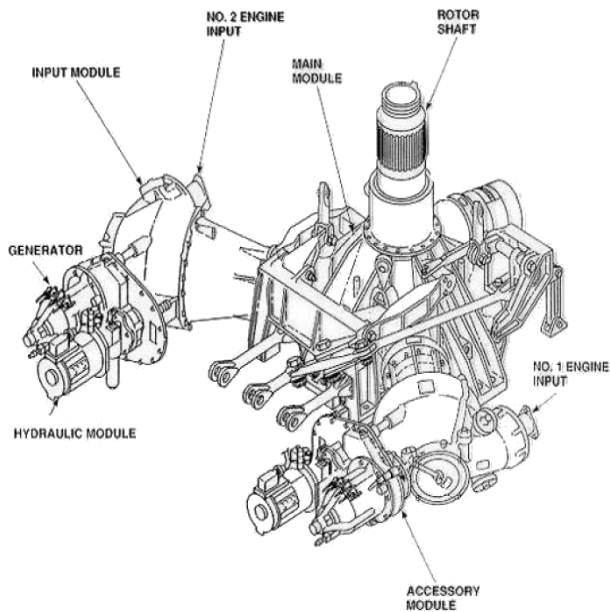
Fig. 1. Black Hawk's Main transmission

The vibration data were recorded during a component endurance test, carried out at Patuxent River, M.D. [8]. Accelerometers were used to acquire the data during the endurance test, at a rate of $100k$Hz. Only the recordings within $\pm 10\%$ of the full torque condition (sixty two data sets, each of 10 seconds duration), were used for this study. During this endurance test severe degradation of the inboard bearing SB-2205 occurred, and six chip lights were retrieved. The first gearbox chip light went on after 10200 minutes of run time had elapsed (which

corresponds to the data set index No. 40). Figure 2b shows a photograph of showing the final condition of the bearing rollers on completion of the endurance test.

A previous study analysing these vibration data was carried out by McInerny [9], which included the computation of power spectral densities and envelope spectra for selected frequency bands as well as trend plots of global indexes such as, deviation standard, kurtosis and wavelet coefficients. It was shown by McInerny that spectral components linked to the cage fault frequency (FTF) were identified in the envelope spectra for some frequency bands. It was also shown that the global indexes calculated showed an evident increase. However, spectral components directly related to the fault in the balls (ball spin frequencies, BSF), were not found.

(a)   (b)
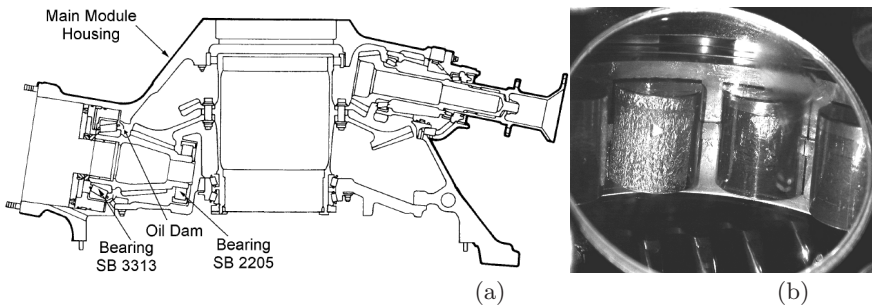
Fig. 2. a) Location of the SB-2205 bearing. b) Condition of the bearing rollers at the end of the endurance test.

In the present study, cyclic spectra and cyclic coherence functions were computed for all the sixty two vibration data registers recorded during the endurance test using equations (6) and (7). Before computing the cyclic spectra of the data, an adaptive strategy based on Adaptive Line Enhancer (ALE) was applied previously, to separate the FOP components and to focus the cyclostationary analysis on the residual signals [10,11]. To illustrate this process of filtering, Figure 3, shows the spectra of the residual signal (error signal, e_k) and the filter output (y_k), after the ALE filter was applied to the vibration data register No. 42 (one of the data registers recorded after the first chip light went on).

To illustrate the results obtained with the cyclic spectral analysis, Figures 4 and 5, show the cyclic coherence function for the residual signal of data set registers No. 08 and No. 42 respectively. As it can be seen in figure 5, the cyclic coherence function revealed the existence of cyclic harmonics (hidden periodicities) linked with the ball spin frequency (2×BSF=361.5Hz) and the fault cage frequency (FTF=35.5Hz) of the inboard roller bearing. Besides, a detailed analysis of the cyclic spectrum let identified, sidebands spaced apart at $\alpha = 35.5$Hz (FTF) around the harmonics at 1×BSF and 2×BSF, indicating some degree of modulation. This cyclic harmonic structure is exactly similar to spectral harmonic structure (f domain) expected for a bearing with defects in the rollers [12].
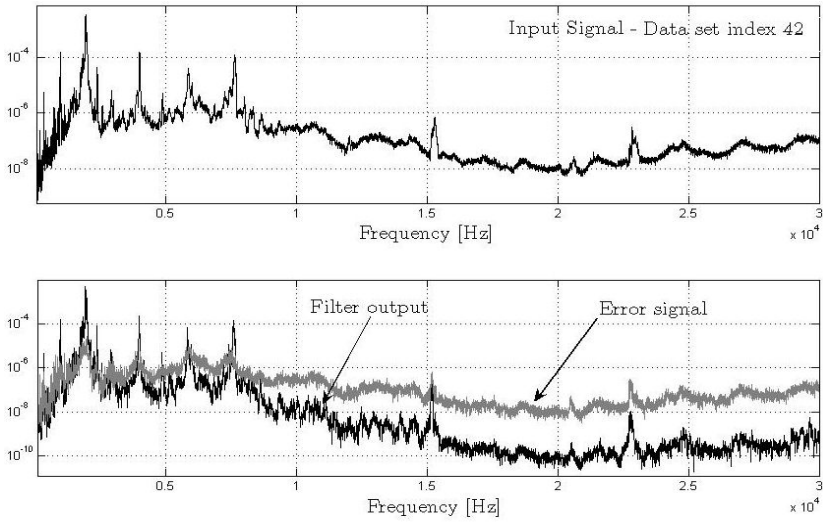
Fig. 3. Adaptive Line Enhancer (ALE), applied to one of the vibration data set, after the first chip light
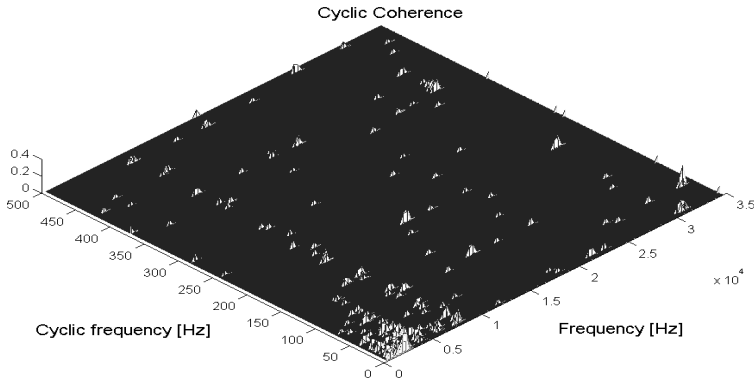
Fig. 4. Cyclic coherence function of fault-free case - Data set index 08. (Only values above 7.5% significance level are displayed).

It is important also to mention that these cyclic spectral components were not present in the cyclic coherence function when it was computed during the initial stages of the endurance test (see figure 4).

Additionally to the analysis of the spectral correlation functions, the cyclic spectra were compared for two different stages of fault, when they were computed at specific cyclic frequencies, linked to the fault bearing frequencies and the shaft rotational speed, as it is suggested in previous studies [2][3]. The results obtained are shown in figure 6. A considerable increase in the cyclostationary energy at the cyclic frequencies related to fault bearing frequencies was detected, as it can be seen in figures 6b, 6c and 6d, which suggests that the cyclic spectra
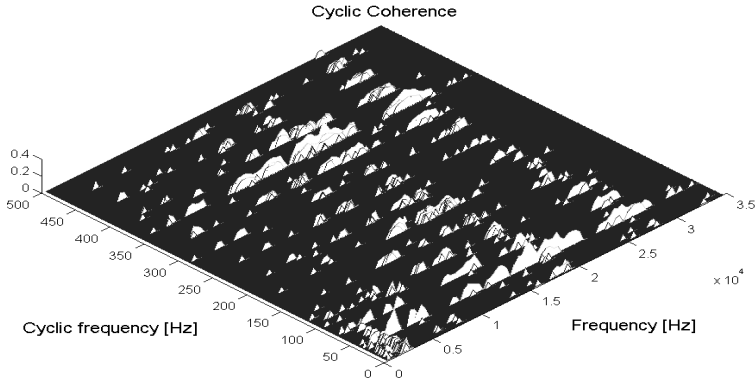
Fig. 5. Cyclic coherence function of faulty case - Data set index 42. (Only values above 7.5% significance level are displayed).
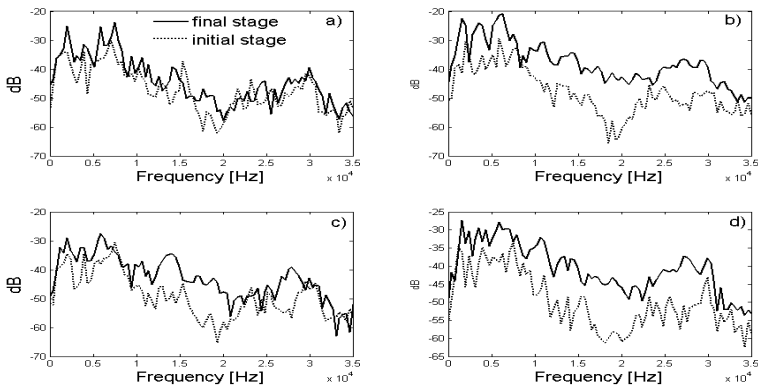
Fig. 6. Cyclic spectra computed at the cyclic frequencies: a) a=95.5 Hz (shaft rotational speed), b) a=35.5 Hz (1xFTF), c) a=180.5Hz (1xBSF), d) a=361.5Hz (2xBSF)

computed at expected fault cyclic frequencies might be used as an indicator of damage intensity. Figure 6a, shows not evidence of increasing of the cyclostationary energy, indicating that the fault in this case is not related to the rotational frequency.

These last results suggest that the change of cyclostationarity should be not only analyzed for $\alpha = \Omega$ [11,13] and better results could be obtained when the change of cyclostationairty is analyzed at cyclic frequencies related to the fault bearing frequencies. These results also confirm the SOP cyclostationary behavior of fault bearings, which has been demonstrated in [7,13]. The SOP in fault bearings is caused mainly to the small randomness caused for the usual slip of the rolling elements and the cage. Therefore, the separation of vibrations produced by faults in gears (mainly in FOP components) from vibrations produced by faulty bearings (mainly SOP components) is a crucial aspect of the diagnosis of faults.
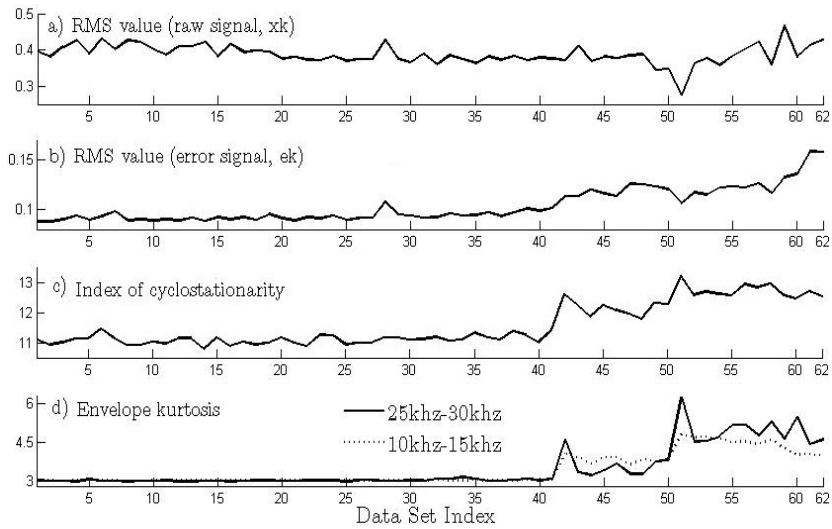
Fig. 7. Global indexes computed for all the vibration data sets

Finally, and to complement the cyclic spectral analysis, different global statistical metrics were computed for all of the data set indexes. It can be seen in figure 7, that the RMS energy computed for the raw signals does not show evidence of great changes during all of the endurance tests. However, the other metrics shown demonstrate an evident increase, especially in the latter stages of the endurance tests, and after the first chip light. The index of cyclostationarity (8) and the envelope kurtosis (computed for two bandwidth frequencies) display the highest increase at the time when the first chip light went on, and only the RMS value computed for the error signal displays some transient increases in an early data set.

5 Conclusions

This study has demonstrated that cyclostationary analysis combined with an appropriate adaptive scheme, or another tool, to remove the FOP components from the signal, can be an efficiently tool to be applied to the vibration monitoring of rotating systems such as the gearbox of a helicopter.

This study has characterized properly the fault of the SB-2205 roller bearing produced during endurance tests of the UH-60A helicopter main gearbox. Through the computation of the cyclic coherence functions the fault frequencies of the bearing (cyclic spectral components at BSF), were detected, in contrast with a previous studies were they were not detected. Besides, an index of cyclostationarity is used as a global indicator and compared with the RMS global value, it demonstrates to have a better sensitivity to the presence of a fault.

Nevertheless, further work should be focus on the testing of these indexes in more detail.

In this study the ACP was used as an estimator for the computation of the spectral correlation density, due to its high computational efficiency, however other estimators should be compared.

References

1. Boustani, R.: Sèparation aveugleà l'ordre deux de sources cyclostationnaires: application aux mesures vibroacoustiques. PhD Thesis, Universitè de Technologie Compiégne (2005)
2. Antoni, J.: Cyclic spectral analysis into practice. Mechanical Systems and Signal Processing 21(2), 597–630 (2007)
3. Gardner, W., Napolitano, A., Paura, L.: Cyclostationary: half a century of research. Signal Processing 86(4), 639–697 (2006)
4. Antoni, J., Bonnardot, F., Raad, A., El Badaoui, M.: Cyclostationary modelling of rotative machine vibration signals. Mechanical System and Signal Processing. 18(6), 1285–1314 (2004)
5. Gardner, W.: Statistical Spectral Analysis. Prentice-Hall, Englewood Cliffs (1991)
6. Bonnardot, F., Randall, R.B., Guillet, F.: Extraction of second- order cyclostationarity sources - Application to vibration analysis. Mechanical System and Signal Processing 19, 1230–1244 (2005)
7. Randall, B., Antoni, J., Chobsaard, S.: The relationship between spectral correlation and envelope analysis in the diagnostics of bearing faults and other cyclostationary machine signals. Mechanical Systems and Signal Processing 15(5), 945–962 (2001)
8. Dawson, F., Killian, K.: Alternate Source Endurance Qualification Test of UH-60 Black Hawk Transmission, Test Report. NAWCAD, Patuxent River, MD (June 2001)
9. McInerny, S.A., Hardman, B., Sun, Q.: Investigation of fault detection algorithms applied to a helicopter input pinion bearing. Technical Report (2004)
10. Lee, S., White, P.: The enhancement of impulsive noise and vibration signals for fault detection in rotating and reciprocating machinery. Journal of Sound and Vibration 217(3), 485–505 (1998)
11. Randall, R.B.: Detection and diagnosis of incipient bearing failure in helicopter gearboxes. Engineering Failure Analysis 11(2), 177–190 (2004)
12. McFadden, P.D., Smith, J.D.: Vibration monitoring of rolling element bearings by the high frequency resonance technique - a review. Tribology International 17(1) (1984)
13. Antoni, J., Randall, R.B.: Differential diagnosis of gear and bearing faults. Journal of Vibration and Acoustics 124(2), 1–7 (2002)

Robust Industrial Machine Sounds Identification Based on Frequency Spectrum Analysis

Antoni Grau, Yolanda Bolea, and Manuel Manzanares

Automatic Control Dept, Technical University of Catalonia UPC, Barcelona, Spain
{antoni.grau,yolanda.bolea,manolo.manzanares}@upc.edu

Abstract. In order to discriminate and identify different industrial machine sounds corrupted with heavy non-stationary and non-Gaussian perturbations (high noise, speech, etc.), a new methodology is proposed in this article. From every sound signal a set of features is extracted based on its denoised frequency spectrum using Morlet wavelet transformation (CWT), and the distance between feature vectors is used to identify the signals and their noisy versions. This methodology has been tested with real sounds, and it has been validated with corrupted sounds with very low signal-noise ratio (SNR) values, demonstrating the method's robustness.

Keywords: wavelets, Fast Fourier Transformation, non-speech sound.

1 Introduction

A common problem encountered in industrial environments is that the electric machine sounds are often corrupted by non-stationary and non-Gaussian interferences such as speech signals, environmental noise, background noise, etc. Consequently, pure machine sounds may be difficult to identify using conventional frequency domain analysis techniques as Fourier transform [1], and statistical techniques such as Independent Component Analysis (ICA) [2]. It is generally difficult to extract hidden features from the data measured using conventional spectral techniques because of the weak amplitude and short duration of structural electric machine signals, and very often the feature sound of the machine is immersed in heavy perturbations producing hard changes in the original sound. For these reasons, the wavelet transform has attracted increasing attention in recent years for its ability in signal features extraction [3][4], and noise elimination [5]. While in many mechanical dynamic signals, such as the acoustical signals of an engine, Donoho's method seems rather ineffective, the reason for their inefficiency is that the feature of the mechanical signals is not considered. Therefore, when the idea of Donoho's method and the sound feature are combined, and a de-noising method based on the Morlet wavelet is added, this methodology becomes very effective when applied to an engine sound detection [6].

In this work, we propose a new approach in order to identify different industrial machine sounds, which can be affected by non-stationary noise sources. This paper is organized as follows. In Section 2 the proposed methodology is overviewed. Next the

Morlet wavelet transform for denoising the acoustical signals is explained as well as the feature extraction procedure. Some interesting experimental results are presented.

2   Methodology

In this section the proposed methodology to identify machine sounds highly corrupted with non-stationary and non-Gaussian perturbations is presented. The original sounds corrupted with noise will be denoted as "noisy" sounds. The procedure consists of the following steps:

1) Given a certain number of "original" sounds recorded from different machines, they will be heavily corrupted with different non-stationary non-Gaussian noises giving different SNR (signal-noise ratio). The problem is that in the temporal space it is impossible to distinguish between two corrupted signals. Due to this reason, we propose the step 2.
2) We will need to work in the frequency space. In order to overcome the lack of identification among noisy sounds, a denoised version is proposed in this article. To carry out the purification (denoising) process, the Morlet wavelet transform (Section 3) will be used as a filter step. A reconstructed version of the noisy signal is generated after a filtering operation, setting to zero some of the wavelet coefficients. Therefore, the frequency spectrum of this denoised signal will be used as a source of the feature extraction process.
3) The features extracted from the frequency spectrum are the basis for identifying the original sounds. This procedure will be done by calculating the distance between the feature vectors extracted from the original signal and the denoised one.
4) To evaluate the robustness of our methodology, we proceed reducing the SNR level (increasing the level of noise) until the distance between the original and its denoised signal exceeds two values: first, the value of the distance between the original signal and its noisy version (d(si, si_denoised)>d(si, si_noisy)), and second, the value of the distance between the original signal and a denoised signal coming from another original signal (d(si, si_denoised)>d(si, sj_denoised)), being si and sj two different original signals. This fact demonstrates the robustness of the proposed methodology because high levels of noise can be added without misidentifying the signals.

3   Wavelet Transform and Feature Extraction

3.1   Review of Wavelet Transform

The wavelet was originally introduced by Goupilland et al. in 1984 [7]. Let $\psi(t)$ be the basic wavelet function or the mother wavelet, then the corresponding family of daughter wavelets consists of

$$\psi_{a,b}(t) = |a|^{-1/2} \psi\left(\frac{t-b}{a}\right) \tag{1}$$

where a is the scale factor and b the time location, and the factor $|a|^{-1/2}$ is used to ensure energy preservation.

The wavelet transform of signal $x(t)$ is defined as the inner product in the Hilbert space of the L^2 norm, as shown in the following equation

$$W(a,b) = \langle \psi_{a,b}(t), x(t) \rangle = |a|^{-1/2} \int x(t) \psi_{a,b}^* dt \tag{2}$$

Here the asterisk stands for complex conjugate. Time parameter b and scale parameter a vary continuously, so that transform defined by Eq. (2) is also called a continuous wavelet transform, or CWT. The wavelet transform coefficients $W(a,b)$ can be considered as functions of translation b for each fixed scale a, which give the information of $x(t)$ at different levels of resolution. The wavelet coefficients $W(a,b)$ also measure the similarity between the signal $x(t)$ and each daughter wavelet $\psi_{a,b}(t)$. This implies that wavelets can be used for feature discovery if the wavelet used is close enough to the feature components hidden in the signal.

For many mechanical acoustic signals impulse components often correspond to the feature sound. Thus, the basic wavelet used for feature extraction should be similar to an impulse. The Morlet wavelet is such a wavelet defined as

$$\psi(t) = \exp(-\beta^2 t^2 / 2) \cos(\pi t) \tag{3}$$

3.2 Feature Extraction Using the Morlet Wavelet

The most popular algorithm of wavelet transform is the Mallat algorithm. Though this algorithm can save a lot of computations, it demands that the basic wavelet is orthogonal. The Morlet wavelet is not orthogonal. Thus, the wavelet transform of the Morlet wavelet has to be computed by the original definition, as shown in Eq. (2). Although the CWT brings about redundancy in the representation of the signal (a one-dimensional signal is mapped to a two-dimensional signal), it provides the possibility of reconstructing a signal. A simple inverse way is to use the Morlet's formula, which only requires a single integration. The formula is:

$$x(t) = C_\psi^{-1} \int W(a,b) \frac{da}{a^{3/2}} \tag{4}$$

where

$$C_{1\psi} = \int_{-\infty}^{\infty} \hat{\psi}^*(\omega) / |\omega| d\omega \tag{5}$$

It is valid when $x(t)$ is real and either $\psi(t)$ is analytic or $\hat{\psi}(\omega)$ is real. The condition is satisfied by the Morlet wavelet. If the wavelet coefficients $W(a,b)$, corresponding to feature components, could be acquired, we could obtain the feature components just by reconstructing these coefficients. In calculations, the feature coefficients should be reserved and the irrelevant ones set to zero, then the signal can be denoised by using formula Eq. (4). Thus, the key to obtaining the denoised signal is how to obtain these feature coefficients. A threshold T_w should be set in advance, but it is not evident to choose it properly. This threshold indicates the value from which wavelet coefficients

must be set to zero. The basic rule for threshold choice is that the higher the correlation between the random variables, the larger the threshold; and the higher the signal-noise ratio (SNR), the lower the threshold. In practice, the choice of the threshold T_w mainly depends on experience and knowledge about the signal. In fact, the quantitative relation between the threshold T_w and the SNR still remains an open question.

Since the sound signal is reconstructed with the modified wavelet coefficients, the frequency spectrum is calculated using the Fast Fourier Transform. In the results, it is easy to appreciate the good level of denoising that wavelet transform is yielding.
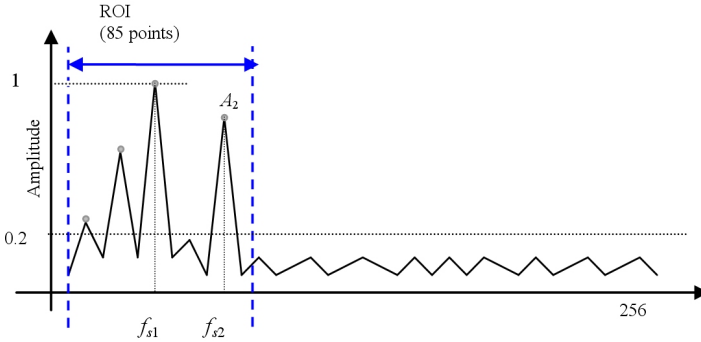
Fig. 1. Definition of features upon the frequency spectrum

Observing in detail such a spectrum, machine sounds have the characteristic of being formed by m harmonics with different amplitude and located at different frequencies. Therefore, these signals are divided in regions-of-interest (ROI) consisting of 85 points (over 256-point FFT). The width of the ROI is chosen so that this area is containing information enough to do the analysis and, consequently, the main fundamental harmonics in the signals can be found inside the ROI. A normalization step is done in the signal spectrums (between [0...1]). Due to the properties of mechanical acoustic signals, the most important parameters that we consider to characterize the machine sounds are: the frequency of the first harmonic (f_{s1}), the amplitude of the second harmonic (A_2) and the number of significant harmonics (with an amplitude > 0.2), note that the first harmonic amplitude will be always 1, that is, the maximal value of normalization. For every sound signal these three features will form the feature vector. In Fig. 1 the features can be observed over a generic spectrum. Nevertheless, other features have been tried such as the frequency of the second harmonic (f_{s2}) but the results do not improve.

3.3   Distance Between Feature Vectors

A distance measure is a function that associates a non-negative numeric value with (a pair of) sequences, with the idea that a short distance means greater similarity. Distance measures usually satisfy the mathematical axioms of a metric. In the Euclidean space $\Re^n$, the distance between two points is usually given by the Euclidean distance (2-norm distance). Other distances, based on other norms, are sometimes used instead. In this article we use the Minkowski distance of order 2 (2-norm distance) defined as:

$$d(x, y) = \sqrt{\sum_{i=1}^{n} |x_i - y_i|^2} \qquad (6)$$

for a point $(x_1, x_2, ...,x_n)$ and a point $(y_1, y_2, ...,y_n)$. Other norms have been tested but the results do not improve, because the distance measure is not relevant. In our opinion, after the tests, the most relevant in the identification process is the feature extraction process. The goodness of the identification depends on the denoising methodology for this kind of signals (machine sounds) and the selection of the most representative features from the spectrum.

For identifying the noisy signals and, effectively, to know what original signal machine sounds they come from, this distance will serve as a dissimilarity measure, defining:

Table 1. Different distances between signals

Acronym	Definition	Description
*ds*ii	$d(s_i, si\_noisy)$	Distance between an original sound and one of its noisy versions
*ds*ij	$d(s_i, s_{j\_noisy})$	Distance between an original sound and one of a noisy version of another original signal. Cross distances.
*ds*ii_denoised	$d(s_i, s_{i\_denoised})$	Distance between an original sound and one of its denoised versions
*ds*ij_denoised	$d(s_i, s_{j\_denoised})$	Distance between an original sound and one of a denoised version of another original signal. Cross distances.

4 Experimental Results

In our experiments, we will demonstrate the identification capacity and the robustness of our methodology when the input signals are highly corrupted with low levels of SNR (high levels of noise).

Initially, we use two original sound signals recorded in real industrial environments: s_1, a car factory assembly line sound; and s_2, a ship engine room sound. These two signals have been corrupted with a non-stationary, non-Gaussian and colored noise, called babble noise (n), with different amplitudes, creating a set of 125 noisy signals with decreasing SNR, ranging from 12 to 0.5. The babble noise [8] represents more than one hundred people speaking in a canteen. All these sounds have been recorded at a frequency sample of 19.98 kHz, 16-bit, mono. Fig. 2 (up) shows original sounds and Fig. 2 (down) their corresponding corrupted sounds before the denoising process. It is important to remark the difficulty to discriminating between both noisy signals.

In the denoising process, the threshold T_w is set to 30% of the maximum wavelet coefficients of the original signals, fulfilling the basic rule stated in that Section 3.2. Fig. 3 shows the similitude among the different spectra for the same signal when it is completely clean (original), when it is completely noisy and finally when it has been denoised after the wavelet reconstruction. It can be observed that denoised spectrum is similar to the clean one, and therefore, the features are quite similar compared with the features obtained from the noisy signal.
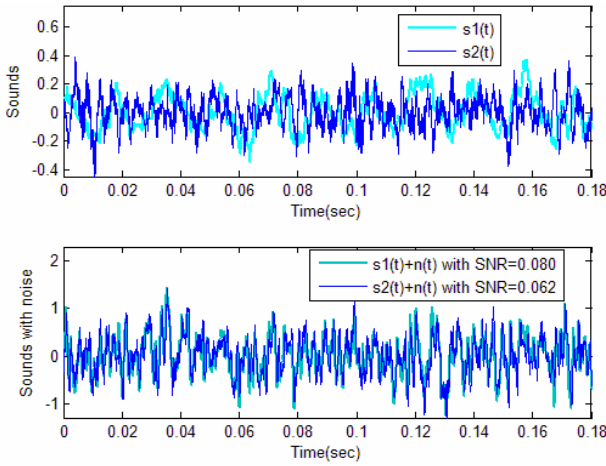
Fig. 2. (Up) Machine sounds; (down) with babble noise
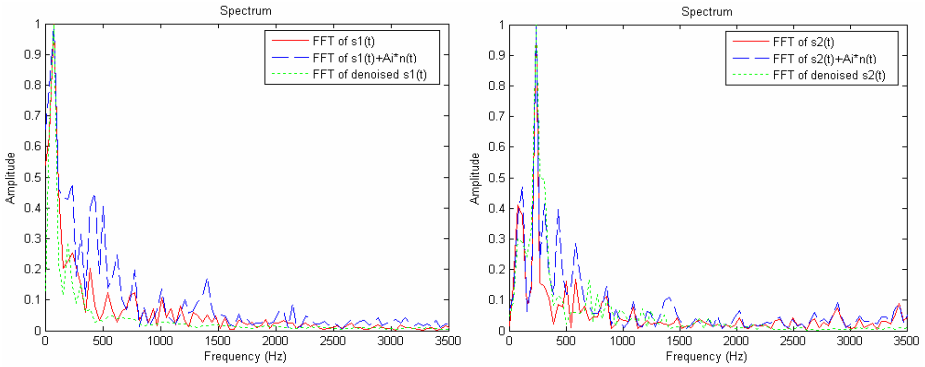
Fig. 3. Spectra of original, noisy and denoised sounds of s_1 (left) and s_2 (right)

Fig. 4 shows the distance between different signals versus the SNR. It can be observed that for both signals (s_1 and s_2) the distance from each original signal to its denoised versions is always lower that the distance between each original signal to its noisy versions, with a wide range of low SNR values. This fact is very important because it demonstrates that the denoising process work very well, reducing the added noise without losing the implicit frequency information of original signal spectrum.

Another consequence is the high rate of discrimination between different original signals and their denoised versions. In the plots in Fig. 4, this fact is represented by the $ds21$, $ds21\_denoised$, $ds12$ and $ds12\_denoised$. The distances of these measures are always higher then the distances between $ds22\_denoised$ and $ds11\_denoised$. Even, the distances $ds22$ and $ds11$, that is, the distances between one signal and its noisy versions are always lower that the cross distances, at least, for values of SNR higher than 2.
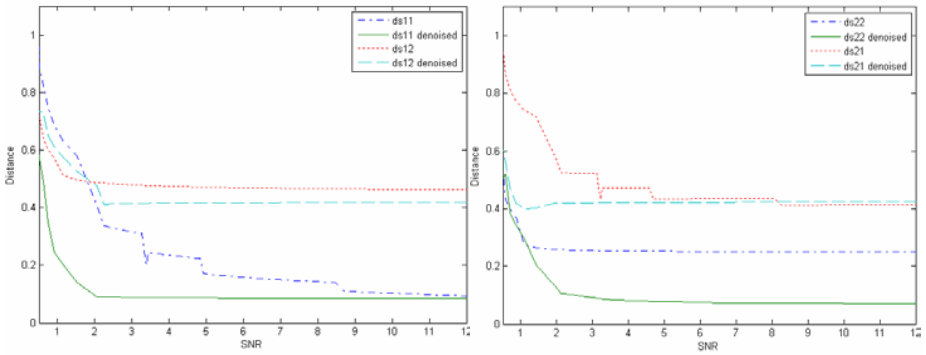
Fig. 4. Distance between signals (see Table 1 for legends)

5   Conclusions

Machine sound varies depending on factors such as background noise, failures of their mechanisms, environmental aspects (speech, superposition...), etc. Besides, when the feature sound is immersed in heavy perturbations as the previously cited is hard to identify. CWT can be used to discover the relevant signal components respect the selected wavelet bases. Then, using a proper basic wavelet, we can reconstruct the sound signal filtering the wavelet coefficients. The machine sound can be denoised following this procedure. Together with a specific feature extraction and identification (based on a basic distance measure) the noisy signals can be effectively identified, even with relatively low signal/noise ratio values.

References

[1] Mori, K., Kasashima, N., Yoshioha, T., Ueno, Y.: Prediction of Spalling on a Ball Bearing by Applying the Discrete Wavelet Transform to Vibration Signals. Wear 195(1-2), 162–168 (1996)
[2] Roberts, S., Everson, R.: Independent Component Analysis: Principles and Practice. Cambridge Univ. Press, Cambridge, UK (2001)
[3] Bolea, Y., Grau, A., Sanfeliu, A.: Non-speech Sound Feature Extraction based on Model Identification for Robot Navigation, 8 Iberoamerican Congress on Pattern Recognition. In: Sanfeliu, A., Ruiz-Shulcloper, J. (eds.) CIARP 2003. LNCS, vol. 2905, pp. 221–228. Springer, Heidelberg (2003)
[4] Mallat, S., Zhang, Z.: Matching pursuits with time-frequency dictionaries. IEEE Trans. on Signal Processing 45(12), 3397–3415 (1993)
[5] Donoho, D.-L.: De-noising by soft-thresholding. IEEE Trans. on Information Theory 33(7), 2183–2191 (1999)
[6] Lin, J.: Feature Extraction of Machine Sound using Wavelet and its Application in Fault Diagnosis. NTD&E International 34, 25–30 (2001)
[7] Goupilland, P., Grossmann, A., Morlet, J.: Cycle octave and related transforms in seismic signal analysis. Geoexploration 23, 85–102 (1984)
[8] http://spib.rice.edu/spib/data/signals/noise/babble

Using Adaptive Filter to Increase Automatic Speech Recognition Rate in a Digit Corpus

José Luis Oropeza Rodríguez, Sergio Suárez Guerra,
and Luis Pastor Sánchez Fernández

Center for Computing Research, National Polytechnic Institute,
Juan de Dios Batiz esq Miguel Othon de Mendizabal s/n, P.O. 07038, Mexico
```
joropeza@cic.ipn.mx, ssuarez@cic.ipn.mx,
            lsanchez@cic.ipn.mx
```

Abstract. This paper shows results obtained in the Automatic Speech Recognition (ASR) task for a corpus of digits speech files with a determinate noise level immerse. The experiments realized treated with several speech files that contained Gaussian noise. We used HTK (Hidden Markov Model Toolkit) software of Cambridge University in the experiments. The noise level added to the speech signals was varying from fifteen to forty dB increased by a step of 5 units. We used an adaptive filtering to reduce the level noise (it was based in the Least Measure Square –LMS- algorithm). With LMS we obtained an error rate lower than if it was not present. It was obtained because of we trained with 50% of contaminated and originals signals to the ASR. The results showed in this paper to analyze the ASR performance in a noisy environment and to demonstrate that if we have controlling the noise level and if we know the application where it is going to work, then we can obtain a better response in the ASR tasks. Is very interesting to count with these results because speech signal that we can find in a real experiment (extracted from an environment work, i.e.), could be treated with these technique and decrease the error rate obtained. Finally, we report a recognition rate of 99%, 97.5% 96%, 90.5%, 81% and 78.5% obtained from 15, 20, 25, 30, 35 and 40 noise levels, respectively when the corpus that we mentioned above was employed. Finally, we made experiments with a total of 2600 sentences (between noisy and filtered sentences) of speech signal.

Keywords: Automatic Speech Recognition, Adaptative Filters, Continuous Density Hidden Markov Models, Gaussian Mixtures and noisy speech signals.

1 Introduction

The science of speech recognition have been advanced to the state where it is now possible to communicate reliably with a computer by speaking to it in a disciplined manner using a vocabulary of moderate size. The interplay between different intellectual concerns, scientific approaches, and models, and its potential impact in society make speech recognition one of the most challenging, stimulating, and exciting fields today. The effect of the noise and filtering on clean speech in the power spectral domain can be represented as:

$$P_Y(\omega_k) = |H(\omega_k)|^2 P_X(\omega_k) + P_N(\omega_k) \tag{1}$$

where $P_Y(\omega_k)$ represents the spectra of the noisy speech $y[m]$, $P_Y(\omega_k)$ represents the power spectra of the noise $n[m]$, $P_X(\omega_k)$ the power spectra of the clean speech $x[m]$, $|H(\omega_k)|^2$ the power spectra of the channel $h[m]$, and ω_k represents a particular Mel-spectra band.

To transform to the log spectral domain we apply the logarithm operator at both sides of the last expression resulting in

$$10\log_{10}(P_Y(\omega_k)) = 10\log_{10}(|H(\omega_k)|^2 P_X(\omega_k) + P_N(\omega_k)) \tag{2}$$

and defining the noisy speech, noise, and clean speech,

$$
\begin{aligned}
y[k] &= 10\log_{10}(P_Y(\omega_k)) \\
n[k] &= 10\log_{10}(P_N(\omega_k)) \\
x[k] &= 10\log_{10}(P_X(\omega_k)) \\
h[k] &= 10\log_{10}(|H(\omega_k)|^2)
\end{aligned}
\tag{3}
$$

results in equations

$$10\log_{10}(P_Y(\omega_k)) = 10\log_{10}\left(10^{\frac{x[k]+h[k]}{10}} + 10^{\frac{n[k]}{10}}\right)$$

$$y[k] = x[k] + h[k] + 10\log_{10}\left(1 + 10^{\frac{n[k]-x[k]-h[k]}{10}}\right)$$

$$\tag{4}$$

Where h[k] is the logarithm of $|H(\omega_k)|^2$, and the similar relationships exist between n[k] and $P_N(\omega_k)$, $x[k]$ and $P_X(\omega_k)$, and y[k] and $P_Y(\omega_k)$.

Last expressions shows that is very difficult to intent to find noise and signal separately. For that is a good recommendation to eliminate the noise embedded into a speech signal using other methods. The different sources of variability that can affect speech determine most of difficulties of speech recognition. During speech production the movements of different articulators overlap in time for consecutive phonetic segments and interact with each other. This phenomenon is known as co-articulation mentioned above. The principal effect of the co-articulation is that the same phoneme can have very different acoustic characteristics depending on the context in which it is uttered [1].

State-of-the-art ASR systems work pretty well if the training and usage conditions are similar and reasonably benign. However, under the influence of noise, these systems begin to degrade and their accuracies may become unacceptably low in severe environments [2]. To remedy this noise robustness issue in ASR due to the static nature of the HMM parameters once trained, various adaptive techniques have been proposed. A common theme of these techniques is the utilization of some form of

compensation to account for the effects of noise on the speech characteristics. In general, a compensation technique can be applied in the signal, feature or model space to reduce mismatch between training and usage conditions [3].

2   Characteristics and Generalities

Speech recognition systems work reasonably well in quiet conditions but work poorly under noisy conditions or distorted channels. The researchers in our speech group (Digital Signal Processing Research Group in the Center for Computing Research) are focused on algorithms to improve the robustness of speech recognition system, so we demonstrated when we employed syllables and Expert Systems for that; we have obtained very good results. Some sources of variability are illustrated in Figure 1.

Speaker-to-speaker differences impose a different type of variability, producing variations in speech rate, co-articulation, context, and dialect, even systems that are designed to be speaker independent exhibit dramatic degradations in recognition accuracy when training and testing conditions differ [4].

Substantial progress has also been made over the last decade in the dynamic adaptation of speech recognition systems to new speakers, with techniques that modify or warp the systems' phonetic representations to reflect the acoustical characteristics of individual speakers [5] [11] [12].
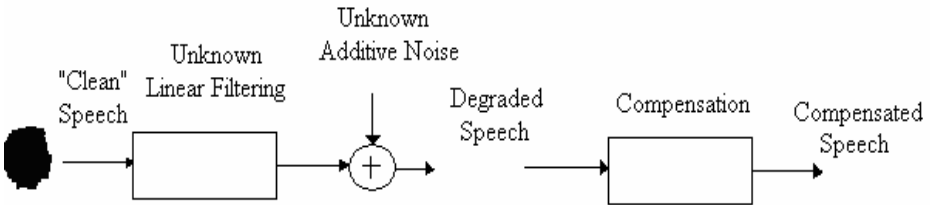
Fig. 1. Schematic representation of some of the sources of variability that can degrade speech recognition accuracy, along with compensation procedures that improve environmental robustness

3   Automatic Speech Recognition Systems

In Automatic Speech Recognition (ASR) systems most of speech energy is under 7 or 7.5 KHz (woman or man voice can change the range mentioned before) dependently. A telephonic lower quality signal is obtained whenever a signal does not have energy out of the band 300-3400 Hz. The vocal tract configuration can be estimated by identifying the filtering performed by the tract vocal on the excitation. Introducing the power spectrum of the signal $P_x(\omega)$, of the excitation $P_v(\omega)$ and the spectrum of the vocal tract filter $P_h(\omega)$, we have:

$$P_x(\omega) = P_v(\omega)P_h(\omega) \tag{5}$$

The speech signal (continuous, discontinuous or isolated) is first converted to a sequence of equally spaced discrete parameter vectors. This sequence of parameter vectors is assumed to form an exact representation of the speech waveform on the basis that for the duration covered by a single vector (typically 10-25 ms) the speech waveform can be regarded as being stationary. In our experiments we used the following block diagram for the isolated speech recognition. The database employed consists of ten digits (0-9) for the Spanish language.

4 Hidden Markov Models

As we know, HMMs mathematical tool applied for speech recognition presents three basic problems [6] y [7]. For each state, the HMMs can use since one or more Gaussian mixtures both to reach high recognition rate and modeling vocal tract configuration in the Automatic Speech Recognition.

4.1 Gaussian Mixtures

Gaussian Mixture Models are a type of density model which comprise a number of functions, usually Gaussian. In speech recognition, the Gaussian mixture is of the form [8] [9], [10], [11] and [12].

$$g(\mu, \Sigma)(x) = \frac{1}{\sqrt{2\pi^d} \sqrt{\det(\Sigma)}} e^{-\frac{1}{2}(x-\mu)^T \Sigma^{-1}(x-\mu)} \tag{6}$$

where μ and Σ in equation 6 represent media and standard deviation of a Gaussian function respectively. Equation 7 shows a set of Gaussian mixtures:

$$gm(x) = \sum_{k=1}^{K} w_k * g(\mu_k, \Sigma_k)(x) \tag{7}$$

In 8, the summarize of the w_k weights give us

$$\sum_{i=1}^{K} w_i = 1 \quad \forall \quad i \in \{1, \dots, K\} \quad w_i \geq 0 \tag{8}$$

As we can deduce, the sum of all w_i is equal to 1. That is an interesting property of the Gaussian Mixtures employed for Automatic Speech Recognition.

4.2 Viterbi Training

We used Viterbi training, in this work for a set of training observations O^r, $1 \leq r \leq R$ is used to estimate the parameters of a single HMM by iteratively computing Viterbi alignments. When used to initialise a new HMM, the Viterbi segmentation is replaced by a uniform segmentation (i. e. each training observation is divided into N equal segments) for the first iteration. Apart from the first iteration on a new model, each training sequence O is segmented using a state alignment procedure which results from maximising

$$\phi_N(T) = \max_i \phi_i(T) a_{iN} \tag{9}$$

For $1<i<N$ where

$$\phi_j(t) = \left[\max_i \phi_i(t-1) a_{ij} \right] b_j(o_t) \tag{10}$$

With initial conditions given by

$$\phi_1(1) = 1 \tag{11}$$
$$\phi_j(t) = a_{1j} b_j(o_1)$$

For $i<j<N$. In this and all subsequent cases, the output probability $b_j(.)$ is as defined in the following equation:

$$b_j(o_t) = \prod_{s=1}^{S} \left[\sum_{m=!}^{M_{js}} c_{jsm} \aleph(o_{st}; \mu_{jsm}, \sum_{jsm}) \right]^{\gamma_s} \tag{12}$$

If A_{ij} represents the total number of transitions from state i to state j in performing the above maximisations, then the transition probabilities can be estimated from the relative frequencies

$$\hat{a}_{ij} = \frac{A_{ij}}{\sum_{k=2}^{N} A_{ik}} \tag{13}$$

The sequence of states which maximises $\phi_N(T)$ implies an alignment of training data observations with states. Within each state, a further alignment of observations to mixture components is made.

We can use two methods for each state and each stream

1.   use clustering to allocate each observation o_{st} with the mixture component with the highest probability

2.   associate each observation o_{st} with the mixture component with the highest probability

In either case, the net result is that every observation is associated with a single unique mixture component. This association can be represented by the indicator function $\psi_{jsm}^r(t)$ which is 1 if o_{st}^r is associated with mixture component m of stream s of state j and zero otherwise.

The means and variances are then estimated via simple averages

$$\hat{\mu}_{jsm} = \frac{\sum_{r=1}^{R} \sum_{t=1}^{T_r} \psi_{jsm}^r(t) o_{st}^r}{\sum_{r=!}^{R} \sum_{t=!}^{r} \psi_{jsm}^r(t)} \tag{14}$$

$$\hat{\sum}_{jsm} = \frac{\sum_{r=1}^{R} \sum_{t=1}^{T_r} \psi_{jsm}^r(t)(o_{st}^r - \hat{\mu}_{jsm})(o_{st}^r - \hat{\mu}_{jsm})'}{\sum_{r=1}^{R} \sum_{t=1}^{T_r} \sum_{t=1}^{M_s} \psi_{jst}^r(t)}$$

5   Experiments and Results

The evaluation of the adaptive filter implemented to reduce noise involved clustering a set of speech data consisting of 100 isolated patterns from a digits vocabulary. The training patterns (and a subsequent set of another 200 independent testing pattern) were recorded in a room free of noise. Only one speaker provided the training and testing data. All training and test recordings were made under identical conditions (we employed a special software created for us to record the sentences, at 16 kbps; mono-channel and the sentence were normalized). The 200 independent testing patterns was addition with a level noise, we obtained a total of 1200 new sentences contaminated (200 per noise level, that is because we used 6 noise levels). After that, we used an adaptive filter to reduce that noise level and the results are shown below, then we obtained another 1200 sentences. Finally, we made experiments with a total of 2600 sentences (between noisy and filtered sentences) of speech signal. Figure 2 shows the adaptive filter algorithm employed. For each corpus created, we used three databases test to recognition task: with same characteristics, noisy and filtered. All sentences were recorded at 16 kHz frequency rate, 16 bits and mono-channel. We use MFCCs with 39 characteristics vectors (differential and energy components). A Hidden Markov Model with 6 states and 1 Gaussian Mixture per state.

Initialise

$$w_k(i) \quad y \quad x_{k-i}$$

Read x_k y y_k
from ADC

Filter x_k

$$n_k = \sum w_k(i)x_{k-i}$$

Compute error

$$e_k = y_k - n_k$$

Compute factor

$$2\mu e_k$$

Update coeficcient

$$w_{k+1}(i) = w_k + 2\mu e_k x_{k-i}$$
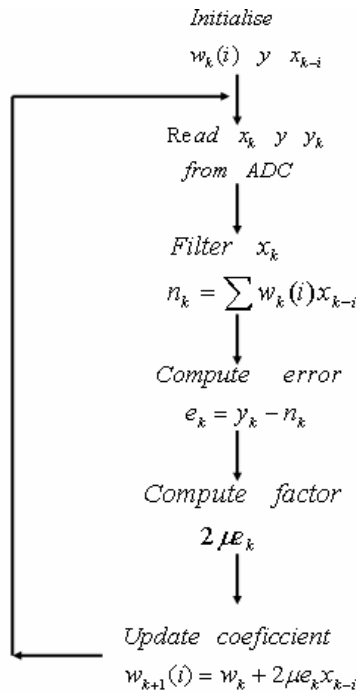
Fig. 2. Adaptive filter algorithm

Table 1. Results obtained with noisy corpus created

Speech signal recognized	speech recognition with noisy corpus created					
	noise level					
	15	**20**	**25**	**30**	**35**	**40**
Noisy	95,5	96,5	98,5	98	99,5	99,5
Original	57	72,5	83,5	91,5	99	99
Filtered	23	50	76,5	90,5	98	99,5

Table 1 Shows the results obtained when we used a noisy corpus to training the ASR. A total of 600 speech sentences were analyzed.

As we can see, when we used a noisy corpus like we hoped, recognition level with noisy database was adequately. When we used high S/N rate (25, 30, 35 and 40 dB), the recognition rate was increased. It is important because it means that the noisy corpus is a good reference. Figure 3 shows a histogram related with the table contents.
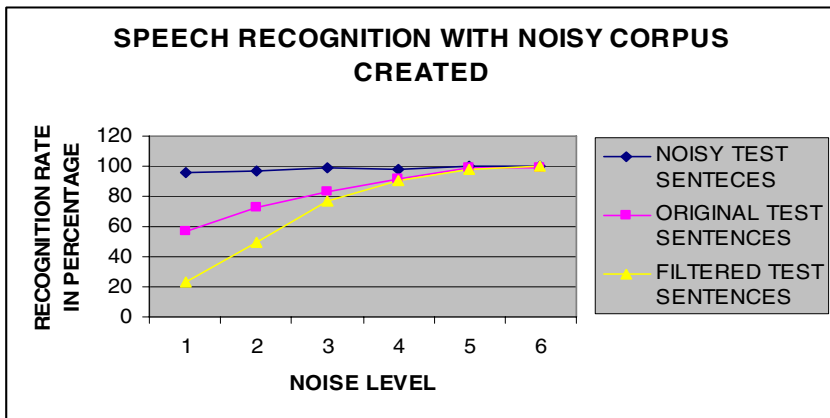
Fig. 3. Block diagram of training step for ASR for isolated words

Table 2. Results obtained with noisy and clean corpus created

Speech signal recognized	speech recognition with noisy and clean corpus created					
	noise level					
	15	**20**	**25**	**30**	**35**	**40**
Noisy	98,5	98	99,5	99	99,5	99,5
Original	19	34	84	91,5	96,5	99
Filtered	78,5	81	90,5	96	95,7	99

Table 2 shows the results obtained when we used a noisy corpus to training the ASR. A total of 600 speech sentences were analyzed.

As we can see, when we used a corpus compound by noisy and original signals, the recognition rate for filtered speech signal was increased considerably. Figure 4 shows that.
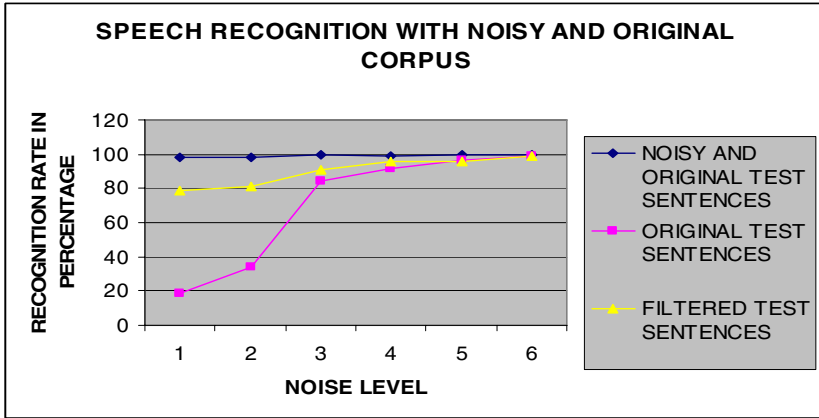
Fig. 4. Block diagram of training step for ASR for isolated words

Table 3 shows the results obtained when we used a noisy corpus to training the ASR. A total of 600 speech sentences were analyzed.

Table 3. Results obtained with clean corpus created

Speech signal recognized	speech recognition with clean corpus created					
	noise level					
	15	20	25	30	35	40
Noisy	99,5	99,5	99,5	99,5	99,5	99,5
Original	16	21,5	18	43	70,5	87
Filtered	18.5	29	33,5	56	99,5	86,5
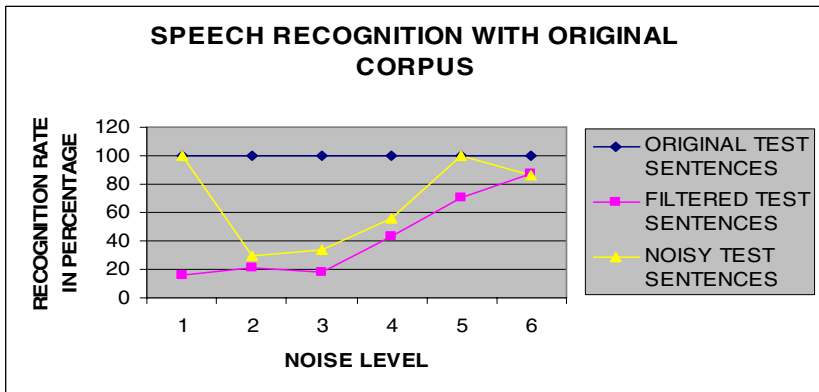
Fig. 5. Block diagram of training step for ASR for isolated words

Finally, with the original corpus the results was not satisfactory, although the recognition rate with filtered signals was better than noisy signals, it was poor and not enough to be considered important as Figure 5 shows.

6   Conclusions and Future Works

The results shown in this paper demonstrate that we can use an adaptive filter to reduce the noise level in an automatic speech recognition system (ASRS) for the Spanish language. The use of this paradigm is not new but with this experiment we propose to reduce the problems find out when we tread with real speech signals. MFCCs and CDHMMs were used for training and recognition, respectively. First, when we used database test with the same characteristics that corpus training a high performance was reached out, but when we used the clean speech database our recognition rate was poor. The most important results extracted of this experiment were when the clean speech was fixed with noisy speech, when we used filtered speech we obtained a high performance in our ASR. For that, our conclusion is that if we want to construct an ASR immerse in a noisy environment, it is going to have a high performance if we included in our database training clean and noisy speech signal. So, if we known the Signal/Noise ratio and it's great than 35%, we can use the filtered signal in an ASR without problems. For future works is recommendable try to probe the results obtained using another methods employed to reduce noise into signal (wavelets i. e.), and extract the results.

References

1. Farnetani, E.: Coarticulation and connected speech processes. In: Hardcastle, W., Laver, J. (eds.) Handbook of Phonetic Sciences, pp. 371–404. Blackwell (1997)
2. Challenges in Adopting Speech Recognition. Communications of the ACM 47(1), 69–75
3. An ASR Incremental Stochastic Matching Algorithm for Noisy Speech Recognition. IEEE Trans. Speech and Audio Processing 9(8), 866–873
4. Cole, R.A., Hirschman, L., et al.: Workshop on spoken language understanding. Tech. Rep. CSE 92-014, Oregon Graduate Institute of Science&Technology, P.O.Box 91000, Portland, OR 97291-1000 USA, (September 1992)
5. Gauvain, J.-L., Lee, C.-H.: Bayesian learning for HMM with GM state observation densities. In: Eurospeech (Eur91), pp. 939–942
6. Lawrence, R., Juang, B.-H.: Fundamentals of Speech Recognition. Prentice Hall, Englewood Cliffs (1993)
7. Jialu, Z.: On the syllable structures of Chinese relating to speech recognition. Institute of Acoustics, Academia Sinica Beijing, China (1999)
8. Bilmes, J.A.: A Gentle Tutorial of the EM Algorithm and its Application to Parameter Estimation for GM and HMM. ICS Institute, Berkeley, CA (1998)
9. Barbara, R.: Gaussian Statistics and Unsupervised Learning. A tutorial for the Course Computational Intelligence Signal Processing and Speech Communication Laboratory (November 15, 2001), www.igi.turgaz.at/lehre/CI

10. Barbara, R.: Hidden Markov Models. A Tutorial for the Course Computational Laboratory. Signal Processing and Speech Communication Laboratory (November 15, 2001), www.igi.turgaz.at/lehre/CI
11. Prasad, K.V., Nagarajan T., Murthy H.A.: Continuous Speech Recognition Using Automatically Segmented Data at Syllabic Units. Department of Computer Science and Engineering. Indian Institute of Technology. Madras, Chennai pp. 600–636 (2002)
12. Paul, M.: Automatic Segmentation of Speech into Syllabic Units. Haskins Laboratories, New Haven, Connecticut 06510 58(4) 880–883 (1975)
13. Huang, X.D., Lee, K.F.: On speaker-independent, speaker-dependent, and speaker-adaptive speech recognition. IEEE Transactions on Speech and Audio Processing 1(2), 150–157 (1993)
14. Schwartz, R., Chow, Y., Kubala, F.: Rapid speaker adaption using a probabilistic spectral mapping. In: ICASSP [ICA87], pp. 633–636

SSM – A Novel Method to Recognize the Fundamental Frequency in Voice Signals

György Várallyay Jr.

Budapest University of Technology and Economics,
Dept. of Control Engineering and Information Technology,
Magyar tudósok krt. 2. IB. 311, H-1117 Budapest, Hungary
varallyay@iit.bme.hu

Abstract. Nowadays the detection of the fundamental frequency (F_0) in voice signals can be evaluated by several algorithms. There are two main attributes of these algorithms: exactness and calculation time. A considerable part of the algorithms are based on the well-known Fast Fourier Transformation (FFT). The Smoothed Spectrum Method is an FFT based process, which was developed for the F_0 detection of recorded voice signals especially the infant cry. As it will be shown the SSM provides a better accuracy than regular FFT based algorithms or the Autocorrelation Function. In case of sound recordings in noisy environment the modified SSM is able to recognize significant noise components in the recorded signal. A further advantage of SSM is that additional information of the analyzed signal can be given to improve the performance of the method.

Keywords: Fundamental frequency detection, voice signals, noise detection.

1 Introduction

The fundamental frequency (F_0) is the lowest useful frequency component in the spectrum. The detection of the fundamental frequency has several applications, *e.g.* in mechanical engineering, in acoustical engineering, etc. In each of these applications various requirements are defined: robustness, calculation time, accuracy, etc [1-3]. In this study a novel method, named *Smooth Spectrum Method* (SSM) will be introduced, which was developed for the F_0 detection of *recorded voice signals* especially the infant cry. This method is based on the spectrum obtained by the well-known *Fast Fourier Transform* (FFT) [4].

Different types of voice signals result different spectrums. Figure 1 (a) shows the short-term spectrum of a sinusoid. An obvious way to estimate its fundamental frequency is to measure the position of the spectral peak. However this procedure fails for the spectrum in Fig. 1 (b) that contains multiple peaks. A simple modification is to accept only the largest peak, but this algorithm fails for the spectrum in Fig. 1 (c) for which the largest peak falls on a multiple of F_0. A simple extension is to select the peak of lowest frequency but this algorithm fails for the signal illustrated in Fig. 1 (d) for which the lowest peak falls on a higher harmonic. Another cue, spacing between partials indicates the correct F_0 for this signal, but not for the signal illustrated in

Fig. 1 (e). In case of recorded acoustic signals narrow-band noises, and/or wide-band noises, and/or significant frequency components (f) might be added into the spectrum from background noises, the noise from the recording device, etc. It might result that some of the useful frequency components of the recorded signal under the noise level will disappear from the spectrum, while significant noise peaks can be treated as a useful frequency component.
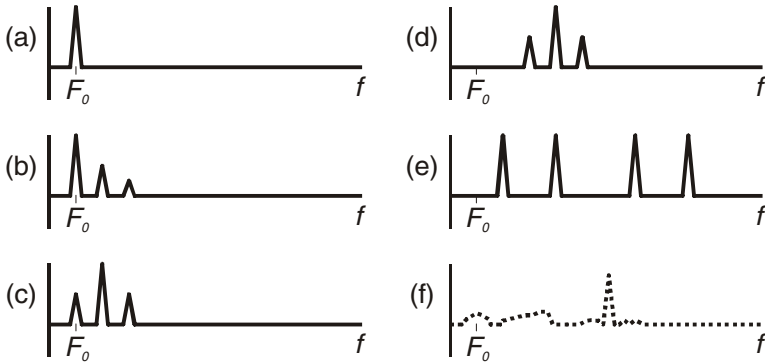
Fig. 1. Spectra of simple signals that illustrate basic spectral F_0 estimation schemes. The spectrum peak determines the F_0 of a pure tone (a) but a complex tone (b) has several such peaks. The largest peak determines the F_0 of the waveform in (b), but not (c). The lowest frequency peak determines the F_0 of the waveform of (c) but not (d). Interpartial spacing determines the F_0 of (d) but not (e). In case of recorded acoustic signals narrow-band noises, and/or wide-band noises, and/or significant frequency components might be added as it is shown in (f).

The inputs of the Smoothed Frequency Method are spectrums obtained from sound recordings of the infant cry. Cry is a multimodal, dynamic behavior; this is the first tool of communication and the sign of life at birth [5]. There are several purposes and ways to analyze the sound of crying: acoustic, physiological, psychological, phonetic, pediatric, etc [6-12]. The infant cry, on the analogy of voice signals, is mostly a harmonic signal, containing the fundamental frequency and its multiple integers, *i.e.* the subharmonics. The fundamental frequency of crying is typically between 200 and 800 Hz [13], while subharmonics can be found for 6000-8000 Hz. The amplitudes of these frequency components are different; there are significant components as well as missing ones, depending on the formant structure of the sound. [14]. In the acoustic analysis of the infant cry the maximum frequency of interest is often above 8000 Hz to be able to analyze special unvoiced sound phonemes.

As the Smoothed Spectrum Method is suitable not only for the F_0 detection of the infant cry but for the F_0 detection of other voice signals, in the following the inputs will be mostly harmonic signals (200 Hz $<F_0<$800 Hz), containing narrow-band and/or wide-band noises and/or significant noise components.

The sampling frequency applied was 44100 Hz; there was a window size of 2048 points. This window length (46.4340 ms) is typical in case of speech processing

or speech recognition, and provides a suitable resolution in the time domain. In the following these values will be used.

In regular FFT based algorithms the frequency resolution of the discrete spectrum is limited. In case of the window length above, the resolution of the spectrum is 21.5333 Hz. The frequency resolution of the FFT spectrums can be decreased theoretically *e.g.* by using a longer window, by zero padding, when possible and allowed. The Smoothed Spectrum Method is such a novel method for fundamental frequency detection, which provides a better accuracy than it could be reached theoretically by regular FFT based algorithms.

2   Methodology

The SSM can be divided into two consecutive parts. In the first part the input spectrum is smoothed and the significant peaks are detected. In the second part the most probable value of the fundamental frequency is calculated by statistical methods.

First, the input FFT spectrum is smoothed by a suitable (*e.g.* bell shape), symmetric kernel function. This smoothing can be realized by weighted addition in a predetermined bandwidth. The purpose of this step is to emphasize the significant peaks in the spectrum (*i.e.* the harmonic components) and to reject the wide-band noises in the spectrum. Figure 2 shows an original spectrum and its smoothed version.
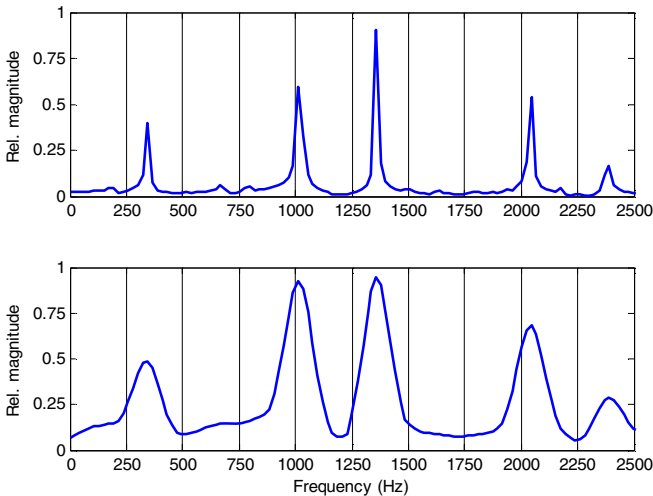
Fig. 2. An original spectrum (A) and its smoothed version (B). The significant peaks of the original spectrum are preserved, while the smaller (noise) components are rejected.

By the detection of the local maxima in the smoothed spectrum the significant peaks of the original spectrum are found. Note that the smoothing of the spectrum does not change the frequency position of the significant peaks.

The second part of the Smoothed Spectrum Method is based on these obtained peaks. As it was shown before there are several types of spectrums. In some cases the

fundamental frequency or higher frequency components are missing, or some significant noise components are present. First, let us see the cases without any noise components.

2.1 SSM Without Noise

In ideal case, the subharmonics (F_{n_ideal}) are whole multiples of the fundamental frequency (F_0).

$$F_{n\_ideal} = F_0 \cdot n \tag{1}$$

From this expression, if a subharmonic of F_0 is detected and its serial number is known, the fundamental frequency can be calculated by a simple division:

$$F_0 = F_{n\_ideal} / n \tag{2}$$

But the distance between two neighboring points in the discrete spectrum is

$$B = F_s / N \tag{3}$$

where F_s is the sampling frequency and N is the window length applied at the FFT. In the worst case a spectral component (F_x) of the signal is placed to $F_x \pm B/2$. In this case (1) is modified as

$$F_n = F_0 \cdot n \pm B/2 \tag{4}$$

From (2) and (4)

$$F_n / n = F_0 \pm \frac{B}{2n} = F_0 \pm \frac{F_s}{2nN} = F_0 \pm h = F_0 \left(1 \pm h'_n\right) \tag{5}$$

Where h is the absolute error of the calculation of F_0, and h' is the relative error:

$$h'_n = \frac{F_s}{2nNF_0} \tag{6}$$

As the sampling frequency (F_s) and the window length (N) are given with the input spectrum, the relative error can be decreased by applying higher n value, *i.e.* determining higher harmonic component in the spectrum.

The significant peaks in the input spectrum are the local maxima in the smoothed spectrum. The positions of these peaks are close to the real subharmonics of F_0. If the frequency values of these peaks are divided by their serial numbers, the resulted ratios will be close to the real F_0 with the relative error from (6).

Example from Figure 2: the fundamental frequency is 340 Hz, the second and the fifth subharmonics are missing. As the frequency resolution of the spectrum (B) is 21.53 Hz, the detected peaks in the smoothed spectrum are at F_{det1}=335.47 Hz, F_{det2}=1027.94 Hz, F_{det3}=1363.41 Hz, F_{det4}=2034.35 Hz and F_{det5}=2369.81 Hz. After the division with their serial numbers the resulted ratios are: 335.47, 342.64, 340.85,

339.06 and 338.54 Hz. The differences between these results and the exact value of the fundamental frequency are within the theoretical error bands.

For these divisions the exact serial numbers of the detected peaks are needed. How could these serial numbers be obtained? By the combination of possible serial numbers the algorithm generates test sequences, and the ratios of the obtained peaks and all of these sequences are calculated. In case of the best sequence of serial numbers the standard deviation of the obtained ratios will be the least.

Continuing the previous example, five test sequences are given, and the ratios are calculated (see Table 1). As the standard deviation of these ratios has the smallest value at the second case, the best sequence of serial numbers is <1,3,4,6,7>.

Table 1. Examples of the sequences of serial numbers. As the standard deviation of the ratios is the smallest in the second line, the best combination is <1,3,4,6,7>.

Sequence of serial numbers	Ratios of the detected peaks and possible sequence of serial numbers (Hz)					Standard deviation (Hz)
	F_{det1}	F_{det2}	F_{det3}	F_{det4}	F_{det5}	
<1,2,3,4,5>	335.47	513.97	454.47	508.59	473.96	72.41
<1,3,4,6,7>	335.47	342.65	340.85	339.06	338.54	2.69
<1,2,4,6,8>	335.47	513.97	340.85	339.06	296.23	85.22
<2,3,4,5,6>	167.73	342.65	340.85	406.87	394.97	95.83
<2,3,4,6,7>	167.73	342.65	340.85	339.06	338.54	77.18

As the least value of the standard deviations is found, the fundamental frequency of the signal can be calculated by the division of the highest detected frequency component and its serial number. In this example the original F_0 at 340 Hz was positioned in the spectrum to 335.47 Hz, while a better estimation (338.54 Hz) was calculated with the SSM.

2.2   SSM with Narrow-Band and/or Wide-Band Noises

In case of wide-band noises, some of the useful peaks in the input spectrum might not be visible; but the Smoothed Spectrum Method can detect the fundamental frequency from the remaining significant peaks.

In case of narrow-band noises, or especially significant noise components, the smoothing of the spectrum might not reject these components. If such a noise component is expected in the signal, the algorithm of the SSM can be modified to recognize the extraordinary peak. In the modified algorithm divisions are evaluated not only with the detected peaks (including the noise peak), but with smaller groups of the detected peaks as well. There will be at least one group, where no noise peak is present.

An example for the recognition of a significant noise component: supposing that the fundamental frequency is 60 Hz, and in the signal there are significant peaks around 40, 60, 120, 180 and 300 Hz. In this example the significant noise component is at 40 Hz. The divisions are evaluated first with all the peaks, second with smaller

Table 2. An example for the recognition of a noise component. The harmonic signal has components at whole multiples of 60 Hz, while an extra peak at 40 Hz illustrates the significant noise component. When the noise component is skipped, the resulted fundamental frequency value differs from the others. That is the indicator of the noise component.

Detected peaks (Hz)	The best sequence of serial numbers after simple SSM	The calculated value of the fundamental frequency (Hz)
40, 60, 120, 180, 300	<2,3,6,9,15>	20
60, 120, 180, 300	<1,2,3,5>	60
40, 120, 180, 300	<2,6,9,15>	20
40, 60, 180, 300	<2,3,9,15>	20
40, 60, 120, 300	<2,3,6,15>	20
40, 60, 120, 180	<2,3,6,9>	20

groups of the peaks. See Table 2 how the modified SSM algorithm detects a noise component.

However the recognition of a noise component needs more SSM divisions, the modified algorithm is able to select the extraordinary peak from the significant peaks detected in the smoothed spectrum.

3   Comparison

To test the accuracy of the Smoothed Spectrum Method, harmonic signals were generated randomly and several fundamental frequency detection algorithms were applied and their results were compared.

There were constant values, as the sampling frequency (F_s=44100 Hz) and the length of the signal (N=2048 points), which resulted a B=21.53 Hz frequency resolution in the FFT spectrum. The fundamental frequency of the generated test signals were integers between 200 and 800 Hz. The amplitudes of the frequency components were randomly generated in each case; a maximum of 10 subharmonics were present.

In the comparison, besides the Smoothed Spectrum Method (SSM) the *Autocorrelation Function* (XCOR) and *Regular FFT* (RFFT) algorithms were applied. The Autocorrelation Function is a special type of the cross-correlation function, which is a typical method for F_0 detection *e.g.* in speech recognition [1, 4]. The Regular FFT algorithms collectively use the resolution of the FFT spectrum; such algorithms are the local maximum detection in the spectrum within a predetermined frequency interval, and the Harmonic Product Spectrum method [2].

For each test signal the value of the fundamental frequency was determined by all of the algorithms mentioned above, and the differences between the exact F_0 and the detected F_0 values were calculated. After this, the mean value of the absolute differences and the standard deviation of the differences were obtained. The following table (Table 3) shows the accuracy of the compared methods.

Table 3. Comparison between the accuracy of F_0 detection algorithms. IDEAL: in ideal case; SSM: by the Smoothed Spectrum Method; XCOR: by the Autocorrelation Function; and RFFT: by Regular FFT algorithms.

	Difference between the original and the detected values on the average (Hz)	Standard deviation of the difference between the original and the detected values (Hz)
IDEAL	0.0000	0.0000
SSM	0.6427	0.7617
XCOR	1.6717	2.2149
RFFT	5.3852	6.2251

As it is shown by Table 3 after the ideal case the Smoothed Spectrum Method provides the least detection error. The Autocorrelation Function also has a better error band than what a Regular FFT algorithm could reach.

Note that in case of regular FFT algorithms, a uniform distribution is expected for the detection difference between 0 and $B/2=10.7666$ Hz, which has an average value at 5.3833 Hz.

4   Discussion and Conclusion

A novel algorithm for fundamental frequency detection of the infant cry was introduced in this study. However the Smoothed Spectrum Method was developed to detect the fundamental frequency of crying signals, its conceptions are relevant for several voice signals, as speech, singing, and musical instruments.

In summary, the algorithm of the Smoothed Spectrum Method is the following:

- Smooth the input spectrum by a chosen kernel function in a chosen bandwidth;
- Detect the local maxima in the smoothed spectrum within a chosen frequency range;
- Generate possible sequences of serial numbers for the detected peaks;
- Divide the peaks with these sequences and calculate the standard deviation of the resulted ratios;
- Choose the smallest standard deviation to find the exact sequence of serial numbers and to calculate the fundamental frequency.

A further advantage of the SSM is that additional information of the analyzed signal can be given to improve the performance of the method. Users can give:

- The type of the kernel function and the bandwidth of smoothing;
- The interval of the local maximum detection in the smoothed spectrum;
- Rules and limitations for generating sequences of serial numbers for the division;
- Rules for detecting and skipping noise-peaks from the division.

For exactness the Smoothed Spectrum Method is a promising algorithm for fundamental frequency detection of voice signals. The modified algorithm of the SSM is able to recognize and eliminate the significant noise components in the signal. The

disadvantage of the SSM might be the calculation time, because it contains numerous divisions.

References

1. Deller, J.R., Proakis, J.G., Hansen, J.H.L.: Discrete-time processing of speech signals. MacMillan Publishing Co, New York (1993)
2. Parsa, V., Jamieson, D.G.: A Comparison of High Precision F0 Extraction Algorithms for Sustained Vowels. J. of Speech, Language, and Hearing Research 42, 112–126 (1999)
3. Cheveigné, A., Kawahara, H.: YIN, a fundamental frequency estimator for speech and music. J. Acoust. Soc. Am. 111, 1917–1930 (2002)
4. Randall, R.B.: Application of B&K equipment to frequency analysis. Brüel & Kjaer Techn. Library, Denmark (1977)
5. Barr, R.G., Hopkins, B., Green, J.A.: Crying as a sign, a symptom and a signal. MacKeith Press, London (2000)
6. Hirschberg, J., Szende, T.: Pathological cry, stridor and cough in infants. Akadémiai Kiadó, Budapest (1982)
7. Várallyay Jr., G., Benyó, Z., Illényi, A.: The development of the melody of the infant cry to detect disorders during infancy. In: Proc. IASTED International Conference on Biomedical Engineering (BioMED 2007), Innsbruck, Austria, February 14-16, pp. 186–191 (2007)
8. Möller, S., Schönweiler, R.: Analysis of infant cries for the early detection of hearing impairment. Speech Commun. 28, 175–193 (1999)
9. Cacace, A.T., Robb, M.P., Saxman, J.H., Risemberg, H., Koltai, P.: Acoustic features of normal-hearing pre-term infant cry. Int. J. Pediatr. Otorhinolaryngol. 33, 213–224 (1995)
10. Várallyay Jr., G.: Future Prospects of the Application of the Infant Cry in the Medicine. Per. Pol. Elec. Eng. 50, 47–62 (2006)
11. Fort, A., Manfredi, C.: Acoustic analysis of newborn infant cry signals. Med. Eng. Phys. 20, 432–442 (1998)
12. Michelsson, K., Michelsson, O.: Phonation in the newborn, infant cry. Int. J. Pediatr. Otorhinolaryngol. 301, S297–S301 (1999)
13. Várallyay Jr., G.: Infant cry analyzer system for hearing disorder detection. Trans. on Automatic Control and Computer Science 49, 57–60 (2004)
14. Wermke, K., Mende, W., Manfredi, C., Bruscaglioni, P.: Developmental aspects of infant's cry melody and formants. Med. Eng. Phys. 24, 501–514 (2002)

Channel / Handset Mismatch Evaluation in a Biometric Speaker Verification Using Shifted Delta Cepstral Features

José R. Calvo, Rafael Fernández, and Gabriel Hernández

Advanced Technologies Application Center, CENATAV, Cuba
`{jcalvo,rfernandez,gsierra}@cenatav.co.cu`

Abstract. This paper examines the application of Shifted Delta Cepstral (SDC) features in biometric speaker verification and evaluates its robustness to channel/handset mismatch due by telephone handset variability. SDC features were reported to produce superior performance to delta features in cepstral feature based Language Identification systems. The result of the experiment reflects superior performance of SDC features regarding to delta features in biometric speaker verification using speech samples from Ahumada Spanish database.

Keywords: biometrics, speaker verification, cepstral features, shifted delta cepstral features, channel mismatch.

1 Introduction

Existing methods of user authentication can be grouped into three classes: possessions (something that you have: a key, an identification card, etc); knowledge (something that you know: a password, a PIN, etc) and biometrics [1]. Biometrics is the science of identifying or verifying the identity of a person based on physiological characteristics (something that you are: fingerprints or face) or behavioural characteristics dependent on physical characteristics (something that you produce: handwritten signature or speech).

Early user authentication was based on possessions and knowledge, but problems associated with these methods, restrict their use. The most important drawbacks of these methods are: possessions can be lost, stolen, shared or easily duplicated; knowledge can be shared, easy to guess, forgotten, and both, knowledge and possessions can be shared or stolen [1]. Consequently it is easy to deny that a given person carried out an action, because only the possessions or knowledge are checked, and these are only loosely coupled to the person's identity. Biometrics provides a solution to these problems by truly verifying the identity of the individual.

As a biometric user authentication method, speech is a behavioural characteristic that is not considered threatening or intrusive by users to provide. The goal of speaker recognition is to extract, characterize, and recognize the information in the speech signal conveying speaker identity [2]. Telephony is the main modality of biometric speaker recognition, since it is a domain with ubiquitous existing hardware and doesn't need for special transducers to be installed.

Current automatic speaker recognition systems face significant challenges caused by adverse acoustic conditions as telephone band limitation and channel and handset variability. Degradation in the performance of speaker recognition systems due to channel mismatch has been one of the main challenges to actual deployment of speaker recognition technologies. Several techniques have been proposed to address this problem, new speech features that are less sensitive to channel effects can be extracted [3], the effect of mismatches can be reduced via cepstral normalization [4, 5], the speaker models can be transformed to compensate for the mismatches [6, 7], and rescoring techniques can be used to normalize the speaker scores and reduce the channel and handset effects [8].

This paper introduces the application of a new set of dynamic cepstral features in speaker recognition: Shifted Delta Cepstral (SDC) features, and evaluates its performance in front of channel/handset mismatch, typical in remote applications. SDC features were recently reported to produce superior performance to delta features in cepstral feature based Language identification [9, 10].

SDC features are obtained by concatenating the delta-cepstral computed across multiple frames of speech. As a combination of dynamic cepstral features, SDC features contain useful information about speaker identity.

Nevertheless, in our knowledge, this is the first attempt on using SDC features for speaker recognition. This evaluation was performed using telephone speech samples of Ahumada Spanish database [11].

2   Biometric Speaker Verification

Voice is a combination of physiological and behavioral characteristics. The features of an individual's voice are based on invariant physiological characteristics, as the shape and size of the vocal and nasal tract, mouth and lips, used in the synthesis of the sound. Nevertheless, this technology is usually classified as a behavioural too, because the way the individual speaks, their attitude and their cultural background strongly influences the resulting speech signal. This behavioral characteristics of a person's speech (and some physiological, too) changes over time due to age, health conditions, emotional state, environmental reasons, etc.

Biometric application of speaker recognition is identified as speaker verification because a user claims to be a client, and the system verifies this claim. Many applications of speaker verification systems are accessed remotely by users and the channel involved in the communication is the telephone. Because the handset and the line can vary from call to call, there is often an acoustic mismatch between the speech collected to train the speaker models and the speech produced by the speakers at run time or during testing. Such mismatches are known to severely affect the performance of the system. However, in a remote banking application, the voice-based technique combined with other user's authentication method, may be preferred since it can be integrated without additional effort, into the existing telephone system.

Speaker verification systems are categorized depending on the freedom in what is spoken; this taxonomy based on increasingly complex tasks also corresponds to the sophistication of algorithms used and the progress in the art over time [1]:

Fixed text: The speaker says a predetermined word or phrase which was recorded at enrolment. The word may be secret, so it acts as a password, but once recorded a replay attack is easy, and re-enrolment is necessary to change the password.

Text prompted: The speaker is prompted by the system to say a specific expression. The system matches the utterance with known text to determine the user. For this, enrolment is usually longer, but the prompted text can be changed at will. Expression as digit strings are more vulnerable than phrases, to splicing-based replay attacks.

Text independent: The system processes any utterance of the speaker. Here the speech can be task-oriented, so it is hard to acquire speech that also accomplishes the impostor's goal.

Combined with utterance verification [2]**:** The system presents to the user, a series of randomized phrases to repeat, and verifies not only the voice matches but also the required phrases match. Additionally, it is possible to use forms of automatic knowledge verification where a person is verified by comparing the content of his/her spoken utterance against the stored information in his/her personal profile.

This paper evaluates the performance of SDC features as a new set of dynamic features for speaker recognition, in a remote speaker verification system using text prompted task using short phrases.

3   Shifted Delta Cepstral Features

First proposed by Bielefeld [12], features called Shifted Delta Cepstral (SDC) are obtained by concatenating the delta-cepstral computed across multiple frames of speech information, spanning multiple frames into the feature vector. Recently, the proposal of using SDC features of a speech signal for language identification with GMM [13] and SVM [14] classifiers, has produced promising results. In our knowledge, this is the first attempt to using SDC for speaker recognition.

Cepstral features contain information about speech formants structure, and delta-cepstral about its dynamics. SDC features evaluate speech spectral dynamics better, because can reflect the movement and position of vocal and nasal articulators if its time interval of analysis is adjusted to include spectral transitions between phonemes and syllables. In each cepstral frame, SDC computation obtains the dynamic of the articulatory movement in next frames, as a pseudo-prosodic feature vector [10] computed without having to explicitly find or model the prosodic structure of the speech signal. Is known that the prosodic structure of the speech conveys important information about the identity of the speaker [15].

The computation of SDC features is a relatively simple procedure [16] and is illustrated in Fig. 1. First, a cepstral feature vector is computed in each frame. A shifting delta operation is applied to frame based cepstral feature vectors in order to create the new combined feature vectors for each frame.

The SDC features are specified by a set of 4 parameters, (*N, d, P, k*) where:

- *N:* number of c cepstral coefficients in each cepstral vector.
- *d:* time advance and delay for the delta computation.
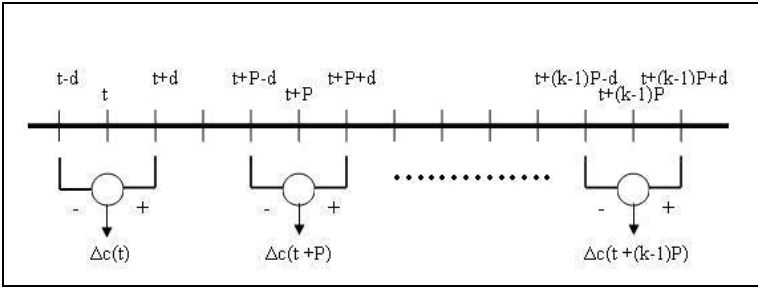
Fig. 1. Computation of SDC feature vector for each cepstral coefficient

- *P:* time shift between consecutive blocks.
- *k:* number of blocks whose delta coefficients are concatenated to form the SDC vector

For the case shown in Fig 1 the final SDC vector at frame time *t* is given by the concatenation from $i = 0$ to *k-1* of all the $\Delta c\,(t + iP)$, where:

$$\Delta c(t + iP) = c(t + iP + d) - c(t + iP - d) \tag{1}$$

Accordingly, kN parameters are used for each SDC feature as compared with 2N for conventional cepstral and delta-cepstral feature vectors. In language identification applications, SDC features substitute cepstral and delta-cepstral features, using different combinations of (N, d, P, k).

More recently, a modified version of SDC was reported to have even higher performance in LID [9], calculated using a recurrent expression:

$$\Delta c(t + iP) = \frac{\sum_{d=-D}^{D} dc(t + iP + d)}{\sum_{d=-D}^{D} d^2} \tag{2}$$

4 Front End Processing

Cepstral coefficients derived from a Mel-frequency filter bank (MFCC) have been used to represent the short time speech spectra. All speech material used for training and testing is pre-emphasized with a factor of 0.97, and an energy based silence removal scheme is used. A Hamming window with 30ms window length and 30% shift is applied to each frame and a short time spectrum is obtained applying a FFT. The magnitude spectrum is processed using a 30 Mel-spaced filter bank, the log-energy filter outputs are then cosine transformed to obtain 12 Mel-frequency cepstral coefficients, the zero cepstral coefficient is not used. Therefore, each window of signal frame is represented by a 12-dimensional MFCC features vector.

In order to reduce the influence of mismatch between training and testing acoustic conditions, a robust feature normalization method for reducing noise and/or channel

effects has been proposed, the Cepstral Mean and Variance Normalization (CMVN) [16]. Assuming Gaussian distributions, CMVN normalizes each component of the feature vector according to the expression:

$$\hat{c}_i[n] = \frac{c_i[n] - \mu_i}{\sigma_i}$$

(3)

where $c_i[n]$ and $\hat{c}_i[n]$ are the i-th component of the feature vectors at time frame n before and after normalization, respectively, and μ_i and σ_i are the mean and variance estimates of the sequence $c_i[n]$.

Delta-cepstral features are obtained for each MFCC features vector, using $d=2$ as time advance and delay for the delta computation, at last, and using equation 2, SDC features are obtained.

Three set of features are used in each one of the experiments:

1. 12 MFCC + 12 delta , dimension 24 (baseline) : MFCC + D
2. 12 MFCC + SDC (12,2,2,2), dimension 36: MFCC + SDC
3. 12 SDC(12,2,2,2), dimension 24: SDC

5   Database and Experiments

Ahumada [11] is a speech database of 103 Spanish male speakers, designed and acquired under controlled conditions for speaker characterization and identification. Each speaker in the database expresses six types of utterances in seven microphone sessions and three telephone sessions, with a time interval between them.

In order to evaluate the performance of SDC features in front to handset and channel mismatch in a remote biometric speaker verification using text prompted phrases, ten phonologically and syllabically balanced phrases in the three telephone sessions of Ahumada were used, the ten phrases are the same for each one of the 103 speakers. The performance of the verification is evaluated using a 64 mixtures GMM/UBM classifier, trained and tested with a subset of 50 speakers of the database; other subset of 50 speakers is used to train the 256 mixtures UBM.

In our approach, the behaviour of a text prompted biometric speaker verification is simulated, so the system is trained with ten phrases of each one of 50 speakers in session T1 and tested with each one of the phrases of the same speakers in session T2 and T3. All 50 speakers were used as targets for their corresponding models and as impostors for the rest of models, so we obtain 500 target and 4500 impostors in each test.

In each telephone sessions, conventional telephone line was used. In session T1, every speaker was calling from the same telephone, in an internal-routing call. In session T2, all speakers were requested to make a call from their own home telephone, trying to search a quiet environment, so the channel and handset characteristics are unknown. In session T3, a local call was made from a quiet room, using 9 randomly selected standard handsets, for each handset, three characteristics are

known: microphone sensibility and frequency response, and the ranges of signal to noise ratio in its associated channel.

Each speaker in session T3 uses one of the 9 handset, then the speakers can be grouped in two classes, for each one of the three measured characteristics:

- Low sensibility (< 1 mV/P) and high sensibility (> 2.5 mV/P) of the microphone.
- Low attenuation level (< 20 dB) and high attenuation level (> 35 dB) of the microphone band pass frequency response.
- Low and high signal to noise ratio mean (threshold: 35 dB) in the channel.

The experiments are organized in the following manner:

1. Evaluation of channel mismatch in uncontrolled conditions: trained with session T1 and tested with session T2
2. Evaluation of channel mismatch due to handset sensibility: trained with speakers in session T1 and tested with speakers in session T3, grouped in two classes, low sensibility (24 speakers) and high sensibility (26 speakers).
3. Evaluation of channel mismatch due to handset frequency response: trained with speakers in session T1 and tested with speakers in session T3, grouped in two classes, low attenuation level (30 speakers)and high attenuation level (20 speakers).
4. Evaluation of channel mismatch due to signal to noise ratio in the channel: trained with speakers in session T1 and tested with speakers in session T3, grouped in two classes, low (19 speakers) and high (31 speakers) signal to noise ratio mean.

6   Results

Evaluation of the results was performed using detection error tradeoff (DET) plot [17].Two indicators are used to evaluate the performance: Equal error rate (EER) and minimum of Detection Cost Function (DCF), defined as:

$$DCF= (C_{FR} * P_{FR} * P_{Target}) + (C_{FA} * P_{FA} * P_{NonTarget}) \tag{4}$$

Where

C_{FR} (cost of a missed detection) = 10

C_{FA} (cost of a false alarm) = 1

P_{Target} (a priori probability of a target speaker) = 0.01

$P_{NonTarget}$ (a priori probability of a non-target speaker) = 0.99

P_{FR} (Miss probability)

P_{FA} (False alarm probability)

The results of the four experiments are reflected in DET plots in figures 2 to 5 and Tables 1 to 4 with values of indicators EER and DCF.

DET plot of experiment 1 reflects a similar behaviour of SDC and MFCC features in front of channel mismatch where the channel and handset characteristics are unknown. Table 1 shows that MFCC + SDC features have better performance that MFCC +D features (better EER and DCF).
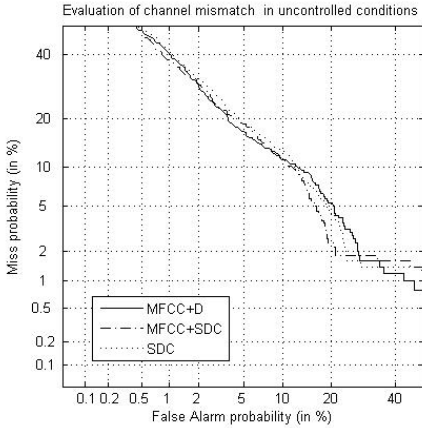
Fig. 2. Experiment 1: T1 train, T2 test
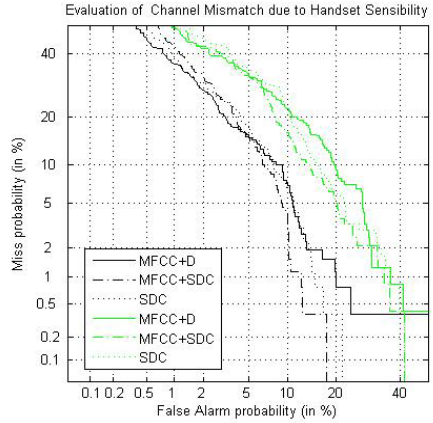
Fig. 3. Experiment 2: T1 train, T3 test black : high sensibility , green: low sensibility
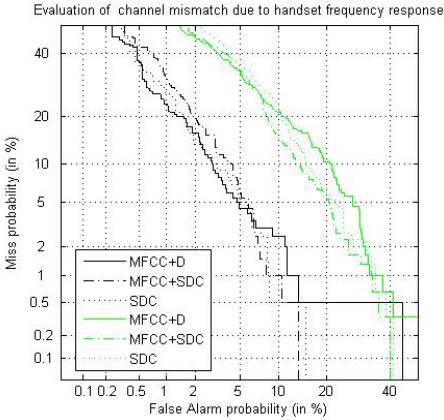
Fig. 4. Experiment 3: T1 train, T3 test black : low attenuation, green: high attenuation
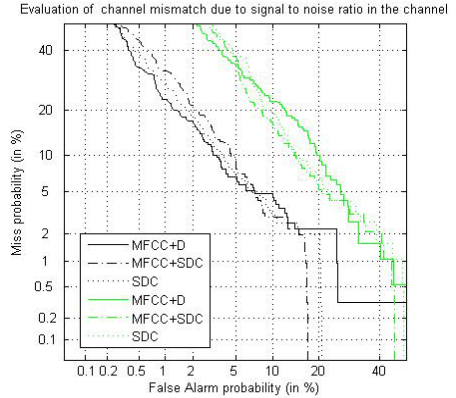
Fig. 5. Experiment 4: T1 train, T3 test black : high s/n, green: low s/n

Table 1. Experiment 1: channel mismatch in uncontrolled conditions

Features	EER	DCF
MFCC +D	0.107	0.048
MFCC+SDC	0.102	0.047
SDC	0.111	0.051

DET plot of experiment 2 reflects a better behaviour of both sets of SDC features compared to MFCC features in front of mismatch due to handset sensibility . Table 2 shows that both sets of SDC features have lower EER and similar DCF that MFCC +D features in both sensibility conditions.

Table 2. Experiment 2: channel mismatch due to handset sensibility

	Low sensibility		High sensibility	
Features	EER	DCF	EER	DCF
MFCC +D	0.154	0.057	0.091	0.045
MFCC+SDC	0.119	0.057	0.080	0.049
SDC	0.132	0.061	0.084	0.046

Table 3. Experiment 3: channel mismatch due to handset frequency response

	High attenuation		Low attenuation	
Features	EER	DCF	EER	DCF
MFCC +D	0.154	0.062	0.049	0.031
MFCC+SDC	0.12	0.064	0.055	0.037
SDC	0.133	0.067	0.05	0.032

DET plot of experiment 3 reflects a better behaviour of both sets of SDC features compared to MFCC features in front of high attenuation of handset frequency response. Table 3 shows that both sets of SDC features have lower EER and similar DCF that MFCC +D features in this condition.

Table 4. Experiment 4: channel mismatch due to signal to noise ratio in the channel

	Low s/n		High s/n	
Features	EER	DCF	EER	DCF
MFCC +D	0.157	0.070	0.058	0.032
MFCC+SDC	0.121	0.072	0.063	0.039
SDC	0.127	0.074	0.061	0.035

DET plot of experiment 4 reflects a better behaviour of both sets of SDC features compared to MFCC features in front of low signal to noise ratio in the channel. Table 3 shows that both sets of SDC features have lower EER and similar DCF that MFCC +D features in this condition.

Results of experiments 2, 3 and 4 reflect a better performance of both sets of SDC features in front of the worst mismatch condition: low handset sensibility, high attenuation in handset frequency response and low signal to noise ratio in the handset associated channel. Table 5 reflects the relative reduction in % of EER, in each experiment for both sets of SDC features respect to MFCC features.

Table 5. Reduction in % of EER for both sets of SDC features respect to MFCC features

Mismatch condition	MFCC + SDC	SDC
low handset sensibility	22	14
high handset attenuation	22	13
low s/n ratio in channel	23	19

7   Conclusions and Future Work

The result of the experiments reflect a superior performance of SDC features respect to MFCC + delta features in speaker verification using speech samples from tele-phone sessions of Ahumada Spanish database.

- Test in uncontrolled conditions (experiment 1) reflects similar behavior of SDC and MFCC features.
- Tests under controlled conditions (experiments 2, 3 and 4) reflect a better behav-iour of SDC respect to MFCC features in front of worst mismatch conditions.
- In these experiments, the EER reduction due to utilization of SDC features in-stead of MFCC features is superior to 22% using MFCC+SDC, and superior to 13% using SDC alone.
- Test under controlled conditions (experiment 2,3 and 4) reflect a similar behavior of SDC respect to MFCC features in front to better mismatch conditions, in ex-periment 2, SDC features have a better behavior than MFCC features in both mismatch conditions.

Shifted Delta Cepstral features must be considered as a new alternative of cepstral features, in order to reduce the effects of channel/handset mismatch in remote speaker verification performance. SDC features appended to MFCC features show the best results, but SDC features instead of MFCC +delta features show a good result too, maintaining the same feature dimensionality (24 dimensions).

Future work will be in the direction of evaluate the influence of SDC parameters d and P. SDC features must be assumed as a pseudo-prosodic vector, and these parame-ters are related with its time-dynamic behaviour. Also, H-Norm score normalization must be applied.

References

1. Ratha, N.K., Senior, A., Bolle, R.M.: Automated Biometrics. In: Singh, S., Murshed, N., Kropatsch, W.G. (eds.) ICAPR 2001. LNCS, vol. 2013, pp. 445–474. Springer, Heidelberg (2001)
2. Ortega-Garcia, J., Bigun, J., Reynolds, D., Gonzalez-Rodriguez, J.: Authentication gets personal with biometrics. IEEE Signal Processing Magazine 50–62 (2004)
3. Heck, L.P., Konig, Y., Sonmez, M.K., Weintraub, M.: Robustness to telephone handset distortion in speaker recognition by discriminative feature design. Speech Communica-tion 31, 181–192 (2000)
4. Mammone, R., Zhang, X., Ramachandran, R.: Robust speaker recognition. IEEE Signal Processing Magazine 58–71 (1996)
5. Rahim, M.G., Juang, B.H.: Signal Bias Removal by Maximum Likelihood Estimation for Robust Telephone Speech Recognition. IEEE Trans. On Speech and Audio Process-ing 4(1), 19–30 (1996)
6. Yiu, K.K., Mak, M.W., Kung, S.Y.: Environment Adaptation for Robust Speaker Verifica-tion. In: Eurospeech 2003, Geneva, pp. 2973–2976 (2003)
7. Teunen, R., Shahshahani, B., Heck, L.P.: A model based transformational approach to ro-bust speaker recognition. In: Proc. ICSLP (2000)

8. Reynolds, D.A: Comparison of background normalization methods for text-independent speaker verification. Proceedings European Conf. on Speech Communication and Technology. Eurospeech (1997)
9. Allen, F.: Automatic Language Identification. PhD Thesis, University of New South Wales, Sydney, Australia (2005)
10. Lareau, J.: Application of Shifted Delta Cepstral Features for GMM Language Identification. MsC Thesis, Rochester Institute of Technology, USA (2006)
11. Javier, O.-G., Joaquin, G.-R., Victoria, M.-A.: AHUMADA A Large Speech Corpus in Spanish for Speaker Characterization and Identification. Speech Communication (31), 255–264 (2000)
12. Bielefeld, B.: Language identification using shifted delta cepstrum. In: Proc. Fourteenth Annual Speech Research Symposium (1994)
13. Torres-Carrasquillo, P.A., Singer, E., Kohler, M.A., Greene, R.J., Reynolds, D.A., Deller Jr., J.R.: Approaches to language identification using Gaussian Mixture Models and shifted delta cepstral features. In: Proc. ICSLP, pp. 89–92 (2002)
14. Singer, E., Torres-Carrasquillo, P.A., Gleason, T.P., Campbell, W.M., Reynolds, D.A.: Acoustic, Phonetic, and Discriminative Approaches to Automatic Language Recognition. In: Proc. Eurospeech 2003, pp. 1345–1348 (2003)
15. Reynolds, D., Andrews, W., Campbell, J., Navrátil, J., Peskin, B., Adami, A., Jin, Q., Klusáček, D., Abramson, J., Mihaescu, R., Godfrey, J., Jones, D., Xiang, B.: Supersid final report: exploiting high-level information for high-performance speaker recognition. Tech. Rep. Workshop, The Centre for Language and Speech Processing (2002)
16. de Wet, F.: Additive Background Noise as a Source of non-Linear Mismatch in the Cepstral and Log-Energy Domain. Computer Speech and Language 19, 31–54 (2005)
17. Martin, A., et al.: The DET curve assessment of detection task performance. Proc. of EuroSpeech 4, 1895–1898 (1997)

Phone-Segments Based Language Identification for Spanish, Basque and English⋆

Víctor Guijarrubia and M. Inés Torres

Departamento de Electricidad y Electrónica
Universidad del País Vasco, Apartado 644, 48080 Bilbao, Spain
{vgga,manes}@we.lc.ehu.es

Abstract. This paper presents a series of language identification (LID) experiments for Spanish, Basque and English. Spanish and Basque are both official languages in the Basque Country, a region located in northern Spain. We focused our research on some techniques based on phone decoding. We propose the use of phone segments as decoding units instead of just phones. We describe a simple procedure to obtain a set of phone segments that typically appear in the languages involved. In comparison with similar techniques that do not rely on phone segments, the choice of these segments as decoding units yields a remarkable improvement in terms of LID accuracy: from 93.02% using phones to 98.32% using phone segments, when applied to trilingual read speech.

Keywords: language identification, phone decoding.

1 Introduction

Language identification is a classical pattern recognition problem that is strongly tied to multilingual speech recognition and dialogue systems.

It has been addressed in the past using a variety of tactics; for instance, those exploiting prosodic cues [1] as rhythm or intonation. Nevertheless, most of them are based on speech recognition approximations: phone decoding approaches [2,3], which rely on phone sequences; Gaussian mixture models [2,4] treating only the acoustic; or large-vocabulary continuous-speech recognition approaches [5], which operate based on full lexical sequences. A thorough analysis discussing the current state of the LID systems can be consulted here [6].

The typical LID system is based on a phone recognition followed by n-gram language modelling (PRLM) or, most commonly, parallel PRLM (PPRLM) [2]. In these cases, some monolingual phoneme decoders are used to tokenise the input sequence, which is then analysed by phonotactic models to predict the spoken language. Although most of these systems use language-dependent phonemes, there are some recent works dealing with unified phoneme sets [7].

The ultimate goal of any LID system is to identify the language being used by an unknown speaker. In some evaluations, like those proposed by the National Institute of Standards and Technology (NIST), 12 or 7 languages are included in those LID systems [6]. However, for multilingual communities high performances are required, but only for the involved languages, typically two or three.

The aim of this work is to build a LID system for Spanish, Basque and English. Basque is a minority language, but it is the joint official language, along with Spanish, for the 2.5 million inhabitants of the Basque Country (northern Spain).

The main differences between Spanish and Basque fall on the lexical units and the morphosyntactic structure. From a phonetic point of view, the set of Basque phones does not differ much from the Spanish one. The two languages share the same vowels (only five). Nevertheless, Basque includes larger sets of fricative and affricate sounds. English, on the other hand, is phonetically very different from Spanish and Basque and includes a larger number of vowel and semi-vowel sounds. In addition, the way to get the phonetic transcription is also different. Whereas for Spanish and Basque the phonetic transcription can be generated by means of a simple set of rules, English transcriptions require the use of a dictionary. Thus, we could presume that English could be discriminated from Spanish and Basque using only acoustic features. However, as suggested in [?], a Basque-Spanish discrimination would require information about how the phones combine in each language.

In this paper, we propose the use of phone segments as the decoding units of a LID system. The fundamental idea is to take advantage of sequences of sounds that appear frequently in each language, with the purpose of improving the phone decoding rates and in order to better identify the language being used. To obtain those segments, we propose a simple technique based on N-gram statistics.

In this sense, the remainder of the paper is organised as follows: Section 2 presents the procedure applied to obtain the phone segments, Section 3 describes each of the LID methods used in this study, Section 4 centres on the main features of the speech databases used in the experiments, Section 5 presents the results obtained for the different LID approaches, comparing LID accuracy values for both phones and phone segments, and finally Section 6 discusses the conclusions of the present work.

2   Obtaining the Phone Segments

We propose the use of phone segments as decoding units, with the idea of getting a better representation of each language. To obtain those segments, a simple procedure based on N-gram statistics was used. This process is summarised in the following points:

– Given the training corpus, identify and extract all the 2-grams, 3-grams, ..., n-grams available. In our case, we chose $n = 5$, because it takes into account the most common prefixes, suffixes and words appearing in the languages.
– Sort them in order of decreasing values of n (5-grams before 4-grams, 4-grams before 3-grams, ...), decreasing number of appearances and according

to inverse alphabetical order. This final condition appears naturally when sorting the n-grams in decreasing number of appearances using the *sort* GNU/Linux command.

– Get the subset of phone n-grams that, while keeping the original order, satisfies a minimum number of occurrences. The idea is to replace all the appearances of a sequence of phones corresponding to a n-gram with a single unit obtained joining all the phones forming that n-gram. Some of the phone n-grams might not appear after this process or might not satisfy the minimum number of occurrences, due to the fact that they could be included in previous phone n-grams. The first of those n-grams not satisfying the minimum number of occurrences is then removed. The process of relabelling and search for not valid n-grams is iteratively repeated until getting the final subset.

3   Language Identification Methods

In order to perform the proposed language identification task, some phone decoding methods were implemented. These techniques rely on acoustic phonetic decoders, which find the best sequence of decoding units depending on the input speech signal. In our case, these decoders are based on the Viterbi algorithm, which, given an input, finds the most likely path through a probabilistic network. When applied to an acoustic phonetic decoder, this network consists of a combination of all the acoustic models, usually being them Hidden Markov Models (HMMs) associated to a previously defined set of phonetic units of the language. In this sense, given a set of acoustic models Λ^l associated to a language l and an input sequence of acoustic observations $O = o_1 \ldots o_T$, a Viterbi decoder finds the best sequence of states $Q = q_1 \ldots q_T$ through the network of models. This can be expressed in a mathematical manner as follows:

$$Q = \underset{q_1 \ldots q_T}{\arg\max} \, P(q_1 \ldots q_T, o_1 \ldots o_T | \Lambda_l) \tag{1}$$

The path Q determines a sequence of decoding units $X^l = X_1 \ldots X_N$, based on the previously defined set of HMMs associated to language l. In this work, we decided to evaluate phones against phone segments as decoding units to assess their impact upon the accuracy of the associated LID system.

The following subsections describe one by one the different techniques that were explored.

3.1   Phone Decoder Scored by a Phonotactic Model (PD+PhM)

For every language being studied, an unconstrained acoustic decoder is applied, resulting in a sequence of decoding units for each language. A language-dependent phonotactic model is then employed to assign a score to each of the sequences for that language. The language of the utterance is selected to be that with the highest score; that is, the language for which

$$L = \arg\max_{l} P(X^l|Ph^l) \tag{2}$$

where Ph^l represents the phonotactic model for language l. Typically, these phonotactic models are modelled using *n-grams*. Thus

$$P(X^l|Ph^l) = \prod_{i=1}^{N} P(X_i^l|X_{i-1}^l, \ldots, X_{i-n+1}^l, Ph^l) \tag{3}$$

A block diagram of the PD+PhM technique is shown in Figure 1. This technique could be considered as a simplification or variation of the commonly used PPRLM technique.
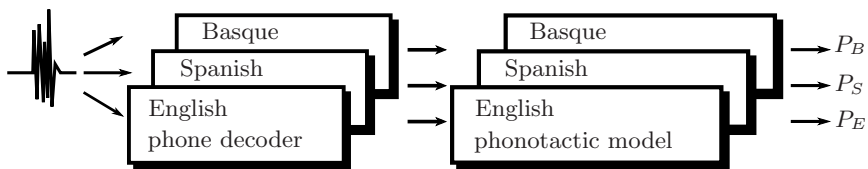
Fig. 1. PD+PhM block diagram. P_B stands for Basque probability, P_S stands for Spanish probability and P_E stands for English probability.

3.2   Phone Decoder Constrained by a Phonotactic Model (PDPhM)

Also known as PPR in the literature [2], this method performs a phone decoding for each language being studied, but constrained by a phonotactic model. That is, in this case, the phonotactic model is used during the decoding process, whereas in the PD+PhM was applied after the decoding.

This way, the decoder is similar to a speech recognition system. In this case, our goal is to find a sequence of phonetic units instead of a sequence of uttered words. In this context, the best sequence of decoding units X^l that fits the input sequence of acoustic observations O is found applying the Bayes' rule

$$P(X^l|O) = P(O|X^l)P(X^l)/P(O) \tag{4}$$

where $P(O|X^l)$ is the probability of the acoustic sequence for that particular phonetic string; this value is computed using the HMMs. $P(X^l)$ is the *a priori* probability of the sequence of decoding units, and is computed using a phonotactic model. In the same way, $P(O)$ represents the *a priori* probability of the acoustic sequence. Typically this parameter is not computed, since it has a constant value across all the possible lexical strings obtained from a given decoding. However, when comparing the output of different recognisers, this probability should also be considered. In this work, we approximated that term using an acoustic normalisation (referred as an acoustic confidence measure), in a similar way as that presented in [9]. This technique reported improvements in other

LID applications [10]. The acoustic likelihood of each of the decoded units is normalised by the likelihood of the best unconstrained phone sequence in that period of time.

Finally, the hypothesised language is assumed to be the one for which

$$L = \arg\max_{l} P(X^l | O) \tag{5}$$

A block diagram of the PDPhM technique is shown in Figure 2.
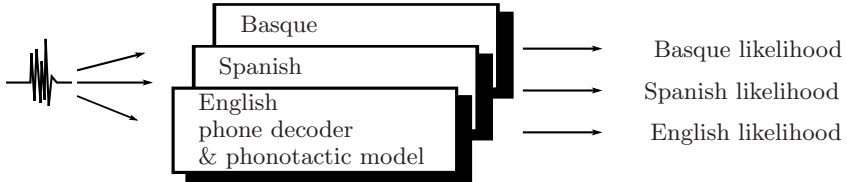
Fig. 2. PDPhM block diagram

4   Speech Corpora

The experiments reported in this paper were performed using several speech databases.

The training of the basic acoustic models for Basque was carried out by means of a phonetically balanced database called EHU-DB16 [11]. This database contains 9394 sentences uttered by 25 speakers and includes around 340000 phones. The resulting models reported phone recognition accuracies of around 74% for this database.

For Spanish, we resorted to the phonetic corpus of the Albayzin database [12], consisting of 4800 sentences uttered by 29 speakers, resulting in around 187000 phones and also being phonetically balanced. The resulting models reported phone recognition accuracies of around 75% for this database.

For English, we chose the *Wall Street Journal 1* database (the SI200 corpus, to be precise). It is composed of more than 30000 sentences uttered by 200 speakers, resulting in more than 66 hours of speech material with around 2 million phones. The resulting models reported phone recognition accuracies of around 58% for this database.

The evaluation set consisted of a weather forecast database recorded initially for Spanish and Basque [13] and later for American English. This database contains 500 different sentences uttered by 36 speakers for every language. The 500 sentences were divided into blocks of 50 sentences each and every speaker uttered the sentences corresponding to one of these blocks. A total of 1800 utterances were recorded for each language. Table 1 summarises the main features of this database. Although there are some spontaneous effects, the data sources are read speech.

Table 1. Main features of the evaluation database

	Spanish	Basque	English
Speakers		36	
Utterances		1800	
Length (hours)	3	3.5	3.4
Average Length of an utterance (sec)	6	7	6.8

It is important to mention that not only do the three languages share the same task and recording conditions, but also two of the languages (Spanish and Basque) share the same speakers. This reduces possible effects benefiting one language from another. Another important aspect to take into account is that silences were not removed from the utterances.

5   Experimental Results

5.1   Experimental Conditions

Within the frame of the experiments that were carried out, the databases were parametrised into 12 Mel-frequency cepstral coefficients with delta and acceleration coefficients, energy and delta-energy. Thus, four acoustic representations were defined. The length of the analysis window was 25 ms and the window shift, 10 ms.

Each phone-like unit was modelled by a typical left-to-right non-skipping self-loop three-state HMM, with 32 Gaussian mixtures per state and acoustic representation. The phone sets were based on the phonemes of each language. A total of 35 context-independent phone-like units were used for Basque, 24 for Spanish and 25 for English. This reduced set of 25 units for English is based on the 39 phone set used by the Carnegie Mellon University (CMU) in its pronouncing dictionary. A previous study was carried out to improve the acoustic decoding accuracies over the Timit database; in this sense, and based on the confusion matrices, some units were merged, leading to the definitive set of units being used. The phone recognition accuracies improved from 59.97 to 65.46. For the segments, the acoustic models were build concatenating the models of their constituent phones.

For the above-mentioned LID techniques, a phonotactic model is also required to score the recognised phone sequence. Moreover, in order to adhere to the phonetic constraints, a *k-testable in the strict sense* (k-TTS) model [14] was used throughout these experiments. The k-TTS are similar to variable-length n-grams, with k and n having approximately the same meaning. Different k values (ranging from $k = 3$ to $k = 5$) were evaluated.

These phonotactic models were trained using several text corpora available at our disposal. For Basque and Spanish, these corpora were phonetically

transcribed based on rules developed by experts, whereas for English the transcription was done using a dictionary; more precisely, the *CMU pronouncing Dictionary* (version 0.6).

5.2   Results of the Experiments

First of all, for every language we needed to obtain a basic set of decoding units consisting in phone segments. For this purpose, the process described in Section 2 was applied. As the training material for each language is different, the minimum number of appearances required to each language was also different. The idea was to get, initially, a similar number of segments for all three languages (around 500). For Spanish and Basque this minimum threshold value was set to 1000 whereas for English it was set to 4000.

Once applied the process described in Section 2, the number of decoding units was 172 for Spanish, 321 for Basque and 221 for English. These units were also used to train the phonotactic models for the segment-based approaches. That is, the phonotactic models of the segment-based approaches are n-grams of phone segments.

In order to carry out Spanish-Basque-English identification experiments, a complete utterance was presented to the LID system, implementing the various approaches described in Section 3.

As mentioned above, one of the aims of the present work was to asses the performance of phone-segment based systems versus those systems that rely on phones only. The results, in terms of LID accuracy, are summarised in Table 2. It is worth pointing out that for both techniques a decoded-string length normalisation was used, since this approximation yielded the best results. Only the PDPhM technique has been applied when using the phone segments (denoted as PDPhM(s) in Table 2). The reasons for this is that the advantage provided by the phone segments is that they help the uttered language while making worse the other languages due to poorer acoustic scores. When using the PD+PhM technique, as the system is not constrained, it is not forced to go through the segments and no real advantage is achieved.

As can be seen, the use of phone segments as decoding units results in a great improvement. Using better phonotactic models, phone segments can yield accuracies of nearly 99%.

One of the differences between the PD+PhM and the PDPhM technique is that the PDPhM includes acoustic scores. Looking at the results for the PD+PhM and PDPhM using phones, we can see that Spanish and Basque benefit form these acoustic scores, whereas English does not. This can be explained by the fact that the Spanish and Basque HMMs are better estimated because they are trained using more reliable phonetic transcriptions. For example, for the PDPhM technique and $k = 4$, the phone recognition rates are around 85% for Spanish and Basque, but only around 60% for English. Note also that whereas the Spanish and Basque transcriptions are completely reliable, the English ones are not. However, for $k = 5$, PD+PhM performs worse than PDPhM. Further investigation should carried out to explain this fact.

Table 2. LID accuracies values for several phonotactic models and according to the techniques described in Section 3

	k	Spanish	Basque	English	Overall
PD+PhM	3	91.71	91.83	80.72	88.09
	4	91.16	94.17	80.72	88.68
	5	92.94	95.17	73.22	87.11
PDPhM	3	99.83	93.72	47.61	80.39
	4	99.89	98.17	63.39	87.15
	5	99.89	98.94	80.22	93.02
PDPhM(s)	3	99.89	99.61	87.83	95.78
	4	99.89	99.67	95.33	98.30
	5	99.89	99.56	95.50	98.32

The use of phone segments improve the results for all the languages. Even if it looks that restricting the decoder is worse for English, when using the phone segments a significant improvement is achieved. For Spanish and Basque the benefits are small, mainly because of the already high accuracies. As commented before, when using the segments, the acoustic scores assigned to the non-uttered languages are much more small, due to they are being forced by the phonotactic model through some predefined paths. However, the uttered language benefits from more reliable paths assigned by the phonotactic model. For example, for $k = 4$ the phone recognition rates in this case are around 95% for Basque and Spanish and around 75% for English. The results clearly demostrate that the phone segments are useful for languages with poorer acoustic modelling. In this work that happened for English, but for other tasks or languages, that could happen for other languages. This also reinforces the idea of exploring a unified phoneme set to overcome similar problems.

6   Concluding Remarks

In this paper we have presented a simple procedure to gather some phone-segments. The use of these phone segments as decoding units resulted in a notable improvement of the associated LID system in terms of accuracy: comparing the results to those obtained using only phones as decoding units, the accuracy increased from 93.02 to 98.32%. The effect of these phone segments is especially significant for English, allowing a remarkable increase in the accuracies. The phone segments help modellize better the language being uttered and worse the others, providing the improvement in the LID accuracies. The phone segments are useful for English in this work, but under different conditions, they could be helpful for others as well.

References

1. Itakahashi, S., Du, L.: Language identification based on speech fundamental frequency. In: EUROSPEECH, Madrid, Spain, vol. 2, pp. 1359–1362 (1995)
2. Zissman, M.A., Singer, E.: Automatic language identification of telephone speech messages using phoneme recognition and n-gram modelling. In: ICASSP, Adelaide, Australia, vol. 1, pp. 305–308 (1994)
3. Navrátil, J., Zühlke, W.: An efficient phonotactic-acoustic system for language identification. In: ICASSP, Seattle, USA, vol. 2, pp. 781–784 (1998)
4. Singer, E., Torres-Carrasquillo, P.A., Gleason, T.P., Campbell, W.M., Reynolds, D.A.: Acoustic, phonetic and discriminative approaches to automatic language identification. In: EUROSPEECH, Geneva, Switzerland, pp. 1349–1352 (2003)
5. Schultz, T., Rogina, I., Waibel, A.: Lvcsr-based language identification. In: ICASSP, Atlanta, USA, pp. 781–784 (1996)
6. Martin, A.F., Le, A.N.: The current state of language recognition: Nist 2005 evaluation results. In: Proceedings of the IEEE Odyssey 2006, the Speaker and Language Recognition Workshop, San Juan, Puerto Rico (2006)
7. Li, H., Ma, B.: A phonotactic language model for spoken language identification. In: ACL 2005, Morristown, NJ, USA, pp. 515–522 (2005)
8. Guijarrubia, V., Torres, I.: Basque-spanish language identification using phonebased methods. In: Proceedings of International Conference of Spoken Language Processing, Pittsburgh, USA, pp. 1780–1783 (2006)
9. Young, S.R.: Detecting misrecognitions and out-of-vocabulary words. In: ICASSP, Adelaide, Australia, vol. 2, pp. 21–24 (1994)
10. Hieronymus, J.L., Kadambe, S.: Spoken Language Identification Using Large Vocabulary Speech Recognition. In: Proceedings of International Conference of Spoken Language Processing, Philadelphia, USA, pp. 1780–1783 (1996)
11. Guijarrubia, V., Torres, I., Rodríguez, L.J.: Evaluation of a Spoken Phonetic Database in Basque Language. In: LREC 2004, Lisbon, vol. 6, pp. 2127–2130 (2004)
12. Moreno, A., Poch, D., Bonafonte, A., Lleida, E., Llisterri, J., Mariño, J.B., Nadeu, C.: Albayzin speech database: Design of the phonetic corpus. In: EUROSPEECH, Lisbon (1993)
13. Pérez, A., Torres, I., Casacuberta, F., Guijarrubia, V.: A Spanish-Basque weather forecast corpus for probabilistic speech translation. In: 5th SALTMIL Workshop on Minority Languages, Genoa, Italy, pp. 99–101 (2006)
14. Torres, I., Varona, A.: K-TSS Language Model in a Speech Recognition System. Computer Speech and Language 15(2), 127–149 (2001)

A New Algorithm to Compute the Distance Between Multi-dimensional Histograms

Francesc Serratosa[1], Gerard Sanromà[1], and Alberto Sanfeliu[2]

[1] Universitat Rovira i Virgili, Spain
[2] Universitat Politècnica de Catalunya, Spain
francesc.serratosa@.urv.cat,
gerard.sanroma@urv.cat,
sanfeliu@iri.upc.edu

Abstract. The aim of this paper is to present a new algorithm to compute the distance between n-dimensional histograms. There are some domains such as pattern recognition or image retrieval that use the distance between histograms at some step of the classification process. For this reason, some algorithms that find the distance between histograms have been proposed in the literature. Nevertheless, most of this research has been applied on one-dimensional histograms due to the computation of a distance between multi-dimensional histograms is very expensive. In this paper, we present an efficient method to compare multi-dimensional histograms in $O(z^2)$, where z represents the number of bins.

Keywords: Multi-dimensional Histogram distance, Earth Movers Distance, Second-Order Random Graphs.

1 Introduction

Finding the distance or similarity between histograms is an important issue in image classification or image retrieval since a histogram represents the frequency of the values of the pixels among the images. For this reason, a number of measures of similarity between histograms have been proposed and used in computer vision and pattern recognition. Moreover, if the position of the pixels is unimportant while considering the distance measure, we can compute the distance between images in an efficient way by computing the distance between their histograms.

Histograms can also be used in structural pattern recognition. For instance, Serratosa defined the Function-Described Graphs [12], which is structure that represents a cluster of Attributed Graphs in which there is a probability density function in each node of the structure described by a histogram. Thus, to compare clusters (that is, to compare Function-Described Graphs), it is needed a distance between histograms to compare each of their nodes. Latter, the same authors defined the Second-Order Random Graphs [13]. This structure represents also a cluster of Attributed Graphs but there is much amount of information since there is a joint probability in each node described by a 2-dimensional histogram. The computational cost of comparing graphs is exponential respect the number of nodes in the worst

case. There are some efficient algorithms that obtain sub-optimal distances in polynomial cost respect the number of nodes. For this reason, it is important to reduce the time consuming comparing their nodes.

Most of the distance measures presented in the literature (there is an interesting compilation in [1]) consider the overlap or intersection between two histograms as a function of the distance value but they do not take into account the similarity on the non-overlapping parts of the two histograms. For this reason, Rubner presented in [2] a new definition of the distance measure between n-dimensional histograms that overcomes this non-overlapping parts problem. It was called Earth Mover's Distance and it is defined as the minimum amount of work that must be performed to transform one histogram into the other one by moving distribution mass.

Often, for specific set measurements, only a small fraction of the *bins* in a histogram contain significant information, that is, most of the *bins* are empty. This is more frequent when the dimensions of the histograms increase. In that cases, the methods that use histograms as fixed-sized structures obtain poor efficiency. In the algorithm depicted by Rubner [2] to find the Earth Mover's Distance the empty-bins where not explicitly considered. They used the simplex algorithm [3] to compute the distance measure and the method presented in [4] to search a good initialisation. The computational cost of the simplex iteration is $O(z'^2)$, where z' is the number of non-empty bins. The main drawback of this method is that the number of iterations is not bounded. Moreover, the initialisation cost is $O(z'^3)$.

To reduce the computational cost, Cha presented in [1] three algorithms to obtain the Earth Mover's Distance between one-dimensional histograms when the type of measurements where *nominal*, *ordinal* and *modulo* in $O(z)$, $O(z)$ and $O(z^2)$ respectively, being z the number of levels or bins.

Finally, Serratosa reduced more the computational cost of comparing one-dimensional histograms in [5]. They presented three new algorithms to compute the Earth Mover's Distance between one-dimensional histograms when the type of measurements where *nominal*, *ordinal* and *modulo*. The computational cost were reduced to $O(z')$, $O(z')$ and $O(z'^2)$ respectively, being z' the number of non-empty bins.

It was presented in [6] an algorithm to compute the distance between histograms that the input was a built histogram (obtained from the target image) and another image. Then, it was not necessary to build the histogram of the image of the database to compute the distance between histograms.

Really few have been done to compare n-dimensional histograms except in [2]. The main drawback of the method presented in [2] is the computational cost. The following papers, make use of colour histograms, although the distance between them is not the main object of the work. One of the earliest papers is [7]. In that paper, the intersection of a pair of colour histograms (three dimensional histogram) was used to obtain a similarity measure between images. More recently, some kernel functions were defined in [8] based on the RGB and HSV histograms. In that paper, the number of bins per each dimension of the histograms had to be reduced to 16 due to run time an space requirements. And in [9], a support vector machine was used to classify images based on colour histograms. The bins of their histograms were not fixed-structures but they were variable depending on the density of the pixels. Finally, in

[10], a tree structure was defined for image retrieval. In each node of the tree, only the average of the histograms were stored.

In this paper, we present an efficient algorithm to compute the distance between n-dimensional histograms with a computational cost of $O(z^2)$. Our algorithm does not depend on the type of measurements (*nominal*, *ordinal* or *modulo*). In the next section, we define the histograms and types of values. In section 3, we give the definitions of distances between histograms and between sets and in section 4 we show the algorithm to compute the distance between histograms. In section 5, we show a separability-class function based on the histogram distance. In sections 6 and 7 we show the experimental validation of our algorithm and the conclusions.

2   Sets and Histograms

Let x be a measurement which can have one of z values contained in the set $X=\{x_1,...x_z\}$. Each value can be represented in a T-dimensional vector as $x_i=(x_i^1, x_i^2,...,x_i^T)$. Consider a set of n elements whose measurements of the value of x are $A=\{a_1,...a_n\}$ where $a_t \in X$ being $a_t=(a_t^1, a_t^2,...,a_t^T)$.

The histogram of the set A along measurement x is $H(x,A)$ which is an ordered list consisting of the number of occurrences of the discrete values of x among the a_t. As we are interested only in comparing the histograms and sets of the same measurement x, $H(A)$ will be used instead of $H(x,A)$ without loss of generality. If $H_i(A)$, $1 \leq i \leq z$, denotes the number of elements of A that have value x_i, then $H(A)=[H_1(A), ...,H_z(A)]$ where

$$H_i(A) = \sum_{t=1}^{n} C_{it}^A \tag{1}$$

and the individual costs are defined as

$$C_{i,t}^A = \begin{cases} 1 & if \ a_t = x_i \\ 0 & otherwise \end{cases} \tag{2}$$

The elements $H_i(A)$ are usually called *bins* of the histogram. Note that z is the number of bins of the histogram. In a T-dimensional histogram with m values per each dimension, the number of bins is $z=m^T$. Therefore, $1 \leq i \leq m^T$.

In this paper, the sets are images. For this reason and for the rest of the paper, the bins of the histograms represent the null or natural numbers, $a_t^i \in \{0, N\}$.

The distance between histograms presented in this paper is used as a fast method for comparing images and image retrieval. The most used colour representations are base on the R,G,B or H,S,I descriptors. The hue parameter (H) is a modulo-type measurement (measurement values are ordered but form a ring due to the arithmetic modulo operation) and the other parameters are ordinal-type measurements.

Corresponding to these types of measurements mentioned before, we define a measure of difference between two measurement levels $a=(a^1, a^2,...,a^T) \in X$ and $b=(b^1, b^2,...,b^T) \in X$ as follows:

$$d(a,b) = \sqrt{\sum_{j=1}^{T} S^2} \qquad \text{where} \tag{3}$$

$$S = \begin{cases} m - \left| a^j - b^j \right| & \text{if } a^j - b^j \le m/2 \text{ and } a^j, b^j \in Modulo\, type \\ \left| a^j - b^j \right| & \text{otherwise} \end{cases} \qquad (4)$$

This measure satisfy the following necessary properties of a metric. Since they are straightforward facts, we omit the proofs. The proof of the triangle inequality for the modulo distance is depicted in [1] for the one-dimensional case ($T=1$).

3   Distance Definitions

In this section we present the distance between sets $D(A,B)$ and the distance between their histograms $D(H(A),H(B))$. It was demonstrated in [11] that both satisfy the necessary properties of a metric and that the distance values are the same, $D(A,B) = D(H(A),H(B))$. This is an important result since we present an algorithm that obtains a good approximation of $D(H(A),H(B))$ with a quadratic computational cost respect the number of *bins* of the histogram z. Moreover, in most of the applications, z is much smaller than n. Another advantage is that the time consuming of the comparison is constant and does not depend on each set.

Given two sets of n elements, A and B, the distance measure is considered as the problem of finding the minimum difference of pair assignments between both sets. That is, to determine the best one-to-one assignment f (bijective function) between the sets such that the sum of all the differences between two individual elements in a pair $a_i \in A$ and $b_{f(i)} \in B$ is minimised. See [11] for more information.

$$D(A,B) = \min_{\forall f A \to B} \left(\sum_{t=1}^{n} d\left(a_t, b_{f(t)}\right) \right) \qquad (5)$$

The distance between histograms that our algorithm computes was presented in [11]. It is a generalisation of the Earth Mover's Distance presented in [2]. Intuitively, given two T-dimensional histograms, one can be seen as a mass of earth properly spread in space, the other as a collection of holes in that same space. Then, the distance measure is the least amount of work needed to fill the holes with earth. Here, a unit of work corresponds to transporting a unit of earth by a unit of ground distance.

More formally, given two histograms $H(A)$ and $H(B)$, where measurements can have one of z values contained in the set $X=\{x_1,...x_z\}$, the distance between the histograms $D(H(A),H(B))$ is defined as follows,

$$D(H(A), H(B)) = \min_{\forall f A \to B} \left(\sum_{i,j=1}^{z} d\left(x_i, x_j\right) g_f\left(i, j\right) \right) \qquad (6)$$

The flow between the *bins* of both histograms is represented by $g_f(i,j)$, that is, the mass of earth that is moved as one unit from the *bin* i to the *bin* j. The product $d(x_i,x_j)g_f(i,j)$ represents the work needed to transport this mass of earth. Notice that $z = m^T$, being m the number of bins per each dimension and T the number of dimensions.

In [11], we determine the flow between *bins* $g_f(i,j)$, as a function of the one-to-one assignment f between the sets A and B used to compute the distance $D(A,B)$ as follows,

$$g_f(i,j) = \sum_{t=1}^{n} C_{i,t}^{A} C_{j,f(t)}^{B} \quad 1 \le i, j \le z \qquad (7)$$

were the costs C are given in (2).

It was demonstrated in [11] that with this new definition, we obtain two advantages; First, there is a relation between distances $D(A,B)$ and $D(H(A),H(B))$ through their definition. Second, the constraints arbitrarily imposed to the flow between *bins* in [2], were converted in deducted properties that make possible to naturally match the distance between histograms to the transportation problem.

4   Algorithm

In this section, we depict an efficient algorithm used to compute the distance between histograms based on a solution to the well-known transportation problem [3]. Suppose that several suppliers, each with a given amount of goods, are required to supply several consumers, each with a given limited capacity. For each pair of suppliers and consumers, the cost of transporting a single unit of goods is given. The transportation problem is then to find a least-expensive flow of goods from the suppliers to the consumers that satisfies the consumer's demand. Our distance between histograms can be naturally cast as a transportation problem by defining one histogram as the supplier and the other one as the consumer. The cost of transporting a single unit of goods is set to the distance between the *bin* of one histogram and the *bin* of the other one, $d(x_i,x_j)$. Intuitively, the solution of the transportation problem, $g_f(i,j)$, is then the minimum amount of "work" required to transform one histogram to the other one subjected to the constraints defined by the properties of the flow $g_f(i,j)$ (see [11]).

The computational cost of the transportation problem is exponential, respect the number of suppliers and consumers, that is, the number of bins of the histograms, z. Fortunately, efficient algorithms are available. One of the most common solutions is the simplex algorithm [3], which is an iterative method that the cost of one simplex iteration is $O(z^2)$. The main drawback is that the number of iterations is not bounded and that this method needs a good initial solution. The Russell method [4] is the most common method used to find the first solution with a computational cost of $O(z^3)$.

In this paper, we present an efficient and not iterative algorithm (figure 1) with a computational cost of $O(z^2)$.

Given a pair of bins from both histograms, i and j, our algorithm finds the amount of goods that can be transported, $g_f(i,j)$, and computes the cost of this transportation,

```
Algorithm Histogram-Distance (H(A),H(B))
i,j = first()
while n > 0 // n: the number of elements of both sets
     gₓ(i,j) = min (Hᵢ(A) , Hⱼ(B))
     Hᵢ(A) = Hᵢ(A) - gₓ(i,j)
     Hⱼ(B) = Hⱼ(B) - gₓ(i,j)
     n = n - gₓ(i,j)
     D = D + gₓ(i,j) * d(xᵢ,xⱼ)
     i,j = next (i ,j)
Return D  //distance between histograms
```

Fig. 1. Algorithm that computes the distance between n-dimensional histograms

$g_f(i,j)*d(x_i, x_j)$. The algorithm finishes when all the goods have been transported, that is, all the elements of the sets, n, have been considered. In each iteration, a pair of bins is selected by the function *next*, in a given order.

4.1   The *Next* Function

Given a pair i,j (i and j are a supplier and a consumer, respectively), the *first* and *next* function returns the first and next pairs of supplier and consumer to be explored, respectively. The first pair of supplier-consumer and the order generated by the *next* function only depends on the dimensionality of histogram and the number of bins but not on the values of the histograms, for this reason, *first* and *next* can be computed a priori.

The order of the pairs i,j is set by decrementing an energy function E as follows,

$$i',j' = next\ (i,j)\quad iff\qquad E(i',j') \le E(i,j) \tag{8}$$

where E is defined as,

$$E(i,j) = Path\_Deviation_j(i) + Path\_Deviation_i(j) \tag{9}$$

The $Path\_Deviation_j(i)$ is the difference between the maximum cost from the bin i to any bin of the histogram and the real cost from this bin to the bin j,

$$Path\_Deviation_j(i) = max\_dist(x_i) - d(x_i, x_j) \tag{10}$$

It represents the worst case that the good can be sent (supplier) or received (consumer) respect the best case. Note that several pairs i,j can obtain the same energy value. In those cases, the order between them is set arbitrarily.

4.2   Computational Cost

Each step of the loop of the algorithm has a constant computational cost. The *next* function is implement as an array that for each pair i,j, returns the next pair i',j'. For this reason, the worst computational cost of our algorithm only depends on the number of iterations. The algorithm finishes when all the goods, n, have been transported and so, the worst case would be in the case that this is achieved at the last transportation from i,j, to i',j'. The number of possible transportations is z^2.

5   Experimental Validation

To verify the performance of the proposed method, we have conducted an experiment on the WANG database. The WANG database is a subset of the Corel database of 1000 images, which were selected manually to form 10 classes of 100 images each. The images are subdivided into 10 classes (e.g. Africa, beach, ruins, food) such that it can be assumed that a user wants to find the other images from a class if the query is from one of these 10 classes.

Our test database was composed by 200 images from the WANG database (20 images for each class). In Figure 2 we can see one representative image of each class. The query set was composed by 20 images (2 images for each class) and the database set was composed by the other 180 images (18 images for each class). We decide that the query image belongs to a class using the 5 nearest neighbours criteria.

Fig. 2. Ten images of WANG database. One of each class.

Given the depth of the pixels, the number of colours of the image, z, and also the computational cost of our algorithm is obtained. Besides, we can deduct the number of bins per dimension, m, depending on the dimensionality of the histogram. Table 1 shows in the last three columns the possible combinations of dimensionality and number of bins per dimension. For instance, a 1D-histogram with 64 bins has the same computational cost, 4096, than a 2D-histogram with 8 bins per dimension and a 3D-histogram with 4 bins per dimension. The empty cells in the table are the ones that m is not a natural number.

Table 1. Relation between the number of bins per dimension, m, and the number of colours, z, and cost, $O(z^2)$ in 1D, 2D and 3D histograms

depth of pixels	z (#colours)	Cost $O(z^2)$	m (1D) $(z=m^1)$	m (2D) $(z=m^2)$	m (3D) $(z=m^3)$
1	2	4	2		
2	4	16	4	2	
3	8	64	8		2
4	16	256	16	4	
5	32	1024	32		
6	64	4096	64	8	4
7	128	16384	128		
8	256	65536	256	16	
9	512	262144	512		8
10	1024	1048576	1024	32	
11	2048	4194304	2048		
12	4096	16777216	4096	64	16

Figure 3 shows the recognition ratio respect the number of colours in 6 different cases. In the first two cases, we have considered only the hue and the luminance. In the other two, we have considered the hue and saturation and also hue and luminance. In the last two cases we have considered the red, green and blue channels and also the hue, saturation and luminance channels. The values in figure 3 that correspond to empty cells in table 1 have been interpolated.
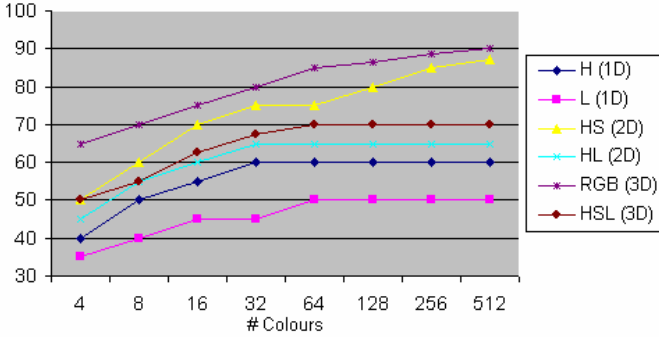
Fig. 3. Recognition ratio respect the number of colours

As we could imagine, when the number of colours increases (that is, the depth of the pixels), also increases the recognition ratio. But also, given a number of colours, it is worth to increase the dimensionality, since the recognition increases with the same computational cost. We can see also, that in this experiments, the Luminance has poor information, since H(1D) has better results than L(1D) and HS(2D) has better results than HSL(3D) or HL(2D).

6   Conclusions and Future Work

We have presented a new distance between multi-dimensional histograms and an efficient algorithm to compute this distance. Our method is useful for comparing multi-dimensional histograms of any type of measurements. The theoretical computational cost is $O(z^2)$, being z the number of bins. From the application point of view, we have seen that it is worth increasing the number of dimensions and reducing the number of bins per each dimension than reducing the number of dimensions in despite of increasing the bins per dimension, with a similar computational cost.

Although the computational cost of $O(z^2)$ can be considered low, in a real application, the run time can be too long when the number of images to be compared and the number of colours per image is high. For this reason, we are thinking about applying the *signature* structure presented in [6] due to the fact that in this structure, the empty bins are not explicitly considered. We will have the advantage that the number of iterations would be reduced (in the cases that the number of colours is high, that is, the histograms are sparse). But we will have the drawback that the computational cost of the function *next* would not be constant. We leave as a future work the implementation of this new method. From a theoretical point of view, we

will propose the new algorithm. And from the practical point of view, we have to show if the reduction of the number of iterations compensates the increase of the computational cost of the function *next*.

References

1. Cha, S.-H., Srihari, S.N.: On measuring the distance between histograms. Pattern Recognition 35, 1355–1370 (2002)
2. Rubner, Y., Tomasi, C., Guibas, L.J.: A Metric for Distributions with Applications to Image Databases. International Journal of Computer Vision 40(2), 99–121 (2000)
3. Numerical Recipes in C: The Art of Scientific Computing, ISBN 0-521-43108-5.
4. Russell, E.J.: Extension of Dantzig's algorithm to finding an initial near-optimal basis for the transportation problem. Operations Research (17), 187–191 (1969)
5. Serratosa, F., Sanfeliu, A.: Signatures versus Histograms: Definitions, Distances and Algorithms. Pattern Recognition 39(5), 921–934 (2006)
6. Jou, F.-D., Fan, K.-C., Chang, Y.-L.: Efficient matching of large-size histograms. Pattern Recognition Letters 25, 277–286 (2004)
7. Swain, M.J., Ballard, D.H.: Indexing via colour histograms. Int. J. Computer Vision (7), 11–32 (1991)
8. Kolesnik, M., Fexa, A.: Multi-dimensional colour Histograms for Segmentation of Wounds in Images. In: Kamel, M., Campilho, A. (eds.) ICIAR 2005. LNCS, vol. 3656, pp. 1014–1022. Springer, Heidelberg (2005)
9. Chapelle, O., Haffner, P., Vapnik, V.N.: Support Vector Machines for Histogram-Based Image Classification. IEEE Trans. On Neural Net. (10) (1999)
10. Gong, Y., Chuan, C.H., Xiaoyi, G.: Image indexing and retrieval based on colour histograms. Multimedia Tools and Applications 2(2), 133–156 (1996)
11. Serratosa, F., Sanromà, G.: An Efficient Distance between Multi-dimensional Histograms for Comparing images. In: SSPR 2006. LNCS (2006)
12. Serratosa, F., Alquézar, R., Sanfeliu, A.: Function-Described Graphs for modeling objects represented by attributed graphs. Pattern Recognition 36(3), 781–798 (2003)
13. Sanfeliu, A., Serratosa, F., Alquézar, R.: Second-Order Random Graphs for modeling sets of Attributed Graphs and their application to object learning and recognition. International Journal of Pattern Recognition and Artificial Intelligence 18(3), 375–396 (2004)

Fuzzy Vector Directional Filters for Multichannel Image Denoising

Alberto Rosales-Silva[1], Volodymyr I. Ponomaryov[1], and Francisco J. Gallegos-Funes[2]

National Polytechnic Institute of Mexico,
Mechanical and Electrical Engineering Higher School
[1] ESIME-Culhuacan; Av. Santa Ana 1000, Col. San Francisco Culhuacan,
04430, Mexico D.F., Mexico
`vponomar@ipn.mx`
[2] ESIME-Zacatenco; Av. IPN s/n, U.P.A.L.M. Col. Lindavista,
07738, Mexico D.F., Mexico
`fgallegosf@ipn.mx`

Abstract. We propose a fuzzy logic recursive scheme using directional processing for motion detection and spatial-temporal filtering to decrease Gaussian noise corruption. We introduce novel ideas that employ the differences between images. That permits to connect these using angle deviations in them obtaining several parameters and applying them in the robust algorithm that is capable to detect and differentiate movement in background of noise in any way.

Keywords: Fuzzy Logic, Video Sequences, Motion, Vectors.

1 Introduction

We consider motion detection in terms of robust change detection in pixels in an image [1]. The proposed method will not be able to distinguish completely changes due to motion from other changes due to rapidly camera zoom in the video sequence analyzed and movement in the scene present. Despite these problems, there exist numerous applications for this kind of motion detection [1-3]. Some techniques detect pixel-by-pixel changes, one of these is to simply substract the color levels of successive frames, and to conclude that the pixel has changed when the outcome exceeds a present threshold. We have developed the mathematical operations to consume less time, that can be achieved dividing different operations depending of parameters obtained using fuzzy logic membership functions. This permits to realize robust noise suppression and movement detection.

The main idea is to use adaptive threshold that is adapted to the local pixel statistics and the spatial pixel context. The proposed method is insensitive to noise; it is locally adaptive to spatially varying noise levels. The presented method uses data incoming during long period of time, and the threshold is adapted to both temporal and spatial information [1-3].

The noise should not be labelled as motion, it is not so important if not every single changed pixel of an object is detected. However, in the case of motion detection

during the denoising processing, where the detection result is used for temporal filtering, undetected changes in an object can lead to motion blur, but in the same time if some noise is labelled as motion it is no so critical. Using fuzzy logic techniques we aim at defining a confidence measure with respect to the existence of motion, to be called hereafter "motion confidence" [2].

2   Framework Method

We expose the framework of the algorithm for simultaneous motion detection and video denoising. The proposed algorithm is shown in Figure 1 where a noisy frame is processed firstly with fuzzy vector motion detection using the current and previous processed frames using a 5x5 window to provide the reference values for following processing stages.
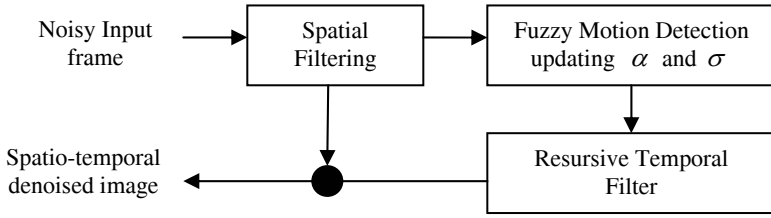
Fig. 1. Proposed denoising scheme using spatial-temporal techniques

2.1   Spatial Filtering

We use the Gaussian estimation algorithm to suppress the noise in the first stage,
Step 1) IF $\theta_c \leq F/255$ THEN Histogram is increased in "1", else is "0".
Step 2) Calculate probabilities for each one of these samples:

$$S = \sum_i Histogram_i \; ; \; p_i = Histogram_i/S \, , \, i=0,\ldots,255. \tag{1}$$

Step 3) Obtain standard deviation σ'_T :

$$\mu = \sum_{i=0}^{255} i \cdot p_i; \, \sigma^2 = \sum_{i=0}^{255} (i-\mu)^2 \cdot (p_i) \, , \, \sigma'_T = \sqrt{\sigma_T^2} \tag{2}$$

where $\theta_c = A(\bar{y}, y_c)$ is the angle deviation, $\bar{y} = \dfrac{1}{N}\sum_{i=1}^{N} y_i$ is the mean value with $i=1,\ldots,N$, $N=9$, and y_c is the central pixel.

Additionally, each plane of the video sequence in RGB space format is processed in an independent way, and the parameters $\sigma'_T = \sigma'_{red} = \sigma'_{green} = \sigma'_{blue}$ are adapted along the video sequence. The angle deviations of central pixel with respect to others in a 3x3 window are found [4]: $\theta_i = A(x_i, x_c)$, $x_i; i=1,\ldots,N-1$; where $i \neq central \; pixel$.

Now, we detect uniform regions using the mean weighted filtering algorithm [5]:

Step 1) IF θ_2 *AND* θ_4 *AND* θ_7 *AND* $\theta_5 \geq \tau_1$ THEN,

$$y_{out} = \sum_{\substack{i=1 \\ i \neq c}}^{N-1} x_i \left[\frac{2}{\left(1 + e^{\theta_i}\right)^r} \right] + x_c \left/ \sum_{i=1}^{N-1} x_i \left[\frac{2}{\left(1 + e^{\theta_i}\right)^r} \right] \right. + 1 \tag{3}$$

Step 2) IF θ_6 *AND* θ_3 *AND* θ_1 *AND* $\theta_8 \geq \tau_1$ THEN, Use Eq. (3).

Such the algorithm can realize the smoothing fast for Gaussian noise. Besides, the central pixel has the highest weight with "1" value to preserve some characteristics in uniform regions. We use a 5x5 processing window to estimate the standard deviation in same way as in the Gaussian estimation algorithm to obtain the values σ_T, and then we compare with the values σ'_T, in order to have a similarity value for each sample and to have a criterion in perform more or less filtering charge. From experiments we obtained that if $\sigma'_T < \sigma_T$, then $\sigma_T = \sigma'_T$, otherwise $\sigma'_T = \sigma_T$, where T can be the component red, green, or blue, that permits to improve temporal filtering algorithm. It has been defined experimentally by optimum PSNR and MAE criteria a threshold $Th_T = 2\sigma_T$ to preserve some important characteristics in a spatially filtered frame that will be used in temporal algorithm.

2.2   Fuzzy Vector Gradient Values

For each pixel *(i,j)* of the any component image, we use a 3x3 neighbourhood window. Each neighbour of *(i,j)* corresponds to one direction as illustrates Table 1.

If A_T denotes one component input image, the definition of the gradient can be defined as $\nabla_{(k,l)} A_T (i, j) = \left| A_T (i + k, j + l) - A_T (i, j) \right|$ with $k, l \in \{-1, 0, 1\}$, where the pair *(k,l)* corresponds to one of the eight directions that are called *the basic gradient values* [2], and *(i,j)* is called the centre of the gradient. To avoid blurred in presence of an edge, it is used not only one basic gradient for each direction but also two related gradient values. The three gradient values for a certain direction are finally connected together into one single value called fuzzy gradient value. Now we take pixels as the vectors to have directional process, taking the same procedure as in gradient values. By this way we obtain Fuzzy vector gradient values that are defined by the *Fuzzy Rule 1*. The two related gradient values in the same direction and the basic gradients are determined by the centres making a right-angle with the direction of the corresponding basic gradient [3].

Table 1. Involved gradient values to calculate the fuzzy vector gradient

Direction	Basic Gradient Involved	Related Gradients Involved
NW	(i, j), (i-1, j-1)	(i+1, j-1), (i-1, j+1)
N	(i, j), (i-1, j)	(i, j-1), (i, j+1)
NE	(i, j), (i-1, j+1)	(i-1, j-1), (i+1, j+1)
E	(i, j), (i, j-1)	(i-1, j), (i+1, j)
SE	(i, j), (i, j+1)	(i-1, j+1), (i+1, j-1)
S	(i, j), (i+1, j-1)	(i, j-1), (i, j+1)
SW	(i, j), (i+1, j)	(i-1, j-1), (i+1, j+1)
W	(i, j), (i+1, j+1)	(i-1, j) (i+1, j)

We can use the threshold Th_T obtained before and use the gradient values to have fuzzy vector gradient values in such a form,

Step 1) IF $\nabla_{\gamma\beta} < T_{s\beta}$ THEN calculate angle deviation in the direction $\alpha_{\gamma\beta}$ and obtain weight value,

$$\alpha'_{\gamma\beta} = 2/\left(1+e^{\alpha_{\gamma\beta}}\right)^r \tag{4}$$

Step 2) Obtain basic vector gradient using membership function.
Step 3) IF $\nabla_{\gamma\beta} > T_{s\beta}$ THEN $\mu_{BIG} = 0$.

where $T_{s\beta} = Th_T$, $\gamma = NW, N, NE, E, SE, S, SW, W$ [6], $\beta = red, gree, blue$ and $r = 1$ channels in video sequence, the membership function is $\mu_{BIG} = \max(x, y)$ with $x = \alpha'_{\gamma\beta}$ and $y = \left(1 - \nabla_{\gamma\beta}/T_{s\beta}\right)$. To obtain the angle deviation in each plane of the image we select to work in the angle formed by vectors in only one coordinate [4]:

$$\alpha = \cos^{-1}\left(\left(r_1 r_2 + g_1 g_2 + b_1 b_2\right)/\sqrt{\left(r_1^2 + g_1^2 + b_1^2\right)\left(r_2^2 + g_2^2 + b_2^2\right)}\right) \tag{5}$$

where, (r_1, g_1, b_1) and (r_2, g_2, b_2) are coordinates of two pixels.

Last algorithm describes the process necessary to determine the basic vector gradient value. To determine related vector gradients the procedure is the following:
Step 1) IF $\nabla_{\gamma\beta(R1,R2)} < T_{s\beta}$ THEN compute angle deviation in direction $\alpha_{\gamma\beta(R1,R2)}$ and obtain weight value [5],

$$\alpha'_{\gamma\beta(R1,R2)} = 2/\left(1+e^{\alpha_{\gamma\beta(R1,R2)}}\right)^r \tag{6}$$

Step 2) Obtain related vector gradient using membership function.
Step 3) IF $\nabla_{\gamma\beta(R1,R2)} > T_{s\beta}$ THEN $\mu_{BIG} = 0$.

where $(R1, R2)$ are the related vector gradients and the membership function is $\mu_{BIG} = \max(x, y)$ with $x = \alpha'_{\gamma\beta(R1,R2)}$ and $y = \left(1 - \nabla_{\gamma\beta(R1,R2)}/T_{s\beta}\right)$.

The fuzzy rule 1 is defined as,

Fuzzy Rule 1: defining the fuzzy vector gradient value $\nabla^F_{\gamma\beta} A_\beta(i,j)$,
IF $\nabla_{\gamma\beta}$ is BIG AND $\nabla_{\gamma\beta R1}$ is BIG, OR $\nabla_{\gamma\beta}$ is BIG AND $\nabla_{\gamma\beta R2}$ is BIG, THEN $\nabla^F_{\gamma\beta} A_\beta(i,j)$ is BIG,

where $\nabla_{\gamma\beta}$ is the basic vector gradient value, and $\nabla_{\gamma\beta R1}$ and $\nabla_{\gamma\beta R2}$ are two related vector gradient values for the direction γ in the channel β.

If basic and related vector gradients are close enough, in absolute difference (absolute norm) or in a vector criterion in angle distances (that is why we change gradient values to vector gradient values), this proposal is developed to obtain robust parameters, giving a better understanding of the nature of pixels in a window processing. Under this criterion we will have values denoted as fuzzy vector gradients that means nearby in pixels related, and they are helpful to suppress Gaussian noise

corruption presented on the sample. So, suppression is done by a weighted mean procedure where nearby close to 1 have the bigger weights in the algorithm due to the proposed procedure used in membership function. This suppresses noise more efficiently but smoothes details and edges, in our complete algorithm the temporal filtering are designed. The reference values where found modifying their parameters according to optimum PSNR and MAE values. Spatial algorithm presents good results in noise suppression compared with some algorithms found in literature [1-3].

The weighted mean algorithm is implemented by:

$$y_{out} = \sum_{\substack{i=0 \\ i \neq c}}^{N-1} y_\gamma \cdot x_{\gamma i} \bigg/ \sum_{i=0}^{N-1} x_{\gamma i} \tag{7}$$

where mean value is found doing multiplication of fuzzy vector gradient value with his respective pixel in that direction γ.

2.3   Temporal Filtering Algorithm

In here, we explain the proposed fuzzy logic recursive motion detector with temporal algorithm. The reference values of spatial filter presented above are used in the final stage in the proposed filter. Only the past and present frames are used to avoid dramatic charge in memory requirements and time processing. The fuzzy logic rules are used in each plane of two frames in independent way.

We found angle deviations and gradient values by the central pixel in present frame respect to his neighbours in past frame, all done by each plane of the frames by using 3x3 window,

$$\theta_i^1 = A\left(x_i^A, x_c^B\right) \; ; \; \nabla_i^1 = \left|x_i^A - x_c^B\right|; i = 1, \ldots, N; \; N = 9 \tag{8}$$

where x_c is central pixel in present frame, and A and B are past and present frames by planes, respectively.

Let us define the membership functions used to obtain a value that indicates the degree, in which a certain gradient value or vector value matches the predicate. If a gradient or a vector value have membership degree one, for the fuzzy set SMALL, it means that it is SMALL for sure in this fuzzy set. Selection of this kind of membership functions is follow from nature of pixels, where a movement is not a linear response, and a pixel has different meanings in each frame of video sequence.

Membership functions SMALL and BIG for angles and gradients are given by [7]:

$$\mu_{SMALL}(M) = \begin{cases} 1 & M < med \\ \exp\left(-\dfrac{(M - med)^2}{2\sigma_S^2}\right) & \text{otherwise} \end{cases} \tag{9}$$

$$\mu_{BIG}(M) = \begin{cases} 1 & M < med \\ \exp\left(-\dfrac{(M - med)^2}{2\sigma_B^2}\right) & \text{otherwise} \end{cases} \tag{10}$$

where $\sigma_S^2 = 0.1$, $\sigma_B^2 = 1000$, and M can be the angle θ or gradient ∇, for angles *med*=0.2 and *med*=0.9 for membership functions SMALL and BIG, respectively, and for gradients *med*=60 and *med*=140 for SMALL and BIG functions, respectively.

Now we use Fuzzy Rules 2, 3, 4, and 5 to acquire corresponding values:

Fuzzy Rules
Fuzzy Rule 2: Defining the fuzzy gradient-vector value $SBB(x,y,t)$.   IF $\theta^1(x,y,t)$ is SMALL AND $\theta^2(x,y,t)$ is BIG AND $\theta^3(x,y,t)$ is BIG AND $\nabla^1(x,y,t)$ is SMALL AND $\nabla^2(x,y,t)$ is BIG AND $\nabla^3(x,y,t)$ is BIG THEN $SBB(x,y,t)$ is true.
Fuzzy Rule 3: Defining the fuzzy gradient-vector value $SSS(x,y,t)$.   IF $\theta^1(x,y,t)$ is SMALL AND $\theta^2(x,y,t)$ is SMALL AND $\theta^3(x,y,t)$ is SMALL AND $\nabla^1(x,y,t)$ is SMALL AND $\nabla^2(x,y,t)$ is SMALL AND $\nabla^3(x,y,t)$ is SMALL THEN $SSS(x,y,t)$ is true.
Fuzzy Rule 4: Defining the fuzzy gradient-vector value $BBB(x,y,t)$.   IF $\theta^1(x,y,t)$ is BIG AND $\theta^2(x,y,t)$ is BIG AND $\theta^3(x,y,t)$ is BIG AND $\nabla^1(x,y,t)$ is BIG AND $\nabla^2(x,y,t)$ is BIG AND $\nabla^3(x,y,t)$ is BIG THEN $BBB(x,y,t)$ is true.
Fuzzy Rule 5: Defining the fuzzy gradient-vector value $BBS(x,y,t)$.   IF $\theta^1(x,y,t)$ is BIG AND $\theta^2(x,y,t)$ is BIG AND $\theta^3(x,y,t)$ is SMALL AND $\nabla^1(x,y,t)$ is BIG AND $\nabla^2(x,y,t)$ is BIG AND $\nabla^3(x,y,t)$ is SMALL THEN $BBS(x,y,t)$ is true.
where $\theta^r(x,y,t)$ are angles values, $\nabla^r(x,y,t)$ are gradient values, and $r = 1,2,3$.

From the result values of each fuzzy rule $(2 - 5)$ we can compare these values in the following way:

Algorithm to Fuzzy Rule $SBB(x,y,t)$
If $SBB(x,y,t)$ is the biggest value found from the others: *Step 1)* IF {($SBB(x,y,t) > SSS(x,y,t)$) AND ($SBB(x,y,t) > BBB(x,y,t)$) AND ($SBB(x,y,t) > BBS(x,y,t)$)} THEN Weighted mean using $SBB(x,y,t)$, $$y_{out} = \frac{\sum p^A(x,y,t) \cdot SBB(x,y,t)}{\sum SBB(x,y,t)}$$ *Step 2)* Update standard deviation for next frames to divide details from uniform regions.

where $SBB(x,y,t)$ value says that central pixel is in movement because of big differences in corresponding local and gradient values, $p^A(x,y,t)$ represents each pixel in last frame that fulfil with the IF condition, and y_{out} is the output filtered in spatial and temporal filtering.

To update standard deviation we need different values by each condition in our algorithm to characterize in an independent manner each region of the image. This is achieved using the expression above, and this expression is always used after by each Fuzzy Rule to update the parameter:

$$\sigma_T' = (\alpha \cdot \sigma_{TOTAL}) + (1-\alpha) \cdot (\sigma_T') \tag{13}$$

where $T = red, green, blue$, $\alpha = \alpha_{SBB} = 0.875$, and $\sigma_{TOTAL} = (\sigma_{red} + \sigma_{green} + \sigma_{blue})/3$.

Algorithm to Fuzzy Rule $SSS(x,y,t)$
If $SSS(x,y,t)$ is the biggest value found from the others: *Step 1)* IF $\{(SSS(x,y,t) > SBB(x,y,t))$ AND $(SSS(x,y,t) > BBB(x,y,t))$ AND $(SSS(x,y,t) > BBS(x,y,t))\}$ THEN Weighted mean using $SSS(x,y,t)$, $$y_{out} = \frac{\sum (p^A(x,y,t)\cdot 0.5 + p^B(x,y,t)\cdot 0.5)\cdot SSS(x,y,t)}{\sum SSS(x,y,t)}$$ *Step 2)* Update standard deviation for next frames to divide details from uniform regions.

where $SSS(x,y,t)$ shows that a central pixel is not in movement because of small differences in all directions, that is why we use pixels in both frames, $p^A(x,y,t)$ and $p^B(x,y,t)$ are the pixels in last and present frames that fulfil with the IF condition will be taken in count to calculate the weighted mean, $\alpha = \alpha_{SSS} = 0.1255$, and y_{out} is the filtered output.

Algorithm to Fuzzy Rule $BBB(x,y,t)$
If $BBB(x,y,t)$ is the biggest value found from the others: *Step 1)* IF $\{(BBB(x,y,t) > SBB(x,y,t))$ AND $(BBB(x,y,t) > SSS(x,y,t))$ AND $(BBB(x,y,t) > BBS(x,y,t))\}$ THEN motion-noise = true. $$y_{out} = \frac{\sum p^A(x,y,t)\cdot SBB(x,y,t)}{\sum SBB(x,y,t)}$$ *Step 2)* If $\sqrt{motion - noise\ confidence} = 1$. then $\alpha = 0.875$, else if $\sqrt{motion - noise\ confidence} = 0$ then $\alpha = 0.125$, else $\alpha = 0.5$. *Step 3)* $y_{out} = (1-\alpha)\cdot(pres\_fr_{central\_pixel}) + \alpha\cdot(past\_fr_{central\_pixel})$

The $BBB(x,y,t)$ value shows that a central pixel and its neighbours do not have relation among the others and it is highly probably that this pixel is in motion or is a noisy pixel. To solve this problem, consider the nine fuzzy gradient-vector values obtained from $BBB(x,y,t)$ and take the central value and at least three fuzzy neighbours values more to detect movement present in the sample. We use the Fuzzy Rule "R" to obtain motion-noise confidence the activation degree of "R" is just the conjunction of the four subfacts, which are combined by a chosen triangular norm defined as $A\ AND\ B = A * B$. Computations are specifically the intersection of all possible combinations of $BBB(x,y,t)$ and three different neighbouring BIG membership degrees $BBB(x+1,y+1,t)$, $(i,j = -1,0,1)$, using triangular norm. This can give 56 different values, which should be summed using algebraic sum $A\ OR\ B = A + B - A * B$ of all instances to obtain the motion-noise confidence.

Algorithm to Fuzzy Rule $BBS(x,y,t)$
If $BBS(x,y,t)$ is the biggest value found from the others: *Step 1)* IF $\{(BBS(x,y,t) > SBB(x,y,t))$ AND $(BBS(x,y,t) > SSS(x,y,t))$ AND $(BBS(x,y,t) > BBB(x,y,t))\}$ THEN Weighted mean using $BBS(x,y,t)$, $$y_{out} = \frac{\sum p^B(x,y,t)\cdot(1 - BBS(x,y,t))}{\sum(1 - BBS(x,y,t))}$$ *Step 2)* Update standard deviation for next frames to divide details from uniform regions.

where, $p^B(x, y, t)$ represents each pixel in present frame that fulfil with the IF condition, and y_{out} is the output filtered in spatial and temporal filtering.

Now it can be applied the *Spatial Filter* to smooth the non-stationary noise left by the preceding temporal filter. This is done by a local spatial filter (see sec. 2.1), which adapts to image structures and noise levels present in the corresponding spatial neighbourhood.

3   Experimental Results

We present the performance of the proposed algorithm obtained by simulation of the proposed techniques. We use "Flowers" and "Miss America" video sequences to qualify effectiveness of this filter to provide a better understanding in the robustness of the fuzzy logic algorithm. Video sequences were contaminated with different Gaussian noise levels, from 0.00 to 0.05 in variance with zero mean. Frames are treated in an RGB color space with 24 bits, 8 bits for each channel, 176x144 pixels in a QCIF format with 100 frames.

The proposed Fuzzy Directional Adaptive Recursive Temporal Filter (FDARTF) was compared with the Vector Median M-type K-nearest Neighbor Filter (VMMKNNF) [8,9] and the Generalized Vector Directional Filter (GVDF) [10,11]. Therefore, the proposed FDARTF filter was compared with other similar algorithms, the Fuzzy Motion Recursive Spatial-Temporal Filter (FMRSTF) [1-3], which works only with gradients, and with an adaptation to this algorithm using angle deviations Fuzzy Vectorial Motion Recursive Spatial-Temporal Filter (FVMRSTF), which was not published yet.

Table 2 presents the performance results in terms of PSNR for the frame #100 of video sequence "Miss America" by use different filters. From the Table 1, one can see that the best results in PSNR criterion are given by the proposed filter.

Table 2. PSNR values for a frame of video sequence "Miss America" by use different filters

Gaussian Noise	VMMKNNF	GVDF	FMRSTF	FVMRSTF	FDARTF
0.001	32.500	33.981	33.765	33.758	33.459
0.002	31.853	32.919	31.912	31.906	33.106
0.003	31.163	32.134	30.860	30.849	32.777
0.004	30.535	31.408	29.963	29.976	32.371
0.005	29.917	30.794	29.283	29.292	31.829
0.006	29.431	30.301	28.791	28.798	31.383
0.007	28.903	29.816	28.332	28.337	30.875
0.008	28.467	29.419	27.977	27.978	30.504
0.009	28.043	29.060	27.538	27.550	30.085
0.01	27.702	28.697	27.259	27.252	29.613
0.015	26.152	27.151	26.062	26.078	28.104
0.02	24.955	25.969	25.163	25.153	26.950
0.03	23.339	24.256	23.859	23.871	25.701
0.04	22.109	22.934	22.872	22.876	24.941
0.05	21.276	21.930	21.986	21.986	24.231

Figure 2 shows the visual results in the frame #100 of video sequence "Flowers" by use in a) *FMRSTF* filter, in b) *FVMRSTF* filter, and in c) the proposed *FDARTF* filter. These images were recovered from Gaussian noise corrupted with variance 0.01, 0.015, 0.02, and 0.03 from top to bottom of Figure 2. From this Figure, one can see that the restored frames by means of use the proposed filters appear to have a better subjective quality.

a)   b)   c)

Fig. 2. Visual results in the frame #100 of video sequence "Flowers", a) Column of restored images by *FMRSTF*, b) Column of restored images by *FVMRSTF*, and c) Column of restored images by *FDARTF*. These images were recovered from Gaussian noise corrupted mages with variance 0.01, 0.015, 0.02, and 0.03 from top to bottom.

4 Conclusions

In this paper a novel robust adaptive recursive scheme for fuzzy logic based motion detection is presented. The proposed algorithm works in a closed loop realizing the spatial and temporal filtering to improve suppression noise performance and preservation of fine details. It is demonstrated that taking into account, both robust characteristics (gradients and vectors) and connecting them together, we can realize a better algorithm, improving the techniques that use such characteristics in a separate form. In future, this idea will be extended to suppress impulsive random noise in multichannel filtering.

References

1. Zlokolica, V., De Geyter, M., Schulte, S., Pizurica, A., Philips, W., Kerre, E.: Fuzzy Logic Recursive Motion Detection for Tracking and Denoising of Video Sequences. In: IS&T/SPIE Symposium on Electronic Imaging, San Jose, California, USA, pp. 771–782 (2005)
2. Zlokolica, V.: Advanced Non-Linear Methods for Video Denoising. PhD Thesis, Gent University (2006)
3. Zlokolica, V., Schulte, S., Pizurica, A., Philips, W., Kerre, E.: Fuzzy Logic Recursive Motion Detection and Denoising of Video Sequences. Journal of Electronic Imaging 15(2), 023008 (2006)
4. Trahanias, P.E., Venetsanopoulos, A.N.: Vector Directional Filters-A New Class of Multichannel Image Processing Filters. IEEE Transactions on Image Processing 2(4), 528–534 (1993)
5. Plataniotis, K.N., Venetsanopoulos, A.N.: Color Image Processing and Applications. Springer, Berlin (2000)
6. Schulte, S., De Witte, V., Nachtegael, M., Van der Weken, D., Kerre, E.: Fuzzy Two-Step Filter for Impulse Noise Reduction from Color Images. IEEE Transactions on Image Processing 15(11), 3567–3578 (2006)
7. Fuzzy Logic Fundamentals, ch. 3, pp. 61–103 (2001) www.informit.com/content/images/ 0135705991/ samplechapter/0135705991.pdf
8. Gallegos-Funes, F., Ponomaryov, V., De-La- Rosa, J.: ABST M-type K-nearest neighbor (ABSTM-KNN) for image denoising. IEICE Trans. Funds. Electronics Comms. Computer Science E88A(3), 798–799 (2005)
9. Ponomaryov, V.I., Gallegos-Funes, F.J., Rosales-Silva, A.: Real-Time Color Imaging Based on RM-Filters for Impulsive Noise Reduction. J. Imaging Science and Technology 49(3), 205–219 (2005)
10. Trahanias, P.E., Karakos, D.G., Venetsanopoulos, A.N.: Directional Processing of Color Images: Theory and Experimental Results. IEEE Trans. Image Process. 5(6), 868–880 (1996)
11. Plataniotis, K.N., Androutsos, D., Vinayagamoorthy, S., Venetsanopoulos, A.N.: Color Image Processing Using Adaptive Multichannel Filters. IEEE Trans. Image Process. 6(7), 933–949 (1997)

EZW-Based Image Compression with Omission and Restoration of Wavelet Subbands

Francisco A. Pujol, Higinio Mora, José Luis Sánchez, and Antonio Jimeno

Specialized Processor Architectures Lab,
Dept. Tecnología Informática y Computación,
Universidad de Alicante
P.O. Box 99, E-03080 Alicante (Spain)
{fpujol,hmora,sanchez,jimeno}@dtic.ua.es
http://www.dtic.ua.es/spa-lab

Abstract. It is well known that multimedia applications provide the user with information through different methods (text, data, graphics, images, audio, video, etc.) which must be digitally represented, transmitted, stored and processed. Due to the fact that there is an increasing interest in developing high definition systems, multimedia applications are demanding, among others, higher bandwidth resources and more memory requirements in embedded devices. Therefore, it is essential to use compression techniques to reduce the time requirements of these new applications. This work aims to design an EZW-based image compression model, which makes use of the omission and restoration of wavelet subbands, providing high compression rates, good quality standards and low computation time requirements. The results obtained show that our method satisfies these assumptions and can be integrated in new multimedia devices.

Keywords: Image Compression, Wavelet Transform, EZW Algorithm.

1 Introduction

Over the last few years there has been a massive demand for multimedia applications in telecommunication systems and, nowadays, it is still required to develop even more sophisticated methods who take into account new user requirements. On the one hand, the standardization of digital photography and the enormous growth in the number of the Internet users, has led to a considerable increase in using the Internet for exchanging images, videos or music. Consequently, file compression has become essential to reduce file size while maintaining maximum quality for these multimedia applications.

In addition, in order to satisfy the needs of both telecommunications platforms (reducing file size to optimize the use of the available bandwidth) and users (obtaining as much quality as possible), new multimedia mobile phone applications, such as video conferencing or capturing and sending still images and videos, need high performance compression schemes.

Furthermore, the JPEG still image compression, which is based in the Discrete Cosine Transform (DCT), became a standard in 1992. In recent years, though, there has been a considerable interest in methods based on the wavelet transform; in fact, the new standard JPEG-2000 uses wavelet-based compression methods [1], [2]. One of the most popular wavelet-based compression methods is known as Embedded Zerotree Wavelet (EZW) algorithm [3], [4]. In recent years, there has been an intensive research on improving this method and related ones, such as the Set Partitioning In Hierarchical Trees coding (SPIHT) [5], the Embedded Block Coding with Optimized Truncation (EBCOT) algorithm [6], and many others [7]. Although wavelet-based compression schemes have both better compression rates and higher quality results than JPEG algorithm, there are still major difficulties in achieving a high performance encoding system, since it is not easy to find an efficient implementation of wavelet transform calculations, which require huge memory sizes and consume many computer resources.

As a consequence, in this work we show a new EZW-based method, which omits and, afterwards, restores different resolution subbands, as it is described later. This algorithm provides better results than basic EZW: (i) considering both subjective and objective global image quality; and (ii) considering the restrictions of computational cost and memory storage of multimedia devices. To complete our task, in Sec. 2 we discuss EZW algorithm and the main advantages and drawbacks that it possess. Then, in Sec. 3 the design of a robust improvement for the EZW compression scheme is shown and, afterwards, Sec. 4 considers some of the experiments completed to verify that our system behaves properly. Finally, some important remarks to our work, as well as some future research tasks, are summarized in Sec. 5.

2 Overview of Image Compression Algorithms

2.1 Fundamentals of Image Compression

A digital image often has a strong correlation between pixels and, therefore, these contain redundant information. What is essential for efficient image coding is to find a representation of the image free from correlation. Thus, research on image compression is focused on reducing the number of bits necessary to represent an image, eliminating spatial redundancy as much as possible.

Lossy methods are most often used for compressing multimedia files, since they can produce a much smaller compressed file than any known lossless method, while still meeting the requirements of the application. Compression occurs by means of a linear transform to remove pixel correlation, then quantizing the resulting transformed coefficients and encoding them with minimum entropy.

Due to the huge amount of data involved and image redundancy, JPEG uses a DCT-based lossy compression scheme. The DCT itself does not carry out any compression, but transforms input data so that redundancy can be easily detected and eliminated. However, wavelet-based compression schemes usually improve image quality for high compression rates. We shall discuss this issue in the following section.

2.2   Wavelet Transform-Based Algorithms

Wavelets have become very popular in last years for different signal processing algorithms. Wavelets are functions defined in finite intervals with an average value of zero [8]; hence, they divide data into different frequency components so that each component can be studied with a resolution matched to its scale.

Wavelet-based image compression uses subband coding, in which an image is split up in frequency bands by means of a filterbank. Thus, a subband coding is a coding technique where the entry signal is filtered and separated in frequency bands combining a high-pass filter and a low-pass filter, with an average value of zero. There is a wide variety of wavelet functions to perform this transform, such as the Daubechies family, the Haar transformn, and many others [9].

The decomposition of images using wavelets is applied in the horizontal and vertical directions. An image is divided into subbands by passing it through a low pass filter and a high pass filter, and both subbands are downsampled by 2. This leads to a 2D signal getting broken down into four subbands, known as LL, LH, HL, and HH. The same procedure can then be applied iteratively to the LL subband, and repeated for as many levels of decomposition as desired.

Once the method is developed, the point is how to compress the wavelet-transformed data from an image. One of the most popular methods to do this is the Embedded Zerotree Wavelet Algorithm (EZW). Let us describe it next.

The EZW Algorithm. In 1993 Shapiro introduced a new algorithm known as *Embedded Zerotree Wavelet* for the entropic coding of the transformed coefficients of an image using the 2D wavelet transform [3]. The EZW algorithm states that if a coefficient at a certain level of decomposition is less than a significant level or threshold T, then all the coefficients of the same orientation in the same spatial location at lower scales of decomposition are not significant compared with T.

For every pass, a threshold T is chosen, against which all the wavelet coefficients are measured. If a wavelet coefficient is larger than T it is encoded and removed from the image, if it is smaller it is left for the next pass. When all the wavelet coefficients have been visited, the threshold is lowered and the image is scanned again to add more detail to the already encoded image. This process is repeated until all the wavelet coefficients have been encoded completely or another criterion has been satisfied.

The main advantage of this encoder is that it lets the encoding process end at any stage and, for this reason, the required compression factor is easily reached by trunking the encoding tree. Likewise, the decoder may also end the decoding process at any stage and, thus, generate a first approximation of the image. EZW encoding does not really compress data, but reorders wavelet coefficients in such a way that they can be compressed very efficiently; as a result, it should be followed by a symbol encoder, such as an arithmetic encoder. This algorithm obtains excellent results and has been object of intensive research since it was developed.

2.3   Discussion

The JPEG compression scheme is simple and has a very good performance, but since the input image is divided into 8×8 blocks, correlation across the block boundaries is not eliminated. This results in noticeable "blocking artifacts", particularly at low bit-rates, as shown in Fig. 1 (a) and (c).

On the contrary, the EZW algorithm provides much better quality results at low bit-rates, as shown in Fig. 1 (b) and (d), where a Daubechies 9/7 wavelet function is used. This is due to the fact that the generated wavelet coefficient tree encodes significant data much more efficiently than the DCT and, consequently, it results in high quality compressed images.

(a)   (b)   (c)   (d)

Fig. 1. EZW compression compared to JPEG: For 0.5 bpp: (a) JPEG; (b) EZW. For 0.25 bpp: (c) JPEG; (d) EZW

Nevertheless, it must be remarked that the time spent to efficiently compress/decompress image data with EZW are much higher that the ones used for standard JPEG. For instance, the compression/decompression time for a 256×256 image is about 27.5 times faster for JPEG than for EZW -using a Pentium M processor and a C++ environment- and, what is more, this fact becomes even worse when image size increases.

To sum up, we can establish the main drawbacks of both systems. Firstly, JPEG algorithm generates a significant loss of quality at low compression rates and, on the other hand, EZW method requires a very high processing time, which makes it difficult to be applied in a real-time condition. Therefore, these two constraints are the initial step to develop a new approach that overcome these problems. This issue is considered in the next section.

3   Omission and Restoration of Wavelet Subbands

As derived from the review of the main methods for image compression, our research has focused on two different aspects: reducing the computation time of wavelet-based methods while keeping as much quality as possible.

In order for the computation time to be decreased, our proposal is based on reducing the image size so that the number of operations for checking descendants in the EZW algorithm would be also reduced. Therefore, the method consists of:

1. Carrying out an iteration of the wavelet transform on the input image.
2. Considering only the LL subband, making the rest of subbands equal to 0.
3. Compressing the LL subband using the EZW algorithm.

This method significantly reduces the processing time for compressing/decompressing an image, as it will be shown in Sec. 4. However, the problem is that by eliminating the subbands, a pixel of the decompressed LL subband is now transformed into a group of four pixels (its descendants) in the restored image, which means quite a visible distortion.

Subsequently, the next step is to improve image quality. In order to minimize distortion when recovering images, the eliminated subbands can be restored, thus reducing the global error. The subband restoration process is carried out once the LL subband has been decompressed, using the EZW algorithm; hence, each 4×4 block B, whose pixels are descendants of another pixel a in the previous subband, will take the value V of their ancestor a. That is, V is the mean value of the descendants of a in the original eliminated subband. As a result, our system distributes the error uniformly so that it is unlikely to be perceptible by the human eye.

As a result, our compression method is called Omission and Restoration of Wavelet Subbands (ORWS), due to the fact that it removes high frequency subbands before the compression and, afterwards, it restores them to minimize distortion. Figs. 2 and 3 show how the ORWS algorithm works.
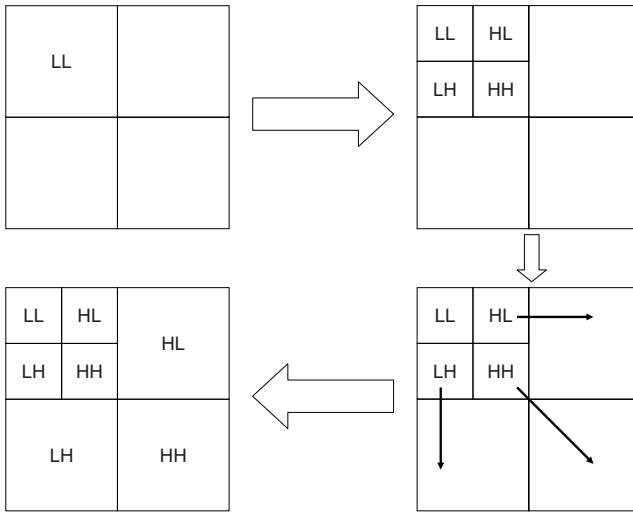
Fig. 2. The subband restoration process

In the next section we shall analyze some different tests carried out to validate our algorithm.
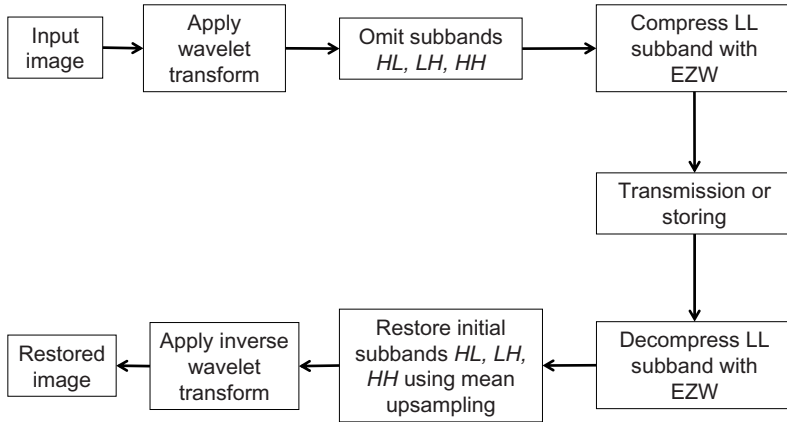
Fig. 3. Block diagram of the ORWS algorithm

4   Experiments

Let us show now the results of some experiments completed for our method. Thus, we will compare the ORWS algorithm with the EZW compression method, and also with standard JPEG compression scheme. The tests have been performed with a series of well-known images, and we found that the results obtained with the ORWS compression scheme confirm the reduction in compression time and the increase in image quality regarding JPEG and EZW algorithms. For illustrations, the results for 512×512, 8-bit gray-level images "Barbara" and "Lena" are shown in Figs. 4 and 5, respectively, using the Daubechies 9/7 wavelet.

Fig. 6 (a) shows the mean gain in the execution time of the ORWS algorithm (compression/decompression) in relation to the EZW method, for all the images in the database. Finally, Fig. 6 (b) compares the performance of ORWS, EZW and JPEG methods by using the mean peak signal-to-noise ratio (PSNR, see [10] for a definition of this ratio) for all the images in the database.
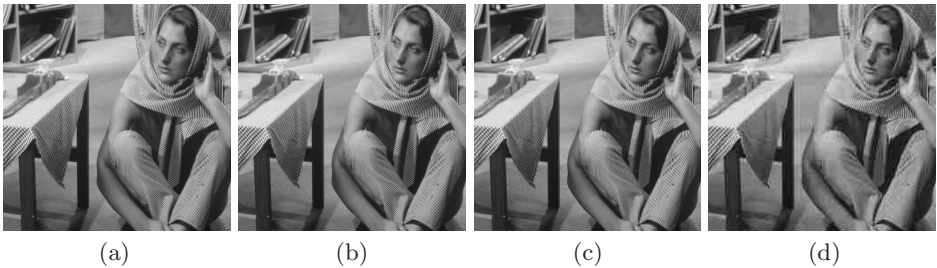
Fig. 4. ORWS for *Barbara*: (a) Original; (b) 0.5 bpp; (c) 0.25 bpp; (d) 0.125 bpp

(a)	(b)	(c)	(d)

Fig. 5. ORWS for *Lena*: (a) Original; (b) 0.5 bpp; (c) 0.25 bpp; (d) 0.125 bpp

(a)

(b)
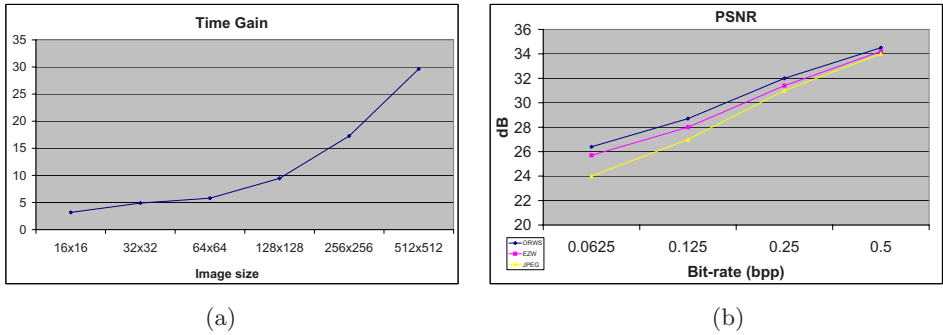
Fig. 6. (a) Time gain of ORWS in relation to EZW; (b) Comparison of PSNR between ORWS, EZW and JPEG

From these results, we must remark that ORWS can run even 30 times faster than EZW (Fig. 6 (a)) and that it leads to higher quality compressed images than EZW and JPEG (Fig. 6 (b)), as it has higher PSNR values. As a result, the ORWS algorithm is a powerful tool for increasing both the computation time of wavelet-based compression schemes and the image quality of EZW and standard JPEG. As a conclusion, our method is a robust technique for compressing images and, consequently, improves existing methods both visually (subjectively) and objectively.

5   Conclusions

With the increasing use of multimedia technologies, image compression requires higher performance as well as new features. From our research, it can be extracted that all the existing compression algorithms have limitations under certain conditions. In particular, JPEG generates low-quality images when high compression rates are needed. On the other hand, EZW method has a very high computation time, which makes it difficult to be included in real-time applications.

In this work, the ORWS algorithm, which is based on the EZW compression method, has been proposed. The experimentation shows that our technique is fast, robust and provides high quality results. To summarize, the main advantages of our algorithm are:

− It is easy to implement and computational costs are low, while keeping good quality standards.
− It improves the quality of DCT-based image compression schemes, such as JPEG, for high compression rates.
− It reduces the processing time of wavelet-based algorithms.

As a future work, we consider the extension of the algorithm to color image compression. It would be also interesting to include other mathematical tools, such as interpolation techniques, to increase the performance of the wavelet subbands restoration process.

References

1. Usevitch, B.E.: A Tutorial on Modern Lossy Wavelet Image Compression: Foundations of JPEG 2000. IEEE Signal Processing Magazine 18, 22–35 (2001)
2. Torres, L., Delp, E.J.: New Trends in Image and Video Compression. In: Proc. of the European Signal Processing Conference (2000)
3. Shapiro, J.M.: Embedded Image Coding using Zerotrees of Wavelet Coefficients. IEEE Transactions on Signal Processing 41, 3445–3462 (1993)
4. Adams, M.D., Antoniou, A.: Reversible EZW-based Image Compression Using Best-Transform Selection and Selective Partial Embedding. IEEE Transactions on Circuits and Systems II: Analog and Digital Signal Processing 47, 1119–1122 (2000)
5. Danyali, H., Mertins, A.: Flexible, Highly Scalable, Object-based Wavelet Image Compression Algorithm for Network Applications. IEE Proceedings Vision, Image and Signal Processing 151, 498–510 (2004)
6. Taubman, D.: High Performance Scalable Image Compression with EBCOT. IEEE Transactions on Image Processing 9, 1158–1170 (2000)
7. Sudhakar, R., Karthiga, R., Jayaraman, S.: Image Compression using Coding of Wavelet Coefficients – A Survey. ICGST International Journal on Graphics, Vision and Image Processing 5, 25–38 (2005)
8. Saha, S.: Image Compression - From DCT to Wavelets: A Review. ACM Crossroads 6, 12–21 (2000)
9. Truchetet, F., Laligant, O.: Wavelets in Industrial Applications: a Review. In: Proc. of the SPIE: Wavelet Applications in Industrial Processing II, pp. 1–14 (2004)
10. Bovik, A.: Handbook of Image and Video Processing. Academic Press, London (2000)

Multi-class Binary Object Categorization Using Blurred Shape Models

Sergio Escalera[1,2], Alicia Fornès[1,3], Oriol Pujol[1,2], Josep Lladós[1,3], and Petia Radeva[1,2]

[1] Computer Vision Center, Universitat Autònoma de Barcelona,
Campus UAB, Edifici O, 08193, Bellaterra, Spain
[2] Dept. Matemàtica Aplicada i Anàlisi, Universitat de Barcelona,
Gran Via 585, 08007, Barcelona, Spain
[3] Dept. Ciències de la Computació, Universitat Autònoma de Barcelona,
Campus UAB, Edifici Q, 08193, Bellaterra, Spain

Abstract. The main difficulty in the binary object classification field lays in dealing with a high variability of symbol appearance. Rotation, partial occlusions, elastic deformations, or intra-class and inter-class variabilities are just a few problems. In this paper, we introduce a novel object description for this type of symbols. The shape of the object is aligned based on principal components to make the recognition invariant to rotation and reflection. We propose the Blurred Shape Model (BSM) to describe the binary objects. This descriptor encodes the probability of appearance of the pixels that outline the object's shape. Besides, we present the use of this descriptor in a system to improve the BSM performance and deal with binary objects multi-classification problems. Adaboost is used to train the binary classifiers, learning the BSM features that better split object classes. Then, the different binary problems learned by the Adaboost are embedded in the Error Correcting Output Codes framework (ECOC) to deal with the muti-class case. The methodology is evaluated in a wide set of object classes from the MPEG07 repository. Different state-of-the-art descriptors are compared, showing the robustness and better performance of the proposed scheme when classifying objects with high variability of appearance.

Keywords: Shape descriptors, Multi-class classification, Adaboost, Error Correcting Output Codes.

1 Introduction

Shape recognition is one of the most popular areas of Pattern Recognition. Its aim consists in solving the problem of modeling and recognizing objects from a large set of classes. It is an extremely difficult task because of the high variability of the object appearance: changes in the perspective and viewpoint, occlusions, rigid and elastic deformations, and high intra-class an low inter-class variabilities. Several applications focus on this type of problems, such as the analysis of handwritten documents (e.g. analysis of old handwritten archive manuscripts and sketching or calligraphic interfaces) [8]. A lot of effort has been made in the

last decade to develop good symbol and shape recognition methods inspired in either structural or statistical pattern recognition approaches. In general, two major focus of interest can be stated: the definition of expressive and compact shape descriptors, and the formulation of robust classification methods according to such descriptors. Zhang [5] reviews the main techniques used in this field, mainly classified in contour-based descriptors (i.e. polygonal approximations, chain code, shape signature, and curvature scale space) and region-based descriptors (i.e. Zernique moments, ART, and Legendre moments [9]). A good shape descriptor should guarantee inter-class compactness and intra-class separability, even when describing noisy and distorted shapes. It has been shown that some object descriptors, robust to some affine transformations and occlusions in some type of objects, are not enough effective in front of elastic deformations. Thus, the research for other descriptors that address the problem of elastic and non-uniform distortions, as well as variations in object styles and blurring, is still required.

Concerning the categorization of objects' classes, many classification techniques have been researched based on both statistical or structural approaches. Elastic deformations of shapes modeled by probabilities tend to be learnt using statistical classifiers. One of the most well-known techniques in this domain is the Adaboost algorithm due to its ability for feature selection and its high performance when applied to binary problems [2]. Although many real problems require multi-classification, designing a single multi-class classifier remains a hard task. In such cases, the usual way to proceed is to reduce the complexity of the problem into a set of simpler binary classifiers and combine them in some way. An usual way to combine these simple classifiers is the voting scheme (one-versus-one or one-versus-all grouping schemes are the most frequently applied). In this way, Dietterich et. al. [11] proposed the Error Correcting Output Codes framework inspired in the signal processing coding and decoding techniques to benefit from error correction properties, obtaining successful results [10][11][3].

The goal of this paper is two-fold: on one hand, we introduce a novel shape descriptor, the Blurred Shape Model (BSM), that encodes the spatial probability of appearance of the shape pixels and their context information. As a result, a robust technique in front of elastic deformations is obtained. On the other hand, we present a successful scheme to describe and classify binary objects. The method aligns object shapes by means of the Hotelling transform and an area density adjustment. Then, the BSM is used for obtaining the shape description. The Adaboost algorithm is proposed to learn the descriptor features that best split classes, and the pairwise scheme (one-versus-one) with Error Correcting Output Codes increases the classification accuracy by correcting possible errors produced by the binary classifiers. A wide set of MPEG07 categories are described and classified with the present methodology, showing high success and better performance compared to the state-of-the-art descriptors.

The paper is organized as follows: Section 2 introduces the Blurred Shape Model descriptor. Section 3 presents the full binary object recognition scheme. Experimental results are shown in section 4, and section 5 concludes the paper.

2   Blurred Shape Model

The Blurred Shape Model (BSM) is based on the object shape description, allowing the definition of spatial regions where some parts of the shape can be involved.

Table 1. Blurred Shape Model algorithm

Given a binary image I,
    Obtain the *shape* S contained in I
    Divide I in $n \times n$ equal size sub-regions $R = \{r_i, ..., r_{n \times n}\}$, with c_i the center of coordinates for each region r_i.
    Let $N(r_i)$ be the neighbor regions of region r_i, defined as $N(r_i) = \{r_k | r \in R, ||c_k - c_i||^2 \leq 2 \times g^2\}$, where g is the cell size.

    For each point $\mathbf{x} \in S$,
        For each $r_i \in N(r_{\mathbf{x}})$,
          $d_i = d(\mathbf{x}, r_i) = ||\mathbf{x} - c_i||^2$
    End_For

    Update the probabilities vector v positions as:
    $v(r_i) = v(r_i) + \frac{1/d}{D_i}, \quad D_i = \sum_{c \in N(r)} \frac{1}{||\mathbf{X} - c||^2}$
    End_For

    Normalize the vector v as: $v = \frac{v(i)}{\sum_{=1}^{2} v(j)} \forall i \in [1, ..., n^2]$

Given a set of object shape points, they are treated as features to compute the BSM descriptor. The image region is divided in a grid of $n \times n$ equal-sized sub-regions (where the grid size identifies the blurring level allowed for the shapes). Each cell receives votes from the shape points in it and also from the shape points in the neighboring sub-regions. Thus, each shape point contributes to a density measure of its cell and its neighboring ones. This contribution is weighted according to the distance between the point and the center of coordinates c_i of the region r_i. Table 1 shows the algorithm.

In fig. 1, a shape description is shown for a MPEG07 sample. Figure 1(a) shows the distances of a shape point to the nearest sub-regions centers. To give the same importance to each shape point, all the distances to the neighbors centers are normalized. The output descriptor is a vector histogram v of length $n \times n$, where each position corresponds to the spatial distribution of shape points in the context of the sub-region and their neighbors ones. Fig. 1(b) shows the vector descriptor updating once the distances of the first point in fig. 1(a) are computed.

The resulting vector histogram, obtained by processing all shape points, is normalized in the range [0..1] to obtain the probability density function (pdf) of $n \times n$ bins. In this way, the output descriptor represents a distribution of probabilities of the object shape considering spatial distortions, where the distortion level is determined by the grid size. Referring the computational complexity, for

(a)   (b)
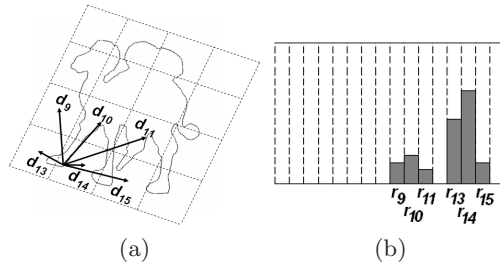
Fig. 1. BSM density estimation example

a region of $n \times n$ pixels, the k relevant shape points considered to obtain the BSM require a cost of $O(k)$ simple operations.

3 Binary Object Recognition Scheme

In this chapter, we present the different methods applied in the scheme shown in fig. 2. First, we describe the Hotelling transform based on principal components and the area density readjustment for aligning the object shape. Then, we discuss the suitability of using Adaboost to train binary classifiers for the object classes and we comment the use of the Error Correcting Output Codes framework to extend the binary classification to the multi-class case.

Fig. 2. Process scheme

3.1 Shape Alignement

Before applying the proposed descriptor, a shape alignement process is performed. This process is composed of two steps: the first step, provides invariance to rotation by means of the Hotelling transform. And the second step deals with the posible mirroring effect.

The Hotelling transform finds a new coordinate system equivalent to locating the main axis of the object. Given a set of n representative object points defined as pairs of coordinates $\mathbf{x} = (x_i, y_i)$, where $i \in [1, .., n]$, the center of mass of the object $m_{\mathbf{X}}$, and the eigenvectors V of the covariance matrix, the new transformation is obtained by means of the projection of the centered points of the object in the following way:

$$\mathbf{x}'_i = V(\mathbf{x}_i - m_{\mathbf{X}}), i \in [1, .., n] \tag{1}$$

Using this transform, we find the common axes for the different object instances. In fig. 3(a), the mean shape for the samples of one MPEG07 category

after applying the Hotelling transform is shown. One can observe that the shapes are not properly aligned. For this reason, a second step, consisting of an area density estimation process is used. Observe fig. 3(b). Horizontal and vertical projections are applied to obtain the area of the object. Then, this area is projected on the two axes, as shown in fig. 3(b). The final alignment is obtained by horizontal and vertical reflection of the object in the direction of the higher area projections. The result of adjusting the alignment is shown in fig. 3(c). Another example of alignment for two MPEG07 object categories is shown in fig. 4.

| (a) | (b) | (c) |
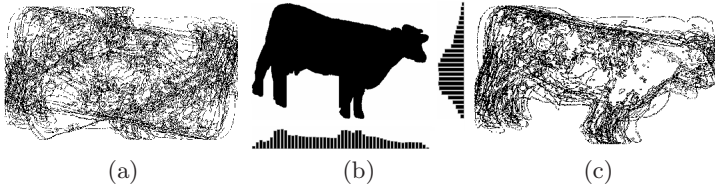
Fig. 3. (a) Mean aligned shape based on principal components. (b) Horizontal and vertical area estimation. (c) Readjusted alignment.

Fig. 4. Mean aligned shapes for two MPEG07 categories

3.2   Adaboost

Different types of objects may share local features [1] (see fig. 5). For this reason, Adaboost [2] has been chosen to boost the BSM models from different classes in order to define a classifier based on the features that best discriminate one class against another. Note that when comparing object descriptors, traditional matching distances take into account all object features for the final classification decision. When objects are very similar, slight deformations in the shared parts may include significant distance errors that finally can lead to a miss-classification of the objects. Observe fig. 5. The two objects have a discriminative region that splits the two categories (marked with a circle). Adaboost focuses on these regions by selecting the highest splitting features.

Fig. 5. Discriminant object regions

3.3   Error Correcting Output Codes

The ECOC framework is a simple but powerful framework to deal with the multi-class categorization problem by embedding binary classifiers. Given a set of N_c classes, the basis of the ECOC framework consists of designing a codeword[1] for each of the classes. Arranging the codewords as rows of a matrix, a "coding matrix" M is defined, where $M \in \{-1, 0, 1\}^{N \times n}$, being n the code length. From the point of view of learning, M is constructed by considering n binary problems, each one corresponding to a matrix column. Joining classes in sets, each dichotomy defines a partition of classes (coded by +1, -1, according to their class set membership, or 0 if the class is not considered by the binary problem).

   In figure 6(d), an example of a coding matrix M design is shown. The matrix is coded using 3 dichotomies $\{h_1, h_2, h_3\}$ for a three multi-class problem (c_1, c_2, and c_3). In fig. 6(a)-(c), three different sub-partition of classes are form, corresponding to all possible pairs of classes. This strategy is also called one-versus-one. Once we define the partitions of classes, each one is coded as a column of the coding matrix M, as shown in fig. 6(d). The dark regions are coded as +1 (first partition of classes), and the grey regions are coded as -1 (second partition of classes). The white regions correspond to the non-considered classes for their respective classifiers. Now, the rows of the matrix M define the codewords $\{Y_1, Y_2, Y_3\}$ for their corresponding classes $\{c_1, c_2, c_3\}$.

   At the decoding step, applying the n trained binary classifiers, a code is obtained for each data point in the test set. This code is compared to the base codewords of each class defined in the matrix M, and the data point is assigned to the class with the "closest" codeword.
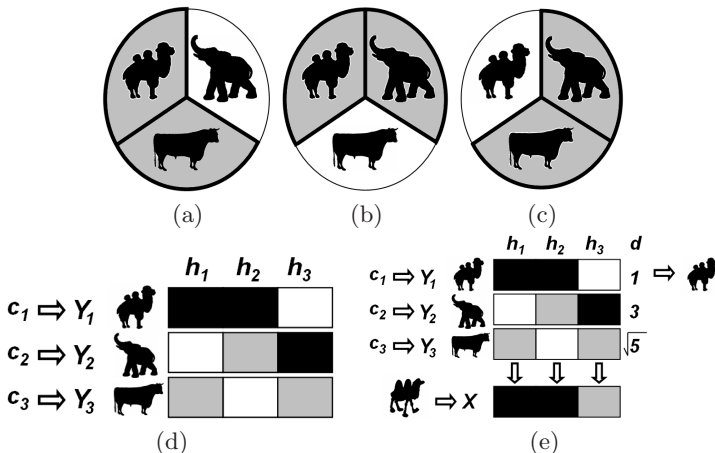
Fig. 6. (a)(b)(c) Three bi-partitions of classes for a three multi-class problem. (d) ECOC coding and (e) decoding for the problem.

---

[1] The codeword encodes the membership information of each binary problem for a given class.

| (a) | (b) | (c) | (d) |
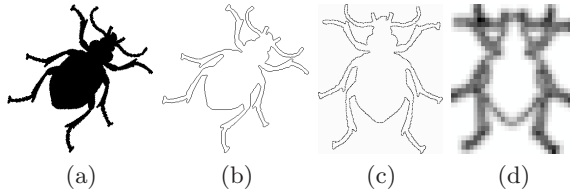
Fig. 7. (a) Input image, (b) contour map, (c) shape alignment, and (d) 32×32 BSM

In fig. 6(e), an input test sample classification is shown. This input is tested using the three binary classifiers, and a codeword X is obtained. Finally, the Euclidean distance is applied between each class codeword and the test codeword X in the form $d(X, Y_i) = \sqrt{\sum_{j=1}^{n}(X(j) - Y_i(j))^2}$, where $i \in [1, .., 3]$. Finally, the test input X is classified by the class with minimum distance c_1.

An example of the process execution is shown in fig. 7. Fig. 7(a) shows an input image, which object shape is obtained in fig. 7(b) by means of a contour map. Shape alignment is performed by means of the Hotelling transform and the area density adjustment in fig. 7(d), and the final BSM of 32×32 grid size is shown in fig. 7(d).

4   Results

To validate the system, first we describe the data, measurements, comparatives, and experiments.

Data: To test the system, we used 23 categories from the MPEG repository database [4]. This database has been chosen since it provides a high intra-class variability in terms of scale, rotation, rigid and elastic deformations, as well as a low inter-class variability. A pair of samples for each of the 23 categories are shown in fig. 8. Each of the classes contains 20 instances, which represents a total of 460 object samples.

Measurements: To analyze the performance of the techniques, the descriptors are trained using 50 runs of Discrete Adaboost with decision stumps, and the one-versus-one ECOC design with the Euclidean distance decoding. The classification score is computed by means of stratified ten-fold cross-validation with two-tailed t-test at 95% of the confidence interval.
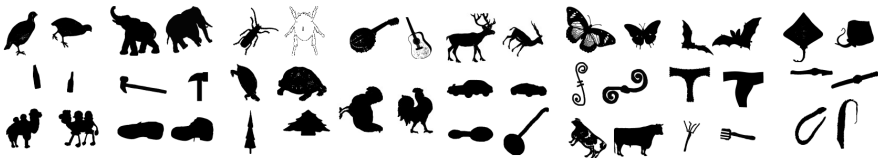
Fig. 8. MPEG07 classes

Comparatives: The methods used for the comparative are: ART, Zoning, Zernique, and CSS curvature descriptors from the standard MPEG [7][5][6].

Experiments: To test the performance of the BSM descriptors, the comparative is applied over the set of 23 MPEG07 classes, classifying by means of 3-Nearest Neighbors to compare the descriptors robustness, and using the whole categorization system with Adaboost and ECOC to show its suitability for multi-class problems. Finally, we discuss the benefits of using the present methodology.

4.1   MPEG07 Classification

The details of the descriptors used for the comparatives are the followings: BSM descriptor is of length 16×16 from the considered regions. The optimum grid size of 16×16 has been estimated applying cross-validation over the training set using a 10% of the samples to validate the different sizes of $n \in \{8, 12, 16, 20, 24, 28, 32\}$. The selected size is the one which attains the highest performance in the training set, defining the optimum grid encoding the blurring degree based on the database distortions. The scores obtained using cross-validation are shown in fig. 9. For a fair comparison, the Zoning descriptor is of the same size (16×16). The parameters for ART are radial order with value 2 and angular order with value 11. Concerning to Zernique, 7 moments are used to estimate the descriptor, and a length of 200 with an initial sigma of 1 increasing per one is applied for the curvature space of the CSS descriptor.
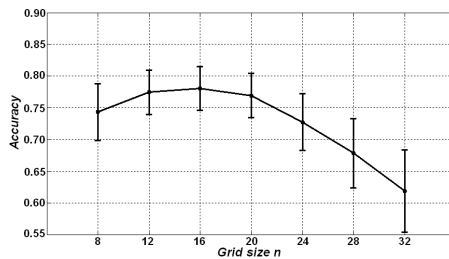
Fig. 9. Cross-validation on the training set for different BSM grid sizes

For this experiment, we started the classification using the first 3 classes of fig. 8. Iteratively, one class is added at each step, and the classification is repeated until the 23 classes are processed. The main objective is to analyze the performance of the techniques when the number of classes increases. The results of the experiment are shown in fig. 10(a). Observing the figure, one can realize that the BSM descriptor attains the best performance for any number of classes in the classification system. Besides, an important point is that its performance does not decrease significatively while increasing the number of classes, obtaining results around 80% in all cases. The second descriptor in the ranking is Zernique, which offers similar performance than BSM when the number of classes is small, but substantially decreases with the number of object categories. Finally, Zoning,

CSS, and ART descriptors offers the worst classification scores in this problem. This can be intuitively justified by the fact that Zoning descriptors are very local, and the database is full of shape variations. This fact also affects to the CSS descriptor, since the points of curvature varies due to the high shape variations among objects.

In order to validate the descriptors independently of the system, the classification for the 23 MPEG07 classes is performed using a simple 3-Nearest Neighbors strategy based on the Euclidean distance. The results are shown in fig. 10(b). One can observe that for the different descriptors the performance decrease considerably. It is intuitively justified by the fact that all features contribute to the final decision, and the non-discriminative ones include distance errors that can miss-classify many samples. Nevertheless, observe that the reduction on the case of the BSM descriptor is less considerable, and it attains the best performance.

Descriptor	$3 - NN$	Our system
BSM	**72.96±3.52**	**79.35±4.17**
Zernique	52.67±5.14	59.52±2.40
Zoning	21.74±2.91	32.07±1.81
CSS	29.50±5.65	28.85±2.42
ART	21.30±3.53	30.35±1.47

(a)   (b)
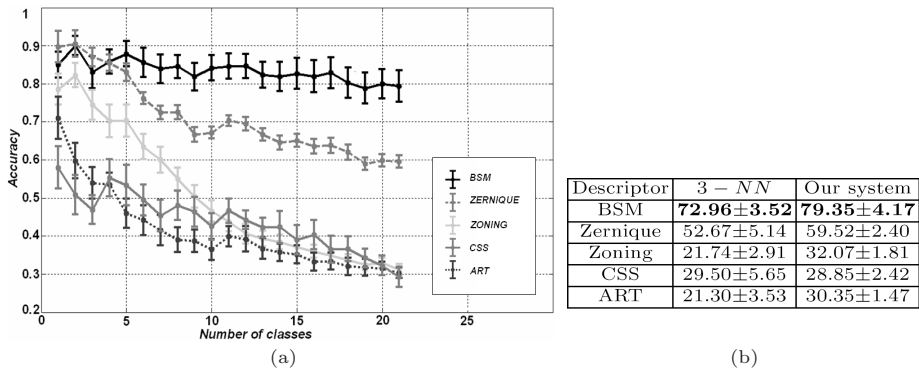
Fig. 10. (a) Classification accuracy on the MPEG07 object categories with our system. (b) Classification on the 23 MPEG07 object categories using 3-Nearest Neighbor and our system.

4.2   Discussion

Concerning the suitability of the presented scheme to deal with multi-class binary object categorization problems, several benefits should be mentioned:

The method is rotation invariant because of the use of the Hottelling transform and the area density adjustment. The method is also scaling and (x, y) stretching invariant because of the use of the $n \times n$ BSM grid. Besides, the BSM descriptor is robust against objects with rigid and elastic deformations since the size of the BSM grid defines the region of activity of the object shape points. The use of Adaboost as base classifier allows to learn difficult classes which may share several object features. The ECOC framework has the property of correcting possible classification errors produced by the binary classifiers, and allows the system to deal with multi-class categorization problems. When the classifiers are trained only few features are selected, and when classifying a new test sample only these features are computed, which makes the approach very fast and suitable for real-time categorization problems.

5   Conclusions

We presented the Blurred Shape Model descriptor, which defines a probability density function of the shape of an object. The shape is parameterized with a set of probabilities that encode the spatial variability of the object, being robust to elastic deformations. Besides, a system to improve the performance of the novel descriptor dealing with multi-class categorization problems is proposed. Adaboost learns the discriminative features that better split object categories, and the binary classifiers are embedded in the Error Correcting Output Codes framework. The evaluation of the system is performed on 23 MPEG07 classes, showing great performance in cases of high intra-class and low inter-class variability, and outperforming the state-of-the-art descriptors while the computational cost is far less.

Acknowledgements

References

1. Torralba, A., Murphy, K., Freeman, W.: Sharing visual features for multiclass and multiview object detection, Technical Report, Massachusetts Institute of Technology Computer Science and Artificial Intelligence (MIT AIM) (2004)
2. Friedman, J., Hastie, T., Tibshirani, R.: Additive logistic regression: a statistical view of boosting. The Annals of Statistics 8(2), 337–374 (1998)
3. Pujol, O., Radeva, P., Vitrià, J.: Discriminant ECOC: a heuristic method for application dependent design of error correcting output codes. IEEE Transaction on Pattern Analysis and Machine Intelligence 28, 1007–1012 (2006)
4. http://www.cis.temple.edu/~latecki/research.html
5. Zhang, D., Lu, G.: Review of shape representation and description techniques. Pattern Recognition 37, 1–19 (2004)
6. Kim, W.: A new region-based shape descriptor, Technical report, Hanyang University and Konan Technology (1999)
7. ISO/IEC 15938-5:2003(E)
8. Lladós, J., Valveny, E., Sánchez, G., Martí, E.: Symbol Recognition: Current Advances and Perspectives. In: Blostein, D., Kwon, Y.-B. (eds.) GREC 2001. LNCS, vol. 2390, pp. 104–127. Springer, Heidelberg (2002)
9. Manjunath, B., Salembier, P., Sikora, T.: Introduction to mpeg-7, Multimedia content description interface. John Wiley and Sons, Chichester (2002)
10. Escalera, S., Pujol, O., Radeva, P.: Decoding of Ternary Error Correcting Output Codes. In: Martínez-Trinidad, J.F., Carrasco Ochoa, J.A., Kittler, J. (eds.) CIARP 2006. LNCS, vol. 4225, Springer, Heidelberg (2006)
11. Dietterich, T., Bakiri, G.: Solving multiclass learning problems via error-correcting output codes. Artificial Intelligence Research 2, 263–286 (1995)

Video Analysis Via Nonlinear Dimensionality Reduction

Alvaro Pardo⋆

DIE, Facultad de Ingeniería y Tecnologías, Universidad Católica del Uruguay
`apardo@ucu.edu.uy`

Abstract. In this work we present an application of nonlinear dimensionality reduction techniques for video analysis. We review several methods for dimensionality reduction and then concentrate on the study of Diffusion Maps. First we show how diffusion maps can be applied to video analysis. For that end we study how to select the values of the parameters involved. This is crucial as a bad parameter selection produces misleading results. Using color histograms as features we present several results on how to use diffusion maps for video analysis.

Keywords: video analysis, dimensionality reduction.

1 Introduction

Most of the available techniques for video analysis begin reducing the amount of information via feature extraction. Usually this means a strong reduction in the amount of data contained in a video sequence. Recently, due to the increase of memory and processing power in actual computers, some algorithms for video analysis are based on a more detailed description of the video using a big number of features [7,10]. Some of these methods can be rooted to image analysis method that use all the pixels and visualize the image as a point in a high dimensional space [7]. Other methods for video analysis recently proposed in the literature use pixel-wise histograms to describe video segments [6]. These methods keep a lot of information from the beginning of the processing. Although, it has been shown that this is beneficial, novel methods for high dimensional data analysis must be developed.

Although the idea of high dimensional data analysis is not new, recently several authors presented new results in this direction. One of the main problems in the context of high dimensional data analysis is dimensionality reduction. The two main goals of this step are: visualization and extraction of smaller set of meaningful and useful coordinates. In what follows we present a brief overview of existing methods for dimensionality reduction.

The most popular method for dimensionality reduction is Principal Component Analysis (PCA). PCA finds the basis of a projection space (of smaller dimension) minimizing the square reconstruction error. It is well known that the

---

subspace which produces the minimum reconstruction error is the subspace with maximum variance. Therefore, this method intends to preserve the covariance structure [9]. PCA has two advantages. First, the projection is performed with a *linear transformation* which is extremely easy to apply. Second, any new vector can be easily projected. Unfortunately, not all spaces are linear and a linear combination of basis vectors will not produce good results. In the same category we can find Independent Component Analysis (ICA) which also uses a linear projection and Multi Dimensional Scaling [9].

The main drawback of the previous methods is that they are not capable of dealing with nonlinear spaces[1]. For this reason, recently several authors presented nonlinear methods for dimensionality reduction. Some of them are graph based methods. Basically, the idea is to discover the underlying structure of the data constructing a graph which joins data points with a given criteria. ISOMAP [11] is one example of these techniques. Other methods such as Locally Linear Embedding (LLE) [8], Laplacian and Hessian Eigenmaps [1,3], and others [5] minimize the reconstruction error using a local linear expansion. That is, each sample is linearly reconstructed using nearby samples. In this way this method overcomes the linear limitation. Diffusion Maps [5,2] provide a unified vision of previous spectral methods in a unified framework. Also, this method includes a natural notion of scale and distance. In next section we review diffusion maps. The weakness of these methods is that is difficult to project a new sample in the obtained projected space. The embedding is given by the data and there is no general method to obtain the projection. In [4] the authors propose a solution to solve the extension to new data points.

Before concluding this section we review some works that apply nonlinear dimensionality reduction for video analysis. In [7] Pless uses Isomap to explore video sequences. The results are for simple sequences. The work is similar to ours but it does not include the notion of scale given by diffusion maps. We also present results with general sequences with transitions. In [10] uses LLE to discover periodicity in video sequences.

The outline of the paper is the following. In next section we present a detailed review of diffusion maps. In section 3 we analyze how to select the appropriate diffusion map parameter values. Then, in section 4 we present several examples of diffusion maps applied to video analysis. Finally in section 5 we discuss our results and present our main conclusions

2   Review of Diffusion Maps

In this section we review Diffusion Maps (DM) following [5]. Let $\Omega = \{x_1, ..., x_n\}$ be a set of data points of dimension N and $d(x_i, x_j)$ a distance between data points. The idea behind DM is to construct a graph with each data point x_i being a vertex and $w(x_i, x_j)$ a weight function between vertices. In what follows we restrict ourselves to $w(x_i, x_j) = \exp(d_\Omega(x_i, x_j)^2)/\sigma^2)$. This graph intends to reflect the knowledge of the local geometry of Ω. Once we have the definition of

---

[1] There are some extensions of PCA and other methods to deal with this problem.

the graph a Markov random walk can be defined over it. If $d(x) = \sum_{z \in \Omega} w(x, z)$ is the degree of node x the quantity $p_1(x, y) = \frac{w(x,y)}{d(x)}$ can be interpreted as the probability of transition from x to y. The 1 means that this transition is made in one step and therefore reflects first order information of the graph structure. Let the matrix P be the one with entries $p_1(x, y)$. Considering powers, P^t, information over larger neighborhoods can be captured. In this way $p_t(x, y)$ means the probability of transition form x to y in t steps. As t increases P^t captures more global information and this enables us to view t as a scale parameter.

If the graph is connected it can be shown that: $\lim_{t \to \infty} p_t(x, y) = \phi_0(y) = \frac{d(y)}{\sum_{\in} d(z)}$ where $\phi_0(x)$ is the stationary distribution. Based on the above elements the distance between points in Ω can be computed as the distance between its corresponding distributions p_t. Thus, the diffusion distance, $D_t(x, y)$ is defined as:

$$D_t^2(x, y) = ||p_t(x, .) - p_t(y, .)||_{1/\phi_0}^2 = \sum_{z \in \Omega} \frac{(p_t(x, z) - p_t(y, z))^2}{\phi_0(z)}.$$

Observe that the distance includes the normalization by $\phi_0(z)$ which is used to decrease the influence of points with small densities. The main result for diffusion distance is the following. The diffusion distance can be expressed as:

$$D_t^2(x, y) = \sum_{i=1}^{n-1} \lambda_i^{2t}(\psi_i(x) - \psi_i(y))^2, \qquad (1)$$

where λ_i and ψ_i are the eigenvalues and eigenvectors of P $(P\psi_i = \lambda_i\psi_i)$. It can be shown that $1 = |\lambda_0| \geq |\lambda_1| \geq ... \geq |\lambda_{n-1}|$ and $\psi_0 = 1$. Due to the ordering of eigenvalues the diffusion distance can be approximated taking only the first coordinates. The number of retained terms depends on the desired precision and on t. The diffusion map is defined as:

$$\Psi_t : x \to \left(\lambda_1^t \psi_1(x), \lambda_2^t \psi_2(x), ..., \lambda_{M(t)}^t \psi_{M(t)}(x)\right)^t, \qquad (2)$$

where $M(t)$ is the number of retained terms. The mapping projects the graph information to a lower dimensional space.

3 Application of Diffusion Maps

DM not only project the data points to a lower dimensional space, but also provide a notion on scale t and precision $M(t)$. This means that we obtain a lower set of coordinates with an associated significance score. In this section we show how to use these ideas for video analysis.

First we must discuss the representation of each image in the video sequence and the associated distance, d_Ω. In this work we will use a representation based on histograms[2]. We describe each frame with its histogram $h_i(q)$. For color

---

[2] We are currently investigating a representation based on pixels.

frames we will take $x_i = \{h_i^R(q), h_i^G(q), h_i^B(q)\}$ a concatenation of the histograms of each color channel. The distance in the original space ,$d_\Omega(x_i, x_j)$, will be the L_2 distance[3]. In following paragraphs we address the specification of the DM parameters: σ and $M(t)$.

How can we select σ? The value of σ must be carefully selected since it determines the final graph and P. This parameter affects the weights, $w(x, y)$, and with them the connection between nodes. If σ is set too big it may cause the graph to be fully connected while a too small value may produce a completely disconnected one. At the end of the day its value is reflected in the graph topology which is in turn what we expect to obtain as a natural description of the data.

To set the value of σ we assume that each point (frame), x_i, must be connected with at least two other points (typically nearby frames). We set the minimum weight for farthest points with distance d_{max} as θ so:

$$\sigma = \frac{d_{max}}{\sqrt{\log(1/\theta)}}.$$

In all the experiments we use $\theta = 0.1$.

How can we decide the value of $M(t)$? It is clear form equation (1) that $M(t)$ determines the precision of the distance approximation. Since are ordered and less or equal than one, we know that to achieve a certain level of approximation we must retain the first coordinates. From equation (2) we conclude that the diffusion map gives a parametrization of the data in a lower dimensional space. Furthermore, the scale of the dimensionality reduction is given by t and the decay of the eigenvalues.

How many data points are needed? In the case of video we may encounter restrictions on the amount of data points available with respect to the dimensionality of the feature space. On one hand DM are insensitive to points density and therefore permit to recover intrinsic data properties [4]. On the other hand, they are more resilient to the number of samples comparing with other existing methods such as [8]. We will confirm this in the experiments where we have in some cases more features than samples. We will have three histograms with 256 bins producing a feature vector of dimension 768 while some of the video sequences have around 300 frames.

Do we need to include temporal information? Traditionally, video analysis is strongly linked to temporal relations. In fact, most of existing methods study the distance between frames at different times[4]. This turns to produce an aperture problem since we observe the data across a given temporal window. Diffusion Maps, and other of the methods reviewed above, enable us to link frames without taking into account small temporal windows. At the end of the day, the method discovers the relevant coordinates within the data and sorts them according to its relevance. This interesting feature comes with the expense

---

[3] Other distance can be used.
[4] Shot detection is a classical example.

of bigger data sets. In the experiments we will show that there is no need to explicitly include temporal information.

4   Experiments

In this section we present a set of experiments of video analysis using the ideas discussed in previous sections. In the two first experiments we show the results for video sequences which contain a smooth transition. Later we will show some results on abrupt changes which are easier to detect.

In the first experiment, see Figure 1 we processed a sequence with a wipe which starts at frame 120 and ends at frame 165. If we observe the first coordinate of the diffusion map at Figure 1 we can see that it correctly detects this smooth transition. From frames 1 to 119 and from frames 166 to 259 this coordinates has little variation. This means that when looking a coarse description these two sets are disjoint. Between frames 120 and 165 we observe a gradual transition between both sets. Therefore, in this case the first coordinate correctly captures the essence of the video sequence. If we observe the remaining coordinates up to the fourth one, we confirm that in finer scales this transition can also be detected. In Figure 1-(b) we depict the video trajectory along the first three

(a)

(b)

(c)
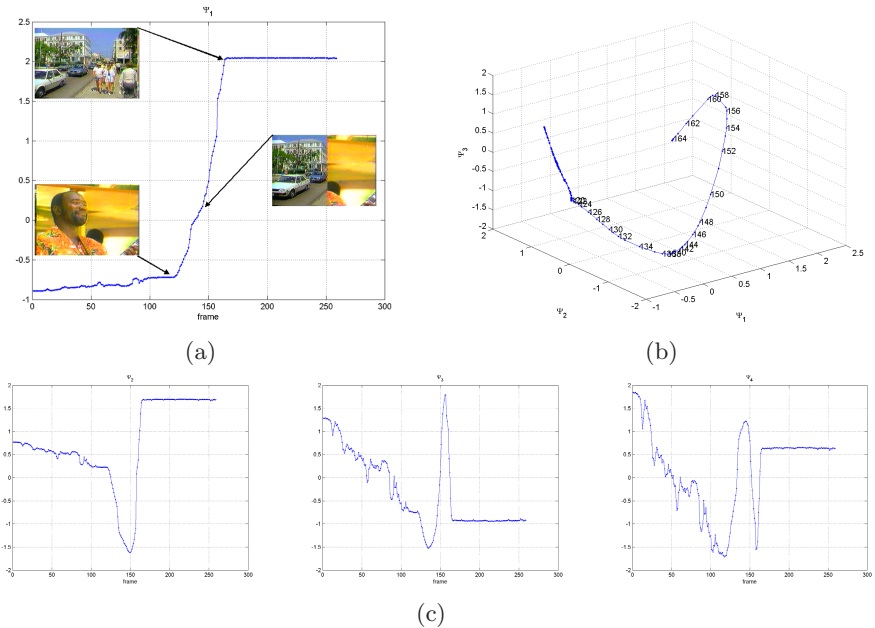
Fig. 1. (a) First coordinate showing clearly showing the structure of the sequence. (b) Video trajectory in the first three coordinates. As we can see the beginning and end of the sequence produces two clusters while the wipe-transition produces a trajectory between them. (c) Remaining coordinates.

(a)

(b)
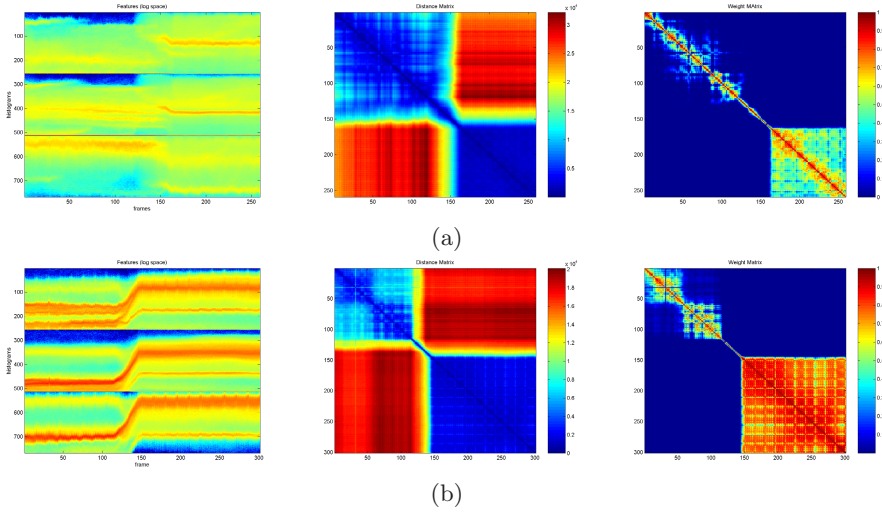
Fig. 2. (a) Features along frames, Distance Matrix and Weight Matrix for sequence in Figure 1. (b) The same for sequence in Figure 3. Observe the video structure.

coordinates. As we can see, there is a transition which expands form frames 120 to 165. To complete the information for this sequence we show the histograms evolution along frames, the Distance and Weight matrices (see Figure 2).

The second experiment presents the results for a dissolve transition. These are the most difficult transitions to detect. As we can see in Figure 3 in this case we can successfully detect the transition. The dissolve starts at frame 115 and ends in frame 145. It is interesting to note the stability of the first coordinate at the beginning and end of the sequences. This shows that the first coordinates classifies, at coarse level, all these frames in the same cluster. This behavior is repeated in the other coordinates. Obviously, as we increase the coordinate number, its corresponding eigenvalues decreases and with it its importance. Finally we note a peak in coordinate Ψ_{10} at frame 31. This is due to an error on the video as can be seen in Figure 3-(b). Therefore, at finer scales we are able to detect such small discrepancies between frames. As we did in the first experiment we show other complementary information in Figure 2.

For our third experiment we used sequence with 1561 frames and mainly abrupt transitions. Observing Figure 4 we see that once again the first components successfully summarize the characteristic of the sequence. If we look at finer scale, in coordinates Ψ_8 to Ψ_{10}, we can see a gradual changes within a shot obtained at coarser scales. This gradual changes are caused by a panning (see $\Psi_1 0$ in Figure 4).

To further evaluate the power of discrimination of the method we tested the algorithm with a small sequence with only smooth transitions. In this case, the first coordinate clearly detects a shot from frames 175 to 200, however, it is difficult to declare other shots while looking only the first coordinate. On the

(a)   (b)

(c)
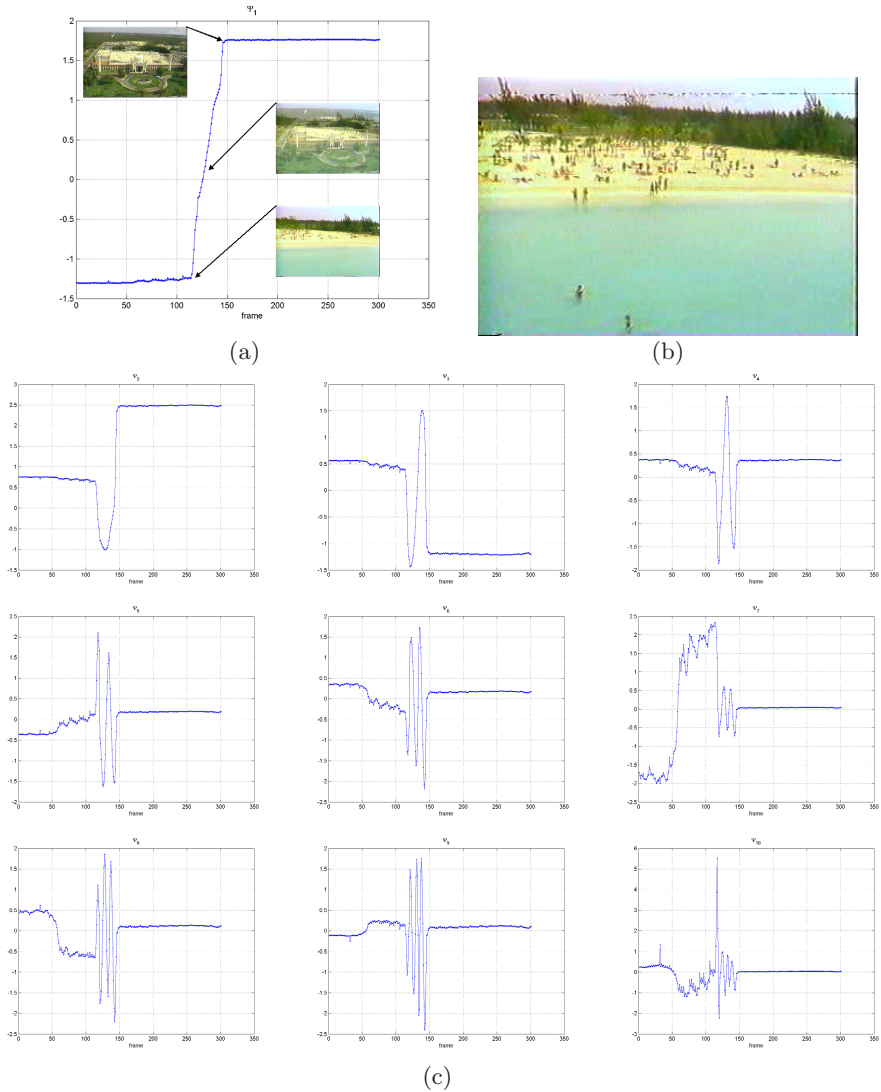
Fig. 3. (a) First coordinate showing clearly showing the structure of the sequence. (b) Frame with error visible at finer scales (c) Remaining coordinates.

other hand, if we observe Ψ_2 we can see a block of frames from frames 45 to 125. However, there is still a big variation within this block which indicates other cluster at finer scale. This is can be confirmed observing Ψ_4, Ψ_5 and Ψ_7. Hence, we conclude that the method effectively detects the structure of the video sequence. However, to do so we must observe several coordinates to discriminate at finer scales.
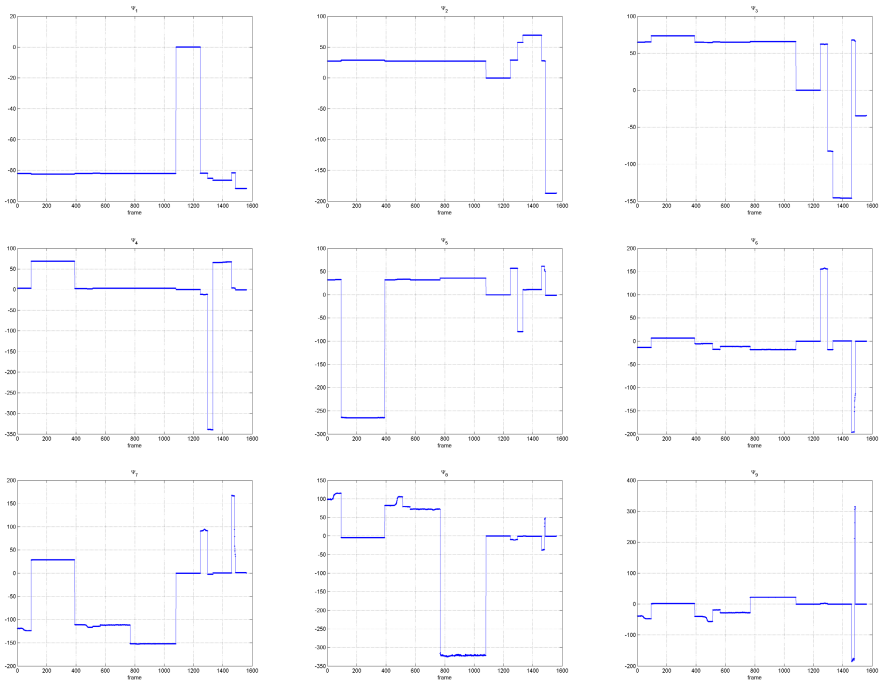
(a)
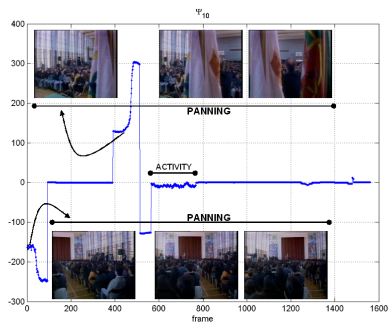
(b)

Fig. 4. (a) First nine coordinates. (b) Details at finer scales showing pannings and some detailed activity within a shot that it is not visible at coarse levels.
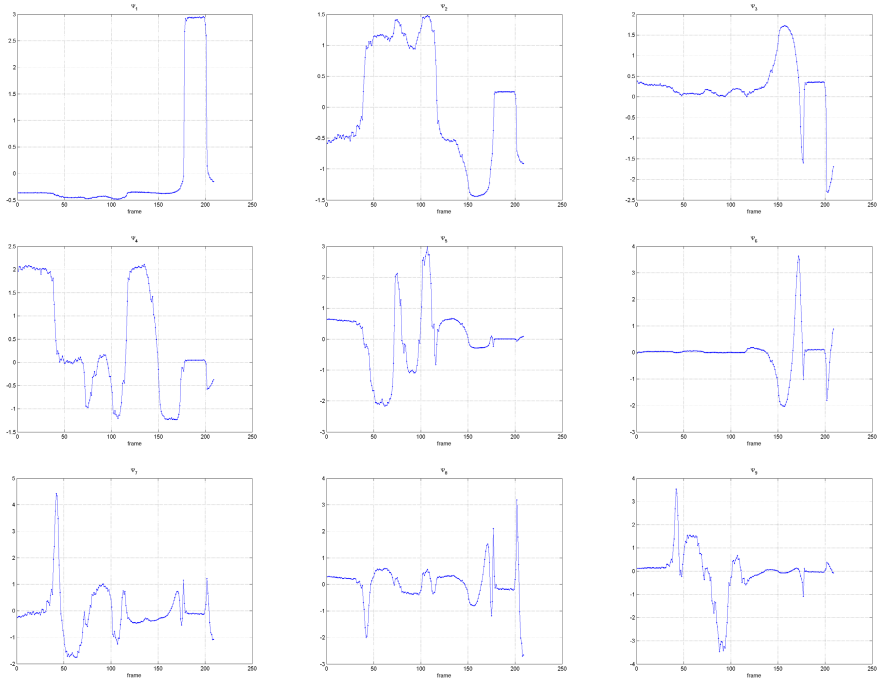
Fig. 5. First nine coordinates for the fourth example

5   Discussion and Conclusions

In this work we study the application of DM to video analysis. We showed
how this method can be successfully applied. We presented estimations for the
method parameters and confirmed this in the experiments. We showed how the
coordinates obtained compress the information of the sequence structure in few
coordinates. Although in several cases the information is compressed in the first
few components, this depends on the sequences, and in some cases we will need
to explore finer scales. This was confirmed with our last experiments. Therefore,
although this are mainly preliminary results, they are very promising. We are
currently testing other descriptions and a more exhaustive evaluation of the
results and their comparison against other methods.

References

1. Belkin, M., Niyogi, P.: Laplacian eigenmaps for dimensionality reduction and data
   representation. Neural Comput. 15(6), 1373–1396 (2003)
2. Coifman, R., Lafon, S.: Diffuion maps. Applied and Computational Harmonic Anal-
   ysis 21, 5–30 (2006)

3. Donoho, D., Grimes, C.: Hessian eigenmaps: locally linear embedding techniques for high dimensional data. Proc. of National Academy of Sciences 100(10), 5591–5596 (2003)
4. Lafon, S., Keller, Y., Coifman, R.: Data fusion and multicue data matching by diffusion maps. IEEE Trans. Pattern Anal. Mach. Intell. 28(11), 1784–1797
5. Lafon, S., Lee, A.B.: Diffusion maps and coarse-graining: a unified framework for dimensionality reduction, graph partitioning, and data set parameterization. IEEE Trans. on Pattern Anal. and Mach. Intell. 28(9), 1393–1403 (2006)
6. Pardo, A.: Pixel-wise histograms for visual segment description and applications. In: Martínez-Trinidad, J.F., Carrasco Ochoa, J.A., Kittler, J. (eds.) CIARP 2006. LNCS, vol. 4225, pp. 873–882. Springer, Heidelberg (2006)
7. Pless, R.: Image spaces and video trajectories: Using isomap to explore video sequences. In: ICCV, pp. 1433–1440 (2003)
8. Roweis, S., Saul, L.: Nonlinear dimensionality reduction by locally linear embedding. Science 290, 2323–2326 (2000)
9. Saul, L., Weinberger, K., Sha, F., Ham, J., Lee, D.: Spectral methods for dimensionality reduction. In: Schoelkopf, B., Chapelle, O., Zien, A. (eds.) Semisupervised Learning, MIT Press, Cambridge (2006)
10. Stich, T., Magnor, M.: Keyframe Animation from Video. In: ICIP 2006, pp. 2713–2716 (2006)
11. Tenenbaum, J.B., de Silva, V., Langford, J.C.: A global geometric framework for nonlinear dimensionality reduction. Science 290, 2319–2323 (2000)

Graph Cuts Approach to MRF Based Linear Feature Extraction in Satellite Images

Anesto del-Toro-Almenares[1,2], Cosmin Mihai[1],
Iris Vanhamel[1], and Hichem Sahli[1]

[1] Vrije Universiteit Brussel, Dept. of Electronics and Informatics,
VUB-ETRO Pleinlaan 2, B-1050, Brussels-Belgium
[2] Univ. Central de Las Villas, Center for Studies on Electronics and
Information Technologies, Carr. a Camanjuani Km 5 $\frac{1}{2}$,
CP-54830, Villa Clara - Cuba
{aalmenar,cmihai,iuvanham,hsahli}@etro.vub.ac.be
http://www.etro.vub.ac.be

Abstract. This paper investigates the use of graph cuts for the minimization of an energy functional for road detection in satellite images, defined on the Bayesian MRF framework. The road identification process is modeled as a search for the optimal binary labeling of the nodes of a graph, representing a set of detected segments and possible connections among them. The optimal labeling corresponds to the configuration that minimizes an energy functional derived from a MRF probabilistic model, that introduces contextual knowledge about the shape of roads. We formulate an energy function modeling the interactions between road segments, while satisfying the regularity conditions required by the graph cuts based minimization. The obtained results show a noticeable improvement in terms of processing time, while achieving good results.

Keywords: road detection, graph cuts, MRF-MAP labeling.

1 Introduction

Several approaches have been proposed for linear feature extraction, most of them dealing with the problem of road extraction in either synthetic aperture radar (SAR) images or optical images (visible range). These approaches can be classified according to the preset objective, the extraction technique applied, the type of sensor used, etc. [1].

Most of the reported schemes are based on two criteria: a local criterion, involving the use of local operators, and a global criterion, incorporating additional knowledge about the structure of the objects to be detected. The methods based on local criteria evaluate local properties on the image by using either an edge or line detector [2] or morphological operators [3]. The performance of these methods can be greatly increased by using techniques that introduce some global constraints in the image analysis process. These techniques lead to an optimal solution through the minimization of a cost function by using dynamic

programming [4], tracking methods [5] or the Bayesian MRF framework [2], [6], [7], [8].

Previous work at VUB-ETRO [8] proposed a method that combines both local and global criteria for the identification of the medial axis of roads and paths in satellite images. The approach consists of two steps Fig. 1.
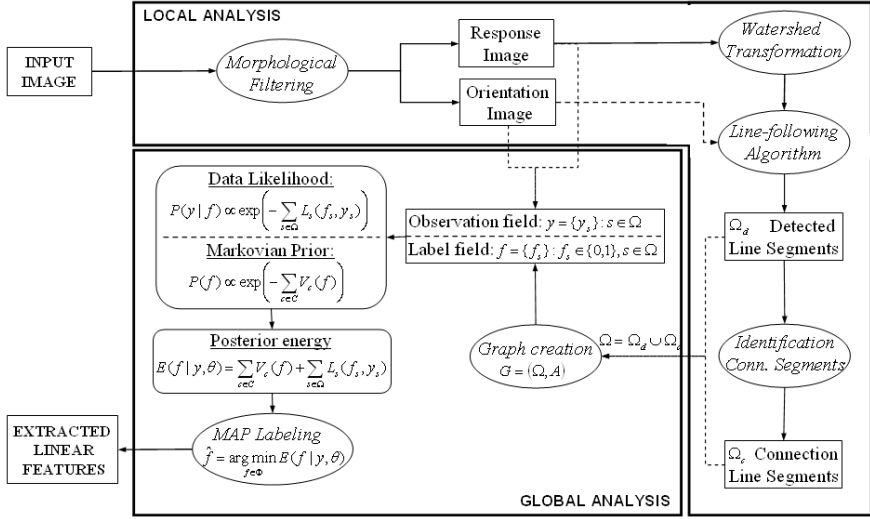
Fig. 1. General algorithm of linear features detection [8]

During a *local analysis*, the detection of elongated structures is performed using a set of soft morphological operators, and a dedicated algorithm is employed for line segment extraction. This results in a set of segments, $\Omega = \Omega_d \bigcup \Omega_c$, with Ω_d the extracted line segments and Ω_c the set of all possible connections between the segments of Ω_d. The elements of Ω are then organized in a graph $G = (\Omega, A)$, where each node $s \in \Omega$ is a line segment, to which we associate a normalized segment length ($l_s \in [0, 1]$), an observation value y_s (defined below), and a label $f_s = 1$ if s belongs to a road, $f_s = 0$ otherwise. An arc, $A_{st} \in A$, between two nodes s and t, correspond to a shared extremity. To each arc A_{st} is associated the angle θ_{st} between the two segments.

A segment linking process is then performed in the *global analysis*. This is based on the Bayesian framework incorporating an observation measure that reflects the likelihood value of each segment as belonging or not to a road, $L(f_s, y_s)$, and a formulation of the potential functions, $V_c(f)$, which describes the probability distributions of the prior model. The identification of the roads is carried out with an appropriate labeling of the graph $G = (\Omega, A)$, in accordance with the observation process $y = (y_1, \ldots, y_m); m = |\Omega|$. A Markov random field (MRF) is defined on the graph and the optimum configuration (labeling) $f = (f_1, \ldots, f_m)$, of the segments of Ω given the observation process y, can be estimated based on the Bayes rule and a MAP criterion that maximizes the *posterior probability*

$P(y|f)$. The *conditional probability distribution* $p(y|f)$ depends on the observation measurements, whereas the *prior probability of labelings* $P(f)$ is based on a Markovian model of road-like objects. From the equivalence between MRF and Gibbs fields [11], both of them can be described with a set of potentials that associate an energy function to the different configurations. The minimization of this energy function gives the optimal solution to the problem.

One of the major drawbacks of the approach in [8] is the time required for solving the MAP estimator by means of the simulated annealing algorithm, which requires exponential time in theory and is extremely slow in practice. The computational task of minimizing the energy associated to a particular problem is usually quite difficult, as it generally requires minimizing a non-convex function in a space with thousands of dimensions. However, recently a new approach for energy minimization has been developed based on graph cuts [9]. The basic idea is to construct a specialized graph for the energy function to be minimized such that the minimum cut on the graph also minimizes the energy (either globally or locally). The minimum cut, in turn, can be computed very efficiently by max flow algorithms [10].

This paper investigates the use of graph cuts for the minimization of an MRF based energy functional of [8]. To this end, we reformulate the Bayesian-MRF framework previously described to fit the graph cuts theory. This energy form turns out to be sufficient to model all the interactions between road segments, while satisfying the regularity conditions required by the graph cuts based minimization.

The paper is organized as follows. Section 2 defines the MAP function to be minimized (subsection 2.1), summarizes the graph cuts theory (subsection 2.2), and formulates the functional of subsection 2.1 in terms of graph cuts (subsection 2.3). Section 3 describes the experiments conducted and a preliminary discussion of the obtained results. Finally, Section 4 exposes the final conclusions and addresses future improvements for the proposed approach

2 Materials and Methods

2.1 MRF-MAP Formulation for Linear Feature Extraction

The MAP-MRF estimation belongs to the general family of variational methods, where the main objective is the minimization of an energy functional that conveys the dependencies on observed data and a series of a priori constraints, according to the MAP criterion [11]. The MAP-MRF framework facilitates the formulation of such an energy term by considering certain independence assumptions for the data likelihoods and introducing prior knowledge in the form of Gibbs distributions. The energy functional for linear feature extraction, defined in [8], is stated in Fig. 1, being θ the set of model parameters. From this expression, the MAP estimation is obtained to be:

$$\widehat{f}^{MAP} = \arg\min_{f \in \mathbb{F}} \left(\sum_{s \in \Omega} L(f_s, y_s) + \sum_{c \in \mathcal{C}} V_c(f) \right) . \tag{1}$$

where $\mathbb{F}$ is the space of all possible configurations $f = \{f_s\} : s \in \Omega, f_s \in \{0,1\}$. $\mathcal{C}$ is the set of all the cliques or clique space of the model. For each detected segment, two cliques are added to $\mathcal{C}$; those conformed by the connection segments sharing one extremity with the detected segment. For more details refer to [8]. The observation, y_s, of a segment s is a function of a saliency measure r_s defined as:

$$r_s = \frac{\overline{R}_s}{|\theta_s - \overline{\alpha}_s| + 1} , \tag{2}$$

where θ_s is the line segment orientation, $\overline{R}_s$ and $\overline{\alpha}_s$ are the mean values, along the line segment, of the response and orientation images, respectively, obtained using soft morphological operators as described in [8] (Fig. 1). The observation values y_s are defined as:

$$y_s = \max_{t \in \mathcal{N}} \left\{ \frac{(r_s + r_t)}{2} \right\} , \tag{3}$$

were $\mathcal{N}_s$ is the neighborhood of segment s. After computed, the y_s are linearly normalized to fit the $[0, 1]$ interval. Analogously:

$$L(f_s, y_s) = (1 - y_s) \left(\min(\frac{y_s}{\tau}, 1) + \log Z_0 \right) . \tag{4}$$

where τ is a model parameter to threshold observation values, and Z_0 is a normalization factor found to be equal to $Z_0 = (1-\tau)(\frac{1}{e}) - \tau(\frac{1}{e}-1)$, with $e = \exp(1)$. The potential functions $V_c(f)$ are defined for each clique according to its size and composition (number and types of segments that conform the clique) as follows:

$$V_c(f_s) = \begin{cases} 0 & \text{if } \forall s \in c, f_s = 0; \\ K_1 + 1 - l_s + \log Z_0 & \text{if } \exists! s \in c \land s \in \Omega_d : f_s = 1; \\ sin(\theta_{st}) + 1 - l_s + l_t + 2\log Z_0 & \text{if } c1; \\ K_2 \sum_{s:s \in c} f_s & \text{otherwise.} \end{cases} \tag{5}$$

where $c1 \equiv \exists!(s,t) \in c \times c \land s \in \Omega_d, t \in \Omega_c : f_s = f_t = 1$. K_1 and K_2 are parameters of the labeling model, defined by the prior road assumptions, and l_s denotes the normalized length of a segment s.

2.2 Energy Minimization Using Graph Cuts

In [9], a systematic and general formulation for energy minimization using graph cuts was presented. The energy form is mainly restricted to functions of binary variables, although it is easily applicable to problems that involve large numbers of labels. Next, we describe the type of energy we are interested to minimize using graph cuts, according to the method described in [9]. Let $x = (x_1, \ldots, x_m) : x_s = \{0,1\}$ be a set of binary-value variables. The type of energy considered has the form:

$$E(x) = \sum_s E_s(x_s) + \sum_{s<t} E_{s,t}(x_s, x_t) \ . \tag{6}$$

That is, the sum of functions involving up to two binary values at a time. A more general energy form, including functions involving up to three binary values, is described in [9].

In order to minimize $E(x)$ (Eq. 6) using graph cuts, a specialized energy graph is created such that the minimum cut on the graph also minimizes $E(x)$ (either globally or locally). The form of the graph depends on the exact form of $E(x)$ and on the number of labels. Let $G = (V, \mathcal{A})$ be a directed graph with non negative edge weights that have two special vertexes (terminals), namely, the source p, and the sink q. A p-q-cut referred simply as cut, $R = \{P, Q\}$ is a partition of the vertexes of V into two disjoint sets P and Q, such that $p \in P$ and $q \in Q$. The total cost of the cut is the sum of the cost of all edges that go from P to Q. The minimum p-q-cut problem is to find a cut R with the smallest cost. The solution to this problem is equivalent to computing the maximum flow from the source to the sink [9]. There are several algorithms that solve this problem in polynomial time with small constants [10]. A cut R is conveniently associated with a labeling f, mapping from the set of vertexes $V - \{p, q\}$ to $\{0, 1\}$, where $f_s = 0$ means that $s \in P$ and $f_s = 1$ means that $s \in Q$. Note that a cut is a binary partition of a graph viewed as a labeling; it is a binary-valued labeling.

The necessary conditions for an energy function to be minimized using graph cuts are described in terms of graph representability, which is conditioned by the regularity of the terms conforming the energy $E(x)$. The regularity condition that must be satisfied is stated as follows:

$$E_{s,t}(0,0) + E_{s,t}(1,1) \le E_{s,t}(0,1) + E_{s,t}(1,0) \ . \tag{7}$$

For a given regular energy function $E(x)$, of the form in Eq. (6), the construction of the energy graph is done for each term separately and then all the sub-graphs merged together. The graph will contain $m + 2$ vertices: $V = \{p, q, v_1, \ldots, v_m\}$; p and q are terminal vertexes, and the non-terminal vertexes v_s will encode the binary variable x_s. For a detailed description of the graph construction process refer to [9].

2.3 Graph Cuts for Linear Feature Extraction

The goal of the graph cuts approach for linear feature extraction is to express the energy of the *global analysis* step, in the form of Eq. (6), while conveying for the assumptions of the prior model. According to the method described in [8], the clique space can contain cliques of size greater than two, since it is possible to have more than two connections at one extremity of a detected segment. This makes infeasible the direct use of graph cuts for the energy form defined by the potential functions described in Eq. (5).

In order to make use of the graph cuts theory, we propose the use of a clique space composed by cliques of size one and two, $\mathcal{C} = \mathcal{C}_1 \cup \mathcal{C}_2$, as follows. $\mathcal{C}_1$ contains

cliques of size one, defined only by a detected segment and $\mathcal{C}_2$ contains cliques of size two, conformed by a detected and a connection segment, sharing one extremity. Thus, the prior energy term in Eq. (1) can exhibit the following form:

$$E_{prior}(f) = \sum_{s \in \Omega} V_1(f_s) \quad + \sum_{(s,t) \in \Omega \times \Omega \ :t \in \mathcal{N}} V_2(f_s, f_t) \,. \tag{8}$$

The key facts used to model the prior knowledge rely on the following assumptions [8]: 1) roads are long structures, 2) roads have low curvature, and 3) multiple connections are rare. From the previous assumptions three constrains should be imposed to the prior model: continuity, co-linearity and penalization of multiple connections. $V_1(f_s)$ is used to account for the extremity penalization in the case of isolated segments, and detected segments with a free extremity situated far from the border of the image. Free extremities at the border of the image are though to belong to a long road not captured by the image, thus no extremity penalization is included.

Let $Ex(s) : \Omega \longrightarrow \{0, 1, 2\}$ be a function that return the number of free extremities of a segment s, excluding the cases when the extremity is at the border of the image, then:

$$V_1(f_s) = f_s \cdot K_{ex} \cdot Ex(s) \,, \tag{9}$$

where K_{ex} is the extremity penalization model parameter, that accounts for assumption 1). Analogously, the use of size two cliques is intended to penalize non co-linear segments while favoring the co-linear ones, and to include a penalization term for unconnected extremities. The definition of $V_2(f_s, f_t)$, for size two cliques, is presented in Table 1.

Table 1. Formulation of the potential function for size two cliques

(f_s, f_t)	$V_2(f_s, f_t)$
0 0	0
0 1	$+\infty$
1 0	$K_{ex} \cdot w_{t|s}^N$
1 1	$K_{co} \cdot \sin \theta_{st}$

Here, K_{co} is a weight to account for assumption 2), by providing a penalty weight for non co-linear segments. It also serves to penalize multiple connections, assumption 3). $w_{t|s}^N$ is a normalized arc measure, defined as the strength of the path determined by the connection segment t in the direction to which it is connected to the detected segment s. This arc measure is computed from the quantities $w_{t|s}$, given by:

$$w_{t|s} = K_{co} \sin \theta_{st} + \begin{cases} (l_s \cdot r_s + l_t \cdot r_t) \cdot (l_s + l_t)^{-1} & \text{if } l_s > l_t; \\ 0.5 \cdot (r_s + r_t) & \text{otherwise.} \end{cases} \tag{10}$$

The quantities $w_{t|s}$, after computed, are normalized locally to fit in the $[0, 1]$ interval to obtain $w_{t|s}^N$. This normalization is accomplished locally among the connection segments sharing the same extremity of a detected segment. $V_2(f_s, f_t)$ is defined based on the belief that every time a connection segment is labeled as zero then the likelihood that the corresponding detected segment is isolated is increased. Note that in the case of a configuration labeling of a connection segment without its corresponding detected segment, a high penalization is included. This corresponds to the analysis that connection segments will not be included without the evidence of a detected segment in one extremity.

From equations (4), (8), (9) and Table 1, we can express the proposed graph cut energy in the form of Eq. (6) as follows:

$$E(f) = \sum_{s \in \Omega} [L(f_s, y_s) + V_1(f_s)] \quad + \sum_{(s,t) \in \Omega \; \times \Omega \; : t \in \mathcal{N}} V_2(f_s, f_t) . \qquad (11)$$

The proof of the required regularity condition, Eq. (7), for the current definition of the clique potentials is straightforward as shown in Eq. (12):

$$V_2(0,0) + V_2(1,1) \leq V_2(1,0) + V_2(0,1) \qquad (12)$$
$$0 + K_{co} \cdot \sin \theta_{st} \leq +\infty + K_{ex} \cdot w_{t|s}^N$$

3   Results and Discussion

In order to validate the proposed approach, some experiments were conducted using images corresponding to the blue channel of two scenes from IKONOS imagery, given in 2.a and Fig. 3.a. Images are available at (http://www.bauv.unibw-muenchen.de/institute/inst10/eurosdr/).

The experiments were carried out as follows: for each image, a graph containing the potential road network was obtained, using the *local analysis* step described in [8] (incises b). Based on this graph, the *global analysis* step (graph labeling) was accomplished using the proposed approach for different sets of parameters settings (incises c and d). Fig. 2.b illustrates the detected candidate road segments of Fig. 2.a, composed of 630 and 441 detected and connection segments, respectively; Fig. 2.c and Fig. 2.d show the obtained road labeling, with parameters $\tau = 0.165$, $K_{co} = 0.01$, $K_{ex} = 0.13$, and $\tau = 0.15$, $K_{co} = 0.008$, $K_{ex} = 0.135$, respectively.

Fig. 3.b illustrates the detected candidate road segments of Fig. 3.a, composed of 870 and 704 detected and connection segments, respectively; Fig. 3.c and Fig. 3.d show the obtained road labeling, with parameters $\tau = 0.15$, $K_{co} = 0.09$, $K_{ex} = 0.12$, and $\tau = 0.155$, $K_{co} = 0.09$, $K_{ex} = 0.135$, respectively.

In both cases, the proposed approach using graph cuts takes less than 1 second for the optimization while the time required by the method reported in [8] takes up to 10 minutes. As can be visually noticed, the obtained results are
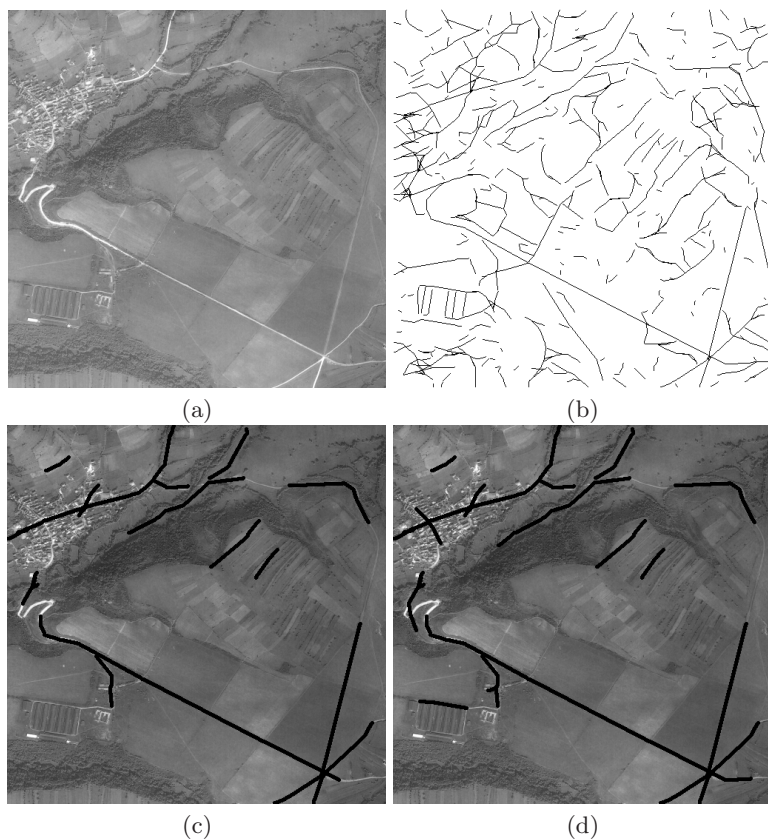
Fig. 2. Image Ikonos1: a) original image; b) candidate road segments; c) road labeling composed by 63 and 51 detected and connection segments; d) road labeling composed by 55 and 45 detected and connection segments

acceptable in terms of false alarms and correct detection of roads. Some false alarms corresponds to the detection of elongated linear structures other than roads, *e.g.* ridges and bright terrain patches. These erroneous detections are thought to be favored by the employed observation model [8], and its ability to effectively describe road and non road linear structures (likelihood value).

Note that the resulting road labeling, is always limited by the quality and completeness of the potential road network, obtained in the *local analysis* step. The setting of the parameters has been made empirically, using the fact that the parameter τ depends on the intensity of the roads. The setting of K_{co}, as expected, was found to be related with the presence of curvilinear roads. Lower values of K_{co} favors the labeling of segments corresponding to curved paths, since its reduces the penalization for non co-linear segments.
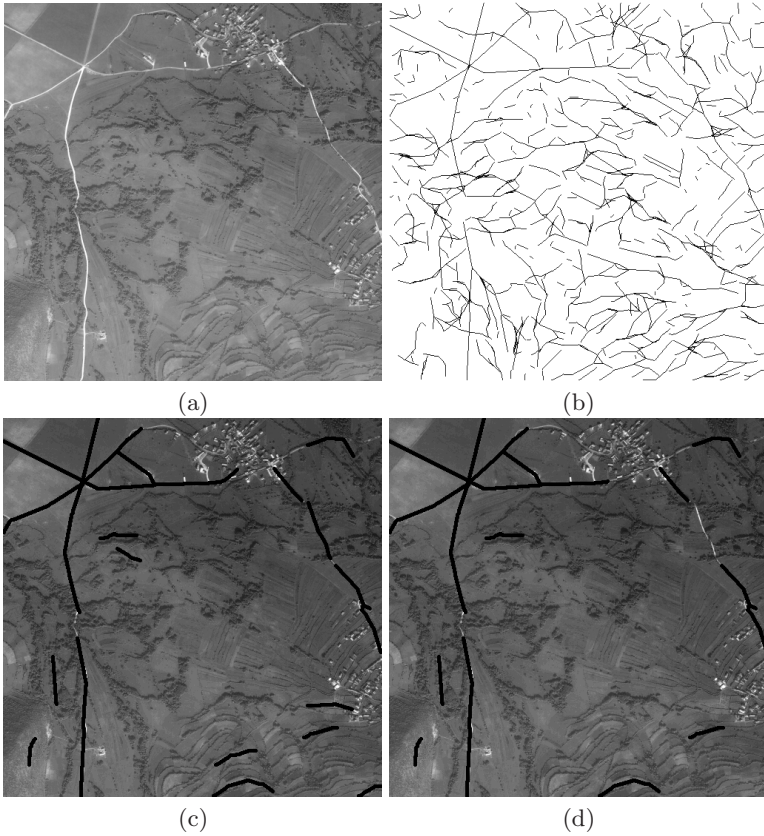
Fig. 3. Image Ikonos3: a) original image; b) candidate road segments; c) road labeling composed by 65 and 49 detected and connection segments; d) road labeling composed by 50 and 39 detected and connection segments

4   Conclusions and Future Work

Despite of its simplicity, the proposed approach shows a noticeable improvement in terms of processing time, while achieving good results. Although the obtained results were satisfactory, these are only preliminary. Improvements should address the observation model, and take into account curvilinear roads as well as the automatic estimation of the involved parameters, by deriving relationships among them. In the future, we aim to tackle these issues and to conduct several experiments to make a comparative analysis with other methods and different optimizers in terms of computational burden and performance.

Acknowledgment

References

1. Mena, J.B.: State of the art on automatic road extraction for GIS update: a novel classification. Pattern Recognition Letters. 24(16), 3037–3058 (2003)
2. Tupin, F., Maitre, H., Mangin, J.F., Nicolas, J.M., Pechersky, E.: Detection of Linear Features in SAR Images: Application to road network extraction. IEEE Trans. on Geoscience and Remote Sensing. 36(2), 434–453 (1998)
3. Chanussot, J., Lambert, P.: An application of mathematical morphology to road network extraction on SAR images. In: Proc. 4th Int. Sym. On Mathematical Morphology and its App. to Image and Signal Processing, Amsterdam, pp. 399–406 (1998)
4. Merlet, N., Zerubia, J.: New prospects in line detection by dynamic programming. IEEE Trans. Pattern Anal. Mach. Intell. 18(4), 426–431 (1996)
5. Geman, D., Jedynak, B.: An active testing model for tracking roads in satellite images. IEEE Trans. Pattern Anal. Mach. Intell. 18(1), 1–14 (1996)
6. Tupin, F., Houshmand, B., Datcu, M.: Road detection in dense urban areas using SAR imagery and the usefulness of multiple views. IEEE Trans. on Geoscience and Remote Sensing. 40(11), 2405–2414 (2002)
7. Katartzis, A., Pizurica, V., Sahli, H.: Application of mathematical morphology and Markov random field theory to the automatic extraction of linear features in airborne images. In: Proc. 5th Int. Sym. On Mathematical Morphology and its Applications to Image and Signal Processing. California, pp. 405–414 (2000)
8. Katartzis, A., Sahli, H., Pizurica, V., Cornelis, J.: A model-based approach to the automatic extraction of linear features from airborne images. IEEE Trans. on Geoscience and Remote Sensing 39(9), 2073–2079 (2001)
9. Kolmogorov, V., Zabih, R.: What energy functions can be minimized via graph cuts? IEEE Trans. Pattern Anal. Mach. Intell. 26(2), 147–159 (2004)
10. Boykov, Y., Kolmogorov, V.: An experimental comparison of min-cut/max-flow algorithms for energy minimization in vision. IEEE Trans. Pattern Anal. Mach. Intell. 26(9) (2004)
11. Li, S.Z.: Markov random field modeling in computer vision, 1st edn. Springer-Verlag, New York Berlin Heidelberg Tokyo (1995)

A Multiple Substructure Matching Algorithm for Fingerprint Verification

Mabel Iglesias Ham, Yilian Bazán Pereira, and Edel B. García Reyes

Adv. Tech.Application Center 7a No. 21812, Siboney, Miramar, 12200, Habana, Cuba
{miglesias,ybazan,egarcia}@cenatav.co.cu

Abstract. In this paper, we represent a fingerprint image with a Delaunay graph formed by minutiae as nodes. The graph has attributes which contributes to the final similarity measure and are invariant under rotation and translation. We design an algorithm for the comparison of these graphs based on the similarities of multiple common substructures. We use different heuristics to tackle the problems of noise, deformation and partial matching found in fingerprint recognition. We match star structures and extend it by edges maintaining the local structural compatibility. Finally, we consolidate the global similarity taking into account the size of the common substructures and the accumulated similarity of all stars involved. We use a simple greedy algorithm obtaining a very efficient performance. We use our proposed method in some experiments with fingerprint images in databases from FVC2002. It shows better results compared to other known algorithms as K-plet, and several others recently published.

Keywords: graph matching, fingerprint recognition, Delaunay triangulation.

1 Introduction

Fingerprints have been widely used in personal identification, access control, financial security, and verification of driver license applicants [1]. However, fingerprint matching is a difficult problem that has not been solved yet for a generic application. The problem of comparing fingerprint impressions appears in two different forms, verification and identification. The verification is applied in systems of access control, where it is needed to determine if a pair of impressions belongs to the same finger or not. Identification, used in forensic applications, refers to the process of establishing the identity of a person from its impression, which entails the comparison of this impression with the one stored in a database returning a list of candidates where it must appear the corresponding one in positive case. Finally the resulting list is examined by the specialist who is the one in charge of giving a final decision.

Minutiae pattern is the most widely used method for representing a fingerprint. Each minutia has some characteristics as coordinates, type and direction. Extraction of minutiae features generally needs a series of processes, including orientation computation, image segmentation, image enhancement, ridge extraction and thinning,

minutiae extraction and filtering. This paper only discusses the process of fingerprint matching.

Fingerprint matching based on minutia features is a well researched problem. Yet, several problems remain as challenges nowadays as tough situations of non-linear distortions, low-quality images and partial prints. A minutia based fingerprint matching system usually returns the number of matched minutiae from query and reference fingerprint and uses it to generate a similarity. Generally, more matched minutiae yield higher similarity scores. We can confidently distinguish a genuine or an imposter fingerprint using the number of matched minutiae when the number of minutiae on both fingerprints is large. However, it is not reasonable to use an absolute number of matched minutiae alone in case of partial fingerprint. A traditional way to calculate the similarity score for a minutiae-based system is $n^2 / (n_1 * n_2)$. Where n_1 and n_2 represent the number of minutiae on query and reference fingerprint, and n is the number of matched minutiae on both prints. This method is unreliable, especially when we are matching fingerprints of different sizes. For this reason we change the similarity score measurement. Kovacs-Vajna [2] has shown that the geometric deformations on local areas can be more easily controlled than global deformation. That is why we pose the problem as a search of multiple common substructures simultaneously on both graph representations of fingerprints and use an accumulative process of evidence about the similarity.

Usually, the point pattern matching methods first align two sets of minutiae and then identify the corresponding ones using an adaptive bounding box to handle the spatial distortion. For that reason we propose a scheme based on graphs, to construct a translation and rotation invariant feature avoiding the alignment step for the local matching. To overcome the effect of missing or fake minutiae in a local area we adopted a Delaunay triangulation graph representing the proximity relations among minutiae.

It is widely believed that if two fingerprints are from the same finger they would share the same local spatial distribution of minutiae. Human experts, in practice, pay special attention to the relative positions among some candidate minutiae pairs. Some approaches in automatic fingerprint matching imitate this observation looking for a global compatibility of the local structures using a graph that represents these local relations [3, 4, 5]. Our idea is similar to the algorithm proposed by Sharat et al., at the ICB2006 [6]. We also, starting in a minutia pair, expand the substructure by the neighbourhood maintaining the local structural compatibility. Nevertheless, we use for the expansion a modification of DFS (depth-first search) strategy instead of BFS (breadth-first search) as Sharat et al. does. The space complexity of DFS is much lower than BFS (breadth-first search). It also lends itself much better to heuristic methods of choosing a likely-looking branch as in our case of study. They used K-plet to represent the topological relationships of the feature set while we use a Delaunay triangulation with the same purpose. In the local matching they employ a dynamic programming approach based on string alignment algorithm and converting the unordered neighbours of each K-plet into an ordered sequence by arranging them in the increasing order of the radial distance. This order is affected because of the fact that distances vary with the translation of minutiae produced by ridge deformations in the process of capturing the image even by different skin conditions or pressure. Meanwhile we use a greedy algorithm for the local matching which is a simpler and

faster heuristic. We obtain a more elaborated consolidation taking into account the similarities of several common substructures representing different areas with low levels of noise. Meanwhile, K-plet uses only the maximum substructure found to measure the global similarity. The K-plet graph does not ensure a connected representation restricting the expansion capacity of the method, not in the case of the Delaunay graph of our proposal.

In section 2, we discuss some issues about the representation of the topological relationships of minutiae. Our heuristic for multiple substructures matching using attributed Delaunay minutiae graphs is given in section 3. The results of the experiments are presented in section 4 using some standard indexes of FVC competition protocol. Finally in section 5, conclusions and future work are presented.

2   Representation

Graphs provide a powerful representation technique in many areas of computer vision including Biometrics. In particular, the structural relationships among minutiae have a good discrimination power. Here the basic idea is to recognise fingerprints by comparing the graph-structure. To the best of our knowledge, four different kinds of representations have been used to capture the local structural information in fingerprints based on minutiae: Minutiae Adjacency Graph (MAG) [7], K-nearest neighbour (K-NN)[4], K-plet[6] and Delaunay triangulation[3, 8, 9].

MAG, K-NN and K-plet do not ensure a connection between all parts of the fingerprint. In MAG two nodes of a graph are considered neighbours if the Euclidean distance between them is less than or equal to a threshold. In K-NN representation, the Euclidean distances between a minutia and its neighbours are calculated and arranged in an increasing order selecting the k-nearest neighbours to form a star. In K-plet to maintain high connectivity at least a neighbouring minutia is chosen in each of the four quadrants sequentially leading to directed edges. The Delaunay triangulation connects two nodes if they have adjacent Voronoi neighbourhoods. Voronoi neighbourhood of a point is the set of points that are nearer to the reference point than to any other point [10, 11]. So in that way points connected by Delaunay triangulation are intuitively neighbours. The Voronoi diagrams and Delaunay triangulation approaches were originally introduced to study proximity relationship among objects in space. Delaunay triangulation ensures connectivity using approximately 2.6 edges by node, which is a very compact and effective representation to propagate matches globally, whilst K-plet needs at least 4 edges by node without warranty of a connected graph.

In this paper, we represent a fingerprint feature set as a Delaunay triangulation. The Delaunay triangulation of a non-degenerate set of points is unique. One problem is that it is sensitive to noise and distortions (e.g, introduced by missing or spurious minutiae points). However, the insertion of a new point in a Delaunay triangulation affects only the nearby triangles. As a result, noise affects the Delaunay triangulation only locally. This means that correct identification will be possible if some regions of the fingerprint have not been seriously affected. In [12] the robustness of various closest point graphs to corruption was investigated. The conclusion reached was that

the Delaunay graph is the most resistant to disruption, a result of considerable significance to the matching of noised fingerprints.

We store translation and rotation invariant attributes as the minutiae type in the nodes; in the edges, the distance between the connected minutiae (D) and the angles between the minutiae directions and the edge in the clock direction ($\alpha 1$, $\alpha 2$), as shown in the Figure1.
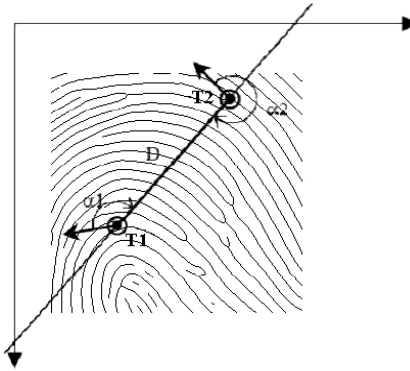
Fig. 1. Minutiae and edge attributes in the graph. T1 and T2 are the types of minutiae; D is the edge length or distance between minutiae and $\alpha 1$, $\alpha 2$ the angles between minutiae directions and the edge in the clock direction.

3   Multiple Substructures Matching: MSM

The heuristic comes from the fact that two fingerprints represented as Delaunay minutiae graphs share common substructures belonging to a set of nodes that remains in both prints with low deformation errors. An example of a common substructure in two fingerprints from the same finger, where the local neighbourhood of two matching nodes looks similar, is shown in the Figure 2.

The method compares each node in the reference graph with each node in the model graph finding a common substructure starting from them simultaneously and propagating the match to other nodes in the neighbourhood eventually.

3.1   Local Substructure Matching (Star Matching)

There are two main processes for the comparison of the local substructures. The first is the measurement of the similarity between the adjacent edges to the central vertex (*Sa*), and the second is the measurement of the similarity between the adjacent vertexes to the central vertex (*Sv*). If both of the previous similarities are greater than zero then they are combined to emit a final similarity score between both stars, giving a predominant weight to the similarity of the adjacent edges, as shown in the following equation (1).

$$St = 0.35 * Sv + 0.65 * Sa \, .\qquad\qquad(1)$$
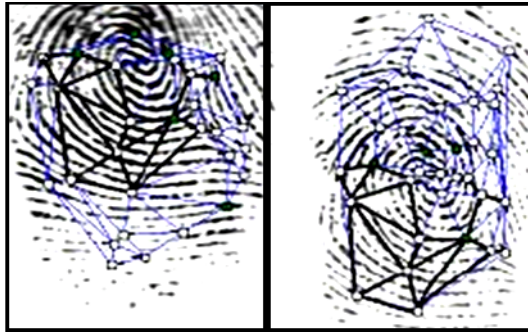
Fig. 2. Example of a common substructure in Delaunay minutiae graphs in two fingerprint images of DB1A FVC2002

3.1.1 Measurement of the Similarity Between the Adjacent Edges to the Central Vertex

A greedy algorithm is used to associate the edges of the first star to the edges of the second local structure. The previously associated edges are marked so they are not associated again in further steps. The similarity of the associated edges are stored and counted. The inferiority in the number of vertexes in the first star is guaranteed by the method. The similarity between two edges is measured as follows.

Two edges ($a1$ and $a2$) are considered similar if the angles $\alpha 1$ and $\alpha 2$ are similar by the formula (**2**) using the difference between angles (*dang1*, *dang2*).

$$dang1 = (\, |a1.\alpha1 - a2.\alpha1| > 180) \; ? \; (360 - |a1.\alpha1 - a2.\alpha1|) : |a1.\alpha1 - a2.\alpha1| \, . \qquad (2)$$
$$dang2 = (\, |a1.\alpha2 - a2.\alpha2| > 180) \; ? \; (360 - |a1.\alpha2 - a2.\alpha2|) : |a1.\alpha2 - a2.\alpha2| \, .$$
$$dang1 < AngleThreshold \, .$$
$$dang2 < AngleThreshold \, .,$$

and the distances (lengths of the edges) are similar by the formula (**3**) using the ratio of length (*Rd*).

$$Rd = |a1.D - a2.D| \, / \, Min(a1.D, a2.D) \, . \qquad (3)$$
$$Rd < DistanceThreshold \, .$$

Finally if the constraints of distance and angles are satisfied the similarity (*s*) of a pair of edges is evaluated as formula 4 shows.

$$s = 1 - Rd \, . \qquad (4)$$

In other cases the similarity is evaluated in zero and it is considered that the edges do not match. Once we have an association of adjacent edges by means of the greedy strategy, the final similarity (*Sa*) is evaluated as appears in the equation bellow (5).

$$Sa = SumEdgesPairSim \, / \, NumEdgesPairs \, . \qquad (5)$$

Where *NumEdgesPairs* is the number of associated adjacent edges and *SumEdgesPairSim* is the sum of the respective similarities.

Our proposal makes a final correction of the similarity score taking into account the type of minutiae in the center of the stars. If there is a coincidence in the minutia

type the final score is increased in a 30% otherwise is decreased in the same percentage.

3.1.2 Measurement of the Similarity Between the Adjacent Vertexes to the Central Vertex

In the star, similarly to the measurement of the matching scores in the adjacent edges, a greedy algorithm is used to associate the vertexes of the first star to the vertexes of the second local structure. The previously associated vertexes are marked so they are not associated again in further steps. The similarity of the associated vertexes are stored and counted. The inferiority in the number of vertexes in the first star is guaranteed by the method. The similarity between two adjacent vertexes is measured as the similarity of its respective adjacent edges using the same procedure defined in section 3.1.1. The final similarity between the adjacent vertexes (*Sv*) is defined as in the equation stated bellow (6).

$$Sv = SumVertexPairSim / MinNumVertexes .\qquad(6)$$

Where *MinNumVertexes* is the number of adjacent vertexes of the first vertex (degree) and *SumVertexPairSim* is the sum of the similarities of the associated vertexes.

3.2 Local Substructure Expansion

Given a vertex pair v1 and v2 not previously marked as belonging to the common substructure, the local star similarity is measured. If they are considered sufficiently similar based on the local similarity, the vertexes are accepted in the common substructure and marked. The expansion is attempted from the first pair of edges (selecting a reference edge adjacent to v1 and comparing to the set of edges adjacent to v2) with similarity greater than zero with the respective adjacent vertexes unmarked. The mentioned adjacent vertexes are then considered as the centers of a new pair of stars for performing a new local matching. If the expansion fails because the new vertexes are not similar enough, then the algorithm will attempt to associate the reference edge in v1 to other consecutive edge in v2 for a possible expansion. The similarities of the pairs of vertexes accepted in the common substructure measured as the star similarities are stored (*sumStarSim*) and counted (*subsSize*). The strategy mentioned is similar to the DFS with the restriction that the traversal is made simultaneously in both graphs and the vertexes are visited only if they have a similar star structure.

The final similarity measure between a common substructure (*Sim*) is evaluated by the expression 10, taking into account a weight in the size of the substructure (*sizeW*) regarding the number of vertexes in the shorter graph (*MinNumVertexes*) as shows the formula 7, and the average of the similarities of its pairs of associated vertexes (*Av*) (8,9).

$$sizeW = subsSize / MinNumVertexes .\qquad(7)$$

If the size of the common substructure is greater than 6 or greater than the 70% of the total of vertexes of the shorter graph then the *Av* is evaluated as follows (8). In other cases formula 9 is used.

$$Av = sumStarSim / subsSize .$$
$$(8)$$

$$Av = sumStarSim / MinNumVertexes .$$
$$(9)$$

$$Sim = sizeW * Av .$$
$$(10)$$

3.3 Global Similarity Consolidation

The human expert performs a first visual comparison of all the minutiae in the reference fingerprint against all minutiae in the query fingerprint taking into account the nearby context. Starting by a pair of minutiae, both neighbourhoods are analyzed looking for matching and expanding the similar area as long as it is possible.

Our proposal reproduces this behavior. The first step is to obtain the graph with the lower number of vertexes (g1) to assume it belongs to the query fingerprint. The bigger graph (g2) represents the reference fingerprint. This is related to the search of a fragment of impression realized by an expert in a stored fingerprint.

The next step is to find the correspondences of vertexes of graph g1 in the set of vertexes of graph g2. Each vertex of g1 is associated with the vertex of graph g2 from which it is obtained the best similarity using a greedy strategy. The previously associated vertexes are marked so they are not used again in the subsequent associations. It is necessary a similarity of the common substructure starting by a pair of vertexes greater than zero to be considered in the association process. The search of the common substructure is made first looking for a local minutia matching (star matching) and finally expanding the common local structure by a minutia in a sequence of local matchings.

It is possible that starting from a pair of common minutiae there is not a connected substructure that contains all the coincidences of both prints even when they belong to the same finger. This is due to the graph deformations produced by missing minutiae or false minutiae occurrence in the feature extraction process, apart from the nonlinear geometric deformations that produce a bound in the possible expansion of the common substructure. This is the reason why, starting by different corresponding minutiae pairs it is possible to find different common substructures. Each of these common substructures contains relevant information for the global similarity of a pair of fingerprints.

There are three cases in the consolidation of the global similarity from the similarities of the multiple common substructures found by each vertex of the reference graph:

1. If the number of vertexes of the reference graph that found a similar substructure is greater than 5 then it is considered that there is a relevant number of representatives and the final similarity is the average of the similarities of the best substructures found by each vertex. This procedure is similar to the expert criterion of the necessity of at least 6 minutiae to emit a relevant similarity score.

2. If the mentioned number is lower than 6 then the ratio regarding the total of vertexes of g1 (the shorter graph) is evaluated. If this ratio is superior to a threshold then the final similarity is the average of the similarities of the best substructures found by each vertex. It is the case when the reference fingerprint is a segment of

impression with a low number of minutiae of which a considerable number reach a local correspondence at least.

3. If the number of associated vertexes is not representative regarding the total of vertexes of the shortest graph, the final global similarity is evaluated in zero.

4   Experimental Results

A series of experiments have been conducted on the test data set of FVC. We use standard indexes of comparison that appear published in the official site for the competition of verification FVC [13] as the EER and FMR. Each FVC databases contains 100 different fingers and 8 impressions for each one yielding a total of 800 fingerprints. For FMR (False Matching Rate) the total number of impostor test is (100*99)/2) = 4950. For FNMR (False Non-matching Rate) the total number of genuine test is (8*7)/2*100 = 2800.

We think it is important to compare our approach with previous methods using local structural similarity. First experiment compares our approach with the algorithm based on graph matching principles presented by Sharat *et al*. at ICB2006 as shown in Table 1.

Table 1. A summary of the comparative results w.r.t. Sharat *et al*. algorithm

Database	Sharat *et al*. Algorithm K-plet		Proposed Approach, MSM	
	EER	FMR100	EER	FMR100
FVC2002 DB1	1.5%	1.65%	0.56%	0.5%

We also compare our algorithm with a minutiae-based matching scheme proposed by Yansong *et al*. at ICPR2006 [14], which introduced a concept of compatibility to the minutiae triangle structures and adopted a relaxation process to adjust the similarity matrix of the minutiae triangle cells between the query and template images. This experiment was performed on the DB1_A of FVC2004. FVC2004 databases are markedly more difficult than FVC2002 and FVC2000 ones, due to the perturbations and geometrical deformations deliberately introduced. Table 2 describes our results compared to Yansong *et al.* algorithm.

Table 2. A summary of the comparative results *w.r.t* Yansong *et al*. algorithm

Database	Yansong *et al*. Algorithm	Proposed Approach, MSM
	EER	EER
FVC2004 DB1	9.4%	8.09%

We compare our approach with a minutiae based fingerprint verification algorithm using Delaunay triangulation presented by Deng and Huo [3], at the AVBPA 2005. This algorithm tries to find the best-matching edge pairs in the local structure instead of finding best-matching minutiae pairs. The global matching score between two fingerprints is calculated by using an aligned-edge-guided triangle procedure. Table 3 describes our results compared to Deng and Huo algorithm.

Table 3. A summary of the comparative results *w.r.t* Deng and Huo algorithm

Database	Deng and Huo AVBPA2005	Proposed Approach, MSM
	EER	EER
FVC2002 DB1	1.82%	0.56%
FVC2002 DB2	1.52%	0.71%

5   Conclusions and Future Work

In this paper, we apply a heuristic method to obtain a similarity measure between two fingerprints represented as attributed Delaunay graphs based on the comparison of multiple common substructures. This algorithm is simple, fast and does not need an explicit alignment between both fingerprints. We obtain a better global similarity measure taking into account the similarities of several common substructures representing correspondences of different areas of the impressions with low distortion errors. Another contribution is that we guarantee a connected graph in order to allow a total global substructure expansion unlike K-plet representation of Sharat *et al*. Also, the space complexity of DFS traversal is much lower than BFS (breadth-first search). It also lends itself much better to heuristic methods of choosing a likely-looking branch as in our case of study.

We compared our method with several algorithms recently published and we obtain better results without many efforts tuning the thresholds. Especially, using FVC2002 DB1 database we reach an EER of 0.56% and FMR100 of 0.5%. We do not tackle the particular problem of correcting the relevant non-linear deformations as included in FVC2004 databases in this contribution. However in a preliminary experiment with FVC2004 DB1A we obtain a better EER index compared with the Yansong *et al* proposal. Nevertheless, we notice that no linear deformation of fingerprint is an important issue to deal with. Also, we want to develop an automatic methodology to learn the thresholds.

References

1. Federal Bureau of Investigation: The Science of Fingerprints: Classification and Uses. Washington, D.C.: U.S. Government Printing Office (1984)
2. Kovacs-Vajna, Z.M.: A fingerprint verification system based on triangular matching and dynamic time warping. IEEE Trans. PAMI 22(11), 1266–1276 (2000)
3. Deng, H., Huo, O.: Minutiae Matching Based Fingerprint Verification Using Delaunay Triangulation and Aligned- Edge-Guided Triangle Matching. In: Kanade, T., Jain, A., Ratha, N.K. (eds.) AVBPA 2005. LNCS, vol. 3546, pp. 270–278. Springer, Heidelberg (2005)
4. Jiang, X., Yau, W.Y.: Fingerprint minutiae matching based on the local and global structures. In: Proc. Internat. Conf. on Pattern Recognition, pp. 1038–1104 (2000)
5. Isenor, D.K., Zaky, S.G.: Fingerprint Identification Using Graph Matching. Pattern Recognition 19(2), 113–122 (1986)
6. Chikkerur, S., Govindaraju, V.: K-plet and CBFS: A graph based fingerprint represent- tation and matching algorithm. In: International Conference on Biometrics (2006)

7. Ratha, N., Bolle, R., Pandit, V., Vaish, V.: Robust fingerprint authentication using local structural similarity. In: 15th IEEE Workshop on Applications of Computer Vision, pp. 29–34 (2000)
8. Bebis, G., Deaconu, T., Georgiopoulos, M.: Fingerprint identification using Delaunay triangulation. In: Int. Conf. on Information Intelligence and Systems, pp. 452–459 (1999)
9. Parziale, G., Niel, A.: A Fingerprint Matching Using Minutiae Triangulation. In: Zhang, D., Jain, A.K. (eds.) ICBA 2004. LNCS, vol. 3072, pp. 241–248. Springer, Heidelberg (2004)
10. Guibas, L., Stolfi, J.: Primitives for the Manipulation of General Subdivisions and the Computation of Voronoi Diagrams. ACT TOG 4(2) (1985)
11. Sloan, S.W., Houlsby, G.T.: An Implementation of Watson's Algorithm for Computing 2-D Delaunay Triangulations. Advanced Engineering Software 6(4) (1984)
12. Tuceryan, M., Chorzempa, T.: Relative Sensitivity of a Family of Closest-Point Graphs in Computer Vision Applications. Pattern Recognition 24(5), 361–373 (1991)
13. FVC2004. Fingerprint Verification Competition, url: http://bias.csr.unibo.it/fvc2004/
14. Feng, Y., Feng, J., Chen, X., Song, Z.: A novel fingerprint matching scheme based on local structure compatibility. In: Int. Conf. on Pattern Recognition (2006)

Bayesian Edge Regularization in Range Image Segmentation

Smaine Mazouzi[1] and Mohamed Batouche[2]

[1] LERI-CReSTIC, Université de Reims, B.P. 1035, 51687, Reims, France
mazouzi@leri.univ-reims.fr
[2] Département d'informatique, Université de Constantine, 25000, Algérie
batouche@wissal.dz

Abstract. We present in this paper a new method for improving range image segmentation, based on Bayesian regularization of edges produced by an initial segmentation. The method proceeds in two stages. First, an initial segmentation is produced by a randomized region growing technique. The produced segmentation is considered as a degraded version of the ideal segmentation, which should be then refined. In the second stage, image pixels not labeled in the first stage are assigned to the resulting regions by using a Bayesian estimation based on some prior assumptions on the region boundaries. The image priors are modeled by a new Markov Random Field (MRF) model. Contrary to most of the authors in range image segmentation, who use surface smoothness MRF models, our MRF model is based on the smoothness of region boundaries, used to improve the initial segmentation by a Bayesian regularization of the resulting edges. Tests performed with real images from the ABW database show a good potential of the proposed method for significantly improving the segmentation results.

Keywords: Image Segmentation, Range Image, Randomized Region Growing, Bayesian Estimation, Markov Random Field.

1 Introduction

Segmenting an image consists in assigning its pixels in homogenous, continuous, and disjoint sets, called image regions. Image segmentation is often essential for high level image analysis and understanding. In an image, a region is defined as the set of contiguous pixels that share a common propriety, called the region homogeneity criterion. In range images, segmentation methods can be divided in two distinct categories: edge-based segmentation methods and region-based segmentation methods. In the first category, pixels which correspond to discontinuities in depth or in surface normals are selected and chained in order to delimit the regions in the image [5,11]. Edge-based methods are well known for their low computational cost; however they are very sensitive to noise. Region-based methods use geometrical surface proprieties to gather pixels with the same properties in disjoint regions [4,1]. Compared to edge-based methods, they are more stable and less sensitive to noise. However, their efficiency depends strongly on the selection of the region seeds.

Few authors have integrated Bayesian inference in range image segmentation. Jain and Nadabar [9] have proposed a Bayesian method for edge detection in range images. Authors use the Line Process (LP) Markov Random Field (MRF) model [7] to label image pixels as EDGE or NON-EDGE pixels. Wang and Wang [15] have presented a hybrid scheme for range image segmentation. First, they proposed a joint Bayesian estimation of both pixel labels, and surface patches. Next, the solution is improved by combining the Scan Line algorithm [11], and the Multi-Level Logistic (MLL) MRF model [14]. In spite of various contributions of the works previously cited, some aspects inherent to range image segmentation were omitted. Indeed, most of the works use markovian models that are based exclusively on the surface smoothness prior. Moreover, the proposed methods proceed by assigning pixels to clusters without ensuring the continuity of the resulting clusters. Typically, in the approach proposed by Wang and Wang [15], pixels belonging to coplanar regions may be labeled equally in any of these regions. The spatial continuity constraint of resulting regions seems that it was not taken into account.

The approach proposed in this paper provides first an initial segmentation version, using an improved region growing technique, and then refines this version by a Bayesian-MRF labeling. The refinement of the initial segmentation consists in a Bayesian regularization of unlabeled pixels. The latter are mostly close to region boundaries. A new Markov random field model is used to model the prior information on region boundaries, assuming that edges in range images are piecewise smooth. The new MRF model uses a high-order neighborhood system, and is based on the assumption that edge pixels are situated on straight lines that represent region boundaries. The use of the ICM algorithm (Iterated Conditional Modes) [3] to search for the optimal solution has allowed us to formulate region continuity by defining a constraint on the possible labels of a given pixel. The experimentations performed with real images from the ABW database [8] show a good potential of the proposed method to improve results in range image segmentation.

The remainder of the paper is organized as follows: In Section 2, we introduce the image segmentation by randomized region growing. Section 3 is devoted to the proposed Bayesian approach for segmentation refinement. We present in this section the new Markov Random Field (MRF) model, as well as the adaptation of the ICM algorithm for the search of the optimal solution. Experimentations are shown in Section 4, in which we present respectively the evaluation framework, parameter selection, and some experimental results. Finally, a conclusion summarizes our contribution.

2   Segmentation by Randomized Region Seed Sampling

A range image is a discretized two-dimensional array where at each pixel (x, y) is recorded the distance $d(x, y)$ between the range finder plane and the corresponding point of the scene. In order to define a homogeneity criterium allowing region growing, we use a new representation (d^*) of the row image, where $d^*(x, y)$

represents the tangent plane to the surface at (x, y). The tangent plane at (x, y) is obtained by the multiple regression method using the set of neighboring pixels situated within a 3×3 window centred at (x, y), and whose depths are close, according to a given threshold (Tr_h). The plane equation in a $3 - D$ coordinate system may be expressed as follows:

$$z = ax + by + c \tag{1}$$

where $(a, b, -1)^T$ is a normal vector to the plane, and $|c|/\sqrt{a^2 + b^2 + 1}$ is the orthogonal distance between the plane and the coordinate origin. We consider that a pixel belongs to a planar region, given its plane equation, if the distance between the respective planes is less than (Tr_h), and the angle between the respective normals is less than Tr_θ, where Tr_h and Tr_θ are respectively the distance and the angle thresholds. The quality of plane estimation $q(x, y)$ at (x, y) according to the regression model is also computed. The latter is used to select the best region seeds in the region growing algorithm.

Inspired from the RANSAC algorithm [6], our region growing technique is based on random sampling of the region seeds. A generated seed is accepted if only the surface estimation quality q at this seed is greater than a given threshold Q. For every accepted seed, a region growing is performed by recursively including homogenous pixels situated on the borders the region in growth. A given seed centred at (x_t, y_t) is formed by the pixels in a $W \times W$ window, belonging to the same plane. The seed quality is represented by the minimum of estimation qualities of pixels that form the seed. Selection-growing process is repeated until no new region can be created. The randomized growing algorithm is described as follows:

```
t=0
Repeat
   Generate a random position (xt,yt)
   If seed quality q>Q then
      Perform a region growing starting from (xt,yt)
   EndIf
   t=t+1
Until none new region was generated since t-DT;  DT>>1
```

Random sampling of region seeds permits to select the best seeds. These latter are characterized by a good quality. It allows to include in a given region the largest possible set of homogenous pixels. Indeed, several seeds within the same region can be generated; however none of these seeds is accepted. The first generated seed for which the quality q is greater than Q will be accepted and considered for region growing.

For each generated region R_l, the residual variance σ_l^2 is calculated as follows:

$$\sigma_l^2 = \sum_{(x,y) \in R} (a_l x + b_l y + c_l - d(x, y))^2 \tag{2}$$

where (a_l, b_l, c_l) are the plane parameters of the region R_l.

3   Edge Regularization as Bayesian Estimation

3.1   Bayesian-MRF Pixel Labeling

We have used the piecewise smoothness of region boundaries as prior to model distributions of pixel labels (MRF) in range images. Let S denote the image lattice. At each site $(x, y) \in S$, $d(x, y)$ is the depth at the site, and $d^*(x, y)$ represents the corresponding tangent plane equation parameters: $d^*(x, y) = (a_{x,y}, b_{x,y}, c_{x,y})$. Let M be the number of regions in the image. So, each site (x, y) can take a label $f_{x,y}$ from the set of labels $L = \{l_1, \ldots, l_M\}$. The labeling set $F = \{f_{x,y}, (x, y) \in S, f_{x,y} \in L\}$, represents a segmentation of the image. If we assume that F is markovian, segmenting S according to the Bayesian-MRF framework [14] can be done by calculating the maximum a posteriori (MAP) of the distribution of the set F: $P(F/d)$, by considering F as a Markov Random Field (MRF).

According to Bayes' rule, the maximum a posteriori $P(F/d)$ is expressed as follows:

$$P(F/d) = \frac{p(d/F)P(F)}{p(d)} \tag{3}$$

$P(F) = Z^{-1}e^{-U(F)}$ is the a priori probability of F obtained according to the Markov-Gibbs equivalence theorem [2].
$Z = \sum_F e^{-U(F)}$ is a normalization constant called the partition function. The a priori energy $U(F)$ is a sum of clique potentials $V_c(F)$ over the set of all possible cliques C: $U(F) = \sum_{c \in C} V_c(F)$.

In order to model the edge smoothness we use cliques formed by 9 sites located in a 3×3 window. Let c_9 be a clique of 3×3 sites centred at (x, y), and let ζ ($\zeta < 0$) a potential parameter. Considering possible configurations in Fig. 1, the potential V_c of cliques in C can be expressed as follows:

$$V_c(c_9(x, y)) = \begin{cases} \zeta \text{ if } \exists(x', y'), (x'', y'') \mid f_{x,y} = f_{x',y'} = f_{x'',y''} \\ \text{and } \phi((x', y'), (x, y), (x'', y'')) = \pi \\ \\ 0 \text{ if } \exists(x', y'), (x'', y'') \mid f_{x,y} = f_{x',y'} = f_{x'',y''} \\ \text{and } \phi((x', y'), (x, y), (x'', y'')) = 2\pi/3 \\ \\ -\zeta \text{ otherwise} \end{cases} \tag{4}$$

where $\phi((x', y'), (x, y), (x'', y''))$ is the angle between the two vectors $(x' - x, y' - y)^T$ and $(x'' - x, y'' - y)^T$.

Configurations used to define V_c depend on the surface type. For images containing polyhedral objects, considered in this work, V_c is defined on the basis that the boundary between two adjacent regions is formed by pixels belonging to the same straight line (Fig. 1). So, configurations which correspond to locally unsmoothed edges are penalized by using a positive clique potential $(-\zeta)$.

The likelihood distribution $p(d/F)$, is obtained by assuming that the observations d are degraded by an independent Gaussian noise: $d(x, y) = a_{f} \, x +$

b_f , $y + c_f$, $+ e(x, y)$, with $e(x, y) \sim N(0, \sigma_f^2$, $)$. So, the likelihood distribution is expressed as follows:

$$p(d/F) = \frac{1}{\prod_{(x,y) \in S} \sqrt{2\pi\sigma_f^2} ,} e^{-U(d/F)} \qquad (5)$$

with the likelihood energy $U(d/F)$ defined by:

$$U(d/F) = \sum_{(x,y) \in S} (a_f , x + b_f , y + c_f , - d(x, y))^2 / 2\sigma_f^2 , \qquad (6)$$

Since $p(d)$ is constant for a fixed d, the solution F^* is obtained by maximizing the a posteriori probability $P(F/d) \propto p(d/F)P(F)$, which is equivalent to minimizing the a posteriori energy $U(F/d) = U(d/F) + U(F)$: $F^* = argmin\{U(d/F) + U(F)\}$.
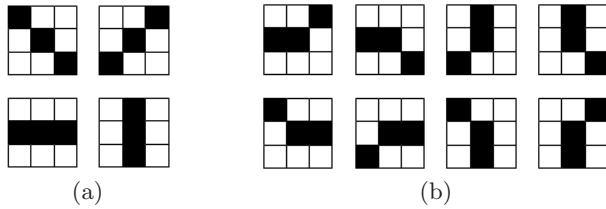
Fig. 1. Clique potential $V_c(c_9)$ defined according to the edge smoothness prior. (a) Full locally smooth edge : $V_c(c_9) = \zeta$; (b) Partial locally smooth edge : $V_c(c_9) = 0$; Otherwise, the edge is not locally smooth : $V_c(c_9) = -\zeta$.

3.2 Searching for the Optimal Solution

By assuming that F is markovian, and the observations $\{d(x, y); (x, y) \in S\}$ are conditionally independent, we have used the ICM algorithm [3] to minimize the a posteriori energy $U(F/d)$. By considering $U(F/d)$ as a sum of energies over all image sites: $U(F/d) = \sum_{(x,y) \in S} U(f_{x,y}/d(x, y))$, we can separate it in two terms:

$$U(F/d) = \sum_{(x,y) \in S'} U(f_{x,y}/d(x, y)) + \sum_{(x,y) \in S-S'} U(f_{x,y}/d(x, y)) \qquad (7)$$

where S' is the set of sites which have not been labeled in the first stage (by region growing): $S' = \{(x, y) \in S \mid f_{x,y} \text{ is undefined }\}$. Assuming the correctness of the labeling of the set $S - S'$ (performed in the first stage), the term $\sum_{(x,y) \in S-S'} U(f_{x,y}/d(x, y))$ is thus constant. Minimizing the energy $U(F/d)$ is equivalent to minimizing the energy $U'(F/d)$ which corresponds to the sites in S':

$$U'(F/d) = \sum_{(x,y) \in S'} U(f_{x,y}/d(x, y)) \qquad (8)$$

The assumption of the correctness of the labeling of $S - S'$ allows also to define a constraint on the set of possible values that a site in S' can have during the execution of the ICM algorithm. Indeed, the label $f_{x,y}^k$ at the iteration k, of a site (x,y) is chosen among the set $L'(x,y) \subset L$ containing the labels of the sites labeled in the first stage, and located in a $W \times W$ window centred at (x,y). Formally, $L'(x,y)$ is defined as follows:

$$L'(x,y) = \{l | \exists (x',y') \in S - S', (x' - x, y' - y) \in [-W/2, W/2]^2 \wedge f_{x',y'} = l\} \ (9)$$

The previous heuristics allow to speed up the calculation of the minimum of the a posteriori energy $U'(F/d)$. They allow also to satisfy the region continuity constraint. For the latter problem, if we assume that the horizontal distance between two coplanar regions R_1 and R_2 is greater than W, labels l_{R_1} and l_{R_2} corresponding respectively to R_1 and R_2, cannot belong to the same set $L'(x,y)$. For example, if the site (x,y) belongs to R_1, it can not be labeled l_{R_2}, although energies $U'(l_{R_1}/d(x,y))$ and $U'(l_{R_2}/d(x,y))$ are equal.

4   Experimentation

Hoover et al. have proposed a dedicated framework for the evaluation of range image segmentation algorithms [8], which has been used in several related works [11,13,4,1]. The framework consists of a set of real range images, and a set of objective performance metrics. It allows to compare a machine-generated segmentation (MS) with a manually-generated segmentation, supposed ideal and representing the ground truth (GT). Instances of region detection are classified into Correct detection, over-segmentation (one region broken is several small regions) , under-segmentation (several regions merged in one large region), missed region and noise region. Region classification is performed according to a compare tool tolerance T; $50\% < T \leq 100\%$ which reflects the strictness of the classification. The 40 real images of ABW set are divided into two subsets: 10 training images, and 30 test images. In this study, four methods, namely USF, WSU, UB and UE, cited in [8] are involved in the result comparison.

4.1   Parameter Selection

Since the evaluation framework provides a set of training images with ground truth segmentation (GT), we have opted to a supervised approach for the estimation of parameters.

For the proposed method, named EBR for Edge Bayesian Regularization, five parameters should be fixed: Tr_θ , Tr_h, W, Q, and ζ . The performance criterion used in parameter selection is the average number of correctly detected regions with the compare tool tolerance T set to 80%. The parameters are divided into two subsets: 1) Tr_θ , Tr_h, W and Q which represent respectively the angle threshold, the depth threshold, the window size, and the seed quality threshold. These parameters are used by the randomized region growing algorithm. 2) The potential parameter ζ, used during the segmentation refinement. For the first

parameter subset, 256 combinations namely $(Tr_\theta, Tr_h, W, Q) \in \{15, 18, 21, 24\} \times \{12, 16, 20, 24\} \times \{5, 7, 9, 11\} \times \{0.90, 0.95, 0.97, 0.99\}$, were run on the training images. Resulting optimal values of the parameters are as follows: $Tr_\theta = 21°$, $Tr_h = 16$, $W = 7$ and $Q = 0.97$. The selected value of W permits to estimate the plane equation by considering a wide neighborhood (W^2 pixels), whereas Q ensure that the plane parameters are reliable, and the window $W \times W$ is not located between two different regions.

We have used the Coding method [2] to estimate the parameter ζ. For each image in the training set, a pair of values of these parameters is calculated. One value of this parameter is calculated for each image in the training set. The average is then computed and used as the final parameter value. The optimal value for each training image is calculated by the simulated annealing algorithm [12], using a Gibbs sampler [7]. The average value of ζ obtained with the training set is -0.587×10^{-4}.

4.2   Experimental Results

Region growing by randomized region seed sampling has provided better results, compared to deterministic region growing (Fig. 2b,c). However, the resulting segmentation often remains unsatisfactory. In Fig. 2c, we can note that most of the unlabeled pixels are situated on the region boundaries. Fig. 2d show the result obtained after edge regularization. Many pixels of boundaries were assigned to certain regions so that resulting edges are more locally smooth.

(a)   (b)   (c)   (d)
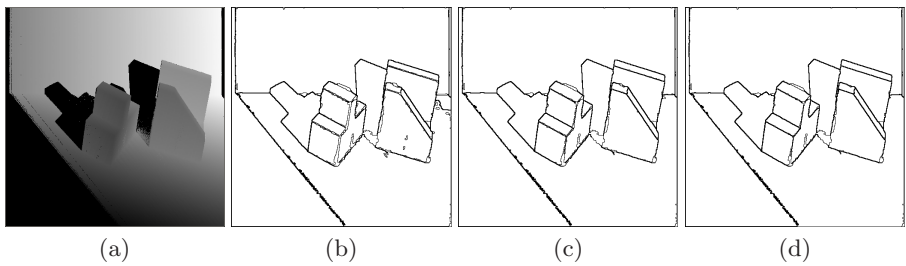
Fig. 2. Result comparison with abw.test.6 image. (a) Range image; (b) Segmentation result by deterministic region growing; (c) Segmentation result by randomized region growing; (d) Segmentation result after edge regularization.

Fig. 3 illustrate the impact of the Bayesian edge regularization on the segmentation results, with all the test images. The two graphs show that segmentation results are significantly improved for the high values of the compare tool tolerance T. Indeed, the edge regularization in range images allows to improve segmentation accuracy, by optimal labeling of pixels close to region boundaries. It was reported that segmentation methods provide better results when they pay particular attention to process region boundaries [8,10].
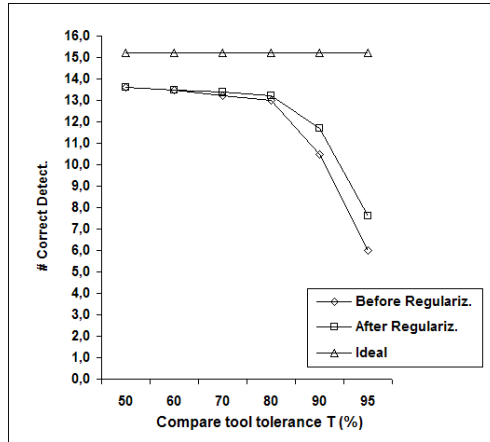
Fig. 3. Comparison of average results before and after edge regularization of the test images, according to T ; $0.5 < T \leq 1.0$

(a)   (b)   (c)
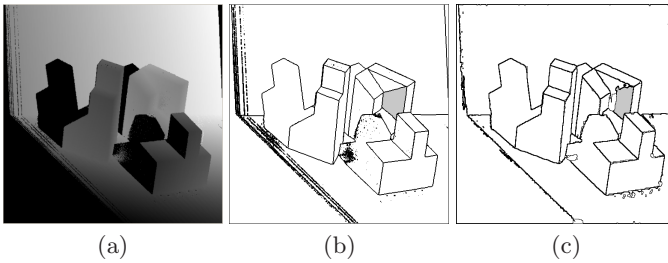
Fig. 4. Segmentation result of abw.test.8 image. (a) Range image; (b) Ground truth segmentation; (c) Segmentation result after edge regularization.

Fig. 4 shows the segmentation result of the image abw.test.8, with the compare tool tolerance T set to 80%. This image was considered as a typical image to compare the involved methods [8,4]. Fig. 4a shows the range image; Fig. 4b shows the ground truth segmentation, whereas 4c represents the segmentation result obtained by our method. Metrics in Table 1 show that all image regions detected by the best-referenced segmenter (UE) were detected by our method. The shadowed region has not been detected by any segmenter, due to high distortions in this region. The incorrectly detected regions are those with small sizes and situated on the horizontal support. Compared to the other methods, values of incorrect detection metrics are also good. Our method is equivalent to UE and scored higher than the others.

Fig. 5 shows the average numbers of correctly detected regions for all test images and according to the compare tool tolerance T; $T \in \{51, 60, 70, 80, 90, 95\%\}$. Results show that the number of correctly detected regions by our method is equivalent to UE and better than those of USF, UB, and WSU. For instance,

Table 1. Comparison results with abw.test.8 image for $T=80\%$

Method	GT	Correct region detection	Over- segmentation	Under- segmentation	Missed	Noise
USF	21	17	0	0	4	3
WSU	21	12	1	1	6	4
UB	21	16	2	0	3	6
UE	21	18	1	0	2	2
EBR	21	18	2	0	1	1
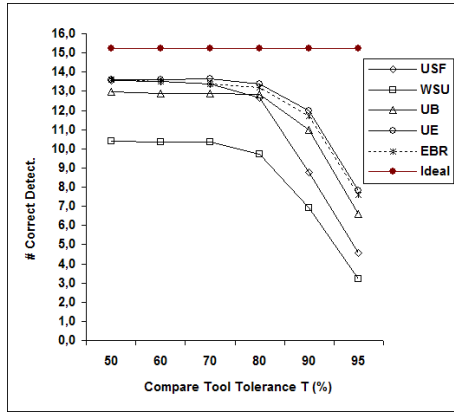
Fig. 5. Average results of correctly detected regions of all methods, according to the compare tool tolerance T ; $0.5 < T \leq 1.0$

our system scored higher than WSU and UB for all the values of the compare tool tolerance T. It scored higher than USF for $T \geq 60\%$. For all incorrect detection metrics (Over-segmentation, Under-segmentation, Missed, Noise), our method has equivalent scores to those of UE and USF. The two latter scored higher than UB and WSU.

5   Conclusion

We have presented in this paper a new Bayesian method for range image segmentation. The refinement of the initial segmentation using the Bayesian-MRF framework has allowed improving significantly the segmentation results. We have presented a new MRF model which allows to model the edge smoothness, considered as the prior assumption on region boundaries in range images. Several tests were performed on real images from the ABW database. The average run time is 8 sec., on a Compaq PC n×8220. The recorded run times were better than those provided by region based methods, and equivalent to edge-based ones. For instance, the average run time for UE algorithm was 6.3 min. Obtained results show the great potential of the proposed method for providing efficient and

accurate range image segmentation. The proposed method scored equivalent results to those of UE algorithm, however, computing time in our case was highly improved.

References

1. Bab Hadiashar, A., Gheissari, N.: Range image segmentation using surface selection criterion. IEEE Transactions on Image Processing 15(7), 2006–2018 (2006)
2. Besag, J.E.: Spatial interaction and statistical analysis of lattice systems. Journal of the Royal Statistical Society, Series B 36, 192–236 (1974)
3. Besag, J.E.: On the statistical analysis of dirty pictures. Journal of the Royal Statistical Society, Series B 48, 259–302 (1986)
4. Ding, Y., Ping, X., Hu, M., Wang, D.: Range image segmentation based on randomized hough transform. Pattern Recognition Letters 26(13), 2033–2041 (2005)
5. Fan, T.J., Medioni, G.G., Nevatia, R.: Segmented description of 3-D surfaces. IEEE Journal of Robotics and Automation 3(6), 527–538 (1987)
6. Fischler, M.A., Bolles, R.C.: Random sample consensus: a paradigm for model fitting with applications to image analysis and automated cartography. Readings in computer vision: issues, problems, and paradigms, pp. 726–740 (1987)
7. Geman, S., Geman, D.: Stochastic relaxation, Gibbs distributions, and the Bayesian restoration of images. IEEE Transactions on Pattern Analysis and Machine Intelligence 6(6), 721–741 (1984)
8. Hoover, A., Jean-Baptiste, G., Jiang, X., Flynn, P.J., Bunke, H., Goldgof, D.B., Bowyer, K.W., Eggert, D.W., Fitzgibbon, A.W., Fisher, R.B.: An experimental comparison of range image segmentation algorithms. IEEE Transactions on Pattern Analysis and Machine Intelligence 18(7), 673–689 (1996)
9. Jain, A.K., Nadabar, S.G.: MRF model-based segmentation of range images. In: International Conference on Computer Vision, pp. 667–671, Osaka (1990)
10. Jiang, X., Bowyer, K.W., Morioka, Y., Hiura, S., Sato, K., Inokuchi, S., Bock, M., Guerra, C., Loke, R.E., Hans du Buf, J.M.: Some further results of experimental comparison of range image segmentation algorithms. In: International Conference on Pattern Recognition, vol. 4, pp. 4877–4882 (2000)
11. Jiang, X., Bunke, H.: Edge detection in range images based on Scan Line approximation. Computer Vision and Image Understanding 73(2), 183–199 (1999)
12. Kirkpatrick, S., Gelatt, C.D., Vecchi, M.P.: Optimization by simulated annealing. Readings in Computer Vision: Issues, Problems, Principles, and Paradigms, pp. 606–615 (1987)
13. Li, S., Zhao, D.: Gradient-based polyhedral segmentation for range images. Pattern Recognition Letters 24(12), 2069–2077 (2003)
14. Li, S.Z.: Markov random field modeling in image analysis. Springer-Verlag, New York, Inc. Secaucus, NJ, USA (2001)
15. Wang, X., Wang, H.: Markov random field modeled range image segmentation. Pattern Recognition Letters 25(3), 367–375 (2004)

Image Segmentation Using Automatic Seeded Region Growing and Instance-Based Learning

Octavio Gómez, Jesús A. González, and Eduardo F. Morales

National Institute of Astrophisics, Optics and Electronics
Computer Science Department,
Luis Enrique Erro Num 1, Puebla, México
{gomezo,jagonzalez,emorales}@ccc.inaoep.mx
http://ccc.inaoep.mx

Abstract. Segmentation through seeded region growing is widely used because it is fast, robust and free of tuning parameters. However, the seeded region growing algorithm requires an automatic seed generator, and has problems to label unconnected pixels (the unconnected pixel problem). This paper introduces a new automatic seeded region growing algorithm called ASRG-IB1 that performs the segmentation of color (RGB) and multispectral images. The seeds are automatically generated via histogram analysis; the histogram of each band is analyzed to obtain intervals of representative pixel values. An image pixel is considered a seed if its gray values for each band fall in some representative interval. After that, our new seeded region growing algorithm is applied to segment the image. This algorithm uses instance-based learning as distance criteria. Finally, according to the user needs, the regions are merged using ownership tables. The algorithm was tested on several leukemia medical images showing good results.

Keywords: Image Segmentation, Seeded Region Growing, Instance-based learning, Color image, Multispectral image.

1   Introduction

The image segmentation process consists in grouping parts of an image into units that are homogeneous with respect to one or more characteristics [2]. Image segmentation can also be viewed as a process of pixel classification in the sense that all pixels that belong to the same region are assigned the same label [6]. Automatic image segmentation is a fundamental step in many image processing applications such as automatic object recognition, because it allows to separate areas of interest of an image and, consequently, reduce the processing effort.

There exist five main approaches to perform image segmentation: thresholding techniques [12], boundary-based methods [9], region-based methods [11] clustering-based techniques [8], and hybrid techniques [4]. A good review of these approaches can be found in [3]. Despite the numerous segmentation algorithms that have been proposed in the literature, image segmentation is still subject of

research, and is not possible to state that the segmentation problem has been solved because of the diversity of applications [17].

Seeded region growing (SRG) is a hybrid method proposed by R. Adams and L. Bischof [1]. This method starts with a set of n initial seeds $A_1, A_2, \ldots, A_n$, and, at each steep, it grows the seeds A_i by merging a pixel x with its nearest neighboring seed region A_i. This algorithm is fast, robust, and free of tuning parameters [6], nevertheless, the algorithm does not automatically generate seeds, and also has problems to label unconnected pixels [6] (the unconnected pixel problem). To deal with the first problem, F. Shih and S. Cheng [14] proposed an automatic seeded region growing algorithm for color image segmentation. The algorithm transforms the input RGB image into a YC_bC_r color space, and selects the initial seeds considering a $3X3$ neighborhood and the standard deviation of the Y, C_b, and C_r components. Afterwards, the seeds are grown to segment the image. Finally, region merging is used to merge similar or small regions. In [6] three methods to automatically generate seeds are proposed. The first one partitions the image into a set of rectangular regions with fixed size and selects the centers of these rectangular regions as the seeds. The second method finds the edges of the image and obtains the initial seeds from the centroid of the color edges. Finally, the third method extends the second method to deal with noise applying an image smoothing filter. A. Tremeau and N. Borel [16] present a color segmentation algorithm that combines region growing with region merging. The algorithm starts with the region growing process taking into account color similarity and spatial proximity, afterwards, the resulting regions are merged on the basis of a criterion that only takes into account color similarity.

This paper introduces a new automatic seeded region growing algorithm called ASRG-IB1 (Automatic Seeded Region Growing - Instance-based Learning) that performs the segmentation of color (RGB) and multispectral images. First, homogeneous seeds are automatically obtained via histogram analysis. The histogram of each band is analyzed to obtain a set of representative pixel values, and the seeds are generated with all the image pixels with representative gray values (section 4.1). Second, a modified seeded region growing algorithm is applied to perform the segmentation. This algorithm makes use of instance-based learning as similarity criteria. Finally, according to user needs, the regions are merged using ownership tables.

This paper is organized as follows. Section 2 gives an overview of the original seeded region growing algorithm and Section 3 gives an overview of instance based learning. In Section 4 our proposed algorithm is described. In Section 5 the experimental results are presented and in Section 6 we present the main conclusions of this work.

2   Seeded Region Growing

To begin, the seeded region growing algorithm needs n seeds $A_1, A_2, \ldots, A_n$. The decision of what is a feature of interest is embedded in the choice of seeds [1].

Let T be the set of all unallocated (non labeled) pixels that border at least one A_i region after m iterations:

$$T = \left\{ x \notin \bigcup_{i=1}^{n} A_i | N(x) \cap \bigcup_{i=1}^{n} A_i \neq \oslash \right\}$$

where $N(x)$ is the second-order neighborhood (8-neighbors) of pixel x. If we have that $N(x)$ intersects only one labeled region A_i, then, we define the label $i(x) \in \{1, 2, \ldots, n\}$ to be an index such that:

$$N(x) \cap A_{i(x)} \neq \oslash$$

If we have that $N(x)$ meets two or more regions A_i then we define $\delta(x, A_i)$ to be a measure of how different is x from the region A_i that $N(x)$ intersects:

$$\delta(x, A_i) = |g(x) - mean_{y \in A_{(\ )}}[g(y)]|$$

were $g(x)$ is the gray value of pixel x. The value of $i(x)$ will be the value of i such that $N(x)$ meets A_i and $\delta(x)$ is minimized:

$$i(x) = \{i | N(x) \cap A_i \neq \oslash \wedge \delta(x)\ is\ the\ minimum\}$$

3   Instance-Based Learning

3.1   Learning Task and Framework

Instance-based learning algorithms are derived from the nearest neighbor pattern classifier. This kind of algorithms stores and uses only selected instances to generate classification predictions by means of a distance function. The learning task of these algorithms is supervised learning from examples.

Each instance is represented by a set of attribute-value pairs, and all instances are described by the same set of n attributes. This set of n attributes defines an n-dimensional instance space. One of the attributes must be the category attribute and the other attributes are predictor attributes.

The primary output of an Instance-based learning algorithm is a function that maps instances to categories called concept description; this concept description includes a set of stored instances and, possibly, information about the classifiers past performance. The set of stored instances can be modified after each training instance is processed. All Instance-based learning algorithms are described by the following three characteristics:

1. *Similarity function:* computes the similarity between a training instance i and the instances stored in the concept description. The similarities are numerical-valued.
2. *Classification function:* This function receives the results of the similarity function and the performance records stored in the concept description. It yields to a classification for the training instance i.

3. *Concept description updater:* Keeps the records of classification performance and decides the instances to be included in the concept description. It yields to a modified concept description.

Similarity and classification functions determine how the instances stored in the concept description are used to predict the category of the training instance i.

3.2   IB-1 Algorithm

IB-1 is the simplest Instance-based learning algorithm. The distance function that it uses is:

$$Distance(x, y) = \sqrt{\sum_{i=1}^{n} f(x_i - y_i)^2}$$

where x is a test instance, y is a trainig instance and x_i is the value of the $i - th$ attribute of instance x. The instances are described by n features. The IB-1 algorithm is presented in Table 1.

Table 1. IB-1 Algorithm (CD = Concept Description)

$CD \leftarrow \oslash$
For each $x \in$ Training set **do**
  1. **For each** $y \in CD$ **do**
    $Dist[y] \leftarrow Distance(x, y)$
  2. $Mdist\leftarrow$ the $y \in CD$ with minimum $Dist[y]$
  3. $class(x) = Mdist$
  4. $CD \leftarrow CD \cup x$

To label an instance, the IB-1 algorithm computes the distance between the test instance and the instances stored in the concept decription, and stores the nearest instance. The class of the test instance will be the class of the nearest instance.

4   ASRG-IB1 Segmentation Algorithm

4.1   Automatic Seed Generation

An overwiew of the automatic seed generation algorithm is shown in Fig. 1.

The first step divides the histogram in subintervals. Let $h_b(p)$ be the histogram function, this function receives a gray value p ($0 \leq p \leq 255$) and returns the number of pixels of band b with gray value equal to p. To divide the histogram we must find the *cut points*. All the gray values p that satisfy the next two conditions will be taken as cut points:

1. $h_b(p - 1) \geq h_b(p)$
2. $h_b(p + 1) > h_b(p)$
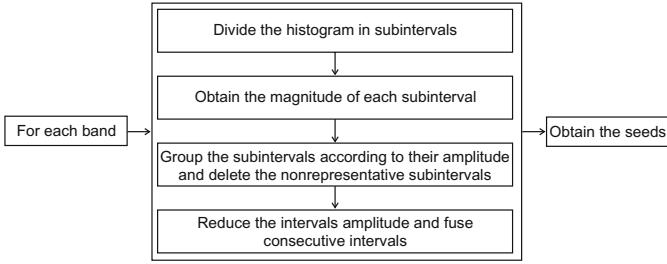
Fig. 1. Overwiew of the automatic seed generation algorithm

Table 2. Subintervals S_j obtained from a given histogram function $h_b(p)$ with q cut points

$S_1 = [0, C_1]$
$S_2 = [C_1 + 1, C_2]$
$S_3 = [C_2 + 1, C_3]$
$\ldots$
$S_m = [C_q, 255]$

The cut points indicate the end and the beginning of each subinterval. Table 2 shows the subintervals S_j obtained from a given histogram function $h_b(p)$ with q cut points, where C_i is a cut point $(1 \leq i \leq q)$, S_j is a subinterval $(1 \leq j \leq m)$ and m is the number of resultant subintervals.

The second step obtains the amplitude of each subinterval. For a given subinterval $S_j = [S_{j,1}, S_{j,2}]$ the amplitude is given by:

$$amp(S_j) = S_{j,2} - S_{j,1} + 1$$

The third step groups the subintervals according to their amplitude to delete the non representative subintervals. For all subintervals S_j with amplitude $amp(S_j) = \alpha$, the most representative subinterval is the one with the largest amplitude:

$$mrs(\alpha) = \arg \max_{\forall S | amp(S) = \alpha} amp(S)$$

A subinterval S_j is nonrepresentative if:

$$amp(S_j) \leq \frac{1}{2} mrs(\alpha)$$

The fourth step reduces the representative intervals amplitude. For a given representative subinterval $S_j = [S_{j,1}, S_{j,2}]$ of band b, the most representative gray value is:

$$mrg(S_j) = \arg \max_{\forall S_{,1} \leq \beta \leq S_{,2}} h_b(\beta)$$

A gray value γ of a representative subinterval S_j of band b is representative if:

$$h_b(\gamma) > \frac{1}{2} mrg(S_j)$$

All the nonrepresentative gray values must be removed from the interval, producing a reduced interval.

Depending of the application, the consecutive resultant reduced intervals can be merged. For example, the reduced intervals [12-18], [19-25] produce the new merged interval [12-25]. Interval merging lower the quantity of homogeneous seeds, and must be avoided if the application needs the highest separation among seeds (i.e. the user needs the maximum level of homogeneity in the regions).

The final step is to generate the seeds. A pixel x is considered as a seed if its gray values on each band fall inside a representative interval of the same band. If the gray values of two seed pixels fall inside the same representative intervals, the pixels will be labeled with the same region ID. The output of the seed generator is a set with n seeds $A_1, A_2, \ldots, A_n$.

4.2   Region Growing and Instance-Based Learning

The region growing algorithm is shown in Fig 2. The automatically generated seeds are used to construct the classifier using the region ID as the class of the pixel. Before the region growing step, the sets of pixels to label P and unallocated (non labeled) pixels Q must be defined. All the seeds must be grouped according to their region ID (region sets R). The region growing step obtains the pixels that must be labeled (set P) and updates the set Q. We use the IB1 classifier to label the regions. Because all the pixels are considered without concerning what regions they meet, pixels that in the original seeded region growing algorithm can not be reached by the region to which they belong (unconnected pixel problem) are labeled. After labeling, the IB1 classifier must be updated to consider the newly labeled instances. The algorithm stops when set Q is empty.
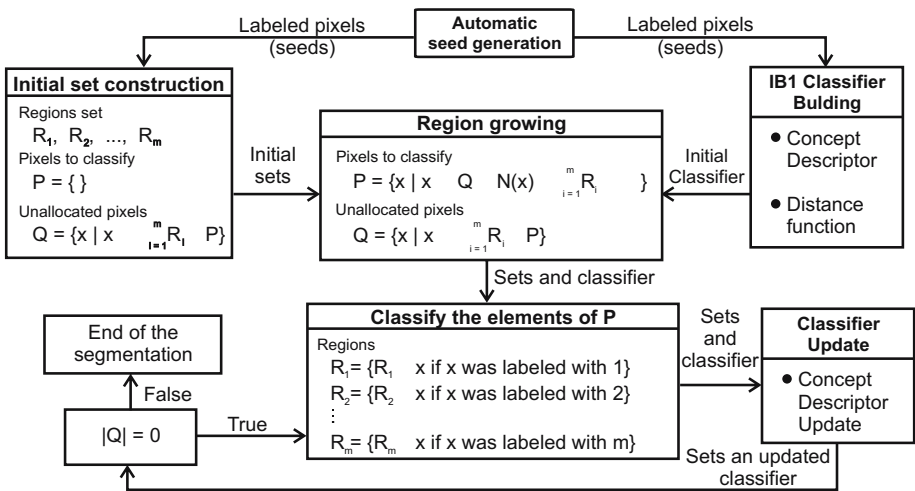
Fig. 2. Region growing algorithm

4.3   Ownership Tables and Region Merging

In many real world applications the user may need the segmentation of an image over different levels of abstraction, for example, in remote sensing, several regions may form a concept (a region with a specific semantic for the user), and these concepts may be merged to form a higher level concept.

At this point, the algorithm has obtained the homogeneous regions of the image, these regions represent a segmentation at the lowest level of abstraction. To complete the task it is necessary to merge the regions according to the user needs.

Ownership tables allow the user to merge regions according to his needs. The user manually selects the regions that must be merged and those regions ID's are stored in a table. An ownership table indicates which regions must be merged to form the concept that the user wants, so, the concept must be completely defined by its ownership table, and distinct concepts can not have the same table. The elements of an ownership table can be of two kinds, ambiguous and unambiguous. The unambiguous elements are regions that only belong to one ownership table and ambiguous elements can belong to two or more tables.

Fig. 3(a) shows a white cell blood with cytoplasm in the bottom. Fig. 3(b) shows the result of the proposed algorithm ASRG-IB1. Finally, Fig. 3(c) shows the result after the user-guided region merging trough ownership tables. An example of an ownership table is shown in Fig. 4.

(a)   (b)   (c)
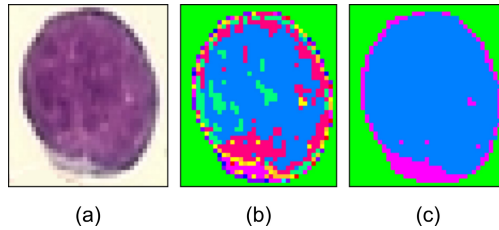
Fig. 3. (a) RGB image of a white blood cell with cytoplasm. (b) Image segmented with ASRG-IB1. (c) Image segmented after region merging.

White corpuscle		Cytoplasm	
	Region 1		Region 4
	Region 2		Region 5
	Region 3		Region 6
			Region 7
			Region 8
			Region 9
			Region 10

Fig. 4. Ownership table for Figure 2(c)

5   Experimental Results

This section shows the results of the proposed algorithm on RGB leukemia medical images. Leukemia is a cancer of the blood characterized by an abnormal proliferation of white blood cells (leukocytes). Experiments were made over thirty distinct images, with the objective of segmenting white blood cells of the image to study their characteristics and determine if a given patient has leukemia.

(a)   (b)   (c)   (d)
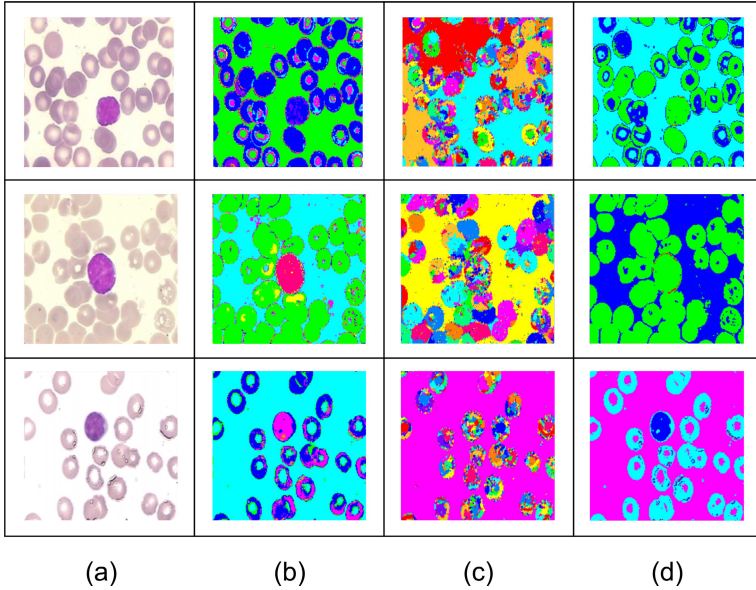
Fig. 5. (a) Original RGB images. (b) Images segmented with ASRG-IB1. (c) Images segmented with region growing. (d) Images segmented with auto threshold.

There is not a generally accepted methodology (in the field of computer vision) which elucidates on how to evaluate segmentation algorithms [10], [15]. Comparing different segmentation algorithms with each other is difficult mainly because they differ in the properties they try to satisfy. Segmentation quality assessment requires a manually generated segmentation (for reference) plus computer-generated segmentations corresponding to different image segmentation algorithms or algorithm parameter settings [10]. In this domain, it is difficult to find or generate manual segmentations so, the most common method for segmentation quality evaluation is a visual inspection made by domain experts.

For this comparison we used the HALCON [7] implementations of the region growing algorithm, and the implementation of the auto threshold algorithm. Auto threshold segments images using multiple thresholding. First, the relative histogram of the gray values are determined, then, relevant minima are extracted from the histogram, which are used successively as parameters for a thresholding operation. The thresholds used are 0, 255, and all minima extracted from the

histogram (after the histogram has been smoothed). For each gray value interval one region is generated. The number of regions is the number of minima + 1.

Results are shown in Fig. 5. It can be observed that the proposed algorithm (b) improves the original instance based algorithm (c) which oversegments the original images (a). The segmentation results of the proposed algorithm are highly competitive with respect to auto-threshold, even more, the proposed algorithm finds more homogeneus regions and allows the user to define a concept hierarchy by means of ownership tables.

6 Conclusions

We presented a new automatic seeded region growing algorithm that makes use of instance based learning as its distance criteria. This algorithm preserves all the advantages of the original SRG algorithm; furthermore, we presented a novel method for automatic seeds generation via histogram analysis, and a region growing scheme that eliminates the unconnected pixel problem when considering all pxeles to label as a single set. Instance based learning is the most suited machine learning algorithm for this task because at each growing step the algorithm is updated, opossed to other algorithms that construct an explicit representation of the training data, and the representation is not updated during the classification step. Finally, ownership tables allow adjusting the segmentation result to the user needs, and make possible the definition of levels of abstraction to represent a concept hierarchy.

References

1. Adams, R., Bischof, L.: Seeded Region Growing. IEEE Transactions on Pattern Analysis and Machine Intelligence 16, 641–647 (1994)
2. Ballard, D.H., Brown, C.M.: Computer Vision, 1st edn. Prentice-Hall, Boston Massachusetts (1982)
3. Cheng, H.D., Jiang, X.H., Sun, Y., Wang, J.: Color image segmentation: advances and prospects. Pattern Recognition 34, 2259–2281 (2001)
4. Cheng, H.D., Jiang, X.H., Wang, J.: Color image segmentation based on homogram thresholding and region merging. Pattern Recognition 35, 373–393 (2002)
5. Dougherty, J., Kohavi, R., Sahami, M.: Supervised and Unsupervised Discretization of Continuous Features. Machine Learning. In: Proceedings of the Twelfth International Conference, vol. 12, pp. 194–202. Morgan Kaufmann, San Francisco (1995)
6. Fan, J., Zeng, G., Body, M., Hacid, M.: Seeded region growing: and extensive and comparative study. Pattern Recognition 26, 1139–1156 (2005)
7. MVTec Software GmbH. Halcon: Machine vison software for business applications. MVTec Software GmbH, Munchen Germany (2007)

8. Jeon, B., Jung, Y., Sang, K.: Image segmentation by unsupervised sparse clustering. Pattern Recognition Letters 27, 1139–1156 (2005)
9. Kass, M., Witkin, A., Terzopoulos, D.: Snakes: Active contour models. In: Proceedings 1st International Conference on Computer Vision. International Journal of Computer Vision, vol. 1, pp. 321–331. Springer-Verlag, Netherlands (1988)
10. Paglieroni, D.W.: Design considerations for image segmentation quality assessment measures. Pattern Recognition 37, 1607–1617 (2004)
11. Pichel, J.C., Singh, D.E., Rivera, F.F.: Image segmentation based on merging suboptimal segmentations. Pattern Recognition Letters 27, 1105–1116 (2006)
12. Quiao, Y., Hu, Q., Qian, G., Luo, S., Nowinski, W.L.: Thresholding based on variance and intensity contrast. Pattern Recognition 40, 596–698 (2007)
13. Quinlan, J.R.: Induction of Decision Trees. Machine Learning 1, 81–106 (1986)
14. Shih, F.Y., Cheng, S.: Automatic seeded region growing for color image segmentation. Image and Vision Computing 23, 877–886 (2005)
15. Siebert, A.: Dynamic Region Growing. Vision Interface 97. Massachusetts Institute of Technology, Cambridge Massachusetts (1997)
16. Tremeau, A., Borel, N.: A region growing and merging algorithm to color image segmentation. Pattern Recognition 30, 1191–1203 (1997)
17. Zouagui, T., Benoit-Cattin, H., Odet, C.: Image segmentation functional model. Pattern Recognition 37, 1785–1795 (2004)

Morphological Distinguished Regions*

Allan Hanbury

Pattern Recognition and Image Processing Group (PRIP),
Institute of Computer Aided Automation, Vienna University of Technology,
Favoritenstraße 9/1832, A-1040 Vienna, Austria
`hanbury@prip.tuwien.ac.at`

Abstract. Distinguished regions can be detected with high repeatability in different images of the same scene. Two definitions of distinguished regions of an image in a mathematical morphology framework are proposed: one based on the use of reconstruction operators on a series of cross sections of a greyscale image, and the second based on extracting regions present in a large number of levels of a watershed segmentation hierarchy. The proposed distinguished regions are evaluated by measuring their repeatability in transformed images of the same scene.

Keywords: distinguished region, hierarchical segmentation, repeatability, watershed.

1 Introduction

Regions that can be detected with high repeatability in different images of the same scene or object have many uses in computer vision. They have been particularly useful for finding correspondences between images for wide-baseline stereo matching [1] and for locating features for object recognition [2]. These regions have been referred to as *invariant regions* [3], *covariant regions* [4] and *distinguished regions* [1]. We use the latter name in this paper.

We investigate distinguished regions that can be extracted within a mathematical morphology framework. The first part, in Section 2, is of more theoretical interest, as we show how a stricter version of the MSER detector [1] can be defined using reconstruction operators on a sequence of cross sections of a greyscale image, in a similar way to which the regional minima and maxima are defined.

We then consider extracting distinguished regions from segmentation hierarchies (Section 3). Hierarchies encoding the fusion of regions created during a watershed flooding of an image have been well studied [5]. These hierarchies have been used to create an image partition containing a specified number of regions by choosing a specific level of the hierarchy [6] or to assist in the manual creation of image partitions by allowing simple fusion and splitting of regions [7]. Nevertheless, the calculation of image features from the complete hierarchy instead of from a single level of the hierarchy has received little attention, showing that

much information available in the hierarchy is ignored. We suggest one possible feature that can be extracted from such a hierarchy, namely the number of levels in which a region of the partition is present. Regions which are present in a large number of levels are considered good candidates for distinguished regions.

Measurements of the repeatability of the proposed distinguished regions across transformed images of the same scene are presented in Section 4.

2   Intensity-Based Distinguished Regions

Of the region detectors described in [4], two operate directly on the intensity values of a greyscale image, while the others make use of the detection of corner points in a scale space or operate on the entropy of the probability density function of intensities in an area. The two intensity-based detectors are the *Intensity Extrema-Based Region Detector* (IBR) [8] and the *Maximally Stable Extremal Region Detector* (MSER) [1].

The IBR begins by locating local intensity extrema in a series of smoothed images. The derivative of the intensity is then evaluated on rays emanating from each local extremum and the derivative extremum on each ray is found. Connecting the positions of these extrema produces an irregularly shaped region, which is replaced by an ellipse having the same shape moments.

An MSER is a connected component of an appropriately thresholded image [4]. Given a greyscale image f with integer greylevels, an *Extremal Region $\mathcal{Q}$* is a connected component with the property that $\forall p \in \mathcal{Q}, q \in \delta^{(1)}(\mathcal{Q}) \setminus \mathcal{Q}$: $f(p) > f(q)$, or alternatively $f(p) < f(q)$. An extremal region is considered to be maximally stable (i.e. to be an MSER) if the following holds [1]: Let $\mathcal{Q}_1, \ldots, \mathcal{Q}_{i-1}, \mathcal{Q}_i, \ldots$ be a sequence of nested extremal regions, i.e. $\mathcal{Q}_i \subseteq \mathcal{Q}_{i+1}$. Extremal region $\mathcal{Q}_{i^*}$ is maximally stable iff $q(i) = |\mathcal{Q}_{i+\Delta} \setminus \mathcal{Q}_{i-\Delta}| / |\mathcal{Q}_i|$ has a local maximum at i^* ($|\cdot|$ denotes cardinality). Δ is a parameter of the method.

As pointed out in [1], the algorithm for locating MSERs is essentially identical to an efficient watershed algorithm [9]. For the watershed, the focus is on finding the positions where two catchment basins merge, whereas for the MSER detection algorithm, the focus is on the rate of change of the area of each catchment basin with increasing threshold. The connected components at which the rate of change of area with threshold is a minimum are chosen as MSERs.

A very strict version of this MSER detection algorithm, in which the connected components for which the rate of change of area with respect to threshold is zero, can be formulated as a morphological reconstruction based operator. We use the following notation (from [10]): $CS_t(f)$ denotes the cross section of greyscale image f at level t (defined as the set of image pixels whose values are greater than or equal to t) and $R_g^\delta(f)$ denotes the morphological reconstruction by dilation of a mask image g from a marker image f. In a similar way to finding the regional maxima and
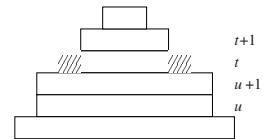
Fig. 1. Greyscale image cross sections

minima in [10], we can see that if a connected component is identical in $\mathrm{CS}_t(f)$ and $\mathrm{CS}_{t+1}(f)$, then it will not be reconstructed by $R_{\mathrm{CS}\ (f)}^\delta [\mathrm{CS}_t(f) \setminus \mathrm{CS}_{t+1}(f)]$ (see levels u and $u+1$ in Figure 1). If however the connected component in $\mathrm{CS}_t(f)$ is larger than the corresponding connected component in $\mathrm{CS}_{t+1}(f)$, then it will be reconstructed (see levels t and $t+1$ in Figure 1, where the hatches represent the set difference between the two levels). Hence the connected components at threshold level t that are identical in level $t+1$ can be found by

$$\mathrm{ST}_t(f) = \mathrm{CS}_t(f) \setminus R_{\mathrm{CS}\ (f)}^\delta [\mathrm{CS}_t(f) \setminus \mathrm{CS}_{t+1}(f)] \tag{1}$$

The binary image containing all the distinguished regions is calculated as the union of $\mathrm{ST}_t(f)$ taken over all greylevels present in the image, or

$$\mathrm{MDR}(f) = \bigcup \mathrm{ST}_t(f) \tag{2}$$

For images which do not contain pixels which assume all possible greylevel values, the values of t should be restricted to the greylevels for which the value of the greylevel histogram $H_t(f)$ is non-zero. This restriction is necessary as $\mathrm{CS}_t(f)$ will be identical to $\mathrm{CS}_{t+1}(f)$ if no pixels with a greylevel of t exist in the image, resulting in all connected components of $\mathrm{CS}_t(f)$ becoming distinguished regions.

Unfortunately it is not possible to find the stable connected components by a single greyscale reconstruction, as is done for the morphological regional maxima and minima, because the structure of a function as a stack of binary cross sections is not kept by the marker image in Equation 1. It may be possible to incorporate the idea of a minimum rate of area change from the MSER calculation through the use of attribute openings, but this remains to be investigated.

In practice, as the result of this algorithm includes very many small connected components, we apply an area opening of size λ to the result:

$$\mathrm{AMDR}(f) = \gamma_\lambda (\mathrm{MDR}(f)) \tag{3}$$

Figure 2(a) shows the regions obtained for an image with $\lambda = 25$ pixels.

3   Hierarchical Watershed-Based Distinguished Regions

We propose distinguished regions calculated from a watershed hierarchy based on volume extinction values [11,5]. The hierarchy is built as follows [5]. During the flooding process on an image, when a lake in a catchment basin is about to overflow, the dissimilarity between this catchment basin and its neighbour into which it would overflow is defined as the measurement of the volume of the full lake. This can easily be represented on a region adjacency graph (RAG), where each node represents a catchment basin, and each edge encodes the dissimilarity between two neighbouring catchment basins. This type of flooding is most often used to obtain a segmentation containing a specific number of regions: in order to obtain a partition with N regions, the $N-1$ edges with the highest dissimilarity values in the minimum spanning tree (MST) of the RAG are cut. Alternatively,

(a) Rec AO25

(b) Ellipses fitted to Rec AO25

(c) HWS Top50

(d) Ellipses fitted to HWS Top50

Fig. 2. (a) Outlines (in white) of the reconstruction-based morphological distinguished regions after an area opening of size 25 pixels. (c) Outlines of the 50 regions having the highest survival values. (b), (d) Ellipses fitted to the regions.

the hierarchy can be visualised as a stack of nested partitions, where the partition at level i contains i regions. This implies that in moving from level i to level $i+1$, one of the regions in level i is split into two regions in level $i+1$.

An obvious candidate for a distinguished region is a region which remains constant over a large number of levels of the hierarchy of partitions. We define the *survival value* of a region which "appears" at some level i (due to a split of a region at level $i-1$), and "disappears" by splitting into two at level $i+n$ to be n. If these survival values are encoded into the regions in each level of the hierarchy, then it is straightforward to find the longest surviving regions by searching for the largest survival values. For efficient searching, the regions in level i which are identical to regions in level $i-1$ are assigned survival values of 0. This avoids having a series of identical regions in subsequent levels with stepwise decreasing survival values, which would lead to multiple detection of a single region. On each level of the hierarchy (except for level 1), there will therefore be two regions with non-zero survival values. These two survival values on the same level are never identical, as both new regions cannot split at the same level. The 50 regions with the highest survival values in a hierarchy of 750 levels are shown in Figure 2(c).

4 Evaluation

We first summarise the framework for evaluating distinguished region repeatability. A description of the experiments and a discussion of the results follows.
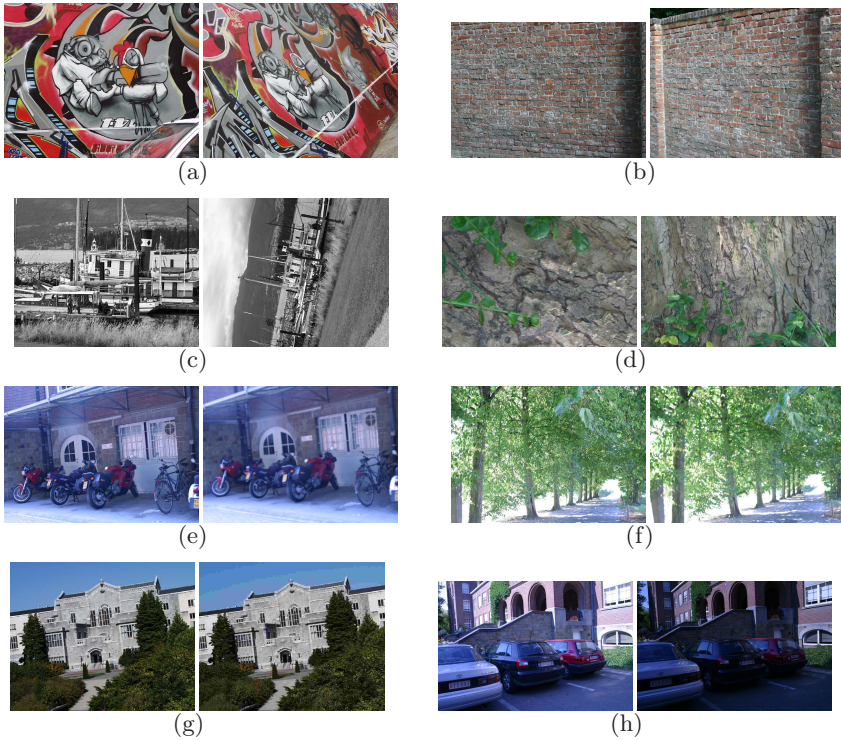
Fig. 3. Part of the evaluation dataset. (a), (b) Viewpoint change, (c), (d) Zoom+rotation, (e), (f) Image blur, (g) JPEG compression, (h) Light change. The leftmost image of each set is the reference image (from [4]).

4.1 Evaluation Framework

The *repeatability* measures the extent to which regions detected in transformed images of the same scene overlap. We use the evaluation framework presented in [4][1]. The framework consists of eight images, where each image is subjected to five transformations, resulting in sets of six images. Examples from the image sets are shown in Figure 3. The homographies between the reference images and the other images for each set have been computed, allowing the overlap between distinguished regions in the reference and another image to be evaluated.

In [4], only elliptical distinguished regions are considered, as these are intrinsically produced by four of the six algorithms tested. For the other algorithms, ellipses approximating the regions are chosen. To be compatible with the framework, we also fit ellipses to the edges of the regions produced by the proposed methods, using the ellipse fitting algorithm in [12]. Examples of the ellipses fitted to the detected regions are shown in Figures 2(b) and (d).

The repeatability is measured between the reference image and another image from the set. The distinguished regions are detected in both images and those

---

[1] http://www.robots.ox.ac.uk/~vgg/research/affine/

from the second image are projected onto the reference image by using the known homography. Two regions are said to form a region-to-region correspondence if the *overlap error* is sufficiently small — in this paper we use 0.4 as was done for the experiments in [4]. The overlap error is defined as [4]

$$1 - \frac{R_\mu \; \cap R_{(H^T \mu H)}}{R_\mu \; \cup R_{(H^T \mu H)}} \qquad (4)$$

where R_u is the region enclosed by the ellipse defined by $x^T \mu x = 1$ and H is the homography relating the images. The *repeatability score* for a pair of images is the ratio between the number of region-to-region correspondences and the smaller number of regions in the pair of images. Only regions located in the part of the scene present in both images are counted. In addition, the regions are transformed to have a normalised size before calculating the overlap, to avoid the problems with regions of different sizes discussed in [4].

4.2   Experiments

The results of the repeatability tests for the eight groups of six images in the dataset are shown in Figures 4 and 5, where the left column shows the repeatability percentage and the right column the number of correspondences. Curves corresponding to six methods are shown in each graph. The curves labelled *MSER* and *Hessian-affine* correspond to the two best performing methods of the six tested in the evaluation of affine covariant region detectors in [4].

For the distinguished regions based on the hierarchical watershed, the number of levels of each hierarchy is set to 750 (limited by the amount of memory on the computer used to perform the experiments). Each image is pre-processed by applying a leveling [13] of size 3 to each channel separately. The hierarchy is built on a gradient image obtained by applying the *saturation weighing-based colour gradient* in the L1 colour space [14]. We evaluate three methods of choosing the distinguished regions. The first two are based on setting a threshold on the minimum number of levels that a region must survive in order to be chosen as a distinguished region. We compared the use of a high threshold of 500 levels (*HWS Th500*) and a low threshold of 100 levels (*HWS Th100*). This evaluates if regions that survive over many levels in the original image also do so in the transformed images, or if choosing a lower threshold, thereby including more regions, leads to higher repeatability. The third method once again tests the repeatability of the regions which survive over many levels by choosing the 50 regions with the highest survival values (*HWS Top50*).

For the reconstruction based distinguished regions (Equation 3), we plot the results obtained using an area opening of size 25 pixels (*Rec. AO25*). Images were converted to greyscale before applying this method.

4.3   Discussion

As has already been pointed out in [4], different algorithms perform better for different transformations, as can be seen by the repeatability results for the
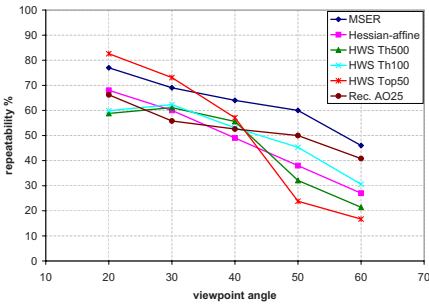
(a) Graf repeatability
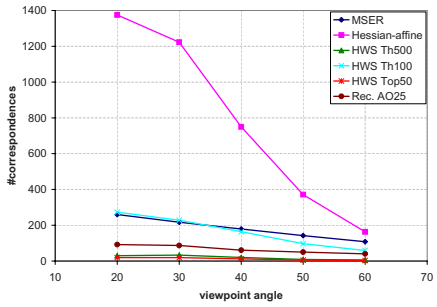
(b) Graf #correspondences
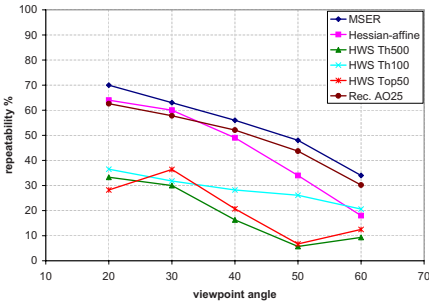
(c) Wall repeatability
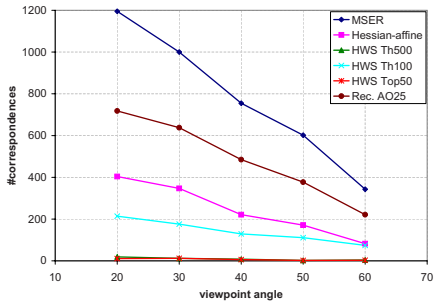
(d) Wall #correspondences
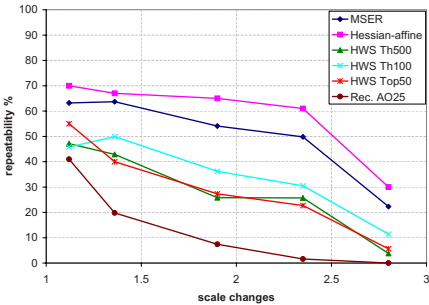
(e) Boat repeatability
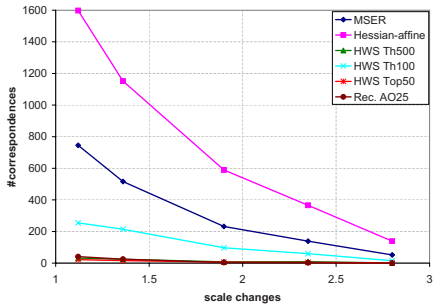
(f) Boat #correspondences
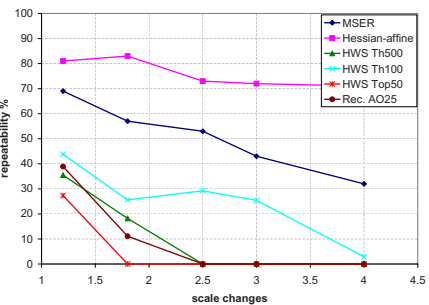
(g) Bark repeatability
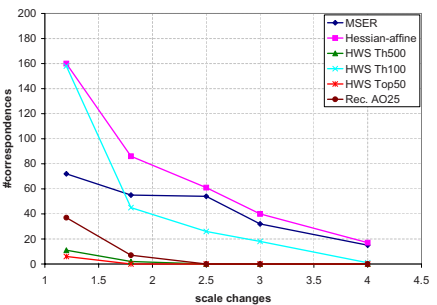
(h) Bark #correspondences

Fig. 4. The repeatability (left column) and number of correspondences (right column) for (a)–(d) viewpoint change and (e)–(h) scale change
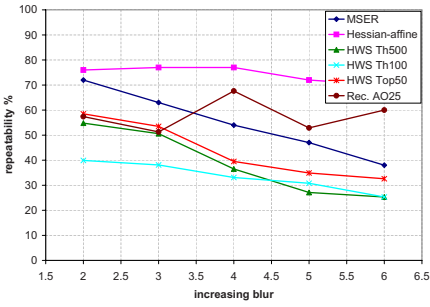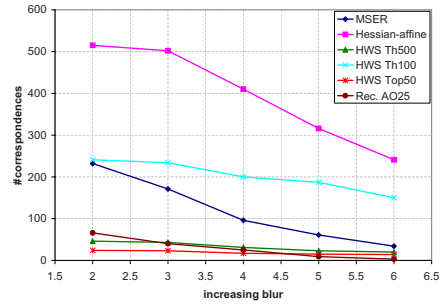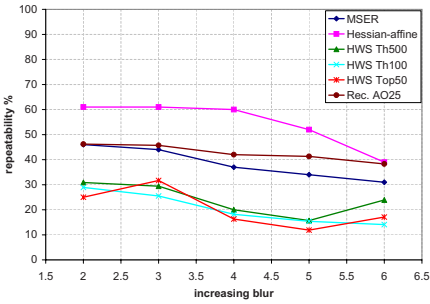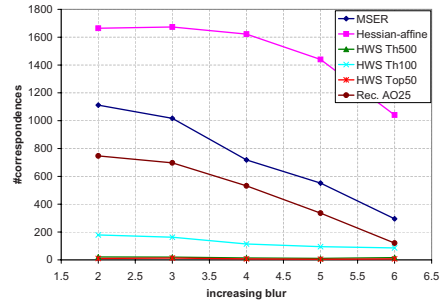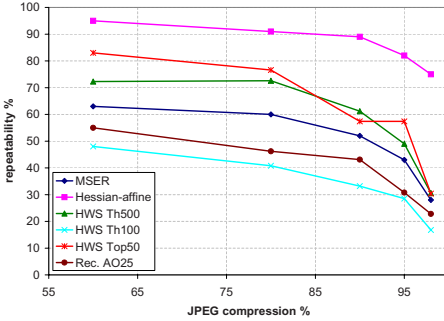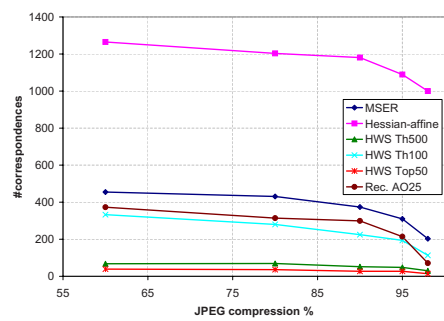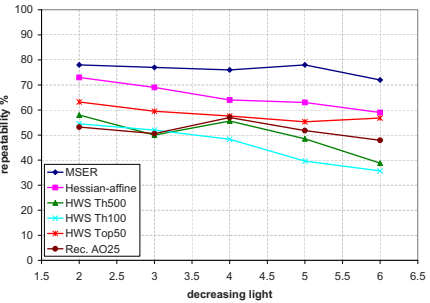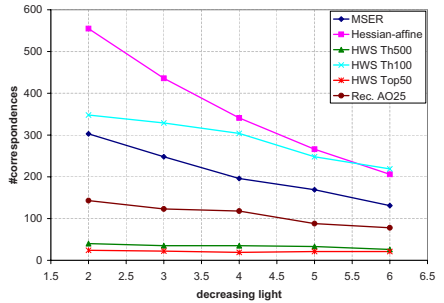
Fig. 5. The repeatability and number of correspondences for (a)–(d) blur, (e)–(f) JPEG compression and (g)–(h) illumination change

MSER and Hessian-affine detectors. The problem of comparing detectors producing different densities of regions is discussed in [4]. They point out that for detectors that produce few regions, the thresholds can be set so that the performance is often better than average. For detectors that produce many regions, the image may be so cluttered with regions that some get matched by accident. For the distinguished regions from the hierarchical watershed, we examine this effect by using the three ways listed above of choosing the number of distinguished regions. The Hessian-affine detector produces the largest number of correspondences for each image sequence except Wall, indicating that the density of the distinguished regions is the highest.

For the viewpoint changes (Figure 4(a)–(d)), the MSER detector has the highest repeatability. For the Graf image, it is interesting that the 50 regions with the highest survival value (*HWS Top50*) are extremely stable for small viewpoint changes and perform the worst for large viewpoint changes. The reconstruction based detector (*Rec. AO25*) performs similarly to the Hessian-affine detector for these images, outperforming it for the three largest viewpoint changes.

The morphological detectors prove to be bad at handling scale changes (Figure 4(e)–(h)). In particular for the Bark image, no matching distinguished regions were found by three of the methods as the zoom-out becomes markedly larger, leading to zero repeatability. Because we are dealing with scale changes, the corresponding regions will occur at different levels of the watershed hierarchy for different images. The fact that the (*HWS Th100*) performs the best among the tested algorithms demonstrates this, as the (*HWS Th500*) and (*HWS Top50*) only choose regions from the lower part of the hierarchy. Increasing the maximum number of levels in the hierarchy should improve the repeatability for scale change. For the blur images (Figure 5(a)–(d)), the reconstruction based approach produces better repeatability results than the MSER for 8 of 10 transformed images, but for a lower number of correspondences.

It is interesting that only for the JPEG compression images (Figure 5(e)–(f)), the two hierarchical watershed based methods in which few distinguished regions are selected perform better than the MSERs. Finally, for the illumination changes (Figure 5(g)–(h)), all morphological methods have a repeatability below that of the MSER and Hessian-affine methods.

In general, the *HWS Th500* and *HWS Top50* curves are very similar, indicating that there is little difference due to these methods of choosing the distinguished regions with the highest survival values. Based on the results, one cannot determine whether it is better to choose a lower survival value threshold (*HWS Th100*) leading to many distinguished regions or a higher threshold, as one of the thresholds does not lead to consistently better results over all transformations.

5   Conclusion

Two methods for calculating distinguished regions in a mathematical morphology framework are proposed. The first is based on reconstructions on a series

of cross sections of a greyscale image and the second extracts regions from a hierarchy calculated using a watershed based on volume extinction values.

Experiments measuring the repeatability of the extracted regions for different types of image transformations are presented. The repeatability falls into the range of the repeatability of the six algorithms tested in [4], without surpassing the best algorithms. One of the drawbacks of the evaluation framework used is that the difference in the number of regions (region density) extracted by each algorithm is not taken into account, which could affect the repeatability results.

The limit of 750 levels of the watershed hierarchy limits the performance, especially for scale changes. The advantage of the hierarchical approach is the extensive information available in the hierarchy for defining distinguished regions. We have so far only looked at one possible feature: the survival value. Use of information on the region shape, region inclusion information, neighbourhood information, etc., is an interesting area for future research.

References

1. Matas, J., Chum, O., Urban, M., Pajdla, T.: Robust wide-baseline stereo from maximally stable extremal regions. Image and Vision Computing 22, 761–767 (2004)
2. Csurka, G., Dance, C.R., Fan, L., Willamowski, J., Bray, C.: Visual categorization with bags of keypoints. In: Workshop on Statistical Learning in Computer Vision (at ECCV) (2004)
3. Dorko, G., Schmid, C.: Selection of scale invariant neighborhoods for object class recognition. In: Proc. of the Int. Conf. on Computer Vision, pp. 634–640 (2003)
4. Mikolajczyk, K., Tuytelaars, T., Schmid, C., Zisserman, A., Matas, J., Schaffalitzky, F., Kadir, T., Van Gool, L.: A comparison of affine region detectors. International Journal of Computer Vision 65(1/2), 43–72 (2005)
5. Meyer, F.: An overview of morphological segmentation. International Journal of Pattern Recognition and Articial Intelligence 15(7), 1089–1118 (2001)
6. Hanbury, A., Marcotegui, B.: Waterfall segmentation of complex scenes. In: Narayanan, P.J., Nayar, S.K., Shum, H.-Y. (eds.) ACCV 2006. LNCS, vol. 3851, pp. 888–897. Springer, Heidelberg (2006)
7. Zanoguera, F., Marcotegui, B., Meyer, F.: A toolbox for interactive segmentation based on nested partitions. In: Proc. of the Int. Conf. on Image Processing (1999)
8. Tuytelaars, T., Van Gool, L.: Matching widely separated views based on affine invariant regions. International Journal on Computer Vision 59(1), 61–85 (2004)
9. Vincent, L., Soille, P.: Watersheds in digital spaces: an efficient algorithm based on immersion simulations. IEEE Trans. Pattern Analysis and Machine Intelligence 13(6), 583–598 (1991)
10. Soille, P.: Morphological Image Analysis, 2nd edn. Springer, Heidelberg (2002)
11. Vachier, C., Meyer, F.: Extinction values: A new measurement of persistence. In: Proc. of the IEEE Workshop on Non Linear Signal/Image Processing, pp. 254–257 (1995)
12. Fitzgibbon, A.W., Pilu, M., Fisher, R.B.: Direct least-squares fitting of ellipses. IEEE Trans. Pattern Analysis and Machine Intelligence 21(5), 476–480 (1999)
13. Meyer, F.: Levelings, image simplification filters for segmentation. Journal of Mathematical Imaging and Vision 20, 59–72 (2004)
14. Angulo, J., Serra, J.: Color segmentation by ordered mergings. In: Proc. of the Int. Conf. on Image Processing. vol. II, pp. 125–128 (2003)

Set of Methods for Spontaneous ICH Segmentation and Tracking from CT Head Images

Noel Pérez[1], José A. Valdés[1], Miguel A. Guevara[1], Luis A. Rodríguez[2], and J. M. Molina[1]

[1] Center for Advanced Computer Sciences Technologies,
Ciego de Ávila University,Ciego de Ávila, Cuba
`{noel,jose,miguel,juanmiguelmolina}`
`@informatica.unica.cu`
[2] Intensive Care Unit, Morón Hospital, Ciego de Ávila, Cuba
`lars@trocha.cav.sld.cav.cu`

Abstract. Spontaneous intracerebral hemorrhage (ICH) is a common cause of stroke, due to this; the early evolution and quantitative analysis of the ICH is important for the treatment and the course of patient's recovery. Computer-based diagnosis systems have played an important role in quantitative analysis of medical images aiding medical personnel in selecting the appropriated treatment of diseases. This paper outlines a set of three methods for ICH segmentation and tracking from computer tomography (CT) head images, based on a suitable combination of digital image processing and pattern recognition techniques. Two of these methods are carried out in a semiautomatic way and the other one is performed in a manual way. Methods developed were tested successfully by medical researchers in a representative dataset of CT head images (patient studies).

Keywords: Intracerebral hemorrhage, medical images analysis, 3D mathematic morphology, segmentation and tracking, deformable models.

1 Introduction

Spontaneous Intracerebral hemorrhage (ICH) is a common cause of stroke, accounting for between 5 and 10% of all strokes. In a consecutive series of 938 stroke patients enrolled into the NINCDS Stroke Data Bank, primary ICH accounted for 10.7% of the cases. The age-adjusted annual incidence rates for primary intracerebral hemorrhage range from 11 to 31 per 100,000 populations in predominantly Caucasian population based-studies with a high rate of computer tomography (CT) scanning [1]. The early evolution and quantitative analysis of the human cerebrovascular illness are significant for the treatment and the course of patient's recovery. Computer-based diagnosis systems have played an important role in quantitative analysis of medical images aiding medical personnel in selecting the appropriated treatment of diseases [2].

Many approaches for ICH segmentation and tracking have been reported in the literature. Cosic and Loncaric [2, 3] proposed a method based on unsupervised fuzzy clustering and expert system-based procedure region labeling techniques that includes

volume measurement of the ICH and the edema regions but not always the automatic method perform a correct segmentation. Majcenic and Loncaric [4] proposed a stochastic method for ICH segmentation based on simulated annealing techniques. However these methods are computationally complex.

This paper outlines a set of three methods for ICH segmentation and tracking from CT head images, two of these methods are performed in a semiautomatic way and the other one in manual way. One of the semiautomatic methods is focused mainly in 3D mathematic morphology operations and the other combine live wire and graphical information retrieval techniques. The manual method use mainly deformable models, but need a major user intervention although it demonstrated a more precise and accurate ICH segmentation. This method was included with the intention to evaluate the semiautomatic methods performance.

The set of methods was used by medical researchers to evaluate the behavior and changes of spontaneous ICH (shape, size, etc.) during the disease course and validated successfully in a representative dataset of 36 ICH CT head images patient studies.

The paper is organized as follows: section 2 outlines the implementation of the proposed set of methods. In section 3 we describe results obtained with the application of methods to a representative dataset of ICH CT head images patient studies. Conclusions and some ideas about the future work are showed in section 4.

2   Proposed Methods

Developed methods for segmentation and tracking of spontaneous ICH from CT head images patient studies are based on suitable combinations of digital image processing and pattern recognition techniques. Included methods were:

1. 3D mathematical morphology based method.
2. Similarity based method.
3. Manual based method.

2.1   3D Mathematical Morphology Based Method

This method relies on the application of 3D mathematical morphology, histogram analysis, optimal thresholding, and prior geometric information techniques. Each patient image study is considered as an anisotropic volume restricted manually to the most outer neighbor ICH slices, with the intention to increase the automation level of the segmentation process and to reduce the computational cost.

The computed tomography images have common intensities frequencies histogram, in that way, we can perform some important correlations between image objects of interest and the characteristics intensities level values of skull, grey matter and white matter. In our work was observed heuristically the ICH intensities frequencies histogram values are related to higher intensities, which was consider as the start point for image segmentation.

2.1.1   Preprocessing
The preprocessing remove short duration impulses and smooth lightly the image edges, applying a median filter slice by slice, in axial form, with a windows of 3x3 pixels.

2.1.2   ICH Auto-detection

Autodetection consists in compute the global maximum, which is used as the threshold value for the ICH segmentation (to produce a binary mask). Hereafter 3D mathematical morphology operations are applied to autodetect the ICH.

Algorithm 1. Semiautomatic method based on 3D mathematical morphology.

1: Define ICH neighbor slices interval.
2: Create an anisotropic volume of interest (VOI) containing the ICH slices.

$$St = \{(x,y,z) \in N^3 : 0 < x < x_f, 0 < y < y_f, z_0 < z < z_f\} ; \quad i = \{i_1, i_2, i_3 ... i_n\} \qquad n = 255$$

x_f and y_f means row and column image size, z_0 and z_f are the most outer neighbor slices. The studies intensities are defined as one-dimensional array i with n intensity levels.

3: Compute $gm = \max(St)$;   gm is the maximum intensity value of St.
4: Obtain ICH binary mask using gm as threshold value.

$$ICHmask_{(x,y,z)} = \begin{cases} 0 & \forall \, St_{(x,y,z)} < gm * 0.90 \\ 1 & \forall \, St_{(x,y,z)} \geq gm * 0.90 \end{cases}$$

5: $mer = ICHmask \ominus se$: where $\ominus$ represent the morphological erosion operation and se is an spherical structuring element (se diameter is set to 5 voxels and it was determine heuristically).
6: Select the fa_mask (biggest foreground connected object in mer), which is a first approach of the ICH segmentation.
7: $ICH\_mask = fa\_mask \oplus se$: ICH_mask is the 3D ICH binary mask.
6: Apply a flood fill operation to avoid holes inside the *ICH_mask*.
7: Multiply the new *ICH_mask* by the original VOI and ICH segmentation is carried out.

2.2   Similarity Based Method

Similarity based method involved two main steps: pick a query object (ICH) and afterward made the automatic ICH retrieval on the remainder patient study.

2.2.1   Select Query Object

Query object selection consists in the extraction of the ICH contour. We used live wire techniques [5] to extract the object edges, and hereafter based on the selected contour are computed automatically the initials reference points with their associated similarity vectors. Reference points and their associated similarity vectors are the query basic elements. The selection of query object (I_n) is made by the following steps:

1. Extract the ICH contour (CT_n).
2. Extract the reference points (set of points that belong to query object contour)
3. Create similarity vectors, from reference points.

Query object elements are formed by the reference points and their associated similarity vectors. The quantity of reference points and their associated similarity vectors is variable and depend of the specific problem domain knowledge.

2.2.1.1   ICH Contour Extraction. We used live wire techniques for object contour extraction (segmentation). Live wire is a recently proposed interactive boundary tracking technique [6] that share some similarities with snakes and it is generally considered in the literature as a competing snake technique. Like snakes, the idea behind the live wire technique is to allow image segmentation to occur with minimal user interaction, while at the same time allowing the user to exercise control over the segmentation process. This technique share two essential components: a local cost function that assigns lower cost to image features of interest, such as edges, and an expansion process that forms optimal boundaries for objects of interest based on the cost function and seed points provided interactively by the user [5]. The contour obtained after live wire application is a not continuous, product of this, we interpolate it with a spline function to obtain a continuous curve to produce a better object contour approximation. The extracted curve is use after to compute the reference points.

2.2.1.2   Reference Points. Reference points are formed by a set of points that are located close or in the object contour with direction $i\theta$, where $i:0..\alpha-1$, $\alpha = \text{int}(360/\theta)$, $0 < \theta \le 180°$ and θ is the displacement angle, taking the object mass center as the center of the coordinates system. The angle θ will be selected by the user and it depend of the problem knowledge domain (Fig. 1). Initial reference points are determined by the following algorithm:

Algorithm 2. Generate Initial Reference Points

1: Select initial slice *I(n)*
2: Select θ, $0 < \theta \le 180°$
3: Select $\mathcal{E}$: admissible (small) distance between $P_i(x, y)$ and *CTn*
4: Compute $P_i(x, y)$: reference points

      coordinates *(X,Y)* of P_i are obtained by the expression:

      $P_i(X,Y) = C_x + r * \cos(i)$, $C_y + r * \sin(i)$

      where $r \in Z^+$, $1 \le r \le R$ and r increase in 1 on each iteration until r = R and R is
      the value in which $d_{Pi}(P_i(X,Y), CT_n) \le \mathcal{E}$,   d is the Euclidian distance
      between $P_i(x, y)$ and CT_n

      Cx and *Cy* are the *(X,Y)* centroid coordinates
5: Store new founded reference points in the $P_i(x, y)$ array

---
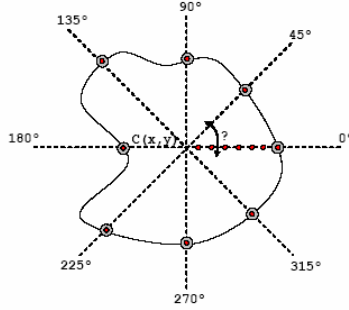
Fig. 1. Reference points obtained with $\theta = 45°, \varepsilon = 0.5$

2.2.1.3   Similarity Vectors. Similarity vectors (S_i) are the basic elements that allow to track the object on the rest of slices (images) belonging to a selected patient study. The reference points represent the centroid ($C_{x,y}$) of the similarity matrixes (Q_i). Similarity matrixes are *MxM* windows, where $M = 2*\delta+1$, δ is a positive integer scalar provided by the user   (Fig. 2). The similarity vectors are obtained from the similarity matrixes using the following mathematic formulation:

$$S_i = \{a_{1,1}... a_{m,1}, a_{1,2}... a_{m,2}, a_{1,m}... a_{m,m}, a_{1,m+1}... a_{m,m+1}\}$$

$$Q_i = \begin{array}{ccccc} a_{11} & a_{12} & a_{13} & \cdots & a_{1m} \\ a_{21} & a_{22} & a_{23} & \cdots & a_{2m} \\ a_{31} & a_{32} & a_{33} & \cdots & a_{3m} \\ \vdots & \vdots & \vdots & & \vdots \\ a_{m1} & a_{m2} & a_{m3} & \cdots & a_{mm} \end{array}$$

where S_i represent the set of similarity vectors corresponding to P_i and Q_i.
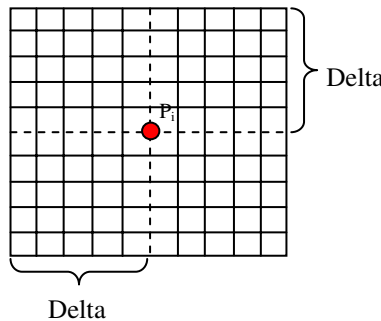
Fig. 2. Similarity matrix

2.2.2   Object Retrieval

Object retrieval (which is carried out in an automatic way) has the aim to track the query object picked over (user selected) slices (images) of patient study. This

algorithm tries to find the points more similar to the current reference points on the slice under processing. The new founded points are used then as the reference points to detect the object in the next slice. This process is repeated over all the slices (selected by the user) that belong to the current patient study.

Object retrieval is in general a process devoted to find a query object on a set of images or images databases [7].

In our case object retrieval has the aim to track (extract) the ICH on a set of slices selected by the user that belong to the patient under study.

Similarity descriptors are critical for the performance of object retrieval process. Several descriptors were evaluated, but the best results were achieved with the distance equation (eq. 1) proposed by Fuertes [8], which we use to select the new reference points belonging to the slice under analysis.

$$d(P_{i(n)}, P_{i(n+1)}) = \sqrt{(S_{i(n)} - S_{i(n+1)})^t * (S_{i(n)} - S_{i(n+1)})} \tag{1}$$

$S_{i(n)}$ is a similarity vector associated to reference point $P_{i(n)}$ in the I_n image, $S_{i(n+1)}$ is a vector associated to the point $P_{i(n+1)}$ in the I_{n+1} slice, t denote a transpose matrix. The new reference points will be those $P_{i(n+1)}$ where $d(P_{i(n)}, P_{i(n+1)})$ is minimum.

The method employ the created similarity vectors on query object to find the reference points related to ICH: the points that identify the ICH occurrence on the rest of slices set of patient under study.

The object retrieval algorithm developed is outline below:

_____

Algorithm 3. Retrieval
_____

1: Select new slice ($I_{(n+1)}$)

2: Compute P_{ik} points

    for each *i* angle

      $P_{ik}(X,Y) = C_{nx} + k * \cos(i), C_{ny} + k * \sin(i)$

      where $k{:}1..D + \sigma$, σ is a value selected by the user, D is the euclidian distance between C_n and $P_{i(n)}$

      Build vector S_{ik} from P_{ik} (see 2.2.1.3)

      Compute R_{ik}

        $R_{ik} = d(S_{ik}, S_{in})$: *d* similarity function (eq. 1)

3: Select $m=k$ where R_{ik} is minimum

4: Created and store $P_{i(n+1)}$ and $S_{i(n+1)}$

  $P_{i(n+1)} = P_{im}(X,Y)$, $S_{i(n+1)} = S_{im}$

5: Build the contour $CT_{(n+1)}$ based on $P_{i(n+1)}$ array

6: Compute the centroid from of $CT_{(n+1)}$

7: if (slice set selected is empty) then end else goto 1
_____

2.3   Manual Method

The manual method uses gradient vector flow (GVF) snake [9, 10] for ICH segmentation, slice by slice. It is divided in two main tasks: first created the initial snake using a spline function (to obtain an approximation of ICH contour), and second the initial snake is deformed to produce the final segmentation.

The following algorithm described the method:

Algorithm 4. Manual Method

1: Select slice *I(n)*
2: Select Query Object
        Extract the ICH contour (*CTn*). (Using spline)
3: GVF snake deformation (*CTn*).

This method was designed (as control method) to produce perfect segmentation patterns which were used to validate semiautomatic methods.

3   Results

We have developed a set of three methods for object segmentation and tracking: 3D mathematical morphology based method (3DMM), similarity based method (SBM) and manual based method. These methods were applied successfully for segmentation and tracking of spontaneous ICH from CT head images. The algorithm prototypes were implemented in MATLAB. These prototypes were validated by medical researchers in a representative dataset of 36 CT head images patient studies. Manual method was used as the control method to produce perfect (correct) segmentation patterns (see Fig.3). The performance of the semiautomatic methods was 83.3%, 30 CT patient studies were segmented and tracked correctly. Both methods do not work correctly in 6 CT patient studies (where the variation in the ICH shape among continuous slices was very high). Despite similar results were found concerning precision and robustness in 30 CT patient studies; some differences were revealed in relation with user intervention, processing time and precision. The 3DMM has the
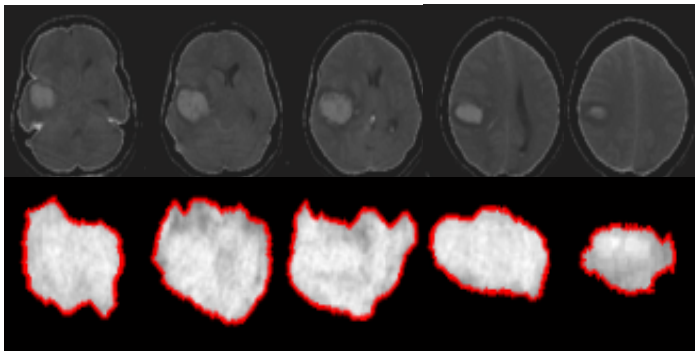
Fig. 3. Manual method results
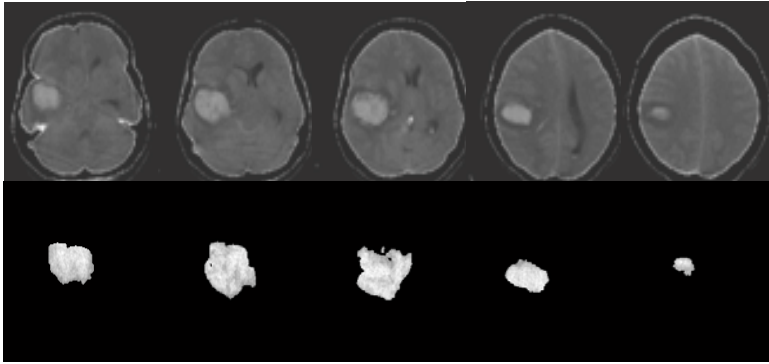
Fig. 4. Semiautomatic 3D mathematical morphology method results
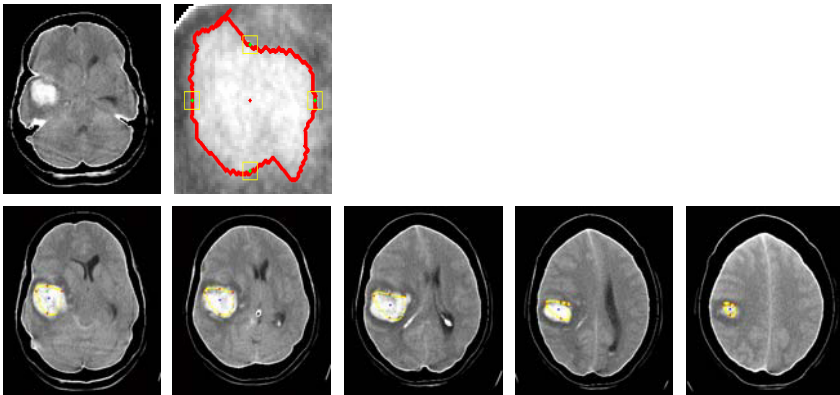
Fig. 5. Similarity method results. From top to bottom and left to right: First ICH slice, ICH query, ICH segmentation and tracking.

advantage to require the least user intervention and processing time, but it has the drawback to be the least precise (see Fig.4). SBM needed more user intervention and more processing time, but segmentation and tracking results achieved were more precise compared with 3DMM (see Fig.5).

4   Conclusion

In this paper we proposed a set of three methods for object segmentation and tracking. Two of these methods can be carryout in a semiautomatic way and one in a manual way (control method). These methods were applied successfully for segmentation and tracking of spontaneous ICH from CT head images. The efficiency of semiautomatic methods was confirmed on a representative dataset 36 patient studies, where these were capable to segment and track correctly the ICH in 30 patient studies (83.3%). Compared with other approaches devoted to ICH segmentation [2, 3, 4, 11] our

approach demonstrated similar or less computational complexity. The algorithms developed will be easily extended, with the corresponding adaptations, to solve others object recognition problems related or not with the medical image analysis area.

Acknowledgments

References

1. Malkoff, A.E.-M.M.D.: Intracerebral Hemorrhage. The Internet Journal of Emergency and Intensive Care Medicine 5(1) (2001)
2. Cosic, D., Loncaric, S.: Computer System for Quantitative Analysis of ICH from CT head Images. In: 19th Annual International Conference of IEEE Engineering in Medicine and Biology Society, Chicago, USA (1997)
3. Loncaric, S., Dhawan, A.P., Cosic, D.: Quantitative intracerebral brain hemorrhage analysis. In: SPIE Medical Imaging, San Diego, USA (1999)
4. Majcenic, Z., Loncaric, S.: CT Image Labeling Using Simulated Annealing Algorithm. In: IX European Signal Processing Conference, Island of Rhodos, Greece (1998)
5. Liang, J., McInerney, T., Terzopoulos, D.: United Snakes. IEEE Trans. Medical Image Analysis 10, 215–233 (2006)
6. Falcão, A.X., Udupa, J.K., Miyazawa, F.K.: Ultra-fast user-steered segmentation paradigm: live-wire-on-the-fly. IEEE Trans. Medical Imaging 19(1), 55–62 (2000)
7. Llerena, Y.: Técnicas para el almacenamiento y recuperación de información gráfica en bases de datos de imágenes. In: CEIS, ISPJAE: Habana, Cuba (2003)
8. Fuertes, J.M.: Recuperación de Imágenes en bases de datos a partir del color y la forma, in E. T. S. de Ingeniería Informática. 1999, Universidad de Granada: Granada.
9. Xu, C., Prince, J.L.: Gradient Vector Flow. A New External Force for Snakes. In: IEEE Conf. on Comp. Vision Patt. Recog. Comp. Soc. Press, Los Alamitos (1997)
10. Xu, C., Prince, J.L.: Snake, shapes, and gradient vector flow. IEEE Trans. Image Processing, 359–369 (1998)
11. Majcenic, Z., Loncaric, S.: CT Image Labeling Using Simulated Annealing Algorithm. In: IX European Signal Processing Conference (1997)

Efficient Rotation-Discriminative Template Matching

David Marimon and Touradj Ebrahimi

Ecole Polytechnique Fédérale de Lausanne (EPFL)
CH-1015 Lausanne, Switzerland
{david.marimon,touradj.ebrahimi}@epfl.ch

Abstract. This paper presents an efficient approach to rotation discriminative template matching. A hierarchical search divided in three steps is proposed. First, gradient magnitude is compared to rapidly localise points with high probability of match. This result is refined, in a second step, using orientation gradient histograms. A novel rotation discriminative descriptor is applied to estimate the orientation of the template in the tested image. Finally, template matching is efficiently applied with the estimated orientation and only at points with high gradient magnitude and orientation histogram similarity. Experiments show a higher performance and efficiency as compared to similar techniques.

Keywords: template, matching, rotation, gradient, histogram.

1 Introduction

Visual matching consists in comparing the visual information extracted from an image patch with the same type of information extracted from another image. Applications that use visual matching are related to region recognition, for instance, object tracking [1,2,3].

Existing techniques can be divided into two categories: trained and non-trained. For the first group, classifiers are trained with a test set of positive and negative patch examples. Research is concentrated on the data set and the classification techniques. These techniques provide an excellent compromise between speed and performance at run-time [4]. However, the time consumed to gather or generate the training data and to train the classifier is generally high. For the second group, attention is paid on the description of the information rather than in the training data or the classification scheme used. Most researchers have focused on descriptors and measures that are robust or even invariant to viewpoint and/or illumination distortions [5]. In this case, descriptors are generally built from a single instance of the patch to recognise. The drawback of such invariance is often a higher computational cost during the matching process.

In this paper, we concentrate on this second category and target fast computation environments such as tracking applications. For this goal, we propose a rotation-discriminative patch descriptor and an efficient hierarchical search strategy divided in three steps. First, similar gradient magnitude is exhaustively

searched within the image. The most similar points are sorted out. Second, the orientation gradient histogram is matched at those points providing a measure of similarity, together with an estimate of the rotation that the patch has undergone. Again, only the most similar points are kept. Finally, template matching is performed at those points by computing the Normalised Cross Correlation (NCC) between the intensity neighbourhood of the point in the image and the patch rotated according to the orientation estimated in the previous step.

2   Related Works

This section takes a more detailed look into non-trained matching techniques related to the proposed method. The matching process is done by comparing the descriptor of a patch with the descriptors obtained at different locations in an image. This description determines in general the robustness of a recognition process facing viewpoint and illumination changes. Consequently, most researchers concentrate their efforts on obtaining invariant descriptors. The reader can find a comparison of descriptors in [5]. Among those descriptors and the related recognition strategies, some have been chosen according to their relation to the method proposed here, for more in depth explanation.

Two descriptors have been used extensively for recognition purposes: templates and distributions. *Templates* are ordered arrays of the pixel values of an image region and have two main advantages. First, the simplicity of construction of this descriptor. Second, that the spatial information of the region is maintained. The drawback is the high sensitivity to viewpoint and illumination changes. Several improvements of template matching techniques exist in literature, either concentrating in illumination changes [1] or also in geometrical variations [2]. *Histograms*, are arrays that model the true distribution by counting the occurrences of pixel values that fall into each bin (range of values). Different information can be used for histogram descriptors, e.g. gray-scale, colour [6,3], and gradient [7]. Histograms have opposite advantages and drawbacks when compared to templates. In other words, histograms loose spatial information while viewpoint invariance can be achieved by construction. Several attempts at combining spatial and distribution information exist, e.g., [8,6,3,7]. Among them, we emphasise a convex monotonic decreasing kernel [3] that weights the contribution of pixels to the histogram. This kernel lessens the weight of peripheral pixels which are the least reliable, being often affected by occlusion, background and viewpoint changes. Also relevant is the use of spatial distribution of gradient histograms achieving high viewpoint invariance [7].

The strategy to locate and match regions inside an image varies depending on the application and often also on the complexity of the descriptor. In applications such as *point correspondence* [7], only locations with high repeatability are considered. Once the detection of possible candidates (usually a large amount of points) in each image is performed, a pair-wise match has to be set. In *line-search* matching, the goal is to iteratively maximise the similarity between the patch and different points of an image. At each iteration, a new position sensed

to increase the similarity is found using, for instance, gradient information [3]. In *window-search* (or exhaustive) matching, the similarity is computed at each point in a test image. As the computational power needed is proportional to the size of the image, it is often applied only when the descriptor is computed rapidly or the size of the image is relatively small [1].

Examples of fast rotation invariant template matching with an exhaustive search are [6, 9]. Fredriksson et al. [6] use an orientation invariant descriptor (colour histogram), to locate points with high probability of match. Although this method is faster than cross correlation by FFT, histograms are not efficiently computed in this work. Ullah et al. [9] presented a two step strategy. First, orientation code histograms (OH) are used to estimate the orientation of a patch in each point of an image. Second, orientation code matching (OCM) at the right orientation is applied only to the best histogram matches. This independent work differentiates from the method proposed here in two main contributions. First and most important, the OC is built only upon the extracted patch at a single orientation achieving less invariance to rotations than our descriptor. Second, that the processing time needed to produce a match is much higher (see Sect. 4).

3   Proposed Method

The problem that we are tackling is template matching of patches that have undergone rotations. A straight approach to this problem would be to generate a number of rotated versions of a patch and to correlate them at each point of the tested image. This window matching process has however a high computational cost. Instead, we propose to estimate first which rotated version has the highest probability of being the adequate to maximise the level of correlation. This is done by comparing the orientation gradient histogram of the patch and that of the neighbourhood extracted at several points in the image. In order to perform most scan operations rapidly we take advantage of the integral image (running sum of image) [4] and the integral histogram (running sum of bins) [10]. In this section, the descriptor used for the recognition of a patch and the proposed matching are detailed.

3.1   Region Description

Gradient information is chosen to generate the descriptor of a patch. One of the reasons lies on the little sensitivity of the gradient to illumination changes, which is one of the problems that recognition has to deal with. As described in Sect. 1, another major problem to tackle is viewpoint invariance. We propose a descriptor that deals with this problem concentrating on rotation robustness and, at the same time, provides orientation information of the region it describes.

Let us first analyse the behaviour of the gradient. From a theoretical point of view, the gradient has a continuous response to a continuous and derivable function. Suppose that a gradient orientation histogram of N bins is computed from a patch $\mathbf{P}$. In this case, a rotation of the patch by δ degrees changes the

values in the histogram. In particular, when $\delta = n \cdot 360/N$ where $n \in \mathbb{Z}$, the histogram would be exactly equal to a perfect shift, and the shift in bins would be equal to n. However, this ideal case is not fulfilled in reality.

Following the observation that histograms change with different orientations, we propose to generate rotated versions of a patch and, from these versions, create a single histogram that can deal with rotations. As mentioned before, orientation histograms repeat approximately their shape every $\Delta = 360/N$ degrees. This can be exploited by aligning the histograms of versions rotated exactly by $k\Delta$ with $k \in \mathbb{Z}$.

The histogram descriptor is obtained as explained next. Firstly, N rotated versions of the patch $\mathbf{P}$ to be matched are pre-computed with an angle of rotation of $n\Delta$ degrees (for $n = 0, .., N-1$) where N is the number of bins. These versions are cropped so as to eliminate additional pixels introduced by the rotation, leading to a vector of rotated versions of the patch $\overrightarrow{\mathbf{P}}_i$, where i indexes the vector. Secondly, the gradient of each of these versions is computed at each point (x, y) as follows

$$
\begin{aligned}
dy(x,y) &= \overrightarrow{\mathbf{P}}_i(x, y+1) - \overrightarrow{\mathbf{P}}_i(x, y-1) \\
dx(x,y) &= \overrightarrow{\mathbf{P}}_i(x+1, y) - \overrightarrow{\mathbf{P}}_i(x-1, y) \\
\nabla_m(x,y) &= \sqrt{dy(x,y)^2 + dx(x,y)^2} \\
\nabla_\theta(x,y) &= \arctan(dy(x,y), dx(x,y)),
\end{aligned}
\tag{1}
$$

where $\arctan(a, b)$ is a function that returns the inverse tangent of $\frac{a}{b}$ in a range $[0, 2\pi]$, ∇_m is the magnitude and ∇_θ is the orientation of the gradient. Then, ∇_θ is quantised in N bins. In order to compact the statistical description of the patch and to reduce the effect of noise, the contribution of each point in $\nabla_\theta(x, y)$ to the corresponding bin is weighted by its magnitude $\nabla_m(x, y)$ (similar to the approach in [7]). It is desirable that the weight of the peripheral pixels is lessened. However, applying a kernel (as presented in [3]) is not possible with the integral histogram approach. We approximate the effect of the kernel by giving double weight to the central part of the patch. Finally, the global histogram of the patch is the mean obtained with the N histograms aligned according to their rotation. Fig. 1 shows an example for 16 bins with the original patch and its rotated versions with the corresponding histogram aligned accordingly.

This average of rotated versions gives a robust descriptor when the rotation of the image is around $n\Delta$ degrees. It could be argued that for non-integer bin-wide angles higher variations will occur. However, experiments shows that, with enough bins, this descriptor is reliable even around $n\Delta + \Delta/2$ degrees (see Sect. 4).

The final region descriptor is composed of the global histogram $\tilde{\mathbf{h}}$, its variance σ^2, its norm and the rotated versions of the template. Our experimentation has shown that using the variance in the matching process enhances the performance.

$$
f(\mathbf{P}) = \left[\tilde{\mathbf{h}}_{\mathbf{P}}, \sigma_{\mathbf{P}}^2, \|\tilde{\mathbf{h}}_{\mathbf{P}}\|, \overrightarrow{\mathbf{P}}_0, \ldots, \overrightarrow{\mathbf{P}}_{N-1} \right].
\tag{2}
$$
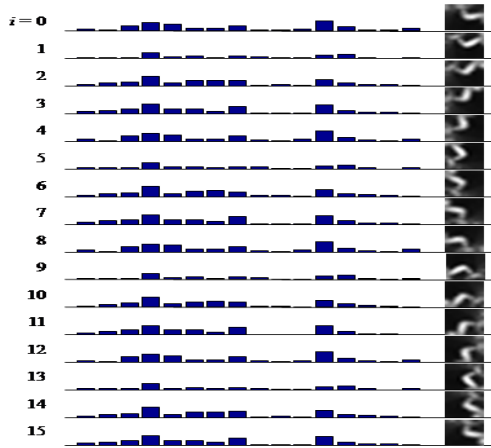
Fig. 1. Example of histogram alignment with $N = 16$ bins. Central column: histograms aligned according to their rotation; right column: corresponding original patch $(i = 0)$ and rotated versions $(i = 1, \ldots, 15)$.

3.2   Rotation-Discriminative Template Matching

This section describes the three hierarchical selection steps performed. Firstly, an exhaustive gradient magnitude comparison is performed. Secondly, the candidates with highest magnitude similarity are kept for orientation gradient histogram matching. This matching provides also an estimate of the rotation between the patch and the image. Finally, template matching is performed at the position of the most similar histograms using the rotation estimated previously.

Gradient magnitude matching. The norm of the histogram $\|\tilde{\mathbf{h}}_{\mathbf{P}}\|$ can be used as a simple feature to rapidly scan the image for similar candidates. From the construction of the histogram it can be found that $\|\tilde{\mathbf{h}}_{\mathbf{P}}\| \simeq \sum_{\mathbf{P}} \nabla_m + \sum_{\mathbf{P}'} \nabla_m$, where $\mathbf{P}'$ is the central part of the patch. Following this observation, we propose to compare this norm with each neighbourhood in a window-search strategy. This can be efficiently performed with the integral image [4] of the magnitude gradient. Given a neighbourhood $\mathbf{R}$ of a point, the measure used to compare the norm is $d_m = \exp{-\alpha \left(1 - \left(\sum_{\mathbf{R}} \nabla_m + \sum_{\mathbf{R}'} \nabla_m\right) / \|\tilde{\mathbf{h}}_{\mathbf{P}}\|\right)^2}$, where α is a factor that weights this similarity according to the variance of the histogram. More precisely, $\alpha = N/(1000 \cdot \|\sigma_{\mathbf{P}}^2\|)$. The points in the image that have a similarity $d_m > 0.9$ are kept as candidates for further matching.

In the worst case where similar magnitude is found all over the image, the number of candidates remains the same after this step. However, based on experiments, this simple selection criteria permits a reduction of the number of candidates by an average factor of 20.

Histogram matching. The gradient orientation histogram matching is applied to the candidates with similar histogram norm. Histogram can be efficiently

computed with the integral histogram approach [10]. The gradient orientation histogram of a region in the image is obtained from the contribution of the quantised $\nabla_\theta(x, y)$ weighted with $\nabla_m(x, y)$ (as for the descriptor of the patch).

The similarity between the histogram of the patch $\tilde{\mathbf{h}}_{\mathbf{P}}$ and that of each candidate is computed with a custom measure to compare orientation histograms (or, generically, circular vectors), the *Circular Normalised Euclidean Distance* (CNED). Not only the CNED measures the distance d between two vectors, but it also determines the circular shift $\hat{s}$ that corresponds to the minimal distance. Mathematically expressed $\mathbf{CNED}(\mathbf{a}, \sigma_{\mathbf{a}}^2, \mathbf{b}) = [\hat{s}(\mathbf{a}, \sigma_{\mathbf{a}}^2, \mathbf{b}) \quad d_{\hat{s}}(\mathbf{a}, \sigma_{\mathbf{a}}^2, \mathbf{b})]^T$, where $\hat{s}(\mathbf{a}, \sigma_{\mathbf{a}}^2, \mathbf{b}) = \arg\min_s d_s(\mathbf{a}, \sigma_{\mathbf{a}}^2, \mathbf{b})$ and

$$d_s(\mathbf{a}, \sigma_{\mathbf{a}}^2, \mathbf{b}) = \sqrt{\sum_{i=0}^{N-1} \frac{(\mathbf{a}(i) - \mathbf{b}((i+s) \bmod N))^2}{\sigma_{\mathbf{a}}^2(i)}}, \tag{3}$$

where $\mathbf{a}$ and $\mathbf{b}$ are vectors of length N, s is the shift that takes a discrete value between 0 and $N - 1$, mod is the modulus function, and $\sigma_{\mathbf{a}}^2$ is the variance associated to vector $\mathbf{a}$. The result of this matching is hence a similarity score $d_{\hat{s}}$ and an estimate of the orientation of the patch $\hat{s} \cdot \Delta$ for each candidate.

Template matching. The magnitude and the orientation histogram discard many unrelated points but the result is still not selective enough (as seen below in Sect. 4). The template is used as a further selection criterion. More precisely, template matching is done using a Normalised Cross Correlation (NCC) between the templates $\mathbf{R}$ centered at those points with high histogram similarity and the template of the patch $\overrightarrow{\mathbf{P}}_{\hat{s}}$.

$$NCC\left(\overrightarrow{\mathbf{P}}_{\hat{s}}, \mathbf{R}\right) = \frac{\sum\sum(\mathbf{R} - \overline{\mathbf{R}}) \cdot (\overrightarrow{\mathbf{P}}_{\hat{s}} - \overline{\overrightarrow{\mathbf{P}}_{\hat{s}}})}{\sqrt{\sum\sum(\mathbf{R} - \overline{\mathbf{R}})^2 \cdot \sum\sum(\overrightarrow{\mathbf{P}}_{\hat{s}} - \overline{\overrightarrow{\mathbf{P}}_{\hat{s}}})^2}}, \tag{4}$$

where $\overline{R}$ is the average value of R. By subtracting this mean value, the result is invariant to uniform illumination changes.

4   Experiments

This section assesses the performance of the proposed method in comparison to other similar techniques. Firstly, the techniques compared are described. Secondly, the set of test images and image patches are presented. Thirdly, the evaluation methodology is explained. Finally, results are depicted and discussed.

The matching techniques compared are: the NCC computed for all the N rotated versions at each point (we call this NCC-R), a gray-level intensity histogram matching (IHM), our own gradient orientation histogram matching (GHM) but computed exhaustively in the image (this is, without magnitude pre-sorting), the technique presented in [9] (OH+OCM), and the final correlation result of our method. In order to do a fair comparison with the IHM, a

Fig. 2. Original images used for the experiments. Average size: 300x225 pixels.

N-bin histogram of the intensity values of each rotated version is computed for each patch. This gives N histograms which are averaged bin-by-bin into a single intensity histogram describing the patch. Moreover, the central part of each histogram is given more weight as for $\mathbf{h_P}$ (see Sect. 3.1). The similarity measure used in this case is the Euclidean distance.

The set of images used for testing is shown in Fig. 2. The first two images (top-left) are custom whereas the other six images are taken from the Visual Geometry Group database [11].

There is one key parameter in the method: the number of bins N in the histogram. This number determines the value of $\Delta = 360/N$ and hence the performance of the method. More concretely, the whole matching is expected to work better for rotations around $k\Delta$ than around $k\Delta + \Delta/2$ (with $k = 0, .., N-1$). Experiments are run on 10, 16 and 20 bins to give an approximate idea of a lower and upper performance bounds. The images are rotated 20 and 70 degrees for a histogram of 10 bins ($\Delta = 36^o$), and 10 and 70 degrees for both 16 bins ($\Delta = 22.5^o$), and 20 bins ($\Delta = 18^o$). These angles correspond to almost best and worst case scenarios for each histogram length.

For each one of the original images, a set of patches is extracted. Their sizes range from 10x10 to 20x20 pixels, which is a common range in related research. Around 20 patches per image are extracted with the Harris corner detector [12]. The main reason behind the choice of this point detector is that patches have more relevant texture information in this case.

The purpose of the compared methods is to find matches. A correct match is found when a point with high similarity coincides with the ground truth. This idea is translated into the concept of *true positive* and of *false positive* in the opposite case. The performance of matching technique can be given by these two values. More precisely, the higher the number of true positives and lower the number of false positives, the better is the result.

The level of similarity that determines a match (or positive) is given by a range, i.e. maximum to minimum similarity, which is not the same for all the considered techniques. Nevertheless, it is possible to find a range that varies

equivalently. In order to find this equivalence, the values of each similarity map are taken, independently, in descending order (highest to lowest similarity) regardless of the value itself. An equivalent level of similarity is found in this case by parsing each list of values. The true positives and false positives can then be defined mathematically. Assume that $d(f_1(a), f_2(b))$ is the similarity between two descriptors $f_1(a)$ and $f_2(b)$ of the respective regions a and b. Given an image $\mathbf{I}$, a rotated version $\hat{\mathbf{I}}$, a patch $\mathbf{P}$ extracted from $\mathbf{I}$ at $(x_{\mathbf{P}}, y_{\mathbf{P}})$, and $(\hat{x}_{\mathbf{P}}, \hat{y}_{\mathbf{P}})$ being the correspondence of $(x_{\mathbf{P}}, y_{\mathbf{P}})$ into $\hat{\mathbf{I}}$, a *true positive* is

$$\text{tp}_{\mathbf{P},\hat{\mathbf{I}},t} = \begin{cases} 1 \text{ if } \exists (x,y) \in \mathbf{G} \mid d(f_1(\mathbf{P}), f_2(\hat{\mathbf{R}}_{x,y})) > t \\ 0 \text{ otherwise,} \end{cases} \tag{5}$$

and conversely, a *false positive* is

$$\text{fp}_{\mathbf{P},\hat{\mathbf{I}},t}(x,y) = \begin{cases} 1 \text{ if} (x,y) \notin \mathbf{G} \mid d(f_1(\mathbf{P}), f_2(\hat{\mathbf{R}}_{x,y})) > t \\ 0 \text{ otherwise,} \end{cases} \tag{6}$$

where $t \in [\max d(f_1(\mathbf{P}), f_2(\hat{\mathbf{R}}_{x,y})), \min d(f_1(\mathbf{P}), f_2(\hat{\mathbf{R}}_{x,y}))]$ and $\mathbf{G}$ is the region $\{\hat{\mathbf{I}}(x,y)|x = \hat{x}_{\mathbf{P}} \pm 1 \text{ and } y = \hat{y}_{\mathbf{P}} \pm 1\}$. A 1 pixel neighbourhood is set to account for sub-pixel location after the image transformation.

The response of each matching method for the best 500 matches is depicted in Fig. 3. The NCC-R indicates a great performance almost independent of the number of candidates. This shows the high selectivity of this kind of map. In the case of the IHM, rotation invariance is evidenced by very similar results throughout the different cases. A poorer selectivity is shown by the GHM as a large number of false positives is obtained in order to get a high probability of having a true positive. The OH+OCM [9] has lower performance probably due to its non-invariant nor robust descriptor. Using only a single version to build the histogram is not enough to effectively face the variations in the histogram due to rotations. The results of the GHM are greatly improved when used as an input for the further template matching step of our method (especially visible as the number of bins grows). Furthermore, the proposed descriptor and similarity measure achieve the desired rotation discrimination and hence accurate matching.

Computational complexity. The efficiency of these methods is contrasted here with the processing time needed to produce a match. Table 1 shows this time (averaged for the patches in the test set) when computed with a Pentium M Processor at 1700 MHz. As it can be seen, the slowest algorithm is the OH+OCM. The main reasons are the circular mask used for matching and, consequently, the impossibility of using the integral histogram approach. The NCC uses the integral image as in [1]. Despite this fast matching implementation, it can be seen that comparing each rotated version of the template is inefficient. The estimation of the orientation in the histogram matching step drastically palliates this inefficiency. Moreover, the hierarchical selection proposed in our work enables a processing time almost as fast as the most simple and efficient
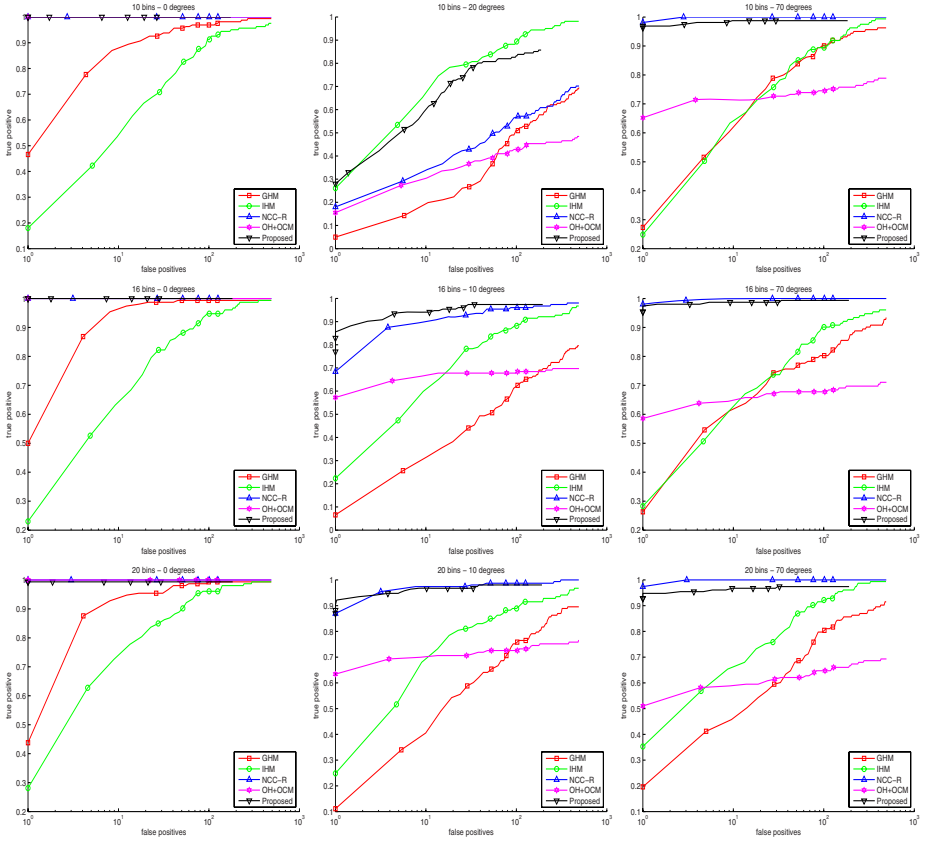
Fig. 3. Mean true positive (vertical axis) and false positives (horizontal) among all the patches. Number of bins: 10 (top), 16 (middle) and 20 (bottom). Rotation angle: 0 degrees (left), $\sim k\Delta + \Delta/2$ (central) and $\sim k\Delta$ (right).

Table 1. Average processing time for a single patch

	10 bins [s]	16 bins [s]	20 bins [s]
OH+OCM	4.4776	4.7115	4.9312
NCC-R	0.9001	1.2506	1.5235
GHM	0.4311	0.8816	1.3014
Proposed method	0.1773	0.2028	0.2584
IHM	0.1085	0.1275	0.1491

strategy, which is the IHM (implemented with the integral histogram). It should be pointed out that reducing the number of candidates would further reduce the computational cost.

5   Conclusions

An efficient method to perform rotation discriminative template matching has been presented. This is achieved with an orientation histogram matching followed by template matching. The main contributions of the method are a rotation-discriminative descriptor and the efficient matching strategy. Experimentation shows that our results are as good as performing NCC of each rotated version of a template but with an average speed up factor of six. In addition, performance and efficiency of our technique is superior to the most similar technique, namely, the OH+OCM [9]. Future path of research will focus on analysing the dependance of the method on the texture information available in the patch.

Acknowledgements

References

1. Lewis, J.: Fast template matching. Vision Interface, 120–123 (1995)
2. Hager, G., Belhumeur, P.: Real-time tracking of image regions with changes in geometry and illumination. In: Computer Vision and Pattern Recognition (CVPR), pp. 403–410 (1996)
3. Comaniciu, D., Ramesh, V., Meer, P.: Kernel-based object tracking. IEEE Trans. on Pattern Analysis and Machine Intelligence 25(5), 564–577 (2003)
4. Viola, P., Jones, M.: Rapid object detection using a boosted cascade of simple features. In: Computer Vision and Pattern Recognition (CVPR). vol. 1, pp. 511–518 (2001)
5. Mikolajczyk, K., Schmid, C.: A performance evaluation of local descriptors. IEEE Trans. on Pattern Analysis and Machine Intelligence 27(10), 1615–1630 (2005)
6. Fredriksson, K., Ukkonen, E.: Faster template matching without FFT. In: Intl. Conf. on Image Processing (ICIP). vol. 1, pp. 678–681 (2001)
7. Lowe, D.: Distinctive image features from scale-invariant keypoints. Intl. Journal of Computer Vision 60(2), 91–110 (2004)
8. Haralick, R., Shanmugam, K., Dinstein, I.: Textural features for image classification. IEEE Trans. on Systems, Man and Cybernetics 3(6), 610–621 (1973)
9. Ullah, F., Kaneko, S.: Using orientation codes for rotation-invariant template matching. Pattern Recognition 37(2), 201–209 (2004)
10. Porikli, F.: Integral histogram: a fast way to extract histograms in cartesian space. In: Computer Vision and Pattern Recognition (CVPR). vol. 1, pp. 829–836 (2005)
11. Visual Geometry Group, Robotics Research Group, Department of Engineering Science, University of Oxford, http://www.robots.ox.ac.uk/~vgg/data.html
12. Harris, C., Stephens, M.: A combined corner and edge detector. In: Alvey Vision Conf. pp. 147–151 (1988)

Texture Classification Through Combination of Sequential Colour Texture Classifiers

Francesco Bianconi[1], Antonio Fernández[2], Elena González[2],
and Fernando Ribas[3]

[1] Università degli Studi di Perugia, Dipartimento Ingegneria Industriale
Via G. Duranti 67 - 06125 Perugia, Italia
`bianco@unipg.it`
[2] Universidade de Vigo, Departamento de Diseño en la Ingeniería
E.T.S.I.I. - Campus Universitario, 36310 Vigo - España
{`antfdez,elena`}`@uvigo.es`
[3] Universidade de Vigo, Departamento de Física Aplicada
E.U.I.T.I. - Torrecedeira 86, 36208 Vigo - España
`fribas@uvigo.es`

Abstract. The sequential approach to colour texture classification relies on colour histogram clustering before extracting texture features from indexed images. The basic idea of such methods is to replace the colour triplet (RGB, HSV, Lab, etc.) associated to a pixel, by a scalar value, which represents an index of a colour palette. In this paper we studied different implementations of such approach. An experimental campaign was carried out over a database of 100 textures. The results show that the choice of a particular colour representation can improve classification performance with respect to grayscale conversion. We also found strong interaction effects between colour representation and feature space. In order to improve accuracy and robustness of classification, we have tested three well known expert fusion schemes: weighted vote, and a posteriori probability fusion (sum and product rules). The results demonstrate that combining different sequential approaches through classifier fusion is an effective strategy for colour texture classification.

Keywords: Classifier fusion, Colour texture classification.

1 Introduction

Texture analysis is recognized as a key point in the development of artificial vision systems. Within texture analysis, classification is a major research topic, due to the numerous applications in areas like medical imaging, remote sensing, quality control and others. Texture classification techniques are very attractive for industrial applications, especially in those situations where it is important to group products in lots according to the criterion of "same visual appearance". In many industrial areas there is a growing interest in systems capable of performing such kind of tasks automatically.

Texture classification involves two major processes: feature extraction and label assignment. The whole formed by these two building blocks is usually referred

to as an *expert*. It is commonly accepted that substantial gain in classification performance can be obtained by combining the results of individual experts [1,2]. In this work we adopted different combination schemes for sequential colour texture classification. The most innovative contributions of this paper are: on the one hand, the use of colour indexing methods that have not been implemented yet in colour texture classification by sequential approaches, and, on the other hand, the combination of sequential colour texture classifiers by classifier fusion.

The remainder of the paper is organized as follows: section 2 describes the colour indexing approach to texture classification. Feature spaces and classifiers used in this work are described in section 3. Combination of experts is detailed in section 4. The experimental activity is described in 5 and its results are presented and discussed in section 6. Final conclusions are reported in section 7.

2   Colour Representation

Several attempts have been made to incorporate colour and texture features during the last years. Up to now, there has been no general consensus about the best way to combine these two properties. It is widely accepted that taking into account colour in texture classification can provide additional information [3]. However some authors argue that colour and texture have to be regarded as separate phenomena [4]. According to Palm [5], the approaches to combine colour and texture can be grouped in parallel, sequential and integrative approaches. In the *parallel* approach, textural features extracted from the luminance plane are considered together with pure chrominance features. *Sequential* methods involve colour histogram clustering before extracting texture features from indexed images. *Integrative* models characterize a texture through spatial interaction within each color plane and between different colour planes.

In this paper we focus on sequential methods. The basic idea is to replace the colour triplet (RGB, HSV, Lab, etc.) by a scalar value, which represents an index of a colour palette. This is usually referred to as *colour indexing*. The selection of a particular technique for colour histogram clustering should be done carefully, since it strongly influences the ability of the features extracted from the indexed images to describe colour texture, no matter the feature space

RGB   GRAY   MINVAR   COLORCUBE
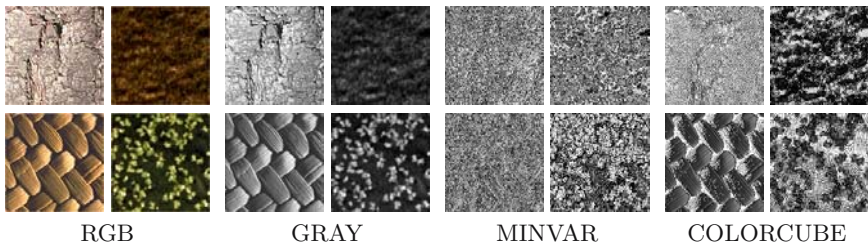
Fig. 1. From left to right: original RGB image; grayscale conversion; minimum variance quantization, colorcube colourmap mapping

considered. Although there is a vast amount of work on the integration of texture and colour in a unique model, few implementations of the sequential scheme have been reported. Song [6] proposed an approach to defect detection in colour textures based on k-means clustering and perceptual merging. More recently, Arvis [7] applied uniform quantization of the 3D colour histogram to texture classification. Uniform quantization involves dividing the color cube into a number of equal-sized boxes. The effects of representing the original images through different colour spaces as well as the effects of varying the number of colour indices have been studied in [8].

Herein we adopted the sequential approach to colour texture analysis, also referred to as chromato-spatial approach. In addition to the classical grayscale conversion, we propose *minimum variance quantization* and *colorcube colourmap mapping* as colour indexing techniques. Different colour representations are likely to produce diverse descriptions of textural data, and thus it makes sense to integrate them through classifier fusion. One can easily realize from figure 1, that the transformed images look significantly different from the original RGB images. Nevertheless, textural data are not lost: they are rather stored in a different way, as it comes out from the results shown in section 6. Based on such idea, we integrated colour indexing methods together with grayscale conversion through different classifier fusion architectures.

In minimum variance quantization the RGB color cube is recursively subdivided into smaller volumes of different sizes (not necessarily cubes). The size of each cluster depends on the distribution of colours in the image [9]. In contrast, colourmap mapping uses a predefined colourmap. Each pixel of the indexed image is then assigned the index of the cluster that contains the colour of the pixel. Applying minimum variance quantization to each image separately does not seem a promising approach, since the meaning of the resulting indices would change from one image to another. Instead, we compute the minimum variance colour map by quantizing the colour distribution of the whole image database (fig. 2). On the other hand, we have chosen Matlab's *colorcube* mapping [10] since it contains as many regularly spaced colours in the RGB space as possible, and thus it can work well in the majority of the situations.

3   Classification Framework

3.1   Feature Extraction

The original RGB images have been converted to single-channel images as described in the previous section. Texture features have been extracted from single-channel images using *Coordinated Clusters Representation* (*CCR*), *Local Binary Patterns* (*LBP*) and *Gabor filters.*

CCR and LBP features represent texture through the histogram of 3x3 binary patterns [11,12]. The only difference between LBP and CCR texture models is that LBP employs a local binarization threshold while CCR uses a global one. In this work we used as binarization threshold the gray level (or colour index) which splits the entropy of the histogram of a single-channel image into two equal

parts. This technique is based on the isentropic quantization approach, which has been successfully applied in the knowledge extraction stage of the construction of fuzzy sets [13]. The dimension of the CCR and LBP feature space is 512 and 256, respectively.

Gabor features consist of the mean and standard deviation of the output of a filter bank applied to the input image. Based on the result of previous work [14,15], we adopted here a filter bank with 4 frequencies and 6 orientations. The dimension of the associated feature space is 48.

3.2   Label Assignment

Label assignment (usually referred to as *classification*), is about assigning a class label to an unknown texture. Many different approaches have been proposed in literature. For a comprehensive review readers are referred to references [16,17,18]. Herein we adopted the well known nearest neighbour approach, which assigns a pattern the class label of the nearest labeled pattern in the feature space.

4   Combination of Experts

Combination of multiple experts has recently emerged as a major topic in pattern analysis and machine intelligence. Though numerous approaches have been proposed and tested, they can be well classified in two main families: *fusion of label outputs* and *fusion of continuous-value outputs* [1,2].

In the first scenario each expert e_k returns, for each point $\mathbf{x}$ in the feature space, a class label j:

$$e_k(\mathbf{x}) = j; \qquad \begin{cases} k = 1, ..., K \\ j \in \{1, ..., n\} \end{cases} \tag{1}$$

where K is the number of experts and n is the number of classes.

In the second scenario each expert produces, for each point $\mathbf{x}$, a vector of *a posteriori* probabilities for that point to pertain to one of the possible classes:

$$e_k(\mathbf{x}) = [P_k(\omega_1|\mathbf{x}), ..., P_k(\omega_n|\mathbf{x})]. \tag{2}$$

Fusion of label outputs is usually based on some voting scheme: majority vote or weighted majority vote. In the first approach it is assumed that all the experts are of identical accuracy. In this case each expert gives the same contribution to the final decision. Weighted voting, instead, tries to give the more competent experts more power in taking the final decision. Weights are usually based on some *a priori* knowledge of experts accuracy.

Three different strategies to combine multiple experts have been considered here: weighted vote, and fusion of *a posteriori* probabilities based on sum and product rule.

4.1   Weighted Vote

For weighted vote to be applied, we need a way to estimate the reliability of each single expert. The accuracy of each expert can be evaluated through its confusion matrix [19,20]. The r_{ij}^k element of the confusion matrix represents the number of samples of class ω_i that have been classified of class ω_j by the expert e_k. In a perfect expert all the elements outside the principal diagonal of the matrix should be zero. Given the confusion matrix R_k of an expert e_k, an event $e_k(\mathbf{x}) = j$ can be described in terms of the conditional probabilities that the propositions $\mathbf{x} \in \omega_i$ are true when the event $e_k(\mathbf{x}) = j$ occurs:

$$P(\omega_i|e_k(\mathbf{x}) = j) = \frac{r_{ij}^k}{\sum_{i=1}^{n} r_{ij}^k} \tag{3}$$

In practice each event $e_k(\mathbf{x}) = j$ gives a different support (or weighted vote) to each hypothesis $\mathbf{x} \in \omega_i$, $i = \{1, ..., n\}$. The total support $S(\omega_i)$ of a proposition $\mathbf{x} \in \omega_i$ given a set of events $e_k(\mathbf{x}) = j$, $j = \{1, ..., n\}$ and $k = \{1, ..., K\}$, is simply computed as the sum of the support of each classifier:

$$S(\omega_i) = \sum_{k=1}^{K} P(\omega_i|e_k(\mathbf{x}) = j) \tag{4}$$

The vector $\mathbf{x}$ is then assigned the label with the highest support.

The confusion matrix needs to be computed before classifying. Here we estimate the confusion matrix of each classifier through cross-validation using the points of the training set.

4.2   Fusion of *a Posteriori* Probabilities

When different experts provide a posteriori class probabilities , such values can be combined in different ways to provide a label output. Despite various approaches have been proposed to this purpose, the simple *sum* and *product* rules have been recognized as reliable and robust [2,20]. A pattern $\mathbf{x}$ is assigned the label j which maximizes the sum (product) of the a posteriori probabilities provided by each expert (eq. 5 and 6).

$$j = \operatorname*{argmax}_{i \in \{1, ..., n\}} \left(\sum_{k=1}^{K} P_k(\omega_i|\mathbf{x}) \right) \tag{5}$$

$$j = \operatorname*{argmax}_{i \in \{1, ..., n\}} \left(\prod_{k=1}^{K} P_k(\omega_i|\mathbf{x}) \right) \tag{6}$$

In order to quantify a posteriori probabilities (sometimes referred to as *memberships*), it seems natural to adopt a distance-based normalized similarity measure: the less the distance between a test point and the nearest labeled neighbour, the highest the probability for that point to belong to the same class of the closest labeled point. We adopted here the following membership:

$$P(\omega_i|\mathbf{x}) = \frac{\dfrac{1}{1 + d(\mathbf{x}, \overline{\mathbf{x}}_i)}}{\displaystyle\sum_{j=1}^{n} \dfrac{1}{1 + d(\mathbf{x}, \overline{\mathbf{x}}_i)}} \tag{7}$$

where d is a generic distance function, and $\overline{\mathbf{x}}_i$ is the pattern of class ω_i closest to $\mathbf{x}$ in the feature space. Equivalent formulations have been proposed by other authors [21,22]. In this work we adopted the L_1 (Manhattan) distance.

5   Experimental Activity

Combined classifiers have been set up using the different colour conversion approaches described in section 2 and the CCR, LBP and Gabor feature spaces. The performance of each single expert and of their combinations has been evaluated over a database of 100 texture classes (fig. 2). Each texture image has been divided into 16 sub-images, resulting in 1600 texture samples. To assess expert performance, we considered the percentage of correctly classified textures. Classification error has been evaluated by split-half validation with stratified sampling [23]. The error is averaged over 100 random partitions of data into training and validation set in order to make the estimation stable.
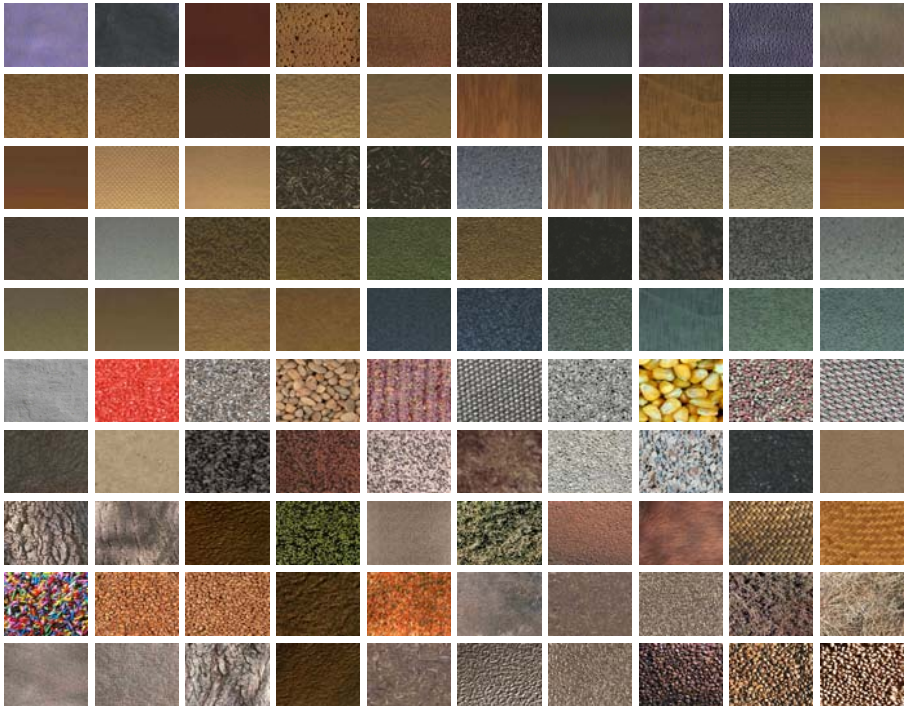
Fig. 2. Experimental dataset
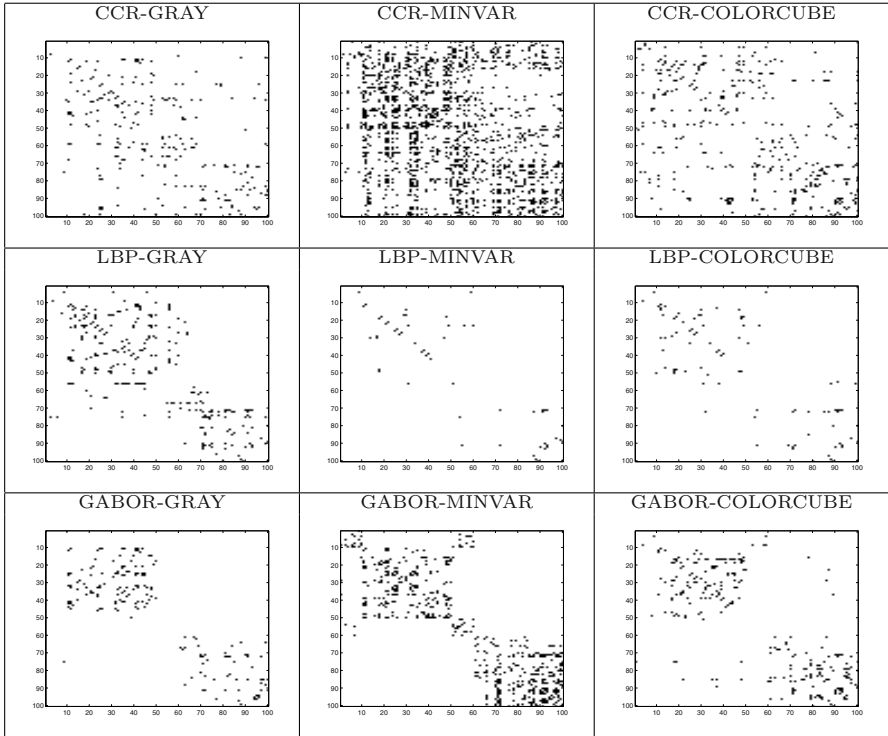
Fig. 3. Simplified representation of the confusion matrices $R_k(i, j)$ of the various classifiers. For visualization purposes the main diagonal of each confusion matrix has been set to 0 (white). Each black point indicates that the k-th classifier makes at least one mistake in classifying a patterns of class i as a pattern of class j.

6 Results and Discussion

The results (table 1) of the experimental activity are suggestive of interesting considerations. First, it appears that the choice of a particular colour representation has significant effects on texture classification. It is worth noticing that switching from grayscale conversion to minimum variance quantization improves performance in the LBP feature space (87,37 % → 97,27 %), but it drastically reduces it in the CCR feature space (87,82% → 53,07 %). Second it results that combining multiple experts provides substantial gain in classification performance. The percentage of correct classification shows significant increase either by adopting different feature spaces -as one could expect- or, more interestingly, by using different colour representations and the same feature space. The best performance is achieved when all the nine possible combinations are employed. The performance of the best combined expert approaches 100 %. Another interesting result is that classifier fusion appears a robust approach: even if we include a classifier that provides poor results (i.e. CCR+MINVAR), the global
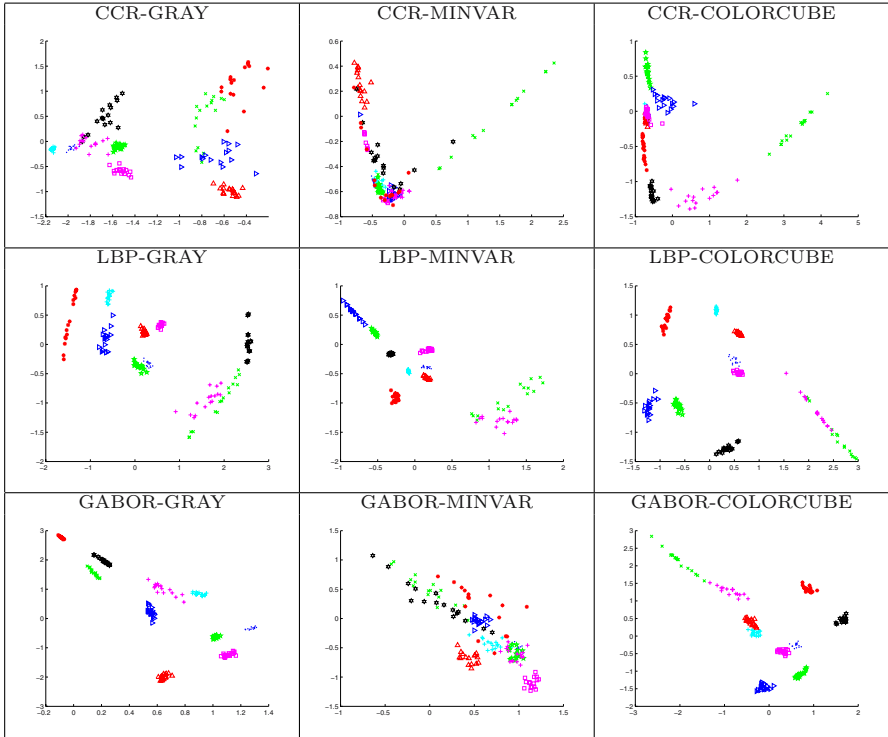
Fig. 4. Representation of the first ten texture classes of the data set of fig. 2 in the first-two principal components space

perfomance is usually better than that of the best clasifier. Only in two cases we have a very slight reduction: GRAY+MINVAR+COLORCUBE (LBP), from 97.27% to 97.23% (probability fusion, sum rule), and from 97.27% to 97.24% (probability fusion, product rule). The results obtained with the three different fusion architectures are essentially the same. Therefore the above conclusions are valid all the fusion schemes considered in this paper.

7   Conclusions

Fusion of classifiers is supposed to work well when there is a reasonable difference among the classifiers, or, in other words, when the classifiers do not make the same mistakes. It is well known that LBP, CCR and Gabor features produce different representations of textures, as we can appreciate in figures 3 and 4. In this study we have demonstrated that diverse descriptions of textural data can also be obtained through different colour representations. This fact can be exploited to improve the overall classification performance by combining multiple experts that result from different feature spaces and colour representations.

Table 1. Performance of single experts and different combinations of experts (expressed as percentage of correct classification). The numerical results corresponding to different fusion schemes are shown in different fonts. Normal font: weighted vote; *italics*: a posteriori probability fusion (sum rule); **boldface**: a posteriori probability fusion (product rule).

	CCR	LBP	GABOR	CCR+ LBP+ GABOR
GRAY	87,82	87,37	88,86	96,40 *95,82* **95,88**
MINVAR	53,07	97,27	78,84	97,88 *98,15* **97,94**
COLORCUBE	87,50	96,14	89,48	97,45 *97,57* **97,44**
GRAY+ MINVAR+ COLORCUBE	96,91 *97,04* **96,92**	97,49 *97,23* **97,24**	97,03 *97,83* **97,73**	99,35 *99,14* **99,18**

Acknowledgements

References

1. Kuncheva, L.: Combining Patterns Classifiers. Wiley-Interscience, Chichester (2004)
2. Kittler, J., Hatef, M., Duin, R., Matas, J.: On combining classifiers. IEEE Transactions on Pattern Analysis and Machine Intelligence 20(3), 226–239 (1998)
3. Drimbarean, A., Whelan, P.: Experiments in colour texture analysis. Pattern Recognition Letters 22(10), 1161–1167 (2001)
4. Mäenpää, T., Pietikainen, M.: Classification with color and texture: jointly or separately? Pattern Recognition Letters 37(8), 1629–1640 (2004)
5. Palm, C.: Color texture classification by integrative co-occurrence matrices. Pattern Recognition 37(5), 965–976 (2004)
6. Song, K., Kittler, J., Petrou, M.: Defect detection in random colour textures. Image and Vision Computing 14, 667–683 (1996)
7. Arvis, V., Debain, C., Berducat, M., Benassi, A.: Generalization of the cooccurrence matrix for colour images: application to colour texture classification. Image Analysis & Stereology 23, 63–72 (2004)
8. van den Broek, E., van Rikxoort, E.: Evaluation of color representation for texture analysis. In: Proc. of the 16th Belgian-Dutch Conference on Artificial Intelligence, Groningen (Holland) (2004)

9. Wu, X.: Color quantization by dynamic programming and principal analysis. ACM Transactions on Graphics 11(4), 348–372 (1992)
10. Various Authors: Matlab release 14. Online documentation (2004)
11. Mäenpää, T., Pietikainen, M.: Texture analysis. In: Handbook of Pattern Recognition and Computer Vision. World Scientific Publishing (2005)
12. Sánchez-Yáñez, R., Kurmyshev, E., Cuevas, F.: A framework for texture classification using the coordinated clusters representation. Pattern Recognition Letters 24(1-3), 21–31 (2003)
13. Ribas, F., Fernández, A.: Generación de etiquetas cualitativas para el modelado de variables meteorológicas en el campo de la dinámica simbólica. In: Actas del Congreso Internacional Conjunto XVI ADM - XIX INGEGRAF, Perugia (Italy) (2007)
14. Bianconi, F., Fernández, A.: Granite texture classification with Gabor filters. In: Actas del XVIII Congreso Internacional de Ingeniería Gráfica, Sitges, Spain (2006)
15. Bianconi, F., Fernández, A.: Evaluation of the effects of Gabor filter parameters on texture classification. Pattern Recognition 40(12), 3325–3335 (2007)
16. Jain, A., Duin, R., Mao, J.: Statistical pattern recognition: A review. IEEE Transactions on Pattern Analysis and Machine Intelligence 22(1), 4–37 (2000)
17. Duda, R., Hart, P., Stork, D.: Pattern Classification, 2nd edn. Wiley-Interscience, Chichester (2000)
18. Theodoridis, S., Koutroumbas, K.: Pattern Recognition, 3rd edn. Academic Press, London (2006)
19. Chen, L., Tang, H.: Improved computation of beliefs based on confusion matrix for combining multiple classifiers. Electronics Letters 40(4) (2004)
20. Xu, L., Krzyzak, A., Suen, C.: Methods of combining multiple classifiers and their applications to handwriting recognition. Man and Cybernetics 22(3), 418–435 (1992)
21. Medasani, S., Kim, J., Krishnapuram, R.: An overview of membership function generation techniques for pattern recognition. International Journal of Approximate Reasoning 19(3-4), 391–417 (1998)
22. Duin, R., Tax, D.: Classifier conditional posterior probabilities. In: Amin, A., Pudil, P., Dori, D. (eds.) SPR 1998 and SSPR 1998. LNCS, vol. 1451, pp. 611–619. Springer, Heidelberg (1998)
23. Steyerberg, E., Harrell, F., Borsboom, G., Eijkemans, M., Vergouwe, Y., Habbema, J.: Internal validation of predictive models: Efficiency of some procedures for logistic regression analysis. Journal of Clinical Epidemiology 54, 774–781 (2001)

Deterministic Component of 2-D Wold Decomposition for Geometry and Texture Descriptors Discovery

Erika Danaé López-Espinoza and Leopoldo Altamirano-Robles

National Institute of Astrophysics, Optics and Electronics,
Computer Science Department,
Luis Enrique Erro 1, 72840 Tonantzintla, México
{danae,robles}@inaoep.mx
http://ccc.inaoep.mx

Abstract. In this paper, the deterministic component of 2-D Wold decomposition is used to obtain texture descriptors in industrial plastic quality images, and hidden geometry of tree crown in remote sensing images. The texture image is decomposed into two texture images: a non-deterministic texture and a deterministic one. In order to obtain texture descriptors, a set of discriminant texture features is selected from the deterministic component. The texture descriptors have been used to distinguish among three kinds of plastic quality. The obtained texture descriptors are compared against texture descriptors obtained from the original image. With the objective to find hidden geometry of tree crown in remote sensing images, the deterministic component of the original image is analyzed. The observed geometry is compared against the modeled geometry in the literature of marked point processes.

Keywords: 2-D Wold Decomposition, Homogeneous Random Fields, Texture, Geometry.

1 Introduction

Texture analysis methods have been traditionally divided into two categories [10]. The first one, called the statistical or stochastic approach, treats textures as statistical phenomena. A textured pattern is characterized by either statistical of image pixel gray values or some stochastic model. The stochastic formulation of a texture is based on a model in which a texture is viewed as a sample of a 2-D stochastic process describable by its statistical parameters. The second category, called the structural approach, introduces the concept of texture primitives, often called textel or textons (texture element). In order to describe a texture, a vocabulary of textels and placement rules that define the exact location of each primitive in the texture are needed. The goal is to describe complex structures with simpler primitives. However, most natural textures do not fall into any of these two categories and it is difficult to classify textures by one single method. Therefore, unified models have been proposed, in which the deterministic and

non-deterministic component of a texture field is separated. The 2-D Wold-like decomposition accomplishes this task. This unified texture model proposed by Francos *et al.* [3] provides a means to analyze the stochastic and deterministic part of a texture separately. The 2-D Wold decomposition has been applied to the image retrieval [6] and for estimating and coding of texture [8]. In [5] a Hough transformation is used to detect spectral evanescent components whereas in [9] a new estimation algorithm of the evanescent field is given. This new method is based on a projection approach and requires a set of projection directions which is obtained by using Farey's series. Now current work propose a new segmentation algorithm which takes into account the deterministic component of 2-D Wold decomposition, as the image of the external field in the MRF model [4]. Moreover, in [11] are explored the properties of higher order statistics and Wold decomposition theory for the sake of finding an algorithm for 3-D texture decomposition.

In the proposed model by Francos, the texture field is assumed to be a realization of a 2-D homogeneous random field. Based on a 2-D Wold-like decomposition of homogeneous random field, the texture field is decomposed into a sum of two mutually orthogonal components: a structural or deterministic component, which results in the structural attributes of the observed realization, and a purely stochastic or purely non-deterministic component, which represents the randomness of the texture field. The deterministic component is further decomposed into a sum of two orthogonal components: a harmonic component and a generalized evanescent component. The harmonic component represents the periodic attributes of the texture, whereas the evanescent components represent directional ones. Then, the perceptual property of texture images, randomness, directional, and periodical are preserved (see Fig. 1).
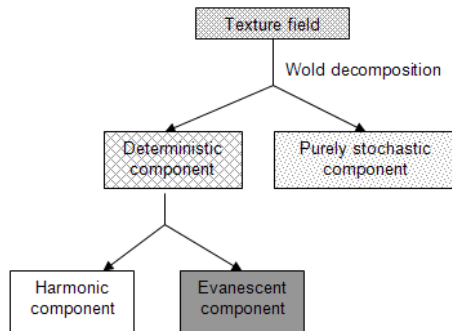
Fig. 1. Wold decomposition

Texture discrimination plays a vital role in real world image segmentation and object extraction. In order to obtain this discrimination, texture exact features have to be extracted. A good texture feature must determinate both similarities into classes and dissimilarities inter classes. In industrial applications is

frequently to classify similar textures belonging to different classes, therefore, is necessary to consider helpful texture descriptors in these classification problems.

Automatic extraction of objects from several remotely sensing images (such as aerial and satellite images) is a very important research task in pattern recognition and image understanding. Many objects in remote sensing have often some regular shape attributes, such circle, ellipse, polygon etc. and they are commonly distributed orderly and aggregated into different object groups. The automatic extraction of tree crown from remotely sensed images by means of marked point processes is reported in [7]. Perrin *et al.* model the stand as a realization of a marked point processes of ellipses or ellipsoids, whose point are the positions of the trees and the marks their geometric features. Moreover, there are other vegetation natural resources important to study in the scale of trees whose geometry is unknown e.g. mangrove.

In this paper, we are motived by Franco's model in which a texture is decomposed into constituent components allowing an analysis of the individual components, the deterministic component is used to obtain texture descriptors of three kinds of plastic quality and to find hidden geometry of tree crown in remote sensing images. The implemented algorithm is based on the harmonic field process of [3] and the evanescent field process of [5]. The obtained texture descriptors are compared against texture descriptors obtained from the original image and the observed geometry is compared against the modeled geometry in the literature of marked point processes.

2   2-D Wold Decomposition of Homogeneous Random Fields

Consider a homogeneous and regular random field $y(m,n)$, $(m,n) \in Z^2$. The 2-D Wold decomposition allows the field to be decomposed in two mutually orthogonal components [3]:

$$y(n,m) = v(n,m) + w(n,m) \tag{1}$$

where $\{v(n,m)\}$ is deterministic and $\{w(n,m)\}$ is non-deterministic. The deterministic component can be decomposed in the harmonic component $\{h(n,m)\}$ and evanescent component $\{g(n,m)\}$:

$$v(n,m) = h(n,m) + g(n,m) \tag{2}$$

In the frequency domain, the spectral distribution fuction (SDF) of $\{y(n,m)\}$ can be uniquely represented by the SDF's of its component fields:

$$F_y(\omega,\upsilon) = F_v(\omega,\upsilon) + F_w(\omega,\upsilon) \tag{3}$$

where $F_v(\omega,\upsilon) = F_h(\omega,\upsilon) + F_g(\omega,\upsilon)$, and the functions $F_h(\omega,\upsilon)$ and $F_g(\omega,\upsilon)$ correspond to spectral singularities supported by point-like and line-like regions,

respectively. Under some assumptions and approximations Francos *et al.* [3] proposed the following models:

The harmonic random field has the following representation:

$$h(n,m) = \sum_{k=1}^{P} \{C_k cos2\pi(n\omega_k + m\upsilon_k) + D_k sin2\pi(n\omega_k + m\upsilon_k)\} \qquad (4)$$

where the C_k's and D_k's are mutually orthogonal random variables, and (ω_p, υ_p) are the spatial frequencies of the kth harmonic. This component generates the 2-D delta functions of the "spectral density" (The 2-D delta functions are singular functions supported on discrete points in the frequency plane).

A model for the evanescent field $\{g(n,m)\}$, which corresponds to the RNSHP (rational non-symmetrical half-plane) defined by $(\alpha, \beta) \in O$ is given by a linear combination of fields $e(n,m)$ of the form:

$$e(n,m) = s(n) \sum_{i=1}^{I} \{A_i cos2\pi m\upsilon_i + B_i sin2\pi m\upsilon_i\} \qquad (5)$$

where $\{s(n)\}$ is a purely non-deterministic 1-D process, I is the number of evanescent components with (α, β) slope and υ_i is the frequency of the ith evanescent component.

The purely non-deterministic component is given by

$$w(n,m) = - \sum_{(0,0) \prec (k,l)} b(k,l)w(n-k, m-l) + u(n,m) \qquad (6)$$

where $\{u(n,m)\}$ is the 2-D white innovations field, whose variance is σ^2.

Further details of the Eq. 4, 5 and 6 can be found in [3].

3   The Texture Model - Implementation

In general, the analysis algorithm of Francos is based on three stages:

- First, the parameters of the harmonic field are estimated (periodic features).
- Second, the evanescent components of the texture field are estimated (global directional features).
- Finally, the parameters of the purely non-deterministic component of the texture field are estimated (random features).

The texture reconstruction is carried out by summing the images obtained by the inverse procedure to the analysis procedure. Further details of the analysis algorithm can be found in [3]. We only analyze the deterministic component of the analysis algorithm, because this component is parameterized independently of the purely non-deterministic component. The deterministic component is obtained through a global thresholding procedure, proposed in [3], which estimate the harmonic texture field, and a Hough transformation procedure proposed in [5], that estimate the evanescent components. The algorithm to obtain the deterministic component was developed in MATLAB 7.1 and the implementation details are shown in the following sections.

3.1   Harmonic Peak Detection

First, we search the presence of the harmonic components before estimating their parameters. The harmonic peaks are detected in the Fourier magnitude image. The periodogram is a frequency estimator for the unknown periodic components by choosing the frequencies of the largest and sharpest isolated peaks of the periodogram. The amplitude threshold value is established to the maximal value of the periodogram. A magnitude histogram is built over the Fourier magnitude image to establish the minimum value or cut frequency. The number of detected spectral peaks are the harmonic component and are denoted by P, see Eq. 4. The parameterization is done by evaluating the amplitude and the phase values of the texture DFT at the frequencies of the detected maxima. The process to estimate harmonic peaks is shown in Fig. 2.
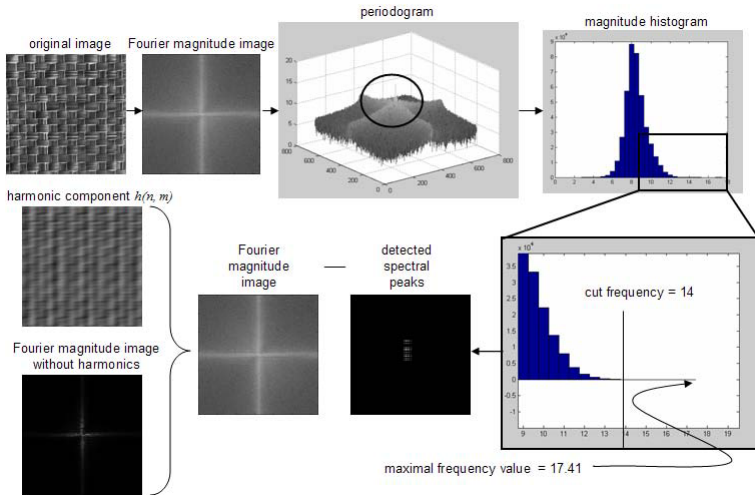
Fig. 2. Process to estimate the harmonic component. Brodatz texture D64 [1].

3.2   Evanescent Line Detection

In this case we search for the frequencies of the periodogram largest peaks such that the peaks are located in neighboring frequencies along one dimension. The Hough transformation method for line detection is used to detect the evanescent lines in the Fourier magnitude image. Prior to applying the Hough transform, the spectral values associated with the harmonic peaks should be removed. Both amplitude and phase components of the DFT are retained to parameterization. The process to estimate evanescent lines is shown in Fig. 3, where six lines are found for the Brodatz texture D64.

Finally, the deterministic component (see Fig 4) is estimated by summing the images obtained by the inverse procedure to the harmonic peaks and evanescent lines detection.
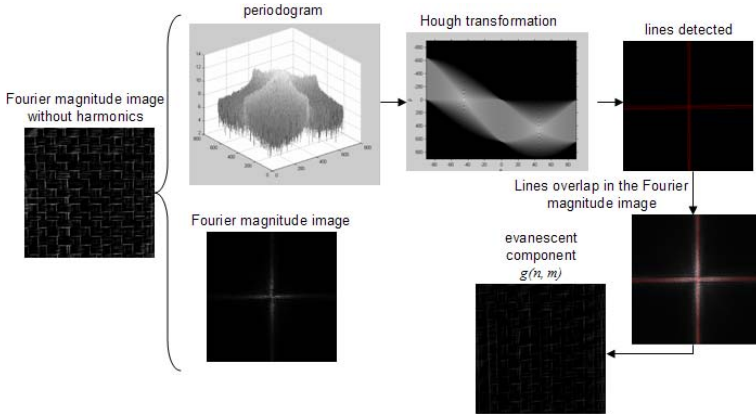
Fig. 3. Process to estimate the evanescent lines
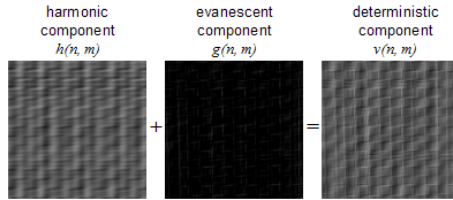
Fig. 4. Structural component of Brodatz texture D64

4 Experimental Results

The experimental results are presented in two parts: first, the deterministic component of Wold decomposition is used to obtain descriptors that discriminate among three classes of plastic quality. Second, the deterministic component is used to extract hidden geometry of trees in texture images.

4.1 Texture Descriptors

The plastic database includes 52 images of plastic quality labeled manually. The images were obtained directly from the industry. The classification error in this manually labeled data is around 40%. The three plastic quality classes are shown in Fig. 5. It can be seen that is difficult to distinguish among the three plastic quality classes because they present very similar characteristics. The database has 15 samples of class 1, 18 samples of class 2 and 19 samples of class 3. The size of the images is 640x640 pixels. For the experiments the images were converted to gray scale.

In this experiment, four texture characteristics were obtained for each image: energy, correlation, homogeneity and contrast. Each characteristic was obtained

Fig. 5. Images of three plastic quality classes. a)class 1 (3), b)class 2 (4-) and c)class 3 (4+).

in four directions (0°, 45°, 90° and 135°). Because manual classification presents high ambiguity, we follow an unsupervised approach. The four characteristics were used as texture descriptors to classify with k-means. The texture characteristics (texture descriptors) were obtained for the original images and the deterministic components. The texture descriptors obtained from deterministic component image (TD-DCI) are compared visually against texture descriptors obtained from original image (TD-OI). The obtained clusters using TD-OI and TD-DCI, are shown in Fig. 6. Graphics 6a, 6c, 6e and 6g show clustering of TD-OI in the directions 0°, 45°, 90° and 135° respectively. Graphics 6b, 6d, 6f and 6h show clustering using TD-DCI in the same directions. In deterministic component, the cut frequency determined for the harmonic component is 9.25 of amplitude, and two evanescent lines for each image were found. It can be seen in graphics that the clusters using TD-DCI are better grouped than TD-OI. Using TD-OI the cluster aren't formed. In the experiments, the classification rate using k-means with TD-DCI is 10% greater than k-means with TD-OI.

4.2 Geometry

The second experiment was carried out on aerial and satellite images. The size of the images is variable. The objective of this experiment is to relate the modeled geometry in [7] for tree crown detection with the geometry observed from the deterministic component of the Wold decomposition. In a marked point process frequently the tree crown is modeled by means of circles and ellipses. Fig. 7 shows the deterministic component obtained from the aerial image (Fig. 7b, 7f) in [7]. The found geometry is represented by circles in the same way as the modeled geometry done by Perrin (Fig. 7c, 7g). A filter to improve the contrast of deterministic component was applied. Obtaining the border of the objects or carrying out visual inspections help us to find the geometry, however, in stochastic textures the geometry is not obvious. Fig. 7d and 7h show the borders obtained from the original image. It can be seen that deterministic component is more similar to modeled geometry than borders. Fig. 8a and 8b show the found ellipses in a CIR (color infrared) image. Fig. 8d and 8f show the circles and triangles geometry found in a high-resolution satellite image.

5   Conclusions

In this paper, the deterministic component of 2-D Wold decomposition was used to obtain texture descriptors and geometry of texture fields. The implemented
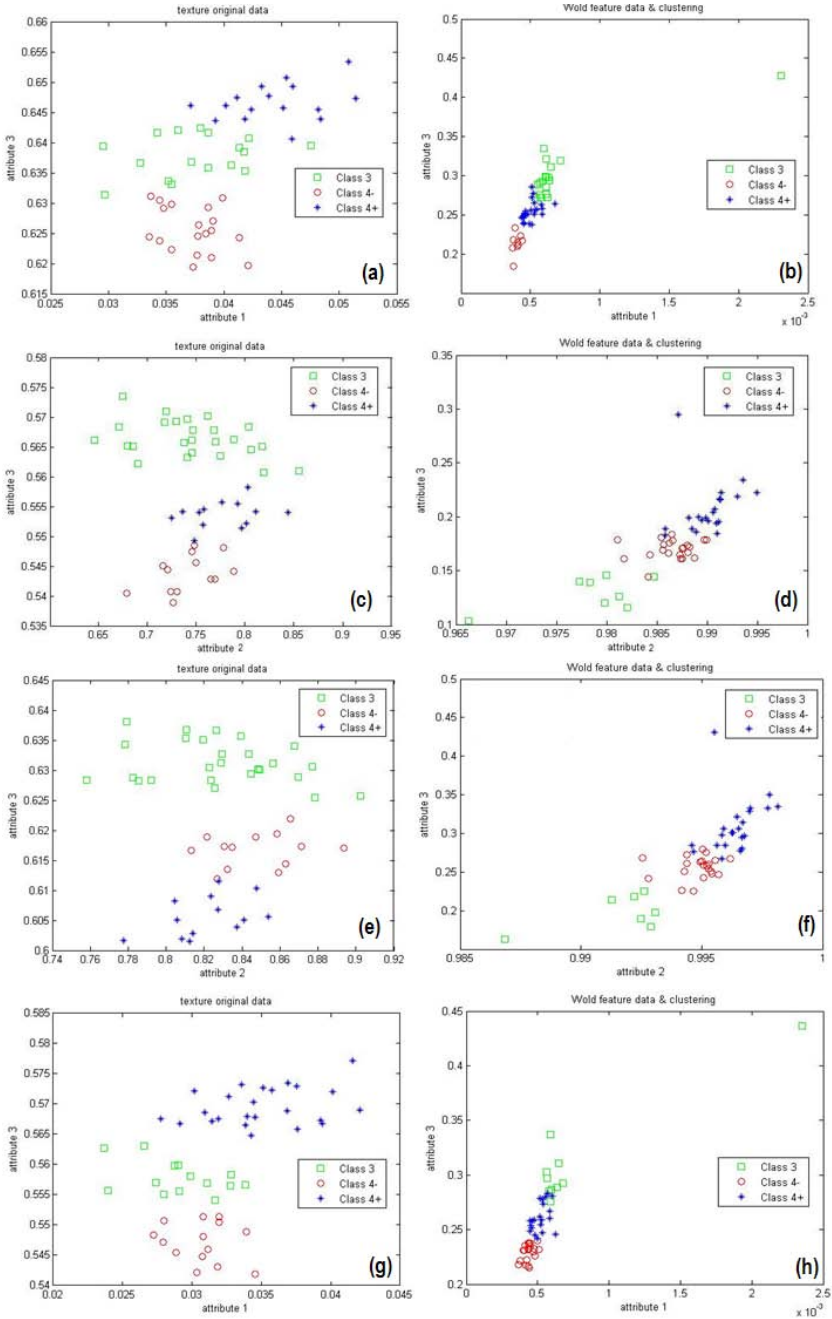
Fig. 6. Comparison of clusters in plastic images (axes x and y attributes, ∗ class 4+, ∘ class 4−, □ class 3). 6a, 6c, 6e and 6g show clusters of TD-OI in 0°, 45°, 90° and 135° respectively; 6b, 6d, 6f and 6h show clusters using TD-DCI in the same directions.
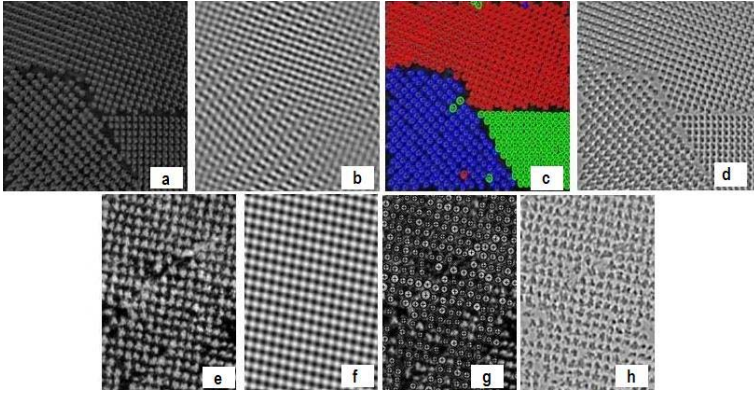
Fig. 7. Geometry: a) and e) original image, b) and f) deterministic component, c) and g) modeled geometry, d) and h) border image
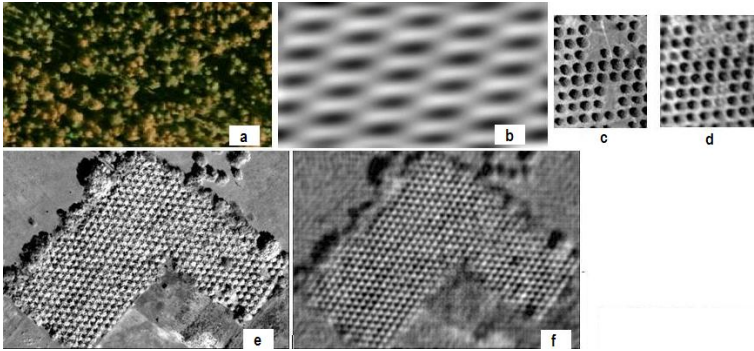
Fig. 8. Geometry for CIR and high-resolution satellite image of permanent cover (agriculture): a), c) and e) original image, b), d) and f) deterministic component

algorithm considers a global thresholding process and other processes based in Hough transformation to estimate the deterministic component. Experimental results show that texture descriptors obtained from deterministic component groups better the classes than texture descriptors from original image. As well, experimental results to find the geometry of tree crown in images show that the obtained geometry from Wold decomposition is the same geometry modeled in marked point processes. Future work involves modeling several covers as a marked point process and defining precisely the geometry obtained from Wold decomposition as the mark of the point process.

References

1. Brodatz, P.: Textures: A Photographic Album for Artists and Designers. Dover Publications, New York (1966)
2. Cross, G., Jain, A.: Markov Random Field Texture Models. IEEE Transactions on Pattern Analysis and Machine Intellige 5, 25–39 (1983)
3. Francos, J.M., Meiri, A.Z., Porat, B.: A Unified Texture Model Based on a 2-D Wold-Like Decomposition. IEEE Transactions on Signal Processing 41, 2665–2678 (1993)
4. Li, F., Peng, J., Zheng, X.: Object-Based and Semantic Image Segmentation Using MRF. EURASIP Journal on Applied Signal Processing 6, 840–883 (2004)
5. Liu, F., Picard, R.W.: A Spectral 2-D Wold Decomposition Algorithm for Homogeneous Random Fields. In: IEEE International Conference on Acoustics, Speech, and Signal Processing, vol. 4, pp. 3501–3504. IEEE Signal Processing Society, Piscataway New Jersey (1999)
6. Liu, F., Picard, R.W.: Periodicity, Directionality, and Randomness: Wold Features for Perceptual Pattern Recognition. Computer Vision & Image. In: Proceedings of the 12th IAPR International Conference on Pattern Recognition, vol. 2, pp. 184–189. IEEE Computer Society, Los Alamitos California (1994)
7. Perrin, G., Descombes, X., Zerubia, J.: 2D and 3D Vegetation Resource Parameters Assesment using Marked Point Processes. In: ICPR 2006, vol. 1, pp. 1–4. IEEE Computer Society, Washington DC USA (2006)
8. Sriram, R., Francos, J.M., Pearlman, W.A.: Texture Coding Using a Wold Decomposition Model. In: Proceedings of the 12th IAPR International Conference on Pattern Recognition. IEEE Transactions on Image Processing, vol. 3, pp. 35–39. IEEE Signal Processing Society, Piscataway New Jersey (1996)
9. Ramananjarasoa, C., Alata, O., Najim, M.: 2-D Wold Decomposition: New Parameter Estimation Approach to Evanescent Field Spectral Supports. In: EUSIPCO, vol. 2, pp. 913–916 (2000)
10. Huang, Y., Chan, K.L.: Texture Decomposition by Harmonics Extraction From Higher Order Statistics. IEEE Transactions on Image Processing 13, 1–14 (2004)
11. Stitou, Y., Turcu, F., Najim, M., Redouane, L.: 3-D Texture Characterization Based on Wold Decomposition and Higher Order Statistics. In: ICASSP, vol. 2, pp. 165–168. IEEE Signal Processing Society, Piscataway New Jersey (2005)

Robust Feature Descriptors for Efficient Vision-Based Tracking

Gerardo Carrera[1], Jesus Savage[1], and Walterio Mayol-Cuevas[2]

[1] Universidad Nacional Autonoma de Mexico(UNAM), Department of Electrical
Engineering, Bio-Robotics Laboratory
Mexico City, Mexico
[2] University of Bristol, Computer Science
Bristol, U.K BS8 1UB

Abstract. This paper presents a robust implementation of an object
tracker able to tolerate partial occlusions, rotation and scale for a variety
of different objects. The objects are represented by collections of interest
points which are described in a multi-resolution framework, giving a
representation of those points at different scales. Inspired by [1], a stack of
descriptors is built only the first time that the interest points are detected
and extracted from the region of interest. This provides efficiency of
representation and results in faster tracking due to the fact that it can
be done off-line. An Unscented Kalman Filter (UKF) using a constant
velocity model estimates the position and the scale of the object, with
the uncertainty in the position and the scale obtained by the UKF, the
search of the object can be constrained only in a specific region in both
the image and in scale.

The use of this approach shows an improvement in real-time tracking
and in the ability to recover from full occlusions.

Keywords: Object tracking, Harris detector, Speeded-Up Robust Fea-
tures (SURF), Unscented Kalman Filter.

1   Introduction

Object tracking is at the core of many interesting computer vision systems. It is
also challenging, due to the large space of object poses, perspective, illumination
and scale changes and clutter. If an object tracker is capable to successfully
solve these problems and at the same time keep the computational complexity
of the tracker as low as possible, then it could facilitate several applications
such as: security and surveillance, traffic management, augmented reality, mobile
robotics, etc.

Recent advances in object detection (e.g. [2] [3]), demonstrate the capabilities
of vision algorithms to deal with large occlusion and viewpoint changes. Usually,
they relay on the detection of key or interesting points to be used as features, and
on the building of descriptors around those points of interest. This robustness
to scale and occlusion usually translates in the expensive computation needed
by those algorithms.

There are numerous approaches to detect interest points [4] [2] [3], most of them differ on the information that the points represent, this yields to a very important issue which is distinctiveness, which means how well the points can be matched in different images. This and the repeatability of the points detected between different images of the same scene under different changes in viewing conditions, are of major concern.

In [5] it was demonstrated that the Harris detector performs well compared to other keypoint detection algorithms in terms of repeatability, but it is well known that this detector is not scale invariant, so to overcome this deficiency, the multi-resolution framework proposed by [1] is used here, where for each point detected, a SIFT-like descriptor is created at several fixed scales. This is done only once and it is computed off-line which overcomes the computational cost of computing the scale space in each frame as done in say SIFT [2] or SURF [6].

To predict scale and object position and their associated uncertainties, an estimator is used. In this case, this is an unscented Kalman filter (UKF) although other estimators are equally applicable.

The goal of this paper is to develop a fast, accurate and efficient tracker that benefits from the repeatability of the computationally expensive detectors created for object recognition and from the well established methods of estimation.

The first part of the algorithm consists of representing the target object with low-level information using interest points extracted from the ROI (see Fig. 1). These interest points are the representation of the object, the use of these points has some advantages, they are locally extracted which gives to the object a robust level of invariance to occlusion as well as to noise and illumination changes. Because the object is often moving and changing its position, it may appear different in each frame so it is important to obtain invariance to some image transformations. This paper it is focused on rotation and scale invariance.

The remainder of this article is organised into 6 parts. Section 2 describes related work, section 3 gives a brief description of the algorithm. Section 4 shows the process of object representation which consists in the detection and the description of the interest points, and describes the object tracking framework using the UKF. Section 5 shows the experiments and the results obtained and finally section 6 provides the conclusion.
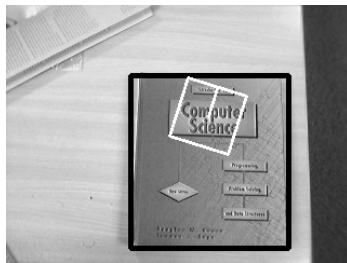
Fig. 1. Region of Interest (black rectangle) showing a single interest point (middle point inside the white rectangle)

2 Related Work

In a typical visual tracker, two components can be distinguished: 1) target or object representation and localisation, and 2) filtering and data association [7]. From the object representation point of view, amongst the wide variety of approaches adopted some employ a reduced amount of information extracted from the object, such as color [8] [9], intensity [10], interest points [11] or spatialized color histograms [12]. Some integrate different representations such as in [13]. There are also approaches that use a well described model of the object, this basis is useful when the goal is to track say solid models. These approaches are based mostly on the contour, edges or on a more detailed representation of an image curve using a parameterisation like B-splines [14]. This level of description can be complicated at best to achieve. There are however examples where this approach works well e.g. [15] [16].

In the second component of a visual tracker, the principal idea is to estimate the next state of the object, using a sequence of noisy measurements made on the system. To do this, an estimator or filter can be used. There are different filters used in tracking problems, under certain circumstances, it is assumed that an optimal solution is given by the Kalman Filter (KF) when the problem is linear, however, in a typical tracking problem there are different factors that make the problem highly not linear.

The Extended Kalman Filter (EKF) is probably the most widely used estimation algorithm for nonlinear systems, unfortunately it exhibits potential drawbacks and serious limitations. First, linearization is only reliable if the error propagation can be approximated by a linear function and can be applied only if the Jacobian matrix exists [17]. Second, the derivations of the Jacobian matrices can be complex, causing implementation difficulties. A most recent alternative is the Unscented Kalman Filter (UKF) [18], which handles the problems caused by linearization providing a mechanism for transforming the mean and covariance information and avoiding the calculus of Jacobian matrices. This estimation algorithm will be described later with more detail. Another more general class of filters are the particle filters which are based on Monte Carlo integration methods. In these filters the current state is represented by a set of randomly generated samples which are used to approximate the filtering distribution, [19] [20] [21]. An issue with particle filters is the need to evaluate and keep a relatively large number of particles and the complication of deciding which hypothesis to use to indicate the location of the object. This work uses the UKF as a good compromise but as mentioned before other estimators and filters can be incorporated.

3 Tracking Algorithm Overview

The first part of the algorithm consists in the object representation, its definition does not assume a fixed form, however, the region of the image to be tracked is delimitated by a rectangle defined by two opposite corners, this generates a

ROI where the interest points are going to be extracted. The interest points are extracted using the Harris detector and the points are not extracted in different scales. To solve this problem, the scale invariance is incorporated in the descriptor building a stack of descriptors at several scales, one for each interesting point, this idea has been proven to work effectively using SIFT descriptors for a visual SLAM system [1].

Once the interest points are extracted and matched against those detected in the first frame, the object center is calculated. It can be obtained in two different ways: the first one is by taking into account the relative coordinates of the points calculated in the first frame to the object center and the scale, the second one is calculating the homography between tracked and original template and getting its center. In the second phase of the algorithm, a UKF estimates frame by frame the center and the scale of the object. This is very important for the performance of this tracker because the interest points are only extracted from a region of the image constrained by the predicted scale covariance and the object center. The predicted scale covariance and the scale predicted are also used to find the region in the stack of descriptors where the system is going to look for possible matches, which makes the matching step computationally easier. It is expected that if the camera looses the object, the uncertainty in the scale and the position of the object will grow until the search region covers the whole image and the complete stack of descriptors in scale (see Fig. 2). If the object is "re-localised" before that moment, an efficient use of the known information would have taken place.
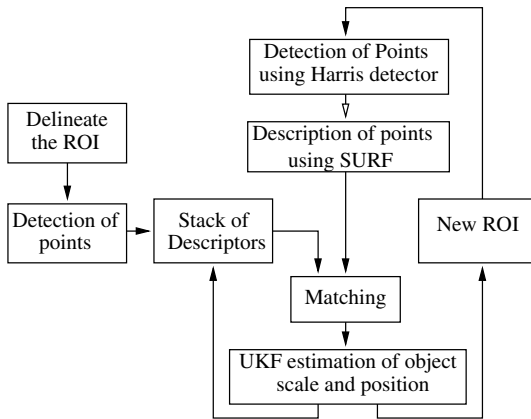
Fig. 2. Block diagram of the object tracking system

One possible problem of this approach is having too many points representing the object, making the matching step more difficult. This is solved in the next stages of the algorithm during the object tracking procedure where the interest points descriptors are built only at a fixed scale and are matched against only those descriptors between a pre-defined range of scales. The interest points description is based in SURF (Speeded-Up Robust Features) [6], which has been

proven to approximate or even outperform previously proposed schemes and the fact that it can be computed faster makes it more reliable for our system. The SURF descriptor will be described in the next section.

4   Object Representation

To extract the interest points, the Harris detector is used [4]. This detector is well known for detecting not only corners but also locations in the image where the signal changes two-dimensionally, this is achieved by using the autocorrelation function defined by (1).

$$c(x, y) = [\Delta x, \Delta y] \ M \ [\Delta x, \Delta y]^T \tag{1}$$

where Δx and Δy are shifts of small windows centered on (x, y). The matrix M denotes the intensity structure of the local neighbourhood, this 2×2 matrix is computed from image derivatives:

$$M = \begin{bmatrix} \sum_W \frac{\partial^2 I}{\partial x^2}(i,j) & \sum_W \frac{\partial^2 I}{\partial x \partial y}(i,j) \\ \sum_W \frac{\partial^2 I}{\partial x \partial y}(i,j) & \sum_W \frac{\partial^2 I}{\partial y^2}(i,j) \end{bmatrix} \tag{2}$$

where (i, j) are the index of the values in the window W over the image I. The location of the feature point is obtained by doing maximum suppression over a 3×3 region using the next function:

$$cornerness = det[M] - \alpha[trace(M)]^2 \tag{3}$$

After the interest points are extracted from the ROI, the description of the interest points is achieved using the fast descriptor coined SURF [6], which makes use of integral images [22] and Haar-wavelets responses. A point $p = (x, y)$ in an integral image $Integral(x, y)$ represents the sum of all pixels in the input image $I(x', y')$ of a rectangular region formed by the point p and the origin.

$$Integral(x, y) = \sum_{x'=0}^{x} \sum_{y'=0}^{y} I(x', y'). \tag{4}$$

The SURF algorithm makes use of the integral image to detect the interest points as well as to describe them.

After computing the integral image, the invariance to rotation is achieved by calculating the Haar-wavelets responses in x and y direction. Because of the use of the integral image, only six operations are needed to compute the response in x or y direction at any scale.

The responses are represented as vectors. To get the dominant orientation, first it is necessary to get the orientation in a sliding window covering an angle of $\pi/3$, by summing all the vectors that are within the window. The longest vector leads the dominant orientation of the feature point.

To compute the descriptor, a square region is defined centered around the feature point and oriented along the dominant orientation. This region is split into 4×4 square sub-regions. In each sub-region, regularly spaced sample points are taken and over these point, the Haar wavelets responses in x and y directions are calculated,

for simplicity they are called d_x and d_y.are also weighted with a Gaussian($\sigma = 3.3s$) centered at the feature point, this is done to achieve robustness towards geometric deformations and localisation errors.

The responses over each sub-region are summed obtaining a vector over each region. These vectors and the sum of the absolute value of the responses over each sub-region give us the total entry of the descriptor. So each sub-region will contribute to the descriptor with 4 values. The structure of the descriptor is then $D = (\sum d_x , \sum d_y , \sum |d_x| , \sum |d_y| , ...)$ where $i = 1, ..., 16$. The descriptor is turned into a unit vector to achieve invariance to contrast [6].

4.1 Multi-resolution Descriptors

Instead of using a scale-space representation to achieve scale invariance, a list of descriptors for each interest point is built at initialisation. Multiple descriptors are constructed at the first frame at different resolutions and they are saved in a stack list, this scheme is useful in two different ways: first, with this approach the scale invariance is achieved and second, an efficient use of computational resources is made. In the subsequent frames the descriptors are computed only in a fixed resolution so this list is used to seek to match those descriptors to those computed at a fixed resolution. In this article the terms resolution and scale are considered equivalent. Not only the size of the region where the descriptor is extracted is scale dependent but also the length between samples, which means that the number of samples is fixed so it is only increased or decreased the size of the window and the length of the sampling interval according to the resolution where the descriptor is going to be computed [1].

In the first frame as it is known the spatial position of the object, it is also known the object center is defined. To be able to calculate the center in subsequent frames, it can be done in two different ways: in the first one it is avoided the calculation of a transforming mapping. In the first frame it is saved for each interest point, the position (x, y) relative to the object center P_c. In the next frames it is used this measure and the scale of the object to get the object center, as it can be seen in the next equation:

$$P_c(x, y) = \frac{\sum_{i=0}^{N}(M_i(x, y)/Scale_i) + p_i(x, y)}{N} \tag{5}$$

where N is the number of points that matches, $M_i(x, y)$ is the measurement of the point relative to the center, $Scale_i$ is the scale of the point and $p_i(x, y)$ is the spatial position of each point.

The second way of doing it, is computing the homography. This is defined as an invertible mapping where a plane can be projected trough a point onto

another plane [23]. In this work it is used an affine mapping for the homography calculation, which includes scales, rotations, translations, and shears. For a robust estimation, the RANSAC algorithm is used to generate a better homography. With this method the object center can be computed in each frame. The idea is that when it calculates a bad homography, the system can still use (5) to get the object center.

4.2 Filtering and Data Association

The tracking process is achieved by predicting the object center position and the scale in the next frame. The Unscented Transform(UT) is used to compute the first two statistical moments for the position and the scale, the means μ_p and μ_s, and variances σ_p^2 and σ_s^2. Using μ_s and σ_s^2 it can be searched in an interval defined by $I = \mu_s \pm 3\sigma_s^2$, in the stack of descriptors, where the matching scale should be found with high probability. With these statistical measures and the size of the ROI obtained in the first frame, the region of the image where the object is located is constrained by, $Width_{newROI} = \frac{Width}{\mu} + k\sigma_s^2$ and $Height_{newROI} = \frac{Height}{\mu} + k\sigma_s^2$, where k is a constant chosen experimentally (see Fig. 3).
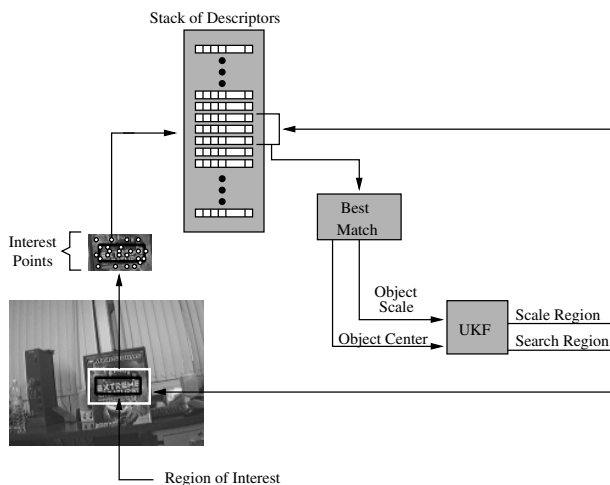
Fig. 3. Schematic view of the object tracking algorithm

Unscented Kalman Filter. The UKF is a variant of the Kalman Filter (KF) for non-linear systems that address the EKF deficiencies. It is based upon the Unscented Transformation (UT) which is a method for calculating the statistics of a random variable which undergoes a nonlinear transformation [18]. A set of sample points are chosen deterministically in order to compute the mean and covariance of the random variable, when these points are propagated through the non-linear system, then information can be extracted about the posterior

mean and covariance with an accuracy up to the 2nd order in the Taylor series expansion. The basic idea then is propagate the mean an covariance information through nonlinear transformations. The UKF is an extension of the UT regarding the recursive nature of the KF. More details about the UKF can be found in [17].

5 Experiments and Results

The system was tested on a 2.2 GHz Pentium 4 PC. The implementation is on Linux in C++ using the openCV library. A firewire camera with FOV of 42° which feeds video at 30 fps at a resolution of 320x240 is used.

Figure 4.I shows a comparative graphic of the tracking system developed in this work vs the naive SURF algorithm, using a video sequence considering changes in scale, rotation, partial occlusions and the total lost of the object. The tracking system shows a fast recovery after temporary total lost of the object. In graphic a), it can be seen that the frame rate is much better through the entire sequence giving a mean of $\mu_{System} = 11.1\ fps$ compared with $\mu_{SURF} = 6.04\ fps$. In graphic b), the number of points detected and matched against the points detected in the first frame are shown.
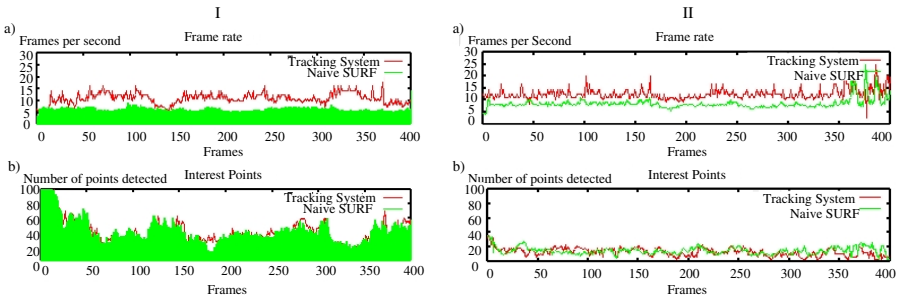
Fig. 4. Graphic showing the performance of the tracking system compared with SURF for two different objects: I) and II)

Figure. 4.II shows a sequence with a different object, where the number of points detected in the first frame is less for the two approaches, 40 for the proposed tracking system and 46 for SURF, compared with those detected from the object I. It can be seen also from this sequence that the frame rate is better in the whole video giving a mean of $\mu_{System} = 12.24\ fps$ compared with $\mu_{SURF} = 8.63\ fps$.

From the graphics b) in Fig. 4 , it can be seen that the amount of points correctly matched for the two objects are roughly the same. Figure 5 shows sample frames of the tracked object over sequence 1. Video sequences of the performance of the method can be seen at [24] and [25].

Fig. 5. Sample images of the test sequence using the proposed tracking system, each image represent the next frames: a)8, b)110, c)139, d)187, e)260, f)380, g)406, h)487, i)337

6   Conclusion

This paper presents a robust implementation of an object tracker using a vision system that takes in consideration partial occlusions, rotation and scale for a variety of different objects. The approach does not assume the form of the object and the results showed that it can track successfully and efficiently identified objects.

By utilising the proposed framework, an efficient implementation of an object tracker is achieved. It is notorious that the use of an estimator (in this case a UKF) of the scale and position of the object, improve the velocity of the algorithm and makes it stable against erratic motion and fast recovery against total lost. The use of the Harris points detector combined with SURF descriptors has proved to give a robust way for an object representation. The scheme of constructing multiple descriptors in the first frame gives to the system the scale invariance and it adds a better performance due to the fact that it is done only once and it avoids the use of scale-space in each frame.

References

[1] Chekhlov, D., Pupilli, M., Mayol-Cuevas, W., Calway, A.: Real-time and robust monocular slam using predictive multi-resolution descriptors. In: 2nd International Symposium on Visual Computing (November 2006)
[2] Lowe, D.: Distinctive image features from scale-invariant keypoints. Int. J. Computer Vision 2(60), 91–110 (2004)
[3] Mikolajczyk, K., Schmid, C.: Scale and affine invariant interest point detectors. IJCV 1(60), 63–86 (2004)
[4] Harris, C.J., Stephens, M.: A combined corner and edge detector. In: Proc. 4th Alvey Vision Conferences, pp. 147–151 (1988)
[5] Schmid, C., Mohr, R., Bauckhage, C.: Evaluation of interest point detectors. International Journal of Computer Vision 2(37), 151–172 (2000)

[6] Bay, H., Tuytelaars, T., Van Gool, L.: SURF: Speeded up robust features. In: Proceedings of the ninth European Conference on Computer Vision (May 2006)

[7] Comaniciu, D., Ramesh, V., Meer, P.: Kernel-based object tracking. IEEE Transactions on Pattern Annalysis and Machine Intelligence 25, 564–577 (2003)

[8] Rasmussen, C., Toyama, K., Hager, G.D.: Traking objects by color alone. Technical report, Yale University (June 1996)

[9] Perez, P., Hue, C., Vermaak, J., Gagnet, M.: Color-based probabilistic tracking. In: ECCV, pp. 661–675 (2002)

[10] Pahlavan, K., Eklundh, J.O.: A head-eye system- analysis and design. CVGIP: Image Understanding 56, 41–56 (1992)

[11] Tissainayagam, P., Suter, D.: Object tracking in image sequences using point features. Pattern Recognition 38, 105–113 (2005)

[12] Comaniciu, D., Ramesh, V., Meer, P.: Real-time tracking of non-rigid objects using mean shift. In: CVPR, pp. 142–149 (2000)

[13] Serby, D., Meier, E.K., Gool, L.V.: Probabilistic object tracking using multiple features. In: ICPR 2004, pp. 184–187 (2004)

[14] Cipolla, R., Yamamoto, M.: Stereoscopic tracking of bodies in motion. Image and Vision Computing 8(1), 85–90 (1990)

[15] Blake, A., Curwen, R., Zisserman, A.: A framework for spatiotemporal control in the tracking of visual contours. Int. J. Computer Vision 11(2), 127–145 (1993)

[16] Blake, A., Isard, M.: Active Contours. Springer, London (1998)

[17] Julier, J., Uhlmann, K.: Unscented filtering and nonlinear estimation. Proceedings of the IEEE 93, 401–422 (2004)

[18] Julier, S.J., Uhlmann, J.K.: A new extension of the kalman filter to nonlinear systems. In: AeroSense: The 11th Int. Symp. on Aerospace/Defence Sensing, Simulation and Controls (1997)

[19] Doucet, A., Godsill, S., Andrieu, C.: On sequential monte carlo sampling methods for bayesian filtering. Statistics and Computing 10(3), 197–208 (2000)

[20] Perez, P., Vermaak, J., Blake, A.: Data fusion for visual tracking with particles. Proceedings of the IEEE 92, 495–513 (2004)

[21] Liu, J., Chen, R.: Sequential monte carlo methods for dynamic systems. American Statistical Association 93, 1032–1044 (1998)

[22] Viola, P., Jones, M.: Rapid object detection using boosted cascade of simple features. Computer Vision and Pattern Recognition 1, 511–518 (2001)

[23] Heckbert Paul, S.: Fundamentals of texture mapping and image warping. Master's thesis, University of California, Berkeley. Dept. of Electrical Engineering and Computer Science (June 1989)

[24] Video of the object I. http://www.youtube.com/watch?v=bpfkVq-w53E

[25] Video of the object II. http://www.youtube.com/watch?v=eR0IMpRKOc8

Smooth Image Surface Approximation by Piecewise Cubic Polynomials

Oliver Matias van Kaick[1] and Helio Pedrini[2]

[1] School of Computing Science,
Simon Fraser University, Burnaby, BC, Canada, V5A 1S6
[2] Department of Computer Science
Federal University of Paraná, Curitiba, PR, Brazil, 81531-990

Abstract. The construction of surfaces from dense data points is an important problem encountered in several applications, such as computer vision, reverse engineering, computer graphics, terrain modeling, and robotics. Moreover, the particular problem of approximating digital images from a set of selected points allows to employ methods that are directed specifically to this task, which take advantage of the fact that all points belong to a common 2D domain. This paper describes a method for approximating images by fitting smooth surfaces to scattered points, where the smooth surfaces are constructed using piecewise cubic approximation. An incremental triangulation algorithm is used to iteratively refine a mesh until a specified error tolerance is achieved. The resulting surface is represented by a network of piecewise cubic triangular patches possessing C^1 continuity. The proposed method is compared against other surface approximation approaches and applied to several data sets in order to demonstrate its performance.

Keywords: Surface modeling, image surface, smooth interpolation.

1 Introduction

Approximation from unorganized data points arbitrarily distributed over 2D or 3D domains is a crucial problem in several scientific and industrial applications. Recent advances in acquisition of high-resolution images, associated with efficient modeling techniques, have allowed the construction of models with high degree of detail. Unless data reduction or compression methods are used, dense data sets cannot be stored, manipulated, or visualized efficiently.

Polygonal surfaces are often used to represent 3D data sets mainly because of their simplicity and flexibility. In the last few years, several polygonal surface algorithms have been proposed in the literature for generating a surface containing a small number of polygons. This is important for processing, visualizing, or transmitting larger surface data sets than the available capabilities of software, computers, and networks permit.

Although piecewise linear approximation approaches are simple in concept and generate compact surfaces, the generalization to a piecewise smooth representation is a natural and, in many cases, a necessary extension. Certain regions

of interest may consist of smoothly curved areas that meet along sharp curves. Modeling such regions as piecewise linear surfaces usually requires a large number of polygons, whereas a curved surface can provide a more compact and accurate model of the surface. Smooth surfaces can also produce superior results for rendering purposes, reducing certain perceptual problems, for instance the appearance of Mach bands along element boundaries [1].

This paper describes a method for approximating digital images or other datasets constrained to a 2D domain, such as digital elevation models. The approximation is constructed by fitting a smooth surface to points selected from the dataset. An incremental triangulation algorithm is used to iteratively refine the mesh that describes the surface until a specified error tolerance is achieved. The approximating surface is represented by piecewise cubic triangular patches possessing C^1 continuity. Two strategies for the refinement method are investigated. The first creates the triangular patches only after the iterative triangulation algorithm is executed, and the second strategy already builds the mesh according to the error generated by the cubic patches. The proposed method is applied to several synthetic and natural data sets to demonstrate its robustness.

Section 2 briefly presents a review of some relevant surface fitting methods found in the literature. Section 3 describes the proposed method. Experimental results are given in Section 4. Some conclusions are summarized in Section 5.

2   Related Work

Techniques for piecewise linear approximation from data points have been proposed by several researchers. The resulting surface can be generally obtained by either refining a coarse triangulation or simplifying a fine triangular mesh until a given tolerance error is achieved.

As an alternative to planar polygonal models, smooth surfaces can be approximated more accurately with higher-order polynomials. Several adaptive methods have been developed for generating piecewise polynomial elements, such as subdivision surfaces [2,3,4,5], hierarchical splines [6], and models composed of triangular patches [1,7,8].

In 1974, Chaikin [9] introduced a method for generating a smooth curve from a control polygon by recursively cutting off the corners of the polygon. This is perhaps the first method of constructing smooth curves of arbitrary topological type. Catmull and Clark [2], and Doo and Sabin [10] generalized the idea to surfaces, where a subdivision surface is defined by repeatedly refining an initial control mesh to produce a sequence of meshes that converge to a limit surface.

The Loop scheme [4] is probably the simplest subdivision method for triangular meshes. Each edge of the mesh is split into two, and new vertices are reconnected to form four new triangles. Vertices are rearranged through an averaging step.

The Butterfly subdivision scheme, proposed by Dyn *et al.* [3], recursively subdivides each triangular face of the control polygon into four triangular faces interpolating the old control points. The subdivision step retains the existing

vertices and splits each edge segment at its midpoint. The Butterfly scheme is proven to achieve tangent plane continuity when applied to regular meshes. A variant of the Butterfly scheme was proposed by Zorin [11], which guarantees that the subdivision produces C^1-continuous surfaces for arbitrary meshes.

A set of spline patches can be derived to fit a smooth surface over irregular polygonal meshes, globally achieving some order of continuity [12,13,14,15,16].

3   Proposed Method

The method proposed for fitting surfaces to scattered points involves two distinct parts, which are the surface approximation method, that creates a triangle mesh from the provided set of points, and the interpolation method, which defines the error between the original data and the triangles. These parts are described in the next two sections.

3.1   Surface Approximation

A refinement method is used in order to generate a piecewise approximation of a certain surface. The algorithm starts with an initial triangulation that covers the boundary of the domain, and iteratively adds new points from the data set until a specified error tolerance is achieved. The resulting surface is formed by C^0 continuous triangular patches.

The Delaunay triangulation is used to construct the mesh, generating the triangulation that maximizes the minimum angle of all triangles. This helps to reduce the occurrence of thin and long triangles since they can lead to undesirable behavior, affecting numerical stability and producing visual artifacts. During the approximation method, the error for each triangle is computed as the sum of the squared difference between each original data point inside the domain of the triangle and its interpolated value. Each triangle has also an associated candidate point, which is the point of the triangle with the maximum difference. Figure 1 presents an example where the points involved in the computation of the triangle error are shown. The candidate point is highlighted in black.

The four steps of the refinement method can be seen in Figure 2, from (a) to (d). At each iteration of the method, for a given mesh (a), the candidate point
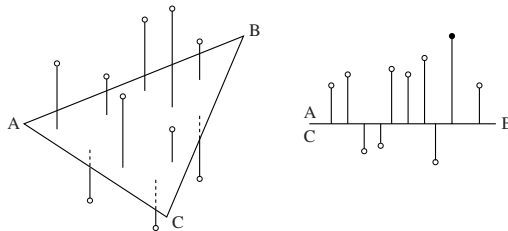
Fig. 1. Vertical error
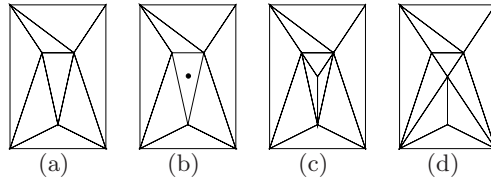
Fig. 2. Surface approximation method

of the triangle with maximum error is inserted into the mesh (b). Three new triangles are created with this vertex (c), and the modified portion of the mesh is retriangulated in order that the triangles maintain the Delaunay property (d).

The error evaluated for a given point clearly depends on the interpolation scheme that is being used. If a linear scheme is used, the value of a point is computed according to the plane defined by the three points of its containing triangle. In this work, we propose a surface approximation method using cubic interpolation, and compare it with linear interpolation. The smooth interpolation can be used either during the iterative construction of the mesh or only to fit a polynomial surface over an already created mesh. Our cubic interpolation method is described in the next section.

3.2   Smooth Surface Interpolation

Our interpolation method uses cubic polynomials to construct C^1 surfaces, which is based on a scheme originally described by Clough and Tocher [17]. It divides each triangle into subtriangles and fits an approximating function over each subtriangle. Certain continuity conditions must be satisfied at every boundary between two adjacent patches in order for the entire surface to be smooth.

Before describing the interpolation method, some preliminary concepts are introduced.

Mathematical Preliminaries
The use of *barycentric coordinates* is a natural way of representing triangular patches, since this guarantees a symmetric influence of all three triangle corners. Let T be a planar triangle defined by the vertices V_1, V_2, V_3. Any point V in T can be expressed in terms of the barycentric coordinates (r, s, t) defined by $V = rV_1 + sV_2 + tV_3$, where $r + s + t = 1$ and $0 \leqslant r, s, t \leqslant 1$.

Bernstein polynomials of degree n over a triangle T can be defined in terms of barycentric coordinates (r, s, t) expressed as

$$B_{i,j,k}^n(r, s, t) = \frac{n!}{i!\ j!\ k!}\ r^i s^j t^k \tag{1}$$

which form a basis for all bivariate polynomials of degree n. The parametric equation for a single triangular Bernstein-Bézier patch is

$$\mathbf{p}(r,s,t) = \sum_{\substack{i+j+k=n \\ i,j,k \geqslant 0}} \mathbf{b}_{i,j,k} \, B^n_{i,j,k}(r,s,t) \tag{2}$$

where the coefficients $\mathbf{b}_{i,j,k}$ are called the Bézier control points of $\mathbf{p}(r,s,t)$.

Taking $n = 3$, Equation 2 gives

$$\begin{aligned}
\mathbf{p}(r,s,t) = r^3\,\mathbf{b}_{3,0,0} + s^3\,\mathbf{b}_{0,3,0} + t^3\,\mathbf{b}_{0,0,3} + 3r^2s\,\mathbf{b}_{2,1,0} + 3r^2t\,\mathbf{b}_{2,0,1} + \\
3rs^2\,\mathbf{b}_{1,2,0} + 3s^2t\,\mathbf{b}_{0,2,1} + 3rt^2\,\mathbf{b}_{1,0,2} + 3st^2\,\mathbf{b}_{0,1,2} + 6rst\,\mathbf{b}_{1,1,1}
\end{aligned} \tag{3}$$

where (r,s,t) are the barycentric coordinates of a point (x,y) relative to the sub-triangle. Figure 3 shows an example of a triangular patch and its corresponding Bernstein polynomials.
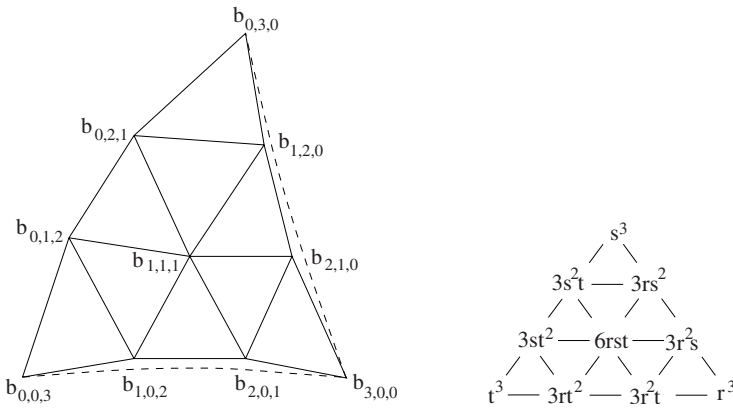
Fig. 3. Cubic triangular Bernstein-Bézier patch and its corresponding Bernstein polynomials

Cubic Interpolant

The Clough-Tocher [17] interpolation scheme, originally developed as a technique in finite element analysis, was used to produce a piecewise cubic polynomial surface during the approximation method. For the surface construction, each triangle is subdivided at the centroid into three subtriangles, and a cubic Bernstein-Bézier polynomial is defined over each subtriangle. Figure 4 illustrates the Clough-Tocher interpolation scheme.

Farin [7] provides a comprehensive description of the conditions for derivative continuity on the common boundary between two adjacent triangular patches. To ensure C^1 continuity, the first derivatives of two adjacent patches $\mathbf{p}$ and $\mathbf{q}$ must join continuously across the shared edge. Our interpolation method is based on the work developed by Quak and Schumaker [18]. Their paper provides a construction such that derivative continuity is achieved on each shared triangle edge.

Our interpolation method is relatively simple to implement since it computes the coefficients of the polynomial for each triangle based only on the elevation values and the estimated values of the first partial derivatives (tangent vectors)
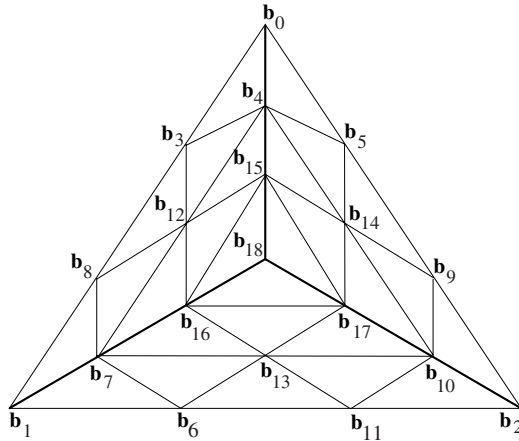
Fig. 4. Clough-Tocher subdivision

at the three vertices of the triangle. The derivative at a vertex is computed as the weighted average of the normals of the triangles adjacent to that vertex.

The 19 Bernstein-Bézier coefficients of the Clough-Tocher interpolation scheme are given by the following equations

$$
\begin{aligned}
\mathbf{b}_0 &= z_0 \\
\mathbf{b}_1 &= z_1 \\
\mathbf{b}_2 &= z_2 \\
\mathbf{b}_3 &= ((x_1 - x_0)z_0^x + (y_1 - y_0)z_0^y)/3 + z_0 \\
\mathbf{b}_4 &= ((x_c - x_0)z_0^x + (y_c - y_0)z_0^y)/3 + z_0 \\
\mathbf{b}_5 &= ((x_2 - x_0)z_0^x + (y_2 - y_0)z_0^y)/3 + z_0 \\
\mathbf{b}_6 &= ((x_2 - x_1)z_1^x + (y_2 - y_1)z_1^y)/3 + z_1 \\
\mathbf{b}_7 &= ((x_c - x_1)z_1^x + (y_c - y_1)z_1^y)/3 + z_1 \\
\mathbf{b}_8 &= ((x_0 - x_1)z_1^x + (y_0 - y_1)z_1^y)/3 + z_1 \\
\mathbf{b}_9 &= ((x_0 - x_2)z_2^x + (y_0 - y_2)z_2^y)/3 + z_2 \\
\mathbf{b}_{10} &= ((x_c - x_2)z_2^x + (y_c - y_2)z_2^y)/3 + z_2 \\
\mathbf{b}_{11} &= ((x_1 - x_2)z_2^x + (y_1 - y_2)z_2^y)/3 + z_2 \\
\mathbf{b}_{12} &= (\mathbf{b}_4 + \mathbf{b}_7 + (\theta_0 - 1)\mathbf{b}_0 + (2 - 3\theta_0)\mathbf{b}_3 + (3\theta_0 - 1)\mathbf{b}_8 - \theta_0\mathbf{b}_1)/2 \\
\mathbf{b}_{13} &= (\mathbf{b}_7 + \mathbf{b}_{10} + (\theta_1 - 1)\mathbf{b}_1 + (2 - 3\theta_1)\mathbf{b}_6 + (3\theta_1 - 1)\mathbf{b}_{11} - \theta_1\mathbf{b}_2)/2 \\
\mathbf{b}_{14} &= (\mathbf{b}_{10} + \mathbf{b}_4 + (\theta_2 - 1)\mathbf{b}_2 + (2 - 3\theta_2)\mathbf{b}_9 + (3\theta_2 - 1)\mathbf{b}_5 - \theta_2\mathbf{b}_0)/2 \\
\mathbf{b}_{15} &= (\mathbf{b}_{14} + \mathbf{b}_4 + \mathbf{b}_{12})/3 \\
\mathbf{b}_{16} &= (\mathbf{b}_{12} + \mathbf{b}_7 + \mathbf{b}_{13})/3 \\
\mathbf{b}_{17} &= (\mathbf{b}_{13} + \mathbf{b}_{10} + \mathbf{b}_{14})/3 \\
\mathbf{b}_{18} &= (\mathbf{b}_{17} + \mathbf{b}_{15} + \mathbf{b}_{16})/3
\end{aligned}
\tag{4}
$$

where

$$
\theta_0 = \frac{(x_c - x_0)(x_1 - x_0) + (y_c - y_0)(y_1 - y_0)}{(x_1 - x_0)^2 + (y_1 - y_0)^2}
$$

$$
\theta_1 = \frac{(x_c - x_1)(x_2 - x_1) + (y_c - y_1)(y_2 - y_1)}{(x_2 - x_1)^2 + (y_2 - y_1)^2} \tag{5}
$$

$$
\theta_2 = \frac{(x_c - x_2)(x_0 - x_2) + (y_c - y_2)(y_0 - y_2)}{(x_0 - x_2)^2 + (y_0 - y_2)^2}
$$

The coordinates of points $\mathbf{b}_0$, $\mathbf{b}_1$, and $\mathbf{b}_2$ are (x_0, y_0, z_0), (x_1, y_1, z_1) and (x_2, y_2, z_2), respectively, and the derivatives at these points are (z_0^x, z_0^y), (z_1^x, z_1^y) and (z_2^x, z_2^y). The point (x_c, y_c) is the centroid of the triangle $(\mathbf{b}_0, \mathbf{b}_1, \mathbf{b}_2)$.

Initially, the derivatives at each data vertex are computed by estimating the normals for each adjacent triangle. Then, three cubic triangular Bézier patches are constructed over each subtriangle. A cubic Bézier patch is defined by 10 control points as shown in Figure 3. The 10 control points of each subtriangle provide the degrees of freedom required to ensure continuity across the element boundaries.

The Bernstein-Bézier representation for subtriangle $(\mathbf{b}_0, \mathbf{b}_1, \mathbf{b}_{18})$ is

$$
\mathbf{p}(r, s, t) = r^3\,\mathbf{b}_{18} + s^3\,\mathbf{b}_0 + t^3\,\mathbf{b}_1 + 3r^2s\,\mathbf{b}_{15} + 3r^2t\,\mathbf{b}_{16} +
$$
$$
3rs^2\,\mathbf{b}_4 + 3s^2t\,\mathbf{b}_3 + 3rt^2\,\mathbf{b}_7 + 3st^2\,\mathbf{b}_8 + 6rst\,\mathbf{b}_{12} \tag{6}
$$

The C^1 cubic surfaces for subtriangles $(\mathbf{b}_1, \mathbf{b}_2, \mathbf{b}_{18})$ and $(\mathbf{b}_0, \mathbf{b}_2, \mathbf{b}_{18})$ are computed analogously.

4   Experimental Results

We compare four surface approximation methods. For the first three methods, a triangle mesh is firstly created according to linear interpolation, and the error of this approximation is compared when the resulting mesh is interpolated using the linear method, our previous quadratic method [1], and the proposed cubic scheme. For the fourth method (labeled *CubicApp*), the described cubic interpolant is directly used during the iterative construction of the triangle mesh, and the error for the triangles and the candidate points is computed according to this scheme.

Our method has been tested and evaluated on several different real and synthetic digital images in order to demonstrate its performance, however, due to limited space, the visual results for only three models are presented in this work. The algorithms were implemented in C programming language on a PC Athlon XP 2000 MHz with 512 Mbytes of main memory.

Table 1 reports the root mean square (RMS) error for a set of reconstructed objects. Figures 5 and 6 show three sets of images obtained by applying the linear and cubic interpolation methods, and their related contour lines. The same number of data points are retained in both methods.

Table 1. Summary of results (RMS Error) for reconstructed objects using 1% of the original points

Model	Linear	Quadratic	Cubic	CubicApp
Columbia	6.84	7.76	7.45	7.43
Crater Lake	5.52	6.93	6.63	6.40
Emory Peak	13.90	16.75	15.62	15.58
Grand Canyon	16.37	19.15	18.52	18.20
Klamath Falls	8.07	10.73	9.59	9.37
Mars	4.91	7.55	7.12	6.83
Peppers	11.22	12.68	12.64	12.53
Rice Lake	1.75	2.16	2.09	2.03

(a) Linear   (b) CubicApp   (c) Linear   (d) CubicApp

(e) Linear   (f) CubicApp   (g) Linear   (h) CubicApp
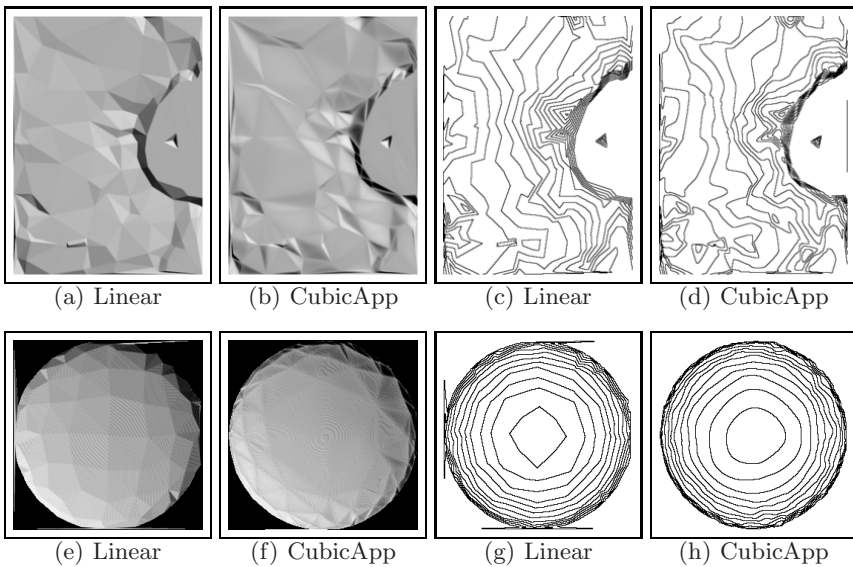
Fig. 5. Approximations of two data sets by the linear and cubic method, respectively. (a) and (b) Crater Lake DEM (336×459 pixels); (c) and (d) Contour lines; (e) and (f) Half-Sphere DEM (256×256 pixels); (g) and (h) Contour lines.

Although the linear method presented lower errors than the smooth interpolation schemes, the cubic interpolation used during the iterative construction of the triangulation resulted in high quality meshes, when compared to the methods that only fit a smooth surface over an already created linear mesh with either the quadratic or cubic scheme. Thus, it appears as a better alternative when lower error approximations with properties such as C^1 continuity and smooth contour lines are required.

(a) Linear   (b) CubicApp

(c) Linear   (d) CubicApp
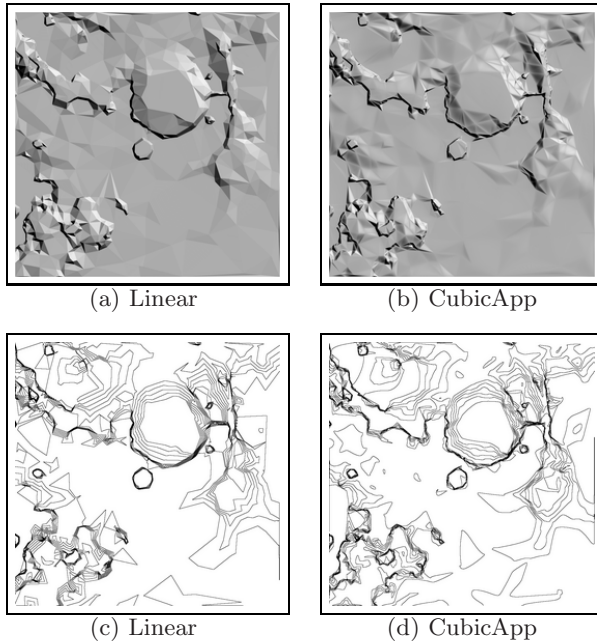
Fig. 6. Approximations of one data set by the linear and cubic method, respectively. (a) and (b) Mars DEM (948×948 pixels); (c) and (d) Contour lines.

5 Conclusions

A method for approximating digital images by smooth surfaces is presented in this paper. The method generates a set of piecewise cubic polynomial patches possessing C^1 continuity. The approximation error that guides the point selection process during the iterative construction of the surface is evaluated according to the interpolation of the cubic polynomials. Therefore, the method selects at a given iteration the point that reduces the maximum error for the current smooth surface.

The results show that the method constructs surfaces of high quality, which are comparable in terms of RMS Error to surfaces constructed by the linear method, but that are more suitable for applications where smooth approximations for digital images or other types of datasets are necessary.

References

1. van Kaick, O.M., da Silva, M.V.G., Schwartz, W.R., Pedrini, H.: Fitting Smooth Surfaces to Scattered 3D Data Using Piecewise Quadratic Approximation. In: IEEE International Conference on Image Processing, Rochester, New York, USA, pp. 493–496. IEEE Computer Society Press, Los Alamitos (2002)

2. Catmull, E., Clark, J.: Recursively generated B-spline surfaces on arbitrary topological meshes. Computer-Aided Design 10(6), 350–355 (1978)
3. Dyn, N., Levin, D., Gregory, J.A.: A Butterfly subdivision scheme for surface interpolation with tension control. ACM Transactions on Graphics 9(2), 160–169 (1990)
4. Loop, C.: Smooth subdivision surfaces based on triangles. Master's thesis, University of Utah, Department of Mathematics (1987)
5. Stam, J.: On subdivision schemes generalizing uniform B-spline surfaces of arbitrary degree. Computer Aided Geometric Design 18, 383–396 (2001)
6. Forsey, D.R., Bartels, R.H.: Surface fitting with hierarchical splines. ACM Transactions on Graphics 14(2), 134–161 (1995)
7. Farin, G.: Curves and Surfaces for Computer-Aided Geometric Design - A Practical Guide. Academic Press, London (1992)
8. Hahmann, S., Bonneau, G.P.: Polynomial surfaces interpolating arbitrary triangulations. IEEE Transactions on Visualization and Computer Graphics 9(1), 99–109 (2003)
9. Chaikin, G.M.: An algorithm for high-speed curve generation. Computer Graphics and Image Processing 3(4), 346–349 (1974)
10. Doo, D., Sabin, M.: Behaviour of recursive division surfaces near extraordinary points. Computer-Aided Design 10(6), 356–360 (1978)
11. Zorin, D., Schröder, P., Sweldens, W.: Interpolating subdivision for meshes with arbitrary topology. In: SIGGRAPH 1996 Conference Proceedings, New Orleans, Louisiana, USA, pp. 189–192 (August 1996)
12. Eck, M., Hoppe, H.: Automatic reconstruction of B-spline surfaces of arbitray topological type. In: ACM SIGGRAPH 1996, pp. 325–334. ACM Press, New York (1996)
13. Zheng, J.J., Zhang, J.J., Zhou, H.J., Shen, L.G.: Smooth spline surface generation over meshes of irregular topology. The Visual Computer 21(8–10), 858–864 (2005)
14. Krishnamurthy, V., Levoy, M.: Fitting smooth surfaces to dense polygonal meshes. In: Computer Graphics Proceedings, Annual Conference Series, pp. 313–324 (1996)
15. Loop, C.: Smooth splines surfaces over irregular meshes. In: Computer Graphics Proceedings, Annual Conference Series, ACM SIGGRAPH, pp. 303–310. ACM Press, New York (1994)
16. Peters, J.: C^1 surface splines. SIAM Journal of Numerical Analysis 32(2), 645–666 (1995)
17. Clough, R., Tocher, J.: Finite element stiffness matrices for analysis of plates in bending. In: Proceedings of Conference on Matrix Methods in Structural Analysis (1965)
18. Quak, E., Schumaker, L.L.: Cubic spline fitting using data dependent triangulations. Computer-Aided Geometric Design 7(1–4), 293–301 (1990)

An Analysis of Automatic Gender Classification

Modesto Castrillón-Santana[1] and Quoc C. Vuong[2]

[1] IUSIANI
Edificio Central del Parque Científico-Tecnológico
Universidad de Las Palmas de Gran Canaria
35017 Las Palmas - Spain
mcastrillon@iusiani.ulpgc.es
[2] Division of Psychology
Henry Wellcome Building for Neuroecology
Newcastle University
Framlington Place
Newcastle upon Tyne
NE2 4HH - UK
q.c.vuong@ncl.ac.uk

Abstract. Different researches suggest that inner facial features are not the only discriminative features for tasks such as person identification or gender classification. Indeed, they have shown an influence of features which are part of the local face context, such as hair, on these tasks. However, object-centered approaches which ignore local context dominate the research in computational vision based facial analysis. In this paper, we performed an analysis to study which areas and which resolutions are diagnostic for the gender classification problem. We first demonstrate the importance of contextual features in human observers for gender classification using a psychophysical "bubbles" technique. The success rate achieved without internal facial information convinced us to analyze the performance of an appearance-based representation which takes into account facial areas and resolutions that integrate inner features and local context.

Keywords: Gender classification, local context, PCA, SVM.

1 Introduction

Humans make use of different static and dynamic features to successfully identify and interact with other people. Gender is one of them.

Gender recognition is an often-studied topic in both the psychology and, since the first work in the early 90s [1,2], the computer vision community. Recently, very high performance was obtained using only facial information [3,4]. To the best of our knowledge, in computer vision this task has been based almost exclusively on internal facial features, except in some recent work which analyzed the discriminative capability of external facial features [5] such as hair [6].

This latter finding is consistent with the human recognition system, which makes use of external and other features for gender recognition, such as gait,

hair, clothes, voice, etc. [7,8]. To illustrate this, if we look at different paintings, e.g., August Macke's *Hat Shop*, or Rene Magritte's *Son of Man*, it is observed that even when internal facial features are not distinguishable at all, different contextual details depicted by the painter allow us to confidently infer the gender of the person depicted. This observation is also supported by psychophysical results, which suggests that local context is a robust cue to gender for low resolution or noisy images [8,9]. This paper investigates the extent to which the facial area and resolution chosen for gender classification influence in the performance of an automatic gender classifier.

Fig. 1. Image samples (62×54) pixels

2   Evidence of Local Context Influence in Human Perception

In the psychology literature, the local context around the face has been established as a source of information to characterize an individual. The local context is defined as the information surrounding the internal features of the face, including hair and possibly the environment surrounding the head (i.e., local background) [10].

According to Torralba [11], object-centered approaches dominate the research in computational vision based facial analysis. Most systems have been designed for a resolution range in which the inner face elements are clearly distinguishable. This focus restricts their reliability due to the fact that these systems are easily fooled in situations with poor viewing conditions in terms of pose, resolution, illumination, etc. Such conditions have been systematically studied in psychophysical experiments [10], and the results suggest that humans make use of the local context as the level of detail decreases to achieve greater robustness. However, Sinha's previous work also suggests that the role of local context is not exclusively utilized at low resolution. Indeed, under some circumstances, the local context provides enough discriminative features which indicates that internal facial details are not the only sources of gender information that are taken into consideration [8,9].

To investigate the influence of local context for gender recognition, we first analyzed which contextual features are used by human observers for gender classification. For that purpose, we used a psychophysical "bubbles" technique [12] to isolate those regions used by humans when only local contextual information around the head and shoulders is available in the image. The technique was used in [12] to identify internal facial features that provided diagnostic information for

Fig. 2. Two different images samples after applying randomly distributed bubble. The inner facial features are always masked but the eye locations are indicated to observers by two red dots. Figure 1 shows some samples without any mask applied but down-sampled to 62×54 pixels.
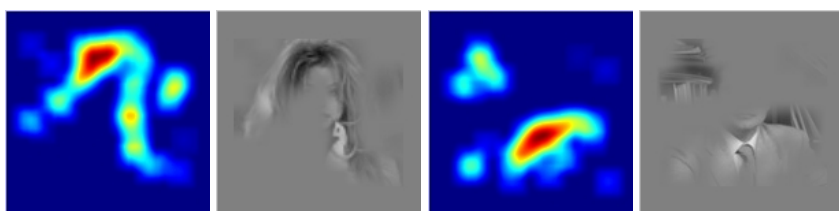
Fig. 3. The left pair shows the diagnostic image and the superimposition of the image with a female sample. The diagnostic image shows diagnostic regions (and their strength) that lead to accurate classification by humans. The right pair shows the results for males.

gender classification. With high-resolution face images, the gender was correctly determined using just the eyes and mouth.

In the current study, images containing aligned male and female face images were revealed through a mask of small randomly distributed Gaussian windows ("bubbles"). That is, the presence of a bubble over a region showed that region. To prevent human observers from making the classification on the basis of internal facial features, the bubbles were never placed on any internal facial region, as shown in Figure 2. Therefore, observers classified the gender based on information contained in the local context surrounding the face. Across observers, masks leading to correct responses are summed and normalized to reveal image regions that were diagnostic for gender classification. The resulting normalized images are referred to as diagnostic images.

The results (i.e. diagnostic images) for a dataset of 962 images (124×108 pixels) are shown in Figure 3. They indicated that the regions used by humans to discriminate gender when internal facial features were not visible depended on the gender of the test face. For male faces, the neck provided the most diagnostic information (i.e., the tie or the shirt neck provided discriminative information). By comparison, for females faces, long hair was frequently used as a diagnostic cue. With these regions observers correctly classified the stimuli $70 - 75\%$ on average, without seeing too much internal facial details.

3   Automatic Gender Classification

The psychophysical results above suggested that the local contextual information around the head and shoulders (e.g., hair, neck tie) provided diagnostic gender information. As we mentioned above, however, automatic gender classification have been predominantly based on internal facial features. For example, the recent work described in [3] used perfectly aligned and cropped frontal faces represented using Principal Components Analysis (PCA). A Support Vector Machine (SVM) classifier [13] was subsequently used to classify the PCA-based representations. This classifier achieved high gender classification performance even at low resolution.

We adopted the same appearance-based representation space, i.e. PCA, and classification approach used by Moghaddam et al. [3]. However, instead of manually collecting a training set for our experiments, we moved to a less restricted scenario in which an automatic face detector [14] provided the input data source extracted from video streams to incrementally build up the training set. In our experiments, gender classification was performed each time a new individual was encountered, but the system used the information extracted to iteratively upgrade the gender classifier.

Our assumption is that the system can be improved by a supervisor which confirms or corrects its classifications. Labelling interactively for learning is not new [15]. The online training is therefore unconstrained in the sense that an individual can be presented in an arbitrary order in front of a camera and labelled by a supervisor.

Fig. 4. Samples of different facial areas used or automatic recognition. From left to right: *Cropped A* (without hair line), *Cropped A IN* (same but with Illumination Normalization [16]), *Uncropped* (including local context), *Cropped B* (including the hair line) and *Eyes*. The first two areas have a dimension of 59×65 pixels, the second two areas 75×90 pixels, and the last area has a dimension of 15×11 pixels.

4   Experiments

4.1   Representation

The initial representation space, based on PCA, has been set up using a dataset of 7000 images taken randomly from the Internet. These images were annotated by hand, and normalized according to eye position to obtain samples that were 59x65 pixels each.
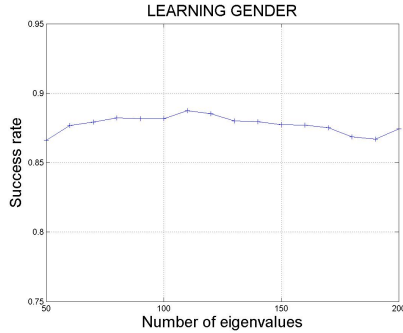
Fig. 5. Correct recognition rate achieved with different classifiers, according to the number of eigenvalues employed, computed offline with around 3400 training images

We randomly selected half of this set for training, and the other half for testing. We then computed a collection of SVM-based classifiers [13] which takes into considering account different number of eigenvalues for the face representation. Based on the results shown in Figure 5, we employed 100 eigenvalues to represent faces in our online experiments.

To test successive meetings, we built up a database which made use of broadcast television. The database contains around 1130 different video streams with resolution equal to or greater than 320×240 pixels. The sequences correspond to approximately 850 different identities. Unfortunately we do not have permission from most of the sources to share the database.

For our face representation, we used incremental PCA (IPCA) approach described in [17,18] instead of using a fixed PCA space. Thus, the learning procedure starts with an initial PCA representation space, and an initially empty training set. The system meets individuals in a random order, after each meeting, it determines a classification (once a sample is available for each class) for that meeting based on some significant exemplars extracted. Incorrectly classified exemplars are then employed to 1) increase the training set to update the gender classifier, and 2) to incrementally update the PCA representation space [17,18].

4.2   Results

As mentioned above, for our experiments, we used an automatic face detector [14] that is freely available for research purposes. To avoid artifacts produced by the order in which videos are presented or meetings held, the experimental procedure was repeated randomly several times for five different facial regions, see Figure 4. We present the results achieved averaged across these repetitions.

Figure 6 presents the results achieved using the different facial areas shown in Figure 4. The plot represents the cumulative success rate of classified meetings. Initially, the system classified gender poorly. However in the final stages, three
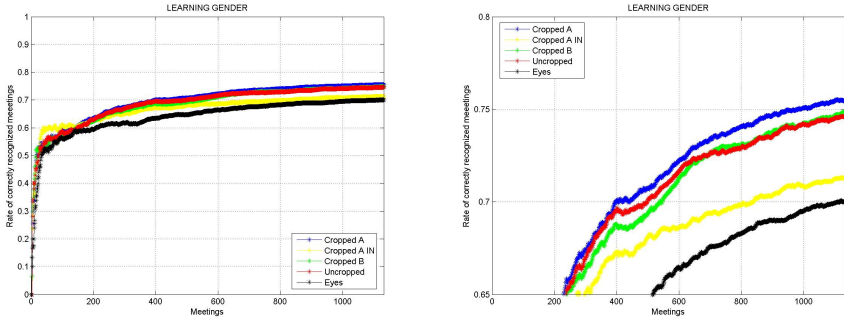
Fig. 6. Gender classification performance evolution (zoomed on the right). For each meeting, the cumulative rate of correct classification is indicated.
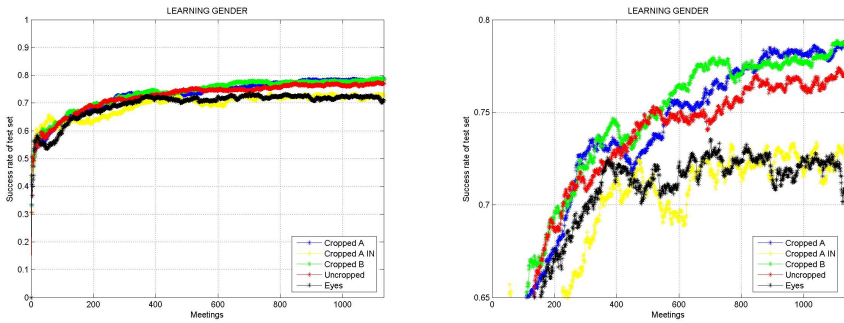
Fig. 7. Gender classification performance evolution (zoomed on the right). For each meeting, the cumulative rate of correct classification is indicated for the independent test set.

curves reported a success rate greater than 75%, which indicates that the system was able to recognize correctly more than 847 sequences of held meetings at that point, and this tendency continued to grow. Two curves in Figure 6 clearly showed relative poor performance: *Eyes*, and *Cropped A IN*.

We were also interested in testing with an independent and larger test set of images of images not contained in the video streams. Figure 7 presents the results achieved using again the facial areas shown in Figure 4 for the test set used to compute the initial PCA (containing 7000 faces annotated by hand). The overall classification performance is slightly better, and again the curves for the *Eyes*, and *Cropped A IN* areas show worst results than the other areas.

Figure 8 left shows the number of samples automatically included in the training set by the different areas. The *Cropped B* appeared to build a training set that
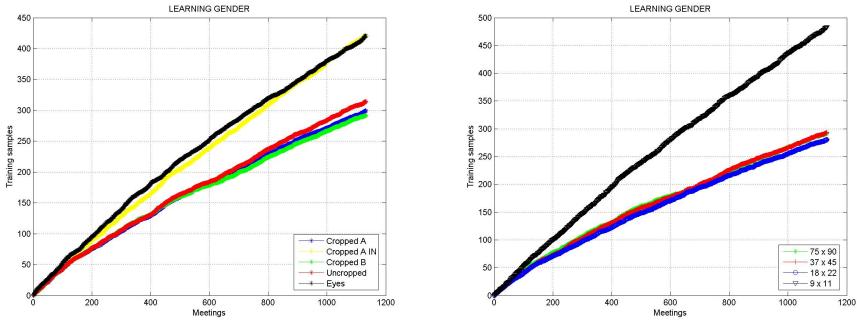
Fig. 8. Gender classification performance evolution. For each meeting, the cumulative size of training set is indicated. Left) comparison of facial areas used, Right) Comparison of resolutions used for *Cropped B*.
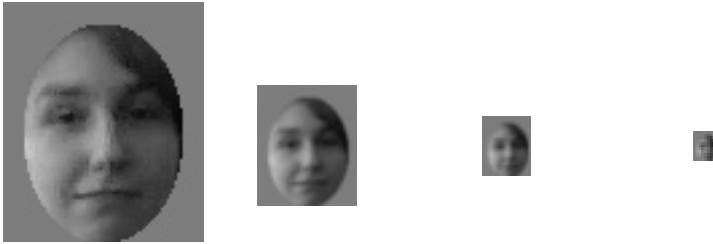
Fig. 9. *Cropped B* samples at three different resolution: a) 75×90, b) 37×45, c) 18×22, and d) 9×11 pixels

was slightly smaller than the *Cropped B* and *Uncropped* areas. The *Cropped B* does not include information related to hair, but does include the forehead which could, in some situations, be affected by hair.

Another question which arose during these experiments was the influence of spatial resolution. In [3], it was stated that the automatic system can easily outperform a human at low resolution. Therefore, we tested four different resolutions, as shown in Figure 9. For resolutions lower than 18×22, we observed a significant reduction in classification performance and an increase in the number of samples, as shown in Figure 8.right. Figures 10 and 11 depict the results for the three best curves (*Cropped A*, *Cropped B* and *Uncropped*) using different resolutions. Based on these results, we do not see a clear advantage in performance for any one of those areas. Overall, however, the lowest resolution revealed a decrease in performance and a corresponding increase in the size of the training set.
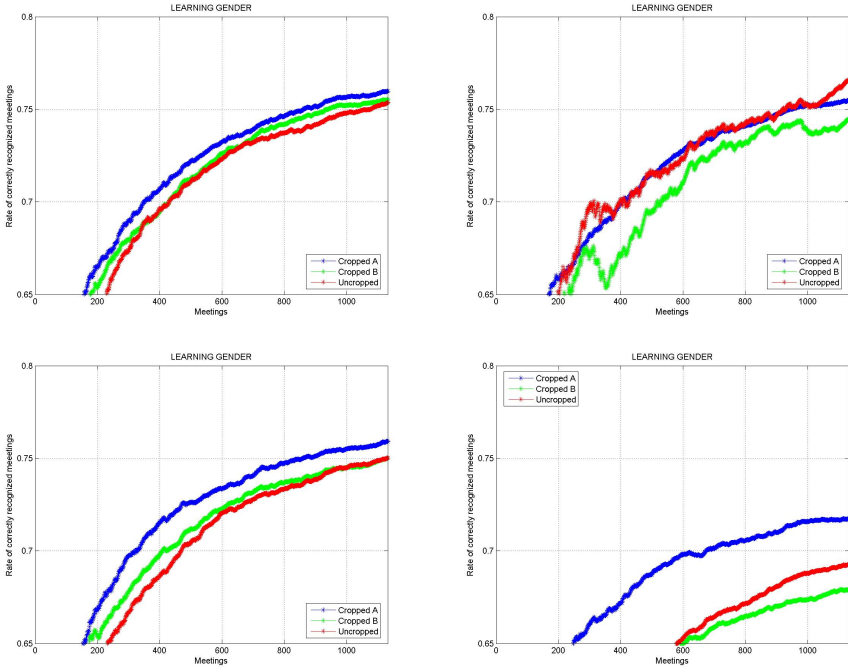
Fig. 10. Cropped A, B and Uncropped at different resolutions (full, half, 1/4 and 1/8) using the meetings results

5   Conclusions and Future Work

In the present work, we first analyzed the influence of outer facial regions on human gender classification performance. The results indicated that humans do not only use inner facial regions to classify gender.

Motivated by the human data, we subsequently employed a state-of-the-art approach to investigate which inner and outer facial areas provided better information for an automatic gender classifier. The entire process is performed automatically from face detection to exemplars selection. Only a supervisor is required to confirm or correct a classification performed by the system. This is the key point for the learning system due to the fact that incorrectly classified patterns are added to the training set.

The resulting classifiers required a much smaller training set: less than 10% that of the classifiers used for offline learning. However, the performance of the offline classifier was still greater.

Our results indicated that the minimal resolution required for gender recognition should not be lower than 18×22. However, we did not find a clear winner in terms of the optimal area for gender classification (among *Cropped A*, *Cropped B* and *Uncropped*). According to this finding, for our configuration the local
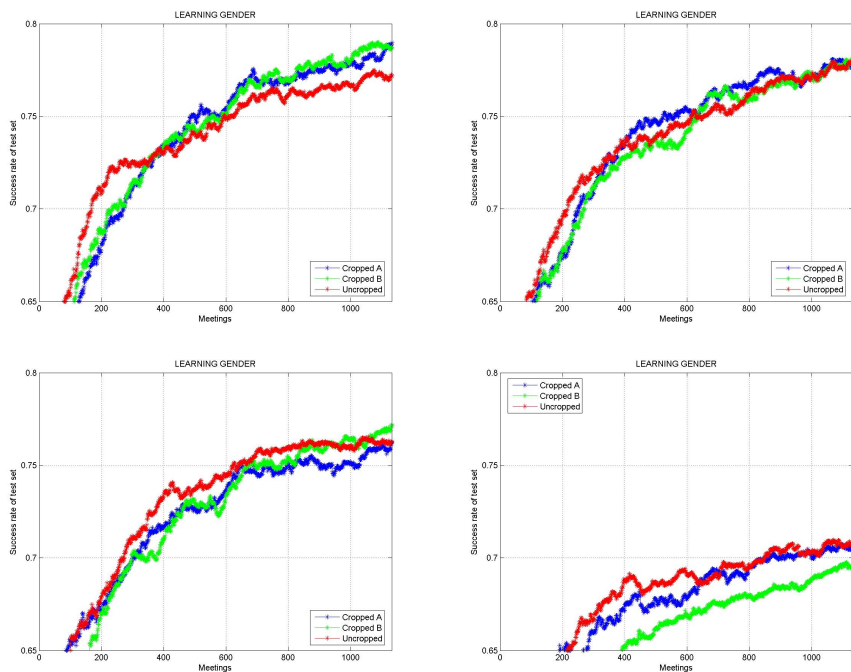
Fig. 11. Cropped A, B and Uncropped at different resolutions (full, half, 1/4 and 1/8) using the independent test set results

context, although useful for humans, does not seem to provide additional information for gender classification if internal features are present.

In the near future we plan to test the possibility of classifying without the availability of inner facial features. Additionally, we would like to test the possibility of combining the different classifiers to get a better metaclassifier for the gender classification problem.

Acknowledgments

References

1. Abdi, H., Valentin, D., Edelman, B.G., O'Toole, A.J.: More about the difference between men and women: evidence from linear neural network and the principal component approach. Perception 24 (1995)

2. Brunelli, R., Poggio, T.: Hyperbf networks for gender classification. In: Proceedings of the DARPA Image Understanding Workshop, pp. 311–314 (1992)
3. Moghaddam, B., Yang, M.-H.: Learning gender with support faces. IEEE Trans. on Pattern Analysis and Machine Intelligence 24(5), 707–711 (2002)
4. Wu, J., Smith, W.A.P., Hancock, E.R.: Learning mixture models for gender classification based on facial surface normals. In: 3rd Iberian Conference on Pattern Recognition and Image Analysis, Girona, Spain, June 2007, pp. 39–46 (2007)
5. Lapedriza, A., Masip, D., Vitria, J.: Are external face features useful for automatic face classification? In: CVPR 2005, vol. 3, pp. 151–157 (2005)
6. Yacoob, Y., Davis, L.S.: Detection and analysis of hair. IEEE Trans. on Pattern Analysis and Machine Intelligence 28(7), 1164–1169 (2006)
7. Bruce, V., Young, A.: The eye of the beholder. Oxford University Press, Oxford (1998)
8. Jarudi, I., Sinha, P.: Relative roles of internal and external features in face recognition. Technical Report memo 225, CBCL (2005)
9. Sinha, P., Poggio, T.: I think I know that face... Nature 384(6608), 384–404 (1996)
10. Sinha, P., Torralba, A.: Detecting faces in impoverished images. AI memo 2001-028, CBCL memo 208, Massachussets Institute of Technology (2001)
11. Torralba, A.: Contextual priming for object detection. International Journal of Computer Vision 53(2), 169–191 (2003)
12. Gosselin, F., Schyns, P.G.: Bubbles: a technique to reveal the use of information in recognition tasks. Vision Research, 2261–2271 (2001)
13. Vapnik, V.: The nature of statistical learning theory. Springer, New York (1995)
14. Castrillón, M., Déniz, O., Hernández, M., Guerra, C.: ENCARA2: Real-time detection of multiple faces at different resolutions in video streams. Journal of Visual Communication and Image Representation, 130–140 (2007)
15. Wersing, H., Kirstein, S., Goetting, M., Brandl, H., Dunn1, M., Mikhailova, I., Goerick, C., Steil, J., Ritter, H., Kierner, E.: Online learning of objects and faces in an integrated biologically motivated architecture. In: ICVS (2007)
16. Xie, X., Lam, K.-M.: An efficient illumination normalization method for face recognition. Pattern Recognition Letters 27(6), 609–617 (2006)
17. Artac, M., Jogan, M., Leonardis, A.: Incremental PCA for on-line visual learning and recognition. In: Proceedings 16th International Conference on Pattern Recognition, pp. 781–784 (2002)
18. Hall, P., Marshall, D., Martin, R.: Incremental eigenanalysis for classification. In: British Machine Vision Conference, vol. 1, pp. 286–295 (1998)

A Method for Segmentation of Local Illumination Variations and Photometric Normalization in Face Images

Eduardo Garea Llano, Jose Luís Gil Rodríguez, and Sandro Vega

Advanced Technology Application Center. 7ma, No. 21812, Siboney, Playa, Cuba, 12200
{egarea,jlgil,svega}@cenatav.co.cu

Abstract. In this paper we present a method for the automatic localization of local light variations and its photometric normalization in face images affected by different angles of illumination causing the appearance of specular light. The proposed approach is faster and more efficient that if the same one was carried out on the whole image through the traditional photometric normalization methods (homomorphic filtering, anisotropic smoothing, etc.). The process consists in using an algorithm for unsupervised image segmentation based on the active contour without edges approach with level set representation model for localization of regions affected by specular reflection combined with a normalization method based on the local normalization that considers the local mean and variance into the located region. The performance of the proposed approach is compared through two experimental schemes to measure how the similarity is affected by illumination changes and how the proposed approach improves the effect caused by these changes.

Keywords: image segmentation, photometric normalization.

1 Introduction

Face recognition algorithms consist in three major parts: Face detection, normalization and face identification [1]. Face recognition starts with the detection of face patterns in sometimes cluttered scenes, continues normalizing the face images to attenuate or eliminate geometrical and illumination problems, then these faces are identified using appropriated classification algorithms, and finally results are post-processed using model-based schemes and logistic feedback [2].

One illumination effect that might cause particular problems in the recognition process is the local reflection of light in the face. Recently many appearance-based algorithms have been proposed to deal with the problem [3-6]. These algorithms work well, but are computationally expensive.

To find a method to efficiently and quickly solve these problems that obtains face images without the specular illumination effect and maintaining the features necessary for identification is a challenge.

In this paper we present a new approach to perform a detection of regions affected by the specular illumination effect by means of a bi-class unsupervised texture image

segmentation method using active contour and connected component analysis and an algorithm proposed by us to attenuate the local specular light through the filtering of the segmented regions by mean value of pixels in the neighbor regions. The first contribution of this paper is the fact that we use the unsupervised texture image segmentation method for region detection. And if in addition we consider that the segmentation turns into a region previously located by the face detector, the normalization process will be extremely fast.

The second contribution of this paper is the fact that this process of photometric normalization is done only in the segmented regions and not on the whole image and only in those images where the illumination problem is present; this clearly reports an important saving of time and calculation

The third contribution of this paper is the proposed method for the local normalization that consider the mean value and variance into the segmented image region by means of a very fast processing implemented through a lookup table.

The effectiveness of the proposed method was evaluated in several experiments using images from the Yale B database, taken a variety of illumination conditions. Obtained results demonstrate that the variations in the image similarity caused by illumination are successfully eliminated or attenuated.

2   Segmentation Algorithm

2.1   Active Contour for Image Analysis

There are two main approaches in active contours based on the mathematical implementation: snakes and level sets. Snakes explicitly move predefines snake points based on an energy minimization scheme, while level set approaches move contours implicitly as a particular level of a function [7].

The classic snakes [8] provide an accurate location of the edges only if the initial contour is given sufficiently near the edges because they make use of only the local information along the contour. Estimating a proper position of initial contours without prior knowledge is a difficult problem. Also, classic snakes cannot detect more than one boundary simultaneously because the snakes maintain the same topology during the evolution stage. That is, snakes cannot split to multiple boundaries or merge from multiple initial contours.

Level set theory has given a solution for this limitation, a formulation to implement active contours, was proposed by Osher and Sethian [7]. They represented a contour implicitly via a two-dimensional Lipschitz-continuous function $\phi(x, y) : \Omega \rightarrow \Re$ defined on the image plane. The function $\phi(x, y)$ is called *level set function*, and particular level, usually the zero level, of $\phi(x, y)$ is defined as the contour.

The advantage of using the zero level is that a contour can be defined as the border between a positive region and a negative region, so the contours can be identified by just checking the sign of $\phi(x, y)$.

Among the different active contours approaches for image segmentation we based our work on the Active Contour without Edges Model. This is a variable model for

2-phase image segmentation. The basic idea is to look for a particular partition of a given image into two regions, one representing the objects to be detected and the other representing the background, if we consider Ω as a bounded open subset of $\Re^2$, with $\partial\Omega$ the boundary, we seek for $\inf F(c^+, c^-, C)$:

$$F(c^+, c^-, C) = \mu \cdot length(C) + \lambda^+ \int_{in(C)} \left| u_0(x, y) - c^+ \right|^2 + \lambda^- \int_{out(C)} \left| u_0(x, y) - c^- \right|^2 \quad (1)$$

where $u_0 : \Omega \to \Re$ is the given image, c^+ and c^- are unknown constants representing the average value of u_0 inside and outside the curve and parameters $\mu > 0$ and $\lambda^+, \lambda^- > 0$ are weights for the regularizing term and the fitting terms respectively. In the level set method, $C \subset \Omega$ is represented by the zero level set of a Lipschitz function $\phi(x, y) : \Omega \to \Re$ such that

$$\begin{aligned} C &= \{(x, y) \in \Omega : \phi(x, y) = 0\} \\ in(C) &= \{(x, y) \in \Omega : \phi(x, y) > 0\} \\ out(C) &= \{(x, y) \in \Omega : \phi(x, y) < 0\} \end{aligned} \quad (2)$$

Using the Heaviside function H defined by:
$$H(x) = \{1, \text{ if } x \geq 0 \quad (3)$$
$$\{0, \text{ if } x < 0$$

We can replace the unknown variable C using eqs. (2) and (3), then the energy functional $F(C, c^+, c^-)$ is transformed to:

$$F(H(\phi), c^+, c^-) = \mu(\int_\Omega |\nabla H(\phi)|) + \lambda_1 \int_\Omega \left| u_0 - c^+ \right|^2 H(\phi) dx + \quad (4)$$

$$+ \lambda_2 \int_\Omega \left| u_0 - c^- \right|^2 (1 - H(\phi)) dx$$

2.2 Segmentation

The main purpose of our method is the segmentation of region affected by non-uniform illumination. Therefore, we need a modification of the Active Contour without Edge model defined on eq.(4), where u_0 is a multispectral image , u_0^i stands for each one of the image features (bands) and $\overline{c_+} = \{c_+^i\}_{i=1}^N$, $\overline{c_-} = \{c_-^i\}_{i=1}^N$ are vector where the ith component represent the pixel values average inside and outside of u_0^i respectively. We can see these changes in the equation (5):

$$F(H(\phi), \overline{c_+}, \overline{c_-}) = \mu(\int_\Omega |\nabla H(\phi)| dx) + \quad (5)$$

$$+ \int_{\Omega} \frac{1}{N} \sum_{i=1}^{N} \lambda_-^i \left| u_0^i - c_-^i \right|^2 (1 - H(\phi)) dx +$$

$$+ \int_{\Omega} \frac{1}{N} \sum_{i-1}^{N} \lambda^i + \left| u_0^i - c_+^i \right|^2 H(\Phi) dx$$

For this algorithm implementation we have been based on [9] where it is proposed a way for implementing optimization problems based on level set representation. When we apply it to solve the functional (eq. 5) the computational cost decreases substantially. Besides, our solution does not need to solve the Euler-Lagrange equation because it computes the energy directly on the functional and analyzes the energy variation when we move a point from inside to outside of the contour or vice versa.

We can approximate the length term $\int |\nabla H(\phi)| dx$ by:

$$\int |\nabla H(\phi)| dx \approx \sum_{i,j} \sqrt{(H(\phi_{i+1,j}) - H(\phi_{i,j}))^2 + (H(\phi_{i,j+1}) - H(\phi_{i,j}))^2} \qquad (6)$$

where $\phi_{i,j}$ is the value of ϕ at the i, j th pixel. Given an initial partition $\phi > 0$ and $\phi < 0$ denoted by ϕ_1 and ϕ_2, assuming that there are m points in ϕ_1 and n points in ϕ_2: let c_i, F_i be the average and energy for ϕ_i, i =1, 2.

If P is the point we want to analyze and its value is x, then if $P \in \phi_1$ the energy variation when we move P from ϕ_1 to ϕ_2 can be computed as:

$$\Delta F_{12} = (x - c_2)^2 \frac{n}{n+1} - (x - c_1)^2 \frac{m}{m-1} \qquad (7)$$

Similarly, if P changes from ϕ_2 to ϕ_1, the change of energy is:

$$\Delta F_{21} = (x - c_1)^2 \frac{m}{m+1} - (x - c_2)^2 \frac{n}{n-1} \qquad (8)$$

According to the needs and characteristics of the image to be segmented it can use or not the length term (8).

Without its consideration our algorithm can be summarized in 5 principal steps:

1. Give any initial partition of the image, set $\phi = 1$ for one part, and $\phi = -1$ for the other part. Calculate initial c_1 and c_2 values.
2. For each image pixel, computes the energy variation on the functional moving the point from ϕ_1 to ϕ_2 or vice versa. If this variation is less than cero, then the value of the function evaluated in this point is changed to its opposite, i.e. if the value of the function was 1 it turns into -1.

3. Apply the connected component filter to the function to eliminate the noise less than a specific size.

4. Recalculate c_1 and c_2 values taking into account the new function ϕ.

5. Repeat steps 2, 3 and 4 while energy decreases.

In case of consider the length term (8), first we apply the algorithm as we have seen before and later, we apply it but this time in the step 2 to calculate the energy variation we take into account the change occurred in the length when we move the point from ϕ_1 to ϕ_2 or vice versa.

3   A Fast Local Photometric Normalization Method

The following proposed method is based on the local normalization algorithm that standardizes the local mean and variance of an image [10], [11]. In our approach we make a filtering by the mean value of the pixels of regions located outside the segmented regions which contains the image parts affected by low frequency illumination effect (specular light) calculated by the expression:

$$I_{(i,j)f} = I_{(i,j)} - \frac{\overline{X}.p}{I_{(i,j)0}} \tag{9}$$

Where, $I_{(i,j)0}$ is the original value of a pixel located at the position i,j of the segmented region containing the part of image affected by illumination.

$I_{(i,j)f}$ is the normalized value of a pixel affected by illumination at the position i,j of the segmented region.

$\overline{X}$. is the mean value of vector formed by pixel values contained in the face region located outside the segmented region that contains the part of the image affected by low frequency illumination effect (specular light). See Fig 1.
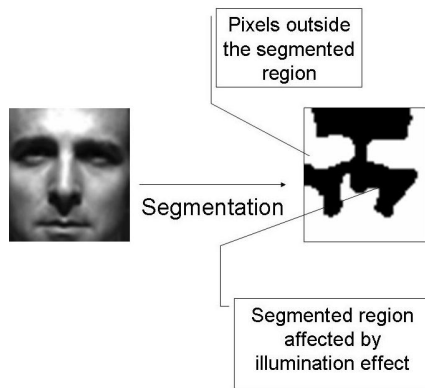
Fig. 1. Distribution of pixel values took for photometric normalization outside and inside of the segmented region

Table 1. Distance intervals and its corresponding coefficients p

No. of interval	Distance Interval	Coefficient p
1	1.2 - 1.5	10
2	1.5 - 1.8	40
…	…	…
20	6.9 - 7.2	760

a)   b)   c)
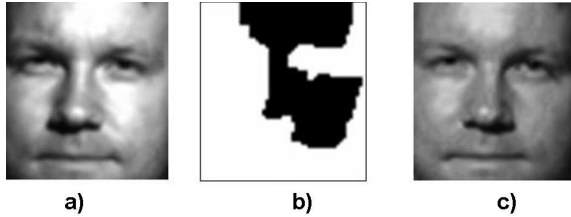
Fig. 2. Example of face image normalization in the Yale B database using the proposed method; a) original image, b) segmented region, c) normalized image

p. is the coefficient that depends of the Euclidean distance between the mean value and each value of the image inside the segmented region, the values of p are increased on a fixed quantity together with the distance interval, Table 1 shows the distance intervals and their corresponding coefficients used by us.

Taking in to account that the segmentation extracts pixels affected by illumination surrounded by non affected pixels, the normalization algorithm works with the values of these non affected pixels, the effect is the change of pixel values inside the region in function of the mean value calculated, without lost of information (see Fig 2).

4   Experiments

4.1   The Yale B Database

We experimented the proposed approach in images from Yale B database [12].

The Yale B database contains 64 different illumination conditions for 10 subjects. The illumination conditions are a single light source, the position of which varies horizontally and vertically. For the evaluation of the effectiveness of the detection process we take a test set composed by 50 images. We take 5 images per subject containing the low frequency illumination effect (specular light). Fig 3 shows an example of used images.

Fig. 3. Example of 5 images per subject with low frequency pixel values in some areas of images (specular light)

4.2   Evaluation of the Performance of Segmentation Combined with the Photometric Normalization

With generated images we compared the results in two experimental schemes. The idea was to measure how the similarity is affected by illumination changes and how the proposed approach improves the effect caused by these changes. Normalized correlation has been chosen as it has proved to be a successful similarity measure in face recognition [13]. For identical images it takes the maximum value equal to unity.

Face detection is achieved trough the Viola and John's algorithm [14], and are implemented at the OpenCV library [15]. There are several advantages offer by this method: The image representation called integral image, allows a very quickly computation of the features used by the detectors. The learning algorithm based on Adaboost, allows to select a small number of features from the initial set, and to obtain a cascade of simple classifiers to discriminate them [14]. A cascade of detectors was used to detect the faces.

To obtain geometrically normalized images we implemented an algorithm [13] that consists of the following steps: Smoothing, rotating, scaling and resampling the input image. The smoothing is performed by convolution with a Gaussian Filter of size5x5, the rotation and scaling outputs an image of size 55 rows x 51 cols. The left-eye is mapped onto the pixel position (19, 38) and the right-eye is mapped onto the pixel position (19, 12).

We compared results obtained in two different representation spaces, one in the image domain and other in the frequency domain using an illumination insensitive representation [13] based in the complex first derivative image to highlight the high frequency content and transformed it to the frequency domain and extracted the real part as illumination insensitive representation.

For the time consuming evaluation we compared the time taken by our method to normalizing of images affected by illumination taking as the region to be normalized the whole image, against the time consumed by four traditional algorithms of photometric normalization [16] (homomorphic filtering, anisotropic smoothing, isotropic smoothing and multiescale retinex) applied to whole image.

For the evaluation of the improvement of the classification task we evaluate our method in a face identification system based in the PCA method [17], since it has demonstrated inconsistent performance when the images have illumination problems [18].

For the evaluation we took one image per person from the mentioned database for the training set and comparing images with illumination problems and images photometrically normalized by our method. In the experiment we made a "close set" identification which evaluates the rate at which an individual in a database is correctly identified. We used the Cumulative Match Characteristic curve (Correct Rate vs. Rank) to analyze the behaviour of the proposed approach . A query is regarded as correct if the true fingerprint is contained in the list outputted by the algorithm

The correct rate is the rate of correct queries to all queries. The rank is the size of the list outputted by the algorithm. For all algorithms, the correct rate increases when the rank increases.

5   Experimental Results

The distributions of normalized correlations were compared in 4 different combinations. In Table 1 we show the different variants of normalized correlations and results of their comparison. We can see that when we applied the proposed approach and compared the normalized correlations in the image domain, we obtained a significant increase of the correlation coefficients of all normalized images respect to the original image.

Table 2. Normalized correlation and its comparison in Yale B database

Correlations	Description	Nc
	In the image domain	
A	10 subjects against the same subjects using 5 different images	0.80
B	10 subjects against the same subjects using 5 different images (with previous photometric normalization).	0.89
	In the frequency domain	
C	10 subjects against the same subjects using 5 different images	0.95
D	10 subjects against the same subjects using 5 different images (with previous photometric normalization).	0.99

A similar result is obtained using the representation in the frequency domain, in this case we obtained high correlation coefficients in both correlations, in concordance with results obtained by Garea and Kittler [12] but when applied the proposed approach the correlation coefficients reached nearer values to one.

The time consuming comparison (Table 2) shows that the proposed normalization method is faster than others traditionally used in computer vision even when it is applied to whole image. Taking in to account that the application of the proposed method will be only in those regions affected by illumination the time processing will decrease significantly.

The experimental results in identification (Fig 4) demonstrate that a high accuracy in the matching process is achieved when the images are previously normalized by our method.

Table 2. Comparison of averages of time consuming in the normalization process in milliseconds

Proposed method	Homomorphic	Multiescale	Anisotropic	Isotropic
0.1	3.4	3.5	10.0	0.8

6   Conclusions

The proposed method of segmentation and photometric normalization offers a set of advantages, the process is carried out only on those affected regions, and as a result we obtain a good save of time with a low computational cost.. The total save of
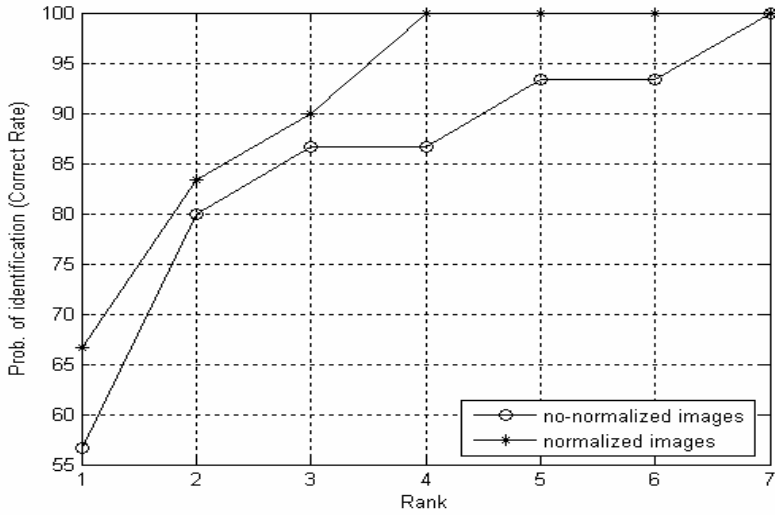
Fig. 4. Cumulative Match Characteristic curve in the Face identification system based on PCA approach

computational cost might be measure not only in the quantity of pixels that it avoids to process and also in the fact of having avoided the use of operations with high computational cost like the logarithms and the transformations to the frequency domain.

The proposed method might be used as a previous step in the general face recognition process and also as an independent process for the improvement of the visual effect of face images.

References

1. Tolba, A.S., El-Baz, A.H., El-Harby, A.A.: Face Recognition: A Literature Review. International Journal of Signal Processing 2(2) (2005)
2. Chellappa, R., Wilson, C.L., Sirohey, C.: Human and machine recognition of faces: A survey. Proc. IEEE 83(5), 705–740 (1995)
3. Belhumeur, P., Kriegman, D.: What is the set of images of an object under all possible lighting conditions. Int. J. of Computer Vision 28, 245–260 (1998)
4. Georghiades, A., Kriegman, D., Belhumeur, P.: From few to many: Generative models for recognition under variable pose and illumination. IEEE PAMI (2001)
5. Riklin-Raviv, T., Shashua, A.: The Quotient image: class-based re-rendering and recognition with varying illumination conditions. In: IEEE PAMI (2001)
6. Lee, K., Ho, J., Kriegman, D.: 9 Points of Light: Aquiring Subspaces for Face Recognition Under Variable Lighting IEEE Proc. Conf. Computer Vision and Pattern Recognition (2001)
7. Osher, S., Sethian, J.: Fronts propagating with curvature dependent speed: Algorithms based on hamilton-jacobi formulations. Journal of Computationl Physics 12–49 (1988)

8. Kass, M., Witkin, A., Terzopoulos, D.: Snakes: Active Contour Models. International. Journal of Computer Vision 1, 321–331 (1987)
9. Song, B., Chan, T.: A Fast Algorithm for Level Set Based Optimization (December 20, 2002) url: http://citeseer.ist.psu.edu/621225.html
10. Xiong, G.: A local normalization algorithm that uniformizes the local mean and variance of an image, URL:http://www.mathworks.com/matlabcentral/fileexchange/loadFile.do?objectId= 8303
11. Biomedical Imaging Group. Local normalization algorithm, http://bigwww.epfl.ch/demo/j
12. The Yale Face Database, URL: http://cvc.yale.edu/projects/yalefaces/yalefaces.html
13. Garea E., Kittler J.,Messer, K., Mendez H., An Illumination Insensitive Representation for Face Verification in the Frequency Domain. IEEE Computer Society. In: ICPR2006, pp. 215–218 (2006) ISBN 0-7695-2521-0
14. Viola, P., Jones, M.: Rapid Object Detection Using a Boosted Cascade of Simple Features. Mitsubishi Electric Research Laboratories, Inc. (2004)
15. Rainer, L.: Haarcascade_frontalface_default.xml. Intel License Agreement For Open Source Computer Vision Library (2000)
16. Gonzales, R., Woods, R., Eddins, S.: Digital Image Processing using Matlab. Ed Pearson pp. 404–405 (2004)
17. Belhumeur, P., Hespanha, J., Kriegman, D.: Eigenfaces vs.Fisherfaces: Recognition using Class Specific Linear Projection. IEEE Trans. Pattern Anal. Mach. Intelligence 19, 711–720 (1997)
18. Short, J., Kittler, J., Messer, K.: A comparison of photometric normalization algorithms for face verification. In: Kanade, T., Jain, A., Ratha, N.K. (eds.) AVBPA 2005. LNCS, vol. 3546, pp. 617–626. Springer, Heidelberg (2005)

Computing the Eccentricity Transform of a Polygonal Shape

Walter G. Kropatsch, Adrian Ion, and Samuel Peltier⋆

Pattern Recognition and Image Processing Group,
Faculty of Informatics, Vienna University of Technology, Austria
{krw,ion,sam}@prip.tuwien.ac.at

Abstract. The eccentricity transform associates to each point of a shape
the distance to the point farthest away from it. The transform is defined
in any dimension, for open and closed manyfolds, is robust to Salt &
Pepper noise, and is quasi-invariant to articulated motion. This paper
presents and algorithm to efficiently compute the eccentricity transform
of a polygonal shape with or without holes. In particular, based on exist-
ing and new properties, we provide an algorithm to decompose a polygon
using parallel steps, and use the result to derive the eccentricity value of
any point.

keywords: eccentricity transform, distance transform, polygon.

1 Introduction

To extract from a set of images the information required for a specific task, a
frequently used design pattern is to repeatedly transform the input image while
gradually moving from the low abstraction level of the input data to the high
abstraction level of the output data. The purpose is to have a reduced amount
of (important) information at the higher abstraction levels. One class of such
transforms that is applied to 2D shapes, associates to each point of the shape a
value that characterizes in some way it's relation to the rest of the shape, e.g.
the distance to some other point of the shape.

Examples of such transforms include the well known distance transform [1],
which associates to each point of the shape the length of the **shortest** path to
the border, the Poisson equation [2], which can be used to associate to each point
the **average** time to reach the border by a random path (average length of the
random paths from the point to the boundary), and the eccentricity transform [3]
which associates to each point the length of the **longest** of the shortest paths to
any other point of the shape. Using the transformed images one tries to come up
with an abstracted representation like the skeleton [4] or shock graph [5] build
on the distance transform, which could be used in e.g. shape classification or
retrieval.

Minimal path computation [6] as well as distance transform [7] are used in
2D and 3D image segmentation.

The eccentricity transform (ECC) has it's origins in the graph based eccentricity [8,9]. It has been defined in the context of digital images in [3,10], where properties and robustness have been shown, and it was applied in the context of shape matching in [11]. The eccentricity transform can be defined for discrete objects of any dimension, closed (e.g. typical 2D binary image) or open sets (surface of an ellipsoid), and for continuous objects of any dimension (e.g. 3D ellipsoid or the 2D surface of the 3D ellipsoid, etc.).

For the case of discrete shapes, a naive algorithm and a more efficient one for 2D shapes without holes, have been presented in [3]. For simply connected shapes on the hexagonal and dodecagonal grid, an efficient algorithm was given in [12]. Regarding continuous shapes, a detailed study has been made for the case of an ellipse, and some preliminary properties regrading rectangles, and a class of elongated convex shapes, have been given [13]. An algorithm for finding the eccentric vertices (furthest points) for the vertices of a simple polygon was given in [14].

This paper presents an algorithm for efficiently computing the eccentricity transform of a polygonal shape. First, the shape is decomposed into patches associated to corner points then these patches are used to compute the eccentricity.

Section 2 gives a short recall of the eccentricity transform and gives the main properties relevant for this paper. Section 3 briefly recalls existing algorithms. Sections 4 and 5 present the proposed algorithm, followed by discussion in Section 6 and possible extentions in Section 7. Section 8 concludes the paper and gives an outlook of the future work.

2   Recall ECC

In this section basic definitions and properties of the eccentricity transform are introduced following [3,11]. Let the shape $\mathcal{S}$ be a closed set in $\mathbb{R}^2$ and $\partial \mathcal{S}$ be its border[1]. A path π is the continuous mapping from the interval $[0, 1]$ to $\mathcal{S}$. Let $\Pi(\mathbf{p_1}, \mathbf{p_2})$ be the set of all paths between two points $\mathbf{p_1}, \mathbf{p_2} \in \mathcal{S}$ within the set $\mathcal{S}$. The geodesic distance $d(\mathbf{p_1}, \mathbf{p_2})$ between two points $\mathbf{p_1}, \mathbf{p_2} \in \mathcal{S}$ is defined as the length λ of the shortest path π, such that $\pi \in \Pi(\mathbf{p_1}, \mathbf{p_2})$, more formally

$$d(\mathbf{p_1}, \mathbf{p_2}) = \min\{\lambda(\pi(\mathbf{p_1}, \mathbf{p_2})_{\pi \in \Pi})\} \text{ where } \lambda(\pi(t)) = \int_0^1 |\dot{\pi}(t)| dt \qquad (1)$$

where $\pi(t)$ is a parametrization of the path from $\mathbf{p_1} = \pi(0)$ to $\mathbf{p_2} = \pi(1)$.

The eccentricity transform of $\mathcal{S}$ can be defined as, $\forall \mathbf{p} \in \mathcal{S}$

$$ECC(\mathcal{S}, \mathbf{p}) = \max\{d(\mathbf{p}, \mathbf{q}) | (\mathbf{q} \in \mathcal{S}\} = \max\{d(\mathbf{p}, \mathbf{q}) | \mathbf{q} \in \partial \mathcal{S}\} \qquad (2)$$

i.e. to each point $\mathbf{p}$ it assigns the length of the shortest geodesics to the points farthers away from it. In [3] it is shown that this transformation is quasi-invariant to articulated motion and robust against salt and pepper noise (which creates holes in the shape).

---

[1] This definition can be generalized to higher dimensions.

2.1   Properties of Eccentric Points

In general, an *extremal point* is a point where a function reaches an extremum (local or global). In the case of the geodesic distance d on a shape $\mathcal{S}$ we call an extremal point $\mathbf{x} \in \mathcal{S}$ a point for which $\exists \mathbf{p} \in \mathcal{S}$ s.t. $d(\mathbf{x}, \mathbf{p})$ is a local maximum.

An *eccentric point* of a shape $\mathcal{S}$ is a point $\mathbf{e} \in \mathcal{S}$ that is farthest away in $\mathcal{S}$ for at least one point $\mathbf{p} \in \mathcal{S}$ i.e. $\exists \mathbf{p} \in \mathcal{S}$ s.t. $ECC(\mathcal{S}, \mathbf{p}) = d(\mathbf{p}, \mathbf{e})$. For a shape $\mathcal{S}$, $E(\mathcal{S}) = \{\mathbf{e} \in \mathcal{S}\}$ denotes the set of all its eccentric points. The set of eccentric points $E(\mathcal{S})$ is a subset of the set of extremal points $X(\mathcal{S}) = \{\mathbf{x}\}$ i.e. $E(\mathcal{S}) \subseteq X(\mathcal{S})$ (eccentric points are global maxima for d, while extremal points only local maxima).

Knowing $E(\mathcal{S})$ can be used to speedup the computation of the $ECC(\mathcal{S})$. Instead of computing for each $\mathbf{p} \in \mathcal{S}$ the length of the geodesics to all the other points of $\mathcal{S}$ and taking the maximum, one can look at the inverse problem and compute the length of the geodesics from all $\mathbf{p} \in E(\mathcal{S})$ to all the points of $\mathbf{p} \in \mathcal{S}$, and for each $\mathbf{p}$ just take the maximum. This reduces the number of shortest path computation steps by $|\mathcal{S}| - |E(\mathcal{S})|$.

The following properties of extremal and eccentric points are relevant for this paper and concern bounded 2D shapes.

Property 1. All eccentric points $E(\mathcal{S})$ of a shape $\mathcal{S}$ lie on the border of $\mathcal{S}$ i.e. $E(\mathcal{S}) \subseteq \partial \mathcal{S}$. (*Proof* due to [3]).

Property 2. Being an eccentric point is not a local property i.e. $\forall B \subset \partial \mathcal{S}$ a boundary part (a 2D open and simple curve), and a point $\mathbf{b} \in B$, we can construct the rest of the boundary $\mathcal{S} \setminus B$ s.t. $\mathbf{b}$ is not an eccentric point of $\mathcal{S}$.
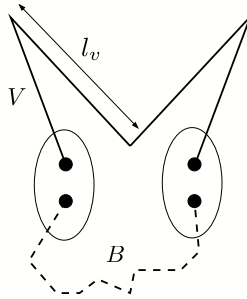
Fig. 1. Adding missing part V to existing one B s.t. no eccentric points lie on B

Proof. Let l_B be the length of B. We construct $\mathcal{S} \setminus B$ with the shape of a capital 'V' glued at its endpoints with the endpoints of B, and the length of the two branches $l_V > 2 * l_B$ (Figure 1). The obtained shape $\mathcal{S}$ will have two eccentric point sets clustered around the tops of the two branches of the 'V', a diamether $\max(ECC(\mathcal{S})) \approx 2 * l_V$, and no eccentric point will lie on B.   □

Property 3. No eccentric points $E(\mathcal{S})$ of a simply connected shape $\mathcal{S}$ lie on concave or straight parts of the border of $\mathcal{S}$ i.e. $\nexists \mathbf{e} \in E(\mathcal{S})$ s.t. $\partial \mathcal{S}$ is concave or straight at $\mathbf{e}$.

Proof. All points at the same distance to a point $\mathbf{p}$ lie on a circle $C(\mathbf{p}, r)$. If the circle is contained in the shape $\mathcal{S}$ then there are points further away to $\mathbf{p}$. A circle C through a point $\mathbf{x} \in C$ is partly inside the shape $\mathcal{S}$ if $\mathbf{x}$ is on a straight or concave part of the boundary. Thus there exists a point $\mathbf{q} \in S$ with $\mathbf{q} \notin C$ s.t. $d(\mathbf{p}, \mathbf{q}) > r$.

A hole can be bypassed in two ways. It partitions the points behind it in two groups: those for which the shortest path passes on one side and, those for which the shortest path passes on the other side of the hole. Shortest paths from both sides meet at the separation curve. Points on the separation curve have on both sides neighbours with smaller distances. Extremal paths never cross the separation curve. Thus, if $\mathbf{x}$ is on the separation curve then it is an extremal point no matter the curvature of $\partial \mathcal{S}$ at $\mathbf{x}$. ☐

Property 4. (from Property 3) All eccentric points $E(\mathcal{S})$ of a simply connected shape lie on convex parts of the border of $\mathcal{S}$ i.e $\forall \mathbf{e} \in E(\mathcal{S}) \Rightarrow \partial \mathcal{S}$ is convex at $\mathbf{e}$.

Properties 1, 3 and 4 also apply to extremal points.

Property 5. For any shape $\mathcal{S}$, all boundary points in convex regions of $\partial \mathcal{S}$ are external points. (Proof similar to Property 3).

From Properties 1-4 we see that for the case of simple polygons all corner points with angles less than 180° makeup the extremal points, but whether such a corner point is actually an eccentric point or not, can be known only after computing $ECC(\mathcal{S})$ for the polygon.

For the case of multiply connected 2D shapes, depending on the number and size of the holes, Properties 3 and 4 do not always hold (for a square with a maximum size square hole, all boundary points are eccentric points). But, due to Property 5, the corner points mentioned above are extremal points and thus still eccentric point candidates (see Section 6 for a discussion).

3   Previous Work - Algorithms

The naive algorithm to compute $ECC(\mathcal{S})$ for a given discrete shape $\mathcal{S}$ has a complexity of $O(|\mathcal{S}|^3)$ in the number of pixels $|\mathcal{S}|$. Eccentric points lie only on the boundary of $\mathcal{S}$. If we assume that the average number of border points $|\partial \mathcal{S}|$ is much smaller than $|\mathcal{S}|$, and we use Dijkstra's algorithm [15] to compute the shortest paths from one point to all other points (runs in $O(|E| + |\mathcal{S}| \log |\mathcal{S}|)$, where $|E|$ is the number of edges i.e. the number of adjacent pixel pairs), we get a complexity of $O(|\partial \mathcal{S}|(|E| + |\mathcal{S}| \log |\mathcal{S}|))$ for a more efficient algorithm. One can also use fast marching [16] for the computation of geodesic length $(O(|\mathcal{S}| \log |\mathcal{S}|))$, a case in which the complexity decreases to $O(|\partial \mathcal{S}||\mathcal{S}| \log |\mathcal{S}|)$.

For continuous shapes, a detailed study of the ellipse and some properties regarding rectangles and a class of elongated shapes are given in [13]. Ellipses can be divided along the short diameter and to each point of the short diameter one eccentric point in each half ellipse can be associated. The eccentricity of any point of the ellipse can be computed in linear time by finding its corresponding point on the short diameter [13]. Also, in the case of the ellipse, the set of eccentric points can be analytically characterized. For the eccentricity of the n corner points of simple polygons, an $O(n \log n)$ algorithm was given in [14].

4   Distances Inside a Polygonal Shape

Given a point $\mathbf{o}$ of the input polygon $\mathcal{S}$ we want to calculate the shortest distance between the point $\mathbf{o} \in \mathcal{S}$ and an arbitrary point $\mathbf{p}$ inside the shape. In a simply connected convex shape it is the length of the straight line $d(\mathbf{o}, \mathbf{p})$ connecting $\mathbf{o}$ and $\mathbf{p}$. However concave portions and holes may not allow straight connections in all cases.

We cover the inside of a polygonal shape by patches $\mathcal{P}_i$ within which the distance of a point $\mathbf{p} \in \mathcal{P}_i$ is the distance to a reference point $\mathbf{r_i} \in \mathcal{P}_i$ plus a handicap h_i:

$$d(\mathbf{p}, \mathbf{o}) = d(\mathbf{p}, \mathbf{r_i}) + h_i \qquad (3)$$

The handicap h_i corresponds to the length of the shortest path inside $\mathcal{S}$ between $\mathbf{o}$ and the reference point $\mathbf{r_i}$.

Create Patch($\mathbf{r}$, h, $\mathcal{P}$)

1. determine the visibility polygon $\mathcal{Q} \subset \mathcal{P}$ delineating the region inside $\mathcal{P}$ that can be reached from reference point $\mathbf{r}$ along a straight line.
2. for all occluding points $\mathbf{t} \in \mathcal{Q}$ do
   Create Patch($\mathbf{t}$, $d(\mathbf{r}, \mathbf{t}) + h$, $\mathcal{P} \setminus \mathcal{Q}$)
3. return patch $\mathcal{Q}$

We initialize the computation backwards from potential eccentric points by creating patches for all corner points $\mathbf{o} \in \mathcal{S}$: Create Patch($\mathbf{o}$, 0.00, $\mathcal{S}$).

Fig. 2 illustrates the first steps. It shows that patches overlap in the shadow of holes. Every hole of the shape can be bypassed by the shortest path on either sides of the hole. Hence all the points in the shadow of a hole can be reached along two alternate paths. Two overlapping patches can be cut along the *separation curve*, which is the curve where the two paths have equal length from $\mathbf{o}$:

$$d(\mathbf{p}, \mathbf{r_1}) + h_1 = d(\mathbf{p}, \mathbf{r_2}) + h_2. \qquad (4)$$

In general the separation curve is a hyperbolic arc. It degenerates into a straight line as in area H of Fig. 2 if the two handicaps are equal.
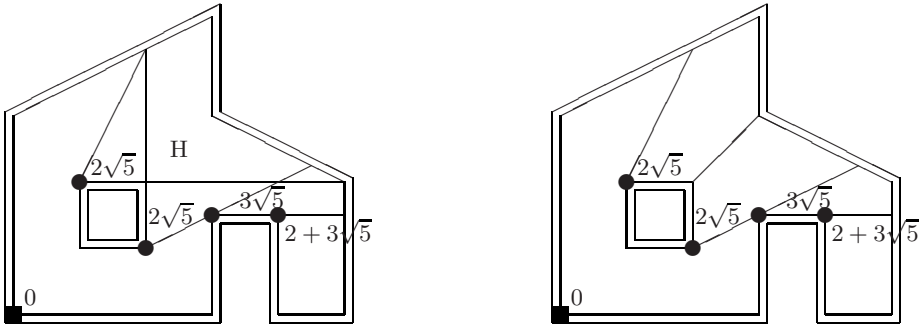
Fig. 2. First patches created by the reference point (bottom-left corner), the obtained handicaps, and the shadow 'H' created by the hole

Assume that the two reference points on the hole are $\mathbf{r_1}$ and $\mathbf{r_2}$ with handicaps h_1 and h_2 respectively. After translating the midpoint $\frac{\mathbf{r_1}+\mathbf{r_2}}{2}$ to the origin and rotating, the two reference points have coordinates $\mathbf{r_1} = (-f, 0)$ and $\mathbf{r_1} = (f, 0)$. Points $\mathbf{p} = (x, y)$ that the same distance to the original point must satisfy

$$d(\mathbf{p}, \mathbf{r_1}) + h_1 = d(\mathbf{p}, \mathbf{r_2}) + h_2 \tag{5}$$

Without restricting generality we assume that $h_2 > h_1$ and set $l = h_2 - h_1$. Then we have $\sqrt{(x+f)^2 + y^2} = \sqrt{(x-f)^2 + y^2} + l$, $(x+f)^2 + y^2 = (x-f)^2 + y^2 + 2l\sqrt{(x-f)^2 + y^2} + l^2$, $4xf - l^2 = 2l\sqrt{(x-f)^2 + y^2}$, $16x^2f^2 - 8xfl^2 + l^4 = 4l^2(x^2 - 2xf + f^2 + y^2)$, $\frac{16f^2 - 4l^2}{l^2(4f^2 - l^2)}x^2 - \frac{4}{4f^2 - l^2}y^2 = 1$, or the hyperbola $\frac{x^2}{(l/2)^2} - \frac{y^2}{f^2 - (l/2)^2} = 1$.

Note that the computation is independent for each starting point $\mathbf{o}$ and hence can be done in parallel.

5   Combining Distance Patches into the ECC-Patches

Every original starting point creates a separate set of patches in which the distance to the original point can be computed locally. Let us call these original patches the *distance patches*. In the following we combine the different sets of patches into a new partition of the ECC. The new patches will be called *ECC patches*.

5.1   The Smallest Common Partition

After creating a partition into patches for all starting points of the given polygon the produced partitions will not coincide with each other. We therefore overlay them to create a finer partition such that every patch of the finer partition fits into any of the distance patches. Fig. 3 shows the first two sets of patches.
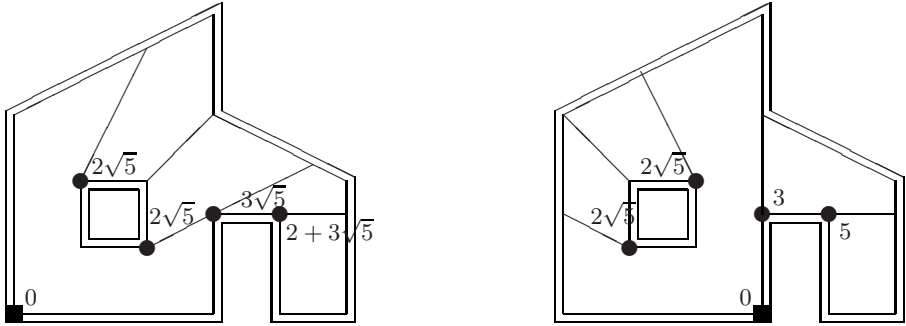
Fig. 3. The first two sets of patches

The resulting finer patches may have as many reference points as there were original points on the polygon since any extremal point on the polygon can be reached from any patch.

5.2 Example with One Concave Part

Fig. 4 shows a simple example with 8 corner points and 11 patches A, B, C, D, E, F, G, H, I, J, K. The table in Fig. 4 lists all the patches together with the reference points leading to all the 8 corner points together with the handicaps.

5.3 Non-maxima Suppression

The ECC computes the longest distance between any point $\mathbf{p}$ inside the shape to the farthest extremal point $\mathbf{x}$ inside the shape along the shortest path inside the shape. Every patch of the refined partition of the shape contains $n \geq 1$ reference points allowing the computation of the length of the shortest paths to any of the n original points.

First a reference point $\mathbf{r}$ may appear several times with different handicaps h depending on the number of paths from original points that go across $\mathbf{r}$. Only the largest handicap must be kept (dropped handicaps are indicated by (h) in Fig. 4).

For the ECC patch we need to keep further only the reference points $\mathbf{r} \in \mathcal{P}$ leading to the farthest extremal point: $\mathrm{argmax}\{d(\mathbf{p}, \mathbf{r}) + h | \mathbf{p} \in \mathcal{P}\}$. In some cases there may be more than one reference point leading to maximal distances in one patch. The patches that have more than one reference point after non-maxima suppression need to be further subdivided along curves separating influence areas of extremal points.

5.4 Subdividing Center Patches

Any remaining patch has two or more reference points $\mathbf{r_i}$. The subdivision can proceed similar to the generation of a weighted Voronoi diagram. Any pair of
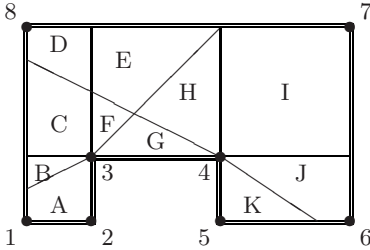
patch		1	2	3	4	5	6	7	8
A	r	1	2	3	3	3	3	**3**	8
	h	0.0	0.0	(0.0)	(2.0)	(3.0)	4.2	**4.5**	0.0
	d_{max}	1.4	1.1	1.4	3.4	4.4	5.6	**5.9**	3.1
B	r	1	2	3	3	3	3	**7**	8
	h	0.0	0.0	(0.0)	(2.0)	(3.0)	4.2	**0.0**	0.0
	d_{max}	1.4	1.4	1.1	3.1	4.1	5.3	**5.6**	2.5
C	r	1	2	3	4	4	**4**	7	8
	h	0.0	0.0	0.0	(0.0)	(1.0)	**2.2**	0.0	0.0
	d_{max}	2.5	2.7	1.8	3.6	4.6	**5.8**	5.4	2.2
D	r	1	2	3	4	4	**6**	7	8
	h	0.0	0.0	0.0	(0.0)	1.0	**0.0**	0.0	0.0
	d_{max}	3.2	3.2	2.2	3.6	4.6	**5.8**	5.0	1.4
E	r	1	3	3	4	4	**6**	7	8
	h	0.0	1.0	(0.0)	(0.0)	1.0	**0.0**	0.0	0.0
	d_{max}	4.2	3.8	2.8	2.8	3.8	**5.0**	4.1	3.0
F	r	1	3	3	4	4	4	**7**	8
	h	0.0	1.0	(0.0)	(0.0)	(1.0)	2.2	**0.0**	0.0
	d_{max}	2.4	2.0	1.0	2.2	3.2	4.4	**4.5**	2.2
G	r	3	3	3	4	4	4	**7**	8
	h	1.4	(1.0)	(0.0)	(0.0)	(1.0)	2.2	**0.0**	0.0
	d_{max}	3.4	3.0	2.0	2.0	3.0	4.2	**4.5**	3.6
H	r	**3**	3	3	4	4	6	7	8
	h	**1.4**	(1.0)	(0.0)	(0.0)	1.0	0.0	0.0	0.0
	d_{max}	**4.2**	3.8	2.8	2.0	3.0	4.1	3.9	3.6
I	r	**3**	3	3	4	5	6	7	8
	h	**1.4**	(1.0)	(0.0)	0.0	0.0	0.0	0.0	0.0
	d_{max}	**5.9**	5.5	4.5	2.8	3.6	3.6	2.8	5.4
J	r	4	4	4	4	5	6	7	**8**
	h	3.4	(3.0)	(2.0)	(0.0)	0.0	0.0	0.0	**0.0**
	d_{max}	5.6	5.2	4.2	2.2	2.2	2.2	3.0	**5.8**
K	r	4	4	4	4	5	6	7	**4**
	h	3.4	(3.0)	(2.0)	(0.0)	0.0	0.0	0.0	**3.6**
	d_{max}	5.2	4.8	3.8	1.8	1.5	2.2	3.6	**5.4**

Fig. 4. Polygon with ECC patches and table of reference points ($\mathbf{r}$), handicaps (h) and distances (d_{max}) of ECC patches (A-K) to corner points (1-8, table header)

reference points $\mathbf{r_1}, \mathbf{r_2}$ subdivides the patch into two half spaces along a second order curve through $N = \frac{\mathbf{r_1}+\mathbf{r_2}}{2} + (h_1 - h_2)\frac{\mathbf{r_1}-\mathbf{r_2}}{|\mathbf{r_1}-\mathbf{r_2}|}$. The remaining reference points are split among the two new patches and the subdivision repeated for all patches having more than one reference point until all patches have only one reference point left.

5.5 Merging Oversegmented Patches

The successive subdivision of patches may have introduced patches that have the same reference point. These patches can be merged in the final ECC-partitions

which subdivides the original shape into patches having exactly one reference point. The ECC value of any point inside the patch can be computed using the reference point $\mathbf{r}$ and its handicap h:

$$ECC(\mathcal{S}, \mathbf{p}) = d(\mathbf{p}, \mathbf{r}) + h \tag{6}$$

6 Discussion

Sections 4 and 5 produce a partition of shape $\mathcal{S}$ into patches $\mathcal{D}(\mathcal{S})$ s.t. the eccentricity tranform is analytically defined in each patch. Given the decomposition $\mathcal{D}(\mathcal{S})$, the computation of the eccentricity of a point $\mathbf{p} \in \mathcal{S}$ is reduced to:

Compute $ECC(\mathcal{S}, \mathbf{p}, \mathcal{D})$:

1. find patch $\mathcal{P} = (\mathbf{r}, h) \in \mathcal{D}$ s.t. $\mathbf{p} \in \mathcal{P}$
2. $ECC(\mathcal{S}, \mathbf{p}) = d(\mathbf{p}, \mathbf{r}) + h$

In a hierarchical structure (e.g. binary trees, quadtrees, irregular pyramids), step 1 runs in logarithmic time in the number of patches. Step 2 executes in a fixed amount of time. The number of patches depends on the number of corner points, the number of holes, and the number of points for which the computation in Section 4 was initialized.

For a simple polygon, the correct eccentricity is computed. In the worst case all corner points are also eccentric points and define at least one patch.

A hole makes the points in the shadow less accessible, which can make border points on the separation curve in the shadow further away than any corner point, and thus eccentric. The assumption that only corner points can be eccentric might not hold, and the number of eccentric points can be infinite. In this case the presented algorithm gives an approximation of the eccentricity transform, less or equal to the correct value. An upper bound for the error is half the length of the longest polygon side. To reduce this upper bound, one can initialize the computation in Section 4 with additional boundary points.

7 Extensions

Circular Arc: Reference point and handicap can also be used to correctly describe shapes with circular arcs. In this case the center of the circle serves as reference point and the radius as handicap. For concave circular arcs the radius carries a negative sign.

3D triangulated surface: In a triangulated surface two adjacent triangles share an edge. The corresponding 3D straight line serves as rotational axis to place the two adjacent triangles into a common plane such that shortest paths become straight lines in this new plane. Therefore the length of the shortest path from a corner to a point in an adjacent triangle can be

computed as the Euclidean distance to the corner after rotating it into the common plane. This can serve as reference point for all straight lines crossing the common edge segment.

8 Conclusion

In this paper an algorithm for efficiently computing the eccentricity transform of a continuous polygonal shape is presented. Corner points are candidates for eccentric points. Parallel steps are used to decompose the shape based on the length and the topology of the shortest paths to each corner point. The resulting decompositions are merged and used to derive the eccentricity transform of the polygon. An algorithm for discrete shapes will be derived from the one presented here. Future work includes a general algorithm for 2D continuous shapes.

References

1. Rosenfeld, A.: A note on 'geometric transforms' of digital sets. Pattern Recognition Letters 1(4), 223–225 (1983)
2. Gorelick, L., Galun, M., Sharon, E., Basri, R., Brandt, A.: Shape representation and classification using the poisson equation. In: CVPR (2), pp. 61–67 (2004)
3. Kropatsch, W.G., Ion, A., Haxhimusa, Y., Flanitzer, T.: The eccentricity transform (of a digital shape). In: 13th International Conference on Discrete Geometry for Computer Imagery, Szeged, Hungary, October 25-27, pp. 437–448. Springer, Heidelberg (2006)
4. Ogniewicz, R.L., Kübler, O.: Hierarchic Voronoi Skeletons. Pattern Recognition 28(3), 343–359 (1995)
5. Siddiqi, K., Shokoufandeh, A., Dickinson, S., Zucker, S.W.: Shock graphs and shape matching. International Journal of Computer Vision 30, 1–24 (1999)
6. Paragios, N., Chen, Y., Faurgeras, O.: 6. In: Handbook of Mathematical Models in Computer Vision, pp. 97–111. Springer, Heidelberg (2006)
7. Soille, P.: Morphological Image Analysis. Springer, Heidelberg (1994)
8. Harary, F.: Graph Theory. Addison-Wesley, Reading (1969)
9. Diestel, R.: Graph Theory. Springer, New York (1997)
10. Klette, R., Rosenfeld, A.: Digital Geometry. Morgan Kaufmann, San Francisco (2004)
11. Ion, A., Peyré, G., Haxhimusa, Y., Peltier, S., Kropatsch, W.G., Cohen, L.: Shape matching using the geodesic eccentricity transform - a study. In: 31st OAGM/AAPR, Schloss Krumbach, Austria, OCG (May 2007)
12. Maisonneuve, F., Schmitt, M.: An efficient algorithm to compute the hexagonal and dodecagonal propagation function. Acta Stereologica 8(2), 515–520 (1989)
13. Ion, A., Peltier, S., Haxhimusa, Y., Kropatsch, W.G.: Decomposition for efficient eccentricity transform of convex shapes. In: Kropatsch, W.G., Kampel, M., Hanbury, A. (eds.) CAIP 2007, Springer, Heidelberg (2007)
14. Suri, S.: The all-geodesic-furthest neighbor problem for simple polygons. In: Symposium on Computational Geometry, pp. 64–75 (1987)
15. Khuller, S., Raghavachari, B.: Basic Graph Algorithms. CRC Press (1998)
16. Sethian, J.: Level Sets Methods and Fast Marching Methods, 2nd edn. Cambridge Univ. Press, Cambridge (1999)

Robust Color Contour Object Detection Invariant to Shadows

Jorge Scandaliaris[1], Michael Villamizar[1], Juan Andrade-Cetto[1],
and Alberto Sanfeliu[1,2]

[1] Institut de Robòtica i Informàtica Industrial (UPC-CSIC)
[2] Dept. System Engineering and Automation, Universitat Politècnica de Catalunya (UPC)
Barcelona, Spain

Abstract. In this work a new robust color and contour based object detection method in images with varying shadows is presented. The method relies on a physics-based contour detector that emphasizes material changes and a contour-based boosted classifier. The method has been tested in a sequence of outdoor color images presenting varying shadows using two classifiers, one that learnt contour object features from a simple gradient detector, and another that learnt from the photometric invariant contour detector. It is shown that the detection performance of the classifier trained with the photometric invariant detector is significantly higher than that of the classifier trained with gradient detector.

Keywords: color invariance, shadow removal, object detection, boosting.

1 Introduction

The motivation of this work is to reduce the effect of shadows when detecting objects in a sequence of outdoor images. We show that the photometric invariant used in this paper is more sensitive to the contours of objects that are not shadows while neglecting shadow contours. Our experiments show a comparison between the proposed method and one using image intensity gradient information only.

There have been other approaches for removing shadows from images. Nadimi *et al.* [1] use a multistage approach based on physical models to detect moving shadows in video. Input video frames are passed through a moving object detection stage and then through a series of classifiers which distinguish object pixels from shadow pixels. They show extensive experimental results demonstrating the usefulness of their approach. Salvador *et al.* [2] exploit spectral and geometrical properties of shadows to segment cast shadows from still and moving images. They make initial hypotheses assuming that cast shadows darken the surfaces where they are cast. They further validate the initial hypotheses using complex hypotheses based on color invariance and geometrical properties, to end with an integration stage that confirms or rejects the hypotheses made.

In this work we also focus on a physical model and strive to remove the effects of shadows, but unlike the aforementioned methods we are concerned with producing a contour image invariant to shadows. This is because we base our boosting algorithm for object detection on contour information and having them invariant to shadows greatly improves the robustness of the detection process.

Our objective is to detect objects in image sequences where there are changes in illumination due to the presence of varying shadows. We use a gradient-like image to perform object detection based on contours in a way different to classical methods. Instead of calculating the gradient modulus from the color images, we detect contours that correspond to material changes using a modification to the approach proposed by Gevers *et al.* [3] based on a combination of photometric invariant contours and an automatic local noise-adaptive thresholding.

Boosting algorithms are very well known methods for fast object detection which are based on building robust classifiers from simple (weak) features [4,5]. We follow the framework addressed in [6], but based on contours instead of intensity images. The use of contour images allows the use of inner and outer object contours to perform robust detection without the drawback of background. Contour features are encoded by Haar operators so that they can be computed in constant time using the intensity integral image. However not all local contours are taken into account for modelling the object as a constellation of Haar operators, since this will require for a large number of weak classifiers. Therefore a learning boosting phase is used in order to select the most discriminant operators and then to linearly combine them for establishing a robust classifier.

To validate our method we have used a sequence of outdoor color images presenting varying shadows to perform object detection. Two boosting classifiers were used, one using simple intensity-based gradient images and the other using the contour images obtained with the proposed method, and their results were compared. We have also compared the effects of shadows in the appearance of spurious contours for intensity-based gradient images and photometric invariant contour images.

2   Robust Physics-Based Contour Detection

2.1   Basic Definitions

Images are the result of complex physical interactions between the light incident over the scene, the surfaces of the objects and the device that acquires the images. Several models of these processes have been developed during the years. One that is commonly used in computer vision applications is the dichromatic reflection model [7]. This model has two terms corresponding to two reflection processes. The light reflected from a surface is a combination of the light reflected at the interface, and the light which enters the substrate and is subsequently reflected back as the result of scattering. It is common to refer to these two reflection components as the interface reflection and the body reflection. The model can be further simplified if the illumination source is assumed to be white or spectrally smooth and the interface reflectance is assumed to be neutral, i.e. the Fresnel reflectance does not depend on wavelength. Under these assumptions the reflection model, expressed in term of the sensor responses, is given by

$$V_k = G_b(\boldsymbol{n}, \boldsymbol{s})E \int_\lambda B(\lambda)F_k(\lambda)\,d\lambda + G_i(\boldsymbol{n}, \boldsymbol{s}, \boldsymbol{v})ESF \qquad (1)$$

where V_k is the kth sensor response, G_b and G_i are geometric terms denoting the geometric dependencies of the body and surface reflection component, that is surface

normal, n, illumination direction, s, and viewing direction, v. $B(\lambda)$ is the surface albedo, E denotes the illumination source, and S denotes the Fresnel reflectance, both assumed independent of λ. $F_k(\lambda)$ denotes the kth sensor spectral sensitivity and $F_k = \int_\lambda F_k(\lambda)\, d\lambda$.

2.2 Color Models

Three color models are used because of their different and complementary properties regarding their response against parameters of the reflection model: RGB, $c1c2c3$ [8] and $o1o2$. In the RGB color model $\{R, G, B\}$ values correspond directly with V_k in (1). The $c1c2c3$ color model is defined by

$$c1(R, G, B) = \arctan(R/\max(G, B)) \tag{2}$$
$$c2(R, G, B) = \arctan(G/\max(R, B)) \tag{3}$$
$$c3(R, G, B) = \arctan(B/\max(R, G)) \tag{4}$$

and the $o1o2$ color model is defined by

$$o1(R, G, B) = (R - G)/2 \tag{5}$$
$$o2(R, G, B) = (R + G)/4 - B/2 \tag{6}$$

It follows from (1) that the RGB color model is sensitive to all parameters of the dichromatic reflection model. Gevers *et al.* [3,8] showed that under the assumptions included in (1) the $c1c2c3$ color model depends only on the sensor spectral sensitivities and the surface albedo or material for dull objects, being independent of shadows and geometry (E and G_b in the model). $c1c2c3$ still vary in the presence of highlights. They also showed that the $o1o2$ color model is invariant to highlights for shiny objects under the same assumptions. $o1o2$ is still dependent on geometry (G_b). These results are summarized in Table 1.

Table 1. Color model sensitivity to parameters of the image formation process. + denotes sensitivity and - invariance of the color model to a particular parameter.

	shadow	geometry	material	highlights
RGB	+	+	+	+
$c1c2c3$	-	-	+	+
$o1o2$	+	+	+	-

2.3 Contour Detection

To compute contours we start by calculating the x and y derivatives for each channel of the three aforementioned color models using Gaussian derivatives. Then the color gradient magnitude for each color model is computed using the Euclidean metric over the various channel derivatives:

$$\nabla C = \sqrt{\sum_{i=1}^{N}\left[\left(\frac{\partial c_i}{\partial x}\right)^2 + \left(\frac{\partial c_i}{\partial y}\right)^2\right]} \tag{7}$$

with C representing each color model, N being their dimensionality, and c_i the particular color channels.

The presence of noise in the images can lead to the appearance of maxima in the gradient modulus that are not related to any parameter of the image formation process (1). If it is assumed that the sensor noise is normally distributed, and that we know the parameters for each particular sensor, then using (14) and (15) (see appendix) the uncertainties associated to the $c1c2c3$ and $o1o2$ color models, as well as the different gradient moduli, can be propagated from the a priori known sensor uncertainties. Once we have the associated uncertainty of a measure, we can use it to eliminate noise, as it is shown in Sect. 2.4.

2.4   Contour Invariance

Once the gradient modulus of each color model is available, it is necessary to combine them to obtain the invariance against the undesired parameters on the image formation process.

Gevers *et al.* classified the edges into shadow-geometry, material and highlights [3]. To achieve this they first calculate the gradient magnitude of the RGB, $c1c2$ and $o1o2$ color models. Then they propagate the RGB uncertainties through the color models up to the gradient magnitudes, and local thresholding was used to binarize the gradient magnitudes to obtain C^b. The assumption that the noise is normally distributed implies that 99% of the values fall within a 3σ margin. If the value of the gradient moduli ∇C is greater than $3\sigma_{\nabla C}$ at a particular (x, y) location then the probability of that contour being due to noise is only of 1%:

$$\nabla C^b(x, y) = \begin{cases} 1 & \text{if } \nabla C(x, y) > 3\sigma_{\nabla C(x,y)} \\ 0 & \text{otherwise} \end{cases} \tag{8}$$

with C^b representing each color model used, that is RGB, $c1c2$ and $o1o2$. Finally a rule-base classifier based on the sensitivity of each color model to the dichromatic reflection model parameters, see Table 1, was used to label the resultant image as follows:

> **if** $\nabla C^b_{RGB} \neq 0$ **and** $\nabla C^b_{c_1 c_2} = 0$ **then**
>   classify as shadow or geometry edge
> **else if** $\nabla C^b_{c_1 c_2} \neq 0$ and $\nabla C^b_{o_1 o_2} = 0$ **then**
>   classify as highlight edge
> **else**
>   classify edge as material edge
> **end if**

We have taken a different approach to obtain the invariant contour image. Rather than classifying edges according to its physical nature we only pursue to detect object contours that are due to material changes, which are the contours relevant for the task we want to solve. Besides, we have realized that a binarized contour image discards information that might be valuable for the detection stage. Then, the contour image that we calculate is a gray-level image, where the image intensity gives a measure similar to a signal to noise ratio.

As in [3], we calculate the gradient magnitudes of the three color spaces defined in Sect. 2.2 and propagate the RGB uncertainties using (15) to obtain the uncertainties associated with the gradient magnitude of each color space, σ_∇ . Instead of performing the local thresholding defined in (8) at this stage, we define a function M in the following way:

$$M = \nabla RGB \cdot \nabla c1c2c3 \cdot \nabla o1o2 \tag{9}$$

M will have a maximum value when the gradient moduli of all color models have simultaneously a maximum, and will have low values when the gradient modulus of any of the color models is low. By looking at Table 1 it is evident that the response of M emphasizes material changes in the image, while minimizing those due to shadow-geometry and highlights.

Then, the uncertainty in the function M is also computed using (15) to yield

$$\sigma_M \le \left(\frac{\partial M}{\partial (\nabla RGB)} \sigma_{\nabla RGB} + \frac{\partial M}{\partial (\nabla c1c2c3)} \sigma_{\nabla c1c2c3} + \frac{\partial M}{\partial (\nabla o1o2)} \sigma_{\nabla o1o2} \right) \tag{10}$$

with $\sigma_{\nabla C}$ being calculated from(15) for each color model

$$\sigma_{\nabla C} \le \frac{\sum_i \left[\left| \frac{\partial c}{\partial x} \right| \cdot \sigma_{\underline{\quad}} + \left| \frac{\partial c}{\partial y} \right| \cdot \sigma_{\underline{\quad}} \right]}{\sqrt{\sum_i \left[\left(\frac{\partial c}{\partial x} \right)^2 + \left(\frac{\partial c}{\partial y} \right)^2 \right]}} \tag{11}$$

with C representing each color model and c_i the particular color channels. The uncertainties $\sigma_{\underline{\quad}}$ and $\sigma_{\underline{\quad}}$ are calculated taking into account that the derivatives are approximated by filtering with a mask, gaussian derivatives in this case. Using (15), it results that the uncertainties can be computed by filtering the uncertainty planes with the absolute value of the mask used for the derivatives. The uncertainty planes are nothing more than the propagation of the RGB uncertainties to the other color models using (14).

The assumption that the noise is normally distributed used in Sect. 2.4 is also used here to obtain a local noise-adaptive threshold for removing noisy measurements from M.

$$M' = \begin{cases} M & M > 3\sigma_M \\ 0 & \text{otherwise} \end{cases} \tag{12}$$

The final result is a gray-level contour image that emphasizes the contribution of material changes and at the same time reduces that of shadow-geometry and highlights on the input images. Note that while a value of zero in M' means there is a probability of 1% of *being wrong*, higher values reduce that probability further. Thus intensity in M' is directly correlated with the probability of a given (x, y) location being a material change.

3   Experiments

In order to evaluate the robustness of the proposed method we have made experiments of detecting an object in a sequence of images, where there are changes in the

illumination of the objects due to varying shadows. For the experiments we have used two boosting classifiers that learn contour object features. One boosting classifier uses contour features coming from a simple gradient detector. The second boosting classifier uses our method, that is the photometric invariant contour detector.[1]

Using both methods, the learning boosting step selected 100 weak classifiers for each method from a learning set of 50 object images and 200 background images. The background images were extracted from patches of outdoor and indoor images using a randomized process. The learning set of images included objects with small variations of position and scale which make this classifier robust against small object transformations.

The two boosting classifiers were tested over a sequence of 934 images where one static object under varying shadows appears. Some frames are shown in Figure 1, where we can also appreciate some detection results. The input color images are on the left column, the results of the classifier based on the simple gradient detector are on the middle column, and the results of the proposed method are on the right column. Each green square in the images represents one object detection. We can see how the classical method is perturbed by the varying shadows, being unable to detect the object under these illumination variations. On the other hand, the classifier based on photometric invariant contours achieves a correct detection thanks to the shadow-free contours, being the contour object features reliable over the sequence. The Figure 3 shows the ROC (*Receiver Operating Characteristic*) curves for both methods. The proposed method overcomes the classical one, achieving 100% detection, meanwhile the simple gradient method performs 79% without false positives.

In Figure 4, there are some test frames when the threshold in boosting classifier is reduced from $\beta = 0.75$ (Figure 1) to $\beta = 0.65$. We can notice that the object is detected in all cases though with many false positives for the method based on simple gradients, unlike the proposed method that continues detecting correctly, demonstrating its robustness and reliability with a relaxed classification threshold.

We have evaluated the influence of shadows both in the proposed photometric invariant contour images and the simple gradient images. The motivation of the experiment was to test the relative increase in contour pixels caused by shadows. To this purpose, a subset of the outdoor image sequence consisting of 87 images from the total of 934 was randomly selected. This subset was enlarged by 3 images selected with the constraint of being shadow free. Because this constraint could not be met over the entire image, the images were cropped around the carton recycle bin used as target object in the detection experiments.

The images were processed and both the gradient and the photometric invariant contour images were obtained. One shadow free contour image was visually inspected for each method. The inspection determined a threshold for each method that produced a binarized image with a similar aspect between them and good correlation between object features and contours. This shadow-free image was used as the reference image, and then the following metric was used for all images

$$E_{bd} = \text{count}\left(\text{abs}\left(\Delta I\right) > k\right)/E_r \tag{13}$$

---

[1] Information about the boosting classifier can be found in [6].

(a)   (b)   (c)
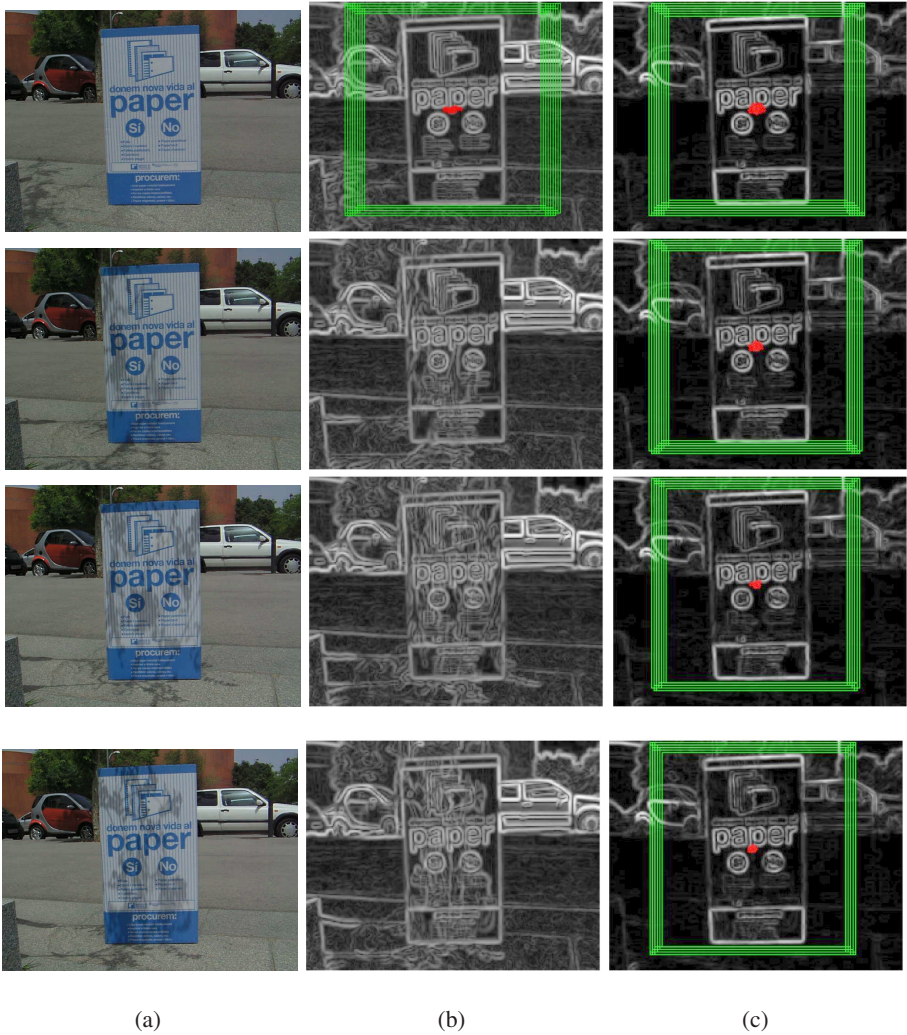
Fig. 1. Test 1. Frames when the threshold β in the boosting classifier is set to 0.75. (a) Input images, (b) gradient based detections and (c) invariant based detections.

with $\Delta I = I_i - I_r$ the difference between a given image and the reference, k the afore-mentioned thresholds, one for each method and $E_r = \text{count}(I_r > k)$ the number of contours in the reference image. E_{bd} is the ratio of the number of incorrectly detected contours to the number of contours in the reference image. The results are shown in Fig. 2. As can be seen, the ratio is small and stable for the proposed method, with a maximum number of misdetected contours of around 3% of the number of contours in the reference image. For the gradient contour image the ratio is unstable and the number of misdetected contours ranges from 35 to 65 percent of the number of contours
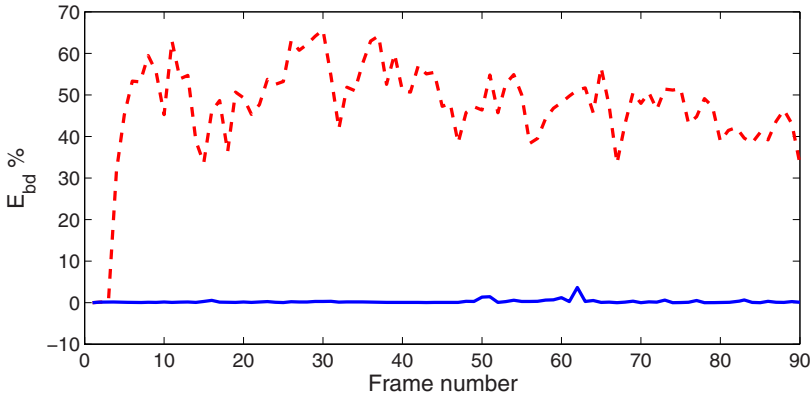
Fig. 2. Percent ratio of the number of misdetected contours to the number of contours in the reference image for the photometric invariant contour image (—), and for the simple gradient contour image (- -)

(a)   (b)
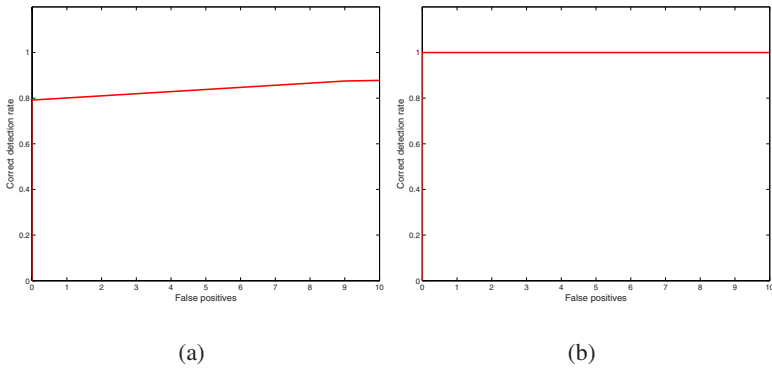
Fig. 3. ROC curves. (a) Simple gradient and (b) photometric invariant contours.

in the reference image. This simple metric clearly shows the impact of the proposed method in the presence of shadows.

4   Conclusions

The proposed method has demonstrated to perform robust object detection in outdoor images under varying shadows and illumination changes, overcoming the classical method relying on a simple gradient detector. This latter method fails due to varying shadows producing *new* object contour features that eventually mislead the classifier. On the other hand, the proposed method based on photometric invariant gives a contour image without shadow effects. This facilitates the identification task, as the classifier focuses on actual object features. The experiments showed the usefulness of the shadow

(a)   (b)   (c)
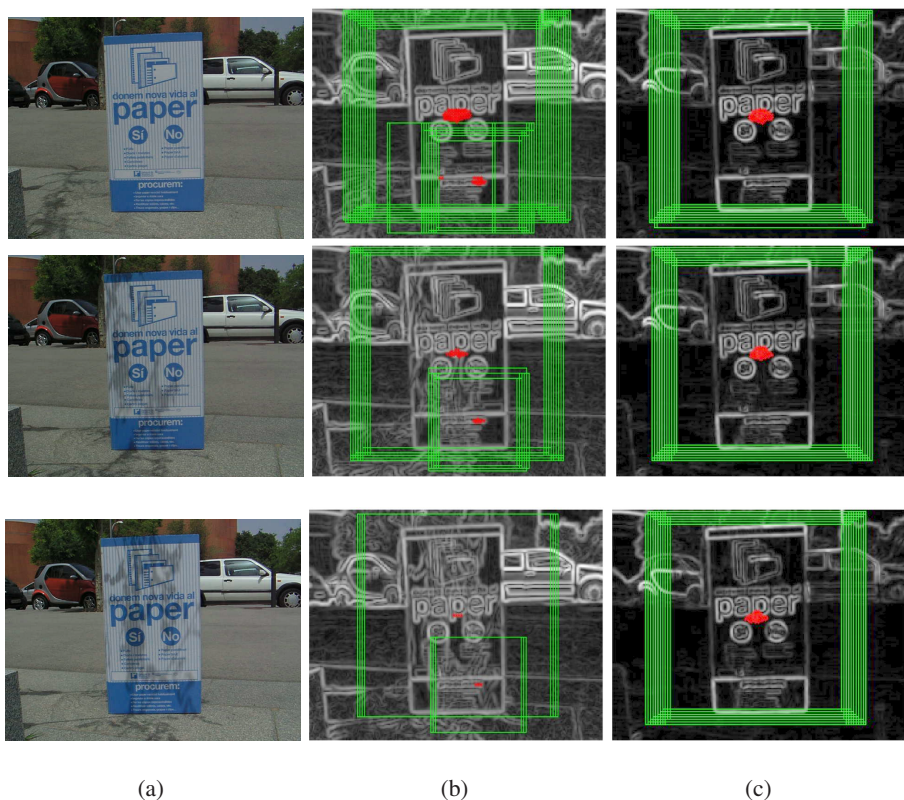
Fig. 4. Test 2. Frames when the threshold β in the boosting classifier is reduced to 0.65. (a) Input images, (b) gradient based detections and (c) invariant based detections.

invariance of the method in a sequence of outdoor images for object detection where the illumination conditions were not controlled.

References

1. Nadimi, S., Bhanu, B.: Physical models for moving shadow and object detection in video. IEEE Trans. Pattern Anal. Machine Intell. 26(8), 1079–1087 (2004)
2. Salvador, E., Cavallaro, A., Ebrahimi, T.: Cast shadow segmentation using invariant color features. Comput. Vis. Image Und. 95(2), 238–259 (2004)

3. Gevers, T., Stokman, H.: Classifying color edges in video into shadow-geometry, highlight, or material transitions. IEEE Trans. Multimedia 5(2), 237–243 (2003)
4. Viola, P., Jones, M.: Rapid object detection using a boosted cascade of simple features. In: Proc. 15th IEEE Conf. Comput. Vision Pattern Recog. Kauai, pp. 511–518. IEEE Computer Society Press, Los Alamitos (2001)
5. Shotton, J., Blake, A.R.C.: Multiclass object recognition with sparse, localized features. In: Proc. IEEE Int. Conf. Comput. Vision, pp. 503–510 (October 2005)
6. Villamizar, M., Sanfeliu, A., Andrade-Cetto, J.: Computation of rotation local invariant features using the integral image for real time object detection. In: Proc. 18th IAPR Int. Conf. Pattern Recog. Hong Kong, vol. 4, pp. 81–85. IEEE Computer Society Press, Los Alamitos (2006)
7. Shafer, S.A.: Using color to separate reflection components. Color Res. Appl. 10(4), 210–218 (1985)
8. Gevers, T., Smeulders, W.M.: Color based object recognition. Pattern Recogn. 32, 453–464 (1999)
9. Taylor, J.R.: An introduction to error analysis. 2nd edn. University Science Books, Sausalito, CA (1997)

Appendix: Error Propagation

Suppose that $x, \ldots, z$ are measured values with uncertainties $\sigma_x, \ldots, \sigma_z$ and the measured values are used to compute the function $q(x, \ldots, z)$. If the uncertainties in $x, \ldots, z$ are independent and random, then the uncertainty in q is [9]

$$\sigma_q = \sqrt{\left(\frac{\partial q}{\partial x}\sigma_x\right)^2 + \cdots + \left(\frac{\partial q}{\partial z}\sigma_z\right)^2} \tag{14}$$

In any case the uncertainty is never larger that the ordinary sum

$$\sigma_q \leq \left|\frac{\partial q}{\partial x}\right|\sigma_x + \cdots + \left|\frac{\partial q}{\partial z}\right|\sigma_z \tag{15}$$

An Evaluation of Video Cut Detection Techniques

Sandberg Marcel Santos[1], Díbio Leandro Borges[2], and Herman Martins Gomes[1]

[1] Departamento de Sistemas e Computação, Universidade Federal de Campina Grande, Av.
Aprígio Veloso s/n, 58109-970 Campina Grande PB, Brazil
`{sandberg,hmg}@dsc.ufcg.edu.br`
[2] Departamento de Ciência da Computação, Fundação Universidade de Brasília, Campus
Universitário Darcy Ribeiro, 70910-900 Brasília DF, Brazil
`dibio@unb.br`

Abstract. Accurate detection of shot transitions plays an important role on automatic analysis of digital video contents, and it is a key issue for video indexing and summarization, amongst other tasks. This work presents in more detail a novel strategy, based on the concept of visual rhythm, to automatically detect sharp transitions or cuts in arbitrary videos. The central part of the work is a comparative evaluation of this strategy versus three other very competitive approaches for video cut detection: one based on the visual rhythm concept, other based on pixel differentiation and a last one based on color histograms. The evaluation carried out demonstrated that the proposed method achieves, on average, higher recall rates at a cost of a slightly lower precision.

Keywords: video cut detection, visual rhythm, pixel differentiation, color histograms, video summarization.

1 Introduction

Digital video applications, such as digital libraries, interactive TV, and multimedia information systems in general, are growing fast due to the advances in multimedia encoding and decoding technologies, increase in computing power and the ever-expanding internet [1]. This has stimulated research in the areas video indexing, retrieval and summarization. While digital videos can be seen as formed by a concatenation of 2-D image samples (frames) of a scene, shots can be seen as a basic functional unit of a video. Shots are defined as uninterrupted sequences of video frames with graphic, spatial and temporal configurations [3]. The automatic detection of shots or the transition between two consecutive shots is an essential part of most video content analysis algorithms.

Gradual and sharp transitions are the two most known types of video transitions [4]. In this paper, we focus on the problem of detecting sharp transitions (or cuts), which is usually taken as a simpler problem than that of gradual transition detection. However the state of the art, as indicated in our literature review, reveals there is still room for improvements in the accuracy of cut detection techniques. In a previous work [13], we proposed an algorithm for video cut detection based on the concept of visual rhythm and compared this algorithm with a previous approach, based on the same principle (the work by Lu et al. [10]). The visual rhythm concept [4] is

explained in more detail in Section 2. In the present paper, the focus was to extend the previous evaluation by incorporating two other widely used and well established techniques based on pixel differentiation (inspired on a measure of motion saliency as given in Wildes [16]), and one based on color histogram (combining the strategies presented by Lienhart [9], and Yeo and Liu [17]).

Next section presents a bibliographic review of related work on video transition detection, including all the competing approaches evaluated in this paper. Section 3 presents technical details of the principal visual rhythm approach. The comparison has been made using a set of arbitrary videos, collected from a public video database [12], which is described in more detail in Section 4. The experimental evaluation and results are also in Section 4. Final considerations and comments on future works are presented in Section 5.

2   Bibliographic Review

There is a variety of methods and techniques proposed to perform the automatic detection of video transitions. Gargi et al. [3], Lienhart [8,9] and Hanjalic [5] developed comparative studies for some of the most representative approaches.

Methods that do not use computed features of compressed videos (e.g. the motion vectors of an *mpeg* video) rely on the assumption that frames from the same shots present a certain visual consistency, whereas frames in the vicinity of video transitions present important variation. Color histograms, pixel differences, edge variation and motion are very popular amongst the kinds of features that have been utilized in the characterization of such variation.

Yeo and Liu [17] and Zhang et al. [19] proposed methods for cut detection designed to distinguish between sharp transitions and sharp illumination variations. Yeo and Liu [17] detected peaks generated by each sharp illumination variation (one at the beginning and another at the end of the variation). Zhang et al. [19], on the other hand, considered models of ideal cut and flashlight detection. Other methods that are based on edge detection, usually demand high computation resources and are sensitive to fast object and camera motion. In order to address these questions, Jun and colleagues [6], proposed to apply a median filter to the features extracted from the video and to compare it to the original signal. A similar work has been done by Leszczuk et al. [7], who implemented a differential motion factor. Other works [15,18] employed a local adaptive threshold, instead of a fixed threshold, to classify an inter-frame variation as sharp or not.

In order to reduce the sensitivity of fast object and camera motion Zheng et al. [20] performed feature extraction (color histogram, pixel differences, standard deviation, mean deviation and motion vectors), in either compressed or uncompressed domains. From the analysis of the variation of these features, decisions (such as the choice for global or local thresholds) are taken and the transition detection is performed.

A popular method for cut detection is based on the concept of visual rhythm [4,10, 11,13]. The visual rhythm is a simplification of a video into a 2-D image [4]. A video sequence is typically seen as having three dimensions: one temporal (corresponding to the frame sequence) and two spatial (corresponding to the XY dimensions of each frame). The visual rhythm approach samples each video frame in such a way that it is

represented by a single 1-D line of pixels. These 1-D lines are, in turn, concatenated to form a 2-D image. Thus, a simplified video representation is obtained with only two dimensions: one temporal (typically the horizontal direction) and another spatial (typically the vertical direction). The 1-D lines that form this new 2-D representation can either be the main diagonal, the central row or the central column of pixels of a video frame. Chung et al. [2] considered the main diagonals as the most interesting lines to use because they contain information from both the lines and the columns of the frame. However, Lu et al. [10] opted to use the horizontal central line, because, according to them, when recording a video, the camera normally moves in the horizontal plane and the camera operator usually locates the interesting objects in the center of the field of view.

After creating the visual rhythm signal, sharp transitions or cuts in a video can be detected using bi-dimensional image processing algorithms. Firstly, different patterns in the signal are identified, and then an association between each video transition event and a pattern in the visual rhythm signal is made. The video cut detection task is therefore to look in the signal for a pattern corresponding to a sharp transition (usually a distinctive vertical line that separates two homogeneous patterns, one to the left and another one to the right of the visual rhythm signal).

One drawback of this approach is that the association between the sharp transition and the line that separates two video shot patterns is not one-to-one. Every sharp transition in the video creates a distinctive vertical line separating two patterns in the visual rhythm; however the contrary is not necessarily true, since this line can represent different video events. An attempt to minimize this problem, presented by Guimarães et al. [4], was to perform a search for vertical lines that separate patterns in different visual rhythms of a same video (obtained from different video samplings).

Other authors consider the problem of cut detection as a problem already solved. However, the results of current approaches are not yet close to perfect detection, so there is still room for improvement. Moreover, due to difficulties in annotating video datasets, most methods are evaluated using only a small number of videos. Existing methods would possibly have reduced performance for larger datasets [19].

3   Main Approach

This section details the main cut detection strategy evaluated in this work. A preliminary evaluation and additional bibliographic references related to this strategy can be found in an earlier paper [13] by the same authors. The strategy is based on the concept of visual rhythm as described in Section 2 and differs from previous works with regards to the computation of the visual rhythm signal and the cut detection rule.

3.1   Description

The approach starts with the following: for each pair of adjacent columns of a generated 2-D visual rhythm image, we compute the integral of the absolute differences of pixel intensities in all lines, according to Equation 1.

$$D_j = \sum_{i=1}^{N} \left| f(i, j) - f(i, j+1) \right| \tag{1}$$

where i and j are line and column indices; D_j is the integral of the absolute differences for columns j and $(j+1)$; N is the total number of lines; $f(i, j)$ is the pixel intensity at line i and column j, and $f(i, j+1)$ is the pixel intensity at line i and column $j+1$.

The values of D_j for each pair of adjacent columns create a 1-D signal that indicates the abrupt changes between the columns of the image (i.e. the sharp transitions between the frames of the video). As an example, Fig. 1(a) presents a sample of one of the videos used in the experiments that are described in Section 4. Figure 1(b) presents a 2-D image (concatenation of diagonal stripes) derived from the video in Fig. 1(a). Finally, Fig. 2 presents the 1-D signal created from the Fig. 1(b).

(a)   (b)
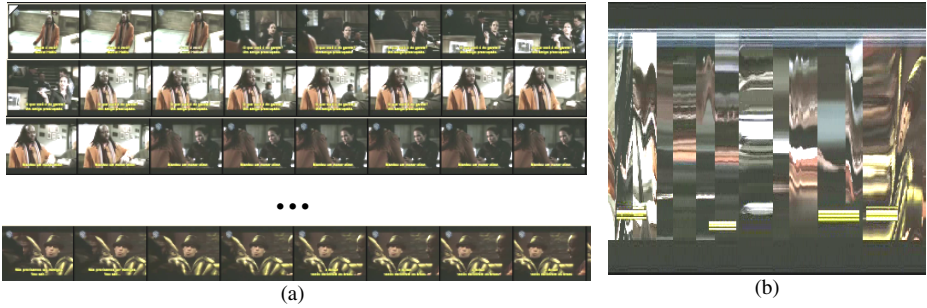
Fig. 1. (a) Sample of one of the videos used in the experiments; (b) 2-D image generated from the video using a concatenation of diagonal frame stripes
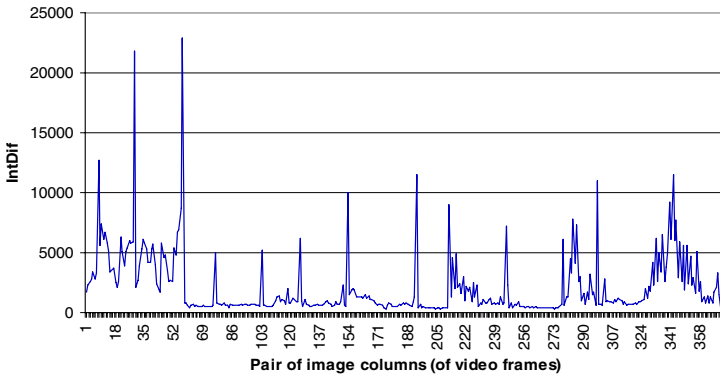
Fig. 2. 1-D signal generated from the visual rhythm image in Fig. 1(b)

The principle of the proposed method is that sharp peaks in the 1-D signal indicate the presence of sharp transitions in the video. Thus, the next step consists in automatically detecting these peaks and labeling the correspondent frames as cuts. Equation 2 formalizes this principle: a point j in the 1-D signal (D_j) is labeled as a sharp peak (indicating a cut or sharp transition) if it is greater than or equal the product between a pre-defined factor (k) and the average of the points inside a window (of size w) centered on the point (frame) j under analysis.

$$\textbf{if } D_j \geq k \times A \textbf{ then } D_j \text{ is a cut,} \tag{2}$$

where $A = \{(j - hw) + [(j - hw) + 1] + \ldots + j + \ldots + [(j + hw) - 1] + (j + hw)\} / w$; and $hw = \left\lfloor w\big/2 \right\rfloor$.

3.2 Finding Best Parameters

The procedure adopted to define the values for window size (w) and factor (k) is described as follows. It is based on an exhaustive search strategy, with the evaluation of possible combinations of window sizes and factors given a sampling interval. The window size w varied from 3 to 15, in steps of 2 (this way, we guaranteed that it is always an odd number, i.e. the window will always have a central point), and the factor k was varied from 1.1 to 3.0, in steps of 0.1. For each window-factor combination and each of the five videos (parameter fitting set), we calculate the precision $P^v_{w,k}$ and recall $R^v_{w,k}$ metrics for the parameter fitting set, where v is a video from the parameter fitting set; $v = 1, 2, \ldots 5$; $w = 3, 5, \ldots 15$; and $k = 1.1, 1.2, \ldots 3.0$. Then, we compute the arithmetic mean between the precision and the recall, which we named the correctness rate (C), presented in Equation 3.

$$C^v_{w,k} = \frac{\left(P^v_{w,k} + R^v_{w,k}\right)}{2} . \tag{3}$$

The window-factor combination which maximized, on average, the correctness rates for the five videos of the parameter fitting set was used to run the proposed algorithm on a new set of five videos (testing set). Precision $P^t_{w,k}$, recall $R^t_{w,k}$ and correctness $C^t_{w,k}$ rates were again computed for the testing set, where t is a video from testing set; $t = 6, 7, \ldots 10$; and (w, k) is the chosen best parameter pair.

Instead of finding the best window-factor combination from just a single pair of video sets (parameter fitting and testing), a cross-validation step was employed. The above procedure was repeated for all possible combinations of parameter fitting and testing sets taken from the complete set of 10 videos available. For each combination of parameter fitting and testing sets, we determined a window-factor pair which maximized the average correctness rates of the correspondent parameter fitting set. The several combinations of parameter fitting experiments were used to calculate the correctness rates of their correspondent testing sets. The averages of the several correctness rates obtained (for the different testing sets) were compared, and the window-factor pair associated with the testing set that presented the highest average correctness rate was defined as the ideal pair. The ideal window size (w) and factor (k) found as described above were 11 and 2.2, respectively.

The purpose of this cross-validation step was to find the best set of parameters to be used in experiments with new videos, taking into account all possible 5-element combinations of the available videos at this stage. A major drawback of this exhaustive search approach was that it was very time consuming. A computationally

more attractive alternative for this task would be to use a genetic algorithm optimization, but this was left as future work.

The videos used in the cross-validation described in this section were random and very diverse in nature, containing samples of indoor and outdoor sports, documentaries, TV series, and advertisements, among others. There was no special concern about selecting videos with static camera. The majority of the videos had camera movements, some especially intense. Video sizes were all of 320×240 pixels, and they have been captured in *mpeg*2 or *avi* formats, and resampled to 12 frames per second to reduce computational processing costs. The approximate length of each video was 31 seconds, resulting in about 375 frames per video. Frames where sharp transitions occur in the videos have been manually annotated.

4   Database, Evaluation and Results

The evaluation described in this section considered five new videos, not used for finding the ideal values of window size and the factor, as described in the previous section. The five new videos were taken from a public video base, the Open Video Project [12]. TRECVID project webpage [14] was also consulted, where annotated transitions are available for some videos of the Open Video Project database. In the TRECVID project, the videos of Open Video Project base are identified by *ids*. The videos selected for the evaluation performed in this paper are listed on Table 1. This table associates each *id* to its corresponding name in the Open Video Project [12].

Table 1. Videos utilized in the evaluation

id	Original Name (Open Video Project [12])	Duration	# of Frames (at 12 fps)
150	Three Smart Daughters (Singer Screen Ad)	1 min 21 s	970
160	Trip, The	48 s	604
169	Wonderful New World of Fords, A (1960 Ford Spot)	3 min	2184
269	Roads to Romance: The Santa Cruz Trail and Land of the Giant Cactus (in Arizona)	3 min	2163
272	She Caught on Quick (Singer Screen Ad)	1 min 15 s	957

These five videos have dimensions of 352×240 pixels, and are in *mpeg* format, sampled at 29.97 frames per second (fps). To reduce computation costs for the experimental evaluation, video frames were resampled to a smaller frame rate of 12 fps (using the Adobe Premiere Pro 1.5 software). This conversion incurred in a few frame drops, but considered unimportant for video cut detection. Besides computational time reduction, there was no other special reason for this chosen frame rate. For cut annotations, we started with the annotations available in TRECVID project webpage [14]. However, a manual revision of the original annotations was needed in order to correct a number of inconsistencies (this has been done in a similar way to the labeling performed for the ten videos used in the cross-validation, as commented in the previous section). Moreover, as the focus of this work is cut detection, gradual transitions (e.g. dissolves or wipes) were not considered.

Finally, cuts were annotated in the present work as frame numbers. This was done simply for convenience, since the raw information processed by our algorithm is at frame level. Time-based annotations can be easily derived from frame-based annotations and vice-versa. In the TRECVID project [14] webpage there is a rule that can help with these conversions. Table 2 presents the reviewed manual annotations for the five videos used in the evaluation. Each video is identified by its respective *id* presented in TRECVID webpage [14].

Table 2. Annotated cuts (indicated by the starting frame number) for the videos used in the experiment. Each cut is exactly 1 frame long

id 150	id 160	id 169	id 269	id 272
56	7	149	387	57
199	44	264	730	112
291	146	284	786	197
315	208	360	969	234
447	250	384	1006	356
686	284	421	1314	377
753	358	484	1442	401
800	422	732	1506	477
	487	925	1666	681
	596	1075	1695	736
		1283	1861	892
		1355	1927	
		1393		
		1552		
		1735		
		1804		
		1837		
		1870		

In Table 3, the results of the application of the main visual rhythm approach are presented on the five new videos obtained from the Open Video Project [12], using a window of size 11, and a factor of 2.2 (ideal window and factor values, determined through the cross-validation experiment explained in Section 3). The columns named "Cuts Detected", "Correct" and "Ground Truth" indicate, respectively, the total number of cuts detected, the number of cuts correctly detected by the approach, and the number of manually annotated cuts in the video. The column named "Precision" was calculated as the number of cuts correctly detected divided by the total number of cuts. The column named "Recall" was calculated as the ratio between the correct detections and the ground truth counts. The lines named "Mean" and "STD" indicate the mean value and standard deviations, respectively. Table 4 summarizes the results for Lu et al.'s visual rhythm approach [10] on the same set of videos. Both statistics in Tables 3 and 4 have been obtained in a previous work of the same authors [13].

In order to better characterize the above results and extend the initial evaluation with other important video cut detection techniques, a method based on pixel differentiation [16], and an approach based on the very popular concept of color histograms [9,17] have been implemented and tested. The goal was to evaluate and discuss precision and recall rates between the four approaches. All algorithms were

Table 3. Results for the main approach [13]

id	Cuts Detected	Correct	Ground Truth	Precision (%)	Recall (%)
150	13	8	8	61.54	100.00
160	13	9	10	69.23	90.00
169	23	17	18	73.91	94.44
269	21	12	12	57.14	100.00
272	18	11	11	61.11	100.00
Mean	17.60	11.40	11.80	64.59	96.89
STD	4.08	3.14	3.37	6.09	4.06

Table 4. Results for the approach by Lu et al. [10]

id	Cuts Detected	Correct	Ground Truth	Precision (%)	Recall (%)
150	1	1	8	100.00	12.50
160	2	1	10	50.00	10.00
169	2	1	18	50.00	5.56
269	2	1	12	50.00	8.33
272	3	3	11	100.00	27.27
Mean	2.00	1.40	11.80	70.00	12.73
STD	0.63	0.80	3.37	24.49	7.61

Table 5. Results for the pixel differentiation approach [16]

id	Cuts Detected	Correct	Ground Truth	Precision (%)	Recall (%)
150	7	3	8	42.86	37.50
160	5	5	10	100.00	50.00
169	12	8	18	66.67	44.44
269	10	6	12	60.00	50.00
272	13	9	11	69.23	81.82
Mean	9.40	6.20	11.80	67.75	52.75
STD	3.01	2.14	3.37	18.56	15.24

Table 6. Resulting statistics for the color histogram approach [9,17]

Id	Cuts Detected	Correct	Ground Truth	Precision (%)	Recall (%)
150	11	5	8	45.45	62.50
160	11	9	10	81.82	90.00
169	12	10	18	83.33	55.56
269	12	4	12	33.33	33.33
272	12	9	11	75.00	81.82
Mean	11.60	7.40	11.80	63.79	64.64
STD	0.49	2.42	3.37	20.48	20.03

applied to the same set of videos. Tables 5 and 6 present the results for pixel differentiation and color histogram approaches, respectively.

Tables 3, 4, 5 and 6 indicate that the novel visual rhythm approach presents recall rates higher than the ones presented by any of the compared approaches. On the other hand, the average precision rates presented by Lu et al.'s algorithm and by the pixel differentiation approach are a little higher. The standard deviations presented by the novel visual rhythm approach are lower for precision and recall when compared to

Lu et al.'s approach, and much lower when compared to the other two. This indicates better regularity in cut detection results, mainly regarding precision. A last consideration to be made upon the two approaches based on the visual rhythm concept is that Lu et al.'s algorithm [10], in general, is more restrictive about classifying frames as cuts. Thus, Lu et al.'s algorithm performs fewer cut detections, which can greatly favor precision, though always in detriment of recall. The novel approach revisited in this paper, in turn, detects more cuts, but in an efficient way, yielding higher recall rates and a small reduction in its average precision, relatively to Lu et al.'s algorithm.

5 Final Considerations

Accurate detection of sharp transitions is foremost important to automatic analysis of digital video contents. This work evaluated some of the most important techniques for video cut detection and presented in more detail a novel strategy based on the concept of visual rhythm to automatically detect sharp transitions or cuts in arbitrary videos.

The novel strategy based on visual rhythm is a simple, yet computationally attractive and of promising performance approach. When compared to three other competing techniques in the literature (based on visual rhythm (by Lu et al. [10]), one based on pixel differentiation (inspired on the work by Wildes [16]) and one based on color histogram [9, 17]), it presented very high recall and average precision rates. However, Lu et al.'s and pixel differentiation approaches performed a little better regarding average precision.

Special care has been taken to perform the evaluation utilizing videos publicly available. Moreover, video cut annotations have been clearly presented in Section 4, so that other groups can build on or confirm the obtained experimental results.

As future work, we intend to improve on this aspect by adding new constraints to the decision we make based on the integral of the absolute differences of pixel intensities for each line and each pair of adjacent columns of the 2-D signal that represents the visual rhythm of the video. Since the cross-validation process to find optimized parameters is very computationally intensive, an optimization process, possibly using genetic algorithms, will be an interesting approach to be investigated.

Another future work is to extend the novel strategy, with the accumulation of other evidences, aiming at: (i) gradual transition (as wipes and dissolves) detection; (ii) the detection of shots within shots (there are situations when a shot is interrupted by other shot and, after some time, the original shot continues from the point where it had stopped; in situations like this, the different pieces of the shot should be considered as only one shot; however, the proposed approach considers each piece as a distinct shot); and (iii) the development of techniques to perform video characterization/indexing/summarization based on the detected shots.

References

1. Bordwell, D., Thompson, K.: Film art: an introduction. Random House, New York (1986)
2. Chung, M.G., Lee, J., Kim, H., Song, S.M.-H., Kim, W.M.: Automatic video segmentation based on spatio-temporal features. Korea Telecom Journal 4(1), 4–14 (1999)

3. Gargi, U., Kasturi, R., Strayer, S.H.: Performance characterization of video-shot-change detection methods. IEEE Trans. on Circuits and Systems for Video Tech. 10, 1–13 (2000)

4. Guimarães, S.J.F., Couprie, M.: Video segmentation based on 2d image analysis. Pattern Recognition Letters 24(7), 947–957 (2003)

5. Hanjalic, A.: Shot boundary detection: unraveled and resolved? IEEE Trans. on Circuits and Systems for VideoTechnology 12(2), 90–105 (2002)

6. Jun, S.-C., Park, S.-H.: An automatic cut detection algorithm using median filter and neural network. Computers and Communications 2, 1049–1052 (2000)

7. Leszczuk, M., Papir, Z.: Accuracy vs. speed trade-off in detecting of shots in video content for abstracting digital video libraries. In: Boavida, F., Monteiro, E., Orvalho, J. (eds.) IDMS 2002 and PROMS 2002. LNCS, vol. 2515, pp. 176–189. Springer, Heidelberg (2002)

8. Lienhart, R.: Reliable transition detection in videos: a survey and practitioner's guide. Int. Journal of Image and Graphics 1(3), 469–486 (2001)

9. Lienhart, R.: Comparison of automatic shot boundary detection algorithms. In: Proc. SPIE Image and Video Processing, pp. 290–301 (1999)

10. Lu, S., King, I., Lyu, M.R.: A novel video summarization framework for document preparation and archival applications, In: IEEE Aerospace Conf. CDROM: IEEEAC paper #1415, pp. 1–10 (2005)

11. Ngo, C.-W., Pong, T.-C., Chin, R.T.: Video partitioning by temporal slice coherency. IEEE Trans. on Circuits and Systems for Video Technology 11(8), 941–953 (2001)

12. Open Video Project, http://www.open-video.org

13. Santos, S.M., Gomes, H.M., Borges, D.L.: A Novel cut detection strategy based on visual rhythm. In: IASTED Int. Conf. on Computational Intelligence, pp. 303—308 (2006)

14. TRECVID – TREC Video Retrieval Evaluation, http://www-nlpir.nist.gov/projects/trecvid/

15. Truong, B.T., Dorai, C., Venkatesh, S.: New enhancements to cut, fade, and dissolve detection processes in video segmentation. In: ACM Int. Conf. on Multimedia, pp. 219–227 (2000)

16. Wildes, R.P.: A measure of motion salience for surveillance applications. In: IEEE Int. Conf. on Image Processing, pp. 183–187 (1998)

17. Yeo, B.-L., Liu, B.: Rapid scene analysis on compressed video. IEEE Trans. on Circuit and Systems for Video Technology 5(6), 533–544 (1995)

18. Yusoff, Y., Christmas, W., Kittler, J.: Video shot cut detection using adaptive thresholding. In: British Machine Video Conf. pp. 362–371 (2000)

19. Zhang, D., Qi, W., Zhang, H.-J.: A new shot boundary detection algorithm. In: IEEE Pacific Rim Conf. on Multimedia, pp. 63–70 (2001)

20. Zheng, W., Yuan, J., Wang, H., Lin, F., Zhang, B.: A novel shot boundary detection framework. In: SPIE Visual Communications and Image Processing, pp. 410–420 (2005)

Surface–Normal Estimation with Neighborhood Reorganization for 3D Reconstruction

Felix Calderon[1], Ubaldo Ruiz[1], and Mariano Rivera[2]

[1] Universidad Michoacana de San Nicolás de Hidalgo
División de Estudios de Posgrado. Facultad de Ingeniería Eléctrica
Santiago Tapia 403 Centro. Morelia, Michoacán, México. CP 58000
`calderon@umich.mx ubaldo@fismat.umich.mx`
[2] Centro de Investigacion en Matematicas A.C.
Apdo. Postal 402, Guanajuato, Gto. Mexico. CP 36000
`mrivera@cimat.mx`

Abstract. Fastest three-dimensional (3D) surface reconstruction algorithms, from point clouds, require of the knowledge of the surface–normals. The accuracy, of state of the art methods, depends on the precision of estimated surface–normals. Surface–normals are estimated by assuming that the surface can be locally modelled by a plane as was proposed by Hoppe *et. al* [1]. Thus, current methods for estimating surface–normals are prone to introduce artifacts at the geometric edges or corners of the objects. In this paper an algorithm for Normal Estimation with Neighborhood Reorganization (NENR) is presented. Our proposal changes the characteristics of the neighborhood in places with corners or edges by assuming a locally plane piecewise surface. The results obtained by NENR improve the quality of the normal with respect to the state of the art algorithms. The new neighborhood computed by NENR, use only those points that belong to the same plane and they are the nearest neighbors. Experiments in synthetic and real data shown an improvement on the geometric edges of 3D reconstructed surfaces when our algorithm is used.

Keywords: Normal Estimation, Point Cloud, Surface Reconstruction.

1 Introduction

The computational representations of physical objects have large and wide applications in distinct areas like industrial design, computer simulations and medicine, among others: an object digitalization can be easily studied, modified or replicated. In a initial stage, a complex real object is detailed scanned, by using of a proper device, for acquiring of a point cloud with thousand or millions of points. In a second stage, a reconstruction algorithm is applied on the point cloud for producing a, generally triangular, mesh that approximates the object surface. Thus the resulting mesh is a suitable representation of the real object.

The reconstruction algorithms must be able to approximate, at a reasonable computational time, the geometric features of the real object. Among the reconstruction algorithms reported in the literature, Multilevel Partition of Unity

Implicits (MPUI) [2] deserves our special attention. Currently, the MPUI is considered as one of the fastest and most up-to-date algorithms for surface reconstruction, however, it is important to notice that the MPUI like the rest of the volumetric methods [1,3,4] requires an estimation of the normal at each point. Clearly, good normal estimations are necessary for a good surface reconstruction.

Some complex three–dimensional (3D) scanner devices estimate the surface normals at the acquisition time. However, in order to eliminate any dependency to those devices it is better to infer such normals from the point set. For instance, Refs. [1,5] reported algorithms for addressing the surface normal problem. But those methods fail, to estimate correctly normals, at sites close to edges or corners. In this paper we propose an edge preserving normal regularization technique based in an adaptive rest condition spring system proposed by Rivera and Marroquin in [6] that allows us to improve the normal-surface estimation at points close to edges and, consequently, improving the quality of the final surface reconstruction.

The paper is organized as follows. In Sect. 2 we present a brief review of the reconstruction algorithms that have been developed. In Sect. 3 we describe a pioneering technique [1], that still, is widely used for normal estimation in point clouds. In Sect. 4 we propose an algorithm for normal estimation that increase the accuracy in regions with edges. In Sect. 5 we compare the performance of the MPUI algorithm [2] when the surface–normal are estimated with the method presented in [1] and with the method we propose here. Finally, some conclusions are discussed in Sect. 6.

2 Surface Reconstruction

Currently, one can distinguish two main lines of research in the field of surface reconstruction from point clouds. The algorithms developed in the context of Computational Geometry (CG) constitute a line of research [7]. In CG-based methods the surface is reconstructed from the Delaunay tetrahedrization of the point cloud [8,9,10]. Unfortunately, CG-based methods are very sensitive to noise and computationally expensive; their computational complexity is of polynomial order with respect the number of points. On the other hand, volumetric methods constitute the alternative research line [1,2,3,4]. In this case, implicit functions are fitted to the point cloud and the surface is extracted (see [11,12,13]) as the zero level set of the computed functions. These methods are used extensive because their better noise tolerance and because they are able to handle large point clouds. However, it is necessary to supply reliable information about the normal at each point. The current state of the art in this approach includes the MPUI algorithm based on quadratic functions [2]. It is one of the few reconstruction algorithms able to process sharp features and also one of the fastest techniques available [2].

The MPUI algorithm works as follows. First it creates an octree-based subdivision of a box that bounds the point cloud. At each cell of the octree the local shape is approximated with a piecewise quadratic function. These functions work

like a signed distance function taking a positive value inside of the point cloud and negative outside of it. The normals of the points are used to distinguish the orientation locally. If the local approximation into a cell is not accurate, then the cell is subdivided; such a procedure is repeated until a desirable accuracy level is reached. The global implicit function describing the surface is given by assembling the local approximations using local weights.

The MPUI algorithm has three types of quadratic functions that allows to model a large variety of point set configurations. Additionally, MPUI provides test–rule for choosing the appropriated quadratic form to fit at each cell. These test–rule give to the algorithm the ability to deal with surface edges. The MPUI algorithm input are the point cloud and the respective surface–normals. In the case were only the point cloud is given (surface normals are not provided), Ohtake *et al.* [2] suggest to compute such surface–normals with the technique proposed by Hoppe *et al.* in [1]. The surface-normal estimation method is described in next section.

3   Standard Surface–Normal Estimation

The estimation of surface–normals from a point cloud is usually done in two stages, as proposed Hoppe *et al.* in [1] (NE–Hoppe). In the first stage the Tangent Plane (TP) is estimated at each point. Thus the Orthogonal unitary vector to the Tangent Plane (OTP) will be used as an approximation of the normal at such point. In the second stage the orientation of the OTP, spatially coherent, is computed.

Given a point set $P = \{\boldsymbol{p}_1, \ldots, \boldsymbol{p}_N\}$ and let be V_i the set of k nearest neighbors (neighborhood) of the point $\boldsymbol{p}_i$. Then the TP at $\boldsymbol{p}_i$ is obtained by fitting a plane to the points in V_i by using a least-squares procedure, then the surface–normal, $\boldsymbol{n}_i$, is the normal to the TP. Hoppe *et al.* [1] proposed to compute, $\boldsymbol{n}_i$, as the third eigenvector (associated with the smallest eigenvalue) of the local covariance matrix:

$$C_i = \sum_{j \in V} (\boldsymbol{p}_j - \boldsymbol{c}_i) \otimes (\boldsymbol{p}_j - \boldsymbol{c}_i) \tag{1}$$

where $\otimes$ denotes the outer product vector operator[1]. If $\lambda_i^1 \geq \lambda_i^2 \geq \lambda_i^3$ are the eigenvalues of C_i, their associated eigenvectors $\boldsymbol{v}_i^1, \boldsymbol{v}_i^2, \boldsymbol{v}_i^3$, respectively, form an orthonormal basis. Then $\boldsymbol{n}_i$ is either $\boldsymbol{v}_i^3$ or $-\boldsymbol{v}_i^3$. The neighborhood size is chosen manually based on visual inspection of the resulting normals and it is the same for each point in the set.

The Oriented OTP (OOTP) is computed such that nearby planes are consistently oriented. The NE–Hoppe algorithm, proposed in [1], considered the state of the art, is following described. First, an Euclidean Minimum Spanning Tree is created over the TP centers $\{\boldsymbol{c}_1, \ldots, \boldsymbol{c}_n\}$ and it is enriched adding the edge $<i, j>$ if either $\boldsymbol{c}_i \in V_j$, or $\boldsymbol{c}_j \in V_i$. Then the edge cost is equaled to $1 - |\boldsymbol{n}_i \cdot \boldsymbol{n}_j|$.

---

[1] If $\boldsymbol{v}$ and $\boldsymbol{u}$ have components v_i and u_j respectively, then the matrix $\boldsymbol{v} \otimes \boldsymbol{u}$ has $u_i v_j$ as its ij-th entry.

Next, the Minimum Spanning Tree of this graph is computed. The OTP whose TP center has the largest z coordinate is forced to point towards $+z$ axis. Rooting the tree at this node, then the tree is traversed in depth first order, if during traversal the current node i has been assigned the orientation $\boldsymbol{n}_i$ and the node j is the next node to be visited, then $\boldsymbol{n}_j$ is replaced with $-\boldsymbol{n}_j$ if $\boldsymbol{n}_i \cdot \boldsymbol{n}_j < 0$.

Pauly *et al.* [5] noticed that nearby points in the neighborhood of a point $\boldsymbol{p}_i$ should have a stronger influence than distant points. Therefore, they assign different weights to elements in the neighborhood by depending on their distance to $\boldsymbol{p}_i$. The weighting function is proposed to be the Gaussian: $w(\boldsymbol{p}_j - \boldsymbol{p}_i) = \exp(-\|\boldsymbol{p}_j - \boldsymbol{p}_i\|^2/(2\sigma^2))$, where σ is chosen as one third of the square distance between $\boldsymbol{p}_i$ and its farthest neighbor: $\sigma^2 = (1/6) \max_{\boldsymbol{p} \in V} \|\boldsymbol{p}_j - \boldsymbol{p}_i\|^2$.

Although the previous algorithms [1,5] work well in the presence of smooth regions and moderate noise, they perform poorly in those regions near corners or edges. If the neighborhood at each of the points has a fixed size and it is constructed using only the Euclidean distance then it is possible that points considered as outliers for a certain region be used in the computation of the normal. Hence, it is important to develop a new robust strategy that estimate the local surface–normal by discarding neighbor points that lay beyond of a surface edge or a corner. Figure 1 shows the normal estimation by different approaches for a step function in two dimensions. Figure 1(a) shows the ground truth and Fig. 1(b) shows the computed normals using neighborhoods based only in a proximity measure, note the effect in corners of the step function. On the other hand, Fig. 1(c) shows the results applying our approach (that will be introduced in next section).

(a)   (b)   (c)
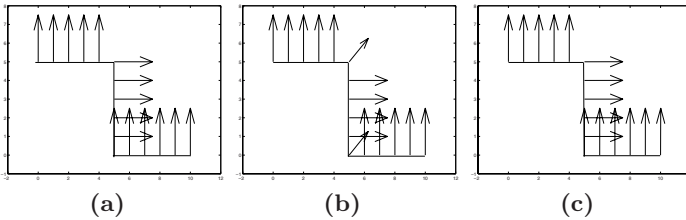
Fig. 1. Normal estimation comparison in two dimensions for a step function. (a) Ground Truth, (b) NE–Hoppe algorithm and (c) NENR algorithm.

4   Normal Estimation with Neighborhood Reorganization (NENR)

The normal estimation using the OOTP is equivalent to apply a low-pass band filter to the point cloud, so the resulting normal, will have a smoothness degree which is proportional to the neighborhood size. If OOTP is used, one is implicitly assumed that the neighborhood around each point may be modelled by simple plane. Such assumption is incorrect at points close to edges or corners. An alternative approach could be to weight each point in the neighborhood; however

the underlying representation of each neighborhood still it is a unique plane. A more appropriated model is to assume a plane–piecewise model. Half-quadratic regularization (HQR) is an edge-preserving regularization technique for restoring piecewise smooth signals [14,15,16,17]; the general HQR energy function is given by

$$U(h,l) = \sum_{i \in \Omega} \left[(h_i - g_i)^2 + \alpha \|\nabla h_i\|^2 (1 - l_i)^2 + \alpha \beta l_i^2 \right];$$ (2)

where g is a given signal, h is the filtering signal with edge-preserving and α, β are parameters which control the signal smoothness. l_i acts as an indicator variable which disconnects the ∇h_i terms with a huge contribution to the general cost function. This technique is also applied by Calderon in [18,19], for Image Registration.

In case of a piecewise constant surface, for a given neighborhood, we approximate this surface by TPs and it is desirable to get out points of the cloud belonging to different TPs. So a new neighborhood is computed considering only the nearest neighbors who belong to the same TP. Figure 2(a) shows the standard plane estimation, for the case of three points on a corner, and Fig. 2(b) shows the plane estimation when a point is rejected, a desirable condition in those cases. We propose a HQR cost function for this purpose and the indicator variable in our case, is used as non-membership term, $l_{ij} = 1$ means that the $j - th$ point, in the original neighborhood, it is not in the same TP that $i - th$ point. The OOTP smoothness is controlled with the parameters α and β. We proposed to compute the surface-normal as the minimization of a constrained HRQ cost function. The additional constraint imposes a unitary norm to the flat piecewise normal vector $\boldsymbol{m}_i$:

$$U(\boldsymbol{m},l) = \sum_{i \in \Omega} \left\{ \|\boldsymbol{m}_i - \boldsymbol{n}_i\|^2 + \alpha \sum_{j \in V} \left[\|\boldsymbol{m}_i - \boldsymbol{m}_j\|^2 (1 - l_{ij})^2 + \beta l_{ij}^2 \right] \right\},$$ (3)

$$\text{s.t.} \qquad \|\boldsymbol{m}_i\| = 1, \qquad \forall i \in \Omega;$$

where $\boldsymbol{n}_i$ is the normal vector computed with the NE–Hoppe algorithm described in Sect. 3 for some neighborhood size. Then by using the Lagrange multipliers, γ, we include the constraint in the Lagrangian:

$$L(\boldsymbol{m},l,\gamma) = U(\boldsymbol{m},l) - \sum_{i \in \Omega} \gamma_i \left(\sum_{d=1}^{3} m_{i,d}^2 - 1 \right)$$ (4)

Then the solution is computed solving the Karush-Khun-Tucker conditions:

$$\nabla_{\boldsymbol{m}} L(\boldsymbol{m},l,\gamma) = 0,$$ (5)
$$\nabla_l L(\boldsymbol{m},l,\gamma) = 0,$$ (6)
$$\|\boldsymbol{m}_i\| = 1;$$ (7)

where ∇_x denotes the partial gradient operator. We propose to use the Gauss-Seidel algorithm, for solving this system of equation, due the fact that the system

of equation has a banded, diagonally dominant and semi-positive defined matrix, so the t-th Gauss-Seidel Iteration is given by the equations (8, 9 and 10):

$$\widehat{m}_{i,d}^{(t)} = \frac{m_{i,d}^{(t)}}{\sqrt{\sum_k \left(m_{i,d}^{(t)}\right)^2}} \qquad \forall i \in \Omega, \tag{8}$$

$$l_{ij}^{(t)} = \frac{\left\|\widehat{\boldsymbol{m}}_i^{(t)} - \widehat{\boldsymbol{m}}_j^{(t)}\right\|^2}{\beta + \left\|\widehat{\boldsymbol{m}}_i^{(t)} - \widehat{\boldsymbol{m}}_j^{(t)}\right\|^2} \qquad \forall <i,j> \in \Omega^2, \tag{9}$$

$$m_{i,d}^{(t+1)} = \frac{n_{i,d} + \alpha \sum_{j \in V} \widehat{m}_{j,d}^{(t)} \left(1 - l_{ij}^{(t)}\right)^2}{1 + \gamma_i + \alpha \sum_{j \in V} \left(1 - l_{ij}^{(t)}\right)^2}. \tag{10}$$
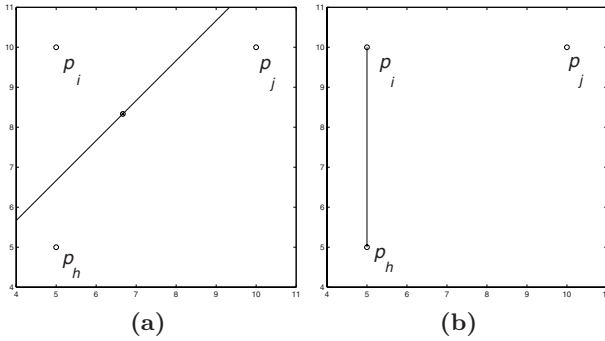
Fig. 2. Different plane estimations using three points on a corner. (a) Plane over the three points and (b) plane over points p_i and p_h when p_j is not included.

The restriction for the equation (3) is fulfill at each iteration according with equation (8), so the Lagrange multiplier γ can take any value, because their contribution to the constrained HRQ cost function will be zero at each iteration, for simplicity we put $\gamma_i = 0$ in equation (10).
The NENR algorithm is resumed in the next steps:

1. Compute the OOTP $\boldsymbol{n}_i$ for some neighborhood with size k
2. Compute the reorganized neighborhood and the filter normal $\boldsymbol{m}_i$ doing
   - (a) Set $\boldsymbol{m}_i^{(0)} = \boldsymbol{n}_i$ and $t = 0$
   - (b) Normalize the vectors $\boldsymbol{m}_i^{(t)}$ applying (8)
   - (c) Compute the memberships $l_{ij}^{(t)}$ using (9)
   - (d) Update the normal vectors $\boldsymbol{m}_i^{(t+1)}$ applying (10)
   - (e) Set $t \leftarrow t + 1$
   - (f) Repeat steps (b-e) until $\left\|\boldsymbol{m}_i^{(t+1)} - \boldsymbol{m}_i^{(t)}\right\| < \varepsilon$

3. Finally compute the robust OTP with the weighted covariance matrix:

$$C_i = \sum_{j \in V} \left(1 - l_{ij}^*\right) \left[(\boldsymbol{p}_j - \boldsymbol{c}_i^*) \otimes (\boldsymbol{p}_j - \boldsymbol{c}_i^*)\right] \tag{11}$$

with

$$\boldsymbol{c}_i^* = \frac{\sum_{j \in V} \left(1 - l_{ij}^*\right) \boldsymbol{p}_j}{\sum_{j \in V} \left(1 - l_{ij}^*\right)} \tag{12}$$

using the finals (optimum) memberships l_{ij}^*, then compute the OOTP as was described in Sect. 3.

5   Experimental Results

We perform experiments in both synthetic and real data, for comparing NE–Hoppe and NENR algorithms. The synthetic data corresponds to a step function and a 3D model with a ground truth while the real data corresponds to 3D models widely used in the literature. All the 3D models were reconstructed using the Ohtake's MPUI implementation available at [20].

The results for the step function in two dimensions are presented in Fig. 1. The normal vectors in Fig. 1(a) were assigned manually according with the step function and the normal field estimated by NE–Hoppe and NENR are shown in Figs. 1(b) and 1(c), respectively. The neighborhood sizes for both algorithms were $k = 2$ and the NENR parameters were $\alpha = 50000$ and $\beta = 0.001$. Note the similarity between the NENR (Fig. 1(c)) and the original normals (Fig. 1(a)) also note the problem presented by NE–Hoppe algorithm in corners of the step function.

For the synthetic 3D model, the normals have been assigned manually according to the characteristics of the surface object and its surface reconstruction is shown in Fig. 3(a). The resulting surface is used as a reference for a qualitative comparison. The MPUI parameters in this case were a grid size of 0.005, and a max error of 0.005 at each cell. For the rest of the parameters we took the default configuration of Ohtake's MPUI implementation. The neighborhood size was taken equal to 15 for both normal estimation algorithms. Additionally, for the NERN algorithm, we took $\alpha = 1000$ and $\beta = 0.01$. The surface reconstructed using the NE–Hoppe is presented in Fig. 3(b). Note that the edges of the reconstructed surface are over–smoothed as a direct consequence of bad normal estimation near these regions. Finally, Fig. 3(c) shows the surface reconstructed using the NENR algorithm. We must notice that NENR algorithm increases the quality of the reconstruction, shown sharped geometric edges without affecting the smooth areas, as you can see comparing Figs. 3(b) and 3(c).

For a quantitative comparison between NERN and NE-Hoppe algorithms, we compute the angle between the ground truth surfaces normals and the estimated normals using both algorithms. The mean angle and standard deviation are shown in Table 1 for the step function (Fig. 1) and the synthetic 3D model (Fig. 3). Note the better results for the normal estimation using NERN than NE-Hoppe in both cases.

(a) *Ground Truth*   (b) *NE–Hoppe*   (c) *NENR*
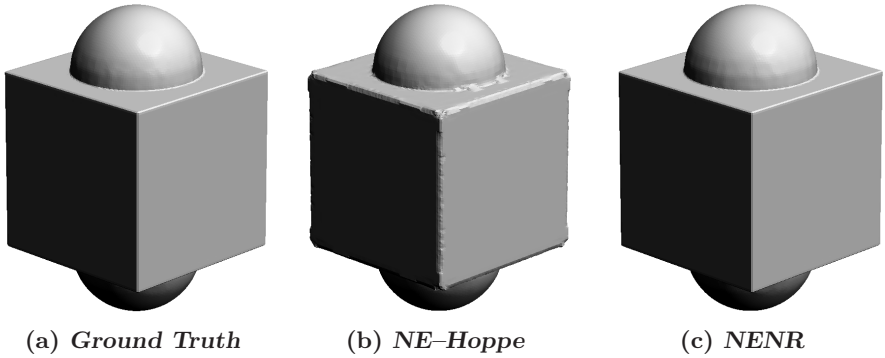
Fig. 3. Surface reconstruction using MPUI and different Surface–Normal Estimations

Table 1. Normal estimation angle between ground truth normals and the estimated normals of both methods

Algorithm	Step Function		Synthetic Model	
	Mean Angle	Std. Deviation	Mean Angle	Std. Deviation
NE-Hoppe	$5.7169°$	$15.2029°$	$7.5544°$	$13.5544°$
NERN	$0.1764°$	$0.1852°$	$0.9973°$	$2.0968°$

(a) *Bunny*   (b) *Golf club*
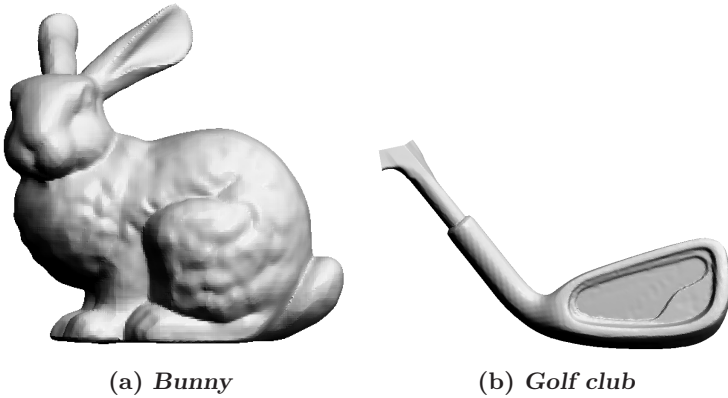
Fig. 4. Surface reconstruction using MPUI and NENR for real models

Figures 4(a) and 4(b) show reconstructions, using the MPUI method with NENR–computed normal, from a couple of real 3D models widely used in the literature. The MPUI parameters for both models were, a grid size of 0.004, and a max error of 0.002 at each cell. The rest of the parameters took the default values setting by the Ohtake's MPUI implementation. For the bunny model the NERN parameters were $k = 15$, $\alpha = 100$, $\beta = 0.01$ and in the case of the golf club model were $k = 12$, $\alpha = 1000$, $\beta = 0.01$.

6   Conclusions

In general, the normal estimation algorithms based on the covariance matrix as NE–Hoppe approximate a neighborhood by a unique plane independently of its local shape. Some algorithms, in order to improve the approximation by a unique plane, reduce the neighborhood size or weight the covariance matrix, nevertheless the approximation continues to be a unique plane.

The NENR algorithm produces a reduction in the neighborhood size, rejecting the neighbors that have large differences. This condition warranties that the neighbors have the same smoothness degree between them. The NERN algorithm was tested using synthetic examples building with shape discontinuities. The experiments presented better quantitative and qualitative results using NENR than NE–Hoppe.

In cases of real models, a couple of experiments were done and the results were very similar for both algorithm, therefore, using NENR in real smooth models does not represent a lost in quality for surface reconstruction. In general, NENR produces a better normal estimation than NE–Hoppe, in places located near to edges, corners and geometric discontinuities. The NERN algorithm does not have troubles with smooth regions or smooth models.

References

1. Hoppe, H., DeRose, T., Duchamp, T., McDonald, J., Stuetzle, W.: Surface reconstruction from unorganized points. In: SIGGRAPH 1992: Proceedings of the 19th annual conference on Computer graphics and interactive techniques, pp. 71–78. ACM Press, New York (1992)
2. Ohtake, Y., Belyaev, A., Alexa, M., Turk, G., Seidel, H.P.: Multi-level partition of unity implicits. In: SIGGRAPH 2003: ACM SIGGRAPH 2003 Papers, pp. 463–470. ACM Press, New York (2003)
3. Bajaj, C.L., Bernardini, F., Xu, G.: Automatic reconstruction of surfaces and scalar fields from 3d scans. In: SIGGRAPH 1995: Proceedings of the 22nd annual conference on Computer graphics and interactive techniques, pp. 109–118. ACM Press, New York (1995)
4. Carr, J.C., Beatson, R.K., Cherrie, J.B., Mitchell, T.J., Fright, W.R., McCallum, B.C., Evans, T.R.: Reconstruction and representation of 3d objects with radial basis functions. In: SIGGRAPH 2001: Proceedings of the 28th annual conference on Computer graphics and interactive techniques, pp. 67–76. ACM Press, New York (2001)
5. Pauly, M., Keiser, R., Kobbelt, L.P., Gross, M.: Shape modeling with point-sampled geometry. In: SIGGRAPH 2003: ACM SIGGRAPH 2003 Papers, pp. 641–650. ACM Press, New York (2003)
6. Rivera, M., Marroquin, J.L.: The adaptive rest-condition spring system: An edge-preserving regularization techique. In: ICIP-2000, vol. II, pp. 805–807. IEEE Signal Processing Society, Vancouver, BC, Canada (2000)
7. O'Rourke, J.: Computational geometry in C. Cambridge University Press, New York (2000)

8. Amenta, N., Bern, M., Kamvysselis, M.: A new voronoi-based surface reconstruction algorithm. In: SIGGRAPH 1998: Proceedings of the 25th annual conference on Computer graphics and interactive techniques, pp. 415–421. ACM Press, New York (1998)
9. Amenta, N., Choi, S., Kolluri, R.K.: The power crust. In: SMA 2001: Proceedings of the sixth ACM symposium on Solid modeling and applications, pp. 249–266. ACM Press, New York (2001)
10. Dey, T.K., Goswami, S.: Tight cocone: a water-tight surface reconstructor. In: SM 2003: Proceedings of the eighth ACM symposium on Solid modeling and applications, pp. 127–134. ACM Press, New York (2003)
11. Lorensen, W.E., Cline, H.E.: Marching cubes: A high resolution 3d surface construction algorithm. In: SIGGRAPH 1987: Proceedings of the 14th annual conference on Computer graphics and interactive techniques, pp. 163–169. ACM Press, New York (1987)
12. Bloomenthal, J.: An implicit surface polygonizer, 324–349 (1994)
13. Hart, J.C.: Sphere tracing: A geometric method for the antialiased ray tracing of implicit surfaces. The Visual Computer 12, 527–545 (1996)
14. Black, M., Rangarajan, A.: On the unification of line processes, outlier rejection, and robust statistics with applications in early vision. Int'l J. Computer Vision 19, 57–92 (1996)
15. Charbonnier, P., Blanc-Feraud, L., Aubert, G., Barluad, M.: Deterministic edge-preserving regularization in computed imaging. IEEE Trans. Image Processing 6, 298–311 (1997)
16. Rivera, M., Marroquin, J.L.: Adaptive rest condition potentials: first and second order edge-preserving regularization. Journal of Computer Vision and Image Understanding 88, 76–93 (2002)
17. Rivera, M., Marroquin, J.: Half–quadratic cost functions with granularity control. Image and Vision Computing 21, 345–357 (2003)
18. Calderon, F., Romero, L.: Non-parametric image registration as a way to obtain an accurate camera calibration. In: Monroy, R., Arroyo-Figueroa, G., Sucar, L.E., Sossa, H. (eds.) MICAI 2004. LNCS (LNAI), vol. 2972, pp. 584–591. Springer, Heidelberg (2004)
19. Calderon, F., Romero, L., Flores, J.: Ga-ssd-arc-nlm for parametric image registration. In: Martínez-Trinidad, J.F., Carrasco Ochoa, J.A., Kittler, J. (eds.) CIARP 2006. LNCS, vol. 4225, pp. 227–236. Springer, Heidelberg (2006)
20. Ohtake, Y.: Mpui implementation in (2003), http://www.mpi-inf.mpg.de/~ohtake/mpu_implicits/

Weighted Principal Geodesic Analysis for Facial Gender Classification

Jing Wu, W.A.P. Smith, and E.R. Hancock

Department of Computer Science, The University of York, York, YO10 5DD, UK
{jwu,wsmith,erh}@cs.york.ac.uk

Abstract. In this paper, we describe a weighted principal geodesic analysis (WPGA) method to extract features for gender classification based on 2.5D facial surface normals (needle-maps) which can be extracted from 2D intensity images using shape-from-shading (SFS). By incorporating the weight matrix into principal geodesic analysis (PGA), we control the obtained principal axis to be in the direction of the variance on gender information. Experiments show that using WPGA, the leading eigenvectors encode more gender discriminating power than using PGA, and that gender classification based on leading WPGA parameters is more accurate and stable than based on leading PGA parameters.

Keywords: Gender classification, facial surface normals, principal geodesic analysis, weighted principal geodesic analysis, gender discriminating power.

1 Introduction

Humans are remarkably accurate at determining the gender of a subject based on the appearance of the face alone. In fact, an accuracy as good as 96% can be achieved with the hair concealed, facial hair removed and no makeup [1]. In recent years, considerable effort has been spent on the statistical feature based approaches [2], [3], [4], [5], [6] to gender classification. Of these, principal component analysis (PCA) is widely used to reduce the dimensionality of the high dimensional facial data. The aim of PCA is to locate the projections that maximize the variance of the data. However, the projections that maximize the variance usually are not the projections that separate the data into distinct clusters, and so, PCA usually does not reveal cluster structure. Therefore, most of the current approaches employ a second step to extract gender relevant features by performing linear discriminant analysis (LDA) on the PCA parameters. Because of the supervised nature of LDA, this two-step feature extraction strategy is unsuitable for unsupervised learning. Another drawback of the current approaches is that most of them are based on 2D intensity information. Although studies [7] have shown that the gender is not only revealed by 2D facial texture, but also has a close relationship with the 3D shape of the human faces, in fact, only a few studies have investigated the role of 3D shape in gender classification [6]. The computation of 3D face shape representation is significantly more complex

than of 2D face texture. Due to the limited effectiveness and high cost of the 3D sensors in the current market, some typical problems with range images including missing data near dark regions and spikes in regions with high reflectivity would also adversely affect the classification accuracy.

In this paper, we address gender classification using the parameterisation of fields of facial surface normals or needle-maps, and propose a one-step feature extraction method. The needle-map is a 2.5-D shape representation which is intermediate between the 2D intensity image and the 3D surface height function [8]. The representation can be acquired from 2D intensity images using shape-from-shading [9]. It therefore avoids the problems caused by the limitation of current 3D sensors, and is invariant to illumination. To parameterize the facial needle-maps, we use weighted principal geodesic analysis (WPGA). This is a novel variant of principal geodesic analysis (PGA) [10], [11], which constructs a weight matrix making use of the a priori knowledge of the gender discriminating power of different regions of the face, and incorporate the weights into PGA. PGA is a generalization of PCA, for data residing on a Riemannian manifold. As a result, PGA is better suited to the analysis of directional data than PCA. By incorporating weights into the analysis of data, we control the data variance structure so that the variance of gender discriminating regions are larger. In this way, the principal axis obtained after the PGA projection are in the direction of the gender discriminating variance. So, WPGA method improves the projections separating clusters in a manner that is consistent with the projection directions that maximize the variance. Therefore, it enables us to extract the gender discriminating features in a single step.

The outline of the paper is as follows. Section 2 first reviews the concepts of the Log and Exponential maps, spherical medians, and the PGA of needle-maps, and then provides the idea of incorporating weights into PGA. Section 3 states the probability based classification strategy. The details of how to construct the weights and experimental results are presented in Section 4. Finally, Section 5 concludes the paper and offers directions for future investigation.

2   Weighted Principal Geodesic Analysis

The surface normal $n \in R^3$ may be considered as a point lying on a spherical manifold $n \in S^2$, therefore, the intrinsic mean and PGA proposed by Fletcher et al. [10] is suitable to analyze the variations of the surface normals.

2.1   The Log and Exponential Maps

If $u \in T_n S^2$ is a vector on the tangent plane to S^2 at n and $u \neq 0$, the exponential map, denoted Exp_n, of u is the point, denoted $Exp_n(u)$, on S^2 along the geodesic in the direction of u at distance $\| u \|$ from n. This is illustrated in Fig. 1. The log map, denoted Log_n is the inverse of the exponential map. The exponential and log maps reserve the geodesic distance between two points, i.e. $d(n_1, n_2) = d(u_1, u_2)$, where $u_1 = Log_n n_1, u_2 = Log_n n_2$.
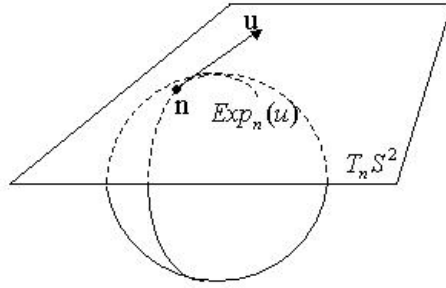
Fig. 1. The exponential map

2.2   Spherical Medians

It is more natural to treat the surface normal as points on a unit sphere: $n_1, \ldots n_N \in S^2$ rather than points in Euclidian space. Instead of the Euclidian mean, we compute the intrinsic mean: $\mu = \arg\min_{n \in S^2} \sum_{i=1}^{N} d(n, n_i)$, where $d(n, n_i) = \arccos(n \cdot n_i)$ is the arc length. For a spherical manifold, the intrinsic mean can be found using the gradient descent method of Pennec [11]. Accordingly, the current estimate $\mu^{(t)}$ is updated as follows: $\mu^{(t+1)} = \text{Exp}_{\mu^{()}}(\frac{1}{N}\sum_{i=1}^{N}\text{Log}_{\mu^{()}}(n_i))$.

2.3   PGA of Needle Maps

PGA is analogous to PCA except that each principal axis in PCA is a straight line, while in PGA each principal axis is a geodesic curve. In the spherical case this corresponds to a great circle. Consider a great circle G on the sphere S^2. To project a point $n_1 \in S^2$ onto a point on G, we use the projection operator $\pi_G : S^2 \longrightarrow G$ given by $\pi_G(n_1) = \arg\min_{n \in G}(n_1, n)^2$. For a geodesic G passing through the intrinsic mean μ, π_G may be approximated linearly in the tangent plane $T_\mu S^2$: $\text{Log}_\mu(\pi_G(n_1)) \approx \sum_{i=1}^{K} V^i \cdot \text{Log}_\mu(n_1)$, where $V_1, \ldots V_K$ is an orthonormal basis for $T_\mu S^2$.

Suppose there are K training needle-maps each having N pixel locations, and the surface normal at the pixel location p for the kth training needle-map is n_p^k. We calculate the intrinsic mean μ_p of the distribution of surface normals $n_p^1, \ldots n_p^K$ at each pixel location p. n_p^k is then represented by its log map position $u_p^k = \text{Log}_\mu (n_p^k)$. $u^k = [u_1^k, \ldots, u_N^k]^T$ is the log mapped long vector of the kth training needle-map. The K long vectors form the data matrix $U = [u^1 | \ldots | u^K]$. The covariance matrix of the data matrix is $L = \frac{1}{K}UU^T$.

The numerically efficient snap-shot method of Sirovich [12] can be used to compute the eigenvectors of L. Accordingly, we construct the matrix $\hat{L} = \frac{1}{K}U^TU$, and find the eigenvalues and eigenvectors. The ith eigenvector e_i of L can be computed from the ith eigenvector $\hat{e}_i$ of $\hat{L}$ using $e_i = U\hat{e}_i$. The ith eigenvalue λ_i of L equals the ith eigenvalue $\hat{\lambda}_i$ of $\hat{L}$ when $i \leq K$. When $i > K$, $\lambda_i = 0$. The m leading eigenvectors of L form the projection matrix $\Phi = (e_1 | e_2 | \ldots | e_m)$.

Given a long vector $u = [u_1, \ldots, u_N]^T$, we can get the corresponding PGA parameters $b = \Phi^T u$. Given the PGA parameters $b = [b_1, \ldots b_m]^T$, we can generate a needle-map using: $n_p = \text{Exp}_\mu ((Pb)_p)$.

2.4   Incorporating Weights into PGA

From above, we can see that PGA, which is a generalization of PCA, captures the directions of the largest variance in the needle-maps. However these variance usually are not associated with the differences in facial shape for different gender. To improve the encoding of gender by the leading eigenvectors, a possible solution is to increase the variance of the normals in the gender discriminating regions, such as eyebrows, nose, etc. Therefore, we introduce the $N \times N$ diagonal weight matrix $W = diag(w_1, \ldots, w_N)$, which gives a weight to each position in the facial needle-map. The positions in the gender discriminating regions are given high weights (w_h), while the other positions are given low weights (w_l). In this way, the normals in the gender discriminating regions have $\frac{w}{w}$ times larger variance than the normals in the other regions. The leading eigenvectors capture the large variance, and therefore, encode gender discriminating information.

In our experiments, the weight matrix is constructed through the angular difference between the intrinsic means of the female facial needle-maps and male facial needle-maps:

$$w_k = 1 - \exp[-\frac{1}{\sigma^2}(\arccos(\bar{n}_k^m \cdot \bar{n}_k^f))^2] \tag{1}$$

where $\bar{n}_k^m$ is the mean unit surface normal direction for males at the image location where k at. $\bar{n}_k^f$ is the corresponding mean unit normal vector for females. Using the intrinsic means reduces the influence of the differences between identities.

Suppose, $U = [u^1 | \ldots | u^K]$ is the data matrix, where $u^k = [u_1^k, \ldots, u_N^k]^T$ is the log mapped long vector of the kth sample data. The weighted covariance matrix is constructed as $L_W = \frac{1}{K}(WU)(WU)^T$. The snap-shot method of Sirovich are used to compute the eigenvectors of L_W. As stated in [13], 5 gender discriminating significant features will achieve the highest classification rate, we maintain the 5 leading eigenvectors to form the projection matrix $\Phi = (e_1 | e_2 | e_3 | e_4 | e_5)$. Given a long vector $u = [u_1, \ldots, u_N]^T$, the corresponding WPGA parameters are computed as $b = \Phi^T(Wu)$.

3   Classification

After the training and test facial needle-maps have been represented by their WPGA parameters, we use the a posteriori class probabilities to classify the test faces to one of the genders.

Let C_f and C_m denote the female and male gender classes, x denote the WPGA parameters of a test facial needle-map. Then according to the Bayes law, the probability that x is of class C_i is:

$$P(C_i|x) = \frac{P(x|C_i)P(C_i)}{\sum_{i \in \{f,m\}} P(x|C_i)} \tag{2}$$

We assume that the distribution of gender is Gaussian, and that the mean and variance of class C_i are μ_i and σ_i. The a priori probabilities are $P(C_f) = P(C_m) = 1/2$. Then,

$$P(x|C_i) = \frac{1}{\sqrt{2\pi\sigma_i^2}} \exp(-\frac{(x-\mu_i)^2}{2\sigma_i^2}). \tag{3}$$

If $P(C_f|x) > P(C_m|x)$, then the face is classified as female. Otherwise, the face is classified as male.

4   Experiments and Discussion

In this section, we first show how the σ value is determined for the weight matrix construction, and compare the gender discriminating power of the WPGA leading eigenvectors with the PGA leading eigenvectors. Then, the gender classification results obtained using WPGA parameters are compared with those obtained using PGA parameters. The Max-Planck Institute for Biological Cybernetics in Tuebingen, Germany provides the database used in our experiments [14], [15]. This database consists of 200 ground truth facial needle-maps, of which 100 are females and 100 are males. The weight matrix is constructed using all 200 faces. Gender classification is performed by randomly choosing 80 females and 80 males as training data, and using the remaining 40 faces for test. We repeated the randomization 10 times and the classification results are the average of the 10 randomizations.

4.1   Construction and Evaluation of the Weight Matrix

We first examine the selection of the value of σ for the weight matrix construction. Next, we evaluate the performance of WPGA by examining the gender discriminating power of the eigenvectors. The discriminating power is calculated using the criterion function introduced in [16], i.e. $J(\xi) = tr(S_w^{-1} S_b) = \sum_{k=1}^{d} \lambda_k$, where S_w and S_b are the within and between class scatter matrices, and λ_k, $k = 1 \ldots d$ are the eigenvalues of the matrix $S_w^{-1} S_b$.

Determination to the σ value. We construct the weight matrices for 10 different values of σ, and obtain 10 different WPGA projection matrices, from each of which we select the 5 leading eigenvectors. The 10 different sets of WPGA parameters for the 200 faces are obtained accordingly. The gender discriminating power is calculated on the 10 sets of WPGA parameters and are shown in Fig. 2. The σ value is selected to give the largest discriminating power. From Fig. 2, we select σ from the shoulder of the curve of discriminating power and this occurs when $\sigma^2 = 0.11$.
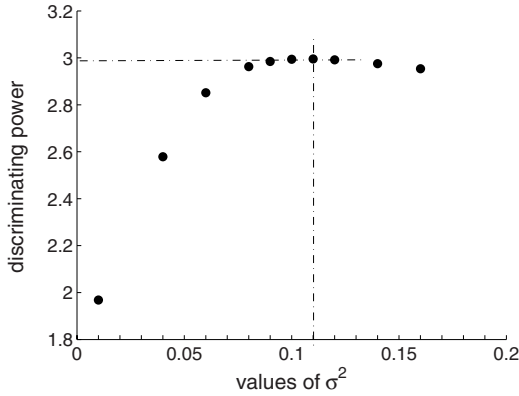
Fig. 2. Selection of σ value
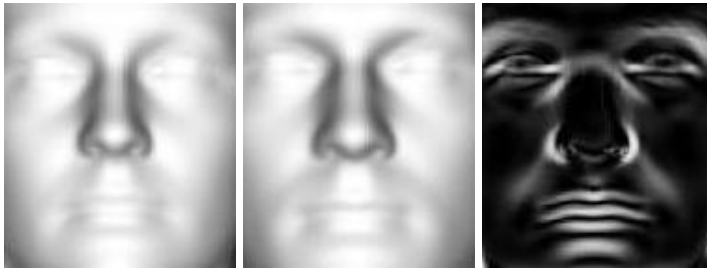
Fig. 3. Construction of the weight matrix. From left to right are the intrinsic mean of female needle-maps, the intrinsic mean of male needle-maps, and the constructed weight matrix.

The intrinsic means of the 100 female needle-maps and the 100 male needle-maps and the weight matrix constructed using $\sigma^2 = 0.11$ are shown in Fig. 3. From the figure, it is clear that the constructed weight matrix has high weights in regions around the eyebrows, nose, and mouth.

Discriminating power. After the construction of the weight matrix, we use it in conjunction with principal geodesic analysis to obtain the projection matrix. The discriminating power of each of the 10 leading WPGA eigenvectors is shown in the left hand panel of Fig. 4, and is compared with those of the 10 leading PGA eigenvectors which are shown in the right hand panel of Fig. 4. From the figure, we see that although the gender discriminating power of the WPGA eigenvectors is not in descending way, it is concentrated in the first 5 eigenvectors. The first 5 WPGA eigenvectors have the 5 largest discriminating power. By comparison, the discriminating power of PGA eigenvectors are more widely distributed. For example, the 8th PGA eigenvector has the 5th largest discriminating power,
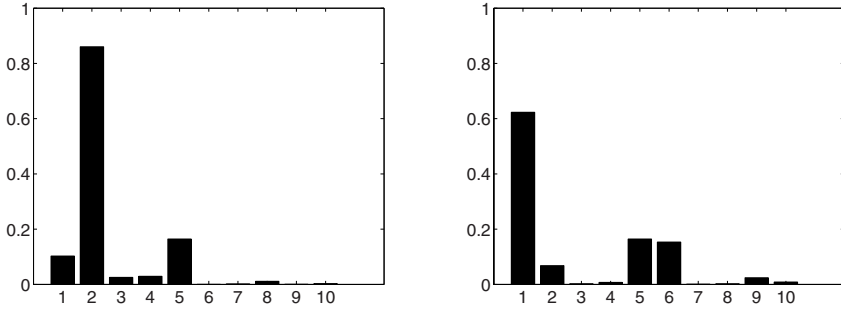
Fig. 4. Discriminating powers of the leading 10 eigenvectors. The left panel is for WPGA and the right panel is for PGA.

and the discriminating power of the 10th PGA eigenvector is larger than that of the 3rd eigenvector. This confirms our assumption that incorporating gender relevant weights into PGA results in better encoding of gender information in the leading eigenvectors. However, in WPGA, the discriminating power of the first and second eigenvectors seem to be swapped, which need further investment in the future.

Fig. 5 shows the plots of cumulative gender discriminating power for the first m ($m = 1 \cdots 20$) WPGA and PGA eigenvectors. From the figure, it is clear that WPGA has significantly larger cumulative discriminating power than PGA when $1 < m < 10$. This gives further confirmation that the first few WPGA eigenvectors encode most of the gender discriminating power, while the
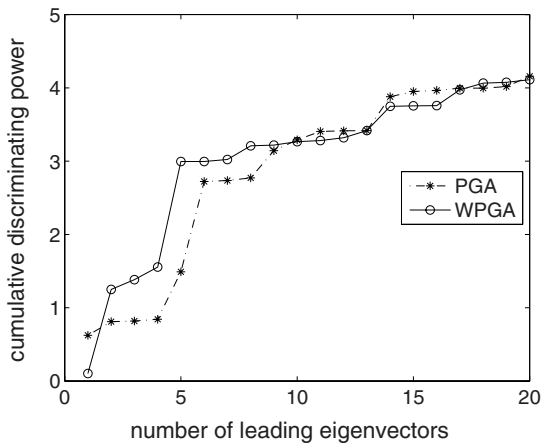
Fig. 5. Cumulative discriminating powers

gender discriminating power encoded in the PGA eigenvectors are more uniformly distributed.

4.2   Classification Results

We randomly selected 80 female needle-maps and 80 male needle-maps from the 200 available for use as training data, and the remaining 40 as test data. We first apply WPGA to the training data to obtain the projection matrix. Then, the construction of separate models for females and males, and gender classification on the test data are both performed on the 5 leading WPGA parameters. We repeat the randomization procedure 10 times. The average classification rates and variance obtained using WPGA and PGA are shown in Table 1, from which it is clear that gender classification performed on the leading WPGA parameters gives improvements not only on the classification rates, but also on the stability of the classification when compared with PCA.

Table 1. Gender classification rates

	Female	Male	Overall
$WPGA$	$93.50\% \pm 0.0450$	$91.00\% \pm 0.0490$	$92.25\% \pm 0.0361$
PGA	$84.00\% \pm 0.1068$	$84.50\% \pm 0.1083$	$84.25\% \pm 0.0448$

5   Conclusion

In this paper, we describe a weighted PGA method to extract gender discriminant features from 2.5D facial needle-maps in a single step, and perform gender classification using the WPGA parameters. Experimental results show that the leading WPGA eigenvectors encode more gender discriminating power than the leading PGA eigenvectors. Moreover, gender classifications based on WPGA parameters achieve more accurate and more stable results than those based on PGA parameters.

There are several potentially interesting avenues for future investigation. First, instead of using ground truth facial needle-maps, we will apply the method to needle-maps recovered from facial images using SFS. Second, we will improve the generalization of the weight matrix. Third, unsupervised learning using the EM algorithm will be used to perform gender classification on the WPGA parameters.

References

1. Burton, A.M., Bruce, V., Dench, N.: What's the Difference Between Men and Women? Evidence from Facial Measurement. Perception 22, 153–176 (1993)
2. Buchala, S., Davey, N., Frank, R.J., Gale, T.M.: Dimensionality reduction of face images for gender classification. Department of Computer Science, The University of Hertfordshire, UK, Technical Report 408 (2004)

3. Buchala, S., Davey, N., Gale, T.M., Frank, R.J.: Principal Component Analysis of Gender, Ethnicity, Age, and Identity of Face Images. In: Proc. IEEE ICMI (2005)
4. Wilhelm, T., Bohme, H.J., Gross, H.M., Backhaus, A.: Statistical and Neural Methods for Vision-based Analysis of Facial Expressions and Gender. In: SMC 2004, pp. 2203–2208. IEEE omnipress (2004)
5. Wilhelm, T., Bohme, H.J., Gross, H.M.: Classification of Face Images for Gender, Age, Facial Expression, and Identity. In: Duch, W., Kacprzyk, J., Oja, E., Zadrożny, S. (eds.) ICANN 2005. LNCS, vol. 3696, pp. 569–574. Springer, Heidelberg (2005)
6. Lu, X., Chen, H., Jain, A.K.: Multimodal Facial Gender and Ethnicity Identification. In: ICB, HongKong, pp. 554–561 (2006)
7. Bruce, V., Burton, A.M., Hanna, E., Healey, P., Mason, O., Coombes, A., Fright, R., Linney, A.: Sex discrimination: how do we tell the difference between male and female faces? Perception 22, 131–152 (1993)
8. Marr, D.: Vision. W.H. Freeman, San Francisco (1982)
9. Smith, W.A.P., Hancock, E.R.: Recovering Facial Shape and Albedo using a Statistical Model of Surface Normal Direction. Tenth IEEE International Conference on Computer Vision 1, 588–595 (2005)
10. Fletcher, P.T., Joshi, S., Lu, C., Pizer, S.M.: Principal geodesic analysis for the study of nonlinear statistics of shape. IEEE Transactions on Medical Imaging 23, 995–1005 (2004)
11. Pennec, X.: Probabilities and statistics on riemannian manifolds: A geometric approach. Technical Report RR-5093, INRIA (2004)
12. Sirovich, L.: Turbulence and the dynamics of coherent structures. Quart. Applied Mathematics XLV(3), 561–590 (1987)
13. Wu, J., Smith, W.A.P., Hancock, E.R.: Learning Mixture Models for Gender Classification based on Facial Surface Normals. In: IbPRIA 2007, vol. 4477, pp. 39–46 (2007)
14. Troje, N., Bulthoff, H.H.: Face recognition under varying poses: The role of texture and shape. Vision Research 36, 1761–1771 (1996)
15. Blanz, V., Vetter, T.: A Morphable Model for the Synthesis of 3D Faces. In: SIGGRAPH 1999 Conference Proceedings, pp. 187–194 (1999)
16. Devijver, P., Kittler, J.: Pattern Recognition: A Statistical Approach. Prentice Hall, Englewood Cliffs (1982)

Range and Intensity Vision for Rock-Scene Segmentation

Simphiwe Mkwelo, Frederick Nicolls, and Gerhard de Jager

[1] Defence Peace Security and Safety,
Council for Scientific and Industrial Research (CSIR)
Meiring Naude road, Lynnwood, Pretoria 0002, South Africa
smkwelo@csir.co.za
http://www.csir.co.za
[2] Department of Electrical Engineering, University of Cape Town, Rondebosch 7700,
South Africa
{fnicolls,gdj}@dip.ee.uct.ac.za
http://www.uct.ac.za

Abstract. This paper presents a methodology for the automatic segmentation of rock-scenes using a combination of range and intensity vision. A major problem in rock scene segmentation is the effect of noise in the form of surface texture and color density variations, which causes spurious segmentations. We show that these problems can be avoided through pre-attentive range image segmentation followed by focused attention to edges. The segmentation process is inspired by the Human Visual System's operation of using a priori knowledge from pre-attentive vision for focused attention detail. The result is good rock detection and boundary accuracy that can be attributed to independence of range data to texture and color density variations, and knowledge driven intensity edge detection respectively. Preliminary results on a limited image dataset are promising.

Keywords: surface texture, color density variations, range image segmentation, intensity edge detection.

1   Introduction

An instrument for measuring rock fragmentation is invaluable to the mining and mineral processing industries where it can be used to monitor, optimize and control blasting and communition. Image processing in particular, has been widely accepted as the analysis method of choice for the estimation of rock-size because of: the non-intrusive nature of the measurement process; the capability of measuring continuously and in real time; the repeatability of measurements given the same scene and lighting conditions; and the absence of moving mechanical parts which implies little or no maintenance.

Intensity image analysis, in particular, has been a research area of focus for many of the recent academic [1], [2], [3] and operational [4], [5], [6] systems, mainly because the imaging sensor is sensitive to shadows which are formed

around the individual particles. These shadows are detected and completed as rock outlines during rock scene segmentation. However, limitations of intensity sensors are well documented [7], [2]: the loss of a dimension due to the projective nature of the sensor; and the loss of small particles due to the limitation in the sensors resolution, etc. These limitations introduce errors into the measurement process which are further increased by errors that can be attributed to the environment under imaging: poor lighting; color density and texture variations.

Lighting conditions can be controlled through the elimination of natural lighting and proper design of synthetic lighting [2]. Color density and texture variations define a rock-scene in intensity but do not necessarily correlate to range image data except perhaps at the edges of rocks. High quality range images of rock-scenes have been segmented using 3D morphological techniques [8] for the purposes of rock-size estimation. However, the processing that is required to produce such high quality data inhibits the practical implementation of such a system in a real plant. Consequently, rapidly generated range imagery of sufficient quality can be complemented with corresponding intensity in a multisensor fusion framework.

A review of current trends and future directions in multisensor integration and fusion is presented in [9], where a distinction between multisensor integration and fusion is made. Multisensor Integration is viewed as the general connectivity of sensors that produce information at system architecture and control level. Fusion, on the other hand, is viewed as the process of combining multisensory information using statistical or mathematical methods. Multisensor integration of infrared and visual sensors has been used for human form detection[10]. Range and intensity images have been fused for mobile robot localization in robotics[11] and deformed object identification and bin picking in materials handling[12]. Range maps have been fused with intensity edge maps to segment noisy range images [13].

We present a methodology that combines the analysis of range and intensity images to address the problem of texture and color density variations during rock edge extraction. Experience and previous work [2] has shown that the human visual system (HVS) is more than capable of rock-scene segmentation and therefore serves as a platform upon which the image analysis is based. Initially, pre-attentive range vision in the form of extracting preliminary rock boundaries from a range image is executed. The boundary information is eventually used as a priori knowledge for focused attention to intensity edges. A description of the pre-attentive range segmentation algorithm is presented in section 2; section 3 describes the focused intensity edge detection algorithm; a methodology for performance evaluation is presented in section 4; Results of the experiments are presented in section 5; and conclusions are drawn in section 6.

2   Pre-attentive Range Vision

Segmentation of range data is an important part of range image perception and understanding. The general problem of range image segmentation is that of partitioning the range image into disjoint surfaces representing individual

objects or a single object. In this work, the former condition is encountered, where each surface represents a single rock in the image. The problem has seen many solutions such as the HK map iterative region growing [14], the effective jump-diffusion method[15], scan-line grouping [13], methods using morphological operators [16], [8] and others. In [13], intensity data in the form of Intensity Edge Maps (IEM) are fused with range data to improve range segmentation. In this work, range segmentations are used to improve intensity image segmentation, see section 2.2. We use a global range segmentation technique referred to as rock model extraction, which is based on morphological operators. Specifically, the watershed and distance transforms are used, as shown in figure 1.
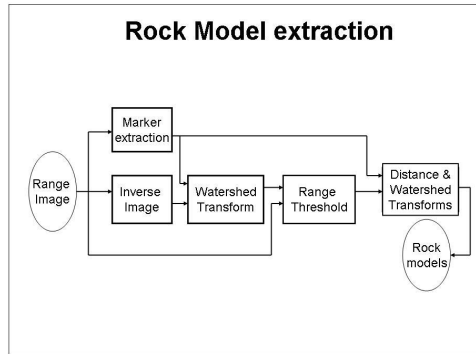
Fig. 1. A block diagram representation of rock model extraction

The processing includes: the estimation of background and foreground range values for range value thresholding to produce a binary image; connected binary models are disconnected using a combination of distance and watershed transforms. As can be seen in figure 2 that the watershed is executed twice for a single range image. The first watershed is used to estimate a range threshold that separates foreground and background range values based on a discrepancy between trough and surface range values. The second watershed combined with the distance transform spatially splits connected binary models that result from the previous process. The distance transform assigns a value for each foreground pixel that is equal to its distance from the background. Consequently, connected binary models will have cone shaped structures whose peaks are centered at the centroids of the models with local minima or saddle points between these peaks. This allows for a watershed transform to create boundaries at the saddle points and hence splitting connected models.

3   Focused Intensity Vision

Perception and understanding of intensity data often requires image segmentation. The segmentation of intensity rock-scenes can be difficult without a priori

knowledge about rocks because of noise, texture and color density variations on rock surfaces. Crida[2] used elliptical models of rocks as a priori knowledge for focused intensity edge detection. He used elliptical probability masks and edge orientations to limit the search for edge pixels. In this work, a similar approach is taken, except a shape model from a range image is used for producing probability masks and edge orientations as shown in figure 2. The process is local by nature and therefore focuses attention to a predefined region-of-interest. Key processing operations in the form of rock edge detection, probability masking and optimization are described in the next section.
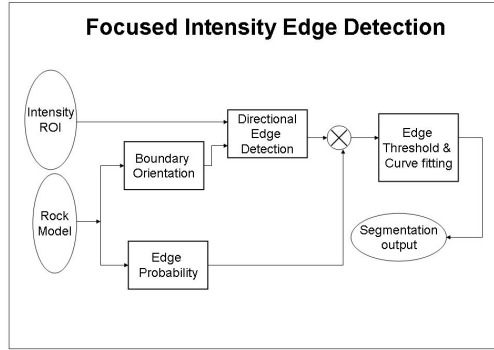
Fig. 2. A block diagram representation of focused intensity edge detection

3.1 Edge Detection, Masking and Optimization

The intensity sub-image is subjected to a directional edge detection process that computes edge-responses based on a variable [3-by-3] convolution kernel whose elements depend on the pixel position and orientation of the boundary model at that point. The practical implementation involves predefining a set of possible kernels for a number of arc intervals of a circle which defines the orientation of edges to be detected. The radial convolutions produce noisy edge responses in areas of mismatches between the kernel orientations and edges. We use probability masks to spatially limit the search area of edges of interest. The masks are created by a dilation of boundary models, distance transformation and normalization. The masking is achieved by multiplying the edge response with the probability mask to remove interior texture and color density noise effects. The masked response is then optimized to narrow edge traces through a radial search for pixels with maximum edge responses. Figure 3 shows input intensity, edge response, probability mask, masked response and optimized response sub-images.

3.2 Rock Shape Extraction

The objective of this stage is to fit the optimized response by a smooth boundary to extract the underlying rock shape. This involves a transformation from an
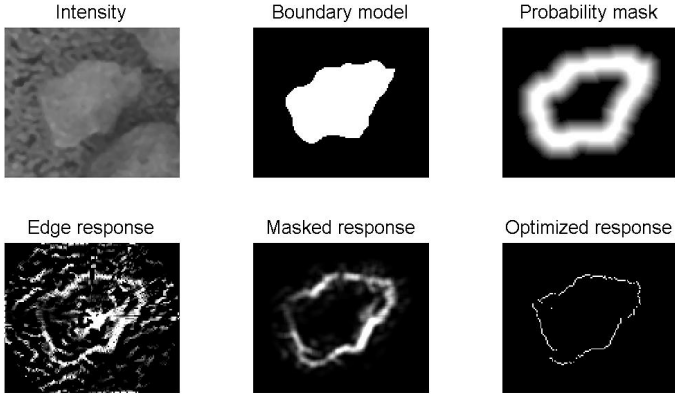
Fig. 3. Image data: intensity, boundary model, probability mask, edge response, masked response and optimized response
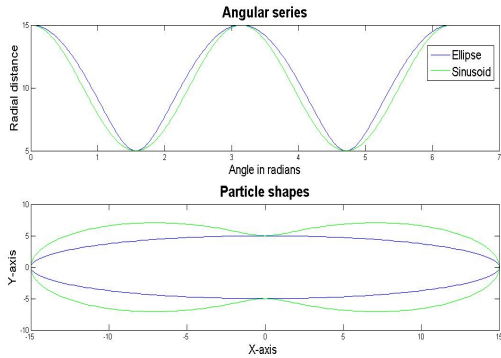
Fig. 4. A sinusoidal signal as an approximation to an elliptical shape

image to an angular-series representation of radial distances. The independent variable becomes angle in radians. The angles range from zero to 2π radians and the distance signal wraps around at the zero and 2π radians interface. A circle of radius r in an image becomes a DC signal of r volts in the angular-series representation. An ellipse becomes an approximately sinusoidal signal with a DC offset equal to the average of the principal components and amplitude equal to the difference in principal components, as shown in figure 4.

In general, however, ore can consists particles with sharp and pointed edges producing irregular and complex angular-series. We use an Nth order least squares polynomial as a first approximation of the angular-series points and hence extract the underlying shape of the projected rock. The least squares formulation determines coefficients

$$\mathbf{c} = [c_N, c_{N-1}, c_{N-2}, ..., c_1]^T ,\tag{1}$$

from the general vector equation

$$\mathbf{y} = \mathbf{Ac} \tag{2}$$

as being $(\mathbf{A}^T\mathbf{A})^{-1}\mathbf{A}^T$. This is known as the pseudo-inverse of matrix $\mathbf{A}$. A single row of the matrix $\mathbf{A}$ has the form $[x^N x^{N-1} x^{N-2}...1]$. The increase in the order of the polynomial will vary the segmentations from simple to complicated models. Least squares is known to perform well provided that there is an effective pre-processing for removing outliers in the data. Because it is not possible to completely remove outliers, it maybe necessary to investigate other curve fitting methods such as Radial Basis functions and robust estimation methods which are known to be less sensitive to outliers.

4 Methodology

A laboratory data set in the form of a calibrated stereo pair of consecutive frames of an intensity rock-scene is used to generate a range image using dense stereo reconstruction [17],[18]. Pre-attentive segmentation of the range image, as described in section 2, is applied to produce boundary models, which are used to automatically select image windows of corresponding intensity rocks. Focused intensity segmentation is achieved through using variable edge orientation kernels and probability masks from the boundary models.

The system's performance is evaluated in terms of a visual measure of error from images coupled with numerical errors between automatically extracted

Table 1. The user-input parameter set

Parameter	value
Polynomial orders	11 and 15
Probability mask width	60% of radial distance
2-tail outlier search regions	50% of range
Intensity Gaussian filter $[size, \sigma]$	$[9, 0.5]$

Range   Intensity and models
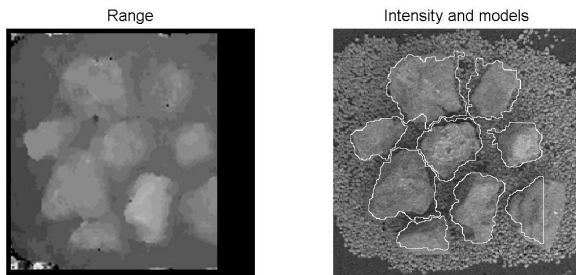
Fig. 5. Experimental data set: the range image and the corresponding reference intensity image overlaid with boundary models

rock-shapes and hand segmented sub-images. Numerical differences in enclosed areas between the segmentations of the system and the human visual system are computed by image subtraction of the system output from the hand segmented images. The percentage error is computed relative to the HVS segmentations. Table 1 shows the user input parameter set that is used during the experiments and figure 5 is the input data-set to be used by the focused intensity segmentation algorithm.

5 Results

This section presents results on a data-set of 8 sub-images. The results are divided into visual and numerical categories based on performances with settings of table 1. The visual data in the form of the input intensity image, extracted model, angular series and segmented rock are shown in figures 6 to 9. Polynomial fitting results with polynomials of order 15 and 11 are shown. The results show, as predicted, that the order 11 polynomial imposes smoothness on the model, while the 15th order can model the intricate complexities of rock shapes. The 15th order polynomial is used for comparisons to hand segmented sub-images.

Table 2 shows the numerical results of a comparison to hand segmented sub-images in terms of over-estimation, under-estimation and overall errors. Results show that the worst performance is produced on image 4 of figure 7, with an overall pixel error 25.5% and an under-estimation component of 24.81%. This image appears not to have clear indications of rock edges of interest. The system performs best on image 5 of figure 8, with a minimum overall error of 4.24%. This image appears to have very good edge information about the rock of interest. Sub-image 3 of figure 7 shows the effect of the sensitivity to outliers of the least squares method. As a result the overall error of 8.59% has an over-estimation component of 6.55%.

These are preliminary results and therefore it is not reasonable to specify averages and standard deviations as the number of image samples is not sufficient.
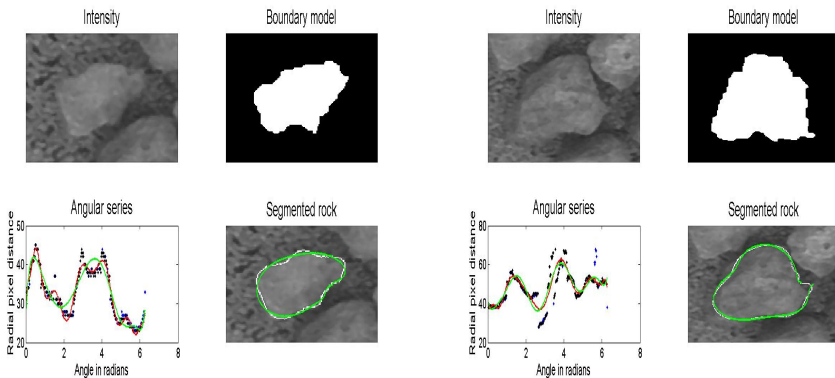
Fig. 6. Rock sub-images 1 and 2 with corresponding results
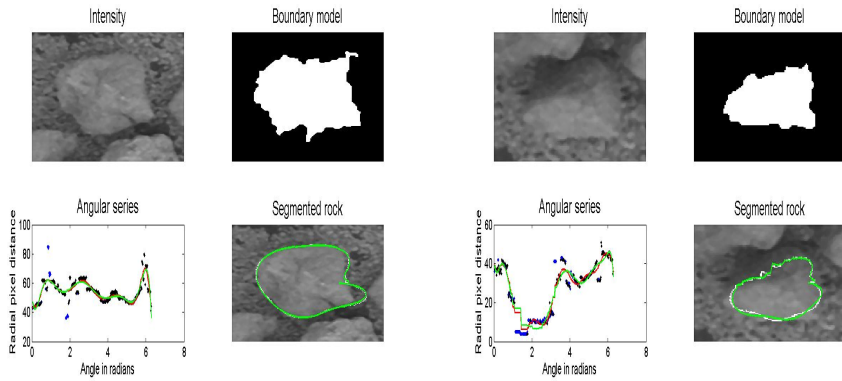
Fig. 7. Rock sub-images 3 and 4 with corresponding results
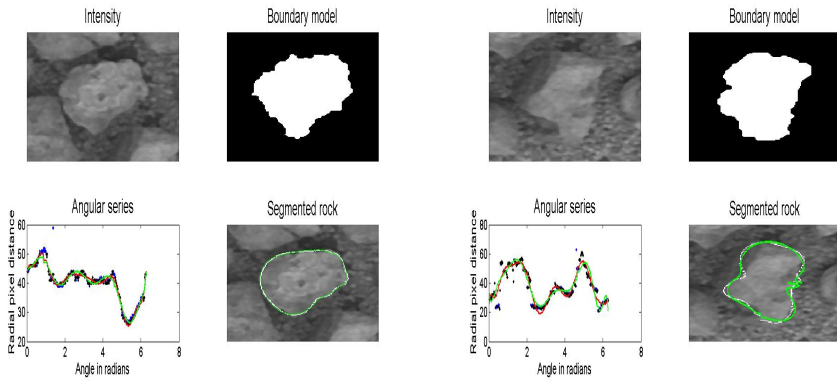
Fig. 8. Rock sub-images 5 and 6 with correpsonding results
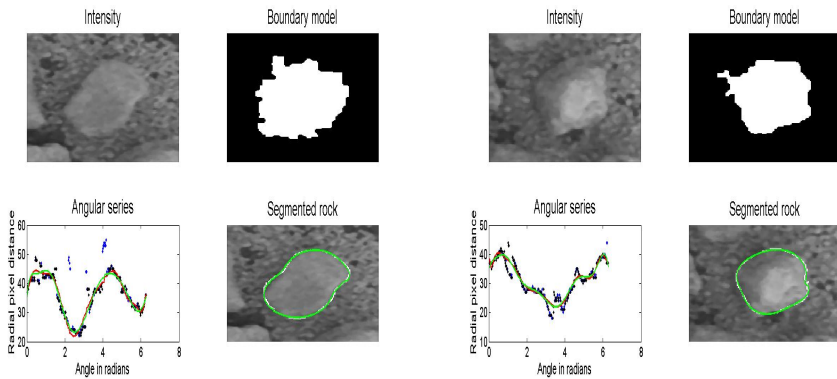
Fig. 9. Rock sub-images 7 and 8 with corresponding results

Table 2. Segmentation error with respect to HVS segmentation results

Image number	under-estimation error	over-estimation error	overall error
image 1	1.85%	4.09%	5.93%
image 2	9.95%	2.96%	12.9%
image 3	2.04%	6.55%	8.59%
image 4	24.81%	0.24%	25.5%
image 5	1.07%	3.17%	4.24%
image 6	18.83%	1.82%	20.65%
image 7	0.92%	4.92%	5.84%
image 8	5.14%	1.66%	6.80%

6 Conclusions

Based on the above findings and results, the following conclusions can be drawn.

– An HVS inspired methodology for rock-scene segmentation that combines intensity and range image analysis to avoid the effects of texture and color density variations is presented.
– Post-processing in the form of angular series representation and polynomial fitting is used to extract the underlying rock shape with good accuracy. However, visual and numerical results seem to agree with literature that the least squares estimator is sensitive to outliers and therefore other estimators must be investigated.
– The system appears to perform very well on the experimental data set. However, more data with variation in texture and color densities is required for a more rigorous evaluation.

References

1. Lange, T.B: Measurement of the size distribution of rocks on a conveyor belt using machine vision, PhD thesis at the University of Witwatersrand (1990)
2. Crida, R.C.: A machine vision approach to rock fragmentation, PhD thesis at the University of Cape Town (1995)
3. Mkwelo, S., De Jager, G., Nicolls, F.: Watershed-based Segmentation of Rock Scenes and Proximitybased Classification of Watershed Regions Under Uncontrolled Lighting. SAIEE Transactions, Research Journal of SAIEE 96(1), 28–34 (2005)
4. Sudhakar, J., Adhikari, G.R., Gupta, R.N.: Comparison of Fragmentation Measurements by Photographic and Image Analysis Techniques. Rock Mechanics and Rock Engineering 39(2), 159–168 (2005)
5. Kemeny, J.: The Split-Online Fragmentation Analysis System (February 12, 2006), www.spliteng.com/splitonline/fragmentation.asp

6. Franklin, J.: Granulometry Analysis Software (February 12, 2006),
   `www.wipware.com/wipfrag.php`
7. Maerz, N.H., Zhou, W.: Optical Digital Fragmentation Measuring Systems-Inherent Sources of Error. FRAGBLAST The International Journal for Blasting and Fragmentation 2(4), 415–431 (1998)
8. Thurley, M.J: Three Dimensional Data Analysis for Separation and Sizing of Rock Piles in Mining. PhD Thesis, Monash University, Department Electrical and Computer Systems Engineering (2002)
9. Luo, R.C., Yih, C.C., Su, K.L.: Multisensor fusion and integration: Approaches, Applications and Future Directions. IEEE Sensors Journal 2(2) (2002)
10. Shah, S., Argarwal, J.K., Eledah, J., Ghosh, J.: Multisensor Integration for scene classification: An experiment in human form detection. In: International Conference on Image Processing, Santa Barbara, October 26-29, 1997 (1997)
11. Neira, J., Tardos, J.D., Horn, J., Schmidt, G.: Fusing range an intensity images for mobile robot localization. IEEE Transactions on robotics and automation 15(1) (1999)
12. Umeda, K., Arai, K.: Industrial vision system by fusing range and intensity image. In: Proc. of IEEE Int. Conf. on Multisensor fusion and integration for Intelligent Systems, October 2-5, 1994 (1994)
13. Zhang, Y., Sun, Y., Sari-Sarraf, H., Aidi, M.A.: Imapact of Intensity Edge Map on Segmentation of noisy range images. In: Proc. of Spie Conf. on Three Dimensional Capture and Applications III, San Jose,CA, vol. 3958, pp. 260–269 (2000)
14. Besl, P.J., Jain, R.C.: Segmentation Through Variable Order Surface Fitting. IEEE Trans. on Pattern Analysis and Machine Intelligence, PAMI 10(2), 167–192 (1988)
15. Han, F., Tu, Z., Zhu, S.: Range image segmentation by an effective jump diffusion method. IEEE Transactions on pattern analysis and machine intelligence 26(9) (2004)
16. Gee, L.A, Abidi, M.A.: Segmentation of range images using morphological operations: Review and examples. In: SPIE Conference on Intelligent Robots and Computer Vision XIV, Philadelphia, PA, vol. 2588, pp. 734–746 (October 1995)
17. Mkwelo, S., De Jager, G., Nicolls, F.: Three Dimensional rock-scene modelling using dense stereo reconstruction. In: 13th Proceedings of PRASA (November 2006)
18. Scharstein, D., Szeliski, R.: A taxonomy and evaluation of dense two frame stereo correspondence algorithms. International Journal of Computer Vision 47(1), 7–42 (2002)

Human Detection in Indoor Environments Using Multiple Visual Cues and a Mobile Robot

Stefan Pszczółkowski and Alvaro Soto

Pontificia Universidad Catolica de Chile
Santiago 22, Chile
`spp@ing.puc.cl`, `asoto@ing.puc.cl`

Abstract. In order to deploy mobile robots in social environments like indoor buildings, they need to be provided with perceptual abilities to detect people. In the computer vision literature the most typical solution to this problem is based on background subtraction techniques, however, in the case of a mobile robot this is not a viable solution. This paper shows an approach to robustly detect people in indoor environments using a mobile platform. The approach uses a stereo vision system that yields a *stereo pair* from which a *disparity image* is obtained. From this disparity image, interesting objects or *blobs* are segmented using a *region growing algorithm*. Afterwards, a color segmentation algorithm is performed on each blob, searching for human skin color areas. Finally, a probabilistic classifier provides information to decide if a given skin region corresponds to a human. We test the approach by mounting the resulting system on a mobile robot that navigates in an office type indoor building. We test the system under real time operation and different illumination conditions. The results indicate human detection accuracies over 90% in our test.

Keywords: human detection, human-computer interaction, face detection.

1 Introduction

An important field in Robotics is *Socially interactive robots* [6], which consists in providing robots with the ability to interact with other agents. To effectively interact socially, robots have to separate possible agents from the rest of the scene. Then, they have to discriminate which of these candidate agents they can interact with. The most common separation is between humans and other objects, like furniture, doors, and decorations.

Serving as a contribution towards the development of socially interactive robots, this paper shows an approach to robustly detect people in indoor environments. Our goal is to mount our system on a mobile robot navigating through an indoor environment, therefore, the use of traditional background subtraction techniques is not a viable solution.

In our case, our approach is based on information provided by a stereo vision system to perform the initial segmentation of candidate humans. We use the fact

that for each person in the scene, its depth is roughly constant and appears on the disparity image as a uniform intensity area. After this initial segmentation, we use color cues to detect skin color pixels that feed a probabilistic classifier that provides the final detection of humans.

The rest of the paper is organized as follows: Chapter 2 reviews relevant previous work on human detection using computer vision techniques. Chapter 3 discusses the main details of our approach to detect people. Chapter 4 shows the results of applying our methodology to real data in real time. Finally, chapter 5 presents the main conclusions of this work.

2   Previous Work

Human detection and tracking are important topics of research in the computer vision literature. Applications for these topics include surveillance, elderly assistance, human-robot interaction, and pedestrian counting, among others [9]. The state of the art in this area can be divided into two main categories: i) Methods that require background substraction as a first step to detect the interesting objects. ii) Methods that perform the detection using moving cameras. Our method belongs to this last category, hence, we concentrate the review here in methods that do not rely in background subtraction techniques, for a more extensive review see [9].

The work in [11] proposes a method based on geometrical structures. It uses the fact that the relative positions of various body parts are common to all humans. On each input image, patches at multiple locations and scales are compared to previously stored templates. Then a threshold is used to classify a patch as a human or a non-human. Recognition rates between 83% and 90% are presented for this method.

The method proposed by [12] deals with the detection of pedestrians from video. The algorithm scans a detector over two consecutive frames of a video sequence and extracts simple rectangular features by evaluating motion and appearance filters. The detector is a cascade of classifiers that is trained using AdaBoost. A static detector only with appearance information is also presented. Results with low false positive rates and detection rates of about 80% are shown.

The work in [10] proposes a method for human detection in video sequences for outdoor surveillance. The technique computes optic flow of several human and non-human motion examples and trains a support vector machine (SVM) with radial basis function (RBF) kernel using these examples. The classifier can be applied to new input video at multiple positions and scales, followed by pruning of detections with large overlap. Good recognition performance for walking people are shown, even in the presence of other moving objects.

Recently, [3] describes a method that uses grids of Histograms of Oriented Gradient (HOG) descriptors for building a support vector machine classifier. It divides the image in small spatial parts (cells) and finds the histograms of edge orientations over all the pixels of the cell. The combined histogram entries form the feature representation after local contrast normalization in overlapping
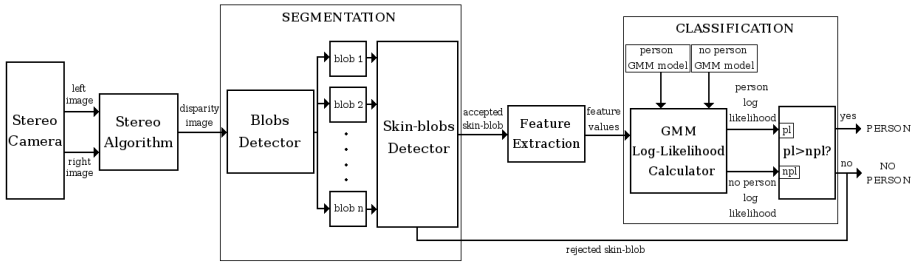
Fig. 1. System diagram. The images obtained from the stereo cameras are passed to the segmentation process, where the stereo blobs and face candidates are detected. Then features are extracted from the face candidates to feed a classifier that distinguishes between person and not person.

descriptor blocks. The inclusion of four different normalizations on each HOG improves performance from 84% to 89%.

3   Our Approach

In this chapter we show the different parts of our approach and how they are integrated to effectively detect people. Figure 1 shows an overview of the approach. It consists of a stereo vision system that yields a *stereo pair* from which a *disparity image* is obtained. From this disparity image, interesting objects or *blobs* are segmented using a *region growing algorithm*. Afterwards, a color segmentation algorithm is performed on each blob, searching for human skin color areas. Then, over each blob a feature extraction process provides information to a probabilistic classifier that finally distinguishes if a given skin region corresponds to a human. In the next, we explain each of these steps in detail.

3.1   Stereo-Based Human Segmentation

The process we developed to make human segmentation is based on the idea that for each person in the scene, its depth is roughly constant and appears on the disparity image as an uniform-intensity area. Based on that, one can separate humans from the background by finding these areas.

To obtain the stereo pair we use the SVS library [8] and the disparity image is calculated using the library implementation of the *Area Correlation Method*. Then, a Breadth First Search (BFS) *region growing* algorithm is performed over the disparity image. This algorithm iteratively looks around each pixel searching for neighbors with similar gray intensity and connecting them. This process yields several regions of connected pixels known as *blobs*. Empirically, we set that blobs smaller than 3.26% of the total image area are filtered out.

Fig. 2. Skin pixel criteria applied to some images. Note that some colors of the T-shirts in the first image are more difficult to filter out due to its similarity to some skin pigmentations.

3.2   Skin-Color Based Segmentation

We want to detect humans, hence, a useful visual cue is skin color. The procedure to obtain skin color blobs consists in searching for skin pixels inside the blobs detected by the stereo vision algorithm (stereo blobs). To effectively classify between *skin* pixels and *non-skin* pixels we used a transformation of the RGB values into a "log color-opponent" space [4]. This space can directly represent the approximate hue of skin color:

$$logVal_1 = \ln(G); logVal_2 = \ln(R) - \ln(G); logVal_3 = \ln(B) - \frac{\ln(R) + \ln(G)}{2} \quad (1)$$

We classify a pixel as *skin*, if it meets the following criteria:

$$logVal_1 \in [3.5, \infty); \quad logVal_2 \in [0.05, 0.8]; \quad logVal_3 \in [-1.25, 0] \quad (2)$$

We set these intervals by sampling 32000 pixels of both *skin* and *non-skin* classes and searching for the optimal thresholds that separate the classes. Figure 2 shows an example of the typical segmentations obtained with this scheme.

Given that our goal is to provided human detection capabilities to a social robot, we focus in detecting people that is standing and facing the robot. Also, due to the biological constraint that humans have their heads in the upper part of their body, we just search for skin pixels in the upper half of the stereo blobs. Here, we find the image row r_{max} and the image column c_{max} with maximum number of skin pixels. If the pixel located at (r_{max}, c_{max}) is a skin pixel, a Breadth First Search region growing algorithm starting on that point finds a *skin-colored blob* and its bounding box; if is not, then a search for a skin pixel is performed over its neighbors. If one of the neighbors is a skin pixel, the region

growing algorithm is done with that neighbors as a starting point, but if none of the neighbors is a skin pixel, then the candidate is rejected.

Finally, over the skin colored blobs obtained, we apply a size based rejection test. Given that the size of the expected color blobs depends of the distance of a potential person from the camera, we use training data to find an adaptive rejection threshold. This threshold depends on the average gray intensity of the corresponding pixels in the disparity image. The following equation shows the relation found between minimum blob area ($minArea$) and average gray intensity ($dispAvg$):

$$minArea = \frac{1.672 \cdot dispAvg^2 - 340.3 \cdot dispAvg + 19310}{2} \tag{3}$$

The numerator in Eq. 3 is obtained by sampling the area of 66 skin-colored blobs known to be real faces versus the average gray intensity of their containing stereo blobs, and fitting the best second-degree curve on the samples. Then, as to ensure that most of the samples are higher than the curve, we set a conservative tolerance for the threshold of 50% below the curve (denominator).

3.3   Feature Extraction

The skin segmentation shown in section 3.2 can yield several types of candidates. For example, for two people very close to each other and producing one blob, we will extract the two faces, but for a person who is waving, we will extract its face and its hand. This originates the need to differentiate between these candidate face blobs. To accomplish this, we extract color features from the color blobs to perform a classification between *face* and *non-face*.

In the computer vision literature there is a large amount of work about different features that can be extracted from a segmented area. We try several of them like Hu moments [7] and Flusser moments [5]. None of these features yielded acceptable results, mainly because skin-colored blobs have a very noisy and non-uniform shape, thus, they did not separate the *face* and *non-face* classes well. Finally, the feature set that provide us the best results is summarized in 3 criteria, that, applied to each RGB channel makes a total of 9 features:

– Normalized Standard Deviation

$$\sigma_{norm}^k = \frac{\sqrt{\frac{1}{N} \sum_{i=1}^{N} \sum_{j=1}^{N} (x_{ij}^k - \bar{x}^k)^2}}{\bar{Y}^2}$$

– Normalized Contrast

$$I_{norm}^k = \frac{\sum_{i=1}^{8} \sum_{j=1}^{8} (i - j)^2 \cdot P^k[i, j]}{\bar{Y}^2}$$

– Normalized Uniformity or Energy

$$E_{norm}^k = \sum_{i=1}^{8} \sum_{j=1}^{8} (P^k[i, j])^2 \cdot \bar{Y}^2$$

where N_i, N_j and N_s are the number of rows, columns and skin pixels of the skin image's bounding box, $k \in \{R, G, B\}$, x_{ij}^k is the value at position (i, j) of the color channel, $\bar{x}^k$ is the mean over all x_{ij}^k on each color channel, $P^k[i, j]$ is the value of the 8x8 co-occurrence matrix [2] at position (i, j) for each color channel, and $\bar{Y}$ is the mean luma component (Y) value of the YCbCr transformation of the skin-colored blob pixels. This value is defined as:

$$\bar{Y} = \frac{1}{N_s} \sum_{(i,j) \in skinBlob} 0.299 * R_{(i,j)} + 0.587 * G_{(i,j)} + 0.114 * B_{(i,j)}$$

Note that all these features are chromatic, hence, they overcome the problem introduced by the very noisy and non-uniform shape of the skin blobs.

σ_{norm}^k deals with the fact that in faces, pixel colors have great variability, because of the presence of hair, eyes, nose, and mouth. In hands, the pixel colors are, generally, less variable. In addition, the standard deviation penalizes the high values the variance takes with very illuminated images, in order to make this feature less responsive to that illumination.

I_{norm}^k and E_{norm}^k deals with the presence of hair, eyes, nose, and mouth in faces by taken into account contrast and uniformity. In these face areas, changes in pixel values tend to increase the contrast and decrease the uniformity. In contrast, the less variable nature of hands pixels tend to decrease the contrast and increase uniformity.

The mean squared luma value $\bar{Y}^2$ is intended to be a normalization value that balances the difference between very illuminated and obscure pictures.

To further improve the extraction of features, we perform an exhaustive feature selection process over all possible subsets of the 9 features. This process receives a feature set and evaluates the average number of blobs that are correctly classified, according to the classification criteria and training set described in section 3.4. This evaluation is performed using a 10-fold cross validation over the entire training data. The results of the best 3 set of features are summarized in Table 1. In our final system we use the set $\{\sigma_{norm}^R, I_{norm}^R, I_{norm}^G\}$.

Table 1. Feature selection results on training data

Feature Set	Average Correctly Classified Points
$\{\sigma_{norm}^R, I_{norm}^R, I_{norm}^G\}$	93.4%
$\{\sigma_{norm}^R\}$	91.1%
$\{\sigma_{norm}^R, \sigma_{norm}^B\}$	84.1%

3.4   Classification

Our approach classifies between *person* and *non-person* classes. The *person* class corresponds to all the skin-colored blobs found to be faces and the *non-person* class correspond to all other skin-colored blobs.

The classifier uses Gaussian Mixture Models (GMMs) to learn each class. These GMMs are trained using the MATLAB toolbox described in [1] with 1000
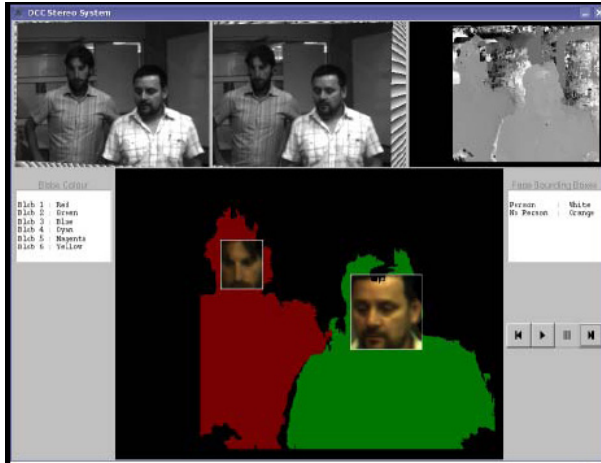
Fig. 3. Example of the operation of the system in an indoor office environment

examples for each class, taking care of having sufficiently different examples, that is, a "face" training set with different skin tonalities and a "non-face" training set representative of our intended scenario. The GMMs are normalized to the [0,1000] range. Every skin color blob is classified according to the likelihood ratio test between the *person* and *non-person* models, using a null threshold.

4   Results

4.1   Person Detection

The first experiment is oriented to measure the performance of the system under two illumination conditions and different distances between the camera and the people being detected.

The test data consists of 100 frames with two people each, corresponding to 20 frames at each of 5 different distances. Experimentally, the maximum distance at which the stereo algorithm begins to capture a person blob is approximately between 360 and 310 cms, and the minimum distance is approximately 130 cms. We test the algorithm in a distance range from 150 to 350 cms. Figure 3 shows an example of the system operating in the office building environment.

The percentage of the people correctly detected as person are shown in figure 4. It is possible to see that, for the corridor location, the system performs better if the people are not too far or too close from the camera. For the office location with good illumination, the algorithm has performances that exceed 95%, except for the case of 250 cms, where a reflex in one of the faces made the feature values lie in a region where both person and no-person likelihoods are very similar.
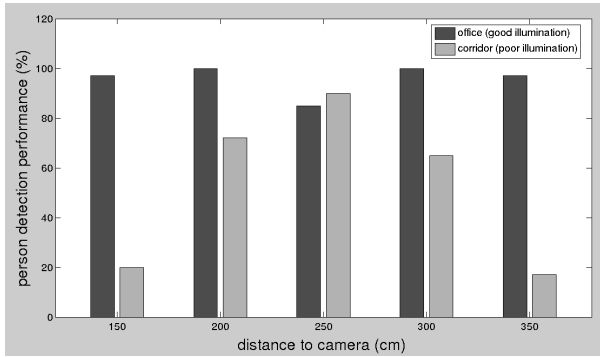
Fig. 4. Detection performance for people at different distances in two environments. Dark bars show performance in a well lighted room. Light bars show performance in a poor lighted corridor.

4.2   GMM Classifier

The second experiment is oriented to illustrate the robustness of the face classifier independently of problems in the initial stereo based segmentation. Therefore the setting of this experiment is similar to the previous one, but it only considers the frames where the stereo algorithm manages to segment the people correctly and at least one face candidate appears inside any of the blobs.

The test data consists of 200 frames with 1 of 5 people appearing in each. This corresponds to 10 frames for each people, acquired at 4 different distances. For this experiment, we consider distances from 150 to 300 cms and the results are shown in figure 5. It can be seen that a good performance (over 90%) is achieved, except for people at 300 cms in the office location. This is due to a moderate amount of false positives (12%). The result shows the robustness of the color based face detector to changes in illumination.

4.3   Real Video

To test our system mounted on a robot under real time operation, we run the system while the robot navigates in a indoor environment. The average robot velocity is around 0.5m/s and the system frame rate is around 2.5 fps. Figure 6 shows a map of the environment and the trajectory followed by the robot.

During its trajectory, the robot encounters 15 people. Table 2 summarizes the test results. One person was not detected because during several consecutive frames appeared standing at a distance that exceeds the detection range of the system. Once this person walked towards the robot, the poor frame rate made the system not to capture an image of this person. The two false positives are due to the arm of a person close to a wooden furniture and with clothes with a similar color to skin.
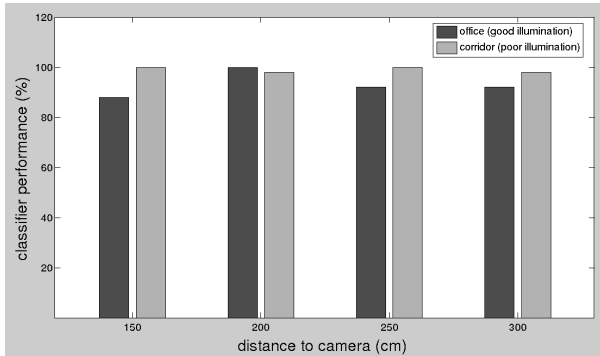
Fig. 5. Classifier performance for skin blobs of people located at different distances in two environments. Dark bars show performance in a well lighted room. Light bars show performance in a poor lighted corridor.
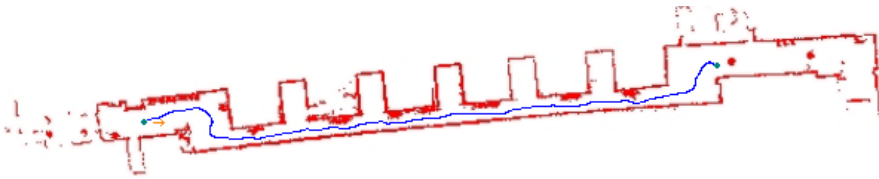
Fig. 6. Robot trajectory in our office environment. The map was obtained with our robot.

Table 2. System performance in the real video test. In the test, the robot meet 15 people.

People Correctly Detected	14
Missed People	1
False Positives	2

5   Conclusions

We have presented a person detection system mounted a moving platform, that is able to operate in real time in indoor buildings. Promising results have been obtained for this system with performance over 90%. The inclusion of a robust skin pixel criteria and an illumination-invariant set of color features are also important contributions of this work.

The results indicate that the stereo vision based segmentation process is vulnerable to changes in illumination conditions and distance from the camera. The color based face segmentation process presents a better result respect to changes in illumination and some vulnerability respect to distance. In the case of our application distance to the camera is not a relevant issue because we have a mobile

platform, however, we still need to further explore the illumination problems of the stereo system.

As future area of research, we can mention: the addition of a pan-tilt mechanism to add target tracking capabilities, the inclusion of probabilistic priors to improve the classification results, and finally, the need to increase the processing frame rate of our system to be able to deal with more crowded scenarios.

Acknowledgments

References

1. Baggenstoss, P.M.: Statistical modeling using gaussian mixtures and HMMs with MATLAB. Naval Undersea Warfare Center, Newport, RI (2002), http://www.npt.nuwc.navy.mil/Csf/htmldoc/pdf
2. Castleman, K.R.: Digital image processing. Prentice-Hall, Englewood Cliffs (1996)
3. Dalal, N., Triggs, B.: Histograms of oriented gradients for human detection. In: IEEE Computer Society Conference on Computer Vision and Pattern Recognition, pp. 886–893. IEEE Computer Society Press, Los Alamitos (2005)
4. Darrell, T., Gordon, G., Harville, M., Woodfill, J.: Integrated person tracking using stereo, color, and pattern detection. In: Proceedings of the IEEE Computer Society Conference on Computer Vision and Pattern Recognition, pp. 601–608. IEEE Computer Society Press, Los Alamitos (1998)
5. Flusser, J., Suk, T.: Pattern recognition by affine moment invariants. Pattern Recognition 26(1), 167–174 (1993)
6. Fong, T., Nourbakhsh, I., Dautenhahn, K.: A survey of socially interactive robots. Robotics and Autonomous Systems, Special issue on Socially Interactive Robots 42(3-4), 143–166 (2003)
7. Hu, M.K.: Visual pattern recognition by moment invariants. IRE Trans. Info. Theory IT(8), 179–187 (1962)
8. Konolige, K.: Small vision system: Hardware and implementation. In: Eighth Symposium on Robotics Research, pp. 111–116 (1997)
9. Ogale, N.A.: A survey of techniques for human detection from video. Master's thesis, University of Maryland (May 2006)
10. Sidenbladh, H.: Detecting human motion with support vector machines. In: ICPR 2004, vol. 2, pp. 188–191 (2004)
11. Utsumi, A., Tetsutani, N.: Human detection using geometrical pixel value structures. In: Proceedings of the Fifth IEEE International Conference on Automatic Face and Gesture Recognition, p. 39. IEEE Computer Society Press, Los Alamitos (2002)
12. Viola, P., Jones, M.J., Snow, D.: Detecting pedestrians using patterns of motion and appearance. In: Proceedings of the Ninth IEEE International Conference on Computer Vision, pp. 734–741. IEEE Computer Society Press, Los Alamitos (2003)

A Method for Estimating Authentication Performance over Time, with Applications to Face Biometrics

Norman Poh, Josef Kittler, Ray Smith, and J. Rafael Tena

CVSSP, University of Surrey, Guildford, GU2 7XH, Surrey, UK
{norman.poh,j.kittler,r.s.smith,j.tena}@surrey.ac.uk

Abstract. Underlying biometrics are biological tissues that evolve over time. Hence, biometric authentication (and recognition in general) is a *dynamic* pattern recognition problem. We propose a novel method to track this change for each user, as well as over the whole population of users, given only the system match scores. Estimating this change is challenging because of the paucity of the data, especially the genuine user scores. We overcome this problem by imposing the constraints that the user-specific class-conditional scores take on a particular distribution (Gaussian in our case) and that it is continuous in time. As a result, we can estimate the performance to an arbitrary time precision. Our method compares favorably with the conventional empirically based approach which utilizes a sliding window, and as a result suffers from the dilemma between precision in performance and the time resolution, i.e., higher performance precision entails lower time resolution and vice-versa. Our findings applied to 3D face verification suggest that the overall system performance, i.e., over the whole population of observed users, improves with use initially but then gradually degrades over time. However, the performance of individual users varies dramatically. Indeed, a minority of users actually improve in performance over time. While performance trend is dependent on both the template and the person, our findings on 3D face verification suggest that the person dependency is a much stronger component. This suggests that strategies to reduce performance degradation, e.g., updating a biometric template/model, should be person-dependent.

Keywords: Biometric authentication, performance assessment, face recognition.

1 Introduction

In general, pattern recognition can be categorized as either static or dynamic [1]. A static pattern does not tend to change dramatically over time whereas a dynamic one does. The latter is problematic because as the variability of dynamic patterns in the same class becomes gradually larger, a classifier that does not update itself will have tremendous difficulty when discriminating between dynamic patterns belonging to different classes.

Biometrics can be considered as a dynamic pattern principally because underlying the metrics are living tissues that tend to modify themselves either as a result of muscle movements or tissue growth (aging). In the former case, the change can take place in seconds whereas in the latter case, the change can be gradual. Apart from this change, variation in patterns can also be caused by an imperfect biometric acquisition process, e.g., in the way a biometric sample is presented and the environmental conditions. These
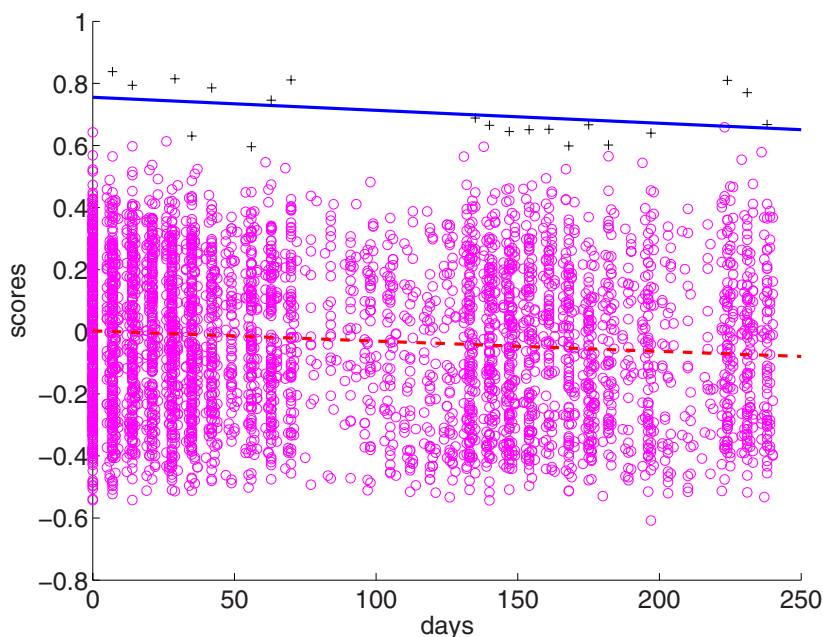
Fig. 1. Scatter plot of genuine user ("+") and impostor ("○") match scores for a single user's template over 250 days (the X-axis). Higher match scores imply genuine user class. The interruption in genuine match scores around the 100-th day is due to no observations being made during the term break. The straight lines are the regression fits on the data (continuous line for the genuine user match scores and dashed line for the impostor ones).

factors cannot often be decoupled but their effects can readily be observed from the resulting match scores.

To give a further motivation, we plotted the class-conditional match scores in Figure 1 of a user selected at random from a face verification system applied to the Face Recognition Grand Challenge (FRGC) database. This database contains images collected over 250 days. Two clusters of scores are available, namely genuine user match scores and impostor match scores. The genuine user match scores are the results of comparing a reference template with query images of the same user. The impostor match scores are the results of comparing the reference template with query images of other users. In this figure, one can observe that genuine user scores are very sparse whereas the impostor match scores, as a result of comparing a sequence of query images from many persons, are very dense.

The ability to track the dynamic change of biometric patterns in terms of performance is valuable because it can determine whether or not a biometric system degrades over time. If it does then preventive measures will have to be taken to maintain the performance. One of the pilot studies in this direction is reported in [2], whereby the performance of four face recognition systems coupled with two face detection algorithms (hence altogether eight systems) were assessed on the FRGC database. This

database contains 250 users whose images were captured over a period of two years. It was observed that all the face identification systems decrease in performance (in terms of rank-1 false rejection) with time-lapse. However, time-lapse is not the only factor; in [2], it was noted that the precision of eye localization is another important factor.

This paper differs significantly from [2] because our concern is with the individual user performance. According to [3], the users in a database can exhibit very different performance. In particular, some users are more easily recognized than the others. As a result, it is reasonable to expect that the performance change will be different from one user to another. We argue that our approach is more useful because it can calculate the person-specific performance. This enables one to sort the users according to their current performance, thereby identifying the weak users in this process. If the performance of these users can be corrected, for instance, by updating the user model, one can potentially improve the overall system performance. Deciding when and how to update a biometric template/model will be investigated in the future.

This paper is organized as follows: Section 2 explains how the user-dependent error over time can be calculated using the proposed procedure; Section 3 describes the database used; Section 4 shows the results and Section 5 presents the conclusions.

2   Modeling Performance over Time on a Per-person Basis

Suppose that each user j in a database has two sequences of scores over time: one from the genuine user set of scores and the other from its impostor counterpart. We denote the two sequences by $\mathbf{y}_j^k = [y_{j,1}^k, \ldots y_{j,N}^k]'$ for genuine user and impostor classes, $k = \{G, I\}$, respectively, and each sequence has N_k number of scores. For clarity, we drop the user index j everywhere. In this study, the impostor scores with respect to the reference user are generated by the rest of the users exhaustively. Therefore, the constraint $N_G \ll N_I$ is true in this case. Note that each sequence of scores has a corresponding time delay sequence $\mathbf{d}_j^k = [d_{j,1}^k, \ldots d_{j,N}^k]'$ or simply $\mathbf{d}^k$ (omitting j).

For the genuine user scores, this time delay sequence is just the time difference between the template and the query image associated with the respective score. Suppose that these images have the following time stamps: $t_0, t_1, \ldots, t_N$. We reserve the first image with time t_0 as a template. This template is then compared to the remaining images in the sequence. The resulting genuine match scores will have the following *relative* time stamps: $\mathbf{d}^G \equiv [d_1^G, d_2^G, \ldots, d_N^G]' \equiv [t_1 - t_0, t_2 - t_0, \ldots, t_N - t_0]'$.

For the impostor sequence, this time delay sequence is with respect to the *relative time difference* between the first impostor attempt and the subsequent impostor attempts by the same impostor. Suppose the image sequence of an impostor has the following time stamps: $t_1, t_2, \ldots t_N$. We define its relative time sequence by $\mathbf{d}^I \equiv [d_1^I, \ldots, d_N^I]' \equiv [t_1 - t_1, t_2 - t_1, \ldots t_N - t_1]'$, i.e., taking the difference between the time stamp of an image in the sequence with the first one. Note that the first element in this list has a time stamp of 0. By so doing, we assume that the time difference between the first impostor attempt and the template has no importance. This is a reasonable assumption given the fact that the two feature sets under impostor matching are not from the same persons.

The goal is to estimate the performance in terms of False Match Rate (FMR) and False Non-Match Rate (FNMR)[1] at a given time d_t for $t = 0, 1, \ldots$ and for each user to an arbitrary precision. This implies that FMR and FNMR are themselves *smooth* functions over time. This is clearly a difficult task since the conditional sequence $\mathbf{y}^k$ has very few data points, especially for the genuine user sequence.

For each sequence k, let us fit a regression function to $(\mathbf{d}^k, \mathbf{y}^k)$. Regression functions are also called smoothers because they give in general a smoothed output of $\mathbf{y}^k$. Some examples are kernel, running mean, running-line, locally weighted running-line, running spline and regression spline smoothers [4, Chap. 3]. We will use a polynomial regression model of order D for this purpose so that we obtain the regression parameter $\mathbf{p} = [p_D, \ldots, p_0]'$. By evaluating the parameter $\mathbf{p}$, we obtain a smoothed conditional score $\mu_t^k = p_0 + p_1 d_t + \ldots + p_D d_t^D$ at time d_t along with standard deviation σ_t^k. By tracing (d_t, μ_t^k) for $t = 0, 1, \ldots$, one obtains a smoothed curve with 95% confidence bound $(d_t, \mu_t^k \pm 2\sigma_t^k)$ for each $k \in \{G, I\}$. In summary, for a given instance of time d_t, we have the parameters $\{\mu_{j,t}^k, \sigma_{j,t}^k\}$ for each class k and for each user j (note that the index j is reintroduced here).

If the conditional regression fit is adequate, then the error residual should be approximately normally distributed. Unfortunately, given a limited number of data points of size N_k, especially for the genuine user sequence, in practice, one has no way of assessing whether the fit is adequate or not. This can be determined subjectively (visually). Another way to proceed is to use a polynomial model with a low degree of freedom D, based on the fact that we have few data points. The consequence is that the fit will lead to a large bias but a low variance. A more in-depth discussion of the bias-variance trade-off in regression can be found in [4, Chap. 3].

Once the regression parameters are found, we can then model instantaneous FMR and FNMR by:

$$\text{FMR}_{j,t}(\Delta) = \Phi\big(\Delta | \mu_{j,t}^I, (\sigma_{j,t}^I)^2\big) \tag{1}$$

and

$$\text{FNMR}_{j,t}(\Delta) = 1 - \Phi\big(\Delta | \mu_{j,t}^G, (\sigma_{j,t}^G)^2\big) \tag{2}$$

for a given threshold Δ in the score space, where $\Phi\big(\Delta | \mu, (\sigma)^2\big)$ is a cumulative normal density function with mean μ and standard deviation σ. Under such condition, a result from [5] shows that at Equal Error Rate (EER), i.e., FMR=FNMR, the user-specific EER is:

$$\text{EER}_{j,t} = \frac{1}{2} - \frac{1}{2}\text{erf}\left(\frac{\text{F-ratio}_j}{\sqrt{2}}\right), \tag{3}$$

where

$$\text{F-ratio}_j = \frac{\mu_{j,t}^G - \mu_{j,t}^I}{\sigma_{j,t}^G + \sigma_{j,t}^I}, \tag{4}$$

and

$$\text{erf}(z) = \frac{2}{\sqrt{\pi}} \int_0^z \exp\left[-x^2\right] dx. \tag{5}$$

---

[1] Also called False Acceptance Rate and False Rejection Rate, respectively when evaluating the overall system performance, as opposed to algorithmic-level performance.

The end results are sequences of user-specific FMR and FNMR over the desired time period d_t estimated to an arbitrary accuracy.

The next issue to be dealt with is to calculate the population performance given the parameters $\{\mu_{j,t}^k, \sigma_{j,t}^k\}$ for each class $k = \{G, I\}$ and *all* the users $j = 1, \ldots, J$ at the desired time d_t. In order to calculate this quantity, we first need to calculate the class-conditional score distributions of the population. From the Gaussian assumption, the user-specific version of this distribution (for a given user j) is $\mathcal{N}(\mu_{j,t}^k, (\sigma_{j,t}^k)^2)$. The population's conditional score distribution must be then a mixture of user-specific score distributions weighted by their respective prior probabilities, i.e., $\sum_{j=1}^{J} \mathcal{N}(\mu_{j,t}^k, (\sigma_{j,t}^k)^2)$ $p(j|k)$. Therefore, the population's FMR is

$$\mathrm{FMR}_t(y) = \sum_{j=1}^{J} \Phi\big(y|\mu_{j,t}^I, (\sigma_{j,t}^I)^2\big) P(j|I). \tag{6}$$

Similarly, the population's FNMR is:

$$\mathrm{FNMR}_t(y) = 1 - \sum_{j=1}^{J} \Phi\big(y|\mu_{j,t}^G, (\sigma_{j,t}^G)^2\big) P(j|G). \tag{7}$$

The population's EER point, i.e., $\mathrm{FMR}_t(y) = \mathrm{FNMR}_t(y)$ can be found numerically.

The section that follows will discuss the database used before applying the proposed procedure on the real data.

3   Experimental Approach

The publicly available FRGC Experiment 3 data [6] is divided into two parts, training and test sets. Each part contains a set of 3D scans together with the corresponding 2D color intensity images. Additionally the 3D coordinates of landmark points located at the eye corners, the tip of the nose and the tip of the chin are also provided for each scan. The data was captured in near frontal pose using a Minolta Vivid 900 range scanner at a resolution of 640×480 and it includes males and females in approximately equal numbers, covering a range of ages and ethnic backgrounds. The training set consists of 943 face scans and images of 270 different subjects, with the number of samples per subject varying from 1 to 8. 410 subjects were included in the test set; with the number of samples per subject ranging from 1 to 22 for a total of 4007 scans and images. It is worth mentioning that 31 samples of the training set were discarded for our experiments, because the provided landmarks were off their mark by more than 50mm.

For the purpose of these experiments we use all of the training data to train face matching algorithms. To study the effects of changes over time we choose a subset of 285 users from the test data such that each one has a sequence of more than 6 accesses within the observed 250 days. Instead of just using the first image as template, we also used the second and third images as templates. When the second image is used for this purpose, the first image is not used to construct the genuine user sequence of

match scores. This makes sense because one cannot compare a template with a sample acquired *before* the template is constructed.

Three sets of face verification experiments are described in this study. These are the PCA baseline system [6] supplied by FRGC (3D-baseline), 3D face verification with an error-correcting output-code based matcher (3D-ECOC) and 2D face verification with a local binary pattern based matcher (2D-LBP).

The 3D-ECOC method follows that described in [7]. Angular linear discriminant analysis is used to establish a low-dimensional feature space in which individuals are reasonably well separated. An error-correcting output code ensemble of Gaussian SVM classifiers is then trained within this feature space and the outputs from this ensemble are used to define a new feature space in which separation is further improved. A final similarity measure between pairs of 3D scans is obtained based on the Manhattan distance in this second feature space.

For the 2D-LBP matcher each face image is subdivided into a 7×6 grid of rectangular non-overlapping regions and a local binary pattern histogram [8] computed for each region. A similarity measure between pairs of images is then computed based on the mean Manhattan difference between corresponding histograms.

The 3D verification experiments require accurate registration and this is performed using the method of dense correspondence with a 3D model as described in [9].

4   Performance Trend Analysis

We first examined if the user-specific performance is template dependent or not. For this purpose, we selected a user at random from the 2D-LBP experiment. Using the first three images in the time-stamped sequence as templates, we plotted the fitted regression function with time being the input (independent) variable and score being the output (dependent) variable (see Figure 2). Their corresponding EERs are also shown at the bottom of each sub-figure. As can be observed, the user-specific performance is template dependent.

We then proceeded to compare the EER trends of different persons but used the first image as a template for all users. The purpose is to examine if the user-specific performance is person dependent or not. The results are shown in Figure 3. As can be observed, different users can exhibit dramatically different EER trend even though the same verification system is used. While most users decrease in performance, there are users who actually improve in performance over time. In any case, the user-specific performance is unlikely to be constant. This experimental result supports our conjecture that biometric authentication (and recognition in general) is a *dynamic* pattern recognition problem. Furthermore, the user-specific performance is both person *and* template dependent. Between the two, the choice of template seems to play a less important part in determining the trend.

Lastly, we plotted the system performance, using DET curves, over the whole population of users for the three different templates used. The results are shown in Figure 4. A DET curve [10] is a plot of false rejection rate (FRR) or FNMR versus false acceptance rate (FAR) or FMR. As can be observed, the DET curve also changes over time. In particular, when we analyzed the EER point in Figure 4(d), we observe that there is a
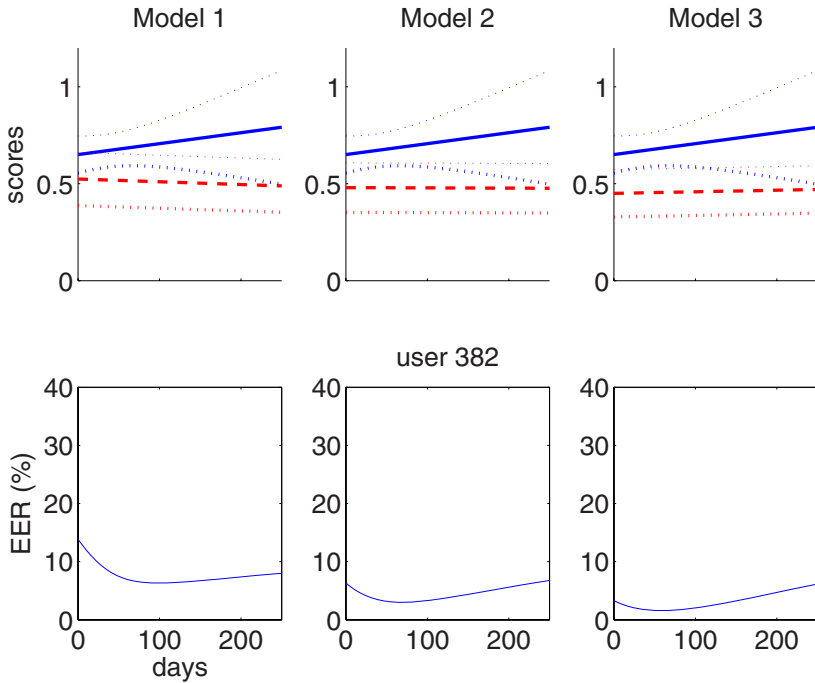
Fig. 2. The evolution of scores as estimated by regression (in the top row of figures) and their corresponding EER trend (bottom row) when using the first (column one), second (column two), third (column three) images according to the time-stamped sequence of a given user. The system used here is the 2D-LBP system. In the top figures, thick continuous lines are the expected trends of the genuine user match scores over time and thick dashed lines are that of the impostor match scores. Around these lines are their corresponding $\pm$ two standard deviations (shown in dotted lines).

general decrease in error rates over time before increasing again. It can be argued that, in general, biometric users become more acquainted with the system. As a result, the system performance may increase with use. However, because biometrics may change over time, the query images may gradually differ from the reference template. As a result, the system may degrade in performance. The system-level performance can be regarded as the *average performance* across users and so the above explanation cannot be readily observed from the set of individual user performance.

5   Conclusions

In this paper, we proposed a method to estimate user-specific performance. This is a difficult problem mainly due to the paucity of the genuine score samples. The availability of scores in time depends very much on how regular a biometric system is used. In the FRGC database, the most frequent interval is 7 days, followed by 14 days. By using an empirical error estimation approach, it is thus possible to estimate the error rate on a
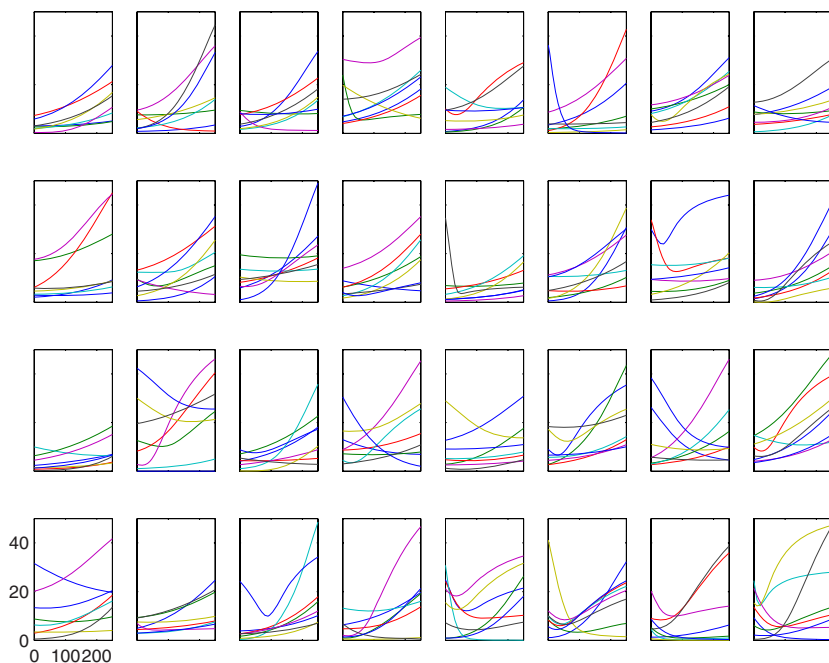
Fig. 3. The EER trend of all 256 users. Each of the 4×8 figures shows the trend of 8 users. The X-axis shows the number of days in $[0, 250]$ and the Y-axis is EER (%) in $[0, 50]$.

per day basis. By imposing the constraints that the user-specific class-conditional score sequence is continuous in time and that it takes on a particular distribution (Gaussian in our case), we demonstrated that our method can estimate the error rate on a per day basis. While the use of Gaussian assumption can be appropriate in our case, we do not claim that this is, in general, the case. The methodology, however, should be equally applicable on other data sets with a sensible choice of distribution.

Our experiments highlight the importance of user-specific performance analysis. This may open up a new research avenue towards customized biometric verification system, i.e., a system that is designed to adapt to the individual characteristic of a user. The proposed method can serve as an evaluation tool for this purpose. Customized biometric system is fascinating because learning with user-specific samples is a difficult task due to the small training sample size.

To the best of our knowledge, our study may be the first attempt to uncover person-dependent performance in a more principled way.

Our experiments show that the impostor score sequence does not need to evolve with time due to the aggregate effect of considering multiple impostor score sequences from a pool of impostors. As a result, modeling the genuine user sequence is of critical importance. Although a polynomial regression was used in this study, it may be logical to replace it with one that does not assume equal variance over the entire score sequence. Another obvious improvement is to replace the Gaussian assumption with a more realistic one.

(a) DET: model 1

(b) DET: model 2

(c) DET: model 3

(d) EER trends: all three models
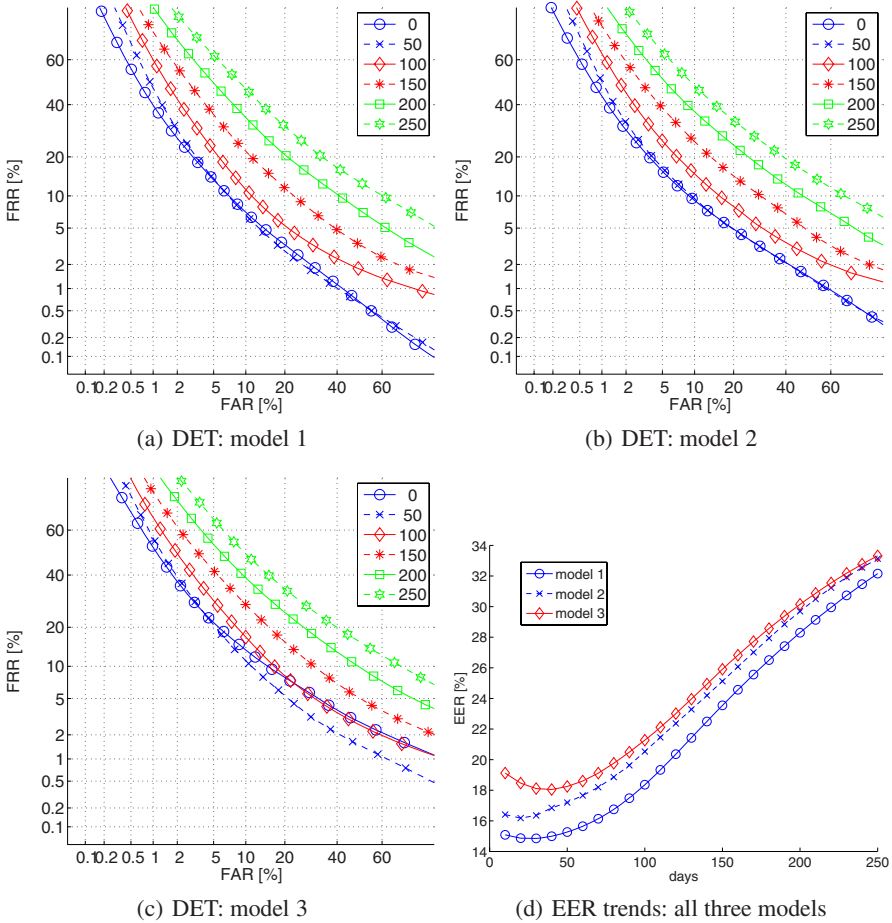
Fig. 4. The evolution of the entire DET curve over the population of users (285 in total) on a 50-day interval given that the (a) first, (b) second and (c) third images in the time-stamped sequence are used as templates. Figure (d) shows the EER trend of the three models over 250 days. The system used here is the 3D-baseline system. The other two systems give similar trends, although their absolute performance differs slightly.

Acknowledgments

References

1. Chen, K.: On the Dynamic Pattern Analysis, Discovery and Recognition, IEEE SMC Society eNewsletter (September 2005)
2. Flynn, P.J., Bowyer, K.W., Phillips, P.J.: Assessment of Time Dependency in Face Recognition: An Initial Study. In: Kittler, J., Nixon, M.S. (eds.) AVBPA 2003. LNCS, vol. 2688, pp. 44–51. Springer, Heidelberg (2003)
3. Doddington, G., Liggett, W., Martin, A., Przybocki, M., Reynolds, D.: Sheep, Goats, Lambs and Woves: A Statistical Analysis of Speaker Performance in the NIST 1998 Speaker Recognition Evaluation. In: ICSLP, Sydney (1998)
4. Hastie, T.J., Tibshirani, R.J.: Generalized Additive Models. Chapman and hall (1990)
5. Poh, N., Bengio, S.: Why Do Multi-Stream, Multi-Band and Multi-Modal Approaches Work on Biometric User Authentication Tasks? In: ICASSP, Montreal, vol. V, pp. 893–896 (2004)
6. Phillips, P.J., Flynn, P.J., Scruggs, T., Bowyer, K.W., Chang, J., Hoffman, K., Marques, J., Min, J., Worek, W.: Overview of the Face Recognition Grand Challenge. In: IEEE Computer Society Conference on Computer Vision and Pattern Recognition, pp. 947–954 (2005)
7. Smith, R.S., Kittler, J., Hamouz, M., Illingworth, J.: Face Recognition Using Angular LDA and SVM Ensembles. In: Proc. 18th Int'l. Conf. on Pattern Recognition, pp. 1008–1012 (2006)
8. Ahonen, T., Hadid, A., Pietikainen, M.: Face Recognition with Local Binary Patterns. In: Proc. European Conference on Computer Vision, Prague, pp. 469–481 (2004)
9. Tena, J.R., Hamouz, M., Hilton, A., Illingworth, J.: A Validated Method for Dense Non-Rigid 3D Face Registration. In: AVSS 2006, p. 81 (November 2006)
10. Martin, A., Doddington, G., Kamm, T., Ordowsk, M., Przybocki, M.: The DET Curve in Assessment of Detection Task Performance. In: Eurospeech 1997, Rhodes, pp. 1895–1898 (1997)

Generalizing Dissimilarity Representations Using Feature Lines

Mauricio Orozco-Alzate[1,2], Robert P.W. Duin[1],
and César Germán Castellanos-Domínguez[2]

[1] Information and Communication Theory Group, Faculty of Electrical Engineering,
Mathematics and Computer Science, Delft University of Technology, P.O. Box 5031,
2600GA Delft, The Netherlands
{m.orozcoalzate,r.p.w.duin}@tudelft.nl
[2] Grupo de Control y Procesamiento Digital de Señales, Universidad Nacional de
Colombia Sede Manizales, Carrera 27 # 64-60, Manizales (Caldas), Colombia
{morozcoa,cgcastellanosd}@unal.edu.co

Abstract. A crucial issue in dissimilarity-based classification is the
choice of the representation set. In the small sample case, classifiers ca-
pable of a good generalization and the injection or addition of extra
information allow to overcome the representational limitations. In this
paper, we present a new approach for enriching dissimilarity representa-
tions. It is based on the concept of feature lines and consists in deriving
a generalized version of the original dissimilarity representation by using
feature lines as prototypes. We use a linear normal density-based classi-
fier and the nearest neighbor rule, as well as two different methods for
selecting prototypes: random choice and a length-based selection of the
feature lines. An important observation is that just a few long feature
lines are needed to obtain a significant improvement in performance over
the other representation sets and classifiers. In general, the experiments
show that this alternative representation is especially profitable for some
correlated datasets.

Keywords: Dissimilarity, representation, feature lines, generalization.

1 Introduction

The nearest neighbor method (k-NN) [1] is a simple and asymptotically well-
behaved classifier, which classifies an object x by assigning it the class label[1]
$\hat{c}$ most frequently represented among the k nearest training objects. In a con-
ventional feature space representation, x is represented as a feature point $\boldsymbol{x}$.
Consider a training set $T = \{\boldsymbol{x}_i^c, 1 \leq c \leq C, 1 \leq i \leq n_c\}$, where C is the number

---

[1] In order to simplify the notation, ours differs from the usual way to denote the set
of class labels, i.e. $\Omega = \{\omega_1, \dots, \omega_c\}$. In this paper, we denote the membership or
association to one of the C classes by using the letter c as a variable running from
1 to C. Besides, when a particular value of c is used as a subscript, it is written
between round brackets.

of classes and n_c the number of objects per class. For $k = 1$, the rule can be written as follows:

$$d(\boldsymbol{x}, \boldsymbol{x}_i^{\hat{c}}) = \min_{1 \leq c \leq C, \ 1 \leq i \leq n} d(\boldsymbol{x}, \boldsymbol{x}_i^c), \tag{1}$$

where $d(\boldsymbol{x}, \boldsymbol{x}_i^c) = \|\boldsymbol{x} - \boldsymbol{x}_i^c\|$ is usually the (weighted) Euclidean or the city block norm. Using the entire training set implies $N = \sum_{c=1}^{C} n_c$ distance calculations; as a result, considerable space requirements to store T and a high computational effort for the evaluation of new objects might be required. A straightforward solution to this drawback is selecting a representation set R, which is chosen to be a subset of T ($R \subseteq T$) or even a distinct set having a cardinality n lower than that of T.

More generally, d might be a dissimilarity measure, metric or not, computed or derived from the objects directly, their sensor representations, or some initial representation [2]; in other words, if a companion feature representation is not necessarily involved, $d(x, p_i)$ denotes a dissimilarity measure between an object and one of the representative objects (prototypes) from R. Those measures, arranged as a vector $D(x, R) = [d(x, p_1), d(x, p_2), \ldots, d(x, p_n)]$, constitute a *dissimilarity representation* of x. For the training set T, it extends to an $N \times n$ dissimilarity matrix $D(T, R)$ and a set S of new objects is provided in terms of their distances to R, i.e. as a matrix $D(S, R)$. Analogously to (1), the 1-NN rule in the dissimilarity representation assigns a new object to the class of its nearest neighbor from R by finding the minimum in the rows of $D(S, R)$.

In addition to the storage and computational disadvantages, the NN rule suffers from other limitations, e.g. sensitivity to noise and potential loss of accuracy when a limited number of prototypes is available or when their representational capacity is not enough to cover the possible variations of data. A number of strategies have been proposed to handle such situations, e.g., modifying the rule [3,4,5], adapting the distance measure [6,7,8,9], expanding the representational capacity of the available feature points [10,11] and building Bayesian classifiers on the dissimilarity representations [12,13]. Combining some of those strategies, taking advantage of their individual properties, may be effective. In particular, we will study the use of the nearest feature line method [10] for generalizing dissimilarity representations and constructing Bayesian classifiers in such a generalized dissimilarity space. The generalization procedure is intended for small sample cases. Its basic rationale is that to enhance the representation using feature lines and to achieve a better generalization, building a Bayesian classifier in the enhanced representation, may improve the performance of both techniques when they are used separately. Our experiments show that the proposed procedure is specially profitable for correlated (cigar-like or elongated) datasets.

The remainder of this paper is organized as follows. Section 2 describes the proposed procedure for generalizing dissimilarity representations. Experiments and results on artificial and real data sets are described in Section 3. Section 4 presents the conclusions and discusses some possibilities for future work.

2   Generalization Procedure

The procedure consists in creating the generalized dissimilarity representation $D_L(T, R_L)$, where L denotes that the representation set is composed by feature lines. In the original dissimilarity space approach, one considers a data-depending mapping $D(x, R) : \mathcal{X} \times \mathcal{X} \to \mathbb{R}^n$ to the so-called *dissimilarity space*, where each dimension corresponds to a dissimilarity $D(\cdot, p_i)$ to a particular object $p_i \in R$. Analogously, for a generalized dissimilarity space, the considered mapping is $D(x, R_L) : \mathcal{X} \times \mathcal{X}_L \to \mathbb{R}^n$. As a result, a *generalized dissimilarity representation* of x corresponds to the vector $D(x, R_L) = [d(x, L_1), d(x, L_2), \ldots, d(x, L_n)]$. In this section we review the nearest feature line method as it was originally proposed for feature space representations. After that, we describe how to build a generalized dissimilarity representation using only the information available at $D(T, R)$; that is, without recurring to an associated feature representation. Indeed, feature vectors might be not available, e.g. when dissimilarities are directly derived from the objects.

2.1   Feature Lines

The *Nearest Feature Line* rule, or *NFL* [10], is an extension of the NN rule. It generalizes each pair of prototype feature points belonging to the same class: $\{\boldsymbol{x}_i^c, \boldsymbol{x}_j^c\}$ by a linear function L_{ij}^c, which is called the *feature line*. The line L_{ij}^c is expressed by the span $L_{ij}^c = \mathrm{sp}(\boldsymbol{x}_i^c, \boldsymbol{x}_j^c)$. The query $\boldsymbol{x}$ is projected onto L_{ij}^c as a point $\boldsymbol{p}_{ij}^c$ (see Fig. 1). This projection can be computed as

$$\boldsymbol{p}_{ij}^c = \boldsymbol{x}_i^c + \tau(\boldsymbol{x}_j^c - \boldsymbol{x}_i^c), \tag{2}$$

where $\tau = (\boldsymbol{x} - \boldsymbol{x}_i^c) \cdot (\boldsymbol{x}_j^c - \boldsymbol{x}_i^c) / \|\boldsymbol{x}_j^c - \boldsymbol{x}_i^c\|^2 \in \mathbb{R}$; τ is called the *position parameter*. The classification of $\boldsymbol{x}$ is done by assigning it the class label $\hat{c}$ most frequently
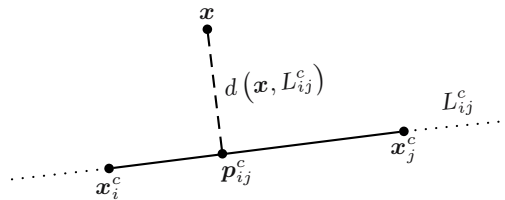
Fig. 1. Feature line L_{ij}^c and computation of the distance to it

represented among the k nearest feature lines; for $k = 1$ that means:

$$d(\boldsymbol{x}, L_{ij}^{\hat{c}}) = \min_{\substack{1 \leq c \leq C, \ 1 \leq i,j \leq n \\ i \neq j}} d(\boldsymbol{x}, L_{ij}^c) \tag{3}$$

where $d(\boldsymbol{x}, L_{ij}^c) = \|\boldsymbol{x} - \boldsymbol{p}_{ij}^c\|$.

2.2   Distances to Feature Lines in Terms of Dissimilarities

Given a dissimilarity matrix $D(T, R)$, deriving the distances to feature lines consists in computing the height h of a scalene triangle as shown in Fig. 2 . Note that d_{ij} must be an intraclass distance. In addition, since any metric triplet d_{ij}, d_{ik} and d_{jk} is Euclidean (i.e. it constitutes a Euclidean triangle), we restrict our experiments to metric distance matrices. Such a restriction does not imply a loss of generality because an embedding can be found to correct a non-metric D, e.g. through a pseudo-Euclidean embedding [14].
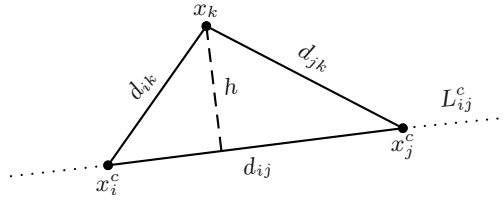
Fig. 2. Scalene triangle for computing the distance to a feature line in terms of dissimilarities

Let define $s = (d_{jk} + d_{ij} + d_{ik})/2$. Then, the area of the triangle is given by:

$$A = \sqrt{s(s - d_{jk})(s - d_{ij})(s - d_{ik})};$$ (4)

but we also know that area, assuming d_{ij} as base, is:

$$A = \frac{d_{ij} h}{2}$$ (5)

We can solve (4) and (5) for h, which is the distance to the feature line, i.e. $d(x_k, L_{ij}^c)$. The generalized dissimilarity representation for a particular object x_k is constructed by arranging all the $n_L = \sum_{c=1}^{C} n_c(n_c - 1)/2$ distances to the feature lines in a vector $D(x_k, R_L)$. As for the original dissimilarity representations, for a training set T it extends to a $N \times n_L$ dissimilarity matrix $D(T, R_L)$. In general, $D(T, R_L)$ is not square and has two zeros elements per column. The information on a set S of new incoming objects is provided in terms of their distances to R_L, i.e., as a generalized dissimilarity matrix $D(S, R_L)$.

2.3   Classification in Dissimilarity Spaces

As $D(\cdot, p_i)$, a dissimilarity $D(\cdot, L_i)$ to a particular feature line $L_i \in R_L$ can be interpreted as an attribute, allowing for building classifiers in such a space. Previous studies [12,13] showed that building Bayesian classifiers in dissimilarity spaces, e.g. a linear normal density based classifier, often outperforms the k-NN rule, especially for small representation sets or non-representative training sets. The use of normal density based classifiers in dissimilarity spaces is

suggested because the summation-based distances are often approximately normally distributed (in fact, a clipped normal distribution due to the nonnegativity of dissimilarities) [13]. There is no practical difference between constructing a classifier on generalized dissimilarities and to build it on non-generalized dissimilarities. Thereby, the classifier definition is the same either the representation is generalized or not. For a two-class problem, a linear decision function (BayesNL) based on the representation set R is given by (The same applies for R_L)

$$
\begin{aligned}
f(D(x,R)) = &\left[D(x,R) - \frac{1}{2} \left(\boldsymbol{m}_{(1)} + \boldsymbol{m}_{(2)} \right) \right]^T \\
&\times \boldsymbol{C}^{-1} \left(\boldsymbol{m}_{(1)} - \boldsymbol{m}_{(2)} \right) + \log \frac{P_{(1)}}{P_{(2)}},
\end{aligned}
\tag{6}
$$

where $\boldsymbol{C}$ is the sample covariance matrix, $\boldsymbol{m}_{(1)}$ and $\boldsymbol{m}_{(2)}$ are the mean vectors, $P_{(1)}$ and $P_{(2)}$ are the class prior probabilities. When $\boldsymbol{C}$ becomes singular, it is regularized by using for example the following strategy [15]: $\boldsymbol{C}^{\lambda}_{reg} = (1 - \lambda)\,\boldsymbol{C} + \lambda\mathrm{diag}(\boldsymbol{C})$. In practice, λ equals 0.01 or less [2]. We keep it fixed to 0.01 in our experiments.

3   Experiments and Results

We test the application of the generalization method on several artificial and real-world datasets. Two selection procedures, random and length-based, are used for selecting prototype feature lines. Due to space constraints and in order to illustrate when the generalization is advantageous, we only present results for some datasets which were found to be benefited by the generalization. In other words, we are not claiming that our strategy gives an overall best solution, but the results do show that there exist problems for which the proposed method is beneficial. The presented results correspond to the following artificial and real-world problems:

Difficult normally distributed classes. It corresponds to a two-dimensional and two-class dataset having very different class variances for the dimensions (see `gendatd` function in [15]). Separation is thereby, for small sample sizes, difficult.

Highleyman classes. A two-dimensional and two-class dataset generated by the Highleyman distribution [16] (see also `gendath` function in [15]).

Wine data. The *Wine* data come from Machine Learning Repositary [17] and describe three types of wine by 13 features.

Laryngeal data. The *Laryngeal* dataset comes from the Bulgarian Academy of Sciences and is available at [18]. The set was originally used for a computer decision support system, in order to aid diagnosis of laryngeal pathology and especially in detecting its early stages. Normal and pathological voices are described by 16 parameters in the time, spectral and cepstral domains.

In all the experiments, a Euclidean distance was chosen for the original dissimilarity representations. The reported results are based on 25 repetitions; however, in order to maintain the clarity of the plots, we do not present the resulting standard deviations. In general, we found that they vary between 2% and 6% of the averaged errors. Implementations are done using PRTools [15].

Figs. 3 and 4 show the classification errors of the 1-NN and BayesNL classifiers applied to the generalized dissimilarity representations, as a function of the number of prototype feature lines chosen by two length-based selection methods: ascending and descending orders. The initial representation set R_L for the ascending method is the shortest feature line, i.e. the shortest base of the triangles (see Fig. 2). Then, the second shortest feature line is added to R_L, followed by the third shortest one and so on. The reverse case corresponds to the selection in descending order. In brief, the first m reported errors (m left most values) in Figs. 3 and 4 correspond to classification using the m shortest/largest feature lines. At the end, when all the $\sum_{c=1}^{C} n_c(n_c - 1)/2$ feature lines are included, the length-ranked representation sets are flipped versions of each other. In these experiments, we use $n_c = 15$. In order to explore its influence, we performed additional experiments for $n_c = 10$ and $n_c = 20$; however, it was not observed a significant difference in the general behavior. The same figures[1] show the best results obtained by the 1-NN and the BayesNL rules in the original dissimilarity spaces. They are plotted as horizontal lines and constitute our reference. In both cases, the representation set R is chosen by random selection. In consequence, such best results do not necessarily correspond to the case of using the entire T for representation.

The BayesNL classifier based on the descending ranked R_L outperforms both the best results in the original dissimilarity space and the other studied alternatives in the generalized one. Comparing the two feature line selection criteria, it is noteworthy that few long feature lines are needed to yield a good result with the BayesNL classifier. This fact may be explained as follows: long feature lines, which are chosen at first by the descending order selection, provide continua across the main direction of data. Such continua, in the case of elongated datasets, resemble the principal axis of an hyperellipse. More generally, they can be interpreted as a piecewise description. In principle (in absence of outliers), the feature lines represent the data as a structural model, i.e. through a *generalization* of their geometric spread. In contrast, for small representation sets and the descending order, the 1-NN method is negatively affected. As claimed in [12] for non-generalized representations, a possible interpretation is that when R or R_L are small, they refer to the objects that differ much from each other, potentially including also outliers.

---

[1] Note that the 1-NN rule, directly applied to the dissimilarity representations $D(S, R)$ or $D(S, R_L)$, consists in looking for the minima in the rows of the matrices. Thereby, its application to those representations corresponds to the 1-NN and the NFL classifiers, respectively. In other words, we are not deriving a new distance representation from the vectors $D(x, R)$ or $D(x, R_L)$.
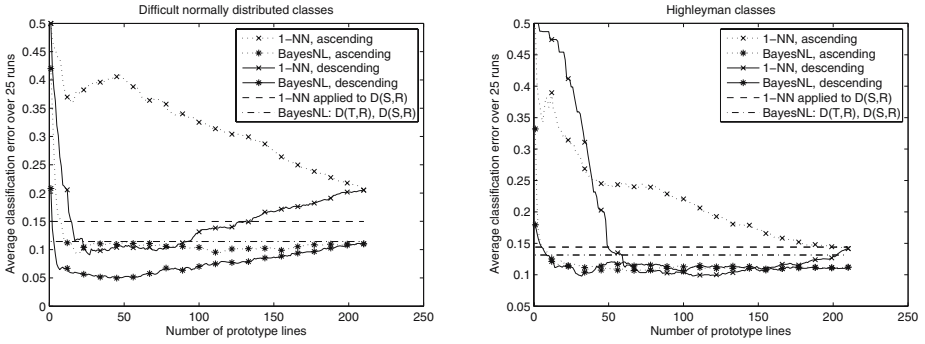
Fig. 3. Artificial data. Average classification errors of the BayesNL and 1-NN classifiers in the generalized dissimilarity space. Feature lines are incrementally included according to their length. Horizontal lines are the best results achieved in the original dissimilarity representations.
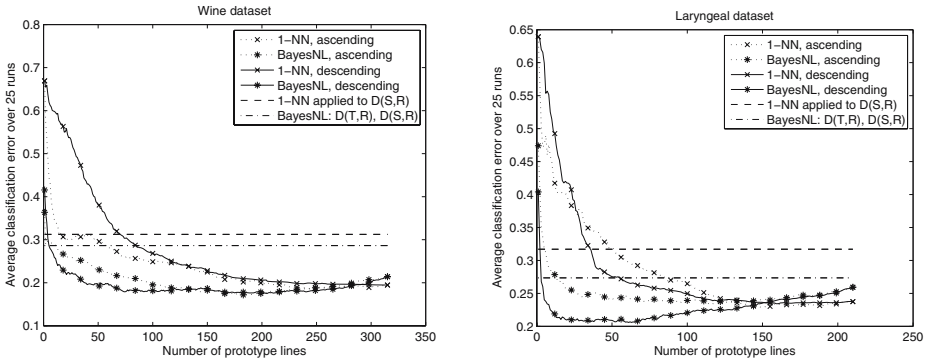
Fig. 4. Real-world data. Average classification errors of the BayesNL and 1-NN classifiers in the generalized dissimilarity space. Feature lines are incrementally included according to their length. Horizontal lines are the best results achieved in the original dissimilarity representations.

Figs. 5 and 6 show the results when the number of the selected prototypes, for both points and lines, is fixed to be a proportion of the cardinality of T: $n = n_L = n_c C/5$. For instance, for the Highleyman classes (two-class problem) and 12 training objects per class, the number of prototypes (points or lines) selected for representation is 5. Again and as expected, the BayesNL classifiers yield a better performance than the 1-NN rules based on the same representations sets either R or R_L.

As an additional criterion to evaluate the discriminative capacity of the generalized dissimilarity representations, we examine the Mahalanobis distance $d_{(i,j)}$ between each pair of classes. The larger Mahalanobis distance, the larger discriminative capacity between data classes. A clear enlargement of such a capacity is observed in Figs. 7 and 8.
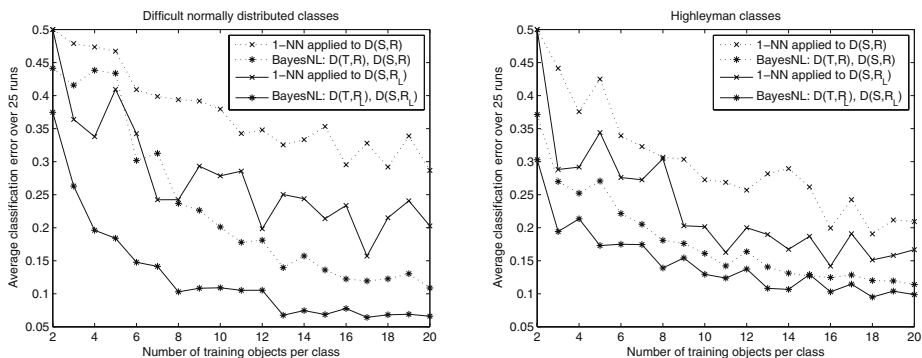
Fig. 5. Artificial data. Average classification errors of the BayesNL and 1-NN classifiers in the original and the generalized dissimilarity spaces. A rule-of-thumb of selecting $n_c C/5$ prototypes is used.
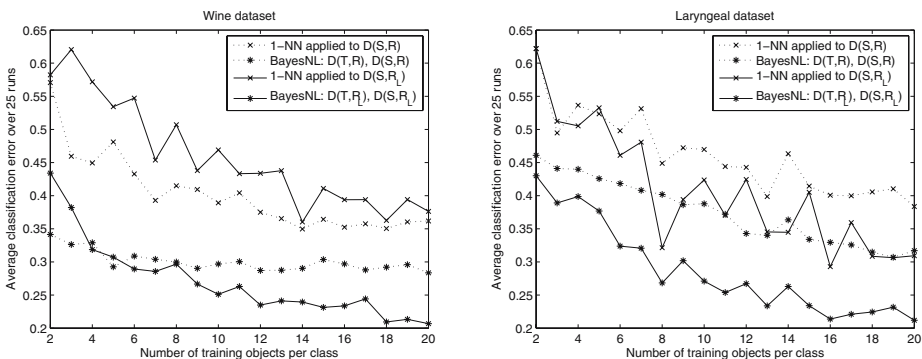
Fig. 6. Real-world data. Average classification errors of the BayesNL and 1-NN classifiers in the original and the generalized dissimilarity spaces. A rule-of-thumb of selecting $n_c C/5$ prototypes is used.

4 Conclusions

Here we have proposed a generalization procedure for dissimilarity representations. The method is based on the feature line concept, which was originally proposed for face recognition problems. Our experiments showed that the generalization procedure, when using a random and a length-based selection of prototype feature lines, seems to be especially profitable for elongated (cigarlike) datasets. Compared to the non-generalized dissimilarity representations, the generalized ones exploit more the intrinsic geometric information available at the pairwise dissimilarities, effectively finding an enriched representation. Additionally, the method is particularly advantageous for small sample size problems because in such sparse spaces, the feature lines are somewhat filling them. Further studies on prototype selection will be conducted as well as on generalization by using feature planes.
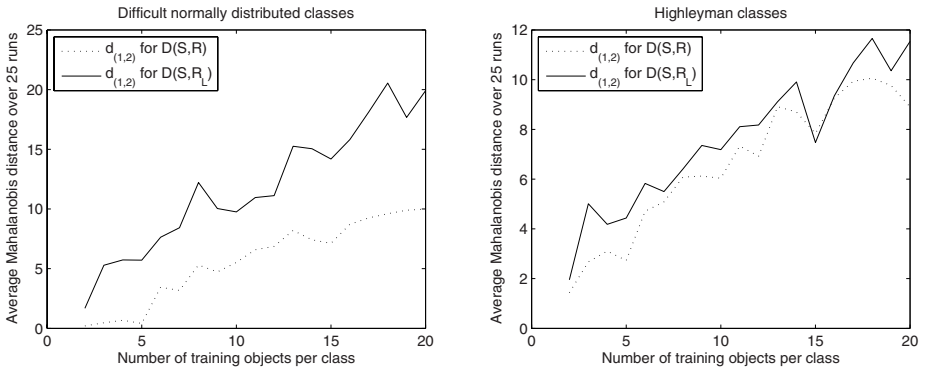
Fig. 7. Mahalanobis distance $d_{(1,2)}$ for the two-class artificial datasets
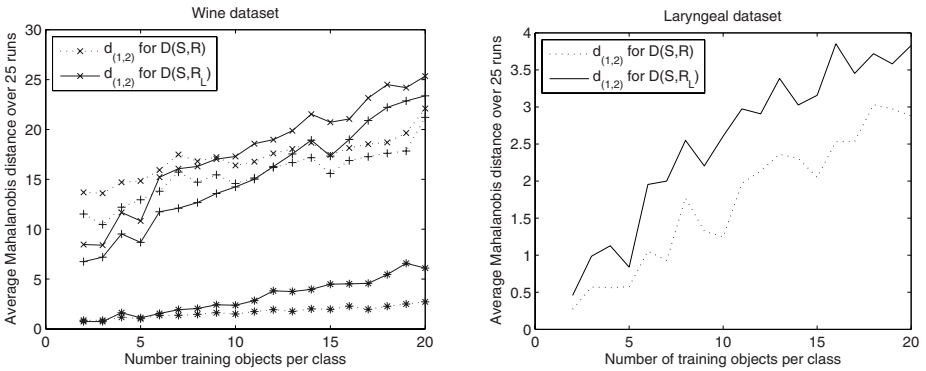
Fig. 8. Mahalanobis distances for the two real-world datasets. Pluses and stars in the left plot correspond to Mahalanobis distances between the other classes, $d_{(1,3)}$ and $d_{(2,3)}$ respectively. They are not specified in the legend for clarity reasons.

References

[1] Cover, T.M., Hart, P.E.: Nearest neighbor pattern classification. Theory IT-13(1), 21–27 (1967)

[2] Pękalska, E., Duin, R.P.W., Paclík, P.: Prototype selection for dissimilarity-based classifiers. Pattern Recognition 39, 189–208 (2006)

[3] Hastie, T., Tibshirani, R.: Discriminant adaptive nearest neighbor classification and regression. In: Touretzky, D.S., Mozer, M.C., Hasselmo, M.E. (eds.) Advances in Neural Information Processing Systems, vol. 8, pp. 409–415. The MIT Press, Cambridge (1996)

[4] Sánchez, J.S., Pla, F., Ferri, F.J.: Improving the k-NCN classification rule through heuristic modifications. Pattern Recognition Letters 19(13), 1165–1170 (1998)

[5] Domeniconi, C., Peng, J., Gunopulos, D.: Locally adaptive metric nearest-neighbor classification. IEEE Trans. Pattern Anal. Mach. Intell. 24(9), 1281–1285 (2002)

[6] Wilson, D.R., Martínez, T.R.: Improved heterogeneous distance functions. J. Artif. Intell. Res (JAIR) 6, 1–34 (1997)

[7] Avesani, P., Blanzieri, E., Ricci, F.: Advanced metrics for class-driven similarity search. In: DEXA 1999: Proceedings of the 10th International Workshop on Database & Expert Systems Applications, p. 223. IEEE Computer Society, Washington, DC, USA (1999)

[8] Paredes, R., Vidal, E.: A class-dependent weighted dissimilarity measure for nearest neighbor classification problems. Pattern Recogn. Lett. 21(12), 1027–1036 (2000)

[9] Wang, J., Neskovic, P., Cooper, L.N.: Improving nearest neighbor rule with a simple adaptive distance measure. Pattern Recogn. Lett. 28(2), 207–213 (2007)

[10] Li, S.Z., Lu, J.: Face recognition using the nearest feature line method. Neural Networks 10(2), 439–443 (1999)

[11] Chien, J.T., Wu, C.C.: Discriminant waveletfaces and nearest feature classifiers for face recognition. IEEE Trans. Pattern Anal. Machine Intell. 24(12), 1644–1649 (2002)

[12] Pękalska, E., Duin, R.P.W.: Dissimilarity representations allow for building good classifiers. Pattern Recognition Lett. 23, 943–956 (2002)

[13] Pękalska, E., Duin, R.P.W.: The Dissimilarity Representation for Pattern Recognition: Foundations and Applications. World Scientific, Singapore (2005)

[14] Duin, R.P.W., Pękalska, E.: Possibilities of zero-error recognition by dissimilarity representations. In: Inesta, J.M., Mico, L. (eds.) PRIS 2002, Alicante, Spain, pp. 20–32. ICEIS Press (April 2002)

[15] Duin, R.P.W., Juszczak, P., de Ridder, D., Paclík, P., Pękalska, E., Tax, D.M.J.: PRTools4: a Matlab Toolbox for Pattern Recognition. Technical report, Information and Communication Theory Group: Delft University of Technology, The Netherlands (2004), http://www.prtools.org/

[16] Highleyman, W.H.: Linear decision functions, with application to pattern recognition. Proceedings of the IRE 50(6), 1501–1514 (1962)

[17] Newman, D.J., Hettich, S.C.L.B., Merz, C.J.: UCI repository of machine learning databases (1998), http://www.ics.uci.edu/~mlearn/MLRepository.html

[18] Kuncheva, L.I.: Real medical data sets (2005) http://www.informatics.bangor.ac.uk/~kuncheva/activities/real_data_full_set.htm

FS-EX Plus: A New Algorithm for the Calculation of Typical FS-Testor Set

Luis Roberto Morales-Manilla and Guillermo Sanchez-Diaz

Center of Technologies Research on Information and Systems, UAEH,
Carr. Pachuca-Tulancingo Km. 4.5, C.P. 42084, Pachuca, Hgo., Mexico
`luisroberto@lycos.com, sanchezg@uaeh.reduaeh.mx`

Abstract. In this paper a novel exterior escale algorithm for the calculation of FS-typical testor set of a learning matrix is proposed. This algorithm allows to use any given similarity function between objects. Besides, results of experiments done, shows the performance obtained by proposed algorithm. A comparison between proposed algorithm and an exhaustive searching algorithm, that is the only one reported on literature that can calculate the complete FS-typical testor set, is also included.

Keywords: FS-testor, feature selection, pattern recognition, typical testor.

1 Introduction

A relevant task in supervised classification is feature selection. This task allows identifying those features that provide relevant information on the classification process. Into the framework of the Logical Combinatorial Pattern Recognition [1] and [2], feature selection is solved using Testor Theory [3]. Yu. I. Zhuravlev introduced the testor concept to pattern recognition problems [4]. Zhuravlev defines a testor like a feature subset that does not confuse objects descriptions which belong to different classes. Subsequently, this concept has extended and generalized to adjust it in other ways [3]. Another generalization model into testor theory is the FS-testors, developed by [5]. This model allows handle any similarity function among objects, opposed as classical testor models. This concept has a special application when qualitative and quantitative features are present (mixed data), using any similarity function among objects. Since computing all typical testors is very expensive, all developed algorithms have exponential complexity. Into the FS-testor model, the run time complexity depends of the similarity function handled. If the similarity function is very complex, then more run time of execution will necessary.

Currently, an exhaustive searching method is the only way in order to calculate the set of FS-typical testors. All feature combinations must be evaluated to determine if FS-testor property is fulfilled. The other way, consists in not to verify this property for every combination, carrying out "skips" of feature combinations over power feature set, we know *a priori* that these combinations do not generate any FS-typical testor.

In this paper, we introduce an algorithm that performs "skips" over power feature set, eliminating a considerable calculations amount.

2   Some Basic Concepts

Let LM be a learning matrix composed by a set of m objects $\Omega = \{O_1, O_2, ..., O_m\}$, described in terms of a set $R = \{X_1, X_2, ..., X_n\}$, with n features of any nature (qualitatives or mixed quantitatives), where every feature X_j, has associated an admissible values set M_j. These objects are grouped on K classes. Every attribute X_j has associated a comparison criterion for the values of X_j, as a function in the form $C_j : M_j x M_j \to L_j$, where L_j it is a totally ordered set.

Let T be a feature combination such that $T \subseteq R$. Besides, let $R^* \subseteq R$ be a reference set. The following definitions were taken from [5, 6, 7].

Definition 1. *The set $T \subseteq R$, is an FS-Differentiating feature set with respect to ν, D', R^* and β of LM if*

$$\forall O_i, O_j \in LM[\nu(\bar{\alpha}(O_i), \bar{\alpha}(O_j)) \notin D'] \Rightarrow$$
$$[\beta(I_{/T}(O_i), I_{/T}(O_j)) \preceq \beta(I_{/R*}(O_i), I_{/R*}(O_j))]$$

where $\bar{\alpha}(O_j) = (\bar{\alpha}_1(O_j), ..., \bar{\alpha}_q(O_j))$ is the membership t-uple and $I_{/T}(O_p) = (x_{p1}(O_j), ..., x_{ps}(O_j))$ the subdescription or partial description of O_j in terms of the features in T.

Definition 2. *The set $T \subseteq R$, is an FS-Characteriziating feature set with respect to ν, D', R^* and β of LM if*

$$\forall O_i, O_j \in LM[\nu(\bar{\alpha}(O_i), \bar{\alpha}(O_j)) \in D'] \Rightarrow$$
$$[\beta(I_{/T}(O_i), I_{/T}(O_j)) \succeq \beta(I_{/R*}(O_i), I_{/R*}(O_j))]$$

Definition 3. *The set $T \subseteq R$, is an FS-testor with respect to ν, D', R^* and β of LM iff T is both FS-differentiating and FS-characteriziating set for LM, with respect to the same parameters.*

In another hand, for the case of FS-typical testors, a partial order relation is required.

Let ν, D', β be given as parameters, and LM, T_1, T_2 and R^* feature subsets of R, where R is the total set of features of LM. The relation of partial order ξ is defined as follows:

Definition 4. *We say that T_1 antecedes to T_2 with respect to ν, D', and β in LM and is denoted by $T_1 \xi T_2$ iff satisfies a) or b):*

a) Exist a pair of objects O_k, O_l of LM such that $\beta(I_{/T_1}(O_k), I_{/T_1}(O_l)) \neq \beta(I_{/T_2}(O_k), I_{/T_2}(O_l))$, and T_1 is an FS-testor for the same parameters ν, D', T_2 and β of LM.

b) For every pair of objects O_i, O_j of MA, $\beta(I_{/T_1}(O_k), I_{/T_1}(O_l)) = \beta(I_{/T_2}(O_k), I_{/T_2}(O_l))$ and $T_1 \xi_2 T_2$ where ξ_2 is the following order relation defined in [8]:

$$T1\xi_2 T2 \Leftrightarrow$$
$$(T_1 \cap T_2) \cup ((support\ T_1 \setminus support\ T_2) \cap T1) \cup ((support\ T_2 \setminus support\ T_1) \cap T_2) = T_2$$

Note that b) is intended for the case where the classes are fuzzy; however, in the case where classes are crisp, the result of this relation is the inclusion of sets.

Taking as base the ralation of parcial order before mentioned, we can give the next definition of FS-typical testor:

Definition 5. *The set* $T \subseteq R$, *is an FS-typical testor with respect to* $\nu, D', R*$ *and* β *of LM, if T is an FS-testor for the same parameters and there are not* T', $T'\xi T$ *that is an FS-testor with respect to* $\nu, D', R*$ *and* β *of LM.*

FS-EX Plus algorithm, in order to fulfill the "skips" over the power feature set, uses the same search order that [9]. This search order was chosen because it allows to the algorithm carry out the big amount of "skips", and these was larger possible.

The algorithm proposed, use the following premises in order to carry out the "skips".

Proposition 1. *Let* $T \subseteq R$ *be a FS-testor. If* $T' \subseteq R$, $T \subseteq T'$ *then* T' *is not a FS-typical testor.*

Proof. As $T \subseteq T'$ (e.g. these are comparable sets) then T antecedes T' by definition 4 (because only it is contemplated inclusion for crisp case). If T' was FS-testor, then by definition 5 of FS-typical testor, T' it is not an FS-typical testor.

Now, if T' was not an FS-testor, then by definition 5 of FS-typical testor, T' can not be neither an FS-typical testor.

Therefore, $T \subseteq T'$ is not an FS-typical testor.   ■

Proposition 2. *Let* $T \subseteq R$, $T' \subseteq R$, *such that* $T \nsubseteq T'$ *and* $T' \nsubseteq T$ *(e.g. these are incomparable sets). If T is an FS-testor with respect to* ν , D', T' *and* β, T *is not an FS-typical testor.*

Proof. As T is an FS-testor with respect to T', then by definition 4, T anteceds T'. And by definition 5, T' isn't an FS-typical testor.   ■

Proposition 3. *Let* $T \subseteq R$ *be an FS-testor. If* $\nexists T' \subseteq R$, *such that* T' *is an FS-testor with respect to* ν , D', T *and* β, *such that* $T' \subseteq T$; *and besides* $\nexists T'' \subseteq R$, *such that* T'' *is an FS-testor with respect to* ν , D', T *and* β, *with* $T \nsubseteq T''$ *and* $T'' \nsubseteq T$, *then T will be an FS-typical testor.*

Proof. a) Suppose that $\exists\ T' \subseteq R$ such that $T' \subseteq T$, T' FS-testor. Then, by proposition 1, T is not an FS-typical testor!

b) Suppose that $\exists\ T'' \subseteq R$ such that $T'' \nsubseteq T$, $T \nsubseteq T''$ and T'' is an FS-testor with respect to ν , D', T and β. Then, by proposition 2, T is not an FS-typical testor!

Therefore T is an FS-typical testor.   ■

3   FS-EX Plus Algorithm

In general, FS-EX Plus algorithm works in the following way. The first combination is generated in the established order and it verifies if this combination is an FS-testor. If so occur, then the combination is saved on a candidates list of FS-typical testors and then all of its consequents supersets in the established order are skipped (proposition 1). In candidates list, all supersets of the current combination are deleted. In other case, the next combination is generated according the established order. This process is repeated until all possible combinations of the power set were generated.

Once the candidates list for FS-typical testors has been obtained, combinations are evaluated in order to eliminate those that being incomparables, and are anteceded among them (proposition 2). One a time all these operations have been done, the final list containing FS-typical testor found (proposition 3) is saved.

Description of the algorithm FS-EX plus
Input: LM (learning matrix)
Output: FSTT (FS-typical testor sets calculated)

1. Inizialitation.- $FSTT = \emptyset$; $Comb = \{X_1\}$

2. Evaluation of candidates.- If last possible feature combination in the search order has been reached, then go to step 5 (e.g. $Comb = \{X_n\}$). On another case, the property of FS-testor is verified. If $Comb$ was FS-testor, then $Comb$ is saved in $FSTT$ ($FSTT = FSTT \cup Comb$). If there are a superset of $Comb$ in $FSTT$, then these supersets are eliminated of $FSTT$ (proposition 1). If $Comb$ was not FS-testor, go to step 4.

3. Skip of non FS-typical testors combinations.- Like $Comb$ was FS-testor, then $FS\_comb = Comb$ and $Comb = Next\_combination(Comb)$ while $Comb$ is a superset of FS_comb. This process means that subsequently supersets of FS_comb are skipped (proposition 1) until $Comb$ is a non superset of FS_comb. Go to step 2.

4. Selection of the new combination to analyze.- The following feature combination for verify is constructed based on before combination generated ($Comb = Next\_combination(Comb)$). Go to step 2.

5. Generation of FS-typical testor set.- The FS-typical testor set is generated. Each Combination $Comb_i \in FSTT$ is compared with remaining combinations of $FSTT$ (e.g. $Comb_j \in FSTT$, $i \neq j$). If $Comb_i$ is and FS-testor with respect to $Comb_j$, then $Comb_j$ is eliminated of $FSTT$ (proposition 2). The FS-typical testor set is composed by the feature combinations of $FSTT$ (proposition 3). The algorithm finish.

Function $Next_combination(Comb)$ return the next feature combination of $Comb$ in the established order of the feature power set.

4   Evaluation

In order of verify the performance of proposed algorithm, a comparison with an exhaustive search algorithm was fulfilled. The exhaustive search algorithm evaluates all possible combinations from the power feature set.

For our comparison, we handled execution times and the number of FS-typical testor obtained, it was used several learning matrices containing real data and that were taken from [10]. Matrices belong to four data bases: Zoo, Votes, Mushroom and Wine.

Values of parameters used in tests were:

$$\nu(\bar{\alpha}(O_i), \bar{\alpha}(O_j)) = \begin{cases} 1, \text{ if } \bar{\alpha}(O_i) = \bar{\alpha}(O_j) \\ 0, \text{ if } \bar{\alpha}(O_i) \neq \bar{\alpha}(O_j) \end{cases}$$

and $D' = \{1\}$, $R^* = R$.

Table 1, shows the results obtained after calculating the FS-typical testors to mentioned matrices taking as similarity function the matching function used in typical testors.

Notation used in the table 1 is as follows:
ECE: Combinations evaluated by exhaustive algorithm
ECFS: Combinations evaluated by FX-EX plus algorithm
TE: Time in seconds used by exhaustive algorithm
TFS: Time in seconds used by FX-EX plus algorithm
NFSTT: Number of FS-typical testors generated

Table 1. Experimental results obtained to Zoo, Votes, Mushroom and Wine data sets

Data set (rows x columns)	ECE	ECFS	TE	TFS	NFSTT
Zoo (101x17)	131071	22315	2145	96	53
Votes (435x16)	65535	65534	1349	1342	3
Mushroom (8124x22)	4194303	22	> 86400	1349	22
Wine (178x13)	8191	146	191	2	67

As we can observe in this results, FS-EX Plus algorithm complies with task of realize a significant less number of evaluations, in contrast with exhaustive search algorithm. However, it could be given the case where for a given matrix, the only FS-testor existing given a similarity function, were the last feature combination, as a result, the number of evaluated combinations in both algorithms would be dramatically the same. But the cause for this would be the chosen similarity function again. This allows to make emphasis in the complexity that involves working with FS-testors model, since in order to such combinations exist inside

Table 2. Time proportion for calculations between exhaustive search and FS-EX Plus algorithms

Data set	time
Zoo	FS-EX plus 22 times more fast than Exhaustive algorithm
Mushroom	FS-EX plus 64 times more fast than Exhaustive algorithm
Wine	FS-EX plus 95 times more fast than Exhaustive algorithm

a learning matrix, it depends of many factors, which ones can be, the learning matrix itself, the similarity function β that is using or even the reference set $R*$ itself who has not either be always the total set of attributes.

From the obtained results, one can observe that FS-EX Plus algorithm found the set of FS-typical testors in the following time proportions:

For the experiment with LM of Mushroom, the process was stopped after 24 hours and was estimated that every realized combination took 164 seconds being evaluated, having to process 4,194303 combinations of attributes. Predicting that exhaustive search algorithm will finish in a few more of 14 years approximately.

5   Conclusions

In this article a novel algorithm of exterior scale to calculate all the set of FS-typical testors was introduced.

The shown performance in the experiments by algorithm was more efficient than exhaustive search algorithm due the "skips" realized over power feature set, avoiding to verify a considerable quantity of combinations that do realizes the exhaustive search algorithm.

Proposed algorithm opens a way for the construction of new exterior escale algorithms to find FS-typical testors. These new algorithms could incorpore some order in the attributes of the learning matrix, or other run over power set of attributes that allows it to decrease the number of combinations to be verified.

It is relevant to say that this algorithm is the first one reported in the literature that does not verify all possible combinations of attributes and generates the total set of FS-typical testors. Besides, currently we do not found a reported in the literature exhaustive search algorithm developed.

References

[1] Ruiz-Shulcloper, J., Abidi, M.: Logical Combinatorial Pattern Recognition: A Review. Recent Research Developments in Pattern Recognition. In: Pandalai, S.G. (ed.) Recent Research Developments in Pattern Recognition, Transworld Research Networks, Kerala, India, pp. 133–176 (2002)

[2] Martinez-Trinidad, J.F., Guzmán Arenas, A.: The Logical Combinatorial approach for pattern recognition an overview through selected Works. Pattern Recognition 34(4), 741–751 (2001)

[3] Lazo-Cortes, M., Ruiz-Shulcloper, J., Alba Cabrera, E.: An overview of the evolution of the concept of testor. Pattern Recognition 34(4), 753–762 (2001)

[4] Dmitriev, A.N., Zhuravlev, Y.I., Krendeliev, F.P.: About mathematical principles and phenomena classification. Diskretni Analiz. 7, 3–15 (1966)

[5] Alba-Cabrera, E.: Novel extensions about testor model for several kinds of similarity functions. Ph. D. thesis, University of Havana, Cuba (1998)

[6] Alba-Cabrera, E., Lazo-Cortés, M.: A Global Solution for the Utilization of Testors in Pattern Recognition Problems. In: Proc. TIARP 1998, pp. 7–22 (1998) (In Spanish)

[7] Alba-Cabrera, E.: A testor concept for any analogy function in a totally ordered set. Integration Journal, Colombia 14(2), 75–82 (1996)

[8] Lazo Cortes, M.: Models based in testor theory for feature selection and supervised classification with non classical objects descriptions. Ph. D. Thesis, UCLV, Cuba (1994)

[9] Santiesteban Alganza, Y., Pons Porrata, A.: LEX: a new algorithm for calculated typical testors. Mathematics Sciences Journal 21(1), 85–95 (2003) (In Spanish)

[10] Newman, D.J., Hettich, S., Blake, C.L., Merz, C.J.: UCI Repository of machine learning databases. Irvine, CA: University of California, Department of Information and Computer Science (1998), http://www.ics.uci.edu/~mlearn/MLRepository.html

Confusion Matrix Disagreement for Multiple Classifiers

Cinthia O.A. Freitas[1], João M. de Carvalho[2], José Josemar Oliveira Jr[2],
Simone B.K. Aires[3], and Robert Sabourin[4]

[1] Pontificia Universidade Católica do Paraná – PUCPR - Brazil
[2] Universidade Federal de Campina Grande – UFCG - Brazil
[3] Universidade Tecnológica Federal do Paraná – Campus Ponta Grossa – UTFP-PG - Brazil
[4] École de Technologie Supérieure - ETS - Canada
`cinthia@ppgia.pucpr.br, carvalho@dee.ufcg.edu.br,`
`josemar@dee.ufcg.edu.br, sbkaminski@pg.cefetpr.br,`
`robert.sabourin@etsmtl.ca`

Abstract. We present a methodology to analyze Multiple Classifiers Systems (MCS) performance, using the disagreement concept. The goal is to define an alternative approach to the conventional recognition rate criterion, which usually requires an exhaustive combination search. This approach defines a Distance-based Disagreement (DbD) measure using an Euclidean distance computed between confusion matrices and a soft-correlation rule to indicate the most likely candidates to the best classifiers ensemble. As case study, we apply this strategy to two different handwritten recognition systems. Experimental results indicate that the method proposed can be used as a low-cost alternative to conventional approaches.

Keywords: multiple classifiers systems, pattern recognition, classifiers diversity, handwriting recognition.

1 Introduction

The traditional pattern recognition approach divides the recognition task in two steps: first, a feature set is extracted from the images; second, the classifier computes the class-conditional probabilities based on the extracted features. Different feature sets can be proposed as well as many distinct classifiers can be designed. Therefore, the problem is to find the best combination of feature set and classifier.

In order to solve this problem many researchers have recently adopted the strategy of utilizing Multiple Classifiers Systems (MCS). The aim is to design a composite system that outperforms any of its individual component classifiers. The underlying principle is that it is more difficult to design one single complex classifier than to optimize a combination of relatively less complex ones. Several combination methods are found in the literature, however, one open question remains: what are the requirements to be fulfilled by the classifier components?

The concept of diversity has been used to answer that question, given that an ensemble of identical classifiers will not outperform its components individually. Evidence indicates that diversity within an ensemble is vital for its success [1] [2]. However, there is no general agreement on how to quantify neither diversity nor its

relation with the ensemble average recognition rate. Aiming to group classification problems in a consistent way, Duin et al. [3] applied disagreement to measure the difference between two distinct classifiers trained on the same classification problem, which may be helpful in selecting appropriate tools for solving those problems. They admit, however, that there is still much to be investigated about disagreement between classifiers, although preliminary results are encouraging.

We are interested in designing a method that does not use first-order information (classifier's score output) to evaluate the ensemble. The idea is to use information from the confusion matrix for each individual classifier and compute distances between those matrices that represent classifier disagreements. Thus, distances will provide a mechanism for *a priori* evaluation of the possible classifier combinations.

2   Distance-Based Disagreement Classifiers Combination

A method for designing pattern recognition systems, known as MCS or committee/ ensemble approach, has emerged over recent years to tackle the practical problem of designing classification systems with improved accuracy and efficiency [1].

Attempts to understand the effectiveness of the MCS framework have prompted the development of several measures, like margin, bias and variance. Recently, many diversity measures have been studied to determine how they correlate with ensemble accuracy [4].

In trying to achieve this goal, the main question is: How can we measure the efficiency of a MCS? Our answer is to measure disagreements between classifiers, using their confusion matrices. This information can provide a mechanism to understand which classifiers can effectively contribute to boost the efficiency of the ensemble.

2.1   Diversity and Disagreement

Diversity measures can be categorized into two types [4]:

- **pair-wise:** calculates the average of a particular distance metric between all possible pairings of classifiers in the ensemble. The distance metric used determines the characteristics of the diversity measure;
- **non-pair-wise:** uses entropy or another similar measure to calculate a correlation of each ensemble member with the averaged ensemble output.

The main difficulty with the use of diversity measures is the so-called accuracy-diversity dilemma. As explained by Hadjitodorov et al., it is not clear how to choose the degree of diversity which produces the best performance, leading to a desired tradeoff between diversity and accuracy [5]. These authors also point that no convincing theory or experimental study has emerged to indicate a reliable measure to predict the generalization error of an ensemble. Other authors have stressed the need to find a balance point between diversity and accuracy [1], [4], reaching no agreement, however, regarding the choice of disagreement measure.

Duin et al. [3], use the disagreement concept to measure the difference between two classifiers C_1 and C_2 trained on a classification problem P_j (j = 1,...,N; N is the size of the set of problems). The disagreement is formulated as in Equation 1:

$$d_j(C_1, C_2) = Prob(C_1(x) \sim= C_2(x) \mid x \in P_j) \tag{1}$$

where $C_i(x)$ returns the label for object x according to classifier C_i. M classifiers constitute an MxM disagreement matrix D_j^C for problem P_j, with elements $D_j^C(m,n)$ $= d_j(C_m, C_n)$.

In this work we take a different approach from that of Duin et al. [3], although also based on disagreement. The idea is to use the confusion matrix for each individual classifier to compute distances that represent classifier disagreements. We call our approach Distance-based Disagreement (DbD) criterion.

2.2   Confusion Matrix

A consistent analysis of classifier behavior can be provided by the semi-global performance matrix, known as the Confusion Matrix. This matrix provides a quantitative performance representation for each classifier in terms of class recognition. The Confusion Matrix can be denoted as in Equation 2 [2]:

$$A = \begin{bmatrix} RR_{1,1} & RR_{1,2} & \cdots & RR_{1,N} \\ \vdots & \vdots & & \vdots \\ RR_{2,1} & RR_{2,2} & \cdots & RR_{2,N} \\ \vdots & \vdots & & \vdots \\ RR_{N,1} & RR_{N,2} & \cdots & RR_{N,N} \end{bmatrix} \tag{2}$$

where $RR_{i,j}$ corresponds to the total number of entities in class C_i which have been classified in class C_j. Hence, the main diagonal elements indicate the total number of samples in class C_i correctly recognized by the system. From matrix A, it is possible to compute a global performance index for classifier A, defined by Equation 3:

$$RR^A = \frac{1}{N} \sum_{i,j=1}^{N} RR_{i,j} \tag{3}$$

For the ensemble of classifiers $A, B, ..., M$ (considering that all confusion matrices are of the same size), a distance measure D^A between classifier A and all other classifiers is provided by Equation 4:

$$D^A = \sum_{i=1}^{N} \sum_{j=1}^{N} \left| RR_{i,j}^A - RR_{i,j}^B ... - RR_{i,j}^M \right| \tag{4}$$

where $RR_{i,j}^k$, k=A,B,...M, are the elements of the confusion matrix for classifier k.

This distance can be similarly calculated for all members of the ensemble. Therefore, for an ensemble of M classifiers, we can define a Distance-based Disagreement (DbD) measure, expressed by Equation 5:

$$DbD = \sum_{k=A,B,\ldots M} D^k \tag{5}$$

which uses information from the confusion matrix of each individual classifier and expresses classifiers disagreement.

2.3 Hypothesis: Soft-Correlation Rule

Our hypothesis is based on the following idea proposed by Hadjitodorov et al. [5]: "The ensembles selected through median diversity will fare better than randomly selected ensembles or ensembles selected through maximum diversity". We are calling this hypothesis the Soft-Correlation Rule. These authors observed that excessively increasing diversity does not lead to more accurate ensembles. They intuitively explain this phenomenon with the notion that in pattern clustering more diversity is associated with many clusters not getting the clustering structure right, leading to lower individual accuracy.

Considering this hypothesis, our proposal is to compute ensemble diversity from the distances (Eq. 4) between confusion matrices of the component classifiers, and to verify whether or not the best ensemble performance corresponds to the median diversity value. This methodology has been applied to two handwriting recognition problem, as described next.

3 Case 1: Character Recognition

For feature extraction, the baseline system for handwritten character recognition used in this work combines global and local (based on a zoning mechanism) approaches, and uses feedforward MLP (Multiple Layer Perceptron) Class-Modular architecture in the classification stage, where the modular MLP classifier consists of K sub-networks, M_i for $0 \leq i \leq K$-1, each responsible for one of the K classes [6].

The system gets as input a 256 grey-level image, as depicted in Fig. 1a. The preprocessing step is composed of binarization and bounding box definition. The feature set is obtained by labeling the background pixels of the input image as belonging to either a concavity or a convexity region [7], as presented in Fig. 1b. The alphabet of symbols was adapted to handwritten characters, resulting in 24 different symbols.

Several authors have presented zoning mechanisms or regional decomposition methods to investigate the recognition of patterns from their parts, similarly to what the human brain does during the reading process. Suen et al. [8] and Li et al. [9] applied a zoning mechanism in their experiments with hand printed characters. They analyzed different zone configurations, framing the character by a rectangle partitioned into Z parts. Based on these studies, we tested several zoning mechanisms, for Z equal to 4, 5 horizontal (5H), 5 vertical (5V) and 7, as shown in Fig. 2. Each image zone defines one classifier and these classifiers combined constitute a MCS. The zoning approach is beyond the scope of this paper [10].
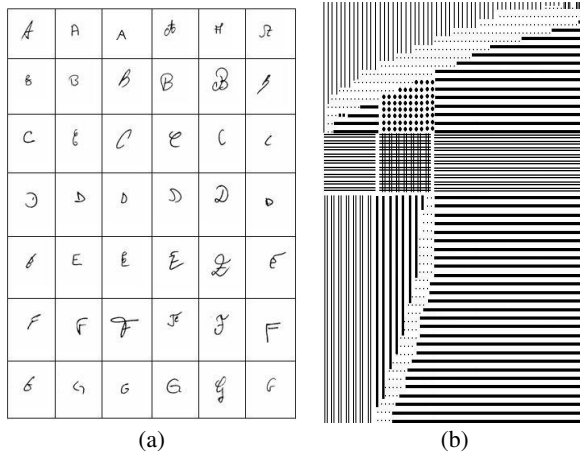
Fig. 1. Feature extraction: a) sample images from the character database and b) feature extraction (character "T")

4   Case 2: Word Recognition

The word recognition problem analyzed in this work is the recognition of handwritten month words on Brazilian bank checks. This is an important task, since it constitutes a sub-problem of bank check date recognition. This study deals only with recognition of the portuguese language month names represented by a limited lexicon of 12 classes: *Janeiro, Fevereiro, Março, Abril, Maio, Junho, Julho, Agosto, Setembro, Outubro, Novembro*, and *Dezembro. S*ome of these classes share sub-strings of characters, therefore adding to the problem complexity.
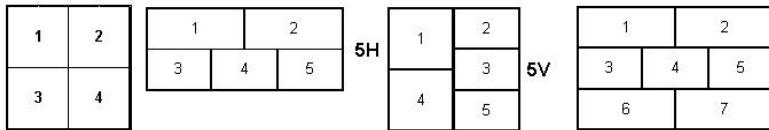
Fig. 2. Zoning mechanism: Z = 4, 5V, 5H and 7 parts

The baseline system utilizes multiple classifiers to avoid the intrinsic difficulties of the lexicon, by combining complementary information obtained from distinct sources (classifiers). Therefore, two different classifiers (Class-Modular Neural Networks [6] and Hidden Markov Models [11]) based on five different feature sets were evaluated. Similarly as used in character recognition, zoning mechanisms were utilized for feature extraction in order to add robustness to the system [8], [9]. The implemented zoning schemes are the following (Fig. 3):

- 2 fixed sub-regions (2-FS): Zoning splits the image in two areas defined at the right and at the left of the word center of gravity (Fig. 3a). These system extracts 14 features from each word in order to generate a feature vector of dimension 24 [12];

- 8 fixed sub-regions (8-FS): Each sample image is divided in 8 sub-regions of equal size (Fig. 3b). This number corresponds to the average number of letters in the lexicon words. In this zoning mechanism, three different feature extraction were evaluated [12]: perceptual, directional, and topological feature sets;
- N-variable sub-regions (N-VS): The features are extracted from the words images and a pseudo-segmentation process is applied to obtain a sequence of corresponding observations (Fig. 3c). Between two black-white transitions over the maximum peak of the horizontal transition histogram, called the Median Line, a segment is delimited and a corresponding symbol is designated to represent the extracted set of features, making up a grapheme [12], [13].

5   Experimental Results

This Section presents the database used in the experiments performed to evaluate the DbD criterion and the experimental results obtained with the MCS applied to the two cases described in Sections 3 and 4.

5.1   Character and Word Databases

The experiments applying characters were carried out using the handwritten character database called IRONOFF (IRESTE/University of Nantes-France), consisting of 26 classes of uppercase characters from Form B [14]. The IRONOFF database was selected because it is fully cursive. Samples were collected from about 700 writers, mainly of French nationality. The off-line data were scanned at 300 dpi with 8 bits per pixel.

To develop the word recognition system it was initially necessary to construct a database that can represent the different handwriting styles present in Brazilian Portuguese language. This was done by collecting samples of each month name, from 500 writers of different levels of education. Each writer was asked to fill a specific form where the word corresponding to each month name would be written once, as presented in Fig. 4 [12].
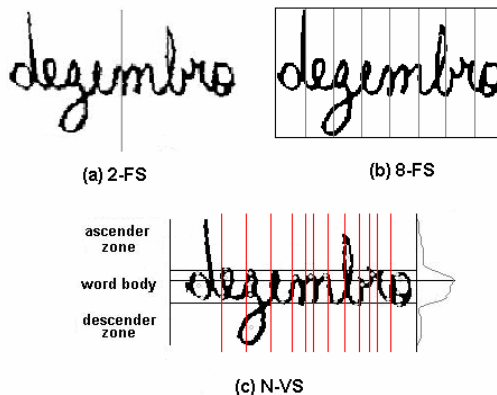
Fig. 3. Example of each zoning mechanism
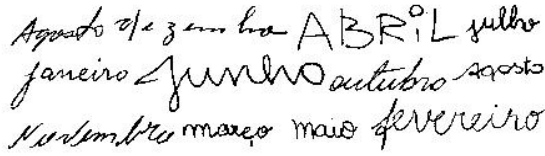
Fig. 4. Sample images from the word database

The databases have a total of 10,510 images of characters and 6,000 images of words, respectively. We split both databases into three sub-sets: Training (60%), Validation (20%), and Test (20%).

5.2 Results

For each zoning Z in the character recognition system presented in Section 3 and for each 2-FS and 8-FS feature set presented in Section 4, one NN was trained and tested, as proposed by Oh et al. [6]. The class decision module considers only the O_0 outputs from each sub-network and uses a simple winner-takes-all scheme to determine the final class.

The N-VS classifier for word recognition was evaluated with the same sets used for the other classifiers and for each class one model was trained and validated. The model that assigns maximum probability to one test image represents the class recognized.

The computational time for the experiments is beyond the scope of this paper. Both systems account for the entire recognition process (preprocessing, feature extraction, recognition, DbD calculation). As described in Section 2.2, the DbD measure is computed from the confusion matrices, therefore after the recognition stage.

Tables 1 and 2 show the results obtained for each zoning scheme both for the character and the word recognition systems, respectively. It can be seen that the best results were obtained using Z=7 for character recognition and 8-FS with directional features for word recognition.

Table 1. Recognition rate for each classifier in character recognition system

Classifier	Recognition Rate (%)
Z=4	83.2
Z=5Vertical	82.4
Z=5Horizontal	84.7
Z=7	**88.9**

Table 2. Recognition rate for each classifier in word recognition system

Classifier	Recognition Rate (%)
2-FS	73.9
8-FS-P (Perceptual)	86.3
8-FS-D (Directional)	**91.4**
8-FS-T (Topological)	85.0
N-VS	81.7

The DbD approach described in Section 2 was applied to the classifiers confusion matrices, for both systems. Distance was calculated considering groups of 2 classifiers. The calculated disagreement measures were compared with the results obtained combining the classifiers outputs with the weighted sum rule (WSC) defined by Kittler et al. [15], as presented in Tables 3 and 4. Other combination rules (average and product) were also tested but the best results were obtained using WSC. The boldfaced entries in the tables correspond to the median diversity ensembles, obtained by the DbD methodology, and to the best recognition rate associated to them.

Tables 3 and 4 show that, in general, the best combination results produced by the WSC rule correspond to one of the median diversity (DbD) values. One exception is the 4-7 combination (last line of Table 3), that achieved the best recognition score (85.8%) with the largest (5.28) DbD value, for the character recognition case. The reason for this deviation is not yet clear (shall be further investigated), however, it does not invalidate the general observed behavior, that recognition rates decay as classifiers diversity moves away from the median values.

Table 3. Classifier combination using DbD – Character recognition system

Character Classifier	DbD	WSC (%)
5H-5V	4.78	83.9
4-5H	4.87	83.4
4-5V	**5.01**	**83.7**
5V-7	**5.13**	**85.2**
5H-7	5.22	85.1
4-7	5.28	85.8

Table 4. Classifier combination using DbD – Word recognition system

Word Classifier	DbD	WSC (%)
8-FS-D – 8-FS-T	1.30	91.7
8-FS-P – 8-FS-T	1.33	89.4
8-FS-P – 8-FS-D	1.34	92.9
8-FS-P – N-VS	1.44	93.2
8-FS-D – N-VS	**1.77**	**95.0**
8-FS-T – N-VS	**1.88**	**93.4**
2-FS – N-VS	2.07	89.9
2-FS – 8-FS-P	2.28	90.3
2-FS – 8-FS-T	2.28	88.9
2-FS – 8-FS-D	2.57	93.9

The DbD measure has also been applied to experiments using three different classifiers for character recognition systems. Preliminary results obtained are shown in Table 5. We can observe that the best results correspond to the diversity (DbD) values close to the median.

Table 5. Classifier combination using DbD– Three different classifiers

Character Classifier	DbD	Recognition Rate (%)
4-5H-5V	27.49	85.8
4-5V-7	**27.52**	**90.9**
Median	27.70	------
4-5H-7	**27,88**	**91,0**
5H-5V-7	29,64	90,1

6 Discussions and Conclusion

This paper proposes an approach to evaluate ensembles of classifiers without actually having to exhaustively combining them to measure classification performance. The main motivation for this is the high computational cost of performing an exhaustive search in classifier combination space when we have a large number of classifiers. The DbD approach uses information from the confusion matrices of each individual classifier to compute distances that represent classifiers diversity. The results obtained with this approach reinforce the idea that median, rather than high, diversity is in general synonymous with high accuracy. The proposed methodology thus constitutes a new method for *a priori* evaluating multiple classifier systems, indicating the strongest candidates to the best classifiers combination. Using this approach, the search space is drastically reduced, in general to two strong candidates, which can then have their performance evaluated to determine the best MCS for the problem at hand. In this work, the method was applied to two handwriting recognition problems, although it can in fact be used for any pattern recognition problem. The validity of the DbD approach is supported by the experimental results. Future work will focus on the analysis of different distance criteria and the application of the DbD measure for ensembles of more than two classifiers, for the word recognition system.

References

1. Windeatt, T.: Diversity Measures for Multiple Classifier System Analysis and Design. Information Fusion 6(1), 21–36 (2005)
2. Zouari, H.K.: Contribution à l'évaluation des méthodes de combinaison parallèle de classifieurs par simulation. Doctor Thesis, Université de Rouen (2004)
3. Duin, R.P.W., Pekalska, E., Tax, D.M.J.: The Characterization of Classification Problems by Classifier Disagreements. In: ICPR 2004, vol. 1, pp. 140–143 (2004)
4. Kuncheva, L.I., Whitaker, C.J.: Measures of Diversity in Classifier Ensembles. Machine Learning 51, 181–207 (2003)
5. Hadjitodorov, S.T., Kuncheva, L.I., Todorova, L.P.: Moderate Diversity for Better Cluster Ensembles (2005), http://www.informatics.bangor.ac.uk/kuncheva/-recent_publications.htm
6. Oh, I.-S., Suen, C.Y.: A Class-Modular Feedforward Neural Network for Handwriting Recognition. Pattern Recognition 35(1), 229–244 (2002)
7. Parker, J.R.: Algorithms for Image Processing and Computer Vision. Jonh Wiley & Sons, Chichester (1997)
8. Suen, C.Y., Guo, J., Li, Z.C.: Analysis and Recognition of Alphanumeric Handprints by Parts. IEEE Trans. on Systems, Man and Cybernetics 24(4), 614–631 (1994)

9. Li, Z.C., Suen, C.Y., Guo, J.: A Regional Decomposition Method for Recognizing Handprinted Characters. IEEE Trans. on Systems, Man and Cybernetics 25(6), 998–1010 (1995)

10. Freitas, C.O.A., Oliveira, L.E.S., Bortolozzi, F., Aires, S.B.K.: Handwritten Character Recognition Using Nonsymmetrical Perceptual Zoning. International Journal of Pattern Recognition and Artificial Intelligence, IJPRAI 21(1), 135–155 (2007)

11. Rabiner, L., Juang, B.H.: Fundamental of Speech Recognition. Prentice-Hall, Englewood Cliffs (1993)

12. Oliveira, Jr.,J.J., Kapp, M.N., Freitas, C.O.A., Carvalho, J.M., Sabourin, R.: Handwritten month word recognition using multiple classifiers. In: XVII Brazilian Symposium on Computer Graphics and Image Processing (SIBGRAPI), vol. 1, pp. 82–89 (2004)

13. Freitas, C.O.A., Bortolozzi, F., Sabourin, R.: Study of Perceptual Similarity Between Differnet Lexicons. International Journal of Pattern Recognition and Artificial Intelligence, IJPRAI 18(7), 1321–1338 (2004)

14. Viard-Gaudin, C.: The Ironoff User Manual. IRESTE, University of Nantes, France (1999)

15. Kittler, J., Hatef, M., Duin, R.P.W., Matas, J.: On Combining Classifiers. IEEE Trans. on PAMI 20(3), 226–239 (1998)

An Empirical Study of the Behavior of Classifiers on Imbalanced and Overlapped Data Sets

Vicente García[1,2], Jose Sánchez[2], and Ramon Mollineda[2]

[1] Lab. Reconocimiento de Patrones, Instituto Tecnológico de Toluca
Av. Tecnológico s/n, 52140 Metepec (México)
[2] Dept. Llenguatges i Sistemes Informàtics, Universitat Jaume I
Av. Sos Baynat s/n, 12071 Castelló de la Plana (Spain)

Abstract. Class imbalance has been reported as an important obstacle to apply traditional learning algorithms to real-world domains. Recent investigations have questioned whether the imbalance is the unique factor that hinders the performance of classifiers. In this paper, we study the behavior of six algorithms when classifying imbalanced, overlapped data sets under uncommon situations (e.g., when the overall imbalance ratio is different from the local imbalance ratio in the overlap region). This is accomplished by analyzing the accuracy on each individual class, thus devising how those situations affect the majority and minority classes. The experiments corroborate that overlap is more important than imbalance for the classification performance. Also, they show that the classifiers behave differently depending on the nature of each model.

Keywords: Imbalance; overlapping; classifiers; performance measures.

1 Introduction

Many traditional approaches to pattern classification assume that the problem classes share similar prior probabilities. However, in many real-world problems, this assumption is grossly violated. Often, the ratios of prior probabilities between classes are extremely skewed. This situation is known as the imbalance problem. A data set is said to be imbalanced when one of the classes (the minority one) is heavily under-represented in comparison to the other (the majority) class.

Most of the research addressing this problem concentrates on balancing the class distribution in the data set. The different proposals can be roughly classified into three categories: assigning distinct costs to the classification errors for positive and negative examples [7], resampling the original training set, either by over-sampling the minority class [5] and/or under-sampling the majority class [11] until the classes are approximately equally represented and, internally biasing the discrimination-based process so as to compensate for the class imbalance [1].

Recently, several works have pointed out that there does not exist a direct correlation between class imbalance and the loss of performance [13]. These studies suggest that the class imbalance is not a problem by itself, but the degradation of performance is also related to other factors. Different works explore the combined effects of class imbalance

with the presence of small disjuncts [10], the size of the training set [9, 12], and the degree of overlapping between classes [2, 13].

In the present work, we study the behavior of six classifiers under the presence of both class imbalance and overlap. This study mainly tries to devise the influence of changes in the overlap region on the classifiers, while keeping the majority/minority ratio constant. The aim is to show that these practical situations affect the classifier performance depending on the characteristics of the particular algorithm used, that is, similar situations may produce different results. In order to accomplish this, we experiment with artificial data sets, employing some performance measures that estimate the accuracy on each individual class.

2   The Classifiers

In this section, we briefly describe the classifiers selected for the present experimental study. All these algorithms work under the assumption that there exists a set of n previously labelled examples (training set, TS), say $\mathcal{X} = \{(x_1, \omega_1), (x_2, \omega_2), \ldots, (x_n, \omega_n)\}$, where each element has an attribute vector x_i and a class label ω_i.

2.1   Nearest Neighbor Rule

One of the most popular non-parametric classification approaches corresponds to the k nearest neighbor (kNN) decision rule [6]. In brief, this classifier consists of assigning a new input sample **x** to the class most frequently represented among the k closest instances in the TS, according to a certain dissimilarity measure (generally, the Euclidean distance metric). A particular case is when $k = 1$, in which an input sample is decided to belong to the class indicated by its closest neighbor.

The characteristics of the kNN classifier need the entire TS stored in computer memory, what causes large time and memory requirements. On the other hand, the kNN rule is extremely sensitive to the presence of noisy, atypical and/or erroneously labelled cases in the TS.

2.2   Naïve Bayes Classifier

The naïve Bayes classifier (NBC) [8] is arguably one of the simplest probabilistic schemes, following from Bayesian decision theory. The model constructed by this algorithm is a set of probabilities, each one corresponding to the probability $P(f_i|c)$ that a specific feature f_i appear in the instances of class c. These probabilities are estimated by counting the frequency of each feature value in the instances of a class in the TS. Given a new instance, the classifier estimates the probability that the instance belongs to a specific class, based on the product of the individual conditional probabilities for the feature values in the instance.

NBC is based on an independent feature model, that is, all the attributes are independent given the value of the class variable. Despite the conditional independence assumption is rarely true in most real-world applications, the algorithm tends to perform well in many scenarios and it learns more rapidly than most induction algorithms.

2.3   C4.5 Decision Tree

The C4.5 algorithm [14] uses a greedy technique to induce decision trees. A decision-tree model is built by analyzing training data and the model is used to classify unseen data. The nodes of the tree evaluate the existence or significance of individual features. Following a path from the root to the leaves of the tree, a sequence of such tests is performed resulting in a decision about the appropriate class of new objects.

The decision trees are constructed in a top-down fashion by choosing the most appropriate attribute each time. An information-theoretic measure is used to evaluate features, which provides an indication of the "classification power" of each feature. Once a feature is chosen, the training data are divided into subsets, corresponding to different values of the selected feature, and the process is repeated for each subset until a large proportion of the instances in each subset belongs to a single class.

2.4   Multilayer Perceptron

The multilayer perceptron (MLP) neural network [3] usually comprises one input layer, one or more hidden layers, and one output layer. Input nodes correspond to features, hidden layers are used for computations, and output layers are the problem classes. A neuron is the elemental unit of each layer. It computes the weighted sum of its inputs, adds a bias term and drives the result thought a generally nonlinear (commonly, sigmoid) activation function to produce a single output.

The most popular training algorithm for MLP is the backpropagation, which takes a set of training instances for the learning process. For the given feedforward network, the weights are initialized to small random numbers. Each training instance is passed through the network and the output from each unit is computed. The target output is compared with the output estimated by the network to calculate the error, which is fed back through the network. To adjust the weights, backpropagation uses gradient descent to minimize the squared error between the target output and the computed output. At each unit in the network, starting from the output unit and moving down to the hidden units, its error value is used to adjust weights of its connections so as to reduce the error. This process of adjusting the weights is repeated for a fixed number of times or until the error is small or it cannot be reduced.

2.5   Radial Basis Function

The radial basis function (RBF) [4] neural network, which has three layers, can be seen as an especial kind of multilayer feedforward networks. Each unit in the hidden layer employs a radial basis function, such as Gaussian kernel, as the activation function. The output units implement a weighted sum of hidden unit outputs. The input into an RBF network is nonlinear. The output is linear. The kernel is centered at the point specified by the weight vector associated with the unit. Both the positions and the widths of these kernels are learned from training instances. Each output unit implements a linear combination of these radial basis functions.

An RBF is trained to learn the centers and widths of the Gaussian function for hidden units, and then to adjust weights in the regression model that is used at the output unit.

To learn the centers of the Gaussian functions, the k-means algorithm can be used, obtaining k Gaussian functions for each attribute in the instance. After the parameters for the Gaussian function at the hidden units have been found, the weights from these units to the output unit are adjusted using a linear regression model.

2.6 Support Vector Machine

Support vector machines (SVMs) [15] are a set of related supervised learning methods used for classification and regression. They belong to a family of generalized linear classifiers. A special property of SVMs is that they simultaneously minimize the empirical classification error and maximize the geometric margin; hence they are also known as maximum margin classifiers.

SVMs map input vectors to a higher dimensional space where a maximal separating hyperplane is constructed. Two parallel hyperplanes are constructed on each side of the hyperplane that separates the data. The separating hyperplane is the hyperplane that maximizes the distance between the two parallel hyperplanes. An assumption is made that the larger the margin or distance between these parallel hyperplanes the better the generalization error of the classifier will be.

3 Performance Evaluation in Class Imbalance Problems

In the literature, there appear many different proposals for measuring the performance of learning algorithms in imbalanced domains. However, they all agree in the need of measuring the classification performance over each individual class, instead of the overall accuracy, because the misclassification costs can be different for each of them. Most of performance measures for two-class problems are built over a 2×2 confusion matrix as illustrated in Table 1.

Table 1. Confusion matrix for a two-class problem

	Positive prediction	Negative prediction
Positive class	True Positive (TP)	False Negative (FN)
Negative class	False Positive (FP)	True Negative (TN)

From the confusion matrix, apart from other more elaborated performance measures, one can obtain several simple metrics on the positive (minority) and negative (majority) classes, along with the overall accuracy and the overall error rate:

True Positive Rate: $TPR = \frac{TP}{TP+FN}$ True Negative Rate: $TNR = \frac{TN}{TN+FP}$

False Positive Rate: $FPR = \frac{FP}{FP+TN}$ False Negative Rate: $FNR = \frac{FN}{TP+FN}$

Accuracy: $Acc = \frac{TP+TN}{TP+FP+FN+TN}$ Error Rate: $Err = \frac{FP+FN}{TP+FP+FN+TN}$

In the present work, since the purpose is to analyze the classifier behavior on each individual class, we adopt the TPR (or a^+) and the TNR (or a^-).

4 Experimental Data Sets and Results

With the aim of analyzing the behavior of each classifier in situations of imbalance and overlap, two groups of experiments have been carried out. In both cases, pseudo-random bivariate patterns have been generated following a uniform distribution in a square of length 100. There are 400 negative examples and 100 patterns from the minority class, keeping the overall majority/minority ratio equal to 4 in all cases.

The experiments have been performed using the Weka toolkit [16] with the learning algorithms described in Sect. 2, that is, 1-NN, NBC, MLP, J48 (a reimplementation of C4.5), RBF, and SVM. We have adopted a 10-fold cross-validation method: each data set was divided into ten equal parts, using nine folds as the TS and the remaining block as an independent test set. This process has been repeated ten times and the results correspond to the average over the 100 runs.

4.1 Constant Imbalance with Increasing Overlap

This experiment will be over a collection of six data sets with increasing overlap. In all cases, the positive examples are defined on the X-axis in the range [50..100], while the majority class instances are generated in [0..50] for 0% of overlap, [10..60] for 20%, [20..70] for 40%, [30..80] for 60%, [40..90] for 80%, and [50..100] for 100% of overlap. Fig. 1 illustrates two of these data sets. It is expected a similar behavior of all classifiers since in the overlap region, the minority class is also under-represented.
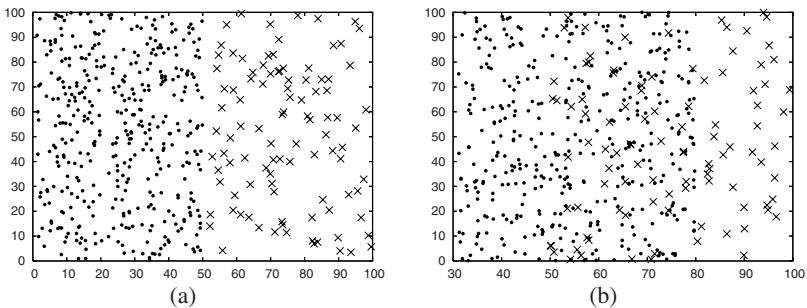
Fig. 1. Two different levels of class overlapping: (a) 0% and (b) 60%

The analysis of Fig. 2 allows to point up a number of results. First, it should be reminded that the majority/minority ratio keeps constant for all data sets. Despite this, the accuracy on the minority class varies in function of the overlap level. While a^+ is close to 100% over the data set with no overlap, it drastically degrades as the overlapping increases (independently of the algorithm used). This corroborates the conclusions of other investigations stating that the loss of classifier performance is not especially due to class imbalance, but to other factors (e.g., overlapping).

Another important observation is the different behavior of the 1-NN classifier on the majority class when compared to the rest of algorithms. In the case of 1-NN,
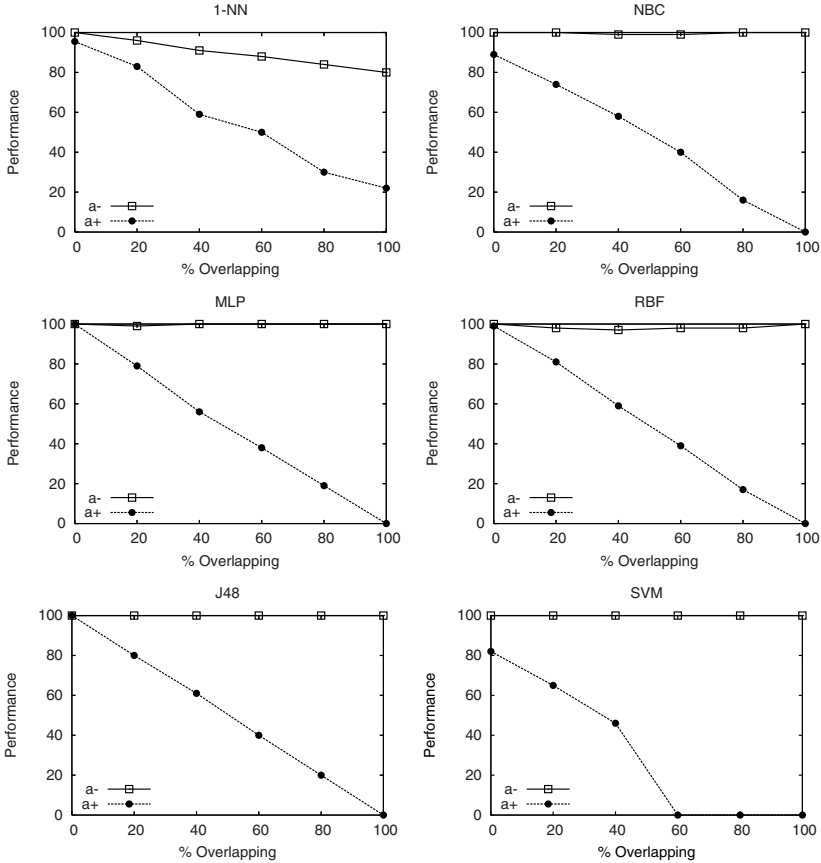
Fig. 2. Classifier performances on each class for the first experiment

the increase of overlapping produces a degradation of the accuracy on the majority class (a^-), due to the local nature of this classifier. Oppositely, the algorithms based on a more global learning keep the a^- close to 100% independently of the overlap degree.

In order to measure whether differences between each pair of classifiers are significant or not, a one-tailed paired t-test has been used as implemented in Weka. Table 2 gives a comparison among the learning algorithms for each individual class. The three values in each entry of this table refer to how many times the algorithm of the column has been significantly-better/same/significantly-worse than the classifier of the row. As can be seen, there exist statistically significant differences when comparing 1-NN with the remaining algorithms. For example, NBC, MLP, J48 and SVM on the majority class have been better than 1-NN in five data sets, whereas on the minority class they have been clearly worse. Comparisons with NBC, MLP, RBF and J48 reveal that in general, differences are not statistically significant. On the minority class, SVM has been significantly worse than any other algorithm.

Table 2. Statistical comparison of the classifiers used in the first experiment

	NBC		MLP		RBF		J48		SVM	
	a^-	a^+	a^-	a^+	a^-	a^+	a^-	a^+	a^-	a^+
1NN	5/1/0	0/1/5	5/1/0	0/3/3	5/1/0	0/3/3	5/1/0	0/3/3	5/1/0	0/0/6
NBC			0/6/0	1/5/0	0/4/2	2/4/0	0/6/0	2/4/0	0/6/0	0/1/5
MLP					0/3/3	0/6/0	0/6/0	1/5/0	0/6/0	0/1/5
RBF							3/3/0	0/6/0	4/2/0	0/1/5
J48									0/6/0	0/1/5

4.2 Changing the Imbalance in the Overlap Region

The second experiment uses a collection of five data sets in which the minority class becomes more representative than the majority one in the overlap region. The aim of this is to analyze the behavior of the classifiers when the overall imbalance is different from the imbalance in the overlap region. To this end, the 400 negative examples have been defined on the X-axis to be in the range [0..100] in all data sets, while the 100 positive cases have been generated in the ranges [75..100], [80..100], [85..100], [90..100], and [95..100] (see Fig. 3 for two examples). The number of elements in the overlap region varies from no local imbalance in the first case, where both classes have the same number of patterns and density, to a critical inverse imbalance in the last case, where the minority class appears as majority in the overlap region due to an increase in density.
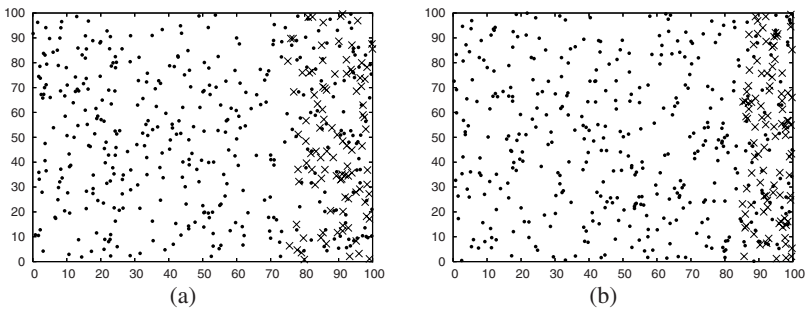
Fig. 3. Two data sets used in the second experiment: (a) [75..100] and (b) [85..100]. Note that the minority class is much denser in the latter case where its samples are confined in a smaller space.

Although in general, the behavior of all classifiers on the minority class improves when this class is denser, thus suggesting the influence of the imbalance in the overlap region, Fig 4 provides some interesting, even surprising results. While the 1-NN performance on the majority class is clearly better than that on the minority one, the other classifiers show a very different behavior. It is especially worth pointing up the results achieved by NBC, in which a^+ is higher than a^- over all data sets. A similar behavior is shown by J48, except when both classes are equally represented in the overlap region (75–100). In this case, the accuracy on the minority class abruptly drops down about
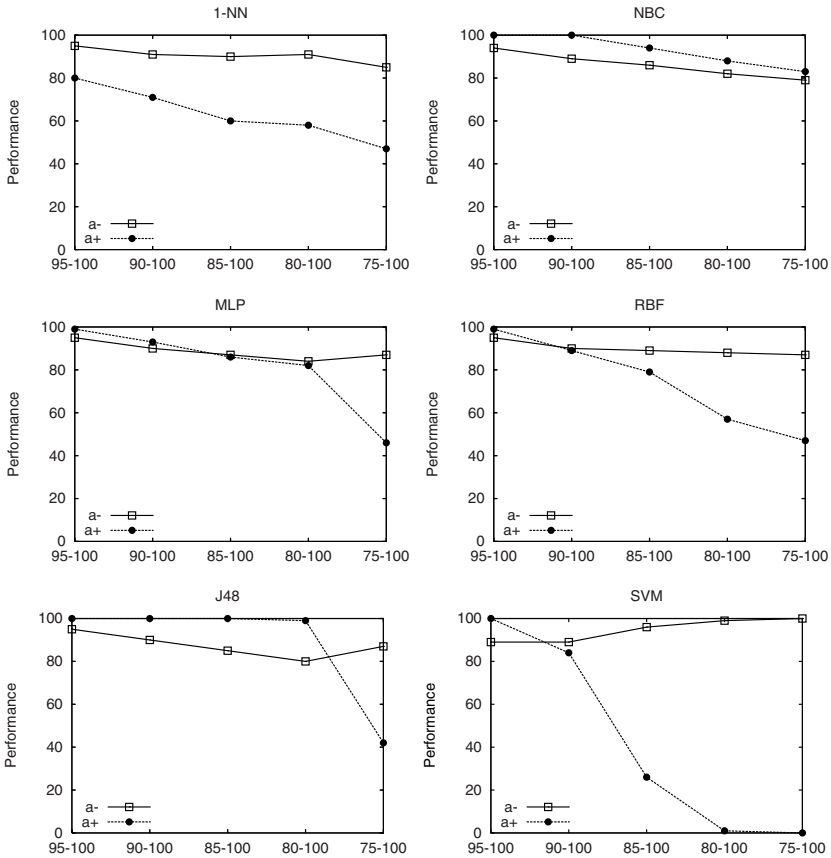
Fig. 4. Classifier accuracies on each class for the second experiment

50 points. Results on SVM show very high accuracy on the minority class for the case [95–100], and close to 0% when this class becomes less dense.

With respect to MLP and RBF, a^+ keeps superior to a^- for the cases in which the majority class is under-represented in the overlap region. Nevertheless, when the number of negative examples is close to the number of positive patterns, the accuracy on the minority class rapidly degrades. In summary, one can observe that in most cases, the performance of NBC, MLP, RBF and J48 on the minority class is higher than that of the majority class, whereas 1-NN and SVM exhibit the opposite behavior. This can be explained by the data characteristics and the operation of both these classifiers. The most surprising effect is on SVM, where a^+ drops down rapidly as the imbalance ratio in the overlap region approaches the overall imabalce.

Analyzing the results in Table 3, it has to be noted that in most cases all classifiers are significantly better than 1-NN in a^+, while there are no significant differences in a^- (except with respect to NBC and SVM). On the other hand, when comparing NBC,

Table 3. Statistical comparison of the classifiers used in the second experiment

	NBC		MLP		RBF		J48		SVM	
	a^-	a^+	a^-	a^+	a^-	a^+	a^-	a^+	a^-	a^+
1NN	0/1/4	5/0/0	0/3/2	4/1/0	0/5/0	3/2/0	0/3/2	4/1/0	3/1/1	2/0/3
NBC			2/3/0	0/3/2	4/1/0	0/1/4	0/4/1	2/2/1	3/1/1	0/1/4
MLP					1/4/0	0/4/1	0/3/2	3/2/0	3/1/1	0/2/3
RBF							0/3/2	3/2/0	3/1/1	0/2/3
J48									3/1/1	0/1/4

MLP, RBF and J48, it seems that there are very few differences. It can be mentioned that the RBF accuracy on the minority class has been significantly worse than that of the NBC four times, while significantly better in the case of a^- also four times. In general, SVM shows the most significant difference in both a^+ (worse) and a^- (better).

5 Conclusions and Future Work

In the framework of imbalanced data sets, recent studies have concluded that performance degradation is not solely caused by class imbalance, but is also related to class overlapping and other data characteristics. In the present work, we have conducted an empirical analysis with the aim of establishing the behavior of several classifiers under combined situations of class imbalance and class overlap. The algorithms here studied correspond to representatives of widely-used models in order to draw more general conclusions: 1-NN, NBC, MLP, RBF, J48, and SVM.

The experiments carried out have revealed some interesting results. First, it has been corroborated that the class imbalance is not a problem by itself, but the loss of performance is also related to other critical factors (class overlap, small disjoints). Second, the combined effects of imbalance and overlap strongly depend on the characteristics of each classifier. Third, it has been observed that 1-NN and SVM are very sensitive to noise in the data set, while NBC seems to be the most tolerant to it. Finally, it has been shown that in certain uncommon situations (like that in the second experiment), the results are quite different from those expected in an imbalanced scenario, that is, the performance on the majority class appears poorer than that on the minority class.

Future research includes an extension of this study to real-world problems. Also, the present work should be complemented with the analysis of other important factors that can strongly affect the classifier performance in imbalanced domains. In particular, we are especially interested in exploring the effects of feature dimensionality. Finally, the use of classifier ensembles with the aim of exploiting the main characteristics of each individual classifier seems an interesting field to be further investigated.

Acknowledgment

References

1. Barandela, R., Sánchez, J.S., García, V., Rangel, E.: Strategies for learning in class imbalance problems. Pattern Recognition 36, 849–851 (2003)
2. Batista, G.E., Prati, R.C., Monard, M.C.: Balancing strategies and class overlapping. In: Proc. 6th Intl. Symposium on Intelligent Data Analysis, Madrid, Spain, pp. 24–35 (2005)
3. Bishop, C.: Neural Networks for Pattern Recognition. Oxford University Press, New York (1995)
4. Buhmann, M., Albowitz, M.: Radial Basis Functions: Theory and Implementations. Cambridge University Press, Cambridge (2003)
5. Chawla, N.V., Bowyer, K.W., Hall, L., Kegelmeyer, W.P.: SMOTE: synthetic minority over-sampling technique. Journal of Artificial Intelligence Research 16, 321–357 (2002)
6. Cover, T.M., Hart, P.E.: Nearest neighbor pattern classification. IEEE Trans. on Information Theory 13, 21–27 (1967)
7. Domingos, P.: Metacost: a general method for making classifiers cost-sensitive. In: Proc. 5th Intl. Conf. on Knowledge Discovery and Data Mining, San Diego, CA, pp. 155–164 (1999)
8. Duda, R.O., Hart, P.E., Stork, D.G.: Pattern Classification and Scene Analysis. John Wiley & Sons, New York (2001)
9. Japkowicz, N., Stphen, S.: The class imbalance problem: a systematic study. Intelligent Data Analysis 6, 40–49 (2002)
10. Jo, T., Japkowicz, N.: Class imbalances versus small disjuncts. ACM SIGKDD Explorations Newsletters 6, 40–49 (2004)
11. Kubat, M., Matwin, S.: Adressing the curse of imbalanced training sets: one-sided selection. In: Proc. 14th Intl. Conf. on Machine Learning, Nashville, USA, pp. 179–186 (1997)
12. Orriols, A., Bernadó, E.: The class imbalance problem in learning classifier systems: a preliminary study. In: Proc. of Conf. on Genetic and Evolutionary Computation, Washington DC, USA, pp. 74–78 (2005)
13. Prati, R.C., Batista, G.E., Monard, M.C.: Class imbalance versus class overlapping: an analysis of a learning system behavior. In: Proc. 3rd Mexican Intl. Conf. on Artificial Intelligence, Mexico City, Mexico, pp. 312–321 (2004)
14. Quinlan, J.R.: C4.5: Programs for Machine Learning. Morgan Kaufmann, San Francisco (1993)
15. Vapnik, V., Kotz, S.: Estimation of Dependences Based on Empirical Data. Springer, New York (2006)
16. Witten, I.H., Frank, E.: Data Mining: Practical Machine Learning Tools and Techniques. Morgan Kaufmann, San Francisco (2005)

Fast *k* Most Similar Neighbor Classifier for Mixed Data Based on a Tree Structure

Selene Hernández-Rodríguez, J. Fco. Martínez-Trinidad,
and J. Ariel Carrasco-Ochoa

Computer Science Department
National Institute of Astrophysics, Optics and Electronics
Luis Enrique Erro No. 1, Sta. María Tonantzintla, Puebla, CP: 72840,
México
{selehdez,ariel,fmartine}@inaoep.mx

Abstract. In this work, a fast *k* most similar neighbor (*k-MSN*) classifier for mixed data is presented. The *k* nearest neighbor (*k-NN*) classifier has been a widely used nonparametric technique in Pattern Recognition. Many fast *k-NN* classifiers have been developed to be applied on numerical object descriptions, most of them based on metric properties to avoid object comparisons. However, in some sciences as Medicine, Geology, Sociology, etc., objects are usually described by numerical and non numerical features (mixed data). In this case, we can not assume the comparison function satisfies metric properties. Therefore, our classifier is based on search algorithms suitable for mixed data and non-metric comparison functions. Some experiments and a comparison against other two fast *k-NN* methods, using standard databases, are presented.

Keywords: Nearest Neighbors Rule, Fast k-Most Similar Neighbors Search, Mixed Data.

1 Introduction

The *k-NN* [1] rule has been a widely used nonparametric technique in Pattern Recognition. However, in some applications, the exhaustive comparison between the new object to classify and the objects in *T* becomes impractical. Many fast *k-NN* classifiers have been designed to avoid this problem; most of them were designed for numerical object descriptions and based on metric properties.

In some applications, the objects are described by numerical and non numerical features (mixed data). In this case, we can not assume the comparison function satisfies metric properties and therefore, we can not use most of the methods proposed for numerical objects. Thus, if a metric is not available but a comparison function that evaluates the similarity between a pair of objects could be defined, the objective would be to find the *k* most similar neighbors (*k-MSN*) and use them for classifying.

The *k-MSN* classifier is based on a training set *T* of *N* objects. Each object is described by *d* features, which can be numerical or non numerical. Given a new object *Q* to classify, the goal consists in finding the *k-MSN* according to a comparison function

and assigning to Q the majority class of its k nearest neighbors. The exhaustive search of the *k-MSN*, as occurs with the *k-NN*, could be very expensive if T is large. Therefore, in this paper we introduce a fast *k-MSN* classifier based on a tree structure, which does not assume the comparison function satisfies any metric property.

This paper is organized as follows: Section 2 provides a brief review of fast *k-NN* classifiers based on tree structures. In Section 2.1 the comparison functions used in this work are described. In Section 3 our fast *k-MSN* classifier is introduced. In Section 4 we report experimental results obtained using our classifier. Finally, in Section 5 we present some conclusions and future work.

2   Related Work

In this section we describe some methods for solving the fast nearest neighbor classification problem.

To avoid the exhaustive search, some methods, based on tree structures, have been proposed. In a preprocessing step, the objects in T are organized in a tree structure. In the classification step, the tree is traversed to find the *k-NN*. The speed up is obtained while the exploration of some parts of the tree is avoided. One of the first fast *k-NN* classifiers, that uses a tree structure, was proposed by Fukunaga and Narendra [2].

In the classifier proposed by Fukunaga and Narendra, each node p of the tree contains four features, which are: the set of objects in the node p (S_p), the number of objects in p (N_p), the centre of the node (M_p) and finally the maximum distance between the centre of p and the objects in the node p (R_p). Given a new object Q to classify, Fukunaga's fast classifier searches the *NN* based on a branch and bound method to traverse the tree. Two pruning rules are used to decide whether a node or an object of the tree is evaluated or not. These rules are based on the triangle inequality. The first pruning rule for nodes of the tree is:

$$B + R_p < D(Q, M_p) \tag{1}$$

Where B is the distance between Q and the current *NN* and D is the distance function. The second pruning rule is applied to the objects that belong to a leaf node of the tree, in order to decide whether or not to compute the distance from the sample Q to the object from the node or not. The pruning rule for every object $o_i \in S_p$ is:

$$B + D(o_i, M_p) < D(Q, M_p) \tag{2}$$

The objects that satisfy condition (2) can not be closer than the current nearest neighbour and therefore, the distance to Q is not computed. The search process finishes when all nodes in the tree have been evaluated or eliminated by the first pruning rule. Finally, the class of the *NN* found in the search process is assigned to Q. An extension to *k-NN* is also proposed in [2], where, in the search process, B is the distance between Q and the current *k-NN* instead of the current *1-NN*. In this case, the majority class of its k nearest neighbors is assigned to Q.

In the last years, some methods have been developed to improve the Fukunaga and Narendra classifier [3,4,5,6,7,8]. The improvements proposed in [3,4,5,6,8] are exact methods to find the *k-NN*. However, finding the *k-NN* (even using a fast method) is a

slow process for some tasks, therefore in [7] Moreno-Seco proposed a fast approximate *k-NN* classifier, where Fukunaga's first pruning rule is modified in order to finish the search when the current nearest neighbor is not too far from the exact nearest neighbor:

$$(1+e)(D(Q,M_p)-R_p) > B \qquad (3)$$

Where *e* is an error margin that allows to decrease the number of comparisons. In this process, lower classification run times are obtained, but reducing the classification accuracy. However, Moreno-Seco's classifier also relies on metric properties to avoid comparisons.

All the mentioned methods, based on tree structures, were designed to work with numerical data when the object comparison function satisfies metric properties.

2.1 Comparison Functions for Mixed Data

In this work, in order to compare objects, the function *F* [10] was used. Let us consider a set of objects $\{O_1, O_2, ..., O_N\}$, each of them described by *d* attributes $\{x_1, x_2, ..., x_d\}$. Each feature could be numerical or non numerical. The function *F* is defined as follows:

$$F(O_1,O_2) = 1 - \frac{|\{x_i \mid C_i(x_i(O_1), x_i(O_2)) = 1\}|}{d} \qquad (4)$$

For qualitative data $C_i(x_i(O_1), x_i(O_2))$ is defined as follows:

$$C_i(x_i(O_1),x_i(O_2)) = \begin{cases} 1 & If \ \ x_i(O_1) = x_i(O_2) \ and \ neither \ x_i(O_1) \ nor \ x_i(O_2) \\ & \qquad is \ a \ missing \ value \\ 0 & otherwise \end{cases} \qquad (5)$$

For quantitative data $C_i(x_i(O_1), x_i(O_2))$ is defined as follows:

$$C_i(x_i(O_1),x_i(O_2)) = \begin{cases} 1 & If \ \ |x_i(O_1) - x_i(O_2)| < \sigma_i \ and \ neither \ x_i(O_1) \ nor \ x_i(O_2) \\ & \qquad is \ a \ missing \ value \\ 0 & otherwise \end{cases} \qquad (6)$$

Where, σ_i is the standard deviation of the attributes x_i. We also used the functions: *HVDM* and *HOEM*, described in [11] and [12] respectively, which allow us to compare objects described by mixed data. Using the functions *F*, *HVDM* and *HOEM* the most similar neighbor is the one that minimizes the function.

3 Proposed Classifier

In this section, an approximate fast *k-MSN* classifier which considers object described by mixed data is introduced. The classifier consists of two phases. The first one, or preprocessing phase, is the construction of a tree structure from *T*, using suitable strategies for mixed data. In the second phase, two fast approximate *k-MSN* search algorithms are used, which are independent of metric properties of the comparison function.

3.1   Preprocessing Phase

In this phase, the training set is hierarchically decomposed to create a tree structure. The *C-Means with Similarity Functions* algorithm *(CMSF)*, which is an extension of the *C-Means* algorithm to work with mixed data, is used. In the original *C-Means* the mean of the objects is considered as the centre of the cluster, meanwhile in *CMSF* an object, which represents the cluster, is used as the centre of it (see [10] for details).

The node 0 (root) of the tree contains the whole set *T*. In order to create the following levels of the tree, each node *n* of the tree is divided in *C* clusters ($c_1,\dots$, c_C), in such way that each cluster c_i represents a descendant node n_i of *n*. Each node is divided again and this process is repeated until a stop criterion is satisfied. In figure 1 the algorithm to construct the tree is described.

Each node *p* of the tree contains three features which are: the set of objects that belong to that node S_p, the number of objects in that node N_p and unlike Fukunaga's and Moreno-Seco's methods a representative object of the node Rep_p.

```
1.      CurrentNode = 0
2.      NodesToDivide = CurrentNode
3.      p = 1
4.      While |NodesToDivide| ≠ 0
5.          CurrentNode = NodesToDivide [1]
6.          To divide the objects belonging from CurrentNode in C clusters
7.          For every cluster c =1:C
8.              cluster(c) = node_p of the tree
9.              node_p is a child of CurrentNode
10.             Compute the features of node_p: S_p, N_p, Rep_p
11.             If a Stop Criterion is satisfied, then node_p is a leaf
12.             Else, node_p is added to the list NodesToDivide
13.             p = p+1
14.         End for every
15.         Eliminate CurrentNode from NodesToDivide
16.     End while
```

Fig. 1. Tree building algorithm

Three different stop criteria are proposed:

1. *Stop criterion based on the node size* (*SCNS*): in this criterion, if a node contains less than *SC* objects ($N_p \leq SC$), then the node is considered as a leaf. This criterion is used in some other works [3,4 and 7]. To implement this criterion, lines 7-14 of the algorithm described in figure 1, are replaced by the algorithm described in figure 2.

```
For every cluster c =1:C
    cluster(c) = node_p of the tree,      node_p is a child of CurrentNode
    Compute the features of node_p: S_p, N_p, Rep_p
    If (N_n ≤ CP) then node_p is a leaf,
    Else node_p is added to the list NodesToDivide
    p = p+1
End for every
```

Fig. 2. Stop criterion based on the node size (SCNS)

2. *Stop criterion based on non homogeneous nodes* (*SCNHN*): it is proposed to consider the number of objects in a cluster and the class of those objects. In this case, if certain percentage of the objects have the same class, then the node is considered a

leaf and is marked with the majority class (even if $N_p > SC$). To implement this criterion, lines 7-14 of the algorithm described in figure 1, are replaced by the algorithm described in figure 3. When the node is generalized by the majority class, through *SCNHN*, an error is introduced. Therefore, a third criterion is proposed.

3. *Stop criterion based on homogeneous nodes* (*SCHN*): In this case, if certain percentage of the objects in a cluster belongs to the same class, two nodes are created. Using the objects that belong to the majority class, a leaf node is created and is marked with the majority class. The rest of the objects are assigned to a second node, which is considered as a leaf if $N_p \leq SC$, otherwise, this node will be divided again. A pseudocode of this criterion is shown in figure 4.

```
For every cluster c =1:C
        cluster(c) = nodep of the tree,       nodep is a child of  CurrentNode
            Compute the features of nodep: Sp, Np, Repp
        For every  j = 1: No.Classes
              PercC (j) = Percentage of the objects in nodep that belong to the class j
            End for every
        PercM  = max (PercC (j),  ∀ j∈[1, No. Classes] )
        If (PercM ≥ thres), then nodep  is a leaf,   NodeCriterion(n) = true
            ClassNode (n) = the majority class of nodep
        Else  If  (Nn ≤ CP) then nodep  is a leaf,    NodeCriterion(n) = false
              Else nodep  is added to the list NodesToDivide
        p = p+1
    End for every
```

Fig. 3. Stop criterion based on non homogeneous leave (SCNHL)

```
For every cluster c =1:C
        For every  j = 1: No.Classes
              PercC (j) = Percentage of the objects in nodep that belong to the class j
        End for every
        PercM = max (PercC (j),
        If  (PercM ≥ Thres),
              N1 = the set of objects of cluster c that belong to the majority class
              N2 = the rest of the objects
              With N1:
                  Sp = N1, nodep is a leaf,        nodep is a child of  CurrentNode
                  Compute the features of nodep: Np, Repp
                  NodeCriterion(n) = true,   ClassNode (n) = the majority class of nodep
              p = p+1
              With N2:
                  Sp = N2, nodep is a child of  CurrentNode
                  Compute the features of nodep: Np, Repp
                  If  (Nn ≤ CP) then nodep  is a leaf,     NodeCriterion(n) = false
                  Else nodep  is added to the list NodesToDivide
        Else,  if  (Nn ≤ CP) then nodep  is a leaf,    NodeCriterion(n) = false
              Else nodep  is added to the list NodesToDivide
        End if
        p = p+1
    End for every
```

Fig. 4. Stop criterion based on homogeneous leave (SCHL)

3.2   Classification Phase

In this phase, in order to avoid the exhaustive tree traversal, the existing fast *k-NN* classifiers rely on pruning rules (based on metric properties). As we are looking a method applicable when the comparison function does not satisfy metric properties,

the pruning rules proposed by Fukunaga and Moreno-Seco would not be appropriate; therefore we propose to stop the search when a leaf of the tree is reached. In the first method (*k-MSN* local search) we propose to use a depth-first search and in the second method (*k-MSN* global search) we propose to use a best-first search. The proposed methods for searching the *k-MSN* are described below:

k-MSN local search method: It begins at the root of the tree, following the path of the most similar node and finishes on a leaf of the tree. A list of the *k-MSN* is stored and updated during the tree traversal. When a leaf node *l* is reached, if *l* is marked with the majority class, then only the representative object Rep_l is considered to update the *k-MSN*. In other case, a local exhaustive search in the node is done and the list of *k-MSN* is finally updated. (see pseudocode in figure 5).

```
Current Node = node 0
While Current Node ≠ Leaf
      DesNodes = descendant nodes of the Current Node.
   MostSimilar Node =    min      (F(Q, Rep_p))
                      ∀ node_p ∈ DesNodes

         Current Node = MostSimilarNode       Update k-MSN  considering MostSimilarNode
End while
If  NodeCriterion(Current Node) = true,
         sim = F(Q, Rep_CurrentNode)           Update k-MSN  considering Rep_CurrentNod
Else,  perform an exhaustive search with the objects in the Current Node  and update k-MSN
Class(Q)=majority class of the k-MSN
```

Fig. 5. *k-MSN* local search method

When a leaf is reached, if the list does not have *k MSN*'s, then the tree traversal makes backtracking to explore nodes closer to *Q*, in order to find *k MSN*'s.

k-MSN global search method: It begins at the root of the tree, comparing *Q* against the descendant nodes of the root, which are added to a list (*List_tree_traversal*). After that, *List_tree_traversal* is sorted in such way that the most similar node to *Q* is in the first place. The most similar node is eliminated from *List_tree_traversal* and its descendant nodes are compared against *Q*, and added to *List_tree_traversal*, which is sorted again. In this search it is possible to reconsider nodes in levels of the tree already traversed if the first node of *List_tree_traversal* belongs to a previous level in the tree (see pseudocode in figure 6). During the tree traversal, another list (*List_k-MSN*) containing the *k* current *MSN* is stored and updated.

```
Current Node = node 0
List_tree_traversal = {0}
While Current Node ≠ Leaf
      Current Node = List_tree_traversal [1]       Delete Current Node  from List_tree_traversal
      DesNodes = descendant nodes of the Current Node.
      Compute the similarity between Q and the nodes in DesNodes
      Add the nodes to List_tree_traversal          Update List_k-MSN
      Order List in such way that the most similar object to Q is the first element of the list.
End while
If  NodeCriterion(Current Node) = true,
         sim = F(Q, Rep_CurrentNode)           Update List_k-MSN, considering Rep_CurrentNod
Else,  perform an exhaustive search with the objects in the Current Node  and update k-MSN
Class(Q)=majority class of the k-MSN
```

Fig. 6. *k-MSN* global search method

When a leaf is reached, if *List_k-MSN* does not contain *k-MSN*, then the first element in *List_tree_traversal* is considered to follow a new route in the tree traversal. The process stops when *List_k-MSN* contains *k-MSN*.

However, using both search methods (*k-MSN* global and *k-MSN* local), it is quite difficult not to have *k MSN*'s during the tree traversal, in applications where the training set is large.

After finding *k-MSN*, the majority class is assigned to the new sample *Q*.

4   Experimental Results

In this section, we report the obtained results of applying the proposed fast approximate *MSN* classifier over 9 datasets from the *UCI* repository [15]. Three of these datasets are numerical (Glass, Iris and Wine), two are non numerical (Hayes and Bridges) and four are mixed (Hepatitis, Zoo, Flag, Echocardiogram). In all the experiments 10-fold-cross-validation was used.

In order to compare our method, Fukunaga's [2] and Moreno-Seco's [7] classifiers were adapted. The adaptation consists in the use of the same tree structure proposed in Section 3 and the same function suitable to work with mixed data, instead of a distance function. There are other methods based in tree structures [13, 14]. However, it is not possible to adapt these methods to work with similarity functions because these methods involve techniques such as *PCA* which are only applicable to numerical data.

The compared five fast *k-NN (k-MSN)* classifiers used in the experimentation were:
1.   The exhaustive *k-NN* classifier (using a dissimilarity function)
2.   Adapted Fukunaga's *k-NN* classifier
3.   Adapted Moreno-Seco's *k-NN* classifier
4.   The proposed classifier using *k-MSN* local search
5.   The proposed classifier using *k-MSN* global search

To compare the classifiers, the accuracy and the number of comparisons between objects were considered.

Before using adapted Moreno-Seco's classifier, some tests with different values of the error margin *e* (*e*=1, 10 and 20) were proved. These experiments were carried out for the three stop criteria described in Section 3.1: *SCNS* (with *SC*=1, 5 and 20), *SCNHL* (with percentage threshold=50, 70 and 100) and *SCHL* (with percentage threshold=50, 70 and 100), were proved. In every experiment, different values of *C* (*C*=3, 5, no. of classes, 4* no. of classes, (.1)* no. of objects and (.3)* no. of objects) in the *CMFS* algorithm, were also proved. In the classification phase, all of the experiments were repeated using *k* = 1, 3 and 5 *MSN*. During the tree construction and the classification phase, the three dissimilarity functions: *HVDM, F* and *HOEM* were tested.

In all of these experiments, while the error margin *e* grows, the number of object comparisons decreases. In the next experiments, adapted Moreno-Seco's classifier was used with *e*=20, because this value needed the smallest number of comparisons with a slightly accuracy reduction.

The parameter *C* of the *CMSF* algorithm corresponds to the number of branches of the nodes in the tree. In order to select the best value of *C*, *C*=3, 5, no. of classes, 4* no. of classes, (.1)* no. of objects and (.3)* no. of objects, were proved. In the tree

construction phase, the three stop criteria described in Section 3.1: *SCNS* (with *SC* = 1, 5 and 20), *SCNHL* (with percentage threshold=50, 70 and 100) and *SCHL* (with percentage threshold=50, 70 and 100), were proved. In the classification phase, all of the experiments mentioned before were repeated using *k* = 1, 3 and 5 *MSN*. During the tree construction and the classification phase, all experiments mentioned before, the three dissimilarity functions: *HVDM, F* and *HOEM* were tested.

According to these experiments, the accuracy does not vary too much with the different values of *C*. However, the number of comparisons between objects increases for the adapted Fukunaga's classifier when *C* grows. In the next experiments *C*=3 was used, because there is not a big variation of the accuracy and the number of objects comparisons is reduced for adapted Fukunaga's and Moreno-Seco's classifiers.

Another important parameter in the tree construction algorithm is the stop criterion. To evaluate the stop criterion, all datasets mentioned before were used. In this experiment, the *HVDM* function and 1-*MSN* were considered.

First, the performance of the classifiers, using the first stop criterion (*SCNS*), was evaluated according different values of the *SC* parameter. From this experiments, *SC*=20 was chosen, since the biggest objects comparison percentage reduction is achieved.

The performance of the classifiers, using the criterion based on non homogeneous nodes (*SCNHN*) was evaluated with a percentage threshold equal to 50, 70, 80 and

Table 1. Evaluation of the different classifiers using *HVDM* function, with *k* = 1, 3 and 5 *MSN*

General averages	Exhaustive *k-NN* classifier		Adapted Fukunaga's *k-NN* classifier		Adapted Moreno-Seco's *k-NN* classifier		Proposed classifier using *k-MSN* local search		Proposed classifier using *k-MSN* global search	
	%Acc	%Com	%Acc	%Com	%Acc	%Com	%Acc	%Com	%Acc	%Com
k=1										
Hep	82,67	100	81,33	126,58	80,71	88,59	82,67	15,75	82,63	13,52
Zoo	97,09	100	94,18	68,25	94,18	23,90	93,09	12,46	93,09	16,76
Flag	53,05	100	50,39	50,38	50,39	44,12	47,84	10,56	48,37	17,41
Echo	83,41	100	81,10	110,29	81,81	75,29	84,89	13,54	84,89	18,50
Hayes	85,71	100	85,25	56,06	84,95	23,25	85,71	14,85	85,71	12,97
Brid	61,82	100	56,09	68,20	54,00	51,55	55,09	9,54	55,09	15,46
Glass	70,06	100	70,06	41,03	67,29	37,80	66,30	7,65	66,30	6,16
Iris	94,67	100	94,67	24,95	92,67	21,37	94,00	14,55	94,00	11,17
Wine	95,49	100	95,49	40,00	95,49	30,73	94,41	11,05	94,41	7,93
General Avg.	**80,44**	**100**	**78,73**	**65,08**	**77,94**	**44,07**	**78,22**	**12,22**	**78,28**	**13,32**
k=3										
Hep	82,67	100	81,29	126,58	81,33	88,59	82,67	15,75	83,92	13,52
Zoo	96,09	100	94,09	68,25	91,09	23,90	95,09	12,46	95,09	16,76
Flag	53,53	100	53,53	50,38	53,53	44,12	50,95	10,56	51,47	17,41
Echo	82,64	100	79,62	110,29	79,56	75,29	80,38	13,54	80,38	18,50
Hayes	85,71	100	85,71	56,06	84,95	23,25	85,71	14,85	85,71	12,97
Brid	57,64	100	56,91	68,20	53,91	51,55	55,91	9,54	55,91	15,46
Glass	68,70	100	68,70	41,03	68,11	37,80	68,66	7,65	68,66	6,16
Iris	94,00	100	94,00	24,95	93,33	21,37	94,00	14,55	94,67	11,17
Wine	95,52	100	95,52	40,00	95,46	30,73	94,41	11,05	93,86	7,93
General Avg.	**79,61**	**100**	**78,82**	**65,08**	**77,92**	**44,07**	**78,64**	**12,22**	**78,85**	**13,32**
k=5										
Hep	84,54	100	83,25	126,58	85,25	88,59	78,83	15,75	78,17	13,52
Zoo	94,09	100	90,18	68,25	88,18	23,90	92,09	12,46	92,09	16,76
Flag	53,66	100	53,63	50,38	53,55	44,12	52,58	10,56	53,11	17,41
Echo	86,43	100	85,66	110,29	85,60	75,29	86,43	13,54	86,43	18,50
Hayes	86,43	100	86,43	56,06	84,89	23,25	85,77	14,85	85,77	12,97
Brid	60,09	100	58,09	68,20	56,09	51,55	56,18	9,54	56,27	15,46
Glass	63,55	100	63,55	41,03	62,64	37,80	63,53	7,65	63,53	6,16
Iris	95,33	100	95,33	24,95	94,00	21,37	94,67	14,55	94,67	12,52
Wine	97,19	100	97,19	40,00	93,82	30,73	94,41	11,05	94,41	7,93
General Avg.	**80,15**	**100**	**79,26**	**65,08**	**78,22**	**44,07**	**78,28**	**12,22**	**78,27**	**13,47**

100. The accuracy is slightly reduced using *SCNHN* (with percentage threshold=50, 70 and 80) in comparison with the criterion based on the node size (*SCNS*, with *SC*=20). However, the comparisons percentage is reduced using *SCNHN*. Using *SCNHN* and *SCHN*, when the percentage threshold grows, both, the accuracy and the objects comparisons percentage increase.

When the percentage threshold is 100, using *SCHN* and *SCNHN* the obtained accuracy and the comparisons percentage are the same, because in both cases, a leaf is marked with the majority class only when all of the objects in the node belong to the same class. In the next experiments, *SCHN* with percentage threshold =100 (which is the same as using *SCNHN*, with percentage threshold =100) and *SC*=20, were used.

In table 1, the obtained accuracy (**%Acc**) and the percentage of objects comparisons (**%Com**) are shown, for *k*=1,3, 5 in *k-MSN* process. The number of comparisons performed by exhaustive search is considered as the 100 percent of comparisons. Using *k*=1, the higher accuracy in average is obtained with the exhaustive *NN* classifier.

The experiments with different *k-MSN* were repeated using *F* and *HOEM* functions. The performance of the different classifiers is similar for *F* and *HOEM* functions. Using *HOEM* function, Fukunaga's classifier is an exact method, it happens because *HOEM* function is a metric. However, for all classifiers the lower accuracy is obtained using *HOEM* function.

In figure 7 a graphic of the accuracy against the comparisons percentage using the different fast *NN* (*MSN*) classifiers, with *k*=1, is shown. From this graph, we can see that all the classifiers obtained similar accuracy but the classifiers proposed in this work (using *MSN* local and *MSN* global search) did the smaller number of comparisons.
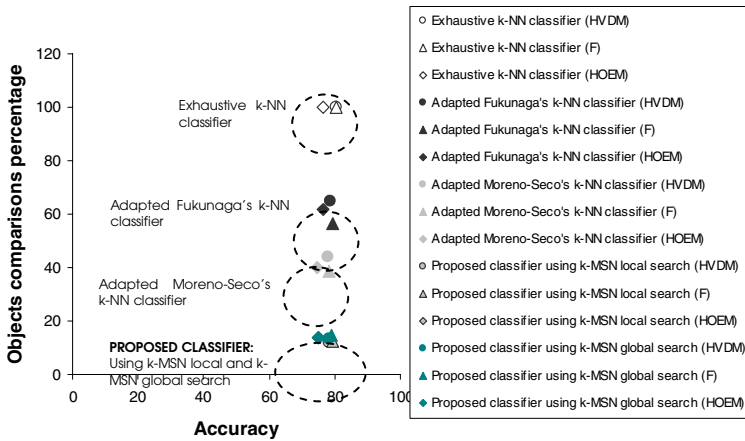
Fig. 7. Accuracy against the comparisons percentage using the different classifiers and three different comparison functions

5   Conclusions

In practical problems, it is frequent to find non numerical object descriptions or even mixed data (numerical and non numerical). Therefore, it is important to use methods that allow us to work with these kind of features.

In this work, an approximated fast *k-MSN* classifier for mixed data was proposed. In order to compare our method, Fukunaga's and Moreno-Seco's classifiers were implemented using the same object comparison functions for mixed data. Based on our experimental results, in comparison with Fukunaga's and Moreno-Seco's classifiers, our method (using *MSN* local and *MSN* global search), obtained a big reduction on the number of comparisons between objects with only a slightly accuracy reduction.

As future work, we plan to look for a pruning rule non based on metric properties, which allow us to reduce the number of objects comparisons, but doing an exhaustive tree traversal during the search process.

References

1. Cover, T.M., Hart, P.E.: Nearest neighbor pattern classification. Trans. Information Theory 13, 21–27 (1967)
2. Fukunaga, K., Narendra, P.: A branch and bound algorithm for computing k-nearest neighbors. IEEE Trans. Comput. 24, 743–750 (1975)
3. Kalantari, I., McDonald, G.: A data structure and an algorithm for the nearest point problem. IEEE Trans. Software Eng. 9, 631–634 (1983)
4. Omachi, S., Aso, H.: A fast algorithm for a k-nn Classifier based on branch and bound method and computational quantity estimation. Systems and Computers in Japan 31(6), 1–9 (2000)
5. Gómez-Ballester, E., Mico, L., Oncina, J.: Some Improvements in Tree Based Nearest Neighbor Search Algorithms. In: Sanfeliu, A., Ruiz-Shulcloper, J. (eds.) CIARP 2003. LNCS, vol. 2905, pp. 456–463. Springer, Heidelberg (2003)
6. Gómez-Ballester, E., Mico, L., Oncina, J.: Some approaches to improve tree-based nearest neighbor search algorithms. Pattern Recognition Letters 39, 171–179 (2006)
7. Moreno-Seco, F., Mico, L., Oncina, J.: Approximate Nearest Neighbor Search with the Fukunaga and Narendra Algorithm and its Application to Chromosome Classification. In: Sanfeliu, A., Ruiz-Shulcloper, J. (eds.) CIARP 2003. LNCS, vol. 2905, pp. 322–328. Springer, Heidelberg (2003)
8. Mico, L., Oncina, J., Carrasco, R.: A fast Branch and Bound nearest neighbor classifier in metric spaces. Pattern Recognition Letters 17, 731–739 (1996)
9. MacQueen, J.B.: Some Methods for classification and Analysis of Multivariate Observations. In: Proceedings of 5-th Berkeley Symposium on Mathematical Statistics and Probability, pp. 281–297. University of California Press, Berkeley (1967)
10. García-Serrano, J.R., Martínez-Trinidad, J.F.: Extension to C-Means Algorithm for the use of Similarity Functions. In: 3rd European Conference on Principles and Practice of Knowledge Discovery in Database Proceedings, Prague, Czech, pp. 354–359 (1999)
11. Wilson, D.R., Martínez, T.: Reduction techniques for instance based learning algorithms. Machine Learning. 38, 257–286 (2000)
12. Wilson, D., Martínez, T.: Improve heterogeneous Distance Functions. Journal of Artificial Intelligence Research 6, 1–34 (1997)
13. McNames, J.: A Fast Nearest Neighbor Algorithm Based on a Principal Axis Search Tree. IEEE Transactions on Pattern Analysis and Machine Intelligence 23(9), 964–976 (2001)
14. Yong-Sheng, C., Yi-Ping, H., Chiou-Shann, F.: Fast and versatile algorithm for nearest neighbor search based on lower bound tree. Pattern Recognition Letters (2006)
15. Blake, C., Merz, C.: UCI Repository of machine learning databases. In: Department of Information and Computer Science, University of California, Irvine, CA (1998), http://www.uci.edu/mlearn/databases/

Conditional Mutual Information Based Feature Selection for Classification Task

Jana Novovičová[1,2], Petr Somol[1,2], Michal Haindl[1,2], and Pavel Pudil[2,1]

[1] Dept. of Pattern Recognition,
Institute of Academy of Sciences of the Czech Republic
{novovic,somol,haindl}@utia.cas.cz
http://ro.utia.cz/
[2] Faculty of Management, Prague University of Economics, Czech Republic
pudil@fm.vse.cz
http://www.fm.vse.cz

Abstract. We propose a sequential forward feature selection method to find a subset of features that are most relevant to the classification task. Our approach uses novel estimation of the conditional mutual information between candidate feature and classes, given a subset of already selected features which is utilized as a classifier independent criterion for evaluation of feature subsets. The proposed mMIFS-U algorithm is applied to text classification problem and compared with MIFS method and MIFS-U method proposed by Battiti and Kwak and Choi, respectively. Our feature selection algorithm outperforms MIFS method and MIFS-U in experiments on high dimensional Reuters textual data.

Keywords: Pattern classification, feature selection, conditional mutual information, text categorization.

1 Introduction

Feature selection plays an important role in classification problems. In general, a pattern classification problem can be described as follows: Assume that feature space $\mathcal{X}$ is constructed from D features $X_i, i = 1, \ldots, D$ and patterns drawn from $\mathcal{X}$ are associated with $|\mathcal{C}|$ classes, whose labels constitute the set $\mathcal{C} = \{c_1, \ldots, c_{|\mathcal{C}|}\}$. Given a training data the task is to find a classifier that accurately predicts the label of novel patterns. In practice, with a limited amount of training data, more features will significantly slow down the learning process and also cause the classifier to over-fit the training data because of the irrelevant or redundant features which may confuse the learning algorithm. By reducing the number of features, we can both reduce over-fitting of learning methods and increase the computational speed of classification. We focus in this paper on feature selection in context of classification.

The feature selection task is to select a subset S of d features from a set of available features $X = \{X_i, i = 1, \ldots, D\}$, where $d < D$ represents the desired number of features. All feature selection (FS) algorithms aim at maximizing some performance measure for the given class and different feature subsets S.

Many existing feature selection algorithms can roughly be divided into two categories: *filters* [1], [2] and *wrappers* [3]. Filter methods select features independently of the subsequent learning algorithm. They rely on various measures of the general characteristics of the training data such as distance, information, dependency, and consistency [4]. On the contrary the wrapper FS methods require one predetermined learning algorithm and use its classification accuracy as performance measure to evaluate the quality of selected set of features. These methods tend to give superior performance as they find features better suited to the predetermined learning algorithm, but they also tend to be more computationally expensive. When the number of features becomes very large, the filter methods are usually to be chosen due to computational efficiency. Our interest in this paper is to design a filter algorithm.

Search scheme is another problem in feature selection. Different approaches such as complete, heuristic and random search have been studied in the literature [5] to balance the tradeoff between result optimality and computational efficiency. Many filter methods [6] evaluate all features individually according to a given criterion, sort them and select the best individual features. Selection based on such ranking does not ensure weak dependency among features, and can lead to redundant and thus less informative selected subset of features.

Our approach to FS iteratively selects features which maximize their mutual information with the class to predict, conditionally to the response of any other feature already selected. Our conditional mutual information criterion selects features that are highly correlated with the class to predict if they are less correlated to any feature already selected.

Experiments demonstrate that our sequential forward feature selection algorithm mMIFS-U based on conditional mutual information outperforms the MIFS methods proposed by Battiti [7] and MIFS-U proposed by Kwak and Choi [8], both of which we also implemented for test purposes.

2   Information-Theoretic Feature Selection

In this section we briefly introduce some basic concepts and notions of the information theory which are used in the development of the proposed feature selection algorithm.

Assume a D-dimensional random variable $Y = (X_1, \ldots, X_D) \in \mathcal{X} \subseteq \mathcal{R}^D$ representing feature vectors, and a a discrete-valued random variable C, representing the class labels. In accordance with Shannon's information theory [9], the uncertainty of a random variable C can be measured by entropy $H(C)$. For two random variables Y and C, the conditional entropy $H(C|Y)$ measures the uncertainty about C when Y is known. The amount by which the class uncertainty is reduced, after having observed the feature vector Y, is called the *mutual information*, $I(C, Y)$. The relation of $H(C)$, $H(C|Y)$ and $I(C, Y)$ is

$$I(C,Y) = I(Y,C) = H(C) - H(C|Y) = \sum_{c \in \mathcal{C}} \int_{\mathbf{y}} p(c, \mathbf{y}) \log \frac{p(c, \mathbf{y})}{P(c)p(\mathbf{y})} d\mathbf{y}, \quad (1)$$

where $P(c)$ represents the probability of class C, $\mathbf{y}$ represents the observed feature vector Y, $p(c, \mathbf{y})$ denotes the joint probability density of C and Y.

The goal of classification is to minimize the uncertainty about predictions of class C for the known observations of feature vector Y. Learning a classifier is to increase $I(C, Y)$ as much as possible. In terms of mutual information (MI), the purpose of FS process for classification is to achieve the highest possible value of $I(C, Y)$ with the smallest possible size of feature subsets.

The FS problem based on MI can be formulated as follows [7]: Given an initial set X with D features, find the subset $S \subset X$ with $d < D$ features $S = \{X_{i_1}, \ldots, X_i\}$ that minimizes conditional entropy $H(C|S)$, i.e., that maximizes the mutual information $I(C, S)$.

Mutual information $I(C, S)$ between the class and the features has become a popular measure in feature selection [7], [8], [10], [11]. Firstly, it measures general dependence between two variables in contrast with the correlation. Secondly, MI determines the upper bound on the theoretical classification performance [12],[9].

To compute the MI between all candidate feature subsets and the classes, $I(C, S)$ is practically impossible. So realization of the greedy selection algorithm is computationally intensive. Even in a sequential forward search it is computationally too expensive to compute $I(C, S)$.

To overcome this practical obstacle alternative methods of $I(C, S)$ computation have been proposed by Battiti [7] and Kwak and Choi [13], [8], respectively. Assume that S is the subset of already selected features, $X \setminus S$ is the subset of unselected features. For a feature $X_i \in X \setminus S$ to be selected, the amount of information about the class C newly provided by feature X_i without being provided by the already selected features in the current subset S must be the largest among all the candidate features in $X \setminus S$. Therefore, the conditional mutual information $I(C, X_i|S)$ of C and X_i given the subset of already selected features S is maximized. Instead of calculating $I(C, X_i, S)$, the MI between a candidate for newly selected feature $X_i \in X \setminus S$ plus already selected subset S and the class variable C, Battiti and Kwak and Choi used only $I(C, X_i)$ and $I(X_s, X_i)$, $X_s \in S$.

The estimation formula for $I(C, X_i|S)$ in MIFS algorithm proposed by Battiti [7] is as follows:

$$I_{Battiti}(C, X_i|S) = I(C, X_i) - \beta \sum_{X \in S} I(X_s, X_i). \tag{2}$$

Kwak and Choi [8] improved (2) in their MIFS-U algorithm under the assumption that the class C does not change the ratio of the entropy of X_s and the MI between X_s and X_i

$$I_{Kwak}(C, X_i|S) = I(C, X_i) - \beta \sum_{X \in S} \frac{I(C, X_s)}{H(X_s)} I(X_s, X_i). \tag{3}$$

In both (2) and (3), the second term of the right hand side is used to estimate the redundant information between the candidate feature X_i and the already selected features with respect to classes C. The parameter β is used as a factor

for controlling the redundancy penalization among single features and has a great influence on FS. The parameter was found experimentally in [7]. It was shown by Peng et al. [11] that for maximization of $I(C,S)$ in the sequential forward selection a suitable value of β in (2) is $1/|S|$, where $|S|$ denotes the number of features in S.

2.1   Conditional Mutual Information

Our feature selection method is based on the definition of the conditional mutual information $I(C, X_i|X_s)$ as the reduction in the uncertainty of class C and the feature X_i when X_s is given:

$$I(C, X_i|X_s) = H(X_i|X_s) - H(X_i|C, X_s). \tag{4}$$

The mutual information $I(C, X_i, X_s)$ satisfies the chain rule for information [9]:

$$I(C, X_i, X_s) = I(C, X_s) + I(C, X_i|X_s). \tag{5}$$

For all candidate features to be selected in the greedy feature selection algorithm, $I(C, X_s)$ is common and thus does not need to be computed. So the greedy algorithm now tries to find the feature that maximizes conditional mutual information $I(C, X_i|X_s)$.

Proposition 1: The conditional mutual information $I(C, X_i|X_s)$ can be represented as

$$I(C, X_i|X_s) = I(C, X_i) - [I(X_i, X_s) - I(X_i, X_s|C)] \tag{6}$$

Proof: By using the definition of MI we can rewrite the right hand side of (6):

$$
\begin{aligned}
I(C, X_i) - [I(X_i, X_s) &- I(X_i, X_s|C)] = H(C) - H(C|X_i) \\
&- [H(X_i) - H(X_i|X_s)] + H(X_i|C) - H(X_i|X_s, C) \\
&= H(C) - H(C|X_i) - H(X_i) + H(X_i|X_s) + H(X_i|C) - H(X_i|X_s, C) \\
&= H(X_i|X_s) - H(X_i|X_s, C) + H(C) - H(C|X_i) - [H(X_i) - H(X_i|C)] \\
&= I(C, X_i) - I(C, X_i) + H(X_i|X_s) - H(X_i|X_s, C). \tag{7}
\end{aligned}
$$

The last term of (7) equals to $I(C, X_i|X_s)$.

The ratio of mutual information between the candidate feature X_i and the selected feature X_s and the entropy of X_s is a *measure of correlation* (also known as *coefficient of uncertainty*) between X_i and X_s [9]

$$CU_{X_i,X_s} = \frac{I(X_i, X_s)}{H(X_s)} = \left(1 - \frac{H(X_s|X_i)}{H(X_s)}\right), \tag{8}$$

$0 \le CU_{X_i,X_s} \le 1$. $CU_{X_i,X_s} = 0$ if and only if X_i and X_s are independent.

Proposition 2. Assume that conditioning by the class C does not change the ratio of the entropy of X_s and the MI between X_s and X_i, i.e., the following relation holds

$$\frac{H(X_s|C)}{I(X_i, X_s|C)} = \frac{H(X_s)}{I(X_i, X_s)}. \tag{9}$$

Then for the conditional mutual information $I(C, X_i | X_s)$ it holds:

$$I(C, X_i | X_s) = I(C, X_i) - CU_{X_{,X}} \ I(C, X_s). \tag{10}$$

Proof: It follows from condition (9) and the definition (8) that

$$I(X_i, X_s | C) = CU_{X_{,X}} \ H(X_s | C). \tag{11}$$

Using the equations (6) and (11) we obtain (10).

We can see from (10) that the second term is the weighted mutual information $I(C, X_s)$ with the weight equal to the measure of correlation $CU_{X_{,X}}$. We propose the modification of the estimation $\tilde{I}(C, X_i | S)$ for $I(C, X_i | S)$ of the following form

$$\tilde{I}(C, X_i | S) = I(C, X_i) - \max_{X_{\ \in S}} CU_{X_{,X}} \ I(C, X_s). \tag{12}$$

It means that the best feature in the next step of the sequential forward search algorithm is found by maximizing (12)

$$X^+ = \arg \max_{X \in X \backslash S} \{I(C, X_i) - \max_{X_{\ \in S}} CU_{X_{,X}} \ I(C, X_s)\}. \tag{13}$$

3   Proposed Feature Selection Algorithm

The sequential forward selection algorithm mMIFS-U based on the estimation of conditional mutual information given in (12) can be realized as follows:

1. *Initialization:*
   Set $S = $ "empty set", set $X = $ "initial set of all D features".

2. *Pre-computation:*
   For all features $X_i \in X$ compute $I(C, X_i)$.

3. *Selection of the first feature:*
   Find feature $X^\star \in X$ that maximizes $I(C, X_i)$;
   set $X = X \setminus \{X^\star\}$, $S = \{X^\star\}$.

4. *Greedy feature selection:*
   Repeat until the desired number of features is selected.
   (a) *Computation of entropy:*
       For all $X_s \in S$ compute entropy $H(X_s)$, if it is not already available.
   (b) *Computation of the MI between features:*
       For all pairs of features (X_i, X_s) with $X_i \in X$, $X_s \in S$ compute $I(X_i, X_s)$, if it is not yet available.
   (c) *Selection of the next feature:*
       Find feature $X^+ \in X$ according to formula (13).
       Set $X = X \setminus \{X^+\}$, $S = S \cup \{X^+\}$.

4 Experiments and Results

Feature selection has been successfully applied to various problems including text categorization (e.g., [14]). The *text categorization* (TC) task (also known as *text classification*) is the task of assigning documents written in natural language into one or more thematic classes belonging to the predefined set $\mathcal{C} = \{c_1, \ldots, c_{|\mathcal{C}|}\}$ of $|\mathcal{C}|$ classes. The construction of a text classifier relies on an initial collection of documents pre-classified under $\mathcal{C}$. In TC, usually a document representation using the *bag-of-words* approach is employed (each position in the feature vector representation corresponds to a given word). This representation scheme leads to very high-dimensional feature space, too high for conventional classification methods. In TC the dominant approach to dimensionality reduction is feature selection based on various criteria, in particular *filter*-based FS.

Sequential forward selection methods MIFS, MIFS-U and mMIFS-U presented in Sections 3 and 2 have been used in our experiments for reducing vocabulary size of the vocabulary set $\mathcal{V} = \{w_1, \ldots, w_{|\mathcal{V}|}\}$ containing $|\mathcal{V}|$ distinct words occurring in training documents. Then we used the Naïve Bayes classifier based on multinomial model, linear Support Vector Machine (SVM) and k-Nearest Neighbor (k-NN) classifier.

4.1 Data set

In our experiments we examined the commonly used Reuters-21578 data set[1] to evaluate all considered algorithms. Our text preprocessing included removing all non-alphabetic characters like full stops, commas, brackets, etc., lowering the upper case characters, ignoring all the words that contained digits or non alphanumeric characters and removing words from a stop-word list. We replaced each word by its morphological root and removed all words with less than three occurrences. The resulting vocabulary size was 7487 words. The ModApte train/test split of the Reuters-21578 data contains 9603 training documents and 3299 testing documents in 135 classes related to economics. We used only those 90 classes for which there exists at least one training and one testing document.

4.2 Classifiers

All feature selection methods were examined in conjuction with each of the following classifiers:

Naïve Bayes. We use the multinomial model as described in [15]. The predicted class for document d is the one that maximizes the posterior probability of each class given the test document $P(c_j|d)$,

$$P(c_j|d) \propto P(c_j) \prod_v^{|\mathcal{V}|} P(w_v|c_j)^N \quad .$$

---

[1] http://www.daviddlewis.com/resources/testcollections/reuters21578.

Here $P(c_j)$ is the prior probability of the class c_j, $P(w_v|c_j)$ is the probability that a word chosen randomly in a document from class c_j equals w_v, and N_{iv} is the number of occurrences of word w_v in document d. We smoothed the word and class probabilities using Bayesian estimate with word priors and a Laplace estimate, respectively.

Linear Support Vector Machines. The SVM method has been introduced in TC by [16]. The method is defined over the vector space where the classification problem is to find the decision surface that "best" separates the data points of one class from the other. In case of linearly separable data the decision surface is a hyperplane that maximizes the "margin" between the two classes. The normalized word frequency was used for document representation:

$$tfidf(w_i, d_j) = n(w_i, d_j) \cdot \log\left(\frac{|\mathcal{D}|}{n(w_i)}\right), \tag{14}$$

where $n(w_i)$ is the number of documents in $\mathcal{D}$ in which w_i occurs at least one.

K-Nearest Neighbor. Given an arbitrary input document, the system ranks its nearest neighbors among training documents, and uses the classes of the k top-ranking neighbors to predict the class of the input document. The similarity score of each neighbor document to the new document being classified is used as a weight if each class, and the sums of class weights over the nearest neighbors are used for class ranking. The normalized word frequency (14) was used for document representation.

4.3   Performance Measures

For evaluating the multi-label classification accuracy we used the standard multi-label measures *precision* and *recall*, both *micro-averaged*. Estimates of micro-averaging precision and recall are obtained as

$$\hat{\pi}_{mic} = \frac{\sum_{j=1}^{|\mathcal{C}|} TP_j}{\sum_{j=1}^{|\mathcal{C}|}(TP_j + FP_j)}, \quad \hat{\rho}_{mic} = \frac{\sum_{j=1}^{|\mathcal{C}|} TP_j}{\sum_{j=1}^{|\mathcal{C}|}(TP_j + FN_j)}.$$

Here TP_j, (FP_j) is the number of documents correctly (incorrectly) assigned to c_j; FN_j is the number of documents incorrectly not assigned to c_j.

4.4   Thresholding

There are two variants of multi-label classification [17], namely ranking and "hard" classifiers. *Hard classification* assigns to each pair document/class (d, c_k) the value YES or NO according to the classifier result. On the other hand *ranking classification* gives to the pair (d, c_j) a real value $\phi(d, c_j)$, which represents the classifier decision for the fact that $d \in c_k$. Then we sort all classes for the document d according to $\phi(d, c_j)$ and the best τ_j classes are selected where τ_j is the threshold for the class c_j. Several thresholding algorithms to train the τ_j exist.
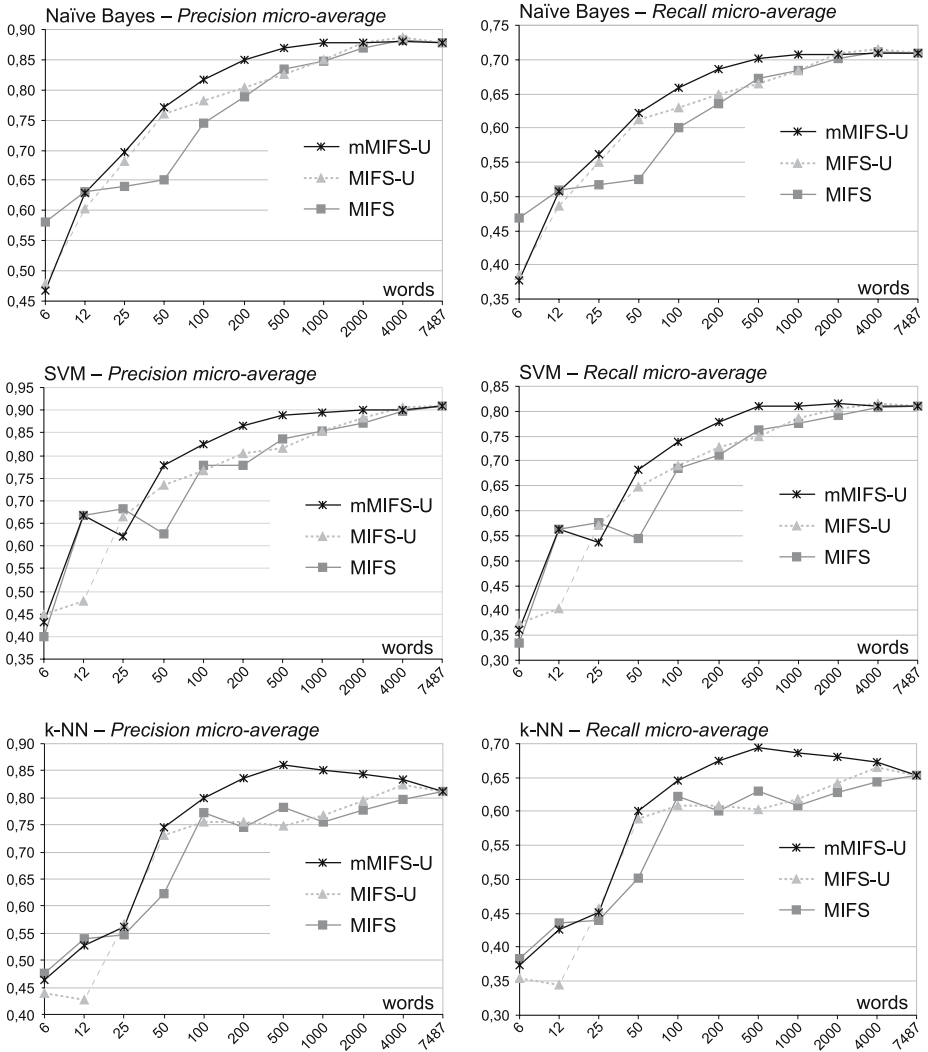
Fig. 1. Classifier performance on Reuters data (90 classes), with Apte split, and RCut-thresholding. Charts of micro-averaged precision, (left-side) and micro-averaged recall (right-side) of Naïve Bayes classifier (1st row), Support Vector Machine (2nd row) and k-Nearest Neighbour (3rd row). Horizontal axes indicate numbers of words.

The commonly used methods RCut, PCut and SCut are described and compared in the paper [18]. It is shown that thresholding has great impact on the classification result. However, it is difficult to choose the best method. We used the RCut thresholding, which sorts classes for the document and assigns YES to the best τ top-ranking classes. There is one global threshold τ (integer value

between 1 and $|\mathcal{C}|$) for all classes. We set the threshold τ according to the average number of classes per one document. We used the whole training set for evaluating the value τ.

The Naïve Bayes and k-NN classifiers are typical tools for ranking classification, with which we used thresholding. In contrast, SVM is the "hard" classifier because there is one classifier for each class which distinguishes between that class and the rest of classes. In fact, SVM may assign a document to no class. In that case we reassign the document to such class that is best according to SVM class rating. This improves the classification result.

4.5   Experimental Results

In total we made 21 experiments, each experiment was performed for eleven different vocabulary sizes and evaluated by three different criteria. Sequential FS (SFS) is not usually used in text classification because of its computational cost due to large vocabulary size. However, in practice we can often either employ calculations from previous steps or make some pre-computations during initialization. Since FS is typically done in an off-line manner, the computational time is not as important as the optimality of the found subset of words and classification accuracy. The time complexity of SFS algorithms is less than $O(|\mathcal{V}'||\mathcal{V}|^2)$ where $|\mathcal{V}'|$ is the number of desired words and $|\mathcal{V}|$ is the total number of words in the vocabulary. The required space complexity is $S(|\mathcal{V}|^2/2)$ because we need to store the mutual information for all pairs of words (w_i, w_s) with $w_i \in \mathcal{V} \setminus S$ and $w_s \in S$. The charts in Figure 1 show the resulting micro-averaged precision and recall criteria. In our experiments the best micro-averaged performance was achieved by the new mMIFS-U methods using modified conditional mutual information.

5   Conclusion

In this paper we proposed a new sequential forward selection algorithm based on novel estimation of the conditional mutual information between the candidate feature and the classes given a subset of already selected features.

– Experimental results on textual data show that the modified MIFS-U sequential forward selection algorithm (mMIFS-U) performs well in classification as measured by precision and recall measures and that the mMIFS-U performs better than MIFS and MIFS-U on the Reuters data.
– In this paper we also present a comparative experimental study of three classifiers. SVM overcomes on average both Naïve Bayes and k-Nearest Neighbor classifiers.

References

1. Yu, L., Liu, H.: Feature selection for high-dimensional data: A fast correlation-based filter solution. In: Proceedings of the 20th International Conference on Machine Learning, pp. 56–63 (2003)
2. Dash, M., Choi, K., Scheuermann, P., Liu, H.: Feature selection for clustering - a filter solution. In: Proceedings of the Second International Conference on Data Mining, pp. 115–122 (2002)
3. Kohavi, R., John, G.: Wrappers for feature subset selection. Artificial Intelligence 97, 273–324 (1997)
4. Liu, H., Yu, L.: Toward integrating feature selection algorithms for classification and clustering. IEEE Transactions on Knowledge and Data Engineering 17(3), 491–502 (2005)
5. Dash, M., Liu, H.: Consistency-based search in feature selection. Artificial Intelligence 151(1-2), 155–176 (2003)
6. Jain, A.K., Duin, R.P.W., Mao, J.: Statistical pattern recognition: A review. IEEE Transactions on Pattern Analysis and Machine Intelligence 22, 4–37 (2000)
7. Battiti, R.: Using mutual information for selecting features in supervised neural net learning. IEEE Transactions on Neural Networks 5, 537–550 (1994)
8. Kwak, N., Choi, C.H.: Input feature selection for classification problems. IEEE Transactions on Neural Networks 13(1), 143–159 (2002)
9. Cover, T., Thomas, J.: Elements of Information Theory, 1st edn. John Wiley & Sons, Chichester (1991)
10. Fleuret, F.: Fast binary feature selection with conditional mutual information. Journal of Machine Learning Research 5, 1531–1555 (2004)
11. Peng, H., Long, F., Ding, C.: Feature selection based on mutual information criteria of max-dependency, max-relevance, and min-redundancy. IEEE Transactions on Pattern Analysis and Machine Intelligence 27(8), 1226–1238 (2005)
12. Fano, R.: Transmission of Information: A Sattistical Theory of Communications. John Wiley and M.I.T.& Sons (1991)
13. Kwak, N., Choi, C.: Improved mutual information feature selector for neural networks in supervised learning. In: Proceedings of the IJCNN 1999, 10th International Joint Conference on Neural Networks pp. 1313–1318 (1999)
14. Forman, G.: An experimental study of feature selection metrics for text categorization. Journal of Machine Learning Research 3, 1289–1305 (2003)
15. McCallum, A., Nigam, K.: A comparison of event models for naive Bayes text classification. In: Proceedings of the AAAI-1998 Workshop on Learning for Text Categorization (1998)
16. Joachims, T.: Text categorization with support vector machines: Learning with many relevant features. In: Nédellec, C., Rouveirol, C. (eds.) ECML 1998. LNCS, vol. 1398, pp. 137–142. Springer, Heidelberg (1998)
17. Sebastiani, F.: Machine learning in automated text categorization. ACM Computing Surveys 34(1), 1–47 (2002)
18. Yang, Y.: A study on thresholding strategies for text categorization. In: Proceedings of ACM SIGIR Conference on Research and Development in Information Retrieval (SIGIR 2001), New Orleans, Louisiana USA (September 9-12, 2001)

Robust Alternating AdaBoost[*]

Héctor Allende-Cid[1], Rodrigo Salas[2], Héctor Allende[1],
and Ricardo Ñanculef[1]

[1] Universidad Técnica Federico Santa María,
Dept. de Informática, Casilla 110-V, Valparaíso-Chile
`vector@inf.utfsm.cl, hallende@inf.utfsm.cl, jnancu@inf.utfsm.cl`
[2] Universidad de Valparaíso, Departamento de Ingeniería Biomédica, Valparaíso-Chile
`rodrigo.salas@uv.cl`

Abstract. Ensemble methods are general techniques to improve the accuracy of any given learning algorithm. Boosting is a learning algorithm that builds the classifier ensembles incrementally. In this work we propose an improvement of the classical and inverse AdaBoost algorithms to deal with the problem of the presence of outliers in the data. We propose the Robust Alternating AdaBoost (RADA) algorithm that alternates between the classic and inverse AdaBoost to create a more stable algorithm. The RADA algorithm bounds the influence of the outliers to the empirical distribution, it detects and diminishes the empirical probability of "bad" samples, and it performs a more accurate classification under contaminated data.

We report the performance results using synthetic and real datasets, the latter obtained from a benchmark site.

Keywords: Machine ensembles, AdaBoost, Robust Learning Algorithms.

1 Introduction

Boosting algorithms, since the mid nineties, have been a very popular technique for constructing ensembles in the areas of Pattern Recognition and Machine Learning (see [2], [6], [8]). Boosting is a learning algorithm to construct a predictor by combining, what are called, weak hypotheses. The AdaBoost algorithm, introduced by Freund and Schapire [6], builds an ensemble incrementally, placing increasing weights on those examples in the data set, which appear to be "difficult". The Inverse AdaBoost [6] is a variant of the classic approach but with exactly the opposite philosophy, it decreases the weights of difficult objects.

In real engineering and scientific applications, data are noisy and present outlying observations. Assumptions of the underlying data generation process no longer holds and the model estimates are badly affected obtaining a poor performance. For example, outliers may occur in recording data.

In this work, we start by empirically demonstrating that the typical boosting algorithm, AdaBoost, is seriously affected by outliers. Similar results were reported in [1] and [2] for this algorithm and in [7] for bagging, another method to build ensembles [4]. Since AdaBoost forces each learner to focus on the difficult examples, learning rounds can strongly depend on isolated examples more than on local patterns of the featured space. Learning such outlying observations could seriously compromise the generalization ability of the final obtained learner. Inverse Boosting on the other hand, systematically ignores difficult examples and hence tends to be more robust than AdaBoost. However this is usually achieved at the expense of a lower performance.

Following this analysis, we propose an improvement of the classical and inverse AdaBoost algorithms to deal with the problem of the presence of outliers in the data. This consists in *Robust Alternating AdaBoost (RADA)*, an algorithm capable to alternate between the classic and inverse AdaBoost to create a more stable algorithm. The RADA algorithm bounds the influence of the outliers to the empirical distribution, detects and diminishes the empirical probability of "bad" samples, and will perform a more accurate classification under contaminated data.

This paper is organized as follows. In section 2, we briefly introduce AdaBoost and Inverse AdaBoost algorithms. In section 3, we make an analysis of the sensitivity of AdaBoost to the presence of outliers. Our proposed algorithm is illustrated in section 4. In section 5 we compare the performance of the classic AdaBoost, inverse AdaBoost and our proposed algorithm called RADA. The last section is devoted to concluding remarks.

2   Boosting Algorithms

The AdaBoost Algorithm [6], introduced in 1995 by Freund and Schapire, has a theoretical background based on the "PAC" learning model [9]. The authors of this model were the first to pose the question of whether a weak learning algorithm that is slightly better than random guessing can be "boosted" in a strong learning algorithm. The classic AdaBoost takes as an input a training set $\mathcal{Z} = \{(x_1, y_1)...(x_n, y_n)\}$ where each x_i is a variable that belongs to $\mathcal{X} \subset \mathbb{R}^d$ and each label y_i is in some label $\mathcal{Y}$. In this particular paper we assume that $\mathcal{Y} = \{-1, 1\}$. AdaBoost calls a weak or base learning algorithm repeatedly in a sequence of stages $t = 1...T$. The main idea of AdaBoost is to maintain a sampling distribution over the training set. This sample set is used to train the learner at round t. Let $\mathcal{D}_t(i)$ be the sampling weight assigned to the example i on round t. At the beginning of the algorithm the distribution is uniform, that is distribution $\mathcal{D}_1(i) = \frac{1}{n}$ for all i. At each round of the algorithm however, the weights of the incorrectly classified examples are increased, so that the following weak learner is forced to focus on the "hard" examples of the training set. The job of each weak or base learner is to find a hypothesis $h_t : \mathcal{X} \to \{-1, 1\}$

appropriate for the distribution $\mathcal{D}_t$. The goodness of the obtained hypothesis can be quantified as the weighted error:

$$\epsilon_t = Pr_{i\sim\mathcal{D}} [h_t(x_i) \neq y_i] = \sum_{i:h_t(x_i)\neq y_i} \mathcal{D}_t(i) \tag{1}$$

Notice that the error is measured with respect to the distribution $\mathcal{D}_t$ on which the weak learner was trained. Once AdaBoost has computed a weak hypothesis h_t, it measures the importance that the algorithm assigns to h_t with the parameter.

$$\alpha_t = \frac{1}{2}\ln\left(\frac{1-\epsilon_t}{\epsilon_t}\right) \tag{2}$$
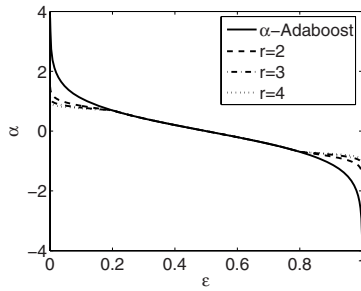
Fig. 1. Graph of the α variable given by equation (4) with the robust parameter values $r = 2, 3, 4$, compared to the AdaBoost α

Figure 1 shows the graph of α_t. After choosing α_t the next step is to update the distribution $\mathcal{D}_t$ with the following rule,

$$\mathcal{D}_{t+1}(i) = \frac{1}{Z_t}\mathcal{D}_t(i)e^{-\alpha_t y_i h_t(x_i)}$$

where Z_t is a normalization factor. The effect of this rule is that, when a example is misclassified its sampling weight for the next round is increased, and the opposite occurs when the classification is correct. This updating rule makes the algorithm to focus on the "hard" examples, instead in the correctly classified examples. After a sequence of T rounds have been carried out, the final hypothesis H is computed as

$$H_T(x) = sign\left(\sum_{t=1}^{T}\alpha_t h_t(x)\right) \tag{3}$$

The other Boosting variant considered in this paper is the Inverse AdaBoost. This algorithm is more robust than the classic approach because it focuses on the correct classified examples, and tries to diminish the influence of the incorrect

examples in the distribution, however the classifiers will tend to be more and more similar, eliminating any diversity in the process [8]. Inverse Boosting is a variant similar to the "hedge" algorithm, first proposed in [6]. The philosophy is completely the opposite to classic boosting. Instead of increasing the sampling probability of the hard examples, we decrease it, thereby gradually filtering them out. Each learner is created to reinforce the knowledge acquired by previous learners, and hence the capability of the algorithm to discover new patterns is low.

3   Empirical Robustness Analysis of AdaBoost

In this section we empirically show that the classic AdaBoost algorithm lacks of robustness and stability under the presence of outlying data.

Suppose that the weak learner h_{t*} at stage t^* correctly learns almost all its training samples $\mathcal{Z}_{t*}$ obtaining a very low classification error (1) ($\epsilon_{t*} \approx 0$), in this case the α_{t*} parameter (2) will approach to infinity. This mean that the weak learner h_{t*} will receive a very high weight in the strong hypothesis $H_T(x)$ and the ensemble decision will strongly depended on this weak learner. If there exists a sample in $\mathcal{Z}$, say (x_j, y_j), that was misclassified by the weak learner h_{t*}, then the expression $\exp(-\alpha_{t*} y_j h_{t*}(x_j))$ will tend to infinity as long as α_{t*} tends to infinity. Then, the sample (x_j, y_j), will obtain a very high weight $0 << \mathcal{D}_{t+1}(j) \approx 1$ for the next round. Due to the high probability of the data (x_j, y_j), it will be sampled several times during the bootstrap step and the weak hypothesis will learn it. If this sample is a "bad" sample (for example an error) or an outlier, an undesired effect of overfitting, poor generalization, very complex model and learning bad data will occur.

If we even construct a robust weak learner (see [1]) it will also be affected by a "bad sample" where most of the data in the bootstrap sample behaves different than the majority of the original sample.

To empirically show the behavior of AdaBoost we create the following synthetic case. We randomly generated 41 samples, where the 20 samples of the class -1 were generated with a gaussian distribution $\mathcal{N}(-2, 1)$, 20 samples with of the class 1 were generated with a gaussian distribution $\mathcal{N}(2, 1)$ and we arbitrarily introduce an additional "bad" sample at location $x = 5$ with target $y = -1$. We bootstrapped only the original 40 samples and construct a weak learner h_1, where

$$h_1(x) = \begin{cases} 1 & |\overline{X}^{[1]} - x| < |\overline{X}^{[-1]} - x| \\ -1 & |\overline{X}^{[1]} - x| \geq |\overline{X}^{[-1]} - x| \end{cases}$$

where $\overline{X}^{[k]} = \frac{1}{n} \sum_{i=1}^{n} x_i^{[k]}$, $k = \{-1, 1\}$, and $x_i^{[k]}$ is the bootstrapped sample i of the class k. Figure 2 shows the empirical distribution at stage 1, 2 and 3 (from left to right), where the first row is the empirical distribution of the AdaBoost algorithm, while the second row is the Robust Alternating AdaBoost algorithm.

Note that in the first round all the samples weight are equal to $\frac{1}{41}$, but in the second round, the misclassified sample number 41 considerably increased its weight over 0.5 in the AdaBoost algorithm while our proposal remains lower. Due to the high weight of this sample, in the next round, the bootstrap sample is composed mostly by this data. The weak learner of stage two learns the outlying sample but at the same time degrades the performance of the strong hypothesis misclassifying other three data that were correctly classify previously. This phenomenon does not occur to our proposal, remaining more stable.
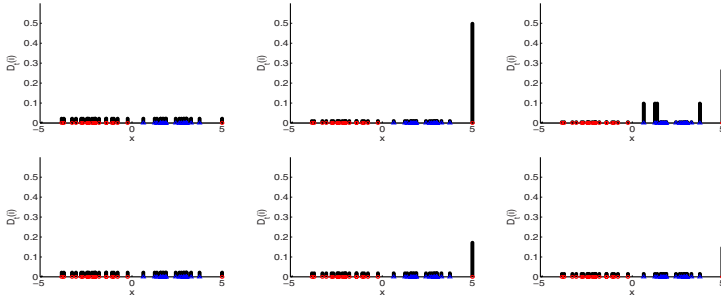
Fig. 2. Empirical Distribution of the AdaBoost **(first row)** and the Robust Alternating AdaBoost **(second row)** algorithms at stages 1 **(left)**, 2 **(middle)** and 3 **(right)**

4   Robust Alternating AdaBoost

In this section we improve the classical and inverse AdaBoost algorithms to deal with the problem of the presence of outliers in the data. Our proposal mainly consists in creating a variant of the AdaBoost algorithm that will alternate between the classic and inverse AdaBoost to create a more stable algorithm that will perform a more adequate classification.

In the previous section we empirically showed that the empirical distribution $D_t(i)$ of the data sample was strongly affected by the presence of outliers. The actualization of the empirical probability $\mathcal{D}_{t+1}(i)$ of the sample (x_i, y_i) depends on its weight of the previous stage $\mathcal{D}_t(i)$, the result of the classification $h_t(x_i)$ compared to the target y_i and the variable α_t. If the weak learner has a very low error ϵ_t, then the α_t variable becomes very large as it is shown in figure 1. Furthermore if the weak learner misclassifies the sample (x_i, y_i), then the new probability weight $\mathcal{D}_{t+1}(i)$ will considerably increase its value. This could mean that if the sample corresponds to an outlying observation that was misclassified by a good learner, it will receive a high probability distribution and will be more probable to be selected more than once, and the next weak learner h_{t+1} will mostly learn this isolated observation. The resulting model could overfit the training data, it could be more complex with several weak learners composing the strong hypothesis, or worst, it could learn erroneous data samples.

To overcome this drawback of the classic AdaBoost, we bound the value of the α_t variable by taking the r-th square root to low values of ϵ_t, i.e., we compute α_t as:

$$\alpha_t = \begin{cases} \frac{1}{2}\sqrt{\ln\left(\frac{1-\epsilon}{\epsilon}\right)} + \alpha_\gamma & \epsilon_t < \gamma \\ \frac{1}{2}\ln\left(\frac{1-\epsilon}{\epsilon}\right) & \epsilon_t \geq \gamma \end{cases} \tag{4}$$

where $\alpha_\gamma = \frac{1}{2}\ln\left(\frac{1-\gamma}{\gamma}\right) - \frac{1}{2}\sqrt{\ln\left(\frac{1-\gamma}{\gamma}\right)}$ is a constant needed so that equation (4) is continuous.

Applying equation (4) will prevent that the empirical distribution considerably grow in one step for any sample. However the empirical distribution is updated at each stage, and after few iterations the probability weight of the samples that were repeatedly misclassified will have bigger values compared to other samples. For this reason we introduce an inverting variable $\beta(i)$ and an age variable $age(i)$ for each sample $i = 1..n$. The variable $\beta(i)$ has an initial value of one, meaning that the algorithm behaves for the sample as the classical AdaBoost, i.e., increases its empirical distribution when it is misclassified and decreases its value otherwise. If the value of $\beta(i)$ is -1, then the algorithm behaves for the sample as the inverse AdaBoost, i.e., decreases its empirical distribution when it is misclassified and increases its value otherwise. The variable $age(i)$ counts the number of times that the sample i was sequentially misclassified, if this number exceeds the threshold τ then the value of $\beta(i)$ is inverted to -1. In other words, the weight of the misclassified sample grows until the number of iterations reaches a limit τ and then begins to decrease. If the $\beta(i)$ was inverted to -1 and the sample was correctly classified in further stages, then the value of $\beta(i)$ is inverted back to 1.

Algorithm 1 shows our proposed *Robust Alternating AdaBoost* algorithm.

5   Experimental Results

In this section we empirically show the performance of our *Robust Alternating AdaBoost* (**RADA**) model proposal compared to classical Adaboost (**ADA**) and Inverse Adaboost (**IADA**) models (see [6] and [8] respectively for further details about these models) in both Synthetic and Real data sets, the latter was obtained from a benchmark site.

The data of both, synthetic and real data sets, were separated in training and test sets. All the results reported were obtained for each model as the mean value of the metrics computed for 20 runs with the same sets of data.

For the synthetic experiment we have created a synthetic data set $\{(x_i, y_i)\}_{i=1}^n$, as an independent sample obtained from a mixture of gaussian distributions labeled with the class $\{-1, 1\}$. For the class $y = -1$, the random variable $X^{[-1]}$ is a mixture of three gaussian distributions with mean $\mu_1^{[-1]} = -10$, $\mu_2^{[-1]} = 0$ and $\mu_3^{[-1]} = 10$ and standard deviation $\sigma_i^{[-1]} = \sigma = 1, i = 1..3$ respectively. For the class $y = 1$, the random variable $X^{[1]}$ is a mixture of two gaussian distributions

Algorithm 1. Robust Alternating AdaBoost

1: Given is the training data set $\mathcal{Z} = \{(x_1, y_1), ..., (x_n, y_n)\}$ with n elements, where $x_i \in \mathcal{X}$ and $y_i \in \mathcal{Y} = \{-1, 1\}$.

2: Initialize the parameters. Pick the age threshold τ, the bound threshold λ and the robust parameter r. Let $T = 0$.

3: Initialize the empirical distribution $\mathcal{D}_1(i) = \frac{1}{n}$, the inverting variable $\beta(i) = 1$ and the age variable $age(i) = 0$ for each data sample $(x_i, y_i), i = 1..n$.

4: **repeat**

5:    Increment T by one.

6:    Take a bootstrap sample $\mathcal{Z}_T$ from $\mathcal{Z}$ with distribution $\mathcal{D}_T$.

7:    Train the weak learner $h_T : \mathcal{X} \rightarrow \{-1, 1\}$ with the bootstraped sample $\mathcal{Z}_T$ as the training set.

8:    Compute the weighted error ϵ_T of the weak hypothesis h_T as

$$\epsilon_T = Pr_{i \sim \mathcal{D}} \ [h_T(x_i) \neq y_i]$$

9:    Compute α_T with equation

$$\alpha_T = \begin{cases} \frac{1}{2}\sqrt{\ln\left(\frac{1-\epsilon}{\epsilon}\right)} + \alpha_\gamma & \epsilon_T < \gamma \\ \frac{1}{2}\ln\left(\frac{1-\epsilon}{\epsilon}\right) & \epsilon_T \geq \gamma \end{cases}$$

10:    Update the empirical distribution as

$$\mathcal{D}_{T+1}(i) = \frac{\mathcal{D}_T(i)}{Z_T} \times e^{(-\alpha \ \beta(i) y \ h \ (x \ ))}$$

where Z_T is the normalization factor.

11:    The strong hypothesis $H_T(x)$ at stage T is given by

$$H_T(x) = sign\left(\sum_{t=1}^{T} \alpha_t h_t(x)\right)$$

12:    Classify the training data set $\mathcal{Z} = \{(x_1, y_1), ..., (x_n, y_n)\}$ with the strong hypothesis $H_T(x)$.

13:    **if** sample (x_i, y_i) is correctly classified by $H_T(x)$ (i.e, $H_T(x_i)y_i > 0$) **then**

14:       Let $age(i) = 0$ and $\beta(i) = 1$.

15:    **else**

16:       Increment $age(i)$ by one.

17:       **if** $age(i) > \tau$ **then** let $\beta(i) = -1$ and $age(i) = 0$

18:    **end if**

19: **until** The stopping criterion is met

20: Output: The strong hypothesis $H_T(x)$

---

with mean $\mu_1^{[1]} = -5$, $\mu_2^{[1]} = 5$ and standard deviation $\sigma_i^{[1]} = \sigma = 1$, $i = 1, 2$ respectively. For each gaussian we generated 20 examples, i.e., the class $y = -1$ has 60 samples while the class $y = 1$ has 40 data. The observational process was obtained by including additive outliers: $Z^{[k]} = X^{[k]} + V\,U$, where $X^{[k]}, k = -1, 1$, are the gaussian variables generated as was previously explained, V is a zero-one process with $P(V \neq 0) = \delta$, $0 < \delta \ll 1$, and U has distribution $\mathcal{N}(0, \sigma_U^2)$

Table 1. Summary results of the performance evaluation of the ADA, IADA and RADA algorithms

Algorithm	% Outliers	T	$CE-Train$	$Min-Train$	$CE-Test$	$Min-Test$
ADA	0	9.8	21.45 ± 7.82	**3.00**	23.60 ± 8.60	**8.00**
IADA	0	8.7	$\mathbf{20.95 \pm 1.10}$	20.00	$23.25 \pm \mathbf{1.02}$	22.00
RADA5	0	7.3	24.50 ± 6.51	9.00	24.30 ± 7.58	10.00
RADA10	0	8.7	22.85 ± 6.67	9.00	$\mathbf{22.10} \pm 6.80$	11.00
RADA20	0	**7.1**	23.00 ± 7.44	7.00	24.55 ± 7.79	10.00
ADA	5	18.8	6.15 ± 2.70	3.00	9.20 ± 3.49	5.00
IADA	5	**14.9**	12.90 ± 7.74	3.00	15.05 ± 7.96	**4.00**
RADA5	5	18.6	6.55 ± 4.81	**2.00**	9.10 ± 4.87	5.00
RADA10	5	17.7	$\mathbf{5.35 \pm 2.43}$	**2.00**	$\mathbf{8.00 \pm 2.27}$	5.00
RADA20	5	17.2	5.90 ± 2.59	**2.00**	9.60 ± 3.30	5.00
ADA	10	17.4	$\mathbf{10.70 \pm 2.34}$	8.00	6.85 ± 4.57	**1.00**
IADA	10	**10.0**	19.80 ± 7.78	7.00	16.65 ± 10.66	2.00
RADA5	10	17.5	11.10 ± 3.65	8.00	6.10 ± 4.40	**1.00**
RADA10	10	18.2	11.80 ± 5.23	**5.00**	6.00 ± 6.64	**1.00**
RADA20	10	16.8	11.25 ± 2.67	8.00	$\mathbf{5.45 \pm 3.71}$	**1.00**
ADA	20	13.5	20.50 ± 8.52	**13.00**	17.25 ± 8.48	8.00
IADA	20	**12.7**	21.00 ± 7.17	14.00	17.55 ± 7.23	9.00
RADA5	20	13.5	$\mathbf{18.55} \pm 6.90$	14.00	16.55 ± 8.46	**7.00**
RADA10	20	16.3	18.65 ± 5.72	**13.00**	$\mathbf{15.25} \pm 6.95$	9.00
RADA20	20	15.6	$18.75 \pm \mathbf{5.34}$	15.00	$16.30 \pm \mathbf{6.42}$	9.00

with variance $\sigma_U^2 \gg \sigma^2$. The generating process was affected with $\delta = 0\%$, 5%, 10% and 20% of outliers and $\sigma_U = 9 * \sigma$. The test set was generated similar to the training set. The classifier used in the algorithms is the Bayesian Classifier (QDA) (see [5]).

Table 1 shows the summary results of the performance evaluation of the ADA, IADA and RADA algorithms, where for the latter the robustifying r parameter has the values $r = 0.05, 0.10$ and 0.20. As we can observe in the *CE-Test* column, the algorithm with better generalization ability was the RADA algorithm with its variants outperforming in most of the experiments the ADA and IADA algorithms with statistical significance. Nevertheless that the ADA obtained good results in the training set, the RADA algorithm with its variants obtained lower error in the test set. Note that in the contaminated cases one of the RADA variants always obtained the best strong hypothesis (see column *Min-Test*). We also observed that when the percentage of outliers was increased all the models became more complex and the performance was degraded. When the percentage of outliers was 0%, the algorithm with best performance and lowest standard deviation was IADA, however in the contaminated data sets, it obtained the worst performance. We can also notice, that RADA10 and RADA20 obtained better results than RADA5, implying that the robust r parameter influences in the performance of the RADA algorithm under contaminated data. The IADA algorithm obtained the simplest model because its mean T value was lower than the other algorithms, this implies that the minimum value was reached with less rounds.

Table 2. Summary results of the performance evaluation of the ADA, IADA and RADA algorithms

Dataset	Algorithm	T	$CE-Train$	$Min-Train$	$CE-Test$	$Min-Test$
Breast Cancer	ADA	6.2	**1.64** $\pm$ 0.82	**0.24**	3.33 $\pm$ 0.29	2.93
	IADA	8.9	2.52 $\pm$ **0.33**	1.96	3.24 $\pm$ **0.27**	2.93
	RADA5	**4.2**	1.86 $\pm$ 0.77	0.49	3.41 $\pm$ 0.41	**2.56**
	RADA10	8.3	2.04 $\pm$ 0.53	0.98	3.30 $\pm$ **0.27**	**2.56**
	RADA20	7.3	1.93 $\pm$ 0.51	0.98	**3.13** $\pm$ 0.37	**2.56**
Diabetes	ADA	24.7	22.33 $\pm$ 1.04	21.30	23.50 $\pm$ 1.27	**20.52**
	IADA	**9.7**	22.47 $\pm$ **0.68**	21.96	23.49 $\pm$ **0.69**	21.82
	RADA5	22.1	22.23 $\pm$ 0.81	21.09	23.40 $\pm$ 1.24	21.82
	RADA10	31.9	**21.87** $\pm$ 0.81	**20.87**	**22.80** $\pm$ 1.08	21.50
	RADA20	30.0	22.58 $\pm$ 0.75	21.74	23.14 $\pm$ 0.90	22.15
Liver Diseases	ADA	24.4	**29.18** $\pm$ 2.25	25.60	40.14 $\pm$ 3.51	38.41
	IADA	31.5	35.77 $\pm$ 3.06	30.44	46.96 $\pm$ 3.88	39.86
	RADA5	24.6	29.95 $\pm$ 2.97	26.57	39.57 $\pm$ **3.15**	35.51
	RADA10	**21.1**	29.78 $\pm$ 2.45	**25.12**	**39.02** $\pm$ 3.84	**31.88**
	RADA20	23.1	30.80 $\pm$ 2.47	**25.12**	39.86 $\pm$ 3.67	34.78

In the real experiment we test the algorithms with three real data sets obtained from the UCI Machine Learning repository [3]. The *Diabetes*, *Liver Diseases* and *Breast-Cancer* data sets were selected. Table 2 shows the summary results of the performance evaluation of the ADA, IADA and RADA algorithms, where RADA has the same robustifying parameters as in the Synthetic Experiments.

The results are shown in table 2. As we can observe in the column *CE-Test*, RADA obtained a better generalization ability than ADA and IADA. Our algorithm outperforms the ADA and IADA algorithms with statistical significance. Furthermore we notice that the algorithms with better results in the 3 different real data sets were RADA10 and RADA20. RADA5 has only a better performance than ADA and IADA in the Diabetes and Liver diseases data sets. In the *CE-Train* column we observe that ADA has better performance in Liver Diseases and Breast-Cancer. In the testing phase, the RADA algorithm and its variants outperform the ADA algorithm. Another drawback of ADA is its standard deviation in the training phase is high compared with RADA.

6   Concluding Remarks

In this paper we have introduced the *Robust Alternating Adaboost* algorithm. This algorithm has the capability to alternate between two differents views of approaching classification problems using a midpoint approach between robustness and sensitivity.

The performance of our algorithm shows better results in the simulation study in both the synthetic and real data sets. In the real case, we investigated three benchmark data known as Breast-Cancer, Diabetes and Liver Diseases. The comparative study with the classic AdaBoost and Inverse AdaBoost without

improvement shows that our Robust Alternating AdaBoost outperforms the alternative models with statistical significance, obtaining good results in both synthetic and real data. Further studies are needed in order to analyze the convergence, and to test this algorithm with other weak learners.

References

1. Allende, H., Nanculef, R., Salas, R.: Bootstrapping neural networks. In: Monroy, R., Arroyo-Figueroa, G., Sucar, L.E., Sossa, H. (eds.) MICAI 2004. LNCS (LNAI), vol. 2972, pp. 813–822. Springer, Heidelberg (2004)
2. Bauer, E., Kohavi, R.: An empirical comparison of voting classification algorithms: Bagging, boosting, and variants. Machine Learning 36(1-2), 105–139 (1999)
3. Blake, C.L., Merz, C.J.: UCI repository of machine learning databases (1998)
4. Breiman, L.: Bagging predictors. Machine Learning 24(2), 123–140 (1996)
5. Duda, R., Hart, P., Stork, D.: Pattern classification. Wiley-Interscience, Chichester (2000)
6. Freund, Y., Schapire, R.: A decision-theoretic generalization of on-line learning and an application to boosting. Journal of Computer and System Sciences 55(1), 119–139 (1997)
7. Kanamori, T., Takenouchi, T., Eguchi, S., Murata, N.: The most robust loss function for boosting. In: Pal, N.R., Kasabov, N., Mudi, R.K., Pal, S., Parui, S.K. (eds.) ICONIP 2004. LNCS, vol. 3316, pp. 496–501. Springer, Heidelberg (2004)
8. Kuncheva, L., Whitaker, C.: Using diversity with three variants of boosting: Aggressive, conservative and inverse. In: Roli, F., Kittler, J. (eds.) MCS 2002. LNCS, vol. 2364, pp. 81–90. Springer, Heidelberg (2002)
9. Valiant, L.G.: A theory of the learnable. Communications of the ACM 27(11), 1134–1142 (1984)

Face Recognition Using Some Aspects of the Infant Vision System and Associative Memories

Roberto A. Vazquez, Humberto Sossa, and Beatriz A. Garro

Centro de Investigación en Computación – IPN
Av. Juan de Dios Batiz, esquina con Miguel de Othon de Mendizábal
Ciudad de México, 07738, México
`ravem@ipn.mx, hsossa@cic.ipn.mx, bgarrol@ipn.mx`

Abstract. Several associative memories (AM) have been proposed in the last years. These AMs have several constraints that limit their applicability in complex problems such as face recognition. Despite of the power of these models, they cannot reach its full power without applying new mechanisms based on current and future studies on biological neural networks. In this research we show how a network of dynamic associative memories (DAM) combined with some aspects of the infant vision system could be efficiently applied to the face recognition problem. Through several experiments by using a benchmark of faces the accuracy of the proposal is tested.

Keywords: Associative memories, face recognition, infant vision system.

1   Introduction

Several statistical computationally expensive techniques such as principal component analysis [2] and factor analysis have been proposed for solving the face recognition problem. These techniques have been combined with neural networks and other classifiers. Although the accuracy of these methods is acceptable, they are computationally expensive techniques. On the other hand, several associative memories (AM) have been proposed in the last years [1], [7], [16] and [17]. These AMs have several constraints that limit their applicability in complex problems such as face recognition. Despite of the power of these AMs, they cannot reach their full power without applying new mechanisms based on current and future studies on biological neural networks. In this research we described how a network of dynamic associative memories (DAM) combined with some aspects of the infant vision system could be applied to the face recognition problem. Through several experiments with a benchmark of faces the accuracy of the proposal is tested.

2   Some Aspects of the Infant Vision System

Vision has been a popular subject of study, but most of the research has focused on the fully developed visual systems of adult humans. To understand the role of the brain in perceptual processes such face recognition, we propose to focus on the visual

system's development from infancy to adulthood. Within a few months of birth, the brain can differentiate faces from other faces or objects. Indeed, an infant can recognize a known face from a stranger's.

Some current researches see for example [11] and [13], have demonstrated that young babies are not capable of detecting subtle features in a face. This fact could suggest that only few information of the face is used by the baby for learning and recognition. However, the question remains: which information the baby uses to recognize a face?

In this research, we conjecture that babies extract the information of a face at random and then use this information for further recognition. We call this information stimulating points SPs.

3   Dynamic Associative Model

This model is not an iterative model as Hopfield's model [1]. The model emerges as an improvement of the model proposed in [9] which is not an iterative model and the results are presented in [18]. Let $\mathbf{x} \in \mathbf{R}^n$ and $\mathbf{y} \in \mathbf{R}^m$ an input and output pattern, respectively. An association between input pattern $\mathbf{x}$ and output pattern $\mathbf{y}$ is denoted as $\left(\mathbf{x}^k, \mathbf{y}^k\right)$, where k is the corresponding association. Associative memory $\mathbf{W}$ is represented by a matrix whose components w_{ij} can be seen as the synapses of the neural network. If $\mathbf{x}^k = \mathbf{y}^k \forall k = 1, \ldots, p$ then $\mathbf{W}$ is auto-associative, otherwise it is hetero-associative. A distorted version of a pattern $\mathbf{x}$ to be recalled will be denoted as $\tilde{\mathbf{x}}$. If an associative memory $\mathbf{W}$ is fed with a distorted version of $\mathbf{x}^k$ and the output obtained is exactly $\mathbf{y}^k$, we say that recalling is robust.

3.1   Building the Associative Memory

The brain is a dynamic, changing neural network that adapts continuously to meet the demands of communication and computational needs [8]. This fact suggests that some connections of the brain could change in response to some input stimuli. We humans, in general, do not have problems to recognize patterns even if these appear altered by noise. Several parts of the brain interact together in the process of learning and recalling a pattern, for details refer to [3] and [6]. Based on the above example we have defined in our model several interacting areas, one per association we would like the memory to learn. Also we have integrated the capability to adjust synapses in response to an input stimulus.

Before an input pattern is learned or processed by the brain, it is hypothesized that it is transformed and codified by the brain. In our model, this process is simulated using the following procedure recently introduced in [10]:

Procedure 1. Transform the fundamental set of associations into codified patterns and de-codifier patterns:

```
Input: FS Fundamental set of associations:
{1. Make d = const and make (x̄¹, ȳ¹) = (x¹, y¹)
```

```
  2. For the remaining couples do {
     For  k = 2  to  p {
              For  i = 1  to  n {
```
$$\overline{x}_i^k = \overline{x}_i^{k-1} + d \; ; \quad \hat{x}_i^k = \overline{x}_i^k - x_i^k \; ; \quad \overline{y}_i^k = \overline{y}_i^{k-1} + d \; ; \quad \hat{y}_i^k = \overline{y}_i^k - y_i^k$$
```
}}} Output: Set of codified and de-codifying patterns.
```

This procedure allows computing *codified patterns* from input and output patterns denoted by $\overline{\mathbf{x}}$ and $\overline{\mathbf{y}}$ respectively; $\hat{\mathbf{x}}$ and $\hat{\mathbf{y}}$ are *de-codifying patterns*. Codified and de-codifying patterns are allocated in different interacting areas and d defines of much these areas are separated. On the other hand, d determines the noise supported by our model. In addition a simplified version of $\mathbf{x}^k$ denoted by s_k is obtained as:

$$s_k = s\left(\mathbf{x}^k\right) = \mathbf{mid} \; \mathbf{x}^k \tag{1}$$

where **mid** operator is defined as $\mathbf{mid} \; \mathbf{x} = x_{(n+1)/2}$.

When the brain is stimulated by an input pattern, some regions of the brain (interacting areas) are stimulated and synapses belonging to those regions are modified.

In our model, the most excited interacting area is call *active region* (AR) and could be estimated as follows:

$$ar = r\left(\mathbf{x}\right) = \arg\left(\min_{i=1}^{p} \left| s\left(\mathbf{x}\right) - s_i \right| \right) \tag{2}$$

Once computed the *codified patterns*, the *de-codifying patterns* and s_k we can build the associative memory.

Let $\left\{ \left(\overline{\mathbf{x}}^k, \overline{\mathbf{y}}^k\right) \middle| k = 1, \ldots, p \right\}, \overline{\mathbf{x}}^k \in \mathbf{R}^n, \overline{\mathbf{y}}^k \in \mathbf{R}^m$ a fundamental set of associations (codified patterns). Synapses of associative memory $\mathbf{W}$ are defined as:

$$w_{ij} = \overline{y}_i - \overline{x}_j \tag{3}$$

After computed the *codified patterns*, the *de-codifying patterns,* the reader can easily corroborate that any association can be used to compute the synapses of $\mathbf{W}$ without modifying the results. In short, building of the associative memory can be performed in three stages as:

```
1.  Transform the fundamental set of association into codified and de-
    codifying patterns by means of previously described Procedure 1.
2.  Compute simplified versions of input patterns by using equation 1.
3.  Build W  in terms of codified patterns by using equation 3.
```

3.2 Modifying Synapses of the Associative Model

As we had already mentioned, synapses could change in response to an input stimulus; but which synapses should be modified? For example, a head injury might cause a brain lesion killing hundred of neurons; this entails some synapses to reconnect with others neurons. This reconnection or modification of the synapses might cause that information allocated on brain will be preserved or will be lost, the reader could find more details concerning to this topic in [5] and [12].

This fact suggests there are synapses that can be drastically modified and they do not alter the behavior of the associative memory. In the contrary, there are synapses that only can be slightly modified to do not alter the behavior of the associative memory; we call this set of synapses *the kernel* of the associative memory and it is denoted by $\mathbf{K_W}$. In the model we find two types of synapses: synapses that can be modified and do not alter the behavior of the associative memory; and synapses belonging to the kernel of the associative memory. These last synapses play an important role in recalling patterns altered by some kind of noise.

Let $\mathbf{K_W} \in \mathbf{R}^n$ the kernel of an associative memory $\mathbf{W}$. A component of vector $\mathbf{K_W}$ is defined as:

$$kw_i = \mathbf{mid}\left(w_{ij}\right), j = 1,\ldots,m \tag{4}$$

According to the original idea of our proposal, synapses that belong to $\mathbf{K_W}$ are modified as a response to an input stimulus. Input patterns stimulate some ARs, interact with these regions and then, according to those interactions, the corresponding synapses are modified. Synapses belonging to $\mathbf{K_W}$ are modified according to the stimulus generated by the input pattern. This adjusting factor is denoted by Δw and could be estimated as:

$$\Delta w = \Delta\left(\mathbf{x}\right) = s\left(\overline{\mathbf{x}}^{ar}\right) - s\left(\mathbf{x}\right) \tag{5}$$

where ar is the index of the AR.

Finally, synapses belonging to $\mathbf{K_W}$ are modified as:

$$\mathbf{K_W} = \mathbf{K_W} \oplus \left(\Delta w - \Delta w_{old}\right) \tag{6}$$

where operator $\oplus$ is defined as $\mathbf{x} \oplus e = x_i + e \;\forall i = 1,\ldots,m$. As you can appreciate, modification of $\mathbf{K_W}$ in equation 6 depends of the previous value of Δw denoted by Δw_{old} obtained with the previous input pattern. Once trained the **DAM**, when it is used by first time, the value of Δw_{old} is set to zero.

3.3 Recalling a Pattern Using the Proposed Model

Once synapses of the associative memory have been modified in response to an input pattern, every component of vector $\overline{\mathbf{y}}$ can be recalled by using its corresponding input vector $\overline{\mathbf{x}}$ as:

$$\overline{y}_i = \mathbf{mid}\left(w_{ij} + \overline{x}_j\right), j = 1,\ldots,n \tag{7}$$

In short, pattern $\overline{\mathbf{y}}$ can be recalled by using its corresponding key vector $\overline{\mathbf{x}}$ or $\tilde{\mathbf{x}}$ in six stages as follows:

```
1. Obtain index of the active region  ar  by using equation 2.
2. Transform  x^k  using de-codifying pattern  x̂^ar  by applying the follow-
   ing transformation:  x̂^k = x^k + x̂^ar .
3. Estimate adjusting factor  Δw = Δ(x̂)  by using equation 5.
```

4. Modify synapses of associative memory $\mathbf{W}$ that belong to $\mathbf{K_W}$ by using equation 6.

5. Recall pattern $\widehat{\mathbf{y}}^k$ by using equation 7.

6. Obtain $\mathbf{y}^k$ by transforming $\widehat{\mathbf{y}}^k$ using de-codifying pattern $\hat{\mathbf{y}}^{ar}$ by applying transformation: $\mathbf{y}^k = \widehat{\mathbf{y}}^k - \hat{\mathbf{y}}^{ar}$.

The formal set of prepositions that support the correct functioning of this dynamic model and the main advantages against other classical models can be found in [19], interesting applications of this model are described in [14] and [15].

In general, we distinguish two main parts for the model: the *active region part* (PAR) which determines the active region; and the *pattern recall part* (PPR). PAR (first step during recall procedure) sends a signal to PPR (remaining steps for recall procedure). This indicates the region activated by the input pattern. A schematic figure of this model is shown in Fig. 1(a).

4 Proposal

As we have previously said, baby's brain can differentiate faces from other faces within a few months of birth. However, they are not capable of detecting subtle features in a face. This fact could suggest the baby uses only few information of the face in order to recognize it.

When babies perceive a scene, we conjecture that babies at random select some stimulating points SPs, and then these information passes through the brain to the visual cortex, where this information is analyzed. Finally the information passes to other regions of the brain involved in learning and recognition processes.

In order to recognize different images of faces we propose to use a network of associative memories nDAMs. Then, we divide the image in different parts (sub-patterns) and over each sub-pattern, we detect subtle features by means of a random selection of SPs. At last, each DAM of the nDAM is fed with these sub-patterns for training and recognition.

4.1 Random Selection Using a Modified DAM

In the DAM model, the simplified version of an input pattern is the middle value of input pattern. This value is computed by using **mid** operator. In order to simulate the random selection of the infant vision system we substitute **mid** operator with **rand** operator defined as follows:

$$\mathbf{rand\ x} = x_{sp} \tag{8}$$

where $sp = random(n)$ is a random number between zero and the length of input pattern. This represents a stimulation point. sp is a constant value computed at the beginning of the building phase. During recalling phase sp takes the same value. **rand** operator uses a uniform random generator to select a component over each part of the pattern. We adopt this operator based on the hypothetical idea about infants are interested into sets of features where each set is different with some intersection

among them. By selecting features at random, we conjecture that at least we select a feature belonging to these sets.

4.2   Implementation of the Proposal

During recalling, each DAM recovers a part of the image based on the AR of each DAM. However, a part of the image could be wrongly recalled because its corresponding AR could be wrongly determined due to some patterns do not satisfy the prepositions that guarantee perfect recall. To avoid this, we use an integrator. Each DAM determines an AR, the index of the AR is sent to the integrator, the integrator determines which was the most voted region and sends to the DAMs the index of the most voted region (the new AR). In Fig. 1(b) a general architecture of the network of DAMs is shown.

(a)   (b)
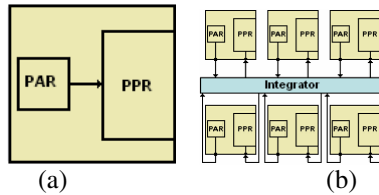
Fig. 1. (a) Main parts of the DAM. (b) Architecture of a network of DAMs.

In order to interconnect several DAMs we disconnect the PAR of its corresponding PPR. The output of the PAR is sent to an external integrator. This integrator receives several signals from different DAMs indicating the AR. At last, based on a voting technique, the integrator "tells" to each DAM which is the most voted AR.

Schematic representation of building and recalling phase are show in Fig. 2. Building of the nDAMs is done as follows:

Let $\left[\mathbf{I}_x^k\right]_{a \times b}$ and $\left[\mathbf{I}_y^k\right]_{c \times d}$ an association of images and r be the number of DAMs.

1. Transform the images into a vector ($\mathbf{x}^k$, $\mathbf{y}^k$) by means of the standard image scan method where vectors are of size $a \times b$ and $c \times d$ respectively.

2. Decompose $\mathbf{x}^k$ and $\mathbf{y}^k$ in r sub-patterns of the same size.

3. Take each sub-pattern (from the first one to the last one (r)), then take at random a stimulating point $sp_i, i = 1, \ldots, r$ and extract the value at that position.

4. Train r DAMS as in building procedure taking each sub-pattern (from the first one to the last one (r)) using **rand** operator.

Pattern $\mathbf{I}_y^k$ can be recalled by using its corresponding key image $\mathbf{I}_x^k$ or distorted version $\tilde{\mathbf{I}}_x^k$ as follows:

1. Transform the images into a vector by means of the standard image scan method.

2. Decompose $\mathbf{X}^k$ in r sub-patterns of the same size.

3. Use the stimulating point, $sp_i, i = 1, \ldots, r$ computed during the building phase and extract the value of each sub-pattern.

4. Determine the most voted active region using the integrator.

5. Substitute **mid** operator with **rand** operator in recalling procedure and apply steps from two to six as described in recalling procedure on each memory.

6. Finally, put together recalled sub-patterns to form the output pattern.

(a)

(b)
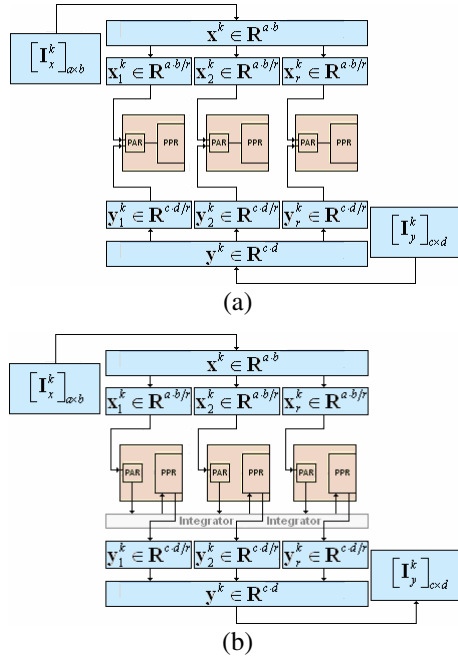
Fig. 2. (a) Schematic representation of building phase. (b) Schematic representation of the recalling phase.

While PCA dimension reduction techniques require the covariance matrix to build an Eigenspace, and then project patterns using this space to eliminate redundant information, our proposal only requires a random selection of stimulating points. This approach contributes to eliminating redundant information, it is less computationally expensive than PCA, and helps the nDAMs or other classification tools to learn efficiently the faces.

The main reason to use a DAM (in our proposal) is to demonstrate that, as in the case of a neural network and other classifiers, DAMs can be used to solve complex problems. To our acknowledgment, nobody had used associative memories this way for face recognition.

5   Experimental Results

We tested the efficiency of the proposal with the benchmark of faces given in [4]. This database contains twenty photos of fifteen different people. Each photo is in colour and of 180×200 pixels. Refer to Fig. 3. Furthermore, people in images appear with different gesticulations which nowadays is still a challenge in face recognition. Due to the level of complexity of this benchmark, we decided to use it to test the accuracy of the proposal. The database of images was divided into two sets of images. First photo of each person (15 in total) was used to train the network of DAMs. The remaining 285 photos (19 for each person) were used to test the efficiency of the proposal.

(a)

(b)
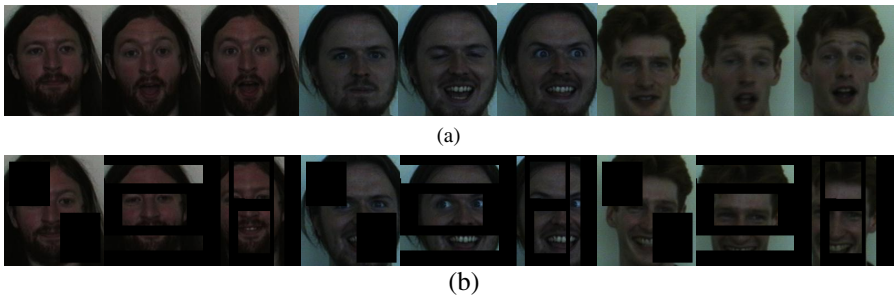
Fig. 3. (a) First 3 images of the photos of 3 people of the 15 used to test the efficiency of the proposal. (b) First 3 images of the photos the 3 people of the 15 used to test the efficiency of the proposal in the presence of occlusions.

To train the nDAM, only one image of the fifteen face classes were used along with the building procedure described in section 4.2. Something important to remark is that each DAM belonging to the nDAM was trained into its auto-associative version, *i.e.* $\mathbf{I}_x^k = \mathbf{I}_y^k$. During recalling phase the second set of images and the recalling procedure described in section 4.2 were used.

The accuracy of the proposal was tested using several configurations, starting with networks composed by one DAM until 1100 DAMs. Because of stimulating points (pixels) were randomly selected, we decided to test the stability of proposal with the same configuration 20 times.

As you can appreciate from Fig. 4(a), the accuracy of the proposal increases when the number of stimulation points (or the number of DAM) also increases. In Fig. 4(a), we can appreciate that after a certain number of stimulating points the accuracy of the proposal tends to be stable. In general, the results obtained in these experiments were around 99 % of recognition.

In addition, the accuracy of the proposal was tested when the testing images were partially occluded. For this, manually one or more parts of each image (of the second set of images) were occluded with regions of different forms and sizes. Figure 3(b) shows the first three images of three people used for testing.

In the previous experiments, the stimulating points were also randomly selected. As you can appreciate from Fig. 4(b), the accuracy of the proposal increases as the

number of stimulating points (or the number of DAM) is increased. In Fig. 4(b), we can appreciate that after a certain number of stimulating points the accuracy of the proposal tends to stabilize. In general, the results obtained in these experiments were around 80 % of recognition.

We have tested the efficiency of the proposal. We have verified that the worst performance was obtained with the images in presence of occlusion. The results obtained with the proposal in the first set of experiments were comparable with those obtained by means of a PCA-based method (99% of accuracy). Although PCA is a powerful technique it consumes a lot of time to reduce the dimensionality of the data. Our proposal, because of its simplicity in operations, is not a computationally expensive technique and the results obtained are comparable to those provided by PCA.
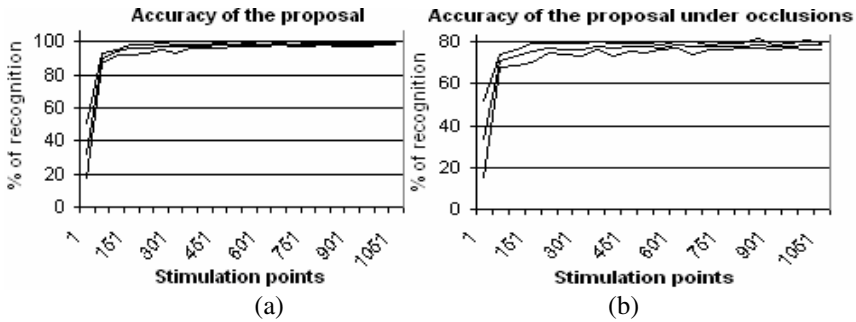
Fig. 4. (a) Behavior of the proposal. (b) Behavior of the proposal in the presence of occlusions. Maximum, average and minimum accuracy are sketched.

6 Conclusions

In this work we have shown that by applying some aspects of the infant vision system it is possible to enhance some associative memories and also make possible its application to complex problems such as face recognition.

Based on some biological aspects of the infant vision system, we have proposed some modifications to the DAM. In addition, we have described the algorithms for training and operation of a network of DAMs.

Through several experiments we have shown the accuracy and the stability of the proposal even in the presence of occlusions. In average the accuracy of the proposal oscillates between 96% and 99%. Important to mention is that, to our knowledge, nobody has reported results of this type using an associative memory for face recognition.

The results obtained with the proposal were comparable with those obtained by means of a PCA-based method. Although PCA is a powerful technique it consumes a lot of time to reduce the dimensionality of the data. Our proposal, because of its simplicity in operations, is not a computationally expensive technique and the results obtained are comparable to those provided by PCA.

Nowadays, we are applying these ideas in 3D object recognition and image retrieval taking into account some other aspects of the vision system.

References

[1] Hopfield, J.J.: Neural networks and physical systems with emergent collective computational abilities. Proc. of the Nat. Academy of Sciences 79, 2554–2558 (1982)

[2] Jolliffe, I.: Principal Component Analysis. Springer, Heidelberg (1986)

[3] Kutas, M., Hillyard, S.A.: Brain potentials during reading reflect word expectancy and semantic association. Nature 307, 161–163 (1984)

[4] Spacek, L.: Collection of facial images: Grimace (1996), Available from http://cswww.essex.ac.uk/ mv/ allfaces/grimace.html

[5] Reinvan, I.: Amnestic disorders and their role in cognitive theory. Scandinavian Journal of Psychology 39(3), 141–143 (1998)

[6] Price, C.J.: The anatomy of language: contributions from functional neuroimaging. Journal of Anatomy 197(3), 335–359 (2000)

[7] Sussner, P.: Generalizing operations of binary auto-associative morphological memories using fuzzy set theory. Journal of math. Imaging and Vision 19(2), 81–93 (2003)

[8] Laughlin, S.B., Sejnowski, T.J.: Communication in neuronal networks. Science 301, 1870–1874 (2003)

[9] Sossa, H., Barron, R.: New associative model for pattern recall in the presence of mixed noise. In: Proc. of the fifth IASTED-SIP2003, vol. 399, pp. 485–490. Acta Press (2003)

[10] Sossa, H., Barrón, R., Vázquez, R.A.: Transforming Fundamental set of Patterns to a Canonical Form to Improve Pattern Recall. In: Lemaître, C., Reyes, C.A., González, J.A. (eds.) IBERAMIA 2004. LNCS (LNAI), vol. 3315, pp. 687–696. Springer, Heidelberg (2004)

[11] Slaughter, V., Stone, V.E., Reed, C.: Perception of Faces and Bodies Similar or Different? Current Directions in Psychological Science 13(9), 219–223 (2004)

[12] Jovanova-Nesic, K., Jankovic, B.D.: The Neuronal and Immune Memory Systems as Supervisors of Neural Plasticity and Aging of the Brainn: From Phenomenology to Coding of Information. Annals of the New York Acad.of Sci. 1057, 279–295 (2005)

[13] Cuevas, K., et al.: Infants Form Associations Between Memory Representations of Stimuli That Are Absent. Psychological Science 17(6), 543–549 (2006)

[14] Vazquez, R.A., Sossa, H.: Associative Memories Applied to Image Categorization. In: Martínez-Trinidad, J.F., Carrasco Ochoa, J.A., Kittler, J. (eds.) CIARP 2006. LNCS, vol. 4225, pp. 549–558. Springer, Heidelberg (2006)

[15] Vazquez, R.A., Sossa, H., Garro, B.A.: A New Bi-directional Associative Memory. In: Gelbukh, A., Reyes-Garcia, C.A. (eds.) MICAI 2006. LNCS (LNAI), vol. 4293, pp. 367–380. Springer, Heidelberg (2006)

[16] Sussner, P., Valle, M.: Implicative Fuzzy Associative Memories. IEEE Trans. on Fuzzy Systems 14(6), 793–807 (2006)

[17] Sussner, P., Valle, M.: Gray-Scale Morphological Associative Memories. IEEE Trans. on Neural Networks 17(3), 559–570 (2006)

[18] Sossa, H., Barron, R., Vazquez, R.A.: Study of the Influence of Noise in the Values of a Median Associative Memory. In: Beliczynski, B., et al. (eds.) ICANNGA 2007, Part II, LNCS, vol. 4432, pp. 55–62. Springer, Heidelberg (2007)

[19] Vazquez, R.A., Sossa, H.: A new associative memory with dynamical synapses (to be submitted, 2007)

Two-Stage ACO to Solve the Job Shop Scheduling Problem

Amilkar Puris[1], Rafael Bello[1], Yaima Trujillo[1], Ann Nowe[2], and Yailen Martínez[1]

[1] Department of Computer Science, Universidad Central de Las Villas, Cuba
[2] CoMo Lab, Department of Computer Science, Vrije Universiteit Brussel, Belgium
{rbellop,ayudier,yaimatr,yailenm}@uclv.edu.cu,
ann.nowe@vub.ac.be

Abstract. In this paper, a multilevel approach of Ant Colony Optimization to solve the Job Shop Scheduling Problem (JSSP) is introduced. The basic idea is to split the heuristic search performed by ants into two stages; only the Ant System algorithm belonging to ACO was regarded for the current research. Several JSSP instances were used as input to the new approach in order to measure its performance. Experimental results obtained conclude that the Two-Stage approach significantly reduces the computational time to get a solution similar to the Ant System.

Keywords: Ant Colony Optimization, Ant System, Job Shop Scheduling Problem.

1 Introduction

This paper introduces a multilevel approach of Ant Colony Optimization to solve the Job Shop Scheduling Problem (JSSP). In the static JSSP, a finite number of jobs need to be processed by a finite number of machines. A job is defined as a predetermined sequence of tasks, each one of those needs to be processed without interruption for a given period of time on a specified machine. The tasks belonging to the same job cannot be processed in parallel and, additionally, each job must be carried out in each machine exactly once. A feasible schedule is an assignment of operations to time slots on a machine without violation of the job shop constraints. A makespan is defined as the maximum completion time of the jobs. The main goal is the accomplishment of a schedule that is able to minimize the JSSP's makespan. Such optimum schedule is the one that minimizes the total idle time for the set of machines. According to the complexity theory [1], the JSSP is characterized as NP-hard combinatorial optimization problem. Since the achievement of exact solutions for such sort of problems is computationally unfeasible [1], different heuristic methods have been applied for solving JSSP.

Ant Colony Optimization (ACO) is a metaheuristic used to guide other heuristics in order to obtain better solutions than those generated by local optimization methods; this meta-heuristic has been successfully applied to various hard combinatorial

optimization problems. In ACO, a colony of artificial ants cooperates in the search of good solutions to discrete problems. Artificial ants are simple agents that incrementally build a solution by adding components to a partial solution under construction. This computational model was introduced by M. Dorigo. Further information about this procedure can be found in [2], [3] and [4].

In the Scheduling field, ACO has effectively dealt with the Flow-shop [5], Resource Constraint Project Scheduling [6] and the Single Machine Total Tardiness problems [7]. ACO has also proven to be profitable in finding out the solutions of other permutation scheduling problems such as the Traveling Salesman [8, 9] and Vehicle Routing problems [10]. However, the application of the ACO to Shop scheduling such as the JSSP and open shop scheduling has demonstrated to be quite difficult [11] and very few papers about the ACO implementation for the JSSP can be found. The first ant system (AS) coping with the JSSP appeared in 1994 [12]; more recently, C. Blum et al. have done significant research on the application of ACO to shop scheduling problems including the JSSP [11, 13]; in 2004, M. Ventresca and B. Ombuki introduced an application of the Ant Colony Optimization metaheuristic to the job shop scheduling problem[14].

It is worthwhile to note that ACO algorithms are appropriate for discrete optimization problems that can be characterized as a graph $G = (C, L)$. Here, C denotes a finite set of interconnected components, i.e. nodes. The set $L \subseteq C \ x \ C$ describes all of the connections (i.e. edges) at the graph (see [6] for a complete description). Every solution of the optimization problem may be expressed in terms of feasible paths across the graph.

In this paper, a new approach of ACO is developed where the underlying idea is to have ants perform the heuristic search as a two-stage process; we focus on the Ant System algorithm belonging to the ACO family because previous studies have shown that it attains the best results [14]. Several JSSP instances were used as input to the new approach in order to measure its performance. Experimental results showed the two-stage approach significantly lowers the computational time to get an Ant System similar solution.

2   Job Shop Scheduling Problem

The JSSP is made up by a finite set J of n jobs to be processed on a finite set M of m machines. Each job J_i must be executed on every machine and consists of m chained operations $o_{i1}, o_{i2},...,o_{im}$ that are to be scheduled in a predetermined given order (precedence constraint).

There is a total of $N = n*m$ operations where o_{ik} is the operation corresponding to job J_i that is to be run on machine M_k during an uninterrupted processing time p_{ik}. The workflow of each job throughout the machines is independent of the other jobs'. At a time, each machine is able to carry out a single job and, besides, each job is to be processed by a single machine simultaneously (capacity constraints). The parameter C_{max} points out the performance measure that should be minimized (longest time required to complete all jobs).

The objective is to determine the starting times ($t_{ik} \geq 0$) for each operation so as to entail a minimization of the makespan in such a way that all of the constraints are met:

$$C_{max}^{*} = \min\{C_{max}\} = \min_{feasible\ schedules}\{\max\{t_{ik} + p_{ik}\} : \forall J_i \in J, \forall M_k \in M\} \qquad (1)$$

Table 1 depicts an example of a JSSP instance whose graphical representation is portrayed in figure 2. Notice that each node represents an operation. Thus, node 1 stands for the first operation of job 1, node 2 symbolizes the second operation and so on. In a general way, a node *i* represents the *(i mod (m+1))* operation of the *job (i div (m+1)) +1*.

Table 1. An example of a simple JSSP instance holding two jobs that must be processed on four machines. The data format is (machine, duration); numbers in bold refer to Figure 2.

(2,10)	(1, 2)	(4,7)	(3, 5)
1	**2**	**3**	**4**
(1,12)	(4,6)	(3,5)	(2,2)
5	**6**	**7**	**8**

2.1 Types of Schedules

According to the schedule properties, any feasible schedule can be categorized into four major kinds: inadmissible, semi-active, active, and non-delay schedules. The number of inadmissible schedules is infinite and most of them contain excessive idle times. A semi-active schedule can be obtained by shifting a schedule forward until no such excessive idle times appears.
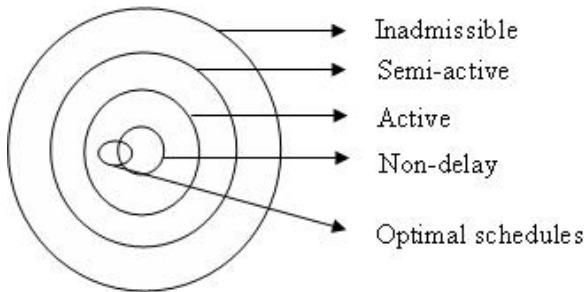
Fig. 1. The hierarchy of feasible schedules

Further improvements on a semi-active schedule can be reached by skipping some operations ahead without bringing about the latter start of other operations regarding the original schedule. However, active schedules allow no such displacement. Thus the optimal schedule is guaranteed to fall within the active schedules. Non-delay schedules build a subset of active schedules. In a non-delay schedule, a machine is never kept idle if some operation is able to be executed. It is remarkable fact that the

best schedule is not necessarily a non-delay one. However, it is easier to generate a non-delay schedule than an active one. The former may be closer to the optimal schedule even if it is not an optimal one. Additionally, there is strong empirical evidence that non-delay schedules bear solutions whose mean quality is higher than those produced by active schedules. Nevertheless, typical scheduling algorithms browse the space of all active schedules in order to assure that the optimum is taken into consideration.

3 Ant Colony Optimization (ACO)

Artificial ants are straightforward agents that incrementally make up a solution by adding components to a partial solution under construction. They are the main component in Ant Colony Optimization (ACO). In such methodology, the ants cooperate in order that good solutions to discrete problems can be found.

Ant System (AS) is the first ACO algorithm; it was introduced by means of the Traveling Salesman Problem (TSP) [7] and [9]. In TSP, we have a group of edges fully connecting the set of N cities $\{c_1, \ldots, c_n\}$; each edge is assigned a weight d_{ij} whose meaning is the distance between cities i and j. The goal is to find the shortest possible trip which comprises each city only once before going back to the starting city. When ACO is used to solve these problems, pheromone trails (τ_{ij}) are associated to the edges and denote the likeliness of visiting city j coming from city i. Initially, the ants are randomly positioned into cities. Throughout the subsequent steps, ant k computes a random proportional rule to decide which city will be visited next according to expression (2):

$$p_{ij}^k = \frac{\left(\tau_{ij}\right)^\alpha * \left(\eta_{ij}\right)^\beta}{\sum_{l \in N_i^k}\left(\tau_{il}\right)^\alpha * \left(\eta_{il}\right)^\beta} \qquad if \quad j \in N_i^k \quad \left(neighborhood \quad of \quad ant\ k\right) \tag{2}$$

where α and β are leveling parameters of the relative importance of the pheromone trail and the heuristic information, respectively. AS ants have a memory (tabu list) that stores visited components of their current path for preventing the chance of returning to an already visited city.

After all ants have made up their tours, the τ_{ij} values are updated in two stages. Evaporation as a fading factor of the pheromone trail is considered in stage 1, yielding lower τ_{ij} which are calculated as shown in expression (3) by using the parameter ξ, *(0 < ξ < 1)*; this step is needed to avoid the unlimited accumulation of pheromone.

$$\tau_{ij} = (1 - \xi) * \tau_{ij} \tag{3}$$

Secondly, all ants increase the value of τ_{ij} on the edges they have traversed in their tours according to the expression below:

$$\tau_{ij} = \tau_{ij} + Inc_{ij} \tag{4}$$

where *Inc_{ij}* is the amount of pheromone dropped by all ants walking across the edge *(i, j)*. Usually, the amount of pheromone dropped by ant k equals to *$1/C_k$*, where C_k is the length of the tour for ant k.

4 Ant System for JSSP

An instance of the JSSP in the ACO algorithm is represented as a graph where the nodes are connected by two kinds of edges; the nodes represent operations, that is, for N jobs and M machines, the graph will include N*M nodes; the oriented edges represent the precedence between operations belonging to the same job and the dashed edges stand for a likely path that ants can go through if the problem constraints are satisfied (See Figure 2).

In order to apply the AS algorithm, a graphical representation **G** of the optimization problem must be built up at first.

The meta-heuristic begins initializing the amount of pheromone in each edge of **G** with some positive real value c. Each ant is then placed into an initial position, which is added to its tabu list; such initial positions are randomly chosen from the possible ones, which are the first operations to execute in each job.

Every agent will independently set up a solution following the probabilistic rule 1, where the heuristic value associated to an operation j is $d_{ij} = 1/Ctime_j$, $Ctime_j$ symbolizes the completion of operation j. After the tabu list of all ants is full (a valid solution has been found), its path length will be determined and the best solution found so far will be recorded.

Next, the pheromone values are recomputed via expressions 2 and 3, where Inc_{ij} in this problem is the better scheduling found in the current cycle. This process is repeated during a given number of cycles.

In the graph displayed in Figure 2, the possible initial positions for the ants are nodes 1 and 5. If ant k chooses node 5, then the likely moves that meet the problem's constraints are either to nodes 1 or 6 and alike.
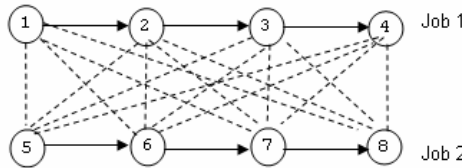
Fig. 2. A graphical representation for the 2-job and 4-machine problem instance shown in Table 1

For this problem we can find the following feasible schedules (solutions):

A: {1-2-3-5-6-7-4-8}, B: {5-6-7-1-2-8-3-4}, C: {1-2-5-6-3-4-7-8}

Table 2. Starting from solution B, an active schedule having a makespan of 30 is built from scratch

	2	4	6	8	10	12	14	16	18	20	22	24	26	28	30
M_1		J_2					J_1								
M_2		J_1											J_2		
M_3										J_2				J_1	
M_4								J_2			J_1				

5 Two-Stage Ant System (TS-AS) in the JSSP

The Two-Stage Ant Colony Optimization (TS-ACO) proposed in this investigation is based on the following idea: to split the search process performed by the ants into two stages so that in the first stage, preliminary results are reached (partial solutions) that behave as initial states for the ulterior search realized during the second stage.

Determining an initial state in which the search process starts has been an interesting issue in heuristic search. Due to the well known influence the initial state has in the search process, the algorithm aims to approximate the initial state to the goal state as much as possible. Of course, it is necessary to regard a fitting balance between the computational cost of achieving the initial state and the overall cost; in other words, the sum of the costs of approximating the initial to the goal state plus the cost of finding the solution beginning at the "enhanced" initial state should not be greater than the cost of seeking the solution from a random initial state.

More formally, the purpose is described as follows: let E_i be an initial state either randomly generated or computed by any other method without a meaningful computational cost; E_i^* is an initial state generated via approximation to the goal state by some method M; $C_M(E_i^*)$ indicates the cost of reaching state E_i^* from E_i through method M and $CC_{HSA}(x)$ is the computational cost of finding a solution from state x utilizing a Heuristic Search Algorithm (HSA). Hence, the objective expression is held so that $C_M(E_i^*) + CC_{HSA}(E_i^*) < CC_{HSA}(E_i)$.

In the TS-AS proposed here, the procedure for calculating E_i^* and the *HSA* are both the AS algorithm, so the objective is $C_{AS}(E_i^*) + CC_{AS}(E_i^*) < CC_{AS}(E_i)$. Since AS is used in both stages, the difference between them is computed by assigning different values to some parameters of the model during each stage. A ratio *(r)* is introduced in order to measure the relative assignment of the values to the parameters of the algorithm in both stages; r indicates the portion of the overall search to be realized at the first stage. For instance, if $r = 0.3$, it means that the first stage will comprise 30% of the overall search and during the second stage, the remaining 70% shall be carried out (an example of the application of this ratio is exhibited in the next section).

Setting the value of r exercises a high influence in the overall performance of the algorithm. The higher value of r, the closer the state E_i^* will be to the goal state. As an outcome, $C_{AS}(E_i^*)$ increases and $CC_{AS}(E_i^*)$ decreases. In addition to this balance between the costs of $C_{AS}(E_i^*)$ and $CC_{AS}(E_i^*)$, the question of how much the search space was explored arises; the greater the rate r is, the lower the search in the second stage is due to several reasons: (I) there are less ants working, (II) the amount of cycles becomes smaller and (III) although the number of possible initial states for the second stage should become greater when r increases, such number is already upper-bounded by the result of the previous stage.

Therefore, a key point is to study what value of rate r is the best in order to reach the best balance between the searches performed during both stages. This value must allow:

- The minimization of $C_{AS}(E_i^*) + CC_{AS}(E_i^*)$.
- An exploration of the search space that guarantees to find good solutions.

When applying AS algorithm to the JSSP, the ants begin the search starting from random initial states; that is, in each cycle an ant commences its trip in a randomly

chosen operation and picks up the next operation through rule (1). At the beginning, no pheromone information is available to lead the search; the heuristic information alone is present.

On the contrary, the TS-AS builds up partial trips (they do not include all the nodes) in the first stage; this information behaves as an initial state for ants during the second stage of the search algorithm. In other words, instead of rebooting the search from scratch, the agents use the information available after the execution of the first stage as the starting point in the second stage.

In JSSP, the parameters whose values depend on the ratio r are: the number of ants (m), the number of cycles (nc) and the number of operations ($co = N * M$) that will be included in each stage.

The parameters values are assigned as illustrated right now: Let be 6 jobs and 5 machines ($J = 6, M = 5, N=30$ *total operations*) and the following parameters for the traditional AS algorithm: $m = 100$, $nc = 100$ and $co = 30$. Setting $r = 0.3$ implies that the values of these parameters for the two stage ACS are computed accordingly as: $m_1 = 100 * 0.3 = 30$, $nc_1 = 100 * 0.3 = 30$ and $cc_1 = 30 * 0.3 = 9$ for the first stage; and $m_2 = 100 * 0.7 = 70$, $nc_2 = 100 * 0.7 = 70$ and $cc_2 = 30$. It means that 30 ants will execute the AS algorithm for the time of 30 cycles, building a sequence of 9 operations. In the second stage, 70 ants will run the AS algorithm throughout 70 cycles shaping the sequence of 30 operations. This signifies that in the first stage, 30% of the ants will be seeking size-lessened solutions (because the sequence comprises only 30% of the nodes) in the 30% of the total number of cycles. In the second stage, the remaining 70% of the ants are used; they will perform the search for the 70% of the total number of cycles so as to discover full problem solutions (including all operations). Once the first stage has finished, a subset of partial solutions is picked up (denoted by *EI*) holding *cs* out of the best solutions (sequences with the best values of the objective function) found during the first stage.

The TS-AS-JSSP algorithm is outlined below:

Input: Parameters beta, rho, epsilon, cc, factor r, number of solutions in EI (cs)
Output: The best solution found.

```
S₁: Set the number of ants either by input data or by using some
method depending on the number of operations.
S₁: Perform Stage 1.
S₁.₁: Compute the parameters for the first stage:
            m₁ = r * m
            nc₁ = r * nc
            cc₁ = r * cc
S₁.₂: Run the AS algorithm that performs nc₁ cycles in the first stage.
S₁.₃: Set of trips ← Trips generated by AS algorithm in the first
stage.
S₂: Perform Stage 2.
S₂.₁: Compute the parameters for the second stage:
            m₂ = m - m₁
            nc₂ = nc - nc₁
            cc₂ = cc
            EI ← Pick up the cs best solutions from the
            set of trips.
S₂.₂: Run the AS algorithm (that performs nc₂ cycles in the second
stage by using the elements of EI as initial states for the ants in
the second stage).
```

6   Experimental Results

Table 3 shows a comparative study between the algorithms AS-JSSP and TS-AS-JSSP using some remarkable JSSP instances found at OR-Library [17] regarding the quality of the solution and the computational cost in time. The same parameters were used in both algorithms for running the tests; that is, the number of ants (m) equals to the number of operations, $nc = 3000$, $\xi = 0.1$, $\alpha = 0.8$ and $\beta = 0.17$. Three different ratios were used for the TS-AS-JSSP algorithm: $r = \{0.2, 0.25, 0.3\}$. For every test, 10 runs on every instance were carried out and the best solution was selected. The columns of Table 3 stand for: the dataset name, the best solution reached for that dataset, the best solution found by the Ant System algorithm, the time cost (in milliseconds) for finding the AS solution, the best solution reported by the two stage approach (including the ratio used in the computation) and finally, the time cost (in milliseconds) for finding the two-stage algorithm solution.

Table 3. A comparative study between Ant System and Two-Stage Ant System

Instance	BK	AS-JSSP	Time1	TS-AS-JSSP	Time2
la01	666	666	157502	666(r=0.3)	53513
la02	660	673	144697	672(r=0.2)	74518
la03	597	627	144107	607(r=0.25)	60210
la04	590	611	144455	594(r=0.3)	53044
la05	593	593	144531	593(r=0.25)	61224
la06	926	926	510077	926(r=0.3)	180915
la07	890	897	509708	890(r=0.25)	224793
la08	863	868	508714	865(r=0.25)	216916
la09	951	951	510802	951(r=0.3)	186744
la10	958	958	508825	958(r=0.25)	178458
la11	1222	1222	1276036	1222(r=0.3)	460834
la12	1039	1039	1269386	1039(r=0.3)	450302
la13	1150	1150	1268055	1150(r=0.3)	462080
la14	1292	1292	1288142	1292(r=0.3)	456755
la15	1207	1251	1271330	1247(r=0.25)	553566
la16	945	978	930177	978(r=0.3)	353844
la17	784	797	927918	800(r=0.2)	510641
la18	848	901	938328	868(r=0.2)	480469
la19	842	892	928723	871(r=0.3)	414511
la20	902	955	933017	936(r=0.3)	354534

These experimental results prove that the two-stage approach algorithm achieved better solutions than the classic Ant System algorithm, additionally lowering the time cost for over 50%. Also, the qualities of the solutions reached by TS-AS- JSSP are higher than those exposed in [14], where the algorithms Max-Min Ant System, PFS and NFS, introduced in [14], are used.

The statistical analysis performed in order to compare the solution values for the mentioned algorithms using Monte Carlo Significance of Friedman's test=0.000 is displayed in Figure 3 a), whereas b) provides the comparison among the algorithms

	Mean Ranks
Optimum	1.50^a
TS-AS-JSSP(0.2)	2.80^b
TS-AS-JSSP(0.25)	3.10^b
AS-JSSP	3.45^{bc}
TS-AS-JSSP(0.3)	4.15^c

a) Statistical analysis for solutions values

	Mean Ranks
TS-AS-JSSP(0.3)	1.00^a
TS-AS-JSSP(0.25)	1.40^{ab}
TS-AS-JSSP(0.2)	2.10^b
AS-JSSP	4.00^c

b) Statistical analysis for time cost

Fig. 3. Statistical Analysis for solutions values (a) and computational cost (b)

with respect to the time needed to get the solution. Mean Ranks with a common letter denote non-significant difference according to Wilcoxon's test, proving that there are not significative differences between the AS and TS-AS in solutions values, and showing an important difference between them in the time cost.

7   Conclusions

This paper introduces a new approach to ant colony optimization to the job shop scheduling problem. It consists of the splitting of the search process performed by ants into two stages. The study was carried out with the use of the Ant System algorithm. In this approach, some parameters (number of ants, number of cycles, etc.) are assigned a different value in each stage according to a ratio r which signals the portion of the overall search that corresponds to each stage.

The algorithm's performance was thoroughly studied by using different ratio values. The best results came up when this value falls within the interval [0.2, 0.3].

This new ACO approach yields a significant reduction of the computational time cost yet preserving the quality of the solutions.

Acknowledgments

References

1. Garey, M.R., D.S.: Computers and Intractability, A Guide to the Theory of NP-Completeness. W.H Freeman and Company (1979)
2. Dorigo, M., et al.: The Ant System: Optimization by a colony of cooperating agents. Man and Cybernetics-Part B 26(1), 1–13 (1996)
3. Dorigo, M., et al.: Ant algorithms for discrete optimization. Artificial Life 5(2), 137–172 (1999)
4. Dorigo, M., Stutzle, T.: Ant Colony Optimization. MIT Press, Cambridge (2004)
5. Stutzle, T.: An ant approach for the flow shop problem. In: EUFIT 1998, Verlag Mainz, Aachen, vol. 3, pp. 1560–1564 (1998)

6. Merkle, D., Middendorf, M., Schmeck, H.: Ant Colony Optimization for Resource Constrained Project Scheduling. IEEE Transactions on Evolutionary Computation 6(4), 333–346 (2002)
7. Merkle, D., Middendorf, M.: Ant Colony Optimization with Global Pheromone Evaluation for Scheduling a Single Machine. Journal of Applied Intelligence 105–111 (2003)
8. Dorigo, M., Gambardella, L.M.: Ant Colony System: A Cooperative Learning Approach to the Traveling Salesman Problem. IEEE Transactions on Evolutionary Computation 1(1), 53–66 (1997)
9. Bullnheimer, B., Hartl, R.F., Strauss, C.: A New Rank Based Version of the Ant System: A Computational Study. Central European Journal for Operations Research and Economics 7(1), 25–38 (1999)
10. Gambardella, L.M., Taillard, E., Agazzi, G.: MACS-VRPTW: A Multiple Ant Colony System for Vehicle Routing Problems with Time Window. In: David Corne, Marco Dorigo, and Fred Glover, editors, New Ideas in Optimization, pp. 63–76. McGraw-Hill, London (1999)
11. Blum, C., Sampels, M.: An ant Colony Optimization Algorithm to tackle Shop Scheduling Problems
12. Colorni, A., Dorigo, M., Maniezzo, V., Trubian, M.: Ant system for Job-shop Scheduling. JORBEL - Belgian Journal of Operations Research, Statistics and Computer Science 34(1), 39–53 (1994)
13. Blum, C., Sampels, M.: An ant Colony Optimization Algorithm for FOP Shop Scheduling: A case study on different pheromone representations. In: CEC 2002, pp. 1558–1563 (2002)
14. Ventresca, M., Ombuki, B.: Ant Colony Optimization for Job Shop Scheduling Problem. From Proceedings pf Artificial Intelligence and Soft Computing (2004)
15. Dorigo, M., Gambardela, L.M.: Ant colonies for the traveling salesman problem. BioSystems (43), 73–81 (1997)
16. Dorigo, M., Stützle, T.: ACO Algorithms for the Traveling Salesman Problem. Evolutionary Algorithms in Engineering and Computer Science: Recent Advances in Genetic Algorithms, Evolution Strategies, Evolutionary Programming, Genetic Programming and Industrial Applications. John Wiley & Sons, Chichester (1999)
17. OR-library, URL http://web.cecs.pdx.edu/ bart/cs510ss/project/jobshop/jobshop/
18. Stutzle, T., Hoos, H.: The Max-Min Ant System. Future Generation Computer System 16(8), 889–914 (2000)

A Novel Hybrid Taguchi-Grey-Based Method for Feature Subset Selection

Hsin-Yun Chang[1] and Chung-Shan Sun[2]

[1] Department of Business Administration,
Chin-Min Institute of Technology
110 Hsueh-Fu Road, Tou-Fen, Miao-Li 305, Taiwan
Department of Industrial Technology Education,
National Kaohsiung Normal University
116 Heping 1st RD., Lingya District, Kaohsiung 802, Taiwan
`ran_hsin@ms.chinmin.edu.tw`
[2] Department of Industrial Technology Education,
National Kaohsiung Normal University
116 Heping 1st RD., Lingya District, Kaohsiung 802, Taiwan
`x9106@ms21.hinet.net`

Abstract. In this paper, a novel hybrid Taguchi-Grey-based method for feature subset selection is proposed. The two-level orthogonal array is employed in the proposed method to provide a well-organized and balanced comparison of two levels of each feature (i.e., the feature is selected for pattern classification or not) and interactions among all features in a specific classification problem. That is, this two-dimensional matrix is mainly used to reduce the feature subset evaluation efforts prior to the classification procedure. Accordingly, the grey-based nearest neighbor rule and the signal-to-noise ratio (SNR) are used to evaluate and optimize the features of the specific classification problem. In this manner, important and relevant features can be identified for pattern classification. Experiments performed on different application domains are reported to demonstrate the performance of the proposed hybrid Taguchi-Grey-based method. It can be easily seen that the proposed method yields superior performance and is helpful for improving the classification accuracy in pattern classification.

Keywords: Feature Subset Selection, Taguchi Methods, Grey-based Nearest Neighbor Rule, Pattern Classification.

1 Introduction

In recent years, different pattern classification approaches have been investigated for classifying new, unseen instances. In a pattern classification model [12], a set of training instances or examples, denoted as training set *TS*, is collected. Each instance or example is described by p features and a class label. Generally, all features of each instance will be taken into consideration during the classification process. Many real-world classification problems, however, involve redundant or irrelevant features that

usually greatly affect the overall classification accuracy.   To improve the performance, various feature selection or feature subset selection methods have been developed. These methods focus on selecting important and relevant features from the original feature set, as well as reducing the dimensionality in a particular classification problem.

Feature subset selection can be viewed as a search problem [15], where each search state in the search space specifies a possible feature subset. If each instance in a specific classification problem contains p attributes, the search space will be composed of 2^p candidate feature subsets. Obviously, exhaustive search through the entire search space (i.e. 2^p candidate feature subsets) has a very high computational cost and thus is usually unfeasible in practice, even for medium-sized p [19]. Consequently, it is difficult to select a best feature subset for pattern classification from the entire search space with respect to the tradeoff between high classification accuracy and small number of selected features.

Two well-known greedy hill-climbing approaches, sequential forward selection (SFS) [17] and sequential backward selection (SBS) [17], are commonly used for feature subset selection.   As mentioned earlier, feature subset selection can be considered as a search problem, where each search state in the search space specifies a possible feature subset. In SFS, the search procedure starts with an empty feature set and then successively adds features one at a time to find the final feature subset. By contrast, in SBS, the search procedure starts with a full feature set and then successively removes features one at a time to find the final feature subset.   In bidirectional feature subset selection methods [19], the search procedure may start with an empty feature set or a full feature set and then add or remove features to or from the search starting point [19] simultaneously. Accordingly, the final feature subset can be obtained. The above sequential search methods for feature subset selection are simple and easy to implement. However, local optimal final feature subsets are often obtained during the search procedure. Another similar sequential search method for feature subset selection is proposed in [11]. First, k features are added (or eliminated) to the candidate feature subset at a time.   Accordingly, l features are eliminated (or added) from the candidate feature subset at a time ($k > l$). These two steps are repeated until a final feature subset is obtained. In this case, the values of k and l, which will significantly affect the final result, should be determined carefully.   To avoid being trapped into local optimal results, random search [4] through the entire search space is also commonly used to find the final feature subset. This method can help the search procedure to escape from local maximums [19] (i.e., non-deterministic heuristic search). However, inconsistent final feature subsets may be derived from different runs [19].

During the search procedure, each feature or generated feature subset should be evaluated by an evaluation criterion. Generally, two kinds of evaluation criteria, independent criterion and dependent criterion [19], are adopted to evaluate each feature or generated feature subset in feature subset selection. An independent criterion [13, 16, 18] is used to evaluate the goodness of each feature or generated feature subset by considering the original characteristics of the training set. In this case, pattern classification methods are not involved in each evaluation process. As for dependent criterion, pattern classification methods are directly used to evaluate the goodness (i.e., classification ability or accuracy) of each feature or generated feature

subset. By contrast, the corresponding feature subset selection methods are named as the wrapper approaches [16]. Generally, the wrapper models, which focus mainly on improving the classification accuracy of pattern classification tasks, often yield superior performance (i.e., high classification accuracy) than the filter models. However, the wrapper approaches are more computational expensive than the filter approaches [16, 19]. As a result, many pattern classification methods that have very high computational costs, such as neural networks [2] and decision trees [20], may not be suitable to be used as evaluation criteria for evaluating each feature or generated feature subset.

In this paper, a novel hybrid Taguchi-Grey-based method for feature subset selection is proposed. The two-level orthogonal array is employed in the proposed method to provide a well-organized and balanced comparison of two levels of each feature (i.e., the feature is selected for pattern classification or not) and interactions among all features in a specific classification problem. That is, this two-dimensional matrix is mainly used to reduce the feature subset evaluation efforts prior to the classification procedure. Accordingly, the grey-based nearest neighbor rule and the signal-to-noise ratio (SNR) are used to evaluate and optimize the features of the specific classification problem. In this manner, important and relevant features can be identified for pattern classification. As a result, the hybrid Taguchi-Grey-based method proposed here has wrapper nature [16] (In wrapper feature subset selection methods, each candidate feature or feature subset is evaluated according to the classification ability obtained by the pattern classification model). That is, features will be selected based on the special properties of the corresponding pattern classification model and thus the goal of feature subset selection method here is to maximize the classification accuracy. Experiments performed on different application domains are reported to demonstrate the performance of the proposed hybrid Taguchi-Grey-based method. It can be easily seen that the proposed method yields superior performance and is helpful for improving the classification accuracy in pattern classification.

The rest of this paper is organized as follows. The concepts of the Taguchi methods used in the proposed method are reviewed in Sections 2. Section 3 proposes a novel hybrid Taguchi-Grey-based method for feature subset selection. In Section 4, an example is given to illustrate the proposed method. In Section 5, experiments performed on different classification problems are reported and discussed. Finally, the conclusions are given in Section 6.

2   Taguchi Methods

In robust design [23], products, processes or equipments can be evaluated and improved by considering different related design parameters (or factors). As a well-known robust experimental design approach, the Taguchi method [22] uses two principal tools, the orthogonal array and the signal-to-noise ratio (SNR), for the above purpose of evaluation and improvement. Consider that a specific object domain (e.g. product, process or equipment) contains q design parameters (or factors). Orthogonal arrays are primarily used to reduce the experimental efforts regarding these q different design factors. An orthogonal array can be viewed as a fractional factorial matrix that

provides a systematic and balanced comparison of different levels of each design factor and interactions among all design factors. In this two-dimensional matrix, each column specifies a particular design factor and each row represents a trial with a specific combination of different levels regarding all design factors. In the proposed method, the well-known two-level orthogonal array is adopted for feature subset selection. A general two-level orthogonal array can be defined as follows.

$$L_w(2^{w-1}),\qquad(1)$$

where $w=2^k$ ($k \geq 1$) represents the number of experimental trials, base 2 specifies the number of levels of each design factor, and w-1 is the number of columns (i.e., the number of design factors) in the orthogonal array.

For example, an orthogonal array $L_{16}(2^{15})$ can be created for a specific object domain that contains 15 design factors with two levels (i.e., level 1 and level 2). Notably, by using the two-level orthogonal array, only 16 experimental trials are needed for the purpose of evaluation and improvement. By contrast, all possible combinations of 15 design factors (i.e., 2^{15}) should be taken into consideration in the full factorial experimental design, which is obviously often inapplicable in practice.

Once the orthogonal array is generated, the observation or the objective function of each experimental trial can be determined. Accordingly, the signal-to-noise ratio (SNR) is used to evaluate and optimize the design parameters (or factors) of the specific object domain. In general, two kinds of signal-to-noise ratios (SNRs), the smaller-the-better and the larger-the-better characteristics [23], are commonly considered for the evaluation task.

Consider that a set of k observations $\{y_1, y_2, \ldots, y_k\}$ is given. In the smaller-the-better characteristic, the signal-to-noise ratio (SNR) is calculated as follows.

$$SNR = -10\log\left(\frac{1}{k}\sum_{i=1}^{k} y_i^{\,2}\right),\qquad(2)$$

Similarly, in the larger-the-better characteristic, the signal-to-noise ratio (SNR) is calculated as follows.

$$SNR = -10\log\left(\frac{1}{k}\sum_{i=1}^{k}\frac{1}{y_i^{\,2}}\right),\qquad(3)$$

The signal-to-noise ratio (SNR) is used to measure the robustness of each design parameter (or factor). That is, "high quality" of a particular object domain can be achieved by considering each design parameter with a specific level having high signal-to-noise ratio (SNR).

In summary, the Taguchi method offers many advantages for robust experimental design. First, the number of experimental runs can be substantially reduced (compared with the full factorial experimental design). Meanwhile, the significance of each design parameter regarding a particular object domain can be analyzed precisely. In the proposed method, the above two useful tools, the orthogonal array and the signal-to-noise ratio (SNR), are employed for feature subset selection.

3   Hybrid Taguchi-Grey-Based Method for Feature Subset Selection

In this section, a novel hybrid Taguchi-Grey-based method for feature subset selection is proposed. Consider that a particular classification task involves a set of m labeled training instances, denoted as $V=\{v_1, v_2, \ldots, v_m\}$. Each instance is described by n attributes, denoted as $F = (f_1, f_2, \ldots, f_n)$. The detailed procedures of the proposed hybrid Taguchi-Grey-based method for feature subset selection are described as follows.

Step1.   Generate the two-level orthogonal array L with respect to the n attributes, features or factors in a specific classification problem. In each experimental trial j in the two-level orthogonal array L, levels 1 or 2 in each column i mean feature i is selected in the corresponding feature set S_j for pattern classification or not, respectively.

Step2.   For each feature set S_j, determine an average classification accuracy regarding the training set V (denoted by $ACC(V, S_j)$) by using the grey-based nearest neighbor rule [8, 9, 10, 14] with leave-one-out (LOO) cross-validation method [5]. Here, $ACC(V, S_j)$ is considered as the observation or the objective function of the experimental trial j in the two-level orthogonal array L.

Step3.   Calculate the corresponding signal-to-noise ratio (SNR) for each level (i.e., levels 1 or 2) of each feature or factor i according to the various observations in the two-level orthogonal array L.

Step4.   Select the features whose SNR for level 1 is greater than that for level 2. These features, denoted as feature subset S, are used as the final feature subset for pattern classification.

The two-level orthogonal array is employed in the proposed method to provide a well-organized and balanced comparison of two levels of each feature (i.e., the feature is selected for pattern classification or not) and interactions among all features in a specific classification problem. In other words, this two-dimensional matrix is mainly used to reduce the feature subset evaluation efforts prior to the classification procedure. Accordingly, the grey-based nearest neighbor rule and the signal-to-noise ratio (SNR) are used to evaluate and optimize the features of the specific classification problem.

Based on the grey-based nearest neighbor rule with leave-one-out (LOO) cross-validation method [5], a classification accuracy with respect to the training set V and a particular feature set S_j (denoted as $ACC(V, S_j)$), can be obtained. Leave-one-out cross-validation implies that each instance in V is considered as the test instance once and other instances in V are considered as the corresponding training instances. In this manner, the grey-based nearest neighbor rule will be carried out m times according to m instances and n features in V. Afterwards, the average classification accuracy is calculated for evaluating the classification performance of the corresponding feature set S_j. The signal-to-noise ratio (SNR) is then used to measure the robustness of each feature of the specific classification problem. That is, high classification performance regarding the classification task can be achieved by

considering each feature with a specific level having high signal-to-noise ratio (SNR). Here, the larger-the-better characteristic, as shown in Eq. (3), is selected for calculating the signal-to-noise ratio (SNR) since maximum classification accuracy is preferred in pattern classification. In the proposed method, feature i with SNR of level 1 greater than that of level 2 means that the feature is suggested to be selected in the final feature subset for pattern classification. By contrast, feature i is suggested to be removed from the original feature set F if the corresponding SNR of level 2 greater than that of level 1. (Notably, levels 1 or 2 of feature i mean the feature is selected in the corresponding feature set S_j for pattern classification or not, respectively.)

4   Illustrative Example

This section gives an example to illustrate the proposed hybrid Taguchi-Grey-based method for feature subset selection. In the Autompg classification problem [3], each instance has seven attributes, denoted by {A, B, C, D, E, F, G}. By using the proposed method, a two-level orthogonal array $L_8(2^7)$ can be generated as Table 1.

Table 1. $L_8(2^7)$ Orthogonal Array

Number of Experimental Trial	Design Factors (Features)						
	A	B	C	D	E	F	G
	Column Number						
	1	2	3	4	5	6	7
1	1	1	1	1	1	1	1
2	1	1	1	2	2	2	2
3	1	2	2	1	1	2	2
4	1	2	2	2	2	1	1
5	2	1	2	1	2	1	2
6	2	1	2	2	1	2	1
7	2	2	1	1	2	2	1
8	2	2	1	2	1	1	2

Restated, in each experimental trial j in the two-level orthogonal array $L_8(2^7)$, levels 1 or 2 of each column i mean feature i is selected in the corresponding feature set S_j for pattern classification or not, respectively. For example, in experimental trial 7, features C, D, G are selected as the final feature subset for pattern classification. By using the two-level orthogonal array $L_8(2^7)$, the experimental efforts regarding feature subset evaluation can be reduced from 128 (i.e., 2^7) trials to eight trials.

Accordingly, for each experimental trial j, the average classification accuracy regarding the training set V and the corresponding feature set S_j (denoted by $ACC(V, S_j)$) can be determined by using the grey-based nearest neighbor rule with leave-one-out (LOO) cross-validation method. Here, $ACC(V, S_j)$ is considered as the observation or the objective function of the experimental trial j in the two-level orthogonal array $L_n(2^{n-1})$. As a result, the experimental layout and signal-to-noise data of the Autompg classification problem can be summarized as Table 2. Here, the larger-the-better characteristic, as shown in Eq. (3), is selected to determine the signal-to-noise ratio (SNR) since maximum classification accuracy is preferred in pattern classification.

Table 2. Experimental layout and signal-to-noise data of the Autompg classification problem

Number of Experimental Trial	Column / Feature							Classification Accuracy (%)	Classification Accuracy SNR (dB)
	A	B	C	D	E	F	G		
1	1	1	1	1	1	1	1	69.10	36.79
2	1	1	1	2	2	2	2	66.58	36.47
3	1	2	2	1	1	2	2	72.86	37.25
4	1	2	2	2	2	1	1	63.07	36.00
5	2	1	2	1	2	1	2	81.16	38.19
6	2	1	2	2	1	2	1	73.62	37.34
7	2	2	1	1	2	2	1	71.11	37.04
8	2	2	1	2	1	1	2	66.83	36.50

Table 3. The signal-to-noise ratios of levels 1 or 2 of each feature regarding the Autompg classification problem

	A	B	C	D	E	F	G
Level 1	36.63	37.20	36.70	37.32	36.97	36.87	36.79
Level 2	37.27	36.70	37.20	36.58	36.93	37.03	37.10

Table 3 lists the signal-to-noise ratios of levels 1 or 2 of each feature regarding the Autompg classification task. As mentioned earlier, the higher the signal-to-noise ratio (SNR), the better the classification performance (i.e., classification accuracy). As a result, features B, D and E, whose SNR for level 1 is greater than that for level 2, are preferred to be selected in the final feature subset for pattern classification. By contrast, features A, C, F, and G, whose SNR for level 2 is greater than that for level 1, are preferred to be removed from the original feature set for pattern classification. Consequently, the final feature subset obtained by using the proposed method for the Autompg classification problem is {B, D, E}. The corresponding classification accuracy is 86.43%, which is significantly better than that of each experimental trial in Table 2.

5   Experimental Results

To demonstrate the performance of the proposed hybrid Taguchi-Grey-based method for feature subset selection, ten real datasets (classification tasks) [3] were used for performance comparison. Table 4 describes the main characteristics of the datasets.

Table 5 represents the classification accuracies (as mentioned earlier) of the above-mentioned grey-based nearest neighbor rule with respect to the above classification problems when the proposed hybrid Taguchi-Grey-based method for feature subset selection is performed or not (In the experiments, the cross-validation technique [21] was used for measuring the classification accuracies). The average classification accuracies regarding these classification problems can be increased from 82.35% to 85.46% when the proposed hybrid Taguchi-Grey-based method for feature subset selection is applied. That is, experimental results demonstrate that the final feature subset obtained by using the proposed method is helpful for pattern classification.

Table 4. Details of experimental classification problems [3]

Classification task	Number of instances	Number of classes	Number of features and their types
Autompg	398	3	7 (2-S, 5-C)
Breastw	699	2	9 (9-C)
Bridges	105	6	12 (9-S, 3-C)
Hcleveland	303	5	13 (8-S, 5-C)
Hepatitis	155	2	19 (13-S, 6-C)
Hhunggarian	294	2	12 (7-S, 5-C)
Tae	151	3	5 (4-S, 1-C)
Voting	435	2	16 (16-S)
Wine	178	3	13 (13-C)
Zoo	101	7	16 (16-S)

C: Continuous, S: Symbolic

Table 5. The classification accuracies (as mentioned earlier) of the above-mentioned grey-based nearest neighbor rule with respect to the above classification problems when the proposed hybrid. Taguchi-Grey-based method for feature subset selection is performed or not.

Classification problem	The proposed method is not used for feature subset selection	The proposed method is used for feature subset selection
Autompg	69.10	**78.89**
Breastw	95.85	**96.57**
Bridges	87.62	**91.43**
Hcleveland	55.78	**57.43**
Hepatitis	80.00	**83.87**
Hhunggarian	75.85	**78.91**
Tae	**66.23**	**66.23**
Voting	92.87	**94.71**
Wine	96.63	**98.87**
Zoo	96.04	**97.03**
Average	81.60	**84.39**

6   Conclusions

In this paper, a novel hybrid Taguchi-Grey-based method for feature subset selection is proposed. The two-level orthogonal array is employed in the proposed method to provide a well-organized and balanced comparison of two levels of each feature (i.e., the feature is selected for pattern classification or not) and interactions among all features in a specific classification problem. Accordingly, the grey-based nearest neighbor rule and the signal-to-noise ratio (SNR) are used to evaluate and optimize the features of the specific classification problem. Experiments performed on different application domains are reported to demonstrate the performance of the proposed hybrid Taguchi-Grey-based method. The proposed method yields superior performance and is helpful for improving the classification accuracy in pattern classification.

References

1. Aha, D.W., Kibler, D., Albert, M.K.: Instance-based Learning Algorithms. Machine Learning 6, 37–66 (1991)
2. Bishop, C.M.: Neural Networks for Pattern Recognition, Oxford (1995)
3. Blake, C.L., Merz, C.J.: UCI Repository of Machine Learning Databases Irvine, CA: University of California, Department of Information and Computer Science (1998), http://www.ics.uci.edu/ mlearn/MLRepository.html
4. Brassard, G., Bratley, P.: Fundamentals of Algorithms. Prentice Hall, New Jersey (1996)
5. Cawley, G.C., Talbot, N.L.C.: Efficient Leave-one-out Cross-validation of Kernel Fisher Discriminant Classifiers. Pattern Recognition 36(11), 2585–2592 (2003)
6. Cover, T.M., Hart, P.E.: Nearest Neighbor Pattern Classification. IEEE Trans. on Information Theory 13(1), 21–27 (1967)
7. Dasarathy, B.V.: Nearest Neighbor (NN) Norms: NN Pattern Classification Techniques. IEEE Computer Society Press, Los Alamitos, California (1990)
8. Deng, J.: The Theory and Method of Socioeconomic Grey Systems. Social Sciences in China 6, 47–60 (1984)
9. Deng, J.: Introduction to Grey System Theory. The Journal of Grey System 1, 1–24 (1989)
10. Deng, J.: Grey Information Space. The Journal of Grey System 1, 103–117 (1989)
11. Doak, J.: An Evaluation of Feature Selection Methods and Their Application to Computer Security. Technical Report, Univ. of California at Davis, Dept. Computer Science (1992)
12. Duda, R.O., Hart, P.E.: Pattern Classification and Scene Analysis. John Wiley & Sons, Chichester (1973)
13. Hall, M.A.: Correlation-based Feature Subset Selection for Machine Learning. PhD Dissertation, University of Waikato (1998)
14. Huang, C.C., Lee, H.M.: An Instance-based Learning Approach based on Grey Relational Structure. Applied Intelligence 25, 243–251 (2006)
15. Inza, I., Larrañaga, P., Sierra, B.: Feature Subset Selection by Bayesian Networks: a Comparison with Genetic and Sequential Algorithms. International Journal of Approximate Reasoning 27, 143–164 (2001)
16. Kohavi, R., John, G.H.: Wrappers for Feature Subset Selection. Artificial Intelligence 97(1-2), 273–324 (1997)
17. Liu, H., Motoda, H.: Feature Selection for Knowledge Discovery and Data Mining. Kluwer Academic, Boston (1998)
18. Liu, H., Setiono, R.: A Probabilistic Approach to Feature Selection - A Filter Solution. In: Proceedings of 13th International Conference on Machine Learning, pp. 319–327 (1996)
19. Liu, H., Yu, L.: Toward Integrating Feature Selection Algorithms for Classification and Clustering. IEEE Trans. Knowl. Data Eng. 17(4), 491–502 (2005)
20. Quinlan, J.R.: Induction of Decision Trees. Machine Learning 1, 81–106 (1986)
21. Stone, M.: Cross-validatory Choice and Assessment of Statistical Predictions. Journal of the Royal Statistical Society B 36, 111–147 (1974)
22. Taguchi, G.: Introduction to Quality Engineering. Tokyo: Asian Productivity Organization (1986)
23. Wu, Y., Wu, A., Taguchi, G.: Taguchi Methods for Robust Design. New York: ASME, pp. 7–10 (2000)

On Using a Pre-clustering Technique to Optimize LDA-Based Classifiers for Appearance-Based Face Recognition[⋆]

Sang-Woon Kim[1] and Robert P.W. Duin[2]

[1] *Senior Member, IEEE.* Dept. of Computer Science and Engineering,
Myongji University, Yongin, 449-728 South Korea
`kimsw@mju.ac.kr`
[2] Information and Communication Theory group,
Delft University of Technology, The Netherlands
`r.p.w.duin@tudelft.nl`

Abstract. Fisher's Linear Discriminant Analysis (LDA) is a traditional dimensionality reduction method that has been proven to be successful for decades. To enhance the LDA's power for high-dimensional pattern classification, such as face recognition, numerous LDA-extension approaches have been proposed in the literature. This paper proposes a new method that improves the performance of LDA-based classification by simply increasing the number of (sub-)classes through clustering a few of classes of the training set prior to the execution of LDA. This is based on the fact that the eigen space of the training set consists of the range space and the null space, and that the dimensionality of the range space increases as the number of classes increases. Therefore, when constructing the transformation matrix, through minimizing the null space, the loss of discriminative information resulted from this space can be minimized. To select the classes to be clustered, in the present paper, the *intraset* distance is employed as a criterion and the k-means clustering is performed to divide them. Our experimental results for an artificial data set of XOR-type samples and a well-known benchmark face database of Yale demonstrate that the classification efficiency of the proposed method could be improved.

Keywords: Face Recognition, Linear Discriminant Analysis (LDA), Pre-clustered LDA (PLDA).

1 Introduction

Over the past two decades, numerous families and avenues for Face Recognition (FR) systems have been developed. This development is motivated by the broad

---

range of potential applications for such identification and verification techniques. Recent surveys are found in the literature [1] and [2] related to FR. As facial images are very high-dimensional, it is necessary for FR systems to reduce these dimensions. Linear Discriminant Analysis (LDA) is one of the most popular linear projection techniques for dimension reduction [3]. LDA has been widely adopted owing to its efficiency, but it does not capture nonlinear manifolds of faces which exhibit pose and background variations[1]. When using LDA methods for dimensionality reduction, thus, they sometimes fail to discover the intrinsic dimension of the image space. To enhance the LDA's power for FR, numerous LDA-extensions including two-stage LDA [3], direct LDA [4], and kernel-based LDA [5] have been proposed in the literature. Beside these, to discover the nonlinear manifold structure, various techniques including LLE (Locally Linear Embedding) [6], LLDA (Locally Linear Discriminant Analysis) [10], SDA (Subclass Discriminant Analysis) [11], and Dissimilarity-Based Classifiers (DBC) [12] have been proposed[2].

The approach that is proposed in this paper concerns treating the nonlinear manifolds of each face class as a set of subclasses when the class is represented by multiple separated Gaussian distributions. LDA methods effectively use the concept of a within-class scatter matrix, S_w, and a between-class scatter matrix, S_b, to maximize a separation criterion, such as $J = tr(S_w^{-1}S_b)$. It is well-known that for c-class (and d-dimensional) problems, S_b has the rank $c - 1$, and subsequently the rank of $S_w^{-1}S_b$ is $c - 1$ [13]. This means that there are, at most, $c - 1$ eigenvectors corresponding to nonzero eigenvalues since the rank of the matrix S_b is bounded by $c - 1$. When solving an eigenvalue problem on the matrix $S_w^{-1}S_b$, $c - 1$ eigenvalues are nonzero and the others are zero. Thus, without losing the criterion value, the d-dimensional input space can be mapped onto the $(c - 1)$-dimensional subspace spanned by the $c - 1$ eigenvectors corresponding to these nonzero eigenvalues. However, the discarded $(d - c + 1)$-dimensional subspace spanned by the $d - c + 1$ eigenvectors, which are corresponding to these zero eigenvalues, may also contain a useful piece of information for discrimination.

From this consideration, in the present paper, a new way of improving the performance of LDA-based classification is proposed. This improvement is achieved by incorporating the clustering technique into the LDA reduction process. A few classes of a training set are first selected. Each of the selected classes is clustered into a set of subclasses by invoking a dividing (or clustering) method prior to the execution of LDA. Consequently, the number of classes of the training set increases from c to $c'(\geq c)$. In this approach, the major problems to be addressed are those of selecting the classes to be clustered and determining the optimal number of Gaussians per class, i.e., the number of clusters. To solve these problems, in this paper, an Eucledian distance called as *intraset distance* and

---

[1] In FR, it is well-known that facial images to be recognized have many kinds of variations, such as pose, illumination, facial expression, distance, and background.

[2] Concerning Linear Dimensionality Reduction (LDR), there are numerous variants of Fisher's LDR. The details of the variants of LDR can be found in the well known literature including [7], [8], and [9].

a k-means clustering algorithm are employed. To select the classes, the intraset distances for all classes are first computed. After sorting them in the descending order, some of the highest variances (i.e., the largest distance) are selected and divided into subclasses by invoking the k-means clustering algorithm. Finally, a classification is performed by invoking a classifier built in the c'-class feature space, where the dimensionality is *maximally* $c' - 1$.

The main contribution of this paper is to demonstrate that the performance of LDA-based classifiers can be improved by employing a pre-clustering step. This has been done by incorporating the clustering technique into the LDA reduction process and by demonstrating its power in classification accuracy. The reader should observe that this philosophy is *quite* simple and distinct from those used in the recently-proposed LLE [6], LLDA [10], or SDA [11] strategies.

2   Optimizing LDA-Based Classification

The fundamental problem that we encounter when classifying the high-dimensional task is that of reducing the dimensionality of the training samples. One of the most popular approaches to solve this problem is employing the LDA. A conventional LDA-based classification method [3] is summarized in the following:

1. Compute two scatter matrices, S_w and S_b, from the training samples, T. Following this, construct a transformation matrix, W, by keeping the eigenvectors corresponding to the nonzero eigenvalues of $tr(S_w^{-1}S_b)$.

2. Project the training set T into a reduced dimensional feature space by using the transformation matrix W, where the dimensionality of the feature space is *maximally* $c - 1$. To test a sample z, compute a feature vector, z', using the same transformation matrix.

3. Achieve a classification based on invoking a classifier built in the feature space and operating on the vector of z'.

In the above algorithm, the classification performance can be improved by increasing the number of classes from c to c'. This increase can be obtained by dividing the manifolds of each class into a set of clusters. Rather than divide *all* classes of T, a few of the classes are bisected in this paper. To choose the classes to be clustered, the distribution variance of each class can be used as a criterion. To measure the variance of the class, the so-called intra-set distance is used. The distance, which is an Euclidean distance, is briefly introduced here.

Intraset Distance: Let $T = \{x_1, \cdots, x_n\} \in \Re^d$ be a set of n feature vectors in a d-dimensional space. Assume that T is a labeled data set so that T can be decomposed into, for example, c disjoint subsets $\{T_1, \cdots, T_c\}$ such that $T = \bigcup_{k=1}^{c} T_k, T_i \cap T_j = \phi, \forall i \neq j$. Then, a criterion associated with T_i is defined

---

[3] For want of a better term, LDA-based classification performed without utilizing the pre-clustering technique will be referred to as "conventional" schemes.

as follow: For an arbitrary pattern $\boldsymbol{x}_j = (x_{j1}, x_{j2}, \cdots, x_{jd})^T \in T_i$, the mean of $d(\boldsymbol{x}_j, T_i - \{\boldsymbol{x}_j\})$ over T_i is called the *intraset distance* of T_i and is denoted by

$$D^2(T_i) = \frac{1}{n_i} \sum_{j=1}^{n} d^2(\boldsymbol{x}_j, T_i - \{\boldsymbol{x}_j\}) \tag{1}$$

$$= \frac{1}{n_i(n_i - 1)} \sum_{j=1}^{n} \sum_{l=1}^{n} \sum_{k=1}^{d} (x_{jk} - x_{lk})^2.$$

By conveniently rearranging the elements in the triple summation of (1) and considering the relations of $\overline{x_{jk}} = \overline{x_{lk}}$ and $\overline{(x_{jk})^2} = \overline{(x_{lk})^2}$ for arbitrary j and l, the intraset distance can be expressed in terms of the unbiased variances of components of the given patterns like: $D^2(T_i) = 2\sum_{k=1}^{d} \sigma_k^2$, where $\sigma_k^2 = \frac{n}{n-1}\left\{\overline{(x_{jk})^2} - (\overline{x_{jk}})^2\right\}$ for all $\boldsymbol{x}_j \in T_i$. Details of the derivation are omitted here in the interest of compactness, but can be found in [14]. This is the rationale of the scheme for employing the intraset distance as a criterion to select the classes to be clustered. To simplify the classification task, in this paper, the chosen classes are divided into *two* clusters. However, this can be expanded into a general solution by utilizing a way of automatically determining the number of clusters and measuring the goodness of the clusters formed. The details of this subject are omitted here, but can be found in [15].

Pre-clustered LDA-Based Classification: As mentioned previously, by the means of clustering the nonlinear manifolds of a class into a set of subclasses, the classification performance of the above conventional method can be improved furthermore. To achieve this, first of all, the intraset distances for all classes are computed to choose the class to be clustered. The proposed approach, which is referred to as a Pre-clustered LDA-based (PLDA) classification, is summarized in the following:

1. Compute the intra-set distances of the input training data set T_i for all i, $1 \leq i \leq c$, and sort them with the intra-set distances in descending order, $D^2(T_1) \geq D^2(T_2) \geq \cdots \geq D^2(T_c)$. Then, set $c' = c$ and $\theta_1 = 1$.
2. Do the following : Increasing i by unity from 1 to the number of classes in T per epoch:
   (a) Cluster the training set of class ω_i, T_i, into two clusters, which are named as T_i and T_{i+c}, and increase the number of *sub*-classes, $c' = c' + 1$.
   (b) Compute two scatter matrices, S_w and S_b, from the training samples, $T = T_1 \cup T_2 \cup \cdots \cup T_{i+c}$. Following this, construct a transformation matrix, W, by keeping the eigenvectors corresponding to the nonzero eigenvalues of $tr(S_w^{-1} S_b)$[4].

---

[4] This step can be different depending on which method is employed. For example, in the direct LDA, this step is performed after doing the *simultaneous* diagonalization of S_b and S_w [13].

(c) Project the training set T into a reduced dimensional feature space by using the transformation matrix W, where the dimensionality of the feature space is *maximally* $c' - 1$. To test a sample z, compute a feature vector, z', using the same transformation.

(d) Achieve a classification based on invoking a classifier built in the feature space and operating on the vector of z'. The classification accuracy for all testing samples is labeled as θ_2. If $\theta_1 - \theta_2 > \rho$, then go to the next step. Otherwise, Step 2 is repeated after $\theta_1 = \theta_2$.

3. Output θ_2 as the final result, then the process terminates.

In Step 2 of the above algorithm, to simplify the classification task for the paper, the maximum iteration number can be limited experimentally. Also, in the same step, the threshold value ρ is determined experimentally.

The computational complexity of the proposed algorithm depends on the computational costs associated with the number of training samples and the clustering algorithm. The time complexity of PLDA can be analyzed as follows: Step 1 requires $O(n^2 \times d) + O(c)$ time. Step 2 requires $O(n) + O(8d^3) + O(n \times d) + O(\gamma_1)$ time (where γ_1 is the time for training a classifier with the training set T) to perform the four sub-steps of computing transformation matrix, projecting data samples onto divided sub-class space, and classifying a test sample with the classifier designed in the sub-class space. Step 3 requires $O(1)$ time to terminate the algorithm. Thus, the total time complexity of the PLDA is $O(n^2 d + d^3 + \gamma_1)$. Then, the space complexity of PLDA is $O(nd)$.

3   Experimental Results : Artificial/Real-Life Data Sets

The proposed method has been tested and compared with conventional methods. This was done by performing experiments on an artificial data set (which is named as XOR4) and a well-known face database, namely, the Yale [5] database.

The data set named "XOR4", which has been included in the experiments as a baseline data set, was generated from a mixture of four 4-dimensional Gaussian distributions as follows: (1) $p_1(x) = \frac{1}{2} N(\mu_{11}, I_4) + \frac{1}{2} N(\mu_{12}, I_4)$ and (2) $p_2(x) = \frac{1}{2} N(\mu_{21}, I_4) + \frac{1}{2} N(\mu_{22}, I_4)$, where $\mu_{11} = [-2, -2, 0, 0]$, $\mu_{12} = [2, 2, 0, 0]$, $\mu_{21} = [2, -2, 0, 0]$, and $\mu_{22} = [-2, 2, 0, 0]$. Also, I_4 is the *4*-dimensional *Identity* matrix. Here, it is clear that each class contains *two* clusters. Thus, this case is better treated as a *four*-class problem rather than a *two*-class one.

The face database captioned "Yale" contains 165 gray scale images of 15 individuals. There are 11 images per subject, one of each for the following facial expression or configurations: center-light, left-light, right-light, with glasses, without glasses, happy, normal, sad, sleepy, surprised, and winking. The size of each image is 243×320 pixels for a total dimensionality of 77760. In this experiment, to reduce the computational complexity, each facial image of Yale database was down-sampled into 61×80 and then represented by a centered vector of normalized intensity values. To obtain a different data set, a part of the

---

[5] http://www1.cs.columbia.edu/ belhumeur/pub/images/yalefaces

down-sampled image, which is 28×23 size and contains only facial components without background, was extracted. This face database is termed as "Yale2" in a subsequent section.

Experimental Method: In this paper, all experiments were performed using a "leave-one-out" strategy. To classify an image of object, that image was removed from the training set and a transformation matrix, W, was computed with the $n-1$ images. Following this, all of the n images in the training set and the test object were translated into a $(c'-1)$-dimensional space using the transformation matrix and recognition was performed based on the algorithm in Section 2. After repeating this n times for every sample, a final result was obtained by averaging them.

To perform the transformation and classification, first of all, the intraset distances for all classes were computed. After computing the distances, the data sets of the classes were sorted in the decreasing order using the intraset distance. Then, the classes of the largest distances were selected and divided into sub-classes by invoking a k-means clustering algorithm. Finally, a classification was obtained by designing a classifier in the sub-classes feature space. In this experiment, to simplify the classification task for the paper, only two, three, or four classes were selected and each of them was divided into *two* sub-classes [6]. Furthermore, to reduce the dimensionality of the clustered data samples, only one approach, namely, the direct LDA, was implemented. However, other approaches including PCA+LDA [3], LDA/GSVD [16], and LDA/QR [17], Kernel-based LDA [5] could have also been considered.

On the other hand, to maintain the diversity between the LDA-based classifications, different classifiers, such as the k-Nearest Neighbor Classifiers ($k = 1, 3$), Nearest Mean Classifiers, Normal Density based Linear Classifier, Uncorrelated Normal Density based Quadratic Classifier, Parzen Density based Classifier, Fisher's Least Square Linear Classifier, and Neural Network Classifier were designed. These classifiers are implemented with PRTools [7] and will be denoted as 1-NN, 3-NN, NMC, LDC, UDC, PZC, FSC, and NNC, respectively, in a subsequent section. Here, NNC is a feed-forward neural net classifier with one hidden layer of 20 sigmoid neurons.

Experimental Results: The run-time characteristics of the proposed algorithm for the artificial data set, XOR4, and the benchmark database, Yale, are reported below and shown in Table 1. The rationality of employing a pre-clustering step in the LDA-based classifiers is investigated first. Following this, a comparison is made between the conventional LDA-based method and the proposed scheme.

First, the results of the dimensionality reduction obtained in Step $2(c)$ of the proposed LDA-based scheme in Section 2 were probed into. Fig. 1 shows plots of two 2-dimensional data sets obtained from the original 4-dimensional data set

---

[6] In this experiment, to implement the normal-density based classifiers, the samples of at least two points were compulsorily assigned to each sub-class.

[7] PRTools is a Matlab Toolbox for Pattern Recognition. PRTools can be downloaded from the PRTools website, http://www.prtools.org/
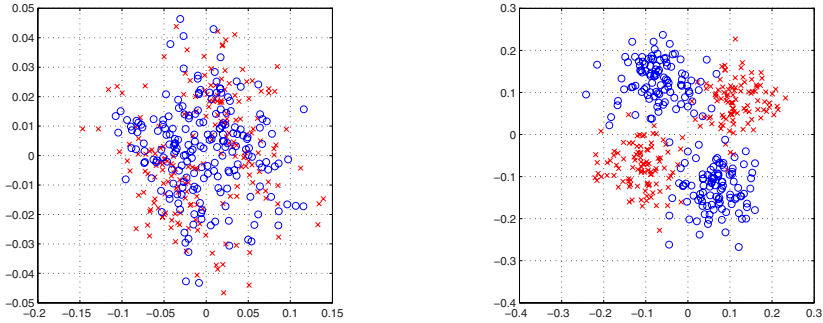
Fig. 1. Plots of the 2-dimensional data set obtained from the original 4-dimensional artificial data set, namely, XOR4. In both pictures, the left is reduced with the direct LDA and the right is obtained with the proposed method, in which the LDA is carried out after doing a pre-clustering.

of XOR4. Here, the left is of the conventional scheme and the right is of the proposed method, respectively. In the conventional scheme, the direct LDA was applied to the original 4-dimensional data set, while the direct LDA was carried out after doing a pre-clustering for the data set in the proposed method.

From the figure, it should be observed that the accuracy of the dimensionality reduction step for the artificial data set can be improved by employing the philosophy of a pre-clustering. This is clearly shown in the classification boundary built between the two classes represented with "×" and "○" in both pictures. This characteristic could be also observed from the real benchmark face database. For the fifteen classes of Yale, the intraset distances obtained with Eq. (1) are sorted as follow:

```
1.0e+007 *
2.9493  2.9240  2.9036  2.8759  2.5882  2.5647  2.1206  2.0010
1.9686  1.9128  1.7468  1.6376  1.6368  1.5628  1.2592
```

From these figures, some of the classes which are ranked among the largest distances are selected and clustered into two sub-classes. Fig. 2 shows faces of an object of Yale and their clustering result. Here, the left picture shows the eleven faces of the object which has the largest distance (i.e., 1.0e+007 * 2.9493) and the right one shows that the faces are divided into two sub-classes. Faces of the two sub-classes are different from each other in the background.

From the above consideration, the rationale of the LDA-based classification for employing the pre-clustering technique is proven to be valid.

Secondly, as the main results, it should be noted that it is possible to improve the classification performance by employing the philosophy of a pre-clustering prior to the execution of the dimensionality reduction step. Table 1 shows a comparison of the classification performances for XOR4 data set and Yale
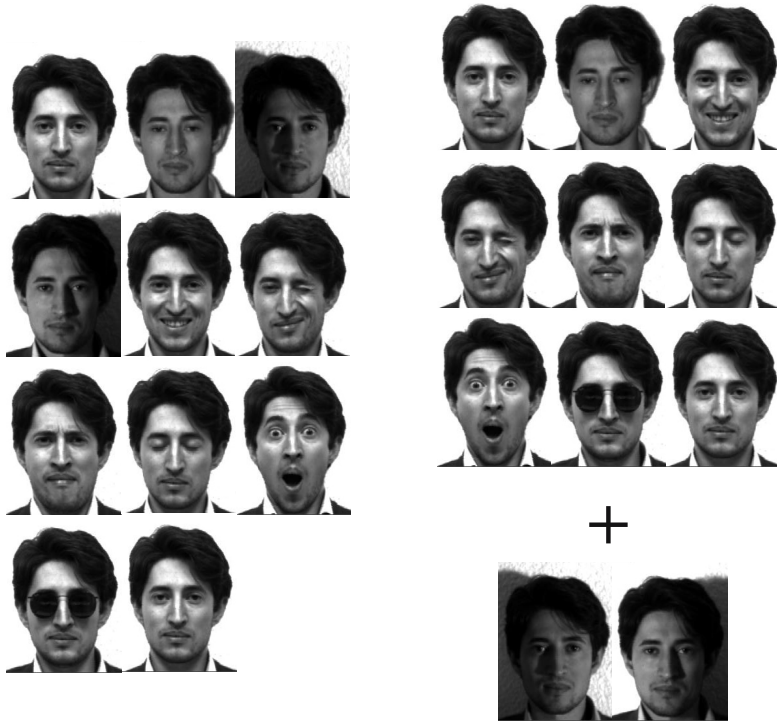
Fig. 2. Faces of an individual selected from Yale database. In the picture, the left eleven faces are of the class that has the largest intraset distance, while the right picture shows that the eleven faces are divided into two sub-classes. The details of the figure are discussed in the text.

database[8]. Here, the abbreviations NON, LDA, and PLDA, which are, respectively, *NON*-reduction classification, the conventional *LDA*-based classification, and the *P*re-clustered *LDA*-based classification, indicate the classification methods employed in this experiment. Especially, *PLDA(2)*, *PLDA(3)*, and *PLDA(4)* are abbreviations of the classifications performed after pre-clustering the selected two, three, and four classes, respectively. For these classification methods, the best results obtained are printed in bold.

From Table 1, it is clear that the classification accuracies for the experimental databases can be improved by employing the pre-clustering technique (see the

---

[8] In Table 1, the symbol "–" indicates that there are *no* results available due to the characteristics of the data set and the out-of-memory problem. First of all, in the implementation of the direct LDA for XOR4, we have a problem in diagonalization of $S_b = \sum_i n_i (m_i - m)(m_i - m)^T$ because two means, namely, the class mean, m_i, and the global mean, m, are (almost) *zero*. Then, to implement the linear/quardratic normal density based classifiers (LDC and QDC) for very high dimensional data, we need three big dimensional matrices, for example, 10304×10304. To be consistent with other methods, however, we did not fix the implementation.

Table 1. A comparison of the classification performances of LDA-based classifiers for XOR4 and Yale. Here, in the second column, the abbreviations NON, LDA, and PLDA(·) indicate *NON*-reduction classification, the conventional *LDA*-based classification, and the *P*re-clustered *LDA*-based classification, respectively. Also the symbol "–" indicates that there are *no* results available due to the characteristics of the data set. The details of the table are discussed in the text.

Dataset Names	Analysis Methods	Experimental Classifiers							
		1-NN	3-NN	NMC	LDC	UDC	PZC	FSC	NNC
XOR4	NON	89.25	92.50	46.50	45.25	44.75	93.00	45.25	85.00
	LDA	–	–	–	–	–	–	–	–
	PLDA(2)	**90.50**	**94.00**	**95.00**	**94.25**	95.25	**94.75**	**94.50**	**94.75**
	PLDA(3)	**90.50**	**94.00**	**95.00**	**94.25**	95.75	**94.75**	**94.50**	94.50
	PLDA(4)	**90.50**	**94.00**	**95.00**	**94.25**	95.75	**94.75**	**94.50**	94.00
Yale	NON	79.39	78.18	78.18	–	–	6.67	**95.76**	58.79
	LDA	89.70	90.91	92.12	92.12	6.67	4.85	81.82	83.03
	PLDA(2)	90.91	93.33	**94.55**	93.94	**87.88**	92.73	91.52	86.06
	PLDA(3)	92.73	**95.76**	93.94	**94.55**	84.85	93.94	92.73	**89.70**
	PLDA(4)	**93.33**	**95.76**	**94.55**	**94.55**	86.67	**94.55**	93.94	87.28
Yale2	NON	78.18	76.97	78.18	**95.15**	73.94	6.67	**89.70**	58.79
	LDA	90.30	89.09	92.12	92.12	**86.06**	90.30	84.24	80.00
	PLDA(2)	90.91	**91.52**	92.12	92.12	84.24	**92.73**	84.24	**81.82**
	PLDA(3)	89.70	89.70	**93.33**	92.73	83.64	90.91	85.45	79.39
	PLDA(4)	**92.12**	**91.52**	**93.33**	93.94	81.82	92.12	87.27	78.18

bold-faced ones). An example of this is the classification accuracy rates (%) obtained with 1-NN classifiers designed for Yale. The classification accuracies of NON, LDA, PLDA(2, 3, 4) methods are 79.39, 89.70, 90.91, 92.73, and 93.33 (%), respectively. Additionally, the classification accuracies of NNC classifiers are 58.79, 83.03, 86.06, 89.70, and 87.28 (%), again respectively. From this consideration, the reader can observe that the classification performance of NON was improved with LDA and further improved with PLDA. The details are omitted here in the interest of compactness. From the table, however, it should be mentioned that the classification accuracies of PLDA(2), PLDA(3), and PLDA(4) are almost the same while the number of classes to be clustered increases. For instance, the accuracy rates obtained with the 1-NN classifier for XOR4 are the same as 90.50 (%). For Yale database, the same characteristics can be observed.

From the above consideration, it should be also observed that the proposed scheme of employing the pre-clustering technique is useful in improving the classification performance.

4   Conclusions

In this paper, a method that seeks to improve the classification performance of LDA-based approaches for appearance-based face recognition is considered. This method involves a pre-clustering step prior to the execution of Fisher's

criterion to find out the nonlinear structure of faces and divide it into a set of clusters. The experimental results for an artificial data set and a well-known face database demonstrate that the proposed scheme is better than the conventional ones in terms of the classification accuracy rates. Even though an investigation has been made, focusing on the possibility of the pre-clustering technique being used to solve the nonlinear-manifolds problem of FR, many problems remain. This classification performance could be further improved by developing an optimal division (or selection) method and by designing suitable classifiers in the divided-class space. The research concerning this is a future aim of the authors.

References

1. Zhao, W., Chellappa, R., Rosenfeld, A., Phillips, P.J.: Face recognition: a literature survey. ACM Compt. Surveys 35(4), 399–458 (2003)
2. Ruiz-del-Solar, J., Navarrete, P.: Eigenspace-based face recognition: a comparative study of different approaches. IEEE Trans. Systems, Man, and Cybernetics-Part C 35(3), 315–325 (2005)
3. Belhumeur, P.N., Hespanha, J.P., Kriegman, D.J.: Eigenfaces vs. Fisherfaces: Recognition using class specific linear projection. IEEE Trans. Pattern Anal. and Machine Intell. 19(7), 711–720 (1997)
4. Yu, H., Yang, J.: A direct LDA algorithm for high-dimensional data - with application to face recognition. Pattern Recognition 34, 2067–2070 (2001)
5. Yang, M.-H.: Kernel eigenfaces vs. kernel Fisherfaces: Face recognition using kernel methods. In: Proceedings of Fifth IEEE International Conference on Automatic Face and Gesture Recognition, pp. 215–220 (2002)
6. Roweis, S., Saul, L.K.: Nonlinear dimensionality reduction by locally linear embedding. Science 290(5500), 2323–2326 (2000)
7. Lotlikar, R., Kothari, R.: Adaptive linear dimensionality reduction for classification. Pattern Recognition 33, 185–194 (2000)
8. Loog, M., Duin, P.W.: Linear dimensionality reduction via a heteroscedastic extension of LDA: The Chernoff Criterion. IEEE Trans. Pattern Anal. and Machine Intell. 26(6), 732–739 (2004)
9. Rueda, L., Herrera, M.: A new approach to multi-class linear dimensionality reduction. In: Martínez-Trinidad, J.F., Carrasco Ochoa, J.A., Kittler, J. (eds.) CIARP 2006. LNCS, vol. 4225, pp. 634–643. Springer, Heidelberg (2006)
10. Kim, T.-K., Kittler, J.: Locally linear discriminant analysis for multimodally distributed classes for face recognition with a single model image. Pattern Anal. and Machine Intell. 27(3), 318–327 (2005)
11. Zhu, M., Martinez, A.M.: Subclass discriminant analysis. IEEE Trans. Pattern Anal. and Machine Intell. 28(8), 1274–1286 (2006)
12. Kim, S.-W.: On solving the small sample size problem using a dissimilarity representation for face recognition. In: Blanc-Talon, J., Philips, W., Popescu, D., Scheunders, P. (eds.) ACIVS 2006. LNCS, vol. 4179, pp. 1174–1185. Springer, Heidelberg (2006)
13. Fukunaga, K.: Introduction to Statistical Pattern Recognition. Academic Press, San Diego (1990)
14. Friedman, M., Kandel, A.: Introduction to Pattern Recognition - Statistical, Structural, Neural and Fuzzy Logic Approaches. World Scientific, New Jersey (1999)

15. Maulik, U., Bandyopadhyay, S.: Performance evaluation of some clustering algorithms and validity indices. IEEE Trans. Pattern Anal. and Machine Intell. 24(12), 1650–1654 (2002)
16. Howland, P., Wang, J., Park, H.: Solving the small sample size problem in face reognition using generalized discriminant analysis. Pattern Recognition 39, 277–287 (2006)
17. Ye, J., Li, Q.: A two-stage linear discriminant analysis via QR-decomposition. IEEE Trans. Pattern Anal. and Machine Intell. 27(6), 929–941 (2005)

Certainty Measure of Pairwise Line Segment Perceptual Relations Using Fuzzy Logic

José Rouco, Marta Penas, Manuel G. Penedo,
Marcos Ortega, and Carmen Alonso-Montes

VARPA Group, Department of Computer Science, University of A Coruña, Spain
{jrouco,mpenas,mgpenedo,mortega,calonso}@udc.es

Abstract. Perceptual grouping is an important part of many computer vision systems. When inferring a new grouping from the primitive features there is always an uncertainty degree on this detection, that might be useful in further reasonings. In this paper, we present a fuzzy logic based system for the computation of the certainties assigned to pairwise line segment relations and introduce its application to the detection of continuity, identity, junction, L-junction, incidence, T-junction and parallelism relations. The results presented show that the proposed method might be very promising for future applications.

Keywords: certainty, fuzzy logic, perceptual grouping.

1 Introduction

A major problem in computer vision and image understanding systems is the organisation of the low level features into meaningful higher level features. The bottom-up process of grouping features by means of perceptual principles like proximity, similarity, continuation, closure and symmetry is referred by the computer vision community as perceptual organisation or perceptual grouping [1,2].

The perceptual grouping is present at several stages of the image understanding process. For example, the edges are combined into line segments or curves and these segments are combined into closed contours. In any case, the lower level features are treated as cues for the detection of the higher level groupings that are considered salient for the scene understanding. This process reduces the complexity of the scene and facilitates the operation of higher level processing for object detection.

The target groupings of a perceptual organisation system should fulfil some properties, in order to be considered salient for scene understanding [2]. First, the groupings should represent significant features of the target objects; also, their features should be invariant to projection and illumination changes; finally, the groupings should be non-accidental, i.e. they should not be easily observed by chance. With these properties, if the salient groupings are present in the input image, it is very likely that the target objects have caused them and, also, the object features that the groupings represent could be inferred from the groupings features. However, in most applications, these groupings can not be categorically

detected in base to the cues provided by the lower level features, but with an associated degree of certainty. Dealing with this uncertainty is an important issue as it may affect further reasonings based on the detected groupings. This paper is focused on the detection of pairwise line segment groupings and in the computation of a subjective measure of its certainty.

The detection of pairwise line segment relations has been a main subject in several perceptual organisation applications [3,4,5,6,7]. The analysis of different distance features using threshold based rules, has been used for the categorical detection of pairwise line segment relations in [3]. Other approaches use probabilities as rank for perceptual relation detection [4,6,5,7]. The idea of non-accidentalness probability for the grouping is used in [4]. However, it is necessary to make assumptions about the distribution of the relation evidences in the background of the target images in order to compute these probabilities. Other approaches like those based in Bayesian inference also need to estimate conditional probabilities about the accidental occurrence of evidences in the image, machine learning techniques have been used to address this problem in [5]. Fuzzy sets have been also used for the detection of perceptual relations in [6,7], these approaches use fuzzy predicates for representing the grouping properties and computing a subjective measure of the relations certainty based on the initial definition of their membership functions.

In this paper, we use fuzzy logic for detecting pairwise line segment relations with an assigned uncertainty. Opposite to previous works, we primarily focus our attention on the definition of a general and configurable approach for computing the suitable certainty measures. The general fuzzy inference system proposed is intended to be extensible and tunable based on the needs of further reasonings. Also, an analysis of the suitable properties for the detection of identity, continuity, junction, incidence and parallelism relations between line segments is performed, along with the proposal of new normalisation equations. This paper is structured as follows. Section 2 defines the fuzzy combination of features proposed. Section 3 describes how the method defined in section 2 is applied to the detection of the target relations. Section 4 show the experimental results for the proposed system. Finally, section 5 exposes the conclusions from our work.

2   Perceptual Grouping with Fuzzy Logic

Fuzzy logic [8] is a multi-valued logic that works with predicates which truth values can not be precisely defined as true or false. Instead, their certainty is quantified in the continuous interval $[0, 1]$. Formally, the truth value of a predicate p over the elements $x \in \mathcal{U}$ in the universe of discourse $\mathcal{U}$ is assigned through a membership function $\mu_p : \mathcal{U} \rightarrow [0, 1]$ The membership function μ_p defines the *fuzzy set* of the elements in $x \in \mathcal{U}$ that satisfy p, and its value represents a measure of the certainty on the predicate p given every element in $\mathcal{U}$.

The truth values of the logical expressions containing logical connectives ($\wedge$,$\vee$) are derived from the truth values of its operands. The membership function of an *and* expression $\mu_{a \wedge b}(x)$ $(x \in \mathcal{U})$ is modelled as a triangular norm, or t-norm,

$\top(\mu_a(x), \mu_b(x))$, while the membership function of an *or* expression $\mu_{a \vee b}(x)$ is modelled as a triangular conorm, or t-conorm, $\bot(\mu_a(x), \mu_b(x))$. The most widely used *t-norm* and *t-conorm* are $\top(a, b) = min\{a, b\}$ and $\bot(a, b) = max\{a, b\}$, respectively.

In this work we model pairwise relations between line segments, like parallelism or collinearity, using predicates in fuzzy logic. Our universe of discourse $\mathcal{U}$ is, therefore, the set of all possible segments pairs $x = (s_1, s_2)$ in an image. The membership function $\mu_R : \mathcal{U} \to [0, 1]$ for a given relation R is modelled as a *logical and* combination:

$$\mu_R(x) = \bigwedge_{f \in \mathcal{F}} \mu_R^f(f(x)) \ . \tag{1}$$

where $\mathcal{F}$ is a set of features, a feature $f \in \mathcal{F} : \mathcal{U} \to C_f$ is a distance measured from the input segment pairs, and $\mu_R^f : C_f \to [0, 1]$ ($\forall f \in \mathcal{F}$) is the membership function of a fuzzy relation R, defined over the set of values C_f that f can take.

The previous definition is flexible enough for representing the most usual relations in perceptual organisation. The definition of the relations and the certainty values associated to them can be refined by adding new features or by adjusting the membership functions. This is very important since the certainty values are likely to be used in further reasoning to detect higher level groupings and, thus, the membership functions may depend on the concrete application domain.

Note that the membership functions over the features could have been modelled as logical combinations of fuzzy linguistic terms (i.e. distance is *low*, *very low*, *medium*, etc.). We think that this option would lead to an extremely difficult to adjust system, since the fuzzy linguistic partitions would be shared by different relations that would add dependencies. In return, it would add an easier to understand knowledge representation of the reasonings, but we think that the knowledge behind the relations in perceptual organisation is simple enough to understand using our simple approach.

3   Line Segment Relations

As previously mentioned, this paper is focused on the detection of several perceptual relations between line segment pairs, concretely: junction, L-junction, T-junction, incidence, parallelism, continuity and identity. Most of these relations are of high significance in different kinds of images, including those containing man-made objects. Section 3.2 describes the features used for the detection and section 3.2 defines the membership functions of the target relations.

3.1   Perceptual Features

Given two line segments s_1 and s_2, the features used for the detection of perceptual relations between them, depicted in figure 1, are: the minimum distance D, the orientation difference α, the overlaps O_{AB} and O_{BA}, and the signed distances from both segments to the intersection of their elongations, I_A and I_B.

(a)   (b)   (c)
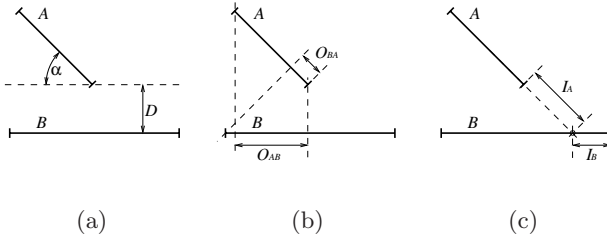
Fig. 1. Perceptual features for pairs of line segments

These distances are normalised in order to preserve the salience of the relations regardless of the segment lengths. The normalisation is very usual in perceptual organisation and the distances are commonly normalised by the length of the longest segment [3,6,5,7]. In this work, we propose a new approach for the normalisation, that is described bellow.

Given the detection of a junction between two segments, a decisive feature would be the Euclidean distance of both segments to their intersection point. If we normalise this distance by the length of the longest segment, then the longer this segment is, the larger this distance can be before a significant loss in the certainty of the relation occurs. For this reason, using this normalisation long segments are more suitable for being related with other segments regardless of their length, which could lead to undesirable high confidence relations with distant and short segments.

Opposite to this, if we normalise this distance by the length of the shortest segment, then weak and blurred edges, that are likely to be detected as short segments, may be involved in meaningful relations that are not detected this way. In many cases, the decision of normalising by one segment length or the other is application dependant. For this reason, the use a weighted average of the segment lengths for normalisation, with parameters that can be independently specified for each feature in base to the final application.

Given two line segments s_1 and s_2, the normalisation length $N_f(s_1, s_2)$ for each feature f is defined as:

$$N_f(s_1, s_2) = w_f \ max\{L_f^*(s_1), L_f^*(s_2)\} + (1 - w_f) \ min\{L_f^*(s_1), L_f^*(s_2)\} \quad (2)$$

$$L_f^*(X) = min\{\lambda_f^+, max\{\lambda_f^-, \ L(X)\}\} \ . \quad (3)$$

where $L(X)$ is the length of the segment X, λ^- and λ^+ are the minimum and maximum segment length normalisation thresholds, and $w_f \in [0, 1]$ is a weighting parameter, used to choose normalisation values varying from the length of the shortest segment when $w_f = 0$, to the length of the longest segment when $w_f = 1$. The parameters λ_f^- and λ_f^+ are chosen in base to the application domain: λ_f^- is the shortest line segment length allowed; λ_f^+ is the maximum segment length considered, with larger lengths truncated to λ_f^+, since larger line segment lenghts do not imply a larger proportional distance for the detection.

The minimum distance $D(s_1, s_2)$, if the segments do not intersect, is computed as the minimum Euclidean distance from each segments' end points to the other segment. If the segments intersect, $D(s_1, s_2)$ is set to 0. In any case, this distance is normalised by $N_D(s_1, s_2)$.

The signed distance to the intersection $I_A(s_1, s_2)$ is computed as the Euclidean distance from the segment s_1 to the intersection point of both segments' elongations. This distance is negative if the intersection point lies inside the s_1 and positive if it lies outside. $I_B(s_1, s_2)$ is computed analogously using s_2, and both distances are normalised by $N_I(s_1, s_2)$. Note that these distances could be infinite if the orientation difference between line segments was low, for this reason, we truncate this feature to the interval $[-1, 1]$.

The $\alpha(s_1, s_2)$ feature is computed as the orientation difference between segments. No segment length dependant normalisation is applied in this case.

The overlap $O(s_1, s_2)$ is defined as the maximum overlap between line segments. It is computed as $max\{O_{AB}(s_1, s_2), O_{BA}(s_1, s_2)\}$, where $O_{AB}(s_1, s_2)$ and $O_{BA}(s_1, s_2)$ are the lengths of the projections of s_1 and s_2 over s_2 and s_1, respectively. Both O_{AB} and O_{BA} are normalised by $max\{L(s_1), N_O(s_1, s_2)\}$ and $max\{L(s_2), N_O(s_1, s_2)\}$, respectively, in such a way that large proportional overlaps of short segments over long segments are penalised.

3.2 Membership Functions

As previously stated in eq. 1, the membership function of each pairwise relation is computed as the *logical and* of the membership functions of the corresponding decisive features. In this section, we define the relations analysed in this work and the membership functions associated to them.

Two line segments are identical if they correspond to the same straight edge. In many cases, segment extraction algorithms detect a blurred edge as two or three overlapped line segments, these line segments can be merged in one as they probably represent an unique straight contour. The membership functions used for the detection of identical line segments are depicted in figure 2. The identity relation depends on the distance D, the orientation difference α and the overlap O. Both, distance D and orientation difference α must be very low in identity relations, as reflected in the functions depicted at figures 2(a) and 2(b) respectively. It is also necessary a significant overlap between lines in order to state the identity, the membership function for the identity relation over the overlap O is depicted in figure 2(c).

Opposite to the identical line segments, two line segments are continuous if one is the collinear continuation of the other. These line segments do not necessarily belong to a single contour but to two nearby contours. We think that the decision whether to merge these segments or not depends on further reasoning that might take into account other relations involving these segments. The membership functions for the continuity detection are depicted in figure 3. Similarly to the identity, the continuity depends on the distance D, the orientation difference α and the overlap O. The orientation difference in continuity relations must be very low, as the membership function in figure 3(b) shows. The overlap must be
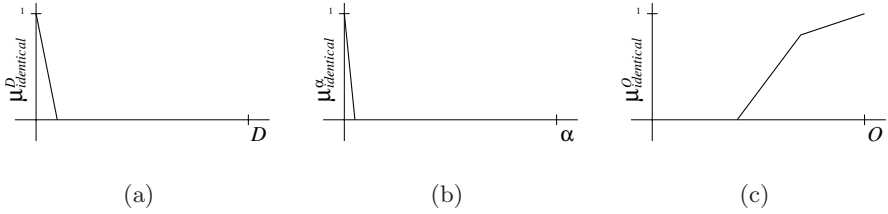
Fig. 2. Feature member functions for identity detection
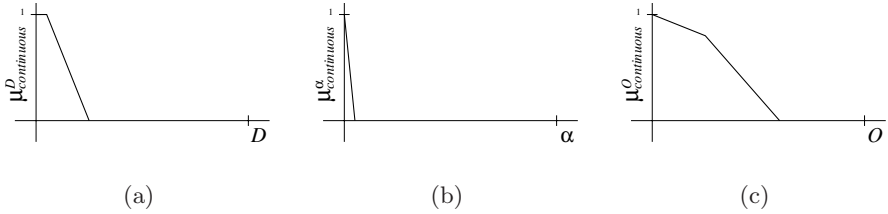
Fig. 3. Feature member functions for continuity detection
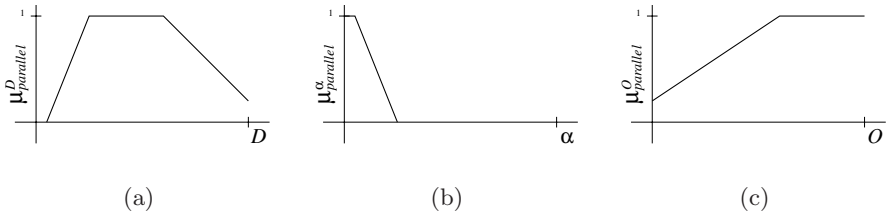
Fig. 4. Feature member functions for parallelism detection

low enough as depicted in figure 3(c). The distance between line segments D, defined as the distance between endpoints since we enforce a low overlap, can be larger than for the identity, as depicted in figure 3(a).

The membership functions used for the parallelism detection are depicted in figure 4. The most important feature for parallelism detection is the orientation difference α, which should not be higher than the transformation caused by the perspective projection. The distance D between parallel segments should not be very low, in order to differentiate this relation from the continuity or the identity. If the distance between segments is too high, the certainty of the relation is lowered, as these lines are less likely to be related. But, in any case, a high distance is not discriminative enough for refusing the parallelism relation, so the membership function for the distance feature is the one depicted in figure 4(b). The high overlap between line segments is also indicative of parallelism but, again, a low overlap is not discriminative enough for refusing the relation, this membership function is depicted in figure 4(c).

(a)   (b)   (c)   (d)
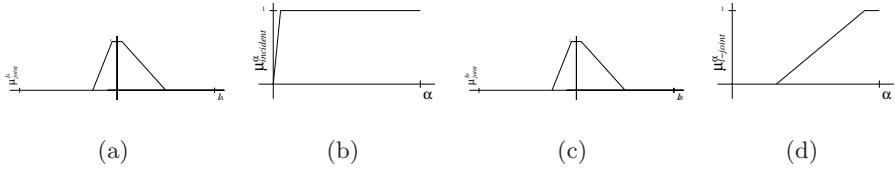
Fig. 5. Feature member functions for junction and l-junction detection

(a)   (b)   (c)   (d)
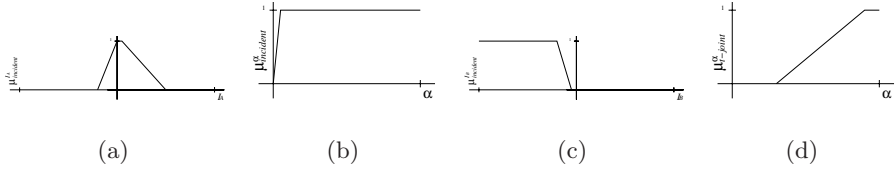
Fig. 6. Feature member functions for incidence and t-junction detection

In this work, we differentiate between regular junctions and L-junctions, being L-junctions those where the orientation difference is close to $\frac{\pi}{2}$. These L-junctions are very likely to be present in images containing man-made objects, since square corners are one of their characteristic features. The membership functions used for the detection of junctions and L-junctions are depicted in figure 5. The distance to the intersection point is the most discriminative feature used for junction detection, line segment pairs with I_A and I_B low positive or very low negative are detected as junctions through the membership functions depicted in 5(a) and 5(c), respectively. The membership function of the orientation difference α, however, is different in junctions and L-junctions. For L-junctions it must be close to $\frac{\pi}{2}$, with some variations allowed due to projection effects, while for junction can be any that is not very low, as depicted in figure 5(d) and 5(c), respectively.

Incidences and T-junctions are the only non-symmetric relations in this paper, with a line segment being incident in a supporting line segment if its endpoints meets the second segment in some location between its endpoints. The membership functions used for the detection of incidences and T-junctions are depicted in figure 6, the only different is the orientation difference, depicted in figure 6(b) and figure 6(d) respectively, that for T-junctions must be close to $\frac{\pi}{2}$. Similarly to junctions, the most decisive feature for the detection of incidences and T-junctions are the distances to the intersection point I_A and I_B. If s_1 is the incident line segment and s_2 is the supporting line segment, the distance to the intersection point I_A, depicted in figure 6(a), must be low and positive or very low and negative, as we penalise more the incidences past the intersection point. Opposite to this, the distance to the intersection point I_B from the supporting line segment s_2 in an incidence relation must be negative and high enough to establish the intersection point lies inside the segment s_2, as the membership function depicted in figure 6(d) represents.

4   Results

We have tested our system with a set of artificially generated segment pairs. Figure 7 shows the associated certainties to the different relations analysed in this paper. We have used the parameters $w_D = 0.5$, $w_I = 0.2$ and $w_O = 0.2$ for the example, but these parameters would not affect the results if they were different, as the line segment lengths of each segment in the pair are very similar in all the examples. Also, the threshold parameters have been set as neutral values as they are of no use for this examples, concretely, we have selected $\lambda_f^- = 0$ and $\lambda_f^+ = \infty$.

	(a)	(b)	(c)	(d)	(e)
Junction	0.0	**0.851**	**0.297**	**0.919**	0.328
Incidence	**1.0**	0.0	0.0	0.003	**0.833**
L-junction	0.0	0.210	0.210	0.681	0.328
T-junction	0.210	0.0	0.0	0.003	**0.833**
Continuity	0.0	0.0	0.0	0.0	0.0
Identity	0.0	0.0	0.0	0.0	0.0
Parallelism	0.0	0.0	0.0	0.0	0.0

	(f)	(g)	(h)	(i)	(j)
Junction	**0.595**	0.0	0.0	0.0	0.0
Incidence	0.0	0.0	0.0	0.0	0.0
L-junction	**0.595**	0.0	0.0	0.0	0.0
T-junction	0.0	0.0	0.0	0.0	0.0
Continuity	0.0	0.0	0.0	0.0	0.0
Identity	0.0	0.0	0.0	0.0	0.0
Parallelism	0.0	**1.0**	**0.627**	**0.699**	**1.0**

	(k)	(l)	(m)	(n)	(o)
Junction	0.0	0.0	0.0	0.0	0.0
Incidence	0.0	0.0	0.0	0.0	0.0
L-junction	0.0	0.0	0.0	0.0	0.0
T-junction	0.0	0.0	0.0	0.0	0.0
Continuity	0.0	**0.604**	**0.853**	**0.707**	0.0
Identity	**0.714**	0.0	0.0	0.0	0.0
Parallelism	0.065	0.061	0.061	0.14	**0.14**

Fig. 7. Resulting relation certainties for 15 testing line segment pairs

The results obtained are coherent with the perceptual interpretation of the relations between the segment pairs. For example, in figure 7(b) the junction certainty is very high (0.851), but the L-junction certainty is lower (0.210) since α is not close to $\frac{\pi}{2}$. As the α gets closer to $\frac{\pi}{2}$, the L-junction certainty increases closely to the junction's, e.g. figures 7(d) and 7(f). Note also that in figures 7(a), 7(c) and 7(f), the minimum distance between segment endpoints are identical, but the certainties for the junction and incidence relations are significantly different, but coherent with how the relations between these segment pairs are subjectively perceived. This is due to the use of the signed distances to the intersection point proposed in this paper for junction, incidence, L-junction and T-junction detection. Parallelisms are also detected with an adequate certainty. For example, in figure 7(h) the parallelism certainty is significantly lower than the one in figure 7(g) due to the higher orientation difference. Also, the low overlapping causes the reduction of this certainty in figure 7(i). Similarly, the continuity certainty is lower for figure 7(l) than for figure 7(m) due to the higher overlap.

5   Conclusions

In this paper, we have introduced a fuzzy logic based method for computing the certainty associated to pairwise line segment relations. The features employed by the method and the effect of normalisation on the final certainty measure has also been widely discussed in the text.

The method proposed is general enough to be suitable for the detection of a wide set of relations: identity, continuity, junction, L-junction, incidence, T-junction and parallelism, among others that could have also been analysed. Also, the method is highly parametrisable, so the certainty associated to each target relations can be tuned in base to the application domain, whether it uses the certainty as a discriminant measure or as a base for further uncertain reasonings. Section 4 show the promising results of this approach that could be of use in environments where subjective scores for perceptual relations are necessary.

Acknowledgements

References

1. Lowe, D.G.: Perceptual Organization and Visual Recognition. Kluwer Academic Publishers, Dordrecht (1985)
2. Nevatia, R.: Perceptual organization for generic object descriptions. In: Boyer, K.L., Sarkar, S. (eds.) Perceptual Organization for Artificial Vision Systems, pp. 173–189. Kluwer Academic, Dordrecht (2000)

3. Iqbal, Q., Aggarwal, J.: Retrieval by classification of images containing large man-made objects using perceptual grouping. Pattern Recognition 35, 1463–1479 (2002)
4. Lowe, D.G.: Three-dimensional object recognition from single two-dimensional images. Artificial Intelligence 31(3), 355–395 (1987)
5. Sarkar, S., Soundararajan, P.: Supervised learning of large perceptual organization: Graph spectral partitioning and learning automata. IEEE Transactions on Pattern Analysis and Machine Intelligence 22(5), 504–517 (2000)
6. Ralescu, A.L., Shanahan, J.G.: Perceptual organization for inferring object boundaries in an image. Pattern Recognition 32, 1923–1933 (1999)
7. Kang, H.B., Walker, E.L.: Perceptual grouping based on fuzzy sets. In: IEEE International Conference on Fuzzy Systems, pp. 651–659. IEEE, New York, USA (1992)
8. Zadeh, L.A.: Fuzzy sets. Information and Control 8(3), 338–353 (1965)

Automatic Image Annotation Using a Semi-supervised Ensemble of Classifiers

Heidy Marin-Castro, Enrique Sucar, and Eduardo Morales

National Institute of Astrophysics, Optics and Electronics,
Computer Science Department,
Luis Enrique Erro 1, 72840 Tonantzintla, México
{hmmarinc,esucar,emorales}@inaoep.mx
http://ccc.inaoep.mx

Abstract. Automatic image annotation consists on automatically labeling images, or image regions, with a pre-defined set of keywords, which are regarded as descriptors of the high-level semantics of the image. In supervised learning, a set of previously annotated images is required to train a classifier. Annotating a large quantity of images by hand is a tedious and time consuming process; so an alternative approach is to label manually a small subset of images, using the other ones under a semi-supervised approach. In this paper, a new semi-supervised ensemble of classifiers, called WSA, for automatic image annotation is proposed. WSA uses naive Bayes as its base classifier. A set of these is combined in a cascade based on the AdaBoost technique. However, when training the ensemble of Bayesian classifiers, it also considers the unlabeled images on each stage. These are annotated based on the classifier from the previous stage, and then used to train the next classifier. The unlabeled instances are weighted according to a confidence measure based on their predicted probability value; while the labeled instances are weighted according to the classifier error, as in standard AdaBoost. WSA has been evaluated with benchmark data sets, and 2 sets of images, with promising results.

Keywords: Automatic image annotation, Semi-supervised Learning, Ensembles, AdaBoost.

1 Introduction

In recent years the amount of digital images in databases has grown impressively. This situation demands efficient search methods to extract images in huge collections according to the user requirements, in what is known as *content–based image retrieval*. To solve this problem, one alternative is to include with each image a list of keywords that describe the semantics of the image. However, this is not practical, because many images do not have an associated caption, and it is too costly to label a huge collection manually. Another alternative is automatic image annotation. Automatic image annotation consists on automatically labeling images, or image regions, with a pre-defined set of keywords, which are

regarded as descriptors of the high-level semantics of the image. Once annotated, the set of keywords obtained are associated to the image for future queries.

Recently, there has been an increasing interest on automatic image annotation [3,8,9,11]. Most methods are based on machine learning techniques, where a set of manually labeled images is used to train a classifier, and then the classifier is used to label the rest of the images. In some cases, the labels are assigned to an specific image region; and in others, labels are globally assigned to each image [9]. A third approach considers salient features in the images, to avoid segmentation [11]. In these approaches the performance of the annotation systems depends on the quantity and quality of the training set, which was manually labeled. However, there is usually a larger set of images that has not been ma-nually labeled, and which in principle could be used to improve the annotation system using a semi-supervised approach.

Semi-supervised methods exploit unlabeled data in addition to labeled data to improve classification performance. This approach could be used with different classification methods, such as neural networks, support vector machines and statistical models. In this work we are interested in improving ensemble methods, in particular AdaBoost [6], using unlabeled data. Ensemble methods work by combining a set of base or *weak* classifiers (usually a simple classifier, such as Naive Bayes) in some way, such as a voting scheme, producing a combined classifier which usually outperforms a single classifier, even a more complex one.

In this paper, a new semi-supervised ensemble of classifiers, called WSA (Weighted Semi-supervised AdaBoost), for automatic image annotation is proposed. It is based on AdaBoost and uses naive Bayes as its base classifier. When training the ensemble of Bayesian classifiers, WSA also considers the unlabeled images on each stage. These images are annotated based on the classifier from the previous stage, and then used to train the next classifier. The unlabeled instances are weighted according to a confidence measure based on their probability; while the labeled instances are weighted according to the classifier error, as in standard AdaBoost. Although there is some previous work in using unlabeled data in ensemble methods [2], they assign a smaller initial weight to the unlabeled data and from then on, the weights are changed as in AdaBoost. In our approach, the weights of unlabeled instances are dynamic, proportional to the probability given by the previous stage. Also, this approach has not been applied to automatic image annotation.

WSA was experimentally evaluated on two set of experiments. In the first one we used two standard data sets from the UCI repository [5], using different percentages of data as labeled and unlabeled. We compared our approach against: (i) supervised AdaBoost and (ii) a semi-supervised version without giving weights to the unlabeled data; using 10 fold cross-validation. In the second experiments we evaluated the performance of image annotation using two subsets of the Corel image data set [4].

The rest of the paper is organized as follows. Section 2 describes the AdaBoost algorithm using Naive Bayes as the base classifier, while section 3 introduces our semi-supervised AdaBoost algorithm with variable weights (WSA). In the next

section we briefly describe how images are segmented, and the visual features obtained per region. In section 5 the experimental results are described, and we conclude with a summary and directions for future work.

2   The AdaBoost Algorithm

We start by describing the base classifier used with AdaBoost.

2.1   Base Classifier

As base classifier we use the naive Bayes classifier, which is a simple method that has shown good performance in many domains. It is also very efficient to train and for classification, which is important when a large number of classifiers is combined. A Bayesian classifier obtains the posterior probability of each class, C_i, using Bayes rule. The naive Bayes classifier (NBC) makes the simplifying assumption that the attributes, A, are conditionally independent between each other given the class, so the likelihood can be obtained by the product of the individual conditional probabilities of each attribute given the class. Thus, the posterior probability, $P(C_i|A_1, \ldots, A_n)$, is given by:

$$P(Ci \mid A_1, \ldots, A_n) = P(C_i)P(A_1 \mid C_i) \ldots P(A_n \mid C_i)/P(A) \qquad (1)$$

In this work we consider the discrete version of the NBC, so the continuous attributes are previously discretized.

2.2   AdaBoost

Our method is based on the supervised multi-class AdaBoost ensemble, which has shown to be an efficient scheme to reduce the rate error of different classifiers, such as trees or neural networks. The main idea of AdaBoost [6] is to combine a series of base classifiers using a a weighted linear combination. Each time a new classifier is generated it tries to minimize the expected error by assigning a higher weight to the samples that were wrongly classified in the previous stages. Ensembles tend to improve the limitations of using a single classifier (e.g., [7]). When the training samples can not provide enough information to generate a "good" classifier; however, the correlated errors of the single classifiers can be eliminated when the decisions of the other classifiers are considered.

Formally, the AdaBoost algorithm starts from a set S of labeled instances, where each instance, x_i, is assigned a weight, $W(x_i)$. It considers N classes, where the known class of instance x_i is y_i. The base classifier is h, and h_t is one of the T classifiers in the ensemble. AdaBoost produces a linear combination of the H base classifiers, $F(x) = \sum_t \alpha_t h_t$, where α_t is the weight of each classifier. The weight is proportional to the error of each classifier on the training data. Initially the weights are equal for all the instances, and these are used to generate the first base classifier, h_1 (using the training algorithm for the base classifier, which

should consider the weight of each instance). Then the error, e_1, of h_1 is obtained by summing the weights of the incorrectly classified instances. The weight of each correctly classified instance is increased by the factor $\beta_t = e_t/(1 - e_t)$, and these weights are used to train the next base classifier. The cycle is repeated until $e_t > 0.5$ or when a predefined maximum number of iterations is reached. Supervised AdaBoost is shown in algorithm 1.

Algorithm 1. AdaBoost algorithm.

Require: S: Labeled instances, T: Iterations, W: weighted vector

Ensure: Final Hypothesis: $H_f = \text{argmax} \sum_{t=1}^{T} log \dfrac{1}{B_t}$

1: Initialize W. $W(x_i)^0 = \frac{1}{NumInst(S)}$

2: **for** t from 1 to T **do**

3:    Normalize W. $W(x_i)^t = \dfrac{W(x_{ })}{\sum_{i=1}^{N} W(x_i)}$

4:    Call weak algorithm. $h_t = C(S, W(x_i)^t))$

5:    Compute the error. $e_t = \sum_{i=1}^{N} W(x_i)^t$ if $h_t(x_i) \neq y_i$

6:    **if** $e_t \geq 0.5$ **then**

7:       exit

8:    **end if**

9:    $B_t = \frac{e}{(1-e_{ })}$

10:    Re-compute W. $W(x_i)^{(t+1)} = W(x_i)^t * B_t$ if $h_t(x_i) = y_i$

11: **end for**

---

3   Variable Weight Semi-supervised AdaBoost

Labeling large sets of instances is a tedious process, so we will like to label only a small fraction of the training set, combining the labeled instances with the unlabeled ones to generate a classifier. This paper introduces a new semi-supervised learning algorithm, called WSA, for image annotation. WSA is based on AdaBoost and uses a naive Bayes classifier as its base classifier. WSA receives a set of labeled data (L) and a set of unlabeled data (U). An initial classifier NB_1 is build using L. The labels in L are used to evaluate the error of NB_1. As in AdaBoost the error is used to weight the examples, increasing the weight of the misclassified examples and keeping the same weight of the correctly classified examples. The classifier is used to predict a class for U with certain probability. In the case of U, the weights are multiplied by the predicted probability of the majority class. Unlabeled examples with high probability of their predicted class will have more influence in the construction of the next classifier than examples with lower probabilities. The next classifier NB_2 is build using the weights and predicted class of $L \cup U$. NB_2 makes new predictions on U and the error of NB_2

on all the examples is used to re–weight the examples. This process continues, as in AdaBoost, for a predefined number of cycles or when a classifier has a weighted error greater or equal to 0.5. The main differences with AdaBoost are: (i) WSA uses labeled and unlabeled data, (ii) the base classifiers create new class labels for the unlabeled instances, and (iii) the weights assigned to the original unlabeled data depends on its predicted probability class. As in AdaBoost, new instances are classified using a weighted sum of the predicted class of all the constructed base classifiers. WSA is described in algorithm 2.

Algorithm 2. Semi-supervised Weighted AdaBoost (WSA) algorithm.

Require: L: labeled instances, U: unlabeled instances, P: training instances, T: Iterations

Ensure: Final Hypotesis and probabilities: $H_f = \text{argmax} \sum_{t=1}^{T} log \frac{1}{B_t}$, $P(x_i)$

1: $W(x_i)^0 = \frac{1}{NumInst(L)}, \forall x_i \in L$
2: **for** t from 1 to T **do**
3: $\quad W(x_i)^t = \frac{W(x_i)}{\sum_{i=1}^{N} W(x_i)} \forall x_i \in L$
4: $\quad h_t = C(L, W(x_i)^t)$
5: $\quad e_t = \sum_{i=1}^{N} W(x_i)^t$ if $h_t(x_i) \neq y_i$
6: $\quad$ **if** $e_t \geq 0.5$ **then**
7: $\quad\quad$ exit
8: $\quad$ **end if**
9: $\quad$ **if** $e_t = 0.0$ **then**
10: $\quad\quad e_t = 0.01$
11: $\quad$ **end if**
12: $\quad B_t = \frac{e}{(1-e)}$
13: $\quad W(x_i)^{(t+1)} = W(x_i)^t * B_t$ if $h_t(x_i) = y_i \forall x_i \in L$
14: $\quad P(x_i) = C(L, U, W(x_i)^t)$
15: $\quad W(x_i) = P(x_i) * B_t \forall x_i \in U$
16: **end for**

---

4   Image Segmentation and Visual Features

Before applying our semi-supervised method for image annotation, we perform two operations on the images: (i) segmentation and (ii) feature extraction.

The Normalized Cuts algorithm [10] was used for image segmentation. This algorithm considers the image as a non–directed complete graph. Each pixel in the image represents a node in the graph. There is an edge between each pair of pixels a y b, with a cost C_{ab} that measures the similarity of a and b. The algorithm finds those edges with a small cost and eliminates them making a cut in the graph. Each one of the edges must keep similar pixels in the same

segments. The minimum cut is performed by using equation (2), where $cut(A, B)$ is a cut between the segments A and B, $volume(A)$ is the sum of each border that touches A and $volume(B)$ is the sum of the borders that touch B.

$$Ncut(A, B) = \frac{cut(A, B)}{Volume(A)} + \frac{cut(A, B)}{Volume(B)} \tag{2}$$

Once the image is segmented, each segment or region is characterized by a set of visual features that describe the region, and which will constitute the attribute vector for WSA. We consider a set of features for color, texture and shape per region:

Color: This feature is the most common in image retrieval. Several representations for this feature have been considered such as the histogram, momentum, sets and color distributions. We use the color histogram in the RGB color space (8 values per band), as well as the mean and variance for each band.

Texture: The perception of textures also plays an important role in content-based image retrieval. Texture is defined as the statistical distribution of spatial dependences for the gray level properties [1]. One of the most powerful tools for texture analysis are the Gabor filters [3], which can be viewed as the product of a low pass (Gaussian) filter at different orientations and scales. A Gabor filter in 2D is given by equation (3).

$$g(x, y) = \left(\frac{1}{2\pi\sigma_x\sigma_y}\right) exp\left[-\frac{1}{2}\left(\left(\frac{x}{\sigma_x}\right)^2 + \left(\frac{y}{\sigma_y}\right)^2\right) + jw\left(xcos\theta\right)\right] \tag{3}$$

where θ represents the orientation of the filter in the range. The constants σ_x and σ_y determine the fall of the Gaussian in the x-axis and the y-axis, respectively. jw represents the frequency along x-axis. To characterize texture we used 4 filters with orientations of 0, 45, 90 and 135 grades, with one scale.

Shape: The following set of features were used to characterize the shape of the region:

1. Area: is an scalar that measures the actual number of pixels the image region.
2. Convex Area: represents the number of pixels in the convex hull of the region.
3. Perimeter: computed as $\sqrt{\frac{4*Area}{\pi}}$.
4. Major and minor axis: measure the longitude in pixels of the major and minor axis of the region.
5. Solidity: computed as $\frac{Area}{Convex\ rea}$.

5 Experiments and Results

WSA was tested on datasets from the UCI Machine Learning Repository [5] and on the Corel image database [4]. For the image collection a user interface, shown in figure 1, was designed to easily label a small set of examples. This tool allows to segment images and to extract their features such as color, texture, and form. Only regions with a *large proportion* of a single object were manually labeled.
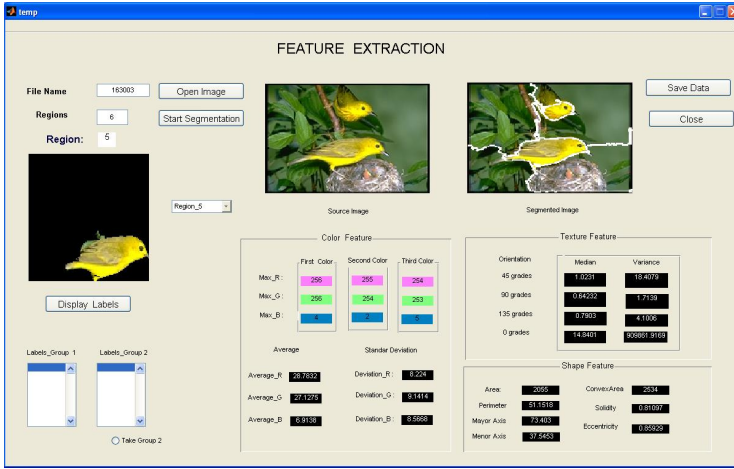
Fig. 1. Graphical user interface for image segmentation, feature extraction and region labeling

WSA was compared against AdaBoost and against a version of WSA without changing the weights of the unlabeled instances using the predicted probability value, which we will call SA. Real valued attributes were discretized in 10 bins using WEKA [12].

The algorithms were evaluated by their predicted precision using 10-fold cross validation for different percentages of unlabeled data on the training sets.

Two datasets were used from UCI repository: *Iris* and *Balance-Scale*, whose characteristics are given in table 1. Figure 2 shows the performance of WSA, SA, and (supervised) AdaBoost on both datasets. As can be seen from the figure, using unlabeled data can improve the performance of AdaBoost, in particular, when there is a large number of unlabeled instances. Also, WSA has a better performance than SA which shows that using the probability class value on the unlabeled instances can have a positive effect as it reduces the unwanted bias that the unlabeled data can produce in the classifier.

WSA was also tested on the Corel images, that are grouped according to different topics, such as, scenes, animals, buildings, airplanes, cars, and persons, among others. The size of these color images is: 192x128 pixels. The images were segmented with normalized cuts (5 regions) and a set of visual features was obtained per region, as describe in section 4. We performed tests in two topics: airplanes and birds. 100 images were randomly selected from the airplane topic; from these images 127 regions were used as the training set. In this test we considered 6 classes. We also used images of bird topic, also with 6 classes, from which 225 regions were considered for training. Table 2 shows the characteristics of these two datasets and the performance obtained by the WSA classifier using different percentage of labeled data. Additionally, figure 3 compares the performance of WSA, SA, and AdaBoost. For the airplanes collection, their is a significant improvement using WSA vs. AdaBoost, for most percentages of

labeled data; while for the birds collection, their accuracy is similar, although slightly better with WSA. In both cases, WSA is superior to SA, which confirms that weighting unlabeled data is important; wrongly labeled data could even decrease the performance of the classifier, as shown in these experiments.
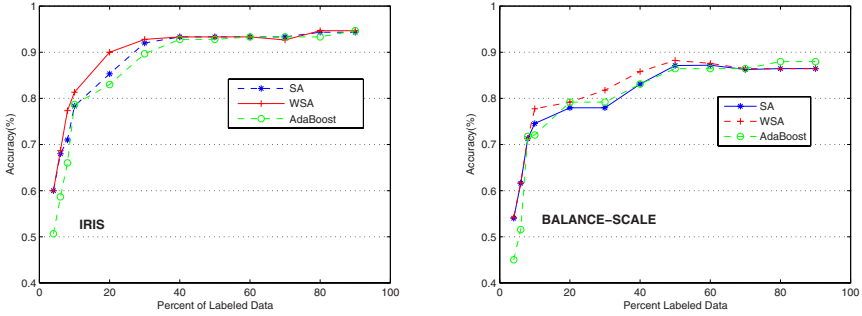
Fig. 2. Performance of WSA (red/cross), SA (blue/asterisk) and AdaBoost (green/circle) on the Iris and Balance-Scale data data sets form the UCI repository
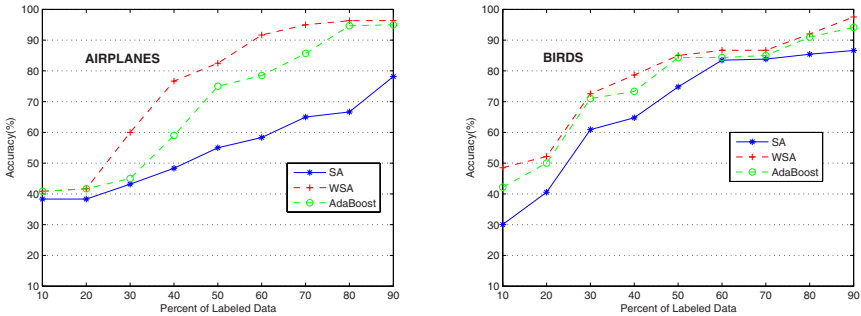
Fig. 3. Performance of SWA (red/cross), SA (blue/asterisk) and AdaBoost (green/circle) on images of airplanes and birds from the Corel database

Table 1. Characteristics of the Iris and Balance-Scale datasets

Datasets	Num-Instances	Num-Attributes	Num-Classes
Iris	150	4	3
Balance-Scale	625	4	3

Table 2. Accuracy with different percentage of labeled data

Dataset	Classes	Num.Inst.	10%	30%	50%	70%	90%
Airplanes	sky, jet, cloud, plane, sunset, helicopter	127	40.83	55.00	76.66	90.08	99.16
Birds	branch, bird, tree, grass, nest, rock	225	32.08	51.16	74.16	86.25	90.10

6   Conclusions

In this paper we proposed WSA, a semi-supervised ensemble of classifiers for automatic image annotation. It is based on AdaBoost using naive Bayes as its base classifier. It incorporates unlabeled instances, which are annotated based on the classifier from the previous stage, and then used to train the next classifier. These unlabeled instances are weighted according to a confidence measure based on the class probability given by the classifier of the previous stage. The main differences between WSA and AdaBoost are: (i) WSA uses labeled and unlabeled data, (ii) the base classifiers create new class labels for the unlabeled instances, and (iii) the weights assigned to the unlabeled data depends on its predicted probability class.

Initial experiments on images and other data show promising results. Using unlabeled data we can improve the performance of AdaBoost, in particular, when there is a large number of unlabeled instances. Also, WSA has a better performance than SA which shows that using the probability class value on the unlabeled instances can have a positive effect as it reduces the unwanted bias that the unlabeled data can produce in the classifier.

As future work we plan to perform a more comprehensive experimentation with other data sets.

References

1. Aksoy, S., Haralick, R.: Textural features for image database retrieval. In: CBAIVL 1998, p. 45. IEEE Computer Society, Washington, DC, USA (1998)
2. Bennett, K., Demiriz, A., Maclin, R.: Exploiting unlabeled data in ensemble methods. In: Proceedings of the Eighth ACM SIGKDD International Conference on Knowledge Discovery and Data Mining, pp. 289–296. ACM Press, New York (2002)
3. Chen, L., Lu, G., Zhang, D.: Content-based image retrieval using gabor texture features. In: PCM 2000, Sydney, Australia, pp. 1139–1142 (2000)
4. Corel. Corel images (2003)
5. Blake, C.L., Newman, D., Hettich, S., Merz, C.: UCI repository of machine learning databases (1998)
6. Freund, Y., Schapire, R.: Experiments with a new boosting algorithm. In: International Conference on Machine Learning, pp. 148–156 (1996)
7. Kuncheva, L.: Using measures of similarity and inclusion for multiple classifier fusion by decision templates. Fuzzy Set and Systems 122(3), 401–407 (2001)
8. Li, W., Maosong, S.: Automatic image annotation based on wordnet and hierarchical ensembles. In: Gelbukh, A. (ed.) CICLing 2006. LNCS, vol. 3878, pp. 417–428. Springer, Heidelberg (2006)
9. de Freitas, N., Duygulu, P., Barnard, K., Forsyth, D.: Object recognition as machine translation: Learning a lexicon for a fixed image vocabulary. In: Proceedings of the 7th European Conference on Computer Vision-Part IV, London, pp. 97–112. Springer-Verlag, Heidelberg (2002)
10. Shi, J., Malik, J.: Normalized cuts and image segmentation. IEEE Trans. Pattern Anal. Mach. Intell. 22(8), 888–905 (2000)
11. Tang, J., Hare, J.S., Lewis, P.H.: Image auto-annotation using a statistical model with salient regions (2006)
12. Witten, I., Frank, E.: Data Mining: Practical machine learning tools and techniques, 2nd edn. Morgan Kaufmann, San Francisco (2005)

Object Selection Based on Subclass Error Correcting for ALVOT

Miguel Angel Medina-Pérez[1], Milton García-Borroto[2],
and José Ruiz-Shulcloper[3]

[1] University of Ciego de Ávila, Cuba
`migue@bioplantas.cu`
`http://www.unica.cu`
[2] Bioplants Center, UNICA, C. de Ávila, Cuba
`mil@bioplantas.cu`
`http://www.bioplantas.cu`
[3] Advanced Technologies Applications Center, MINBAS, Cuba
`jshulcloper@cenatav.co.cu`
`http://www.cenatav.co.cu/`

Abstract. ALVOT is a supervised classification model based on partial precedences. These classifiers work with databases having objects described simultaneously by numeric and nonnumeric features. In this paper a new object selection method based on the error per subclass is proposed for improving the accuracy, especially with noisy training matrixes. A comparative numerical experiment was performed with different methods of object selection. The experimental results show a good performance of the proposed method with respect to previously reported in the literature.

Keywords: Partial precedence, mixed and incomplete data, editing method.

1 Introduction

In general, the *better* the training matrix the higher the accuracy of supervised classifiers. The accuracy of a classifier depends on the way that it is measured, and in this paper it is directly proportional to the well classification ratio. On the other hand, the quality measure of the training matrix is considered as a function of the classifier accuracy. Improving the accuracy is usually accomplished by removing *noisy* as well as *redundant* objects. Several techniques have been developed to deal with these two problems: editing and condensing methods respectively [1].

In real world problems, sometimes the objects are described simultaneously in terms of numeric and nonnumeric features. Some of the object descriptions could also be incomplete (missing values). In these cases, we are talking about mixed and incomplete data (MID). For this kind of data, the tools of the Logical Combinatorial Pattern Recognition (LCPR) [2] have shown a good behavior.

ALVOT [3, 4], introduced by Zhuravlev, is a model of supervised classification based on partial precedence. Partial precedence is the principle of calculating the

object similarities using comparisons between their partial descriptions. A partial description is a combination of feature values that should have a clear meaning in the problem domain. This is the way that physicians, and other natural scientists, establish comparisons among objects in practice [4]. This model of algorithms has been applied to different real world situations. In these cases new comparison criteria of feature values and similarity functions between sub-description of objects were introduced, allowing to work with MID.

Any algorithm of ALVOT model A works in six stages:

Stage 1.- Determine the <u>support sets system</u> Ω_A, which is a set of subsets of features

Stage 2.- Find out the <u>feature values comparison criteria and similarity function</u> between sub-descriptions of objects $\beta(\Omega O, \Omega O_i)$, $\Omega \in \Omega_A$. ΩO is a sub-description of object O using only features in Ω; and β is a similarity function

Stage 3.- Rule $\Gamma_\Omega(O_i, O)$ for evaluating the partial similarity between a fixed sub-description of a new object O and the corresponding sub-descriptions of previously classified objects O_i (<u>partial evaluation by rows</u>)

Stage 4.- Rule $\Gamma_\Omega^j(O)$ for summarizing the partial evaluation by rows of a fixed sub-description of a new object O for class K_j (<u>partial evaluation by class</u>)

Stage 5.- Rule $\Gamma^j(O)$ for summarizing all partial evaluations by class with respect to the whole support sets system of a new object O (<u>total evaluation by class</u>)

Stage 6.- <u>Decision-making rule</u> $\Gamma_A(O)$ based on the total evaluation by class.

Some authors have faced the problem of improving the efficiency of an ALVOT classifier reducing the size of the training matrix. This is usually achieved with some negative impact in the classifier accuracy. In this paper a different approach is considered. We present an efficient method for improving the accuracy of the ALVOT classifiers.

2 Previous Works

The first editing method for ALVOT was introduced in [5, 6]. This method uses a set of genetic algorithms to select the support sets system, the features weights, and the objects in the training matrix respectively. Nevertheless, there are several problems where this optimization procedure can not be applied, because the parameters have a meaning in the problem definition domain. For example, the specialist might determine the support sets system and assign the feature weights according to his background knowledge. He can also use some procedures, with a comprehensive meaning in his model. Based on these facts, we compared our algorithm only with the object selection procedure (GA-ALVOT).

The chromosomes used by the genetic algorithm were binary strings consisting of m bits, one for each object, representing the subsets of those which are selected. The i th bit has value 1 when the respective element is included, and 0 otherwise.

In general, the algorithm works as follows:

1. The initial population is generated randomly. The population size and iteration number are input parameters of the algorithm.
2. The population's individuals are sorted according to their fitness. The first and last individuals are crossed, the second is crossed with the penultimate and this process is repeated until finishing the population. They are crossed using a 1-point crossover operator in the middle of the individual. The fitness function is the ratio of well classified objects.
3. For each individual in the population the mutation operator is applied. It takes randomly an individual's gene and changes its value. The fitness is evaluated for this new population.
4. The original individuals together with those obtained by crossing and mutation are sorted in descending order according to their fitness and those with highest fitness are chosen (taking into account the population size). The new population is used in the next iteration of the algorithm.

This method has an important random component, so two different executions of the algorithm with the same data could have dramatically different results. As pointed out by Kuncheva and Bezdek [7] selecting prototypes by Random Searches and Genetic Algorithms could be computationally demanding and, for large data sets, may be infeasible.

In the first numerical experiment of this paper our proposed method shows a clear superiority with respect to the GA-ALVOT. In the second experiment was considered larger training matrixes intentionally noised. Because the computational demanding of GA-ALVOT and its behavior in the first experiment, this procedure was not taken into consideration.

For selecting objects for ALVOT we can apply classical editing methods based on NN rule. An analogue solution was reported by Decaestecker [8] and Konig et. al [9], in which the training matrix is edited for a Radial Based Function network, using a procedure originally designed for k-NN. A deep study about editing methods is outside of the scope of this paper, but a review can be found in [1]. Considering we are working with MID, in this paper we use the Compact Set Editing method (CSE) [10].

Despite the fact that these procedures can be applied, as was shown in [11], a better solution could be achieved considering the way ALVOT works.

In [11] a method to select objects for ALVOT was introduced (Voting based Object Selection, VOS). In VOS the objects are selected according to their *voting power* in the training data, which is calculated with the equation (1).

$$\iota(O) = \frac{V_{K_j}(O)}{\alpha_{K_j}(O)+1} - \max_{i \neq j}\left\{\frac{V^{'}_{K_i}(O)}{\alpha^{'}_{K_i}(O)+1}\right\}, \quad i \neq j \qquad (1)$$

where:

- $V_{K_j}(O) = \dfrac{1}{|K_j|-1} \displaystyle\sum_{\substack{O_l \in K_j \\ O_l \neq O}} I(O, O_l)$, summarizes the votes that $O \in K_j$ gives to the

  objects of the class K_j.

- $V'_{K_i}(O) = \dfrac{1}{|K_i|} \displaystyle\sum_{O_l \in K_i} I(O, O_l)$, summarizes the votes that $O \in K_j$ gives to the

  objects of the class K_i, $i \neq j$.

- $I(O, O_l) = \begin{cases} \dfrac{1}{|\Omega_A|} \displaystyle\sum_{\Omega \in \Omega_A} \dfrac{1}{|K_j|-1} \cdot \rho(O) \cdot \rho(\Omega) \cdot \beta(\Omega O, \Omega O_l) & \text{if } O_l \in K_j \\[4mm] \dfrac{1}{|\Omega_A|} \displaystyle\sum_{\Omega \in \Omega_A} \dfrac{1}{|K_j|} \cdot \rho(O) \cdot \rho(\Omega) \cdot \beta(\Omega O, \Omega O_l) & \text{if } O_l \in K_i \end{cases}$; a

  voting function obtained from ALVOT stages 3 to 5. This function expresses the
  vote that the object O gives to O_l, being $\rho(O)$ the weight of the object O,
  $\rho(\Omega) = \displaystyle\sum_{\chi_i \in \Omega} \rho(\chi_i)$, and $\rho(\chi_i)$ the weight of the feature χ_i.

- $\alpha_{K_j}(O) = \dfrac{1}{|K_j|-1} \displaystyle\sum_{\substack{O_l \in K_j \\ O \neq O_l}} \left| V_{K_j}(O) - I(O, O_l) \right|$; the deviation between the mean

  $V_{K_j}(O)$ and the vote that the object O gives to the objects in K_j; so when the
  deviation decreases, the values of $\iota(O)$ increases.

- $\alpha'_{K_i}(O) = \dfrac{1}{|K_j|} \displaystyle\sum_{O_l \in K_i} \left| V'_{K_i}(O) - I(O, O_l) \right|$; the deviation between the mean

  $V'_{K_i}(O)$ and the vote that the object O gives to the objects in K_i; so when the
  deviation decreases, the values of $\iota(O)$ increases.

The expression (1) was modified with respect to [11]. Instead $\alpha_{K_j}(O) + (1 - V_{K_i}(O))$ and $\alpha'_{K_i}(O) + (1 - V'_{K_i}(O))$ here we use $\alpha_{K_j}(O) + 1$ and $\alpha'_{K_i}(O) + 1$, respectively.

In general, the algorithm VOS works as follows:
- Calculate the voting power of each object using (1)
- Select an initial solution, formed by $\min_{i \in 1...s} \left\{ \left| \{ O \in K_i : \iota(O) > 0 \} \right| \right\}$ objects with
  highest voting power per class, being s the number of classes.
- Add (remove) the object per class with greater (lower) $\iota(O)$, until the original
  accuracy is at least (at most) achieved.

In order to improve the results of VOS, in this paper we take into consideration the inner structure of the classes while selecting objects.

3   The Inner Structure of the Classes in Supervised PR Problems

In many classification problems, a class is not uniformly formed. This fact depends on the level of generality of the properties that determine each class. Consider, for example, in the universe of all humans we can define two classes: *S* is the class of all who are *sick*, and *H* is the class of all who are *healthy*. In the class *S* are grouped together many different objects with many different diseases, which compose *subclasses* inside the outer class. Intuitively, if an object belongs to a subclass its most similar neighbor must be in the same set, so one way is to consider that a subclass should be a union of compact sets [10]. The compact set criterion induces a unique partition for a given data set, which has the property that one object x and all its most similar neighbors belong to the same cluster, and also, those objects for which x is its most similar neighbor.

Frequently in some compact sets there are objects with low similarity. Consequently, this structure is not appropriate for editing. That is why in this paper we introduce a new algorithm to generate the inner structure of the classes, named the Hierarchical Strongly Connected Components (HiSCC) algorithm. A strongly connected component of a direct graph is a maximal subset of vertices containing a directed path from each vertex to all others in the subset.

This algorithm assumes the following issues: a) The similarity between two components is computed as the global minimum similarity between two elements, one in each component (group-minimum); b) The maximum β-similarity graph is a direct graph where each vertex is connected to the vertexes with maximum value of similarity to it, if this value is above β. The algorithm works as follows:

Step 1: Construct the maximum β-similarity graph, G_0.

Step 2: Compute the set of all strongly connected components (SCC) of G_0, which are the initial solution SC_0.

Step 3: Construct the maximum β-similarity graph G_i, where the nodes are the elements of SC_{i-1}, and the inter-component similarity is the group-minimum.

Step 4: Find the strongly connected components of G_i in the current iteration, SC_i

Step 5: If the number of elements in SC_i and SC_{i-1} differs, go to step 3.

4   Object Selection Based on Subclass Error Correcting for ALVOT

Based on the previous structuralization of the classes, a new method for editing ALVOT is introduced. Let A be an algorithm of ALVOT and T a training matrix formed by objects in $K_1,...,K_s$ classes.

Subclass Error Correcting Object Selection (SECOS) algorithm works as follows:

Step 1: Eliminate from T all the objects with negative voting power, which are calculated with the equation (1). Let $T^{'}$ be the result matrix. (Noise filtering procedure)

Step 2: Cluster the matrix $T^{'}$ using HiSCC algorithm. Let $K_i^a \subseteq K_i$, $K_j^b \subseteq K_j$ where $i \neq j$ and K_i^a, K_j^b are subclasses

Step 3: Build the validation matrix V, selecting the object with worst voting power from each cluster with cardinal greater than 1.

Step 4: Build a confusion matrix E_A of A. This is a square matrix where $E_A\left[K_i^a, K_j^b\right]$ represents the number of objects belonging to the cluster $K_i^a \subseteq K_i$; that were classified by A as elements of K_j^b

Step 5: Select K_i^a and K_j^b with highest $E_A\left[K_i^a, K_j^b\right]$, $i \neq j$.

Step 6: Select $X = \left\{ O \in K_j^b : V_{K_i^a}(O) > \frac{1}{\left|K_i^a\right|} \sum_{O' \in K_i^a} V_{K_i^a}(O') \right\}$, and sort them descending according to $V_{K_i^a}(O)$, the summarization of the votes that O gives to the objects of the subclass K_i^a. For every $O \in X$, classify the validation matrix V using ALVOT trained with $T^{'} \backslash \{O\}$, until a better accuracy is achieved, and go to step 4. If no object O exists or no improvement of the accuracy could be achieved, go to step 5 and select a different pair of subclasses

Step 7: If no new pair of subclasses K_i^a and K_j^b can be found in step 5, finish.

5   Experimental Results

The experiments were made using 7 databases from UCI [12] Repository of Machine Learning, with mixed and incomplete data. A description of these databases can be found in Table 1. We conducted two different experiments. The first one was the accuracy comparison of A trained with the original matrix, and the edited matrix with GA-ALVOT, CSE, VOS and SECOS respectively. The results of this experiment are shown in table 2 and 3.

In the second experiment, we consider two databases. The training matrixes were intentionally noised interchanging the classes of fixed percent of objects. For example, in the Australian database we got from the respective training matrix 40% of the objects belonging to class 2 and put them in class 1, and vice versa. With these training matrixes the algorithms ALVOT, VOS, CSE and SECOS were executed. In table 4 the results of this experiment are shown.

Table 1. Databases used in the experiments

Database	Objects	Features	Missing Values	Classes
Breast-cancer	286	9	9	2
Breast-cancer-breast	286	9	9	2
Credit-screening	690	15	37	2
Credit-screening-A9	690	15	37	2
Credit-screening-A12	690	15	37	2
Hepatitis	155	19	75	2
Australian	690	14	37	2

Breast-cancer-breast is the same database as Breast-cancer, but with the feature breast used as class feature. Credit-screening-A9 (Credit-screening-A12) is the same database as Credit-screening, but with the feature A9 (A12) used as class feature.

Each database was split taking 70% for training and 30% for testing, repeating the process 5 times and averaging the results.

In our experiments we used a voting algorithm A with the following parameters:
- The support sets system was the set of all typical testors of the training matrix.

- $\beta(\Omega O_i, \Omega O_j) = \dfrac{\sum\limits_{\chi_p \in \Omega} C_p(\chi_p(O_i), \chi_p(O_j))}{|\Omega|}$; partial similarity function, where

  Ω is a subset of features, C_p the comparison criterion for the feature χ_p, and $\chi_p(O_i)$ is the value of the feature χ_p in the object O_i.

- $C_p(\chi_p(O_1), \chi_p(O_2)) = \begin{cases} 1 & \text{if } |\chi_p(O_1) - \chi_p(O_2)| < \sigma_p \\ 0 & \text{otherwise} \end{cases}$;similarity compare-

  son criteria for numeric features, where σ_p is the standard deviation of the values of the feature χ_p in the training matrix.

- $C_p(\chi_p(O_1), \chi_p(O_2)) = \begin{cases} 1 & \text{if } \chi_p(O_1) = \chi_p(O_2) \\ 0 & \text{otherwise} \end{cases}$; similarity comparison

  criteria for non-numeric features.

- $\Gamma_\Omega(O_p, O) = \rho(O_p) \cdot \rho(\Omega) \cdot \beta(\Omega O_p, \Omega O)$; partial evaluation by rows for a fixed support set, where $\rho(\Omega) = \sum\limits_{\chi_i \in \Omega} \rho(\chi_i)$. In the experiments $\rho(O_p) = 1$ was used.

- The weight of the feature χ_i is calculated, following [13], with the equation:

  $\rho(\chi_i) = \alpha \cdot P(\chi_i) + \beta \cdot L(\chi_i)$ with $\alpha, \beta > 0$ and $\alpha + \beta = 1$, being α and

β two parameters, which weight the influence of $P(\chi_i)$ and $L(\chi_i)$ respectively in $\rho(\chi_i)$. We used $\alpha = \beta = 0.5$. $P(\chi_i)$ is computed: $P(\chi_i) = \dfrac{\tau(i)}{\tau}$, where $\tau(i)$ is the number of typical testors, which contain the feature χ_i and τ the amount of all typical testors. $L(\chi_i)$ is computed: $L(\chi_i) = \dfrac{\sum\limits_{t \in \Psi^*(\chi_i)} \dfrac{1}{|t|}}{\left|\Psi^*(\chi_i)\right|}$, where $\Psi^*(\chi_i)$ is the family of all typical testors, which contain the feature χ_i

- $\Gamma_\Omega^j(O) = \dfrac{1}{\left|K_j\right|} \sum\limits_{O_t \in K_j} \Gamma_\Omega(O_t, O)$; partial evaluation by classes for a fixed support set

- $\Gamma^j(O) = \dfrac{1}{\left|\Omega_A\right|} \sum\limits_{\Omega \in \Omega_A} \Gamma_\Omega^j(O)$; total evaluation by classes

- $\Gamma_A\left(\Gamma^1(O), \ldots, \Gamma^s(O)\right)$; the majority vote.

The quality function used was the well classification ratio.

The accuracy of the original ALVOT A, GA-ALVOT, VOS, CSE, and SECOS with the edited matrixes respectively, is shown in Table 2. The accuracy of A could be improved in 3 cases. In 2 of them, SECOS achieved the highest value.

The compression ratios achieved by the algorithms are shown in Table 3.

Table 2. Accuracy of A without editing compared with edited by respective methods

Database	A	GA-ALVOT	CSE	VOS	SECOS
Breast-cancer	0.75	0.71	0.75	0.76	**0.78**
Breast-cancer-breast	**0.58**	0.52	0.57	0.57	0.57
Credit-screening	**0.81**	0.79	0.79	0.79	0.79
Credit-screening-A9	0.73	**0.74**	**0.74**	0.71	0.72
Credit-screening-A12	**0.64**	0.62	0.61	0.62	0.62
Hepatitis	0.73	0.74	0.68	0.75	**0.78**

The performance of each editing method in the presence of noisy databases is shown in table 4. Because of the stability of the ALVOT classifier, its accuracy can not be degraded with low levels of noise. Nevertheless if the noise introduced is too much, the degradation is drastic, and no meaningful comparison can be done. That is why we only present the results for noise of 30% and 40%. The results show that SECOS is less sensitive to noise than other editing methods, and also it improves original ALVOT. This behavior can be explained because it starts with a noise filtering procedure.

The CSE editing method, although with acceptable behavior in experiment 1, has worse results in the presence of noise. We suppose this happens because CSE does not select objects taking into consideration the way ALVOT works.

Table 3. Compression ratio

Database	GA-ALVOT	CSE	VOS	SECOS
Breast-cancer	**0.51**	0.41	0.35	0.41
Breast-cancer-breast	**0.53**	0.36	0.36	0.46
Credit-screening	0.50	**0.52**	0.51	0.20
Credit-screening-A9	**0.50**	0.48	0.26	0.21
Credit-screening-A12	0.49	0.38	0.23	**0.51**
Hepatitis	0.51	0.54	**0.65**	0.32

Table 4. Accuracy of A with larger and noised training matrixes

Database/noise	A	VOS	CSE	SECOS
Australian	0.85			
Australian/30%	0.84	**0.85**	**0.85**	**0.85**
Australian/40%	0.82	0.81	0.70	**0.84**
Credit-screening	0.86			
Credit-screening/30%	0.86	**0.86**	0.85	0.85	**0.86**
Credit-screening/40%	0.81	0.81	0.75	**0.82**

6 Conclusions

ALVOT is a model for supervised classification based on partial precedences. It is mainly used in problems where the objects are described in terms of numeric and nonnumeric features simultaneously with missing values.

Speeding up ALVOT through object selection has been faced in some papers, but it is usually achieved with some degradation of the classifier accuracy. In this paper a method for improving the accuracy of ALVOT is presented: Subclass Error Correcting Object Selection (SECOS).

SECOS first eliminates noisy objects using the voting power concept. Then it decomposes each class in subclasses by HiSCC, a new subclass detecting algorithm. Finally, a confusion matrix by subclasses is used to select the objects to be eliminated.

Two different experiments were carried out. In the first, the comparisons with other methods showed that only in 3 databases of 6 the ALVOT accuracy could be improved. In 2 of them, SECOS achieved the highest value. In the second experiment artificial disturbance was introduced and it showed that the accuracy of ALVOT could be affected by noisy objects. The proposed algorithm improved the accuracy of the classifier in all databases so it can be used to detect noisy objects and improve the accuracy of ALVOT.

References

1. Bezdek, J.C., Kuncheva, L.I.: Nearest Prototype classifiers designs: an experimental study. International Journal of Intelligent Systems 16, 1445–1473 (2001)
2. Martínez Trinidad, J.F., Guzmán-Arenas, A.: The logical combinatorial approach to Pattern Recognition, an overview through selected works. Pattern Recognition 34, 741–751 (2001)
3. Zhuravlev, Y.I., Nikiforov, V.V.: Recognition algorithms based on voting calculation. Journal Kibernetika 3, 1–11 (1971)
4. Ruiz-Shulcloper, J., Abidi, M.A.: Logical Combinatorial Pattern Recognition: A Review. In: Pandalai, S.G. (ed.) Recent Research Developments in Pattern Recognition. Transword Research Networks, USA, pp. 133–176 (2002)
5. Carrasco-Ochoa, J.A., Martínez-Trinidad, J.F.: Editing and Training for ALVOT, an Evolutionary Approach. In: Liu, J., Cheung, Y.-m., Yin, H. (eds.) IDEAL 2003. LNCS, vol. 2690, pp. 452–456. Springer, Heidelberg (2003)
6. Carrasco-Ochoa, J.A., Martínez-Trinidad, J.F.: Combining Evolutionary Techniques to Improve ALVOT Efficiency. WSEAS Transactions on Systems 2, 1073–1078 (2003)
7. Kuncheva, L.I., Bezdek, J.C.: Nearest prototype classification: clustering, genetic algorithms or random search. IEEE Transactions on Systems, Man and Cybernetics. Part C 28, 160–164 (1998)
8. Decaestecker, C.: NNP: A neural net classifier using prototype. International Conference on Neural Networks, San Francisco, California, pp. 822–824 (1993)
9. König, A., Rashhofer, R.J., Glesner, M.: A novel method for the design of radial-basis-function networks and its implication for knowledge extraction. International Conference on Neural Networks, Orlando, Florida 1804–1809 (1994)
10. García-Borroto, M., Ruiz-Shulcloper, J.: Selecting Prototypes in Mixed Incomplete Data. In: Sanfeliu, A., Cortés, M.L. (eds.) CIARP 2005. LNCS, vol. 3773, pp. 450–459. Springer, Heidelberg (2005)
11. Medina-Perez, M.A., García-Borroto, M., Villuendas-Rey, Y., Ruiz-Shulcloper, J.: Selecting objects for ALVOT. In: Martínez-Trinidad, J.F., Carrasco Ochoa, J.A., Kittler, J. (eds.) CIARP 2006. LNCS, vol. 4225, pp. 606–613. Springer, Heidelberg (2006)
12. Merz, C.J., Murphy, P.M.: UCI Repository of Machine Learning Databases. University of California at Irvine, Department of Information and Computer Science, Irvine (1998)
13. Lazo-Cortés, M., Ruiz-Shulcloper, J.: Determining the feature informational weight for non-classical described objects and new algorithm to calculate fuzzy testors. Pattern Recognition Letters 16, 1259–1265 (1995)

CT-EXT: An Algorithm for Computing Typical Testor Set

Guillermo Sanchez-Díaz[1] and Manuel Lazo-Cortés[2]

[1] Center of Technologies Research on Information and Systems, UAEH,
Carr. Pachuca-Tulancingo Km. 4.5, C.P. 42084, Pachuca, Hgo., Mexico
sanchezg@uaeh.reduaeh.mx
[2] Institute of Cybernetics, Mathematics and Physics,
15 No. 551 Vedado, C.P. 10400, Havana, Cuba
mlazo@get.tur.cu

Abstract. Typical testors are a useful tool for feature selection and for determining feature relevance in supervised classification problems, especially when quantitative and qualitative features are mixed. Nowadays, computing all typical testors is a highly costly procedure; all described algorithms have exponential complexity. Existing algorithms are not acceptable methods owing to several problems (particularly run time) which are dependent on matrix size. Because of this, different approaches, such as sequential algorithms, parallel processing, genetic algorithms, heuristics and others have been developed. This paper describes a novel external type algorithm that improves the run time of all other reported algorithms. We analyze the behaviour of the algorithm in some experiments, whose results are presented here.

Keywords: feature selection, pattern recognition, typical testors.

1 Introduction

Feature selection is a significant task in supervised classification and other pattern recognition areas. This task consists of identifying those features that provide relevant information for the classification process. In Logical Combinatorial Pattern Recognition [6,8], feature selection is solved by using Testor Theory [5]. Yu. I. Zhuravlev introduced the use of the testor concept in pattern recognition problems [4]. He defined a testor as a set of features that does not confuse objects descriptions belonging to different classes. This concept has since been extended and generalized in several ways [5]. This concept is especially well suited to problems which involve qualitative and quantitative features (mixed data) and even incomplete descriptions.

Computing all typical testors is very expensive procedure; all described algorithms have exponential complexity. In addition to sequential algorithms, different methods, such as parallel computing [14], genetic algorithms used for calculating a subset of typical testors [13], etc. But even through the application of these techniques, the run time of existing algorithms continues to be unacceptable owing to several problems which are dependent on matrix size.

The present paper proposes a novel external type algorithm, named CT-EXT, for calculating the typical testor set of a learning matrix. The classic concept of a testor, where classes are assumed to be both hard and disjointed, is used. The comparison criteria used for all features are Boolean, regardless of the feature type (qualitative or quantitative). The similarity function used for comparing objects is also Boolean. These concepts are formalized in the following section.

2 Preliminary Concepts

Let $U = \{O_1, O_2, \cdots, O_s, \cdots\}$ be a universe of objects, $\Omega = \{O_1, O_2, \cdots, O_m\}$ is a subset of U, $I(O_1), I(O_2), \cdots, I(O_m)$, are the object descriptions in terms of the set of features $R = \{X_1, X_2, \cdots, X_n\}$, where each feature X_i, has a set of admissible values M_i (M_i is the domain of X_i) associated to it.

Each object description can be represented as $I(O_i) = (X_1(O_i), X_2(O_i), \cdots, X_n(O_i)$. Let us consider a function $C_i : M_i \times M_i \to L_i$, where L_i is a totally ordered set, such as if C_i is a dissimilarity criterion, then $C_i(X_i(O_s), X_i(O_s)) = min\{y|y \in L_i\}$, and if C_i is a similarity criterion, then $C_i(X_i(O_s), X_i(O_s)) = max\{y|y \in L_i\}$ [10] . This function can be regarded as the comparison criterion for the feature X_i.

Set U is a union of a finite number of c disjoint subsets $K_1, \cdots, K_c$, which are called classes. Each object O has an associated c-tuple of membership degrees, which describes the belonging of the object O to the classes $K_1, \cdots, K_c$. This c-tuple of membership degrees is denoted by $\alpha(O)$. Then, $\alpha(O) = (\alpha_1(O), \cdots, \alpha_c(O))$, where $\alpha_i(O) = 1$ means that $O \in K_i$ and $\alpha_i(O) = 0$ means that $O \notin K_i$ [10]. The information containing both descriptions and c-tuple of membership degrees of objects in Ω is used as learning data for classification, and we call it a Training Sample (TS).

Other denominations like Learning Sample or Learning Matrix (LM) are also used. Table 1 shows the general scheme of a learning matrix.

Table 1. General Learning Matrix scheme

Objects	Features			l-uple of belonging
O_1	$X_1(O_1)$	$\cdots$	$X_n(O_1)$	$\alpha_1(O_1), \cdots, \alpha_c(O_1)$
$\vdots$	$\vdots$	$\vdots$	$\vdots$	$\vdots$
O_p	$X_1(O_p)$	$\cdots$	$X_n(O_p)$	$\alpha_1(O_p), \cdots, \alpha_c(O_p)$
O_q	$X_1(O_q)$	$\cdots$	$X_n(O_q)$	$\alpha_1(O_q), \cdots, \alpha_c(O_q)$
$\vdots$	$\vdots$	$\vdots$	$\vdots$	$\vdots$
O_m	$X_1(O_m)$	$\cdots$	$X_n(O_m)$	$\alpha_1(O_m), \cdots, \alpha_c(O_m)$

The supervised pattern recognition problem for an object $O \in U - \Omega$ consists in determining $\alpha(O)$ using the learning matrix and the description of object O.

Given LM and n bi-valued comparison criteria $C_1, \cdots, C_n$, a comparison matrix denoted by DM is created. We consider all comparison criteria as dissimilarity ones. This comparison matrix is called a dissimilarity matrix. Rows of DM are obtained from feature by feature comparison of every pair of objects from LM belonging to different classes. As all are dissimilarity criteria, if the objects under comparison are not similar in terms of a feature, a value of 1 is assigned in the corresponding column. If this is not the case, a value 0 is assigned.

Each row of DM may be represented by the set of column indexes, in which this row has a value of 1. This set indicates the features in which the compared objects are not similar.

It is important to realize that each row of DM may contain redundant information.

Let f and g be two rows of DM and let F and G be their associated set of column indexes, respectively. We say that f is a sub-row of g if $F \subset G$. We say that f is a basic row of DM if f has no sub-rows in DM.

A sub-matrix containing all basic rows in DM (without repetitions) is called a basic matrix and we identify it with BM.

Commonly, algorithms used for computing typical testors make use of BM instead of DM or LM by two reasons: 1) unnecessary comparisons among objects are avoided, BM contains the comparisons among the "most similar" objects, and 2) typical testors calculated over BM are the same as those calculated over DM or LM [10]. This is because BM contains all information needed to calculate typical testors of LM.

Definition 1. *A feature subset $T \subseteq R$ which does not confuse any two objects belonging to different classes is called testor. A typical testor is an irreducible testor (if any feature of T (column of LM) is eliminated, then the new set is not a testor [10]).*

3 Previous Algorithms

Algorithms for computing typical testor set can be divided into external type and internal type algorithms. External type algorithms consider the whole power set of features of BM in order to determine whether a feature subset is a typical testor or not, by using a previously defined total order. These algorithms take advantage of several properties for skipping over several sets and thus avoid the analysis of every combination of features. Examples of this kind of algorithms are: BT and TB [9], REC [7], CER [2] and LEX [15].

On the other hand, internal type algorithms analyze BM based on several conditions that guarantee that a feature subset is a typical testor. Instead of verifying whether a set of features is a typical testor, as external type algorithms do, internal type algorithms build typical testors through different strategies. Some of these algorithms are: CC [1] and CT [3].

Generally speaking, external type algorithms work in the following fashion: each combination (feature subset) is represented by a characteristic n-tuple, a total order is defined in the power set of features (natural order over the

characteristic n-tuples, lexicographic order, etc.), a property that characterizes a typical testor is defined. Starting from an initial combination, the algorithm moves about the power set verifying the fulfillment of the property. If the feature combination under analysis is a typical testor, then it is saved. In all cases, the algorithm skips those consecutive feature combinations which may be said, with certainty, not to be typical testors, either because they are not testors or because they are testors but not typical. The characterizing property is verified row by row in BM, in consideration only of columns belonging to the current combination.

The blind generation of feature combinations, which does not take into account how much each feature contributes to the combination under construction, is one of the main limitations of this kind of algorithm.

The most significant difference between LEX and all other external type algorithms is that LEX incorporates into the combination under construction those features that maintain the fulfilment of the typical testor characterizing property. However, the verification of this property for each new added feature is a costly process.

Internal type algorithms build feature combinations considering values in BM. These algorithms take into account elements with a value of 1 in BM in order to generate maximal feature combinations in such a way that the involved columns represent a typical testor. There are two strategies: i) building incremental combinations knowing that they are testors and trying to successfully complete a typical testor and ii) building incremental combinations that have the typicity property and trying to successfully complete a testor. These algorithms have the disadvantage that they generate many repetitions of feature combinations.

4   The Proposed Algorithm CT-EXT

CT-EXT is an external type algorithm which uses the same lexicographic total order that the LEX algorithm uses. The CT-EXT algorithm generates incremental feature combinations reducing, step by step, the number of objects belonging to different classes that are confused, until a combination which is a testor is obtained. Subsequently, CT-EXT verifies whether the generated combination is a typical testor. As well as LEX, CT-EXT rules out those feature combinations that can generate a testor which is not a typical testor, preserving those candidates capable of generating a typical testor only. If a testor is generated, all its consecutive supersets (in the lexicographic order previously introduced into the power set of features) are not analyzed. They are skipped because these feature combinations are testors, but not typical testors.

The Algorithm's name (CT-EXT) is obtained by combining CT (because of the similarities in behaviour it presents with respect to the CT algorithm) and EXT (because it carries out its search over the power set of features). Meaning, it is an EXTernal type algorithm.

In addition to this, to improve the performance of the algorithm, a convenient order is introduced into BM, in a similar way as the case studied in [12]. The algorithm has the following theoretical bases.

Definition 2. *Let f_i be a row of BM. We say that f_i is a zero row of $S \subseteq R$, and we denote it by $f_i^0(S)$, if $\forall X_p \in S$, $f_i[p] = BM[i,p] = 0$.*

Definition 3. *In terms of BM, a testor $T \subseteq R$ is a feature set such that there are no zero rows of T in BM.*

From this definition, if T is a testor then, any superset of T is a testor too.

Definition 4. *Let f_i be a row of BM. We say that f_i is a typical row of $S \subseteq R$ with regard to X_q, and we denote it by $f_i^1(S,q)$ if $\exists X_q \in S$, such that $f_i[q] = BM[i,q] = 1$, and $\forall X_p \in S$, $X_p \neq X_q$, $f_i[p] = BM[i,p] = 0$*

Definition 5. *In terms of BM, $T \subseteq R$ is a typical testor if T is a testor and $\forall X_j \in T, \exists f_i^1(T,j)$*

This means that in a typical testor, for all features, there exists a row in BM in the sub matrix associated to T, having a value of 1 in the position corresponding to that feature, and values of 0 in all remaining positions (there are no zero rows, and if any column of T is eliminated, at least one zero row appears, and the testor property is not fulfilled). Although we have defined a typical testor here in terms of BM, normally it is defined as an irreducible testor (as in definition1).

Definition 6. *Let $T \subseteq R$ and $X_j \in R$, $X_j \neq T$. We denote by $\sum_T f^0$ the number of zero rows of T. We say that X_j contributes to T if, and only if, $\sum_{T \cup \{X\}} f^0 < \sum_T f^0$.*

This definition indicates that one feature contributes to a feature combination if for some zero rows in BM, considering only T, the new feature has a value of 1 in at least one of these zero rows. So, adding this feature to T, there are less zero rows of the incremented feature combination than of T.

Being $T \subset T \cup \{X_j\}$, it is not possible that $\sum_T f^0 < \sum_{T \cup \{X\}} f^0$. If we increase the feature combination either the zero rows are maintained and in this case the column added does not contribute to the combination, or the number of zero rows decreases.

Proposition 1. *Let $T \subseteq R$ and $X_j \in R$, $X_j \neq T$. If X_j does not contribute to T, then $T \cup \{X_j\}$ can not generate any typical testor.*

Proof. Let $T \subseteq R$ and $X_j \in R$, such that X_j does not contribute to T. Suppose that $T' = T \cup \{X_j \cup Z\}$ is a typical testor. Then, according to definition 5, there exists for X_j at least a typical row in BM. Then, $f_i[j] = BM[i,j] = 1$, and $\forall X_p \in T', X_p \neq X_j, f_i[p] = BM[i,p] = 0$. Thus, we have that f_i is a zero row of $T \cup Z$ and therefore, of T too. So, $\sum_{T \cup \{X\}} f^0 < \sum_T f^0$ and we obtain that X_j contributes to T, which contradicts the formulated hypothesis and then, we have that there are no typical testors that include $T \cup \{X_j\}$.

Proposition 2. *Let $T \subseteq R$, $Z \subseteq R$, $Z \neq \emptyset$. If T is a testor, then $T \cup Z$ is a testor too, but it is not a typical testor.*

Proof. Being T a testor, we have that $\sum_T f^0 = 0$, therefore, any feature $X_p \in Z$ contributes to T. Since $T \cup Z$ is a superset of T, then $T \cup Z$ is a testor, but following proposition 1, it can not generate any typical testor.

Description of the algorithm CT_EXT

Input: BM (Basic Matrix)

Output: TT (set of all typical testors)

1. **Ordering rows and columns in BM**.- The row with less quantity of values 1, is set as the first row of BM. Columns of BM are ordered, from left to right, each having a value of 1 in the first row and each subsequent column having a value 0 in the first row of BM. The order of the columns into each group (with the same value of 1 or with the same value of 0) is irrelevant.
2. **Initializing**.- $TT = \emptyset$ (typical testors set); $T = \emptyset$ (current feature combination); $j = 1$ (first feature of BM to be analyzed)
3. **Adding a new feature generator of feature combinations**.- If X_j has a value of 1 in the first row of BM then X_j is added to T ($T = T \cup \{X_j\}$), go to step 5. In another case, the algorithm finishes (any new feature combination will not generate a typical testor, because all these combinations have a zero row).
4. **Evaluating the new feature**.- The new feature is added to the current combination ($T = T \cup \{X_j\}$), and it is verified whether this new feature contributes to the current combination. If the answer is negative, go to step 6.
5. **Verifying testor property**.- Verify whether T is a testor, if yes then verify whether it is a typical testor. If T is a typical testor, the combination is saved in TT ($TT = TT \cup T$). If this is not the case, go to step 7.
6. **Eliminating the last feature analyzed**.-The last feature analyzed X_j is eliminated from T ($T = T \backslash \{Xj\}$). If X_j does not contribute to T, then no combination containing T is verified (proposition 1). Go to step 7. If the combination was a testor, then no consecutive superset of the current combination is analyzed (proposition 2). If $T = \emptyset$ then $j = j + 1$, go to step 3.
7. **Selecting a new feature to analyze**.- The next non-analyzed feature in the current combination is selected. If $j < n$ then $j = j + 1$, and go to step 4. If this is not the case, go to step 6.

5   Experiments

In order to evaluate the performance of the proposed algorithm, a comparison with three algorithms reported in the literature (BT, CT and LEX) was made. The first algorithm selected is a classical external type algorithm, which uses the

last reported algorithm which incorporates several improvements in performance [12]. The second algorithm is an internal type algorithm which has the best run times compared with other internal type algorithms [11]. The final algorithm, LEX, reported the best run time execution of all algorithms.

In order to compare run times, we use several BM with different dimensions. Some of them were randomly generated; one was taken from real medical diagnosis problems. In table 2, the experimental results obtained with the algorithms are shown.

The matrices used are denoted by $M_{rows \times columns}$, and TT denotes the number of typical testors found by algorithms. The experiments were conducted in a Pentium IV, with 2Ghz, and 1 Mbyte of RAM. The execution times are presented in seconds.

Table 2. Run time execution in seconds of several algorithms

Algorithm	$M_{10 \times 10}$	$M_{10 \times 34}$	$M_{15 \times 15}$	$M_{209 \times 32}$	$M_{20 \times 38}$	$M_{10 \times 42}$	$M_{269 \times 42}$	$M_{209 \times 47}$
BT	0	14	0	25	105	14	> 43200	> 43200
CT	0	0	0	39	0	0	38691	8026
LEX	0	0	0	14	0	0	2530	1799
CT_EXT	**0**	**0**	**0**	**3**	**0**	**0**	**928**	**483**
TT	30	935	178	6405	2436	935	302066	184920

Experiments show that the LEX algorithm has the best performance of all algorithms (BT and CT). The BT algorithm was unable to find the typical testors whole set for the two largest matrices for more than 12 hours, and the execution was aborted. In all experiments, the proposed algorithm provides faster run times than the other algorithms. As Table 2 shows, CT-EXT run time execution achieves reductions between 63% and 78% with respect to LEX algorithm.

6   Conclusions

This paper proposes a novel external type algorithm which affords the best performance of all algorithms reported in the literature. With this algorithm, thus, we provide researchers and applied scientists who might be interested in calculating typical testors for high dimensional matrices with a useful tool.

Like LEX, the proposed algorithm does not generate a great quantity of comparisons, because it does not verify many feature combinations which, as one may determine a priori, do not generate typical testors. The main difference with respect to LEX is that LEX verifies, as a first condition, whether the combination under analysis has typical rows. In contrast, CT-EXT verifies, first of all, if the combination generated has less zero rows than previous combinations. From this point of view, CT-EXT resembles the REC algorithm, although REC directly works with the learning matrix [7].

In addition to this, an analogy between algorithms LEX and CC can be noted, because both algorithms generate combinations focusing on typical rows. On the other hand, an analogy between algorithms CT-EXT and CT is that these algorithms generate combinations guarantying that they are testors, and, after that, both algorithms verify whether the testor is typical or not. The order introduced into rows and columns of BM, allows us to avoid the analysis of a great quantity of feature combinations.

The CT-EXT and LEX algorithms represent a new kind of algorithm for computing all typical testors. Their chief characteristic is that both algorithms analyze a typical testor candidate before inserting new feature in current combination. They are less blind than their predecessors. Based on experimental results, we can conclude that the proposed algorithm has the highest performance score.

References

1. Aguila Feroz, L., Ruiz Shulcloper, J.: Algorithm CC for the elaboration of k-valued information on pattern recognition problems. Cuba 5(3), 89–101 (1984) (In Spanish)
2. Ayaquica Martinez, I.Y., Jimenez Jacinto, V.: A new external type algorithm for the calculation of tipical testors. In: Proc. TIARP 1997, pp. 141–148 (1997) (In Spanish)
3. Bravo, A.: Algorithm CT for calculating the typical testors of k-valued matrix. Revista Ciencias Matematicas, Cuba 4(2), 123–144 (1983)
4. Dmitriev, A.N., Zhuravlev, Y.I., Krendeliev, F.: About mathematical principles and phenomena classification. Diskretni Analiz 7, 3–15 (1966)
5. Lazo-Cortes, M., Ruiz-Shulcloper, J., Alba Cabrera, E.: An Overview of the evolution of the concept of testor. Pattern Recognition 34(4), 753–762 (2001)
6. Martinez-Trinidad, J.F., Guzman Arenas, A.: The Logical Combinatorial approach for pattern recognition an overview through selected Works. Pattern Recognition 34(4), 741–751 (2001)
7. Morales, R.: A classification system and pattern recognition. B. Sh. Thesis, Mexico, UNAM (1988) (In Spanish)
8. Ruiz-Shulcloper, J., Abidi, M.: Logical Combinatorial Pattern Recognition: A Review. Recent Research Developments in Pattern Recognition. In: Pandalai, S.G. (ed.) Recent Research Developments in Pattern Recognition, Transworld Research Networks, Kerala, India, pp. 133–176 (2002)
9. Shulcloper, J.R., Bravo, M.A.Y., Aguila, F.L.: Algorithms BT and TB for calculating all typical tests. Revista Ciencias Matematicas, Cuba 6(2), 11–18 (1982) (In Spanish)
10. Ruiz Shulcloper, J., Guzman Arenas, A., y Martinez Trinidad J.: Logical combinatorial pattern recognition approach". Advances on pattern recognition series, Edit. Instituto Politecnico Nacional, Mexico (1999) (In Spanish)

11. Sanchez Diaz, G,: Developing and implementing efficient algorithms (batch and parallel) for calculating typical testors of a basic matrix. Master Thesis, BUAP, Puebla, Mexico (1997) (In Spanish)
12. Sanchez Diaz, G., y Lazo Cortes, M.: Modifications to BT algorithm for improving its run time execution. Revista Ciencias Matematicas, Cuba 20(2), 129–136 (2002) (In Spanish)
13. Sanchez Diaz, G., Lazo Cortes, M., y Fuentes Chavez, O.: Genetic algorithm for calculating typical testors of minimal cost. In: Proc. SIARP 1999, pp. 207–213 (1999) (In Spanish)
14. Sanchez Diaz, G., Lazo Cortes, M., Garcia Fernandez, J.: Parallel and distributed models for calculating typical testors. In: Proc. TIARP 1997, pp. 135–140 (1997) (In Spanish)
15. Santiesteban Alganza, Y., Pons Porrata, A.: LEX: A new algorithm for calculating typical testors. Revista Ciencias Matematicas, Cuba 21(1), 85–95 (2003) (In Spanish)

Evaluating a Zoning Mechanism and Class-Modular Architecture for Handwritten Characters Recognition

Sandra de Avila[1], Leonardo Matos[1], Cinthia Freitas[2],
and João M. de Carvalho[3]

[1] Federal University of Sergipe, Comp. Depart., São Cristóvão, SE, Brazil
[2] Pontifical Catholic University of Parana, Curitiba, PR, Brazil
[3] Federal University of Campina Grande, Campina Grande, PB, Brazil
{sandraeliza,lnmatos}@ufs.br, cinthia@ppgia.pucpr.br,
carvalho@dee.ufcg.edu.br

Abstract. In this article we propose a feature extraction procedure based on directional histograms and investigate the application of a nonconventional neural network architecture, applied to the problem of handwritten character recognition. This approach is inspired on some characteristics of the human visual system, as it focus attention on high spatial frequencies and on the recognition of local features. Two architectures were tested and evaluated: a conventional MLP (Multiple Layer Perceptron) and a class-modular MLP. Experiments developed with the Letter database produced a recognition rate of 93.67% for the class-modular MLP. Other set of experiments utilized the IRONOFF database resulting in recognition rates of 89.21% and 80.75% for uppercase and lowercase characters respectively, also with the class-modular MLP.

Keywords: Handwritten characters recognition, Class-modular architecture, Directional histogram.

1 Introduction

The recognition of handwritten characters has been a topic widely studied during the recent decades because of both the theoretical challenges in pattern recognition and its many possible applications, such as automatically processing postal ZIP codes from mail pieces and money amount in bankchecks. However, it proves to be a challenging problem due to the large variance the data may exhibit. Not only there are changes and distortions from one writer to another, but even for samples produced by the same writers [11].

In this paper we propose three steps approach for recognition of handwritten characters: (1) preprocessing, (2) feature extraction and (3) classification. The role of *preprocessing* is to segment the pattern of interest from the background. *Feature extraction* represents the image of each character by a set of significant features, i.e., each character is represented by a feature vector. *Classification* recognizes the class to which the analyzed character belongs, according to the provided features.

The experimental results we present were obtained with the IRONOFF database [13] from Nantes University, France, that contains off-line character images of the English alphabet, with 10685 instances of lowercase and 10681 instances of uppercase characters. In addition, some preliminary tests were performed with the Letter database from

UCI repository of machine learning [5]. The preliminary tests were used to investigate only the classifier effectiveness, since the feature extraction procedure is already performed for this database. Both databases are similar, as they contain equal number of classes (26) and approximately the same number of classes instance: 20000 (Letter) and 21366 (IRONOFF).

This paper is organized as follows. Section 2 presents the feature extraction procedure for handwritten characters recognition; Section 3 describes the architecture and training of the class-modular neural network; Section 4 presents experimental results and some discussions; finally, Section 5 draws some concluding remarks.

2 Feature Extraction Procedure

Studies in the area of vision show that human visual perception is strongly influenced by high spatial and temporal frequency features [1]. Contours or edges, where the contributions of high spatial frequencies dominate, plays a primordial role in the recognition of forms and interpretation of visual stimulus, as the sense of deepness. Since handwriting characters are visual representations of handmade strokes, most relevant information for the recognition task is extracted from contours.

In this article we present a feature extraction procedure based on directional and curvature histograms for the contour image. A histogram is a frequency distribution of some punctual feature, i.e. a feature of an isolated pixel. Some punctual features used by Shi et al. [10] are gradient and curvature.

Several existing operators can be used to calculate an image gradient. In order to make gradient computation more efficient, we create a gray scale image from the original binary one using a spatial lowpass filter. This grayscale image is used to obtain the gradient phase and curvature.

The directional histogram is a useful tool for emphasizing differences between segments of character contours. It captures the slant of other characteristics concerning their shape. Nevertheless the histograms does not point out where those features occur. An isolated histogram can detect an interesting feature, like a rounding stroke, but it does not reveal where it is located on the character contour. Hence, it does not provide sufficient information for distinguishing, for example, between digits six and nine, as it does not points out where the looping is. In order to mitigate this problem, we developed a zoning mechanism which allows associating directional and curvature features with the position where they occur.

The zoning mechanism adopted does not impose zones of fixed dimension, as it splits the image into non-overlapping regions, therefore avoiding the need to perform a scale normalization preprocessing. Thus, the image preserves all the original geometric properties. The association of directional and curvature histograms with zones of different sizes captures structural information about the character image. In a typical image of digit two, for instance, the pixels with high curvature usually occur in the upper right and bottom left corner, it is also usual that a straight line segment covers the bottom of the image and a rounding segment is present at the top. This kind of information is captured when zones of relative size are associated with the use of histograms.

2.1   Algorithm

The algorithm that summarizes the feature extraction process discussed in this section is stated as follows in two phases. The first performs the preprocessing operations and the second the features vector extraction.

Preprocessing

1. The contour of the input image is saved in a list of points. Both the inner and outer contours were used in this work.
2. A spatial lowpass filter is applied to the binary input image r times in order to yield a grayscale image. In the experiments described in this paper we used $r = 4$ (Fig. 1(a)).
3. A normalization procedure is applied to the image of step 2 in order to limit the grayscale variation to the interval $[0, 1]$.
4. Curvature (Fig. 1(b)) and gradient phase (Fig. 1(c)) are computed for the grayscale image from step 3, as described in Shi et al. [10], only for the pixels saved in step 1.

(a) Pseudo-grayscale   (b)   Curva-ture   (c) Phase
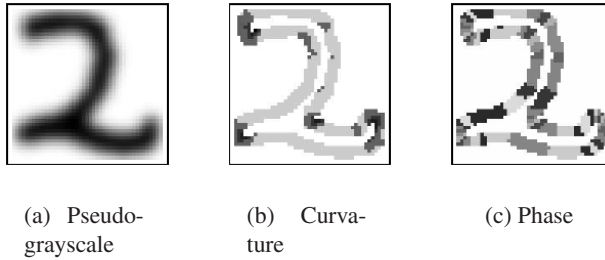
Fig. 1. Feature extracted from image

Feature Extraction Procedure

1. Image $F_{r \times c}$ is partitioned into zones with approximately the same size. If $r \approx c$ it is segmented into 16 zones (4×4). If $r > 1.25c$, F is segmented into 5×4 zones. If $c > 1.25r$, F is segmented into 4×5 zones (Fig. 2).
2. The interval $[0, \pi]$ is partitioned into 10 classes of equal amplitude $\pi/10$. If two angles differ from each other by π radians, they are considered the same.
3. The curvature is computed as in Shi et al. [10] and the interval $[-\infty, \infty]$ is divided into 5 classes.
4. For each zone the number of pixels from each class of direction and curvature is counted. This leads to histograms with 15 classes.
5. Each histogram is normalized.
6. The histograms are concatenated in order to compose the feature vector.

(a) Horizontal   (b) Ver-
                      tical
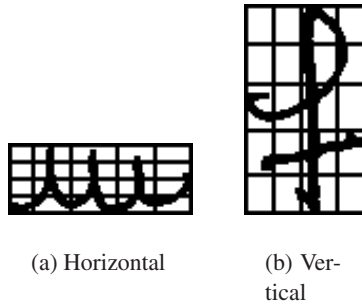
Fig. 2. Rectangular images zones

3   Classification

In character recognition systems, the type or format of the extracted features must match
the requirements of the chosen classifier [12]. Multi-Layer Perceptron Neural networks
(MLP-NN) classifiers have proven to be powerful tools in pattern recognition [14]. This
work investigates two MLP architectures: Conventional and Class-modular, such as Oh
and Suen [6] and Kapp et al. [3]. The class-modular architecture is described next.

3.1   Class-Modular Architecture

According to Oh and Suen [6], one property of the conventional MLP architecture is
that all K classes share one single network. The essential task in designing a charac-
ter recognition system is to choose features with good discriminative power and the
network should segment the chosen feature space between into the K classes regions.
However, determining the optimal decision boundaries for the K-classification network
for character recognition in a high-dimensional feature space is very complex and can
seriously limit the recognition performance of character recognition systems using MLP.

The conventional MLP-NN architecture has a "rigid" structure in which all the K
classes are altogether intermingled. This architecture cannot be locally modified or op-
timized for each class. Principe et al. [8] and Oh and Suen [6] mention specific con-
vergence problems with one large network, when the training set is not large enough
compared with the classifier size, i.e., the number of free parameters in the classifier.

To overcome such limitations Oh and Suen [6] introduce the class modularity con-
cept to the MLP classifier. To implement this concept, the original K-classification
problem is decomposed into K 2-classification subproblems, one for each of the K
classes. A 2-classification subproblem is solved by the 2-classifier specifically designed
for the corresponding class. The 2-classifier is in charge of only one specific class, dis-
criminating that class from the other $K - 1$ classes.

The MLP for a 2-classifier is illustrated in Fig. 3(a). The modular MLP classifier
consists of K subnetworks, M_{wi} for $0 \leq i < K$, each responsible for one of the K
classes. The specific task of M_{wi} is to classify two groups of classes, Ω_0 and Ω_1 where
$\Omega_0 = \{w_i\}$ and $\Omega_1 = \{w_k | 0 \leq k < K$ and $k \neq i\}$.

Designing subnetworks M_{wi} follows the same way as for the conventional MLP. In each of the subnetworks, the three layers are fully connected. The input layer has d nodes to accept the d-dimensional feature vector. The output layer has two output nodes, denoted by O_0 and O_1 for Ω_0 and Ω_1, respectively.

The architecture for the entire network constructed by K subnetworks is shown in Fig. 3(b). The feature module extracts a feature vector X which is shared by all K classes. X is applied to the input layer of all subnetworks and each M_{wi} uses its own weights set to produce an output vector $D = (O_0, O_1)$. The values of O_0 constitutes the final decision [6] [3].

(a) A subnetwork M_{wi}.   (b) Whole network.
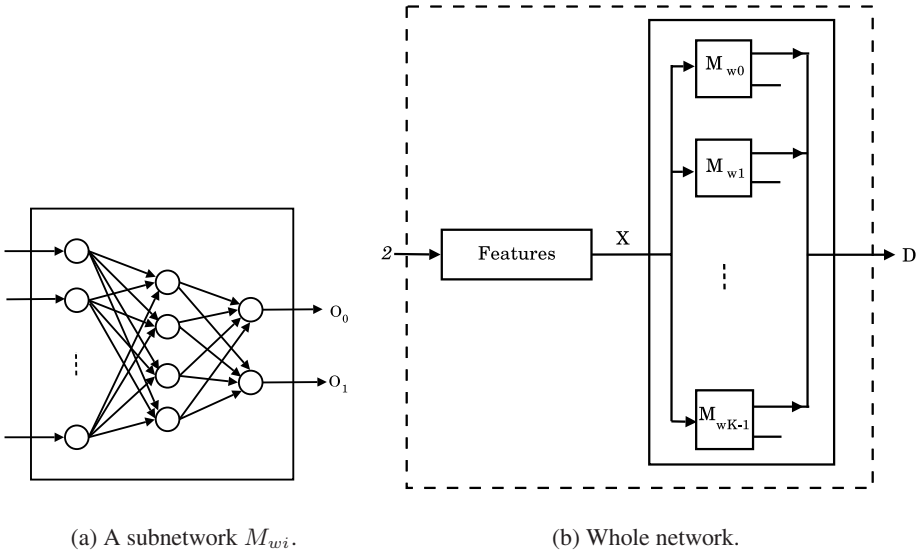
Fig. 3. Class-modular MLP architecture [6]

For training, each of the K 2-classifiers (subnetworks) is trained independently of the other classes, the error-backpropagation algorithm being applied in the same way as for the conventional MLP. A distinct training set is built for each subnetwork, as follows: the samples in the original training set are organized into two groups, Z_{Ω_0} and Z_{Ω_1} such that Z_{Ω_0} has the samples from classes in Ω_0 and Z_{Ω_1} the ones from classes in Ω_1. For recognition of the input character patterns, the class decision module considers only the values of Z_{Ω_0} from each subnetwork and employs a simple winner-takes-all scheme to determine the final class. Therefore, the winner class is associated with the subnetwork which provides the largest output to the desired pattern.

Oh and Suen [6] presented the effectiveness and superiority of the class-modular MLP compared to the classical nonmodular approach, as shown in Table 1.

Kapp et al. [3] compared the conventional and class-modular architectures for handwritten recognition applied to bankchecks. Experiments confirm that the modular network shows a superior recognition performance. The recognition rates obtained were 77.08% for the nonmodular network and 81.75% for the modular network.

Table 1. Recognition rates for test set of [6]

	Classes	Conventional (%)	Modular (%)
Numerals	10	94.15	97.30
English capital letters	26	81.03	91.11
Touching numeral pairs	100	57.06	75.18
Hangul characters	352	22.46	68.75

Freitas et al. [2] investigated many non-symmetrical zoning mechanisms for hand-written characters recognition, based on analysis of confusion matrix of individuals classifiers (class-modular). The recognition rates obtained were: 4 zones = 82.89%, 5Horizontal zones = 81.75%, 5Vertical zones = 80.94%, 7 = 84.73% and 5Horizontal-5Vertical-7 zones = 85.9%. The database used in experiments was IRONOFF, specifically uppercase characters.

The partitioning strategy of the training set discussed in this article is known in literature as "one-vs-all" classification. This is a common way to deal with binary classifiers, such as SVM (Support Vector Machine), to solve the problem of multiclass classification. Rifkin and Klatau [9] reviewed extensively the existing literature concerning one-vs-all approach and they also defended the superiority of that approach, as we did in this section.

Therefore, there is considerable evidence regarding the effectiveness and superiority of the class-modular architecture, compared to the conventional architecture, in terms of recognition performance. The experiments and results that we describe next, support this conclusion.

4   Experiments and Results

The conventional and modular networks were implemented via the SNNS[1] simulator. For training, both for the Letter and the IRONOFF databases, we used the same parameter values, shown in Table 2. The results obtained for each database are presented next.

4.1   Experiments for Letter Database

For the conventional network, the MLP was composed by 16 neurons in the input layer, one hidden layer with 64 neurons and 26 neurons in the output layer. Training terminated at the 1000-th epoch. The achieved recognition rate was 83.10%.

For the class-modular networks, each one of the K 2-classifiers consists of an input layer of 16 neurons, one hidden layer of 64 neurons and an output layer of 2 neurons. The maximum number of training epochs was 100.

The metrics for classifier performance evaluation were *sensitivity*, i.e., the percentage of positive instances that were classified as positive (true positive), and *specificity*, i.e., the percentage of negative instances that were classified as negative (true negative). These metrics were extracted from the confusion matrix for a two-class classification problem.

---

[1] Available in <www-ra.informatik.uni-tuebingen.de/SNNS/>

Table 2. Parameter values applied for training of the conventional and the modular networks

Parameter	Value
Layers	3
Learning algorithm	*backpropagation*
Learning rate	0.02
Activation function	sigmoid
Initial weights	random $[-1,1]$

The average rates obtained for the set of K 2-classifiers were 90.19% (sensitivity) and 99.81% (specificity). The higher specificity rate is justified by the fact that training and test sets for a 2-classifier are not balanced between the two classes, as the number of negative samples is much higher than the number of positive samples.

The global classifier output is achieved by combining the 2-classifiers individual outputs. In this work we used a simple winner-takes-all scheme to determine the final class. The global recognition rate by using the Letter database was 93.67%. This is a significant improvement compared to the 83.1% recognition rate produced by the conventional neural network, obtained despite having used a winner-takes-all strategy in decision module.

4.2 Experiments for IRONOFF Database

The IRONOFF database contains a large diversity of handwritten character images, provided from several authors with distinct age, sex and social level. It captures the diversity of writing style that is a major source of difficult in handwritten character recognition. In Fig. 4 we show some samples from uppercase and lowercase off-line character images from IRONOFF database.

For the lowercase and uppercase characters sets we used the same nonmodular MLP. The network consists of an input layer of 375 neurons, which corresponds to length the feature vector, one hidden layer of 256 neurons and an output layer of 26 neurons Training terminates at the 1000-th epoch. The recognition rates obtained were 56.14% to lowercase characters and 63.49% to uppercase characters.

The class-modular networks were composed by 375 neurons in the input layer, 256 neurons in an one hidden layer and 2 neurons in the output layer. It was use 250 epochs for training.

The same metrics applied to the Letter database to classifier performance evaluation were used to IRONOFF database. Therefore, the sensitivity and specificity average rates were for lowercase characters 70.35% and 90.84% and for uppercase characters 84.29% and 99.86%, respectively. The global recognition rate for lowercase characters was 80.75% and for uppercase characters was 89.21%. These results match the best available thus far in the literature for the IRONOFF database, as illustrated in Table 3.
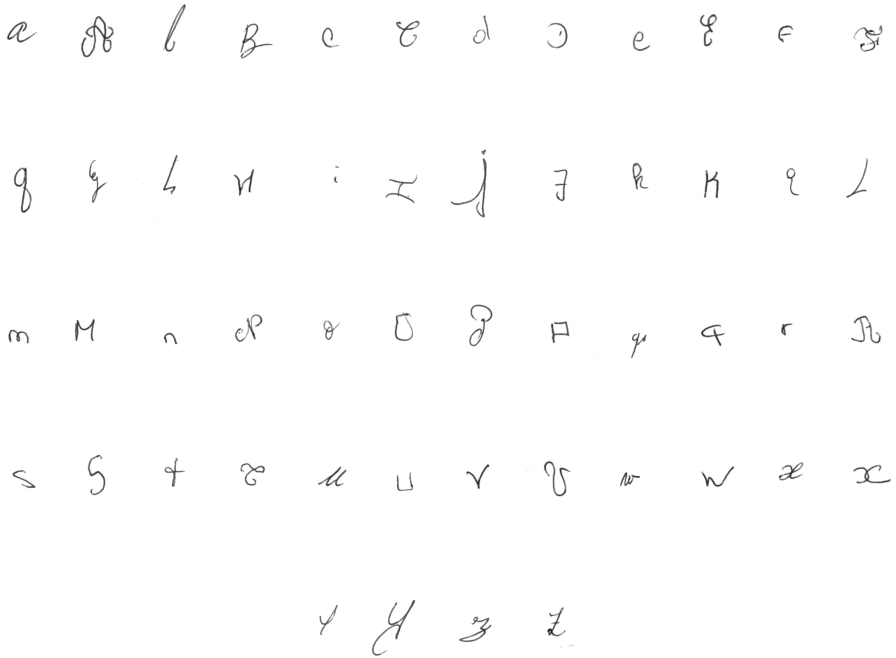
Fig. 4. IRONOFF's samples

4.3   Discussions

Some concluding remarks can be made based on the experimental results reported in the previous section.

- The class-modular network is superior in terms of convergence over the conventional network. This is due to the fact that, for the modular network, the classifier has been decomposed into much smaller subclassifiers, with fewer parameters to estimate.
- The class-modular network has a better performance than the non-modular network, in terms of recognition power.

In addition, training for the class-modular architecture can be easily parallelized, because each sub-network is trained independently of the others, differently from classical architecture in which all the classes are altogether intermingled.

The experimental results for the class-modular classifier are comparable to the best reported in the literature for IRONOFF database (see Table 3). In fact, both the class-modular architecture and the feature extractor proved to be quite appropriate for the handwritten characters recognition problem. The feature extraction method had already produced, in a previous work, one of the best recognition rates for the NIST database [4]. Furthermore, to the best of our knowledge, the combination of these two approaches had not yet been reported by anyone, being therefore an original contribution of this work.

Table 3. Recognition rates

	Letter (%)	Lowercase (%)	Uppercase (%)
Poisson et al. [7]	–	80.5	**89.9**
Freitas et al. [2]	–	–	85.9
Matos [4]	95.6	–	–
Rifkin and Klatau [9]	**96.4**	–	–
Conventional	83.1	56.1	63.5
Class-modular	93.6	**80.7**	89.2

5   Conclusions

In this paper we propose and evaluate a zoning mechanism as well as a class-modular architecture for the recognition of handwritten characters.

Directional histograms applied to the zones were used for feature extraction. This approach was inspired on some aspects of the human visual system, which focus special attention on high spatial features and on the recognition of local features.

The experimental results reveal the superiority of the class-modular network in terms of convergence and recognition rate, over a conventional MLP-NN. The results match the best recognition rates reported in the literature, as shown in Table 3.

The original contribution of this paper is the proposal of a zoning mechanism which combined to a class-modular architecture provides an efficient classifier for the handwritten character recognition problem.

References

1. Cormack, L.K., Bovik, A.l.: Computation models of early human vision in Handbook of image and video processing, p. 891. Academic Press, San Diego (2000)
2. Freitas, C.O.A., Oliveira, L.E.S., de Bortolozzi, F., Aires, S.B.K.: Handwritten character recognition using non-symmetrical perceptual zoning. International Journal of Pattern Recognition and Artificial Intelligence 21, 1–21 (2007)
3. Kapp, M.N., Freitas, C.O.A., Sabourin, R.: Methodology for the design of NN-based month-word recognizers written on brazilian bank checks. International Journal of Image and Vision Computing, Image and Vision Computing 25, 40–49 (2007)
4. Matos, L.N.: Utilização de redes bayesianas como agrupador de classificadores locais e global. PhD thesis, Federal University of Campina Grande, Brazil (2004)
5. Newman, D.J., Hettich, S., Blake, C.L., Merz, C.J.: UCI repository of machine learning databases, Irvine, CA: University of California, Department of Information and Computer Science (1998)
6. Oh, I.-S., Suen, C.Y.: A class-modular feedforward neural network for handwriting recognition. Pattern Recognition 35(1), 229–244 (2002)
7. Poisson, E., Viard-Gaudin, C., Lallican, P.M.: Multi-modular architecture based on convolutional neural networks for online handwritten character recognition. In: IEEE Proceedings of the 9th International Conference on Neural Information Processing, vol. 5, pp. 2444–2448 (2002)

8. Principe, J.C., Euliano, N.R., Lefebvre, W.C.: Neural and adaptive systems: fundamentals through simulations. John Wiley & Sons, New York, USA (1999)

9. Rifkin, R., Klautau, A.: In defense of one-vs-all classification. The Journal of Machine Learning Research 5, 101–141 (2004)

10. Shi, M., Fujisawa, Y., Wakabayashi, T., Kimura, F.: Handwritten numeral recognition using gradient and curvature of grayscale image. Pattern Recognition 35(10), 2051–2059 (2002)

11. Suen, C.Y., Guo, J., Li, Z.C.: Analysis and recognition of alphanumeric handprints by parts. IEEE Transactions on Systems, Man and Cybernetics 24(4), 614–631 (1994)

12. Trier, O., Jain, A., Taxt, T.: Feature extraction methods for character recognition – a survey. Pattern Recognition 29(4), 641–662 (1996)

13. Viard-Gaudin, C., Lallican, P.M., Binter, P., Knerr, S., The, I.R.E.S.T.E.: on/off IRONOFF) dual handwriting database. In: Proceedings of the Fifth International Conference on Document Analysis and Recognition, pp. 455–458, Bangalore, India (1999)

14. Zhang, G.P.: Neural networks for classification: a survey. IEEE Transactions on Systems, Man and Cybernetics, Part C: Applications and Reviews 30(4), 451–462 (2000)

Median M-Type Radial Basis Function Neural Network

José A. Moreno-Escobar[1], Francisco J. Gallegos-Funes[1],
and Volodymyr I. Ponomaryov[2]

National Polytechnic Institute of Mexico,
Mechanical and Electrical Engineering Higher School
[1] Av. IPN s/n, U.P.A.L.M. SEPI-ESIME, Edif. Z, Acceso 3, Tercer Piso,
Col. Lindavista, 07738, Mexico, D. F., Mexico
j.augusto.moreno@gmail.com, fgallegosf@ipn.mx
[2] Av. Santa Ana 1000, Col. San Francisco Culhuacan, 04430, Mexico, D. F., Mexico
vponomar@ipn.mx

Abstract. In this paper we present the capability of the Median M-Type Radial Basis Function (MMRBF) Neural Network in image classification applications. The proposed neural network uses the Median M-type (MM) estimator in the scheme of radial basis function to train the neural network. Other RBF based algorithms were compared with our approach. From simulation results we observe that the MMRBF neural network has better classification capabilities.

Keywords: Radial Basis Functions, Rank M-type estimators, Neural Networks.

1 Introduction

The artificial neural networks are nonparametric pattern recognition systems that can generalize by learning from examples [1,2]. They are particularly useful in problems where decision rules are vague and there is no explicit knowledge about the probability density functions governing sample distributions [1,2].

Recently, we proposed the robust Rank M-type (RM) estimators for image denoising applications [3,4]. The combined RM-estimators use different rank estimators such as the Median, Wilcoxon and Ansari-Bradley-Siegel-Tukey estimators, and the M-estimator with different influence functions to provide better robustness. The performances of the RM-estimators are better in comparison with original R- and M- estimators [3,4].

In this paper is proposed the Median M-Type Radial Basis Function (MMRBF) Neural Network for image classification purposes. The neural network uses the Median M-Type (MM) estimator in the scheme of radial basis function to train the neural network according with the schemes found in the references [5,6].

The rest of this paper is organized as follows. The RBF neural network is presented in section 2. In section 3 we formulate the proposed MMRBF neural network. Experimental results of classification capabilities for simulated images by using our method and other RBF based networks are presented in section 4. Finally, we draw our conclusions in section 5.

2   Radial Basis Function Neural Network

The Radial Basis Functions (RBF) have been used in several applications for pattern classification and functional modeling [7]. These functions have been found to have very good functional approximation capabilities [7]. The RBF have their fundamentals drawn from probability function estimation theory. In the RBF neural networks each network input is assigned to a vector entry and the outputs correspond either to a set of functions to be modeled by the network or to several associated classes [1,2,8,9]. The structure of the RBF neural network is depicted in Figure 1. From Figure 1, each of N_k components of the input vector $\mathbf{X}$ feeds forward to M basis functions whose outputs are linearly combined with weights $\left\{\lambda_j\right\}_{j=1}^{M}$ into the network output $Y_k(\mathbf{X})$.
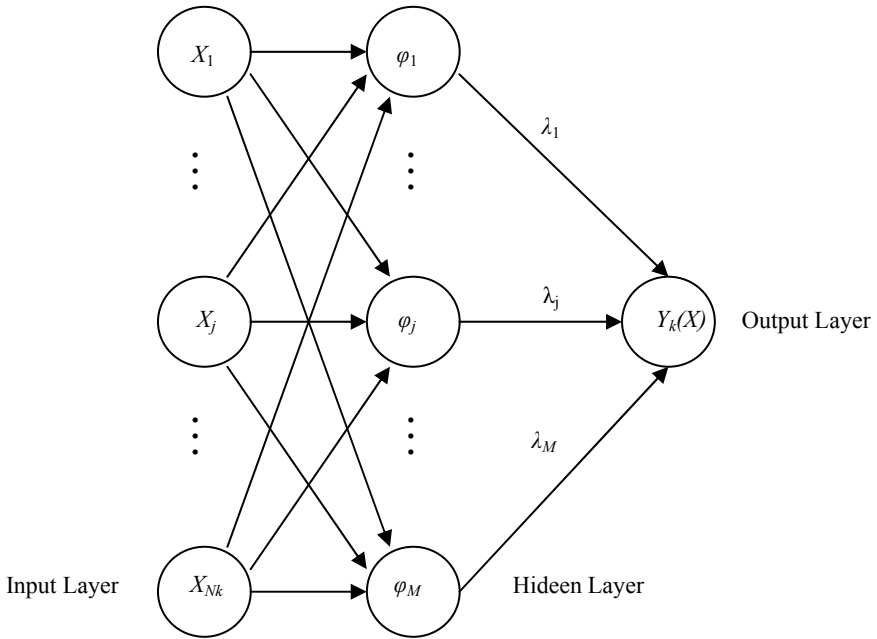
Fig. 1. Structure of Radial Basis Function Neural Network

2.1   Activation and Output Layer

Several functions have been tested as activation functions for RBF neural networks. In pattern classification applications the Gaussian function is preferred, and mixtures of these functions have been considered in various scientific fields [8,9].

The Gaussian activation function for RBF neural networks is given by [1,2]:

$$\phi_j(\mathbf{X}) = \exp\left[-\left(\mu_j - \mathbf{X}\right)^T \sum_j^{-1}\left(\mu_j - \mathbf{X}\right)\right] \tag{1}$$

where $\mathbf{X}$ is the input feature vector, μ_j is the mean vector and Σ_j is the covariance matrix of the jth Gaussian function. Geometrically, μ_j represents the center or location and Σ_j the shape of the basis functions. Statistically, an activation function models a probability density function where μ_j and Σ_j represent the first and second order statistics. A hidden unit function can be represented as a hyper-ellipsoid in the N-dimensional space.

The output layer implements a weighted sum of hidden-unit outputs [1,2]:

$$\psi_k(\mathbf{X}) = \sum_{j=1}^{L} \lambda_{jk} \phi_j(\mathbf{X}) \tag{2}$$

where L is the number of hidden units, M is the number of outputs with $k=1,\ldots,M$. The weights λ_{kj} show the distribution of the hidden unit j for modeling the output k.

2.2 Learning Techniques of RBF Networks

Radial Basis Functions have interesting properties which make them attractive in several applications. A combined unsupervised-supervised learning technique has been used in order to estimate the RBF parameters [8]. In the unsupervised stage, k-means clustering algorithm is used to find the pdf's parameters, LMS or instead pseudo-inverse matrix can be used in the supervised stage to calculate the weights coefficients in the neural network [8].

3 Median M-Type Radial Basis Function Neural Network

In here, we present the use of the RM-estimator as statistic estimation in the Radial Basis Function network architecture. The combined RM-estimators can use different rank estimators such as the Median, Wilcoxon or Ansari-Bradley-Siegel-Tukey [3,4]. In our case we use the MM-estimator with different influence functions.

3.1 Activation Function

The Gaussian activation function is the most used function in the RBF networks. We tested with different activation functions and we chose the inverse multiquadratic function [8,9] due this function provided the best results:

$$\phi_j(\mathbf{X}) = \frac{1}{\sqrt{\mathbf{X}^2 + \beta_j^2}} \tag{3}$$

where $\mathbf{X}$ is the input feature vector, β_j is a real constant. In our simulation results $\beta_j=1$.

3.2 K-Means Algorithm

In our case we use the clustering k-means algorithm to estimate the parameters of the MMRBF neural network [1,2]. The k-means algorithm is used in the unsupervised

stage. The input feature vector $\mathbf{X}$ is classified in k different clusters. A new vector $\mathbf{x}$ is assigned to the cluster k whose centroid μ_k is the closest one to the vector. The centroid vector is updated according to,

$$\mu_k = \mu_k + \frac{1}{N_k}(\mathbf{x} - \mu_k)$$

(4)

where N_k is the number of vectors already assigned to the k-cluster. The centroids can be updated at the end of several iterations or after the test of each new vector. The centroids can be calculated with or without the new vector. By other hand, the steps for the k-means algorithm are the following:

Step 1	Select an initial partition with k clusters. Repeat steps 2 through 4 until the cluster membership stabilizes.
Step 2	Generate a new partition by assigning each pattern to its closest cluster center.
Step 3	Compute new cluster centers as the centroids of the clusters.
Step 4	Repeat steps 2 and 3 until an optimum value of the criterion function is found.

3.3 Median M-Type (MM) Estimator

The Median M-type (MM) estimator is used in the proposal RBF neural network [3,4]. The non-iterative MM-estimator used as robust statistics estimate of a cluster center is given by,

$$\mu_k = \mathrm{med}\{\mathbf{X}\tilde{\psi}(\mathbf{X}-\theta)\}$$

(5)

where $\mathbf{X}$ is the input data sample, $\tilde{\psi}$ is the normalized influence function ψ: $\psi(\mathbf{X}) = \mathbf{X}\tilde{\psi}(\mathbf{X})$, $\theta = \mathrm{med}\{X_k\}$ is the initial estimate, and $k=1, 2,\ldots,N_k$.

3.4 Influence Functions

In our experiments we use the following influence functions [3]:

-   The simple cut (skipped mean) influence function,

$$\psi_{\mathrm{cut}(r)}(X) = X \cdot 1_{[-r,r]}(X) = \begin{cases} X, & |X| \le r \\ 0, & \text{otherwise} \end{cases}$$

(6)

-   and the Tukey biweight influence function,

$$\psi_{\mathrm{bi}(r)}(X) = \begin{cases} X^2(r^2 - X^2), & |X| \le r \\ 0, & \text{otherwise} \end{cases}$$

(7)

where X is a data sample and r is a real constant. The parameter r depends of the data to process and can be change for different influence functions.

4   Experimental Results

The described MMRBF neural network has been evaluated, and their performance has been compared with the Simple RBF, α-Trimmed Mean RBF, and Median RBF neural networks [5,6,8].

The images used to train the proposed MMRBF neural network and other networks used as comparative are shown in Figure 2. In this figure, the first six images of Group A have common texture or filling which is different form the six first images of Group B. The last two images of each group have a texture or filling that is similar to the opposite group, that is, the last two images of Group A have similar filling than the images of Group B, and vice versa. The main idea here of using textures in figures is to try to simulate medical image textures.
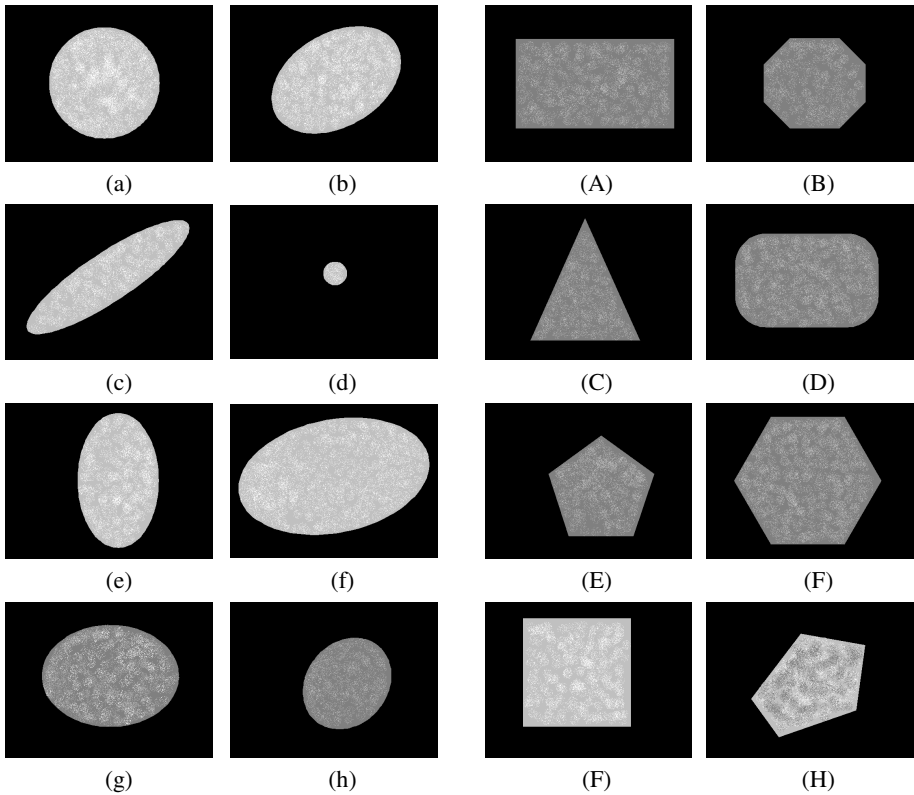
Fig. 2. Training images

To train the networks for getting the appropriate pdf's parameters were used 10 images as the ones shown in Figure 2. The objective of this experiment is to classify between 2 main groups:

Group A	contains circles and ellipses. The geometric shapes of this group are denoted with small letters in Figure 2.
Group B	contains many kinds of polygons. The geometric shapes of this group are denoted with capital letters in Figure 2.

In the segmentation stage were obtained 3 numerical data or characteristics, which are compactness, average gray value, and standard deviation [10,11].

To train the networks implemented in this work we used the block diagram depicted in Figure 3: having the images, the first step is extracting numerical data form them. Afterwards we determined the center of the activation functions. The number of elements used in each activation function depends on the algorithm implemented. The number of elements used to train the comparative Simple RBF, α-Trimmed Mean RBF, and Median RBF neural networks varies in accordance to the training algorithms found in references [5,6,12]. In the case of the proposed MMRBF we use eq. (5) in combination with eq. (6) and (7) to determine the elements to be used.

The number of images used to train the networks was 10 (five of each group). The training results are shown in Table 1.

In the test stage we use 30 images (15 of each group), these images are of different form that the images used in the training stage. Figure 4 presents some images used in the test stage. The results obtained are shown in Table 2.
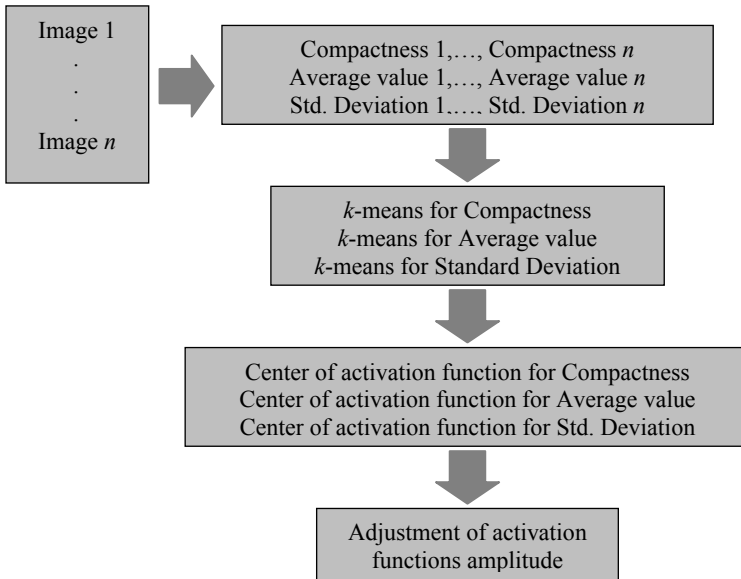
Fig. 3. RBF training block diagram

Table 1. Results obtained with different RBF algorithms in training stage

		Group A	Group B	Total
SIMPLE RBF	Efficiency	60%	100%	80%
	Uncertainty	0%	0%	0%
	Error	40%	0%	20%
MEDIAN RBF	Efficiency	60%	100%	80%
	Uncertainty	0%	0%	0%
	Error	40%	0%	20%
α-TRIMMED MEAN RBF	Efficiency	80%	100%	90%
	Uncertainty	0%	0%	0%
	Error	20%	0%	15%
MMRBF Simple Cut	Efficiency	67%	100%	83.5%
	Uncertainty	0%	0%	0%
	Error	33%	0%	16.5%
MMRBF Tukey	Efficiency	67%	100%	83.5%
	Uncertainty	0%	0%	0%
	Error	33%	0%	16.5%
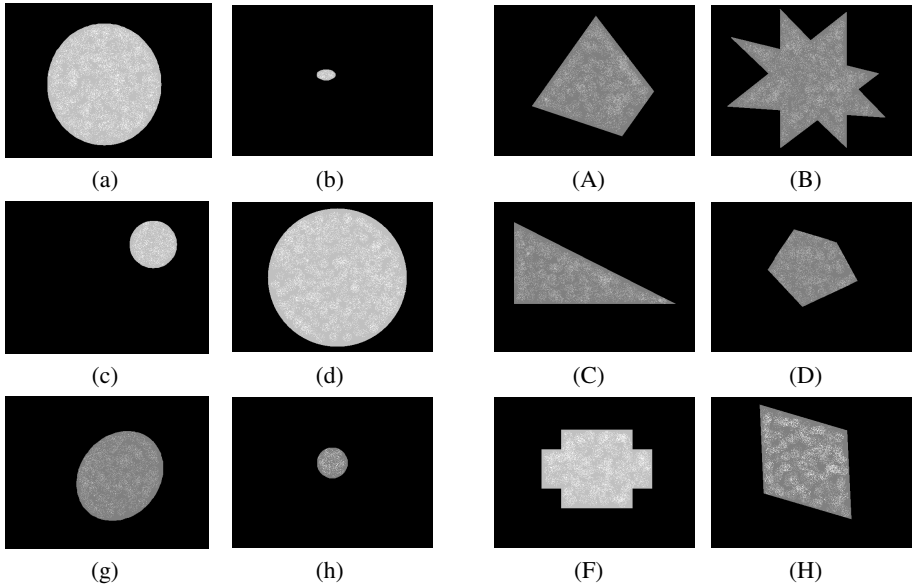
Fig. 4. Some images used in test stage

Table 2. Results obtained with different RBF algorithms in test stage

		Group A	Group B	Total
SIMPLE RBF	Efficiency	67%	93%	80%
	Uncertainty	0%	0%	0%
	Error	33%	7%	20%
MEDIAN RBF	Efficiency	67%	93%	80%
	Uncertainty	0%	0%	0%
	Error	33%	7%	20%
α-TRIMMED MEAN RBF	Efficiency	67%	87%	77%
	Uncertainty	0%	0%	0%
	Error	33%	13%	23%
MMRBF Simple Cut	Efficiency	67%	100%	83.5%
	Uncertainty	0%	0%	0%
	Error	33%	0%	16.5%
MMRBF Tukey	Efficiency	67%	100%	83.5%
	Uncertainty	0%	0%	0%
	Error	33%	0%	16.5%

From previous tables (see Tables 1 and 2) we can appreciate that the difference between algorithms is not big, and that percentages of efficiency, uncertainty and error vary from training stage to test stage. It is evident that if we use more images in the training stage the capabilities of proposed MMRBF neural network can be increased in the test stage in terms of efficiency, uncertainty, and error.

Tables 3 and 4 show a comparison between the RBF algorithms implemented here.

Table 3. Efficiency comparison between the RBF algorithms implemented in training stage

Neural Networks	SIMPLE RBF	MEDIAN RBF	α-TRIMMED MEAN RBF
MMRBF Simple Cut	3.5%	3.5%	-6.5%
MMRBF Tukey	3.5%	3.5%	-6.5%

Table 4. Efficiency comparison between the RBF algorithms implemented in test stage

Neural Networks	SIMPLE RBF	MEDIAN RBF	α-TRIMMED MEAN RBF
MMRBF Simple Cut	3.5%	3.5%	6.5%
MMRBF Tukey	3.5%	3.5%	6.5%

We can see from Tables 3 and 4 that α-TRIMMED MEAN RBF had the best efficiency in training stage, but in test stage the best results are given by the proposed MMRBF neural network.

5   Conclusions

We present the MMRBF neural network, it uses the MM-estimator in the scheme of radial basis function to train the proposed neural network. The results obtained with the use of the proposed MMRBF are better than others results obtained with RBF algorithms used as comparative. In future, the proposed network will be extended to real-world datasets such as mammographic imaging.

Acknowledgements

References

1. Haykin, S.: Neural Networks, a Comprehensive Foundation. Prentice-Hall, Englewood Cliffs (1994)
2. Rojas, R.: Neural Networks: A Systematic Introduction. Springer, Berlin (1996)
3. Gallegos, F., Ponomaryov, V.: Real-time image filtering scheme based on robust estimators in presence of impulsive noise. Real Time Imaging. 8(2), 78–90 (2004)
4. Gallegos-Funes, F., Ponomaryov, V., De-La Rosa, J., ABST,: M-type K-nearest neighbor (ABSTM-KNN) for image denoising. IEICE Trans. Fundam. Electron. Commun. Comput. Sci. E88-A(3), 798–799 (2005)
5. Bors, A.G., Pitas, I.: Median radial basis function neural network. IEEE Trans. Neural Networks. 7(6), 1351–1364 (1996)
6. Bors, A.G., Pitas, I.: Object classification in 3-D images using alpha-trimmed mean radial basis function network. IEEE Trans. Image Process. 8(12), 1744–1756 (1999)
7. Buhmann, M.D.: Radial Basis Functions: Theory and Implementations. Cambridge Monographs on Applied and Computational Mathematics (2003)
8. Karayiannis, N.B., Weiqun Mi, G.: Growing radial basis neural networks: merging supervised and unsupervised learning with network growth techniques. IEEE Trans. Neural Networks. 8(6), 1492–1506 (1997)
9. Karayiannis, N.B., Randolph-Gips, M.M.: On the construction and training of reformulated radial basis function neural networks. IEEE Trans. Neural Networks. 14(4), 835–846 (2003)
10. Ritter, G.: Handbook of Computer Vision Algorithms in Image Algebra. CRC Press, Boca Raton-New York (2001)
11. Myler, H.R., Weeks, A.R.: The Pocket Handbook of Image Processing Algorithms in C. Prentice-Hall, Englewood Cliffs (1993)
12. Musavi, M.T., Ahmed, W., Chan, K.H., Faris, K.B., Hummels, D.M.: On the training of radial basis function classifiers. Neural Networks. 5, 595–603 (1992)

A Precise Electrical Disturbance Generator for Neural Network Training with Real Level Output

Antonio García, Carlos León, Iñigo Monedero,
and Jorge Ropero

Escuela Técnica Superior de Ingeniería Informática
Departamento de Tecnología Electrónica
Avda, Reina Mercedes s/n
41012 Sevilla (Spain)
imonedero@us.es

Abstract. Power Quality is defined as the study of the quality of electric power lines. The detection and classification of the different disturbances which cause power quality problems is a difficult task which requires a high level of engineering expertise. Thus, neural networks are usually a good choice for the detection and classification of these disturbances. This paper describes a powerful tool, developed by the Institute for Natural Resources and Agrobiology at the Scientific Research Council (CSIC) and the Electronic Technology Department at the University of Seville, which generates electrical patterns of disturbances for the training of neural networks for PQ tasks. This system has been expanded to other applications (as comparative test between PQ meters, or test of effects of power-line disturbances on equipment) through the addition of a specifically developed high fidelity power amplifier, which allows the generation of disturbed signals at real levels.

Keywords: Power quality, electrical disturbance, neural network.

1 Introduction

Power Quality (PQ) is defined as the study of the quality of electric power lines. PQ has been a topic of consideration for the last two decades, and has recently acquired intensified interest due to the wide spread use of electronic devices in complicated industrial processes and the generalized power quality of commercial electric power [1]. Thus nowadays, customers demand higher levels of PQ to ensure the proper and continued operation of such sensitive equipment.

The poor quality of electrical power is normally attributed to power line disturbances such as waveshape faults, overvoltages, capacitor switching transients, harmonic distortion and impulse transients. Thus, electromagnetic transients, which are momentary voltage surges powerful enough to shatter a generator shaft, can cause catastrophic damage suddenly. Harmonics, sometimes referred to as electrical pollution, are distortions of the normal voltage waveforms found in ac transmission, which can arise at virtually any point in a power system. While harmonics can be as destructive as transients, often the greatest damage from these distortions lies in the loss of

credibility of the power utilities vis-a-vis their customers. The classification and identification of each one of the disturbances is normally carried out from standards and recommendations depending on where the utilities operate (IEEE in the United States, UNE in Spain, etc).

The detection and classification of the different disturbances which cause power quality problems is a difficult task which requires a high level of engineering expertise [2]. Due to the above mentioned difficulties, artificial intelligence tools [3] emerge as an interesting alternative in the detection of electrical disturbances. The main intelligent tools of interest include expert systems, fuzzy logic and artificial neural networks (ANNs) [4].

<u>Neural Networks on Power Quality</u>

For the detection and classification of disturbances, ANNs can be combined with mathematical analysis such as Fourier and Wavelet transforms for the generation of signal features which serve as inputs in the network [5]. Thus, feature extraction by wavelet transforms provides an unique characteristic which can represent every single PQ disturbance at different resolutions using the technique called multi-resolution signal decomposition or multi resolution analysis. In this way, while the detection of the power quality signals has tended to be easy, their classification is still a difficult task in which ANNs play an important role [6][7][8].

Pattern recognition in ANNs generally requires preprocessing of data, feature extraction and final classification. One of the most important tasks in the design and development process of an ANN is to generate an adequate number of training patterns in order to approximate future inputs. Sometimes an optimal design of the ANN is found but the limited number of train patterns does not give good results. In particular, in PQ a great numbers of electrical patterns are necessary due to the multiple combinations of different disturbances which can coincide in one or various samples. Another additional problem with ANNs applied to PQ is the impossibility of getting real patterns directly from the power line due to the irregularity in the apparition of disturbances.

2   Electrical Disturbance Generator

2.1   General Description

Initially the function of this system was to allow the generation of training signals at level of files of data. Nevertheless, as we described next, has added to an interface (D/A converter and power amplifier) that allows the generation of these signals at the levels of tension of power grid with medium power levels.

This Generator of disturbances, therefore, it has been developed in two different stages: the generator of electrical patterns and the power amplifier:

In one first stage the generating subsystem of patterns has been developed (named with the acronym PANDORA). This system allows the programmable generation of signals that emulate the operation of the power grid, allowing the easy addition of disturbances on it.
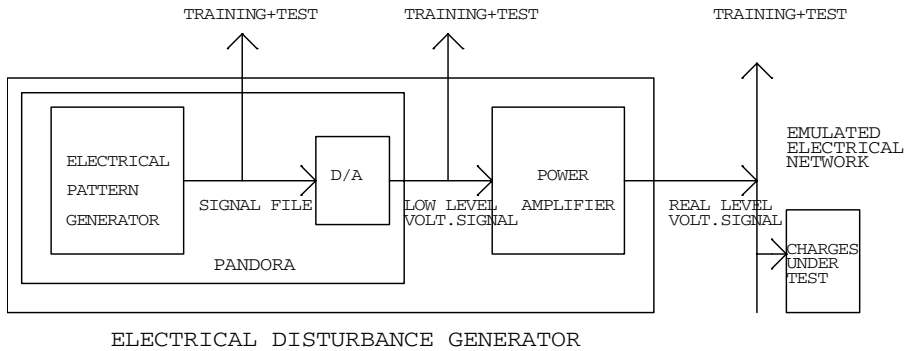
Fig. 1. Electrical Disturbance Generator. General Scheme.

The PANDORA allows to obtain the signals at level of files (sequence of numeric data) and by means of the use of a D/A board of signals of tension of low level (tensions between +/- 10 volts. and powers of milliwatts). These two forms of outputs have been used to train the ANN of the system detector of disturbances, and later to check its operation.

The second stage has corresponded to the design, implementation, and test of the power amplifier. The function of this amplifier is to elevate the level of the signals coming from the PANDORA, until real existing in the network (the signals of the order of 230 volts rms and values of power of the order of at least hundreds of watts).

The amplifying system, in combination with subsystem PANDORA, completes the functionality of the generating system of disturbances allowing:

1. The systematic test at levels of real power grid of our detector of disturbances in a reasonable term. Until the development of the amplifying system, the single detector of disturbances could be made a will of complete form by means of its connection to real power grid. The tests made in this sense have been quite satisfactory, and the detector has worked correctly before the disturbances that have taken place. Nevertheless, considering, that real power grid has relatively high quality, this is, that the disturbances that take place are, in general, little frequent, and in addition unforeseeable, the produced disturbances are few for an extensive time of operation

2. The comparison of our detector of disturbances with other similar equipment of the market. This is an essential task as opposed to demonstrate the advantages of our system of detection of disturbances to the alternative techniques. With the Electrical Disturbance Generator is possible to establish systematic protocols of comparative tests between equipment based on different techniques and to verify the limits and precision of the different techniques.

3. Test of equipment under disturbances of the network [10][11]. The possibility of having a system able to generate signals equivalent to those of real power grid, with the possibility of generating of arbitrary form disturbances in the same one it allows a fan of very interesting possibilities:

* It allows the manufacturers of equipment to have a tool to the test of its equipment before the disturbances that can take place in power grid, allowing to the verification of its immunity or its improvement before this type of effects.

* It allows the providing companies to make defensive analyses before claims of the users by failures of equipment, demonstrating, for example, that this equipment fails before disturbances that do not leave the limits established by the norm.

2.2 Programmable Electrical Pattern Generator (PANDORA)

For the task of training neural networks for the detection and classification of electrical disturbances we are developing an electrical pattern generator. The objective of this generator is to create an unlimited number of patterns to be used by a classification system.

In particular, we are developing a classification system in the Electronic Technology Department at the University of Seville and the Institute for Natural Resources and Agrobiology. The system is a real-time detector of power line disturbances based on artificial intelligence techniques (in particular, a first version based on ANNs) is being developed. We are going to use the Electrical Pattern Generator in order to carry out the ANN training.

The Electrical Pattern Generator make it possible to configure parameters such as the duration of the sample, the frequency of the signal and the number of samples in an ideal cycle (50Hz or 60Hz) and to add one or more disturbances. From the selected parameters, the generator creates a text file with the voltage values of the sample. The structure of the file consists of a header with the file information (name, number of sample cycles and sampling period) and a data column corresponding to the voltages of each of the samples.

The type of disturbances includes: impulse, oscillation, sag, swell, interruption, undervoltage, overvoltage, harmonics, flicker and frequency variations. In amplitude disturbances (impulses, sags, swells, interruptions, undervoltages and overvoltages), the tool allows us that parameters such as amplitude, start time, final time, rising and falling slope, be configured. The edition of harmonics allows the configuration of amplitude and phases as far as forty harmonic levels including the possibility of adding them an offset. In the flicker menu the start time can be set and the final time of the flicker, its RMS, frequency and phase.
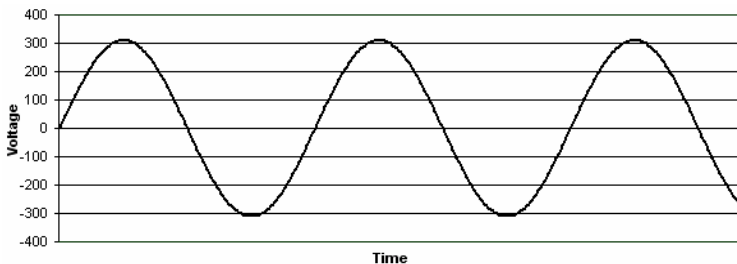
Fig. 2. Ideal signal (one-phase representation)

Models of disturbances

1.- Harmonic distortion

Harmonic distortion is defined as the phenomenon in which diverse sinusoidal signals with diverse frequencies which are multiples of the fundamental frequency are superposed on the ideal signal (Figure 3).
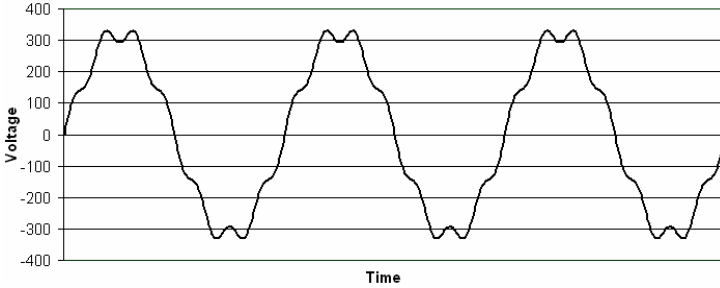
Fig. 3. Harmonic distortion

The following mathematical model was implemented in the generator:

$$C(t) = A + \sum_{i=1}^{N} A_i \sin(2\pi f_i t + \varphi_i) \tag{1}$$

- A: DC term (V).
- A_i: Amplitude of the ith harmonic of signal (V).
- f_i: Frequency of the ith harmonic of signal (Hz)
- φ_i: Phase of the ith harmonic (Rad)
- i: Harmonic order ($i = 1,.., N$).

In our harmonic model $C(t)$ is considered as consisting of a fundamental and 39 harmonic components.

2.- Frequency deviation

Frequency deviation is a signal disturbance added to the harmonic distortion. The model consists of the frequency modulation of the signal $C(t)$ by means of the carrier signal $M(t)$, which is named modulating signal.
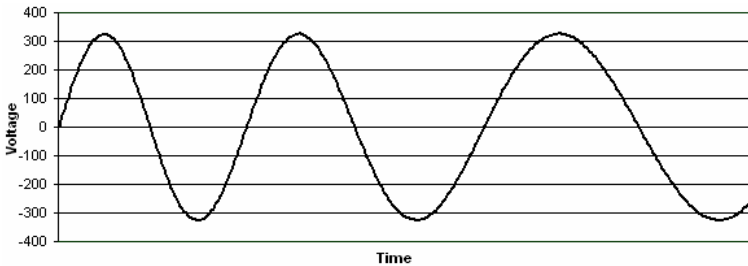
Fig. 4. Frequency deviation

The mathematical expression of this signal is:

$$M(t) = B + \sum_{j=1}^{40} B_j \, sin(\, 2\pi j f_m t + \varphi_j \,)$$ (2)

- B: DC term (V).
- B_j: Amplitude of the jth harmonic of signal (V)
- f_m: Fundamental frequency (Hz)
- φ_i: Phase of the ith harmonic (Rad)

Considering (1) and (2) the resultant signal would end up as:

$$X(t) = A + \sum_{i=1}^{40} A_i \, sin\left[2\pi i f_c t + \varphi_i + B + \sum_{j=1}^{40} B_j \, sin(\, 2\pi j f_m t + \varphi_j \,) \right]$$ (3)

which shows the harmonic content and frequency modulation.

The addition of another kind of disturbance was carried out from the previous expression $X(t)$. Therefore, the previous expression would be the result of an ideal electrical signal or a frequency or/and harmonic disturbed signal.

3.- Flicker

Flicker (Figure 5) is considered an amplitude modulation of the carried signal X (t), which changes in function of the modulating signal F(t) [9]. The modulating signal has sinusoidal form with prefixed random amplitude, frequency (usually around 30 Hz) and an initial phase.
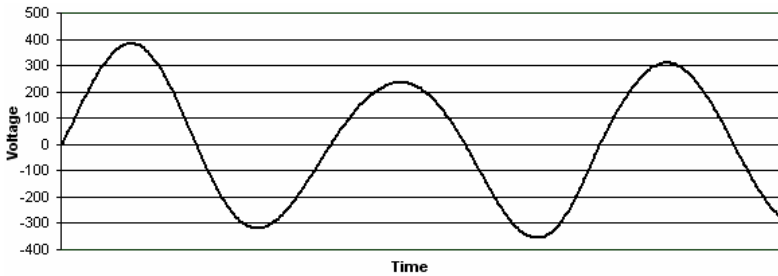
Fig. 5. Flicker

The equation which defines the mathematical model implemented by the pattern generator is:

$$Z(t) = F(t)X(t) = \left[1 + A_{fk} \, sin(2\pi f_{fk} t + \varphi_{fk}) \right] X(t)$$ (4)

- A_{fk}: flicker amplitude
- f_{fk}: flicker frequency
- φ_{fk}: flicker phase

4.- Overvoltages, swells, undervoltages and sags.

In this kind of disturbances the amplitude of the signal rises (overvoltages or swells) or falls (undervoltages and sags) a certain value along a time interval.
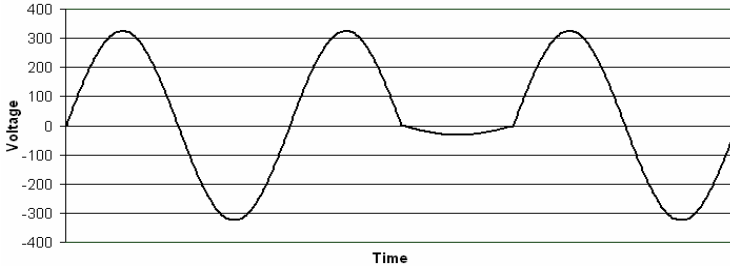
Fig. 6. Sag

In the development of the disturbance generator, a trapezoidal model for the ampli-tude evolution (lineal slope) was considered. The model makes it possible to ap-proximate the amplitude disturbances most frequently encountered in power systems. Figure 7 shows a graphical of the model used for overvoltages or swells (inverse trapeze for undervoltages and sags).
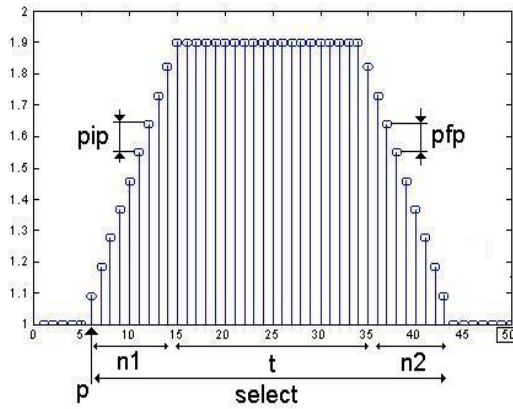
Fig. 7. Overvoltage and swell model

- p: initial sample of the trapeze
- pip: slope of the initial ramp
- pfp: slope of the final ramp
- n1: number of samples of the initial ramp
- n2: number of samples of the final ramp
- t: number of samples when the climb is reached
- select: total number of samples

5.- Transients

The electrical pattern generator models transients as a damped sine through a super-posed exponential function, which is added to $X(t)$ at a certain point.
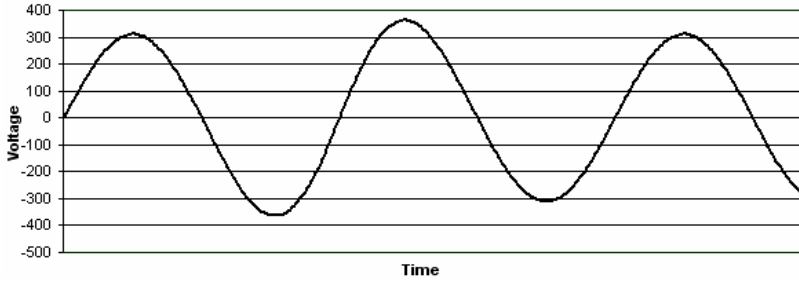
Fig. 8. Overvoltage
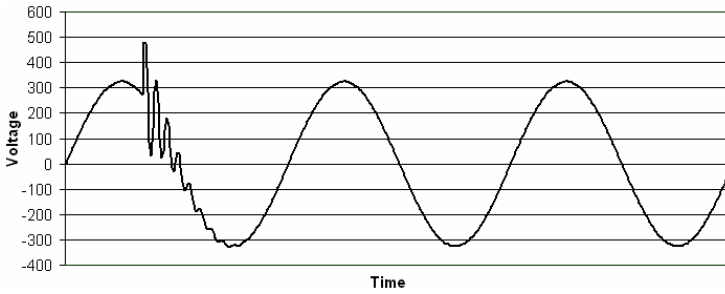
Fig. 9. Transient

The implemented mathematical model obeys to:

$$T(t) = e^{-at} A_r \, sin(\, 2\pi f_r t + \varphi_r \,) \tag{5}$$

- a: transitory exponent.
- A_r: amplitude of the ripple (V)
- f_r: frequency of the ripple (Hz)
- φ_r: initial phase of the ripple (Rad)

6.- Noise

The generator makes it possible to add Additive White Gaussian Noise (AWGN) (Figure 10) in order to simulate more realistic signals of the power line.
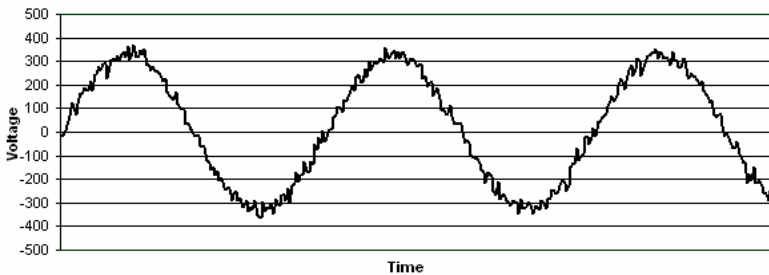
Fig. 10. Additive White Gaussian Noise (AWGN)

2.3   The Power Amplifier

The power amplifier was specifically developed for the application. The main requirements were:
- Output Voltage up to: +/- 600 volts (instantaneous), 400 (RMS)
- Power, up to 200 watts.
- Band Width (minimum) (25 Hz to 5 Khz)
- High fidelity. That implies: THD<0.2%, and SNR>60dB.

Architecture

This amplifier consists of:
- Module 1.- Electronic Voltage Amplifier. Class AB on C.I. (LM3886 of National Sem.). It will amplify the signals at medium levels of tension (20~40 volts rms) with medium powers (> 100 watts).
- Module 2.- Coupler Transformer. It will elevate the voltage (trafo ratio 1:10) at the required levels of tension. It will establish an input/output galvanic isolation.
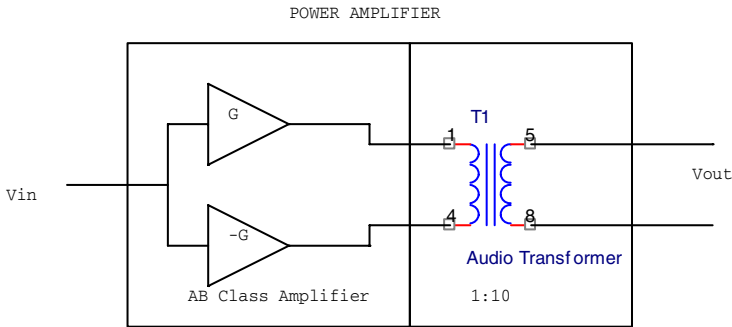
Fig. 11. Proposed Amplifier Architecture

The use of a transformer like element of connection to the load isolates the input and the output and allows to work with amplifiers at low voltage level. A medium power (500watts) audio professional transformer has been chosen to avoid the problems of bandwidth limitation and distortion that implies another type of transformers.

For the electronic amplifier the chosen configuration has been type AB as opposed to other types (example: D Type), due to its smaller distortion. On the other hand, the levels of power output are not as elevated as that the energy efficiency was the key question. It has been decided on a design based on Power Linear I.C. (LM3886 of National Sem.) to simplify the design because the device includes all the protection subsystems.

System Tests

The system was put under a complete set of typical tests, and the obtained general results have been satisfactory in all the parameters:

Table 1. Test results

Characteristics	
1.-Input Impedance	>25 Koh
2.- Output Imp.	<10 Oh
5.- Gain	Up to 450
6.- Band width	<10Hz/>20Khz
7.- Vout(max)	420(rms) +/-600(inst.)
8.- Power (Note 1)	160 watts
9.- SNR out	>63dB

A characteristic that specially has been studied has been the harmonic distortion of the amplifier. In order to guarantee the global operation of the equipment, it has been necessary to carry out measures of this parameter at different input frequencies and different power outputs.
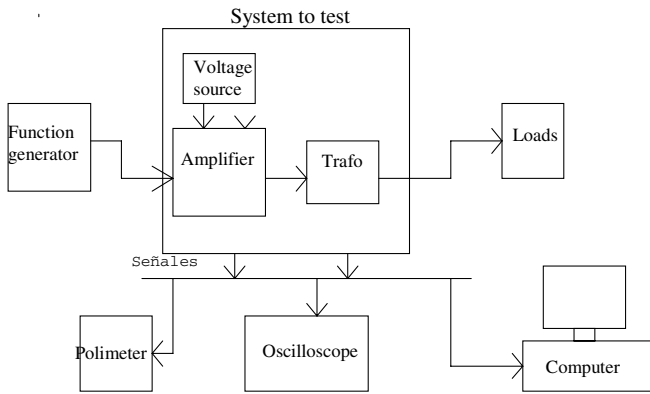
Fig. 12. Scheme of the assembly to test the amplifier
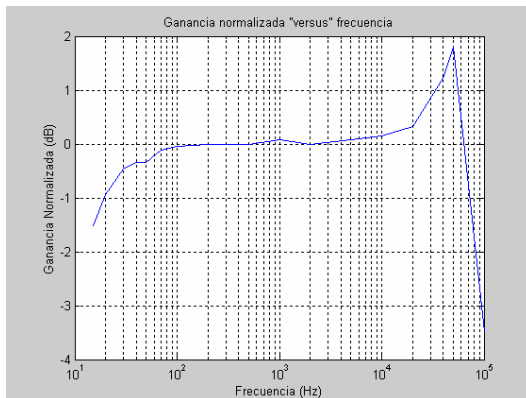
Fig. 13. Gain 'versus' frequency (BW)

We developed a low cost experimental tool, based on PC with standard audio board and MATLAB©, for the measurement of Harmonic Distortion.
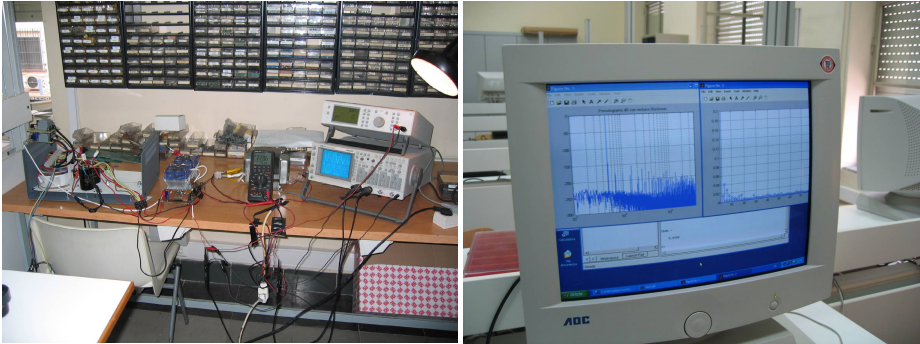
Fig. 14. Experimental setup and Harmonic Distortion Measurement System

This tool, based on DFT, allows us to measure for different inputs frequencies and output powers the n order Harmonic Distortion Index HDi, and the Total Harmonic Distortion (THD). The THD of the amplifier fulfilled the requirements (THD<0.2%) for all the bandwidth (25Hz-5Khz) and for powers up to 160 watts.
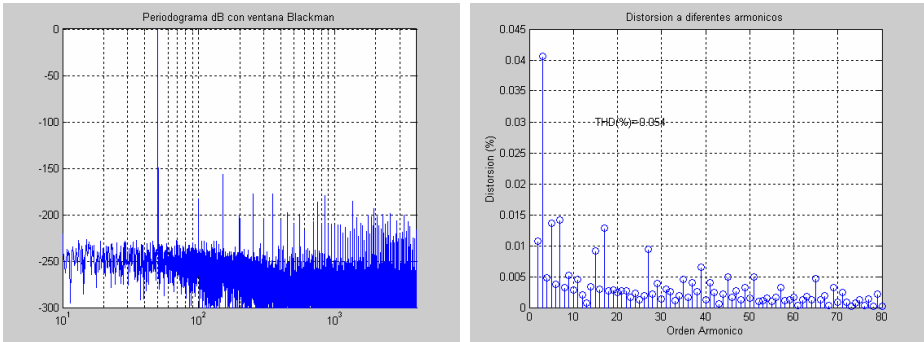
Fig. 15. Periodogram of output signal (Input 0Hz) and Measurement of HDi index and THD

3   Conclusions

Today it is known that neural networks are a good choice for detecting and classifying electrical power disturbances. Often the problem lies in generating a sufficient number of training patterns to get that neural networks obtain good results in future inputs.

We have developed an electrical pattern generator which is capable of generating common disturbances which can be found in a power line with the aim of making the training of neural networks easier. The tool can generate a set of disturbance data which include: impulse, oscillation, sag, swell, interruption, undervoltage, overvoltage, harmonics, flicker and frequency variations. In addition, it can add different

kinds of noise to the generated signals. This generator has been recently patented by the University of Seville.

We have added a high fidelity power amplifier specifically developed for the application that allows obtained outputs at real level in terms of voltage and with small power levels (up to 200 watts). This paper describes the generator, the different mathematical models for each disturbance as well as the power amplifier and the global performance of the system.

Acknowledgments

References

[1] McGranaghan, M., Roettger, B.: Economic Evaluation of Power Quality. 0272-1724/02 (2002)
[2] Hussain, A., Sukairi, M.H., Mohamed, A., Mohamed, R.: Automatic Detection Of Power Quality Disturbances and Identification of Transients Signals. In: International Symposium on Signal Processing and its Applications, Kuala Lumpur, Malaysia, August 13-16, 2001 (2001)
[3] Adapa, R.: Power Quality Analysis Software, 0272-1724/02 IEEE (2002)
[4] Anis Ibrahim, W.R., Morcos, M.M.: Artificial Intelligence and Advanced Mathematical Tools for Power Quality Applications: A Survey. 668 IEEE Transactions on Power Delivery 17 (2002)
[5] Zheng, G., Shi, M.X., Liu, D., Yao, J., Mao, Z.M.: Power Quality Disturbance Classification Based on Rule-Based and Wavelet-Multi-Resolution Decomposition. In: Proceedings of the First International Conference on Machine Learning and Cybernetics, Beijing, November 4-5 (2002)
[6] Lai, L.L.: Wavelet-based Neural Network for Power Quality Recognition. 0-7803-7322-7, IEEE (2002)
[7] Xiangxun, C.: Wavelet-based Measurement and Classification of Power Quality Disturbances, 0-7803-7242-05/02, IEEE (2002)
[8] Borrás, D., Castilla, M., Moreno, N., Montaño, J.C.: Wavelet and neural structure: a new tool for diagnostic of power system disturbances. IEEE Trans. on Industry Applications 37(1), 184–190 (2001)
[9] Bhargava, B.: Arc Furnace Flicker Measurements and Control. IEEE Transactions on Power Delivery 8(1), 409–423 (1993)
[10] Topalis, F.V., Gonos, I.F., Vokas, G.A.: Arbitrary wavvform generator for harmonic distortion test on compact fluorescent lamps. Measurement 30, 257–267 (2001)
[11] Anderson, L.M., Bowes, K.B.: The effects of Power-line disturbances on consumer electronic equipment. IEEE Transactions on Power Delivery 5(2), 1062–1065 (1990)

A New Algorithm for Training Multi-layered Morphological Networks

Ricardo Barrón, Humberto Sossa, and Benjamín Cruz

Centro de Investigación en Computación-IPN
Av. Juan de Dios Bátiz esquina con Miguel Othón de Mendizábal
Mexico City, 07738, Mexico
`rbarron@cic.ipn.mx`, `hsossa@cic.ipn.mx`,
`benjamincruz@sagitario.cic.ipn.mx`,

Abstract. In this work we present an algorithm for training an associative memory based on the so-called multi-layered morphological perceptron with maximal support neighborhoods. We compare the proposal with the original one by performing some experiments with real images. We show the superiority of the new one. We also give formal conditions for correct classification. We show that the proposal can be applied to the case of gray-level images and not only binary images.

Keywords: Associative memories, Morphological neural networks, maximal support neighborhoods.

1 Introduction

Neural networks have shown to be an excellent alternative to face problems where it is difficult to find no algorithmic solution. Based on the functioning of the human nervous system, lots of researchers have proposed different neural processing models. Probably the best know model is the Back-propagation Neural Network [1], [2] and [3].

The study of the internal structure of neural cells has revealed that all cells have the same simple structure, independently of their size and shape. Information from a cell voyages through the signals that neurons send to other neurons through their dendrites. It is believed that the cellular body adds up the received signals; when enough inputs are available a discharge is produced. Initially, this discharge occurs in cellular body, it then propagates between the axon until the synapses that sends a new signal to the other neurons.

An artificial neural network can be seen as a non-linear mapping between two pattern spaces: the input pattern set and the output pattern set. Normally the internal parameters of this mapping are determined by means of a training process and are denoted as synaptic weights.

In the decade of the 50's, Rosenblatt ([2], [3]) introduces the well-known perceptron, which is the classical model that has been used for most of the actual developments. However, in the 90's, Ritter et al., ([4], [5], [6]) and Sussner [12] presented a new kind of neural network model, the so-called morphological neural

network. Here, the classical operations of multiplication and addition are replaced by summations and **max** (or **min**), respectively. One difference between this model and the classical models is the computational cost when computing the value of i-th neuron at time $t+1$ that in this model is less.

In the last years it has been found that, apparently the processing of information not only occurs at the cellular body but also at the dendrites [7]. This affirmation could give an explanation of the great efficiency of our nervous system, since processing of the information happens practically along the communication channel.

The material just presented along with the morphological paradigm is the departure point of this paper.

2 Associative Memory Based on the Morphological Perceptron

In [7] it is presented how a morphological perceptron allows classifying any compact set in the pattern's domain, which can be used to build an associative memory able to recall patterns affected by mixed noise. The idea is to build a three layer associative memory (an of input, one hidden, and of output) as can be appreciated in Figure 1.
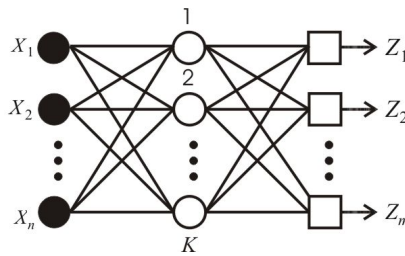
Fig. 1. Associative memory of three layers based on the morphological perceptron

First layer works as register of the number of elements of the input pattern. Second one (the hidden layer) is composed of morphological perceptrons [7], one for each class, while the output layer is formed by perceptrons based on the **max** operator with a linear gating function, one perceptron for each component of the output patterns.

The perceptrons of the hidden layer are morphological perceptrons with one input dendrite. The classified region is thus a hyper-rectangle in $\mathbf{R}^n$, whose goal is to classify the corresponding pattern inside the on-region. For the better functioning of this model, the perceptron outputs a zero in its on-region and $-\infty$ in its complements.

The output of a perceptron at the output layer is given as

$$z_i = \bigvee_{k=1}^{K} \left[y_i^k + \varphi_k(x) \right] \tag{1}$$

where y_i^k is the i-th component of the k-th output pattern, and $\varphi_k(x)$ is the output of the k-th perceptron of the hidden layer. Thus, when taking the **max** of the

outputs of the perceptrons φ_k that output a $-\infty$ unqualify pattern y^k as possible output of the associative memory. To train this associative memory, we have simply to define the supports of each key pattern. In this case the on regions of the corresponding patterns represent these supports.

From [3], during training, all supports of the memory are built as hyper-cubes of side equal to α, where α is obtained as

$$\alpha < \frac{1}{2}\min_{i<j} d\left(x^i, x^j\right) \tag{2}$$

where $d\left(x^i, x^j\right)$ is defined as

$$d\left(x^i, x^j\right) = \max\left\{\left|x_l^i - x_l^j\right|_{l=1,\ldots n}\right\} \tag{3}$$

and $\left(x^i\right) i = 1,\ldots,m$ is the set of key patterns.

To avoid collisions at the moment of classification it is necessary that the supports are disjoint two by two. This is not demonstrated in [7]. Next a brief proof that this happens is given.

Proposition 1. *Let M a multi-layered associative memory. If each key pattern* x^k *has a support* $S_k = \left\{x : d\left(x, x^k\right) < \alpha\right\}$*, with* α *as defined in equation* (2)*, then it hold that* $S_i \cap S_j = \varnothing, \forall i \neq j$.

Proof. Let us suppose that $\exists_{i \neq j}$ such that $S_i \cap S_j \neq \varnothing$, this means that there is a x such that $d\left(x, x^i\right) < \alpha$ and $d\left(x, x^j\right) < \alpha$. When summing and using triangles' inequality we get: $d\left(x^i, x^j\right) \leq d\left(x, x^i\right) + d\left(x, x^j\right) \leq \left(\alpha + \alpha = 2\alpha\right)$, then $d\left(x^i, x^j\right) < 2\alpha$, or in other words $\dfrac{d\left(x^i, x^j\right)}{2} < \alpha$!!, which is a contradiction, thus the proposition hold.

One of the drawbacks of this method to construct the supports is that if two of them are of them too close, the (radius) of the neighborhood's supports reduce drastically.

In [7] it is proposed another method to increase the neighborhoods of the supports by means of the kernels' method. According to [7], with this the range of permissible noise is increased. However, this method makes expensive the computational cost and besides it imposes restrictions over the patterns very difficult to get.

3 Proposed Training Algorithm

In the content of this work, let us suppose that a pattern is represented in terms of n object features; then at each coordinated axis we can compute the variation obtained

per feature by ordering all components. By computing the average of variability per pattern it is possible to define a threshold. For practical purposes, this threshold allows to consider if two patterns can be considered to be the same from the point of view of one of their components. This way we avoid having very tiny supports with respect to the coordinated axis. This way the drawback of the algorithm described in last section is surpassed.
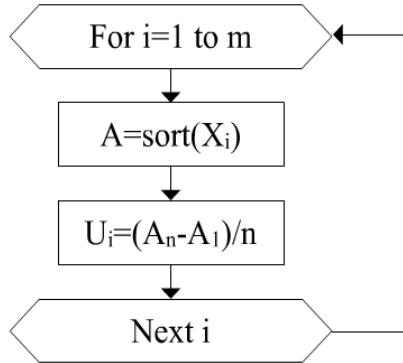
Fig. 2. Flowchart to get average variation threshold

The algorithm to find the average variation threshold by axis is observed in Fig. 2. In this case, X is a matrix of $n \times m$. At j-th column it is j-th pattern, while at i-th line are the m features of the i-th axis of each pattern. In U_i it is the average variation threshold for the i-th axis. The key point for the training of the multi-layered morphological perceptron consists on constructing the supports for each pattern. In general these supports must be disjoint two by two to avoid that two patterns be assigned to the same output. This is fulfilled in the proposed algorithm thanks to the following:

Proposition 2. *Let Ω_i and Ω_j two arbitrary supports corresponding to different patterns in $\mathbf{R}^n$, built according to average variation threshold, then it holds that $\Omega_i = \Omega_j$ or $\Omega_i \cap \Omega_j = \varnothing$.* [13].

Proof. Let x^i and x^j the corresponding patterns to supports Ω_i and Ω_j, respectively, then we have two cases:

a. If it holds that $\left| x_k^i - x_k^j \right| < U_k, \forall_{k=1,...n}$, with U_k is the average variation. If this holds then $\Omega_i = \Omega_j$.

b. If $\exists_{k=1,...,n}$ such that $\left| x_k^i - x_k^j \right| > U_k$ would imply that at $k-th$ coordinate, the support does not coincide and on the axis they are disjoint, thus they are disjoint in $\mathbf{R}^n$.

Evidently, when the patterns are too close, the neighborhoods would present occlusions. In these cases $\Omega_i = \Omega_j$ for $i \neq j$, one variant of this algorithm would be to consider that $\Omega_i \cap \Omega_j \neq \varnothing$, but that each neighborhood is centered at its respective key pattern. The advantage of this enhancement is that neighborhoods allowing more noise to be added to the patterns will be enlarged.

4   Numerical Examples

Example No. 1. Let the following set of key patterns in R^n:

$$\left\{ x^1 = \begin{bmatrix} 3 \\ -4 \end{bmatrix}, x^2 = \begin{bmatrix} -1 \\ -4 \end{bmatrix}, x^3 = \begin{bmatrix} -2 \\ 2 \end{bmatrix}, x^4 = \begin{bmatrix} -2 \\ -3 \end{bmatrix}, x^5 = \begin{bmatrix} 4 \\ 5 \end{bmatrix}, x^6 = \begin{bmatrix} -3 \\ 2 \end{bmatrix} \right\} \quad (4)$$

a) Solution obtained by means of algorithm proposed in [7]:

By applying the algorithm proposed in [7], according to equation (**2**) $\alpha = 0.5$. Figure 3 shows the neighborhoods obtained when using this value of α.
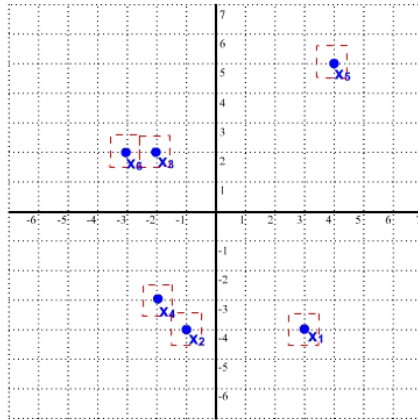
Fig. 3. Neighborhoods obtained when algorithm proposed in [7] is used

b) Solution obtained by means of algorithm proposed in this paper (first variant):

When using the algorithm to get the maximal support neighborhoods, by applying the flowchart shown in Figure 3, we get the threshold value U as:

$$U = \begin{bmatrix} 1.166 \\ 1.5 \end{bmatrix} \quad (5)$$

The neighborhoods obtained by using this threshold value are shown in Figure 4. The differences can be immediately appreciated. In this second case the range on noise for each pattern, as can be appreciated, is bigger.
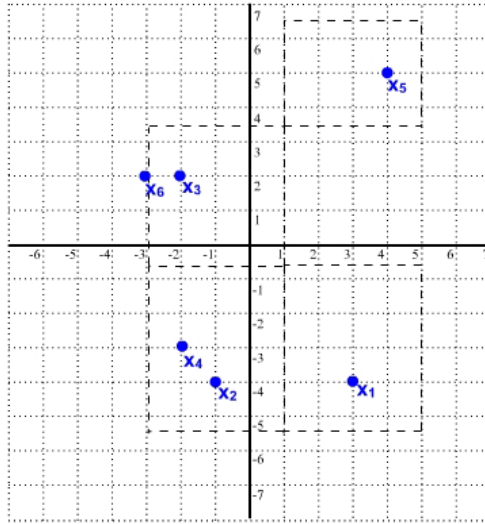
Fig. 4. Neighborhoods obtained when using first variant of the proposed algorithm

c) Solution obtained by means of algorithm proposed in this paper (second variant):

We apply the same procedure used by the first variant, but in this case the neighborhoods are centered at the corresponding key patterns. The threshold is the same given by equation (5).
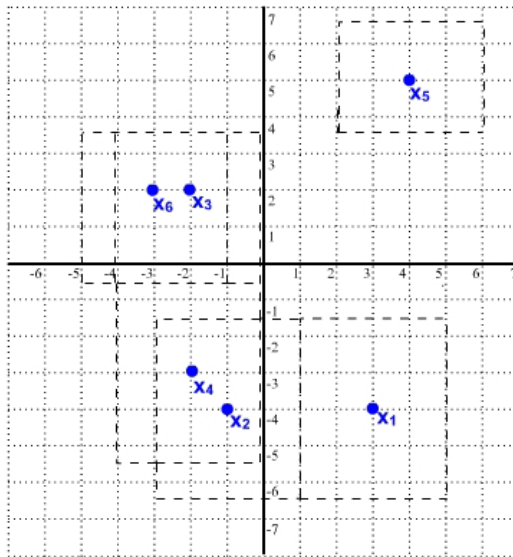
Fig. 5. Neighborhoods obtained when using second variant of the proposed algorithm

The neighborhoods obtained are shown in Fig. 5. Due to the neighborhoods are now centered at their respective key patterns, in this case the support for noise is bigger. Note also the occlusions between classes that do not occur in the first variant.

In the following section we show how the proposal described in this paper can be used not only to recall binary patterns but also gray-level patterns such images.

5   Experiments with Real Patterns

For this experiment we used the images shown in Fig. 6. These images are gray-level of 262×326 elements. They were perturbed with noise from 5% to 15%, in steps of 5%.

Fig. 6. Original images of experiments

The input key patterns where formed by describing each image by means of known Hu invariants ([10], [11]). Figures 7 to 9 show graphically the results obtained when using the algorithm proposed in [7], and the algorithm proposed in this paper to the images is shown in Figs. 10 to 12. From all of these figures we can observe that when adding, even small quantities of noise to the patterns, the original algorithm proposed in [7] fails to recall practically of the patterns, while the proposal, although with modest percentage, several of the desired patterns are correctly recalled.

(a)

(b)
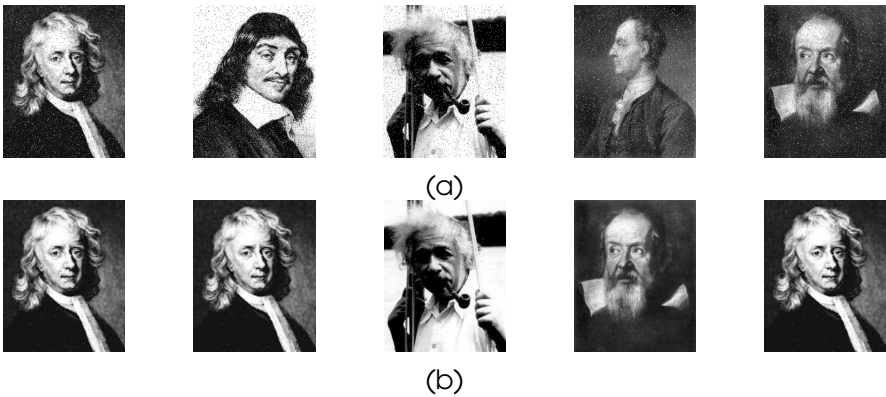
Fig. 7. (a) Images altered wit 5% of noise. (b) Images recalled using [7].

Fig. 8. (a) Images altered wit 10% of noise. (b) Images recalled using [7].

Fig. 9. (a) Images altered wit 15% of noise. (b) Images recalled using [7].
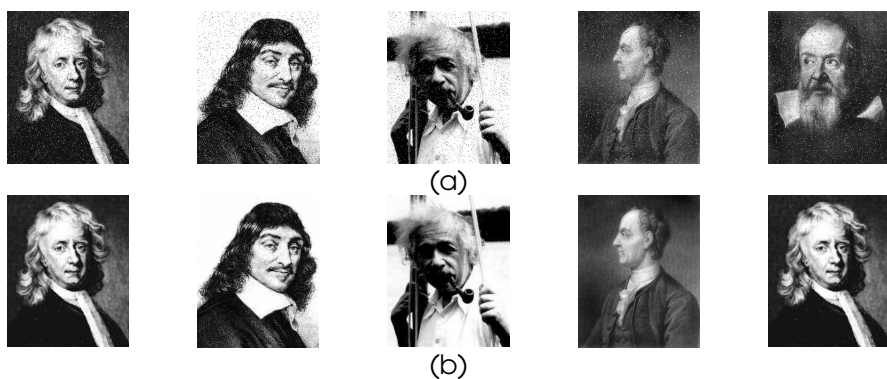
Fig. 10. (a) Images altered wit 5% of noise. (b) Images recalled using the proposal.
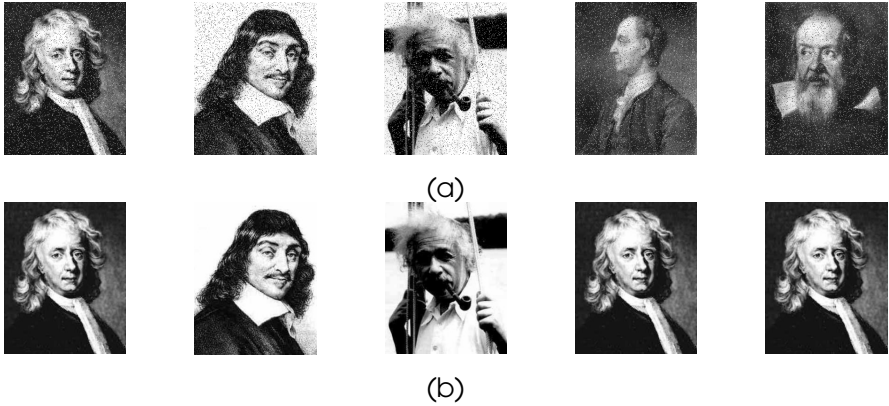
Fig. 11. (a) Images altered wit 10% of noise. (b) Images recalled using the proposal.
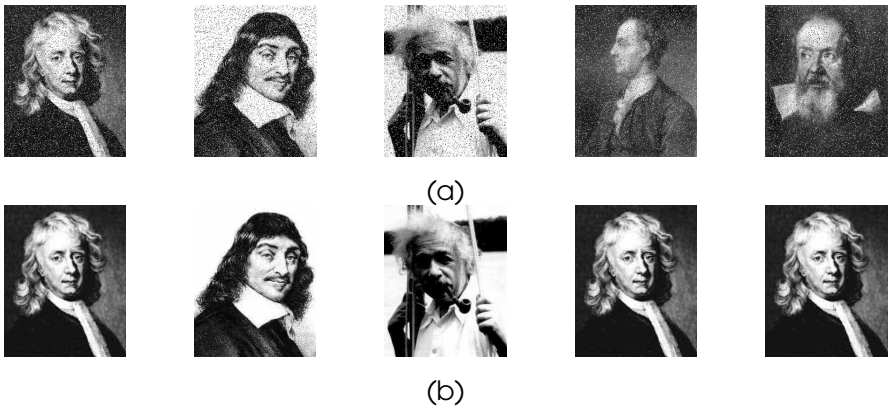
Fig. 12. (a) Images altered wit 15% of noise. (b) Images recalled using the proposal

6   Conclusions

In this paper we have presented an algorithm to train the multi-layered morphological perceptron that allows to build more efficient support neighborhoods, since the point of view of pattern recall, from the set of key pattern patterns of the training set of an associative memory in both its auto-associative or hetero-associative way of operation. By several experiments with real patterns, we have shown that the proposal can be used to recall gray-level images and not only binary images. We show the superiority of the new one.

References

[1] Bishop, C.: Neural Networks for Pattern Recognition. Oxford University Press, Oxford England (1995)

[2] Rossenblatt, F.: The perceptron: a probabilistic model for information storage and organization in the brain. Psychological review 65, 386–408 (1958)

[3] Rossenblatt, F.: Principles of Neurodinamics: Perceptrons and the theory of brain mechanism, Spartians Books, Washington D.C (1962)

[4] Ritter, G.X., et al.: An introduction to morphological Neural Networks. In: Proceedings of the 13International Conference on Pattern Recognition, pp. 709–717 (1996)

[5] Ritter, G.X., et al.: Morphological associative memories. IEEE Transactions on Neural Networks C-9, 281–293 (1998)

[6] Ritter, G.X.: Morphological Perceptrons. ISAS'97, Intelligent Systems and Semiotics, Gaithersburg, Maryland (1997)

[7] Ritter, G.X.: A new auto-associative memory based on lattice algebra. In: Proc. 9CIARP 2004, La Havana, Cuba pp. 148–155 (2004)

[8] Kishan, M., et al.: Elements of Artificial Neural Networks. The MIT Press, Cambridge, Massachusetts, London, England (1997)

[9] Pessoa, L.F.C., et al.: Morphological/Rank Neural Networks and their adaptative optimal image processing. IEEE International Conference on Acoustic, Speech, and Signal Processing 6, 3399–3402 (1996)

[10] Hu, M.K.: Pattern recognition by moments invariants. Proceeding of the IRE 49, 1428 (1961)

[11] Hu, M.K.: Visual pattern recognition by moments invariants, IRE Transactions on Information Theory, 179–187 (1962)

[12] Sussner, P.: Morphological Perceptron Learning. In: Proceedings of the 1998 International Symposium on Intelligent Systems and Semiotics, pp. 477-482, Gaithersburg, Maryland (1998)

[13] Barron, R., et al.: New Improved Algorithm for the training of a Morphological Associative Memory, Research in Computer Science. Special Issue: Neural Networks and Associative Memories 21, 49–59 (2006)

Joint Diagonalization of Kernels for Information Fusion

Alberto Muñoz and Javier González

Universidad Carlos III de Madrid, c/ Madrid 126, 28903 Getafe, Spain
{alberto.munoz,javier.gonzalez}@uc3m.es

Abstract. Information Fusion is becoming increasingly relevant in fields such as Image Processing or Information Retrieval. In this work we propose a new technique for information fusion when the sources of information are given by a set of kernel matrices. The algorithm is based on the joint diagonalization of matrices and it produces a new data representation in an Euclidean space. In addition, the proposed method is able to eliminate redundant information among the input kernels and it is robust against the presence of noisy variables and irrelevant kernels.

The performance of the algorithm is illustrated on data reconstruction and classifications problems.

Keywords: Information Fusion, Approximate Joint Diagonalization, Kernel Methods, Support Vector Machines.

1 Introduction

Fusion information techniques are becoming increasingly relevant in different fields such as classifier combination [9] or image processing [17]. Data fusion processes combine different sources of information to feed some data processing algorithm. For instance, in the problem of kernel combination [4], there are several metrics available and the task is to produce a single kernel to increase the classification performance of Support Vector Machine algorithms. In image fusion [3], a typical problem considers different satellite pictures, with different resolutions and different color qualities, and the task is to produce a picture that has maximum resolution and the best color quality. In the field of Information Retrieval, the goal can be to classify a set of web pages [8], and the information that has to be combined lies in the co-citation matrix and in the terms-by-documents matrix.

In this paper we approach the problem of information fusion in the context of kernel methods. Consider a set of kernels $K_1, ..., K_t$. By the Mercer theorem [11] each positive-definite kernel K_i induces a transformation of the data set into a (possibly) high dimensional Euclidean space $\mathbb{R}^n$. Thus, each kernel induces a particular representation of the data set using some basis $\{v_i\}$ for $\mathbb{R}^n$. If we want to combine the information provided by a set of kernels, we will have to find some 'common' basis $\{v^*\}$ from the individual basis $\{v_i\}$, such that the inmersion

of the data set in the resulting $\mathbb{R}^{n^*}$ contains all the relevant information from the individual kernels K_i.

Any technique to produce the desired combination basis needs to take into account the problem of information redundance. To illustrate this problem, let us consider a data set, and two representations given by two projections on two pairs of principal axes: (x, y) and (x, z), where the x variable is present in both representations. If we use the direct sum of the corresponding spaces as solution for the combination problem, we will have the representation (x, y, x, z). Thus, the weight of the x variable will be doubled when using the Euclidean distance and the results of the classification and regression algorithms will be distorted. In the general case the correlation between the variables will cause similar problems.

The Joint Diagonalization (JD) is a procedure that can be applied for fusion information purposes. The basis $\{v_i\}$ for the individual representation spaces are given by the eigenvectors of the K_i matrices. JD is able to produce a new basis $\{v_i^*\}$ from the $\{v_i\}$ basis and provides information to weight the new variables. Redundant kernel information can be removed during the process and the problem of overweighting variables avoided.

The paper is organized as follows. In Section 2 we review the simultaneous diagonalization process and introduce the case for more than two kernels. In Section 3 a new algorithm for kernel fusion is presented based on the joint diagonalization of matrices. Finally, in Section 4 the performance of the new data fusion methodology is tested using an ilustrative example.

2   Joint Diagonalization of Matrices

The calculus of eigenvalues is an usual task in many pattern recognition algorithms such as FDA [10], Kernel PCA [13,1], or Kernel Canonical Correlations [6] among others. Given a matrix $A \in \mathbb{R}^{n \times n}$ the diagonalization process seeks matrices V orthogonal and D diagonal such that $AV = VD$, or equivalently:

$$A = VDV^T. \tag{1}$$

When A is symmetric then a solution always exists and the elements of D are real numbers.

Some algorithms require the simultaneous diagonalization of two matrices. For instance, in FDA the *within-class* scatter matrix and the *between-class* scatter matrix have to be simultaneously diagonalized to find discriminative directions.

It is well known that exact simultaneous diagonalization is always possible [12]. This problem is referenced in the literature as the Generalized Eigenvalue Problem. Given two matrices $A, B \in \mathbb{R}^{n \times n}$ the problem is stated as finding $V \in \mathbb{R}^{n \times n}$, and two diagonal matrices D_1 and D_2 such that $AV = BVD$. In other terms,

$$V^T A V = D_1$$
$$V^T B V = D_2. \tag{2}$$

The base of vectors given by the columns of V is not necessarily orthonormal. This base is not unique and it is proven that V is orthogonal when the matrices A and B conmute, that is when $AB = BA$. If B is non-singular, the problem can be solved as and ordinary eigenvalue problem where the target matrix is $B^{-1}A$. See [7,5] and references therein for further details.

Next we afford the problem of diagonalization of more than two matrices at the same time.

2.1 Approximate Joint Diagonalization Algorithm

Given a set of matrices $S = \{A_1, ..., A_t\}$ it is not possible in general to achieve perfect joint diagonalization in a single step, unless $A_i A_j = A_j A_i \ \forall i, j \in \{1, ..., t\}$. These restrictions do not hold for most theoretical or practical problems. In practice we will have to find an orthonormal change of basis which makes the matrices in S 'as diagonal as possible' in a sense that will be detailed right away.

In this paper we consider the Approximate Joint Diagonalization (AJD) of symmetric matrices [14,2,15]. Given a square matrix A, we can measure the deviation of A from diagonality by defining

$$off(A) = \|A - diag(A)\|_F^2 = \sum_{i \neq j} a_{ij}^2, \tag{3}$$

where $\|A\|_F = \sum_i \sum_j a_{ij}^2$ is the Frobenius norm. If A is a diagonal matrix then $off(A) = 0$, while $off(A)$ will take small positive values when the off-diagonal values of A are close to zero.

Given the set S, the target is to find an orthonormal matrix V such that the departure from diagonality of the transformed matrices $D_i' = V^T A_i V$ is as small as possible $\forall i \in \{1, ..., t\}$. Therefore the goal will be to minimize

$$J(V) = \sum_{k=1}^{t} off(V^T A_k V)$$
$$s.t.$$
$$\|V^T V - I\|_F = 0$$
$$\|diag(V - I)\|_F = 0, \tag{4}$$

where the restrictions have to be included to achieve orthonormality and to avoid the trivial solution $V = 0$. After solving (4) we will obtain quasi diagonal matrices $D_1', ..., D_t'$, where $D_i' = V^T A_i V \ \forall i \in \{1, ..., t\}$.

There is no closed solution for the problem in (4) and some type of numerical approach has to be adopted. We will apply the algorithm described in [2,16]. The idea is to generate a sequence of similarity transformations of the initial matrices that drive to zero the off-diagonal entries. The convergence of the algorithm is proven to be quadratic and the obtained eigenvalues and eigenvectors are robust against small perturbations of the data.

3   Fusion Joint Diagonalization Algorithm (FJDA)

As already mentioned, Approximate Joint Diagonalization involves the computation of a base of orthogonal vectors in which the set of kernels approximately diagonalize. We will obtain relevant information about the data structure by analyzing the resulting eigenvalues, or equivalently, the diagonal matrices obtained from the joint diagonalization procedure. The ideas are similar to that used in Principal Components Analysis, where the covariance matrix is diagonalized and the resulting eigenvalues can be interpreted as the weights of the new variables.

Let $\{v_1, ..., v_n\}$ be the column vectors of the matrix V obtained from the JD algorithm (the $\{v_i^*\}$ vectors in the introduction). These vectors constitute the basis where both kernels diagonalize and can be interpreted as the *average eigenspace* of the kernels. A detailed analysis of the kernels redundancy can be done in terms of the values of the diagonal matrices $D_1', D_2', ..., D_t'$ obtained. Given the kernel K_l, their components can be interpreted as follows:

- $D_l'(i,i) = 0$: the vector v_i is irrelevant for the kernel K_l. That is, the i-th variable v_i is in the null space of K_l.
- $D_l'(i,i) \neq 0$: in this case v_i is a relevant component for K_l.
- $D_l'(i,j)$: These values can be interpreted as the interactions among the new variables. Due to the JD operation, $D_l'(i,j) \approx 0$.

Given V and $D_1', D_2', ..., D_t'$, the straightforward sum of the kernel matrices can be reexpressed as:

$$\sum_{i=1}^{t} K_i = V^T \left(\sum_{i=1}^{t} D_i' \right) V \qquad (5)$$

Given that the *off-diagonal values* of $\{D_1', ..., D_t'\}$ are quite close to zero, $D_l'(i,i)$ can be interpreted as the weight that kernel K_l assigns to the i-th variable in the new basis. Since the new base is orthogonal, independent information is given by each component. The straightforward sum of kernels implies to include redundances in the operation and to overweight variables that appear in more than one kernel at the same time. In order to avoid these redundances, the sum of the quasi-diagonal matrices of expression (5) can be replaced by the function $F(D_1', D_2', ..., D_t')$ defined as follows:

$$F(D_1', D_2', ..., D_t') = \begin{cases} max\{D_1'(i,j), ..., D_t'(i,j)\} & \text{if } i = j \\ 0 & \text{if } i \neq j \end{cases} \qquad (6)$$

The justification of this choice is as follows. The relevance of the $i-th$ variable in the basis induced by kernel K_l is given by $D_l'(i,i)$. The use of the max function guarantees that the i-th variable will be relevant in the resulting combined basis if this is the case for any of the individual representations. Thus, the weight of ith variable in the fusion kernel will be $max\{D_1'(i,i), ..., D_t'(i,i)\}$.

The final algorithm for kernel fusion is shown in Table 1 and it provides a global framework for kernel fusion. Notice that, since the matrix V is orthogonal and the diagonal matrices of $F(D_1', D_2', ..., D_t')$ are positive, K^* is always a Mercer kernel matrix.

Table 1. Scheme of the Fusion Joint Diagonalization Algorithm in three steps

INPUT: Kernel matrices $K_1, ..., K_n$
OUTPUT: Kernel combination K^*
1.- $(V, D'_1, ..., D'_n) = AJD(K_1, ..., K_n)$
2.- $D^* = F(D'_1, ..., D'_n)$
3.- $K^* = V^T D^* V$

4   Experiments

In order to validate the effectiveness of the proposed methodology some experimental results are shown in this section. First, the algorithm is tested in a data reconstruction example where partial information about the data is given. Finally, the methodology is successfully tested in a real classification problem..

4.1   Simulated Example

In this example we illustrate the performance of the new JD algorithm in a data structure recovery task.

We consider two different one-dimensional random projections π_1 and π_2 of the spiral data in Figure 1 and calculate the kernel matrices K_1 and K_2 by applying the linear kernel $k(x, y) = x^T y$ to the projected data points, that is, $K_i(x, y) = \pi_i(x)^T \pi_i(y)$. We add a corrupted (random) representation of the data and calculate K_3 from this representation in the same way. K_3 plays the role of a non informative (non-related) piece of information in the system. This situation happens when the distance function is not appropiate for the data set under consideration or when we try to use irrelevant information to solve a problem. The task is to recovery the original data set from the three projections.

Two fusion schemes were compared in the experiment: The straightforward sum of kernels $K^{sum} = K_1 + K_2 + K_3$ and the combination K^* calculated with the Fusion Joint Diagonalization Algorithm. In Figure 2 the results are shown. It is clear that our procedure is able to recover the original data set structure while the straightforward sum of kernels fails on the task of recovering the data set structure.

4.2   Sonar Data

In this example we perform a study of classification of sonar signals [18]. The goal is to discriminate between two types of signals: those bounced off a metal cylinder and those bounced off a roughly cylindrical rock. The data set has 208 observations measured on 60 variables that take values in the interval $[0, 1]$. Each value represents the *energy within a particular frequency band, integrated over a certain period of time*. The goal is classify the objects as rocks or mines.
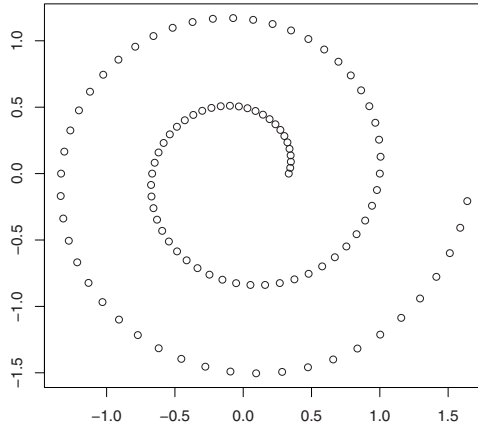
Fig. 1. Spiral data
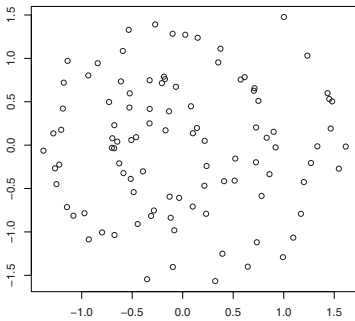
(a) Direct fusion of kernels for the Spiral data
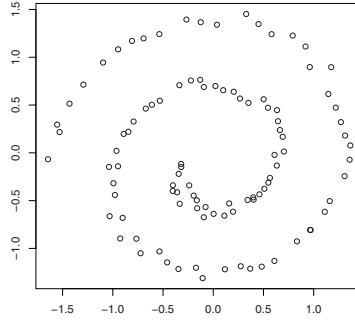
(b) Fusion Joint Diagonalization Algorithm applied to the Spiral data set

Fig. 2. Representations for recovered data structures after the direct combination of three kernels and after the Fusion Joint Diagonalization algorithm

We consider two Radial Basis Funtion kernels $K_i(x, y) = e^{-\gamma \|x-y\|^2}$, $i \in \{1, 2\}$, where $\gamma = 1$ and $\gamma = 0.1$. We want to combine K_1 and K_2 using the straightforward sum and the AJD fusion method. In order to evaluate the performance of both fusion approaches we will feed one SVM classifier with the resulting fusion kernels. The penalty value C is set to one in all the experiments. Table 2 shows the classification results for the SVM classifier using four different kernels: the individual kernels K_1 and K_2, and the two fusion kernels: Sum for the straightforward sum and KAJD for the AJD kernel.

It is apparent from the results that K_1 performs better than K_2. When the straightforward sum is considered, the performance of the SVM is worse than in the case of using the RBF kernel with $\gamma = 1$. It seems that the bad performance

Table 2. Percentage of missclassied data, and percentage of support vectors for the Sonar data set after 10 runs. Standard deviations in brackets.

Kernel	Train Error	Test Error	%SV
K_1 ($\gamma = 1$)	1.144 (0.460)	15.952 (0.372)	40.0 (0.0)
K_2 ($\gamma = .1$)	16.56 (0.077)	25.761 (0.170)	48.7 (0.0)
KSum	1.325 (0.516)	16.666 (0.380)	76.6 (1.8)
KAJD	0.783 (0.499)	15.238 (0.404)	82.9 (2.2)

of K_2 damages the performance of the straightforward sum approach. On the other hand, the kernel obtained by the AJD algorithm shows a better classification performance than the other fusion method and also than the individual kernels.

5   Conclusions and Future Work

In this work, we present a new framework for information fusion when the sources of information are given by a set of kernel matrices. The algorithm, based on the Approximate Joint Diagonalization of matrices, produces a new representation of the data set in a Euclidean space, where the basis is created from the representations induced by the individual kernels. In addition our method is able to eliminate redundant information from the individual kernels. The proposed fusion scheme has been tested in a couple of significative examples. Furthermore, the procedure is shown to be robust against the inclusion of noisy variables.

Future research will include the study of Joint Diagonalization Algorithms that take into account the label information in classification problems and also JD algorithms specific for regression problems.

References

1. Bach, F.R., Jordan, M.I.: Kernel Principal Components Analysis. Journal of Machine Learning Research 3, 1–48 (2002)
2. Cardoso, J.F., Souloumiac: A Jacobi Angles for Simultaneous Diagonalization. SIAM J. Mat. Anals. Applied 17(1), 161–164 (1996)
3. Choi, M., Young, R., Nam, M.-R., Kim, H.O.: Fusion of Multispectral and Panchromatic Satellite Images Using the Curvelet Transform. Geoscience and Remote Sensing Letters 2(2) (2005)
4. Martin de Diego, I., Moguerza, J.M., Muñoz, A.: Combining Kernel Information for Support Vector Classification. In: Roli, F., Kittler, J., Windeatt, T. (eds.) MCS 2004. LNCS, vol. 3077, pp. 102–111. Springer, Heidelberg (2004)
5. Epifanio, I., Gutierrez, J., Malo, J.: Linear transform for simultaneous diagonalization of covariance and perceptual metric matrix in image coding. Pattern Recognition 36, 799–1811 (2003)

6. Gretton, A., Herbrich, R., Smola, A., Bousquet, O., Schölkop, B.: Kernel methods for measuring independence. J. Machine Learning Research 6, 2075–2129 (2005)
7. Hua, Y.: On SVD estimating Generalized Eigenvalues of Singular Matrix Pencils in Noise. IEEE Transactions on Signal Processing 39(4), 892–900 (1991)
8. Joachims, T., Cristianini, N., Shawe-Taylor, J.: Composite Kernels for Hypertext Categorisation. In: Proceedings of the International Conference on Machine Learning, pp. 250–257 (2002)
9. Kittler, J., Hatef, M., Duin, R.P.W., Matas, J.: On combining classifiers. IEEE Transactions on Pattern Analysis and Machine intelligence 20(3), 226–239 (1998)
10. Mika, S., Ratsch, W.G., Scholkopf, B., Muller, K.-R.: Fisher Discriminant Analysis with Kernels. In: Proceedings of IEEE Neural Networks for Signal Processing Workshop, IEEE Computer Society Press, Los Alamitos (1999)
11. Moguerza, J., Muñoz, A.: Support Vector Machines with Applications. Statistical Science 21(3), 322–336 (2006)
12. Beresford, P.N.: The Symmetric Eigenvalue Problem. Classics in Applied Mathematics. SIAM (1997)
13. Schölkopf, B., Smola, A.J., Müller, K.R.: Nonlinear Component Analysis as a Kernel Eigenvalue Problem. Neural Computation 10, 1299–1319 (1998)
14. Wax, M., Sheinvald, J.: A least-squares approach to joint diagonalization. IEEE Signal Processing Lett. 4, 52–53 (1997)
15. Bunse-Gerstner, A., Byers, R., Mehrmann, V.: Numerical methods for simultaneous diagonalization. SIAM Journal on Matrix Analysis and Applications 14(4), 927–949 (1993)
16. Yeredor, A.: Non-Orthogonal Joint Diagonalization in the Least-Squares Sense With Application in Blind Source Separation. IEEE Transactions on Signal Processing. 50 (7), 1545–1553 (2002)
17. Piella, G., Heijmans, H.: Multiresolution Image Fusion Guided by a Multimodal Segmentation. In: Proceedings of ACIVS 2002, Ghent, Belgium (September 9-11, 2002)
18. Newman, D.J., Hettich, S., Blake, C.L. and Merz, C.J.UCI Repository of machine learning databases. Irvine, CA: University of California, Department of Information and Computer Science 1998, http://www.ics.uci.edu/mlearn/MLRepository.html

Support Vector Regression Methods for Functional Data

Noslen Hernández[1], Rolando J. Biscay[2], and Isneri Talavera[1]

[1] Advanced Technologies Applications Center
nhernandez@cenatav.co.cu
[2] Institute of Mathematics, Physics and Computation

Abstract. Many regression tasks in practice dispose in low gear instance of digitized functions as predictor variables. This has motivated the development of regression methods for functional data. In particular, Naradaya-Watson Kernel (NWK) and Radial Basis Function (RBF) estimators have been recently extended to functional nonparametric regression models. However, these methods do not allow for dimensionality reduction. For this purpose, we introduce Support Vector Regression (SVR) methods for functional data. These are formulated in the framework of approximation in reproducing kernel Hilbert spaces. On this general basis, some of its properties are investigated, emphasizing the construction of nonnegative definite kernels on functional spaces. Furthermore, the performance of SVR for functional variables is shown on a real world benchmark spectrometric data set, as well as comparisons with NWK and RBF methods. Good predictions were obtained by these three approaches, but SVR achieved in addition about 20% reduction of dimensionality.

Keywords: Support Vector Regression, Functional Data, Kernel Function.

1 Introduction

The fast development of instrumental analysis equipment, such as spectrophotometers, chromatographs, signal analyzers and other modern measurement devises, provides huge amount of data as high-resolution digitized functions. As a consequence, regression tasks in which the predictor variable is some type of Functional Data (FD), instead of a low-dimensional vector, are quite common. For example, it is very important nowadays the prediction of chemical physical properties of a product from its spectral function [4], [16].

The direct application of classical multivariate regressions methods for this type of data exhibits serious limitations. Indeed, digitized functions (e.g., spectral data) are generally represented by high-dimensional vectors whose coordinates are strongly correlated. Furthermore, usually the dimension of such vectors greatly exceeds the number of independent observations (e.g., the number of measured spectra). In such situations, standard regression analysis leads to ill-posed inverse problems, which cause a number of difficulties.

As an alternative, Functional Data Analysis is an extension of traditional multivariate analysis that is specifically oriented to deal with observations of functional nature [12]. For this, each individual is characterized by one or more continuous real-valued functions, rather than by a finite-dimensional vector. This allows for applying functional processing techniques such as derivation, integration, etc. On this basis, over the last years several classical multivariate statistical methods have been extended to FD. In respect to regression, first works in this direction were focused on linear models. In particular, least squares methods have been elaborated for linear regression with functional predictors (see, e.g., [11], [12], and references therein). Also, some dimensionality reduction approaches for linear regression, such as principal component regression and partial least squares, have been generalized to FD [1], [3], [9]. More recently, a number of estimation methods for functional nonparametric regression models have been also introduced. Namely, estimators based on functional data adaptations of classical neural networks [13], Naradaya-Watson Kernel (NWK) estimators [6], [7] and regularization in Reproducing Kernel Hilbert Spaces (RKHS) [9]— the latter including Radial Basis Function (RBF) methods. Likewise their classical counterparts in multivariate analysis, these nonparametric techniques provides high flexibility to approximate a wide class of functional regressions. However, a difficult with them is that a high amount of computer memory is required to encode the estimates in order to make future predictions (e.g., the whole data set has to be retained for predicting by NWK and RBF methods).

In the present paper, the drawback just mentioned is approached by introducing Support Vector (SV) regression methods on functional spaces. Though SV regression have been studied by several authors in the more general framework of abstract RKHS methods (see, e.g., [15], [5], [2]), to our knowledge no work have been carried out to deal with its application to FD. On the basis of the RKHS framework we study some properties of SV regression for FD, emphasizing specificities related with the construction of nonnegative definite (nnd) kernels on functional spaces. Furthermore, the feasibility and practical performance of SV regression for FD, as well as comparisons with NWK and RBF estimators, are shown on a real world benchmark spectrometric data set.

2 Estimation of Abstract Nonparametric Regression Models by Regularization in Reproducing Kernel Hilbert Spaces

Estimation methods for very general regression models have been elaborated by several authors on the basis of regularization in RKHS (see, e.g., [15], [5], [2], and references therein, for definitions and detailed expositions). We will here briefly describe this abstract framework before considering its specification for regression with FD in the next Section.

Let $\mathcal{X}$ be a linear space with norm $\|\|_{\mathcal{X}}$, and $\mathbb{R}^{\mathcal{X}}$ be the set of functions from $\mathcal{X}$ into $\mathbb{R}$. Suppose it is given some positive definite (pd) function (or kernel) $\kappa : \mathcal{X} \times \mathcal{X} \to \mathbb{R}$. It is known that there exists a RKHS $\mathcal{H}_\kappa \subset \mathbb{R}^{\mathcal{X}}$ with reproducing

kernel κ. The norm on $\mathcal{H}_\kappa$ will be denoted by $\|\|_{\mathcal{H}}$. Consider the abstract nonparametric regression model:

$$Y = \Psi(X) + e,$$

where (X, Y) is a random variable on some probability space $(\Omega, \mathcal{F}, P)$ with values in $\mathcal{X} \times \mathcal{Y}$, $\mathcal{Y} \subset \mathbb{R}$, e is a real-valued random variable with zero mean, which is assumed to be independent from (X, Y), and Ψ is an unknown mapping $\mathcal{X} \rightarrow \mathbb{R}$. The variables X and Y are interpreted, respectively, as the predictor and response variable in this regression model. The problem of interest is to estimate the regression mapping Ψ on the basis of data (X_i, Y_i), $1 \le i \le n$, formed by independent and identically distributed observations of (X, Y).

For this, let $\mathcal{H}_0$ be a given finite-dimensional linear subspace of $\mathbb{R}^{\mathcal{X}}$ with basis $G_1, ..., G_m$, such that the matrix $(G_j(X_i))$, $1 \le i \le n$, $1 \le j \le m$, has rank m. Denote by $\mathcal{H} = \mathcal{H}_\kappa + \mathcal{H}_0$ the space of functions $F = F_\kappa + F_0$ with $F_\kappa \in \mathcal{H}_\kappa$ and $F_0 \in \mathcal{H}_0$. Henceforth, it will be assumed that $\Psi \in \mathcal{H}$. To assess the closeness of each $F \in \mathcal{H}$ to the unknown Ψ, suppose that a function $c : \mathcal{X} \times \mathcal{Y} \times \mathcal{H} \rightarrow \mathbb{R}_+$ (called a contrast function) has been specified. The risk of approximating Ψ by an element $F = F_\kappa + F_0 \in \mathcal{H}$ is then quantified by

$$R(F) = E(c(X, Y, F(X))),$$

where E is the expectation with respect to the distribution of (X, Y). The corresponding empirical risk and the regularized empirical risk are defined, respectively, as

$$R_{emp}(F) = \frac{1}{n} \sum_{i=1}^{n} E(c(X_i, Y_i, F(X_i)))$$

and

$$R_\lambda(F) = R_{emp}(F) + \lambda \|F_\kappa\|_{\mathcal{H}} ,$$

where $\lambda \ge 0$ is a a given constant (regularization hyperparameter). The regularized estimate $\widehat{\Psi}_\lambda$ of Ψ is defined through the optimization problem

$$\widehat{\Psi}_\lambda = \arg \min_{F \in \mathcal{H}} R_\lambda(F).$$

As has been pointed out by several authors, this general framework provides an unified treatment of several approaches to nonparametric regression, in dependence of the specification of the contrast function c (see, e.g., [5] and references therein). In particular:

$c1$) Regularized least squares regression methods correspond to the quadratic contrast

$$c(X, Y, F(X)) = (Y - F(X))^2.$$

More particularly, standard RBF regression methods are obtained when the quadratic contrast is adopted, $\mathcal{X}$ is a subspace of $\mathbb{R}^d$ (for some $d \in \mathbb{N}$), and the kernel has the radial form $\kappa(x, x) = g(\|x\|)$ for some function $g : \mathbb{R}_+ \rightarrow \mathbb{R}$. Here, $\|x\|$ is the euclidean norm on $\mathbb{R}^d$.

$c2$) Support Vector regression methods correspond to the so-called ϵ-insensitive contrast function

$$c\left(X, Y, F\left(X\right)\right) = |Y - F\left(X\right)|_{\epsilon} = \max\left(|Y - F\left(X\right)| - \epsilon, 0\right),$$

where $\epsilon \geq 0$ is some given constant. In this case, $\mathcal{H}_0$ is taken as either the one-dimensional space generated by the constant function $G_1\left(x\right) \equiv 1$ or $\mathcal{H}_0 = \{0\}$.

3   Support Vector Estimators for Functional Nonparametric Regression

The general framework for regression estimation through regularization in RKHSs, as sketched above, can be applied for any specification of the space $\mathcal{X}$, the pd kernel κ on $\mathcal{X}$, the contrast function c, and the finite-dimensional subspace $\mathcal{H}_0$ of $\mathbb{R}^{\mathcal{X}}$.

Classical applications of RKHS methods for regression deal with situations in which $\mathcal{X} \subset \mathbb{R}^d$, and so $\mathcal{H} \subset \mathbb{R}^{\mathcal{X}}$ is constituted by multivariate functions $F : \mathcal{X} \subset \mathbb{R}^d \to \mathbb{R}$. This is the setting of multivariate regression methods, in which the regression mapping Ψ to be estimated is a *multivariate function*, i.e., a function on $\mathbb{R}^d$.

On the contrary, functional nonparametric regression models deal with cases in which $\mathcal{X} \subset \mathbb{R}^{\mathcal{T}}$ is a set of functions $x : \mathcal{T} \to \mathbb{R}$, where $\mathcal{T}$ is an infinite-dimensional set. For example, in some practical situations of interest, $\mathcal{T} = [a, b]$ is a closed interval in $\mathbb{R}$, and $\mathcal{X}$ is the space $L^2\left([a, b], \mathbb{R}\right)$ of squared-integrable functions defined on $[a, b]$. Thus, in regression models with FD the unknown regression mapping Ψ is a *functional* defined on a normed space $\mathcal{X}$ of real-valued functions.

The estimation of functional regression models by RKHS methods have been recently initiated in [9] under the quadratic contrast, hence providing regularized least squares estimates. These are instances of the general class ($c1$) described in the previous Section.

In the present work we introduce methods to estimate regression models for FD adopting the ϵ-insensitive contrast function, i.e. we adapt to functional data the general approach ($c2$) mentioned above.

It is known that under quite general conditions on the contrast function c (which are satisfied by both the quadratic and the ϵ-insensitive contrasts), the regularized estimate $\widehat{\Psi}_{\lambda}$ in any abstract regression model has the following explicit form: for all $x \in \mathcal{X}$,

$$\widehat{\Psi}_{\lambda}\left(x\right) = \sum_{i=1}^{n} a_i \kappa\left(x_i, x\right) + \sum_{j=1}^{m} b_j G_j\left(x\right)$$

for some a_i, $b_j \in \mathbb{R}$ that depend only on the hyperparameter λ and the matrices $K = \left(\kappa\left(x_i, x_j\right)\right)$, $G = \left(G_j\left(x_i\right)\right)$.

Therefore, once the kernel κ is given, the numerical computation of RKHS-based regularized estimators $\widehat{\Psi}_{\lambda}$ in regression for FD input (i.e., when $\mathcal{X}$ is a

space of functions) is exactly the same as in regression for multivariate input (i.e., when $\mathcal{X}$ is a subspace of some finite-dimensional linear space $\mathbb{R}^d$).

Furthermore, both for quadratic and ϵ-insensitive contrast functions (i.e., for regularized least squares and SV regression approaches), many properties of the estimator $\widehat{\Psi}_\lambda$ in the FD setting can be quite directly derived from known results in the framework of abstract regression models. For example, if $\mathcal{Y}$ is bounded by a constant $M_{\mathcal{Y}}$ and κ is bounded by a constant M_κ then, for any $\lambda \geq 0$,

$$R_{emp}\left(\widehat{\Psi}_\lambda\left(x\right)\right) - R\left(\widehat{\Psi}_\lambda\left(x\right)\right) \to 0$$

in probability exponentially fast as $n \to \infty$ ([10], see also [2] and [15]). Likewise, some results on uniform convergence in probability

$$R_{emp}\left(F\right) - R\left(F\right) \to 0$$

over sets of the form $\left\{F : \|F\|_{\mathcal{H}} \leq A\right\}$, $A \in \mathbb{R}$, are discussed e.g. in [5].

However, RKHS-based regularization has important specificities in case of regression models for functional data. Some of them, mainly related with the interpretation and construction of pd kernels on functional spaces, are discussed bellow.

4 Nonnegative Definite Kernels on Functional Spaces

Nonnegative definite (nnd) kernels on finite-dimensional linear spaces $\mathbb{R}^d$ are usually constructed on the basis of classical differential operators or completely monotone functions of order $q \in \mathbb{N}$, from which standard spline and RBF approximations to multivariate functions are derived [18]. Unfortunately, these approaches are not directly applicable to obtain nnd kernels on infinite-dimensional spaces. This difficulty poses a challenge to the RKHS approach to regression for FD.

In this Section we will give some results that allow for the construction of some classes of nnd kernels on functional spaces. It will be assumed that $\mathcal{X}$ is some (infinite-dimensional) separable normed space. Thus, all results are applicable to typical problems with FD, in which $\mathcal{X} \subset \mathbb{R}^{\mathcal{T}}$ and $\mathcal{T}$ is an interval of the real line. Notations and definitions introduced in the previous Sections are assumed.

The following lemma can be easily proved.

Lemma 1. *Let*

$$\varphi\left(x\right) = E\left(e^{iW(x)}\right)$$

be the characteristic function of a stochastic process $(W\left(x\right) : x \in \mathcal{X})$ on $\mathcal{X}$. If $x \to W\left(x\right)$ is a linear functional, and if for all $x \in \mathcal{X}$, the distribution of the

random variable $W\left(x\right)$ is symmetric around zero, then

$$\kappa\left(x, \acute{x}\right) = \varphi\left(x - \acute{x}\right)$$

is a (real-valued) nnd kernel on $\mathcal{X}$.

A direct consequence of this lemma is the following well-known fact. If $\mathcal{X}$ is a separable Hilbert space and $h \succ 0$ then the Gaussian function

$$\varphi(x) = e^{-\frac{1}{h}\|x\|^2}$$

defines a nnd kernel on $\mathcal{X}$ (called the Gaussian kernel [15]) by means of

$$\kappa(x, \acute{x}) = \varphi(x - \acute{x}) = e^{-\frac{1}{h}\|x - \acute{x}\|^2}.$$

Indeed, it is known that there exists a probability space Ω and a Gaussian and linear stochastic process $(W(x) : x \in \mathcal{X})$ on Ω with zero mean (called the isonormal or Gaussian process on $\mathcal{X}$) such that

$$E(W(x)W(\acute{x})) = (x, \acute{x}),$$

where (x, x) is the scalar product in $\mathcal{X}$. Hence, the conditions of the lemma 1 are satisfied by taking

$$\varphi(x) = E\left(e^{iW(x)}\right) = e^{-\frac{1}{h}\|x\|^2}.$$

Lemma 1 provides other interesting classes of nnd kernels, as the one stated in the following theorem.

Theorem 1. *Let $\mathcal{T}$ be an interval of $\mathbb{R}$, $\alpha \in (0, 2]$, $h \geq 0$, and $\mathcal{X}$ be a set of measurable functions $\mathcal{X} \subset \mathbb{R}^{\mathcal{T}}$ such that*

$$\|x\|_L = \left(\int_{\mathcal{T}} |x(t)|^\alpha \, dt\right)^{\frac{1}{\alpha}}$$

is finite for each $x \in \mathcal{X}$. Then,

$$\kappa(x, \acute{x}) = e^{-\frac{1}{h}\|x - \acute{x}\|}$$

is a nnd kernel on $\mathcal{X}$ (which we will call an "α-stable kernel").

Indeed, define

$$W(x) = \frac{1}{h} \int_{\mathcal{T}} x(t) \, dZ(t), \tag{1}$$

where $(Z(t) : t \in \mathcal{T})$ is a standard symmetric α-stable Levy motion [14] Then, it can be shown that W satisfies the conditions of lemma 1.

Notice that, more generally, also as a consequence of lemma 1, if the stochastic process $(Z(t) : t \in \mathcal{T})$ is any semimartingale whose increments have symmetric distributions, and if the stochastic integral (1) is well-defined for all $x \in \mathcal{X}$, then

$$\kappa(x, \acute{x}) = E\left(e^{i(W(x) - W(\acute{x}))}\right)$$

is a nnd kernel.

The investigation of the variety of kernels for FD provided by these results is an interesting issue for further research. As a first step in this direction, in the next Section we will restrict to explore the performance of SV regression with Gaussian kernels on a real FD set.

5   Application to Real Data

The main objective in this section is to demonstrate the feasibility of Support Vector Regression (SVR) for FD, and its behavior regarding RBF and NWK estimators.

The considered experimental data comes from the food industry named Tecator [17], It consist of 215 near-infrared absorbance spectra of meat samples, recorded on a Tecator Infratec Food and Feed Analyzer. Each observation consists in a 100-chanel absorbance spectrum in the 850-1050 nm wavelength range. Each spectrum in the data base is associated to a content description of meat sample, obtained by analytic chemistry; the percentage of fat, water and protein are reported. The regression problem consists in the prediction of the fat percentage from the spectrum.

From the 215 spectra, 43 are kept aside as a testing set and the 172 remaining sample is used for model estimation (training set). It should be mentioned that the spectra are finely sampled, leading to very smooth curves. Each function was represented by a 4th order B-spline approximation with 32 basis functions. The adopted kernel was the Gaussian kernel with the L_2 norm of the second derivative of the spectrum. This norm was computed on the basis of the B-spline representation of the spectrum. All calculations were performed using Matlab. For SVR, the LIBSVM implementation embedding in a Matlab toolbox was used.

Table 1. Prediction accuracy for different regression estimators

	rmse	max Abs Error	max. Rel. Error	Avrg. Rel. Error
SVR	0.5451	1.2933	0.1653	0.0276
RBF	0.9279	2.8486	0.3061	0.0512
NWK	1.4563	5.6000	0.2196	0.0642

In order to select best hyperparameter values (λ , ϵ, h) to train the SVR, 10 folds Cross-Validation over a grid search was done. For RBF and NWK estimates, Generalize Cross-Validation [18] was applied to tune the hyperparameters.

Figure 1 contains plots of predicted values versus real values of the response variable in the testing sample for each regression method: SVR, RBF and NWK. It is clear that prediction accuracies (generalization capabilities) are quite good for all these methods but SVR seems to exhibit the best one.

This is quantitatively confirmed in Table1 which summarizes the values of several measures of prediction accuracy over the testing sample for each method: root mean squared error (rmse), maximum absolute error (max Abs Error), maximum relative error (max. Rel. Error) and average relative error (Avrg. Rel Error). SVR shows the best predictive behavior in terms of all error measures while the NWK method is the worst one, particularly in respect to the maximum absolute error.
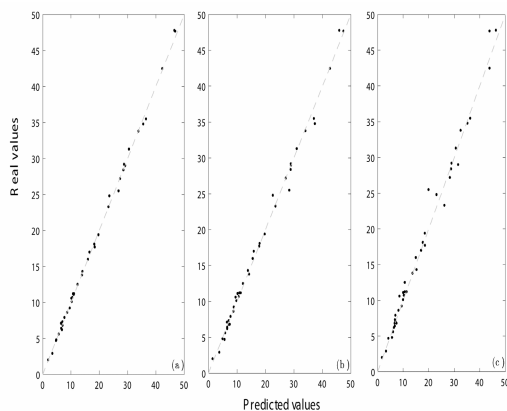
Fig. 1. Real values vs. Predicted values for a) SVR, b) RBF, and c) NWK estimates
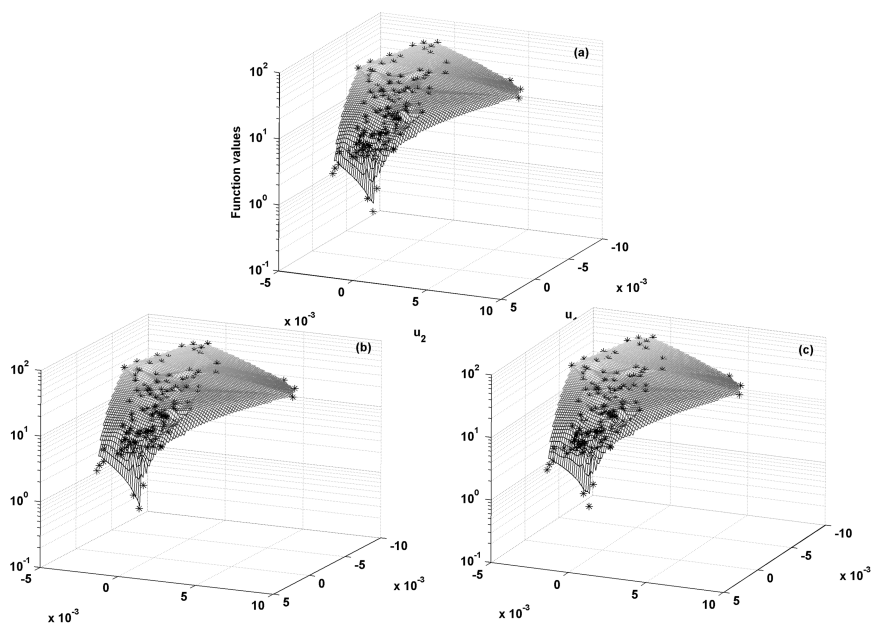
Fig. 2. Functional regression estimates for (a) SVR, (b) RBF, (c) NWK estimator

In order to aid to a better understanding of the different regression estimators in terms of prediction capabilities and shapes of the regression estimates, a graphic representation of the fitted regression functional would be convenient. However, their complete visualization is not possible due to the fact that they live in an infinite dimensional space. To overcome this, a (metric) multidimensional scaling transformation to the two-dimensional euclidean space was applied

to the inter-distance matrix among all spectra (distances computed according to the L_2 norm of second derivatives mentioned above). In this way each spectra x_i is (approximately) represented by a point (u_i, v_i) in the plane. For each method, Figure 2 shows the (interpolated) surface formed by the predicted values $\widehat{y}_i$ (vertical axis) as a function of the multidimensional scaling representations (u_i, v_i), $i = 1, ..., n$ (in the horizontal plane). The points (u_i, v_i, y_i) that represents the original fat percentage values y_i corresponding to the spectra x_i are also plotted as asterisks.

It is observed that Figure 2 further corroborates the nice goodness of fit attained by the three estimation methods considered, as well as the shape similarity of their estimates of the regression functional.

However, two advantages of SVR should be highlighted. First, it showed a slightly better prediction accuracy as reflected by all error measures in Table 1. Second, SVR achieved about 20% of dimensionality reduction by retaining from the original data (100%) only a proper subset of selected support vectors (80 %). This is in contrast to the other two methods that require to keep all the training data to predict a future sample.

6   Conclusions and Final Remarks

This paper demonstrates the theoretic and practical viability of SVR methods for functional data inputs.

A comparison of the prediction errors among SVR and two other regression methods for functional nonparametric regression, namely RBF and NWK estimators, is presented on a spectroscopy benchmark data set. SVR exhibits the best performance in terms of absolute and relative measures of prediction accuracy, closely followed by RBF. An additional advantage of SVR was its capability for dimensionality reduction, which was around 20% in the analyzed data set. This in contrast to the other two methods that must retain all the training data in order to make a prediction for a new sample.

Notwithstanding, it should be noted that computing SVR estimates involves slightly larger learning times and number of tuning hyperparameters than RBF and NWK methods.

On the theoretic side, we emphasize the important open problem of developing methods for constructing nnd kernels with desired smoothness properties on infinite-dimensional functional spaces. Results derived in the present paper offer some classes of nnd kernels for functional data, such as α-stable kernels that have long tails. Further research is necessary to explore their practical relevance, and to widen the toolkit of nnd kernels for FD.

We also recommend to take into account in future investigations on similar data sets the possible influence of spectral preprocessing in the quality of regression estimates.

We conclude that SVR for FD appears as a promising and competitive tool for functional nonparametric regression tasks in practice due to its approximation flexibility and its capability for dimensionality reduction.

References

1. Aguilera, A.M., Ocana, F., Valduama, M.J.: An approximated principal component prediction model for continuous-time stochastic processes. Appl. Stochastic Models Data Anal. 13, 61–72 (1999)
2. Bousquet, O., Elisseef, A.: Stability and Generalization. J. of Machine Learning Research 1 (2002)
3. Cardot, H., Ferraty, F., Sarda, P.: Functional linear model Statist. Probab. Lett. 45, 11–22 (1999)
4. Geladi, P.: Chemometrics in spectroscopy: Part 1. Classical Chemometrics. Spectrochem. Acta, Part B 58, 767–782 (2003)
5. Eugeniou, T., Pontil, M., Poggio, T.: Regularization networks and Support Vector Machines. In: Smola, A.J., Bartlettt, P.L., Schölkopf, B. (eds.) Advances in Large Margin Classifiers, pp. 171–203. The MIT Press, Cambridge (2000)
6. Ferraty, F., Vieu, P.: Nonparametric models for functional data with application in regression, time series prediction and curve discrimination. J. Nonparametric Statist. 16, 11–125 (2004)
7. Ferraty, F., Vieu, P.: Nonparametric Functional Data Analysis. Springer Series in Statistics (2006)
8. Frank, J., Friedman, J.H.: A statistical view of some chemometrics regression tools. Technometrics 35, 109–148 (1993)
9. Preda, C., Saporta, G.: PLS regression on stochastic processes. Comput. Statist. Data Anal. 48, 149–158 (2005)
10. Preda, C.: Regression models for functional data by reproducing kernel Hilbert space methods. J. Statistical Planning and Inference 137, 829–840 (2007)
11. Some tools for functional data analysis. J. R. Stat. Soc. Ser. B 53, 539–572 (1991)
12. Ramsay, I., Silverman, B.: Functional Data Analysis. Springer, Heidelberg (1997)
13. Rossi, F., Conan-Gues, B.: Functional Multilayer perceptron: a nonlinear tool for functional data analysis. Neural Networks 18, 45–60 (2005)
14. Samorodnitsky, G., Taqqu, M.S.: Stable Non-Gaussian Random Processes. Chapman & Hall, New York (1994)
15. Schölkopf, B., Smola, A.: Learning with Kernels. The MIT Press, Cambridge (2002)
16. Swierenga, H.: Multivariate Calibration Model in Vibrational Spectroscopic Applications. PhD. Thesis, Univ. of Nijmegen, Nijmegen (2000)
17. Tecator dataset. available on statlib: http://lib.stat.cmu.edu/datasets/tecator
18. Wahba, G.: Spline Models for Observational Data. SIAM, Philadelphia (1990)

Monitoring Nonlinear Profiles Using Support Vector Machines

Javier M. Moguerza[1], Alberto Muñoz[2], and Stelios Psarakis[3]

[1] University Rey Juan Carlos, Camino del Molino s/n, 28943 Fuenlabrada, Spain
`javier.moguerza@urjc.es`
[2] University Carlos III, c/ Madrid 126, 28903 Getafe, Spain
`alberto.munoz@uc3m.es`
[3] Athens Univ. of Econ. and Business, 76 Patission Str., 10434 Athens, Greece
`psarakis@aueb.gr`

Abstract. In this work we focus on the use of SVMs for monitoring techniques applied to nonlinear profiles in the Statistical Process Control (SPC) framework. We develop a new methodology based on Functional Data Analysis for the construction of control limits for nonlinear profiles. In particular, we monitor the fitted curves themselves instead of monitoring the parameters of any model fitting the curves. The simplicity and effectiveness of the data analysis method has been tested against other statistical approaches using a standard data set in the process control literature.

Keywords. Kernel methods, Statistical Process Control, Support Vector Machines.

1 Introduction

The technique of Statistical Process Control (SPC) was introduced by Shewhart in 1924 [9]. The basic tools of SPC are the control charts. The central aim of control charts is the monitoring of processes, where the performance is determined by quality characteristics. In particular, control charts are useful to test the stability of a process. The process is often represented by a curve or function (called profile) that involves a response variable Y and a number of explanatory variables $(X_1, X_2, \ldots)$. The simplest profiles are generated by linear models, but often more realistic nonlinear models are demanded.

In this paper, we are concerned with a different class of profile data that cannot be adequately represented by a linear structured model. This kind of data are generally known as nonlinear profiles. Very little work has been done for monitoring of nonlinear profiles (see [17,5,3]). For an overview of profile monitoring techniques see [18].

There are two phases involved in the SPC methodology. In Phase I, an historical amount of process data is available and has to be analyzed. The targets here are to test the stability of the process, to understand the variation in the process over time and to model the in-control process performance. In Phase II,

the goal is to monitor the process. Using on-line data, the system (adjusted in Phase I) has to perform a quick detection of shifts.

In Multivariate SPC, when the underlying distribution of the quality characteristics is not multivariate normal, the design of the control limits is not trivial, and regression Support Vector Machines (SVMs) may be used to design a control boundary limits which adapt to the shape of the data. In this work we propose a technique for Phase I analysis of nonlinear profiles using SVMs.

The rest of the paper is organized as follows. In Section 2 some background on profiles is given. In Section 3 SVMs for regression are briefly described. In Section 4 we show how to use SVMs for the monitoring of nonlinear profiles, and our method is compared to other state-of-the-art methods. Section 5 concludes.

2 Basics on Profiles

Profile data consist of a set of measurements with a response variable Y and one or more explanatory variables $X^{(i)}$, $i \in \{1, \ldots, k\}$. The explanatory variables are used to assess the quality of a manufactured item. In the case of linear profiles we have a linear regression model with a response variable Y and the vector of explanatory variables $X = (X^{(1)}, \ldots, X^{(k)})^T$,

$$Y = A_0 + A_1^T X + \varepsilon \ ,$$

where ε is the random error, A_0 is a constant and A_1 is a vector of parameters.

Applying the linear profile, we have to pool n set points $x_1, \ldots, x_n \in \mathbb{R}^k$. For the sample i the process output is:

$$y_i = A_0 + A_1^T x_i + \varepsilon_i \ , \ \text{with } i \in \{1, \ldots, n\} \ ,$$

where ε_i are random variables, independent and normally distributed with mean zero and variance σ^2. The estimations of the vector A_1 and the intercept A_0 can be obtained using the least squares method (see [4]).

The extension of the linear model to the nonlinear case is

$$Y = f(X, \beta) + \varepsilon \ ,$$

where ε is the random error, β is a vector of parameters and f is a nonlinear function. Unlike linear profiles, which can be represented by a linear regression model whose regression model parameters can be used for monitoring and detection, nonlinear profiles are often sampled into high dimensional data vectors and analyzed by non-parametric methods. Examples of nonlinear profiles are given in [15,16].

3 Regression Support Vector Machines in a Nutshell

It is usual in SVMs tutorials to consider the regression problem from a geometric point of view. Consider a regression problem where the regression function is

nonlinear. The idea underlying Regression Support Vector Machines [13,2] is to map the data into a "Feature Space" so that the estimated regression function becomes linear. This mapping, denoted Φ in the sequel, determines a dot product K in the Feature Space, called kernel, of the form $K(x, y) = \Phi(x)^T \Phi(y)$.

Regression SVMs work by solving the following optimization problem:

$$
\begin{aligned}
\min_{w,b,\xi,\xi'} \quad & \frac{1}{2}\|w\|^2 + C\sum_{i=1}^{n}(\xi_i + \xi_i') \\
\text{s.t.} \quad & (w^T\Phi(x_i) + b) - y_i \leq \varepsilon + \xi_i \; i = 1, \ldots, n\,, \\
& y_i - (w^T\Phi(x_i) + b) \leq \varepsilon + \xi_i' \; i = 1, \ldots, n\,, \\
& \xi_i, \xi_i' \geq 0 \qquad\qquad\qquad i = 1, \ldots, n\,.
\end{aligned}
\tag{1}
$$

Notice that ε appears only in the constraints, forcing the solution to be calculated taking into account a confidence band around the regression equation (see Figure 1).
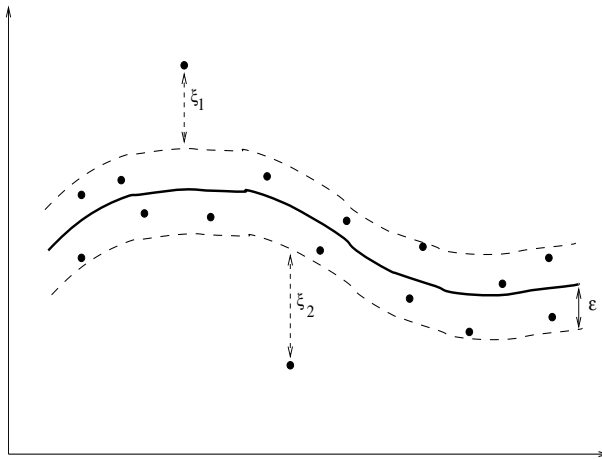
Fig. 1. Support Vector Regression

The ξ_i and ξ_i' are slack variables that allow for some data points to stay outside the confidence band determined by ε. This is the standard support vector regression formulation. This optimization problem is convex and therefore, it has no local minima. The linear regression equation will take the form:

$$
R^*(x) = w^{*T}\Phi(x) + b^*\,,
$$

where w^* and b^* are the values of w and b at the solution of the previous optimization problem. Notice that the inclusion of the mapping implies nonlinearity.

It can be shown that the problem described above can be stated as a regularization problem [12]. Regularization methods include, among others, smoothing splines [14] or kriging [1]. Regularization allows the construction of smooth

functions. In fact, it can be shown (see, for instance [7,8]) that the previous problem can be formulated as a regularization problem of the form:

$$\min_{f \in H} \ \frac{1}{n} \sum_{i=1}^{n} L(y_i, f(x_i)) + \mu \|f\|_K^2 \,, \tag{2}$$

where $\mu > 0$, H_K is the Reproducing Kernel Hilbert Space (RKHS) associated to the kernel K, $\|f\|_K$ denotes the norm of f in the RKHS, (x_i, y_i) are the sample data points, and $L(y_i, f(x_i)) = (|f(x_i) - y_i| - \varepsilon)_+$, $\varepsilon \geq 0$ is known as the 'ε-insensitive loss' function. By the Representer Theorem (see, for instance [7]), the solution to problem (2) has the form $f(x) = \sum_{i=1}^{n} \alpha_i K(x_i, x) + b$, where x_i are the sample data points. Notice that the penalization term $\mu \|f\|_K^2$ in eq. (2) favours the choice of smooth solutions to the optimization problem under consideration. It is immediate to show that $\|f\|_K^2 = \|w\|^2$, where $w = \sum_i^n \alpha_i \Phi(x_i)$ and Φ is the mapping defining the kernel function. In this way, $R^*(x) = f(x)$.

4 An Application of SVMs to Nonlinear Profiles

We will apply Regression SVMs to the example given in [15,16,18]. The data set is made up of 24 curves, each one corresponding to a vertical density profile (VDP). These data come from the manufacture of engineered woodboards. In the production of engineered wood boards the control of the density properties of the boards produced is crucial. Multiple measurements on a sample (usually a 2×2 inch piece) to form the vertical density profile of the board have been taken. Figure 2 shows the 24 profiles. Each one consists of 314 measurements taken 0.002 inches apart. The VDPs are divided in three groups. Each group is made up by boards selected in the same 8-hour shift. Group 1 consists of 9 boards $(1,\ldots, 9)$, group 2 consists of 11 boards $(10,\ldots, 20)$, and group 3 consists of 4 boards $(21,\ldots, 24)$.
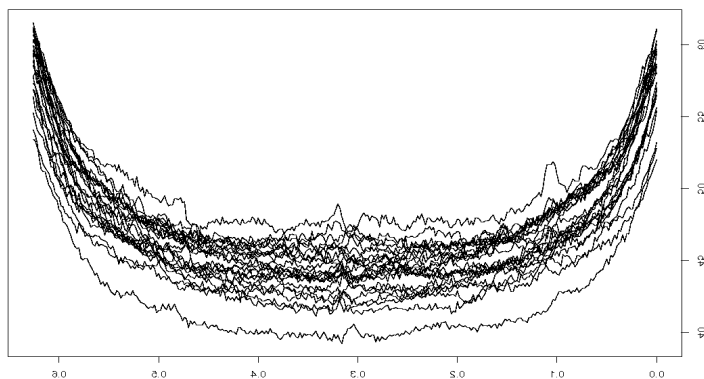
Fig. 2. 24 profiles. Each one consists of 314 measurements

The way in which we will apply Regression SVMs for profile monitoring falls into the area of Functional Data Analysis [11]. We will calculate the control limits by regularizing the percentile curves obtained from the profiles. Figure 3 shows, in bold, the 0.005 and 0.095 percentiles for the 24 curves. Between both percentiles, 99% percent of the curves should be contained. In the following application we will use the Gaussian kernel $K(x, y) = e^{-\|x-y\|^2/\sigma}$ with $\sigma = 0.025$, and in the SVM formulation we will take $C = 100$. The parameters have been fixed by cross-validation (see [14] and [6] for details).
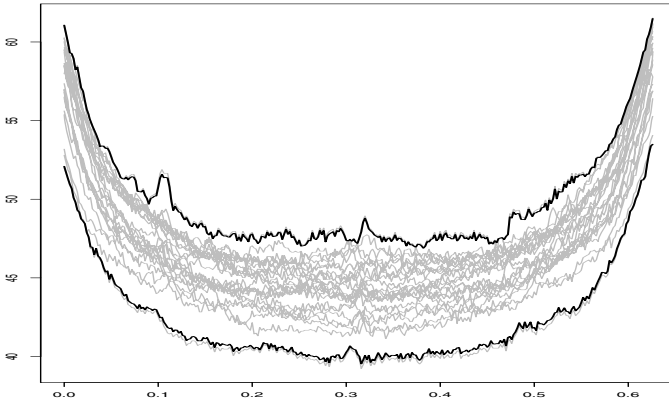
Fig. 3. 0.005 and 0.095 percentiles for the 24 curves

In order to obtain smooth control limits, we regularize these percentile curves using a Regression Support Vector Machine. Figure 4 shows the 24 curves and the regularized control limits in bold.

Using these control limits, outlying profiles can be calculated. In this application, we will consider a profile as out of bounds if its regularized version at some moment comes out of the band delimited by the upper or lower regularized control limits. The use of the regularized version of the profiles is justified by the need of avoiding the effect of the peaks of the nonregularized curves. Figure 5 shows the estimated curve for one of the profiles, in particular for the profile named 10. Figure 6 shows the regularized curves for all the profiles, and the control limits (the two bold curves).

Using our methodology, three profiles are obtained as out of bounds, in particular, profiles 3, 6 and 16. The regularized version of curve 3 is out of bounds 279 times, curve 6 is out of bounds 296 times and curve 16 is out of bounds 11 times. The remaining curves remain always between the control limits. Since each profile consists of 314 measurements, we may design a measure (taking values between 0 and 1) to decide how outlying is a profile (the proportion of time that its regularized version is out of control). In this way, the results for these three profiles are 0.89, 0.94 and 0.035, respectively. Figure 7 shows the outlying regularized profiles (black lines) and the control limits (dashed lines).
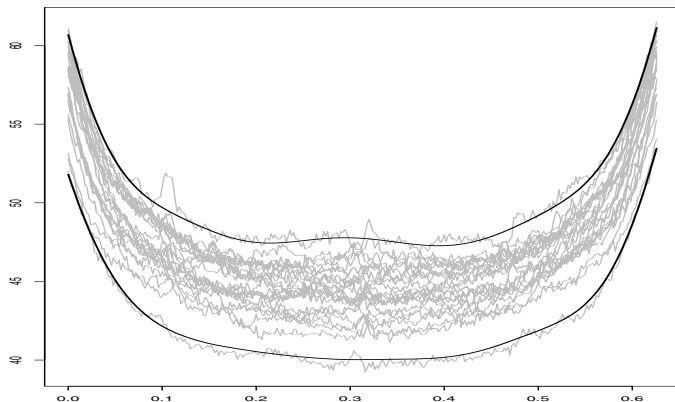
Fig. 4. The 24 curves and the regularized control limits in bold
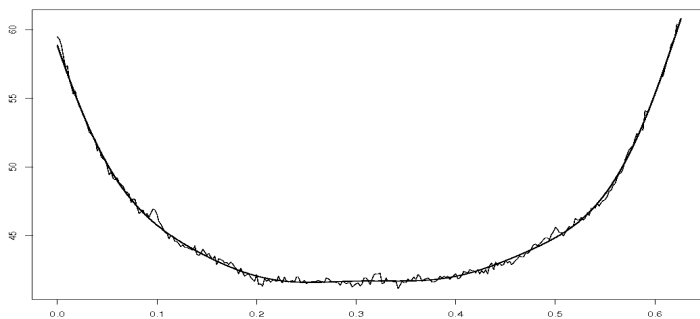
Fig. 5. Profile 10 and its corresponding regularized curve

Curves 3 and 6 are the ones clearly out of bounds, being their corresponding values for the outlying measure high, that is, 0.89 and 0.94 respectively. Curve 16 is out of bounds only in the tails of the lower control limit (being its measure 0.035, a low value). For the shake of completeness, Figure 8 shows the regularized control limits and the non-regularized version of the outlying curves.

Notice that using less restrictive criterions in order to decide whether a given curve is out of bounds (for instance, a percentage of times coming out of the limits), fewer curves would be considered as outlying ones.

4.1   Comparison with Other Methods

The analysis of nonlinear profiles has been previously afforded using standard statistical methods. In particular, in [17] three methods are applied to this data set. These methods are based on the monitoring of the parameters obtained by estimating each VDP using a 'bathtub' function model. Given the data points
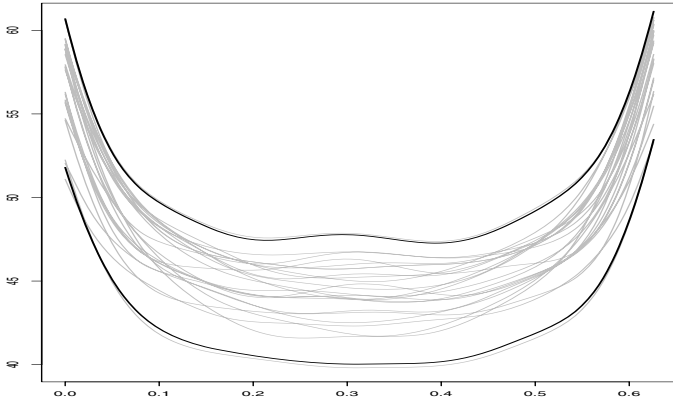
Fig. 6. The 24 regularized curves and the regularized control limits in bold

(x_i^k, y_i^k) for the ith profile (in our case $i \in \{1, \ldots, 24\}$, $k \in \{1, \ldots, 314\}$), the following model has to be estimated:

$$f_i(x_i^k, \beta_i) = \begin{cases} a_{i1}(x_i^k - d_i)^{b_{i1}} + c_i & , x_i^k > d_i \, , \\ a_{i2}(-x_i^k + d_i)^{b_{i2}} + c_i & , x_i^k \leq d_i \, , \end{cases} \tag{3}$$

where x_i^k is the kth regressor variable value for the ith profile, and $\beta_i = (a_{i1}, a_{i2}, b_{i1}, b_{i2}, c_i, d_i)^T$ is the vector of parameters corresponding to the model estimating the ith profile. Notice that there exists a 'bathtub' model for each of the 24 profiles. Once β_i has been estimated by $\hat{\beta}_i$, $i \in \{1, \ldots, 24\}$, three covariance matrices S_1, S_2 and S_3 (for methods 1, 2 and 3, respectively) are calculated (see [17] for details). Then three T^2-statistics of the form $T_i^2 = (\hat{\beta}_i - \bar{\hat{\beta}}_i)^T S_i^{-1}(\hat{\beta}_i - \bar{\hat{\beta}}_i)^T$, $i \in 1, 2, 3$ are calculated in order to monitor the parameters simultaneously. These T_i follow standard statistical distributions and control limits can be calculated.

In [17] it is shown that, for the three statistics, board 15 is outlying. For two of the three statistics board 18 is borderline, while the third statistic indicates that boards 4, 9, 18 and 24 are outliers. It is apparent that none of these boards are outliers as they are included within the calculated control limits.

4.2 Principal Component Analysis

The results obtained with the regularization methodology are coherent with the ones of the following experiment. We have considered each profile as a single data point of dimension 314. Then, we have made a Principal Component Analysis (PCA) on the 24 profiles. The first principal component explains 98% of the variability. Figure 9 shows the 24 profiles projected on this first principal component, with profiles 3, 6 and 16 in bold. It is clear that the most outlying
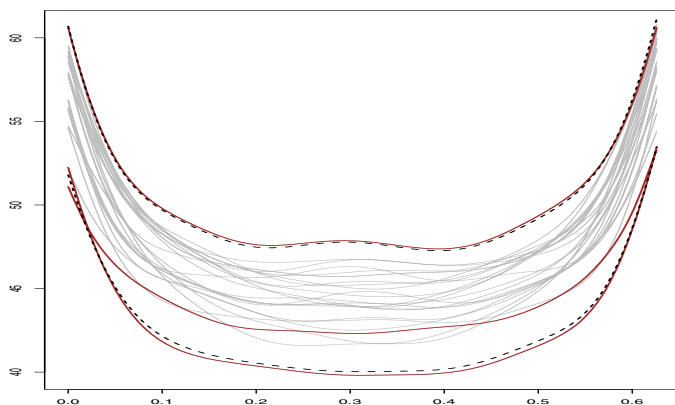
Fig. 7. Outlying regularized curves. Control limits in dashed.
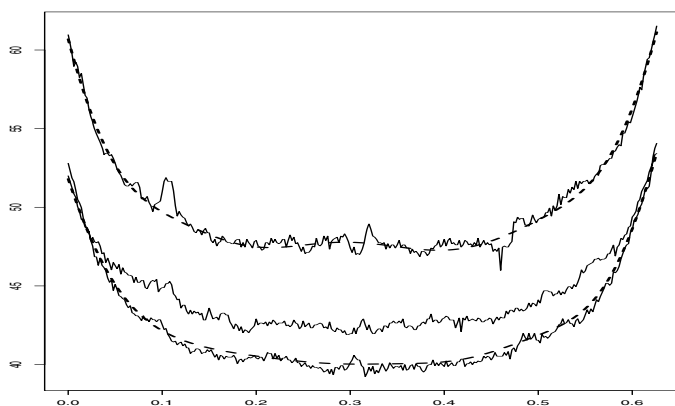
Fig. 8. Regularized control limits (dashed) and the non-regularized version of the outlying curves
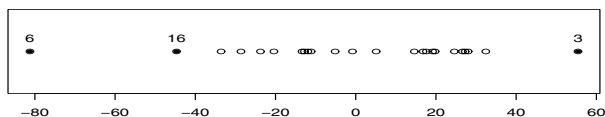
Fig. 9. The 24 profiles projected on the first principal component, with profiles 3, 6 and 16 in bold

profiles are these three ones, being profiles 3 and 6 the most outlying ones. The PCA method can be considered a qualitative method rather than a quantitative one. Therefore, it does not provide a decision value to determine if a given profile can be considered as an outlier, while the method that we propose does.

5   Conclusions

In this work we have developed a new methodology based on Functional Data Analysis for the construction of control limits for nonlinear profiles. Our technique is not based in the monitoring of the parameters of any model fitting the curves. Instead, we monitor the fitted curves themselves. Therefore, we do not need to find a particular nonlinear regression model that must adapt to the particular shape of the profiles in each case. The use of the regularized curve corresponding to each profile has the effect of automatically considering the variability within the profile. Similarly, by building the percentile curves and the control limits we are taking into account the variability among different profiles.

The simplicity and effectiveness of the data analysis method has been tested against other statistical approaches using a standard data set in the process control literature. In particular we have shown that our method outperforms other state-of-the-art methods in term of outlying board detection.

Further research will include the study of density estimation methods to detect the outlying curves, by considering the profiles as data points in a functional data space. To this aim, we will extend the techniques presented in [10] to the functional data case.

References

1. Cressie, N.: Statistics for Spatial Data. Wiley, Chichester (1993)
2. Cristianini, N., Shawe-Taylor, J.: An Introduction to Support Vector Machines. Cambridge University Press, Cambridge (2000)
3. Ding, Y., Zeng, L., Zhou, S.: Phase I Analysis for Monitoring Nonlinear Profiles in Manufacturing Processes. Journal of Quality Technology 38(3), 199–216 (2005)
4. Draper, N., Smith, H.: Applied Regression Analysis. Wiley, Chichester (1997)
5. Jensen, W.A., Birch, J.B., Woodall, W.H.: Profile Monitoring via Linear Mixed Models. Journal of Quality Technology (to appear, 2007)
6. Keerthi, S.S., Lin, C.J.: Asymptotic behaviors of support vector machines with Gaussian kernel. Neural Computation 15, 1667–1689 (2003)
7. Moguerza, J.M., Muñoz, A.: Support Vector Machines with Applications. Statistical Science 21(3), 322–336 (2006)
8. Moguerza, J.M., Muñoz, A.: Rejoinder to Support Vector Machines with Applications. Statistical Science 21(3), 358–362 (2006)
9. Montgomery, D.C.: Introduction to Statistical Quality Control, 2nd edn. Wiley, Chichester (1990)
10. Muñoz, A., Moguerza, J.M.: Estimation of high density regions using One-Class Neighbor Machines. IEEE Trans. on Pattern Analysis and Machine Intelligence 28(3), 476–480 (2006)
11. Ramsay, J.O., Silverman, B.W.: Functional Data Analysis. Springer, Heidelberg (1997)

12. Tikhonov, A.N., Arsenin, V.Y.: Solutions of ill-posed problems. John Wiley & Sons, New York (1977)
13. Vapnik, V.: The Nature of Statistical Learning Theory. Springer, New York (1995)
14. Wahba, G.: Spline Bases, Regularization, and Generalized Cross Validation for Solving Approximation Problems with Large Quantities of Data. In: Cheney, W. (ed.) Approximation Theory III, pp. 905–912. Academic Press, London (1980)
15. Walker, E.: Determining the Smoothing Parameter in Penalized Regression Splines Using Model Selection Criteria. Talk to the IMPS, Osaka, Japan (2001)
16. Walker, E., Wright, W.P.: Comparing Curves with Additive Models. Journal of Quality Technology 34(1), 118–129 (2002)
17. Williams, J.D., Woodall, W.H., Birch, J.B.: Statistical Monitoring of Nonlinear Product and Process Quality Profiles. Quality and Reliability Engineering International (to appear, 2007)
18. Woodall, W.H., Spitzner, D.J., Montgomery, D.C., Gupta, S.: Using Control Charts to Monitor Process and Product Quality Profiles. Journal of Quality Technology 36, 309–320 (2004)

MP-Polynomial Kernel for Training Support Vector Machines

Iván Mejía-Guevara[1] and Ángel Kuri-Morales[2]

[1] Instituto de Investigaciones en Matemáticas Aplicadas y Sistemas (IIMAS),
Universidad Nacional Autónoma de México (UNAM),
Circuito Escolar S/N, CU, 04510 D. F., México
`imejia@uxmcc2.iimas.unam.mx`
[2] Departamento de Computación, Instituto Tecnológico Autónomo de México,
Río Hondo No. 1, 01000 D. F., México
`akuri@itam.mx`

Abstract. In this article we present a new polynomial function that can be used as a kernel for Support Vector Machines (SVMs) in binary classification and regression problems. We prove that this function fulfills the mathematical properties of a kernel. We consider here a set of SVMs based on this kernel with which we perform a set of experiments. Their efficiency is measured against some of the most popular kernel functions reported in the past.

Keywords: MP-Polynomial Kernel, Kernel Methods, Support Vector Machine.

1 Introduction

Kernel methods have been a matter of study in the last years given their remarkable power and robustness to tackle nonlinear systems. Any kernel method solution comprises two parts: a) A module that performs the mapping into a high dimensional feature space and b) A learning algorithm designed to discover linear patterns in that space. Part (b) has been the focus of research in statistics and machine learning for decades, while part (a) rests on kernel functions. These kernel functions make it possible to represent linear patterns and ensure adequate representational power in higher-dimensional spaces [1]. In particular, a SVM is a kernel method that has been successfully used in recent years for the solution of a multiplicity of practical applications.

The use of kernel functions in SVMs aims at the solution of non-linearly separable classification and non-linear regression problems. Some conditions must be fulfilled by those functions in order to be considered valid kernels. The main purposes of this article are: a) To propose a new polynomial kernel, b) To describe its implementation in SVMs and c) To compare its efficiency in the solution of classification and regressions tasks with some other kernels which have been used in previous applications of SVMs. In section 2, some important concepts regarding the characterization of kernel functions are discussed. In section 3 we

review the main elements of an SVM for classification and regression problems. In section 4 a new kind of polynomial kernel is advanced and we prove that this kernel fulfills the conditions of section 2. Finally, in section 5, some experiments are performed to exemplify our approach. We close with some conclusions and future work considerations.

2   Kernel Functions

All the concepts and formal statements presented here were taken from [1], where a complete analysis of kernel methods and their applications is presented.

Definition 1 (finitely positive semi-definite functions). *A function:*

$$\kappa : XxX \to R, \tag{1}$$

satisfies the finitely positive-definite property if it is a symmetric function for which the matrices formed by restriction to any finite subset of the space X are positive semi-definite.

A formal characterization of a Kernel function is shown here as follows:

Theorem 1. *(Characterization of kernels) A function*

$$\kappa : XxX \to R, \tag{2}$$

which is either continuous or has a countable domain, can be decomposed

$$\kappa(x, z) = \langle \phi(x), \phi(z) \rangle \tag{3}$$

into a future map ϕ into a Hilbert space F applied to both its arguments followed by the evaluation of the inner product in F if it satisfies the finitely positive-definite property.

Some properties of Kernels, which are called closure properties [1], are as follows:

$$
\begin{aligned}
\kappa(x, z) &= \kappa_1(x, z) + \kappa_2(x, z) \\
\kappa(x, z) &= a\kappa_1(x, z) \\
\kappa(x, z) &= \kappa_1(x, z)\,\kappa_2(x, z) \\
\kappa(x, z) &= f(x)\,f(z) \\
\kappa(x, z) &= \kappa_3(\phi(x), \phi(z)) \\
\kappa(x, z) &= x^T B z
\end{aligned}
\tag{4}
$$

where κ_1 and κ_2 are Kernels over XxX, $X \subseteq R^n$, $a \in R^+$, $f(.)$ a real valued function on X, $\phi : X \to R^N$ with κ_3 a kernel over $R^N xR^N$, and **B** a symmetric positive semi-definite $n_x n$ matrix.

The characterization of kernel functions, kernel matrices and the previous properties are needed to decide whether a candidate kernel is a valid one and to combine simple kernels to obtain more complex and useful ones.

3   Support Vector Machine

In the last decade of the past century the SVM approach was discovered by [2] and has been studied and applied in multiple practical applications [3] [4] [5]. A broad and conscientious exposition of this methodology can be found in [6] and [7].

3.1   Classification

In the case of binary pattern classification with SVM, a training sample $\tau = \{x_i, d_i\}_{i=1}^{N}$ is considered where x_i is the input pattern and d_i is the target output. When attempting pattern classification, the goal is to find a hyper-surface that allows the separation of the objects in the sample into two classes: the first class should be on one side of the surface $d_i = 1$ and the second class on the other side $d_i = -1$. The distance of the nearest points of both classes is called the margin of separation and the optimal surface considered to have been found when such margin is maximized. The optimal surface is known as Optimal Hyperplane (OHP)[2].

The objective of the SVM is to find the OHP for a given training set. This results in a constrained optimization problem. In practice a Quadratic Optimization Problem (QOP) is formulated in order to solve it. However, its dual formulation is more adequate, since only the Lagrange Multipliers (LMs) of the QOP need to be found. The dual form is as follows:

$$Max_\alpha \ \sum_{i=1}^{N} \alpha_i - \frac{1}{2} \sum_{i=1}^{N} \sum_{j=1}^{N} \alpha_i \alpha_j d_i d_j K\left(x_i, x_j\right)$$

$$s.t. : \ \sum_{j=1}^{N} \alpha_i^* d_i = 0 \tag{5}$$

$$0 \le \alpha_i \le C$$

The solution of (5) is given by $\alpha_i, i = 1, 2, ..., N$; C is known as the *regularization parameter* and appears in (5) as an upper bound for each α_i. This parameter controls the trade-off between the complexity of the SVM and the number of acceptable misclassifications (a low value for C corresponds with a higher proportion of errors allowed in the solution, while fewer errors are permissible for high C values). The kernel function, $K\left(x, x_i\right)$, is used to construct a decision surface that is nonlinear in the input space but whose image in the feature space is linear. Once the solution of (5) is found, a function classifier is determined through the following expression:

$$f\left(\mathbf{x}\right) = \sum_{i=1}^{N} \alpha_i K\left(x, x_i\right) + b \tag{6}$$

where the points corresponding with $\alpha_i \ne 0$ are called support vectors.

3.2   Nonlinear Regression

In the case of nonlinear regression problems, the training set is analogous to the one used for classification problems; however, the values for d_i are continuous. Given this training set, the goal of SVM is to find a function $f(\mathbf{x})$ such that $\left| f(x) - \hat{d}_i \right| < \epsilon$ for each element and a small ϵ. In other words, errors are disregarded as long as they are smaller than a properly selected ϵ. The function $f(\mathbf{x})$ has the a similar form as in the classification problems and it can also be found by solving a QOP. The dual form of this optimization problem is, as before, more appropriate. The dual formulation is as follows:

$$Max_{\alpha,\alpha^*} \quad -\frac{1}{2} \sum_{i=1}^{N} \sum_{j=1}^{N} \left(\alpha_i - \alpha_i^* \right) \left(\alpha_j - \alpha_j^* \right) K\left(x_i, x_j \right)$$

$$-\epsilon \sum_{i=1}^{N} \left(\alpha_i + \alpha_i^* \right) + \sum_{i=1}^{N} y_i \left(\alpha_i - \alpha_i^* \right) \qquad (7)$$

$$s.t.: \sum_{j=1}^{N} \left(\alpha_i - \alpha_i^* \right) = 0$$

$$\alpha_i \alpha_i^* \in [0, C]$$

The regularization parameter $C > 0$ determines the tradeoff between the flatness of $f(x)$ and the acceptable number of points with deviations larger than ϵ. The value of ϵ is inversely proportional to the number of support vectors $((\alpha_i - \alpha_i^*) \neq 0)$ [7]. An adequate determination of C and ϵ is needed for a proper solution. Their determination is explained in section 4.

Once the solution of (7) is obtained, the support vectors are used to construct the following regression function:

$$f(\mathbf{x}) = \sum_{i=1}^{N} \left(\alpha_i - \alpha_i^* \right) K\left(x, x_i \right) + b \qquad (8)$$

We wish to emphasize that in both formulations (classification and regression) the kernel is used to train the SVM and to construct the classifier and regression function, respectively.

3.3   Polynomial Kernel

Many functions can be used as kernels, but only if they fulfill Mercer's theorem [8] and the conditions of section 2. Some of the most popular kernels discussed in the literature are the radial basis functions, the perceptrons and the algebraic polynomials. In this paper we focus on the last one and we compare its accuracy versus the one obtained with more complex polynomials.

$$K(\mathbf{x}, \mathbf{x}_i) = (1 + \mathbf{x}.\mathbf{x}_i)^p \qquad (9)$$

For instance, if m=2 and p=2, equation (9) is as follows:

$$K\left(\mathbf{x}, \mathbf{x}_i\right) = 1 + x_1^2 x_{i1}^2 + 2x_1 x_2 x_{i1} x_{i2} + x_2^2 x_{i2}^2 + 2x_1 x_{i1} + 2x_2 x_{i2} \tag{10}$$

Of particular interest here is the degree of this kind of kernel which corresponds to the parameter p in (9). The selection of this parameter is very important not only for SVMs but also for other approaches where polynomial kenels are used. This parameter determines the complexity of the model and affects its accuracy. For that reason, different approaches have been proposed in the past for its optimal selection [9] [10].

4   MP-Polynomial Kernel

Consider the following function:

$$F\left(\mathbf{x}\right) = \sum_{j_1}^{\rho} \sum_{j_2}^{\rho} \cdots \sum_{j}^{\rho} a_{j_1, j_2, \ldots, j} \left(x_1^{j_1} x_2^{j_2} \ldots x_m^j\right) \tag{11}$$

We algebraically show that function (11) may be used as a valid kernel. The first disadvantage in trying to use this expression is that it holds as an argument an m-dimensional vector whereas a kernel requires two arguments. This problem was solved considering the following expression:

$$K\left(\mathbf{x}, \mathbf{x}_i\right) = \sum_{j_1}^{\rho} \sum_{j_2}^{\rho} \cdots \sum_{j}^{\rho} \left(x_1^{j_1} x_2^{j_2} \ldots x_m^j\right) \cdot \left(x_{i1}^{j_1} x_{i2}^{j_2} \ldots x_{im}^j\right) \tag{12}$$

where $\mathbf{x}$ is a vector representing an element of the training set, with m independent variables and x_i, the i-th object taken from this set. Notice that the functional structure of (11) and (12) is rather similar except for the term $\left(x_1^{j_1} x_2^{j_2} \ldots x_m^j\right)$, which was gotten from the elements of x_i, but that it may be considered as a constant. The structure of (12) now does indeed have a kernel structure. It just remains to be proven that it complies with the mathematical requirements, as is now established:

Proposition 1. *The expression in (12) is a function with domain in $R^m x R^m$ and satisfies the required conditions for being a valid kernel.*

Proof (of proposition). The first step in this proof relies on the observation that the expression in (12) may be represented in the form:

$$K\left(\mathbf{X}, \mathbf{X}_i\right) = \left[X_{j1} \otimes X_{j2} \otimes \cdots \otimes X_{jm}\right]^T \cdot \left[X_1 \otimes X_2 \otimes \cdots \otimes X_m\right] \tag{13}$$

where,

$$X_i = \begin{pmatrix} x_i^0 \\ x_i^1 \\ x_i^2 \\ \ldots \\ x_i^{(1+p)} \end{pmatrix}, \ X_{ji} = \begin{pmatrix} x_{ji}^0 \\ x_{ji}^1 \\ x_{ji}^2 \\ \ldots \\ x_{ji}^{(1+p)} \end{pmatrix},$$

and $\otimes$ is Kronecker's matrix product. Therefore, expounding and applying the properties of a kernel we get:

$$
\begin{aligned}
K\left(\mathbf{X}, \mathbf{X}_i\right) &= \left[X_{j1} \otimes X_{j2} \otimes \cdots \otimes X_{jm}\right]^T \cdot \left[X_1 \otimes X_2 \otimes \cdots \otimes X_m\right] \\
&= \Phi\left(X_j\right)^T \cdot \Phi\left(X\right) \\
&= \left[\Phi_1\left(X_j\right), \cdots, \Phi_{(1+p)}\left(X_j\right)\right] \cdot \left[\Phi_1\left(X\right), \cdots, \Phi_{(1+p)}\left(X\right)\right]^T \\
&= \sum_{k=1}^{(1+p)} \Phi_k\left(X_j\right) \cdot \Phi_k\left(X\right) \\
&= \sum_{k=1}^{(1+p)} i_k^T \left[x_{j1} \otimes x_{j2} \otimes \cdots \otimes x_{jm}\right]^T \cdot i_k^T \left[x_1 \otimes x_2 \otimes \cdots \otimes x_m\right] (14)
\end{aligned}
$$

where i_k^T is a vector having $0's$ in all his positions except for the kth one, in which it takes the value of 1.

$$
K\left(\mathbf{X}, \mathbf{X}_i\right) = \sum_{k=1}^{(1+p)} \left(x_{j1}^{[k]} \cdot x_{j2}^{[k]} \cdots x_{jm}^{[k]}\right)^T \cdot \left(x_1^{[k]} \cdot x_2^{[k]} \cdots x_m^{[k]}\right) \tag{15}
$$

In (15) we find a scalar product which may be grouped in couples as $x_{j1}^{[k]} x_1^{[k]}$ and from properties (4) the scalar product represents a kernel; in fact, it is the simplest possible one. Hence, we may put:

$$
K\left(\mathbf{X}, \mathbf{X}_i\right) = \sum_{k=1}^{(1+p)} \kappa\left(x_{j1}^{[k]}, x_1^{[k]}\right) \cdots \kappa\left(x_{jm}^{[k]}, x_m^{[k]}\right) \tag{16}
$$

Finally, according to properties (4), the kernel product is in itself a kernel, so we have that:

$$
K\left(\mathbf{X}, \mathbf{X}_i\right) = \sum_{k=1}^{(1+p)} \kappa^{[k]}\left(x_j, x\right) \tag{17}
$$

This last expression is simple a summation of kernels which, from properties (4), also results in a valid kernel, which completes the proof.

We had called this new kernel as MP-Polynomial Kernel (MPK). A simple example of this kernel is as follows: if we assume two independent variables (m=2) and a degree p=2. Then $K\left(\mathbf{X}, \mathbf{X}_j\right) = \left[X_{j1} \otimes X_{j2}\right]^T \cdot \left[X_1 \otimes X_2\right]$, where:

$$
X_1 \otimes X_2 = \left[x_1^0 x_2^0, x_1^0 x_2^1, x_1^0 x_2^2, x_1^1 x_2^0, x_1^1 x_2^1, x_1^1 x_2^2, x_1^2 x_2^0, x_1^2 x_2^1, x_1^2 x_2^2\right]
$$
$$
X_{j1} \otimes X_{i2} = \left[x_{j1}^0 x_{i2}^0, x_{j1}^0 x_{i2}^1, x_{j1}^0 x_{i2}^2, x_{j1}^1 x_{i2}^0, x_{j1}^1 x_{i2}^1, x_{j1}^1 x_{i2}^2, x_{j1}^2 x_{i2}^0, x_{j1}^2 x_{i2}^1, x_{j1}^2 x_{i2}^2\right]
$$

which yields:

$$
K\left(\mathbf{X}, \mathbf{X}_i\right) = (x_1^0 x_{j1}^0)(x_2^0 x_{i2}^0) + \ldots + (x_1^2 x_{j1}^2)(x_2^2 x_{i2}^2) \tag{18}
$$

Given this result, it turns out that it is possible to train an SVM using this new kernel. It only remains to verify the convenience of its adoption in practical cases. To this effect we performed a set of experiments regarding binary classification (i.e. the one involving only two classes) and non-linear regression. An important point in showing the validity of MPK is that its use is not limited to applications involving SVMs but, rather, it may also be applied as the basis for other kernel based methods.

5   Experiments and Results

It is well known that two key properties are required for a kernel to be used in practice [1]. The first one requires that the kernel retains the measure of similarity appropriate to the particular task or domain. The second is that its evaluation should not be computationally intensive. The purpose of this section is determine experimentally if these properties are fulfilled by the MPK.

Two different tasks were tackled in this section: binary classification and regression. The dataset for classification was taken from UCI Machine Learning Repository. It refers to the identification of two kinds of diabetes. In case of regression, the data also has to do with diabetes, but now it refers to the study of the factors affecting patterns of insulin-dependent diabetes mellitus in children[1]. The diabetes classification (DC) dataset consist of 750 instances and 8 features. The diabetes-regression (DR) dataset has 43 cases and 2 features.

To analyze the performance of SVM in the solution of these tasks we used two popular kernels (polynomial in (9) and Gaussian) to compare their accuracy and efficiency with the MP-Polynomial Kernel.

In the case of classification, one statistical approach suggested by [11] was used. This test is known as 5x2cv paired t test, based in 5 iterations of 2-fold cross-validation. In each replication of the test, the available data are partitioned into two equal-sized sets S1 and S2. The comparison of two different algorithms, for example RBF-SVM vs MPK-SVM[2], is made by subtracting their corresponding error estimates in the application of 2-fold cross-validation in each replication. The means and variances (s_i^2) are also successively estimated and finally a t statistic is defined:

$$\widetilde{t} = \frac{p_{(1)}^1}{\sqrt{\frac{1}{5}\sum_{i=1}^5 s_i^2}} \tag{19}$$

This is called 5x2vc $\widetilde{t}$ statistic and it has an approximate t distribution with 4 degrees of freedom. The value of $p_{(1)}^1$ represents the difference between the estimated errors for the two algorithms in the first replication. The comparison of two algorithms is based on the null hypothesis that there is no difference between their performances. The null hypothesis is rejected if $|\tilde{t}| > t_4$.

---

[1] This dataset can be downloaded from:
http://www.liacc.up.pt/ ltorgo/Regression/DataSets.html
[2] RBF-SVM stands for an SVM trained with a Radial Basis Function kernel and similar to MPK-SVM.

The results of the comparison of MPK-SVM vs the other kernels are shown in Table 1. It is important to remark that we used Matlab's program of [12] which was designed to train SVM for classification and regression problems. We modified this algorithm in order to compute the MPK.

The results of the tests for the diabetes classification problem are shown in Table 1, where the values of the $\tilde{t}$ statistics for the hypothesis: 1) $\hat{p}_p - \hat{p}_{mp} = 0$, 2) $\hat{p}_p - \hat{p}_g = 0$ and 3) $\hat{p}_{mp} - \hat{p}_g = 0$, where $\hat{p}_p$, $\hat{p}_{mp}$ and $\hat{p}_g$ are the estimated errors for PK-SVM[3], MPK-SVM and RBF-SVM, respectively, are shown in the second column. The third column of Table 1 indicates that there is no statistical evidence to reject the null hypothesis in any case, i.e., there is no strong evidence supporting the idea that any algorithm is better than any other one. The parameter selection for the SVM was determined using 6-fold Cross Validation, so that the parameters for the polynomial kernels (MPK-SVM and PK-SVM) are C=16, p=1 and for the RBF-SVM are C=2, $\sigma_k = 0.6$. In the case of regression

Table 1. Hyphotesis tests for classification accuracy

Test	t-statistic	Null Hyp
PK-SVM vs MPK-SVM	-0.12	No reject
PK-SVM vs RBF-SVM	0.41	No reject
MPK-SVM vs RBF-SVM	0.41	No reject

problems, the models were chosen once the parameters ϵ, C, p and σ were calibrated. Regarding the model trained with the radial basis kernel, the couple [C, ϵ] was determined following the methodology proposed by [13], where the value of C is calculated as the maximum value resulting from $\{\bar{y} - 3 * \sigma_y, \bar{y} + 3 * \sigma_y\}$ and the computation of ϵ was determined by $\epsilon = \sigma\tau\sqrt{ln(n)/n}$, being τ, σ and n, a parameter set to 3 [13], the noise deviation and the number data train, respectively. The calculation of σ required the computation of $\frac{\sum_{=1}(y_ - \hat{y}_)^2}{n-d}$; in this case, $\hat{y}$ represent the target values when a high order polynomial function is estimated using the training data. We applied the Genetic Multivariate approach [14] to estimate this polynomial and tried several degrees, choosing the one with the smallest Press statistic and the σ according with the best parameter of the radial basis function gotten from the application of Leave-one-Out Cross Validation (LoOCV). The Press statistic is used for model selection and is obtained by adding the square of the residual errors that result from training the SVM N times and leaving one observation out every time to determine the residual at every step[15]. Actually, the Press statistic and the methodology of LoOCV are equivalent in this case, since for any particular observation the squared residual and the mean squared error for that observation are the same. The parameters obtained from this method were: C=6.9082, $\sigma_k = 0.6$ and $\epsilon = 0.6779$

Since a similar analytical approach is not possible to calibrate C for polynomial kernels, we apply LoOCV for that purpose. We look for the best value that

---

[3] Stands for SVM trained with a classical polinomial kernel.

belongs to this set (1, 2, 4, 8, 16, 32, 64, 128, 254, 512, 1024). In the case of ϵ we used the value estimated for the radial basis function. The p parameter of the kernel function was chosen according with the lowest Press statistic (or LoOCV error) which reflects the best selection for the C parameter. The best values for C and p were 2 and 1, respectively.

In table 2, the Press statistic indicates that the MP-polynomial performs as well as the classical polynomial kernel; RBF based SVM performs better than SVMs based on the other polynomials. R^2 (which is a measure of the expressive capabilities of the learning machine) also supports that result. The LoOCV error is presented in column 3; it yields similar results.

Table 2. Hyphotesis tests for regression accuracy

Model	Press	R^2	LoO error
PK-SVM	14.4	0.34	0.34
MPK-SVM	14.5	0.33	0.34
RBF-SVM	12.5	0.43	0.29

According to the results shown, it is possible to assert that MP-polynomial kernel performs as well as the alternative classical counterparts tested in this paper for both classification and regression problems. Moreover, this kernel can also be used to represent the decision or regression function, derived from the application of SVMs, as an algebraic explicit expression, in which the relationship among independent variables and their powers is straightforward. This result has been explored with succes in the past using traditional polynomial kernels, where the resulting algebraic structure was compared with the one gotten from the application of Multivariate Polynomial Analysis [14]. However, two different structures were obtained. Fortunately, with the use of MPK is now possible to get the same algebraic stuctures with the use of those approaches and, hence, comparisons between them become also straighforward.

6   Conclusions

A new polynomial kernel (which we called "MP-Polynomial Kernel") is used to train a SVM in the solution of classification and regression problems. The characterization and mathematical proof of this function as a valid kernel was shown. The results of the experiments show that the use of this function for training SVMs is adequate in terms of accuracy. This conclusion is gotten by comparing its performance with other popular (polynomial and Gaussian) kernel functions. The statistical tests confirm this fact. An important advantage that we pointed out is the use of MP-polynomial kernel in the construction of an explicit algebraic expression as decision function of a SVM and its comparison with similar ones derived from other techniques. The use of this new kernel as a basis in applications with other kernel methods is a matter of future work.

References

1. Shawe-Taylor, J., Cristianini, N.: Kernel Methods for Pattern Analysis. CUP (June 2004)
2. Boser, B.E., Guyon, I., Vapnik, V.: A training algorithm for optimal margin classifiers. In: COLT, pp. 144–152 (1992)
3. Blanz, V., Scholkopf, B., Bulthoff, H.H., Burges, C., Vapnik, V., Vetter, T.: Comparison of view-based object recognition algorithms using realistic 3d models. In: ICANN, pp. 251–256 (1996)
4. Muller, K.-R., Smola, A.J., Ratsch, G., Scholkopf, B., K.J., Vapnik, V.: Predicting time series with support vector machines. In: ICANN, pp. 999–1004 (1997)
5. Weston, J., Gammerman, A., Stitson, M., Vapnik, V., Vovk, V., Watkins, C.: Density estimation using support vector machines (1997)
6. Burges, C.J.C.: A tutorial on support vector machines for pattern recognition. Data Mining and Knowledge Discovery 2(2), 121–167 (1998)
7. Smola, A., Schölkopf, B.: A tutorial on support vector regression (2004)
8. Haykin, S.: Neural networks: A comprehensive foundation. MacMillan, New York (1994)
9. Friedrichs, F., Igel, C.: Evolutionary tuning of multiple svm parameters. Neurocomputing 64, 107–117 (2005)
10. Min, J.H., Lee, Y.: Bankruptcy prediction using support vector machine with optimal choice of kernel function parameters. Expert Syst. Appl. 28(4), 603–614 (2005)
11. Dietterich, T.G.: Approximate statistical test for comparing supervised classification learning algorithms. Neural Computation 10(7), 1895–1923 (1998)
12. Gunn, S.: Support vector machines for classification and regression. Technical report (April 07, 1998)
13. Cherkassky, V., Ma, Y.: Practical selection of SVM parameters and noise estimation for SVM regression. Neural Networks 17(1), 113–126 (2004)
14. Kuri-Morales, A., Mejía-Guevara, I.: Analysis of algebraic expressions derived from genetic multivariate polynomials and support vector machines: A case study. In: Martínez-Trinidad, J.F., Carrasco Ochoa, J.A., Kittler, J. (eds.) CIARP 2006. LNCS, vol. 4225, pp. 974–984. Springer, Heidelberg (2006)
15. Rice, J.A.: Mathematical Statistics and Data Analysis. Duxbury Press, Good intermediary statistics book (1995)

Adaptive ECG Compression Using Support Vector Machine

Sándor M. Szilágyi[1], László Szilágyi[1,2], and Zoltán Benyó[2]

[1] Sapientia - Hungarian Science University of Transylvania,
Faculty of Technical and Human Science, Târgu-Mureş, Romania
`szs@ms.sapientia.ro`
[2] Budapest University of Technology and Economics,
Dept. of Control Engineering and Information Technology, Budapest, Hungary

Abstract. An adaptive, support vector machine based ECG processing and compression method is presented in this study. The conventional pre-filtering algorithm is followed by a characteristic waves (QRS, T, P) localization. The regressive model parameters that describe the recognized waveformes are determined adaptively using general codebook information and patient specific data. The correct regocnition ratio of the QRS waves was above 99.9% using single channels from the MIT-BIH database files. The adaptive filter properly eliminates the perturbing noises such as 50/60 Hz power line or abrupt baseline shift or drift. The efficient signal coding algorithm can reduce the redundant data about 12 times. The good balance among proper signal quality for diagnosis and high compression rate is yielded by a support vector machine based system. The properly obtained wave locations and shapes, using a high compression rate, can form a solid base to improve the diagnosis performance in clinical environment.

Keywords: signal compression, QRS clustering, support vector machine, adaptive estimation.

1 Introduction

Nowadays the computerized ECG signal processing can be considered a well-developed application. An on-line performing analyzer and encoder system must be able to evaluate the signal with maximum few seconds delay to recognize in time the potentially dangerous and life threatening arrhythmia. These systems are based on filtering, beat detection (recognition and clustering), classification, storage and diagnosis.

Despite the presence of serious perturbation, a reliable analysis must involve at least the detection of QRS complexes, T and P waves, automatic rhythm analysis, classification and diagnosis, enabling physicians to derive more information for cardiac disease diagnosis. To perform a reliable evaluation of the ECG, it is important to correctly determine the position and amplitude of every characteristic event, as they play an important role at producing the diagnosis. The performance of an optimally functioning computerized ECG filtering algorithm

is limited by the ability to separate the signal from artifacts, and by the amount and nature of distortion introduced by the filter. As a filter can perform much better using some predefined patient specific information, it is desired to use a post-filtering step to reduce the signal distortion. The speed and accuracy requirements during ECG processing represent a hard task, the varying shape of the ECG and the subjectivity of the diagnosis make it even harder.

The most important task in the ECG signal processing is the accurate localization of QRS complexes. The established QRS places constitute the basic a-priori information for all further processing steps. Many times the recorded ECG is disturbed by different kind of noises that can imply a pre-filtering or discarding of the studied segment. To assure the good quality of the ECG, and to prevent the loss of clinically significant information, the usage of human and artificial noise detection schemes is required. As the perturbing noise can only be diminished, but not eliminated from the measured signal, it is important to use processing methods with good noise susceptibility. The non-linear behavior of the human body requires adaptive processing that follows the patient's state.

The design of an optimal matched filter can increase the signal-to-noise ratio, but the non-stationary nature of the signal and noise in an ECG represents an obstacle in the application of these filters for QRS detection. A linear filter cannot properly whiten the non-linear ECG signal. Artificial neural networks (ANN) [12] are inherently non-linear models, so an ANN-based filtering is potentially useful. In practical use, the ANN model can adapt far better than linear models. The number of input units corresponds to the filter order that should not be increased too much, in order to assure constantly good transient properties. The selection of the right number of hidden layers is important to provide good learning speed and adaptation at the same time. After pre-processing, filtering, evaluation and model's parameter estimation, the signal reconstruction is needed. In this step, the post-filtering method knows the main ECG specific information, and can better separate all artificial noises. To create an efficient filter, it is necessary to use all ECG and patient dependent information. This problem can be handled only if the computer knows the formation of the ECG signal.

The collected noise during ECG signal acquisition makes almost meaningless the usage of loss-free compression [4]. In this paper we focused on lossy methods as a compromise between bandwidth and final reconstruction possibility, using sophisticated medical knowledge-based reconstruction algorithms [9]. The signal's main characteristics are represented by exponential parameterization that is delivered by a processing system that uses support vector machine (SVM) [5]. This robust model involves the filtering, analysis and compression step of an automatic ECG evaluation method.

2   Materials and Methods

The proposed complex ECG signal compression algorithm can be divided into the following steps (see Fig. 1):

- Irregular signal recognition and processing;
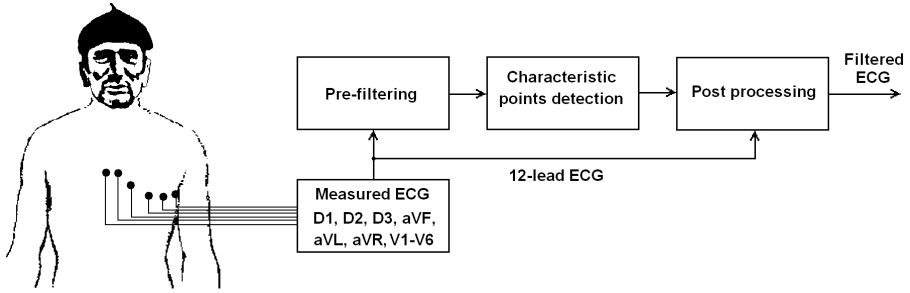
Fig. 1. The proposed ECG signal filtering, processing and compression

- Pre-filtering;
- Segmentation into R-R intervals, R-R period based filtering;
- Create/update a temporal template bank for whole beats;
- Determine all recognizable characteristic points (for R, T and P waves);
- R, T and P wave location based filtering;
- Extract the waveform estimation model's parameters;
- Post-filtering using pattern database and the model-based estimation;
- Complete the general and patient specific template bank for all recognized waves;
- Adjust long term prediction;
- Adaptive smoothing and advanced distortion analysis;
- Residual signal estimation, entropy coding, data storage, back-estimation;
- Medical parameter estimation and computer aided diagnosis.

Before starting the characteristic waveforms (R, T and P waves) recognition and proceed an accurate segmentation, we need to pre-filter the signal in order to eliminate all perturbing phenomena, like noise caused by the electrical network, the perturbing artifacts caused by bad contacts, motion or breathing. The elimination of the noise caused by the electrical network is recommended by windowed FFT and IFFT combined with a parameter estimator and filter, which contains the following steps:

- Perform a windowed FFT for an interval of length between five and twenty seconds. All intervals are overlapped by at least fifty percent of their length;
- Estimate the amplitude and phase of the 50 (60) Hz component and its harmonics from the amplitudes and phases of the adjacent frequencies;
- Modify the signal spectra;
- Process the IFFT algorithm;
- Performed a regressive elimination of the artificial noise caused by modifications in signal's spectra.

In our approach, because the studied signal has a non-linear behavior, we define a non-linear adaptive estimation algorithm. The main drawback of this

method is the cumbersomeness to determine the optimal phase of the 50 (60) Hz component of the measured ECG signal, but paper [8] presents how to handle this problem.

In high frequency noise elimination, the non-linear parameter estimation methods could reach better performance than transformation methods.

Let $\hat{X}_L(n)$ and $\hat{X}_R(n)$ the n-th left and right aimed estimation, defined as:

$$\hat{X}_L(n) = p_L \cdot \widetilde{X}_L(n) = p_L \sum_{i=-q}^{q} a_{L,i} X(n-i) + (1-p_L) \sum_{i=1}^{q} b_{L,i} \hat{X}_L(n-i) \quad (1)$$

$$\hat{X}_R(n) = p_R \cdot \widetilde{X}_R(n) = p_L \sum_{i=-q}^{q} a_{R,i} X(n-i) + (1-p_R) \sum_{i=1}^{q} b_{R,i} \hat{X}_R(n-i) \quad (2)$$

where $a_{L,i}$, $a_{R,i}$, $b_{L,i}$ and $b_{R,i}$ are prediction coefficients, p_L and p_R are balance probabilities determined by the dispersions

$$\sigma_{\hat{X}\ -X}(n,l), \sigma_{\hat{X}\ -X}(n,l), \sigma_{\widetilde{X}\ -X}(n,l) \text{ and } \sigma_{\widetilde{X}\ -X}(n,l), \quad (3)$$

constrained by the condition $p_L + p_R = 1$. For better separation of the signal from the noise, the length l should select more than one R-R period. On-line processing requires the estimation to be delayed with at least $3 \cdot q$ samples, but preferably with more than one R-R interval, in order to minimize the differences of the efficiency between $\hat{X}_L(n)$ and $\hat{X}_R(n)$. The resulting sample $\hat{X}(n)$ is obtained by the following formula:

$$\hat{X}(n) = p \sum_{i=-q}^{q} a_i \hat{X}_L(n-1) + (1-p) \sum_{i=-q}^{q} b_i \hat{X}_R(n-1). \quad (4)$$

The high level of the noise can massively degrade the performance of the parameter extraction models. In this situation, a well constructed transformation algorithm can outperform the parameter estimation procedure. Our proposed transformation method for QRS complex detection uses wavelets. The selected mother wavelet is:

$$\Psi(t) = \frac{1}{\sqrt{2\pi\sigma}} \cdot \exp\left(-\frac{t^2}{2\sigma}\right) \cdot \sin(2\pi \cdot \alpha \cdot t \cdot \exp(-\beta|t|)) \quad (5)$$

Parameters α and β are selected according to the highest frequency in ideal (noise free) ECG signal, while σ is the dispersion that acts like an attenuation factor for the wavelet's shape. After the analysis of more than 100 recordings, we obtained as a good robust result $\alpha = 100$ and $\beta = 1/3$. The robustness in this step is far more important, than a local performing index.

The first step in the recognition of the characteristic waveforms of the ECG consists of accurate detection of the QRS beats. These waveforms contain most of the signal's power, so they must be included into the template collection. This collection may be altered during ECG processing.

Although the automated waveform classification based on a decision tree algorithm could produce remarkable results, the self-organizing (SO) adaptive clustering [3] based method have several advantages:

- It is not susceptible to variations of beat morphology and temporal characteristics;
- It can perform a real-time unsupervised learning;
- It needs much less amount of knowledge for the same performance.

The clusters are built up according to the following rules:

- $\sigma_i \leq \sigma_{\mathrm{Max}}$; σ_{Max} is predetermined; $i = 0 \ldots n$;
- The mean value of a cluster is M_i and is determined in such a way, that σ_i to be minimal;
- For every R (T and P) wave, which belongs to a cluster

$$||X|| = \sum_{i=0}^{n} \left(\frac{X_i - M_i}{\sigma_i} \right)^2 \leq R_{\mathrm{Max}}, \qquad (6)$$

where R_{Max} is predetermined; X is a vector, representing a wave in the space.

Each waveform in the template bank is represented by 8 characteristic points that were selected using a shape estimation error minimization process. The indicator vector of each waveform is represented as $\bar{X}^T = (p_0(X), \ldots, p_{n-1}(X))$ where n is the number of clusters and $p_I(X)$ is the probability that X belongs to the cluster C_I, having the value:

$$p_I(X) = \prod_{k=0}^{7} \frac{1}{\sigma_{I,k}} \exp \left(-\frac{(X_k - M_{I,k})^2}{2\sigma_{I,k}} \right). \qquad (7)$$

The clustering process must work properly even if the studied patient manifests abnormal QRS wave patterns. To assure this, the main database must contain the most specific abnormal waveforms that are patient-free. It case of heavily patient dependent waveforms, such as ectopic beats, the studied waveforms are collected and included in a new, patient dependent cluster. These clusters are representative only for a patient but not for a larger group.

The optimal filter is based on the pre-processed signal and the template bank. Let

$$\bar{X}(n) = \sum_{k=0}^{nr-1} \left(s_k \cdot \sum_{i=-q}^{q} a_{F,i} \cdot X_k(n-i) \right) \qquad (8)$$

and

$$\widetilde{X}(n) = p_{F,X-\widetilde{X}}(n) \cdot \bar{X}(n) + (1 - p_{F,X-\widetilde{X}}(n)) \cdot \sum_{i=-q}^{q} b_i B(m, i) \qquad (9)$$

be the processed data. The low value of p_F, $p_F < 0.2$, justifies the need of the collection B, whose m-th element has the maximal correlation value with $\bar{X}(n)$.

The characteristic point localizer algorithm is performed in a similar way to the template bank building method. An important difference consists in the appliance manner of pre-filtered data. Firstly the template bank is created for

every recognizable event. With the aid of pre-filtered data, we can minimize the isoelectric line displacement caused problem. Such a pre-filtered and denoised signal consist the entrance of a SVM trained ANN. This kind of formulation of learning leads to quadratic programming with linear constraints.

The problem of learning SVM [11] is formulated as a task of separating learning vectors X_i into two classes of destination values $d = +1$ or $d = -1$ using maximal possible separation margin, that gives a high robustness to the obtained solution. The maximization task of function $Q(\alpha)$ is defined as follows:

$$Q(\alpha) = \sum_{i=-p}^{p} \alpha_i - \frac{1}{2} \sum_{i=-p}^{p} \sum_{j=-p}^{p} \alpha_i \cdot \alpha_j \cdot d_i \cdot d_j \cdot K(x_i \cdot x_j) \tag{10}$$

with linear constraints $\sum_{i=-p}^{p} \alpha_i \cdot d_i = 0$, where $0 \leq \alpha_i \leq C$ [1,10]. The α values are Lagrange multipliers, and function K represents the kernel, p is the number of learning pairs and C is a user defined constant (in our study C was selected between 0.1 and 0.5). In this case we applied radial Gaussian kernel function. The output signal $y(x)$ of the SVM network in retrieval mode (after learning) is determined as the combination of kernels

$$y(x) = \sum_{i=1}^{N} \alpha_{SVi} \cdot d_i \cdot K(x_{SVi} \cdot x) + w_{opt} \tag{11}$$

where N_{SV} is the number of support vectors and w_{opt} is the optimal weight vector. Although SVM separates the data into two classes, the recognition of more ones is straightforward by applying either 'one against one' or 'one against all' methods [2]. After the ANN is trained, we used it to estimate the ECG as an output of a whitening filter.

The non-linear intermediate result is:

$$Z_p(t) = f \left(\sum_{k=-j}^{j} c_{pk}(t) \cdot X(t+k) \right), \tag{12}$$

where $X_k(t) = Y(t+k)$, and $f()$ is a normalized Gauss function. The c_{pk} weight coefficients connect the input and the hidden layers. The output of the filter is:

$$Y_w(t) = Y(t) - \hat{Y}(t) = Y(t) - \sum_{p=-i}^{i} c_p(t) \cdot Z_p(t). \tag{13}$$

The adaptive behavior of the filter is assured by the permanent variance of the genetic search method based upon least mean square (LMS) algorithm computed coefficients [4]. Both the input signal and the selected template are processed through the main filter. During this process, the template bank is changing adaptively. The whitened template is:

$$T_{w,r}(t) = T(r) - \sum_{p=-i}^{i} c_p(t) \cdot Z_p(t), \tag{14}$$

where $r = j, \ldots, L - j$, and L is the size of the template. The output of the matched filter will be:

$$Y_w(t) = \sum_{r=j}^{L-j} T_{w,r}(t) \cdot Y_w(t - L + r). \tag{15}$$

After the signal is filtered, a smoothing operation should be performed to reduce the size of the compacted data. The compression strength should be selected in accordance with the diagnosis performance decrease from the recovered signal. The main aim of this algorithm is to decrease the length of the compressed signal and to keep the data quality as high as possible. Let

$$\widetilde{X}_{[\text{sm}]}(n) = \frac{1}{k}\left(\sum_{i=1}^{k-1} \widetilde{X}_{[\text{sm}]}(n - i\tau) + \widetilde{X}(n)\right), \tag{16}$$

where $k = 2^j$, with j and τ positive integers, and $\widetilde{X}(n) = Y_w(n)$. Normally the adjacent samples are highly correlated, and we select the positive integer τ that minimizes the auto-correlation function of the ECG signal. Usually the sampling delay τ is about half a QRS complex duration. The inverse transform is given by:

$$\widetilde{X}(n) = k \cdot \widetilde{X}_{[\text{sm}]} - \sum_{i=1}^{k-1} \widetilde{X}_{[\text{sm}]}(n - i\tau). \tag{17}$$

In the meantime of the transform, the values of $\widetilde{X}(n)$ and $\widetilde{X}_{[\text{sm}]}(n)$ can be modified with $k/2$ in order to reduce the reconstruction error or the dispersion of the smoothed signal. The efficiency of this algorithm highly depends on the chosen values for k and τ.

Because the variance of the filtered and optionally smoothed signal $\sigma_{\widetilde{X}_{[\text{sm}]}}(n, l)$ is too high to allow sufficient compression rate, a linear prediction transform is needed. This method eliminates the redundancy due to correlation between adjacent samples and beats. The resulting data

$$Y(n) = P(n) \cdot \sum_{i=1}^{q} a_{E,i}\widetilde{X}(n - i) + (1 - P(n)) \cdot \sum_{i=-q}^{q} b_{E,i}B(m, i), \tag{18}$$

where $P(n) = p_{E,\widetilde{X}_{[\text{sm}]} - B(m)}(n))$, support the calculation of the residual signal $r(n) = Y(n) - \widetilde{X}_{[\text{sm}]}(n)$.

Verifying processes determine the compression caused performance decrease in accordance to square error and diagnostic robustness. More iterations should be calculated to determine the optimal set of parameters. In most cases, the estimation errors have nearly normal distribution. In order to reduce the length of the residual data, an adaptive method-based entropy coding is needed. For every moment we determine the dispersion $\sigma_r(n, l)$ and the probability $p_{\sigma (n,l)}(r(n, l))$ of the errors. The output value is obtained by:

$$N_{[act]}(n, k) = I_1(n-k+1)+p_1(n-k+1)\cdot I_2(n-k+2)+\prod_{i=1}^{k-1} p_i(n-k+i)\cdot I_k(n) \tag{19}$$

using $p_i(n - k + i) = p(r(n - k + i), l)$ and $I_{k-i} = \int_{-\infty}^{r(n-i)} p_{k-i}(n - i)dr$.
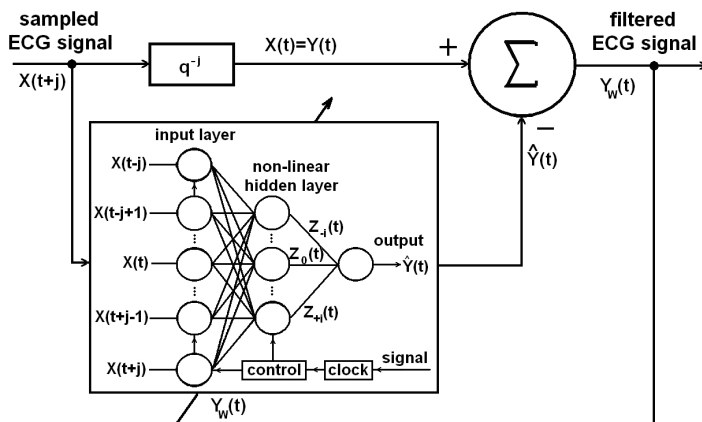
Fig. 2. The structure of the ANN-based adaptive filter

Table 1. Representation of the entropy coder's performance using 32 parameters

MIT-BIH record no.	Theoretic entropy	Huffman code size	SVM-based coding
102	161677	193419	163589
103	171223	201448	173295
107	169442	200102	171142
202	162735	192781	164814
205	182493	214923	184456
220	167321	198274	169121
223	180039	211952	181935
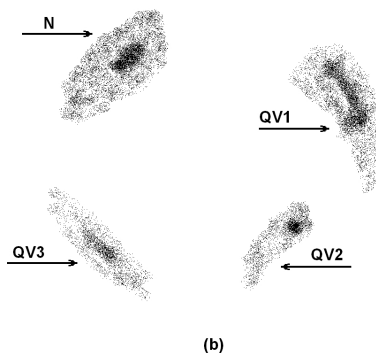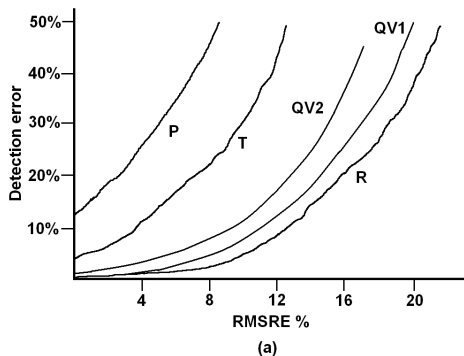
Fig. 3. (a) The recognition ratio of R, T, P and QV1, QV2 waves plotted against RM-SRE; (b) Representation of various beat forms: the normal QRS beats are represented by N, and three different ventricular extra beats are represented by QV1, QV2 and QV3 in plain representation (the calculation space has 32 dimensions, and the two most significant orthogonal combinations were selected for planar representation)

3   Results

For a better comparability we used the MIT-BIH arrhythmia database for evaluation. All processing steps were tested on the ECG registrations of MIT-BIH database (sampled at 360 Hz with 11-bit resolution) and our own recordings (sampled at 200-500 Hz with 12-bit resolution). Most of these files contain one or two channels. The performance is determined by the number of estimation parameters, smoothing strength, resolution and sampling rate. The entropy coding can decrease at least 12 times the theoretical 'waste', compared with Huffman coding, during signal compacting.

The characteristic wave recognition performance heavily depends on the level of allowed root mean square error during signal compression. Figure 3(a) represents the level of detection error of P, T and R waves when the relative RMSE varies from 0 to 20%. We investigated the detection error in function of the nature of R wave. The ventricular ectopic beats QV1 and QV2 included in this study were treated patient specific. Figure 3(b) illustrates the separation problem of various QRS waveforms in a 32-dimensional parameter space.

4   Discussion and Conclusion

Table 1 illustrates the compaction effectiveness for some of the most perturbed files, whose noise level and missed R wave detection rate was almost maximal. The new coding formula (19) has far better results than the adaptive Huffman coding. The elements distribution is close to normal and its change is not recommended without further knowledge. The smoothing strength should be adjusted by k and τ (see (16), (17)). Experiments show that (Fig. 3) the R wave can be accurately recognized even if RMSRE is about 10%. For T and P wave detection [7] the root mean square error must not exceed 3-5% of the signal's power. S (J), Q points and U wave cannot be recognized in most of the cases if RMSRE is higher than 1%. The lower amplitude of the T and P waves is the main reason of the lower detection rate. The amplitude of the QV1 and QV2 ectopic beats is about the same as in case of R waves, but the uncommon patient-specific shape of them inhibit the usage of a priori waveforms (we considered new patients, so the database had not any information about them). It can be observed a smoother shape of the performance graph for the studied QV1 and QV2 ectopic beats caused by the much lower available occurrence (almost 100 times less).

An experimental real-time processing using this method needs a powerful computer able to perform massively parallel algorithms. In Holter telemetry and diagnostic systems [6], where a vast amount of data is acquired and transmitted by radio wave, the compression is an unavoidable step of the computerization. Sophisticated long computation and lingering unpack of the signal could be the major disadvantages of this process. Although quite often the calculation term doesn't admit on-line computerization (in multitasking mode), the rapid evolution of the computers will shortly change this fact.

References

1. Burges, C.: A tutorial on support vector machines for pattern recognition. In: Fayyad, U. (ed.) Knowledge Discovery and Data Mining, pp. 1–43. Kluwer, Norwell, MA (2000)
2. Crammer, K., Singer, Y.: On the learnability and design of output codes for multiclass problems. In: Proc. 13th Conf. Comput. Learn Theor. pp. 35–46 (2000)
3. Lagerholm, M., Peterson, C., Braccini, G., Edenbrandt, L., Sörnmo, L.: Clustering ECG complexes using Hermite functions and self-organizing maps. IEEE Trans. Biomed. Eng. 47, 838–848 (2000)
4. Nave, G., Cohen, A.: ECG Compression Using Long-Term Prediction. IEEE Trans. Biomed. Eng. 40, 877–885 (1993)
5. Osowski, S., Hoai, L.T., Markiewicz, T.: Support vector machine-based expert system for reliable heartbeat recognition. IEEE Trans. Biomed. Eng. 51, 582–589 (2004)
6. Szilágyi, S.M.: Non-Linear Adaptive Prediction Based ECG Signal Filtering. In: Proc. 21st Ann. Int. Conf. IEEE EMBS, Atlanta, p. 286 (1999)
7. Szilágyi, S.M., Szilágyi, L.: Wavelet Transform and Neural-Network-Based Adaptive Filtering for QRS Detection. In: Proc. 22nd Ann. Int. Conf. IEEE EMBS, Chicago, pp. 1267–1270. Chicago (2000)
8. Szilágyi, S.M., Benyó, Z., Dávid, L.: Iterative ECG Filtering for Better Malfunction Recognition and Diagnosis. In: Proc. 5th IFAC Symp. Model. Contr. Biomed. Syst. Melbourne, pp. 295–300 (2003)
9. Szilágyi, S.M., Szilágyi, L., Benyó, Z.: ECG Signal Compression and Noise Distortion Effect Analysis. Proc. World Congr. Med. Phys. Biomed. Eng. Sydney, IFMBE Proc. 4, 4391 (2003)
10. Smola, A., Scholkopf, B.: A tutorial on support vector regression. Royal Holloway College, Univ. London, NeuroColt Tech. Rep. NV2-TR-1998-030
11. Vapnik, V.: Statistical learning theory. Wiley, New York (1998)
12. Xue, Q., Hu, Y.H., Tompkins, W.J.: Neural-Network-Based Adaptive Matched Filtering for QRS Detection. IEEE Trans. Biomed. Eng. 39, 317–329 (1992)

Incremental Multiple Sequence Alignment⋆

Marcelino Campos, Damián López, and Piedachu Peris

Departamento de Sistemas Informáticos y Computación
Universidad Politécnica de Valencia
Camino de Vera s/n
46071 Valencia (Spain)
{mcampos,dlopez,pperis}@dsic.upv.es

Abstract. This work proposes a new approach to the alignment of multiple sequences. We take profit from some results on Grammatical Inference that allow us to build iteratively an abstract machine that considers in each inference step an increasing amount of sequences. The obtained machine compile the common features of the sequences, and can be used to align these sequences. This method improves the time complexity of current approaches. The experimentation carried out compare the performance of our method and previous alignment methods.

Keywords: Grammatical inference, processing of biosequences, multiple alignment of sequences.

1 Introduction

Multiple alignment of biological sequences [1] is one of the commonest task in bioinformatics. Some applications of this task are: to find diagnostic patterns in order to characterize protein families; to detect or demonstrate homology between new sequences and existing families of sequences; to help predict the secondary and tertiary structures of new sequences; to suggest oligonucleotide primers for PCR; or as a essential prelude to molecular evolutionary analysis.

In order to perform an exact alignment, it is necessary to consider an n-dimensional space, where n denotes the number of sequences. There are some strategies used to avoid the high computational cost of the multiple alignment of sequences. One of the most successful strategies used is the so named *progressive alignment* (i.e. [2]). This approach considers evolutionary relations to build a phylogenetic tree. Following its branching order it is possible to align first the those most related sequences, gradually adding in more distant sequences/alignments. A pairwise alignment procedure is used in each alignment step. This approach can deal with alignments of virtually any number of sequences, obtaining good results.

Two main problems arise when this approach is used. The first one is due to the greedy nature of the method that does not guarantee that the global optimal solution would be obtained. The second problem consist on the choice of the alignment

parameters. Usually, a distance matrix between symbols and two gap penalties are chosen: the opening and the extension of a gap. On the one hand there is no way to obtain a consensus matrix for every kind of sequences, on the other hand the gap penalty values are key to obtain good results when divergent sequences are to be aligned. Furthermore, in protein sequence alignments, gaps do not occur randomly (they occur more often between secondary structures than within).

Other successful approach aims to reduce the greedy effect of the progressive alignment method by considering a library of local and global alignments instead of a distance matrix [3]. Due to the fact that a given pair of symbols can be treated in many ways in the library, the score given to a pair of symbols is position dependent. This lead to a more flexible approach and a better behaviour, avoiding errors in early stages of the process.

Inductive Inference is one of the possibilities to tackle the problem of Automatic Learning. This approach uses a set of facts (training data) in order to obtain the most suitable model, that is, the model that compile better the features of the data. Once the inference process is finished, the model obtained is able to correctly process data that shares some common features with the training set. When the inductive process obtains a formal language as the model, then the approximation is known as *Grammatical Inference* (GI) [4,5,6,7,8,9].

The *Error Correcting Grammar Inference* algorithm (ECGI) [10] builds iteratively a finite automaton (learns a regular language) from the training data. Each step considers the automaton of the previous step (the first step it considers the empty automaton) and a new sample from the training data. The algorithm uses an edit distance algorithm to detect the set of operations of minimum cost needed to force the automaton to accept the sample. These operations are used to modify the automaton, adding new states and transitions in such a way that neither loops nor cycles are added (the resulting automaton accepts a finite language). This GI method has been successfully applied in some pattern recognition tasks [11,12].

In our work we used this algorithm to learn a language from biological sequences. Once the finite automaton is obtained, it is possible to extract an alignment using the automaton's accepting path of each sequence. This step is bounded by a polynomial because the automaton lacks of loops. Our approach improves the time complexity of current procedures.

This paper is organized as follows: section 2 introduces some notation and definitions as well as the ECGI algorithm. Section 3 explains the proposed alignment method and analyzes its time complexity. Section 4 shows the experimentation carried out and comparative results with current alignment methods. The conclusions and some lines of future work end the paper.

2 Definitions and Methods

2.1 Theoretical Concepts

Let a finite deterministic automaton be a system $A = (Q, \Sigma, \delta, q_0, F)$ where: Q is a finite set of states; Σ is a finite alphabet; $q_0 \in Q$ is the initial state; $F \subseteq Q$ is

the set of accepting or final states and $\delta : Q \times \Sigma \to Q$ is the set of transitions of the automaton. It is possible to change the definition of the transition function to allow multiple transitions from a state on the same symbol $\delta : Q \times \Sigma \to 2^Q$. Such an automaton is referred to as non-deterministic finite automaton. Both types of automata recognize the same class of formal language. Finite automata can be extended to process strings of symbols, to do so, the transition function has to be extended to consider strings. Let p, q be states in Q, let a be a symbol in Σ and w a string, in the following we show the extension for the non-deterministic case:

$$\delta : Q \times \Sigma^* \to 2^Q$$
$$\delta(q, \lambda) = q$$
$$\delta(q, wa) = \bigcup_{p \in \delta(q,w)} \delta(p, a)$$

A string w over Σ is accepted by a finite automaton A if and only if $\delta(q_0, w) \cap F \neq \emptyset$. The set of strings accepted by the automaton is denoted by $L(A)$. Let Σ^* be the set of words of any length over Σ. Let $L \subseteq \Sigma^*$ be a language over the alphabet. L is a regular language if and only if there exists a finite automaton A such that $L(A) = L$. Please, refer to [13] for further definitions.

2.2   The Error Correcting Grammar Inference

The Error Correcting Grammar Inference (ECGI) algorithm proposed by Rulot and Vidal [10] was originally designed to recognize isolated words. Nevertheless, due to its features, it has been used in many others pattern recognition tasks. The ECGI solve two basic drawbacks of grammatical inference when applied to pattern recognition tasks. First, these algorithms are usually extremely recursive, that is, they ignore the relative position of the different substructures of the training sample. Second, grammatical inference algorithms, usually, do not maintain position-dependent features of the strings, which are key in some tasks. The ECGI algorithm obtains a finite language that preserves the main common features of the samples together with this relative position.

ECGI algorithm is an iterative process. ECGI considers one new sample and the current automaton and finds the most similar string to the sample (applying a criterion of similarity between strings that take into account a distance measure). The algorithm detect those transitions with minimum edition cost to be added in order to accept the new sample. The search of the most similar string to the sample in the automaton is made by a standard Error-Correcting Syntax Analysis method (Viterbi). An example of run is shown in Figure 1.

The language inferred by the automaton with ECGI method contains the training samples, is finite (therefore regular) and is not deterministic. The automaton obtained is ambiguous and without cycles. Due to its heuristic nature, the inference algorithm obtains different result depending on the samples order. The algorithm has been successfully applied to syntactic pattern recognition
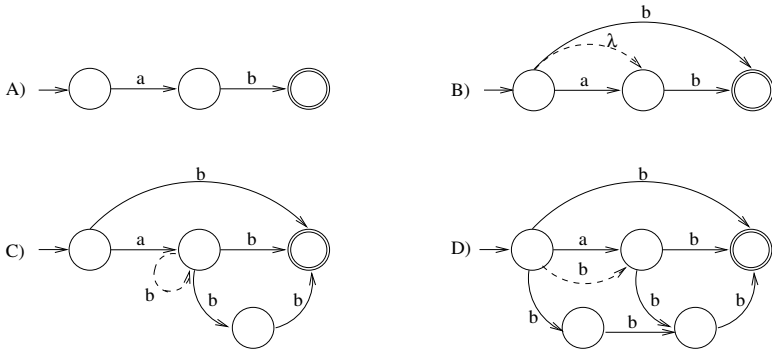
Fig. 1. Example of run of the original ECGI algorithm when the set $S = \{ab, b, abb, bbb\}$ is considered as the training sample. Dashed lines show error transitions. Note that the processing of the first string of the training set S returns the canonical automaton (see A). In order to avoid lambda transitions, the ECGI algorithm adds a transition to the next state (see B). Loops are avoided by the creation of a new state (see C), substitution are treated in the same way (see D). Note that, in the resulting automaton, all the incoming transitions to each state are labeled with the same symbol.

tasks [11,12], where the best performance of the algorithm is obtained when the longest samples are supplied first.

3   Incremental Alignment of Biosequences

3.1   Description of the Alignment Procedure

The method we propose for the multiple sequence alignment consist on two steps: the first one considers the set of sequences and obtains an automaton with a modified ECGI algorithm; the second step uses the learned automaton and the same set of sequences to construct the multiple alignment.

The Error-Correcting Syntax Analysis method used by the original ECGI algorithm considers three weights: to substitute, to insert and to erase a symbol. The modification we introduce allows the use a parameterizable distance matrix among the symbols and three gap-related penalties: to open, to extend and to close a gap. This modification of the analysis step does not add time complexity to the algorithm, and basically aims to change, in a somewhat biological way, the set of non-error transitions of the automaton obtained in each analysis. The use of such gap penalties is justified biologically and widely used by existing approaches. The alignments obtained this way have lesser and more concentrate gaps. Figure 2 shows the different behavior of the modified algorithm when the same sample is considered.

The alignment method we propose uses the set of sequences to align as the training set. Once inferred the automaton, the sequences are processed to obtain the accepting path in the automaton. We considered those states used by more

With original ECGI
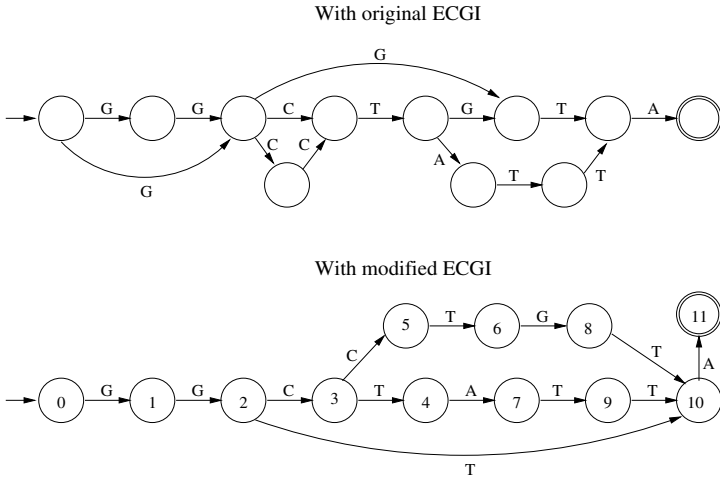
With modified ECGI

Fig. 2. Final automaton obtained by the original and modified ECGI algorithms. The same set of samples $S = \{GGCCTGTA, GGCTATTA, GGTA\}$ has been used. The optimal parameters were used to carry out this examples (see Section 4 for details). Note that the addition of gap penalties modifies the set of non-error transitions, and therefore, the final result.

```
PROGRAM: MULTIPLE SEQUENCE ALIGNMENT
INPUT:  STRINGS[]
OUTPUT:  ALIGNMENT


BEGIN

    AUT  ←————————  result of the ECGI algorithm using as input the strings into STRING[];
    PATHS[]  ←————  set of paths obtained by Viterbi's analysis using the automaton AUT and STRINGS[];
    ALIGNMENT  ←  aligment obtained using the set of paths PATHS[], the automaton AUT and STRINGS[];

END
```

Fig. 3. Multiple sequence alignment algorithm based on Grammatical Inference

than one sequence as synchronization points. This is justified because, each step, the error-correcting inference method looks for the best accepting path for the samples, adding the minimum cost transitions needed to accept the sample. The lack of loops allow to efficiently process the sequences in a parallel way, adding gaps when one synchronizing state is reached by some sequences but not all that use the state. The description of the algorithm is showed in Figure 3 and an example of multiple alignment in Figure 4.

In order to compare the performance of our approach, two alignment programs have been selected. The first one, Clustal-W [2], is probably the most widely used by the biological community. T-Coffee [3] is the second program considered. Briefly, T-Coffee could be seen as a refinement of the progressive approach to multiple alignment that avoids the use of a distance matrix. These two programs

	original ECGI	modified ECGI
string 1	GGCCTG.TA	GGCCTGTA
string 2	GG.CTATTA	GGCTATTA
string 3	.G...G.TA	GG....TA

Fig. 4. Alignment example using the automata from Figure 2. Considering the version that uses the modified ECGI, please note that the state 10 is a synchronizations point for all the strings. Note that the third string reaches this state with its third symbol. The other two strings need to analyze several symbols to reach the same state. Therefore, somewhat the third string "has to wait", and a gap is opened. The gap is closed when all the strings reach the synchronization state. Also note that the original ECGI automaton lead to an alignment that contains more gaps than the alignment obtained when the modified ECGI algorithm is used.

allow us to compare the GI approach in terms of computational complexity as well as their experimental behaviour.

3.2 Computational Complexity

In the following let n denote the number of sequences to align and let M denote the length of the longest sequence. The time complexity of Clustal-W algorithm is $\mathcal{O}(n^2 M^2)$. The time complexity of T-Coffee is higher than the complexity of Clustal-W algorithm ($\mathcal{O}(n^2 M^2) + \mathcal{O}(n^3 M) + \mathcal{O}(n^3) + \mathcal{O}(nM^2)$).

The approach we propose needs $\mathcal{O}(n)$ steps to build the automaton and each one can be carried out in $\mathcal{O}(M^2)$, therefore, the automaton can be obtained with complexity $\mathcal{O}(nM^2)$. The second step implies the alignment of the sequences, and can be carried out with complexity $\mathcal{O}(nM)$. Therefore, the final time complexity of our alignment method is $\mathcal{O}(nM^2)$, therefore improving previous results.

4 Experimental Results

In order to carry out the experimentation, a benchmark database of RNA alignments was considered [14]. Structural alignment of RNA remains as an open problem despite the effort on the development of new alignment procedures to protein sequences. This dataset is divided into five subsets that take into account structural features. In their work, Gardner et al., compare the performance of several methods. Their results were the reason to select Clustal-W and T-Coffee as the two better methods.

From the five subsets of the database, one of them was thought to be untrustworthy, and was not considered. Further testing has shown the alignments of the set to be perfectly reliable and were considered in our work.

To assess the performance of the results, two different scores have been used [15]. The *sum-of-pairs score* (SPS) increases with the number of sequences correctly aligned. Therefore, it is useful to measure whether the program succeeds in aligning some of the sequences in an alignment. The *column score* (CS) is a

more strict parameter and it is a way to test whether the program aligns or not all the sequences properly.

Given an alignment of N sequences and M columns, let $a_{i1}, a_{i2}, \ldots, a_{in}$ denote the symbols on the ith column. p_{ijk} is defined such that $p_{ijk} = 1$ if symbols a_{ij} and a_{ik} are aligned with each other in the reference alignment and $p_{ijk} = 0$ otherwise. Let the score S_i be defined as follows:

$$S_i = \sum_{j=1}^{N} \sum_{\substack{k=1 \\ k \neq j}}^{N} p_{ijk}$$

let M_r denote the length of the reference alignment and S_{ri} the score of the ith column for the reference alignment. The SPS for the alignment is then:

$$SPS = \frac{\sum_{i=1}^{M} S_i}{\sum_{i=1}^{M} S_{ri}}$$

For any given alignment described as above, let $C_i = 1$ if all the symbols in the ith column are aligned in the reference, otherwise let $C_i = 0$. Then, CS for the alignment is obtained as follows:

$$CS = \frac{\sum_{i=1}^{M} C_i}{M}$$

Clustal-W and T-Coffee software were downloaded from the European Bioinformatics Institute (*http://www.ebi.ac.uk/*). The experiments were run with the DNA default parameters for each program because they are reported as the most suitable ones. We tested both the basic ECGI algorithm and the modified one. The same alignment scheme explained in Section 3 was followed in any case.

All the parameters used in the alignment step of our approach were empirically set to: an identity distance matrix with substitution value set to 6; a gap open penalty set to 10; a gap extension penalty set to 6.66; and a closing gap penalty set to 0.5. The original version of the ECGI algorithm showed poor performance (results not showed). The main reason of this behaviour was the high amount of gaps introduced in the alignment, mainly due to the lack of gap penalties.

Experiments were carried out for each alignment group in the dataset. From the data shown we can consider that, no matter which group is considered, there is no substantial difference in the behaviour of the methods tested. Three homology levels were studied: low homology for sequences below the 50% of identity, medium homology for sequences between 50% and 70% of identity, and high homology for sequences over 70% of identity. No relevant difference in the methods' performance was observed. Finally, Figure 5 shows the global results. From the data obtained we conclude that all the three methods behave in the same way. Table 1 summarizes all the results.
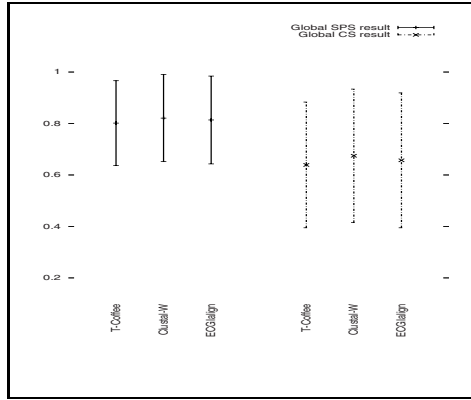
Fig. 5. Global experimental results

Table 1. Summary of the experimental results

		T-Coffee		Clustal-W		ECGIalign	
		SPS	CS	SPS	CS	SPS	CS
Results by group	G1	0.698	0.506	0.700	0.508	0.682	0.476
	G2	0.895	0.773	0.927	0.836	0.906	0.800
	G3	0.835	0.679	0.856	0.719	0.836	0.679
	G4	0.802	0.665	0.849	0.731	0.868	0.755
	G5	0.782	0.582	0.779	0.593	0.780	0.583
Results by homology	Low	0.735	0.536	0.749	0.562	0.746	0.549
	Med	0.868	0.736	0.903	0.801	0.892	0.780
	High	0.910	0.831	0.928	0.863	0.929	0.862
Global results		0.801	0.638	0.820	0.674	0.813	0.656

5 Conclusions and Future Work

Multiple alignment of biological sequences is one of the commonest task in bioinformatics and have several important applications. Structural alignment of RNA remains as an open problem despite the effort on the development of new alignment procedures to protein sequences. In this work, we address this task using only the sequences of the molecules to align.

Inductive inference is one of the possibilities to tackle the problem of Automatic Learning. In our work we used a grammatical inference algorithm and biological information to learn a finite automaton. This automaton is used to obtain an alignment using the each sequence accepting path in the automaton.

It is important to note that the time complexity of our approach to multiple sequence alignment improves previous results. Our method achieves the same performance but reduces by one degree the time complexity of previous approaches ($\mathcal{O}(nM^2)$) instead $\mathcal{O}(n^2M^2)$ where n denotes the number of sequences to align and M denotes the length of the longest sequence).

Several lines of work remain open and could lead to improve our results. As noted above, ECGI algorithm obtains different automata when the training set is ordered in different ways. Therefore it should be possible to improve the results by ordering the samples as a preprocessing of the training set. Nevertheless this preprocessing would lead to an increasing of the time complexity, and it has to be studied whether the performance worth the increased complexity.

Another important feature of the grammatical inference algorithms is that the more data available, the best results obtained. Therefore, it has to be studied whether the more sequences considered, the better alignment results obtained.

One of the drawbacks of previous alignment methods is the greedy behaviour of the approach that makes impossible of change first stages alignments. It can be argued that our approach can also produce bad first-stage decisions. In order to smooth this greedy behaviour, it should be possible to take advantage of the ambiguity of the automata by using stochastic automata. In this way, those better accepting paths in the automata would be selected, leading to better alignment results.

References

1. Notredame, C.: Recent progresses in multiple sequence alignment: a survey. Pharmacogenomics 3(1), 1–14 (2002)
2. Thompson, J., Higgins, D., Gibson, T.: Clustal-w: improving the sensitivity of progressive multiple sequence alignment through sequence weighting, position-specific gap penalties and weight matrix choice. Nucleic Acid Research 22(22), 4673–4680 (1994)
3. Notredame, C., Higgins, D., Heringa, J.: T-coffee: a novel method for fast and accurate multiple sequence alignment. J. Mol. Biol. 302, 205–217 (2000)
4. Fu, K., Booth, T.: Grammatical inference: Introduction and survey - Part I. IEEE Transactions on Pattern Analysis and Machine Intelligence 8(3), 343–359 (1975)
5. Fu, K., Booth, T.: Grammatical inference: Introduction and survey - Part II. IEEE Transactions on Pattern Analysis and Machine Intelligence 8(3), 360–375 (1975)
6. Angluin, D., Smith, C.: Inductive inference:Theory and Methods. Computing Surveys 15(3), 237–269 (1983)
7. Miclet, L.: Grammatical inference. In: Syntactic and Structural Pattern Recognition. Theory and Applications. Series in Computer Science, vol. 7, pp. 237–290 (1990)
8. Sakakibara, Y.: Recent advances of grammatical inference. Theoretical Computer Science 185, 15–45 (1997)
9. Sakakibara, Y.: Grammatical inference in bioinformatics. IEEE Transactions on Pattern Analysis and Machine Intelligence 27(7), 1051–1062 (2005)
10. Rulot, H., Vidal, E.: An efficient algorithm for the inference of circuit-free automata. In: Syntactic and Structural Pattern Recognition. NATO Asi Series, pp. 173–184 (1988)
11. Prieto, N., Vidal, E.: Learning language models through the ecgi method. Speech Communication 11, 299–309 (1992)
12. Vidal, E., Rulot, H., Valiente, J.M., Andreu, G.: Application of the error-correcting grammatical inference algorithm (ECGI) to planar shape. In: Grammatical inference: theory, applications and alternatives. vol. IEE. Digest No: 1993/092 (1993)

13. Hopcroft, J., Ullman, J.: Introduction to Automata Theory, Languages and Computation. Addison-Wesley Publishing Company, Reading (1979)
14. Gardner, P., Giegerich, R.: A comprehensive comparison of comparative rna structure prediction aproaches. BMC Bioinformatics 5 (2004)
15. Thompson, J., Plewniak, F., Poch, O.: A comprehensive comparison of multiple sequence alignment programs. Nucleic Acid Research 27(13), 2682–2690 (1999)

Mass Spectrometry Based Cancer Classification Using Fuzzy Fractal Dimensions

Tuan D. Pham

Bioinformatics Applications Research Center
School of Mathematics, Physics, and Information Technology
James Cook University
Townsville, QLD 4811, Australia
tuan.pham@jcu.edu.au

Abstract. Cancer classification using high-throughput mass spectrometry data for early disease detection and prevention has recently become an attractive topic of research in bioinformatics. Recently, several studies have shown that the synergy of proteomic technology and pattern classification techniques is promising for the predictive diagnoses of several cancer diseases. However, the extraction of some effective features that can represent the identities of different classes plays a critical factor for any classification problems involving the analysis of complex data. In this paper we present the concept of a fuzzy fractal dimension that can be utilized as a novel feature of mass spectrometry (MS) data. We then apply vector quantization (VQ) to model the class prototyes using the fuzzy fractal dimensions for classification. The proposed methodology was tested with an MS-based ovarian cancer dataset. Using a simple VQ-based classification rule, the overall average classification rates of the proposed approach were found to be superior to some other methods.

Keywords: Feature extraction, fuzzy fractal dimension, fuzzy c-means, vector quantization, mass spectrometry data, cancer classification.

1   Introduction

Proteomics has increasingly been a major role in the discovery of disease pathways and biomarkers for new drug treatment and development [1,2]. In comparison with transcriptional profiling in functional genomics, proteomics has some obvious advantages in that it provides a more direct approach to studying cellular functions because most gene functions are characterized by proteins, and more insight on exploring gene functions by studying protein expression.

The identities of expressed proteins in a protemome can be determined by protein separation, identification, and quantification. Protein separation methods involve two-dimensional gel electrophoresis followed by gel image processing. Once proteins are separated, protein differential expression can be characterized using mass spectrometry (MS) which is a high-resolution technique for determining molecular masses. A mass spectrometry dataset consists of relative intensities at chromatographic retention time and the ratios of molecular mass over charge

(m/z). Thus the mass spectrum for a sample is a function of the molecules and used to test for presence or absence of one or more molecules which may relate to a diseased state or a cell type. Proteomic patterns have recently been used for early detection of cancer progressions [3,4]. Obviously, early detection of such diseases has the potential to reduce mortality. In fact, it has been forseen that advances in mass-spectrometry based diagnostics may lead to a new revolution in the field of molecular medicine [5,4,6].

Several methods for classification of normal and diseased states using mass spectrometry data have been recently developed. Petricoin *et al.* [3] applied cluster analysis and genetic algorithms to detect early stage ovarian cancer using proteomic spectra in serum generated by mass spectrometry to distinguish neoplastic from non-neoplastic disease within the ovary. Lilien *et al.* [7] applied principal component analysis and a linear discriminant function to classify ovarian and prostate cancers using whole spectrum surface-enhanced laser desorption/ioinization time of flight (SELDI-TOF) mass spectronometry data of human serum. Wu *et al.* [8] compared the performance of several methods for the classification of mass spectrometry data. These classification methods include linear discriminant analysis, quadratic discriminant analysis, k-nearest neighbor algorithm, bagging and boosting classification trees, support vector machine, and random forest. The authors tested these methods against ovarian cancer and comtrol serum samples obtained from the National Ovarian Cancer Early Detection Program clinic at the Northwestern University hospital (USA) and found that the random-forest based classifier outperformed other methods in the discrimination of normal individuals from cancer patients based on mass spectrometry data.

Tibshirani *et al.* [9] proposed a probabilistic approach for sample classification from protein mass spectrometry data. These authors applied the so-called peak probability contrast technique to determine a set of common peaks of the ovarian cancer MALDI-TOF (matrix-assisted laser desoprtion and ionization time-of-flight) data. Based on the assumption that mass spectrometry involves complex functional data where the features of interest are the peak signals, Morris *et al.* [10] applied wavelet transforms and peak detection for feature extraction of MS data. This procedure consists of two steps as follows. Firstly the MS peaks are extracted; and secondly the resulting mass spectral peaks are then quantified. Yu *et al.* [11] developed a method for dimensionality reduction for high-throughput MS data. This method consists of four steps for data preprocessing based on binning, Kolmogorov-Smirnov test (KS-test), restriction of coefficient variation, and wavelet transforms. These authors applied the support vector machines (SVM) to train the wavelet coefficients of an ovarian high-resolution SELDI-TOF dataset, and reported that the SVM based classifier outperformed several other classification algorithms such as voted perceptron, discriminant analysis, decision tree analysis, naive Bayes, bagging and boosting classification trees, and random forest.

In this paper, we introduce the concept of a fuzzy fractal dimension and its vector quantization for extracting a novel feature of mass spectrometry signals

and classification respectively. Application of such computational framework has never been explored before for the analysis of proteomic data.

2 Feature Extraction by Fuzzy Fractal Analysis

The fractal dimension [12] is a mathematical expression of the space filling properties of an object whose concept leads to many different types of fractal dimensions [13]. The simplest form of fractal dimensions is the self-similarity dimension. The self-similarities of the line, square, and cube are equal to 1, 2, and 3 respectively. Consider a geometrically self-similar fractal object which consists of line segments. If each line segment is divided into M smaller line segments, then N smaller objects are produced. Furthermore, if the object is geometrically self-similar, then each of the objects of smaller sizes is an exact but reduced size copy of the whole object. The self-similarity dimension d is then expressed as [13]

$$N = M^d \tag{1}$$

which can be written in a another form as

$$d = \frac{\log(N)}{\log(M)} \tag{2}$$

Because the self-similarity dimension requires that each smaller subject formed by the division of the whole object must be an exact copy of the whole object, it can only be used to study objects that are geometrically self-similar. Such a fractal dimension is not very useful for analyzing many real objects that usually have irregular shapes. Thus more general fractal dimensions have been developed as more general forms of the fractal dimension. Two such popular forms are known as the capacity and the Hausdorff dimensions. The capacity of an object can be determined by covering it with balls of a radius r. The smallest number of balls $N(r)$ that covers all the parts of the object is counted. Then the radius of the previous balls is reduced and again $N(r)$ is counted. The capacity is the value of $\log N(r) / \log(1/r)$ in the limit as r shrinks to 0. The relationship of the capacity and the self-similarity dimensions is that if $M = 1/r$, then $N = M^d$. The Hausdorff-Besicovitch dimension is similar, but not identical, to the capacity dimension. In the capacity dimension, the object is covered with the number of balls $N(r)$ of a given radius r; whereas in the Hausdorff dimension, the object is covered with sets.

There are two general principles of the concept of the fractal dimension: the scaling dimension and the Hausdorff dimension [14]. The first principle, which is often called the telescope-microscope principle, states that the decrease of the measuring scale of an object by a factor s is equivalent to the increase of the measuring scale of the object by the factor s. The second principle states that any measurement of the "mass" of a fractal of the Hausdoff dimension d contained in a box of side s is proportional to s^d. There are many natural ways for computing the mass of a fractal set such as the box counting method [13],

the area-perimeter method [15], and the mass-radius method [12]. We develop herein a new method for obtaining the fractal dimension using the framework of the fuzzy c-means algorithm, that can be useful for extracting some novel feature of mass spectrometry data and easily implemented by the vector quantization technique for pattern classification.

Let M_{fc} be the fuzzy c-partition space, and $J : M_{fc} \times \mathcal{R}^{cp} \to \mathcal{R}^+$ be [17]

$$J_m(\mathbf{U}, \mathbf{v}) = \sum_{k=1}^{n} \sum_{i=1}^{c} (u_{ik})^m (d_{ik})^2 \tag{3}$$

where $\mathbf{U} \in M_{fc}$ is a fuzzy partition of $\mathbf{X} = (\mathbf{x}_1, \mathbf{x}_1, \dots, \mathbf{x}_n)$; $\mathbf{v} = (\mathbf{v}_1, \mathbf{v}_2, \dots, \mathbf{v}_c)$ $\in \mathcal{R}^{cp}$ with $\mathbf{v}_i \in \mathcal{R}^p$ is the cluster center of u_i, $1 \le i \le c$; $d_{ik} = ||\mathbf{x}_k - \mathbf{v}_i||$ and $|| \cdot ||$ is any inner product induced norm on $\mathcal{R}^p$; and $m \in [1, \infty)$.

Observation of (3) reveals that d_{ik} is the the measure of dissimilarity between each data point $\mathbf{x}_k$ and fuzzy cluster center $\mathbf{v}_i$, whose squared distance is then weighted by the term $(u_{ik})^m$. Thus, J_m is a square error clustering function, and solutions for this fuzzy clustering algorithm is to

$$\text{minimize}_{M \ \times \mathcal{R}} \quad J_m(\mathbf{U}, \mathbf{v}) \tag{4}$$

There exists an infinite family of fuzzy clustering algorithms – one for each $m \in [1, \infty)$ – via the conditions for solutions of (4).

In the fuzzy c-means (FCM) algorithm; c, the number of clusters, needs to be given. In many practical cases, c is unknown. It is reasonable to expect cluster substructure at more than one value of c, and therefore necessary to estimate the most plausible value of c for the cluster analysis. This problem is known as cluster validity. It is very difficult to formulate the cluster validity problem in a mathematically tractable manner, because the basic question is imposed on the definition of a cluster. For fuzzy clustering, one should examine which pairs of fuzzy groups/classes overlap, and this leads to the question of how fuzzy a fuzzy c-partition is. A heuristic solution to this problem is to calculate the measure of fuzziness in $\mathbf{U}$, and then assign c as the most valid value that has the least fuzzy partitions.

The first functional designed for cluster validity measure is the partition co-efficient [17]. This partition coefficient of a fuzzy c-partition of $\mathbf{U} \in M_{fc}$ of $\mathbf{X}$ is expressed as

$$F(c) = \frac{1}{n} \sum_{k=1}^{n} \sum_{i=1}^{c} (u_{ik})^2 \tag{5}$$

Another equivalent expression for (5) that emphasizes various properties of F is the Euclidean inner product for two matrices $\mathbf{I}, \mathbf{J} \in \mathbf{V}_{cn}$ is $< \mathbf{I}, \mathbf{J} >= \text{Tr}(\mathbf{IJ}^T)$, where Tr is the trace of a matrix, and $\mathbf{J}^T$ is the transpose of $\mathbf{J}$. And (5) has alternative forms

$$F(c) = \frac{\text{Tr}(\mathbf{UU}^T)}{n} = \frac{< \mathbf{U}, \mathbf{U} >}{n} = \frac{||\mathbf{U}||^2}{n} \tag{6}$$

Now it can be analyzed that: if $F(c) = 1$ then $\mathbf{U}$ contains no fuzzy clusters ($\mathbf{U}$ consists of only zeros and ones); if $F(c) = 1/c$ (all elements in $\mathbf{U}$ is equal to $1/c$) then $\mathbf{U}$ is completely fuzzy; and in general $1/c \leq F(c) \leq 1$. As $F(c)$ increases, the partition of the data sets is more effective. Thus the formal strategy for selecting the most valid c^* is as follows. Let Ω_c represents any finite set of optimal $\mathbf{U}$'s $\in M_{fc}$, and $c = 2, 3, \ldots, n - 1$. The optimal c^* is determined by direct search

$$c^* = \arg\max_c[\max_\Omega F(c)] \tag{7}$$

An observation of the relationship between c and $F(c)$ reveals that $F(c)$ can be interpreted as a type of the measure of the fuzziness or the "fuzzy mass" of the partition space $\mathbf{U}$ as a function of the number of clusters of size c. Based on the second principle of dimension for fractals, $F(c)$ is equivalent to the approximate power law

$$F(c) \propto c^d \tag{8}$$

where d_{fcm} is called the FCM-based fractal dimension or the fuzzy fractal dimension (FFD) of $\mathbf{U}$, which can be determined as

$$d_{fcm} = \lim_{c \to c^*} \frac{\log F(c)}{\log c} \tag{9}$$

It can be further shown that if the plot of $\log F(c)$, the vertical axis, versus $\log c$, the horizontal axis, is represented by a straight line using the method of least squares; then a straight line in a x-y diagram can be expressed as

$$\log F(c) = d_{fcm} \log c + b \tag{10}$$

where d_{fcm} is the slope of the line, and b is the intercept of the fitting line with the vertical axis. Alternatively,

$$F(c) = b\, c^d \tag{11}$$

Thus, the fuzzy fractal dimension d_{fcm} expression in (9), in the limit where c approaches c^*, can be determined as the slope of the plot of $\log F(c)$ versus $\log c$. The basic idea is that if an object is self-similar, then the slope of $\log F(c)$ versus $\log c$ is the same as the limit of $\log F(c)/\log c$ as c approaches c^*. However, the determination of the slope is much easier than c^*.

For recognition or classification of complex patterns, it has been reported that the use of a single fractal dimension is not sufficient enough to obtain good results; and therfeore suggested multifractal models [16]. Based on the minimization of J_m expressed in (4), an infinite set of the FCM-based fractal dimensions $\mathcal{D}_{fcm}$ can be obtained in terms of the weighting exponent m:

$$\mathcal{D}_{fcm} = \bigcup_{m=1}^{\infty} d_{fcm}^m \tag{12}$$

To obtain a finite vector of fuzzy fractal dimensions, we set the range for m with some discrete values being greater than one (as $m = 1$, the FCM algorithm becomes a hard-clustering case). We now turn our discussion on the

implemenation of the fuzzy fractal dimensions for pattern classification using vector quantization approach in the next section.

3   Classification Using FFD-Based Vector Quantization

To obtain the set of codewords or codevectors which can be modeled as the prototype of a certain class, we apply the method for quantizing the vectors of the fuzzy fractal dimensions. Let $\mathbf{a}_t$ be a vector of fuzzy fractal dimensions; and the codebook of the vectors of fuzzy fractal dimensions be $C = \{\mathbf{c}_1, \mathbf{c}_2, \ldots, \mathbf{c}_L\}$, where $\mathbf{c}_j = (c_{j1}, c_{j2}, \ldots, c_{jp})$, $j = 1, 2, \ldots, L$ are codewords, Each codeword $\mathbf{c}_j$ is assigned to an encoding region R_j in the partition $\{R_1, R_2, \ldots, R_L\}$. The source vector $\mathbf{a}_t$ can be represented by the encoding region R_n and expressed by

$$V(\mathbf{a}_t) = \mathbf{c}_n, \text{ if } \mathbf{a}_t \in R_n \tag{13}$$

The main idea of the vector quantization (VQ) is to find an optimal codebook such that for a given training set and a codebook size, the average distortion in representing each vector $\mathbf{a}_t$ by the closest codeword $\mathbf{c}_n$ is minimum. One of the most popular methods for VQ design is the LBG (Linde, Buzo and Gray) algorithm [18]. The LGB-VQ method requires an initial codebook, and iteratively bi-partitions the codevectors based on the optimality criteria of nearest-neighbor and centroid conditions until the number of codevectors is reached.

For the particular study, the MS cancer classification system based on the fuzzy fractal analysis and VQ-codebook approach works as follows. In the training phase, the MS signals are analyzed by the fuzzy fractal analysis to obtain the vectors of fuzzy fractal dimensions (FFD). The training FFD vectors are then quantized using the number of codebooks according to the number of different classes. In the testing phase, an input unknown MS signal, denoted as s, is analyzed by the fuzzy fractal analysis resulting in the FFD vector. The dissimilarity between the FFD vector of the unknown sample and each trained codebook is computed. The dissimilarity measure of the unknown sample s and a particular known class represented by the codebook C^i is determined using the minimum rule:

$$D(s, C^i) = \min_{1 \leq j \leq L} D(\mathbf{x}_m, \mathbf{c}_j^i) \tag{14}$$

where D is a measure of dissimilarity taken as the L_2 norm, $\mathbf{x}_m$ is the FFD vector of the unknown sample s, $\mathbf{c}_j^i$ is the j FFD-VQ codevector of a particular known class represented by codebook C^i.

The unknown sample s is assigned to class i^* if the dissimilarity measure of its FFD vector $\mathbf{x}_m$ and the FFD-VQ codebook $\mathbf{C}^i$ is minimum, that is

$$\text{assign } s \text{ to class } i^* \text{ if}$$
$$i^* = \arg\min_i D(s, C^i) \tag{15}$$

4   Experiment

The ovarian high-resolution SELDI-TOF mass spectrometry dataset, which can be obtained from the FDA-NCI Clinical Proteomics Program Databank was used to test the proposed approach. The dataset was generated using a non-randomized study set of ovarian cancers and control specimens on an ABI Qstar fitted with a SELDI-TOF source to study ovarian cancer case versus high-risk control. The dataset consists of 100 control samples and 170 cancer samples. Figures 1 and 2 show the typical MS signals of ovarian control and ovarian cancer respectively.

A vector of 8 fuzzy fractal dimensions is extracted for each sample by using 8 arbitrary values for the FCM weighting exponent m ranging from 1.5 to 5.0 with the interval of 0.5. Two codebooks of 8 and 16 codevectors were used to generate the two prototypes for the control and cancer classes respectively. The validation of the classification of the proposed approach was designed with similar strategies to those carried out in [11], who applied support vector machine (SVM) for the classification, so that comparisons can be made. The first measure of performance is the k-fold cross validation where $k = 2, 3, \ldots, 10$, and each k-fold validation was carried out 1000 times. The second measure of performance is the leave-one-out cross validation.

It is noted that the raw ovarian high-resolution SELDI-TOF dataset used by Yu *et al.* [11] consists of 95 control samples and 121 cancer samples; while the raw ovarian high-resolution SELDI-TOF dataset we used to test the performance of the proposed approach has 100 control samples and 170 cancer samples. In the leave-one-out cross validation, the proposed method only misclassified 2 control and 2 cancer samples in comparison with 6 control and 2 cancer samples being misclassified by the SVM [11]; and 4 control and 2 cancer samples misclassified by the linear predictive coding (LPC)-VQ method [19]. It was also reported that the principal component analysis (PCA) was applied to reduce the large number of
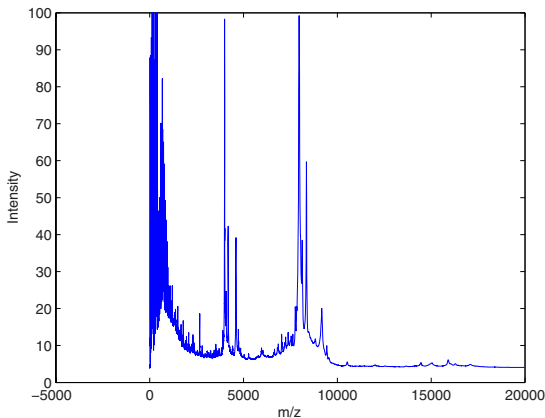
Fig. 1. MS-based ovarian control data
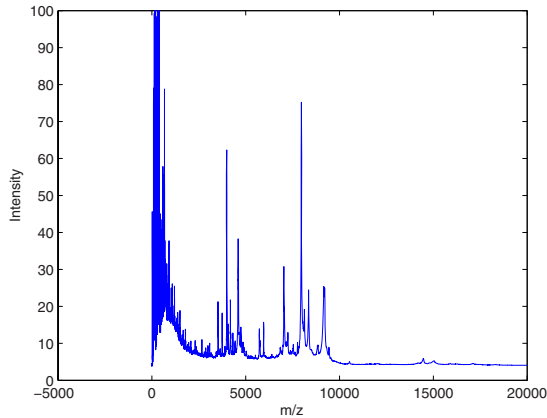
Fig. 2. MS-based ovarian cancer data

Table 1. k-fold cross validation results for ovarian cancer data

	SVM		LPC-VQ		FFD-VQ	
k	Control mean	Cancer mean	Control mean	Cancer mean	Control mean	Cancer mean
2	0.8930	0.9492	0.9224	0.9637	0.9314	0.9707
4	0.9058	0.9722	0.9327	0.9811	0.9450	0.9766
6	0.9094	0.9760	0.9348	0.9825	0.9531	0.9818
8	0.9098	0.9784	0.9362	0.9852	0.9570	0.9862
10	0.9096	0.9801	0.9377	0.9885	0.9564	0.9890

features and the PCA-reduced first nine components were used to train the SVM-based classifer [11]. For leave-one-out cross-validation, 9 control and 2 cancer samples were misclassified by the SVM using the PCA reduced dataset. Table 1 shows the mean classification values of the k-fold cross validation obtained from the SVM classification on the preprocessed data, the LPC-VQ, and the FFD-VQ. Except for $k = 2$ and 6, where the cancer means obtained from the LPC-VQ method are highest; the overall results show that the proposed method is most favorable for MS-based ovarian cancer classification than the other two approaches. We also report herein that the Hurst components [16] for all the MS samples are close to one showing the persistency in the MS samples and hence confirms the reliability of the fractal dimensions.

5   Conclusion

Fuzzy fractal dimensions (FFDs) have been used as an effective features for classification of cancers using MS data. The use of the fuzzy fractal dimensions

is suitable for this study because it can capture the inherent spatial information of the MS data, and can be applied to other classification methods.

It has been predicted that the advancement of proteomics pattern diagnostics will lead to a revolution in the field of molecular medicine such as the concept of personalized medicine [20]. It is because this technology not only represents a new model for disease detection but it is also clinically feasible [6]. It is still now the clinical impact of proteomic pattern diagnostics is in the very early stage where the results have not been validated in large trials. Furthermore, recent research outcomes have illustrated the role of MS-based proteomics as an indispensible tool for molecular and cellular biology and for the emerging field of systems biology [2].

Given these promising results, identifying biomarkers using MS data is a challenging task which requires the combination of the contrast fields of knowledge of modern biology and computational methodology. We have presented in this paper a novel application of fuzzy fractal analysis for extracting a novel feature of mass spectrometry data. The simple decision logic of the VQ-based classification rule is effective for the implementation of the fuzzy fractal dimensions of MS-based cancer data.

References

1. Griffin, T., Goodlett, D., Aebersold, R.: Advances in proteomic analysis by mass spectrometry. Curr. Opin. Biotechnol. 12, 607–612 (2001)
2. Aebersold, R., Mann, M.: Mass spectrometry-based proteomics. Nature 422, 198–207 (2003)
3. Petricoin, E.F., et al.: Use of proteomic patterns in serum to identify ovarian cancer. Lancet 359, 572–577 (2002)
4. Conrads, T.P., Zhou, M., Petricoin III, E.F., Liotta, I.L., Veenstra, T.D.: Cancer diagnosis using proteomic patterns. Expert Rev. Mol. Diagn. 3, 411–420 (2003)
5. Petricoin, E.F., Liotta, L.A.: Mass spectrometry-based diagnostics: The upcoming revolution in disease detection. Clinical Chemistry 49, 533–534 (2003)
6. Wulfkuhle, J.D., Liotta, L.A., Petricoin, E.F.: Proteomic applications for the early detection of cancer. Nature 3, 267–275 (2003)
7. Lilien, R.H., Farid, H., Donald, B.R.: Probabilistic disease classification of expression-dependent proteomic data from mass spectrometry of human serum. J. Computational Biology 10, 925–946 (2003)
8. Wu, B., Abbott, T., Fishman, D., McMurray, W., Mor, G., Stone, K., Ward, D., Williams, K., Zhao, H.: Comparison of statistical methods for classification of ovarian cancer using mass spectrometry data. Bioinformatics 19, 1636–1643 (2003)
9. Tibshirani, R., Hastie, T., Narasimhan, B., Soltys, S., Shi, G., Koong, A.: Sample classification from protein mass spectrometry, by 'peak probability contrasts'. Bioinformatics 20, 3034–3044 (2004)
10. Morris, J.S., Coombes, K.R., Koomen, J., Baggerly, K.A., Kobayashi, R.: Feature extraction and quantification for mass spectrometry in biomedical applications using the mean spectrum. Bioinformatics 21, 1764–1775 (2005)
11. Yu, J.S., Ongarello, S., Fiedler, R., Chen, X.W., Toffolo, G., Cobelli, C., Trajanoski, Z.: Ovarian cancer identification based on dimensionality reduction for high-throughput mass spectrometry data. Bioinformatics 21, 2200–2209 (2005)

12. Mandelbrot, B.B.: How long is the coast of Britain? Statistical self-similarity and fractional dimension. Science 156, 636–638 (1967)
13. Liebovitch, L.S.: Chaos Simplified for the Life Sciences. Oxford University Press, New York (1998)
14. Hastings, H.M., Sugihara, G.: Fractals A User's Guide for the Natural Sciences. Oxford University Press, New York (1993)
15. Lovejoy, S.: Area-perimeter relation for rain and cloud areas. Science 216, 185 (1982)
16. Sun, W., Xu, G., Gong, P., Liang, S.: Fractal analysis of remotely sensed images: A review of methods and applications. Int. J. Remote Sensing 27, 4963–4990 (2006)
17. Bezdek, J.C.: Pattern Recognition with Fuzzy Objective Function Algorithms. Plenum Press, New York (1981)
18. Linde, Y., Buzo, A., Gray, R.M.: An Algorithm for Vector Quantization. IEEE Trans. Communications 28, 84–95 (1980)
19. Pham, T.D., Chandramohan, V., Zhou, X., Wong, S.T.C.: Robust feature extraction and reduction of mass spectrometry data for cancer classification. In: Proc. IEEE-ICDM Workshop on Data Mining in Bioinformatics, pp. 202–206 (2006)
20. Ginsburg, G.S., McCarthy, J.J.: Personalized medicine: revolutionizing drug discovery and patient care. Trends Biotechnol. 19, 491–496 (2001)

Bayesian Detection of Coding Regions in DNA/RNA Sequences Through Event Factoring

Renatha Oliva Capua[1], Helena Cristina da Gama Leitão[1], and Jorge Stolfi[2]

[1] Institute of Computing, Federal Fluminense University (UFF)
Rua Passo da Pátria, 156, Bloco E – 24210-240 Niterói, RJ – Brazil
`{rcapua,hcgl}@ic.uff.br`
[2] Institute of Computing, University of Campinas (UNICAMP)
Cx. Postal 6176 – 13081-970 Campinas, SP – Brazil
`stolfi@ic.unicamp.br`

Abstract. We describe a Bayesian inference method for the identification of protein coding regions (active or residual) in DNA or RNA sequences. Its main feature is the computation of the conditional and *a priori* probabilities required in Bayes's formula by factoring each event (possible annotation) for a nucleotide string into the concatenation of shorter events, believed to be independent. The factoring allows us to obtain fast but reliable estimates for these parameters from readily available databases; whereas the probability estimation for unfactored events would require databases and tables of astronomical size. Promising results were obtained in tests with natural and artificial genomes.

Keywords: coding regions, ab-initio DNA tagging, Bayesian inference.

1 Introduction

We describe here a new statistical inference method for finding protein-coding regions in genomes. Our method is well-grounded on Bayesian inference theory, and is easily adapted to different genome models.

1.1 Coding and Non-coding Regions

The *protein-coding regions* of a genome specify the sequence of aminoacids in some protein, according to the well-known *protein genetic code* [1]. A coding region is *active* if it is still transcribed by the organism in appropriate circumstances. Such regions comprise only a fraction of an organism's genome — varying from almost 100% in viruses, prokaryotes, and archaea, to 10% or less in eukaryotes. Another important fraction of the genome, which may be dominant in eukaryotes, consists of *fossil coding regions* — copies of active coding regions of some ancestral genome, which have become inactive or un-transcribable due to mutations and truncations. These fossil regions may be embedded in any non-functional part of the genome, such as between genes and in the introns of eukaryotes. Finally, genomes are believed to contain *junk regions* that are

the result of "accidental" events — such as single-base insertions and duplication of pre-existing junk sequences. The primary goal of a *genome classification algorithm* is to identify the protein-coding regions of a given genome.

1.2 Homology-Based Methods

The most successful genome classifiers are the *homology-based methods*, that rely on the detection of known gene expression clues (operons, mRNA splicing markers) and comparison with previously identified bio-sequences, from the same organism or from other organisms [2].

By their own nature, homology-based methods can identify only coding regions that are still active, or that can still be recognized (by similarity) as descendants of active regions in some ancestral genome. They cannot distinguish truly junk regions from fossil coding regions which are not similar to any known active region. Homology methods may also fail to identify an active coding region if its nucleotide sequence is "new to science" (not represented in available databases) — a situation which is not as rare as one may think [3].

1.3 Ab-Initio Methods

To distinguish fossil coding regions from junk and other types of DNA, one must resort to *ab initio* genome classifiers — algorithms that rely only on the fact that protein-coding regions, being constrained to represent useful and functioning proteins, have different local statistics than other parts of the genome.

The ab-initio approach imposes certain limitations on the performance and results of the classifier. Being based on statistical (rather than logical) inference, the result too is usually probabilistic rather than categorical, and subject to mistakes due to freak coincidences. Moreover, since the differences between coding and non-coding regions are small, one must analyze relatively long segments of the genome in order to get confident and accurate classifications. For this reason, ab-initio methods cannot be expected to detect very short coding or non-coding regions, or locate the exact transition point between two adjacent regions.

1.4 Previous Work

There are many ab-initio classifiers described in the literature [4], but none is definitely better than all the others [5]. They use various mathematical models and algorithms, such as neural networks [6], signal processing [7], and Markov models (generally between 2nd and 5th order) [8]. While all those classifiers rely on statistical differences between coding and non-coding regions, their statistical models and inference rules are often ad-hoc and/or hidden in an inscrutable computation model. Methods that explicitly use statistical inference include those of Fickett [3] and Staden and McLahan [9].

1.5 Outline of Method

Our algorithm breaks the input sequence into overlapping windows, typically 10 to 100 bases long, and uses Bayesian inference to determine the probability that

each window belongs to a coding region or to a non-coding region, or contains a transition between two such regions.

Direct estimation of the conditional probabilities required by Bayes's formula, with any useful accuracy, would require labeled databases ("training sets") and tables of astronomical size. Our algorithm avoids the problem by factoring each possible labeling of the window into a sequence of short events, whose probabilities can be easily and accurately estimated from existing databases [10].

2   Definition of the Problem

2.1   Genome Model

In our model, the classifier's input is a DNA sequence, represented as a string $b = (b_0, b_1, \ldots, b_{n-1})$ where each b_i is a letter from the *base alphabet* $\mathcal{B} = \{A, T, C, G\}$. The string b is assumed to be the concatenation of several non-empty *regions*, each being either *coding* or *non-coding*. We assume furthermore that each coding region derives from a *gene*, a concatenation of three-letter *codons*. However, in order to account for mRNA editing in active coding regions, and accidental truncations in fossil coding regions, we allow that a coding region of the input string may be an arbitrary substring of its original gene.

2.2   Genome Labelings

A (*full*) *labeling* of the input string is another string $e = (e_0, e_1, \ldots, e_{n-1})$, with the same length n, where each e_i is a letter from the *label alphabet* $\mathcal{E} = \{N, D, E, F\}$. In the *true* or *correct* labeling, the label e_i is N if nucleotide b_i belongs to a non-coding region; otherwise it is D, E, or F according to whether b_i descends from the first, second, or third base, respectively, of a codon in the original gene. Needless to say, the true labeling of a natural genome is usually unknown (and, in fact, essentially unknowable).

A full labeling e of the input string implies a *weak label-ing* $c = (c_0, c_1, \ldots, c_{n-1})$, where each c_i is N if e_i is N, and K (meaning "a coding base") if e_i is D, E, or F. A full label-ing also implies a *frame labeling* $\phi = (\phi_0, \phi_1, \ldots, \phi_{n-1})$, where each ϕ_i is either '−', 'o', '+' or '?', depending on the full label e_i and the value of $i^* = i \bmod 3$ according to the table at right.

Table 1.

	e_i			
i^*	D	E	F	N
0	o	+	−	?
1	−	o	+	?
2	+	−	o	?

Note that the frame label is constant (−, o, or +) within each coding region, and specifies one of the three possible *codon read-ing frames* [1] for that region.

2.3   Window Probabilities and Ergodicity

We define a *window* of the input genome as any finite set of consecutive indices $w = \{r, r+1 \ldots, s\} \subseteq \{0, 1, \ldots, n-1\}$. The *size* of that window is $|w| = s - r + 1$;

its *content* is the basis sequence $b[w] = (b_r, b_{r+1}, \ldots, b_s)$; and its *true labeling* is the label sequence $e[w] = (e_r, e_{r+1}, \ldots, e_s)$.

We assume that the input genome is *ergodic*; in the sense that, considering all possible input genomes, the probabilities $\Pr(b[w] = \beta \wedge e[w] = \eta)$, for each window w and each pair $\beta \in \mathcal{B}^{|w|}$ and $\eta \in \mathcal{E}^{|w|}$, depend only on η and β (and on the window size $|w|$), but not on the position of the window w. Then we can write simply $\Pr(\eta) = \Pr(e[w] = \eta)$, $\Pr(\beta) = \Pr(b[w] = \beta)$, $\Pr(\eta \mid \beta) = \Pr(e[w] = \eta \mid b[w] = \beta)$, and so on, where w is any window of size $|\beta| = |\eta|$.

2.4 Classifier Output

The goal of our algorithm is to compute, for each input base b_i, four real numbers $\mathtt{P}[i, \mathtt{N}]$, $\mathtt{P}[i, \mathtt{D}]$, $\mathtt{P}[i, \mathtt{E}]$, and $\mathtt{P}[i, \mathtt{F}]$, where $\mathtt{P}[i, \varepsilon]$ is the probability that ε is the true full label of input base b_i. Note that from this data one can compute the probability that base b_i belongs to a coding region, namely $\mathtt{P}[i, \mathtt{K}] = \mathtt{P}[i, \mathtt{D}] + \mathtt{P}[i, \mathtt{E}] + \mathtt{P}[i, \mathtt{F}]$; and also a probability for each frame label (?, -, o, or +). See Fig. 1.

```
...
681 A    0.398 *0.601  0.000   0.000 D:N*    0.398 *0.601 K:N*
682 A   *0.668  0.000  0.331   0.000 N:N.   *0.668  0.331 N:N·
683 G   *0.548  0.000  0.000   0.451 N:N.   *0.548  0.451 N:N·
684 T    0.161 *0.838  0.000   0.000 D:N*    0.161 *0.838 K:N*
685 A   *0.593  0.000  0.405   0.000 N:N.   *0.593  0.406 N:N·
686 T    0.447  0.000  0.000  *0.552 F:F.    0.447 *0.552 K:K·
687 A    0.120 *0.879  0.000   0.000 D:D.    0.120 *0.879 K:K·
688 C    0.449  0.000 *0.549   0.000 E:E.    0.449 *0.550 K:K·
689 C    0.276  0.000  0.000  *0.723 F:F.    0.276 *0.723 K:K·
690 C    0.077 *0.921  0.000   0.000 D:D.    0.077 *0.922 K:K·
...
```

Fig. 1. Sample output from our classifier

The first two columns of Fig. 1 are the index i and the contents b_i of each base. The next four columns show the computed probabilities $\mathtt{P}[i, \varepsilon]$ for each full label $\varepsilon \in \{\mathtt{N}, \mathtt{D}, \mathtt{E}, \mathtt{F}\}$; the most likely label is flagged with '*'. The next column has the format $X : YZ$; where X is the label ε with largest $\mathtt{P}[i, \varepsilon]$, Y is the user-given "true" label e_i, and Z is '.' if $X = Y$, '*' otherwise. The next three columns give similar probabilities for the weak label c_i (N or K).

3 Description of the Algorithm

3.1 Classifying Bases by Context

In our method, the four probabilities $\mathtt{P}[i, \varepsilon]$, for each index i, are estimated by analyzing the base b_i and the p nearest bases on either side of it; where p is a user-specifiable parameter.

Let $W_i^p = \{i - p, i - p + 1, \ldots, i + p\}$ be the window with size $k = 2p + 1$ centered at position i; and let $\beta = b[W_i^p]$ be its (known) content. Its (unknown) true labeling $e[W_i^p]$ could be any string in $\mathcal{E}^k$. Our algorithm actually computes (implicitly or explicitly) a probability $\Pr(\eta \mid \beta) = \Pr(e[W_i^p] = \eta \mid b[W_i^p] = \beta)$ for each possible labeling $\eta \in \mathcal{E}^k$, taking into account its known content β. These probabilities are then combined into the four probabilities $\mathtt{P}[i, \varepsilon]$ according to the central label η_p of η; that is, $\mathtt{P}[i, \varepsilon] = \sum \{ \Pr(\eta \mid \beta) : \eta \in \mathcal{E}^k \wedge \eta_p = \varepsilon \}$

3.2   Window-Based Bayesian Inference

In theory, the probabilities $\Pr(\eta \mid \beta)$ could be obtained by analysis of a *training set* — a reference database of labeled genomic sequences, whose labels can be assumed to be true. Specifically, we can use the approximation $\Pr(\eta \mid \beta) \approx \#(\eta \wedge \beta) / \#(\beta)$, where $\#(\beta)$ is the the total number of windows in the training set with content β, and $\#(\eta \wedge \beta)$ is the number of windows with labeling η and content β.

However, this approximation is accurate only if $\#(\beta)$ is sufficiently large, and is in fact useless if $\#(\beta) = 0$. By a rough estimate, using this method with $k = 21$ (a rather modest window size) would require a training set with more than $4^{21} = 10^{12}$ *correctly labeled* bases — far beyond what is currently available.

To circumvent this problem, we first use Bayes's inference formula to express the "deductive" conditional probabilities $\Pr(\eta \mid \beta)$ in terms of the "generative" probabilities $\Pr(\beta \mid \eta)$. For all $\beta \in \mathcal{B}^k$ and all $\eta \in \mathcal{E}^k$

$$\Pr(\eta \mid \beta) = \frac{\Pr(\beta \wedge \eta)}{\Pr(\beta)} = \frac{\Pr(\beta \mid \eta) \Pr(\eta)}{\sum_{\sigma \in \mathcal{E}} \Pr(\beta \mid \sigma) \Pr(\sigma)} \tag{1}$$

3.3   The Independence Hypotheses

In order to apply formula (1), we need to know $\Pr(\beta \mid \eta)$; which is the probability that a random window of the genome with length $k = |\eta| = |\beta|$, whose true labelling is η, contains the bases $(\beta_0, \beta_1, \ldots, \beta_{k-1})$. We also need $\Pr(\eta)$; which is the probability that η is the true labeling of any k consecutive bases of the genome, *a priori* (i.e. independently of which bases are found at those positions).

Needless to say, we cannot estimate these probabilities by counting frequencies in some training set, since the frequency approximation $\#(\beta \wedge \eta) / \#(\eta)$ is just as impractical for $\Pr(\beta \mid \eta)$ as $\#(\beta \wedge \eta) / \#(\beta)$ is for $\Pr(\eta \mid \beta)$. We get around this problem by making certain *independence assumptions* about the statistics of the input data. In our tests, specifically, we assumed that

H1.   Within a gene, each codon is independently chosen.
H2.   Within a non-coding region, each base is independently chosen.
H3.   There is no correlation between the contents of distinct regions.

These assumptions seem to hold for available labeled genomes [9]. They imply, in particular, that there is no correlation between the content of coding and non-coding regions; and that any two adjacent non-coding regions can be treated as

Table 2. Frequencies $\Pr(\beta \mid \texttt{DEF})$ of codons in the exons of Reese's human genome sample. See Sec. 4.2 for details on the data set.

Codon	Freq	Codon	Freq	Codon	Freq	Codon	Freq
AAA	0.018	TAA	0.001	CAA	0.010	GAA	0.023
AAT	0.013	TAT	0.010	CAT	0.008	GAT	0.018
AAC	0.021	TAC	0.018	CAC	0.015	GAC	0.028
AAG	0.035	TAG	0.001	CAG	0.036	GAG	0.045
ATA	0.004	TTA	0.003	CTA	0.005	GTA	0.005
ATT	0.012	TTT	0.013	CTT	0.010	GTT	0.008
ATC	0.024	TTC	0.024	CTC	0.022	GTC	0.016
ATG	0.022	TTG	0.010	CTG	0.051	GTG	0.033
ACA	0.011	TCA	0.008	CCA	0.014	GCA	0.013
ACT	0.011	TCT	0.011	CCT	0.018	GCT	0.019
ACC	0.023	TCC	0.018	CCC	0.025	GCC	0.036
ACG	0.007	TCG	0.005	CCG	0.008	GCG	0.010
AGA	0.008	TGA	0.002	CGA	0.006	GGA	0.014
AGT	0.008	TGT	0.008	CGT	0.005	GGT	0.012
AGC	0.020	TGC	0.014	CGC	0.016	GGC	0.030
AGG	0.010	TGG	0.014	CGG	0.013	GGG	0.017

a single region. On the other hand, one observes quite unequal frequencies for the 64 possible codons, as shown in Table 2.

The irregularities of Table 2 imply significant differences in nucleotide frequencies between coding and non-coding regions. Table 3 shows the frequencies of nucleotides A, T, C, G observed in Reese's data set, in five contexts: respectively, in the first, second, and third base of codons within

Table 3. Observed base frequencies

	D	E	F	K	N
A	0.248	0.300	0.144	0.231	0.263
T	0.160	0.263	0.184	0.203	0.278
C	0.261	0.235	0.351	0.283	0.227
G	0.330	0.200	0.318	0.283	0.232

the exons (columns D, E, F), in any position within the exons (K), and outside the exons (N).

Note that the codon frequencies shown in Table 2 differ significantly from those that one would expect if the three letters were chosen independently with the probabilities of columns D, E, and F of Table 3. These discrepancies imply significant correlations between bases b_i and b_j in coding regions, whenever $|i - j| \leq 2$.

3.4   Factoring the Productive Probabilities

Hypotheses H1–H3 allow us to break down the factor $\Pr(\beta \mid \eta)$ of Formula (1) into products of probabilities of *atomic events* which are easier to estimate. Firstly, suppose that a window labeling η can be split as $\eta'\eta''$, where the last label ε' of η' and the first label ε' of η'' are any pair in $\mathcal{E}^2$ except NN, DE, EF, or FD.

In that case, the sub-windows of the input genome corresponding to η' and η'' necessarily belong to distinct regions. Then, by assumption H3, and elementary probability calculus, we have

$$\Pr(\beta \mid \eta) = \Pr(\beta' \mid \eta') \Pr(\beta'' \mid \eta'') \tag{2}$$

for any strings β, β', β'' such that $|\beta'| = |\eta'|$ and $|\beta''| = |\eta''|$. Moreover, by assumptions H1 and H2, Formula (3) holds also when the label pair $\varepsilon'\varepsilon''$ is NN (two consecutive non-coding bases) or FD (the boundary between two codons).

In other words, we can split β and η between any two codons, any two non-coding bases, or at any place that, according to η, is obviously the boundary between two distinct regions. It follows that, for any $\beta \in \mathcal{B}^k$ and $\eta \in \mathcal{E}^k$,

$$\Pr(\beta \mid \eta) = \prod_{j=1}^{m} \Pr(\beta_j \mid \eta_j) \tag{3}$$

where

- $\eta = \eta_1 \eta_2 \cdots \eta_m$, and $\beta = \beta_1 \beta_2 \cdots \beta_m$;
- for each j, $\beta_j \in \mathcal{B}^{|\eta|}$;
- for each j, $\eta_j \in \{\text{N}, \text{DEF}, \text{DE}, \text{EF}, \text{D}, \text{E}, \text{F}\}$;
- for each j, $(\eta_j, \eta_{j+1}) \notin \{(\text{D}, \text{EF}), (\text{DE}, \text{F}), (\text{D}, \text{E}), (\text{E}, \text{F})\}$.

Note that the deductive probabilities $\Pr(\eta \mid \beta)$ cannot be factored in this way; that is the reason why we need formula (1).

3.5   Relevant Labelings

In principle, the Bayesian inference Formula (1) should be evaluated for all possible labelings $\eta \in \mathcal{E}^k$; which is obviously impractical for k beyond 10 or so. Fortunately, most of those labelings turn out to be so unlikely that they can be ignored, without significant effect on the classification. More precisely, we replace Formula (1) by the approximation

$$\Pr(\eta \mid \beta) \approx \frac{\Pr(\beta \mid \eta) \Pr(\eta)}{\sum_{\sigma \in Z} \Pr(\beta \mid \sigma) \Pr(\sigma)} \tag{4}$$

The set of relevant labelings Z is a parameter of the algorithm. As shown in Secs. 3.4 and 3.6, the algorithm's running time is proportional to $nk \, \# Z$, and one can get useful results with a set Z of size $O(k)$.

3.6   Estimating the a Priori Labeling Probabilities

Besides the generative probabilities $\Pr(\beta \mid \eta)$, Bayes's Formula (1) also requires the a priori probabilities $\Pr(\eta)$ for each labeling $\eta \in \mathcal{E}^k$. Since the genome is assumed to consist of relatively long regions, each uniformly coding or uniformly non-coding, there is substantial correlation between the *labels* of adjacent bases

— even in non-coding regions and across codon boundaries. As a consequence of these long-range correlations, there is no factoring result analogous to Formula 3 for the a priori probabilities $\Pr(\eta)$.

To compute $\Pr(\eta)$, we need to extend the genome model with information about the lengths of coding and non-coding regions, and how the former are cut out from the ancestral genes. For the tests reported below, we assumed that:

L1.   Coding and non-coding regions alternate in the input string.
L2.   Every region is at least k bases long.
L3.   The mean lengths $\mu_{\mathtt{K}}, \mu_{\mathtt{N}}$ of coding and non-coding regions are known.
L4.   The first (or last) base of a coding region may have true label D, E, or F, with equal probability.

Assumptions L1–L4 greatly reduce the window labelings η that need to be considered, from $\mathcal{E}^k$ to the following possibilities:

E1.   The window is totally non-coding, i.e. the true labeling η is NNN....
E2.   The window is totally coding, i.e. η is DEFDEF..., EFDEFD..., or FDEFDE....
E3.   The window straddles the boundary between two regions, one coding and one non-coding.

There is only one window labeling of type E1, three of type E2, and $6(k-1)$ of type E3 (since there are $k-1$ positions for the transition within the window, two choices for the order of η' and η'', and three choices for the first coding label). That makes $6k-2$ labelings to consider for each window.

Given hypotheses L1–L4, the *a priori* probability $\Pr(\eta)$ of each labeling η depends only on the mean lengths $\mu_{\mathtt{K}}$ and $\mu_{\mathtt{N}}$ of coding and non-coding regions. Namely, we expect one N-K transition and one K-N transition every $\mu_{\mathtt{K}} + \mu_{\mathtt{N}}$ bases, and each of these transitions will be straddled by $k-1$ windows. It follows that $\Pr(\eta)$ is, for each type,

$$ \text{E1:} \quad \frac{\mu_{\mathtt{N}} - k + 1}{\mu_{\mathtt{K}} + \mu_{\mathtt{N}}} \qquad \text{E2:} \quad \frac{1}{3}\frac{\mu_{\mathtt{K}} - k + 1}{\mu_{\mathtt{K}} + \mu_{\mathtt{N}}} \qquad \text{E3:} \quad \frac{1}{6}\frac{1}{\mu_{\mathtt{K}} + \mu_{\mathtt{N}}} \tag{5} $$

4   Experimental Results

4.1   Test Runs

We tested the algorithm on a set **H** of natural eukaryotic DNA sequences, as well as on a randomly generated artificial dataset **A**. Both datasets were processed with windows of size 1, 3, 5, 9, 17, 33, 65, and 129.

4.2   The Natural Dataset

The natural dataset **H** was a collection of annotated human DNA sequences prepared by Martin Reese [11]. The collection comprises 462 separate files, each

covering one human gene (or part of one gene). After excluding a few unsuitable files (such as genes which had been tagged by software), there remained 448 files with 5,258,181 nucleotide bases, 439,761 of them (8.4%) belonging to exons. The average length of exon and non-exon regions were $\mu_K = 160$ and $\mu_N = 1516$, respectively.

Within exons, we set each "true" label e_i to D, E, or F according to its position in the expressed gene (after mRNA splicing). For all other bases, we set e_i to N. The atomic probabilities $\Pr(\beta \mid \eta)$ of tables 3 and 2 were obtained by counting occurrences of β and η in a subset of these sequences (with about 3.21 million bases), assuming the e labeling as "true", as described in Sec. 3.4. The rest of the data set (about 2.05 million bases) was then classified with our algorithm, and the output was scored using the same labeling e as the truth.

4.3   The Artificial Dataset

The artificial dataset **A** consisted of a single sequence with 45,000 nucleotide letters, obtained by concatenating coding and non-coding regions, alternately. Each region was independently generated according to hypotheses H1–H3, using the probabilities of Table 3 for each base in non-coding regions, and of Table 2 for each codon in coding regions. The first and last codons were truncated so that each coding region was equally likely to begin or end with a D, E, or F base. The length of each region was $100 + \ell$ where ℓ was drawn from an exponential distribution, with mean 50 for coding regions and 800 for non-coding regions — resulting in mean lengths $\mu_K = 150$ and $\mu_N = 900$, respectively. The true labeling e_i of each base was recorded during its generation.

4.4   Scoring Table and Mean Hit Score

To evaluate the performance of the algorithm, we compared its probability estimates $P[i, \varepsilon]$ for each base b_i with the corresponding "true" label e_i. Specifically, we computed the *scoring table*

$$SC[\varepsilon, \varepsilon'] = \frac{1}{n} \sum_{i=0}^{n-1} (e_i = \varepsilon') \, P[i, \varepsilon] \tag{6}$$

for all $\varepsilon, \varepsilon' \in \mathcal{E}$; where the factor $(e_i = \varepsilon')$ is 1 if the equality holds, 0 otherwise. We can use the sum $\sigma = \sum_\varepsilon SC[\varepsilon, \varepsilon]$ of the diagonal elements of that table as the *mean hit score* of the classifier.

4.5   Test Results

Table 4 shows the mean hit scores obtained by the algorithm on the two data sets, as a function of the window length k. The columns σ_{KN} and σ_{DEF} are the scores achieved on the weak K/N classification problem and on the reading frame identification problem, respectively.

Table 4. Hit scores for the human (**H**) and artificial (**A**) test data

k	H		A	
	σ_{KN}	σ_{DEF}	σ_{KN}	σ_{DEF}
1	0.14	0.36	0.15	0.36
3	0.17	0.40	0.18	0.39
5	0.19	0.45	0.19	0.43
9	0.24	0.55	0.24	0.49
17	0.33	0.68	0.36	0.58
33	0.52	0.81	0.54	0.69
65	0.73	0.92	0.69	0.80
129	0.83	0.98	0.76	0.86

Figure 2 shows the variation of $\mathrm{P}[i, \mathrm{K}]$, the estimated probability of b_i belonging to a coding region, along a segment of the **A** sequence, with $k = 9$ (top), $k = 33$ (middle), and $k = 129$ (bottom). The dashed line is the output of the ideal classifier (1 when $e_i = \mathrm{K}$, 0 when $e_i = \mathrm{N}$). Note that the coding region at bases 335-405 was was practically indistinguishable with $k = 9$, but clearly and confidently detected with $k = 129$.
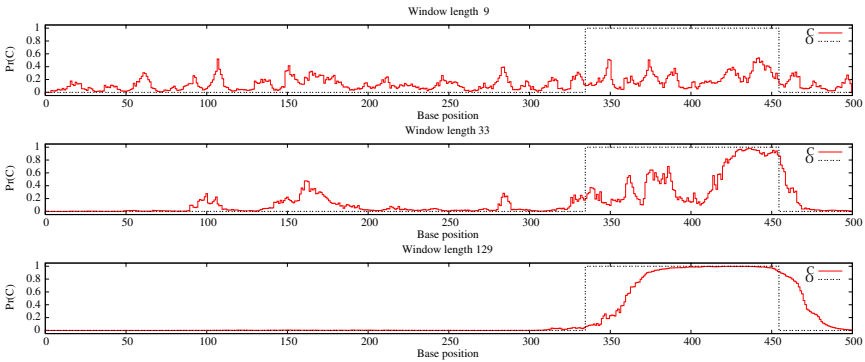
Fig. 2. Graph of $\mathrm{P}[i, \mathrm{K}]$ for the artificial dataset **A**

4.6   Discussion of Test Results

While the test with natural data would seem more relevant for users, it was distorted by the use of an incorrect reference labeling. The non-exon DNA regions, which we assumed to be entirely non-coding (N), surely contained many undocumented fossil coding regions, which we should have labeled with D/E/F. This mislabeling of fossil regions had also the effect of "blurring" already small differences between the probabilities $\Pr(\beta \mid \eta)$ of coding and non-coding regions.

Nevertheless, the algorithm performed fairly well on the natural dataset **H**, with a hit score $\sigma_{\mathrm{DEF}} = 0.857$ on the frame labeling problem. While the test with artificial data **A** used the same tables $\Pr(\beta \mid \eta)$, which were distorted

by the mislabeling above, the algorithm's performance was much better, with $\sigma_{\text{DEF}} = 0.982$ on the frame labeling problem — presumably, because the output was scored against the correct labeling. In any case, the performance obtained in both tests is only a lower bound on the performance that one could obtain with better-labeled natural training set.

5   Conclusions and Future Work

The main advantages of our method are consistency, correctness, and flexibility, at a modest computational cost. The use of Bayesian inference ensures that the proposed algorithm produces the best possible classification. The inclusion of coding/non-coding transitions in the Bayesian inference leads to sharp estimates for the position of those transitions for large $|w|$. The methods is easily adapted to other statistical models by changing the set of allowed window labelings Z, the probability tables $\Pr(\beta \mid \eta)$, and the a priori probabilities $\Pr(\eta)$.

References

1. Meidanis, J., Setubal, J.C.: Introduction to Computational Molecular Biology. PWS Publishing Company (1997)
2. Batzoglou, S., Pachter, L., Mesirov, J.P., Berger, B., Lander, E.S.: Human and mouse gene structure: Comparative analysis and application to exon prediction. Genome Research (10), 950–958 (2000)
3. Fickett, J.W.: Recognition of protein coding regions in DNA sequences. Nucleic Acids Research 10(17), 5303–5318 (1982)
4. Sagot, C.M.M.F., Schiex, T., Rouzé, P.: Recognition of protein coding regions in DNA sequences. Nucleic Acids Research 30(19), 4103–4117 (2002)
5. Pertea, M., Salzberg, S.L.: Computational gene finding in plants. Plant Molecular Biology 48(1-2), 39–48 (2002)
6. Farber, R., Lapedes, A., Sirotkin, K.: Determination of eukaryotic protein coding regions using neural networks and information theory. Journal of Molecular Biology (226), 471–479 (1992)
7. Kotlar, D., Lavner, Y.: Gene prediction by spectral rotation measure: A new method for identifying protein-coding regions. Genome Research 13(8), 1930–1937 (2003)
8. Majoros, W.H., Pertea, M., Salzberg, S.L.: Efficient implementation of a generalized pair hidden Markov model for comparative gene finding. Bioinformatics 21(9), 1782–1788 (2005)
9. Staden, R., McLachlan, A.D.: Codon preference and its use in identifying protein coding regions in long DNA sequences. Nucleic Acids Res. 10(1), 141–155 (1982)
10. Capua, R.O., da Gama Leitão, H.C., Stolfi, J.: Uma abordagem estatística para identificação de éxons. In: WOB 2004, Brasília, DF (2004)
11. Reese, M.: Database with human genome sequences (2005), http://www.fruitfly.org/seq_tools/datasets/Human/multi_exon_GB.dat

Coding Region Prediction in Genomic Sequences Using a Combination of Digital Signal Processing Approaches

Aníbal Rodríguez Fuentes[1], Juan V. Lorenzo Ginori[1], and Ricardo Grau Ábalo[2]

[1] Center for Studies on Electronics and Information Technologies
[2] Center for Studies on Informatics, Universidad Central "Marta Abreu" de Las Villas,
Carretera a Camajuaní, km 5 ½, Santa Clara, VC, CP 54830, Cuba
anibalr@uclv.edu.cu, juanl@uclv.edu.cu, rgrau@uclv.edu.cu
http://www.fie.uclv.edu.cu

Abstract. Identifying protein coding regions in DNA sequences is a basic step in the location of genes. Several approaches based on signal processing tools have been applied to solve this problem, trying to achieve more accurate predictions. This paper presents a new predictor that improves the efficacy of three ones that use the Fourier Transform to predict coding regions, and that could be computed using an algorithm that reduces the computation load. ROC curves are used to demonstrate the efficacy of the proposed predictor, based on the computation of 25 DNA sequences from three different organisms.

Keywords: Bioinformatics, Digital Signal Processing, Fourier Transform, Coding region prediction, Computational load reduction.

1 Introduction

The genomic information is usually represented by sequences of nucleotide symbols in the strands of DNA molecules, by symbolic codons (triplets of nucleotides), or by symbolic sequences of amino acids in the corresponding polypeptide chains. When representing by sequences of nucleotide symbols, the alphabet consists of the letters A, T, C and G; represent adenine, thymine, cytosine, and guanine respectively. The segments of DNA molecule responsible for protein synthesis are the genes. The regions containing useful information from genes are called exons; in eukaryotes these regions are separated by introns, whereas in prokaryotes they are continuous.

The computational recognition of genes is one of the challenges in the analysis of newly sequenced genomes, and it is a basic step to an understanding of the genome. It is needed to find accurate and fast tools to analyze genomic sequences and annotate genes. A number of methods have been proposed for gene and exon detection, based on distinctive features of protein-coding sequences, and among them many techniques using digital signal processing [1-8] have been used and shown to be successful; based on the period-3 periodicity present in most of genome exons due to the non-uniform distribution of codons in coding regions.

In this paper we propose a new coding region predictor based on a combination of others approaches that use the Short Time Fourier Transform (STFT) [1-3], and that could be computed using an algorithm [9] design for the authors to improve the

computational load. In order to validate the results of the proposed predictor, ROC curves are used, which show a slight increase of the efficacy of the predictor when compared with the others that use STFT.

2 Materials and Methods

In the following paragraphs there is a presentation of the new predictor we propose, introducing firstly the technique we used to convert the genomic information to a numerical sequence. In this work we have made extensive use of a fast algorithm previously developed by the authors [9], in order to reduce the computational load associated to the use of the predictor . At the end a brief presentation of ROC curves is made as a validation approach.

2.1 Obtaining Numerical Sequences from Genomic Information

There are several approaches [2, 6-8, 10, 11] to convert genomic information in numeric sequences using its different representations. The most relevant for the application of signal processing tools are the assignation of complex numbers to each base of the nucleotide sequence, and the indicator sequences. The complex numbers to be assigned are selected according to their mathematical properties, their relation with the bases and the properties of the resulting numeric sequence. Indicator sequences are defined as binary sequences for each base, where 1 at position k indicates the presence of the base at that position, and 0 its absence. For example, for the DNA sequence x[k] = TACAGAACTTAGC…the binary indicator sequences for each base are:

$$x_A[k] = 0101011000100\ldots$$
$$x_T[k] = 1000000011000\ldots$$
$$x_C[k] = 0010000100001\ldots$$
$$x_G[k] = 0000100000010\ldots \quad (1)$$

One of the advantages of using indicator sequences lies in their simplicity, and in the possibility of providing a four-dimensional representation of the frequency spectrum of the character string, when computing the Discrete Fourier Transform of each indicator sequence.

2.2 Combining Approaches Based on Discrete Fourier Transform

The Discrete Fourier Transform (DFT) has been used by several authors to predict coding regions in large DNA sequences. Based on the non-uniform distribution of codons in coding regions, a three-periodicity is present in most of genome coding regions, which show a notable peak at frequency component N/3 when calculating their DFT [12, 13]. Taking into account the validity of this result the Short Time Fourier Transform has been applied to large DNA sequences to predict coding regions, using a sliding window along the sequence, calculating the Fourier Transform of each subsequence, and taking only the N/3 frequency component. In [1] Tiwari introduces the Spectral Content Measure (SCM), defined as:

$$S[k] = \left| X_A[k] \right|^2 + \left| X_T[k] \right|^2 + \left| X_C[k] \right|^2 + \left| X_G[k] \right|^2 . \tag{2}$$

Here $X_A[k]$, $X_T[k]$, $X_C[k]$ and $X_G[k]$ are the frequency component at k of the Fourier Transform for the indicator sequences. In [2] Anastassiou introduces a new predictor, which he called Optimized Spectral Content Measure (OSCM), and that was defined as:

$$W = \left| aA(s) + tT(s) + cC(s) + gG(s) \right|^2 . \tag{3}$$

where $A(s)$, $T(s)$, $C(s)$ and $G(s)$ are the frequency component at N/3 of the Fourier Transform for sequence s. The values a, t, c and g are numerical complex constants obtained as a solution of an optimization problem proposed by the author to maximize the discriminatory capacity between coding and non-coding regions. This predictor demonstrated to be significantly better than the Spectral Content Measure for the sequences analyzed by Anasstasiou.

Using an expression similar to (3), Kotlar proposes in [3] the Spectral Rotation Measure (SRM) (4), where μ_A, μ_T, μ_C and μ_G are the approximated average values, in coding regions, of $\arg(A(s))$, $\arg(T(s))$, $\arg(C(s))$, and $\arg(G(s))$ respectively; and σ_A, σ_T, σ_C and σ_G are the angular deviation corresponding to $A(s)$, $T(s)$, $C(s)$, and $G(s)$. The magnitude shown in equation (4), proposed by Kotlar, achieves an increase in the magnitude on coding regions when computing this measure.

$$\left| V \right|^2 = \left| \frac{e^{-i\mu_A}}{\sigma_A} A(s) + \frac{e^{-i\mu_T}}{\sigma_T} T(s) + \frac{e^{-i\mu_C}}{\sigma_C} C(s) + \frac{e^{-i\mu_G}}{\sigma_G} G(s) \right|^2 . \tag{4}$$

In his paper Kotlar demonstrates on all experimental exons, and for all non-coding strands of length greater that 50 bp from the first 15 Chromosomes of S. cerevisiae, that this predictor is more efficiently that the other two exposed methods. The measures were calculated using chromosome 16 of S. cerevisiae,

Based on these three predictors we designed a new predictor defined as a linear combination of them. In order to determine the linear combination coefficients, we first considered the True Positive Fraction (The fraction of bases in the sequence that are predicted as coding regions, when they are truly inside a coding region) detected only by each predictor using a sample composed by 25 DNA sequences from different sizes and belonging to three different organisms. In Figure 1 it is shown the distribution of these fractions associated to each predictor for all possible decision thresholds using a sliding window of length 351, which is a typical value according to [2] when computing the DFT.

The distribution of the true positive fraction detected only by the Optimized Spectral Content Measure appeared as hardly noticeable, which led us to eliminate this predictor from the lineal combination. The performance of the two remaining predictors when using the ROC analysis is very similar (Figure 2), and after analyzing the similarity of the mean squared error of each predictor, we obtained the following equation:
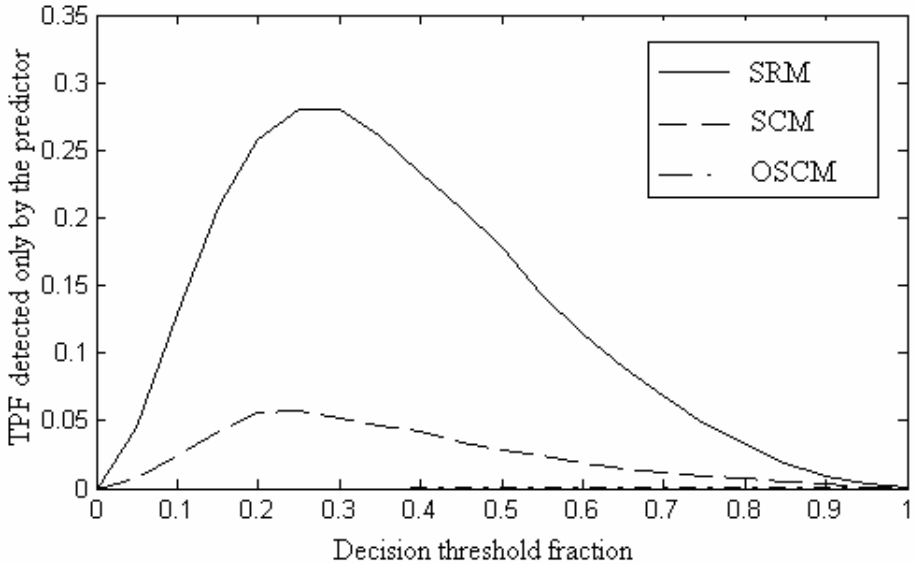
$$P[k] = mR[k] + nS[k] . \tag{5}$$

Fig. 1. Distribution of the true positive fraction detected only by each predictor for all possible decision thresholds

Where $R[k]$ and $S[k]$ are the Spectral Rotation Measure and the Spectral Content Measure respectively, and m and n are the inverse of the maximum value reached by the corresponding predictor when computing the sequence. The objective of the previous multiplication of the measures by the values m and n is to normalize these measures before adding them.

2.3 Reducing the Computational Load

The use of two predictors and a lineal combination of these predictors increases the computational load of the approach. Using the algorithm proposed by the authors in a previous paper [9] to calculate the DFT for sliding windows, which reduced at great extent the computational load associated to this task, we also reduced the general computation load, considering that the N/3 frequency component coefficient of the Discrete Fourier Transform for each window is computed once per indicator sequence.

2.4 Evaluation Method: ROC Curves

In order to measure and compare the efficacy of the proposed predictor with the other three, we have used receiver operating characteristic (ROC) curves [14, 15], which provide a global representation of the prediction accuracy.

When we evaluate a dichotomic test (results can be only interpreted as positives or negatives), the sensibility is defined as the probability an individual be correctly classified when its real status is the one defined as positive, regarding the condition studied by the test. It's also known as True Positive Fraction (TPF). The specificity is the probability an individual be correctly classified when its real status is the one

defined as negative. It is the result to subtract the False Positive Fraction (FPF) from 1.

In Table 1 it is shown the statistical procedure to obtain the sensibility and the specificity, considering the problem of coding region prediction in DNA sequences.

Table 1. Statistical procedure to obtain the sensibility and the specificity in coding region prediction

	Coding region	Non-coding region
Positive Prediction	True Positive (TP)	False Positive (FP)
Negative Prediction	False Negative (FN)	True Negative (TN)

Sensibility (Ss) = TP/(TP+FN) = TPF
Specificity (Sp) = TN/(TN+FP) = True Negative Fraction = 1 – FPF

Basically the ROC curve plots for every possible decision threshold, which ranges from zero to the maximum value reached by the predictor, the pair (1-Sp, Ss) when computing the whole sequence and the results are compared with the real values. The closer the ROC curve is to a diagonal, the less useful is the predictor in order to discriminate coding and non-coding region of a DNA sequence. The more the curve moves to the upper left corner on the graph, the better the predictor.

3   Results

For the validation of the experiments all the techniques were applied to 25 genomic sequences with different features and sizes, belonging to three organisms: S. *cerevisiae*, S. *pombe* and C. *elegans*. These sequences can be retrieved directly from the Genbank database, maintained by National Center for Biotechnology Information (NCBI) [16].

Figure 2 shows the ROC curves associated to each predictor when computing the 25 selected DNA sequences, using a sliding window of size 351. Notice that the graph corresponding to the proposed predictor (solid line) is more effective than the three others. The approximated values when calculating the area under the curve for each predictor are: Proposed Predictor: 0.7767, Spectral Content Measure: 0.7352, Optimized Spectral Content Measure: 0.7319 and Spectral Rotation Measure: 0.7351; demonstrating that the Proposed Predictor increases the efficacy of the Spectral Content Measure in 6.12%. Using sliding window of lengths 180, 480 and 702 we obtained similar results.

Figure 3 shows the graph obtained at using the proposed predictor to a DNA sequence composed by 16680 bp inside chromosome X of S. *cerevisiae*. Real coding regions are represented using the rectangles.

In order to evaluate the computation time of the proposed predictor when using the fast algorithm described in [9], in Table 2 it is shown the average execution time, in seconds, when compute the Spectral Rotation Measure using the direct (traditional)
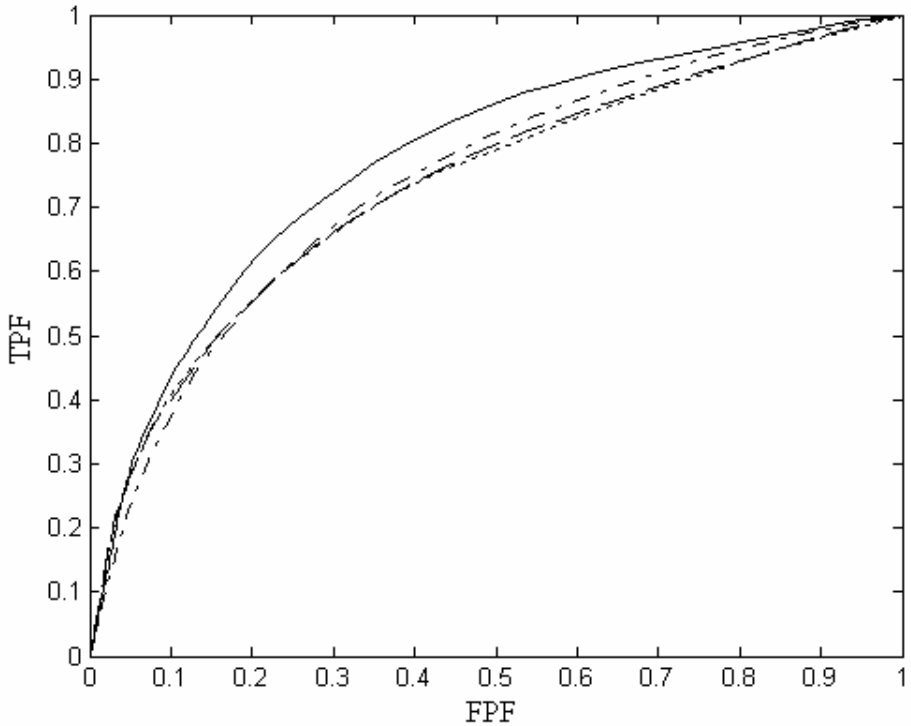
Fig. 2. ROC curves associated to each predictor. Proposed Predictor (Solid line), Spectral Content Measure (dash dot), Optimized Spectral Content Measure (dotted), Spectral Rotation Measure (dashed line).
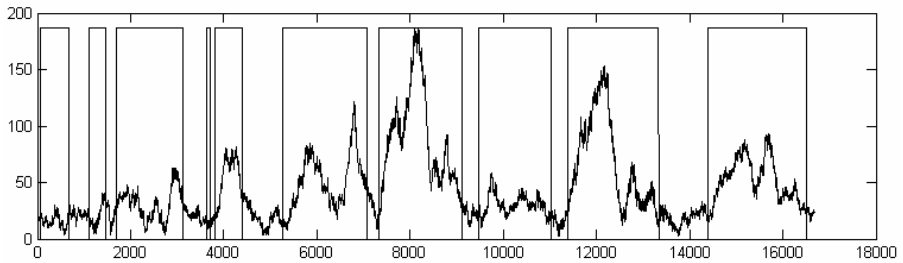
Fig. 3. Application of the proposed approach to a sequence contains 16680 bp inside chromosome X of S. *cerevisiae*. Rectangles indicate real coding regions.

method and the proposed predictor using the fast algorithm for two sequences with different lengths and using two different window lengths, under the same conditions.

The percentage of time used by the proposed predictor using the fast algorithm is about 3% of the time employed to compute the Spectral Rotation Measure using the direct method.

Table 2. Computation time comparison, in seconds, between the SRM using the direct method and the proposed preditor using the fast algorithm for different DNA strings

DNA stretch length	8000 bp		16680 bp	
Window Length	**351**	**702**	**351**	**702**
Spectral Rotation Measure using direct method	1.4210	2.1700	2.9030	4.6050
Proposed predictor using the fast algorithm	0.0470	0.0620	0.0930	0.1090

4   Conclusions

The prediction of coding regions in large DNA sequences is a basic problem to annotate genes. Digital Signal Processing techniques have been used successfully to solve this problem; however the current tools are still unable to predict all the coding regions present in a DNA sequence.

   In this work, a new predictor is proposed based on the linear combination of two other methods that showed good efficacy individually and also on a fast algorithm previously developed by the authors to reduce the computational load. The efficacy of the proposed predictor was evaluated by means of ROC curves, which showed a better performance in coding regions detection when compared to the previous methods. A computation time comparison between the Spectral Rotation Measure using the direct method and the proposed predictor using the fast algorithm demonstrated that even when combining two predictors the computational load does not increase significantly.

References

1. Tiwari, S., et al.: Prediction of probable genes by Fourier analysis of genomic sequences. CABIOS 113, 263–270 (1997)
2. Anastassiou, D.: Genomic signal processing. IEEE Signal Processing Magazine 18(4), 8–20 (2001)
3. Kotlar, D., Lavner, Y.: Gene Prediction by Spectral Rotation Measure: A New Method for Identifying Protein-Coding Regions. Genome Research 13(8), 1930–1937 (2003)
4. Vaidyanathan, P.P., Yoon, B.-J.: Gene and exon prediction using allpass-based filters. ONR (2002)
5. Akhtar, M., Ambikairajah, E., Epps, J.: Detection of Period-3 Behavior in Genomic Sequences Using Singular Value Decomposition. In: IEEE-International Conference on Emerging Technologies, pp. 13–17 (2005)
6. Berger, J.A., Mitra, S.K., Astola, J.: Power spectrum analysis for DNA sequences. In: ISSPA 2003, Paris, France, pp. 29–32 (2003)
7. Dodin, G., et al.: Fourier and Wavelet Transform Analysis, a Tool for Visualizing Regular Patterns in DNA Sequences. J. Theor. Biol. 206, 323–326 (2000)
8. Berger, J.A., et al.: New approaches to genome sequence analysis based on digital signal processing. University of California (2002)

 9. Fuentes, A.R., Ginori, J.V.L., Ábalo, R.G.: Detection of Coding Regions in Large DNA Sequences Using the Short Time Fourier Transform with Reduced Computational Load. In: Martínez-Trinidad, J.F., Carrasco Ochoa, J.A., Kittler, J. (eds.) CIARP 2006. LNCS, vol. 4225, pp. 902–909. Springer, Heidelberg (2006)
10. Cristea, P.D.: Conversion of nucleotides sequences into genomic signals. J. Cell. Mol. Med. 6(2), 279–303 (2002)
11. Su, S.-C., Yeh, C.H., Kuo, C.J.: Structural Analysis of Genomic Sequences with Matched Filtering. IEEE Signal Proccessing Magazine 3, 2893–2896 (2003)
12. Tsonis, A.A., Elsner, J.B., Tsonis, P.A.: Periodicity in DNA coding sequences: Implications in gene evolution. J. Theor. Biol. 151, 323–331 (1991)
13. Chechetkin, V.R., Turygin, A.Y.: Size-dependence of three-periodicity and long-range correlations in DNA sequences. Phys. Lett. A 199, 75–80 (1995)
14. Swets, J.A., Pickett, R.M.: Evaluation of diagnostic systems: methods from signal detection theory. Academic Press, Nueva York (1982)
15. Zweig, M.H., Campbell, G.: Receiver-operating characteristic (ROC) plots: a fundamental evaluation tool in clinical medicine. Clin. Chem. 39, 561–577 (1993)
16. GenBank database, NCBI

Using Typical Testors for Feature Selection in Text Categorization

Aurora Pons-Porrata[1], Reynaldo Gil-García[1], and Rafael Berlanga-Llavori[2]

[1] Center of Pattern Recognition and Data Mining,
Universidad de Oriente, Santiago de Cuba, Cuba
{aurora,gil}@csd.uo.edu.cu
[2] Computer Science,
Universitat Jaume I, Castellón, Spain
berlanga@lsi.uji.es

Abstract. A major difficulty of text categorization problems is the high dimensionality of the feature space. Thus, feature selection is often performed in order to increase both the efficiency and effectiveness of the classification. In this paper, we propose a feature selection method based on Testor Theory. This criterion takes into account inter-feature relationships. We experimentally compared our method with the widely used information gain using two well-known classification algorithms: k-nearest neighbour and Support Vector Machine. Two benchmark text collections were chosen as the testbeds: Reuters-21578 and Reuters Corpus Version 1 (RCV1-v2). We found that our method consistently outperformed information gain for both classifiers and both data collections, especially when aggressive feature selection is carried out.

Keywords: feature selection, typical testors, text categorization.

1   Introduction

Text Categorization (TC - also known as text classification) is the task of assigning documents to one or more predefined categories (classes or topics). This task relies on the availability of an initial corpus of classified documents under these categories (known as training data). Depending on the application, TC may be either single-label (i.e., exactly one category must be assigned to each document) or multi-label (i.e., several categories can be assigned to each document).

Text Categorization is an important component in many information management tasks such as spam filtering, real time sorting of email or files into folders, document routing, document dissemination, topic identification, classification of Web pages and automatic building of Yahoo!-style catalogs. That is why during the last decade there has been a great interest from researchers.

TC literature mainly relies on Machine Learning methods such as probabilistic classifiers, decision trees, nearest neighbour classifiers, support vector machines and classifier committees, to mention a few. However, a major difficulty of text categorization problems is the high dimensionality of the feature space, which can be tens or hundreds of thousands of terms for even a moderate-sized text collection.

Most of the features are irrelevant and others introduce noise that diminishes the classifier effectiveness. Thus, feature selection becomes a crucial task for improving both the efficiency and effectiveness of the classification algorithms. Moreover, feature selection techniques reduce overfitting (i.e., the tendency of the algorithm to better classify the data it has been trained on than new unseen data), and makes the problem more manageable for the classifier.

Let τ be the original set of features and φ a certain feature selection criterion function. Without any loss of generality, let us consider a higher value of φ to indicate a better feature subset. Formally, the problem of feature subset selection consists of finding a subset $\tau' \subseteq \tau$ such that $|\tau'| \ll |\tau|$ and $\varphi(\tau') = \max_{t \subseteq \tau} \varphi(t)$ [1].

According to John et al. [2] there are two main approaches to feature subset selection used in Machine Learning: wrapper and filtering. The idea of the wrapper approach is to select feature subset using the evaluation function based on the same algorithm that will be used for learning on domain represented with selected feature subset. This can result in a rather time consuming process, since, for each candidate feature subset that is evaluated during the search, the target learning algorithm is run usually several times. This approach has the advantage of being tuned to the learning algorithm being used. However, the sheer size of the space of different term sets makes its cost-prohibitive for standard TC applications. On the contrary, in the filtering approach a feature subset is selected independently of the learning method that will use it. It keeps terms that receive the highest score according to a function that measures the "importance" of the term for the TC tasks. Because of computational complexity the filtering approach is preferable over the wrapper approach to feature subset selection in TC. We will explore this solution in this paper.

The filtering methods can be also divided into two categories: Best Individual Feature (BIF) selection methods and global subset selection methods. In the former, some evaluation function that is applied to a single feature is used. All the features are independently evaluated, a score is assigned to each of them and the features are sorted according to the assigned score. Then, a predefined number of the best features is taken to form the best feature subset. BIF selection methods completely ignore the existence of other words and the manner how the words work together. Scoring of individual features can be performed using some of the measures used in machine learning, for instance: information gain [3], document frequency, mutual information, χ^2 statistic [4] and odds-ratio [5]. The mathematical definitions of these functions are summarized in [6]. Yang et al. [4], Mladenic et al. [7], Rogati et al. [8] and Forman [9] give experimental comparison of the above mentioned measures in text categorization tasks. Information gain was reported to work well on text data.

As opposed to the BIF methods the global selection procedures reflect to a certain extent the dependencies between words. These methods include, for instance, forward and backward selection algorithms and oscillating search. Forward selection algorithms start with an empty set of features and add one feature at a time until the final feature set is reached. Backward elimination algorithms start instead with a feature set containing all features and remove features one at a time. Oscillating search [10] is not dependent on pre-specified direction of search. It is based on repeated modification of the current subset of features by alternating the so-called

down- and up-swings. However, these sequential methods can show to be too slow to yield results in reasonable time, because of their combinatorial nature.

In this paper, we propose a new feature selection method based on Testor Theory [11] for text categorization tasks. This criterion not only takes into account inter-feature relationships but also it is computationally feasible. We experimentally compared our method with information gain using *k*-nearest neighbour and Support Vector Machine classifiers over two benchmark text collections. We found that our method consistently outperformed information gain for both classifiers when aggressive feature selection is carried out.

2   Basic Concepts

Before presenting our feature selection method, we review the main definitions of the *Testor Theory* [11].

Let ζ be the set of training samples, each of them described in terms of features $\tau=\{t_1,\ldots,t_n\}$ and grouped into the classes $C_1,\ldots,C_r$, $r \geq 2$. Each feature t_i takes values in a set D_i, $i = 1,\ldots,n$. Let M be the training matrix, whose rows represent the training samples and columns represent the features describing them.

A comparison criterion of dissimilarity $\psi_i : D_i \times D_i \rightarrow \{0,1\}$ is associated to each t_i ($i=1,\ldots,n$). Applying these comparison criteria for all possible pairs of objects belonging to different classes in M, a Boolean comparison matrix is built. Notice that the number of rows in the comparison matrix is $m' = \sum_{i=1}^{r-1} \sum_{j=i+1}^{r} |C_i||C_j|$, where $|C_i|$ denotes the number of objects in class C_i.

In the Testor Theory, the set of features $\pi = \{t_{i_1},\ldots,t_{i_k}\} \subseteq \tau$ and their corresponding set of columns $\{i_1,\ldots,i_k\}$ of a matrix M is called a *testor*, if after removing from M all columns except $\{i_1,\ldots,i_k\}$, all rows of M corresponding to distinct classes are different. In terms of the comparison matrix, a testor can be described as a set of features for which a whole row of zeros does not appear in the remainder comparison submatrix, after removing all the other columns. A testor is called *irreducible* (*typical*) if none of its proper subsets is a testor [11].

Thus, the set of all typical testors of a matrix M contains the combinations of features that distinguish the classes.

3   Proposed Feature Selection Method

Broadly speaking, our approach to feature selection is a combination of the individual and global approaches. More specifically, we use individual feature selection by applying word frequency criterion to select a first subset of features. Then, we apply Testor Theory to select the subset of these features that better discriminate the different target classes. Thus, this approach takes profit from both viewpoints: individual filtering speeds-up notably the selection of features and the global one takes into account possible feature correlations and discriminating power. Moreover, Testor Theory provides us a natural method to select for each class, independently of its weight and training set size, the set of features that better discriminates their

examples from the rest of classes. This approach alleviates the problem of unbalanced classes, which is a very common problem in TC, and implies that aggressive feature selection affect to all the classes not only the smaller ones. Next paragraphs describe in detail how Testor Theory is applied to filter features.

In our text categorization problem, ζ is the set of training documents, τ contains all terms occurring in the documents and $C_1,\ldots,C_r$ are the categories. Each document d_j is represented as a vector of term weights $d_j = (w_1^j,\ldots,w_n^j)$. The selection of terms includes removing tags and stop words, lemmatization and proper name recognition. Weights are computed by using the standard *ltc* variant of *tf-idf* function [12], i.e.,

$$w_i^j = (1+\log TF(t_i,d_j))\cdot\log\frac{|\zeta|}{df(t_i)}, \text{ where } TF(t_i,d_j) \text{ denotes the number of times } t_i$$

occurs in d_j and $df(t_i)$ is the number of documents in ζ in which t_i occurs at least once.

The representative of a category C_i, denoted as $\bar{c}_i$, is calculated as the average of

the documents of that category, that is, $\bar{c}_i = \left(\dfrac{\sum\limits_{d_j\in C_i} w_1^j}{|C_i|},\ldots,\dfrac{\sum\limits_{d_j\in C_i} w_n^j}{|C_i|} \right)$.

Given a category C_i, let $T(C_i) = \{t_1,\ldots, t_{n_{c_i}}\}$ be the most frequent terms in the representative $\bar{c}_i$, i.e., the terms t_j such that $w_j^{\bar{c}_i} \geq \varepsilon$, $j = 1,\ldots, n_{c_i}$ and ε is an user-defined parameter that represents the minimum frequency required to consider a term in the global subset selection process.

For each category C_i, we construct a matrix $MR(C_i)$, whose columns are the terms of $T(C_i)$, and its rows are the representatives of all categories, described in terms of these columns. Notice that this matrix is different in each category.

In order to calculate the typical testors, we considered two classes in the matrix $MR(C_i)$. The first class is only formed by $\bar{c}_i$ and the second one is formed by the other category representatives. Notice that our goal is to distinguish the category C_i from the other categories.

For the calculus of the typical testors, the key concept is the comparison criterion of the values of each feature. In our case, the features that describe the documents are the terms and its values are the weights of terms. The comparison criterion applied to all features is:

$$\psi(w_k^{\bar{c}_i}, w_k^{\bar{c}_j}) = \begin{cases} 1 & if\ w_k^{\bar{c}_i} - w_k^{\bar{c}_j} \geq \delta \\ 0 & otherwise \end{cases},$$

where $w_k^{\bar{c}_i}, w_k^{\bar{c}_j}$ are the weights in the category representative $\bar{c}_i$ and $\bar{c}_j$ in the column corresponding to the term t_k respectively, and δ is a dissimilarity threshold (in our experiments we use $\delta=0.15$). As it can be noticed, this criterion considers the two values (weights of the term t_k) different if the term t_k is frequent in category C_i and not frequent in category C_j.

In order to determine all typical testors of each matrix $MR(C_i)$, we use the algorithm LEX [13], which computes efficiently the typical testors of a data

collection. Finally, the selected feature subset is the union of typical testors of all categories. Notice that, unlike global feature selection methods, the number of desired features is not fixed beforehand, but it depends on the ε parameter.

The proposed feature selection method is summarized as follows:

```
Algorithm Feature selection
Input: M: training matrix.
       ε: term frequency threshold.
Output: τ′: set of selected features.
1. For each category C:
   a. Construct the matrix MR(C).
   b. Calculate the typical testors of the matrix MR(C),
      regarding two classes: C and its complement.
   c. Let U(C) be the union of all typical testors
      found in the step b.
2. τ′ = ⋃ U(C)
        C
```

4   Experimental Results

As mentioned before, Information gain had been one of the best performing feature selection measures for text categorization. It takes into account the presence of the term in a category as well as its absence and can be defined by

$$IG(t_k, C_i) = \sum_{C \in \{C_i, \overline{C_i}\}} \sum_{t \in \{t_k, \overline{t_k}\}} P(t, C) \cdot \log_2 \frac{P(t, C)}{P(t) \cdot P(C)}$$ [6]. In this formula, probabi-

lities are interpreted on an event space of documents (e.g. $P(\overline{t_k}, C_i)$ indicates the probability that, for a random document d, term t_k does not occur in d and d belongs to category C_i), and are estimated by maximum likelihood. We use the maximum value over all categories as the global score.

In this section, we compare the proposed feature selection method with Information gain. With this aim, two high-performing classifiers for the experiments: k-Nearest neighbour (parallel implementation, [14]) and Support Vector Machines (LibSVM, [15]) are selected. We used the standard C-SVC form of the SVM classifier with C=1, the linear kernel and tolerance of termination criterion = 0.1. No data scaling has been done. We also used the binary approach, which extends the one-against-all multi-class method for multi-label classification.

4.1   Data Sets

In our experiments two benchmark text collections were chosen as the testbeds: Reuters-21578[1] and Reuters Corpus Version 1 (RCV1-v2) [16]. The distribution of training documents into the categories is quite unbalanced in both collections.

---

[1] The Reuters-21578 collection may be freely downloaded from http://kdd.ics.uci.edu.

Reuters-21578 consists of a set of 12902 news stories classified under 135 categories related to economics. In this paper, we used the subset of 90 categories with at least one positive training example and one test example. This collection is partitioned (according to the "ModApté" split we have adopted) into a training set of 7058 documents and a test set of 2740 documents. The dimension of the document space is 26602 terms.

RCV1-v2 collection consists of over 800000 newswire stories that have been manually classified into 103 categories. The topic codes were selected as class labels. This collection is partitioned (according to the LYRL2004 split we have adopted) into a training set of 23149 documents and a test set of 781265 documents. The dimension of the document space is 47152 terms.

As we used a parallel implementation of k-Nearest neighbour classifier [14], our experiments are carried out over the entire RCV1-v2 collection. However, SVM is unable to handle such a collection, and consequently we used a small percentage (2%) of it. The documents were randomly chosen, and split into a 70% training set and 30% test set, while maintaining the distribution of the class probabilities in the original training and test sets. The resulting set has 11224 training documents and 4815 test documents.

4.2 Results

The first experiments are conducted to compare the categorization performance of our feature selection method (TT) against Information Gain (IG) using k-NN and SVM classifiers on the two above-mentioned Reuters collections. In our experiments, we set $\varepsilon = \{0.1, 0.15, 0.2, 0.25, \ldots, 0.7\}$ to obtain feature subsets of different sizes. For instance, we obtained a subset of 502 features in Reuters-21578 and 639 features in RCV1-v2 collection when ε is fixed to 0.4. Figures 1, 2, 3 and 4 show the classifiers performance w.r.t. different feature subset selections (including all features). Effectiveness is evaluated with both micro-averaged and macro-averaged F1 measures. Whereas micro-F1 depends on the size of the evaluated categories, macro-F1 depends on the number of categories to be evaluated. Thus, a classifier that behaves well on large categories will obtain a high micro-F1 value, but if it does not with small ones it will obtain low macro-F1. This is because in text collections, large categories cover a very large portion of the collection and small categories are much more numerous than large ones. As a result, when applying feature selection it is more difficult to improve macro-F1 values than micro-F1 ones.

Several observations can be made by analyzing the results in Figures 1, 2, 3 and 4. First, our feature selection method consistently outperformed information gain for both classifiers and both data collections at all number of selected features. The increase of performance is much larger for macro-averaged F1 (27% for Reuters-21578 and 18% for RCV1-v2 in average) than micro-averaged F1 (0.37% for Reuters-21578 and 5% for RCV1-v2 in average). This fact seems to suggest that our feature selection method is more insensitive to the problem of unbalanced class distribution. Another interesting observation is that the lesser number of selected features, the higher increase of performance is obtained.
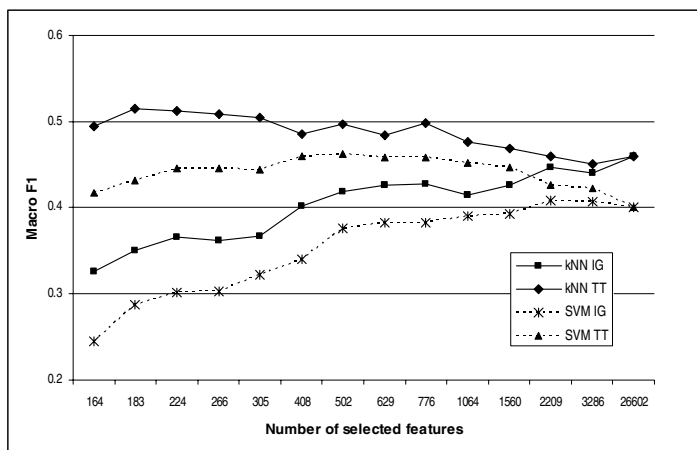
Fig. 1. Macro-averaged F1 scores for Reuters-21578 collection
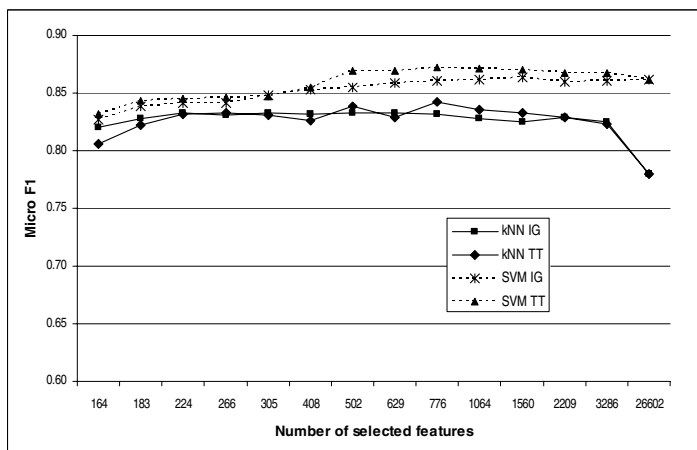
Fig. 2. Micro-averaged F1 scores for Reuters-21578 collection

A second fact that also emerges clearly from the figures is that our method achieves better F1 scores with very aggressive feature selection than those obtained when all features are regarded for both classifiers and both text collections.

Finally, in Figure 1 we observe that a good feature selection method enables *k*-NN classifier surpasses SVM's performance.

Our second experiment was focused on evaluating the time performance of our feature selection method (see Fig. 5). It can be seen that the behaviour is exponential as the number of selected features increases. From a practical point of view this is not a problem. Notice that execution times are negligible for aggressive feature selections,
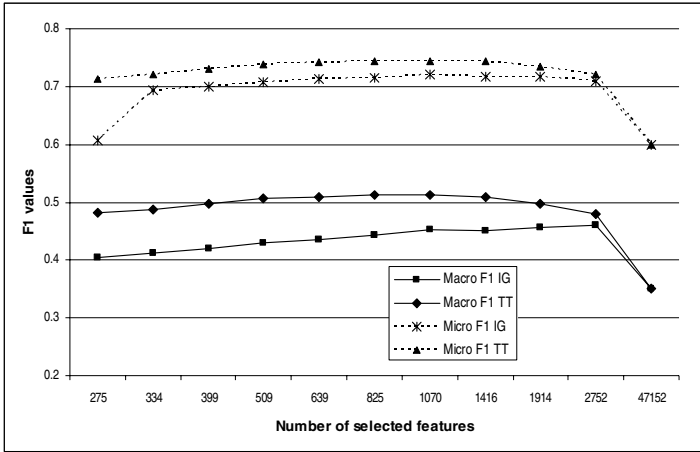
Fig. 3. F1 scores for *k*-NN classifier on the entire RCV1-v2 collection
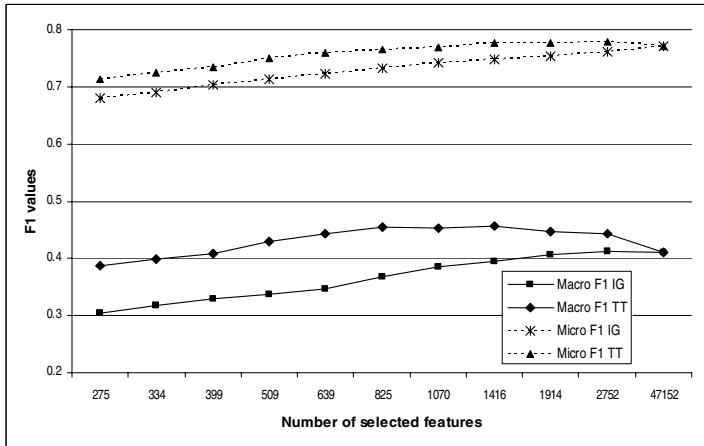
Fig. 4. F1 scores for SVM classifier on the small percentage (2%) of the RCV1-v2 collection

at the same time that good effectiveness improvements are achieved for them (see Figures 1-5). When the feature selection is not so aggressive (e.g. 2209 features), the combinatorial explosion arises but at the same time effectiveness improves very slightly. In this way, this indicates that global methods (as ours) are useful when applying aggressive feature selection, and that individual methods (e.g. *tf-idf*) are useful when selecting large feature subsets.

Comparing to other global methods, our execution times contrast with, for example, the 11 hours that Oscillating search takes to select around 2000 features in a subset of our test collection [17].
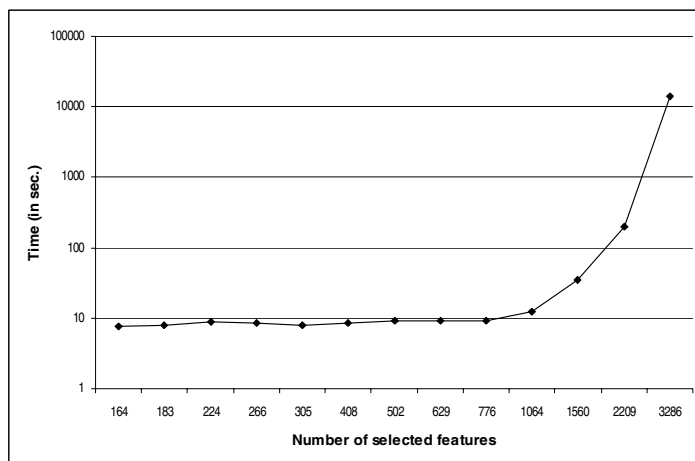
Fig. 5. Computational time of our feature selection method over Reuters-21578 collection

5   Conclusions

In this paper, a feature selection method that combines word frequency criterion and Testor Theory for Text Categorization tasks has been proposed. This method not only takes into account feature relationships and discriminating power but also it is computationally feasible. In this sense, it takes advantages from both individual and global methods for feature selection.

The experiments were conducted on two benchmark text collections (Reuters-21578 and RCV1-v2) using two high-performing classifiers (*k*-nearest neighbour and SVM). Results show that our method consistently outperformed information gain, especially when aggressive feature selection is carried out. The better performance improvements are obtained with respect to macro-averaged F1. This suggests that the proposed method is not affected by unbalanced class distribution.

The proposed method achieves good F1 scores with very aggressive feature selection, and even better than those obtained when all features are regarded. Thus, it may significantly ease the application of more powerful and computationally intensive machine learning methods to very large text categorization problems which are otherwise intractable.

As future work, we plan to study how this feature selection method can be applied in the context of adaptive document filtering tasks.

References

1. Jain, A.K., Duin, R.P.W., Mao, J.: Statistical Pattern Recognition: A Review. IEEE Transactions on Pattern Analysis and Machine Intelligence 22(1), 4–37 (2000)
2. John, G.H., Kohavi, R., Pfleger, K.: Irrelevant Features and the Subset Selection Problem. In: Proceedings of the 11th International Conference on Machine Learning, pp. 121–129 (1994)
3. Lewis, D.D.: An evaluation of phrasal and clustered representations on a text categorization task. In: Proceedings of 15th ACM International Conference on Research and Development in Information Retrieval, Denmark, pp. 37–50. ACM Press, New York (1992)
4. Yang, Y., Pedersen, J.O.: A Comparative Study on Feature Selection in Text Categorization. In: Proc. of the 14th International Conference on Machine Learning, pp. 412–420 (1997)
5. Mladenic, D.: Feature subset selection using in text learning. In: Proceedings of the 10th European Conference on Machine Learning, pp. 95–100 (1998)
6. Sebastiani, F.: Machine Learning in automated text categorization. ACM Computing Surveys 34(1), 1–47 (2002)
7. Mladenic, D., Grobelnik, M.: Feature selection for unbalanced class distribution and naive bayes. In: Proc. of the 16th International Conference on Machine Learning, pp. 258–267 (1999)
8. Rogati, M., Yang, Y.: High-performing feature selection for text classification. In: Proceedings of the 11th International Conference on Information and Knowledge Management, pp. 659–661. ACM Press, New York (2002)
9. Forman, G.: An extensive empirical study of feature selection metrics for text classification. Journal of Machine Learning Research 3, 1289–1305 (2003)
10. Somol, P., Pudil, P.: Oscillating Search Algorithms for Feature Selection. In: Proc. of the 15th IAPR International Conference on Pattern Recognition, Barcelona, pp. 406–409 (2000)
11. Lazo-Cortés, M., Ruiz-Shulcloper, J., Alba-Cabrera, E.: An overview of the evolution of the concept of testor. Pattern Recognition 34(4), 753–762 (2001)
12. Salton, G., Buckley, C.: Term-weighting approaches in automatic text retrieval. Information Processing and Management 24, 513–523 (1988)
13. Santiesteban, Y., Pons-Porrata, A.: LEX: a new algorithm for the calculus of typical testors. Mathematics Sciences Journal 21(1), 85–95 (2003)
14. Gil-García, R., Badía Contelles, J.M., Pons-Porrata, A.: Parallel nearest neighbour algorithms for Text Categorization. In: Kermarrec, A.-M., Bougé, L., Priol, T. (eds.) Euro-Par 2007. LNCS, vol. 4641, pp. 328–337. Springer, Heidelberg (2007)
15. Chang, C.C., Lin, C.J.: LIBSVM: a library for support vector machines (2001), Software available at http://www.csie.ntu.edu.tw/ cjlin/libsvm
16. Lewis, D., Yang, Y., Rose, T., Li, F.: Rcv1: A new benchmark collection for text categorization research. Machine Learning Research 5, 361–397 (2004)
17. Novovicová, J., Somol, P., Pudil, P.: Oscillating Feature Subset Search Algorithm for Text Categorization. In: Martínez-Trinidad, J.F., Carrasco Ochoa, J.A., Kittler, J. (eds.) CIARP 2006. LNCS, vol. 4225, pp. 578–587. Springer, Heidelberg (2006)

Towards Automatic Generation of Conceptual Interpretation of Clustering⋆

Alejandra Pérez-Bonilla[1,2] and Karina Gibert[1]

[1] Dep. of Statistics and Operations Research, Technical University of Catalonia.
Campus Nord; Edif. C5. C/ Jordi Girona 1-3; 08034 Barcelona, Spain
[2] Department of Industrial Engineering, University of Santiago of Chile
Avda. Ecuador 3769, Santiago, Chile.
{alejandra.perez,karina.gibert}@upc.edu

Abstract. In this paper the *Methodology of conceptual characterization by embedded conditioning CCEC*, oriented to the automatic generation of conceptual descriptions of classifications that can support later decision-making is presented, as well as its application to the interpretation of previously identified classes characterizing the different situations on a WasteWater Treatment Plant (WWTP). The particularity of the method is that it provides an interpretation of a partition previously obtained on an *ill-structured domain*, starting from a hierarchical clustering. The methodology uses some statistical tools (as the *boxplot multiple*, introduced by Tukey, which in our context behave as a powerful tool for numeric variables) together with some machine learning methods, to learn the structure of the data; this allows extracting useful information (using the concept of *characterizing variable*) for the automatic generation of a set of useful rules for later identification of classes. In this paper the usefulness of *CCEC* for building domain theories as models supporting later decision-making is addressed.

Keywords: Hierarchical clustering, class interpretation, Knowledge Discovery and Data Mining.

1 Introduction

In automatic classification where the classes composing a certain domain are to be discovered, one of the most important required processes and one of the less standardized one, is the interpretation of the classes, closely related with *validation*[1] and critical in the later usefulness of the discovered knowledge. The interpretation of the classes, so important to understand the meaning of the obtained classification as well as the structure of the domain, use to be done in an artistic-like way. But this process becomes more and more complicate as the number of classes grows. This work tries to face the problem of the automatic generation of useful interpretations of classes in such a way that decisions about the treatment of a new object can be modelled, to develop, in the long term, a software tool which supports decision-making.

⋆ This research has been partially financed by the project TIN 2004-01368.

Conceptual characterization by embedded conditioning (CCEC)[2] is the proposal presented in this paper to cover these goals. Given a clustering, *CCEC* provides an automatic interpretation for it that supports the later construction of intelligent decision support systems for assisting decision-making. A particular application to WWTP is addressed. The presented proposal integrates different findings from a series of previous works [3][4] in a single methodological tool which takes advantage of the hierarchical structure of the clustering to overcome some of the limitations observed in [3], [5]. The application is presented in next section in order to be used for illustration in §3.

This paper is organized as follows: After the introduction, WWTP are presented in §2 as well as, the description of the specific data base that has been analyzed, the basic concepts are in §3. The §4 presents the proposed methodology *CCEC* and the results of applying *CCEC* to the data described in §5. Finally in §6 the conclusions and the future work are addressed.

2   Application

In this paper a real WWTP is used to validate the proposed methodology [4]. First, a very brief description of the general WWTP process is briefly introduced the water flows sequentially through three or four processes (see [6] for a detailed description of the process): *(i):* In the *pretreatment*, an initial separation of solids from wastewater is performed. *(ii) Primary* treatment consists of leaving the wastewater in a settler for some hours. Solids will deposit down the settler and could be sent out. *(iii) Secondary* treatment occurs inside a biological reactor; a population of microorganisms (biomass) degrades the organic matter solved in the wastewater. *(iv)* In the *advanced* treatment another settler is used to separate the water from the biomass. The settler output (solids or biomass) produces a kind of mud which is the input of another process called *sludge line*. Next the plant used in this research described is a WWTP is located in Catalunya (Spain). Data analyzed in this work is a sample of 396 observations taken from September the first of 1995 to September the 30th of 1996. Each observation refers to a daily mean, and it is identified by the date itself.

The state of the Plant is described through a set of 25 variables, considered the more relevant upon expert's opinions. They can be grouped as: *(i)* Input (measures taken at the entrance of the plant): Q-E: Inflow wastewater (daily m^3 of water);FE-E Iron pre-treatment (g/l); pH-E; SS-E: Suspended Solids (mg/l); SSV-E: Volatile suspended solids (mg/l); COD-E: Chemical organic matter (mg/l); BOD-E: Biodegradable organic matter (m/l). *(ii)* After Settler (measures taken when the wastewater comes out of the first settler): PH-D: pH; SS-D: Suspended Solids (mg/l); SSV-D: Volatile suspended solids (mg/l); COD-D: Chemical organic matter (mg/l); BOD-D: Biodegradable organic matter (m/l). *(iii)* Biological treatment (measures taken in the biological reactor): Q-B: Biological reactor-flow; V30: Index at the biological reactor (measures the sedimentation quality of the mixed liquor, in ml/l); MLSS-B: Mixed liquor suspended solids at the biological reactor; MLVSS-B: Mixed liquor volatile

suspended solids: MCRT-B: Mean cell residence time at the biological reactor. *(iv)* Output (when the water is meeting the river): PH-S: pH ; SS-S: Suspended Solids (mg/l); SSV-S: Volatile suspended solids (mg/l); COD-S: Chemical organic matter (mg/l); BOD-S: Biodegradable organic matter (m/l). *(v)* Other variables: QR-G: Recirculated Flow ; QP-G: Purged flow; QA-G: Air inflow.
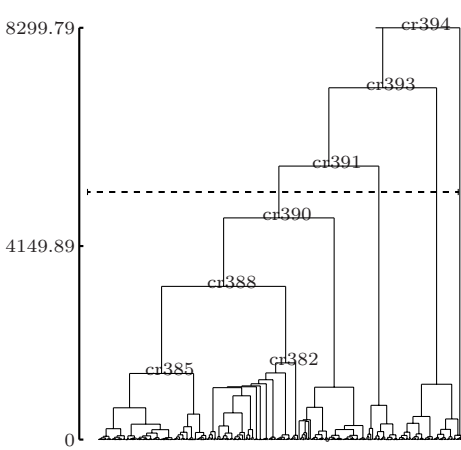
The standard input of a clustering algorithm use to be a data matrix with the values of K variables $X_1 \dots X_K$ (numerical or not) observed over a set $\mathcal{I} = \{1, \dots n\}$ of individuals. Variables are in columns, while individuals in rows. Cells contain the value (x_{ik}), taken by individual $i \in \mathcal{I}$ for variable X_k, ($k = 1 : K$). The set of values of X_k is named $\mathcal{D}^k = \{c_1^k, c_2^k, ..., c_s^k\}$ for categorical variables and $D^k = r_k$ for numerical ones, being $r_k = [minX_k, maxX_k]$ the range of X_K. A partition in ξ classes of $\mathcal{I}$ is denoted by $\mathcal{P}_\xi = \{C_1, ..., C_\xi\}$, and $\tau = \{\mathcal{P}_1, \mathcal{P}_2, \mathcal{P}_3, \mathcal{P}_4, ..., \mathcal{P}_n\}$ is an indexed hierarchy of $\mathcal{I}$. Finally, $\mathcal{P}_2 = \{C_1, C_2\}$ is a binary partition of $\mathcal{I}$. Usually, τ is the result of a *hierarchical clustering* over $\mathcal{I}$, and it can be represented in a graphical way in what is known as a *dendrogram* (or hierarchical tree, see figure 1, [4]).

Fig. 1. *Left:* Hierarchical tree $[\tau_{Gi2,R1}^{En,G}]$[2]; *Right:* Notation

The data base previously presented, was classified in a previous work [4] by using clustering based on rules [3], producing the hierarchical tree of Figure 1(left).

The Figure 2 contains the *class panel graph* [7] of the 25 variables regarding the top partition $\mathcal{P}_2 = \{C_{393}, C_{392}\}$ where the *multiple boxplot*[8] of variables for each class are displayed. As usual in hierarchical clustering, the final partition is the horizontal cut of the tree that maximizes the ratio between *heterogeneity* between classes with respect to *homogeneity* within classes, what guaranties the *distinguishability* of classes. The result is a 4-classes partition $\mathcal{P}_4 = \{C_{392}, C_{389}, C_{390}, C_{383}\}$.

3   Basic Concepts

Four main concepts are in the kernel of this work (basic notation is introduced in Figure 1(right)):

- Variable X_k is *Totally characterizing* of class $C \in \mathcal{P}$, if all the values taken by X_k in class C are *characteristic* of C (objects of other classes take other values). As an example, see variables Q-E or QR-G in Figure 2.
- Variable X_k is *Partially characterizing* of class $C \in \mathcal{P}$ if there is at least one characteristic value of C, although the class can share some other values
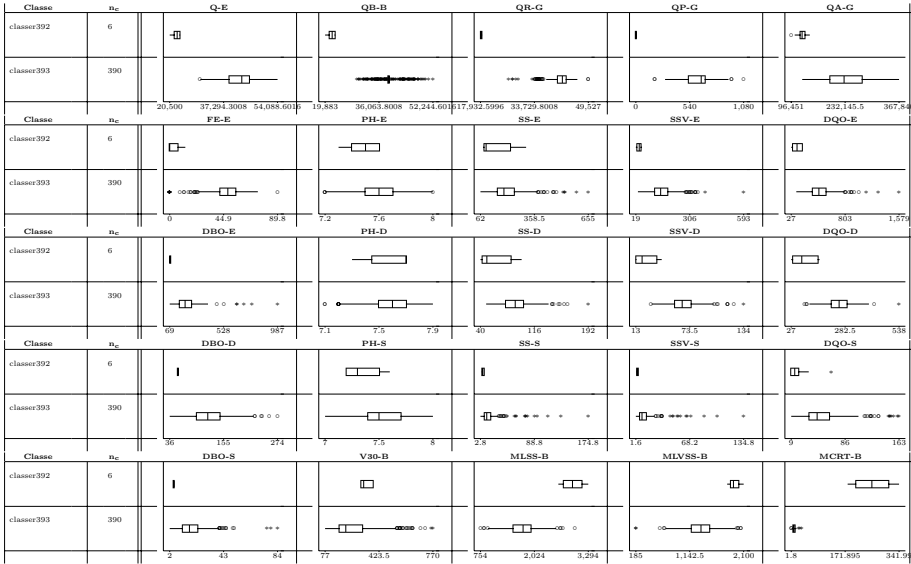
Fig. 2. class panel graph of $\mathcal{P}_2$

with other classes. See PH-E in Figure 2, which is partially characterizing the class C_{392} if it takes very low or high values.

- Covering (Cov): Given a rule $r : x_{ik} \in I_s^k \longrightarrow C$ the covering of r is the number of objects in $\mathcal{I}$ that satisfy the rule. $Cov(r) = card\{i \in C \;\; tq \;\; x_{ik} \in I_s^k\}$
- Relative covering ($CovR$): Given a rule, the relative covering is the proportion of of class C that satisfy the rule. $CovR(r) = \dfrac{card\{i \in C \;\; tq \;\; x \;\; \in I \;\;\}}{card\{C\}} * 100$

Boxplot based discretization (BbD) is presented in [2], [9] and revised in [10], as an efficient way of transforming a numerical variable into a qualitative one in such a way that the cut points for discretizing identify where the subsets of intersecting classes between classes change and, given $X_k, \mathcal{P}$, it consists of the following steps:

1. Calculate the *minimum* (m_C^k) and *maximum* (M_C^k) of X_k inside any class. Built $\mathcal{M}^k = \{m_{C_1}^k, \ldots, m_C^k, M_{C_1}^k, \ldots, M_C^k\}$, where $card(\mathcal{M}^k) = 2\xi$
2. Built the *set of cutpoints* $\mathcal{Z}^k$ by sorting $\mathcal{M}^k$ in increasing way into $\mathcal{Z}^k = \{z_i^k \; ; \; i = 1 : 2\xi\}$. At every z_i^k the intersection between classes changes arity.
3. Built the *set of intervals* I^k *induced by* $\mathcal{P}$ *on* X_k by defining an interval I_s^k between every pair of consecutive values of $\mathcal{Z}^k$. $\mathcal{I}^k = \{I_1^k, \ldots, I_{2\xi-1}^k\}$ is the boxplot based discretization of X_k. The $I_s^k, s \in \{1, 2\xi - 1\}$, intervals are variable length and the intersection among classes changes from one to another.

As an example, Table 1(left) contains descriptive statistics of Q-E versus $\mathcal{P}_2$. In the right hand side of Table 1 the set of minimums and maximums of every class

Table 1. (*left*): Summary statistics for Q-E vs $\mathcal{P}_2$; (*right*): $\mathcal{M}^{Q-E}$, Set of extreme values of Q-E$|\mathcal{C} \in \mathcal{P}_2$ and $\mathcal{Z}^{Q-E}$, corresponding ascendant sorting

	Class	**C393**	**C392**
Var.	N = 396	$n_c = 390$	$n_c = 6$
Q-E	$\bar{\mathbf{X}}$	42,112.9453	22,563.7988
	S	4,559.2437	1,168.8481
	min	29,920	20,500
	max	54,088.6016	23,662.9004
	N*	1	0

$\mathcal{M}^{Q-E}$	$\mathcal{Z}^{Q-E}$
29,920	20,500
20,500	23,662.9004
54,088.6016	29,920
23,662.9004	54,088.6016

$\mathcal{M}^{Q-E}$ is sorted into Z^{Q-E} and its values can be considered as the cut points of a discretization of Q-E in 3 intervals: $I^{Q-E} = \{I_1^{Q-E}, I_2^{Q-E}, I_3^{Q-E}\}$, with $I_1^{Q-E} = [20500.0, 23662.9]$, $I_2^{Q-E} = (23662.9, 29920.0)$, $I_3^{Q-E} = [29920.0, 54088.6]$. Thus, I^{Q-E} is a discretization of X_k which takes 3 values. Only elements of C_{392} can take value I_1^{Q-E}. Only elements of C_{393} take value I_3^{Q-E} and I_2^{Q-E} is empty. For variable $I^{SS-S} = \{I_1^{SS-S}, I_2^{SS-S}, I_3^{SS-S}\}$, with $I_1^{SS-S} = [2.80, 3.200)$, $I_2^{SS-S} = [3.20, 20.00]$, $I_3^{SS-S} = (20.0, 174.8]$. Only elements of C_{391} can take value I_1^{SS-S}; along I_2^{SS-S}, C_{391} is intersecting with C_{389} and along I_3^{SS-S} does not intersect. The values of $\mathcal{M}^k$ are identifying the points where intersections among classes change.

The methodology *boxplot based induction rules (BbIR)* is presented in [9]. It is a method for generating probabilistic concepts with a minimum number of attributes in the antecedent, using of the boxplot based discretization of X_k.

1. Use the *boxplot based discretization* to build $r_s : \mathcal{I}^k = \{I_1^k, I_2^k, I_3^k, \ldots, I_{2\xi-1}^k\}$.
2. Build table $I^k \times P$ where rows are indexed by $s \in \{1, 2\xi - 1\}$, and columns by $C \in \{1, \xi\}$.
3. Built the table $I^k \mid \mathcal{P}$ by dividing the cells of $I^k \times P$ by the row totals. Cells,
$$p_{sc} = P(C|I^k = I_s^k) = P(i \in C|x_{ik} \in I_s^k) = \frac{card\{i : x \in I \wedge i \in C\}}{card\{i \in \mathcal{I} : x \in I\}} = \frac{n_c}{\sum_\forall n_c}$$
   If $\exists C : p_{sc} = 1$ & $Cov(r_s) = 100\%$, then X_k is a *totally characterizing variable* of C.
4. For every cell in table $I^k \mid \mathcal{P}$ produce the rule: If $x_{ik} \in I_s^k \xrightarrow{p_c} i \in C$
   For example, see Table 2(left) $I^{Q-E} \times P_2$, since $card\{i \in \mathcal{I} : x_{ik} \in I_1^{Q-E}\} = card\{i \in \mathcal{I} : i \in C_{392}\} = card\{i \in \mathcal{I} : x_{ik} \in I_1^{Q-E} \wedge i \in C_{392}\} = 6$. Then $p_{1C_{392}} = 1$ and the rule: $x_{Q-E,i} \in (23662.9, 29920.0] \xrightarrow{1.0} C_{392}$ is generated.

From $I^{Q-E} \mid \mathcal{P}_2$ (see Table 2(center)) the following system of probabilistic rules, can be induced for the variable Q-E:

$$r_{1,classer393}^{Q-E} : x_{Q-E,i} \in [20500.0, 23662.9] \xrightarrow{0.0} classer393$$
$$r_{1,classer392}^{Q-E} : x_{Q-E,i} \in [20500.0, 23662.9] \xrightarrow{1.0} classer392$$
$$r_{3,classer393}^{Q-E} : x_{Q-E,i} \in [29920.0, 54088.6] \xrightarrow{1.0} classer393$$
$$r_{3,classer392}^{Q-E} : x_{Q-E,i} \in [29920.0, 54088.6] \xrightarrow{0.0} classer392$$

Finally too more concepts are used in this work.

Table 2. (*left*): $I^{Q-E} \times P_2$; (*center*): $I^{Q-E} \mid \mathcal{P}_2$ table; (*right*): $\mathcal{P}_2 \times \mathcal{P}_3$

	C^2_{392}	C^2_{393}
I^{Q-E}_1	6	0
I^{Q-E}_2	0	0
I^{Q-E}_3	0	389

	C^2_{392}	C^2_{393}
I^{Q-E}_1	1	0
I^{Q-E}_2	0	0
I^{Q-E}_3	0	1

P_3 vs P_2	C^2_{393}	C^2_{392}
C^3_{392}	0	6
C^3_{391}	320	0
C^3_{389}	70	0

4   The Metodology

CCEC takes advantage of the existence of τ, and uses the property of any binary hierarchical structure that $\mathcal{P}_{\xi+1}$ has the same classes of $\mathcal{P}_\xi$ except one, which splits in two subclasses in $\mathcal{P}_{\xi+1}$. Binary hierarchical structure will be used by *CCEC* to discover particularities of the final classes step by step also in hierarchical way. The *CCEC* [2] allows generation of automátic conceptual interpretations of a given partition $\mathcal{P} \in \tau$. The steps to be followed are described bellow. The application to the WWTP is illustrated in section §5:

1. Cut the tree at highest level (make $\xi = 2$ and consider $\mathcal{P}_2 = \{C_1, C_2\}$).
2. Use *the boxplot based discretization* presented in [9] and revised in [10], to find (total or partial) characteristic values for numerical variables [5].
3. Use *boxplot based induction rules (BbIR)*, to induce a the knowledge Base describing both classes.
4. For classes in $\mathcal{P}_2$, determine concepts $A^{\xi,X}_1$: "$[X_k \in I^k_s]$", $A^{\xi,X}_2$: $\neg A^{\xi,X}_1$ associated to C_1, C_2, by taking the intervals provided by a totally characteristic variable or the partial one with greater relative covering and $p_{sc} = 1$.
5. Go down one level in the tree, by making $\xi = \xi + 1$ and so considering $\mathcal{P}^{\xi+1}$. As said before $\mathcal{P}^{\xi+1}$ is *embedded* in $\mathcal{P}^\xi$ in such a way that there is a class of $\mathcal{P}^\xi$ split in two new classes of $\mathcal{P}^{\xi+1}$, namely $C^{\xi+1}_i$ and $C^{\xi+1}_j$ and all other classes are common to both partitions.
Since in the previous step $C^{\xi+1}_i \cup C^{\xi+1}_j$ were conceptually separated from the rest, at this point it is only required to find the variables which separate (or distinguishes) $C^{\xi+1,X}_i$ from $C^{\xi+1,X}_j$, by repeating steps 2-4. Suppose $B^{\xi+1,X}_i$ and $B^{\xi+1,X}_j$ the concepts induced from $C^{\xi+1,X}_i$ and $C^{\xi+1,X}_j$, in the step $\xi + 1$.
6. Integrate the extracted knowledge of the iteration $\xi + 1$ with that of the iteration ξ, by determining the compound concepts finally associated to the elements of $\mathcal{P}_{\xi+1}$. The concepts for the classes of $\mathcal{P}_{\xi+1}$ will be: $A^{\xi+1,X}_q = A^{\xi,X}_q$, $A^{\xi+1,X}_i = \neg A^{\xi,X}_q \wedge B^{\xi+1,X}_i$ and $A^{\xi+1,X}_j = \neg A^{\xi,X}_q \wedge B^{\xi+1,X}_j$
7. Make $\xi = \xi + 1$, and return to the step 2) repeating until $\mathcal{P}_\xi = \mathcal{P}$.

5   Results

The 2-class Partition. For the presented data, $\mathcal{P}_2 = \{C_{393}, C_{392}\}$. Figure 2 shows the *class-panel graph* of $\mathcal{P}_2$ [7]. As stated in §3, I^k is built using *Boxplot*

based discretization (BbD) for all variables. Table 2(left) shows the crossing of I^{Q-E} and $\mathcal{P}_2$. Then the $I^k \mid \mathcal{P}_2$, table is built and totally characterizing variables are identified as those with $I^k \mid \mathcal{P}$ table having one 1 per row. Next is to use *BbIR* to generate all the rules induced for $\mathcal{P}_2$. Only rules with $p_{sc} = 1$ are considered. Totally characterizing variables are those with $p_{sc} = 1$ and $CovR = 100\%$ (Q-E, QB-B, QR-G, QP-G, MCRT-B). In this case any of them is useful for conceptualization. Here Q-E is choosen. The Table 3 shown the knowledge Base whit certain rules ($p_{sc} = 1$) for *classer*392.

Since Q-E is a totally characterizing variable the following concept association can be done:

- $A_{C_{392}}^{2,Q-E} =$ "$x_{Q-E,i} \in [20500.0, 23662.9]$" is associated to C_{392}
- $A_{C_{393}}^{2,Q-E} =$ "$x_{Q-E,i} \in [29920.0, 54088.6]$" is associated to C_{393}

Or, in other words:

- Class C_{392}, "Low values of Inflow wastewater".
- Class C_{393}, "High values of Inflow wastewater".

Being *low* and *high* defined according to the above numeric limits. Any totally characterizing variable could be used instead. The next step is to go one level down the tree.

The 3-class partition. Take $\mathcal{P}_3 = \{C_{392}, C_{391}, C_{389}\}$ and first identify correspondences between the classes of $\mathcal{P}_2 = \{C_{393}, C_{392}\}$ and $\mathcal{P}_3 = \{C_{392}, C_{391}, C_{389}\}$. Table 2(right) shows the crossing and elicits that class C_{393} splits into C_{391} (referred as C_i^3 in methodology), C_{389} (referred as C_j^3 in methodology) while C_{392} remains in both $\mathcal{P}_2$ and $\mathcal{P}_3$ (C_{392} is referred as C_i^2 in methodology). From the previous iteration it is already known that there is a common characteristic of both C_{391} and C_{389} (Q-E is greater) which distinguishes them from C_{392} (with lower Q-E). Thus, it is only required to find the separation between C_{391} and C_{389}. A similar procedure as the used in previous step for separating C_{392} and C_{393} was used with all the variables regarding C_{391} and C_{389}.

Totaly characterizing variables do not exists here. So partially characterizing variables with greater relative covering are considered, in this case SS-D and SSV-D, using variable SS-D for this example. The following system of probabilistic rules than can be induced for the variable SS-D in $\mathcal{P}_3 \setminus \{C_{392}\}$:

$r_{2,classer391}^{SS-D} : x_{SS-D,i} \in [63, 136] \xrightarrow{0.8547} classer391$

$r_{3,classer391}^{SS-D} : x_{SS-D,i} \in (136, 192] \xrightarrow{1.0} classer391, being \; B_{391}^{3,SS-D} = x_{SS-D,i} \in (136, 192]$

$r_{1,classer389}^{SS-D} : x_{SS-D,i} \in [48.0, 63) \xrightarrow{1.0} classer389 \;\;, being \; B_{389}^{3,SS-D} = x_{SS-D,i} \in [48, 63)$

Combining with the results of previous iteration of *CCEC* leads on the following interpretation of $\mathcal{P}_3$:

-Class C_{392} is such that "Q-E is in $[20500.0, 23662.9]$" $(A_{392}^{2,Q-E})$

-Class C_{391} is such that "Q-E is in $[29920.0, 54088.6]$" and

"SS-D is in $(136,192]$" $(\neg A_{392}^{2,Q-E} \wedge B_{391}^{3,SS-D})$

-Class C_{389} is such that "Q-E is in $[29920.0, 54088.6]$" and

"SS-D is in $[48, 63)$" $(\neg A_{392}^{2,Q-E} \wedge B_{389}^{3,SS-D})$

Table 3. Knowledge Base for classer392

Concep.	Rules		Cov	CovR
$A_{392}^{2,Q-E}$	$r_{1,cla\ \ er392}^{Q-E}:$	$x_{Q-E},\ \in [20500.0, 23662.9] \xrightarrow{1.0} classer392$	6	100%
$A_{392}^{2,QB-B}$	$r_{1,cla\ \ er392}^{QB-B}:$	$x_{QB-B},\ \in [19883.0, 22891.0] \xrightarrow{1.0} classer392$	6	100%
$A_{392}^{2,QR-G}$	$r_{1,cla\ \ er392}^{QR-G}:$	$x_{QR-G},\ \in [17932.6, 18343.5] \xrightarrow{1.0} classer392$	6	100%
$A_{392}^{2,QP-G}$	$r_{1,cla\ \ er392}^{QP-G}:$	$x_{QP-G},\ \in [0.0, 0.0] \xrightarrow{1.0} classer392$	6	100%
$A_{392}^{2,QA-G}$	$r_{1,cla\ \ er392}^{QA-G}:$	$x_{QA-G},\ \in [96451.0, 124120.0) \xrightarrow{1.0} classer392$	3	50%
$A_{392}^{2,SSV-E}$	$r_{1,cla\ \ er392}^{SSV-E}:$	$x_{SSV-E},\ \in [19.0, 30.0) \xrightarrow{1.0} classer392$	1	16,7%
$A_{392}^{2,DQO-E}$	$r_{1,cla\ \ er392}^{DQO-E}:$	$x_{DQO-E},\ \in [27.0, 100.0) \xrightarrow{1.0} classer392$	3	50%
$A_{392}^{2,DBO-E}$	$r_{2,cla\ \ er392}^{DBO-E}:$	$x_{DBO-E},\ \in [73.0, 73.0] \xrightarrow{1.0} classer392$	1	16,7%
$A_{392}^{2,SS-D}$	$r_{1,cla\ \ er392}^{SS-D}:$	$x_{SS-D},\ \in [40.0, 48.0) \xrightarrow{1.0} classer392$	2	33,33%
$A_{392}^{2,SSV-D}$	$r_{1,cla\ \ er392}^{SSV-D}:$	$x_{SSV-D},\ \in [13.0, 30.0) \xrightarrow{1.0} classer392$	3	50%
$A_{392}^{2,DQO-D}$	$r_{1,cla\ \ er392}^{DQO-D}:$	$x_{DQO-D},\ \in [27.0, 90.0) \xrightarrow{1.0} classer392$	3	50%
$A_{392}^{2,DBO-D}$	$r_{2,cla\ \ er392}^{DBO-D}:$	$x_{DBO-D},\ \in [54.0, 54.0] \xrightarrow{1.0} classer392$	1	16,7%
$A_{392}^{2,MLSS-B}$	$r_{3,cla\ \ er392}^{MLSS-B}:$	$x_{MLSS-B},\ \in (2978.0, 3294.0] \xrightarrow{1.0} classer392$	2	33,33%
$A_{392}^{2,MLVSS-B}$	$r_{3,cla\ \ er392}^{MLVSS-B}:$	$x_{MLVSS-B},\ \in (2054.0, 2100.0] \xrightarrow{1.0} classer392$	1	16,7%
$A_{392}^{2,MCRT-B}$	$r_{3,cla\ \ er392}^{MCRT-B}:$	$x_{MCRT-B},\ \in [179.8, 341.99] \xrightarrow{1.0} classer392$	6	100%

Table 4. Knowledge Base for classer389

Concep.	Rules		Cov	CovR
$B_{389}^{3,Q-E}$	$r_{3,cla\ \ er389}^{Q-E}:$	$x_{Q-E},\ \in (52255.8, 54088.6] \xrightarrow{1.0} classer389$	3	4,28%
$B_{389}^{3,QB-B}$	$r_{3,cla\ \ er389}^{QB-B}:$	$x_{QB-B},\ \in (49695.8, 52244.6] \xrightarrow{1.0} classer389$	3	4,28%
$B_{389}^{3,QR-G}$	$r_{1,cla\ \ er389}^{QR-G}:$	$x_{QR-G},\ \in [26218.0, 27351.0) \xrightarrow{1.0} classer389$	2	2,85%
$B_{389}^{3,QP-G}$	$r_{1,cla\ \ er389}^{QP-G}:$	$x_{QP-G},\ \in [188.0, 327.6) \xrightarrow{1.0} classer389$	2	2,85%
$B_{389}^{3,QA-G}$	$r_{1,cla\ \ er389}^{QA-G}:$	$x_{QA-G},\ \in [124120.0, 136371.0) \xrightarrow{1.0} classer389$	2	2,85%
$B_{389}^{3,PH-E}$	$r_{3,cla\ \ er389}^{PH-E}:$	$x_{PH-E},\ \in (7.9, 8.0] \xrightarrow{1.0} classer389$	1	1,42%
$B_{389}^{3,SS-E}$	$r_{1,cla\ \ er389}^{SS-E}:$	$x_{SS-E},\ \in [62.0, 82.0) \xrightarrow{1.0} classer389$	1	1,42%
$B_{389}^{3,SSV-E}$	$r_{1,cla\ \ er389}^{SSV-E}:$	$x_{SSV-E},\ \in [30.0, 60.0) \xrightarrow{1.0} classer389$	2	2,85%
$B_{389}^{3,DQO-E}$	$r_{1,cla\ \ er389}^{DQO-E}:$	$x_{DQO-E},\ \in [100.0, 158.0) \xrightarrow{1.0} classer389$	1	1,42%
$B_{389}^{3,DBO-E}$	$r_{1,cla\ \ er389}^{DBO-E}:$	$x_{DBO-E},\ \in [69.0, 90.0) \xrightarrow{1.0} classer389$	5	7,14%
$B_{389}^{3,SS-D}$	$r_{1,cla\ \ er389}^{SS-D}:$	$x_{SS-D},\ \in [48.0, 63.0) \xrightarrow{1.0} classer389$	24	34,28%
$B_{389}^{3,SSV-D}$	$r_{1,cla\ \ er389}^{SSV-D}:$	$x_{SSV-D},\ \in [30.0, 47.0) \xrightarrow{1.0} classer389$	25	35,71%
$B_{389}^{3,DBO-D}$	$r_{1,cla\ \ er389}^{DBO-D}:$	$x_{DBO-D},\ \in [36.0, 56.0) \xrightarrow{1.0} classer389$	5	7,14%
$B_{389}^{3,DBO-S}$	$r_{1,cla\ \ er389}^{DBO-S}:$	$x_{DBO-S},\ \in [2.0, 4.0) \xrightarrow{1.0} classer389$	2	2,85%
$B_{389}^{3,MLSS-B}$	$r_{3,cla\ \ er389}^{MLSS-B}:$	$x_{MLSS-B},\ \in (2696.0, 2978.0] \xrightarrow{1.0} classer389$	1	1,42%
$B_{389}^{3,MCRT-B}$	$r_{3,cla\ \ er389}^{MCRT-B}:$	$x_{MCRT-B},\ \in [28.8, 34.4] \xrightarrow{1.0} classer389$	1	1,42%

Since anyone of these interpretations is based on non totally characterizing variables, some degree of certainty should be associated depending on the probabilities of the corresponding generated concepts. The interpretation with the highest global degree of certainty is the one that intends to be refined in the following iteration. Table 4 showns the Knowledge Base with certain rules ($p_{sc} = 1$) induced for *classer*389.

Table 5. Knowledge Base for classer383

Concep.	Rules	Cov	CovR
$\neg C_{390}^{4,SS-E}$	$r_{3,cla\ \ er383}^{SS-E}:\ x_{SS-E},\ \in (480.0, 655.0] \xrightarrow{1.0} classer383$	5	14,70%
$\neg C_{390}^{4,SSV-E}$	$r_{3,cla\ \ er383}^{SSV-E}:\ x_{SSV-E},\ \in (336.0, 593.0] \xrightarrow{1.0} classer383$	4	11,76%
$\neg C_{390}^{4,DQO-E}$	$r_{3,cla\ \ er383}^{DQO-E}:\ x_{DQO-E},\ \in (1279.0, 1579.0] \xrightarrow{1.0} classer383$	1	2,94%
$\neg C_{390}^{4,DBO-E}$	$r_{3,cla\ \ er383}^{DBO-E}:\ x_{DBO-E},\ \in (382.0, 987.0] \xrightarrow{1.0} classer383$	7	20,58%
$\neg C_{390}^{4,MLVSS-B}$	$r_{1,cla\ \ er383}^{MLVSS-B}:\ x_{MLVSS-B},\ \in [185.0, 611.0) \xrightarrow{1.0} classer383$	2	5,88%
$\neg C_{390}^{4,MCRT-B}$	$r_{1,cla\ \ er383}^{MCRT-B}:\ x_{MCRT-B},\ \in [1.8, 6.2] \xrightarrow{1.0} classer383$	1	2,94%

The final partition. The process would continue separating the classes C_{390} and C_{383} of the following partition $\mathcal{P}_4$, see figure 1(left), which are the subdivision of C_{391}. Similarly, the following interpretation of $\mathcal{P}_4$, which is the final partition [4] is obtained with the following Knowledge Base with certain rules for classer383(Table 5) and classer390 (Table 6):

And de final interpretation is:

– Class C_{392} is such that $A_{392}^{2,Q-E}$
– Class C_{389} is such that $\neg A_{392}^{2,Q-E} \wedge B_{391}^{3,SS-D}$
– Class C_{390} is such that $\neg A_{392}^{2,Q-E} \wedge \neg B_{391}^{3,SS-D} \wedge C_{390}^{4,DBO-E}$
– Class C_{383} is such that $\neg A_{392}^{2,Q-E} \wedge \neg B_{391}^{3,SS-D} \wedge \neg C_{390}^{4,DBO-E}$. Or, in other words:
– Class C_{392}, "*Low values for Inflow wastewater*"
– Class C_{389}, "*High values for Inflow and few Suspended solids at the settler*"
– Class C_{390}, "*High values of Inflow wastewater, high Suspended solids at the exit and few Biodegradable organic matter at the input*"
– Class C_{383}, "*Medium-high values of Inflow wastewater, high Suspended solids at the settler and high Biodegradable organic matter at the input.*"

This set of rules can, in fact, be considered as a domain model which can support later decision on the treatment to be applied to a new day, provided that a standard treatment is previously associated to every class by experts. In this association the possibility of easily interpreting the classes is critical as well as to provide the experts means for easily understanding the meaning of the classes. In this sense the proposed method provides simple and short rules which use to be easier to handle than those provided by other induction rules algorithms. This final interpretation is consistent with the one provided by the experts and presented in [4].

6   Conclusions and Future Work

In this paper the first approach of a methodology to generate automatic interpretations from a group of classes is presented. Concepts associated to classes are built taking advantage of hierarchical structure of the underlying clustering. The *Conceptual characterization by embedded conditioning CCEC* [2] is a quick and effective method that generates a conceptual model of the domain, which will be from great support to the later decision making based on a combination

Table 6. Knowledge Base for classer390

Concep.	Rules	Cov	CovR
$C_{390}^{4,Q-E}$	$r_{1,cla\_er390}^{Q-E}:\ x_{Q-E,}\ \in [29920.0, 34284.4)\ \xrightarrow{1.0}\ classer390$	9	3,15%
$C_{390}^{4,QB-B}$	$r_{3,cla\_er390}^{QB-B}:\ x_{QB-B,}\ \in (39000.0, 49695.8]\ \xrightarrow{1.0}\ classer390$	60	21,06%
$C_{390}^{4,QR-G}$	$r_{3,cla\_er390}^{QR-G}:\ x_{QR-G,}\ \in (44568.6, 49527.0]\ \xrightarrow{1.0}\ classer390$	13	4,56%
$C_{390}^{4,QP-G}$	$r_{3,cla\_er390}^{QP-G}:\ x_{QP-G,}\ \in (831.1, 1080.0]\ \xrightarrow{1.0}\ classer390$	56	19,64%
$C_{390}^{4,QA-G}$	$r_{1,cla\_er390}^{QA-G}:\ x_{QA-G,}\ \in [136371.0, 156320.0)\ \xrightarrow{1.0}\ classer390$	7	2,45%
$C_{390}^{4,FE-E}$	$r_{3,cla\_er390}^{FE-E}:\ x_{FE-E,}\ \in (63.3, 89.8]\ \xrightarrow{1.0}\ classer390$	7	2,45%
$C_{390}^{4,PH-E}$	$r_{3,cla\_er390}^{PH-E}:\ x_{PH-E,}\ \in (7.8, 7.9]\ \xrightarrow{1.0}\ classer390$	8	2,80%
$C_{390}^{4,SS-E}$	$r_{1,cla\_er390}^{SS-E}:\ x_{SS-E,}\ \in [82.0, 114.0)\ \xrightarrow{1.0}\ classer390$	4	1,40%
$C_{390}^{4,SSV-E}$	$r_{1,cla\_er390}^{SSV-E}:\ x_{SSV-E,}\ \in [60.0, 92.0)\ \xrightarrow{1.0}\ classer390$	7	2,45%
$C_{390}^{4,DQO-E}$	$r_{1,cla\_er390}^{DQO-E}:\ x_{DQO-E,}\ \in [158.0, 414.0)\ \xrightarrow{1.0}\ classer390$	113	39,64%
$C_{390}^{4,DBO-E}$	$r_{1,cla\_er390}^{DBO-E}:\ x_{DBO-E,}\ \in [90.0, 220.0)\ \xrightarrow{1.0}\ classer390$	126	44,21%
$C_{390}^{4,PH-D}$	$r_{1,cla\_er390}^{PH-D}:\ x_{PH-D,}\ \in [7.2, 7.3)\ \xrightarrow{1.0}\ classer390$	3	1,05%
$C_{390}^{4,SS-D}$	$r_{3,cla\_er390}^{SS-D}:\ x_{SS-D,}\ \in (112.0, 192.0]\ \xrightarrow{1.0}\ classer390$	30	10,52%
$C_{390}^{4,SSV-D}$	$r_{3,cla\_er390}^{SSV-D}:\ x_{SSV-D,}\ \in (92.0, 134.0]\ \xrightarrow{1.0}\ classer390$	11	3,85%
$C_{390}^{4,DQO-D}$	$r_{3,cla\_er390}^{DQO-D}:\ x_{DQO-D,}\ \in (329.0, 538.0]\ \xrightarrow{1.0}\ classer390$	22	7,71%
$C_{390}^{4,DBO-D}$	$r_{3,cla\_er390}^{DBO-D}:\ x_{DBO-D,}\ \in (224.0, 274.0]\ \xrightarrow{1.0}\ classer390$	4	1,40%
$C_{390}^{4,PH-S}$	$r_{3,cla\_er390}^{PH-S}:\ x_{PH-S,}\ \in (7.8, 8.0]\ \xrightarrow{1.0}\ classer390$	16	5,61%
$C_{390}^{4,SS-S}$	$r_{3,cla\_er390}^{SS-S}:\ x_{SS-S,}\ \in (29.0, 174.8]\ \xrightarrow{1.0}\ classer390$	25	8,77%
$C_{390}^{4,SSV-S}$	$r_{3,cla\_er390}^{SSV-S}:\ x_{SSV-S,}\ \in (19.0, 134.8]\ \xrightarrow{1.0}\ classer390$	38	13,3%
$C_{390}^{4,DQO-S}$	$r_{3,cla\_er390}^{DQO-S}:\ x_{DQO-S,}\ \in (95.0, 163.0]\ \xrightarrow{1.0}\ classer390$	24	8,4%
$C_{390}^{4,DBO-S}$	$r_{3,cla\_er390}^{DBO-S}:\ x_{DBO-S,}\ \in (35.0, 84.0]\ \xrightarrow{1.0}\ classer390$	4	1,40%
$C_{390}^{4,V30-B}$	$r_{1,cla\_er390}^{V30-B}:\ x_{V30-B,}\ \in [77.0, 140.0)\ \xrightarrow{1.0}\ classer390$	26	9,12%
$C_{390}^{4,MLSS-B}$	$r_{3,cla\_er390}^{MLSS-B}:\ x_{MLSS-B,}\ \in (2248.0, 2696.0]\ \xrightarrow{1.0}\ classer390$	17	5,96%
$C_{390}^{4,MLVSS-B}$	$r_{3,cla\_er390}^{MLVSS-B}:\ x_{MLVSS-B,}\ \in (1726.0, 2054.0]\ \xrightarrow{1.0}\ classer390$	18	6,31%
$C_{390}^{4,MCRT-B}$	$r_{3,cla\_er390}^{MCRT-B}:\ x_{MCRT-B,}\ \in (16.0, 28.8]\ \xrightarrow{1.0}\ classer390$	8	2,81%

of boxplop based discretization and an interactive combination of concepts upon hierarchical subdivisions of the domain. This is a preliminary proposal that has been applied with success to real data coming from a WWTP. Benefits of those proposal are specially interesting in the interpretation of partitions with great number of classes. Automatic generation of interpretations cover the important goal of KD of describing the domain [11]. However, in this proposal a direct connection between the generated concepts and the automatic rules generation allows direct construction of a decision model for the domain oriented to later class prediction. As a matter of fact, automatic production of probabilistic or fuzzy classification rules regarding concepts provided by *CCEC* is direct, as discussed in [12]. By associating an appropriate standard treatment to every class a model for deciding the appropriate treatment of a concrete day upon a reduced number variables is obtained together with an estimation of the risk associated to that decision (which is related with the certainty of the rule). At present other automatic criteria for deciding which variable is kept at every iteration (here the covering of the all concepts was used) and how to propagate uncertainty from

one iteration to the next is in progress (here rules with $p_{sc} = 1$ are used). The idea is to use an approach which avoids the explicit construction of all the concepts to evaluate their coverage. Comparison of rules produced with *CCEC* and other inductive methods ID3-like is also in progress, as well as validation with a second real WWTP from Slovenia.

References

1. Gordon, A.D.: Identifying genuine clusters in a classification. Computational Statistics and Data Analysis 18, 561–581 (1994)
2. Gibert, K., Pérez-Bonilla, A.: Ventajas de la estructura jerárquica del clustering en la interpretración automática de clasificaciones. In: III TAMIDA, pp. 67–76 (2005)
3. Gibert, K.: The use of symbolic information in automation of statistical treatment for ill-structured domains. AI Communications 9, 36–37 (1996)
4. Gibert, K., Roda, I.: Identifying characteristic situations in wastewater treatment plants. In: Workshop BESAI (ECAI), vol. 1, pp. 1–9 (2000)
5. Gibert, K., Aluja, T., Cortés, U.: Knowledge Discovery with Clustering Based on Rules. Interpreting results. In: Żytkow, J.M. (ed.) PKDD 1998. LNCS, vol. 1510, pp. 83–92. Springer, Heidelberg (1998)
6. Metcalf, E.: Wastewater engineering treatament. Disposal and reuse. McGraw-Hill 4th edn. revised by George Tchobanoglous, Franklin L. Burton NY.US (2003)
7. Gibert, K., Nonell, et al.: Knowledge discovery with clustering: impact of metrics and reporting phase by using klass. Neural Network World 4/05, 319–326 (2005)
8. Tukey, J.: Exploratory Data Analysis. Addison-Wesley, Reading (1977)
9. Gibert, K.: Técnicas híbridas de Inteligencia Artificial y Estadística para el descubrimiento de conocimiento y la minería de datos. In: Thompson (ed.) Tendencias de la minería de datos en España, pp. 119–130 (2004)
10. Gibert, K., Pérez-Bonilla, A.: Revised boxplot based discretization as a tool for automatic interpretation of classes from hierarchical cluster. In: Series Studies in Classification, D.A., pp. 229–237. Springer, Heidelberg (2006)
11. Fayyad, U., et al.: From Data Mining to Knowledge Discovery: An overview. In: Advances in Knowledge Discovery and Data Mining, AAAI/MIT Press (1996)
12. Gibert, K., Pérez-Bonilla, A.: Taking advantage of the hierarchical structure of a clustering for automatic generation of classification interpretations. In: 4th EUSFLAT, España, pp. 524–529 (2005)

ACONS: A New Algorithm for Clustering Documents

Andrés Gago Alonso, Airel Pérez Suárez, and José E. Medina Pagola

Advanced Technologies Application Center (CENATAV),
7a ♯ 21812 e/ 218 y 222, Rpto. Siboney, Playa, C.P. 12200, La Habana, Cuba
{agago,asuarez,jmedina}@cenatav.co.cu

Abstract. In this paper we present a new algorithm for document clustering called Condensed Star (ACONS). This algorithm is a natural evolution of the Star algorithm proposed by Aslam *et al.*, and improved by them and other researchers. In this method, we introduced a new concept of star allowing a different star-shaped form; in this way we retain the strengths of previous algorithms as well as address previous shortcomings. The evaluation experiments on standard document collections show that the proposed algorithm outperforms previously defined methods and obtains a smaller number of clusters. Since the ACONS algorithm is relatively simple to implement and is also efficient, we advocate its use for tasks that require clustering, such as information organization, browsing, topic tracking, and new topic detection.

Keywords: Clustering, Document processing.

1 Introduction

Clustering is the process of grouping a set of data objects into a set of meaningful subclasses, called clusters; these clusters could be disjoint or not. A cluster is a collection of data objects that have high similarity in comparison to one another, but are very dissimilar to objects in other clusters.

Initially, document clustering was evaluated for improving the results in information retrieval systems [9]. Clustering has been proposed as an efficient way of finding automatically related topics or new ones; in filtering tasks [2] and grouping the retrieved documents into a list of meaningful categories, facilitating query processing by searching only clusters closest to the query [10].

Several algorithms have been proposed for document clustering. One of these algorithms is Star, presented and evaluated by Aslam *et al.* [1]. They show that the Star algorithm outperforms other methods such as Single Link and Average Link in different tasks; however, this algorithm depends on data order and produces illogical clusters. Another method that improves the Star algorithm is the Extended Star method proposed by Gil *et al.* [6]. The Extended Star method outperforms the original Star algorithm, reducing considerably the number of clusters; nevertheless this algorithm can leave uncovered objects and

in some cases produce unnecessary clusters. Another version of the Extended Star method was proposed by Gil *et al.* to construct a parallel algorithm [7]. However, this version also has some drawbacks.

In this paper we propose a new clustering method, called Condensed Star or ACONS. In ACONS, we introduced a new definition of star allowing a different star-shaped sub-graph, in this way we retain the strengths of previous algorithms as well as solve the above-mentioned drawbacks. The experimentation – comparing our proposal against the original Star and the Extended algorithms – shows that our method outperforms those algorithms.

The basic outline of this paper is as follows. Section 2 is dedicated to related work. Section 3 contains the description of the ACONS method. The experimental results are discussed in section 4. The conclusions of the research and some ideas about future directions are exposed in section 5.

2   Related Work

In this section we analyze the Star algorithm and two proposed versions of the Extended Star method for document clustering, and we show their drawbacks.

The Star algorithm was proposed by Aslam *et al.* in 1998 [1], with several extensions and applications in filtering and information organization tasks [2,3]. They formalized the problem representing the document collection by its similarity graph, finding overlaps with dense sub-graphs; it is done so because the clique cover of the similarity graph is an NP-complete problem, and it does not admit polynomial time approximation algorithms. With this cover approximation by dense sub-graphs, in spite of loosing intra-cluster similarity guarantees, we can gain in computational efficiency.

Let $V = \{d_1, ..., d_N\}$ be a collection of documents and $Sim(d_i, d_j)$ a similarity (symmetric) function between documents d_i and d_j, we call similarity graph to an undirected and weighted graph $G = \langle V, E, w \rangle$, where vertices correspond to documents and each weighted edge corresponds to the similarity between two documents. Considering a similarity threshold σ defined by the user we can define a thresholded graph G_σ as the undirected graph obtained from G by eliminating all the edges whose weights are lower than σ. The Star algorithm approximate a clique cover of G_σ using denser star-shaped sub-graphs [1].

This algorithm has some drawbacks: (i) dependency on the data order processing, and (ii) production of "illogical" clusters, since two star centers are never adjacent. These drawbacks were properly explained in [6]. The Extended Star algorithm was proposed by Gil *et al.* to solve the aforementioned drawbacks [6]. They represent also the document collection by its thresholded similarity graph, defining a new notion of star center, obtaining as a consequence, different star-shaped clusters that are independent of data order.

Unlike the Star algorithm, the obtained clusters are independent of data order. Nevertheless, the Extended Star algorithm has also some drawbacks. First of all, it can leave uncovered vertices, producing an infinite loop. This situation is illustrated in Fig. 1 (A).
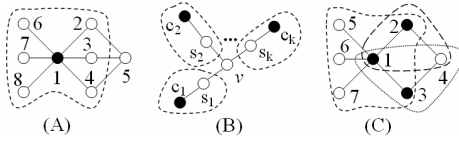
Fig. 1. Drawbacks of Extended algorithm

This situation is not an isolated case. We can generalize that any time that there is a vertex v – such as the illustrated in graph (B) of Fig. 1 – that satisfies the condition described in (1), then the algorithm produces an infinite loop, leaving the vertex v uncovered.

$$\forall s_i, 1 \le i \le k, |v.Adj| > |s_i.Adj| \land \forall c_i, 1 \le i \le k, |c_i.Adj| > |v.Adj| \ . \quad (1)$$

In this graph, each s_i represents the corresponding neighbours (adjacent vertices) of v, and c_i, is the adjacent center of s_i with highest degree. In (1) and in the following expressions, $x.Adj$ represents the set of adjacent vertices of the vertex x.

The second drawback of this algorithm is that it can produce unnecessary clusters, since more than one center can be selected at the same time. As can be noticed in graph (C) of Fig. 1, vertex 2 and vertex 3 should not be centers at the same time because we only need one of them to cover vertex 4.

A different version of the Extended Star algorithm was proposed by Gil *et al.* to construct a parallel approach [7]. This new version is also independent of data order, and solves the first drawback of the former Extended Star algorithm, but it can produce unnecessary clusters and illogical (less dense) clusters.

3   ACONS Algorithm

In this section we introduce a new concept of star allowing a different star-shaped form and as a consequence a new method, called ACONS, is obtained. As with the aforementioned algorithms, we represent the document collections by its thresholded similarity graph G_σ.

3.1   Some Basic Concepts

In order to define this new star concept and to describe the method, we define a finite sequence of directed graphs called transition graphs. Each new transition graph removes the unnecessary edges to get better clusters. Thus, the last transition will hold the vertices with real possibilities to be centers.

We call the *first transition* of $G_\sigma = \langle V, E_\sigma \rangle$ to the directed-graph $G_\sigma^{(0)} = \langle V, E_\sigma^{(0)} \rangle$ resulting from adding the directed-edge (v, u) to $E_\sigma^{(0)}$ iff the edge $(v, u) \in E_\sigma$.

Let $n \ge 0$ be an integer number, we call the *next transition* of $G_\sigma^{(n)} = \langle V, E_\sigma^{(n)} \rangle$, to the directed-graph $G_\sigma^{(n+1)} = \langle V, E_\sigma^{(n+1)} \rangle$, resulting from adding the directed--edge (v, u) to $E_\sigma^{(n+1)}$ iff $(v, u) \in E_\sigma^{(n)}$ and $v.out[n] \ge u.out[n]$, where $v.out[n]$

denote the *out-degree* of v in $G_\sigma^{(n)}$, i.e the number of edges $(v, x) \in E_\sigma^{(n)}$. It is important to notice that as $G_\sigma^{(n)}$ is not affected in the construction of $G_\sigma^{(n+1)}$, we can conclude that this process does not depend on data order.

Thus, starting from G_σ, we can construct a *sequence of graph transitions* $\{G_\sigma^{(0)}, G_\sigma^{(1)}, \ldots, G_\sigma^{(n)}, \ldots\}$. Furthermore, the integer positive sequence $\{e_n\}_{n=0}^\infty$, where $e_n = |E_\sigma^{(n)}|$, is decreasing and there is a unique integer $h \geq 0$ such that the finite sequence of terms $\{e_n\}_{n=0}^h$ is strictly decreasing and the sequence $\{e_n\}_{n=h}^\infty$ is constant. Then we say that $G_\sigma^{(h)}$ is the *last transition* of G_σ. Given $u, v \in V$, we say that u is an *r-satellite* of v, if $0 \leq r \leq h$ and $(v, u) \in E_\sigma^{(r)}$. We denote $v.Sats[r] = \{u \in V \mid u \text{ is an } r\text{-satellite of } v\}$ as the set of all r-satellites of v.

A *condensed star-shaped sub-graph* of $m+1$ vertices in G_σ, consists of a single center c and m adjacent vertices, such that $c.out[h] > 0$. Each isolated vertex in G_σ will be considered as a degenerated condensed star-shaped sub-graph with only one vertex.

Starting from this definition and guaranteing a full cover C of G_σ, this method should satisfy the following post-conditions:

$$\forall x \in V , x \in C \vee x.Adj \cap C \neq \emptyset , \tag{2}$$

$$\forall c \in C, \forall u \in c.Sats[h] , c.out[h] \geq u.out[h] . \tag{3}$$

The first condition (2) guarantees that each object of the collection belongs at least to one group, as a center or as a satellite. On the other hand, the condition (3) indicates that all the centers satisfy the condensed star-shaped sub-graph definition.

3.2   ACONS Algorithm

In order to define the ACONS algorithm, we introduce the concepts of voting-degree of a vertex and the redundancy of a center.

Let $G_\sigma^{(h)}$ be the last transition of G_σ and $v \in V$ a non-isolated vertex. The *voting-degree* $(v.vd)$ of a vertex v is $v.vd = |\{u \mid v \in u.Electees\}|$, where $u.Electees = \arg\max_x \{x.out[h] \mid x \in u.Adj \cup \{u\}\}$.

Let C be a set of centers obtained by the algorithm, a center vertex c will be considered *redundant* if it satisfies the following conditions:

1. $\exists d \in c.Adj \cap C, d.out[h] > c.out[h]$, i.e. vertex c has at least one adjacent center (with greater out-degree) on its neighborhood.
2. $\forall s \in c.Sats[h], s \in C \vee |s.Adj \cap C| > 1$, i.e. vertex s has more than one adjacent center (a neighboring center different to c) on its neighborhood or vertex s is a center.

The logic of the ACONS algorithm is to generate a cover of G_σ by the densest condensed star-shaped sub-graphs. The centers are selected from a candidates list, formed by the vertices with positive voting-degree in the last transition of G_σ. The algorithm is summarized in Fig 2.

The functions *FindFirstTransition* and *FindLastTransition* are applied to construct the first and the last transition of G_σ based on the concepts and definitions

---

Algorithm 1: ACONS

Input: $V = \{d_1, d_2, \ldots, d_N\}$, σ-similarity threshold
Output: SC-Set of clusters

1 // Phase 1
2 $G_\sigma^{(0)} :=$ FindFirstTransition(V, σ);
3 $G_\sigma^{(h)} :=$ FindLastTransition$(G_\sigma^{(0)})$;
4 **forall** *vertex* $v \in V$ **do** $v.Electees := \arg\max_x\{x.out[h] \mid x \in v.Adj \cup \{v\}\}$;
5 **forall** *vertex* $v \in V$ **do** $v.vd := |\{u \mid v \in u.Electees\}|$;
6 $L := \{v \in V \mid v.vd > 0\}$;
7 // Phase 2
8 $C := \{v \in V \mid v.Adj \neq \emptyset\}$;
9 $U := \emptyset$;
10 **while** $L \neq \emptyset$ **do**
11 $v := \arg\max_x\{x.vd \mid x \in L\}$;   // Only one vertex is selected
12   **if** $v.Adj \cap C \neq \emptyset$ **then** $C := C \cup \{v\}$
13   **else**
14 $F = \{u \in v.Sats[h] \mid u.Adj \cap C \neq \emptyset\}$;
15   **if** $F \neq \emptyset$ **then**
16   **if** $\exists f \in F, v.out[h] > f.out[h]$ **then** $C := C \cup \{v\}$
17   **else** $U := U \cup \{v\}$;
18   **end**
19   **end**
20 $L := L \setminus \{v\}$;
21 **end**
22 // Phase 3
23 **forall** *vertex* $v \in U$ **do**
24   **if** $\exists u \in v.Sats[h], u.Adj \cap C \neq \emptyset$ **then** $C := C \cup \{v\}$;
25 **end**
26 // Phase 4
27 "Sort C in ascending order by out-degree";
28 $SC := \emptyset$;
29 **forall** *center* $c \in C$ **do**
30   **if** c *is redundant* **then** $C := C \setminus \{c\}$
31   **else** $SC := SC \cup \{\{c\} \cup c.Adj\}$;
32 **end**

Fig. 2. Pseudo-code of ACONS Algorithm

mentioned in section 3.1. Both functions are very easy to be implemented, because it is not necessary to preserve all transition states.

The algorithm is made up of five phases: (1) computes the last transition of G_σ, and calculates the candidates list L using voting-degrees, (2) determines centers list C and uncertain centers lists U from L, (3) processes U to find new centers, and (4) removes from C the redundant centers and constructs the set of clusters.

The phase (1) is very important, because it guarantees the selection of vertices that actually have real possibilities to be selected as center, i.e. vertices that could form a dense condensed star-shaped sub-graph. Notice that the starting candidates list L after phase (1) is made up of the vertices $v \in V$ with $v.vd > 0$. Thus, the vertices outside L are isolated or satellites with at least one adjacent vertex in L.

The isolated vertices are selected as centers at the beginning of the phase (2). Afterward, the vertices of L are processed in a decreasing order regarding the voting-degree; in this way, we ensure that any selected center will satisfy the post-condition (3). In each iteration, the vertex v is processed considering the following situations:

1. If v has not been covered yet by an adjacent vertex $c \in C$ then we add v to C; thus we try to reduce the overlapping among sub-graphs and ensure that v is covered at least by itself.
2. If v has some adjacent vertex f that has not been covered yet and satisfy:
   (a) If f has a lesser out-degree than v then we add v to C; thus we ensure that such vertex f will belong to a sub-graph denser than the one it can form.
   (b) Otherwise, v is added to uncertain list U postponing the selection of v as center.

At the end of each iteration, we remove the vertex v from L to guarantee the phase (2) ending.

During phase (3) all of the vertices $v \in U$ are processed in the insertion order, selecting v as center if it is needed to cover some adjacent vertex. Thus, each vertex s outside C has at least one adjacent vertex in C, i.e. the post-condition (2) is fulfilled. Finally (phase(4)), we check the redundancy of each vertex to eliminate the redundant centers in C .

3.3   General Considerations of ACONS Algorithm

The ACONS method – as the original Star algorithm and the two versions of the Extended algorithm – generates clusters which can be overlapped and guarantees also that the pairwise similarity between satellites vertices in a condensed star-shaped sub-graph be high.

As we can see in Fig. 3, unlike its previous algorithms, the ACONS algorithm can not produce illogical clusters because all the centers satisfy the condensed
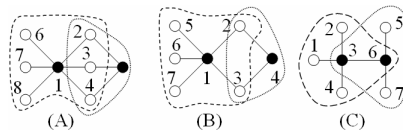

Fig. 3. Solutions to uncovered vertices (A), unnecessary clusters (B) and illogical clusters (C)

star-shaped sub-graph definition. The ACONS algorithm does not produce uncovered vertices – this property is ensured by the fulfillment of postcondition (2) – and avoid the generation of unnecessary clusters presented in graph (A) and (C) of Fig. 1 respectively.

The dependence on data order is a property that the Extended Star method certainly solves. Nevertheless, as we had previously indicated, it is necessary only when that dependence affects the quality of the resulting clusters. Thus, the ACONS algorithm solves the dependence on data order (for non symmetric or similar solutions) observed in the Star algorithm.

4   Experimental Results

In this section we present the experimental evaluation of our method, comparing its results against the Extended Star method and the original Star algorithms. The produced clustering results are evaluated by the same method and criterion to ensure a fair comparison across all algorithms.

Two data sets widely used in document clustering research were used in the experiments: TREC-5 and *Reuters*-21578. These are heterogeneous regarding document size, cluster size, number of classes, and document distribution. The data set TREC-5 contains news in Spanish published by AFP during 1994 (http://trec.nist.gov); *Reuters*-21578 was obtained from http://kdd.ics.uci.edu . We excluded from data sets the empty documents and also those documents do not have an associated topic.

In our experiments, the documents are represented using the traditional vector space model. The index terms of documents represent the lemmas of the words appearing in the texts. Stops words, such as articles, prepositions and adverbs are removed from document vectors. Terms are statistically weighted using the term frequency. We use the traditional cosine measure to compare the documents.

The literature abounds in measures defined by multiple authors to compare two partitions on the same set. The most widely used are: Jaccard index, and F-measure.

Jaccard index.- This index (noted j) takes into account the objects simultaneously joined [8]. It is defined as follows:

$$j(A, B) = \frac{n_{11}}{\frac{N(N-1)}{2} - n_{00}} \ . \tag{4}$$

In this index, n_{11} denotes the number of pairs of objects which are both in the same cluster in A and are also both in the same cluster in B. Similarly, n_{00} is the number of pairs of objects which are in different clusters in A and are also in different clusters in B.

The performances of the algorithms in the document collections considering Jaccard index are shown in Fig. 4 (A) and (B).

F-measure.- The aforementioned index and others are usually applied to partitions. In order to make a better evaluation of overlapping clustering, we have

considered F-measure calculated over pairs of points, as defined in [4]. Noted as *Fmeasure*, this measure is the harmonic mean of *Precision* and *Recall*:

$$Fmeasure = \frac{2 * Presicion * Recall}{Presicion + Recall} \quad, \tag{5}$$

where:

$$Presicion = \frac{n_{11}}{Number\ of\ identified\ pairs}, \quad Recall = \frac{n_{11}}{Number\ of\ true\ pairs} \quad .$$

The performances of the algorithms in the document collections considering F-measure are shown in Fig. 4 (C) and (D).
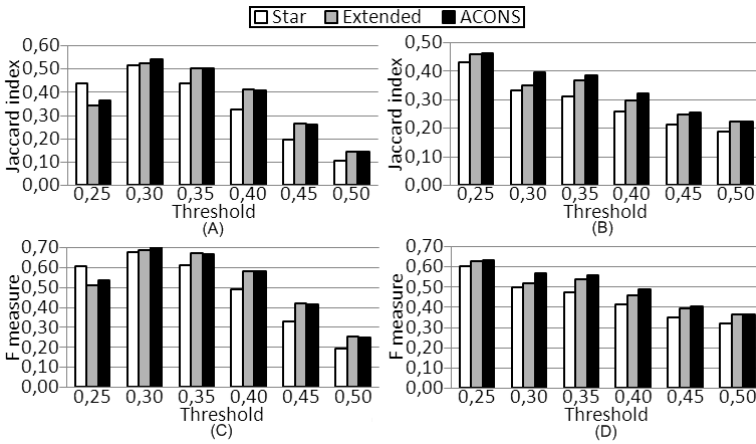
Fig. 4. Behavior in AFP (A,C) and Reuters (B,D) collections with Jaccard index and F-measure

As can be noticed, the accuracy obtained using our proposed algorithm is in most cases (for all the indexes) comparable with that obtained from the other methods investigated; moreover, our proposal can outperform those methods for all the indexes. But, this behavior is not homogeneous for all similarity thresholds; for each collection, there is a minimum value for which ACONS outperforms previous Star methods. Starting from this minimum value, the accuracy of ACONS is in general as good as, or even in many cases higher than, the others.

Furthermore, ACONS in all cases obtains lesser clusters than the other algorithms (see Fig. 5), and in most cases obtains denser clusters. This behavior could be of great importance for obtaining a minimum quantity of clusters without loosing precision.

It is important to notice that the Extended algorithm could cover all the vertices, but only in these experiments. Nevertheless, as it was explained, theoretically the Extended algorithm may fail with other repositories.
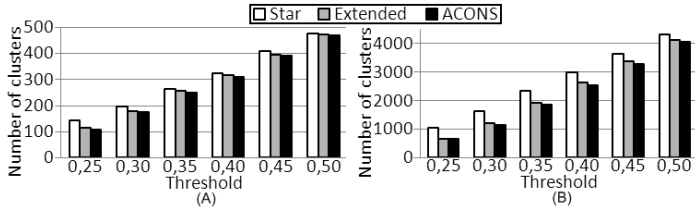
Fig. 5. Number of generated clusters in AFP (A) and Reuters (B) collections

Despite the experiments carried out by Aslam *et al.* in [1], and in order to ensure the effectiveness of our proposed algorithm, we made a new experimentation to compare the performance of ACONS algorithm against the Single Link and Average Link [5] algorithms, which uses different cost functions. For a fair comparison across all algorithms, we used the same thresholds of the previous experiments, stopping the execution of the Single Link and Average Link algorithms when the two selected clusters to be joined do not satisfy the current threshold, meaning that the evaluation of the cost function for all pair of clusters in the current algorithm return a value greater than the selected threshold. After that, we evaluated each algorithm considering the Jaccard index and F-measure, and we selected the average value of each algorithm for the selected measures for all thresholds.

The performances of the algorithms in the document collections considering Jaccard index, and F-measure are shown in Fig. 6.
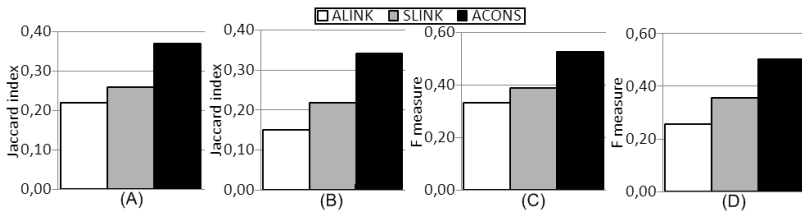

Fig. 6. Behavior in AFP (A,C) and Reuters (B,D) collections with Jaccard index and F-measure

As we can see, our proposal also outperforms the Single Link and Average Link algorithms in both collections. Thus, the ACONS algorithm represents a 68.2% improvement in performance compared to average link and a 42.3% improvement compared to single link in AFP collection considering the Jaccard index; if we consider F-measure, then the ACONS algorithm represents a 57.6% improvement in performance compared to average link and a 33.3 improvement compared to single link in the same collection. In the case of the Reuters collection the improvements are higher and even in some cases it doubles the result.

5   Conclusions

In this paper we presented a new clustering algorithm called Condensed Star (ACONS). As a consequence, we obtained different star-shaped clusters. This algorithm solves the drawbacks observed in Star and Extended Star methods: the dependence on data order (for non symmetric or similar solutions), the production of uncovered vertices and the generation of illogical and redundant clusters.

We compared the ACONS algorithm with the original Star and the Extended Star methods. The experimentation shows that our proposal outperforms previous methods for all the measures and aspects. These performances prove the validity of our algorithm for clustering tasks.

This algorithm can be used for organizing information systems, browsing, topic tracking and new topic detection. Although we employ our algorithm to cluster documents collections, its use is not restricted to this area, since it can be applied to any problem of pattern recognition where clustering is needed.

As a future work, we want to do some other experiments considering other representations of the documents and other similarity measures. These experiments could help us to decide a priori how to choose the threshold value in order to obtain the best performance of our algorithm.

References

1. Aslam, J., Pelekhov, K., Rus, D.: Static and Dynamic Information Organization with Star Clusters. In: Proceedings of the 1998 Conference on Information Knowledge Management, Baltimore (1998)
2. Aslam, J., Pelekhov, K., Rus, D.: Using Star Clusters for Filtering. In: Proceedings of the Ninth International Conference on Information and Knowledge Management, USA (2000)
3. Aslam, J., Pelekhov, K., Rus, D.: The Star Clustering Algorithm for Static and Dynamic Information Organization. Journal of Graph Algorithms and Applications 8(1), 95–129 (2004)
4. Banerjee, A., Krumpelman, C., Basu, S., Mooney, R., Ghosh, J.: Model Based Overlapping Clustering. In: Proceedings of International Conference on Knowledge Discovery and Data Mining (KDD) (2005)
5. Duda, R., Hart, P., Stork, D.: Pattern Classification. John Wiley & Sons, Chichester (2001)
6. Gil-García, R.J., Badía-Contelles, J.M., Pons-Porrata, A.: Extended Star Clustering Algorithm. In: Sanfeliu, A., Ruiz-Shulcloper, J. (eds.) CIARP 2003. LNCS, vol. 2905, pp. 480–487. Springer, Heidelberg (2003)
7. Gil-García, R.J., Badía-Contelles, J.M., Pons-Porrata, A.: Parallel Algorithm for Extended Star Clustering. In: Sanfeliu, A., Martínez Trinidad, J.F., Carrasco Ochoa, J.A. (eds.) CIARP 2004. LNCS, vol. 3287, p. 402. Springer, Heidelberg (2004)
8. Kuncheva, L., Hadjitodorov, S.: Using Diversity in Cluster Ensembles. In: Proceedings of IEEE SMC 2004, The Netherlands (2004)
9. van Rijsbergen, C.J.: Information Retrieval, Buttersworth, London, 2nd edn. (1979)
10. Zhong, S., Ghosh, J.: A Comparative Study of Generative Models for Document Clustering. In: Proceedings of SDM Workshop on Clustering High Dimensional Data and Its Applications (2003)

Mixed Data Object Selection Based on Clustering and Border Objects

J. Arturo Olvera-López, J. Francisco Martínez-Trinidad, and J. Ariel Carrasco-Ochoa

Computer Science Department
National Institute of Astrophysics, Optics and Electronics
Luis Enrique Erro No. 1, Sta. María Tonantzintla, Puebla, CP: 72840, Mexico
{aolvera,fmartine,ariel}@ccc.inaoep.mx

Abstract. In supervised classification, the object selection or instance selection is an important task, mainly for instance-based classifiers since through this process the time in training and classification stages could be reduced. In this work, we propose a new mixed data object selection method based on clustering and border objects. We carried out an experimental comparison between our method and other object selection methods using some mixed data classifiers.

Keywords: Supervised Classifiers, Object Selection, Clustering, Mixed Data.

1 Introduction

The supervised classification is a process that assigns a class or label to new objects according to their features using a set of previously assessed objects called training set, denoted in this paper as T.

In practice, T contains objects with useless information for the classification task, that is, superfluous objects. Due to the superfluous objects in a training set, it is necessary to select those objects (in T) that give relevant information for the classifier. This selection process is known as object selection. The main goal of an object selection method is to obtain a set $S \subset T$ such that S preserves the classification accuracy.

Several methods have been proposed for solving the object selection problem, the *Condensed Nearest Neighbor* (*CNN*) [1] and the *Edited Nearest Neighbor* (*ENN*) [2] are two of the first proposed methods for object selection. The *CNN* method starts with $S = \varnothing$ and its initial step consists in randomly including in S one object belonging to each class. After the initial step, each object in T is classified (with *k-NN*) using S as training set, if an object O is misclassified then O is included in S to ensure that new objects near to O will be classified correctly. The *ENN* rule consists in discarding from T those objects that do not belong to their k nearest neighbors' class. This method is used as noise filter because it deletes noisy objects, that is, objects with a different class in a neighborhood. An extension of *ENN* is *REEN* (*Repeated ENN*) [3] which applies *ENN* repeatedly until all objects in S have the same class that the majority of their k nearest neighbors.

Other object selection methods are the *DROP* (*Decremental Reduction Optimization Procedure*) which were proposed in [4], their selection criterion is based on the concept of *associate*. The *associates* of an object *O* are those objects such that *O* is one of their *k* nearest neighbors. These methods discard the object *O* if its associates can be classified correctly without *O*.

In [5] the *Iterative Case Filtering algorithm* (*ICF*) was proposed, this method is based on the *Reachable*(*O*) and *Coverage*(*O*) sets which are the neighborhood set and the associates set described above. *ICF* discards an object *O* if |*Reachable*(*O*)| > |*Coverage*(*O*)|.

Clustering can be used for object selection [6, 7] so that after splitting *T* in *n* clusters, *S* is the set of centers of each cluster. In [8] the *CLU* object selection method is based on this rule and it was applied to the signature recognition problem.

In a training set, the border objects of a class are located in a region where there are objects from different classes. These objects give useful information to the classifier for preserving the class discrimination regions [4, 5]. On the other hand, interior objects of a class (objects that are not border) could be less useful. In this paper, we propose a mixed data object selection method based on clustering; our method finds and retains border objects and some interior objects.

In order to show the performance of the proposed method, we present an experimental comparison between our method and some other object selection methods using the obtained object sets as training for different mixed data classifiers.

This paper is structured as follows: in section 2 our object selection method is introduced, in section 3 we report experimental results obtained by our method, and finally, in section 4 some conclusions and future work are given.

2   Proposed Method

In a training set, interior objects could be deleted without loosing classification accuracy. In this paper we propose a method called *MOSC* (*Mixed data Object Selection by Clustering*) which finds and retains border objects and some interior objects. The selection criterion in *MOSC* is based on clustering, mainly on non homogeneous clusters.

An homogeneous cluster is a set of objects such that all objects belong to the same class whereas in a non homogeneous cluster there are objects belonging to different classes.

In order to find border objects, the *MOSC* method generates clusters and analyses non homogeneous clusters since border objects are located in regions which contain similar objects belonging to different classes.

In order to handling mixed data, *MOSC* uses the *k-means with similarity functions* algorithm (*kMSF*) [9] for creating clusters. This algorithm is based on the same idea as *k-means* but for comparing objects it uses a similarity function and instead of computing means, it computes representative objects for each cluster. The *kMSF* algorithm determines the representative object in a cluster A_j using the next expression (for more details see [9]):

$$r_{\substack{A_i \\ O_j \in A_i \\ A_q \neq A_i}}(O_j) = \frac{\beta_{A_i}(O_j)}{\alpha_{A_i}(O_j) + (1 - \beta_{A_i}(O_j))} + \eta_{A_q}(O_j) \tag{1}$$

Where

$$\beta_{A_i}(O_j) = \frac{1}{|A_i| - 1} \sum_{\substack{O_j, O_q \in A_i \\ O_j \neq O_q}} \Gamma(O_j, O_q) \tag{2}$$

$$\alpha_{A_i}(O_j) = \frac{1}{|A_i| - 1} \sum_{\substack{O_j, O_q \in A_i \\ O_j \neq O_q}} \left| \beta_{A_i}(O_j) - \Gamma(O_j, O_q) \right| \tag{3}$$

$$\eta_{A_k}(O_j) = \sum_{\substack{q=1 \\ i \neq q}}^{n} (1 - \Gamma(O_q^r, O_j)) \tag{4}$$

$\Gamma(O_j, O_q)$ is the similarity between objects O_j and O_q, O_q^r is the representative object in cluster q and n is the number of clusters. $\beta_{A_i}(O_j)$ is the average similarity of O_j with the other objects in the same cluster A_i. The $\alpha_{A_i}(O_j)$ function evaluates the variance between $\beta_{A_i}(O_j)$ and the similarity between O_j and the other objects in A_i and $\eta_{A_k}(O_j)$ is the average dissimilarity of O_j with the other representative objects.

The most representative object O_{Ri} in A_i must be the most similar in average with other objects in the cluster and the most dissimilar with respect to the other representative objects. These properties directly depend on $\beta_{A_i}(O_j)$ and $\eta_{A_k}(O_j)$ values respectively then O_{Ri} is that object that maximizes the expression $r_{A_i}(O_j)$.

The *MOSC* method (figure 3.1) starts creating n clusters. Once the clusters have been obtained, for each cluster A_j it is necessary to decide whether A_j is homogeneous or not.

If the cluster A_j is non homogeneous then A_j contains some objects located at critical regions, that is, border objects. In order to find the border objects, *MOSC* finds the majority class objects. Once these objects have been found, the border objects in the majority class are those objects that are the most similar to an object in A_j belonging to different class, and by analogy, the border objects of A_j in the other classes are those objects that are the most similar to each border object in the majority class.

If the cluster A_j is homogeneous then the objects in A_j are interior objects and they could be discarded from T without affecting the classification accuracy. Therefore, *MOSC* finds the representative object of the homogeneous cluster A_j and discards the remaining objects so that A_j is reduced to its representative object.

The objects selected by *MOSC* are the representative objects from each homogeneous cluster and the border objects from each non homogeneous cluster.

MOSC (Training set *T*, number of clusters *n*): object set *S*
$S = \varnothing$
Clust= *kMSF*(*T*, *n*)   // create *n* clusters from *T*
For each cluster A_j in *Clust*
  If A_j is non homogeneous then
    Find the majority class C_M in cluster A_j
    For each class C_k in A_j ($C_k \neq C_M$)
      For each object O_j belonging to class C_k
        Find $O_c \in C_M$, the most similar object to O_j with class C_M
        $S = S \cup \{ O_c \}$
        Find O_M , the most similar object to O_c with class different to C_M
        $S = S \cup \{ O_M \}$
  Else   // A_j is homogeneous
    O_i = representative object of the cluster A_j
    $S = S \cup \{ O_i \}$
Return *S*

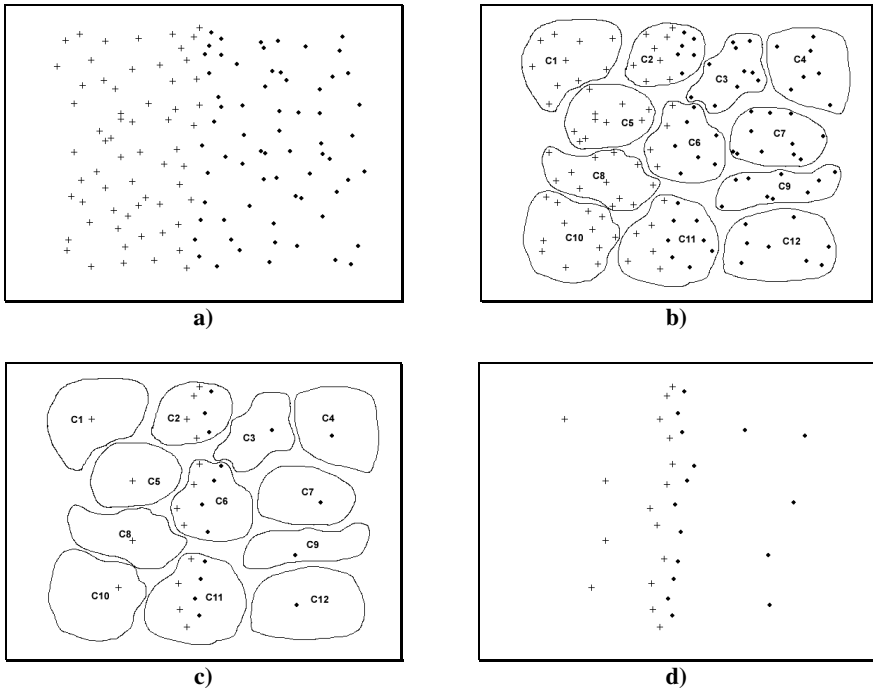**Fig. 3.1.** *MOSC* method for object selection

Fig. 3.2. a) Dataset with classes "+" and "•". **b)** Clusters created from the dataset. **c)** Objects selected in each cluster. **d)** Objects set obtained by *MOSC*.

To illustrate in a graphical way how *MOSC* finds border objects let us consider the dataset shown in figure 3.2a which is a bi-dimensional dataset created by hand with objects belonging to the classes "+" and "•". In figure 3.2b, the clusters (C1…C12) created from the dataset are depicted, the non homogeneous clusters are C2, C6 and C11 whereas the remaining clusters are homogeneous.

In the clusters C6 and C11 the minority class is "+", then the border objects in the most frequent class (•) are the most similar objects to each minority class object (+). On the other hand, the border object in class "+" are the most similar objects (belonging to class "+") to each border object in class "•".

The same process described before is applied to cluster C2 where the minority class is "•". The objects selected in each cluster are depicted in figure 3.2c and the objects set obtained by *MOSC* is depicted in figure 3.2d. We can observe that *MOSC* finds border objects and some interior objects (representative objects in the homogeneous clusters).

3   Experimental Results

In this section, we report the results obtained applying the *MOSC* method over ten datasets from the UCI dataset repository [10], four of them (*Glass, Iris, Liver, Wine*) are full numeric and the other six datasets are mixed. For all the experiments 10-fold cross validation is reported.

We show a performance comparison among *MOSC, CLU* and the *DROP* methods because according to the results reported in [4, 5], the *DROP* methods outperform to other relevant object selection methods such as *ENN, RENN* and *ICF*. We also compare against *CLU* because it is also an object selection method based on clustering.

For *MOSC* and *CLU* it is necessary to generate *n* clusters, $n \geq c$, where *c* is the total number of classes in the dataset. For these methods, we used the *k-means with similarity functions* algorithm for creating clusters.

In this work we used the next similarity function:

$$\Gamma(O_j, O_q) = 1 - \frac{HVDM(O_j, O_q)}{m} \tag{5}$$

Where *HVDM* (*Heterogeneous Value Difference Metric*) [4] is the function used and proposed by the *DROP*s authors and *m* is the number of features.

In order to choose the number of clusters *n* to be used in our experiments, we carried out an experiment over ten datasets using different values for *n* to choose the best ones where *MOSC* and *CLU* had the best performance in the average case. In table 4.1 we show the classification accuracy obtained by *MOSC* and *CLU* using the values *n= 2c, 4c, 6c, 8c* and *10c*. For testing the object sets selected by *MOSC* and *CLU*, the *k-Most Similar Neighbor* (*k-MSN*) classifier (*k=3*) was used, that is, *k-NN* but using a similarity function instead of a distance function for comparing objects. Also we show the classification obtained by the original training set (*Orig.*).

According to the results shown in table 4.1, the best value for *n* using *MOSC* was *n=8c* and the best one for *CLU* was *n=10c*, therefore these values were used in all the experiments reported in the next tables.

Table 4.1. Classification accuracy obtained by *CLU* and *MOSC* using different number of clusters

Dataset		Number of clusters								
		n=2c		n=4c		n=6c		n=8c		n=10c	
	Orig.	CLU	MOSC	CLU	MOSC	CLU	MOSC	CLU	MOSC	CLU	MOSC
Bridges	66.09	46.09	45.45	51.63	51.63	53.54	56.54	58.36	59.45	61.27	61.09
Echocardiogram	95.71	89.82	94.46	85.90	86.42	90.71	86.42	94.10	91.42	90.71	85.53
Glass	71.42	42.85	54.71	50.45	62.27	55.64	64.04	61.29	64.48	62.00	63.52
Heart Cleveland	82.49	73.00	69.98	74.61	71.26	73.00	73.27	75.29	72.26	76.33	74.00
Heart Swiss	93.72	84.61	73.07	69.23	67.69	84.61	83.91	74.88	79.55	84.61	86.21
Hepatitis	79.29	79.25	77.25	77.50	73.12	75.00	75.37	75.87	79.29	73.66	75.54
Iris	94.66	64.64	90.66	89.33	92.66	88.66	91.33	91.33	94.66	90.00	90.00
Liver	65.22	55.03	57.98	53.94	59.68	48.19	59.40	46.40	59.40	51.89	59.15
Wine	94.44	73.33	86.66	88.88	88.88	92.22	94.44	90.00	91.11	94.44	94.44
Zoo	93.33	76.66	84.44	84.44	90.00	91.11	92.22	90.00	90.00	90.00	91.11
Average	**83.64**	68.53	73.47	72.59	74.36	75.27	77.69	75.75	78.16	77.49	78.06

In table 4.2 we report the results obtained by *DROP3, DROP5* (the best *DROP* methods reported in [4]), *CLU* and *MOSC* over the ten datasets. For each method we show the classification accuracy (*Acc.*) and the percentage of the original training set that was retained by each method (*Str.*), that is, 100*|S|/|T|. In addition, we show the classification obtained by the original training set (*Orig.*). The classifier used was *k-MSN* with *k=3* (the value of *k* reported in [4] for *DROP* methods, using *k-NN*). At the bottom of each table we show the average accuracy and storage obtained by each method.

Table 4.2. Classification (*Acc.*) and retention (*Str.*) results obtained using: the original training set (*Orig.*), *DROP3, DROP5, CLU* and *MOSC*

Dataset	Orig.		DROP3		DROP5		CLU		MOSC	
	Acc	Str.	Acc	Str.	Acc	Str.	Acc	Str.	Acc	Str.
Bridges	66.09	100	56.36	14.78	62.82	20.66	61.27	63.68	59.45	51.79
Echocardiogram	95.71	100	92.86	13.95	88.75	14.87	90.71	30.03	91.42	23.87
Glass	71.42	100	66.28	24.35	62.16	25.91	62.00	31.15	64.48	48.33
Heart Cleveland	82.49	100	78.89	11.44	79.87	14.59	76.33	18.33	72.26	26.21
Heart Swiss	93.72	100	93.72	1.81	93.72	1.81	84.61	18.06	79.55	15.89
Hepatitis	79.29	100	78.13	11.47	75.42	15.05	73.66	14.33	79.29	10.46
Iris	94.66	100	95.33	15.33	94.00	12.44	90.00	22.22	94.66	25.48
Liver	65.22	100	67.82	26.83	63.46	30.59	51.89	6.44	59.40	46.44
Wine	94.44	100	94.41	15.04	93.86	10.55	94.44	37.03	91.11	34.69
Zoo	93.33	100	90.00	20.37	95.56	18.77	90.00	76.41	90.00	50.24
Average	**83.64**	100	81.38	15.54	80.96	16.52	77.49	31.77	78.16	33.34

In figure 4.1, the classification (horizontal axis) versus retention (vertical axis) scatter graphic from results shown in table 4.2 is depicted. On this kind of graphic, the most located at right the best classification accuracy and the most located at bottom the best retention percentage.

Based on the results in table 4.2 and figure 4.1, we can observe that in the average case, the best object selection methods were *DROP3* and *DROP5*. The classification accuracy obtained by *MOSC* and *CLU* were smaller than those obtained by *DROPs* but *OSC* outperformed *CLU*.

The best methods in table 4.2 were the *DROPs* since the classifier was *k-MSN* and the *DROP*s are based on the Nearest Neighbor or Most Similar Neighbor rules, how-ever it is important to test the object sets selected (obtained in the previous experi-ment by *DROPs, CLU* and *MOSC*) as training sets for other classifiers, in particular we are interested in testing with classifiers that allow handling mixed data.
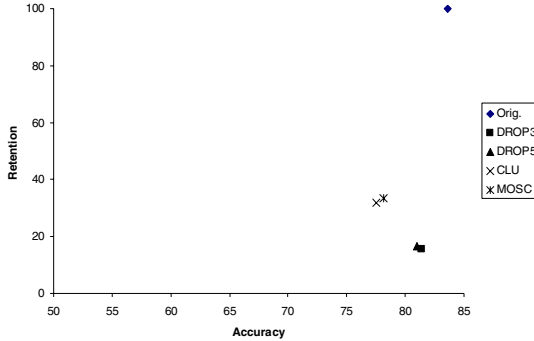

Fig. 4.1. Scatter graphic from results shown in table 4.2

Therefore, another experiment was done using the object set obtained by *DROPs, CLU* and *MOSC* as training sets for the *C4.5* [11] and *ALVOT* [12] classifiers, which allow handling mixed data. For *ALVOT,* we used as support sets system all the fea-tures subsets with cardinality 3. The row evaluation function for a fixed support set Ω was:

$$\Gamma_\Omega(O_p,O) = \beta_\Omega(O_p,O) \tag{6}$$

Where $\Omega \in \Omega_A$, Ω_A is the support set system, and $\beta(O_p,O)$ is the similarity func-tion shown in (5) but comparing only the features of Ω.

The class evaluation function for a fixed support set Ω was:

$$\Gamma_\Omega^j(O) = \frac{1}{m_j} \sum_{t=1}^{m_j} \Gamma_\Omega(O,O_t) \tag{7}$$

Where m_j is the number of objects in the *j*-th class.

The evaluation by class for the whole support set system Ω_A was obtained using the next expression:

$$\Gamma_j(O) = \frac{1}{|\Omega_A|} \sum_{\Omega \in \Omega_A} \Gamma_\Omega^j(O) \tag{8}$$

Finally, a new object is assigned to the class where it obtains the higher evaluation.

The *C4.5* and *ALVOT* results are reported in tables 4.4-4.5 and figures 4.2-4.3 re-spectively.

Table 4.4. Classification results obtained using the original training set (*Orig.*) and the object sets obtained by *DROPs, CLU* and *MOSC* as training for the *C4.5* classifier

Dataset	Orig.	DROP3	DROP5	CLU	MOSC
Bridges	65.81	47.90	39.54	55.45	59.17
Echocardiogram	95.71	84.10	92.85	93.21	95.89
Glass	67.29	60.19	53.76	58.35	62.22
Heart Cleveland	71.96	68.59	72.16	76.57	73.59
Heart Swiss	93.71	93.71	93.71	84.61	82.81
Hepatitis	76.70	63.33	63.41	71.58	65.68
Iris	93.99	92.66	90.66	92.66	93.99
Liver	63.67	59.48	63.67	57.96	61.11
Wine	94.44	84.43	78.88	86.65	86.65
Zoo	93.33	81.10	88.88	92.21	93.33
Average	81.66	73.55	73.75	76.93	77.44
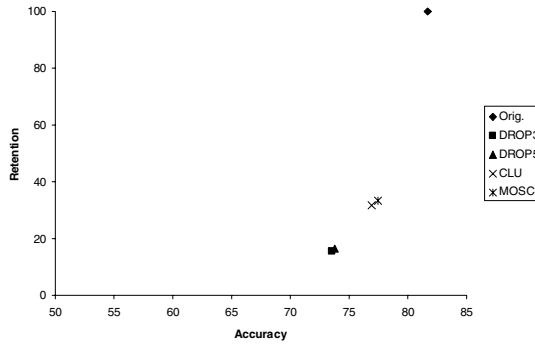
Fig. 4.2. Scatter graphic from results shown in table 4.4

Table 4.5. Classification results obtained using the original training set (*Orig.*) and the object sets obtained by *DROPs, CLU* and *MOSC* as training for the *ALVOT* classifier

| Dataset	Orig.	DROP3	DROP5	CLU	MOSC
Bridges	22.81	23.09	27.27	22.81	20.00
Echocardiogram	93.21	93.21	90.35	93.21	87.50
Glass	40.56	29.95	28.09	40.90	40.56
Heart Cleveland	72.59	73.26	73.89	73.26	72.30
Heart Swiss	66.53	76.23	76.23	76.21	76.00
Hepatitis	81.12	35.12	41.87	24.08	45.58
Iris	86.66	88.66	88.66	87.33	88.66
Liver	48.44	48.57	54.77	48.07	48.44
Wine	90.00	83.69	89.86	92.22	92.22
Zoo	96.66	90.00	84.44	96.66	96.66
Average	69.86	64.18	65.54	65.48	66.79
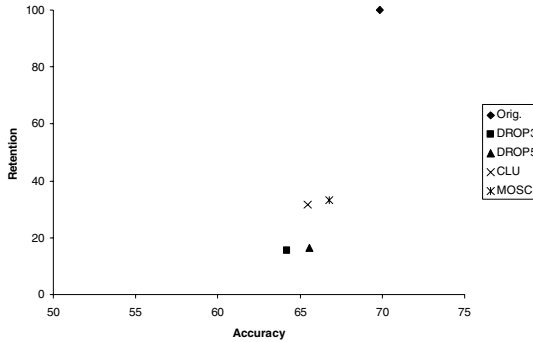
Fig. 4.3. Scatter graphic from results shown in table 4.5

Based on the results shown in tables 4.4 and figure 4.2, in the average case, for *C4.5*, the best object selection method was *MOSC* followed by *CLU*, that is, in this experiment, the subsets obtained by the *DROP*s were not as good as the obtained by *MOSC*.

According to results shown in table 4.5 and figure 4.3, again (as in table 4.4), in the average case for *ALVOT*, the best method was *MOSC* followed by *DROP5* and *CLU* respectively. Notice that in table 4.5, there are some low accuracy results; this is due to the *ALVOT* sensitivity to imbalanced classes.

4   Conclusions

The object selection is an important task for instance-base classifiers since through this selection the times in training and classification could be reduced. In this paper we proposed and compared the *MOSC* object selection method based on clustering. This method finds some interior and border objects since through these last it is possible to preserve discrimination capability between classes in a training sample. In addition, *MOSC* allows handling not only numeric but also nominal data which is useful since in practice it is very common to face with mixed data problems.

The experimental results showed that *MOSC* is a good method for solving the object selection problem when a classifier different from *k-MSN* is used. Since most of the object selection methods follow the nearest or most similar neighbor rule, the object sets obtained by these methods have not a good performance when they are used as training for other classifiers which are not based on the nearest or most similar neighbor rules, as it can be seen in our experimental results. These results showed that the objects sets selected by *MOSC* had a better average performance when they are used as training for the *C4.5* and *ALVOT* classifiers.

As future work, we will do experiments using other mixed data clustering methods and we will propose another way for selecting border objects in non homogeneous clusters.

References

1. Hart, P.E.: The Condensed Nearest Neighbor Rule. IEEE Transactions on Information Theory 14(3), 515–516 (1968)
2. Wilson, D.L.: Asymptotic Properties of Nearest Neighbor Rules Using Edited Data. IEEE Transactions on Systems, Man, and Cybernetics 2(3), 408–421 (1972)
3. Tomek, I.: An Experiment with the Edited Nearest-Neighbor Rule. IEEE Transactions on Systems, Man, and Cybernetics 6(6), 448–452 (1976)
4. Wilson, D.R., Martínez, T.R.: Reduction Techniques for Instance-Based Learning Algorithms. Machine Learning 38, 257–286 (2000)
5. Brighton, H., Mellish, C.: Advances in Instance Selection for Instance-Based Learning Algorithms. Data Mining and Knowledge Discovery 6, 153–172 (2002)
6. Leung, Y., Zhang, J.S., Xu, Z.B.: Clustering by scale-space filtering. IEEE Trans. on Pattern Analysis and Machine Intelligence 22, 1396–1410 (2000)
7. Spillmann, B., Neuhaus, M., Bunke, H., Pękalska, E., Duin, R.P.W.: Transforming Strings to Vector Spaces Using Prototype Selection. In: Yeung, D.-Y., Kwok, J.T., Fred, A., Roli, F., de Ridder, D. (eds.) Structural, Syntactic, and Statistical Pattern Recognition. LNCS, vol. 4109, pp. 287–296. Springer, Heidelberg (2006)
8. Lumini, A., Nanni, L.: A clustering method for automatic biometric template selection. Pattern Recognition 39, 495–497 (2006)
9. García-Serrano, J.R., Martínez-Trinidad, J.F.: Extension to C-means algorithm for the use of similarity functions. In: Żytkow, J.M., Rauch, J. (eds.) Principles of Data Mining and Knowledge Discovery. LNCS (LNAI), vol. 1704, pp. 354–359. Springer, Heidelberg (1999)
10. Blake, C., Keogh, E., Merz, C.J.: UCI repository of machine learning databases. In: Department of Information and Computer Science, University of California, Irvine, CA (1998), http://www.ics.uci.edu/ mlearn/MLRepository.html
11. Quinlan, J.R.: C4.5: Programs for Machine Learning. Morgan Kaufmann, San Francisco (1993)
12. Ruiz-Shulcloper, J., Abidi, M.A.: Logical Combinatorial Pattern Recognition: A Review. In: Pandali, S.G. (ed.) Recent Research Developments in Pattern Recognition. Transword Research Networks, USA, pp. 133–176 (2002)

Modification of the Growing Neural Gas Algorithm for Cluster Analysis

Fernando Canales and Max Chacón

Universidad de Santiago de Chile; Depto. de Ingeniería Informática,
Avda. Ecuador No 3659 - PoBox 10233; Santiago - Chile
`fernando.canales.cifuentes@gmail.com, mchacon@diinf.usach.cl`

Abstract. In clusters analysis, a problem of great interest is having methods that allow the representation of the topology of input space without the need to know additional information about it. This gives rise to *growing competitive neural* methods which are capable of determining the structure of the network autonomously during the process of training. This work proposes a variation of the *Growing Neural Gas* (*GNG*) algorithm, calling *GNG with post-pruning* (*GNG-PP*), and a method of clustering based on the search for topological neighborhoods generated by the former. These were combined in a three-phase process to clustering the *S&P100* set, which belongs to the macroeconomic field. This problem has a high dimensionality in the characteristics space. Its results are compared to those obtained by *SOM*, *Growing Cell Structures* (*GCS)*, and a non-neural method. Evaluation of the results was made by means of the *kappa* coefficient, using as evaluation set the GICS industrial classification. The results show that when using the proposed methods the best clustering are generated, obtaining a kappa coefficient of *0.5643* in the GICS classification.

Keywords: clustering, vectorial quantization, GNG, S&P100.

1 Introduction

The discovery of structures that allow the representation of data spaces has led to the creation and use of a large variety of techniques.

The most widely used methods for this purpose are those of *unsupervised competitive self-learning*, in particular neural networks, which are capable of creating topological representations by means of the distribution of a set of neurons over the input data, capturing most of the relations of the original space [1].

This is known as *vectorial quantization* and allows reducing the original data set to a smaller one, but equally representative, allowing work to be done on the vectors instead of doing it directly on the data. By means of this technique it is possible to solve, for example, the data clustering problem [2].

The most traditional *competitive learning* method is that of Kohonen's *Self-Organizing Maps* (*SOM*), which however present some limitations in practical problems because they require previous knowledge to define the structure of the network, i.e., its configuration and the number of neurons.

In view of this, neural methods arise that incorporate a new philosophy in their operation: the *growth of neurons*. In these it is the network itself what determines autonomously its structure, whether it is the required *number of neurons*, the *connections* between them, or the possible eliminations of both [3].

Examples of these are the *Growing Cell Structures* (GCS) and *Growing Neural Gas* (GNG) networks

In this paper a proposal is made of a variation of the GNG algorithm, called *GNG with post-pruning* (GNG-PP), which allows eliminating and repositioning neurons so that vectorial quantization is improved. Furthermore, a clustering method is proposed whose operation is based on the topological information acquired during the training process, through the same neural method, called *Neighborhood Clustering*.

These methods will be applied to the clustering of data by means of a three-phase process. First, quantize the input space by means of a GNG network with post-pruning (GNG-PP). In a second stage, use the *Neighborhood* method to clustering the quantization vectors, and finally, associate the data with the closest vectors according to a measure of distance, identifying them with the cluster to which the related vector belongs.

To evaluate the results obtained, use was made of the *S&P100* set, belonging to the macroeconomic field, which contains the stock market variation indices of *Standard & Poor's* stock market of the 100 largest companies in the USA in terms of capital market. This data set has the peculiarity that each subject (company) is represented in a very high space dimensionality with 249 characteristics, which transforms it into an icon for evaluation. The clustering were evaluated by means of the *kappa* coefficient because the real classification of the companies was known, in this case the *Global Industry Classification Standard* (GICS).

Finally, the results are compared with those obtained by a traditional neural method (SOM), a growing one (GCS), and a non-neural one, which has been found to be one of the most efficient in the treatment of these kinds of problems.

2   Methods

2.1   Growing Neural Gas with Post-Pruning (GNG-PP)

The GNG algorithm [4] gets a series of characteristics from other self-organizing methods (SOM [5], NG [1, 6] and GCS [7]) for quantizing the input space.

But it incorporates others like the no need to predefine a topological structure or to maintain the consistent structure of the network during the training. It also introduces the concepts of *local error* for each neuron, and *age* for each connection, allowing them to be created and eliminated at any time, giving the network greater flexibility in the representation sought [3].

Another of its characteristics is that it bases its topological preservation capacity in obtaining the *induced Delaunay triangulation* (IDT) [8], which allows the input space to be divided into regions or clusters of vectors (during its vectorial quantization process), generating neural connections *only in those areas of space where data are found*. It is precisely the generation of the IDT what allows GNG to find clusters in the data space.

However, one of the risks of working with growing networks is that an inadequate training termination criterion can be chosen, and therefore the model obtained would not truly represent the input space. An example of this could be to use very few training steps or a very high range of quantization error.
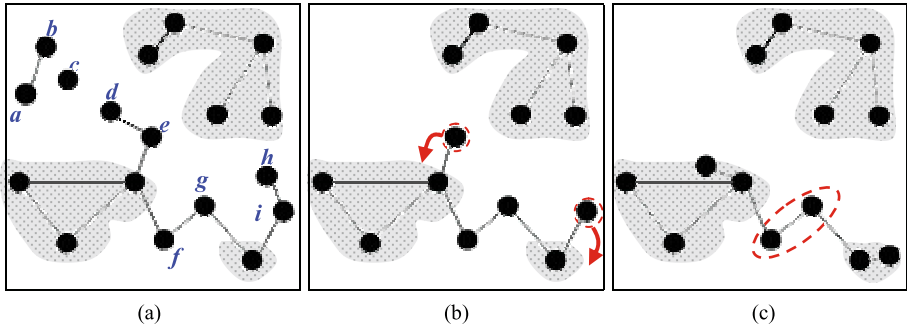

Fig. 1. Post-pruning process: (a) Identification of the non useful neurons. (b) Elimination of neurons and identification of new coordinates. (c) Final GNG model. In each image the shaded regions represent input data distributions.

To solve this problem it is proposed to carry out a *post-pruning* of the GNG models once the training stage has ended, with the purpose of eliminating and/or re-localizing the neurons that do not contribute to decreasing the quantization error. The general operation of the method is the following:

i)   As initial information it uses the neural model (neurons and connections) obtained by GNG.

ii) The closest vector is associated with each datum by means of the calculation of a distance measure.

iii) The neurons that are not useful for minimizing the quantization error, i.e. those to which no data were associated in the previous step, are identified, and they are assigned to set V_{in}. In Figure 1.a it would be $V_{in}=\{a,b,c,d,e,f,g,h,i\}$.

iv) The neurons of V_{in} are eliminated and/or relocalized. In this step, one of three cases may occur:

- If a disconnected neuron is found, such as *c* in the example, it is *eliminated*.
- If neurons connected only to neurons belonging to V_{in} are found, they are also *eliminated* together with their connections. In the example, *a, b, d* and *h*.
- If neurons connected at least to a *useful* neighbor are found, they are not eliminated (in the example, *e, f, g* and *i*). Here, two cases must be distinguished:

  a) If the neuron has only one *useful* neighbor, then it will be *relocated* in a zone where it can help to decrease the quantization error, but without losing the connection (neurons highlighted in Figure 1.b). The new location is given by a differential of the position of the *useful* neuron to which it is connected.

  b) If the neuron is connected to more than one *useful* neighbor, it cannot be displaced (neurons highlighted in Figure 1.c).

The treatment process of the *non useful* neurons is done in the same order in which it was presented, with the purpose of *relocalizing* the largest possible number of neurons, eliminating first all the model's *leftover* nodes.

2.2 Clustering by Neighborhoods

Although growing methods are capable of finding the clusters in the input space, they do not provide information on *which neurons are part of each cluster*. To solve this a method is proposed that identifies the groups of vectors from the following concepts:

Direct and indirect neighbors. The former are those that have a direct connection that joins them, while the latter, in spite of not being connected directly, are related by means of direct neighbors common to them (see Figure 2.a).

Neighborhood. It is formed by the set of *direct* and *indirect* neighbors of a set of neurons. In the case of Figure 2.b there are 2 neighborhoods, *A* and *B*.
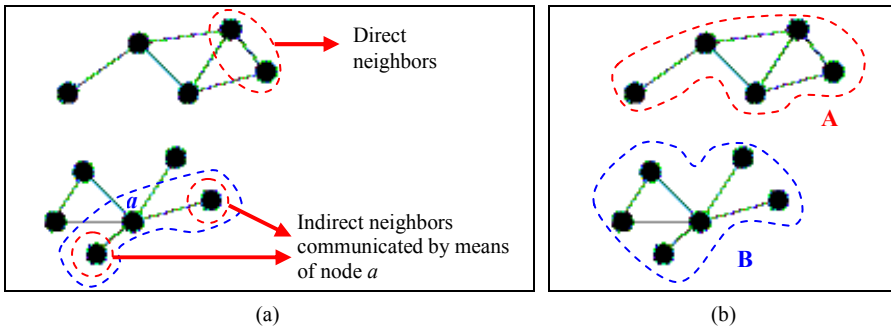
Fig. 2. Neighborhood relations: (a) Direct and indirect. (b) Neighborhoods.

The general operation of the method is the following:

i)   Initialize the label index: *i=1*.
ii) Look for the first neuron $v \in A$ not associated with any cluster, where *A* corresponds to the structure or set of neurons of the network.
iii) Determine the direct neighbors of neuron *v*:

$$N_d(v) = \{ \forall i \in A \mid (v,i) \in C \} \tag{1}$$

where *C* is the set of connections of the structure. Figure 3 shows an example in which $N_d(v)=\{a,b,c,d,e\}$.

iv) Determine the direct neighbors of each neuron of the set $N_d(v)$ that do not belong to the same set:

$$N_d(w) = \{ \forall j \in A \mid (w,j) \in C \land j \notin N_d(w) \}, \ \forall \ w \in N_d(v) \tag{2}$$

In the example we have that $N_d(b)=\{f,g\}$, therefore the indirect neighbors of *v* will be: $N_i(v)=\{f,g\}$.

v) Join in set *N* the direct and indirect neighbors of *v*. In the example, it would be *N={a,b,c,d,e,f,g}*.

vi) Label, in set *M*, all the nodes belonging to *N* (including neuron *v*), associating them to neighborhood *i*:

$$M(k) = i, \forall \ k \in N \cap v \qquad (3)$$

In the example it would be *M(a)={1}, M(b)={1}, ..., M(v)={1}*, as shown in Figure 3.b.

vii) Continue the revision, returning to step iii), with the following unrevised element in *N*. In the example, it would be to continue with *v=a*.

viii) If there are no unrevised elements in *N*, increase the label index: *i=i+1*.

ix) If there are unmarked neurons of *A*, return to step ii), otherwise the algorithm is ended. In the example, it would be to continue with neuron *q* (see Figure 3.b).

(a)   (b)
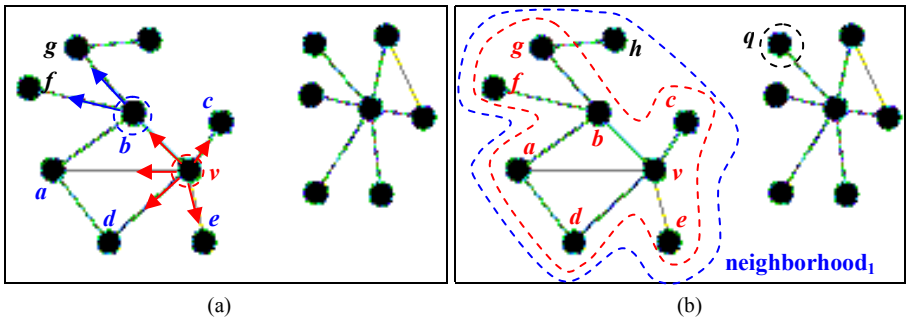
Fig. 3. Clustering by neighborhoods: (a) Direct and indirect neighbors of neuron '*v*'. (b) Mark of the neurons associated with '*v*' (inner segmented line), identification of '*neighborhood₁*' (outer segmented line) and next unmarked neuron (node *q*).

2.3 Clustering Strategy

A clustering in phases approach presented in [2] will be used:

Phase 1: Vectorial quantization
In this phase a vectorial quantization of the data input space is made, generating a structure formed by vectors and neighborhood relations between them reflecting their topological characteristics.

Phase 2: Clustering of quantization vectors
In this phase the clustering of the vectors obtained in the previous phase takes place. In this case it is proposed to use the *by Neighborhood* method for this purpose.

Phase 3: Association of data and vectors
Once all the model's neighborhoods have been identified, each datum is associated with the nearest vector from a distance measure (for example, *Euclidian*), identifying them with the cluster or neighborhood to which the related vector belongs.

3 Experimental Results

3.1 Data

Standard & Poor's 100 [1] (S&P100) index is one of the main of *stock market* indicators in the USA, which measures the performance of the largest 100 companies (over US$ 6 trillion) in terms of market capitalization.

For any given company, the values of the S&P index are related to the time series of the price of its own stock in a given time period.

In this work the set of data was calculated, as indicated in Inostroza-Ponta et al. [9], i.e., the experimental value y_i at time t is given by:

$$y_i(t) = \frac{P_i(t-h) - 2 \cdot P_i(t) + P_i(t+h)}{P_i(t-h)} \tag{4}$$

where $P_i(t)$ corresponds to the price of the stock of company i in week t, h represents the interval used to calculate the price variation of the stock (in this case it corresponds to one week), and $P_i(t - h)$ is the normalization to eliminate any influence introduced by the current stock price.

In this way the experimental set was formed by 100 registers (one per company) and 249 columns or dimensions (associated to the value y_i). In this case use was made of the S&P indices between the years 1999 and 2004.

3.2 Clustering Evaluation

The *kappa coefficient* was used to obtain a measure of the quality of the clustering obtained. This is an indicator of the agreement between the *values estimated by the model* and the *true values of the evaluation set* [10].

It was chosen to use this index because the real classification of the S&P set was known beforehand. In this case the evaluation set corresponds to the *Global Industry Classification Standard* [2] (GICS), which classifies the companies in four levels, with different subclassifications according to it (see Table 1). However, in this study only the first two levels will be considered.

Table 1. Classification of companies by level according to GICS

Level No.	Level Name	No. of subclassifications
1	Sector	10
2	Group of industries	22
3	Industries	39
4	Industrial branch	53

---

[1] www2.standardandpoors.com/portal/site/sp/en/us/page.topic/indices_rtv
[2] www2.standardandpoors.com/portal/site/sp/en/us/page.topic/indices_gics

3.3   Results

The clustering were made by means of the strategy of three phases, varying the vectorial quantization algorithm for *phase 2* and using a *Euclidian* distance relation in *phase 3*.

In this case neural methods were used to quantize the space: a fixed one with topological structure and predetermined shape (SOM), a growing one with rigid dimensional structure (GCS), and the proposed algorithm (GNG-PP).

In the case of the SOM, the clustering strategy was to use each neuron of the network as a group by itself [2], so two configurations were used, one of 5x2 and one of 5x4 neurons (SOM-1 and SOM-2 models, respectively), because it was attempted to obtain a sensitive clustering both at level 1 and at level 2 of the GICS classification.

In both cases it was decided to use hexagonal lattices because in them, in contrast with rectangular lattices, the neurons have not only vertical and horizontal connections, so the evolution of their neighborhood zones affects a greater number of neurons at a time, achieving greater capacity to adapted to the input space.

In the case of growing methods, the values of the training parameters were defined from their function within the corresponding algorithm [4, 7, 11]. In the case of the learning rates (ε_b and ε_n) small values were chosen with the aim of moving the neurons from their random initial positions, with some balance, in all directions. It must always be true that $\varepsilon_b \gg \varepsilon_n$, because otherwise it would be the neighbors and not the winner neuron that would move faster toward the input vector, reflecting the existing topology inadequately.

With respect to the decrease in the local error rates of each neuron (α and β), their values are associated with the purpose of increasing the influence of the most recent errors in order to avoid an uncontrolled growth of the local errors.

In the case of the growth parameter λ, use was made of values associated with the capacity of each network to generate the vectors clusters by means of pruning neurons during the training. In this way, in the case of GCS the network was increased every 500 training steps, because in each elimination of leftover neurons it is possible to eliminate many others to maintain consistent the structure of growing cells.

For GNG-PP this was done only every 100 steps, trying to generate models with no more than 100 neurons, avoiding the creation of too many nodes with respect to the total data (in this case only 100 companies). For the same reason, 100 were used as maximum age for each connection (a_{max}).

As to the threshold for the elimination of neurons in GCS (η), its value was used according to a recommendation from the literature [7].

Finally, the termination criterion used for the growing methods was the number of training steps. Because of this and due to the pruning characteristics of each method, more than twice the number of steps was used to train the GCS network compared to GNG-PP, to try to generate a more robust model in terms of the number of final neurons. Table 2 shows the values used for each parameter in each neural model.

Using these training values, the clustering with each growing method were generated, finding the groups autonomously and automatically. In the case of

Table 2. Values of the training parameters for the growing methods

Method	Training	ε_b	ε_n	a_{max}	λ	α	β	η
GCS	110000	0.01	0.00010	-	100	0.5	0.0005	0.09
GNG-PP	50000	0.01	0.00005	100	500	0.05	0.0005	-

Table 3. Classification of companies by level according to GICS

Method	# Groups	# Neurons	Kappa Level 1	Kappa Level 2
GNG-PP	20	98	0.5643	0.4622
Non neural	10	-	0.5242	0.3618
SOM-2	20	20	0.5078	0.3441
GCS	7	124	0.3792	0.2347
SOM-1	10	10	0.3690	0.2349

GNG-PP there were 20 clusters, and in that of GCS there were 7, with 98 and 124 neurons, respectively. Table 3 presents a summary with the results obtained by each method considering only levels 1 and 2 of the GICS classification.

As to the GNG model without *post-pruning*, 21 groups were obtained in 110 neurons, 12 of which were not useful in vectorial quantization. Using *post-pruning*, 3 of them were eliminated and 9 were relocated in positions of the space where they contributed to decrease the *quantization* and *topological* errors [5, 12], in that way improving the characterization of the input space.

Furthermore, the results obtained by a *non neural* method presented in Inostroza-Ponta et al. [9] were added; it considers that each market stock is a node of a graph, and that each edge has a weight associated with the correlation between the stock. Thus, the method divides the graph recursively into disconnected subgraphs forming the clusters. As far as we can tell, this is the most efficient method for solving this problem.

With respect to the visualization of the results, it was decided to use the projection algorithm of the GCS method [7], because the model proposed by Fritzke does not have characteristics that restrict it exclusively to the growing cell method, so it was used without any modification.

The projection for GNG was restricted only to a bidimensional space, favoring its ease of visualization over the possible loss of topological characteristics. This means that it is possible that the distances represented in the projection may not be strictly related to the real positions of the *n*-dimensional space.

Figure 4 shows the projection obtained by the GNG-PP model for the S&P100 set, giving an approximate idea of what happens in the *n*-dimensional input space. It also shows the projection obtained by means of a classical method: *Multidimensional Scaling* (MDS) [13]. This carries out the space transformation in a *metric* and *nonmetric* way, and that would indicate if the relation between the initial proximities matrix and the distances of the new space will be *linear* or *nonlinear*.
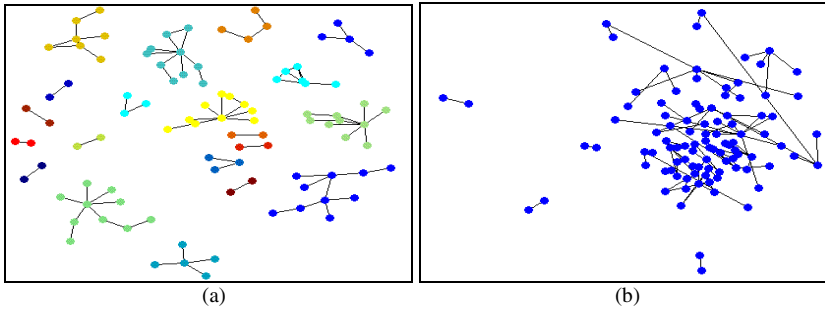
Fig. 4. Projection of the GNG-PP model (generated from the S&P100 set) obtained by: (a) the growing method. (b) MDS.

4   Discussion and Conclusions

After the clustering made of the S&P100 set, it was found that the GNG algorithm with *post-pruning* got the best kappa coefficients, both for level 1 and for level 2 of the GICS classification. This is because GNG has a series of improvements that distinguish it from the other methods used and also make it a method sensitive to the characterization of data spaces.

In the SOM models, since they have a rigid, predefined topological structure and are not capable of making prunings in their network, there are limitations in the results obtained, because they lead to the use of alternatives such as forcing each neuron to be a cluster by itself.

Therefore, a bad choice of the number of neurons would make it lose capacity for the topological representation of the space, generating very poor quality clustering. This is the case of both SOM models, whose results are incapable of improving the results obtained by GNG-PP.

With respect to the use of growing methods, one of their greatest limitations is that they are extremely sensitive to the values of their training parameters, because an incorrect choice of them can generate very poor results or processes that would use much computer time and resources to generate them.

In the case of GCS, its weak results can be due, together with the above, to the fact that at each pruning of the network useful units were eliminated in the vectorial quantization with the purpose of maintaining the cell structure consistent, losing too much topological information.

However, for GNG the influence of its parameters is attenuated, in terms of data clustering, because none of them have a direct influence in the partition of the space. On the other hand, by not depending on a rigid topological structure and allowing each neuron to have different numbers of neighbors, greater flexibility is achieved in the characterization of the original space, giving the possibility of relocating neurons in places where they can help in improving its quantization.

Also, by using *post-pruning*, it is possible to eliminate neurons which, being useless in the characterization of the input space, can generate a distortion in the number of clusters found.

In this way more robust models are constructed, in terms of the quantization of the input space, making use of most of the neurons that were incorporated in the process of growth of the network. In the case of S&P100, the results obtained by the *non-neural* method were even improved, in spite of the fact that GNG-PP bases its operation exclusively on the calculation of distances, and may achieve results as robust as this method that uses optimization techniques in the fractioning of the data set.

As to the projection achieved by GNG-PP, it turns it into an important aid in the cluster analysis, because it makes it possible to appreciate visually how the groups are distributed in the plane, keeping most of the topological relations of the *n*-dimensional original vector space.

The above is because the space transformation is obtained during the training of the network, and therefore reflects all the changes produced in the model until it represents the input space of the data. This is precisely what does not happen with the MDS projection method, which depends on the type of transformation used (either *metric* or *non-metric*).

Finally, it is important to mention that the evaluation has been made with a case study whose difficulty is centered in its high dimensionality. It would also be of interest to evaluate this method with benchmarks in which the number of cases is significant, such as the case of applications in the field of bioinformatics.

References

1. Martinetz, T., Schulten, K.: A neural gas network learns topology. Artificial Neural Networks, pp. 397–402. Elsevier Science Publishers, Amsterdam, Holanda (1991)
2. Vesanto, J., Alhoniemi, E.: Clustering of the self-organizing map. IEEE 3, 11 (2000)
3. Fritzke, B.: Growing self-organizing networks - Why? ESANN, Belgium pp. 61–72 (1996)
4. Fritzke, B.: A growing neural gas network learns topology. Advances in Neural Information Processing Systems, Cambridge, USA (1995)
5. Kohonen, T.: Self-organized formation of topologically correct feature maps. Biological Cybernetics 43, 59–69 (1982)
6. Martinetz, T., Berkovich, S., Schulten, K.: Neural gas network for vector quantization and its application to time-series prediction. IEEE 4, 4, 218–226 (1993)
7. Fritzke, B.: Growing cell structures - a self-organizing network for unsupervised and supervised learning. Neural Networks 1441–1460 (1994)
8. Martinetz, T.: Competitive hebbian learning rule forms perfectly topology preserving maps. In: ICANN 1993, pp. 427–434 (1993)
9. Inostroza-Ponta, M., Berretta, R., Mendes, A., Moscazo, P.: An automatic graph layout procedure to visualize correlated data. In: IFIP 19th World Computer Congress, Artificial Intelligence in Theory and Practice, August 21-24, Santiago. Chile, pp. 179–188 (2006)
10. Landis, J.R., Koch, G.G.: The measurement of observer agreement for categorical data. Biometrics 33, 159–174 (1977)
11. Fritzke, B.: Some competitive learning methods. Biophysics Systems, Institute for Neural Computation, Ruhr-Universitat Bochum, Germany (1997)
12. Fritzke, B.: Kohonen feature maps and growing cell structures - A performance comparison. Advances in Neural Information Processing Systems 5, 115–122 (1993)
13. Kruskal, J.B.: Multidimensional scaling by optimizing goodness of fit to a nonmetric hypothesis. Psychometrika 29, 1–27 (1964)

Bagging with Asymmetric Costs for Misclassified and Correctly Classified Examples[*]

Ricardo Ñanculef[1], Carlos Valle[1], Héctor Allende[1], and Claudio Moraga[2,3]

[1] Universidad Técnica Federico Santa María,
Departamento de Informática, CP 110-V Valparaíso, Chile
{cvalle,jnancu,hallende}@inf.utfsm.cl
[2] European Centre for Soft Computing 33600 Mieres, Asturias, Spain
[3] Dortmund University, 44221 Dortmund, Germany
mail@claudio-moraga.eu

Abstract. Diversity is a key characteristic to obtain advantages of combining predictors. In this paper, we propose a modification of *bagging* to explicitly trade off diversity and individual accuracy. The procedure consists in dividing the bootstrap replicates obtained at each iteration of the algorithm in two subsets: one consisting of the examples misclassified by the ensemble obtained at the previous iteration, and the other consisting of the examples correctly recognized. A high individual accuracy of a new classifier on the first subset increases diversity, measured as the value of the Q statistic between the new classifier and the existing classifier ensemble. A high accuracy on the second subset on the other hand, decreases diversity. We trade off between both components of the individual accuracy using a parameter $\lambda \in [0, 1]$ that changes the cost of a misclassification on the second subset. Experiments are provided using well-known classification problems obtained from UCI. Results are also compared with *boosting* and *bagging*.

Keywords: Ensemble Methods, Bagging, Diversity, Neural Networks, Classification Algorithms.

1 Introduction

Ensemble methods actually constitute an active research area that has lead to a family of learning algorithms applied to a wide range of problems including classification, clustering and regression. These methods are based on the idea of combining a set of simple predictors instead of using only one, maybe more complex. The interesting point is that with an appropriate design, the expected performance of the combined predictor can be better than the average performance of the individual predictors, even if these are weakly good. A key characteristic to obtain such behavior seems to be *diversity* of the combined predictors. This is

---

intuitively clear, since combining a set of identical models is hardly better than using any single member of the set.

A well-studied method for ensemble generation is *bagging*, introduced by Breiman in [3]. Bagging can be described as an algorithm with only an implicit search for diversity, because no information about the predictions of the other models is incorporated to generate each predictor. Recent works [10] [9] have shown that the action of bagging is to control the effective influence of training examples in the estimation process, which is implicitly implemented by the bootstrapping plan carried out at each round of the algorithm. According to this reasoning, the robustness of bagging to overfitting, is not related to the independence of the different bagging rounds. An explicit search for diversity could hence be incorporated, allowing visibility between the learners while preserving the robustness characteristic of bagging.

In this paper we focus on binary classification, that is, we are given with a set of examples $S = \{(x_k, y_k); k = 1, \dots, m\}$, obtained sampling independently a distribution $P(\mathbf{x}, \mathbf{y})$, where $x_k \in \mathbb{R}^p$ represents a set of features and $y_k \in \{-1, 1\}$ a class label. We are asked to build a classifier $M : \mathbb{R}^p \to \{-1, 1\}$ capable to recognize the class corresponding to a given $\mathbf{x}$, specifically we are asked to minimize the misclassification probability $E_P(\mathbf{x} \neq M(\mathbf{y}))$.

In this type of problems, diversity can be quantified using the so called Q statistic [13] [11]. For a pair of classifiers, this measure depends on the frequency with which the classifiers coincide and disagree in the recognition and misclassification of the training examples. As stated in [5], diversity can be harmful if this is maximized at the expense of the individual accuracy and hence, an imperfect correlation between diversity and accuracy is observed in practice [11]. In this paper, we propose a modification of bagging, to explicitly trade off diversity and individual accuracy, decomposing the training objective of each learner in a component that contributes to diversity and other that decreases diversity. This algorithm has the same spirit of some algorithms proposed for regression problems, for example the *negative correlation algorithm* [6].

We start by presenting in section 2 the bagging algorithm [3] and a possible justification of its effectiveness. In section 3 we briefly review the concept of diversity in ensembles. In section 3 we show how to modify bagging to explicitly balance diversity and local accuracy. This algorithm inherits the robustness of bagging to overfitting because it preserves at each iteration, the resampling plan characteristic of bagging. In the final section we provide experimental results on classification problems obtained from UCI[2] and systematically used in the literature to analyze classifier ensembles. We also compare the algorithm with other methods, boosting and bagging, using different numbers of component learners.

2   Bagging

One of the most widely used techniques for creating an ensemble is *bagging* (short for Bootstrap Aggregation Learning), where a base classifier is provided with a set of patterns obtained randomly resampling the original set of examples

and then trained independently of the other classifiers. The final hypothesis is obtained as the signum of the averaged predictions. The algorithm is summarized in figure (1)

1: Let $S = \{(x_i, y_i); i = 1, \ldots, m\}$ be training set.
2: Generate T bootstrap samples S^t, $t = 1, \ldots, T$ from S.
3: **for** $t = 1$ to T
4:     Train the classifier f_t with the set of examples S^t to minimize the classification error $\sum_j I(y_j \neq f_t(x_j))$, where $I(S)$ is the indicator of the set S.
5:     Set the ensemble predictor at time t to be $F^t(x) = sgn\left(\frac{1}{t}\sum_{i=1}^{t} f_i^t(x)\right)$.
6: **end for**

Fig. 1. Bagging

Breiman [3] presents bagging as a procedure capable to reduce the variance of predictors mimicking averaging over several training sets.

In [14] it is shown that for well behaved loss functions, bagging can provide generalization bounds with a rate of convergence of the same order as Tikhonov regularization. The key observation is that using bagging, an α-stable algorithm can becomes strongly α-stable with appropriate sampling schemes. Strongly α-stable algorithms provide fast rates of convergence from the empirical error to the true expected prediction error.

The key fact in the previous analysis is that certain sampling plans allow some points to affect only a subset of learners in the ensemble. The importance of this effect is also remarked in [10] and [9]. In these works, empirical evidence is presented to show that bagging equalizes the influence of training points in the estimation procedure, in such a way that points highly influential (the so called leverage points) are down-weighted. Since in most situations leverage points are badly influential, bagging can improve generalization by making robust an unstable base learner. From this point of view, resampling has an effect similar to robust M-estimators where the influence of sample points is (globally) bounded using appropriate robustifying functions.

Since in uniform resampling all the points in the sample have the same probability of being selected, it seems counterintuitive that bagging has the ability to selectively reduce the influence of leverage points. The explanation is that leverage points are usually isolated in the feature space. To remove the influence of a leverage point it is enough to eliminate this point from the sample but to remove the influence of a non-leverage point we must in general remove a group of observations. Now, the probability that a group of size K be completely ignored by bagging is $(1 - K/m)^m$ which decays exponentially with K. For $K = 2$ for example $(1 - K/m)^m \sim 0.14$ while $(1 - 1/m)^m \sim 0.368$. This means that bootstrapping allows the ensemble predictions to depend mainly on "common" examples, which in turns allows to get a better generalization.

3   Diversity for Classifier Ensembles

Several works have revealed that diversity is a very important characteristic to get real advantages of combining predictors [13] [11] [12] [5]. In regression problems, diversity can be rigorously defined by the so called *ambiguity decomposition* [5]. It can be easily proved that if a set of individual regressors $f_1, f_2, \ldots, f_m$ are linearly combined as $F = \sum_i w_i f_i$, the quadratic loss of the ensemble prediction $F(x)$ at a fixed pattern (x, y) can be decomposed as

$$(y - F)^2 = \sum_i w_i (y - f_i)^2 - \sum_i w_i (f_i - F)^2 \tag{1}$$

This decomposition states that the ensemble accuracy not only depends on the individual accuracies but also on the variability of the individual predictions around the combined prediction. From this result, is clear that differences between individual outputs contribute toward the overall ensemble accuracy, if the individual accuracies are maintained. We can hence define the level of diversity in the ensemble as the second term of equation (1), computed and averaged over the training examples. Similar measures of diversity can be obtained in terms of the correlation between the individual errors.

In classification problems, predictors are usually not aggregated using simple linear combinations and hence equation (1) does not hold. Moreover, if base classifiers can only output discrete class labels, quadratic loss cannot properly be used. Definition of diversity for a set of classifiers is hence a more complex task that has been tackled on different ways. Great part of the work examining classifier diversity is due to Kuncheva [13] [11]. In [13], several diversity measures are analyzed, which can be separated between pairwise and non-pairwise measures. Pairwise measures compute a statistic between a pair of classifiers based on the complete set of examples, and then this is averaged over all possible pairings. Non-pairwise measures in contrast, compute a statistic for each example based on the predictions of the set of classifiers and then the average among the examples. The pairwise measures analyzed in [13] depend on the frequency with which a pair of classifiers agree or disagree in the recognition of a training example. Given two classifiers f_i, f_j we can count the number of examples N^{11} for which both are correct, the number of examples N^{00} for which both are incorrect, the cases N^{10} for which f_i is correct but f_j incorrect and the cases N^{01} for which f_j is correct but f_i incorrect. These four types of situations can be summarized in the following table:

	f_j correct	f_j incorrect
f_i correct	N^{11}	N^{10}
f_i incorrect	N^{00}	N^{01}

From these statistics, several metrics of diversity can be derived. Since different measures show great similarity, Kuncheva recommends the use of the so called Q statistic for easy of interpretation. For a pair of classifiers f_i and f_j this is computed as

$$Q(f_i, f_j) = \frac{N^{11}N^{00} - N^{10}N^{01}}{N^{11}N^{00} + N^{10}N^{01}} \qquad (2)$$

If the classifiers tend to misclassify and correctly classify the same instances, the Q statistic will take a positive value achieving a maximum of $+1$. If on the other hand, the classifiers show different patterns of errors, the Q statistic will take a negative value with a minimum value of -1. For independent classifiers $Q = 0$.

4 Bagging with Asymmetric Costs for Misclassified and Correctly Classified Examples

According to the taxonomy proposed in [5] for diversity creation methods, manipulation of the training data is one the most investigated techniques for ensemble generation. In particular, resampling of the training set is part of the two currently most successful ensemble algorithms: boosting [7] and bagging [3]. Bagging can be considered as an implicit method to generate diversity because it does not use any information about the behavior of the other learners to manipulate the training data. This algorithm can however significatively decrease the generalization error of the base learner because, as we have explained in the previous sections, resampling limits the influence of isolated examples on the ensemble, stabilizing the overall prediction. In contrast to bagging, *Adaboost* is an algorithm explicitly designed to focus each learner in the instances of the training set where the previous learners perform bad.

Suppose we generate an ensemble sequentially, adding at each step t a new classifier h_t to the ensemble generated in the previous steps. Suppose we generate the new classifier to maximize the Q statistic between the existing classifier H_{t-1} (resulting from the combination of the previously generated classifiers) and the new classifier. Hence, if the ensemble correctly classifies a subset C of examples of the training set S and misclassifies a subset M, the new classifier h_t has to misclassify all the examples in the set C but correctly recognize the patterns in M. In this case, $Q(H_{t-1}, f_t) = -1$ and diversity is clearly maximized. However, for reasonable aggregation functions this procedure has only sense if the existing classifier has an accuracy lower than 50% or the margin for the classification of the correctly classified examples is wide enough. It would be possible to overcome this problem using instance-dependent aggregation functions, but this is out of the scope of this paper. On the other hand, the problem of determining which classifiers behave well for a given instance is a classification problem itself, which could be even more complex than the original classification problem. As stated by [5], the problem is that diversity can be harmful if individual accuracy is completely sacrificed to obtain differences between the predictors outputs. For this reason it is difficult to speak about a perfect correlation between the diversity measure and the ensemble accuracy [11]. The latter observation holds also for regression ensembles where clear diversity measures can be defined. For example, the ambiguity decomposition and similar decompositions in regression estimation, have lead to algorithms that look for an adequate tradeoff between

individual accuracy and diversity. In the *negative correlation algorithm* [6] this achieved training each learner with the objective function

$$E_i = \sum_{(x_i,y_i)\in S} (y_i - f(x_i))^2 + \lambda \sum_{i\in S}(f_i - \bar{F})^2 \tag{3}$$

where $\bar{F}$ is the ensemble output. It can be shown that diversity can decrease the ensemble accuracy if this is not balanced with other components of the ensemble error. In this spirit, we propose an algorithm to explicitly trade off diversity and individual accuracy. The procedure works iteratively, by adding a new classifier h_t to the existing ensemble H_{t-1} at each step $t = 1, 2, \ldots, M$. Following bagging, each learner is trained using a bootstrap sample S^t of the original set of examples S. Bootstrapping at each iteration allows us to inherit the robustness of bagging to overfitting, which is not based on the independence of the different bagging steps, but on the effects of the resampling plan. Instead of generating each learner independently of the others, we propose to train the learner at step t with the following objective function

$$E_t = \sum_{(x_i,y_i)\in M_{t-1}} I(y_i \neq h_t(x_i)) + \lambda \sum_{(x_i,y_i)\in C_{t-1}} I(y_i \neq h_t(x_i)) \tag{4}$$

where M_{t-1} is the set of examples incorrectly classified by the ensemble obtained at step $t - 1$ and C_{t-1} the set of correctly recognized examples. Note that $I(S)$ is the indicator of the set S. Hence, the first component of equation (4) is the total classification error on the set M_{t-1} and the second is the total error on the set C_{t-1}. The greater the first term, the greater the Q statistic between the new classifier and the existing ensemble. Optimization of the second term in contrast, monotonically decreases diversity measured as the value of the Q statistic. Both components of E_t contribute to the individual accuracy of the new classifier. In other words, equation (4) represents a tradeoff between individual accuracy that contributes to generate diversity and individual accuracy that decreases diversity. Note that if $\lambda = 1$, the algorithm coincides with bagging and accuracy is optimized independently of the diversity the new classifier incorporates to the ensemble. If λ is allowed to increase beyond 1, then accuracy that damages diversity would be preferred over accuracy compatible with diversity generation. If λ is allowed to go below 0, then it leads to a better optimization of the Q statistic, but both individual and ensemble accuracy can be seriously damaged, especially when the existing ensemble has performance over the 50%.

Algorithm (2) summarizes the proposal of the paper. The implementation of this procedure can be carried out in several ways. The most natural of them is to consider weights for each example: a weight $\lambda_i = 1$ for the examples (x_i, y_i) misclassified by the previous ensemble and a weight $\lambda_i = \lambda$ for the correctly recognized examples. Another possibility, if the base learner cannot manipulate weights for each example, is to use a sampling plan with probabilities coinciding with the desired weights. This approach is used for example in the *adaBoost* algorithm [7] [8].

The resultant algorithm is similar in spirit to the half-and-half bagging algorithm proposed by Breiman [4]. In this method predictors are generated

1: Let $S = \{(x_i, y_i); i = 1, \ldots, m\}$ be training set.
2: Generate T bootstrap samples S^t, $t = 1, \ldots, T$ from S.
3: Train the classifier f_1 with S^1 to minimize $\sum_j I(y_j \neq f_t(x_j))$
4: **for** $t = 2$ to T
5:     Classify each example x_j of S^t using the classifier ensemble F^{t-1}. If the example is correctly classified put it in the set C_{t-1}, otherwise put it in the set M_{t-1}.
6:     Train the classifier f_t to minimize

$$E_t = \sum_{j \in M_{t-1}} I(y_j \neq h_t(x_j)) + \lambda \sum_{j \in C_{t-1}} I(y_j \neq h_t(x_j))$$

$$= \sum_{j \in S_t} \lambda_j I(y_j \neq h_t(x_j))$$

where $\lambda_j = 1$ if $(x_j, y_j) \in M_{t-1}$ and $\lambda_j = \lambda$ if $(x_j, y_j) \in C_{t-1}$.
7:     Set the ensemble predictor at time t to be $F^t(x) = sgn\left(\frac{1}{t} \sum_{i=1}^{t} f_i^t(x)\right)$.
8: **end for**

Fig. 2. The proposed algorithm

sequentially using different subsets of the original training set. At each round, an example is randomly selected and classified by the learners previously generated that did not use the example in their training sets. If the example is misclassified by majority voting on the latter predictions this is incorporated in a set M. Otherwise the example is incorporated in a set C. This process is repeated until the sizes of M and C are equal to $s = n/4$, where n is the total number of examples. The next classifier is trained on the examples of M and C with equal costs. It should be noted that the number of correctly classified examples will be in general greater than the number of misclassified examples, especially when several rounds of the algorithm have been elapsed. Hence, this method implicitly puts more focus than standard bagging in the misclassified examples. The constant proportion of the correctly classified examples in the next training sample on the other hand, ensures each learner achieves a reasonable individual accuracy of the original training set and that misclassified examples do not dominate excessively the next training round. This is a clear difference with the *adaBoost* algorithm [7] [8]. In contrast to standard bagging, adaBoost forces the learners to focus on the difficult training examples and pay less attention to the examples correctly classified by the last predictor. This is achieved by computing example weights and then bootstrapping the training data with probabilities coinciding with these weights. Although very effective in practice, adaBoost is highly more sensitive to leverage points (in particular outliers) than bagging [1]. In some rounds, adaBoost could be completely dominated by few isolated examples more than in local patterns present in the data. With the algorithm proposed in this section, the relative importance of a misclassified example with respect to an already recognized example is kept constant and hence the former cannot dominate excessively.

5   Experimental Results and Discussion

In this section we present results of empirical studies to evaluate the proposed algorithm. In the whole set of experiments, two real and well-known data sets were used, namely *Phoneme* and *Diabetes*. A detailed description of these data

Table 1. Analysis of the parameter λ

	Phoneme		Diabetes	
λ	Training Error	Testing Error	Training Error	Testing Error
0.0	0.2730 ± 0.0810	0.2793 ± 0.0758	0.3503 ± 0.0383	0.3935 ± 0.0368
0.1	0.1687 ± 0.0154	0.1810 ± 0.0111	0.1939 ± 0.0048	0.2600 ± 0.0101
0.2	0.1643 ± 0.0073	0.1777 ± 0.0102	0.1927 ± 0.0049	0.2465 ± 0.0113
0.3	0.1676 ± 0.0090	0.1762 ± 0.0094	0.1896 ± 0.0042	0.2359 ± 0.0107
0.4	0.1659 ± 0.0062	0.1786 ± 0.0077	0.1911 ± 0.0040	0.2384 ± 0.0097
0.5	0.1661 ± 0.0077	0.1774 ± 0.0110	0.1884 ± 0.0035	0.2375 ± 0.0097
0.6	0.1709 ± 0.0081	0.1811 ± 0.0103	0.1892 ± 0.0036	0.2329 ± 0.0105
0.7	0.1691 ± 0.0059	0.1814 ± 0.0107	0.1891 ± 0.0040	0.2314 ± 0.0098
0.8	0.1717 ± 0.0072	0.1805 ± 0.0104	0.1900 ± 0.0033	0.2338 ± 0.0093
0.9	0.1675 ± 0.0065	0.1811 ± 0.0082	0.1908 ± 0.0040	0.2316 ± 0.0095
1.0	0.1730 ± 0.0045	0.1850 ± 0.0118	0.1919 ± 0.0040	0.2333 ± 0.0115

Table 2. Experimental results on the *Phoneme* dataset

N	Boosting	Bagging	Proposal $\lambda = 0.3$
Training Set			
2	0.1992 ± 0.0178	0.1973 ± 0.0186	0.1893 ± 0.0165
4	0.1885 ± 0.0098	0.1846 ± 0.0134	0.1665 ± 0.0077
6	0.1822 ± 0.0111	0.1776 ± 0.0046	0.1726 ± 0.0167
8	0.1840 ± 0.0139	0.1748 ± 0.0043	0.1648 ± 0.0067
10	0.1786 ± 0.0075	0.1777 ± 0.0092	0.1662 ± 0.0088
12	0.1769 ± 0.0071	0.1746 ± 0.0066	0.1654 ± 0.0117
14	0.1753 ± 0.0074	0.1760 ± 0.0076	0.1609 ± 0.0067
16	0.1751 ± 0.0065	0.1737 ± 0.0051	0.1642 ± 0.0087
18	0.1754 ± 0.0062	0.1725 ± 0.0046	0.1587 ± 0.0062
20	0.1746 ± 0.0075	0.1712 ± 0.0048	0.1570 ± 0.0049
Testing Set			
2	0.2058 ± 0.0193	0.2093 ± 0.0205	0.1972 ± 0.0155
4	0.1978 ± 0.0125	0.1965 ± 0.0158	0.1764 ± 0.0101
6	0.1910 ± 0.0161	0.1904 ± 0.0116	0.1822 ± 0.0174
8	0.1937 ± 0.0190	0.1865 ± 0.0112	0.1752 ± 0.0099
10	0.1882 ± 0.0094	0.1863 ± 0.0110	0.1768 ± 0.0118
12	0.1862 ± 0.0093	0.1848 ± 0.0083	0.1765 ± 0.0039
14	0.1863 ± 0.0101	0.1849 ± 0.0082	0.1733 ± 0.0131
16	0.1872 ± 0.0122	0.1853 ± 0.0084	0.1729 ± 0.0091
18	0.1886 ± 0.0123	0.1846 ± 0.0095	0.1729 ± 0.0129
20	0.1867 ± 0.0130	0.1837 ± 0.0091	0.1674 ± 0.0101

Table 3. Experimental results on the *Diabetes* dataset

N	Boosting	Bagging	Proposal $\lambda = 0.7$
		Training Set	
2	0.2247 ± 0.0068	0.2083 ± 0.0058	0.2092 ± 0.0062
4	0.2080 ± 0.0061	0.1986 ± 0.0046	0.1966 ± 0.0043
6	0.2013 ± 0.0053	0.1944 ± 0.0045	0.1921 ± 0.0037
8	0.1956 ± 0.0052	0.1921 ± 0.0044	0.1894 ± 0.0042
10	0.1920 ± 0.0054	0.1919 ± 0.0040	0.1891 ± 0.0040
12	0.1896 ± 0.0053	0.1905 ± 0.0038	0.1890 ± 0.0036
14	0.1869 ± 0.0055	0.1899 ± 0.0038	0.1889 ± 0.0039
16	0.1850 ± 0.0054	0.1895 ± 0.0037	0.1880 ± 0.0035
18	0.1835 ± 0.0055	0.1892 ± 0.0035	0.1863 ± 0.0036
20	0.1818 ± 0.0053	0.1892 ± 0.0035	0.1860 ± 0.0036
		Testing Set	
2	0.2616 ± 0.0126	0.2467 ± 0.0106	0.2465 ± 0.0107
4	0.2650 ± 0.0125	0.2386 ± 0.0087	0.2386 ± 0.0104
6	0.2621 ± 0.0117	0.2354 ± 0.0105	0.2349 ± 0.0109
8	0.2561 ± 0.0110	0.2343 ± 0.0111	0.2314 ± 0.0101
10	0.2589 ± 0.0125	0.2333 ± 0.0115	0.2314 ± 0.0098
12	0.2588 ± 0.0121	0.2340 ± 0.0104	0.2316 ± 0.0105
14	0.2573 ± 0.0112	0.2305 ± 0.0108	0.2297 ± 0.0104
16	0.2560 ± 0.0116	0.2302 ± 0.0097	0.2319 ± 0.0097
18	0.2596 ± 0.0117	0.2321 ± 0.0099	0.2323 ± 0.0093
20	0.2590 ± 0.0110	0.2306 ± 0.0102	0.2317 ± 0.0095

sets can be obtained from [2]. For comparison purposes, three algorithms will be evaluated: Boosting, Bagging, and the proposed algorithm. In addition, neural networks with five sigmoidal hidden units and trained with standard backpropagation were employed as base learners. For each experiment, t-student confidence intervals will be reported with a significance of 0.02 obtained after 50 simulations. The estimation process is carried out with a 75% of the available observations and testing with the rest 25%.

Table (1) shows the proposed algorithm performance by using different values of parameter λ in the *Phoneme* and *Diabetes* datasets.

Table (2) and table (3) show confidence intervals for the *mse* of Boosting, Bagging and the proposed algorithm versus the number of learners in the ensemble, obtained with the *Phoneme* and *Diabetes* dataset respectively. In this experiment, we use the test error optimal values of λ found in the previous experiment. It should be remarked that these values of λ are the optimal found with 10 base learners.

For this paper only two benchmark problems have been chosen, which however allow us to draw preliminary representative conclusions. Table (1) shows clearly that the optimal value of λ is problem dependent, as it was already shown in the case of *Negative Correlation* applied to regression problems [6]. In both benchmarks however, the optimal value of λ was lower than 1. It should be

remarked $\lambda = 1$ is equivalent to bagging. This parameter may be selected using a validation set or adjusted with an evolutionary algorithm. Table (2) illustrates that the proposed method, with $\lambda = 0.3$ reaches a lower mean square error than Boosting and Bagging on the test set. It is known that the Diabetes classification problem suffers from "missing information" and mse results at the level of 0.25 are already considered to be good. Boosting reaches this level with 16 base learners in the ensemble. Bagging obtains the best result (mse 0.2302) with an ensemble of the same size. The proposed method, with $\lambda = 0.7$, obtains a result (mse 0.2314) which is better than Boosting and slightly weaker than Bagging using however only 8 base learners.

References

1. Bauer, E., Kohavi, R.: An empirical comparison of voting classification algorithms: Bagging, boosting, and variants. Machine Learning 36(1-2), 105–139 (1999)
2. Blake, C.L., Merz, C.J.: UCI repository of machine learning databases (1998)
3. Breiman, L.: Bagging predictors. Machine Learning 26(2), 123–140 (1996)
4. Breiman, L.: Half and half bagging and hard boundary points. Technical report, Statistics Department, University of California (1998)
5. Brown, G., Wyatt, J., Harris, R., Yao, X.: Diversity creation methods: A survey and categorisation. Information Fusion Journal 6(1), 5–20 (2004)
6. Brown, G., Wyatt, J.L.: Negative correlation learning and the ambiguity family of ensemble methods. In: Windeatt, T., Roli, F. (eds.) MCS 2003. LNCS, vol. 2709, Springer, Heidelberg (2003)
7. Freud, Y., Schapire, R.: A decision-theoretic generalization of on-line learning and application to boosting. J. of Computer and System Sciences 55(1), 119–137 (1997)
8. Freud, Y., Schapire, R.: A short introduction to boosting. Journal of Japanese Society for Artificial Intelligence 14(5), 771–780 (1999)
9. Grandvalet, Y.: Bagging down-weights leverage points. In: IJCNN, vol. IV, pp. 505–510 (2000)
10. Grandvalet, Y.: Bagging equalizes influence. Mach. Learning 55(3), 251–270 (2004)
11. Kuncheva, L.: That elusive diversity in classifier ensembles. In: Perales, F.J., Campilho, A., Pérez, N., Sanfeliu, A. (eds.) IbPRIA 2003. LNCS, vol. 2652, pp. 1126–1138. Springer, Heidelberg (2003)
12. Kuncheva, L.: Combining Pattern Classifiers: Methods and Algorithms. Wiley InterScience, Chichester (2004)
13. Whitaker, C., Kuncheva, L.: Measures of diversity in classifier ensembles. Machine Learning 51, 181–207 (2003)
14. Poggio, T., Rifkin, R., Mukherjee, S.: Bagging regularizes. Technical Report 214/AI Memo 2002-003, MIT CBCL (2002)

Distribution-Based Semantic Similarity of Nouns[*]

Igor A. Bolshakov and Alexander Gelbukh

Center for Computing Research (CIC), National Polytechnic Institute (IPN),
Av. Juan Dios Bátiz s/n, Col. Nueva Industrial Vallejo,
07738, Mexico City, Mexico
igor@cic.ipn.mx, gelbukh@gelbukh.com,
www.Gelbukh.com

Abstract. In our previous work we have proposed two methods for evaluating semantic similarity / dissimilarity of nouns based on their modifier sets registered in Oxford Collocation Dictionary for Student of English. In this paper we provide further details on the experimental support and discussion of these methods. Given two nouns, in the first method the similarity is measured by the relative size of the intersection of the sets of modifiers applicable to both of them. In the second method, the dissimilarity is measured by the difference between the mean values of cohesion between a noun and the two sets of modifiers: its own ones and those of the other noun in question. Here, the cohesion between words is measured via Web statistics for co-occurrences of words. The two proposed measures prove to be in approximately inverse dependency. Our experiments show that Web-based weighting (the second method) gives better results.

Keywords: Semantic relatedness, word space model, lexical resources, Web as corpus, natural language processing.

1   Introduction

Several works evaluate semantic similarity or dissimilarity between words, see [3, 11] and references therein. The majority of evaluations are based on semantic hierarchies of WordNet [4, 5]. In this class of methods, semantic dissimilarity between words is considered proportional to the number of steps separating corresponding nodes of the hierarchy. The nodes are synsets that include the words under evaluation, while the arcs are subset-to-superset links between the synsets. The greater the distance, the greater dissimilarity. This measure proved to be useful in many applications and tasks of computational linguistics, such as word sense disambiguation [9], information retrieval, etc.

Another possible way for estimation of semantic proximity of words consists in comparing the sets of other words frequently co-occurring in texts in close vicinity to the two words in question [6]. The more similar the recorded beforehand sets of standard neighbors of any two words of the same POS, the more semantically similar the

---

words [7]. As applied to nouns, the accompanying words are primordially their modifiers. In European languages, these are usually adjectives or participles; in English these are also nouns staying in preposition and used attributively.

We evaluate semantic similarity or dissimilarity of English nouns by two methods in this paper. Both of them are based on those standard modifier sets for few tens of commonly used English nouns that are registered for them in OCDSE that seems the most reliable source of English collocations so far [10]. The nouns were preferred with more numerous collections of modifiers recorded.

In the first method, the similarity $Sim(N_1, N_2)$ of the noun N_1 to the noun N_2 is measured by the ratio of the number of modifiers commonly applicable to the both nouns and the number of modifiers of N_2.

In the second method, we weight the relatedness between the noun and its modifiers by the Web co-occurrence statistics. Namely, the dissimilarity $DSim(N_1, N_2)$ of N_1 from N_2 is measured by the residual of two mean values of specially introduced *Stable Connection Index. SCI* is exteriorly like Mutual Information of two words [8] and operates by raw statistics of Web pages containing these words considered separately and in their close co-occurrences. In contrast to Mutual Information, it does not require repetitive evaluation of the total amount of pages under search engine's control. One mean value covers *SCI*s of all 'noun → its own modifier' pairs, another mean value covers *SCI*s of all 'N_1 → a modifier of N_2' pairs. English modifiers usually precede their nouns forming bigrams with them, thus facilitating reliable Web statistic evaluations. In other words, *Sim* is determined through coinciding modifiers of nouns, while *DSim* is determined through alien modifiers.

The main idea of the two methods discussed here was briefly presented in our previous work [2]. In this paper, we give more details on the experiments conducted to compare these two methods.

Namely, our experimental data show that though the *Sim* and *DSim* measures can be rather arbitrary in each specific case, on average they show an inverse monotonic interdependence. However, in our experiments *DSim* showed higher resolution. By higher resolution we mean that while many noun pairs have zero *Sim* values as measured according to the OCDSE, they differ significantly in their *DSim* values.

2   Modifier Sets Selected for Evaluations

English nouns with all their recorded modifiers—both adjectives and nouns in attributive use—were taken from OCDSE. The nouns were picked up in rather arbitrary manner, without taking into account their mental similarity. Our only preferences were with the nouns with larger modifier sets.

For 32 nouns taken, total amount of modifiers (partially repeating) is 1964, and the mean modifiers group size equals to 61.4, varying from 39 (for *comment* and *disease*) to 119 (for *eyes*). The second and the third ranks determined by the set sizes are with *expression* (115) and *effect* (105). The nouns selected and sizes of their modifier sets are shown in Table 1.

We have limited the number of nouns to 32 units, since the total amount of accesses to the Web in experiments of the second method (cf. Section 5) grows approximately as a square of the number of words in question, so that, taking into

Table 1. Selected nouns and sizes of their modifier sets

S/N	Noun	MSet Size	S/N	Noun	MSet Size
1	*answer*	44	17	*effect*	105
2	*chance*	43	18	*enquiries*	45
3	*change*	71	19	*evidence*	66
4	*charge*	48	20	*example*	52
5	*comment*	39	21	*exercises*	80
6	*concept*	45	22	*expansion*	44
7	*conditions*	49	23	*experience*	53
8	*conversation*	52	24	*explanation*	59
9	*copy*	61	25	*expression*	115
10	*decision*	40	26	*eyes*	119
11	*demands*	98	27	*face*	96
12	*difference*	53	28	*facility*	89
13	*disease*	39	29	*fashion*	61
14	*distribution*	58	30	*feature*	51
15	*duty*	48	31	*flat*	48
16	*economy*	42	32	*flavor*	50

account limitations of Internet searchers and the general trend of all statistics to grow, we could afford several days to acquire all necessary statistics but not a month.

Some nouns (*conditions, demands, enquiries, exercises,* and *eyes*) were taken in plural, since they are used with the recorded modifier sets in plural more frequently than in singular.

3   Influence of Intersection of Modifier Sets

In our first method, the similarity $Sim(N_i, N_j)$ is defined through the intersection ratio of modifier sets $M(N_i)$ and $M(N_j)$ of the two nouns by the formula

$$Sim\left(N_i, N_j\right) \equiv \frac{\left|M\left(N_i\right) \cap M\left(N_j\right)\right|}{\left|M\left(N_i\right)\right|}, \tag{1}$$

where $|M(N_i)|$ means cardinal number of the set $M(N_i)$, $\cap$ designates set intersection.

With such definition, the similarity measure is generally asymmetric: $Sim(N_i, N_j) \neq Sim(N_j, N_i)$, though both values are proportional to the number of commonly applicable modifiers. We can explain the asymmetry by means of the following extreme case. If $M(N_i) \subset M(N_j)$, each member of $M(N_i)$ has its own counterpart in $M(N_j)$, thus $Sim(N_i, N_j)$ reaches the maximum equal to 1 (just as when $M(N_i) = M(N_j)$), but some members of $M(N_j)$ have no counterparts in $M(N_i)$, so that $Sim(N_j, N_i) < 1$.

To better visualize the similarity, we put to Table 2 symmetric ratios

$$Sym\left(N_i, N_j\right) \equiv \frac{\left|M\left(N_i\right) \cap M\left(N_j\right)\right|}{\sqrt{\left|M\left(N_i\right)\right|\left|M\left(N_j\right)\right|}}.$$

Table 2. Similarity measure for the 32 nouns

	1	2	3	4	5	6	7	8	9	10	11	12	13	14	15	16	17	18	19	20	21	22	23	24	25	26	27	28	29	30	31
2	9																														
3	5	7																													
4	2	7	3																												
5	10	2	4	2																											
6	7	2	9	2	5																										
7	6	11	7	2	11	6																									
8	10	2	2	4	11	4	4																								
9	4	6	0	7	6	2	13	4																							
10	12	5	11	0	0	7	9	2	6																						
11	5	9	12	10	6	9	12	1	3	8																					
12	6	10	28	2	2	18	4	4	21	11	14																				
13	0	0	2	2	3	0	2	2	0	0	2	4																			
14	0	4	6	0	8	4	8	5	3	0	5	14	2																		
15	0	2	2	6	7	6	0	2	0	0	9	2	0	4																	
16	0	2	7	2	0	5	2	2	2	5	11	8	0	8	2																
17	9	3	20	3	3	3	4	1	0	3	7	13	2	1	0	8															
18	9	0	4	6	12	9	0	8	2	7	8	4	0	2	9	7	4														
19	9	6	6	4	0	9	4	2	6	10	9	12	0	2	0	6	12	11													
20	10	11	2	0	4	6	6	8	5	2	3	13	4	0	0	0	5	0	7												
21	10	2	7	2	5	12	6	6	6	11	8	5	2	3	5	3	2	7	4	9											
22	0	5	25	2	0	4	2	0	4	5	14	23	0	8	0	16	9	4	6	6	7										
23	4	4	3	2	4	2	4	11	4	4	6	4	4	2	2	0	5	0	8	8	6	2									
24	35	6	5	2	10	19	7	13	3	4	5	11	2	2	4	0	5	14	8	9	10	0	5								
25	8	1	3	3	7	6	5	5	4	1	5	5	3	2	1	0	5	6	10	9	5	0	6	12							
26	4	4	2	0	3	3	1	3	1	3	6	9	0	1	1	0	1	3	5	4	2	4	4	2	11						
27	3	2	1	3	2	2	3	8	4	2	3	1	2	0	0	0	1	2	4	4	1	0	3	4	12	9					
28	5	8	3	2	3	8	11	4	8	3	9	6	2	4	2	3	1	3	5	6	9	2	4	6	1	1	0				
29	8	2	5	2	2	10	4	7	3	2	8	4	0	3	2	2	4	2	6	7	7	2	0	10	1	1	5	4			
30	0	2	8	2	2	15	6	2	4	9	8	23	2	0	0	6	12	2	3	19	9	8	4	2	7	1	3	7	4		
31	0	7	5	2	0	0	0	0	2	2	1	2	0	0	0	0	1	0	0	0	2	0	0	1	3	1	2	0	2		
32	4	6	5	2	2	2	4	4	5	2	7	6	2	4	0	4	4	2	5	8	3	0	4	7	8	4	7	4	2	10	0

Because of the symmetry, we may consider the elements (in percents) only with $i \in [1, ..., j-1]$ (numbers at the left border and the bottom of the Table 2 are as in Table 1) and $j \in [1, ..., 32]$.

The average value of $Sym(N_i, N_j)$ in Table 1 is the 0.05. It reaches the maximum 0.35 for the pair {*answer*, *explanation*}, which are semantically closest words among these few under consideration. The following pairs decreasing in similarity are {*change, difference*}, {*change, expansion*}, {*difference, expansion*}, {*difference, feature*}, {*change, effect*}, {*comment, explanation*}, {*concept, difference*}, {*economy, expansion*}, {*concept, feature*}, etc. Some meaning clusters could be already seen, but we should admit that a more trustworthy clustering needs a vaster set of nouns and vaster sets of modifiers.

Quite dissimilar pairs (with zero *Sym* value) are quite numerous (76): {*change, copy*}, {*charge, decision*}, {*comment, decision*}, {*answer, disease*}, {*chance, disease*}, etc. The nouns for human features *eyes* and *face* proved to be very productive in modifiers (119 and 96 relatively) but very specific (their *Sym* measures are close to zero for majority of noun pairs).

4   Words Cohesion in Internet

Any words W_1 and W_2 may be considered forming a stable combination if their co-occurrence number $N(W_1, W_2)$ in a text corpus divided by S (the total number of words in the corpus) is greater than the product of relative frequencies $N(W_1)/S$ and $N(W_2)/S$ of the words considered apart. Using logarithms, we have a measure of word cohesion known as log-likelihood ratio or Mutual Information [8]:

$$MI(W_1, W_2) \equiv \log \frac{S \cdot N(W_1, W_2)}{N(W_1) \cdot N(W_2)}.$$

MI has important feature of scalability: if the values of all its building blocks S, $N(W_1)$, $N(W_2)$, and $N(W_1, W_2)$ are multiplied by the same factor, *MI* preserves its value.

Any Web search engine automatically delivers statistics on a queried word or a word combination measured in numbers of relevant Web pages, and no direct information on word occurrences or co-occurrences is available. We can re-conceptualize *MI* with all $N()$ as numbers of relevant pages and S as the page total managed by the engine. However, now $N()/S$ are not the empirical probabilities of corresponding events: the words that occur at the same a page are indistinguishable in the raw statistics, being counted only once, and the same page is counted repeatedly for each word included. We only hope that the ratios $N()/S$ are monotonically connected with the corresponding empirical probabilities for the events under consideration.

In such a situation a different word cohesion measure was construed from the same building blocks [1]. It conserves the feature of scalability, gives very close to *MI* results for statistical description of rather large sets of word combinations, but at the same time is simpler to be reached, since does not require repeated evaluation of the whole number of pages under the searcher's control. The new cohesion measure was named Stable Connection Index:

$$SCI(W_1, W_2) \equiv 16 + \log_2 \frac{N(W_1, W_2)}{\sqrt{N(W_1) \cdot N(W_2)}}. \tag{2}$$

The additive constant 16 and the logarithmic base 2 were chosen rather arbitrary. The constant 16 does not affect the comparisons discussed in this paper and is included purely for sake of tradition (since this is how the notion of *SCI* has been introduced previously); the reader can safely ignore it.

Since our experiments with Internet searchers need minimally several days to perform, some additional words on Web searchers are worthwhile here.

The statistics of searcher have two sources of variation in time. The first one is monotonic growing because of steady enlargement of searcher's DB. In our experience, for huge searcher's BDs and the queried words forming stable combinations, the

raw statistics $N(W_1)$, $N(W_2)$, $N(W_1, W_2)$ grow approximately with the same speed, so that *SCI* keeps its value with the precision to the second decimal digit, even if the statistics are got in different moments along the experimental day.

The second, fluctuating source of instability of Internet statistics is selection by the searcher of a specific processor and a specific path through searcher's DB—for each specific query. With respect to this, the searchers are rather different. For example, Google, after giving several very close statistics for a repeating query, can play a trick, suddenly giving twice fewer amount (with the same set of initial snippets!), thus shifting *SCI* significantly. Since we did not suffer of such troubles so far on behalf of AltaVista, we preferred it for our experiments.

5   Dissimilarity Based on Mean Cohesion Values

Consider first the mean cohesion values

$$\frac{1}{|M(N_i)|} \sum_{x \in M(N_i)} SCI(N_i, x)$$

between the noun N_i and all modifiers in its own modifier set $M(N_i)$. One can see in Table 3 that all mean *SCI* values are positive and mainly rather big (4 to 8), except for *enquiries.* As to the latter, we may suppose that occurrence statistics of British National Corpus—the base for selection of collocations in OCDSE—differ radically from Internet statistics, probably because OCDSE is oriented to the British variant of the English language, while Internet is mostly composed of texts written in American English or in international sort of English. Hence the collocations *intellectual / joint / open / critical / sociological... enquiries,* being rather rare in whole Internet, were inserted to OCDSE by purely British reasons. This is not unique case of British vs. USA language discrepancies. We had rejected orthographic differences like *flavour* vs. *flavor*, but we did not feel free to sift out such OCDSE collocations as *coastal flat* 'property by the sea,' which proved to be rare in Internet as a whole.

When calculating the SCI value of 'noun → modifier of a different noun' pairs that mainly are not normal collocations, we frequently observe the cases with zero co-occurrence number in Internet. Then formula (2) gives *SCI* value equal to $-\infty$. To avoid the singularity, we take the value -16 for such cases, i.e. the maximally possible positive value, but with the opposite sign.

We define the dissimilarity measure as

$$DSim(N_i, N_j) = \frac{1}{|M(N_i)|} \sum_{x \in M(N_i)} \left(SCI(N_i, x) - SCI(N_j, x) \right) \qquad (3)$$

i.e., as the mean difference between the *SCI* value of the modifiers of N_i with N_i and N_j, respectively. Note that in this formula the noun in question is compared with the set of its own modifiers defined by the dictionary and with the set of the modifiers of the other noun. Two things can be observed as to this definition.

Table 3. The mean SCI values of nouns with their own modifiers

S/N	Noun	Mean SCI	S/N	Noun	Mean SCI
1	*answer*	6.3	17	*effect*	6.7
2	*chance*	4.9	18	*enquiries*	1.4
3	*change*	6.5	19	*evidence*	8.0
4	*charge*	5.6	20	*example*	6.1
5	*comment*	4.4	21	*exercises*	4.0
6	*concept*	5.9	22	*expansion*	6.4
7	*conditions*	6.5	23	*experience*	7.7
8	*conversation*	6.0	24	*explanation*	6.1
9	*copy*	5.4	25	*expression*	4.9
10	*decision*	7.2	26	*eyes*	6.0
11	*demands*	4.1	27	*face*	5.7
12	*difference*	6.2	28	*facility*	4.5
13	*disease*	8.3	29	*fashion*	5.1
14	*distribution*	6.7	30	*feature*	5.9
15	*duty*	5.6	31	*flat*	4.3
16	*economy*	6.7	32	*flavor*	6.1

First, the formula is not symmetric. As it was discussed above, we consider the relations between different nouns more as inclusion than as distance: *cat* is a perfect *animal*, i.e., in our terminology we would say that *cat* is no different from *animal*, while *animal* by no means is a perfect *cat*.

Another observation about this definition is more theoretical. It seems to be contradicting: while we use the objective reality, the Web (as corpus) to measure the relatedness between a noun and a modifier, we seemingly arbitrary restrict the set of participating modifiers to be considered by those found in a dictionary, which were subjectively selected by a lexicographer. What is more, this seemingly leads to the necessity to use in our method a specialized large lexical resource, which does not exist in all languages, and it is not clear how the results obtained with different such resources would coincide.

Though we did not conduct any corresponding experiments, we believe that the formula above can be modified to use the whole set of words of the language (occurring in a large corpus or in the Web). The formula is then to be modified to take into account the cohesion between each word and the noun in question; those words that have low value of such cohesion would be weighted out. However, this would be a bit impractical. So we here use an approximation to such a totally unsupervised approach. Our approximation takes advantage of an already existing resource to roughly indicate which words are expected to correlate with the given noun.

Note that in this sense the second method can be thought of as a weighted variant of the first one.

Table 4 shows the pairs with the smallest and the greatest dissimilarity measure in our small dataset. One can notice the pairs with the smallest dissimilarity, such as {*enquiries, explanation*}, do have similar or related meaning, while those with greater dissimilarity, such as {*disease, enquiries*}, look totally unrelated.

Table 4. Most and least similar noun pairs in our sample

Least dissimilar noun pairs				Most dissimilar noun pairs			
Noun$_1$	Noun$_2$	DSim	Sim	Noun$_1$	Noun$_2$	DSim	Sim
enquiries	*explanation*	0.3	0.156	*disease*	*enquiries*	18.5	0.000
enquiries	*distribution*	0.5	0.022	*eyes*	*enquiries*	15.8	0.017
enquiries	*comment*	0.6	0.111	*effect*	*enquiries*	14.8	0.029
enquiries	*conversation*	0.6	0.089	*face*	*enquiries*	14.7	0.010
enquiries	*change*	0.9	0.044	*experience*	*enquiries*	14.4	0.000
difference	*change*	1.1	0.321	*disease*	*economy*	14.2	0.000
enquiries	*fashion*	1.1	0.022	*disease*	*chance*	14.0	0.000
enquiries	*charge*	1.2	0.067	*flavor*	*enquiries*	14.0	0.020

In fact, the very small DSim measure can indicate that the words are nearly synonyms or nearly antonyms, but this results from a different our research.

6   Comparison and Discussion

Comparing the *Sim* and *DSim* values for the 16 pairs in Table 4, one can see that the pairs with maximal *Sim* values usually have minimal *DSim* values and vice versa, i.e. an inverse monotonic dependency exists between the two measures. More representative comparison is given in Figure 1 that gives correlations between *Sim* and *DSim* on the plane.

A statistically proved inverse monotonic dependency is quite clear form Figure 1. One can also comprehend that *DSim* has higher resolution for semantically most different nouns. Indeed, the numerous pairs with zero *Sim* values have quite diverse *DSim* values, from 14.0 for {*disease, flat*} to 4.2 for {*flat, answer*}. Hence the use of *DSim* measure seems preferable.

7   Conclusions and Future Work

Two methods of numerical evaluation of semantic similarity of any nouns is proposed. The evaluations are based on comparison of standard modifiers of the nouns registered in OCDSE. The first method evaluates similarity by the portion of common modifiers of the nouns, while the second one evaluates dissimilarity by the change of the mean cohesion of a given modifier set with its own noun and an alien one.

Cohesion measurements are based on raw Web statistics of occurrences and co-occurrences of supposedly cohesive words. It is shown that dissimilarity measured through the Web has higher resolution and thus may have greater reliability.

Both methods do not depend on language and can be easily tested on the resources of other languages. Currently we are conducting experiments with Spanish and Russian, which are morphologically-rich languages. For English, it is worthwhile to repeat evaluations for a greater number of nouns and for different source of modifiers sets, e.g. for a large corpus of American origin. Finally, we believe that this method can be applied to words of parts of speech other than nouns, though one should be much more careful with, say, verbs, where the co-occurrence patterns are much more lexicalized and less semantic than those of nouns.
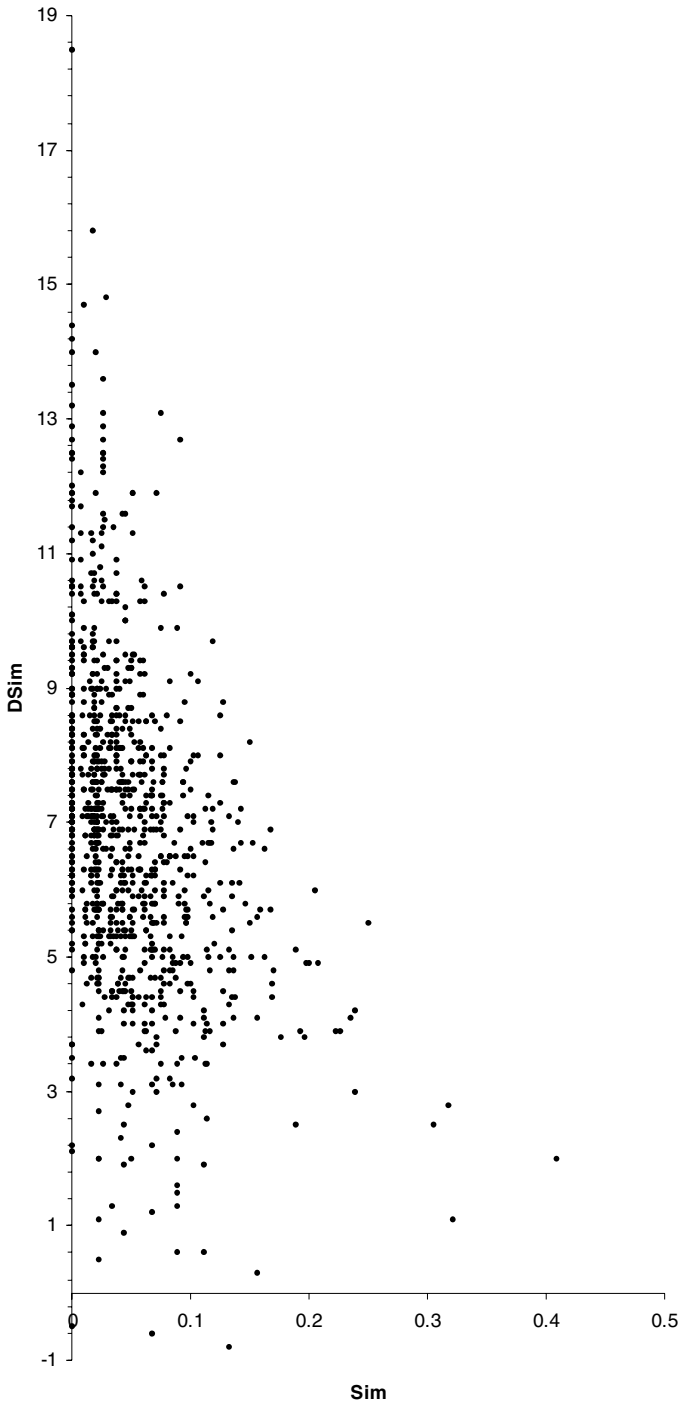
Fig. 1. Correlations between *Sim* and *DSim*

References

1. Bolshakov, I.A., Bolshakova, E.I.: Measurements of Lexico-Syntactic Cohesion by means of Internet. In: Gelbukh, A., de Albornoz, Á., Terashima-Marín, H. (eds.) MICAI 2005. LNCS (LNAI), vol. 3789, pp. 790–799. Springer, Heidelberg (2005)
2. Bolshakov, I.A., Gelbukh, A.: Two Methods of Evaluation of Semantic Similarity of Nouns Based on Their Modifier Sets. In: LNCS, vol. 4592, Springer, Heidelberg (2007)
3. Cilibrasi, R.L., Vitányi, P.M.B.: The Google Similarity Distance. IEEE Transactions on Knowledge and Data Engineering 19(3), 370–383 (2007), www.cwi.nl/ paulv/ papers/tkde06.pdf
4. Fellbaum, C. (ed.): WordNet: An Electronic Lexical Database. MIT Press, Cambridge (1998)
5. Hirst, G., Budanitsky, A.: Correcting Real-Word Spelling Errors by Restoring Lexical Cohesion. Natural Language Engineering 11(1), 87–111 (2005)
6. Keller, F., Lapata, M.: Using the Web to Obtain Frequencies for Unseen Bigram. Computational linguistics 29(3), 459–484 (2003)
7. Lin, D.: Automatic retrieval and clustering of similar words. In: COLING-ACL 1998, Canada (1998)
8. Manning, C.D., Schütze, H.: Foundations of Statistical Natural Language Processing. MIT Press, Cambridge (1999)
9. McCarthy, D., Koeling, R., Weeds, J., Carroll, J.: Finding Predominant Word Senses in Untagged Text. In: Proc. 42nd Annual Meeting of the ACL, Barcelona, Spain (2004)
10. Oxford Collocations Dictionary for Students of English. Oxford University Press (2003)
11. Patwardhan, S., Banerjee, S., Pedersen, T.: Using Measures of Semantic Relatedness for Word Sense Disambiguation. In: Gelbukh, A. (ed.) CICLing 2003. LNCS, vol. 2588, Springer, Heidelberg (2003)

Segment-Based Classes for Language Modeling Within the Field of CSR

Raquel Justo and M. Inés Torres

Dept. of Electricity and Electronics, University of the Basque Country. Spain
`raquel.justo@ehu.es, manes@we.lc.ehu.es`

Abstract. In this work, we propose and formulate two different approaches for the language model integrated in a Continuous Speech Recognition System. Both of them make use of class-based language models where classes are made up of segments or sequences of words. On the other hand, an interpolated model of a class-based language model and a word-based language model is explored as well. The experiments carried out over a spontaneous dialogue corpus in Spanish, demonstrate that introducing segments of words in a class-based language model a better performance of a Continuous Speech Recognition system can be achieved.

Keywords: language model, classes, segments of words.

1 Introduction

Within the field of Continuous Speech Recognition (CSR) the use of a language model (LM) is required in order to represent the way in which the combination of words is carried out in a specific language. Nowadays, Statistical Language Models (SLMs), based on n-grams, are the most commonly used approach in CSR [1]. They learn the frequency of occurrence of word sequences from a training corpus. Specifically, word n-gram LMs have demonstrate their effectiveness when it comes to minimizing the *word error rate* (WER) [2]. Alternatively, some formalism based on regular grammars and context free grammars have also been used in language modeling [3]. Language constraints, such as long-term dependencies, could be better modeled under this kind of syntactic approaches. However, they still present difficulties of learning and integrating, e.g. into a Continuous Speech Recognition system, when dealing with complex, real tasks.

In this work, we take advantage of both approaches by using *k-testable in the strict sense* (k-TSS) LMs. k-TSS languages are a subclass of regular languages and can be inferred from a set of positive samples by an inference algorithm [4]. k-TSS LMs are considered as the syntactic approach of the well-known n-gram models, where n is represented by k in the k-TSS model. This syntactic approach leads to the use of a Stochastic Finite State Automaton (SFSA) to represent the LM at decoding time. Moreover, the required smoothing, needed to deal with unseen events, is carried out by interpolating K k-TSS models, where $k = 1, \ldots, K$, into

a unique smoothed SFSA under a backing-off structure [5]. Then, acoustic models can easily be incorporated to this network into a CSR system.

Large amounts of training data are required to get a robust estimation of the parameters defining the mentioned models. However, there are numerous CSR applications, e.g. human-machine dialogue tasks, for which the amount of training material available is rather limited. One of the ways to deal with sparseness of the data is to cluster the vocabulary of the application into a smaller number of classes. Thus, an alternative approach, as a class n-gram LM, could be used [6,7].

A class n-gram LM is more compact and generalizes better on unseen events. Nevertheless, it only captures the relations between the classes of words, while it assumes that the inter-word transition probability depends only on the word classes. This fact degrades the performance of the CSR system. To avoid the loss of information associated with the use of a class n-gram LM, other authors have proposed different approaches, e.g. model interpolation, aiming to take advantage of both the accurate modeling of word n-grams for frequent events, and the predictive power of class n-gram models for unseen or rare events [6,8,9].

On the other hand, using phrases or word segments is a technique that has already successfully been used in language modeling for speech recognition [10,11,12] and machine translation [13]. In this work, a LM based on classes made up of segments of words is employed in order to combine the benefits of word-based and class-based models. That is, a class n-gram (k-TSS in our case) LM is generated to deal with the sparseness of the data. However, the proposed classes consist of sequences or segments of words, instead of being made up of isolated words. Therefore, the relations between words can be captured inside each class.

We propose and formulate in this work two different approaches to class k-TSS LMs based on word segments. Both are fully explained in Section 2. On the other hand an interpolated model is proposed as well. Such a model is defined as a linear combination of a word-based and a class-based LM, where classes are made up of segments of words.

The proposed models were integrated into a CSR module in a dialogue system application. The task consists of telephone queries about long-distance train timetables, destinations and fares uttered by potential users of the system. Several series of experiments were carried out on a spontaneous dialogue corpus in Spanish, in order to asses the proposed models (Section 5). These experiments show that the integration of word segments into a class-based LM yields a better performance of the CSR system.

2 Word Segments in Class-Based Language Models

Two different approaches to class-based LMs are formulated below. Both of them are generated introducing segments or sequences of words inside the classes of a class-based LM. However, in the first approach, M_{sw}, the words in a segment are separately studied and the transition probability among them is calculated.

In the second approach instead, M_{sl}, the words in a segment are joined and the whole segment is treated as a unique new "word" or lexical unit. Finally, a hybrid model is proposed as a linear combination of a word based and a class-based LM.

2.1 LMs Based on Classes of Word Segments: M_{sw}

Our goal is to estimate the probability of a sequence of N words $\bar{w} = w_1, w_2, \ldots$, w_N in accordance with a LM based on classes consisting of segments.

Let us define a segmentation (s) of the sequence of words into M segments, as a vector of M indexes, $s = (a_1, \ldots, a_M)$, such that $a_1 \leq \ldots \leq a_M = N$. The $\bar{w}$ sequence of words can be represented in terms of such segmentation as follows:

$$\bar{w} = w_1, \ldots, w_N = w_{a_0=1}^{a_1}, \ldots, w_{a_{M-1}+1}^{a_M=N} \tag{1}$$

where $w_{a_{i-1}+1}^{a_i} = w_{a_{i-1}+1}, \ldots, w_{a_i}$. The set of all possible segmentations of a $\bar{w}$ sequence of words is denoted as $S(\bar{w})$.

On the other hand, let $C = \{c_i\}$ be a previously defined set of classes, selected using any classification criteria. Each class consists of a set of segments previously defined as well. Each segment within a given class is made up of a sequence of several words. If the words in $\bar{w}$ are classified using the C set of classes, the corresponding sequence of classes is written as $\bar{c} = c_1, c_2, \ldots, c_T$ where $T \leq N$.

In this work, only segmentations compatible with the possible sequences of classes $(\bar{c})$ associated to each sequence of words are considered. This set of segmentations is denoted by $\mathcal{S}_{\bar{c}}(\bar{w})$. That is, only segmentations having the following form will be considered

$$\bar{w} = w_1, \ldots, w_N = w_{a_0=1}^{a_1}, \ldots, w_{a_{T-1}+1}^{a_T=N} \tag{2}$$

where $w_{a_{i-1}+1}^{a_i}$ must be a segment belonging to the c_i class.

The segmentation of a sequence of words can be understood as a hidden variable. In this way, the probability of a sequence of words $\bar{w}$, according to a LM based on classes made up of segments (M_{sw}), can be obtained by means of Equation 3

$$P_{M_{sw}}(\bar{w}) = \sum_{\forall \bar{c} \in \mathcal{C}} \sum_{\forall s \in \mathcal{S}_{\bar{c}}(\bar{w})} P(\bar{w}, \bar{c}, s)s = \sum_{\forall \bar{c} \in \mathcal{C}} \sum_{\forall s \in S_{\bar{c}}(\bar{w})} P(\bar{w}, s|\bar{c})P(\bar{c}) =$$
$$= \sum_{\forall \bar{c} \in \mathcal{C}} \sum_{\forall s \in \mathcal{S}_{\bar{c}}(\bar{w})} P(\bar{w}|s, \bar{c})P(s|\bar{c})P(\bar{c}) \tag{3}$$

being $\mathcal{C}$ the set of all the possible class sequences, given a predetermined set of classes C.

The probability of a given sequence of classes, $p(\bar{c})$, can be calculated as a product of conditional probabilities, as Equation 4 shows. The history (c_1^{i-1}) is usually truncated to the n most recent categories, when classical n-grams are used, or to the k_c most recent categories under the k-TSS approach, where k_c is the maximum length of the considered class history.

$$P(\bar{c}) = \prod_{i=1}^{T} P(c_i|c_1^{i-1}) \simeq \prod_{i=1}^{T} P(c_i|c_{i-k_c+1}^{i-1}) \tag{4}$$

The term $P(s|\bar{c})$, on the other hand, could be estimated using different approaches: zero or higher-order models, assuming that all the segmentations have the same probability, etc. Let us assume, in this work, the segmentation probability to be constant $P(s|\bar{c}) = \alpha$, as proposed in several phrase-based statistical machine translation works [14].

Finally, $P(\bar{w}|s,\bar{c})$ is estimated in accordance with zero-order models. Thus, given a sequence of classes $\bar{c}$, and a segmentation s, the probability of a segment given a class c_i only depends on this c_i class, but not on the previous ones, as Equation 5 shows.

$$P(\bar{w}|s,\bar{c}) \simeq \prod_{i=1}^{T} P(w_{a_{i-1}+1}^{a_i}|c_i) \tag{5}$$

The term $P(w_{a_{i-1}+1}^{a_i}|c_i)$ represents the probability of a sequence of words, which must be a segment, given the class of this segment and is estimated using a k-TSS model as shown below.

$$P(w_{a_{i-1}+1}^{a_i}|c_i) \simeq \prod_{j=a_{i-1}+1}^{a_i} P(w_j|w_{j-k_w+1}^{j-1},c_i) \tag{6}$$

where k_w stands for the maximum length of the word history that is considered in each class c_i.

Summing up, the probability of a sequence of words can be computed from Equation 7:

$$P_{M_{sw}}(\bar{w}) \simeq \alpha \sum_{\forall \bar{c} \in \mathcal{C}} \sum_{\forall s \in \mathcal{S}_{\bar{c}}(\bar{w})} \prod_{i=1}^{T} \left[\left[\prod_{j=a_{i-1}+1}^{a_i} P(w_j|w_{j-k_w+1}^{j-1},c_i) \right] P(c_i|c_{i-k_c+1}^{i-1}) \right] \tag{7}$$

Under this approach, several SFSAs need to be integrated into the CSR system: a SFSA representing the transition probabilities among classes as well as one additional SFSA for each class, representing the transition probabilities among the words contained in the segments of the class. Moreover, acoustic models should also be integrated in the search network. A static full integration of all these models is computationally prohibitive, thus, each SFSA is integrated "on the fly" [15] in the search network only when needed.

2.2 LMs Based on Classes of Linked Words: M_{sl}

In a second approach, we propose a LM based on classes consisting of joined sequences of words. In this approach each segment, $w_{a_{i-1}+1}^{a_i}$, will be considered as a new lexical unit that cannot be divided into different words. Let us denote each lexical unit by l_i, where $l_i \in \{\Sigma\}$, being $\{\Sigma\}$ the previously defined set of all the possible segments that will be inside the classes. The same hypothetical sets of segments and classes of 2.1 are considered here but assuming now that the segments cannot be separated in different words. Thus, a sequence of lexical units $\bar{l} = l_1, \ldots, l_M$ corresponds to a specific segmentation (s) of the sequence of words $\bar{w}$.

$$\bar{w} = \underbrace{w_{a_0=1}^{a_1}}_{l_1}, \dots, \underbrace{w_{a_{M-1}+1}^{a_M}}_{l_M} \tag{8}$$

Assuming again that only segmentations compatible with a given class sequence $(\bar{c} = c_1, \dots, c_T)$ are to be considered; the possible sequences of lexical units, for a given sequence of words, will have the following form $\bar{l} = l_1, \dots, l_T$, where l_i is a segment belonging to c_i.

A sequence of lexical units involves a specific segmentation itself, thus, in this case, $\bar{l}$ is considered as a hidden variable and the probability of a sequence of words is given by Equation 9.

$$P_{M_{sl}}(\bar{w}) = \sum_{\forall \bar{c} \in \mathcal{C}} \sum_{\forall \bar{l} \in \mathcal{L}_{\bar{c}}(\bar{w})} P(\bar{w}, \bar{c}, \bar{l}) = \sum_{\forall \bar{c} \in \mathcal{C}} \sum_{\forall \bar{l} \in \mathcal{L}_{\bar{c}}(\bar{w})} P(\bar{w}, \bar{l}|\bar{c}) P(\bar{c}) =$$
$$= \sum_{\forall \bar{c} \in \mathcal{C}} \sum_{\forall \bar{l} \in \mathcal{L}_{\bar{c}}(\bar{w})} P(\bar{w}|\bar{l}, \bar{c}) P(\bar{l}|\bar{c}) P(\bar{c}) \tag{9}$$

being $\mathcal{C}$ the set of all the possible class sequences, given a predetermined set of classes C. $\mathcal{L}_{\bar{c}}(\bar{w})$ is the set of all the possible sequences of lexical units compatible with the given sequence of words and the possible sequences of classes.

The third term in Equation 9, $P(\bar{c})$, is estimated as stated in Equations 4 (see previous Section).

The second term in Equation 9 is the probability of a sequence of lexical units given a sequence of classes. Assuming again zero-order models, this probability is calculated as:

$$p(\bar{l}|\bar{c}) = \prod_{i=1}^{T} P(l_i|c_i) \tag{10}$$

A k-TSS model, with $k = 1$, i.e. an unigram, has been used to estimate this kind of probability for each class.

Finally, the fist term in Equation 9, $P(\bar{w}|\bar{l}, \bar{c})$ is equal to 1 when the sequence of lexical units, $\bar{l}$, and the sequence of classes, $\bar{c}$, are compatible with the sequence of words, $\bar{w}$, and 0 otherwise. Taking into account that the restriction $\bar{l} \in \mathcal{L}_{\bar{c}}(\bar{w})$ has been established, the term $P(\bar{w}|\bar{l}, \bar{c})$ is equal to 1 in all the cases we have considered.

Summing up Equation 9 can be rewritten as follows:

$$P_{M_{sl}}(\bar{w}) \simeq \sum_{\forall \bar{c} \in \mathcal{C}} \sum_{\forall \bar{l} \in \mathcal{L}_{\bar{c}}(\bar{w})} \prod_{i=1}^{T} \left[P(l_i|c_i) P(c_i|c_{i-k_c+1}^{i-1}) \right] \tag{11}$$

Here, smoothed k-TSS models are used again to represent the class based LM. The corresponding SFSAs are integrated in the search network represented by Equation 11 "on-the-fly" only when required.

2.3   Interpolating an M_{sw} Model and a Word-Based LM, M_h

The interpolation of a class-based and a word-based LM has demonstrated to outperform both mentioned models. In this work a hybrid model (M_h) is defined

as a linear combination of a a word-based LM, M_w, and a LM based on classes made up of word segments, M_{sw}. Using such a model the probability of a word sequence is given by Equation 12.

$$P_{M_h}(\bar{w}) = \lambda P_{M_w}(\bar{w}) + (\lambda - 1)P_{M_{sw}}(\bar{w}) \tag{12}$$

In the above equation, the term $P_{M_w}(\bar{w})$ is the probability of a word sequence using a classical word-based language model, and in this work, a k-TSS model was used to estimate this probability, as Equation 13 shows.

$$P_{M_w}(\bar{w}) = \prod_{i=1}^{N} P(w_i|w_1^{i-1}) \simeq \prod_{i=1}^{N} P(w_i|w_{i-k+1}^{i-1}) \tag{13}$$

The term $P_{M_{sw}}$ is the probability given by Equation 7 in Section 2.1.

3   Classes and Word Segments

In order to deal with the proposals presented in the previous Section, a set of segments and a set of classes formed by those segments needed to be obtained from the selected corpus. Two different types of criteria were used.

Statistical classes and segments: In this case, we first obtained a set of segments using a statistical criterion. The most frequent n-grams of the corpus were selected as segments. In this sense, and in order to avoid rare or unimportant n-grams, a minimum number of occurrences was required. In the experiments shown in Section 5 the n-grams (where $1 \leq n \leq 5$) appearing in the corpus a number of times above a prefixed threshold were included in the set of the defined segments. Then, a segmented training corpus was generated with the set of segments. Finally, different sets of statistical classes constituted by the defined segments were obtained with the aid of *mkcls* [16].

Linguistic classes and segments: In this case, the set of segments and the set of classes were simultaneously obtained under a linguistic criterion by applying a rule based method. These classes are independent of the task and consist of word segments having the same linguistic function in the sentence. This set of classes, as well as the segments the classes are made up of, were provided by *ametzagaina*[1]. Furthermore, they provided us with the segmented and classified corpus. An example of some employed classes and segments appears below:

- **IZ** (stands for a noun phrase, NP): "el próximo viernes", "un billete de ida y vuelta", "el de las once", ...
- **LO-que** (stands for any phrase ending with the word "que"): "el que", "los que", "un euromed que", "dígame los que", ...
- **PR-despues** (stands for a prepositional phrase, PP, beginning with the word "después"): "después de las dos", "después de las quince", ...

---

[1] Ametzagaiña R&D group, member of the Basque Technologic Network, http://www.ametza.com

4   Task and Corpus

The experiments were carried out over a task-oriented corpus that consists of human-machine dialogues in Spanish, DIHANA (acquired with a Consortium of Spanish Universities) [17]. In this corpus, 225 speakers ask by telephone for information about long-distance train timetables, fares, destinations and services.

Table 1. Features of the corpus

		DIHANA
Training	Sentences	8,606
	Different sent.	5,590
	Words	77,476
	Vocabulary	865
Test	Sentences	1,348
	Words	12,365
	Vocabulary	503
	OOV	72
	PP ($k = 3$)	14.59

Table 2. Different sets of classes and segments

	linguistic	statistical				
$|C|$	57	50	100	200	300	400
$|\Sigma|$	3,851	1,289				
total no. cat.	55,053	57,078				
total no. seg.	55,053	57,078				

A total of 900 dialogues were acquired using the Wizard of Oz technique. This task has intrinsically a high level of difficulty due to the spontaneity of the speech and the problematic derived from the acquisition of large amount of transcriptions, of human-machine dialogues, for training purpose. Therefore, it is well-suited to study the improvements associated to modifications in the LM. The features of the corpus are detailed in Table 1.

As already mentioned in Section 3, different sets of classes were obtained using two different classification criteria: a linguistic criterion and a statistical one. Furthermore, two different sets of segments were obtained, also using two different criteria and the techniques described in Section 3. Table 2 shows the statistics of the resulting groups of classes and segments, as well as the total number of classes and segments that are in the training corpus once it has been segmented or classified.

5   Experiments and Results

The LMs proposed in this work were fed into an CSR system, which was subsequently evaluated in terms of WER. The CSR system makes use of the Viterbi Algorithm to search for the best sequence of uttered words for a given sequence of acoustic observations. Thus, the decoder finds the best sequence of states through a probabilistic network, combining classes, segments, words and acoustic models (The acoustic models are continuous Hidden Markov Models).

Three series of experiments were carried out in order to evaluate the proposed approaches in Section 2.

Firstly, the **LM based on classes consisting of word sequences, M$_{sw}$**, was fed into the CSR system, according to Equation 7. Making use of this LM, different experiments were carried out, choosing for all of them a value of $k_c = 3$ and $k_w = 2$. First of all, the set of linguistic classes was employed. Then, five experiments were carried out using 50, 100, 200, 300 and 400 statistical classes respectively.

On the other hand, **LMs based on classes consisting of linked words, M$_{sl}$**, were integrated into the CSR system according to Equation 11. A value of $k_c = 3$ was established. Experiments were carried out using the same sets of linguistic and statistical classes described above. The same sets of segments were also employed here.

Finally the **hybrid model** was integrated into the CSR system according to Equation 12. For the M_{sw} model a value of $k_c = 3$ and $k_w = 2$ was established, whereas for the classical word-based model, M_w, a value of $k = 3$ was employed. On the other hand, the λ parameter was selected to obtain the best WER result ($\lambda = 0.1$). The same experiments with the same mentioned sets of classes and segments were repeated with this model.

Table 3 illustrates WER results using the proposed LMs and the classical word-based LM mentioned above, M_w, (with a value of $k = 3$) as a baseline.

First of all, looking at the results in Table 3 it can be concluded that statistical classes yield better results than linguistic ones, even when the number of classes is similar (50 statistical classes vs. 57 linguistic classes).

The results obtained in Table 3 were also compared with the values of WER obtained in another work [18], over the same task and using a classical class-based model with classes made up of isolated words. As shown in the mentioned work, class-based LMs using 50, 75 and 100 statistical classes achieve WER values of 24.20, 23.05 and 22.22 respectively. It can be concluded from this, that better results are obtained when using word segment based classes (in both M_{sw} and M_{sl} models), than when employing classical class-based LMs using classes made up of isolated words.

Regarding the results obtained with the M_{sw} model, when 50 classes were used the results improve by 7%, whereas for 100 classes the corresponding improvement equals 4.5%. Nevertheless, using a word based LM (M_w), WER values are lower

Table 3. WER results for a classical word based LM (M_w) and for the proposed LMs (M_{sw}, M_{sl} and M_h) using different sets of classes: 57 linguistic classes and 50, 100, 200, 300 and 400 statistical classes respectively

WER (%)					
no. cat.		M_{sl}	M_{sw}	M_h	M_w
ling.	57	22.78	25.97	20.04	
statis.	50	20.96	22.52	19.23	
	100	19.83	21.21	18.84	19.84
	200	19.42	20.79	18.14	
	300	19.27	20.66	18.22	
	400	19.63	21.38	18.52	

than those obtained for the M_{sw} model and the selected sets of classes and segments. This could be due to some strong assumptions made in the definition of the model.

On the other hand, regarding the experiments carried out with the M_{sl} model, a significant drop of the WER is observed compared to the previous model (M_{sw}) for all of the selected sets of classes. The best result is obtained for 300 statistical classes, achieving an improvement of a 6.7% with respect to the value obtained in the same conditions for the M_{sw} model. Furthermore, the result obtained with 300 statistical classes and an M_{sl} model improves the WER values obtained with the word based LM (M_w) by a 2.8%.

However, the use of a hybrid model, interpolating the M_{sw} and the M_{sl} models, outperforms the results obtained with all the previous proposals. Moreover, the best result is obtained for 200 statistical classes where an improvement of a 8.56% is observed with respect to the word-based LM.

6   Concluding Remarks and Future Work

In this work, we propose and formulate two different approaches to language models, which are based on classes made up of segments of words. On the other hand, an interpolated LM was explored as well. The proposed models were integrated into a CSR system in order to evaluate them in terms of WER. The experiments carried out show that using a LM based on classes consisting of segments of words instead of a classical class n-gram (or k-TSS) LM, a better performance of a CSR system can be achieved. On the other hand, although some of the results attained with the class-based models in this work, outdo those obtained with a classical word-based LM, the observed improvement is not very significant. Therefore, the interpolation of a word-based LM and a LM based on classes made up of segments of words was employed. Using such a model a better performance of a CSR system can be achieved compared to a word-based LM.

However, since the M_{sl} model provides better results than the M_{sw} one, it could be interesting, for further work, to explore the interpolation of the M_{sl} model and a LM based on the same words or lexical units that M_{sl} employs.

References

1. Jelinek, F.: Statistical Methods for Speech Recognition. MIT Press, Cambridge (1998)
2. Gupta, V., Lenning, M., Mermelstein, P.: A language model for very large-vocabulary speech recognition. Computer Speech and Language 6(2), 331–344 (1992)

3. Benedí, J.M., Sánchez, J.A.: Estimation of stochastic context-free grammars and their use as language models. Computer Speech and Language 19(3), 249–274 (2005)
4. García, P., Vidal, E.: Inference of k-testable languages in the strict sense and application to syntactic pattern recognition. IEEE Trans. Pattern Anal. Mach. Intell. 12(9), 920–925 (1990)
5. Torres, I., Varona, A.: k-tss language models in speech recognition systems. Computer Speech and Language 15(2), 127–149 (2001)
6. Brown, P.F., Pietra, V.J.D., Souza, P.V.d., Lai, J.C., Mercer, R.L.: Class–based n-gram Models of Natural Language. Computational Linguistics 18(4), 467–480 (1992)
7. Niesler, T.R., Woodland, P.C.: A variable-length category-based n-gram language model. In: IEEE ICASSP 1996, Atlanta, GA, vol. I, pp. 164–167. IEEE, Los Alamitos (1996)
8. Niesler, T., Whittaker, E., Woodland, P.: Comparison of part-of-speech and automatically derived category-based language models for speech recognition. In: ICASSP 1998, Seattle, pp. 177–180 (1998)
9. Zitouni, I.: Backoff hierarchical class n-gram language models: effectiveness to model unseen events in speech recognition. Computer Speech and Language 21(1), 99–104 (2007)
10. Deligne, S., Bimbot, F.: Language modeling by variable length sequences: Theoretical formulation and evaluation of multigrams. In: Proc. ICASSP 1995, Detroit, MI, pp. 169–172 (1995)
11. Ries, K., Buo, F.D., Waibel, A.: Class phrase models for language modelling. In: Proc. ICSLP 1996, Philadelphia, PA, vol. 1, pp. 398–401 (1996)
12. Kuo, H.K.J., Reichl, W.: Phrase-based language models for speech recognition. In: Proceedings of EUROSPEECH 99, Budapest, Hungary, vol. 4, pp. 1595–1598 (September 1999)
13. Marcu, D., Wong, W.: A phrase-based, joint probability model for statistical machine translation (EMNLP), Philadelphia, PA (July 6-7, 2002)
14. Zens, R., Ney, H.: Improvements in phrase-based statistical machine translation. In: Proc. of the Human Language Technology Conf (HLT-NAACL), pp. 257–264 (2004)
15. Caseiro, D., Trancoso, I.: Transducer composition for on-the-fly lexicon and language model integration. In: Proceedings ASRU 2001 - IEEE Automatic Speech Recognition and Understanding Workshop, Madonna di Campiglio, Italy (December 2001)
16. Och, F.J.: An efficient method for determining bilingual word classes. In: Proceedings of the ninth conference on European chapter of the Association for Computational Linguistics, Morristown, NJ, USA, Association for Computational Linguistics, pp. 71–76 (1999)
17. Benedí, J., Lleida, E., Varona, A., Castro, M., Galiano, I., Justo, R., López, I., Miguel, A.: Design and acquisition of a telephone spontaneous speech dialogue corpus in Spanish: DIHANA. In: Proc. of LREC 2006, Genoa, Italy (May 2006)
18. Justo, R., Torres, M.I., Benedí, J.M.: Category-based language model in a spanish spoken dialogue system. Procesamiento del Lenguaje Natural 37(1), 19–24 (2006)

TextLec: A Novel Method of Segmentation by Topic Using Lower Windows and Lexical Cohesion

Laritza Hernández Rojas and José E. Medina Pagola

Advanced Technologies Application Centre (CENATAV)
7a #21812 e/ 218 y 222, Rpto. Siboney, Playa. C.P. 12200, C. Habana, Cuba
{lhernandez,jmedina}@cenatav.co.cu

Abstract. The automatic detection of appropriate subtopic boundaries in a document is a difficult and very useful task in text processing. Some methods have tried to solve this problem, several of them have had favorable results, but they have presented some drawbacks as well. Besides, several of these solutions are application domain dependant. In this work we propose a new algorithm which uses a window below the paragraphs to measure the lexical cohesion to detect subtopics in scientific papers. We compare our method against two algorithms that use the lexical cohesion too. In this comparison we notice that our method has a good performance and outperforms the other two algorithms.

Keywords: Text processing, Segmentation by topic, Lexical cohesion.

1   Introduction

The concept of segmentation in text processing has been used with different interpretations. For example, Boshakov and Gelbukh in 2001 structured it as: thematic (topic) and lexico-grammatical segmentation [3]. In this work, we will focus on topic segmentation.

A document usually contains several pieces of text about a more specific content (subtopic) regarding the content of the whole text (topic). Such pieces are formed by textual units (words, sentences or paragraphs). The marks, subtitles or comments that can identify the subtopics are not always used by the authors of the documents. The pieces of text obtained by means of automatic processing, that identify the subtopics that form the text, are known as segments, and this process is known as Texts Segmentation by Topic.

The process of segmentation by topic is useful in several text processing tasks. For example, Texts Summarization, News stories segmentation from broadcast news, Information Retrieval and others [1], [5], [10], [11], [13].

The segmentation methods by topic are used in Information Retrieval specifically in Passages Retrieval to return segments or passages more related with the user's queries instead of the whole document. Text Summarization would be more robust by knowing all the subtopics that form a document, because they can be used as a guide to select the main ideas which may include a summary of the whole document.

The segmentation that we will propose in this work will be used in a scientific information retrieval system to find document segments that topically satisfy specific requirements or profiles.

A scientific paper is usually a text of multiple paragraphs that explicitly explain or teach about a topic, in which the most significant words that form a subtopic are frequently reiterated.

Although there are some approaches to solve the segmentation problem, the results that they achieve do not always have a high quality.

This and all the reasons exposed here have motivated our work. We propose in this paper a new segmentation algorithm, which is based on the following assumption: if a lexical terms group (vocabulary) is used during the course of the discussion of a subtopic and this subtopic changes, a significant portion of this vocabulary changes too.

We have structured the present work as follows. In Section 2 we briefly explain some previous works to solve the segmentation problem and their drawbacks. In Section 3 we describe the proposed method. In the last section we present the experimental results by using a textual corpus which we prepared with articles selected from the ICPR '2006 proceedings.

2   Methods of Segmentation by Topic

Many of the researches about segmentation by topic use the linguistic term Lexical Cohesion. This term was defined by Halliday and Hasan in 1976 as a sense relationship that exists among the textual units in a text [4]. The repetition or lexical reiteration, synonymy and others are mechanisms that indicate sense relationships.

The results of these researches have shown that the Lexical Cohesion is a very useful way to detect the subtopics changes inside a text, because the textual units that are strongly related by Lexical Cohesion usually constitute a segment about a simple subtopic [5], [6],[9],[12].

We consider proper to mention that there are some works in segmentation focused on discovery of topical units and not on subtopic structure inside documents although this is not the goal of this work.

The Stokes, Carthy and Smeaton's work is an example of the previous one. This work is called SeLeCT, which is intended to distinguish individual news stories from a broadcast news programme [12]. SeLeCT is based on an analysis of the lexical cohesion strength among the textual units using a linguistic technique that is called Lexical Chaining [13].

Ponte and Croft proposed a method that has as application goal the topic tracking of broadcast speech data and topic identification in full-text databases. Their work is focused on text with relatively small segment sizes and for which sentences inside a segment have relatively few words in common turning segmentation into a more difficult problem. This method uses a query expansion technique to find common features for the topic segments [8].

Next we will describe two segmentation methods that are focused on the identification of subtopic structures in documents; they are based on lexical reiteration to detect relationship among textual units.

2.1 Segmentation Proposed by Hearst

We found that the most interesting research in identification of subtopic structures is the Hearst work. She proposed an algorithm which he called TextTiling. This algorithm splits explanatory texts into discourse units of multiple paragraphs. In contrast to many discourse models that assume a hierarchical segmentation model, the author has the goal of identifying subtopic boundaries by attempting only a linear segmentation. Also, Hearst assumes that if a lexical terms group (vocabulary) is used during the course of the discussion of a subtopic and this subtopic changes, then a significant portion of this vocabulary changes too.

The algorithm has three main parts: pre-processing, lexical score determination and boundary identification.

In the first one stopwords are eliminated and a morphological analysis is applied to the text. Besides, the text is subdivided into sequences of a predefined size of the resulting words, without considering punctuation marks, which she called sentences (pseudosentences).

Then a lexical score is determined. TextTiling proposes two lexical score methods. The first method compares adjacent blocks of sentences, and assigns a similarity score between two blocks according to how many words they have in common, the sentences blocks are represented by the Vector Space Model. The second method, called vocabulary introduction, forms text intervals with sentences and assigns a lexical score to the midpoint of the interval, based on how many new words (words not seen before in the text) appear around this midpoint.

Finally, the identification of the limit is made identically for the two lexical scoring methods. Keeping in mind this lexical score, a depth score is assigned to each gap between blocks with lowest lexical scores, called valleys.

The depth score of a valley corresponds to how strongly the features for a subtopic changed on both sides of the valley and is based on the distance from the valley to the two peaks that make it up. In other words, if a low lexical score is preceded and is followed by a high lexical score this is assumed as an indicator of a change in the vocabulary, which will correspond, according to what the author assumed, to a subtopic change.

Then, the depth scores are sorted and used to determine segment boundaries. The larger the score, the more likely the boundary occurs at that location [5].

This algorithm maintains a good performance, but it presents a drawback that causes the interruption of a segment that contains a simple subtopic; this problem also produces many segments that surpass the considered valid amount. This occurs when there is a short paragraph or other (e.g. paraphrase) which interrupts a cohesive text chain. TextTiling does not detect this behavior. In these anomalous cases, TextTiling gets a notable low score and, then, assigns a segment boundary.

2.2 Segmentation Proposed by Heinone

Unlike Hearst, Heinone proposed a method which uses a sliding window to determine, for each paragraph, which is the most similar paragraph inside the window. The sliding window will be formed by several paragraphs on both sides (above and below) of every processed paragraph.

This segmentation method is especially useful when it is important to control the segment length. The author uses a dynamic programming technique that guarantees to get segments of minimum cost. The segment cost is obtained by a lexical cohesion curve among the paragraphs, a preferential segment size specified by the user, and a defined parametric cost function [6].

Firstly, as in TextTiling, Heinone suggests a text preprocessing stage. Then, the paragraphs are represented by the Vector Space Model similar to TextTiling as well.

Later, a cohesion vector ($Cohe_1...Cohe_n$) is built for the document, where each paragraph is associated with the highest similarity value inside its window.

As the algorithm considered the segment length, a length cost function $clen(x, p, h)$ is used to evaluate the closeness between the real and the preferential segment length, where x is the real segment length, p the preferential segment length, and h a scale parameter to adjust the length.

The algorithm calculates, in a sequential way from the first to the last one, the minimum cost segmentation by paragraph. To this end, the following expressions were considered:

$$Cost_i = \min(CostS(S_i^i)...CostS(S_i^1)) \ , \tag{1}$$

$$Cost_0 = 0 \ , \ Cohe_0 = 0 \ , \tag{2}$$

$$CostS(S_i^k) = Flon(S_i^k) + Cohe_{k-1} + Cost_{k-1} \ , \tag{3}$$

$$Flon(S_i^k) = clen(\text{"amount of words in segment from k to i"}, p, h) \ , \tag{4}$$

were S_i^k is a segmentation that considers a segment from k-th to i-th paragraphs.

Besides, for each paragraph, its segment boundary is defined, which is the last paragraph of the previous segment. This boundary is determined by the expression:

$$LimP_i = k - 1 \ \ were \ \ Cost_i = CostS(S_i^k) \ . \tag{5}$$

This method achieves a good assessment among the segment length, the preference length and the similarity value associated with each paragraph. Besides, the use of a sliding window can diminish the interruption of a cohesive text chain, in contradistinction to Hearst's proposal.

However, this method entails a shortcoming as well. The cohesion vector associates each paragraph with the highest similarity value in its window, but this value can belong to a paragraph above or below the paragraph in question. In case the value belongs to a paragraph above, the algorithm – not distinguishing this situation – could decide to include the paragraph in the segment below. As we can observe, it is incorrect to allow the similarity value to be chosen with paragraphs above to decide the inclusion of a paragraph in a segment below. This weakens the method assumptions by enabling low cohesion segments to be obtained.

On the other hand, for each paragraph, the method looks for the most similar paragraph inside its window, causing that other very similar paragraphs are underestimated.

Besides, this method has another drawback; it requires an approximate subtopic length, which is an unpredictable value that is not always the same for all the subtopics. Lastly, when the cost length function establishes a matching between the approximate and real length, the algorithm can interrupt the segment cohesion.

3   Segmentation Method TextLec

We propose a novel method called TextLec, which intends to segment scientific papers into subtopics. With TextLec we solve the drawbacks aforementioned. We also use term repetitions as a mechanism to indicate the lexical cohesion among the text units.

In this work we take the paragraph as the minimum text unit, because, as we have said before, our work is intended to the segmentation of multiple paragraphs.

We assume a lineal segmentation and also that whenever there is a subtopic change we are in the presence of a vocabulary change, just as Hearst assumed. Besides, we consider that: the neighbor paragraphs that maintain a considerable lexical cohesion among them, regarding the use of a lexical terms group, should belong to the same segment.

We establish that, if the value that expresses the lexical cohesion between two paragraphs is bigger than a similarity threshold U, then these paragraphs have a considerable lexical cohesion among them. From now on, we only use the term *cohesive* to refer to paragraphs whose lexical cohesion is bigger than the threshold U.

With the frequency of the resulting terms after a preprocessing, we represent the paragraphs with the Vector Space Model. We will compute the lexical cohesion by applying the cosine measure.

For each paragraph, we define a lower window to find inside a cohesive paragraph that will be, opposite to Heinone, the farthest cohesive paragraph.

We only use a lower window to distinct if paragraphs, above or below, are cohesive, and to diminish the possibility of wrongly including a paragraph into a segment. Besides, we decided to take the farthest cohesive paragraph inside each window instead of the most cohesive; so, we do not leave all the potential cohesive paragraphs, what diminishes the possibility of excluding a paragraph incorrectly from a segment. This also allows us to avoid more efficiently the effect of paragraphs that interrupt a coherent text chain.

Besides, with the control of the farthest cohesive paragraph we can determine a possible end of a segment.

Another interesting aspect of this method is that by increasing the window size we are able to obtain longer segments, because we increase the possibility of finding a farthest cohesive paragraph, although the segment cohesion would decrease.

3.1   Preliminary Conditions

We use the vector *Parf* with the purpose of controlling the farthest cohesive paragraph inside the window for each paragraph. It is possible that a paragraph does not have any cohesive one inside its window; in this case, we consider that the paragraph is cohesive at least to itself.

On the other hand, we use the variable *MaxBel* to control the possible end (lower boundary) of the segment in process while the segmentation algorithm is executed. This variable will allow knowing the farthest cohesive paragraph from the segment in process. Therefore, the paragraph controlled by *MaxBel* will be possibly the one that closes the segment.

Besides, we use the vector *Lim* to control, for each segment, the lower boundary, where Lim_k will contain the finish paragraph of segment *k*. For example, if $Lim_k = 5$, then we will get a segment *k* that finishes in paragraph 5.

3.2 Segmentation Process

The segmentation process that we propose will include paragraphs into a segment until finding a paragraph that is not cohesive with any paragraph inside the segment and also if there is no paragraph inside the segment cohesive with a paragraph below it.

We show the segmentation algorithm pseudo-code in Fig. 1.

```
Algorithm: TextLec
Input:   Parf - vector of more similar paragraph below
         N - total of paragraphs
Output: Lim - boundary of segments
  1)  MaxBel = Parf₁;
  2)  k = 1;
  3)  for i = 2 to N do begin
  4)     if MaxBel = i-1; then begin
  5)        Limₖ = MaxBel;
  6)        k = k + 1;
  7)     end
  8)     MaxBel = max( Parfᵢ, MaxBel );
  9)  end
 10)  Limₖ = N
```

Fig. 1. Pseudo-code of TextLec Algorithm

We suppose that the texts will have one paragraph at least, and we also suppose that we will also obtain a segment formed by one paragraph at least. Then we have as initial values: $MaxBel = Parf_1$ and $k = 1$.

During the execution, we analyze the other paragraphs and we determine whether we include a paragraph or not in the segment that we are building. During this process, a paragraph *i* can be in any of the following situations:

- There is no paragraph inside the segment that is cohesive with *i* or cohesive with a paragraph below *i*, (*MaxBel* = *i* - 1). In this case we take the paragraph $i - 1$ as lower boundary of the segment, and we include *i* into a new segment.
- The paragraph *i* is cohesive with some paragraph inside the segment, (*MaxBel* = *i*). In this case we include *i* into this segment.
- There is no a paragraph inside the segment, that is cohesive with *i*, but there is at least one inside cohesive with a paragraph below *i*. Then, we do not interrupt this segment and we include *i* into it.

After the inclusion of the paragraph *i* into a segment we verify if the cohesive paragraph with *i* is farthest than *MaxBel*; in this case, we update *MaxBel*.

When the process finishes all the lower boundary of the segments are into *Lim*, and *k* is the amount of detected segments.

4   Evaluation

The evaluation of the segmentation by topic has two major related difficulties. The first one is given by the subjective nature of detecting the appropriate subtopic boundaries, in which several human readers can even disagree, regarding where boundaries should be placed and how fine-grained an analysis should be. This makes it difficult for us to select a reference segmentation to compare our results. Usually, this difficulty is solved by comparing the segmentation results against the marks or subtitle that the authors use to identify the subtopics inside a document; but these marks are not always specified. Some authors evaluate the algorithm in terms of how well it distinguishes entire articles from one another when they are concatenated into one file and where different topics are distinguished. Another way is to compare the results against a manual segmentation based on the several human judgments, which make a "gold standard" [5], [7], [12].

The second difficulty is that error importance depends on the applications where the segmentation techniques are necessary. For example, in Information Retrieval it can be accepted that the segment boundaries will differ in a few sentences from the real segment boundaries. However, in order to segment news stories from broadcast news the accuracy of boundaries location is very important [7].

On the other hand, finding an appropriate evaluation metric to determine the segmentation algorithm accuracy has generated much debate. Two of the evaluation measures that have been used by many authors are Precision and Recall, which are standard measures in Information Retrieval experimentations. In the estimation of the segmentation accuracy, the Precision and the Recall are defined likes this.

Precision: The percentage that represents the segment boundaries correctly detected by the algorithm from all boundaries detected by it.

Recall: The percentage that represents the segment boundaries correctly detected by the algorithm from all boundaries in the reference segmentation.

Precision and Recall are usually very convenient in applications where the accuracy of boundaries location is very important. But in applications where it is not very necessary they have some problems. These measures strongly penalize the algorithm when boundaries that do not agree exactly with the reference segmentation are detected, because they are not sensitive to the proximity between the boundaries of both segmentations. Another difficulty with Precision and Recall is that there is inherent tradeoff between precision and recall; improving one tends to cause the score for the other to decline [2], [7]. This difficulty is usually solved in Information Retrieval with F-measure; it is defined as:

$$F\text{-}measure = 2 \times \frac{Precision \times Recall}{Precision + Recall} \ . \tag{7}$$

F-measure has been used in segmentation as well. Nevertheless, we should note that as F-measure depends on Precision and Recall it shows the first problem, i.e., it is not sensitive to the proximity between the boundaries of both segmentations.

Pevzner and Hearst proposed a metric to improve the segmentation evaluation process, called WindowDiff [7]. WindowDiff uses a sliding window of length k to find disagreements between the reference and algorithm segmentation.

In the segmentation literature there are many authors that experiment with several window sizes, i.e., with several k values. In this work we take k as the half of the average true segment size in the reference segmentation.

The boundaries amount inside the window of both segmentations is determined for each window position; the algorithm is penalized if the amount of boundaries disagrees. Later, all penalizations found are added. This value is normalized and the metric takes a value between 0 and 1. WindowDiff takes a score of 0 if the algorithm assigns all boundaries correctly and it takes a score of 1 if it differs completely from the reference segmentation. The WindowDiff formal expression is defined as follows:

$$WindowDiff\,(ref,hyp) = \frac{1}{N-k}\sum_{i=1}^{N-k}(|\,b(ref_i,ref_{i+k})-b(hyp_i,hyp_{i+k})\,|> 0)\;, \qquad (8)$$

where $b(i,j)$ represents the number of boundaries between positions i and j in the text and N represents the textual units number in the whole text, regarding goal applications; ref is the reference segmentation and hyp the algorithm segmentation.

In this section we show the result of the three segmentation methods: TextTiling, the Heinone's, and TextLec. The corpus that we used in the experimentation was built joining 14 different papers taken from The 18th International Conference on Pattern Recognition ICPR'2006 proceedings. The resultant corpus has 305 paragraphs and an average of 22 paragraphs approximately for each paper.

We chose from all the marks or subtitles inside the papers defended by the authors those that, in our opinion, have the clearest boundaries to select the reference segmentation based on our judgment. Also, we added to the reference segmentation the boundaries among each different article.

We show the comparison among the three algorithms by calculating the Precision, Recall and metric WindowDiff values for each one, regarding the reference segmentation. These values are shown in Table 1.

Table 1. Precision, Recall and metric WindowDif values for three segmentation methods: TextLec TextTiling, and the Heinone's

Algorithms	Precision	Recall	F-measure	WindowDiff
TextLec	61,74	52,59	56,8	0,21
TextTiling	45,90	62,22	52,83	0,33
Heinone's	45,24	42,2	43,67	0,26

In the experimentation we can notice a better performance in TecxLec compared to the other two algorithms. TextLec obtained a better WindowDiff value, i.e., closer to 0. Also, both values, Precision and Recall, are greater than 50%, but we should notice that if the amount of obtained boundaries increases then the Recall may improve but,

at the same time, Precision may decline. For example, TextTiling has a recall value higher than TextLec, but it has a lower precision value and lower than 50%. In any case, TextLec has a higher F-measure value than the TextTiling and Heinone's algorithm.

5   Conclusion

The use of text methods of segmentation by topic would improve the results of many text processing tasks; for example, Text Summarization, News stories segmentation from broadcast news, Information Retrieval, and others. We proposed here a new segmentation algorithm, which has as a goal the segmentation of scientific papers to apply its results on a scientific information retrieval system.

We based our research on term repetition as a lexical cohesion mechanism to determine strongly cohesive segments. The paragraphs were represented by the Vector Space Model. We measure the lexical cohesion by computing the similarity among the paragraphs, and using the cosine measure. In this way we could diminish the possibility of interrupting the subtopic coherence obtaining more cohesive segments, what increases the TextLec performance when we compare it with other segmentation algorithms.

As future work, we propose to continue improving this method looking for other computational models to represent the textual units, and determining with greater robustness the lexical cohesion between these textual units, to detect the subtopics in a document with better precision.

References

1. Angheluta, R., Busser, R., Moens, M.F.: The Use of Topic Segmentation for Automatic Summarization. In: Proceedings of the ACL-2002, Post-Conference Workshop on Automatic Summarization (2002)
2. Beeferman, D., Berger, A., Lafferty, J.: Text segmentation using exponential models. In: Proceedings of the Second Conference on Empirical Methods in Natural Language Processing, pp. 35–46 (1997)
3. Bolshakov, I.A., Gelbukh, A.: Text segmentation into paragraphs based on local text cohesion. In: Proceedings of the 4th International Conference on Text, Speech and Dialogue, Lecture Notes in Artificial Intelligence, pp. 158–166 (2001)
4. Halliday, M.A.K., Hasan, R.: Cohesion in English. Longman Group, New York (1976)
5. Hearst, M.A.: TextTiling: Segmenting Text into Multi-paragraph Subtopic Passages. In: Computational Linguistics, vol. 23(1) (1997)
6. Heinonen, O.: Optimal Multi-Paragraph Text Segmentation by Dynamic Programming. In: Proceedings of COLING-ACL 1998, Montreal, Canada, Cite as: arXiv:cs/9812005v1 [cs.CL] pp. 1484–1486 (1998)
7. Pevzner, L., Hearst, M.A.: A Critique and Improvement of an Evaluation Metric for Text Segmentation. In: Computational Linguistics, vol. 16(1) (2000)
8. Ponte, J.M., Bruce Croft, W.: Text segmentation by topic. In: Peters, C., Thanos, C. (eds.) ECDL 1997. LNCS, vol. 1324, pp. 113–125. Springer, Heidelberg (1997)

9. Reynar, J.C.: An automatic method of finding topic boundaries. In: Proceedings of the 32nd annual meeting on Association for Computational Linguistics, Las Cruces, New Mexico, Student session, Cite as arXiv:cmp-lg/9406017 v1 7 Jun 1994 cmp-lg/9406017 7 Jun 1994 (1994) pp. 331–333 (1994)
10. Reynar, J.C.: Topic Segmentation: Algorithms and Applications. Thesis Doctoral, Presented to the Faculties of the University of Pennsylvania, Pennsylvania (1998)
11. Reynar, J.C.: Statistical Models for Topic Segmentation. In: Proceedings of the 37th annual meeting of the Association for Computational Linguistics on Computational Linguistics, pp. 357–364 (1999) ISBN:1-55860-609-3
12. Stokes, N., Carthy, J., Smeaton, A-F.: SeLeCT: A Lexical Cohesion Based News Story Segmentation System. AI Communications 17(1), 3–12 (2004)
13. Stokes, N.: Applications of Lexical Cohesion Analysis in the Topic Detection and Tracking Domain. Thesis Doctoral, Department of Computer Science Faculty of Science, National University of Ireland, Dublin (2004)

European Portuguese Accent in Acoustic Models for Non-native English Speakers

Carla Simões[1,2], Carlos Teixeira[2], Miguel Dias[1], Daniela Braga[1], and António Calado[1]

[1] Microsoft Language Development Center, Av. Prof. Doutor Aníbal Cavaco Silva, 2744-010 Porto Salvo, Portugal
[2] Departamento de Informática, Faculdade de Ciências da Universidade de Lisboa, Campo Grande, 1749-016 Lisboa, Portugal
`{t-carlas,midias,i-dbraga,i-antonc}@microsoft.com,`
`carlos.teixeira@di.fc.ul.pt`

Abstract. The development of automatic speech recognition systems poses several known difficulties. One of them concerns the recognizer's accuracy when dealing with non-native speakers of a given language. Normally a recognizer precision is lower for non-native users, hence our goal is to improve this low accuracy rate when the speech recognition system is confronted with a foreign accent. A typical usage scenario is to apply these models in applications where European Portuguese is dominant, but where English may also frequently occur. Therefore, several experiments were performed using cross-word triphone based models, which were then trained with speech corpora containing European Portuguese native speakers, English native speakers and English spoken by European Portuguese native speakers.

Keywords: Acoustic Models, European Portuguese accent, Speech Recognition.

1 Introduction

The tremendous growth of technology increased the need of integration of spoken language technologies into our daily applications, providing an easy and natural access to information. These applications are of different nature with different user interfaces. Besides voice enabled Internet portals or tourist information systems, Automatic Speech Recognition (ASR) systems can be used in home user experiences where TV and other appliances could be voice controlled, discarding keyboards or mouse interfaces, or in mobile phones and palm-sized computers for a hands-free and eyes-free manipulation.

When we think of the potential of ASR systems we must deal with the problem of language-dependency. This includes the non-native speaker's speech with different phonetic pronunciations from those of the language native speakers. The non-native accent can be more problematic than a dialect variation on the language. This mismatch depends on the individual speaking proficiency and speaker's

mother tongue. Consequently, when the speaker's native language is not the same as the one that was used to train the recognizer, there is a considerable loss in recognition performance. Teixeira et al. [1], [2] have identified a drop of approximately 15% in the recognition accuracy when using a recognizer of native speakers. This paper describes several experiments and results using Portuguese speaker's using English, in order to improve the recognition performance of English language in a speech recognizer system within a European Portuguese dialogue system.

1.1 Approach and Related Work

A considerable number of methods and experiments for the treatment of non-native speech recognition has already been proposed by other authors. The simplest idea is to use non-native speakers' speech from a target language and train new acoustic models. This method is not reasonable because it can be very expensive to collect data that comprehends all the speech variability involved. An alternative is to apply speaker adaptation techniques such as Maximum Likelihood Linear Regression (MLLR) or Maximum A Posteriori (MAP) adaptation on speaker-independent context to reduce the disparity between the foreign accent and the native accent [3][12]. There is also research on the use of multilingual models using statistical data-driven models known as Hidden Markov Models (HMMs). The purpose is to develop standard acoustic models of phonemes where the similarities of sounds between languages are explored [4], [5], [6]. Another possibility is to include pronunciation variants to the lexicon of the recognizer using acoustic model interpolation [7], where each model of a native-speech recognizer is interpolated with the same model from a second recognizer which depends on the speaker's accent. Stefan Steidl et al. [8] considers that acoustic models of native speech are sufficient to adapt the speech recognizer to the way how non-native speakers pronounce the sounds of the target language. The HMM states from the native acoustic models are interpolated with each other in order to approximate the non-native pronunciation. Another approach is the training of selective data [11], where training samples from different sources are selected concerning a desired target task and acoustic conditions. The data is weighted by a confidence measure in order to control the influence of outliers. An appliance of such method is selecting utterances from a data pool which are acoustically close to the development data.

In this work we apply a number of acoustic modeling techniques to compare their performance on non-native speech recognition. The case of study is focused on English language spoken by European Portuguese speakers. Initially we explore the behavior of an English native model when tested with non-native speakers as well as the performance of a model only trained with non-native speakers. HMMs can be improved by retraining on suitable additional data. Regarding this we have trained a recognizer with a pool of accents, using utterances from English native speakers and English spoken by Portuguese speakers. Furthermore, we used adaptation techniques such as MLLR to reduce the variance between an English native model and the adaptation data, which in this case refers to the European Portuguese accent when speaking English language. To fulfill that task a native English speech recognizer is adapted using the non-native training data. Afterwards, we explore the pronunciation

adaptation through adequate correspondences between phone sets of the foreign and target languages. Considering Bartkova et al. [6], we extended this approach when training new models with a new phone set, created by mapping the English and the Portuguese phone sets in order to support English words in a Portuguese dialogue system.

1.2 Overview

This article is organized as follows: the training and test corpora are presented in section 2. The training process, parameters and baseline systems are described in section 3. The several accomplished experiments such as pooling models, accent adaptation and new phone set mapping are described and discussed in section 4. A brief conclusion and reference to future work is presented in section 5.

2 Corpora

Our study was based on an experimental corpus of English spoken by European Portuguese speakers. This corpus is part of a larger one used in the Teixeira and Trancoso [2]. There are approximately 20 speakers (10 male and 10 female) for each accent, but only the male sub-set corpus was used in these experiments. To accomplish the experiments related with the application of the adaptation techniques or updating models, a native English Corpus (Teixeira and Trancoso) was used [2]. The audio files were sampled at 8 kHz with 16 bits-linear precision. Each speaker has recorded two times approximately 227 English isolated words. The training and the test set are then separated to build a combined model for a speaker-independent speech recognition system. Table 1 shows the implied corpus and the partition for training and testing data set in this study.

Once the wave files were organized, the word level transcriptions were mapped into monophone level and then to triphone level. This procedure is further explained in the following sections. The phone sets of the languages presented in this study are defined using the SAMPA phonetic alphabet.

Table 1. Database overview

Data	Partition	Speakers	Utterances	Minutes
Non-native Data	Training	8	3468	35
	Testing	3	1221	12
Native Data	Training	7	3476	34
	Testing	2	996	9

3 Acoustic Model

All the experiments described in this paper are based on HMMs. Recognition was done using the Viterbi algorithm [9], used for obtaining the best sequence of states that match the sequences of speech frames that correspond to a certain unit. Our

system is a cross-word triphone system and it is developed in an HTK based training tool [14] [15]. Each HMM has 3 states; each state represents a short segment of speech. This segment is the result of splitting the spoken utterances into frames of 10 milliseconds each. This representation is described mathematically by Gaussians probability distributions. Multiple mixture Gaussians are used and acoustically similar information is shared across HMMs by sharing/tying states called senones [16].

To train a set of HMMs, every file of training data must have an associated phone level transcription. The starting point of phone transcription is an orthographic transcription in HTK label format, a Master Label File (MLF), which is a single file containing a complete set of transcriptions. This allows the same transcriptions to be used with different versions of the speech data to be stored in diferent locations.

The training begins by converting word level transcriptions into monophone level transcriptions. Once reasonable monophone HMMs have been created, a *forced alignment* of the training data can be performed. Concerning this, a new phone level MLF is created in which the choice of pronunciations depends on the acoustic evidence. This new MLF can be used to perform a final re-estimation of the monophone HMMs. These models are iteratively updated by repeatedly traversing the training data and mapping the models to the monophone labels in the transcription.

After producing an initial monophones' model, the respective cross-word triphones are cloned for each monophone. This is done in two steps, first, the monophone transcriptions are converted to cross-word transcriptions and the cross-word triphones re-estimated to produce initial single-mixture models. Then, similar acoustic states of these triphones are clustered and tied to ensure that all state distributions can be robustly estimated. Since the system size is vastly reduced at this stage, we can increase the number of mixtures per senone. This leads to an initialized cross-word acoustic model, which is used to run through the training data and re-label the transcriptions to allow multiple pronunciations. After that these cross-word transcriptions are re-used to update the cross-word acoustic model leading once again to the final cross-word triphone system (Fig. 1 represents the training process described above) [14].

To carry out the experiments we have defined 1500 tying states (senones). For an initial number of mixtures we have a total of 12 mixtures and as a final smoothing stage we reduce the average total mixtures of the final system to 8 mixtures. For

Feature Extraction			
Monophone Generation			
Initialization	Alignment	Update	Triphone Cloning
Triphone Clustering			
Clustering	Mix-Up	Alignment	Mix-Down
Triphone Training Model			
Clustering	Mix-Up	Pruning	Final Training
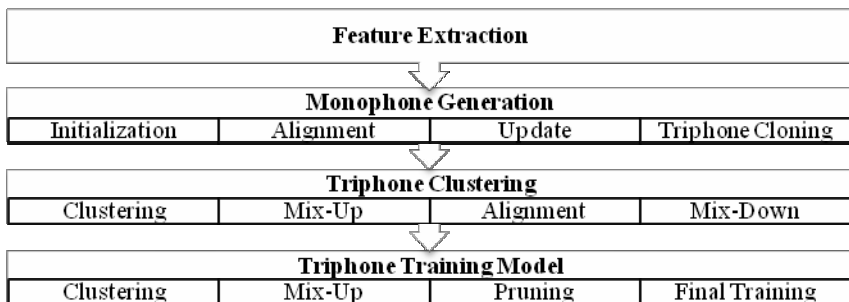
Fig. 1. Training Acoustic Models Flowchart

testing the several speech recognition systems we have defined a set of data dedicated to testing (see Table 1). Because we are talking about command and control systems, a grammar, which specifies the sequences of recognizable words, had to be defined. For that purpose a context free-grammar (CFG) was built with all the words found in the test set.

3.1 Baseline Systems

Both non-native and native acoustic models were trained with the respective training set described in Table 1. The training lexicon that lists the phonetic pronunciation of all the words in the corpus uses the English phone set. The parameters and training procedure are the same for the two models. The non-native and native speech engines were tested with the same corpus. Table 2 shows the performance on the non-native and native test set when using the both models. The remaining scores show better recognition performance when non-native models are used for the foreign accent.

Table 2. Accuracy rate on non-native and native data (WER %)

Models	Non-Native Models	Native Models
Non-Native test set	6.28%	13.41%
Native test set	22.89%	4.09%

4   Experiments and Results

We explore different acoustic modeling methods to test their efficiency for recognition improvement on non-native speech. The results refer to experiments with cross-word triphone models which were obtained in a process reported in [14]. The different experiments and their results are described in the following sections.

4.1 Pooled Models

Non-native speech recognition can be viewed as speaker independent recognition problem, for which the traditional approach has been pooling all the speech data from as many speakers as possible as if it would belong to a single speaker. Pursuing this idea the native model was retrained with the available non-native data (pooled models). As we can see (Fig. 2) the improvement from pooling the native and non-native training data indicates that recognition of non-native data can profit from native data. Since both corpus have almost the same training utterances, one way of weighting the non-native training utterances is to set up the weight parameter of the non-native training corpus.

The optimal weighting factor was found to be 2.0 for non-native data where recognition scores reveal a Word Error Rate (WER) of 6.02% (non-native test) and 4.17% (native test). The recognition performance is slightly better when comparing these results with the English baseline system (Table 2). In [13] a pooled model using English native data and German accent shows an accuracy increasing of 1.2%.
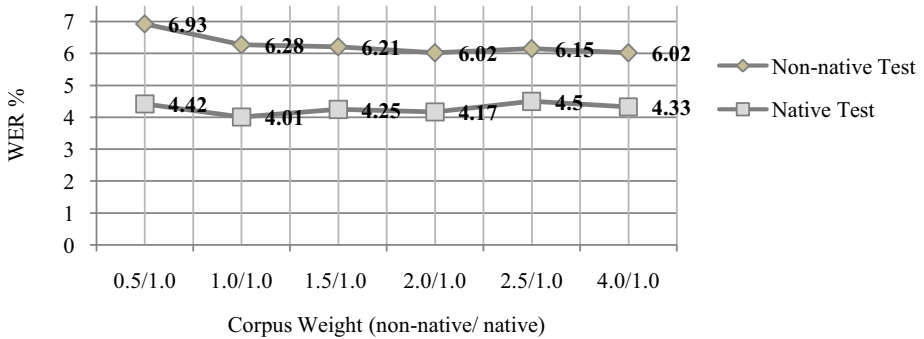
Fig. 2. Pooled models using different corpus weights for non-native corpus

4.2 Adapting English Native Model

The adaptation of acoustic models reduces the mismatch between a certain model set and the adaptation data. Adaptation can be at speaker level, environment or characteristics of a group of speakers such as foreign accent. The most used techniques are the Maximum Likelihood Linear Regression (MLLR) [12] and the maximum a-posteriori (MAP) [3]. MLLR computes a set of transformations, where one single transformation is applied to all models in a transformation class. More specifically it estimates a set of linear transformations for the context and variance parameters of a Gaussian mixture HMM system. The effect of these transformations is to shift the component means and to alter the variances in the initial system so that each state in the HMM system is more likely to generate the adaptation data.

In MAP adaptation we need a prior knowledge of the model parameter distribution. The model's parameters are re-estimated individually requiring more adaptation data to be effective. When larger amounts of adaptation training data become available, MAP begins to perform better than MLLR, due to this detailed update of each component.

Since we have a small amount of data in this experiment we used only the MLLR method, applied to English native model (baseline model) adapted with non-native corpus. Each model adaptation was iterated 4 times. Adaptation has improved performance on non-native recognition, revealing 6.21% WER for non-native test. On a native English test no changes were found, giving the same WER as the native model, 13.41%.

4.3 Mapping English Phonemes into Portuguese Phonemes

Speaking a foreign language can change the native phonological structure (e.g. the English pharyngeal voiceless fricative in <hit> is commonly not articulated by Portuguese native speakers when speaking in English, since this phoneme is not present in the Portuguese phone set) or adapt unfamiliar sounds to similar/closer ones from their native phoneme inventory [6][10]. This also depends on the speaker proficiency, which will determine how different a native accent is from a foreign accent.

In order to get better recognition results on non-native accents, English phonemes were mapped into Portuguese phonemes. The mapping was done by a linguist expert who defined which phoneme inventory should be taken into account to describe a

standard Portuguese English pronunciation. This phoneme inventory was selected bearing in mind the pronunciation of a Portuguese prestigious group/community, with a good knowledge of English language. As prestigious group we mean the higher literacy level group that uses a dominant variant or pattern dialect of a given language [17] [18].

Using the phonetic inventory SAMPA, 33 phones were defined to transcribe the English language when spoken by native Portuguese speakers. The majority of English phones suffered a direct mapping, except those that represent non Portuguese existing sounds. One example of that is the dental voiceless fricative [T] (e.g. <thriller>, <thirties>), that in European Portuguese language is converted to a dental voiceless plosive [t] or alveolar voiceless fricative [s]. We consider that the prestigious group recognizes this sound so we have included it in our new phone set. Another non existing sound in European Portuguese is the pharyngeal voiceless fricative [h] (e.g. <hang>). However, for the prestigious group there is, for example, differentiation in pronunciation between <and> and <hand>, which made us include this phone in the English-Portuguese mapped phone set.

Finally, another important difference we need to consider is the approximant [r] (e.g. <red>). This phone does not exist in the European Portuguese phone set. Despite this, in some words, when a Portuguese speaker uses English, like <red>, we can say [R E d] (PT SAMPA), in other cases such as <car> we say [k a r] (PT SAMPA). For this reason we added this phone to the new mapped phone set.

Afterwards, new word transcriptions of the corpus vocabulary were required, following an accurate process accomplished by the linguist expert. The initial English phonetic transcription was directly mapped to the Portuguese form (using the new phone set), which is not enough for a reliable representation of English spoken with a Portuguese accent. An improved phonetic transcription was accomplished by modifying the phonetic transcription of each word, taking into account the Portuguese prestigious accent while using English. An example of that adaptation is the way an English or a Portuguese speaker will pronounce words that end with a plosive consonant such as [t] (e.g <art>). In English we should transcribe the word <art> like [Q r t] (PT SAMPA) but in Portuguese we say [Q r t @] (PT SAMPA).

Results reveal 7.26% of WER for the new trained models using the phone set described above. The recognition accuracy has decreased, when comparing it with the baseline non-native system or the pooled model experiment, but it is still far from the English native model when tested with a non-native test set. This is an encouragement for continuing exploring this subject.

Another experiment was training a pooled model using this new phone set, but instead of using the English native model, we experimented it with a Portuguese native model. Doing this we are representing a European Portuguese recognition system that also supports English words with a Portuguese accent. The Portuguese native model was trained with 87 hours of speech for a total of 553 speakers (266 male and 287 female). The audio files were sampled at 16 kHz with 16 bits-linear precision. The results of such experiment were encouraging, as the system reveals 9.81% of WER when testing with the non-native test set. This value is still above the baseline English system results, which means that an accurate phonetic representation may improve recognition performance of non-native speakers.

5   Conclusions

In this paper we have explored several ways of adapting automatic speech recognition systems to non-native speakers. The results presented in this paper show that a small amount of data can be successfully used for the improvement of non-native accent recognition. Even though some applied methods reveal worst performance results when compared to the only non-native trained models, there are considerably improvements on the English native models recognizing non-native accents.

The following graphic (Fig. 3) gives the best results and its proportion between methods. As we can infer from the last experience, where we use the mapped phone set to train new models, the test using the English native test corpus was not performed. In this experiments we work with a different phone set from the one used in the English native model, so the results related with testing those models with English native speaking are not relevant for the experiment.
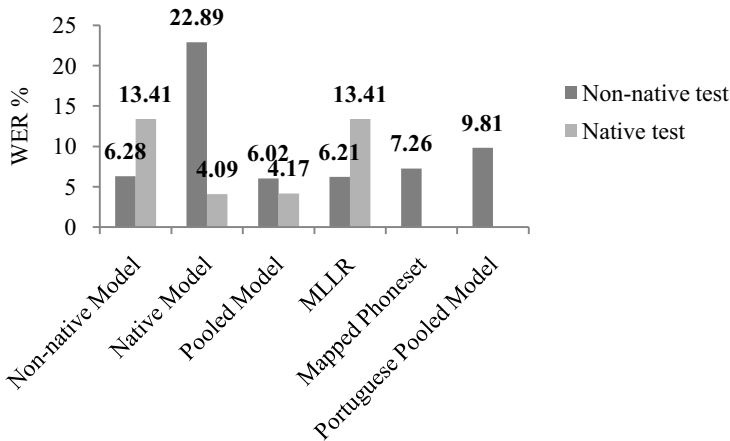
Fig. 3. Best results of the different experiments

In the future, we plan to explore some of these methods, especially to continue the study of pronunciation in the context of Portuguese speaking foreign words, in order to improve recognition performance of dialogue systems.

References

1. Teixeira, C., Trancoso, I., Serralheiro, A.: Recognition of Non-Native Accents. In: Eurospeech, vol. 5, pp. 2375–2378 (1997)
2. Teixeira, C., Trancoso, I.: Word Rejection using Multiple Sink Models. In: Proc. ICSLP, pp. 1443–1446, Banff (1992)
3. Zavaliagkos, G., Schwartz, R., Makhoul, I.: Batch, Incremental and Instantaneous Adaptation Techniques for Speech Recognition. In: Proc. ICASSP (1995)
4. Kunzmann, S., Fischer, V., Gonzalez, J., Emam, O., Gunther, C., Janke, E.: Multilingual Acoustic Models for Speech Recognition and Synthesis, IEEE. In: ICASSP (2004)

5. Kohler, J.: Multi-lingual Phoneme Recognition Exploiting Acoustic-Phonetic Similarities of Sounds, Siemens AG, Munich, Germany
6. Bartkova, K., Jouvet, D.: Multiple models for improved speech recognition for non-native speakers. In: SPECOM (2004)
7. Livescu, K., Glass, J.: Lexical Modelling of Non-Native Speech for Automatic Speech Recognition. In: ICASSP (2000)
8. Steidl, S., Stemmer, G., Hacker, C., Nöth, E.: Adaptation in the Pronunciation Space for Non-Native Speech Recognition. In: ICSLP, Korea (2004)
9. Rabiner, L.R.: A tutorial on hidden Markov models and selected applications in speech recognition. Proceedings of the IEEE 77(2), 257–286 (1989)
10. Flege, J.E., Schirru, C., MacKay, I.: Interaction between the native and second language phonetic subsystems. Speech Communication 467–491 (2003)
11. Arslan, L.M., Hansen, J.H.L.: Selective Training in Hidden Markov Model Recognition. IEEE Transactions on Speech and Audio Processing 7(1), 46–54 (1999)
12. Leggetter, C.J., Woodland, P.C.: Speaker Adaptation of HMMs Using Linear Regression (1994)
13. Wung, Z., Schultz, T., Waibel, A.: Comparison of Acoustic Model Adaptation Techniques on Non-Native Speech, IEEE. In: ICASSP (2003)
14. Morton, R.: The Training Guide, A Guide for Training Acoustic Models, Microsoft Document
15. Young, S., Kershaw, D., Odell, J., Ollason, D., Valtchev, V., Woodland, P.: The HTK Book (1999)
16. Woodland, P., Young, S.: The HTK Tied-State Continuous Speech Recognition. In: Proc. Eurospeech (1993)
17. Ferreira: Variação linguística: perspectiva dialectológica, in Faria et al. 1996. Introdução á Linguística Geral e Portuguesa, Lisboa, Caminho: 483
18. Fromkin, Rodman: Introdução á Linguagem, Coimbra, Almedina: 273

A Statistical User Simulation Technique for the Improvement of a Spoken Dialog System⋆

Lluís F. Hurtado, David Griol, Emilio Sanchis, and Encarna Segarra

Departament de Sistemes Informàtics i Computació (DSIC)
Universitat Politècnica de València (UPV)
Camí de Vera s/n, 46022 València, Spain
{lhurtado,dgriol,esanchis,esegarra}@dsic.upv.es

Abstract. In this paper, we present a statistical approach for the automatic generation of dialogs by means of a user simulator. This technique can be used to generate dialogs with reduced effort, facilitating the evaluation and improvement of spoken dialog systems. In our approach for user simulation, the user answer is selected taking into account the history of the dialog and the last system turn, as well as the objective(s) set for the dialog. The user model is automatically learned from a training corpus that is labeled in terms of dialog acts. This methodology has been evaluated within the framework of the DIHANA project, whose goal is the design and development of a dialog system to access a railway information system using spontaneous speech in Spanish.

Keywords: spoken dialog systems, user simulation, dialog management, dialog system evaluation.

1   Introduction

A dialog system is a man-machine interface that is able to recognize and to understand a spoken input and to produce an oral output as answer. Different modules usually take part in order to carry out this final goal: they must recognize the pronounced words, understand their meaning, manage the dialog, make the error handling, access to the databases and generate the oral answer. Nowadays, diverse projects have developed systems to provide information and other services automatically; for example, information and booking of airplane and train trips [1] [2] [3] [4] and other types of information [5] [6] [7].

An important area of research within the framework of dialog systems is the development of techniques that facilitate the evaluation of these systems and the learning of an optimal strategy for dialog management. A technique that has attracted increasing interest in the last decade is based on the automatic generation of dialogs between the Dialog Manager (DM) and an additional module, called user simulator, which represents user interactions with the dialog system. The user simulator makes it possible to

generate a great number of dialogs in a very simple way. Therefore, this technique reduces the time and effort that would be needed for the evaluation of a dialog system with real users each time the system is modified.

The construction of user models based on statistical methods has provided interesting and well-founded results in recent years and is currently a growing research area. The overall goal of techniques of this kind is to learn optimal strategies for dialog management from training data. A probabilistic user model can be trained from a corpus of human-computer dialogs to simulate user answers. Therefore, it can be used to learn a dialog strategy by means of its interaction with the DM. In the literature, there are several approaches that are related to the development of corpus-based methods for user simulation. These describe different alternatives for carrying out the evaluation of the techniques and for learning optimal management strategies and evaluating the dialog system [8] [9] [10] [11]. A summary of user simulation techniques for reinforcement learning of the dialog strategy can be found in [12].

We have developed different statistical approaches for the design of a DM [13] [14] and for user modeling [15]. The methodology that we present in this paper for developing a user simulator extends our work to model the system behavior, which is described in [14]. The user simulator is automatically learned from a training corpus that is labeled in terms of dialog acts. In our system, both DM and user behaviors are corpus-based.

The new user turn is selected by taking into account the information provided by the simulated user throughout the history of the dialog, the last system turn, and the objective(s) set for the dialog. The user turn, which is represented as dialog acts, is selected using the probability distribution provided by a neural network. With this methodology, an initial dialog corpus can be extended by increasing its variability and detecting dialog situations in which the DM does not provide an appropriate answer.

This approach has been used for the construction of a user simulator within the framework of the DIHANA project [16]. This project undertakes the design and development of a dialog system for access to an information system using spontaneous speech. The domain of the project is the query to an information system about railway timetables, fares, and services in Spanish.

Section 2 briefly presents the main characteristics of the dialog system developed for the DIHANA project. It also describes a corpus and the semantic and dialog-act labeling that is used for learning the user model. Section 3 presents the proposed user simulator. Section 4 and 5 present an evaluation of this approach and our conclusions.

2   The System Architecture

Within the framework of the DIHANA project, we have developed a mixed-initiative dialog system to access information systems using spontaneous speech [16]. We have built an architecture that is based on the client-server paradigm. The system consists of six modules: an automatic speech recognition (ASR) module, a natural language understanding (NLU) module, a dialog manager (DM), a database query manager, a natural language answer generator, and a text-to-speech converter.

We are currently using the CMU Sphinx-II system (*cmusphinx.sourceforge.net*) in our speech recognition module. For speech output, we have integrated the Festival
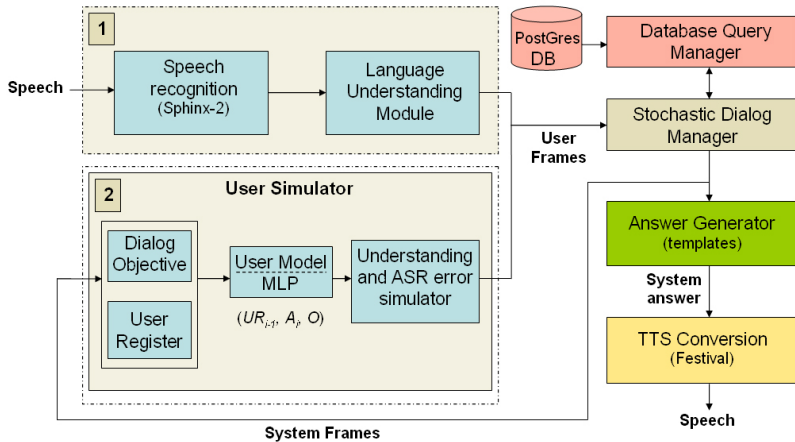
Fig. 1. Architecture of the DIHANA dialog system. [1] Interaction with real users. [2] Operation with the user simulator.

speech synthesis system (*www.cstr.ed.ac.uk/projects/festival*). The specific information relative to our task is stored in a PostGres database using dynamic information extracted from the web.

Our dialog system has two operation modes. First, the system uses the ASR and the NLU modules for the normal interaction between the system and the real users. Second, the system allows the automatic acquisition of dialogs by means of the user simulator module. Figure 1 shows the modular architecture of our system: (1) the interaction with real users and (2) the operation with the user simulator.

The behavior of the principal modules that make up the dialog system is based on statistical models that are learned from a dialog corpus that was acquired and labeled within the framework of the DIHANA project.

2.1 The DIHANA Corpus

A set of 900 dialogs (6,280 user turns) was acquired for the DIHANA project using the Wizard of Oz technique (WOz). Real ASR and NLU modules were used for the acquisition and the WOz played the role of the DM following a predefined strategy. Five files were stored for each acquired dialog: the output of the recognizer, the output of the understanding module, the answer (dialog act) generated by the system, the values of the attributes during the successive turns, and the queries made to the Database. This information is used to model the behavior of the system depending on the succession of dialog acts, the semantic representation of the user turn, and the values associated to the attributes (and their confidence scores). The characteristics of this corpus are shown in Figure 2.

For the acquisition, a set of 300 scenarios were defined. These scenarios can be classified into two categories depending on the number of objectives. Type S1 defined only one objective for the dialog and Type S2 defined two objectives.

Number of users	225
Number of dialogs/user	4
Number of user turns	6280
Average number of user turns/dialog	7
Average number of words/user turn	7.74
Vocabulary	823
Duration of the recording (hours)	10.8

Fig. 2. Main characteristics of the DIHANA corpus

In order to learn statistical dialog models, the dialogs were labeled in terms of dialog acts. The user dialog acts correspond to the classical frame representation of the meaning of the utterance. In other words, one or more concepts represent the intention of the utterance, and a sequence of attribute-value pairs contains the information about the values given by the user. The Understanding Module takes the sentence supplied by the recognition process as input and generates one or more frames as output. In this task, we defined eight concepts and ten attributes. There are two kinds of concepts:

1. *Task-dependent concepts*: they represent the concepts the user can ask for, such as *Hour*, *Price*, *Train-Type*, *Trip-Time* and *Services*.
2. *Task-independent concepts*: they represent typical interactions in a dialog, such as *Affirmation*, *Negation* and *Not-Understood*.

The attributes are: *Origin*, *Destination*, *Departure-Date*, *Arrival-Date*, *Departure-Hour*, *Arrival-Hour, Class*, *Train-Type*, *Order-Number* and *Services*.

The system turns were labeled using a set of three-level dialog acts. The first level describes the general acts of any dialog independently of the task. The second level represents the concepts involved in the turn and is specific to the task. The third level represents the values of the attributes given in the turn. The following labels were defined for the first level: *Opening*, *Closing*, *Undefined*, *Not-Understood*, *Waiting*, *New-Query*, *Acceptance*, *Rejection*, *Question*, *Confirmation* and *Answer*. The labels defined for the second and third level were the following: *Departure-Hour*, *Arrival-Hour*, *Price*, *Train-Type, Origin*, *Destination*, *Date*, *Order-Number*, *Number-Trains*, *Services*, *Class*, *Trip-Type*, *Trip-Time* and *Nil*. Each turn of the dialogs was labeled with one or more dialog acts. From this kind of detailed dialog act labeling and the values of attributes obtained during a dialog, it is straightforward to construct a sentence in natural language.

An example of the user/system labeling is shown below:

User turn:
I would like to know the timetables from Valencia to Madrid.
Semantic representation:
(Hour)
Origin: Valencia
Destination: Madrid

System turn:
Do you want timetables to Madrid?
Three-level labeling:
(Confirmation:Arrival-Hour:Destination)

A more detailed description about the WOz acquisition and the corpus labeling can be found in [14].

3 The User Simulator

In our system, the user simulator replaces the functions performed by the ASR and the NLU modules. It generates frames in the same format defined for the output of the NLU module, i.e, in the format expected by the DM.

The methodology that we have developed for user simulation is based on the statistical modelization of the sequences of user and system dialog acts. As stated above, the user answers are generated taking into account the information provided by the simulator throughout the history of the dialog, the last system turn, and the objective(s) predefined for the dialog. A labeled corpus of dialogs is used to estimate the user model. The formal description of the proposed model extends the methodology proposed in DIHANA for dialog management:

Let A_i be the output of the dialog system (the system answer) at time i, expressed in terms of dialog acts. Let U_i be the semantic representation of the user turn. We represent a dialog as a sequence of pairs (*system-turn, user-turn*):

$$(A_1, U_1), \cdots, (A_i, U_i), \cdots, (A_n, U_n)$$

where A_1 is the greeting turn of the system (the first turn of the dialog), and U_n is the last user turn. We refer to a pair (A_i, U_i) as S_i, the state of the dialog sequence at time i.

Given this representation, the objective of the user simulator at time i is to find an appropriate user answer U_i. This selection, which is a local process for each time i, takes into account the sequence of dialog states that precede time i, the system answer at time i, and the objective of the dialog $\mathcal{O}$. If the most probable user answer U_i is selected at each time i, the selection is made using the following maximization:

$$\hat{U}_i = \underset{U_i \in \mathcal{U}}{\operatorname{argmax}} P(U_i | S_1, \cdots, S_{i-1}, A_i, \mathcal{O})$$

where set $\mathcal{U}$ contains all the possible user answers.

As the number of possible sequences of states is very large, we establish a partition in this space (i.e., in the history of the dialog preceding time i).

Let UR_i be the user register at time i. The user register is defined as a data structure that contains the information about concepts and attribute values provided by the user throughout the previous history of the dialog. The information contained in UR_i is a summary of the information provided by the sequence $S_1, \ldots, S_{i-1}$. Different state sequences can lead to the same UR.

The partition that we establish in this space is based on the assumption that *two different sequences of states are equivalent if they lead to the same UR.* This assumption

provides a great reduction in the number of different histories in the dialogs at the expense of a loss in the chronological information. However, we do not consider the order in which the information is supplied by the user to be a relevant factor in determining the next user turn U_i.

After applying the above considerations and establishing the equivalence relations in the histories of the dialogs, the selection of the best U_i is given by:

$$\hat{U}_i = \underset{U_i \in \mathcal{U}}{\operatorname{argmax}} P(U_i | UR_{i-1}, A_i, \mathcal{O}) \tag{1}$$

In our previous work on dialog management, we proposed the use of a multilayer perceptron (MLP) to obtain the system answer. In this work, we also propose using the MLP to make the assignation of a user turn. The input layer receives the current situation of the dialog, which is represented by the term $(UR_{i-1}, A_i, \mathcal{O})$ in Equation 1. The values of the output layer can be viewed as the a posteriori probability of selecting the different user answers defined for the simulator given the current situation of the dialog. The choice of the most probable user answer of this probability distribution leads to Equation 1. In this case, the user simulator will always generate the same answer for the same situation of the dialog. Since we want to provide the user simulator with a richer variability of behaviors, we base our choice on the probability distribution supplied by the MLP on all the feasible user answers.

3.1 Codification Defined for the MLP Classifier

For the DIHANA task, the UR is a sequence of 15 fields that correspond to the five concepts (*Hour*, *Price*, *Train-Type*, *Trip-Time*, and *Services*) and ten attributes (*Origin*, *Destination*, *Departure-Date*, *Arrival-Date*, *Departure-Hour*, *Arrival-Hour, Class*, *Train-Type*, *Order-Number*, and *Services*) defined for our task. For the user simulator to determine the next user turn, we have assumed that the exact values of the attributes are not significant. Even though these values are important for accessing the database and for constructing the output sentences of the system, the only information necessary to determine the next user action is the presence or absence of concepts and attributes. Therefore, the information we used from the UR is a codification of this data in terms of two values, $\{0, 1\}$, for each field in the UR according to the following criteria: **0** if the concept is not activated, or the value of the attribute is not given; **1** if the concept or attribute is activated.

For the DM of the DIHANA task, we have defined a total of 51 possible system answers taking into account the different combinations of three-level labeling. Thus, the system answer is modeled using a variable with 51 bits.

3.2 The Error Simulator

Our corpus includes information about the errors that were introduced by the ASR and the NLU modules during the acquisition. This information also includes confidence measures, which are used by the DM to evaluate the reliability of the concepts and attributes generated by the NLU module.

An error simulator module has been designed to perform error generation and the addition of confidence measures in accordance with an analysis made of our corpus. This information modifies the frames generated by the user simulator. Experimentally, we have detected 2.7 errors per dialog. This value can be modified to adapt the error simulator module to the operation of any ASR and NLU modules. As future work, we want to make a more detailed study of the errors introduced in our corpus.

4   Evaluation

To carry out the evaluation of the simulation process, 50,000 dialogs of each one of the two types of scenarios defined (Type S1 and Type S2) were generated.

Two criteria were defined for closing the dialog. The first criterion consists of finalizing the dialog when the number of system turns exceeds a threshold obtained experimentally. The second criterion is applied to generate a user request to close the dialog when the manager has provided the set of information defined for the objective(s) of the dialog. The successful dialogs are those that end when the second criterion is applied.

We defined five measures for the evaluation of the simulated dialogs: the number of successful dialogs (SD), the average number of turns per dialog (NT), the number of different successful dialogs (DD), the number of turns of the shortest dialog (TS), and the number of simulated dialogs that are contained in our initial corpus (CD). Using these measures, we tried to evaluate the success of the simulated dialogs as well as its efficiency and variability with regard to the different objectives.

Table 1 shows the values of the different measures obtained for the simulated corpus of 100,000 dialogs. Taking the two types of scenarios into account, the simulator generated a total of 22,614 dialogs that achieved their objectives (22.6%). The number of simulated dialogs that were initially contained in the WOz corpus, CD, corresponds to only a small partition of these dialogs (1.2%). It can be viewed that Type S2 dialogs are more complicated to simulate due to the two objectives must be satisfied.

Table 1. Evaluation of the simulated corpus

Type	SD	NT	DD	TS	CD
S1	18,400	10.4	11,550	5	224
S2	4,214	12.1	3,833	7	42

First, we evaluated the behavior of the original DM that was learned using the training corpus (obtained by WOz). Then, we evaluated its evolution when the successful simulated dialogs were incorporated to the training corpus. A new DM model was learned each time a new set of simulated dialogs was generated. For this evaluation, we used a test partition that was extracted from the DIHANA corpus (20% of the samples). We considered four measures: the number of unseen situations (*#unseen*), i.e. the dialog situations that are present in the test partition but not in the corpus used for learning the DM; the number of answers provided by the DM that would cause the failure of the dialog (*#error*); the percentage of answers provided by the DM that exactly

follow the strategy defined for the WOz to acquire the training corpus (*%strategy*); and the percentage of answers provided by the DM that are coherent with the current state of the dialog although they do not follow the original strategy defined for the WOz (*%coherent*).

Figure 3 and Figure 4 respectively show how *#unseen* and *#error* decreased when the training corpus was enriched by adding the simulated dialogs, which is the expected behavior. These measures continued to decrease until 60,000 dialogs were simulated.
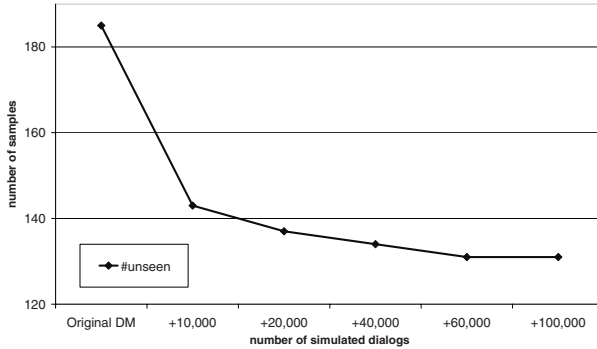
Fig. 3. Evolution of the *#unseen* with regard to the incorporation of new simulated dialogs
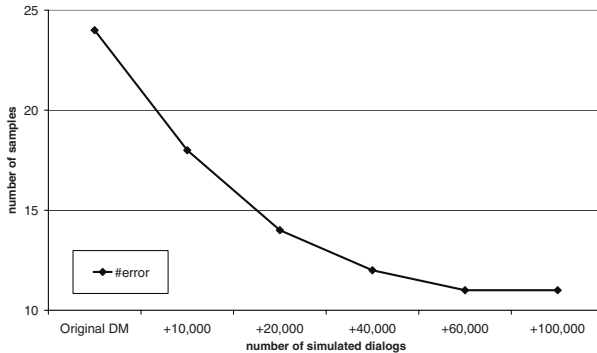
Fig. 4. Evolution of the *#error* with regard to the incorporation of new simulated dialogs

Figure 5 shows the evolution of *%strategy* and *%coherent*. It can be observed that the DM improved the generation of coherent answers when the new dialogs were incorporated. In addition, the number of coherent answers that are different from those defined in the WOz strategy was increased. In other words, the original strategy was modified, thereby allowing the DM to tackle new situations and generate new coherent answers.
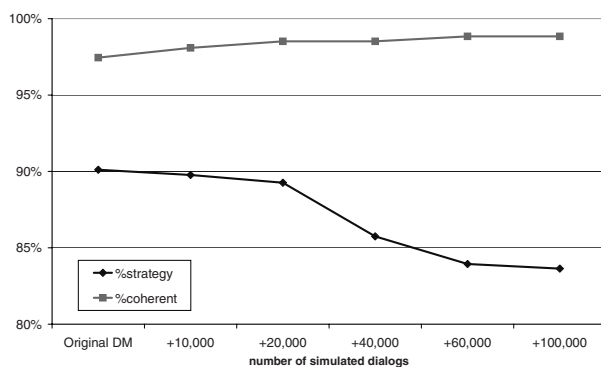
Fig. 5. Evolution of the *%strategy* and *%coherent* with regard to the incorporation of new simulated dialogs

5   Conclusions

In this paper, we have presented a corpus-based approach for the development of a user simulator. The proposed methodology allows the generation of new dialogs with little effort. We have described an evaluation of this methodology within the framework of a dialog system, in which both the DM and the user simulator are statistically modeled from a data corpus. The definition of the user register allows the user simulator to take into account the complete history of the dialog in order to generate the next user turn.

The results of the evaluation demonstrate that the coverage of the DM is increased by incorporating the successful simulated dialogs and that the number of unseen situations can be reduced. A study of the evolution of the strategy followed by the DM has also been carried out. This study shows how the DM modifies its strategy by detecting new correct answers that were not defined in the initial strategy. As future work, we plan to apply this technique to a new domain, the booking of sports installations, to evaluate the task-portability.

References

1. Seneff, S., Polifroni, J.: Dialogue management in the Mercury flight reservation system. In: Proc. ANLP-NAACL 2000, Satellite Workshop pp. 1–6 (2000)
2. Lamel, L., Rosset, S., Gauvain, J., Bennacef, S., Garnier-Rizet, M., Prouts, B.: The LIMSI ARISE System. Speech Communication 4(31), 339–353 (2000)
3. Rudnicky, A., Thayer, E., Constantinides, P., Tchou, C., Shern, R., Lenzo, K., Xu, W., Oh, A.: Creating natural dialogs in the Carnegie Mellon Communicator system. Proceedings of Eurospeech 1(4), 1531–1534 (1999)
4. Ward, W., Pellom, B.: The CU Communicator system. In: Proc. of ASRU-IEEE Workshop, Keystone, Colorado (USA) (1999)
5. Bohus, D., Grau, S., Huggins-Daines, D., Keri, V., Krishna, G., Kumar, R., Raux, A., Tomko, S.: Conquest - an open-source dialog system for conferences. In: Proc. HLT-NAACL 2007, Rochester, NY (2007)

6. Litman, D., Singh, S., Kearns, M., Walker, M.: Njfun: a reinforcement learning spoken dialogue system. In: Proceedings of the ANLP/NAACL 2000 Workshop on Conversational Systems, Seattle, USA, Association for Computational Linguistics pp. 17–20 (2000)
7. Zue, V., Seneff, S., Glass, J., Polifroni, J., Pao, C., Hazen, T., Hetherington, L.: Jupiter: A telephone-based conversational interface for weather information. IEEE Trans. on Speech and Audio Proc. 8(1), 85–96 (2000)
8. Georgila, K., Henderson, J., Lemon, O.: User Simulation for Spoken Dialogue Systems: Learning and Evaluation. In: Proc. of Interspeech 2006-ICSLP, Pittsburgh, pp. 1065–1068 (2006)
9. Pietquin, O., Dutoit, T.: A probabilistic framework for dialog simulation and optimal strategy learning. IEEE Transactions on Speech and Audio Processing 14, 589–599 (2005)
10. Scheffler, K., Young, S.: Automatic learning of dialogue strategy using dialogue simulation and reinforcement learning. In: Proc. Human Language Technology, San Diego, pp. 12–18 (2002)
11. Cuayáhuitl, H., Renals, S., Lemon, O., Shimodaira, H.: Learning multi-goal dialogue strategies using reinforcement learning with reduced state-action spaces. In: Proc. of InterSpeech'06-ICSLP, Pittsburgh, pp. 469–472 (2006)
12. Schatzmann, J., Weilhammer, K., Stuttle, M., Young, S.: A Survey of Statistical User Simulation Techniques for Reinforcement-Learning of Dialogue Management Strategies. Knowledge Engineering Review 21(2), 97–126 (2006)
13. Griol, D., Hurtado, L., Segarra, E., Sanchis, E.: Managing unseen situations in a stochastic dialog model. In: Proc. of AAAI Workshop Stadistical and Empirical Approaches for Spoken Dialogue Systems, Boston, pp. 25–30 (2006)
14. Hurtado, L.F., Griol, D., Segarra, E., Sanchis, E.: A stochastic approach for dialog management based on neural networks. In: Proc. of Interspeech 2006-ICSLP, Pittsburgh, pp. 49–52 (2006)
15. Torres, F., Sanchis, E., Segarra, E.: Learning of stochastic dialog models through a dialog simulation technique. In: Proc. of Eurospeech 2005, Lisbon, pp. 817–820 (2005)
16. Griol, D., Torres, F., Hurtado, L., Grau, S., García, F., Sanchis, E., Segarra, E.: A dialog system for the DIHANA Project. In: Proc. of SPECOM 2006, S. Petersburgh (2006)

A New Approach for Cervical Vertebrae Segmentation

Saïd Mahmoudi and Mohammed Benjelloun

Computer Science Department, Faculty of Engineering,
rue de Houdain 9 Mons, B-7000, Belgium
{Said.Mahmoudi,Mohammed.Benjelloun}@fpms.ac.be

Abstract. Efficient content-based image retrieval of biomedical images is a challenging problem of growing research interest. This paper describes how X-ray images of the spinal columns are analyzed in order to extract vertebra regions and contours. Our goal is to develop a computer vision tool able to determine a global polygonal region for each vertebra in first time. After this step, we apply a polar signature system in order to extract the effective contour of each vertebra. Finally, we use an edge closing method exploiting a polynomial fitting. The aim is to propose a closed contours detection representing each vertebra separately. We suggest an application of the proposed method which consists on an evaluation of vertebra motion induced by their movement between two or several positions.

Keywords: Vertebral Mobility Analysis, X-ray Images, Region Vertebra Selection, Contour Detection, Template Matching, Polar Signature.

1 Introduction

Medical staffs often examine X-rays of spinal columns to determine the presence of abnormalities or dysfunctions and to analyze the vertebral mobility. Nevertheless, the result is generally qualitative and subjective. To help them to establish a good diagnosis, medical image processing and analysis applications automate some tasks dealing with the interpretation of these images. It permits the extraction of quantitative and objective parameters related to the form and the texture included in pictures. These image parameters allow to measure, compare and detect the changes between images. X-ray images segmentation is an essential task for morphology analysis and motion estimation of the spinal column. Several methods have been proposed in the literature to analyze and to extract vertebra contours from X-ray images [11]. Extensive research has been done by Long et al. [1,9] to automatically identify and classify spinal vertebrae. They formulated the problem of spine vertebra identification by three level of processing: In the first stage they used an heuristic analysis combined with an adaptive thresholding system to obtain basic orientation data, providing basic landmarks in the image; in the second stage, boundary data for the spine region of interest were defined by solving an optimization problem; the third stage was expected

to use deformable template processing to locate individual vertebra boundaries at finely grained level. The main drawback of this approach is the need of a good grayscale thresholding. Stanley and Long [2] proposed a new method of subluxation detection. They used the spatial location of each vertebra in the spinal column and the variation in its position. They applied a second order spinal column approximation by using vertebral centroids. The goal of their approach was to quantify the degree to which vertebra areas within the image are positioned on their posterior sides.

In an other work, Kauffmann et al. [4] first detected the axis of the spinal column by manually placing points along it and fitting a curve through them. The fitted curve was used to initialize and rigidly match templates of vertebral body with the image data to obtain vertebral outlines. Verdonck et al. [5] manually indicated specific landmarks in the image and founded others using an interpolation technique. The landmarks, together with a manually indicated axis of the spinal column, were used to automatically compute endplates on vertebrae and the global outline of the spine.

Techniques using Hough transform [6,7] and Active Shape Models [8] are other examples of the various approaches developed. These methods use a large set of templates to capture the great variability in vertebra shapes. But, in most of the cases, it leads to prohibitive computation time, as in the case of Hough transform, and usually needs a large and accurate training set in the case of Active Shape Models.

In this work, we propose a new segmentation approach applied to vertebral mobility analysis. The proposed segmentation approach is based on a first semi-automatic step of region vertebra selection. After this, we achieve vertebra contour detection using a polar signature system followed by a polynomial fitting process. The extraction of some quantitative measures of particular changes between images acquired at different moments allows determining vertebral mobility. For instance, to measure and compare the corresponding vertebrae between several images, we analyze vertebra edges extracted from some images corresponding to the cervical vertebra of the same person, in flexion, neutral and extension positions. This paper is organized as follows: In section 2 we present the principles of the region vertebra selection process. After this we describe in section 3 the polar signature system used for vertebra contours detection. In section 4, we describe the numerical segmentation results given by this method, and presented by the angular measures of each vertebra. These results allow the estimation of vertebral mobility.

2   Region Vertebra Selection

This first step allows the creation of a polygonal region for each vertebra. This will facilitate edge detection, and also make easier other processing like determining relative positions between vertebrae. Each region represents a specific geometrical model based on the geometry and the orientation of each vertebra. We propose a process where the user has to click once inside each vertebra.

We initially place a click by vertebra, towards the center of the vertebra. These landmarks represent the starting points $P(x_i, y_i)$ for the construction of vertebra regions, figure (1-a). After this, we compute the distance between each two contiguous points $(D_{i,i+1})$, equation (1), and the line L_1, figure (1-b), which connects the contiguous points, by a first order polynomial, equation (2).

(a)   (b)
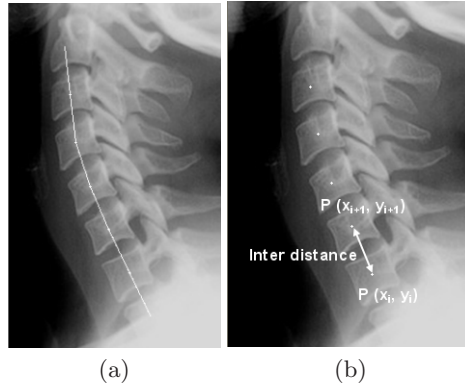
Fig. 1. (a) : The first order polynomial function: (L_1) between the click points. (b): The inter vertebral distance computation, $P(x_i, y_i)$ and $P(x_{i+1}, y_{i+1})$ are the click points associated to the first and the second vertebrae.

$$D_{i,i+1} = \sqrt{(P(x_i, y_i) - P(x_{i+1}, y_{i+1}))^2} \tag{1}$$

$$L_1 = f\left[a, b; P(x_i, y_i), P(x_{i+1}, y_{i+1})\right] \tag{2}$$

The calculated distance between the click points allows the estimation of the inter vertebral distance. We use the line L_1 and the consecutive click points to carry out a relative estimation of order zero for the angles between vertebrae.

On the other hand, the line L_1 will be used as reference for a template displacement by the function $T(x, y)$. This template function represents an intervertebral model, which is calculated according to the area shapes between vertebrae. To build the function $T(x, y)$, we analyzed the figures (2-a) and (2-b). The figure (2-b) presents the intensity values distribution along the line L_1. We notice that this intensity deployment can be decomposed of two main shapes: vertebral and inter-vertebral areas. We focus our analysis on the inter-vertebral area which takes a valley form. So, we propose a template function $T(x, y)$ with an opposite exponential trajectory. This function is given by equation (3). This template function depends on a new reference plane on the direction of L_1. Figure (2-c) is a three dimensional representation of the template function $T(x, y)$ which is built by auto repetition of $T(x, y)$ along an axis.

We use the L_1 function and the inter vertebral distances to calculate the inter vertebral angles (α_{iv}) and to determine a division line for each inter vertebral area. The goal of the proposed template matching process is to find the position
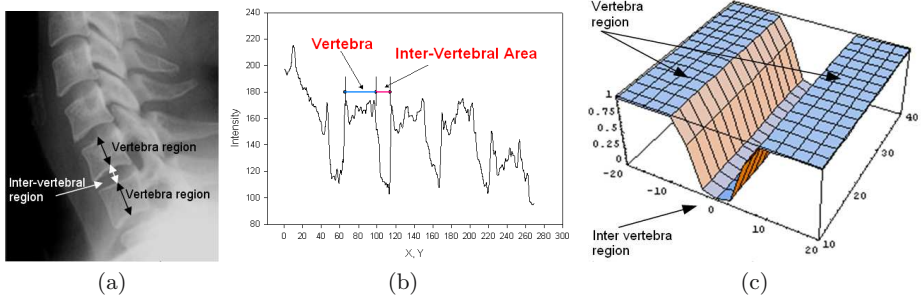
Fig. 2. (a): Representation of the vertebra area and the inter vertebra region; (b): Distribution of the of intensity values along the line L_1; (c): Three dimensional representation of the template function proposed

on the image which is best correlated with the template function (See [3] for more detail). So, for each vertebra, the template function $T(x, y)$ is first placed on the geometrical inter-vertebral central point $P(x_{ic}, y_{ic})$, which represents the average position between each two contiguous click points: $P(x_i, y_i)$ and $P(x_{i+1}, y_{i+1})$. The new reference plane is created with $P(x_{ic}, y_{ic})$ as center. The X axis of this plane is the line L_1. The Y is axis therefore easily created by tracing the line passing through $P(x_{ic}, y_{ic})$ and orthogonal to L_1. We notice that the orientation angle of this second axis present the initial value of the orientation angle α_{iv}. To determine the points representing border's areas, we displace the template function $T(x, y)$, equation (3), between each two reference points $P(x_i, y_i)$ and $P(x_{i+1}, y_{i+1})$, along the line L_1. Then, we compute the correlation degree D_C between the template function and the image $I(x, y)$. The central geometrical point is moved in the two directions in top and bottom along the L_1 axis for a distance equivalent to a parameter T_r fixed experimentally according to the X-ray images used at $\pm 25\%$ of the inter-vertebral distance $(D_{i,i+1})$. Also, for each position on the line L_1 obtained by this translation, we operate a shift of the orientation angle α_{iv} using an angle parameter β_r, fixed experimentally at $\pm 30°$, $(T(x, y) \pm \beta_r)$, with a step of $2°$.

$$T(x, y) = \left(1 - e^{(-rx_l^2)}\right) \quad with \quad r = k/D_{i,i+1} \tag{3}$$

With $k = 0.1$ an empirical value and x_l the coordinate of the point (x, y) in the new reference plane.

The correlation degree is a similarity measurement which permits to obtain the ideal template function that joins perfectly the borders between the areas of vertebrae. The maximum correlation value D_C between templates function $T(x, y)$ and the image $I(x, y)$ for all the analyzed positions will correspond to the most stable position. This position corresponds to an angle α_{iv} and a position $P(x_{iM}, y_{iM})$ for the template function, i.e. the position on the image $(P(x_i, y_i) \pm T_r * D_{(i,i+1)}, \pm \beta_r)$ in which the template function $T(x, y)$ is best placed. In figure (3-a), the click points $P(x_i, y_i)$ are represented. In figure (3-b),

we present the inter-vertebral points $P(x_{iM}, y_{iM})$ given by the proposed procedure. In figure (3-c), boundary lines between vertebrae are traced according to the angle α_{iv} given by the same procedure and centered on the points $P(x_{iM}, y_{iM})$). To obtain vertebral regions, we connect the extreme points of the boundary lines, figure (3-d).

The Results obtained by the region vertebra segmentation method in flexion and neutral and extension positions are represented in figure 4. Already at this step, we can estimate vertebral mobility. Indeed, the mobility of the vertebrae can be approximated by the mobility of their anterior sides. We rely on angular variations measurements and comparisons to determine this one. Once all the segments that represent each polygonal region are found, we extract the segments representing the anterior (frontal) faces ([3]). After this, we can make a first estimation of the orientation angle belonging to each vertebra, the angular variation between two consecutive vertebrae and the angular variation for the same vertebra in two different positions. But, to have better precision, we apply the contour detection of each vertebra inside its area. This process allows the computation of some parameters characterizing each vertebra, like their positions, dimensions, orientation, and other cervical information.

| (a) original image reference | (b) order points given by template matching process | (c) boundary lines between vertebrae | (d) vertebrae regions |
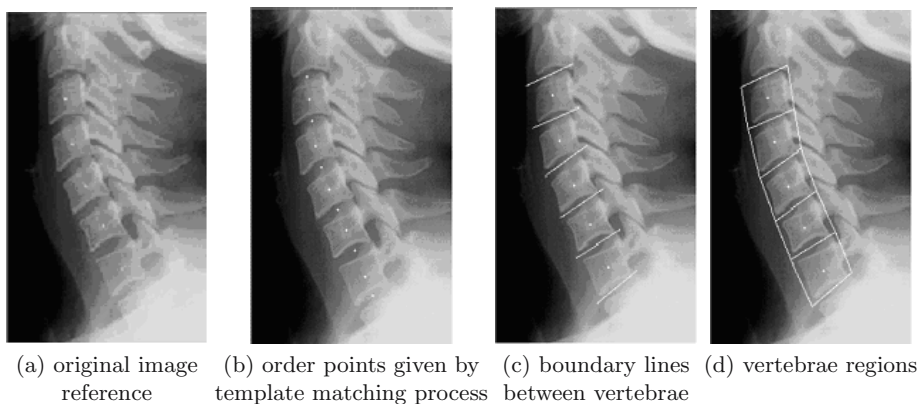
Fig. 3. Results obtained by the region vertebra segmentation method

3   Contour Detection

After the region localization step, we proceed to vertebra contours detection. To this aim, we use a polar signature method [12] applied to each vertebra region. A general approach to determine the polar signature of objects boundaries is illustrated in figure (6). We choose to use this polar signature approach in order to explore all region points likely to be corresponding to vertebra contours.

A polar signature technique applied to vertebra region is represented in figure (7). The center point of the polar signature system is the click point. We
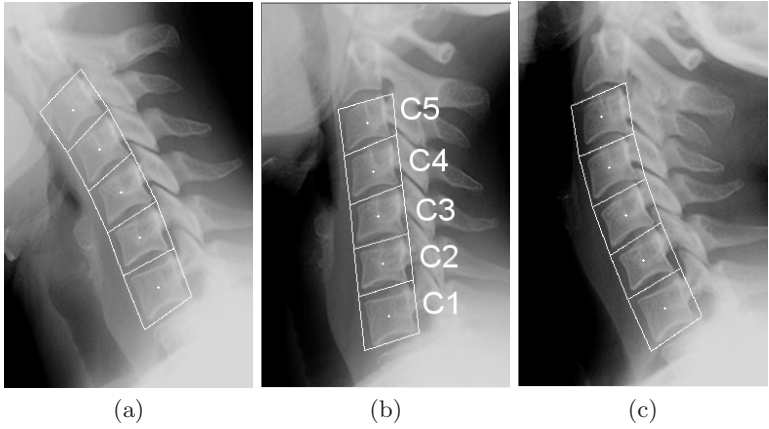
Fig. 4. Results obtained by the region vertebra segmentation method for three X-ray images of the spinal column in three positions: (a): flexion position, (b): reference position, (c): extension position
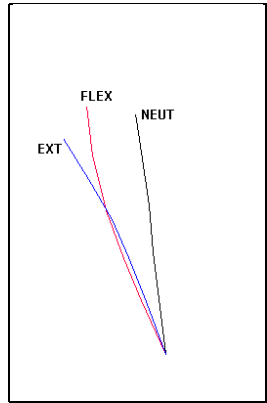
Fig. 5. Graphical comparison between three cervical spine positions using a frontal face computing by Region vertebra segmentation
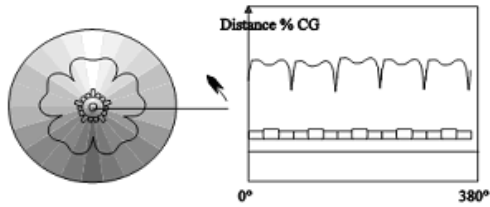
Fig. 6. Example of contour points obtained by a polar signature approach

make the radial vector turn by 360° around the central points with a step parameter, Δ_α degree. More Δ_α is high, more the computing time is less. But more Δ_α is high, more the contour is open. In order to get a closed contour, we apply an edge closing method to the contours obtained, a polynomial fitting to each face for each vertebra. In deed, for a better approximation of vertebra contours, we use a second degree polynomial fitting [10]. We achieve this 2D polynomial fitting by the least square method, figures (8-a, 8-b).

(a) Polar signature system (b) Polar signature direction (c) Research area in Gradient intensity
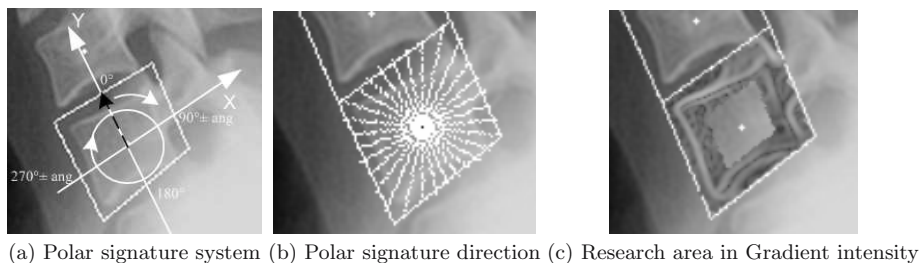
Fig. 7. Polar signature applied to vertebra region
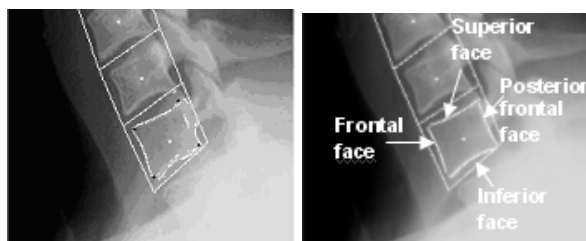
Fig. 8. (a) Contour and corners points, (b) Polynomial fitting for each vertebra face

4   Experimental Results

We apply the proposed method to a large set of X-ray images of the cervical spinal column. We have tested the algorithm on a set of 100 images belonging to real patients. The figure (9). shows the results obtained by applying the proposed method to three X-ray images of the cervical spinal column. We notice that the process of region selection, figure (3) gives good results and permits to isolate each vertebra separately in a polygonal area. On the other hand, contours extracted with the polar signature system combined with template matching process are given with high precision. The great advantage of our method is the fact that segmentation results are presented by closed contours. This will essentially facilitate the use of these results for image indexing and retrieval.
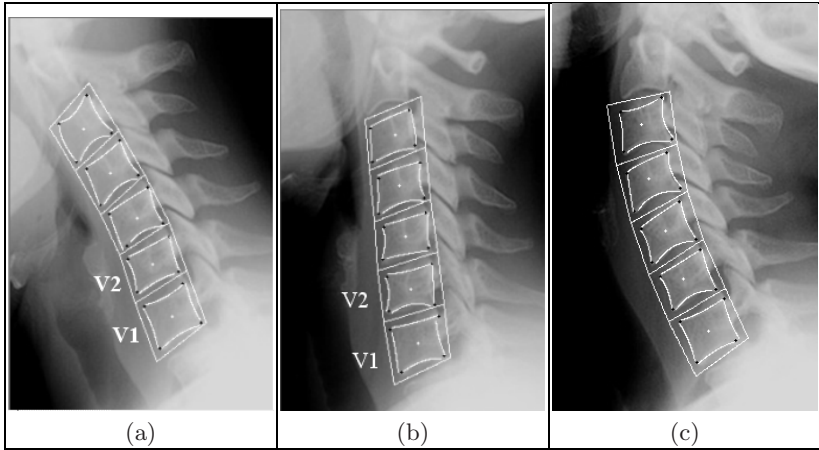
Fig. 9. Results obtained by the proposed contour vertebra selection method
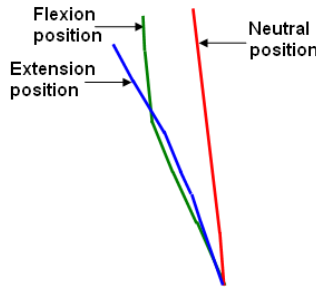
Fig. 10. Graphical comparison between three spine positions

Vertebral mobility is estimated by the computation of the orientation angles belonging to each face of the contour. In table 1, we present some quantitative measurements of the orientation angle for each vertebra face. So, we present the orientation angles for the five vertebrae belonging to the images (a), (b) and (c) in figure (9). This allows motion head estimation and vertebral mobility computation. The error margin by applying only region segmentation method instead of the region vertebra segmentation combined with polar signature is shown in table (2). The results given in table (2) are corresponding to the neutral position and the frontal faces of vertebrae $V1$ to $V5$. Two graphical representation of the angular variation between these three positions using region and contour detection with polar signature methods are shown in figures (5) and (10). It will be noticed that if figures (5) and (10) resemble, the error margin Delta is rather significant. This shows the utility of an additional treatment like the polar signature.

Table 1. Orientation angles for the five first vetebrae in figure. 9, with $S_p = 1°$

PF: Posterior face	FF: Frontal face	SF: Superior face	IF: Inferior face

		PF	FF	SF	IF			PF	FF	SF	IF			PF	FF	SF	IF
	V_1	114.0	113.6	25.3	29.3		V_1	103.8	102.0	15.6	18.5		V_1	117.0	113.5	26.9	29.8
(a)	V_2	107.7	106.4	26.8	25.5	**(b)** V_2		93.1	91.7	13.1	8.6	**(c)**	V_2	111.5	110.5	12.7	28.2
	V_3	112.0	110.0	32.4	29.7		V_3	101.1	90.0	15.2	8.1		V_3	112.6	106.2	34.0	31.4
	V_4	119.5	113.8	37.2	37.3		V_4	102.1	91.6	16.4	14.3		V_4	112.5	99.4	23.2	24.5
	V_5	124.6	127.6	49.4	43.0		V_5	104.3	91.7	23.5	17.9		V_5	107.1	90.0	18.8	13.3

Table 2. Error margin between (R.V): frontal face detection with only region vertebra selection method and (S.P): frontal face detection with polar signature approach

R.V + S.P.	R.V.	Delta
101,6	99	101,6-99=2,6
91,7	95,9	-4,2
90	94,9	-4,9
91,6	98,3	-6,7
91,7	98,1	-6,4

5   Conclusion

In this a paper, a new method of vertebra segmentation has been proposed. The goal of this work was to propose a method for closed contours detection representing each vertebra separately. This method permits to overcome some classical problems related to closed contours extraction. Our approach lies on three steps. First, we proposed a region vertebra selection. This step allows the creation of a polygonal region for each vertebra and facilitate edge detection. In the second step we applied a polar signature to extract the effective contour of each vertebra. Finally, we used an edge closing method exploiting a polynomial fitting. We have applied, with good results, the method to a large set of real images. The major advantage of the polar signature is the facility and the precision of the results. But, if the precision is obtained by increasing azimuths number, the cost in time computing can be sometimes unfavorable according to images complexity. After the contour segmentation process, we have estimated vertebral mobility. The applied techniques have given good results to measure the mobility of cervical vertebrae. For this, we calculated the angular variations between two consecutive vertebrae within the same image as well to measure the angular variation of a vertebra in several images, in particular between three cervical spine positions. In our future works, we are aiming to develop a template matching method for all the process of contour extraction, and also limiting to only one the number of click points initially placed by the user. Currently we are developing a content based image retrieval system by using the results presented in this paper.

References

1. Long, L.R., Thoma, G.R.: Identification and classification of spine vertebrae by automated methods. SPIE Medical Imaging 2001 Image Processing, vol. 4322 (2001)
2. Stanley, R.J, Seetharaman, S., Long, R.L., Antani, S., Thoma, G.: Downey Ed. image analysis techniques for the automated evaluation of subaxial subluxation in cervical spine x-ray images. In: Proceeding of the 17th IEEE symposium on computer-based medical systems CMBS 2004 (2004)
3. Benjelloun, M., Téllez, H., Mahmoudi, S.: Template matching method for vertebra region selection. In: ICTTA 2006, Damascus, Syria (April 2006)
4. Kauffman, C., Guise, J.: Digital radiography segmentation of scoliotic vertebral body using deformable models. SPIE Medical Imaging vol 3034, pp. 243–251 (1997)
5. Verdonck, B., Nijlunsing, R., Gerritsenand, F., Cheung, J., Wever, D., Veldhuizen, A., Devillers, S., Makram-Ebeid, S.: Computer. In: Proceeding of International Conference of Computing and Computer Assisted Interventions. LNCS, pp. 822–831. Springer, Heidelberg (1998)
6. Howe, B., Gururajan, A., Sari-Sarraf, H., Long, R.: Hierarchical Segmentation of Cervical and Lumbar Vertebrae Using a Customized Generalized Hough Transform. In: Proc. IEEE 6th SSIAI, p. 182–186, Lake Tahoe, NV, March (2004)
7. Tezmol, A., Sari-Sarraf, H., Mitra, S., Long, R., Gururajan, A.: A Customized Hough Transform for Robust Segmentation of Cervical Vertebrae from X-Ray Images. In: Proc. 5th IEEE Southwest Symposium on Image Analysis and Interpretation, santa Fe, NMexico, USA (2002)
8. Roberts, M.G., Cootes, T.F., Adams, J.E.: Linking Sequences of Active Appearance Sub-Models via Constraints: an Application in Automated Vertebral Morphometry. In: Proc. BMVC 2003, vol.1, pp. 349–358 (2003)
9. Long, L.R., Thoma, G.R.: Use of shape models to search digitized spine X-rays. In: Proc. IEEE Computer-Based Medical Systems, Houston, TX, pp. 255–260 (June 2000)
10. Keren, D.: Topologically Faithful Fitting of Simple Closed Curves. IEEE Transactions on PAMI 26(1) (2004)
11. Rico, G., Benjelloun, M., Libert, G.: Detection, Localization and Representation of Cervical Vertebrae. In: Computer Vision Winter Workshop 2001; Bled, Slovenia; pp. 114–124 (February 2001)
12. Lie, W.N., Chen, Y.C.: Shape representation and matching using polar signature. In: Proc. Intl. Comput. Symp. 1986, pp. 710–718 (1986)

Automatic Clump Splitting for Cell Quantification in Microscopical Images

Gloria Díaz, Fabio Gonzalez, and Eduardo Romero

Bioingenium Research Group, National University of Colombia,
Bogotá, Colombia
{gmdiazc,fagonzalezo,edromero}@unal.edu.co
http://www.bioingenium.unal.edu.co

Abstract. This paper presents an original method for splitting over-lapped cells in microscopical images, based on a template matching strategy. First, a single template cell is estimated using an Expectation Maximization algorithm applied to a collection of correctly segmented cells from the original image. Next, a process based on matching the template against the clumped shape and removing the matched area is applied iteratively. A chain code representation is used for establishing best correlation between these two shapes. Maximal correlation point is used as an landmark point for the registration approach, which finds the affine transformation that maximises the intersection area between both shapes. Evaluation was carried out on 18 images in which 52 clumped shapes were present. The number of found cells was compared with the number of cells counted by an expert and results show agreement on a 93 % of the cases.

Keywords: Cell quantification, Overlapping objects, Segmentation, Clump splitting.

1 Introduction

Clumping of objects of interest is a relatively frequent phenomenon in different computer vision domains. Its identification results crucial in many cytological applications [1,2,3], in which the expected result is a population count; although human experts are capable of separating the constituent objects, most real applications require a count of a large number of these objects, thereby many conclusions of cytological studies lye on statistical or qualitative approaches [4]. Manual methods have been replaced in hematological cell counting by automated techniques because of a superior repeatability and the avoidance of the many error sources present in manual methods [4]. Besides, manual strategies are in general limited in cases such as random aggregates of cells produced by smearing failures or dye deterioration [4].

Available clump splitting methods are based on prior knowledge about shape, size or region gray level intensities [5,6,7]. These methods include mathematical morphology [3,8,9], watershed techniques [10,11] and concavity analysis [12,13,3].

Di Ruberto [8] applies a size defined disk as a structural element to separate clumped red cells while Ross [9] complements it using a gray level granulometry for separating objects in the image. Concavity analysis methods are based on the hypothesis that superimposed objects can be separated at some specific cut points in which either the curvature abruptly changes or the overlapped objects present differences in the gray level intensities. The drawback of these methods is that they are only applicable for objects with specific shapes and sizes. On the other hand, Kumar [3] proposes a method based on a concavity analysis, adaptable to many shapes and sizes and which depends on a set of parameters that are obtained from a large set of training samples. However, this method is not accurate enough (79%), many samples are synthetic and there is not a study of the degree of overlapping at which the method is capable to deal with.

The clump-splitting method herein proposed addresses the issue that for the particular case of cytology, the *a priori* information about the predominant cell shape and size are already present in the image. For this, a cell model obtained from the image is used for separating cell aggregates. This approach is simple and permits reliable quantification, independent of any pre-determined geometric feature (shape and size). It enables the accurate splitting of clumps composed of cells of different sizes and with a variable degree of overlap. This paper is organized as follows: the construction of a cell model template, estimated from single cells segmented from actual microscopical images is presented in Section 2.2. This template is then used for an efficient search of similar objects in the clumped shapes via a template matching approach, (Section 2.3). Finally, some preliminary results and conclusions are presented in Sections 3 and 4 respectively.

2   Methodology

In figure 1 the main steps of the whole process are illustrated. Firstly, single and clumped cells are extracted from an initial image. Then, single cells are used for estimating a cell model, an estimation which is formulated as a maximum likelihood problem and solved with an Expectation Maximization algorithm. The cell model is finally used as a template for splitting cells in clumped shapes. This approach searches the better matching between a chain code representation of the contours of the clumped shape and the cell model.

2.1   Single Cell Extraction

Cell features are highlighted using very specific histological procedures, which mostly consist in coloring the different cell components so that color is essentially the base of any differential diagnosis and the main strategy for finding objects in histological samples [14]. Single cell extraction can be achieved through a variety of segmentation techniques [15]. Cells are herein extracted from a binary partition of the image, obtained from a process in which objects are segmented
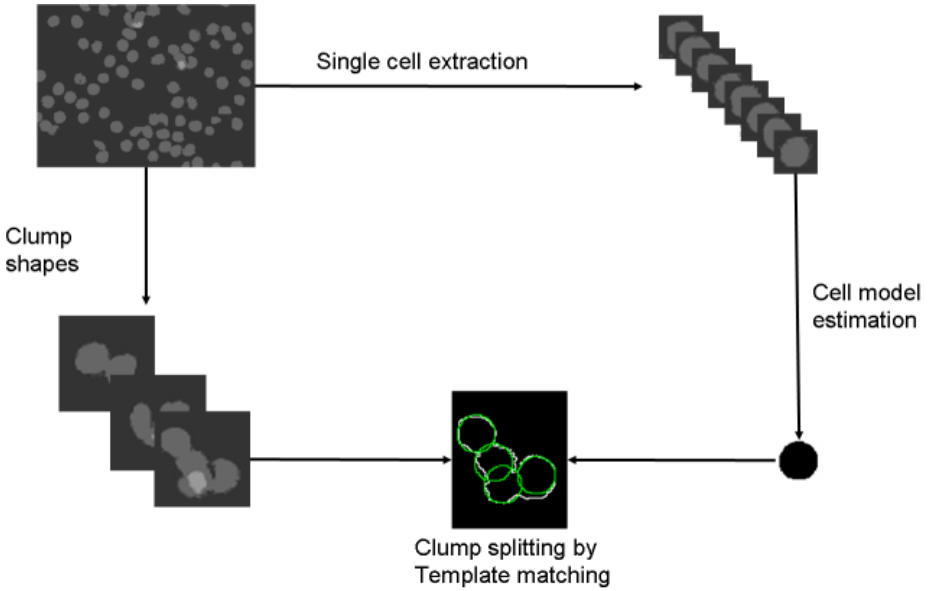
Fig. 1. Proposed method: single and clumped cells are extracted from a initial segmentation. Single cells are then used for estimating a cell model, which is used for splitting clumped shapes via a template matching strategy.

using a color strategy. Therefore, searched objects in these histological images are clustered using their color characteristics.

The problem of color segmentation can be formulated as to find the set of boundaries in the RGB cube, which optimally separates tissues. This corresponds to assign to each image pixel a particular class, based on the color structure of the image. Colour classification at the level of pixel is thus the first step for identifying fundamental relationships in the digital image. Evaluation images were segmented using a trained neural network, a multilayer perceptron with one hidden layer, which classified pixels using the RGB cube as the parameter space. Training points were selected by a pathologist from one image and applied to the whole set of histological images. It was needed two training sets, one drawn from images of malaria and the other from plasmocytoma images.

Once pixels are separated into their constituent classes, they are assembled together into objects using neighbor information. Formally, this is a connected operator graph [16], which uses filtering operations for finding relevant morphological structures. This image representation easily permits separation of the single and clumped objects in the image. The graph is constructed with the number of levels needed to represent the hierarchical relationships of the image. Once the graph representation is complete, a number of connected operators are then successively applied for removing redundant information and identifying interest objects. Finally, single cells are extracted and aligned into the same axis

using a standard principal component analysis (PCA) [15] and the single cells bounding boxes dimensions are set to the bounding box of the larger feature.

2.2 Template Construction Via the EM Algorithm

For the cell template construction, we assume that each single cell drawn from the image is one instance of a true model. Each is assumed to be generated from a process that modifies the true model by adding a random noise, which models the complex interaction of factors such as the biological variability, the histological procedure and the illumination capturing conditions.

Let $D_i = (D_i^1, \ldots, D_i^n)$ be a vector of n elements, which stores the n binary pixel values of a single cell image, with $i = 1 \ldots N$ and N the number of single cells extracted from the image. Let I be a vector of n elements too, which stands for the pixel values of the ideal cell (true model) so that

$$D_i^j = T_i(I^j) \tag{1}$$

where T is a stochastic function that generates the model instance and is defined as follows

$$T_i(1) = \begin{cases} 1 \text{ with probability } p_i \\ 0 \text{ with probability } 1 - p_i \end{cases} \qquad T_i(0) = \begin{cases} 1 \text{ with probability } 1 - q_i \\ 0 \text{ with probability } q_i \end{cases} \tag{2}$$

Where p_i and q_i control the probability of error on the generated instance. A T_i with $p_i = q_i = 1$ means that instances generated by T_i corresponds to the true model. The problem is then to find the p_i and q_i values which maximise the likelihood of the instances being generated from the model:

$$(p, q, I) = \arg\max_{p,q,I}(L(D|p, q, I)) \tag{3}$$

where the likelihood

$$L(D|p, q, I) = \prod_{i=1}^{N} \prod_{j=1}^{n} P(D_i^j | p_i, q_i, I^j) \tag{4}$$

$$= \prod_{i=1}^{N} \prod_{j=1}^{n} P(D_i^j | p_i, q_i, I^j = 1)^{I^j} P(D_i^j | p_i, q_i, I^j = 0)^{1-I^j} \tag{5}$$

$$= \prod_{i=1}^{N} \prod_{j=1}^{n} p_i^{I^j D_i^j} q_i^{(1-I^j)(1-D_i^j)} (1 - p_i)^{I^j(1-D_i^j)} (1 - q_i)^{(1-I^j)D_i^j} \tag{6}$$

A first naive approximation to this problem could be an intensive search of the parameters, but this is no feasible because of the size of the parameter space, which is potentially infinite. An alternative approach is to iteratively improve

the estimation of the optimal parameters. For this purpose, a Expectation Maximization (EM) strategy was adapted from the original work of Warfield [17].

The main idea of the approach is to consider the true model (I) as a hidden variable, which is estimated from the observed data and a set of values for the parameters p_i and q_i. The initial values of p_i and q_i are further improved by local optimization. The process of alternatively estimate I (expectation step) and improve the p_i and q_i values (maximization step) is iterated until convergence. This convergence is guaranteed since the likelihood function has an upper bound, as was stated in [18].

The initial parameter estimates p_i and q_i are set to 0.9, as the fundamental hypothesis in this work is that the instances do not differ too much from the true model. The final estimation of I corresponds to the true model that will be later used as a template to find cells in the input image.

2.3   Splitting Via Template Matching Strategy

Tradionally, template matching techniques have been considered as expensive regarding computational resources since the template must slide over whole image. However, the approach herein used is mainly based on a simplified version of both the template and the clumped shape through a chain code representation, which searches for an anchorage point that results in a "best match" when the two shapes are superimposed.

A chain code is typically used to represent the object boundary by a sequence of straight-line segments with their associated directions. A randomly selected pixel from the object boundary is chosen as the initial point. Afterwards, the pixel's neighbors are numbered from 0 to 7 (8-neighbor mask) and the pixels belonging to the boundary are selected following a clockwise direction. Finally, the obtained chain code is normalized for achieving an invariant representations regarding the initial point and orientation [15]. This normalization is performed computing the distance difference between two consecutive segments and assuming that the chain code is a circular sequence.

Once a chain code representation is achieved for both the clumped and template shapes, a maximal correlation point is determined in the registration phase. This point is from now on a landmark which limits transformations of the found template shape. Provided that our true model may differ from cells which result trapped into aggregates and which generally are deformed because of the contact with other cells, this landmark is used to bond both the ideal model contour and the clump boundary and constitutes the initial search point. Registration is addressed to find the affine transformation which maximises the intersected areas between the two shapes: the template and the clumped. Overall, the template size (width and height) was varied from 70% to 120% for allowing to find a "best match", even if the cell was deformed into the clump. Likewise, orientation was varied in steps of 5%, sliding the template code over the clumped shape. After a first cell is found, its corresponding intersection surface is eliminated of the clumped shape as well as its equivalency from the chain code. Procedure is iterated until the remaining area is lower than 0.2 of the original clumpled shape.

3   Experimentation

3.1   Experimental Setup

In the present investigation we performed evaluations on two different types of cells. Figure 2 displays two microscopical images obtained from the two cell types: plasmocytoma (left panel) and thin blood smears infected with malaria parasite (right panel). Upper row displays the original digital images, while bottom row shows the obtained images using the segmentation approach described before. Our objective was thus to find the cells within the clumped shapes, formed after the segmentation process.
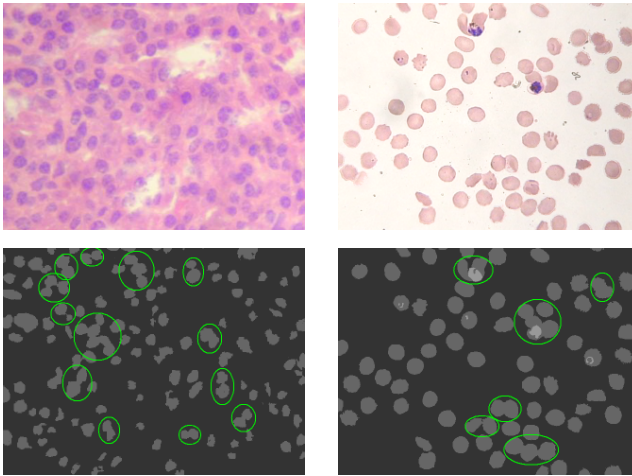
Fig. 2. Fist row corresponds to the original microscopical images. Bottom row displays segmented images obtained from the original ones. Several clumped shapes appear in both cases, a result of the overlapped cells.

A group of 18 microscopical images was used for evaluation, 14 from thin blood stained samples and 4 from a plasmocytoma slide, chosen from two different unrelated studies. These samples corresponded to a two very different tissues, each entailed with different color properties.

3.2   Results and Discussion

Figure 3 shows the final and intermediate results. Upper row (First row) displays, from left to right different microscopical images, among which the first two are extracted from thin healthy blood samples and the next five are extracted from thin blood samples infected with Plasmodium falciparum. In the same row the last five images come from a plasmocytoma slide, characterized by large nuclei with different shapes, sizes and in which the variable to determine is the number of nuclei.

a)

b)

c)

d)

e)
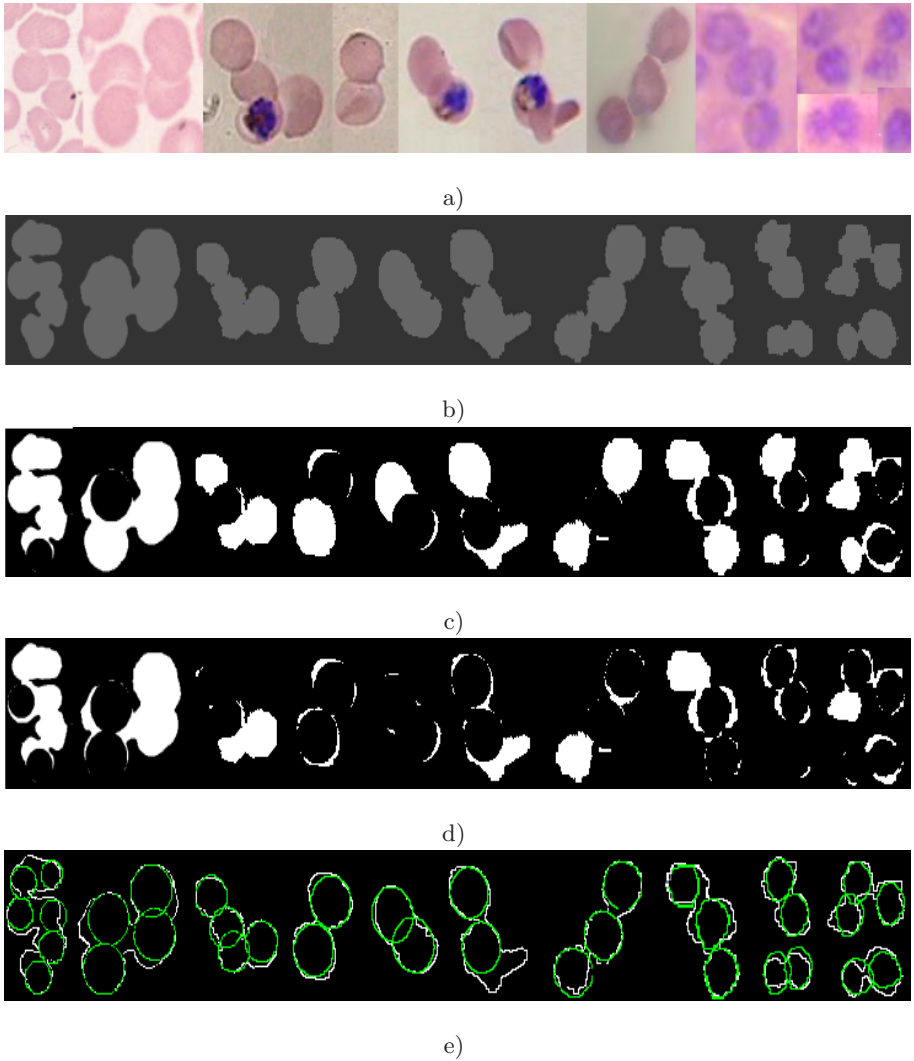
Fig. 3. Figure illustrates the whole process using actual cytological images from different tissues. From the upper to the lower row: row a) displays the original digital images and the first five images from left to right correspond to red cells infected by *plasmodium falciparum*; the rest of the row shows images from a plasmocytoma, a kind of cancer in the lymphatic system. Row b) depicts the binarized images after the color classifier has segmented objects, rows c) and d) show first and second iterations of the proposed method and finally, row e) shows the superimposed results of the splitting cells and the clumped contour shape.

From upper to lower row, results shown in Figure 3 summarise the entire process: row *a* illustrates some examples of sets of cells which are touching or overlapping each other in the two cases herein evaluated (thin blood stains and

plasmocytoma). Row b shows results after the binarization strategy for every original image in the upper row. It should be strengthen out that at this state, the graph has been already constructed and every single cell has been ruled out so that the graph is uniquely composed of clumped shapes. Notice that the color strategy can also produce overlapping shapes because of the segmentation process, see for example the eighth panel (from left to right) of row a and observe the resulted segmentation at the corresponding image in row b. Overall, cells are easily separated using color differences. However, the segmentation process may result in complex shapes such as the shown in the mentioned panel. For this reason, yet color characteristics are at the base of differences among objects, they are difficult to establish since histological objects are complex mixes of different intensities and chrominances which are seen in the RGB space as boundaries varying from one image to other. Rows c and d illustrate the splitting process i.e. a first best matching is shown in row c while a second best matching is displayed in row d. Observe that there is no a systematic trend about a preferred initial location among the whole set of assessed shapes. Finally, row e shows the original clumped contour superimposed with the different locations at which the template has found a relevant shape.

The proposed technique was applied to the set of evaluation images, the identified cells were quantified and the results compared against a manual quantification. In every case, the algorithm was able to match a shape which definitely was an actual cell, a finding which was correlated with the results obtained from observations performed by an expert on the whole set of images. Automatic quantification (the number of found cells for these shapes) coincided in 49 of 52 clumped shapes, resulting in a 93% agreement. Failures were mostly due to an overlapping larger than 50% or to very deformed cells which have lost their geometrical properties and were very different from the estimated template. Regarding time performance, the whole process for a 640×480 image size was $0.7 \pm 0.17\,s$.

4   Conclusions

Automatic methods for performing a precise cell counting are limited by a large number of artifacts, among which the formation of clumped shapes is one of the most frequent. In this research, an entirely automatic method is proposed for splitting cells within clumped shapes. The process starts by performing a binarization of the microscopical image, after which every single cell is counted and stored for the construction of a model cell. This cell model is inferred from single cells by an Expectation Maximization algorithm applied at the level of each pixel. The clumped and template contours are then transformed into a chain code, which is used for the registration phase. Registering is performed through affine transformations of the template, under the restriction that the maximal correlation point between the two shapes is fixed. The proposed method has shown to be robust by splitting cells of diverse sizes and shapes whose overlap varies, it is also reliable and reproducible on the test group of evaluation images.

Future work includes the evaluation of the proposed method in different applications domains and the exploration of different representation alternatives for the true cell model.

References

1. Ong, S.H., Jayasooriah, Y.H.H., Sinniah, R.: Decomposition of digital clumps into convex parts by contour tracing and labelling. Pattern Recognition Letters 13, 789–795 (1992)
2. Bowie, J., Young, I.: An analysis technique for biological shape-ii. Acta Cytologica 21, 455–464 (1977)
3. Kumar, S., Ong, S., Ranganath, S., Ong, T., Chew, F.: Arule based approach for robust clump splitting. Pattern Recognition 39, 1088–1098 (2006)
4. Hall, R., Malia, R.G.: Medical Laboratory Haematology, 2nd edn. Butterworth-Heinemann Ltd. (1991)
5. Wang, Z., Ben-Arie, J.: Model based segmentation and detection of affine transformed shapes in cluttered images. In: International Conference on Image Processing (1998)
6. Gadkari, M.S., Refai, H.H., Sluss, J.J., Broughan, T.A., Broughan, T.A., Naukam, R.: The detection of single hepatocytes within clusters in microscopic images. In: Proceedings of the IEEE Southwest Symposium on Image Analysis and Interpretation (2004)
7. Wurflinger, T., Stockhausen, J., Meyer-Ebrecht, D., Bocking, A.: Robust automatic coregistration, segmentation, and classification of cell nuclei in multimodal cytopathological microscopic images. Computerized Medical Imaging and Graphics 28, 87–98 (2004)
8. di Ruberto, C., Dempster, A., Khan, S., Jarra, B.: Analysis of infected blood cell images using morphological operators. Image and Vision Computing 20(2), 133–146 (2002)
9. Ross, N.E., Pritchard, C.J., Rubin, D.M., Dusï, A.G.: Automated image processing method for the diagnosis and classification of malaria on thin blood smears. Medical and Biological Engineering and Computing 44, 427–436 (2006)
10. Nilsson, B., Heyden, A.: Segmentation of dense leukocyte clusters. In: Proceedings of the IEEE Workshop on Mathematical Methods in Biomedical Image Analysis (2001)
11. Althoff, K.: Implementation and evaluation of stem cell segmentation techniques. Technical report, Chalmers University of Technology (2003)
12. Liu, L., Sclaroff, S.: Deformable model guided region split and merge of image regions. Image and Vision Computing 22, 343–354 (2004)
13. Poon, S.S.S., Ward, R.K., Palcic, B.: Automated image detection and segmentation in blood smears. Cytometry 13, 766–774 (1992)

14. Junqueira, L.C., Carneiro, J.: Basic Histology, 10th edn. MacGraw Hill, New York (2003)
15. Gonzlez, R.C., Woods, R.E.: Digital Image Processing. Prentice-Hall, Englewood Cliffs (2002)
16. Braga-Neto, U.: Multiscale connected operators. Journal of Mathematical Imaging and Vision 22, 199–216 (2005)
17. Warfield, S.K., Zou, K.H., Wells, W.M.: Simultaneous truth and performance level estimation (staple): An algorithm for the validation of image segmentation. IEEE Transactions On Medical Imaging 23, 903–921 (2004)
18. Dempster, A., Laird, N., Rubin, D.: Maximum-likelihood form incomplete data via the em algorithm. Journal of Royal Statistical Society 39, 34–37 (1977)

A Semi-supervised Learning Method for Motility Disease Diagnostic

Santi Seguí[1], Laura Igual[1], Petia Radeva[1,2], Carolina Malagelada[3],
Fernando Azpiroz[3], and Jordi Vitrià[1,2]

[1] Computer Vision Center, Universitat Autònoma de Barcelona, Bellaterra, Spain
[2] Computer Science Department, Universitat Autònoma de Barcelona,
Bellaterra, Spain
[3] Hospital de Vall d'Hebron, Barcelona, Spain

Abstract. This work tackles the problem of learning a robust classification function from a very small sample set when a related but unlabeled data set is provided. To this end we define a new semi-supervised method that is based on a stability criterion. We successfully apply our proposal in the specific case of automatic diagnosis of intestinal motility disease using video capsule endoscopy. An experimental evaluation shows the viability to apply the proposed method in motility disfunction diagnosis.

Keywords: Feature Extraction, Intestinal Motility Diseases, Semi-Supervised Learning, Suppor Vector Machine, Wireless Capsule Video Endoscopy.

1 Introduction

In many pattern classification problems, the acquisition of labeled training data is costly and/or time consuming, whereas unlabeled samples can be obtained more easily. Semi-supervised learning addresses this problem by using unlabeled data, together with the labeled data, to build better classifiers. Because semi-supervised learning requires less human effort and gives higher accuracy, it is of great interest both in theory and in practice [1,2].

Semi-supervised methods can be seen as a solution to the problem of generalizing from small samples. Successful learning from a very small number of training samples requires the introduction of a certain hypothesis bias using additional information, and one such source of information may be unlabeled data. Semi-supervised learning methods use unlabeled data to either modify or reprioritize hypotheses obtained from labeled data alone. Although not all methods are probabilistic, it is easier to look at methods that represent hypotheses by $p(y|x)$, and unlabeled data by $p(x)$. Generative models have common parameters for the joint distribution $p(x, y)$. It is easy to see that $p(x)$ influences $p(y|x)$. Mixture models with EM are in this category, and to some extent self-training. Many other methods are discriminative, including transductive SVM, Gaussian processes, information regularization, and graph-based methods.

The simplest method of incorporating unlabeled data into a new model is self-training [3]. In self-training a classifier is first trained with the small amount of labeled data. The classifier is then used to classify the unlabeled data. Typically the most confident unlabeled points, together with their predicted labels, are added to the training set. The classifier is re-trained and the procedure repeated. Self-training has been applied to several natural language processing tasks like word sense disambiguation [4] or to classify dialogues as 'emotional' or 'non-emotional' [5], and also to computer vision problems like object detection from images [6].

Co-training is another way to train models from unlabeled data [7]. Unlike self-training, co-training requires multiple learners, each with a different "view" of the data. When one learner is confident of its predictions about the data, we apply the predicted label of the data to the training set of the other learners.

A variation suggested by Dasgupta et al. [8] is to add data to the training set when multiple learners agree on the label. If this is the case, we can be more confident that the data was labeled correctly than if only one learner had labeled it.

In the case of supervised learning, a learned function generalizes well if it does about as well on new inputs as on the old ones. Given an appropriate measure for the 'cost' of an error, the most common approach for assuring that a learning algorithm holds the previous property is to choose the least expensive function over the set of training samples, an approach to learning called *empirical risk minimization*. A classical result in learning theory shows that the functions learned through empirical risk minimization generalize well only if the 'hypothesis space' from which they are chosen is simple enough. The classical definition of a 'simple enough' hypothesis space is based on the *Vapnik-Chervonenkis* dimension [9], but although this approach has generated powerful learning algorithms, the complexity of hypothesis spaces for many realistic scenarios quickly becomes too hard to measure with this definition.

Recently Poggio et al. [10] proposed an elegant solution to this difficulty that shifts attention away from the hypothesis space. Instead, they require the learning algorithm to be stable if it is to produce functions that generalize well. An algorithm is stable if the removal of any one training sample from any large set of samples results almost always in a small change in the learned function.

We formulate our problem as follows: given a reduced set of labeled samples belonging to two different classes and a set of unlabeled samples, the task is to learn a binary classification function that generalizes well when tested by a Leave-One-Out Cross-Validation method. The problem is challenging because the number of labeled samples is small and we cannot use classical re-sampling methods to assess generalization capacity of the classifier when considering unlabeled data. To this end we introduce a stability criterion based on data perturbation methods that allows us to select which unlabeled samples are added to the learning set in order to modify the generated hypothesis. This method is applied to a Support Vector Machine classifier trained with the problem of intestinal motility disease diagnosis.

This paper is organized as follows. In the next section we describe the proposed semi-supervised learning method and the stability criterion. In Section 3 we explain the problem, the diagnostic of intestinal motility disfunction using the video capsule endoscopy. In Section 4 we expose the experimental results, comparing the results when using a supervised learning method with the obtained results when using the proposed semi-supervised learning method. Finally, Section 5 ends the paper with our conclusions and future work.

2   Semi-supervised Learning Based on Stability Criterion

In view of these considerations, we propose a semi-supervised method that uses a stability criterion to add samples to the training data set. The proposed stability criterion differs slightly from the one defined by Poggio et al. [10] in order to be used with small sample sets. We define a statement as follows:

Stability Criterion: *"An algorithm is stable if adding one training sample from a set of samples results in a small change in the learned function".*

In order to use the stability criterion during the application of a semi-supervised method, we need to define how to measure *small changes in the learned function* when adding a training sample. To this end we adopt the following strategy (see Fig. 1):

1. Given a binary classification problem with two class labels $\{-1, +1\}$, a training set with an additional training sample, and a learning method that is able to assign a confidence level to the classification of any sample, perform a Leave-One-Out Cross-Validation test over the training set, including the new training sample.
2. At each stage of the Cross-Validation test, repeat n times the following procedure:
   (a) Add random noise to the samples, creating a perturbed data set.
   (b) Build a classifier and classify the "left out" sample.
   (c) Return the class and the confidence level of the sample classification.
3. Compute the mean confidence classification level for each sample and rank all training samples from both classes by assigning the lowest rank to the most confident sample from class -1 and the highest rank to the most confident sample from class +1.
4. Compute a measure of stability of the algorithm for the additional training sample by comparing the produced rankings (a learned function is stable if the sample ranking change is insignificant). To compare two rankings we can use Spearman's rank coefficient [11]. This is a non-parametric measure of correlation that assesses how well an arbitrary monotonic function can describe the relationship between two variables, without making any assumptions about the frequency distribution of the variables. The coefficient is defined as:

$$r_{ab} = 1 - 6 \sum_{i=1}^{N} \frac{(d_i^a - d_i^b)^2}{N(N^2 - 1)} \tag{1}$$

where the sum is taken over all samples d, d_a and d_b, are the obtained ranks of the d sample using two differently perturbed data sets a and b, respectively, and N is the number of samples. At the end we average the pairwise rank correlation coefficient over all n iterations. We consider that the example with the highest correlation coefficient is the most stable for the classifier.
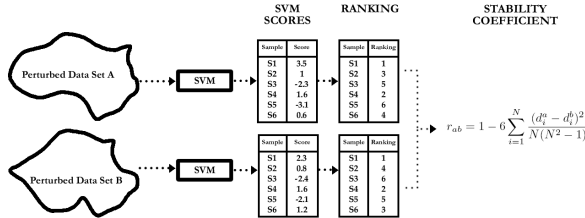
Fig. 1. Strategy to measure the stability coefficient. The obtained ranks for data set A and B are $d^a = \{1, 3, 5, 2, 6, 4\}$ and $d^b = \{1, 4, 6, 2, 5, 3\}$, respectively, and N=6.

Table 1. Stability based semi-supervised learning algorithm

1. Pick one classification method.
2. Train a classifier f using the labeled data set $(x, y) \in (X_l, Y_l)$.
3. Use f to classify all unlabeled items $x \in X_u$.
4. Compute the stability criterion for each $x \in X_u$.
5. Pick from the unlabeled data set the sample x^* with the highest stability on the results of the classification, and add $(x^*, f(x^*))$ to labeled data.
6. Repeat this procedure until all samples from the unlabeled data set are added to the labeled data set.

Once we know how to measure the stability criterion we can define our stability based semi-supervised learning algorithm. The basic idea is to add at each step the sample from the unlabeled data set which presents the highest stability with respect to the classifier. Table 1 summarizes the proposed algorithm.

3   Applying to Intestinal Motility Analysis

With the recently appeared Wireless Capsule Video Endoscopy (WCVE) a new field of research is opened to study small intestine affections. Currently, the most extended diagnosis test for small bowel motility disorders is intestinal manometry [12]. This technique has some drawbacks: it is highly invasive, require the hospitalization of the patient and monitorization of the whole process by medical staff, and also the acquired information is limited to examination of some kind of information.

The WCVE is an ingestible device provided with all the suitable technologies for image acquisition, including auto illumination and radio frequency emission.

For more details see [13]. The capsule is swallowed by the patient and emits a radio frequency which is received and stored by an external machine. The result is a video which records the "travel" of the capsule along the intestine with a frame ratio of two frames per second.

The human intestine is the portion of the alimentary canal extending from stomach to the anus. It is divided in two segments, the small intestine and the large intestine. The small intestine is subdivided into duodenum, jejunum and ileum, and the large intestine is subdivided into cecum, colon and rectum. We are interested in the part of the intestine comprised between post-duodenum and cecum, because in the other part of the video we can not extract reliable information. In the portion of the video corresponding to this part, we can observe three different elements or events: the intestine wall, the intestinal content, and some artefacts related with the movement of the intestine. In Fig. 2 we can see an example of the intestine image visualized by the WCVE. In this image the lumen and the intestinal wall are visualized. The lumen is the cavity where digested food goes thought and from where the nutrients are absorbed. It can be recognized in the video images as a dark area. In order to quantify the infor-
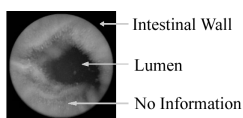
Fig. 2. Example of intestinal video image

mation that is visualized in the video, we have to extract the values related to several features. All these analyzed features are, according to medical experts, important in the diagnostic of the intestinal motility disfunctions. The features that we analyze from the video are:

Static rate. Static frames appears when the camera has a null apparent motion and the visualized frames are almost the same. The experts believe that a high level of static frames could be considered as a symptom of intestinal disease. An example of this kind of sequences can be seen in Fig. 3 - 1st row. We characterize this feature with Earth Mover Distance method (EMD) [14]. From this feature we are interested in quantifying the next information: *percentage of static frames in the video*; *percentage of static frames in those parts of the video that turbid is not present*; *the mean length of the static sequences*; and the *static level of the video*, all of them computed with the mean of the static level of each frame.

Turbid. The turbid is food in digestion or intestinal juices. The food appears as small pieces through the gut and the intestinal juices could be presented as liquid or bubbles (Fig. 3 - 2nd row). For details about turbid detection using WCVE see [15]. Related with turbid we get the next values: *percentage of turbid frames in the video*; *percentage of turbid frames that are apparently stopped*; and *static level in the parts that the turbid is not present*.
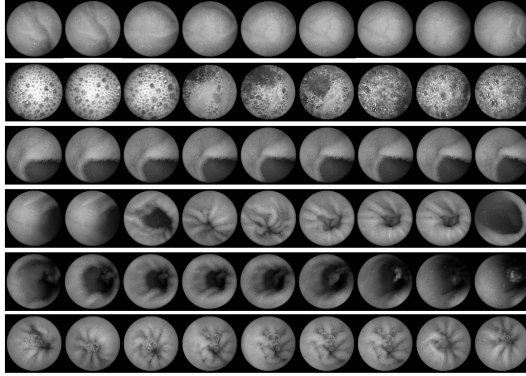
Fig. 3. Some different intestinal video images. From top to bottom: Static Sequence, Turbid frames examples, Tunnel Sequence, Occlusive contraction, Non-Occlusive contraction and Sustained Contraction.

Tunnel. A tunnel is a sequence of frames where the lumen appear static for a long period of time (Fig.3 - 3rd row). The interpretation of the tunnel is that the intestine is relaxed, and there is not contractile movement.

The tunnel is described in terms of the lumen area of a sequence of nine frames. In order to estimate the area of the lumen, a Laplacian of Gaussian filter is applied (LoG)[16]. For further details about detecting these frames see [17]. We are interested in assessing: *percentage of tunnel in the video*; *percentage of tunnel in those frames that turbid is not present*; *the mean length of the tunnel sequences*; and *the level of static level of all tunnel frames.*

Contractions. Intestinal contractions are the result of muscular stimulation produced by the nervous system. The analysis of these contractions has been proved to be a meaningful method for diagnosis several intestinal dysfunctions [18]. From a physiological point of view, intestinal contractions can be divided into the following three groups:

- Occlusive contractions: the lumen in the central frame of these contractions is completely closed. These are considered as the classical intestinal contractions (Fig.3 - 4th row).
- Non-occlusive contractions. In this type of contraction the lumen never appears completely closed. The origin of this kind of contraction is based in the physiological fact that the intestinal wall do not perform enough pressure during the contractile activity (Fig.3 - 5th row).
- Sustained contractions. They are produced by the muscular tone, and can be visualized as a continuous closing of the intestinal lumen (Fig.3 - 6th row).

The method to classify frames as contractions has been described elsewhere and is called Cascade [17]. Each step of the Cascade receives as input the output of the previous step. The initial input is all the frames of the video, and the output is the set of frames where a contraction is suggested to appear.

We use a Relevance Vector Machine classifier (RVM) [19] in order to detect the non-occlusive contractions from all the contraction set detected by the system . The principal feature to characterize this type of contraction is the area of the lumen in each frame. Generally, in non-occlusive contractions the lumen area of the central frame is bigger than it is in the rest of the contractions. This area is estimated in the same way as is done in the tunnel frame detection. The resulting vector of nine lumen areas is used as feature vector to the classification of occlusive or non-occlusive contractions.

We are interested in analyzing: *the number of contractions per minute in the video*; *the number of contractions per minute in those parts that the turbid is not present*; and *the percentage of the contractions that are non-occlusive.*

Wrinkle pattern level presence. The wrinkle star pattern is an omnipresent characteristic of the sustained contractions. In the frames where the wrinkle pattern appears we observe strong edges of the folded intestinal wall, distributed in a radial way around the intestinal lumen. In order to localize this pattern in video frames an accurate wrinkle detection is essential. For more information about this method see [20]. The output is the level of wrinkle presence in each frame. Related with this feature we get: *the percentage of video frames with wrinkles*; *the percentage of the frames without turbid where the winkle star pattern appears*; *the mean length of the wrinkle sequences*; *the percentage of frames with a very low level of wrinkle presence*; *the percentage of frames with a high level of wrinkle presence*; and *the percentage of contractions with wrinkles.*

All these features are assembled in an 21-dimensional feature vector that is used to diagnose subjects in intestinal motility disfunctions.

4   Experimental Results

In this section we evaluate the proposed method over our problem. Our video set is provided by the Digestive Diseases Department of General Hospital Vall d'Hebron in Barcelona, Spain. This video set was obtained using the wireless endoscopic capsule developed and provided by Given Imaging, Ltd., Israel. All videos were created at the same conditions, patients and healthy volunteers were in fasting (without eating and drinking in the previous 12 hours). There are three different group of videos, one from patients, another from healthy volunteers, and finally another one from persons with non conclusive manometric diagnose that are used as unlabeled data. Healthy volunteers were randomly selected from a bigger pool of subjects without any symptom. We consider these subjects as healthy subjects without performing a manometry test, because the probability to be patient is too small and anyone of them has any symptom to be patient, statistically the probability of error is very low. Our data set is composed by 50 healthy volunteers, 15 patients and 17 unlabeled subjects. It is important to notice that the intestinal motility diseases are very odd ones. This is the reason why the number of available patient cases is very low.

We evaluate the performance of this methodology using a Leave-One-Out Cross-Validation Method [21] with the data set. Before performing this test

we normalize the data with zero mean and standard deviation set to one. The results are validated using several measures that are described in terms of true positives (TP), true negatives (TN), false positives (FP), and false negatives (FN) as follows: $Error = $ FP + FN, $Sensitivity= TP/(TP + FN)$, $Specificity= TN/(TN + FP)$, $Precision= TP/(TP + FP)$ and $False\ Alarm\ Ratio, FAR = FP(TP + FN)$. Table 2 summarizes these definitions.

Table 2. Validation Measures

Error	Sensitivity	Specificity	Precision	FAR
$FP + FN$	$\frac{TP}{TP+FN}$	$\frac{TN}{TN+FP}$	$\frac{TP}{TP+FP}$	$\frac{FP}{TP+FN}$

In order to perform our classification test we use the Support Vector Machine classifier (SVM) [22]. SVM classifier looks for the hyperplane which separates positive and negatives samples, maximizing the distance to the hyperplane. The original algorithm by V. Vapnik was a linear classifier, however there is a way to create non-linear classifiers by applying the kernel trick to the SVM framework. We used the SVM classifier with the radial basis function kernel [23] represented by:

$$K_{rbf}(x, x_i) = exp\frac{-|x - x_i|^2}{2\sigma^2} \tag{2}$$

where the parameter σ will be found by Cross-Validation in each test.

Our first test is performed only using the supervised data (healthy volunteers and patients). In the first row of Table 3 we display the obtained results for this test. We get a 4.61% of error, 80.00% of sensitivity, and specificity, precision and FAR are: 100.00%, 100.00% and 0.00% respectively. It means that all healthy subjects are correctly classified, but three patients are considered as healthy subjects.

The previous test present an important drawback, the limited size of the data set. In order to overcome this problem and be able to get better results we perform another test using both, the supervised and unsupervised data set in the proposed semi-supervised learning method. Before using this algorithm we have to define two important issues:

– Which binary classifier is used and how we estimate the confidence level of the sample classification, and
– How we perturb the original data.

For the first issue we again use an SVM classifier. To get the classification confidence value of a given classified sample, we take the distance from this sample to the SVM hyperplane. To create the perturbed data set we choose to add a percentage f of Gaussian noise to the original data set. We test our method with different percentages of noise obtaining the same results when $0\% <= f <= 40\%$. Finally for this percentage was fixed to $f = 20\%$.

The semi-supervised learning method labels 8 examples of the unsupervised data set (of 17 elements) as patients and 9 of these examples as healthy volunteers. We use this new training set in order to perform the validation for proposed method of our problem. As we can see in the second row of Table 3 we get 1.53% of error, 93.00% of sensitivity, and specificity, precision and FAR are: 100.00%, 100.00% and 0.00% respectively. It means that the system only fails in one case, when it considers one example of the patients as a healthy subject.

Table 3. Classification Results

	Error	Sensitivity	Specificity	Precision	FAR
supervised learning	4.61%	80.00%	100.00%	100.00%	0.00%
semi-supervised learning	1.53%	93.33%	100.00%	100.00%	0.00%

5   Conclusions

In this paper we proposed a new semi-supervised learning method for the diagnostic of intestinal motility dysfunctions. The principal difficulty of this problem is the low number of patients samples available. However, we have another set of unlabeled data and we propose to use it with the semi-supervised learning method.

We propose the stability as the criterion used in the semi-supervised learning method. The stability measure that has been defined is based on the Spearman's Rank Correlation.

The performed experiments show that using this semi-supervised learning method with an unlabeled set of samples results in an improvement of results. It is important to notice that we obtain this improvement of the results avoiding the computation of the error (on the unsupervised data) as the criterion to be optimized.

Even if the tests have been performed on a very small data set the WCVE and this method is very promising in order to diagnose intestinal motility dysfunctions. The good results demonstrate that this method could be a candidate to replace, in a close future, the most used diagnosis tests for intestinal motility dysfunctions, the manometry test.

Acknowledgements

References

1. Chappelle, O., Schölkopf, B., Zien, A.: Semi-supervised learning. Unpublished book. MIT Press (to appear)
2. Seeger, M.: Learning with Labeled and Unlabeled Data. Technical report, Edinburgh (2000)
3. Zhu, X.: Semi-Supervised Learning Literature Survey. Technical Report 530, Computer Sciences, University of Wisconsin-Madison (2005), http://www.cs.wisc.edu/~jerryzhu/pub/ssl_survey.pdf
4. Yarowsky, D.: Unsupervised Word Sense Disambiguation Rivaling Supervised Methods. In: Proceedings of Association for Computational Linguistics (1995)
5. Maeireizo, B., Litman, D., Hwa, R.: Co-training for predicting emotions with spoken dialogue data. In: ACL (2004)
6. Rosenberg, C., Hebert, M., Schneiderman, H.: Semi-supervised self-training of object detection models, I: 29–36 (2005)
7. Blum, A., Mitchell, T.: Combining Labeled and Unlabeled Data with Co-Training. In: Proceedings of Computational Learning Theory (1998)
8. Dasgupta, S., Littman, M.L., Mcallester, D.A.: Pac generalization bounds for co-training. In: Dietterich, T.G., Becker, S., Ghahramani, Z., NIPS (eds.) NIPS, pp. 375–382. MIT Press, Cambridge (2001)
9. Vapnik, V.: The Nature of Statistical Learning Theory. Springer, Heidelberg (2000)
10. Poggio, T., Rifkin, R., Mukherjee, S., Niyogi, P.: General conditions for predictivity in learning theory. Nature 428, 419–422 (2004)
11. Callan, J.P., Connell, M.E.: Query-based sampling of text databases. Information Systems 19(2), 97–130 (2001)
12. Hansen, M.B.: Small intestinal manometry. Physiological Research 51, 541–556 (2002)
13. Iddan, G., Meron, G., et al.: Wireless capsule endoscopy. Nature 405, 417 (2000)
14. Rubner, Y.: The earth movers distance as a metric for image retrieval. International Journal of Computer Vision 40, 99–121 (2000)
15. Vilarino, F., Spyridonos, P., Pujol, O., Vitria, J., Radeva, P.: Automatic detection of intestinal juices in wireless capsule video endoscopy. ICPR 4, 719–722 (2006)
16. Russ, J.: The Image Processing Handbook. CRC Press (1999)
17. Vilariño, F., Spyridonos, P., Vitrià, J., Azpiroz, F., Radeva, P.: Cascade analysis for intestinal contraction detection. CARS, 9–10 (2006)
18. Quigley, E.M.: Gastric and small intestinal motility in health and disease. Gastroenterology Clinics of North America 25, 113–145 (1996)
19. Tipping, M.: The relevance vector machine. In: Advances in Neural Information Processing Systems, Morgan Kaufmann, San Francisco (2000)
20. Spyridonos, P., Vilariño, F., Vitrià, J., Radeva, P.: Anisotropic feature extraction from endoluminal images for detection of intestinal contractions. LNCS (2006)
21. Stone, M.: Cross-validatory choice and assessment of statistical predictions (with discussion). Journal of the Royal Statistical Society B 36, 111–147 (1974)
22. Vapnik, V.: The Nature of Statistical Learning Theory. Springer, New York (1995)
23. Keerthi, S.S., Lin, C.J.: Asymptotic behaviors of support vector machines with gaussian kernel. Neural Computation 15, 1667–1689 (2003)

Lung Structure Classification Using 3D Geometric Measurements and SVM

João Rodrigo Ferreira da Silva Sousa, Aristófanes Corrêa Silva,
and Anselmo Cardoso de Paiva

Federal University of Maranhão - UFMA
Av. dos Portugueses, SN, Campus do Bacanga, Bacanga
65085-580, São Luís, MA, Brazil
j.rodrigo.sousa@gmail.com, ari@dee.ufma.br,
paiva@deinf.ufma.br

Abstract. In this paper, a set of three features for aiding classification of lung nodule bearing candidates based upon morphological characteristics is proposed. Metrics were validated using Support Vector Machine (SVM) technique as classifier. Preliminary results indicate the efficiency of the adopted measurements, taking into account the sensitivity and specificity high rates obtained from the studied samplings.

Keyword: Lung Nodule, Classification, Geometric Measures, SVM.

1 Introduction

In the last years lung cancer is gaining attention from the scientific community due to its high occurrence among people and also due to the difficulty to treat it. Nevertheless, it is well known that the principal cause of the illness is associated with the smoking habits, especially among males population, in such a way that the chances for a positive diagnostic increase from 20 to 30 times amongst smokers [1].

Research has been performed in the computer field aiming at producing tools to aid the physician in the analysis of computer tomography imaging (CT). Those tools can be divided into two main groups: lung nodule detection and diagnosis aiding ones.

Lung nodule detection is characterized by the identification, from a set of CT images, of a region presenting features that identify it as lung nodule. To do this, in general, a two fold process is conducted: first, the various structures existing in the parenchyma are segmented; next, the structures are classified as to identify which among them represent the nodules and which are associated to the rest of structures that lay, usually, in the lung parenchyma (non-nodules).

In the area of lung structures classification through CT, significant progress has been observed. Several discriminatory measures have been proposed as to differentiate nodules from non-nodules. There are morphological approaches that use geometrical structure characteristics, both bi-dimensional and three-dimensional, to describe them. [2] introduced a new characteristic able to

estimate the nodule tissue radial distribution in a non binary way, getting promising target hitting [3]; on the other hand, he developed a method for rebuilding lung trees supported on highlighting filters, demonstrating its applicability as an aid tool for nodule detection.

There are, also, works that adopt texture characteristics to describe lung tissue and thus, identify it. In [4], for example, there were used 22 characteristics texture based to classify the regions of a CT image from 6 possible groupings, among which the nodule, bronchial-vascular and normal.

In most of the works, once the structures' representative characteristics have been calculated, classifiers for identifying them within the group of nodule or non-nodules are used. One of the classifiers that became very popular because of its high generalization capacity is the Support Vector Machine (SVM), already used in several researches [5], [2], [6]. Neural networks and grouping algorithms are other very popular type of classifiers, also presenting satisfactory results.

In spite of these developments, however, there is not yet a methodology neither in the segmentation area nor in the classification one, which could be considered as definitive for lung nodules identification. Most of them still need improvements concerning target hitting rates or generalization capacity, making it still an open problem.

In fact, lung structures classification is still facing several difficulties. One of them, for example, says respect to the tissue density, which is very alike among the blood vessels and some kind of nodules, leading the classifier to commit same mistakes.

Another difficulty concerns the malignant nodules form. This kind of nodule usually presents spikes and branching due to its disordered nature. The classification problem derived from this is that these branches are similar to the vessels irrigating the nodule which, in its turn, are also numerous in the case of a malignant lesion.

Thus, a great deal of the problem faced by researchers is linked with the difficulty of proposing measures for describing the lung parenchyma inner structures, in such a way as to allow a maximization of the used classifier target hitting rates. This dilemma can still be aggravated by the fact that, under certain aspects such as tissue density or form, a nodule could be considered similar to a lung's normal structure, confusing the classifier.

Besides the techno-scientific challenges above, this problem presents social motivation due to its close association with human health. Hence, the present work aims at contributing with the automation efforts for detecting lung nodules while proposing some novel discriminatory characteristics for the parenchymal structures using them, associated to a SVM classifier, to compare its efficiency with other traditional approaches.

This work is organized as follows: In Section 2, the methodology and the features proposed for the geometrical description of the structures under analysis is explicated. Next, in Section 3, presents the criteria and parameters used in the analysis of the proposed characteristics, as well as the results obtained with them and their comparison with other studies results. Finally, Section 4 closes

the study by analyzing the viability of the described features supported by the obtained results.

2   Methods

In this Section, the proposed method for lung nodules detection is presented and demonstrated the data base formation process used in trials and method validation. Next, three new classification features based upon objects' morphology is also presented. Finally, the SVM technology, basement of the classifier, is introduced.

2.1   Pulmonary Structures Segmentation

The images were acquired with a Helical GE Pro Speed tomography under the following conditions: tube voltage 120 kV, tube current 100 mA, image size 512×512 pixels, voxel size $0.67 \times 0.67 \times 1.0$ mm and reconstruction interval of 1 mm. The images were quantized in 12 bits and stored in the DICOM format [7].

It is important to stand out that the CT exam was performed with no contrast injection, which may be clinically used in order to increase the diagnosis readiness but also carries some morbidity and occasional mortality by allergic complications.

It is also necessary to highlight that the nodules were previously diagnosed by physicians and that the final diagnosis of benignity or malignancy was posteriorly confirmed by histopathological exam of the surgical specimen or by radiologic 3-year stability, which explains the reduced size of our sample.

Nodules were semi-automatically segmented by a specialist physician who used the Lung Nodule Analysis System (Bebúi). This system, proposed in [8], allows the three-dimensional segmentation of the lung nodule by means of a region growing algorithm starting from given seed indicated by the specialist physician. A preliminary segmentation is, next, submitted to the users' approval through the observation of two dimension slices. At this point, if necessary, the physician may manually tune the segmentation as to increase the results accuracy.

Other parenchymal structures, such as blood vessels and bronchia, were automatically segmented through a serial processing of the TC data, under a segment modularizing scheme. This segmentation scheme uses parameters dynamically defined through properties obtained from the images of each examination. This approach avoids the dependency on parameters statically defined which could embarrass the generality of the method.

The entirely automatic processing starts by removing from the bulk the dense tissues involving the lung, mainly composed by muscles and bones, through a selective threshold algorithm by location. Next, by using the morphology technique known as rolling ball, the lung walls are restored as not to neglect peripheral nodules. The next step is to remove from lungs the soft tissues, principal constitutive of the parenchyma, preserving only the structures

contained in it, what is again performed aided by a dynamical threshold. Finally, by using region growing algorithm, each structure is identified and isolated. Samples of the segmented structures through the described methods can be seeing in Figure 1. Figures 1a and 1b represent normal lung structures automatically segmented, while the ones of Figures 1c and 1d isolated lung nodules segmented by the Bebúi system.

Fig. 1. Structures sampling present in the parenchyma. c and d are isolated lung nodules.

Considering both methods, it was possible to build a database with samples corresponding to nodules segmented by the Bebúi system and the rest of the lung parenchymal structures.

In total, 38 samples were used, corresponding to benign and malignant nodules which volume varied between $0.06cm^3$ and $88cm^3$. There were also used 228 structures belonging to the class non-nodule, among which blood vessels and bronchia.

2.2   Proposed Features

As to allow classification and attain satisfactory target hitting rates, it is important to use the under analysis structures' characteristics. Thus, this Section presents the proposal of three new measurements based on the object's geometry (morphology) to be classified.

Spherical Disproportion.   Morphologically it is well known that blood vessels are very different than lung nodules, when observed three dimensionally. While the former presents elongated shape, being possible branches formation, the latter presents a compact and round feature.

Conducting the analysis under this aspect, the measurement of the round disproportion can tell us until which extent certain structure presents unsmooth surface with respect to another totally round surface. This is got by means of a comparison between the estimation of the area the volume should have, if it were totally spherical, and its actual area.

It must be noted the difference between border voxels and surface area. The set of border voxels of an object forms a volume, i.e, it is a three dimensional magnitude, while the outside area is a surface, hence a bi-dimensional one.

In such a way, the spherical disproportion is calculated by Equation 1:

$$D = \frac{A}{4\pi R^2} \tag{1}$$

where A is the object's surface area, R is the estimated sphere's radius with the same volume as the object. The estimated radius (R) is obtained by

$$R = \sqrt[3]{\frac{3V}{4\pi}} \qquad (2)$$

where V is the object's volume.

The Spherical Disproportion assumes smaller values for round objects and higher values for irregular or elongated objects. The measurement also presents invariant properties with respect to the rotation, translations and to the scale.

Spherical Density. As already said, the various structures, nodular or not, found at the lung parenchyma, have more or less compact formats according to their own nature. In such a way, more compact structures are very similar to spheres, while less compact structures look differently.

A very ordinary measurement for measuring how compact a structure is consists in comparing its volume with that one of the minimum box [9]. There are, however, variations of this technique through which it is possible to use the convex hull [10] or, yet, other geometrical figures such as ellipses [9]; but in general, the method encloses the calculation of an object's circumscribed figure and compare its volume with the one occupied by the object under study.

These techniques, nevertheless, face the problem of calculating the best object circumscribed figure alignment or inconsistencies related with the lack of alignment, such as different values for identical objects, but with different rotation, that is, they are not rotationally invariant.

The spherical density, on the other hand, uses a sphere, a figure rotationally invariant, but without having to calculate optimal measurements to circumscribe it to the object. What is in fact done is to use a sphere which volume is the same as the one of the object under study, with origin in the object's center of mass. Thus, the measurement of the spherical density will consist in this sphere's percentage that, in fact, also corresponds to the objects'.

Figure 2 visually represents this feature in 2D format, even though the feature is in 3D, as to easy the visualization and the understanding through a media that is also bi-dimensional. Note that, in Figure 2a, the object occupies most of the circle, resulting in a high spherical density, In Figures 2b and 2c occurs the opposite due to greater dispersion of the object's volume, in such a way that the resulting spherical density assumes smaller values.

Spherical Density is calculated by:

$$\frac{100 \cdot n}{V}. \qquad (3)$$

In this paper, the following notation was used: every time x, y and z, together or separately, would appear underlined, it would indicate a point coordinates, whereas whenever they appear in between parenthesis, they will be indexing an antecedent variable with respect to the respective axis in the objects voxels grid. Thus, in Equation 3, $p(x, y, z)$ is the voxel value with coordinates x, y and z, n
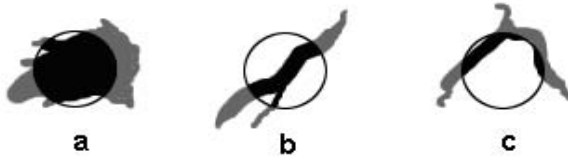
Fig. 2. Spherical Density bi-dimensional Illustration

is the amount of voxels p such that $p(x, y, z) \neq 0$ and $(x - M_x)^2 + (y - M_y)^2 + (z - M_z)^2 \leq R^2$, V is the object's volume, R is the estimated radius obtained through Equation 2 and M_x, M_y, M_z is the object's center of mass coordinate.

The Spherical Density presents the property of getting close to zero in very elongated objects or with external mass center, while it assumes values close to 100 for more round volumes, even though the interval [0,1] could be used without affecting the results just by removing the constant in the Equation 3. Besides this, it is an invariant measurement with respect to changes in the object concerning rotation, translation and scale; being, thus, a very fair stable measurement to be used as a reliable morphological describer.

Weighted Radial Distance. Feature that calculate the flatness or lengthening of an object based on circumscribed images or on global characteristics are flawed because they fail in measuring these objects' real peculiarities.

In Figure 3 one can notice that, even when the three objects minimum boxes factually present the same dimensions, the own objects themselves are very different. Measurements taken upon these boxes' dimensions run the risk of falling into significant lack of accuracy.
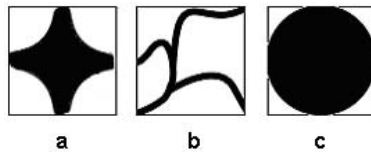
Fig. 3. Objects represented in their minimum boxes

Global measurements such as area and volume not always are ideal descriptors for certain objects' characteristics as it is known, again, that those ones holding the same measurements may present very different shapes.

The Weighted Radial Distance ponders the degree of flatness of an object, starting from voxels' local measurements, increasing the overall precision of this descriptor.

The idea behind this measurement lays in the distance relationship between the volume's voxels and its own medial axis. In very elongated volumes, the voxels, in average, tend to be at a short distance from the medial axis, while in more concentrated volumes the voxels assume longer radial distances.

Nevertheless, the mean radial distance with respect to the medial axis, even when it already supplies an idea of the objects' degree of flatness, is not a consistent measurement, once volume objects will tent to present higher coefficients.

Thus, the Radial Distance is taken in a pondered fashion, so assuring that the volume's dimension will not interfere in the measurement magnitude, but just in its format.

The Weighted Radial Distance can be obtained by means of

$$P = R^{-1} \sum_{x,y,z} c(x,y,z) \tag{4}$$

where R is the estimated radius obtained through Equation 2, $c(x,y,z)$ is the weighting coefficient applied to each voxel by means of

$$c(x,y,z) = \frac{3}{4\pi} \left[[r(x,y,z) + 0,5]^3 - [r(x,y,z) - 0,5]^3 \right]^{-1} \tag{5}$$

and $r(x,y,z)$ is the radial distance of a voxel with coordinates x,y,z.

The radial distance $r(x,y,z)$, as explained before, is the voxel's distance to medial axis at that point. It is calculated by the inverse distance transform.

Initially, the distance's transform is done in a smooth manner on the volume, assigning to each voxel an index which represents its degree of remoteness from the borders. The most inner voxels, which are part of the medial axis, will present, then, higher values.

The inverse radial distance is but nothing else than the reversal of the ascendant direction of those values, given the value zero to the central voxels and to the remaining ones, as they go away, successively higher values until the borders are reached.

It is important to notice that the same result can not be obtained just from the conventional radial distance calculation based in the origin. This happens because the former is based upon the distance with respect to a single central point, while the radial distance calculated through the described process obtains the voxels distance with respect to the object medial axis, which is formed by a series of points.

The Weighted Radial Distance presents the property of assuming values close to unity in not very elongated volumes, and higher values for more elongated volumes. It is also an invariant measurement for rotations, translations and scales.

2.3   Support Vector Machine

The Support Vector Machine (SVM) introduced by V. Vapnik in 1995 is a method to estimate the function classifying the data into two classes [11]. The basic idea of SVM is to construct a hyperplane as the decision surface in such a way that the margin of separation between positive and negative examples is maximized. The SVM term come from the fact that the points in the training set

which are closest to the decision surface are called support vectors. SVM achieves this by the structural risk minimization principle that is based on the fact that the error rate of a learning machine on the test data is bounded by the sum of the training-error rate and a term that depends on the Vapnik-Chervonenkis (VC) dimension.

In the proposed work, the characteristics obtained from each candidate trough of the Equations 2, 3 and 4 had to be supplied to the classifier in such a way as allowing it to evaluate the classes separation hyper-plane and, next, classify other objects.

Nevertheless, each characteristic varies in different value bands, which would lead to a tendency, by the part of the classifier, for super-estimating the relevance of some of them, due to a greater interval variation. As to avoid this fact to become a problem, it is necessary to proceed with a quantization as to translate all the intervals of each characteristic to a common variation band.

The interval selected in this work was [-1,1], once it is conventionally accepted and used with SVM.

After the quantization of all the intervals, the characteristics obtained in such a way give raise to the x points of the input space.

2.4   Validation of the Classification Methods

In order to evaluate the classifier in respect to its differentiation ability, we have analyzed its sensitivity, specificity and accuracy. Sensitivity is defined by $TP/(TP + FN)$, specificity is defined by $TN/(TN + FP)$, and accuracy is defined by $(TP + TN)/(TP + TN + FP + FN)$, where TP is true-positive, TN is true-negative, FN is false-negative, and FP is false-positive. Herein, true-positive means Mass samples were correctly classified as Mass. The meaning of the others are analogous.

3   Results

The adopted SVM classifier was the libsvm [12] library configured to use, during classification, the Gaussian RBF kernel due to its well known generalization power.

The target hitting statistical evaluation procedure conducted the samples cross validation, taking for each iteration a pair of two elements arbitrarily grouped for testing purposes, and the remaining ones for training, i.e., the diverse samples compounding the data base were occasionally, and at different iterations, used for both, training and validation, according to the group they belonged at that very moment. This sort of validation allowed the use of all samples as to obtain a more consistent training, as well as a more precise validation.

This procedure for targer hitting evaluation was separately conducted for all three measurements, all together with the three proposed measurements. According within this criterion, it was verified that, among the proposed characteristics, the one who presented the best results was the Spherical Density.

This feature, alone, was able to attain a rather good target hitting degree, as can be checked in Table 1.

Table 1. The proposed features comparison

Features	Sensitivity %	Specificity %	Accuracy %
Spherical Disproportion	78.94	100	96.99
Spherical Density	100	99.56	99.62
Weighted Radial Distribution	71.05	97.36	93.60
The three proposed features	100	100	100
Radial Volume distribution	91.40	99.5	-

Nevertheless, the most important was that the remaining proposed features, together with the Spherical Disproportion, even though they did not do in isolation such a good classification, characterize the nodule candidate in such a precise way that, the total target hitting rate reached 100%.

Based on the presented results, we have observed that this new methodology provides significant support for a more detailed clinical investigation. Nevertheless, there is the need to perform tests with a larger database and more complex cases in order to obtain a more precise behavior pattern.

For comparison, Table 1 also presents the results obtained from other approaches. The Radial Volume Distribution was proposed by [2], who demonstrated this as having a very high descriptive power.

4   Conclusion

This paper presented a set of three geometrical measurements to be used in the discrimination between nodules non-nodules. The results of the classification based upon these measurements were compared with the results obtained from other works, verifying that the proposed measurements present a rather good discrimination power.

It was also confirmed that, once each measurement was destined to describing a morphological aspect different of that one of the candidates, they, in isolation, can not fully characterize them. However, the set of features proved to be fairly efficient in the candidates' description, reaching 100% correct classification in the test samples.

The size of the samples used for tests, however, was too small for getting any definitive conclusion, but the statistics obtained from the tests, specially the ones concerning the target hitting rate, showed that the proposed measurements appear themselves as viable alternatives for geometrical objects description for a variety of applications, particularly in the medical area for classifying lung nodules.

Acknowledgements

References

1. Partnership, N.L.C.: Frequently asked questions (2007), Available at http://www.nationallungcancerpartnership.org
2. Bi, J., Periaswamy, S., Okada, K., Kubota, T., Fung, G., Salganicoff, M., Rao, R.B.: Computer aided detection via asymmetric cascade of sparse hyperplane classifiers. In: KDD 2006, pp. 837–844. ACM Press, New York (2006)
3. Agam, G., Armato III, S.G., Wu, C.: Vessel tree reconstruction in thoracic ct scans with application to nodule detection. IEEE Trans. Med. Imaging 24, 486–499 (2005)
4. Uppaluri, R., Hoffman, E., Sonka, M., Hartley, P., Hunninghake, G., Mclennan, G.: Computer recognition of regional lung disease patterns. American Journal of Respiratory and Critical Care Medicine 160, 648–654 (1999)
5. Korfiatis, P., Kalogeropoulou, C., Costaridou, I.: Computer aided detection of lung nodules in multislice computed tomography (2006)
6. Mousa, W.A.H., Khan, M.A.U.: Lung nodule classification utilizing support vector machines. In: ICIP (3), pp. 153–156 (2002)
7. Clunie, D.A.: DICOM Structured Reporting. PixelMed Publishing, Pennsylvania (2000)
8. Silva, A.C.: Algoritmos para Diagnostico Assistido de Nodulos Pulmonares Solitarios em Imagens de Tomografia Computadorizada. PhD thesis, PUC-Rio (2004)
9. Gurcan, M.N., Sahiner, B., Petrick, N., Chan, H.P., Kazerooni, E.A., Cascade, P.N., Hadjiiski, L.M.: Lung nodule detection on thoracic computed tomography images: Preliminary evaluation of a computer-aided diagnosis system. Medical Physics 2552–2558 (2002)
10. Silva, A., Carvalho, P.C., Nunes, R., Gattass, M.: Algorithms for assisted diagnosis of solitary lung nodules in computerized tomography images. Technical Report TR-2004-02, IMPA - Visgraf Laboratory (2004)
11. Burges, C.J.C.: A Tutorial on Support Vector Machines for Pattern Recognition. Kluwer Academic Publishers, Dordrecht (1998)
12. Chang, C.C., Lin, C.J.: LIBSVM: a library for support vector machines (2001), Available at http://www.csie.ntu.edu.tw/~cjlin/libsvm

Edge Detection in Ventriculograms Using Support Vector Machine Classifiers and Deformable Models

Antonio Bravo[1], Miguel Vera[2], and Rubén Medina[3]

[1] Grupo de Bioingeniería, Universidad Nacional Experimental del Táchira,
Decanato de Investigación, San Cristóbal 5001, Venezuela
abravo@unet.edu.ve
[2] Laboratorio de Física, Departamento de Ciencias, Universidad de Los
Andes–Táchira, San Cristóbal 5001, Venezuela
[3] Grupo de Ingeniería Biomédica (GIBULA), Universidad de Los Andes,
Facultad de Ingeniería, Mérida 5101, Venezuela

Abstract. In this paper a left ventricle (LV) contour detection method is described. The method works from an approximate contour defined by anatomical landmarks extracted using Support Vector Machine (SVM) classifiers. The LV contour approximation is used as an initialization step for the deformable model algorithm. An optimization method based on a gradient descend algorithm is used to obtain the optimal contour that provides a minimum energy value. Both classifier and edge detection method performances have been validated. The error is determined as the difference between the shape estimated by the algorithm and the shape traced by an expert.

Keywords: anatomical landmarks, left ventricle, support vector machines, edge detection, deformable models.

1 Introduction

Segmentation and contour extraction are fundamental tasks in high–level image analysis. The main goal is to divide an image into parts that have a strong correlation with objects or real shapes contained in the image [1].

In cardiac medical imaging modalities, anatomical boundaries cannot be detected by algorithms that use only edge or region information. Low contrast, noise, and non–uniformity of regional intensities are some of the problems associated with cardiac imaging modalities. These problems are always present in ventriculograms. The left ventricle boundary detection in X–ray ventriculograms is a rather complicated task because of the presence of fuzzy superposition of anatomical structures [2].

The aim of this paper is to develop a method combining both SVM and deformable model approaches for LV contour detection.

1.1 Support Vector Machines

Support vector machine is a methodology based on the Vapnik–Chenovenkis learning theory and the structural risk minimization principle [3]. SVMs are efficient non–parametric classification and regression tools [4,5]. In classification problems SVMs are used for constructing a discriminant function to separate classes using vectors nearest to the decision boundary. The examples or training set for a two–class classification problem can be represented as: $\mathcal{S} = \{(\mathbf{x}_i, y_i)\}_{i=1}^{l} \subset \mathbb{R}^N \times \{+1, -1\}$.

The classification task (from $\mathcal{S}$) addresses the general problem of finding a discrimination function defined from an input space $\mathbb{R}^N$ into an unordered set of classes $\{+1, -1\}$. This discrimination function in some m–dimensional feature space is a separating hyper-plane expressed as follows:

$$f(\mathbf{x}) = \text{sign}(\mathbf{w} \cdot \mathbf{x} + b) \ , \tag{1}$$

where $\mathbf{w}$ is normal to the hyper-plane, b is the bias, $\|\mathbf{w}\|$ is the Euclidean norm of $\mathbf{w}$, and $|b|/\|\mathbf{w}\|$ is the perpendicular distance from the origin to the hyper-plane.

The SVM objective is to find the hyper-plane with minimum norm $\|\mathbf{w}\|^2$. The classification problem using linear machines trained on non–separable examples [6,7], can be formulated as a quadratic programming problem where the optimal solution is obtained using Lagrange Multipliers. This solution can be written as:

$$\mathbf{w} = \sum_{i=1}^{l} \lambda_i y_i \mathbf{x}_i \ , \tag{2}$$

where $\{\lambda_1, \ldots, \lambda_l\}$ are positive Lagrange multipliers. In (2), the examples for which $\lambda_i > 0$ are known as *support vectors* and correspond to the critical elements of the training set. In real classification tasks a linear SVM is not appropriate because the classes are generally separated by a non–linear function [7]. In this case, the examples are projected to a feature space of higher (possibly infinite) dimensions via a nonlinear mapping function $\mathbf{\Phi}(\cdot)$. This projection process is applied to transform the non–linear problem in the N–space to a linear problem in the M–space. The SVM solution can be written as:

$$f(\mathbf{x}) = \text{sign}\left(\sum_{i=1}^{l} \lambda_i y_i \mathbf{\Phi}(\mathbf{x}_i) \cdot \mathbf{\Phi}(\mathbf{x}) + b\right) \ . \tag{3}$$

1.2 Deformable Models

A deformable model is a parametric contour $\mathcal{C}$ located in the image plane $(u, v) \in \mathbb{R}^2$. This contour could be represented as a controlled continuity spline expressed as $\mathbf{p}(s) = (\mathbf{u}(s), \mathbf{v}(s))^\top$, where $\mathbf{u}$ and $\mathbf{v}$ are vectors of coordinate functions and $s \in [0, 1]$ is the parametric domain [8]. The left ventricle shape defined by contour $\mathcal{C}$ is modeled by the following functional:

$$\mathcal{E}(\mathbf{p}) = \mathcal{I}(\mathbf{p}) + \mathcal{P}(\mathbf{p}) + \mathcal{R}(\mathbf{p}) \ . \tag{4}$$

This functional represents the contour energy that includes the internal energy $\mathcal{I}(\mathbf{p})$, the image energy $\mathcal{P}(\mathbf{p})$ and the external energy $\mathcal{R}(\mathbf{p})$. The optimal contour shape corresponds to the minimum of this energy function. The internal deformation energy (5) incorporates the smoothness and bending properties of the contour.

$$\mathcal{I}(\mathbf{p}) = \int_s \alpha(s) \left| \frac{\partial \mathbf{p}}{\partial s} \right|^2 + \beta(s) \left| \frac{\partial^2 \mathbf{p}}{\partial s^2} \right|^2 ds \ , \tag{5}$$

where $\alpha(s)$ and $\beta(s)$ are weighting coefficients for the smoothness and bending terms respectively. The functional representing the image energy (6) is generally based on the edge detection theory. Several approaches use the theory proposed by Marr and Hildreth [9], where the intensity changes can be detected by finding the maximum or the minimum of $\mathbf{G}_\sigma * \mathbf{I}$ that represents the convolution of an image $\mathbf{I}$ with a bi-dimensional Gaussian kernel $\mathbf{G}_\sigma$. The image energy pushes the deformable model toward the contour that constitutes the target features.

$$\mathcal{P}(\mathbf{p}) = -|\nabla \mathbf{G}_\sigma * \mathbf{I}(\mathbf{p})| \ , \tag{6}$$

where σ is the spread parameter (standard deviation) of the Gaussian kernel.

The energy constraints $\mathcal{R}$ imposes additional external forces leading to the minimum energy corresponding to the contour. Different approaches for defining the external constraint forces have been reported by Kass [8].

2   Method

2.1   Initialization

The proposed method uses the traditional deformable contour model for detection of the left ventricle boundary. This deformable model uses a parametric contour $\mathbf{p}(s)$ (see section 1.2) as the input. This parametric contour is deformed in order to minimize the energy functional (4). The deformable model is very sensitive to initialization. Therefore, selecting the initial contour is a very important stage.

Our initial contour is estimated from myocardial landmarks extracted using an approach based on machine learning [10]. This approach uses support vector machines (SVM) to localize left ventricle landmarks in ventriculographic sequences. The apex (AP), the basal regions (BA2, BP3, BP4) and the aortic valve sides (VA, VP) are selected as landmarks of interest to construct the SVM classifier (see Figure 1).

A SVM classifier is constructed using the Gaussian Radial Basis Function as parametric kernel. The MatLab Support Vector Machines library is used for performing the training based on a set of 1500 patterns.

SVM Training. Each LV landmark is a 31×31 pixel pattern manually traced by a cardiologist. A total of 300 patterns constitutes the landmarks dataset (50 patterns for each landmark). A similar procedure is used for obtaining a dataset of 1200 non–landmark pixel patterns generated from angiographic images without
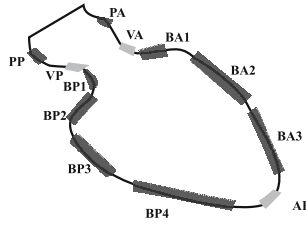
Fig. 1. Fifteen anatomical landmarks established by the American Heart Association

including any landmark information. The training process is used to construct a decision surface. This surface enables classification of input pixel patterns as left ventricle landmarks or non–landmarks. During the test phase a set of 116 images not included in the training set was used. A landmark recognition rate of 98.35 % was obtained.

SVM Based Landmark Detection. The left ventricle approximate border is constructed from landmark points extracted by the SVM classifier. Given the input ventriculographic image, landmarks are located by exhaustively scanning the image for landmark-like patterns. Landmark localization is performed using a 31×31 sliding window whose content is analyzed by the SVM to determine whether a landmark is present or not. Each landmark is identified by the center point of the 31×31 pattern considered. After all landmark points are identified, they are joined clockwise starting from VA landmark point and ending in the VP landmark point. Identification of the VA landmark is performed using prior knowledge about the upper part of the aortic valve localization in ventriculographic images.

Initial Contour Estimation. Five more points are estimated using a linear interpolation method from the previously calculated points (AP, BA2, BP3, BP4, VA, VP). The five new points are obtained as follows: the midpoint of the line described by VA and BA2 landmarks is computed. This midpoint is used to construct a new line perpendicular to the line described by VA and BA2 landmarks. The maximum image gradient is searched over this perpendicular line, and the first new point of the set is the one located at the maximum gradient along the line. The remaining points are obtained following the same process between the corresponding pair of landmarks: BA2–AP, AP–BP4, BP4–BP3, and BP3–VP. At the end, a new set of eleven points is available to describe the initial LV contour. This set of points is used to generate the parameterized contour using the b–spline method [11]. A final discrete set of evenly distributed points is determined by re-sampling the parameterized contour providing the initial contour for the deformable model.

2.2   Edge Enhancement

The approaches based on gradient have been widely used for edge enhancement [9,12] while smoothing filters have been used for minimizing noise content. We

propose four different techniques to enhance the edges of the left ventricle cavity in the angiographic images. These techniques are based on four smoothing filters: 1) the averaging filter [13], 2) the Gaussian filter [2], 3) the similarity filter [14], and 4) the top–hat morphological filter [15]. Once smoothed, the images are processed using an optimal gradient operator [16]. The filters are applied after the initial contour detection. The smoothing filters are applied to the input image, the gradient operator is applied to the smoothed images.

The averaging filter. According to this filter, if a pixel value in the input image ($\mathbf{I}_{\text{in}}$) is greater than the average of its neighbors plus a certain threshold ε, then the pixel value in the output image ($\mathbf{I}_{\text{average}}$) is set to the average value, otherwise the output pixel is set to the pixel value in the input image. The threshold value ε was set to the standard deviation of the input image.

The Gaussian filter. Gaussian filtering is a frequently used technique for image smoothing. Each pixel value in the output image ($\mathbf{I}_{\text{Gauss}}$) is the result of the convolution between the input image ($\mathbf{I}_{\text{in}}$) and a kernel that represents a 2–D Gaussian distribution.

The Similarity filter. This filter quantifies the difference between the gray–level values of pixels in the original image $\mathbf{I}_{\text{in}}$ and in the smoothed image ($\mathbf{I}_{\text{average}}$) based on a similarity criterion [14]. The similarity filter is constructed using the procedure proposed in [17]:

- For each $p_{\mathbf{I}_{\text{in}}}(i,j) \in \mathbf{I}_{\text{in}}$ and each $p_{\mathbf{I}_{\text{average}}}(i,j) \in \mathbf{I}_{\text{average}}$ obtain the feature vectors $\mathbf{pv}_{\mathbf{I}_{\text{in}}} = [I_1, a]$ and $\mathbf{pv}_{\mathbf{I}_{\text{average}}} = [I_2, b]$. Where, I_1 and I_2 denote the intensities associated with pixel (i,j) and, a and b are the intensity average in a $l \times l$ neighborhood around the pixel (i,j).
- The filter output or similarity image ($\mathbf{I}_{\text{S}}$) is obtained according to equation (7).

$$\mathbf{I}_{\text{S}} = \omega_1(I_1 - I_2)^2 + \omega_2(I_1 - b)^2 + \omega_3(I_2 - a)^2 \ , \tag{7}$$

where ω_1, ω_2 and ω_3 were set to one.

The top–hat morphological filter. The top–hat is a gray-level morphological operator that can be used as a nonlinear filtering technique. These filters preserve the location of the border transition, and at the same time denoise the image. We consider the white top–hat (WTH) and its dual, the black top–hat (BTH). The white top–hat is defined as the difference between the average image and the opened Gaussian filtered image. The black top–hat is obtained by subtracting the average image from the closed Gaussian filtered image. A disk structuring element (D) of size 11×11 is used for both the opening and closing operators. Opening ($\circ$) and closing ($\bullet$) morphology operators are derived from the basic operations of erosion ($\ominus$) and dilation ($\oplus$) [18]. The top–hat images $\mathbf{I}_{\text{BTH}}$ and $\mathbf{I}_{\text{WTH}}$ are calculated according to equation (8).

$$\mathbf{I}_{\text{BTH}} = \mathbf{I}_{\text{average}} - (\mathbf{I}_{\text{Gauss}} \bullet \text{D}), \quad \mathbf{I}_{\text{WTH}} = \mathbf{I}_{\text{average}} - (\mathbf{I}_{\text{Gauss}} \circ \text{D}) \ . \tag{8}$$

The optimal gradient operator. These operators can be constructed using a consistency criterion as proposed in [16]. The optimum 5×5 operator ($\nabla_{5 \times 5}$)

developed by Ando [16, p. 258] is used to obtain $x-$ and $y-$directional gradients associated with the smoothed images.

2.3   Left Ventricle Deformable Model

Shape model. The shape model used in our approach is a bi-dimensional dynamic parametric contour $\mathcal{C}$. The smoothness constraint force in the shape model is represented by the internal energy term $\mathcal{I}(\mathbf{p})$. In this paper, we use the internal energy formulation proposed by Kass [8], which is related to the local contour curvature. The internal energy is represented by a linear combination of smoothness and bending contour properties as expressed in (5). This energy term is discretized using the finite difference scheme.

The image energy term $\mathcal{P}$, in the contour energy functional (9), is defined as the average of the gradient magnitude for the smoothed images.

$$\mathcal{P}(\mathbf{p}) = -\gamma\frac{1}{3}\left(\|\nabla\,\mathbf{I}_{\mathrm{Gauss}}(\mathbf{p})\| + \|\nabla\,\mathbf{I}_{\mathrm{WTH}}(\mathbf{p})\| + \|\nabla\,\mathbf{I}_{\mathrm{BTH}}(\mathbf{p})\|\right)\ , \qquad (9)$$

where ∇ represents the optimum gradient operator $\nabla_{5\times5}$ proposed in [16] and γ is a weighting constant.

Our deformable model incorporates a regularization term $\mathcal{R}$ for attracting the deformable model towards the cardiac cavity edge. The restriction term $\mathcal{R}$ allows to reorient the direction field associated with the image energy term. The restriction is defined from the similarity image obtained using (7). This functional is expressed according to (10) where κ is a weighting constant.

$$\mathcal{R}(\mathbf{p}) = -\kappa\|\nabla\,\mathbf{I}_{\mathrm{S}}(\mathbf{p})\|\ . \qquad (10)$$

Shape evolution. The dynamics of this model is established according to deformable model theory (see Section 1.2). In this kind of models, the energy functional $(\mathcal{E})$ gives rise to forces deforming the model. The LV shape model energy $(\mathcal{E})$ is minimized by using an iterative optimization process based on a gradient descent algorithm. The aim of this iterative optimization process is to express the current contour shape based on the knowledge of the corresponding previous contour energy. The normalized equation is given by (11).

$$\mathbf{p}^{k+1} = \mathbf{p}^k + \delta\frac{\mathcal{E}(\mathbf{p}^k)}{\|\mathcal{E}(\mathbf{p}^k)\|}\ , \qquad (11)$$

with δ denoting the gradient descent step size and k the iteration number.

3   Results

The proposed method has been tested with mono–plane sequences of ventriculographic images that have been acquired from patients using a digital flat–panel X–rays system (Innova$^{\mathrm{TM}}$ 4150, General Electric Medical System). These images

were acquired using the right anterior oblique (RAO 30°) view. Each image has a resolution of 512×512 pixels. Each pixel is represented with 8 bits.

The SVM classifier was constructed using the Gaussian radial basis function as a parametric kernel. Our SVM anatomical landmarks classifier is constructed using the Least Squares Support Vector Machines library [19]. The support vectors obtained in the training stage are used to construct the decision surface used to detect the LV landmarks in the original image. The proposed approach has been tested with ventriculograms acquired at several instants of the cardiac cycle. In figure 2, results of the LV landmarks extraction approach for the ventriculogram sequences are shown. Validation of the approach is performed by quantifying the difference between the LV landmark location obtained with respect to the LV landmark located by a cardiologist. The average of the errors obtained ($mean \pm standard\ deviation$) for five sequences of ventriculograms in the RAO view, including 163 images is 2.17 mm $\pm$ 0.93 mm.
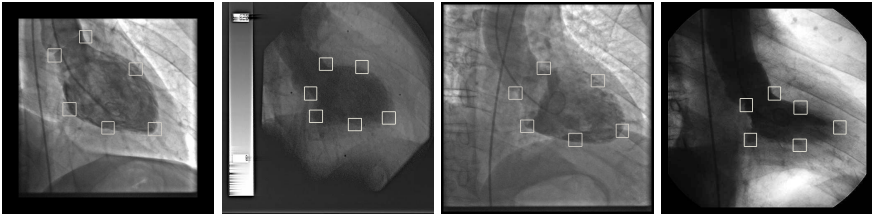
Fig. 2. Bounding white boxes represents the anatomical landmarks obtained

The ventriculographic images are enhanced using the techniques described in section 2.2. Figure 3 shows the enhancement procedure for an end–diastole ventriculogram image. The smoothed image using the Gaussian filter is shown in figure 3.a. Figures 3.b and 3.c show the top–hat images (obtained using equation (8)). The similarity image is shown in figure 3.d. Figures 3.e–3.h show the gradient magnitude images obtained from the smoothed images.

The approximate contour is constructed using the procedure described in section 2.1. This approximation is used to initialize our deformable model method. Given the initial contour, the forces associated with the model and its dynamics can be obtained using equations (5), (9), (10) and (11) using the information extracted from preprocessed images as these shown in figure 3. Two of the five sequences analyzed are used to train and initialize the parameter set as follows. The detection process is applied by varying each parameter value. For each parameter, a comparison between the resulting contour and the contour traced by the cardiologist is obtained. The optimal parameter values are $\{\alpha = 0.005, \beta = 0.00005, \gamma = 0.01, \kappa = 0.01, \delta = 0.5\}$. Figure 4 shows the results of the edge detection process. The image shows a zoom of the LV region where the initial and final contours are located. Figure 4.a shows the approximate contour used to initialize the deformable model. The approximate contour evolution towards the optimum contour is shown in figure 4.b, where the initial contour is

(a) (b) (c) (d)

(e) (f) (g) (h)
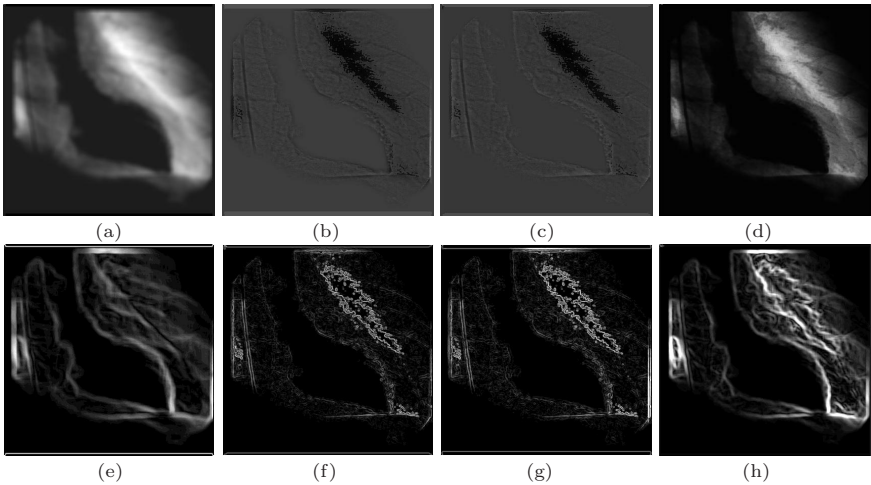
Fig. 3. Edge enhancement results. a) Gaussian filtered image. b) Black top–hat image. c) White top–hat image. d) Similarity image. e) Gradient magnitude for the Gaussian image. f) Gradient magnitude for the Black top–hat image. g) Gradient magnitude for the White top–hat image. g) Gradient magnitude for the Similarity image.

indicated by white dash-dotted line and the final contour by black dash-dotted line. Figure 4.c shows the contour energy behavior where the minimum energy state is reached after few iterations. Figure 5 shows the results obtained for the end diastole images in four ventriculographic sequences. The contours traced by the expert are shown using white dash-dotted lines and the final segmentations are shown using black dash-dotted lines. The performance of the segmentation method is validated using the approach proposed by Suzuki [20, p. 335]. Five ventriculogram sequences including a total of 163 images are considered during the validation process. Comparison between the segmented contours and the contours traced by a cardiologist shows an average contour error E_C of 5.97 % and an average area error E_A of 3.71 %.

(a) (b) (c)
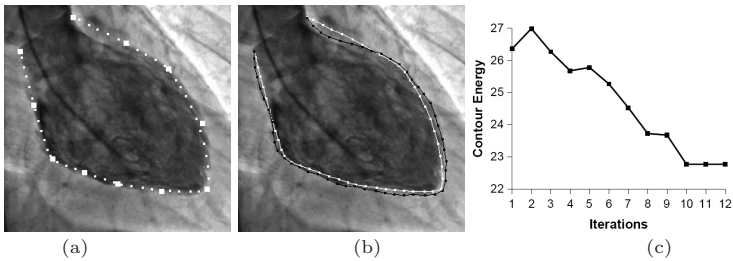
Fig. 4. Edge detection process. a) Initial contour (white dash-dotted line). c) Evolution to final contour (black dash-dotted line). c) Contour energy evolution.
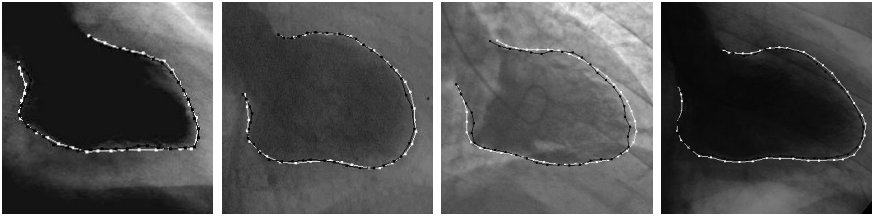
Fig. 5. Results of the left ventricle segmentation. Ground truth contour indicated by a white dash-dotted line. Contour extracted by the proposed approach is shown using a black dash-dotted line.

4   Conclusions

This paper has presented an automatic method for segmentation of the LV shape using SVM and deformable models. The accurate initialization of the deformable model is performed based on landmarks extracted using Support Vector Machine classifiers. The SVM classifier approach does not require preprocessing of the input data. The deformable model incorporates information about the ventricular edge by means of an energy functional expressed as a linear combination of the gradient magnitude estimated from several edge enhanced images.

The proposed segmentation method is accurate for automatically detecting the left ventricle contour in ventriculograms. The accuracy has been accessed by tests performed for the SVM based initialization approach as well as the validation for the complete segmentation method. Further research is aimed at using a multi-class SVM and at performing a more complete validation.

Several efforts to develop an automatic contour detection method for ventricular images have been reported so far [20,1,21]. However, these methods have not been subjected to an extensive clinical validation. In this paper, we have proposed an alternative automatic method that can be implemented easily. It enables the quantitative analysis of the cardiovascular function based on ventriculograms.

Acknowledgments

References

1. Sui, L., Haralick, R., Sheehan, F.: A knowledge–based boundary delineation system for contrast ventriculograms. IEEE Trans. Inform. Technol. Biomed. 5(2), 116–132 (2001)
2. Pratt, W.: Digital Image Processing. John Wiley - Sons, USA (1978)
3. Vapnik, V.: The Nature of Statistical Learning Theory. Springer, New York (1995)

4. Osuna, E., Freund, R., Girosi, F.: Training support vector machines: an application to face detection. In: CVPR 1997, San Juan, Puerto Rico, pp. 130–136 (1997)
5. Smola, A.J.: Learning with Kernels. PhD thesis, Technische Universit
6. Burges, C.: A tutorial on support vector machines for pattern recognition. Knowledge Discovery and Data Mining 2(2), 121–167 (1998)
7. Osuna, E., Freund, R., Girosi, F.: Support vector machines: Training and applications. Technical report, Artificial Intelligence Laboratory, Massachusetts Institute of Technology (1997)
8. Kass, M., Witkin, A., Terzopoulos, D.: Snakes: Active contours models. Int. J. Comput. Vis. 1, 321–331 (1987)
9. Marr, D., Hildreth, E.: Theory of the edge detection. Proccedings of the Royal Society of London 207, 187–217 (1980)
10. Vera, M., Bravo, A.: Left ventricle image landmarks extraction using support vector machines. In: Proceedings of 2nd International Conference on Computer Vision Theory and Applications, Barcelona, Spain, pp. 339–343 (2007)
11. Barsky, B.A.: Computer Graphics and Geometric Modeling Using Beta–Splines. Springer, USA (1988)
12. Canny, J.: A computational approach to edge detection. IEEE Trans. Pattern Anal. Machine Intell. PAMI-8, 679–698 (1986)
13. Gonzalez, R., Woods, R.: Digital Image Processing. Addison–Wesley Publishing Company, New-Jersey (1992)
14. Haralick, R., Shapiro, L.: Computer and Robot Vision, vol. I. Addison-Wesley Publishing Company, USA (1992)
15. Hanbury, A., Serra, J.: Morphological operators on the unit circle. IEEE Trans. Image Processing 10(12), 1842–1850 (2001)
16. Ando, S.: Consistent gradient operators. IEEE Trans. Pattern Anal. Machine Intell. 22(3), 252–264 (2000)
17. Bravo, A., Medina, R., Diaz, J.A.: A clustering based approach for automatic image segmentation: An application to biplane ventriculograms. In: Martínez-Trinidad, J.F., Carrasco Ochoa, J.A., Kittler, J. (eds.) CIARP 2006. LNCS, vol. 4225, pp. 316–325. Springer, Heidelberg (2006)
18. Serra, J.: Image Analysis and Mathematical Morphology. A Press, London (1982)
19. Suykens, J., Gestel, T.V., Brabanter, J.D., Moor, B.D., Vandewalle, J.: Least Squares Support Vector Machines. World Scientific, Singapore (2002)
20. Suzuki, K., Horiba, I., Sugie, N., Nanki, M.: Extraction of left ventricular contours from left ventriculograms by means of a neural edge detector. IEEE Trans. Med. Imag. 23(3), 330–339 (2004)
21. Oost, E., Koning, G., Sonka, M., Oemrawsingh, P.V., Reiber, J.H.C., Lelieveldt, B.P.F.: Automated contour detection in x–ray left ventricular angiograms using multiview active appearance models and dynamic programming. IEEE Trans. Med. Imag. 25(9), 1158–1171 (2006)

Breast Cancer Diagnosis Based on a Suitable Combination of Deformable Models and Artificial Neural Networks Techniques

Yosvany López[1], Andra Novoa[1], Miguel A. Guevara[1], and Augusto Silva[2]

[1] Center for Advanced Computer Sciences Technologies, Ciego de Ávila University, Cuba
[2] IEETA, Aveiro University, Portugal
{yosvany,andra}@informatica.unica.cu,
{mangel,asilva}@ieeta.pt

Abstract. According to the World Health Organization (WHO) breast cancer is the most common cancer suffered by women in the world, which during the last two decades has increased the women mortality in developing countries. Mammography is the best method used for screening; it is a test producing no inconvenience and with small diagnostic doubts of breast cancer since the preclinical phase. For this reason, unfailing Computer-Aided Diagnosis systems for automated detection/classification of abnormalities are very useful and helpful to medical personnel. In this work is proposed a novel method that combines deformable models and Artificial Neural Networks among others techniques to diagnose diverse mammography abnormalities (calcifications, well-defined / circumscribed masses, spiculated masses, ill-defined masses, architectural distortions and asymmetries) as benign or malignant. The proposed algorithm was validated on the Mammographic Image Analysis Society (MiniMIAS) database in a dataset formed by 100 mammography images, which were selected randomly.

Keywords: Breast cancer, mammography images, deformable models, artificial neural networks.

1   Introduction

According to the World Health Organization (WHO) breast cancer is the most common cancer suffered by women in the world with 1151298 cases in 2002. During the last two decades this disease has increased the women mortality in developing countries having, up to date, 31% of cases. Breast cancer is one of the major causes of death in women aged 35 – 64 years in Latin America.

Mammography is the best method used for screening; it is a test producing no patients inconvenience and with small diagnostic doubts of breast cancer since the preclinical phase. For this reason, unfailing Computer-Aided Diagnosis (CAD) systems for automated detection/classification of abnormalities are very useful and helpful, providing a valuable "second opinion" to medical personnel [1, 2].

Several methods have been reported to detect the presence of abnormalities in digital mammograms. Basically is possible to classify the developed methods in two classes: methods for enhancing mammography abnormalities details (only to be classified by specialized medical personnel) and automatic or semiautomatic CAD methods (in which is produced an automatic or semiautomatic abnormalities classification). Some of CAD methods reported are: methods for masses detection using multiple circular path convolution neural networks models [3], the combination of Artificial Neural Networks (ANN) and Wavelet Transform (WT) for detecting microcalcifications [4], CAD algorithms to identify breast nodule malignancy combining multiple sonographic features and ANN classifiers [5], learning contextual relationships in mammograms based on hierarchical pyramid ANN [6], neural-genetic algorithms for feature selection to classify microcalcifications [7], and methods for discrimination and classification of mammograms in benign, malignant and normal tissues using independent component analysis and ANN [8] among others techniques.

Methods mentioned before represent important approximations (with interesting results) to improve (in major or minor degree) the mammography image analysis process, but in general (at present) reported techniques are paying attention only to classify some specific class of masses or calcifications and not put together the complete classification problem. Wide-ranging techniques including the possibility to classify calcifications and diverse classes of masses are still a not solved problem.

In this work we propose a new method that combines deformable models and ANN among others techniques to diagnose a wide range of mammography abnormalities classes (calcifications, well-defined/circumscribed masses, spiculated masses, ill-defined masses, architectural distortions and asymmetries) as benign or malignant tissues. The proposed algorithm was validated on the Mammographic Image Analysis Society (MiniMIAS) database, with a dataset formed by 100 images selected randomly, of which 60 images were used in the training set and the rest for method evaluation.

The remainder paper is organized as follows: section 2 describes the technical aspect related with the new proposed method. Section 3 outlines the achieved results. Conclusions are presented in section 4, where also are included some ideas for future work.

2   Proposed Method

The developed method includes five steps: region of interest (ROI) selection, adjust image intensities, segmentation, features extraction and abnormalities classification. An algorithm prototype was implemented in MATLAB (version 7.0) to test the proposed method on the MiniMIAS database. The MiniMIAS (MiniMammographic) is a reduce version of Mammographic Image Analysis Society (MIAS) database with a resolution of 200 microns by pixel and clipped/padded so that every image size is equal to 1024 x 1024 pixels. We selected randomly a representative dataset that included examples of diverse classes of abnormalities: calcifications, well-defined/circumscribed masses, spiculated masses, ill-defined masses, architectural distortions and asymmetries. The dataset was composed by 100 images, of which 60 images were used in the training set and the rest for method evaluation.

2.1   ROI Selection

ROI Selection is a fundamental step because the selected region represents the mammography image part used as input for the developed algorithm. This process allows that the user select for processing only regions suspicious to contain abnormalities (see Fig. 1b).

2.2   Adjust Image Intensities

One of the most common defects of photographic or electronic images is poor contrast resulting from a reduced, and perhaps nonlinear, image amplitude range. Image contrast can be often improved by amplitude rescaling of each pixel. Adjust image intensities is a conventional contrast enhancement technique. To enhance the mammography images contrast we map the grayscale intensity values of input mammography images to new values such that 1% of data is saturated at low and high intensities to produce a new image in which the contrast is increased (see Fig. 1c).

2.3   Segmentation

Segmentation is considered an important step in any image analysis process because correct objects segmentation can reduce drastically the time and the computational cost of any image analysis process. Deformable models (snakes) have been used successfully in many and diverse image segmentation tasks. Our method used a novel variant of deformable models: the live wire techniques to produce faster and precise abnormalities segmentation of selected ROIs (see Fig.1d).

Live wire (or intelligent scissors) is an interactive boundary tracing technique, considered as a competing technique to snakes. This technique allows (with minimal user interaction) to exercise control over the segmentation process. Live wire have two essential components: a local cost function that assigns lower cost to image features of interest (edges) and an expansion process to form optimal boundaries for objects of interest, based on the cost function and seed points provided by the user. Boundary finding in live wire can be formulated as a directed graph search for an optimal (minimum cost) path using Dijkstra´s algorithm in the underlying graph model. A more profound live wire technique definition, with examples of applications to medical images are presented in [9],[10],[11] and [12].

We apply the live wire technique to produce the first curve contour approximation E (edge points) of the abnormality present in the selected ROI (see Fig. 1d). Due to E be not a continuous curve we interpolate E using a spline function to produce a continuous curve: a better abnormality approximation. Final E contour is used after to compute the morphometric feature vector of the abnormality under study.

2.4   Feature Vector

Diverse sets of morphometric features were evaluated and tested [13], but based on statistical evaluations we selected a set of five features to include in the feature vector (related with shape and size), which were sufficient to classify correctly the abnormalities under study. These features are: object area, brightness, object shape,

roughness and elongation. For computing these features we take as input the edge pixels that belong to the closed curve (contour) represented by E. Mathematic formulation used for computing the features was the following:

- O set of pixels that belong to the abnormality segmented
- $E \subset O$ edge pixels (subset of O)
- $Area = |O|$
- $Perimeter = length(E)$
- $Elongation = \dfrac{diam}{DIAM}$, where *diam* and *DIAM* represent the minimum and maximum diameters
- $Roughness = \dfrac{Perimeter^2}{4 \times \pi \times Area}$
- $Shape = \dfrac{Perimeter \times (diam + DIAM)}{8 \times (Area)}$
- $Brightness = mean(O)$ Intensity levels average of pixels that belong to the selected abnormality
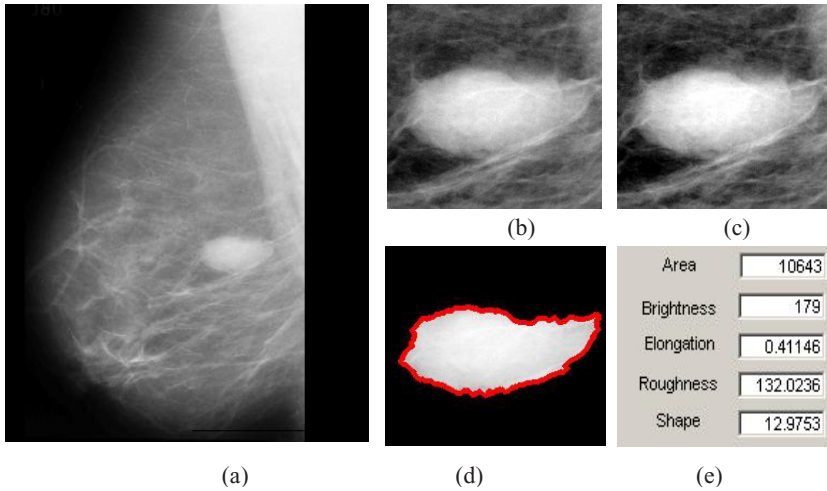
Fig. 1. a) Original Image, b) ROI selected, c) Adjusted intensities of (b), d) Segmented abnormality, e) Feature vector computed from (d)

2.5 Abnormalities Classification

Semiautomatic or automatic abnormalities classification has the aim to offer one "second opinion" (diagnostic) to medical personnel about abnormalities present on the mammography images. We designed and tested different ANN models to classify

abnormalities under study, but better results were obtained with Feedforward Backpropagation (FFBP) and Learning Vector Quantization (LVQ) ANN models. These neural networks models were trained with 60 vectors, which contain the computed features described before in 2.4 (including benign and malignant examples) representative of diverse abnormalities classes: calcifications, well-defined/ circumscribed masses, spiculated masses, ill-defined masses, architectural distortion and asymmetries.

2.5.1 Feedforward Backpropagation Neural Network

The Feedforward Backpropagation (FFBP) is one of the more studied neural network by the scientific community and the most common used in many medical applications. Morphologically, the FFBP is formed by a set of organized neurons in layers: hidden and output layers. Network architecture is determined by the number of neurons in the hidden layers.

The learning process of a FFBP network is characterized to be supervised, the network parameters (known as weights) are estimated from a group (pairs) of training patterns composed for input and output patterns $\{(x^t, y^t)\}t = 1..n$.

The backpropagation algorithm [14] is a generalization of the delta rule proposed by Widrow-Hoff [15]. The term "backpropagation" refers to the form in that the error gradient function is calculated for the FFBP network. Therefore, the network adjust takes place as a result of the estimation of weights parameters. The learning involves an adjustment of the weights comparing the desired output with the network answer so that the error is minimized.

Our FFBP network was designed with three layers: two hidden layers with 14 and 8 neurons respectively and an output layer with 12 neurons. Each neuron from output layer represent one (benign or malignant) abnormality class (calcifications, well-defined/circumscribed masses, spiculated masses, ill-defined masses, architectural distortions and asymmetries). The logarithmic sigmoid (*logsig*) was the transfer function used on the three layers. Mathematical definition of this function is the following: $\text{logsig}(n) = 1 / (1 + \exp(-n))$.

A MATLAB network implementation can be observed below in Fig.2.
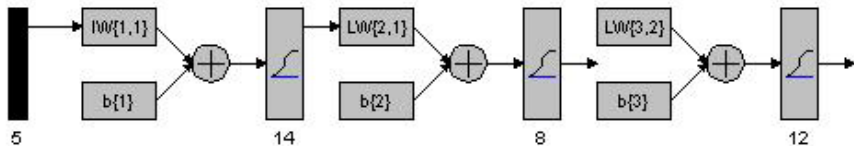
Fig. 2. Feedforward Backpropagation Neural Network

2.5.2 Learning Vector Quantization

Learning Vector Quantization (LVQ) is a precursor of the well-known self-organizing maps (also called Kohonen feature maps) and like them it can be seen as a special kind of ANN[16]. Both types of networks represent a set of reference vectors, the positions of which are optimized with a given dataset. A neural network for learning

vector quantization consists of two layers: an input layer and an output layer. It represents a set of reference vectors, the coordinates of which are the weights of the connections leading from the input neurons to an output neuron. Hence, one may also say that each output neuron corresponds to one reference vector. The learning method of learning vector quantization is often called competition learning, because it works as follows: for each training pattern the reference vector that is closest to it is determined. The corresponding output neuron is also called the winner neuron. The weights of the connections to this neuron - and this neuron only: the winner takes all - are then adapted. The direction of the adaption depends on whether the class of the training pattern and the class assigned to the reference vector coincide or not. If they coincide, the reference vector is moved closer to the training pattern, otherwise it is moved farther away. This movement of the reference vector is controlled by a parameter called the learning rate. It states as a fraction of the distance to the training pattern how far the reference vector is moved. Usually the learning rate is decreased in the course of time, so that initial changes are larger than changes made in later epochs of the training process. Learning may be terminated when the positions of the reference vectors do hardly change anymore.

We utilized an LVQ network formed by a competitive layer (input layer) of 16 neurons and a linear layer (output layer) of 12 neurons. Each neuron from linear layer represent one (benign or malignant) abnormality class (calcifications, well-defined/ circumscribed masses, spiculated masses, ill-defined masses, architectural distortions and asymmetries), that we consider the adequate design to classify the abnormality classes under study.

A MATLAB network implementation can be observed in Fig.3.
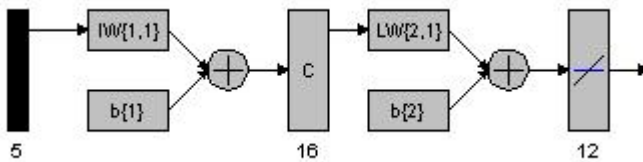
Fig. 3. Learning Vector Quantization Neural Network

3   Results and Discussions

Proposed method was evaluated in the MiniMIAS (MiniMammographic) database. MiniMIAS is a reduce version of MIAS database, with a resolution of 200 microns by pixel and clipped/padded so that every image size is equal to 1024 x 1024 pixels. MiniMIAS have included an information file with several details as: image reference number, type of background tissues, class of abnormality present, severity of abnormality (benign or malignant), the x, y coordinates of the abnormality center and an approximated radius (in pixels) of a circle, which enclose the abnormality. This information file was used to select correct ROI surrounding the abnormalities.

We selected randomly a representative dataset (including examples of all abnormalities classes: calcifications, well-defined/circumscribed masses, spiculated masses, ill-defined masses, architectural distortions and asymmetries) formed by 100 images, of which 60 images were used in the training set and 40 for method evaluation.

FFBP and LVQ developed networks models were then trained with a matrix formed by the 60 vectors representing the selected morphometric features (abnormality area, brightness, roughness, shape and elongation). These vectors were computed from abnormalities presents on the images ROIs belonging to the training set.

Classification results are expressed in terms of three parameters: True Positive (**TP**), False Positive (**FP**) and False Negative (**FN**). A **TP** is obtained when a mammogram abnormality is classified into the correct (benign or malignant) class. When a benign mammogram abnormality is incorrectly classified into another benign class or into a malignant class, it is defined as a **FP**. A **FN** is obtained when a malignant mammogram abnormality is incorrectly classified into another malignant class or into a benign class**.**

Table 1 resume obtained results with the application of both (FFBP and LVQ) developed neural networks models to the simulation set formed by 40 abnormalities vectors (not includes in the training set). Calcifications, other ill-defined masses and well-defined/circumscribed masses were the classes with major incidence of true positives. Spiculated masses and architectural distortion were the classes with minor incidence of true positives classifications.

Summarizing was observed that FFBP model had a better performance in relation with the LVQ model. FFBP model obtained a classification score of 97.5%, 39 true positives, only 1 false positive and 0 false negative versus LVQ model with a classification score of 72.5%, 29 true positives, 5 false positives and 6 false negatives.

Table 1. Classification score

Anormalities	No. ROIs	Neural Networks							
		FFBP				LVQ			
		TP	FP	FN	(%)	TP	FP	FN	(%)
Calcifications	7	7	-	-	100	7	-	-	100
Well-defined/ Circumscribed Masses	7	7	-	-	100	6	1	-	85.7
Spiculated Masses	7	7	-	-	100	3	2	2	42.9
Other Ill-defined Masses	7	7	-	-	100	7	-	-	100
Architectural Distortion	6	5	1	-	83.3	2	2	2	33.3
Asymmetry Masses	6	6	-	-	100	4	-	2	66.6
Total	40	39	1	-	**97.5**	29	5	6	**72.5**

4   Conclusions

We have developed a new method based on the suitable combination of deformable models and ANN capable to classify correctly (as benign or malignant) six different

types of breast cancer abnormalities on mammography images. Also was demonstrated that a simple set of five morphological features (feature vector) computed from segmented abnormality edges are sufficient to obtain good (true positives) classification results. A full prototype was implemented in MATLAB (version 7.0) to test the algorithm performance, which was verified successfully with two different neural networks models: FFBP (97.5%) and LVQ (72.5%) true positives in a dataset of 40 vectors not include in the networks training set.

Our future work will be focused to enrich the feature vector with new features and to improve the networks models that allow better abnormalities classification.

Acknowledgments

References

1. Nishikawa, S.R., Papaioannou, J., Onsis, R., Haldemann Heusler, R.A., Giger, M.L., et al.: Performance of a prototype clinical intelligent mammography workstation. In: Digital mammography, Elsevier, Amsterdam (1996)
2. Roehrig, J.D.T., Hasegawa, A., Hunt, B., Marshall, J., Romsdahl, H., et al.: Clinical results with R2 ImageChecker system. In: Digital mammography, Kluwer academic Publishers, Dordrecht (1998)
3. Shih-Chung, B.L.H.L., Wang, Y., Kinnard, L., Freedman, M.T.: Multiple Circular Path Convolution Neural Network System for Detection of Mammographic Masses. IEEE Transaction on Medical Imaging 150–158 (2002)
4. Sepehr M.H.Jamarani, B.G.R.-r., Behnam, C.H.: A Novel Method for Breast Cancer Prognosis Using Wavelet Packet Based Neural Network. In: IEEE Engineering in Medicine and Biology 27th Annual Conference, Shanghai, China (2005)
5. Segyeong Joo, Y.S.Y., Moon, W.K., Kim, H.C.: Computer-Aided Diagnosis of Solid Breast Nodules: Use of an Artificial Neural Network Based on Multiple Sonographic Features. IEEE Transaction on Medical Imaging 1292–1300 (2004)
6. Paul Sajda, C.S., Pearson, J.: Learning Contextual Relationships in Mammograms Using a Hierarchical Pyramid Neural Network. IEEE Transaction on Medical Imaging 239–250 (2002)
7. Ping Zhang, B.V., Kumar, K.: Neural vs. statistical classifier in conjunction with genetic algorithm based feature selection. Pattern Recognition Letters 1–11 (2004)
8. Lúcio, F.A., Campos, A.C.S., Barros, A.K.: Diagnosis of Breast Cancer in Digital Mammograms Using Independent Component Analysis and Neural Networks. In: Sanfeliu, A., Cortés, M.L. (eds.) CIARP 2005. LNCS, vol. 3773, Springer, Heidelberg (2005)
9. Artur Chodorowski, U.M., Langille, M., Hamarneh, G.: Color Lesion Boundary Detection Using Live Wire. Medical Imaging (2005)
10. Jianming Liang, T.M., Terzopoulos, D.: United Snakes. Medical Image Analysis p. 215–233 (2006)

11. Ghassan Hamarneh, J.H.: DTMRI: Segmentation using DT-Snakes and DT-Livewire. In: IEEE International Symposium on Signal Processing and Information Technology (2006)
12. Kelvin Poon, G.H.: Rafeef Abugharbieh, Segmentation of Complex Objects with Non-Spherical Topologies from Volumetric Medical Images using 3D Livewire (2006)
13. Karsten Rodenacker, E.B.: A feature set for cytometry on digitized microscopic images. Analytical Cellular Pathology 1–36 (2003)
14. Hinton, G.E., William, D.E.R.R.J.: Learning internal representation by back-propagation errors. Nature 323, 533–536 (1986)
15. Widrow, B.: M.E.H. Adaptive switching circuits. in IRE WESCON Convention Record, New York IRE (1960)
16. Kohonen, T. (ed.): Self-Organization and Associative Memory, 2nd edn. Springer, Berlin (1987)

Infected Cell Identification in Thin Blood Images Based on Color Pixel Classification: Comparison and Analysis

Gloria Díaz, Fabio Gonzalez, and Eduardo Romero

Bioingenium Research Group, National University of Colombia,
Bogotá, Colombia
{gmdiazc,fagonzalezo,edromero}@unal.edu.co
http://www.bioingenium.unal.edu.co

Abstract. Malaria is an infectious disease which is mainly diagnosed by visual microscopical evaluation of Giemsa-stained thin blood films using a differential analysis of color features. This paper presents the evaluation of a color segmentation technique, based on standard supervised classification algorithms. The whole approach uses a general purpose classifier, which is parameterized and adapted to the problem of separating image pixels into three different classes: parasite, blood red cells and background. Assessment included not only four different supervised classification techniques - KNN, Naive Bayes, SVM and MLP - but different color spaces -RGB, normalized RGB, HSV and YCbCr-. Results show better performance for the KNN classifiers along with an improving feature characterization in the normalized RGB color space.

Keywords: Cell detection, Supervised classification, Color spaces, Performance comparison.

1 Introduction

Malaria is a leading cause of morbidity and mortality in tropical and sub-tropical countries, with an estimated of 300 to 500 worldwide million infections per year and 1 to 2 million deaths [1]. Plasmodium falciparum is the most mortal of the four species. In recent years, many research works have been addressed to development of new therapeutic alternatives for control of this disease [2], which involves in vitro drug susceptibility analysis by parasitism level quantification. Although different approaches have been developed for determining the level of infected erythrocytes with Plasmodium falciparum, visual microscopical evaluation of Giemsa-stained thin blood films is so far the most widely used in development countries. Its main drawback is that it is a subjective and time consuming method which demands trained technical personnel. In this context, development of mechanisms that automate the process of evaluation and quantification in thin blood films, becomes a high priority.

Several digital image processing techniques have been previously used for detecting malaria parasites on Giemsa stained slides [3], [4], [5], [6], [7].Plasmodium

falciparum parasites are highlighted in a dark purple colour, while erythrocytes are colored in slight pink colors. Object detection has been performed using a threshold on single components of the RGB and HSV histograms [3], [6]. Likewise, parasite detection has been achieved in two consecutive steps: a former stained/non-stained pixel classification - based on the RGB values - is followed by setting the pixel to any of the parasite/non-parasite categories - based on other features such as shape, color and Hu moments [4]. Finally, the color co-occurrence matrix has been calculated for pixel classification in cells previously detected by a template matching strategy [5].

In this paper, we present a very simple approach for automatic identification of infected and no infected erythrocytes in thin blood images by means of a supervised pixel classification method. Herein, an exhaustive study of the effect of selecting both a color space representation and a particular classifier on actual Plasmodium falciparum slides is presented. We investigated four color spaces (RGB, normalized RGB, HSV and YCbCr) and four supervised classification algorithms (Naive Bayes, SVM, KNN and Neural network). A separate analysis was performed only on the chrominance component of each color space. This paper is organized as follows: color representations and color pixel classification algorithms are described in Section 2, comparison results are presented in section 3 and discussion and conclusions are given in Section 4.

2 Cell Identification Based on Pixel Classification

The overall approach for identification of cells proposed in this paper is illustrated in figure 1. First, a set of training samples was manually extracted by an expert. Each training sample corresponded to a pixel labeled as erythrocyte, parasite or background. Then, a classification model was trained using these sample pixels, which was used for classifying the whole color space (RGB, normalized RGB, HSV or YCbCr). The classified color space was so used as a look-up table (LUT) for classifying pixels. Finally, the image was re-colored in three gray level values (background, erythrocyte and parasite) and a a two-scan connected component labeling algorithm [8] was applied for identifying and counting the objects present in the image.

2.1 Color Representation

As mentioned before, different color spaces were used to building the pixel classification model since features are differently represented in each. For instance, Di Ruberto found found that it is easier to identify parasites in the S component of the HSV color space [3]. The different color spaces assessed in this work are described in the following subsections.

RGB. This color space is used for acquiring and displaying color digital images. Each color pixel is represented by its three components: R(Red), G(Green) and B(Blue).
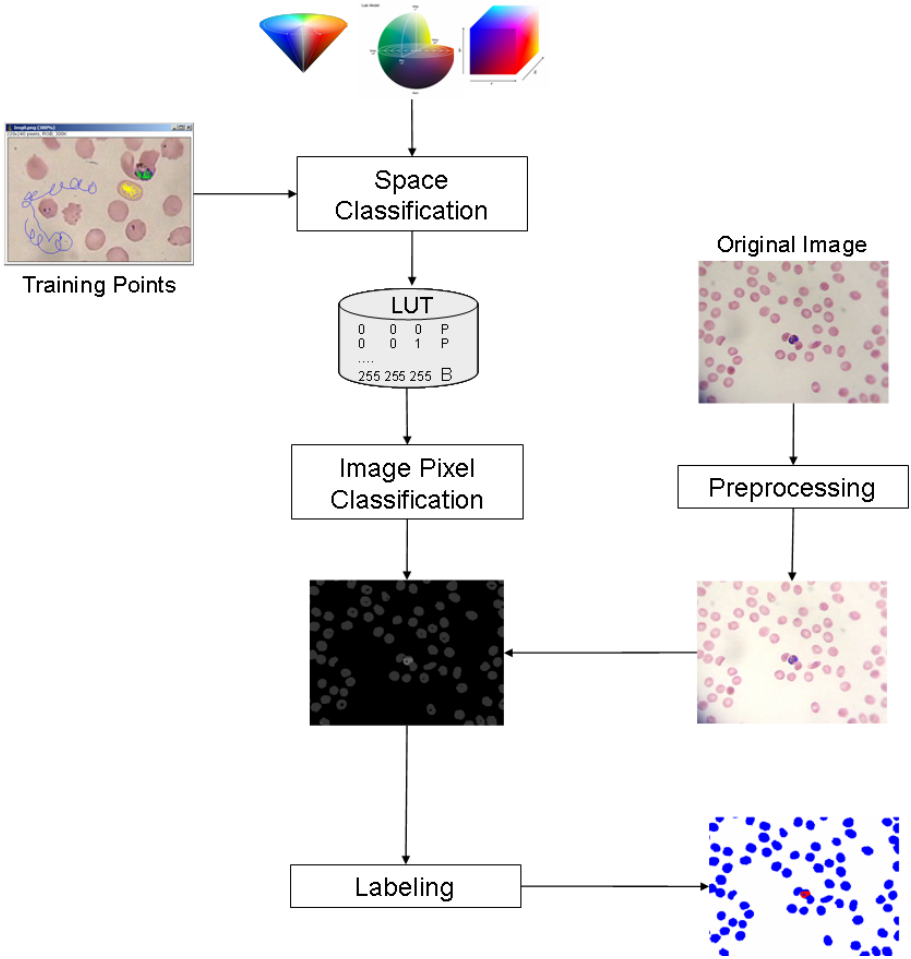
Fig. 1. The main steps of the whole erythrocytes and parasites detection

Normalized RGB (RGBn). This transformation is obtained by a simple procedure of RGB normalization:

$$
\begin{aligned}
r_N &= \frac{R}{R+G+B} \\
g_N &= \frac{G}{R+G+B} \\
b_N &= \frac{B}{R+G+B}
\end{aligned}
\tag{1}
$$

This nonlinear transformation reduces the sensitivity of the distribution to color variability, making it more robust to illumination changes than RGB. Since $r + g + b = 1$, when two components are given, the third component can be determined. Thus, only two of these three were used.

HSV. This transformation decorraleted color and intensity information in the image. Color information is represented by hue and saturation components, while intensity is determined by the value component. Hue defines the basic color in the pixel, saturation measures its colorfulness related to its brightness and value corresponds to the luminance color.

YCbCr. Is a family of color spaces commonly used to represent digital video. Luminance information is stored as a single component (Y), and chrominance correspond to the two color-difference components (Cb and Cr). We have used the YCbCr transformation specified in the ITU-R BT.601 standard for computer-display oriented applications.

2.2 Classification Models

Supervised learning is the area of machine learning or pattern recognition, that addresses the problem of building models for performing classification or regression tasks. This is one of the areas more deeply and extensively studied in machine learning. Tens of algorithms have been proposed, ranging from biologically inspired to pure statistical techniques. Each has its own weaknesses and strengths and, according to the No-Free Lunch Theorem [9], there is not one that could be deemed as superior to the rest for any classification task. In general, one algorithm may outperform another algorithm in a particular task, but may under perform in other task. According to the previous discussion different algorithms were tried. The chosen algorithms are representative of the state of art and of different approaches to supervised learning.

The Naive Bayes Approach. Likely, this is the simpler classifier and is based on the hypothesis that features are conditionally independent, which in terms of the Bayes theorem amounts to

$$P(C|x_1, x_2, \ldots, x_n) = \frac{1}{K} P(C) \prod_{i=1}^{n} P(x_i|C) \qquad (2)$$

where K is a constant dependent only on x_i and $P(c)$ is a prior probability of the class C, which is herein calculated during the training phase by merely counting the number of occurrences in the training data set.

The k-NN decision rule. The k-nearest neighbors method is well known used in the pixel classification problems [10][11]. It is an intuitive method that classifies unlabeled samples based on their similarity with samples in the training set. Given the knowledge of N prototype features (vectors of dimension Σ) and their correct classification into M classes, the k-NN rule assigns an unclassified pattern to the class that is most heavily represented among its k neighbors in the pattern space (under some appropriate metric).

A Neural Network strategy (MLP). Networks with organizations that emulate nervous system connections have been used in a large variety of image

segmentation problems. Herein, a Multi Layer Perceptron (MLP) trained using back-propagation was used [12]. The idea of this method is to connect layers of "neurons", while the particular neuron response is modeled with a continuous sigmoid approximation .

The *SVM* algorithm. A support vector machine (SVM) is a classification model that finds an optimal separating hyperplane that discriminates two classes. In principle, a SVM is a linear discriminator, however it can perform non-linear discrimination thanks to the fact that it is a kernel method. In this work, a version of SVM that uses sequential minimal optimization algorithm is used [13]. The multi-class classification problem is solved creating one classifier for each pair of the target classes, ignoring instances that belong to other classes and estimating a probability for each target class. Absolute probability estimate for each class is computed combining the probability estimate from all pairwise classifiers.

3   Experimentation

3.1   Data Set

A total of 25 microscopical fields from three different thin blood films were digitized using a Sony high resolution digital video camera Handycam DCR-HC85 (640×480 pixels to 1200×16000), coupled to a Carl Zeiss Axiostar Plus microscope, provided with Carl Zeiss 426126 and 456006 adapters (Carl Zeiss, Light Microscopy, Gottingen, Germany). Use of intermediate lens and a $\times 100$ power objective yielded a total of $\times 1006$ magnification. Optical image was a $102 \times 76 \mu m^2$ for a 640×480 image size, resulting in a total resolution of $0.0252 \, \mu m^2/pixel$. A total of 1226 erythrocytes and 60 parasites were found in these images, indicating that the most relevant class (parasite) was barely represented by a 5 %.

Before applying the classification process, a correction of the luminance differences in the original image is performed through a local low pass filter. This filter is essentially a local adaptive filter, defined for a window size of the larger image feature, i.e. a typical erythrocyte size. Firstly, the $m \times n$ RGB luminance and chrominance image components are decorrelated through a YCbCr transformation. Luminance channel is split into disjoint regions of approximately the larger feature in the image and a mean pixel value is calculated from each. These mean values make up a matrix which is smoothed out using a moving smaller window, whose size is adjusted in order to eliminate the tiling effect of the filter. Afterward, luminance is corrected by ruling out the lower frequencies found before. Finally, the color image is re-constructed using this luminance correction and the original chrominance information. Figure 2 displays two microscopical images obtained from thin blood smears. Upper row displays the original digital images, while bottom row shows the obtained images using the proposed filter.
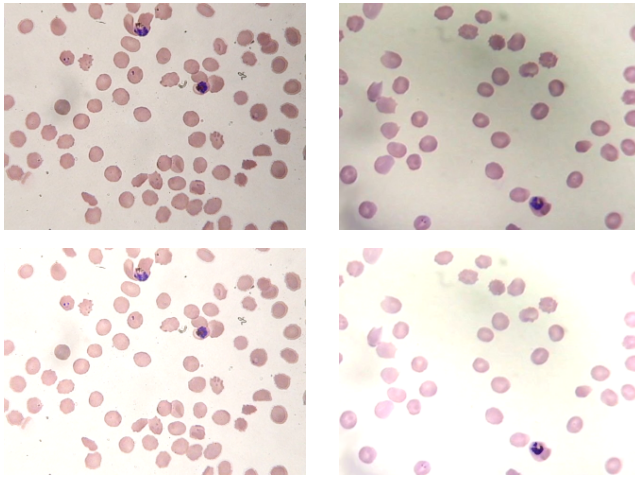
Fig. 2. Pre-processed image results. Fist row corresponds to the original microscopical images, bottom row displays filtered images obtained from the original ones.

3.2   Experimental Setup

Four classification algorithms were assessed (Naive Bayes, KNN, SVM and MLP). Each classification model was tuned independently for its own particular set of parameters as follows: k-NN was assessed by varying the k odd nearest neighbors between 1 and 15. SVM was evaluated with different kernels i.e. radial or polynomial [13]. In both cases C gap was set to 1. Additionally, in the former case the γ parameter was varied between 100 and 1000 with increment steps of 100, while an optimal polynomial degree was determined for the later case $(1, 2, 3)$. The Bayes algorithm was trained with a normal distribution and a 95 % confidence interval. The neural network was provided with a hidden layer on which the number of neurons was varied between 3 and 9, with increment steps of 3 and error rates among $(0.005, 0.1, 0.2, 0.5, 0.9)$. All classifiers were trained using sets of 500, 1000 and 2000 pixel samples, classified manually by an expert in two representative images.

The different color spaces stand for the characteristic spaces so that six different feature vectors were analyzed : four complete (RGB, HSV, YCbCr, normalized RGB) and two incomplete color spaces (HS, CbCr).

3.3   Evaluation

Classification performance was assessed based on a reference-manual segmentation, using two strategies: pixel classification and interest-object detection (erythrocytes and parasites) rates. In this analysis, performance estimation through a conventional accuracy comparison results inappropriate because of the high imbalanced class distribution of parasites related to erythrocytes and background. That is to say, the assessment may report a high accuracy even if parasites are

not identified. As an alternative to accuracy, we used the F-measure, or effectiveness measure, [14] computed as $F_\beta = \frac{(1+\beta)*RC*PR}{\beta*PR+RC}$, with RC (recall) defined as $\frac{TP}{TP+FN}$ and PR (precision rate) computed as $\frac{TP}{TP+FP}$, where TP stands for the true positives, FN for the false negatives and FP for the false positives. The $\beta > 0$ coefficient controls the relative importance of recall and precision rates; $\beta = 1$ gives the same importance to both measures, whilst precision rate is more important with a higher value of β. Herein, β was set to 2/3, since we attempt to detect as many objects as possible even at expense of lower precision. $F_\beta = 1$ means a perfect score, i.e. $PR = RC = 1$.

Pixel wise evaluation is performed by comparing re-colored images, generated by each set of training points and classifier parameters, with a manual segmentation. In this case, the test set is composed of labeled pixels. Precision and recall are calculated based on the number of rightly/wrongly classified pixels.

Interest-object wise evaluation is based on the objects identified by a method that includes the classification process as the first step. After the application of the classification method, objects are identified as follows: a basic filtering process is performed for keeping only relevant objects in the image; thus, small or large regions identified as flaws (particulate matter from the stain or from fragments of released hemazoin, acquisition artifacts) are removed; likewise, near unconnected segments are evaluated for establishing their relevance to a given parasite, if they are relevant they are considered as a unique object.

For interest-object wise evaluation, the test set is composed of images where interest-objects (erythrocytes and parasites) are labeled. Precision and recall are calculated based on the rightly/wrongly identified objects.

3.4   Results and Discussion

As it was mentioned before, training sets with different sizes were used. It was noticed that, in all the cases, increasing the size of the training set from 500 to 2000 did not improve significantly the performance of the different classifiers. Therefore, all subsequent experiments were performed using a 500 elements training data set.

The different classification algorithms were trained and evaluated with different parameter values, as mentioned in the experimental setup (for the sake of brevity, these intermediate results are not shown). The best parameter values for each algorithm were identified: K = 15 for KNN, error rate = 0.1 and 6 neurons in hidden layer for MLP, polynomial degree = 1 for SVM with polynomial kernel (SVM_P) and $\gamma = 100$ for SVM with radial base kernel.

Effectiveness measure results for pixel wise and interest-object wise evaluations are shown in Tables 1 and 2. The F-measure is reported independently for the erythrocyte (F_β^{Er}) and parasite (F_β^P) classes, respectively.

Pixel Wise Evaluation. Pixel wise evaluation results are shown in Table 1. F_β values suggest that performance is good for the erythrocyte class, while it is not as good for the parasite class. The pattern is the same for all classifier algorithms and color spaces. Our hypothesis is that the complex mix of colors,

present in the parasites, makes it difficult to discriminate individual pixels using only color information.

The best overall performance is accomplished by the combination of a KNN classifier and YCbCr color space, with $F_\beta^{Er} = 0.95$ and $F_\beta^P = 0.72$. However, there are other combination that produce similar results such as KNN classifier and normalized RGB color space ($F_\beta^{Er} = 0.95$ and $F_\beta^P = 0.71$), MLP-classifier and normalized RGB color space ($F_\beta^{Er} = 0.94$ and $F_\beta^P = 0.71$) and SVM_P-classifier and YCbCr color space ($F_\beta^{Er} = 0.94$ and $F_\beta^P = 0.72$).

From the point of view of color space, normalized RGB and YCbCr have better performance. This indicates that these color spaces emphasize the differences between classes. From a classifier stantpoint KNN, MLP and SVM_P clearly outperform SVM_{RBF} and Naive Bayes.

Table 1. F_β measure results for pixel wise evaluation for different classification algorithms and color spaces. F-measure is reported independently for the erythrocyte (F_β^{Er}) and parasite (F_β^P) classes.

Color Space	Naive Bayes		KNN $k = 15$		MLP $er = 0.1, n = 6$		SVM_P $degree = 1$		SVM_{RBF} $\gamma = 100$	
	F_β^{Er}	F_β^P	F_β^{Er}	F_β^P	F_β^{Er}	F_β^P	F_β^{Er}	F_β^P	F_β^{Er}	F_β^P
RGB	0.88	0.13	0.95	0.69	0.95	0.68	0.94	0.68	0.92	0.17
HSV	0.90	0.35	0.89	0.70	0.90	0.68	0.89	0.65	0.89	0.05
HS	0.90	0.37	0.91	0.72	0.90	0.62	0.89	0.67	0.94	0.62
RGBn	0.95	0.52	**0.95**	**0.71**	**0.94**	**0.71**	0.94	0.70	0.93	0.45
YCbCr	0.89	0.52	**0.95**	**0.72**	0.94	0.68	**0.94**	**0.72**	0.86	0.07
CrCb	0.84	0.68	0.85	0.71	0.86	0.63	0.86	0.70	0.86	0.50

Interest-Object Wise Evaluation. Table 2 shows the results of the interest object wise evaluation. The best overall performance is clearly accomplished by the combination of a KNN-classifier and normalized RGB color space with $F_\beta^{Er} = 0.99$ and $F_\beta^P = 0.83$, followed by SVM_P-classifier and YCrCb color spaces ($F_\beta^{Er} = 0.97$ and $F_\beta^P = 0.81$). This means that normalized RGB and YCrCb color spaces produced again the best results. This is no really surprising as object identification is based on pixel classification.

With regard to the classifier algorithm, SVM_{RBF} and Naive Bayes produced the best results for erythrocyte detection, however their performance on parasite detection was really poor. Both KNN and SVM_P produced a good balance of parasite and erythrocyte detection.

An interesting finding in these results, is the fact that the performance is much better at the level of object identification than at the level of pixel classification. The main reasons is that pixel classification is more sensitive to noise, while the

Table 2. F_β measure results for erythrocytes and parasites detection. for different classification algorithms and color spaces. F-measure is reported independently for the erythrocyte (F_β^{Er}) and parasite (F_β^P) classes.

ColorSpace	Naive Bayes		KNN $k = 15$		MLP $er = 0.1, n = 6$		SVM_P $degree = 1$		SVM_RBF $\gamma = 100$	
	F_β^{Er}	F_β^P	F_β^{Er}	F_β^P	F_β^{Er}	F_β^P	F_β^{Er}	F_β^P	F_β^{Er}	F_β^P
RGB	0,98	0,19	0,99	0,76	0,99	0,78	0,93	0,73	0,99	0,18
HSV	0,97	0,43	0,96	0,75	0,97	0,72	0,96	0,71	0,98	0,11
HS	0,97	0,44	0,97	0,75	0,97	0,65	0,95	0,74	0,99	0,67
RGBn	0,99	0,57	**0,99**	**0,83**	0,98	0,78	0,96	0,74	0,98	0,40
YCrCb	0,97	0,47	0,97	0,77	0,98	0,77	**0,97**	**0,81**	0,98	0,10
CrCb	0,95	0,80	0,92	0,81	0,94	0,72	0,90	0,76	0,95	0,51

object identification process is able to eliminate this noise thanks to the filtering process that improves the results of the pixel classification step.

4   Conclusions

A simple an efficient method for parasite and erythrocyte detection in thin blood images was proposed. The approach is based on a classification process that finds boundaries that optimally separate a given color space in three classes, namely, background, erythrocyte and parasite. The classified color space is stored and used as a look-up table for classifying pixels from new images.

The method was evaluated at two levels: pixel classification and object detection. Different classification algorithms and color spaces were evaluated. KNN algorithm with normalized RGB color space was found to have higher detection performance compared to other tested classifiers. Furthermore, this color space requires less computational resources as only two components are needed to fully determine a point in this space (the third one is calculated from the first two). Color spaces traditionally used as RGB or HSV produced poorer results. The performance result at the object-identification level was superior to the performance at the pixel-classification level. This shows that the filtering step used by the object-identification process is able to reduce noise, making the overall process robuster.

Future work is focused on evaluating the feasibility of using combined color spaces and more specialized classification algorithms.

Acknowledgments

References

1. WMR, UNICEF: World malaria report. Technical report, WMR and UNICEF (2005)
2. OPS: The health in the americas. Technical Report 1, Pan-american organization of the Health (1998)
3. di Ruberto, C., Dempster, A., Khan, S., Jarra, B.: Analysis of infected blood cell images using morphological operators. Image and Vision Computing 20(2), 133–146 (2002)
4. Tek, F., Dempster, A., Kale, I.: Malaria parasite detection in peripheral blood images. In: Proceeding of British Machine Vision Conference (2006)
5. Halim, S., Bretschneider, T.R., Li, Y., Preiser, P.R., Kuss, C.: Estimating malaria parasitaemia from blood smear images. In: Proceedings of the IEEE International Conference on Control, Automation, Robotics and Vision (2006)
6. Ross, N.E., Pritchard, C.J., Rubin, D.M., Dus, A.G.: Automated image processing method for the diagnosis and classification of malaria on thin blood smears. Medical and Biological Engineering and Computing 44, 427–436 (2006)
7. Sio, S.W.S., Sun, W., Kumar, S., Bin, W.Z., Tan, S.S., Ong, S.H., Kikuchi, H., Oshima, Y., Tan, K.S.W.: Malariacount: an image analysis-based program for the accurate determination of parasitemia. Microbiological Methods 68 (2007)
8. di Stefano, L., Bulgarelli, A.: A simple and efficient connected components labeling algorithm. In: Proceedings of the 10th International Conference on Image Analysis and Processing (1999)
9. Wolpert, D., Macready, W.: No free lunch theorems for optimization. IEEE Transactions on Evolutionary Computation 1, 67–82 (1997)
10. Cover, T., Hart, P.: Nearest neighbor pattern classification. IEEE Transactions on Information Theory IT-13, 21–27 (1967)
11. Fix, E., Hodges, J.: Discriminatory analysis, non-parametric discrimination. Technical Report Project 21-49-004, Rept. 4, Contract AF41(128)-131, USAF School of Aviation Medicine, Randolf Field, Texas (February 1951)
12. Rumelhart, D., Hinton, G., Williams, R.: Parallel Distributed Processing: Explorations in Macrostructure of cognition, vol. I. Badford Books, Cambridge. MA (1986)
13. Platt, J.: Machines using sequential minimal optimization. In: Schoelkopf, B., Burges, C., Smola, A. (eds.) Advances in Kernel Methods - Support Vector Learning, MIT Press, Cambridge (1998)
14. Daskalaki, S., Kopanas, I., Avouris, N.: Evaluation of classifiers for an uneven class distribution problem. Applied Artificial Intelligence 20, 381–417 (2006)

Coregistration of Small Animal PET and Autoradiography for *in vivo–ex vivo* Comparison

Soo-Min Song[1], Min-Jeong Kim[1], Joung-Min Lee[1], Hye-Jin Park[1],
KyeongMin Kim[2], Gi-Jeong Cheon[2], and Myoung-Hee Kim[1,3,*]

[1] Department of Computer Science and Engineering
Ewha Womans University, Seoul, Korea
{smsong,kimmj,clrara,tlseo}@ewhain.net
[2] Korea Institute of Radiological and Medical Sciences, Seoul, Korea
{kmkim,larry}@kcch.re.kr
[3] Center for Computer Graphics and Virtual Reality
Ewha Womans University, Seoul, Korea
mhkim@ewha.ac.kr

Abstract. Non-invasive imaging of small animal and its quantification techniques are needed to be evaluated by comparison with *ex vivo* image. To overcome the existing method, hand-operated comparison with the unaided eye observation, we present an algorithm that matches the target area in PET scanned *in vivo* with an autoradiography image acquired *ex vivo*. We applied a coregistration algorithm that uses voxel similarity to find the corresponding slices and to make quantitative measurements. Automatic matching of *in vivo* and *ex vivo* images is novel, and can provide better validation than manual matching techniques.

Keywords: Image registration, in vivo-ex vivo validation, small animal image.

1 Introduction

Small experimental animals such as mice and rats play a crucial role in enhancing our understanding of human disease. *In vivo* animal imaging technologies enable the development of a disease in its early stage, or the efficacy of a drug to be observed. These technologies allow repetitive, long-term follow-up studies and replace invasive and destructive observations by biopsy or histology. Many methods have been proposed for non-invasive extraction of quantitative information about a target area, and they can achieve better results than measurement using a caliper. Nevertheless, image-based analysis can be inaccurate. So in existing preclinical experiments the animal is sometimes sacrificed after non-invasive image analysis to obtain physical measurements *in vitro* or *ex vivo* for comparison. In comparing two images, it is difficult to find the same region of interest in both, and this is usually done manually until now. Besides, a quantitative comparison between the images may also be performed with the unaided eye[1,2] so the evaluation cannot be achieved objectively.

---

* Corresponding author.

To overcome this approach, we propose an algorithm that automatically finds the same target area and extract its quantitative characteristics both in *in vivo* and *ex vivo* images using image registration. We also estimate the error range to establish the robustness of this approach to image quantification.

Nevertheless of necessity of *in vivo - ex vivo* image matching, existing image registration algorithms applied to small animal images have been designed to compare only between *in vivo* images so far. Furthermore, most of their methods are based on hardware or stereotactic approaches. Jan[3] proposed a way of combining PET, CT, and SPECT images using a calibration phantom and an animal holder, and Chow[4] aligned coordinate systems between images by moving the imaging cylinder. Rowland[5] and Shen[6] developed respectively, MRI-PET, MRI-SPECT image registration algorithms to observe structural and functional information simultaneously. In this paper we suggest the scheme of finding corresponding positions between *in vivo – ex vivo* images using an automatic and robust registration.

In Section 2 we described the features of the *in vivo* and *ex vivo* images used in this study, and the intensity-based image matching method used for automatic inter-image comparison. Section 3 explains how we evaluated the matching method by quantifying the overlapped images. Experimental results and conclusions follow in Sections 4 and 5.

2   Coregistration of *in vivo* and *ex vivo* Images

In this section, we introduce two input image modalities: PET (Positron Emission Tomography) image which is acquired *in vivo* and autoradiography, which is obtained *ex vivo*. And we present an inter-image matching algorithm that performs registration based on voxel intensity statistics.

2.1   Image Characteristics and Preprocessing

PET provides a dynamic view of functional information about living animals, enabling the detection of biological and biochemical changes at the molecular level, using a radiotracer as a marker for a specific physiological function. In the resulting images we can see the distribution of the marker from the intensity of the radiation. The resulting data can quantify the distribution, and kinetics of a drug, and its likely mode of action on body function such as metabolism and blood flow. However, because of the low resolution and blurring artifact of PET images, it is difficult to determine the exact shape of a target area.

Autoradiography also involves injecting a radioactive tracer, but in this case the animal is then sacrificed to get more detailed anatomical information. The animal's organs are then sliced up and each slice is imaged with a detector that is sensitive to radiation.

Even though both PET and autoradiography use a radiotracer to visualize metabolic functions, autoradiography image shows fine anatomical structures because the sliced specimen is laid in contact with the radiation detector. To obtain autoradiography images after taking PET images of the small animal requires a preparation procedure that includes sacrificing, freezing and sectioning. During this

time the radio-isotope used will decay, so we have to choose a radio-tracer with a long half-life so that the radioactivity remains strong until image acquisition is completed.

The image acquisition protocol is described in Fig. 1.
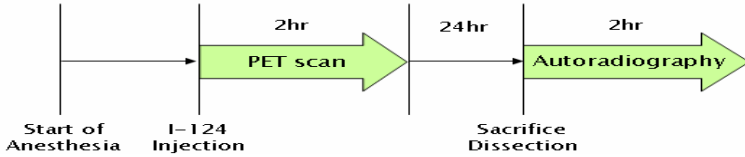
Fig. 1. Imaging protocol

However, much care is taken, the images acquired will still have some drawbacks. The slice thickness for autoradiography is 30~50μm. This is so thin that some data can be lost during the slicing process (Fig. 2(a)), which can lead to inconsistency with PET data, and incorrect registration. Therefore we specify a small ROI (region of interest) as a boundary box at a preprocessing step (Fig. 2(c)). Only this region is considered during the subsequent image registration procedure, which speeds up the algorithm and makes it robust.

(a)   (b)   (c)
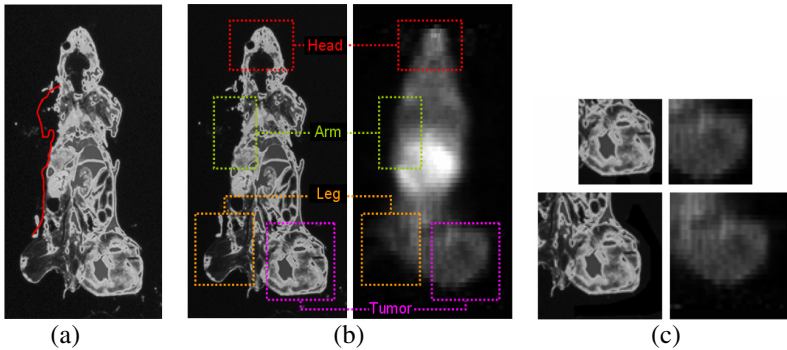
Fig. 2. Resolving problems with input images: (a) partial data loss, (b) inconsistency between PET and autoradiography data, (c) ROI(tumor area)

2.2   Registration Using Voxel Similarity

To compare a target area in PET and autoradiography data, it is necessary to match the same position in both images and then overlay them. PET is scanned for animal whole body three dimensionally at one time, but autoradiography is obtained slice by slice fashion. Because of the difficulties of slicing with uniform thickness, whole-body imaging by autoradiography is practically impossible. So when one autoradiography image is acquired during the experiment, finding corresponding image slice which shows the same tissue in PET volume data is needed. This matching processing is done by image registration.
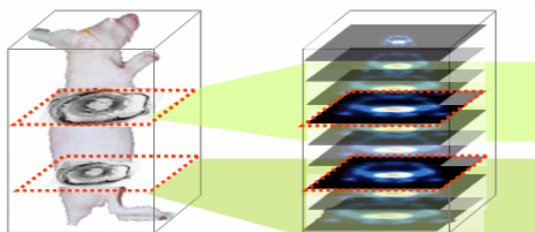
Fig. 3. Concept of finding corresponding slices in PET and autoradiography images

Image registration is the process of aligning images in order to correspond with their features[7]. In this process, one input image should be defined as a reference volume and the other is a test volume. And the test volume is repeatedly transformed until the most similar image is found.

In this paper, autoradiography image is treated as a reference because it has to be used as a validation standard and furthermore, when an image with higher resolution is used as a reference, image processing time and artifact due to the voxel interpolation can be reduced[8]. And to determine similarity between two images, we used an intensity based approach which does not need to extract feature points such as points or surfaces because it is difficult to segment geometrical structures in blurry PET image. In intensity based method the transformation factor can be computed by maximizing a similarity measure assuming statistical dependency between the intensity value of the two images.

In this study, we used mutual information[9], one of the most widely used measure in multi-modal image registration. Mutual information stems from information theory and statistics and it is expressed as the difference between the sum of the entropies of the individual images, H(A) and H(B), and the joint entropy of the combined image where they overlap, H(A,B) [10]. The entropy of a single image can be computed from the probability distribution of its intensities, and the joint entropy of two images can be estimated by computing a joint histogram of paired intensities. So this is a measure of the extent to which one image explains the other.

$$I(A,B) = \frac{H(A) + H(B)}{H(A,B)}. \tag{1}$$

However, mutual information measure is sensitive to the changes of the number of overlapped voxels and changes in overlap of very low intensity regions such as noise in the background. To overcome these kind of problems modified version by normalization has suggested and has proved very robust[11].

During the process of image registration two images A and B can should be corresponded by searching for an optimal transformation T which has the maximum normalized mutual information. Finding the transformation factor is represented as Eq. (2) where the original image A(x) and the transformed image B(T(x)), where x is a voxel in image A, and the closest voxel in image B is T(x), so that

$$\hat{T} = \arg\max_{T} I(A(x), B(T(x))). \tag{2}$$

At this point, this requires the specification of the degrees of freedom of transformation. We assumed the animal body is fixed which means that there're no movements or structural changes to the animal during the whole image acquisition. Because the animal stays motionless because of gas anaesthesia during PET scanning and the animal is immediately sacrificed after PET acquisition and slicing for autoradiography is started as soon as cadaveric stiffening is apparent. Therefore we only applied the rigid transformation.

3   Quantitative Measurement and Its Validation

To validate the accuracy of image-based analysis, comparing the quantitative information by measuring the size, length, or biological activity of target tissue is required. Therefore, once the corresponding image slices have been found, we delineate the target area and extract its characteristics quantitatively from both *in vivo* and *ex vivo* image. In this section, we describe the target area detection algorithm and the methods of quantitative measurement used to obtain both morphological and biological information, shown in Fig. 4.
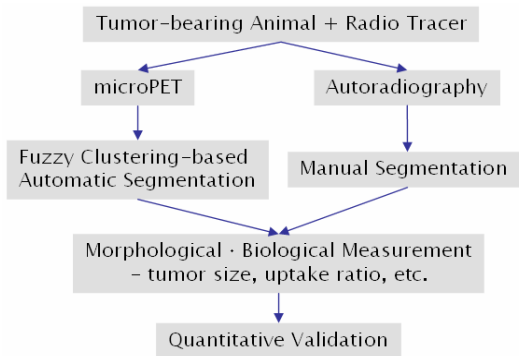
Fig. 4. Quantification of the target area

3.1   Target Area Detection

In this study, two image scans are acquired from a tumor-bearing mouse to observe metabolic activity in the tumor tissue and its growth rate. We segment the tumor area manually in the autoradiography data, because it is used as the reference standard in this study, as this data obtained *ex vivo* and shows the anatomical structure in fine resolution.

We now present a target area delineation algorithm to detect the tumor area in the PET data automatically [12] in two steps using a clustering algorithm. The tumor tissue looks bright compared to the surrounding normal tissue because of its high glucose uptake. We therefore can identify tumor tissue and other several types of normal tissue using voxel intensity.

In the first step, we use an iterative thresholding method to separate the foreground, which is the whole of the body area, from the background in a very noisy PET image. Then, we calculate a membership function for each element in the foreground using the fuzzy C-means(FCM) objective function:

$$J(U,V) = \sum_{j=1}^{c}\sum_{i}^{n}[u_j(x_i)]^b \cdot \| x_i - m_j \|, \tag{3}$$

Under the condition

$$\sum_{j=0}^{c} u_j = 1, \sum_{j=0}^{c} u_j > 0, u_j \in [0,1], \tag{4}$$

Where U is the matrix that contains the membership value of pixel x_i with respect to each cluster, u_i is an element of that matrix, and m_j is the center of class j. Voxel clustering is done by minimizing this equation using the following iteration:

$$m_j = \frac{\sum_{i=1}^{n}[u_j(x_i)]^b \cdot x_i}{\sum_{i=1}^{n}[u_j(x_i)]^b} , \tag{5}$$

$$u_j(x_i) = \frac{(\frac{1}{\| x_i - m_j \|^2})^{\frac{1}{(b-1)}}}{\sum_{k=1}^{c}(\frac{1}{\| x_i - m_j \|})^{\frac{1}{(b-1)}}} . \tag{6}$$

However, after intensity-based clustering, the tumor cluster may still include regions corresponding to normal organs such as the heart or bladder, which also show high intensity value because of glucose metabolism. To separate the tumor from this false positive region, we use a geometric clustering algorithm in which connected voxels are regrouped into the same cluster.

In Fig. 5(a) shows an image segmented into three clusters using brightness; the second cluster(shown in blue) is then divided into two using connectivity information. The small pink region is finally selected as the target area.

(a)   (b)
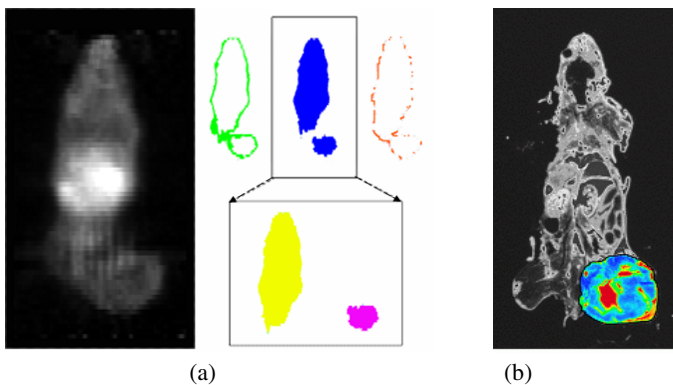
Fig. 5. Target area segmentation: (a) segmentation of PET data by fuzzy clustering, and (b) manual segmentation of autoradiography data

3.2 Measurement of Morphological and Biological Information

Morphological information can be used to estimate the state of tumor growth, regression and regrowth. We compute the tumor size by counting the number of voxels in target area and multiplying by the voxel size in millimeters. To determine the length of the boundary of the tumor, we use a chain code algorithm to extract a contour and then count voxels along the line. We calculate the eigenvectors of the contour and consider its first principal axis as a diameter.

We can also extract biological information by computing metabolic activity, as a standard uptake value(SUV), in the tumor tissue:

$$SUV = meanROIactivity(mC_i / cc)/(injectedDose(mC_i)/bodyWeight(g)) \tag{7}$$

This functional gives the information about tumor viability or a metabolic disorder. It can allow the stage of cancer to be determined, whether it is malignant or benign, and the efficacy of an anti-cancer drug observed.

4 Implementation and Experimental Results

We used PET and autoradiography to measure a tumor in a mouse. Hummm Burkitt Lymphoma Raji cell was injected into the right thigh of C57BR/cdJ SCID mouse and I-124 was injected into a vein as a biotracer. The spatial resolution of the PET scan was 256x256x63 and the voxel size was 0.85x0.85x1.21㎜ The resolution of each autoradiography slice was 1050x1998 and the voxel size was 40㎛ To match PET and autoradiography data using image registration algorithm, every image slice of PET volume was compared to find the one which has the most similar intensity distribution with an autoradiography image.

Fig. 6 (a), (b) are the ROI of each input image in coronal view that is used in registration process. On this region, normalized mutual information is calculated and the plot of voxel similarity for a series of PET image slices is shown in Fig. 6 (d). The image which has the maximum value has to be transformed and Fig. 6 (c) shows its result. Table 1. provides quantitative comparisons for a selection of image pairs. It shows that, as the voxel similarity increases, the differences in quantitative parameters are reduced.

(a)   (b)   (c)   (d)
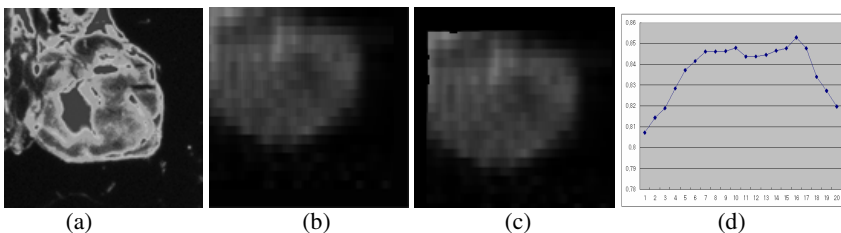
Fig. 6. PET-autoradiography Coregistration using voxel similarity: autoradiography, (b) PET, (c) registration result, (d) similarity measure

Table 1. Quantitative comparison of target area characteristics

	Auto-radiography	PET (33th image)	PET (37th image)	PET (40th image)
Similarity measure	.	1.4864	1.5949	1.5827
Radius(mm)	0.85	0.83	0.85	0.86
Length(mm)	4.5	4.3	4.6	4.5
Size(mm^3)	6529.23	6246.07	6624.60	6701.91
SUV	10.04	9.7	9.8	11.20

Because we consider the animal fixed during the image acquisition procedure, the registration error within any specific region of the mouse can be expected to be the same as the calculated for the global registration error. Therefore, the transformation parameters calculated for the small ROI can be applied to the entire image. After we have done this, we overlaid three images of the animal section changing the transparency to provide an intuitive understanding (Fig. 7).
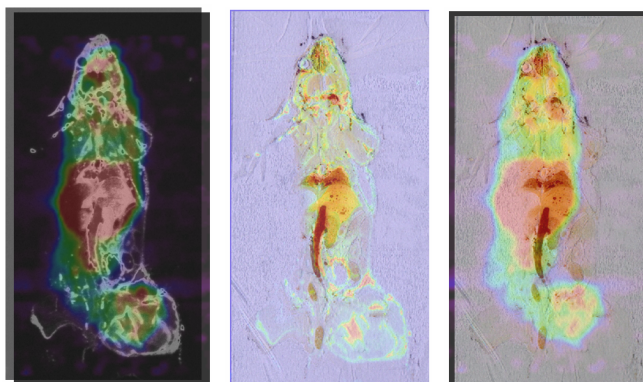
Fig. 7. PET, autoradiography, and visible-light images of a single section of the tumor-bearing mouse

5   Conclusions and Future Work

We have developed a coregistration algorithm to match *in vivo* PET and *ex vivo* autoradiography data. This allows image processing algorithms, including target area detection and quantification, applied to *in vivo* images to be validated by comparison with an *ex vivo* image. This comparison shows an error-rate within 0.1~0.2 %, which suggests that the proposed algorithm for *in vivo* quantification is sufficiently accurate. Results are proven robust even when the experimental image, especially autoradio-graphy, has partial data missing problem which is frequently occurred during the image acquisition.

In the future, we plan to develop inter-image matching algorithms to compare autoradiography with other *in vivo* image modalities.

Acknowledgements

References

1. Chen, X., Park, R., Hou, Y., Tohme, M., Shahinian, A.H., Bading, J.R., Conti, P.S.: microPET and Autoradiographic imaging of GRP Receptor Expression with 64Cu-DOTA-[Lys3]Bombesin in Human Prostate Adenocarcinoma Xenografts. The Journal of Nuclear Medicine 45(8) (2004)
2. Chang, C.H., Fan, K.H., Chen, T.J., Hsu, W.C., Jan, M.L., Tsai, T.H., Kao, P.F., Chen, C.F., Fu, Y.K., Lee, T.W.: Dynamic Evaluation of 18F-FDG Uptake by MicroPET and Whole-Body Autoradiography in a Fibrosarcoma-bearing Mouse Model. Journal of Formosan medical Association 103(11) (2004)
3. Jan, M.L., Chuang, K.S., Chen, G.W., Ni, Y.C., Chen, S., Chang, C.H., Wu, J., Lee, T.W., Fu, Y.K.: A three-Dimensional Registration Method for Automated Fusion of micro PET-CT-SPECT Whole-Body Images. IEEE Trans. on Med. Img. 24(7) (2005)
4. Chow, P.L., Stout, D.B., Komisopoulou, E., Chatziioannou, A.F.: A Method of Image Registration for Animal, Multi-modality Imaging. Physics in Medicine and Biology 51, 379–390 (2006)
5. Rowland, D.J., Garbow, J.R., Laforest, R., Snyder, A.Z.: Registration of 18f-FDG microPET and small-animal MRI. Nuclear medicine and Biology 32, 567–572 (2006)
6. Shen, D., Liu, D., Cao, Z., Acton, P.D., Zhou, R.: Coregistration of Magnetic Resonance and Single Photon Emission Computed Tomography Images for Noninvasive Localization of Stem Cells Grafted in the Infarcted Rat Myocardium. Mol. Imaging Biol. 9, 24–31 (2007)
7. Hajnal, Hill, Hawkes: Medical Image Registration. CRC Press (2001)
8. Pluim, J.P., Maintz, J.B., Viergever, M.A.: Interpolation artifacts in mutual information-based image registration. Computer Vision and Image Understanding 77(2), 211–232 (2000)
9. Woods, R.P., Mazziotta, J.C., Cherry, S.R.: MRI-PET registration with automated algorithm. Journal of Computer Assisted Tomography 17(4), 536–546 (1993)
10. Pluim, J.P., Maintz, J.B., Viergever, M.A.: Mutual Information based Registration of Medical Images: a survey. IEEE Trans. On Medical Imaging 22, 986–1004 (2003)
11. Studholme, C., Hill, D.L.G., Hawkes, D.J.: An overlap Invariant Entropy Measure of 3D Medical Image Alignment. Pattern Recognition. 32, 71–86 (1999)
12. Lee, J., Song, S., Kim, K.M., Kim, M.-H.: Tumor detection from small animal PET using clustering method based on intensity and connectivity, World Congress on Medical Physics and Biomedical Engineering (2006)

Noise Pattern Recognition of Airplanes Taking Off: Task for a Monitoring System

Luis Pastor Sánchez Fernández, Oleksiy Pogrebnyak, José Luis Oropeza Rodríguez, and Sergio Suárez Guerra

Center for Computing Research, National Polytechnic Institute
Av. Juan de Dios Batiz s/n casi esq. Miguel Othon de Mendizabal, Col. Nueva Industrial Vallejo. CP 07738. Mexico City, Mexico
{lsanchez,olek,joropeza,ssuarez}@cic.ipn.mx

Abstract. This paper presents an original work for aircraft noise monitoring systems and it analyzes the airplanes noise signals and a method to identify them. The method uses processed spectral patterns and a neuronal network feed-forward, programmed by means of virtual instruments. The obtained results, very useful in portable systems, make possible to introduce redundancy to permanent monitoring systems. The noise level in a city has fluctuations between 50 dB (A) and 100 dB (A). It depends on the population density and its activity, commerce and services in the public thoroughfare, terrestrial and *aerial urban traffic*, of the typical activities of labor facilities and used machinery, which give varied conditions that must be faced of diverse ways within the corresponding normalization. The sounds or noises that exceed the permissible limits, whichever the activities or causes that originate them, are considered events susceptible to degrade the environment and the health.

Keywords: Aircraft, monitoring, noise, pattern, recognition.

1 Introduction

The goal of this research stage is to make aircrafts noise signals analysis, that allows creating a recognition method, that will do possible to identify types or class of aircrafts by means of its noise patterns. These types of aircrafts can be of propeller, turbojet and reaction. On the other hand, it is possible to classify the aircrafts as long reach (high power), medium reach (medium power) and short reach (low power).

Committees of Aerial Transport and Environmental propose an aircraft classification based on the level of noise emission. The proposed common classification of aircraft is based on the principle that the aircraft operator should pay a fair price that should be proportional to its noise impact, independently of the weight of the aircraft or of the transport service rendered. Such data would make it possible to recognize the environmental merits of larger aircraft, even if these aircraft are noisier in absolute terms when compared to smaller aircraft [1].

Much of this work involves the collection and analysis of large amounts of aircraft noise data from the Noise and Track Keeping systems (NTK) installed at airports.

Like any other measured quantity, aircraft noise measurements are subject to some uncertainty, which can influence the quality of the final measured result [2].

The uncertainty contributions for a typical noise study can be considered in two groups. The first group includes the components of uncertainty associated with the measurement of aircraft noise at a particular monitoring location. The second group includes the components of uncertainty associated with any subsequent data analysis that may be carried out [2], [3], [4]. The overall accuracy of any type of measurement is limited by various sources of error or uncertainty. Components of uncertainty can essentially be classified as either *random* or *systematic* in nature. When making a series of repeated measurements, the effect of the former is to produce randomly different results each time, which are all spread or scattered around an average (mean) value. In contrast, systematic components of uncertainty cause the measurement to be consistently above or below the true value. For example, when measuring the time with a watch that has been set 1 minute slow, there will be a systematic error (or bias) in all the measurements. In a well-designed measurement study, the systematic components of uncertainty should generally be smaller than the random components [2], [5]. Possible sources of uncertainty for aircraft noise measurements include not only the noise instrumentation itself, but also variations in the noise source and propagation path, meteorological variations, the local environment at the measurement site, and also any variance due to data sampling - all of these individual uncertainty components can influence the quality of the final measured result [1]. *An internationally accepted procedure for combining and expressing measurement uncertainties is given in the ISO Guide to the Expression of Uncertainty in Measurement [6], [7], [8].*

2   Diagrams and Description of Typical Architecture of an Aircraft Noise Monitoring Station [9], [10]

Generally, a noise monitoring *complex* system detects, identifies and analyses the noise produced by arriving and departing aircrafts. The Fig. 1 presents a typical architecture of aircraft noise monitoring stations. The noise monitoring system (NMS) measures aircraft noise according to defined criteria. The first step of the system is the collection of the detected aircraft noise, the second the attribution of the noise to a specific aircraft movement. To perform the correlation of the aircraft noise, additional information is necessary, which will be described later.

2.1   EMU - Environmental Monitoring Unit

The EMU consists of: a) a digital microphone; b) a local unit for data backup; c) a modem for transmitting data to the central processing system.

2.1.1   Microphone Unit
Each unit is mounted at the end of a mast and equipped with a digital microphone, an anti-wind and bird guard and a lightning arrestor. The microphone captures the analogue noise signal and performs the critical conversion of the signal immediately at the microphone head, and transmits the noise data in digital form to the EMU's
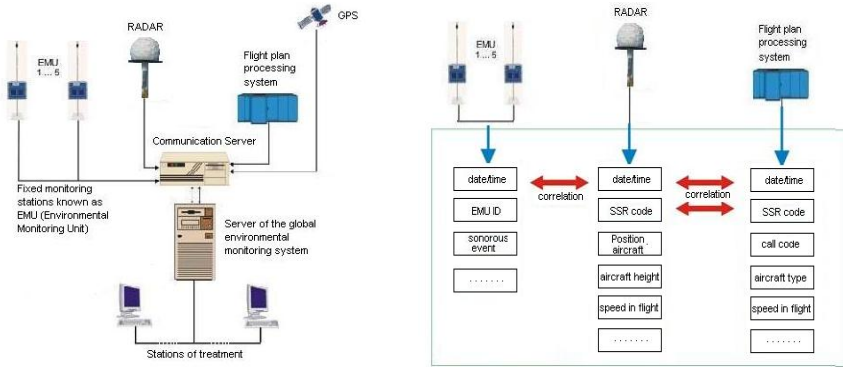
Fig. 1. Typical architecture of aircraft noise monitoring stations and correlation principle

electronics. The immediate conversion to a digital signal provides a higher immunity to interference. The unit guarantees an omni directional detection of noise with high reception qualities. The 5 local units are synchronized by the central system GPS clock.

2.2   Central Processing System

All the data collected via network or modem from the airport radar, the flight plan processing system and the EMUs are put through to the central processing system which consists of **Comm**unication **S**erver and **G**lobal **E**nvironment **M**onitoring **S**ystem (GEMS). The Communication Server collects: a) the noise events of the five EMUs; b) the radar aircraft tracks; c) the flight plans from FDP (**F**light **D**ata **P**rocessor); d) the GPS (**G**lobal **P**ositioning **S**ystem) to guarantee the synchronization of the noise monitoring system.

The GEMS processes and correlates the data acquired by the Communication Server in order to identify an aircraft that produced a noise event. The essential processing in the GEMS consists of: a) correlating the real time data from the Communication Server; b) archiving the acquired data, and generating reports about individual events, daily, monthly or annual summaries.

Identification of the noise event: The EMU continuously analyses the incoming noise signal to identify the source of noise. By using various detection algorithms it is possible to identify noise generated by an aircraft flying past, known as event. The process of identifying a noise event is based on threshold and time change criteria. The incoming data are noise events, aircraft flight plans and Radar information. The correlation principle is observed in the right side of Fig 1.

3   Aircrafts Noise Patterns

The used airplanes noises in this work have been acquired by means of MP201 microphone. It is a good choice for use in IEC61672 class 1 sound level meters and other noise measurements requiring class 1 accuracy [11]. It is a 1/2" prepolarized

free-field measurement microphone. The data acquisition card is USB-9233. It is a four-channel dynamic signal acquisition module for making high-accuracy measurements from IEPE sensors. The USB-9233 delivers 102 dB of dynamic range. The four USB-9233 input channels simultaneously acquire at rates from 2 to 50 kHz. In addition, the module includes built-in antialiasing filters that automatically adjust to your sampling rate. The USB-9233 uses a method of A/D conversion known as deltasigma modulation. If the data rate is 25 kS/s, each ADC actually samples its input signal at 3.2 MS/s (128 times the data rate) and produces samples that are applied to a digital filter. This filter then expands the data to 24 bits, rejects signal components greater than 12.5 kHz (the Nyquist frequency), and then digitally resamples the data at the chosen data rate of 25 kS/s. This combination of analog and digital filtering provides an accurate representation of desirable signals while rejecting out-of-band signals. The built-in filters automatically adjust themselves to discriminate between signals based on the frequency range, or bandwidth, of the signal.

In this work, the noise samples were acquired with sampling frequencies of 22050 Hz (Samples/second: S/s) and 11025 Hz (S/s), monophonic and during 24 seconds. In general, this interval is greater than to aircraft takeoff time, or greater to the time in which the produced noise affects the zones near an airport. It is possible to extend this sampling time interval (>24 seconds). For a same aircraft, many *noise events* were acquired, taken for different meteorological conditions, several microphone orientations and background noises. The takeoff direction is always the same one and this reduces the disturbances of Doppler Effect.

3.1   Aircraft Noise Signals Analysis

The Fig. 2 and Fig. 3 present examples of some aircrafts noise signals.
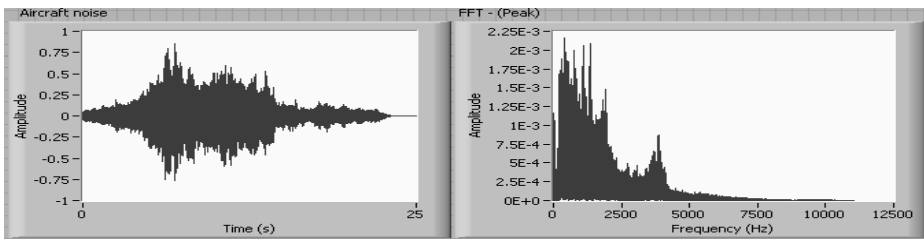
Fig. 2. Noise of Falcon aircraft taking off, with sampling frequency of 22050 Hz

For all used aircraft noises *the typical form of the amplitude spectrum* is observed from 0 to 5000 Hertz, for this reason, in this work was used a sampling frequency of 11025 Hz, in order to reduce the number of taken samples in 24 seconds (264600 samples). The amplitude spectrum has 132300 harmonics, with $\Delta f = 0.04167$ Hz. In other aircraft noise analyses, the recommended sampling frequency is 25 Ks/s and D, C and A-weighting filters.
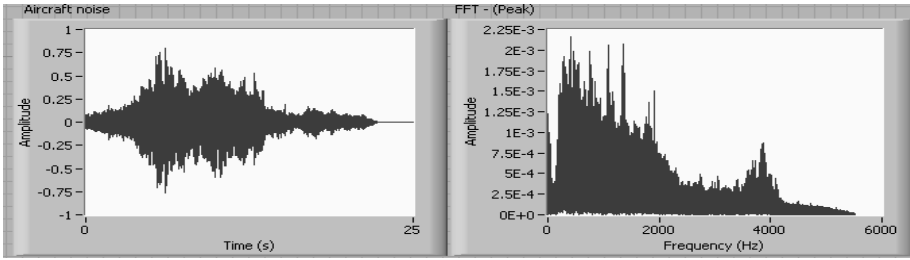
Fig. 3. Noise of Falcon aircraft taking off, with sampling frequency of 11025 Hz

3.1.1 Reduction of the Spectral Resolution

It is necessary to reduce the spectral resolution because of the following reasons:

1. The amplitude spectrum has 132300 harmonics and its processing will be very complex.
2. It is only of interest the spectral form.

The following hypotheses are presented:

1. Any reduction method of spectral resolution introduces a tolerance in the initial and final times within the measurement interval of aircraft noise.
   For example, a feedforward neural network is trained with one noise pattern which was acquired from zero seconds from the aircraft takeoff until 24 seconds later. In run time, if the aircraft takeoff noise is acquired from 5 seconds until 24 seconds, this time displacement of 5 seconds will affect little the spectral form if its spectral resolution has been reduced.
2. A median filter (moving average filter) creates a typical form of the aircrafts takeoff noises spectrums.
3. The decimation of average spectrum, with a rate X, conserves the spectral form of aircrafts takeoff noises.

3.1.2 Spectral Estimation

In the present work is used the *Bartlett-Welch* method [12] for spectral estimation. The Bartlett method consists on dividing the received data sequence into a number K, of non-overlapping segments and averaging the calculated Fast Fourier Transform.

It consists of three steps:

1. The sequence of N points is subdivided in K non overlapping segments, where each segment has length M.

$$x_i(n) = x_i(n + iM), \ i = 0,1,...,K-1, \ n = 0,1,...,M-1 \qquad (1)$$

2. For each segment, periodogram is calculated

$$\hat{P}_{xx}(f) = \frac{1}{M}\left|\sum_{n=0}^{M-1} x_i(n)e^{-j2\pi fn}\right|^2, \ i = 0,1,...,K-1 \qquad (2)$$

3. The periodograms are averaged for the K segments and the estimation of the Bartlett spectral power can be obtained as:

$$\hat{P}_{xx}^{B}(f) = \frac{1}{K}\left|\sum_{i=0}^{K-1} \hat{P}_{xx}^{(i)}(f)\right|^2 \qquad (3)$$

The statistical properties of this estimation are the following ones:

The average value is:

$$\left\langle \hat{P}_{xx}^{B}(f) \right\rangle = \frac{1}{K} \sum_{i=0}^{K-1} \overline{\hat{P}_{xx}^{(i)}(f)} = \overline{\hat{P}_{xx}^{(i)}(f)} = \sum_{m=-(M-1)}^{M-1} \left(1 - \frac{|m|}{M}\right) r_{xx}(m) e^{-j2\pi fm}$$

$$= \frac{1}{M} \int_{-1/2}^{1/2} P_{xx}(a) \left(\frac{\sin \pi (f-\alpha) M}{\sin \pi (f-\alpha)}\right)^{2} d\alpha, \tag{4}$$

where $\dfrac{1}{M} \dfrac{\sin \pi (f-\alpha)}{\sin \pi (f-\alpha)} = W_{B}(f)$ it is the frequency characteristic of the Bartlett

window: $w_{B}(m) = \begin{cases} \left(1 - \dfrac{|m|}{N}\right), & |m| \le M-1 \\ 0, & |m| > M-1 \end{cases}$ (5)

The true spectrum is convolutioned with the frequency characteristic of the Bartlett window $w_{B}(m)$. Reducing the length of the data window of N points to M=N/K, it results in a window whose spectral wide has been increased by the factor k. Consequently, ***the frequency resolution has decreased for the factor k,*** in exchange for a variance reduction.

The variance of the Bartlett estimation is:

$$\mathrm{var}\left[\hat{P}_{xx}^{B}(f)\right] = \frac{1}{K^2} \sum_{i=0}^{K-1} \mathrm{var}\left[\hat{P}_{xx}^{(i)}(f)\right] = \frac{1}{K} \mathrm{var}\left[\hat{P}_{xx}^{(i)}(f)\right] = \frac{1}{K} P_{xx}^2(f) \left[1 + \left(\frac{\sin 2\pi fM}{M \sin 2\pi f}\right)^2\right] \tag{6}$$

Welch Method [12], [13], [14]: unlike in the Bartlett method, the different data segments are allowed to overlap and each data segment is windowed.

$$x_i(n) = x(n+iD), \ n = 0,1,...,M-1, \ i = 0,1,...,L-1 \tag{7}$$

Where iD is the point of beginning of the sequence i-th. If D=M, the segments are not overlapped. If D=M/2, the successive segments have 50% of overlapping and the obtained data segments are L=2K.

Another modification proposed by Welch to the Bartlet method consists on using a window for the data segments before calculating the periodogram. The result is the "modified" periodogram:

$$\tilde{P}_{xx}^{(i)}(f) = \frac{1}{MU} \left| \sum_{n=0}^{M-1} x_i(n) w(n) e^{-j2\pi fn} \right|^2, \ i = 0,1,...,L-1 \tag{8}$$

Where U is a normalization factor for power of the function window and it is selected as:

$$U = \frac{1}{M} \sum_{n=0}^{M-1} w(n) \tag{9}$$

The Welch estimation of spectral power is the average of these modified periodograms:

$$P_{xx}^{W}(f) = \frac{1}{L} \sum_{i=0}^{L-1} \tilde{P}_{xx}^{(i)}(f) \tag{10}$$

The average of the Welch estimation is:

$$\left\langle P_{xx}^{W}\left(f\right)\right\rangle = \frac{1}{L}\sum_{i=0}^{L-1}\overline{\tilde{P}_{xx}^{(i)}\left(f\right)} = \overline{\tilde{P}_{xx}^{(i)}\left(f\right)} = \frac{1}{MU}\int_{-1/2}^{1/2} P_{xx}\left(a\right)W\left(f-\alpha\right)d\alpha \tag{11}$$

Where $W\left(f\right) = \dfrac{1}{MU}\left(\dfrac{\sin\pi\left(f-\alpha\right)M}{\sin\pi\left(f-\alpha\right)}\right)^{2} = \dfrac{1}{MU}\Im\left\{w\left(n\right)\right\}$ \hfill (12)

The normalization factor assures that: $\displaystyle\int_{-1/2}^{1/2} W\left(f\right)df = 1$

The variance of the Welch estimation is:

$$var\left[\hat{P}_{xx}^{W}\left(f\right)\right] = \frac{1}{L^{2}}\sum_{i=0}^{L-1}\sum_{j=0}^{L-1}\left\{\left[\overline{\tilde{P}_{xx}^{(i)}\left(f\right)\tilde{P}_{xx}^{(j)}\left(f\right)}\right]^{2} - \left[\left\langle\hat{P}_{xx}^{W}\left(f\right)\right\rangle\right]^{2}\right\} \tag{13}$$

Why Welch method is introduced?

- Overlapping allows more periodograms to be added, in hope of reduced variance.
- Windowing allows control between resolution and leakage.

The Welch method is hard to analyze, but empirical results show that it can offer lower variance than the Bartlett method, but the difference is not dramatic.

·Suggestion is that 50 % overlapping is used.

In this paper, the data segment of 264600 samples, acquired in 24 seconds, is divided in 24 segments: K=24, with 50% of overlapping, therefore, L=2K=48 overlapped data segments, later is applied the FFT (periodogram) to each segment and they are averaged.

3.2 Examples of Some Aircrafts Noise Patterns
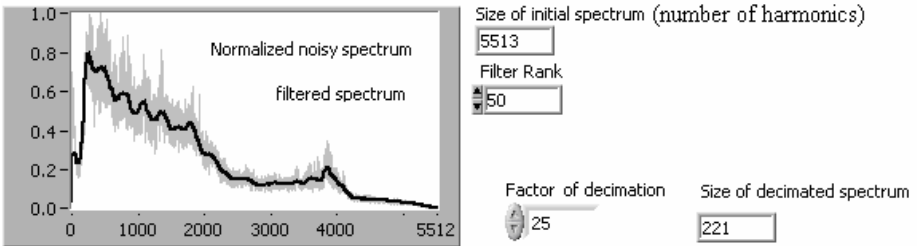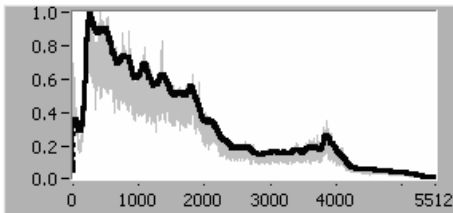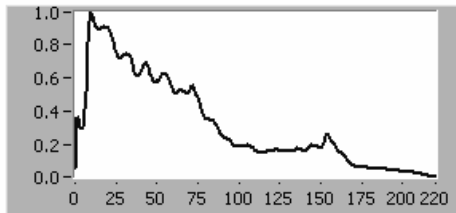
Fig. 4. Example of noise pattern of Falcon aircraft taking off (turbojet)
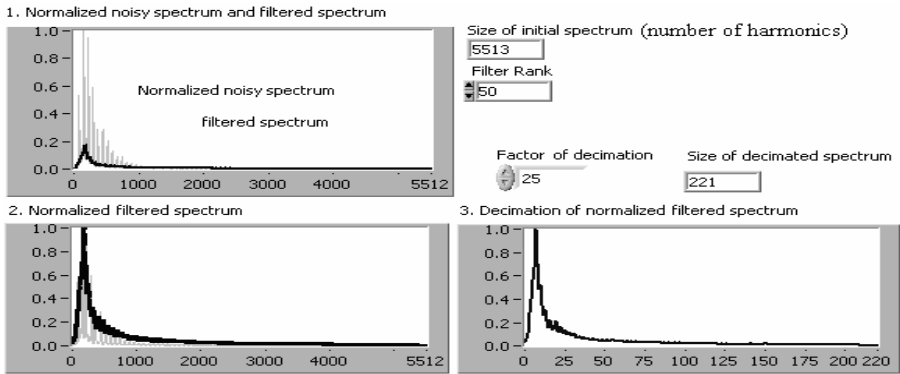
Fig. 5. Example of noise pattern of T6 aircraft taking off (propeller)
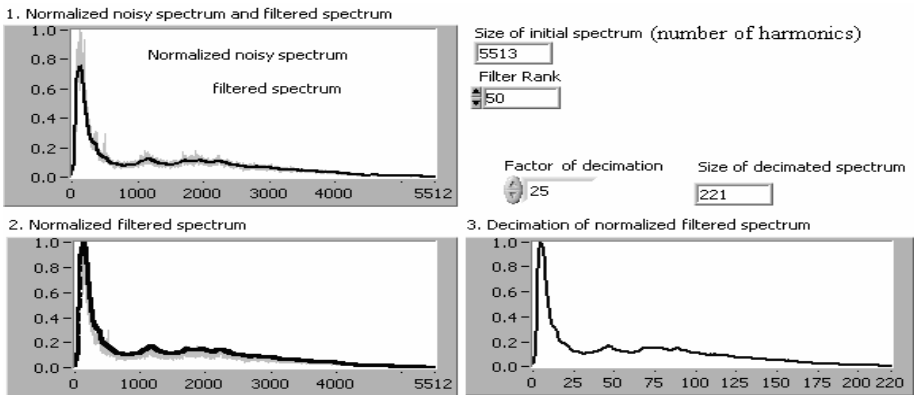
Fig. 6. Example of noise pattern of f Boeing 707 aircraft taking off

In this stage, 16 aircrafts types were tested with 12 patterns by aircraft. In all, the neural network was trained with 192 patterns. Ninety and six patterns were used for testing.

4   Neural Network

The neural network has 221 inputs. Every input is a normalized harmonic and some examples were presented in Fig. 4, 5 and 6. The output layer has 16 neurons, corresponding to the 16 recognized aircrafts. After several tests, the neural network was successful with a hidden layer of 14 neurons. The activation functions are tan-sigmoid. The Fig 7 presents the topological diagram and training performance. The training performance was successful with an error of $1.51281e^{-10}$ in 300 epochs. The training finished in 19 minutes in a Pentium IV of 3 GHz.

Input: 221 neurons
(aircrafts noise harmonics)

Output layer: 16 neurons
(aircrafts type)
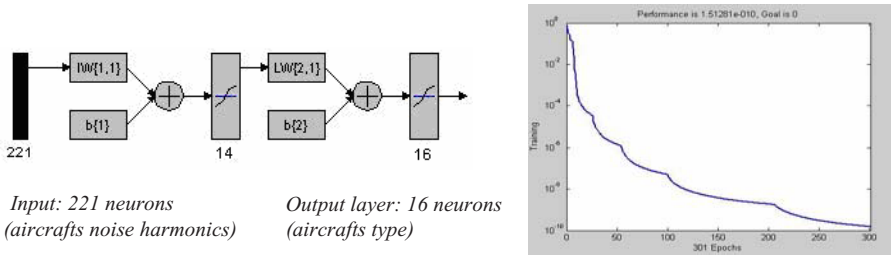
Fig. 7. Neural network topology and training performance

5   Analysis of Results

For aircraft noise used in neural network training, the recognition was successful. For an aircraft noise non-used in the training, the neural network non-recognized a specific aircraft and the program presented a message with three aircrafts whose mixed noise patterns have similarity to the acquired noise event (see Fig. 8). Table 1 shows results of a test of aircrafts recognition.
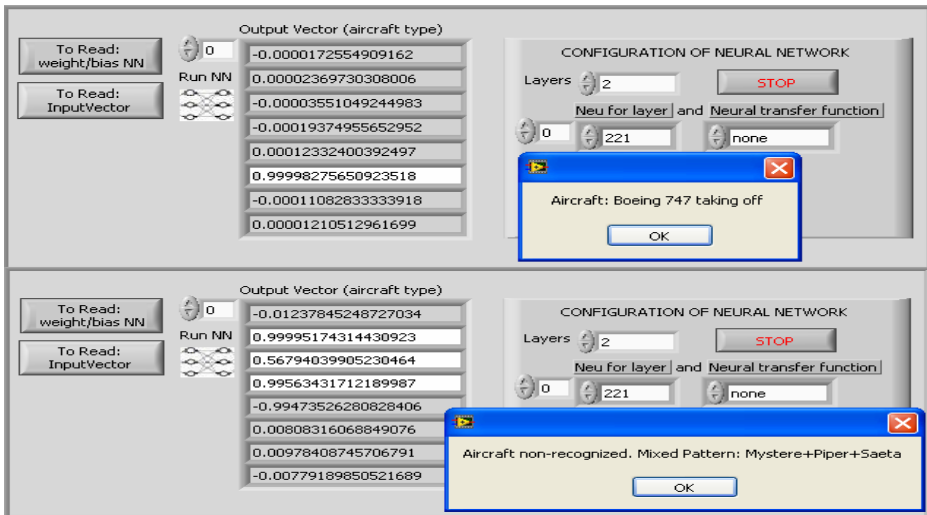
Fig. 8. Example of two tests of patterns recognition and non-recognition

Table 1. Certainty of recognized aircrafts in the first test

Aircrafts type	Evaluated Aircrafts	Recognized aircrafts with certainty of more than 80%	Recognized aircrafts with certainty of mote than 60% and less than 80%
Propeller	5	4	1
Turbojet	17	13	4
Reaction	4	4	0

6   Conclusions and Future Work

The presented work tested successfully a methodology to create aircrafts noise patterns. It combines the decrease of spectral resolution, a moving average filter and decimation of average spectrum, this method allows reducing the number of significant harmonics in amplitude spectrum, so that a feedforward neural network with 221 inputs can recognize the aircraft type. The decrease of spectral resolution using the Bartlett-Welch method introduces a tolerance in the initial and final times within the measurement interval of aircraft noise, which produces a better recognition of the patterns when the measurements can have uncertainties. This research tests the feasibility to identify the aircraft that produces a certain noise level, having only noise information. The obtained results make possible to introduce redundancy to permanent monitoring systems of aircraft noise (Fig. 1). These results are very useful in portable systems. The noise intensity and others environmental contamination indicators are calculated by statistical methods using noise time series. The next tests will include more aircrafts types using a distributed and portable system.

References

1. Kendall, M.: EU proposal for a directive on the establishment of a community framework for noise classification of on civil subsonic aircraft for the purposes of calculating noise charges, European Union (2003)
2. White, S.: Precision of Aircraft Noise Measurements at the London Airports. Environmental Research and Consultancy Department. Civil Aviation Authority. Department for Transport. Ercd Report 0506. ISBN 0-117905-19-4. London (2005)
3. Holding, J.M.: Aircraft noise monitoring: principles and practice. IMC measurement and Control 34(3), 72–76 (2001)
4. Holding, J.M., Sheldon, M.: An expert system for aircraft recognition using acoastics. IMC measurement and Control 34(3), 77–80 (2001)
5. Doebelin, E.O.: Measurement Systems Application and Design. McGraw-Hill, New York (1998)
6. BIPM, IEC, IFCC, ISO, IUPAC, IUPAP, OIML, Guide to the Expression of Uncertainty in Measurement, International Organization for Standardization (ISO), Geneva (1995)
7. Bell, S.: A Beginner's Guide to Uncertainty of Measurement, Measurement Good Practice Guide No. 11(2) National Physical Laboratory (March 2001)
8. Craven, N.J., Kerry, G.: A Good Practice Guide on the Sources and Magnitude of Uncertainty Arising in the Practical Measurement of Environmental Noise, University of Salford (October 2001)
9. Luxembourg Airport Authority: Aircraft noise monitoring stations (2005)
10. Lochard Expanding Environmental Capacity (2006)
11. International Electrotechnical Commission (IEC): Standard IEC61672: Electroacoustics-sound level meters (2002)
12. Oppenheim, A.V., Schafer, R.W.: Discrete-Time Signal Processing, pp. 311–312. Prentice Hall, Englewood Cliffs, NJ (1989)
13. Welch, P.D.: The Use of Fast Fourier Transform for the Estimation of Power Spectra: A Method Based on Time Averaging Over Short, Modified Periodograms. IEEE Trans. Audio Electroacoust. AU-15, 70–73 (1967)
14. Thompson, S.C.: Spectral Estimation of Digital Signaling Using The Welch Method. Center for Wireless Communications, Department of Electrical and Computer Engineering, University of California at San Diego (2004)

Echocardiographic Image Sequence Compression Based on Spatial Active Appearance Model

Sándor M. Szilágyi[1], László Szilágyi[1,2], and Zoltán Benyó[2]

[1] Sapientia - Hungarian Science University of Transylvania,
Faculty of Technical and Human Science, Târgu-Mureş, Romania
`szs@ms.sapientia.ro`
[2] Budapest University of Technology and Economics,
Dept. of Control Engineering and Information Technology, Budapest, Hungary

Abstract. This paper presents a new method for echocardiographic image sequence compression based on active appearance model. The key element is the intensive usage of all kind of a priori medical information, such as electrocardiography (ECG) records and heart anatomical data that can be processed to estimate the ongoing echocardiographic image sequences. Starting from the accurately estimated images, we could obtain lower amplitude residual signal and accordingly higher compression rate using a fixed image distortion. The realized spatial active appearance model provides a tool to investigate the long term variance of the heart's shape and its volumetric variance over time.

Keywords: Echocardiography, active appearance model, image compression, QRS clustering.

1 Introduction

Echocardiography is a popular medical imaging modality due to its noninvasive and versatile behavior. There are no known side effects, and the measuring equipment is small and inexpensive relative to other options, such as MRI or CT. Reducing storage requirements and making data access user friendly are two important motivations for applying compression to ultrasound images, with the retention of diagnostic information being critical [2]. A typical echocardiography image consists of a non-rectangular scanned area, and a passive background, which may contain patient related text or limited graphics (e.g. a single channel ECG signal). The resulting spatial variation in image statistics presents a hard task to coding methods that use a single partition strategy. For example, many modern image compression algorithms, such as zero-tree coding [16] and set partitioning in hierarchical trees (SPIHT) [8,15] are based on the wavelet transform, which partitions the input images into frequency bands whose size decreases logarithmically from high frequencies to low ones. This kind of decomposition strategy works well when the input images are statistically homogeneous, but not in the case of echocardiography image sequences.

In paper [5] is presented the investigation results of the improved transformation based lossy compression techniques for ultrasound and angiography images.

The goal of the study was to clarify, where the compression process could be improved for the medical application. It was proved that wavelet transform outperforms discrete cosine transform applied to ultrasound image sequence. The analysis of international image compression standards was carried out with special attention to the new still image compression standard: Joint Photographic Experts Group (JPEG) 2000. The JPEG2000 compression is better than ordinary JPEG at higher compression ratio levels. However, some findings revealed this consideration is not necessarily valid for lower compression levels. In study [17] the qualities of the compressed medical images such as computed radiography, computed tomography head and body, mammographic, and magnetic resonance T1 and T2 images were estimated using both methods. The negative effect of blocking artifacts from JPEG was decreased using jump windows.

The impact of image information on compressibility and degradation in medical image compression was presented in paper [7]. This study used axial computed tomography images of a head. Both JPEG and JPEG 2000 compression methods were evaluated using various compression ratios (CR) and minimal image quality factor (MIQF).

In pattern recognition research the dimensionality reduction techniques are widely used since it may be difficult to recognize multidimensional data when the number of samples in a data set is comparable with the dimensionality of data space. Locality pursuit embedding (LPE) is a recently proposed method for unsupervised linear dimensionality reduction. LPE seeks to preserve the local structure, which is usually more significant than the global structure preserved by principal component analysis (PCA) and linear discriminant analysis (LDA). In paper [25] the supervised locality pursuit embedding (SLPE) is investigated. These dimensionality reduction methods can improve the understanding level of the medical information borrowed in the recorded image sequences [24].

Usually the medical applications do not tolerate much loss in fidelity, so the distortion free methods, such as context-based adaptive lossless image coding (CALIC) [22] have been recently adapted to "near-lossless" situations [23] with good results. Erickson et al. [4] have compared SPIHT and JPEG methods to compress magnetic resonance imaging (MRI) and ultrasound images. They concluded that wavelet-based methods are subjectively far superior to JPEG compressed at moderately high bit rates. Medical images are typically stored in databases, so it is possible for computers to extract patterns or semantic connections based on a large collection of annotated or classified images. Such automatically extracted patterns can improve the processing and classifying performance of the computers.

In the recent past, researchers in the image analysis community have successfully used statistical modeling techniques to segment, classify, annotate and compress images. Particularly, variations of hidden Markov models (HMMs) have been developed and successfully applied for image and video processing. The key issue in using such complex models is the estimation of system parameters, which is usually a computationally expensive task. In practice, often a tradeoff is accepted between estimation accuracy and running time of the parameter

estimation method [9]. The matching pursuit (MP) signal coding technique was developed by Mallat and Zhang [12] and enhanced to code the motion prediction signal by Neff and Zakhor [14]. The task of the MP coder is to measure the energy of different subunits, each of which represents a motion residual.

Such a statistical information-based estimation highly depends on biological parameters. In our case, the most important task in efficient echocardiography image compression is the accurate detection of QRS complexes from the simultaneously measured ECG signal. Due to the semi-periodic behavior of the ECG signal and echocardiography image sequences, the parameters of the patient model can be more precisely estimated.

Active appearance models (AAM), introduced by Cootes et al. [3], are promising image segmentation tools that may provide solutions to most pending problems of echocardiography, as they rely on both shape and appearance (intensity and/or texture) information. Bosch et al. [1] proposed a robust and time-continuous delineation of 2-D endocardial contours along a full cardiac cycle, using an extended AAM, trained on phase-normalized four-chamber sequences.

An accurate investigation of the physiology and patho-physiology of the heart, besides studying the electrical activity and spatial distribution of its structures, must also consider the movement of these structures during normal and abnormal cardiac cycles. In this order, simultaneous ECG signal and ultrasound image sequence recording is proposed [20], which reliably supports the localization of the investigated events.

Several papers have already reported the usage of spatial AAM [13,18]. The present work has the following contributions: (1) we developed a heart reconstruction algorithm including time-dependent wall boundaries, to estimate the image variances, that allow a better compression rate than conventional methods at a fixed image quality; (2) reported techniques classify ultrasound images only as belonging to systolic or diastolic interval. Our approach distinguishes normal and extra beats, and processes the corresponding images accordingly.

2   Materials and Methods

Simultaneous echocardiography sequence recording and ECG signal measurement were carried out at the County Medical Clinic of Târgu-Mureş, using a 2-D echocardiograph that produces 30 frames per second, and a 12-lead ECG monitoring system that samples at 500 Hz frequency and 12-bit resolution. Each image frame received a time stamp, which served for synchronization with ECG events. Two different series of measurements were recorded. The first series, which served for AAM training, consisted of 35 patients (12 of whom having extraventricular beats), 20 ultrasound sequences for each patient, of 10-15 seconds length each, with previously established transducer placements. Based on these data, an a priori information database was created, which organized the ultrasound images grouped by corresponding ECG events.

The second series of measurements, which involved 8 patients, consisted of two stages. In the first stage, the same measurements were performed, as in the

first series, in order to provide patient-specific training data for the AAM. In the second stage, several measurements of the same individuals but recorded in different moments were performed using different placements and positions of the transducer. In this order, image sequences were recorded at 8 parallel cross sections in horizontal and rotated (45° to the left and to the right) positions with a 1 cm inter-slice distance. We used 10 common axis planes that were placed at the front, lateral and back side of the torso, resulting for each patient $10 \times 8 \times 3 = 240$ image sequences of 2-3 seconds duration.

The duration of the recorded image sequences was restricted by the semiperiodic behavior of the ECG signal. The spatial movement of the heart is constrained by the course of the depolarization-repolarization cycle [19]. The studied ECG parameters were: shape of QRS beat, QT and RR distances. These parameters characterize the nature of a QRS complex, and were determined as presented in [19]. ECG event clustering was accomplished using Hermite functions and self-organizing maps [10]. Two main event clusters were created: normal and ventricular extra beats. This latter group, because of the patient specific manifestation of ventricular extras, had to be dealt with separately patient by patient. QRS beats not belonging to any cluster were excluded from further processing, together with their corresponding ultrasound sub-sequences. A further condition for normal QRS complexes to be included was having RR distance between 700-800 ms and QT distance between 350-400 ms. A detailed presentation of ECG processing is presented in Fig. 1.

The time-varying evolution of the cardiac volume is determined by the interconnection of electrical and mechanical phenomena. In a whole cardiac cycle there are two extremity values. The maximal volume can be coupled with the starting moment of ventricular contraction. The moment of minimal volume shortly precedes the termination of ventricular contraction, but is much more difficult to identify, due to the dead time of a normal cardiac cell. This delay is caused by the behavior of a regular cardiac cell, whose electric response precedes with 60-80 ms the mechanical contraction [21]. The combination of the electrical and mechanical properties of the heart and the usage of knowledge-base allowed us to create a performance evaluation module, shown in Fig. 2, that determines the most probable wall position. This image presents an overview of the image processing and volumetric reconstruction procedure. The first algorithmic step is noise elimination. Speckle noise represents a major difficulty to most ultrasound imaging applications [6]. In our case, the suppression of such phenomena was accomplished using the well-known motion adaptive spatial technique presented in [20]. Due to the measuring technique of traditional echocardiography, the obtained images are distorted. In order to become suitable input for 3-D processing, they need to go through a normalization transform. Every recorded ultrasound slice is represented by a plane, whose spatial alignment depends on the position and rotational angle of the transducer. The normalization process also takes into consideration the distance of each image pixel from the transducer.

The AAM was trained using the spatial position of each slice recorded in the first measurement series. By averaging these spatial distributions, a mean 4-D
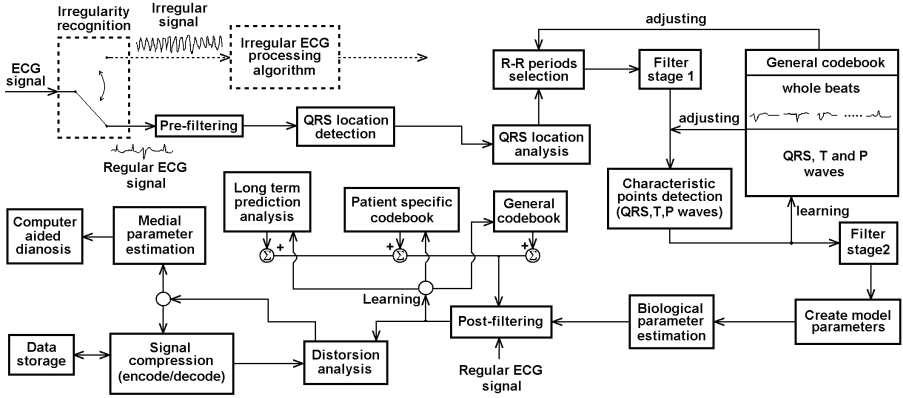
Fig. 1. The proposed ECG signal filtering, processing and compression
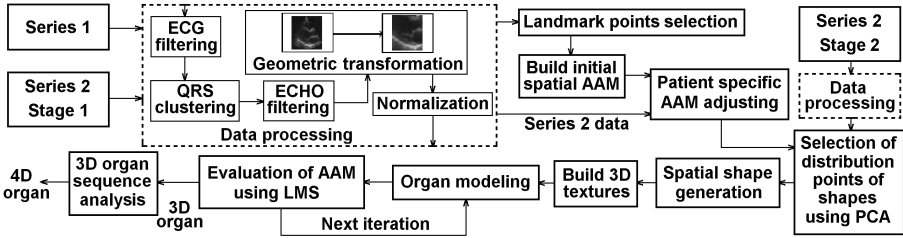
Fig. 2. The data recording and analyzing procedure: all echocardiography and ECG data go through the same processing module. The AAM is constructed from the measurements of series 1, and fine tuned afterward using the patient specific data resulting from series 2 stage 1. Stage 2 data serve for the detailed cardiac volumetric analysis. Reconstructed 3-D objects are finally aligned using an iterative LMS-based algorithm.
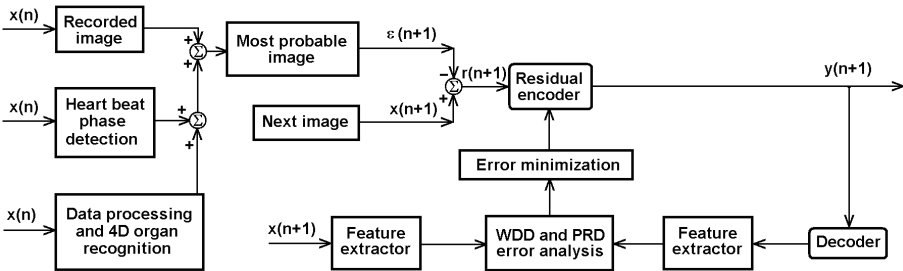
Fig. 3. Residual data construction and distortion analysis using the recorded image, heart beat phase information and AAM-based 4D organ shape to determine the most probable image in the next cycle. As the $y(n+1)$ output signal is obtained, a WDD and PRD-based distortion analysis is performed, using image features given by AAM.

heart shape model is obtained, which will be the base shape of the AAM [1,11]. Landmark points are determined as by Mitchell et al. [13]. The sparse character of the obtained spatial description model doesn't allow the landmark points have 3-D texture information, so we restricted the texture to 2-D.

Subjects have their own specific, time-dependent inner structure, which cannot be properly approximated from a population of few dozens of individuals. In order to make further adjustments to the AAM, the base structure was adjusted to the patient using the measurements made in the second series, first stage. The landmark points determined on the images recorded during the second stage of the second series allowed us to create a 3-D distribution point model, which was established according to [13]. Having the distribution points established, the AAM will be enabled to adjust itself to a diversity of biological factors like the phase of ECG and breathing. A detailed description of the manifestation of these phenomena and the model adaptation is given in [18]. Our algorithm acts similarly, but it treats the cardiac cycle differently: not only systolic and diastolic phases are distinguished, but also a QRS complex clustering is performed to give different treatment to normal and ventricular cardiac cycles.

Spatial texture maps are determined via averaging [18]. The visual aspect of the heart and its environment, because of their mutual motion, is changing in time. AAM models only include information on the texture situated within the model. The time dependent representation of the ultrasound slices obtained from the large stack of sequences enabled us to accurately determine the 4-D structure of the heart [13]. The iterative algorithm of the AAM demands the comparison of measured and expected shapes. The AAM was adjusted using a quadratic cost function, until the desired accuracy was obtained.

Due to its adaptive behavior, the compression method can handle patient-dependent data and efficiently separate the measured artifacts from the useful signal. The proposed signal compression algorithm consists of the following steps:

- Intelligent image sequence analysis and filtering, that involves the automatic recognition of echocardiography image, ECG signal and various changing and constant labels and letters that appear on the recorded image sequence;
- Background selection (the constantly dark region);
- ECG signal processing (see Fig. 1);
- Segmentation of ultrasound image (see Fig. 2);
- Calculation of the heart's 4-D shape (3-D + time) using AAM;
- Estimation of probable image;
- Residual signal estimation, 2-way entropy coding and back-estimation.

Compression results were evaluated using the percentage root mean square difference (PRD) and weighted diagnostic distortion (WDD) [26]. WDD measures the relative preservation of the diagnostic information (e.g. location, duration, intensity, shapes, edges) in the reconstructed image. These diagnostic features were determined by physicians. The distortion estimation and signal (ultrasound image and all auxiliary data) coding process is presented in Fig. 3.

3 Results

Figure 4(a) presents two series of ultrasound slices indicating the contour of the left ventricle of the 2nd patient, detected during a ventricular contraction. The two columns of slices show two different views, having 60° angle difference. The four slices in each column represent subsequent images of the sequence, showing the approximately 100 ms duration of a ventricular contraction. Figure 4(b) exhibits the same ultrasound slices after being normalized, that is, transformed to Euclidean space. Figure 4(c) shows two different reconstructed 3-D shapes of the left ventricle.

Figure 5 presents the decoded echocardiography images at various compression rates. The variation of RMSE level against inverted compression rate is shown in Fig. 5(e). The RMSE graph was created for an averaged normal QRS beat shape, and average RR and QT distances.

(a)   **(b)**   **(a)**   **(b)**   **(c)**
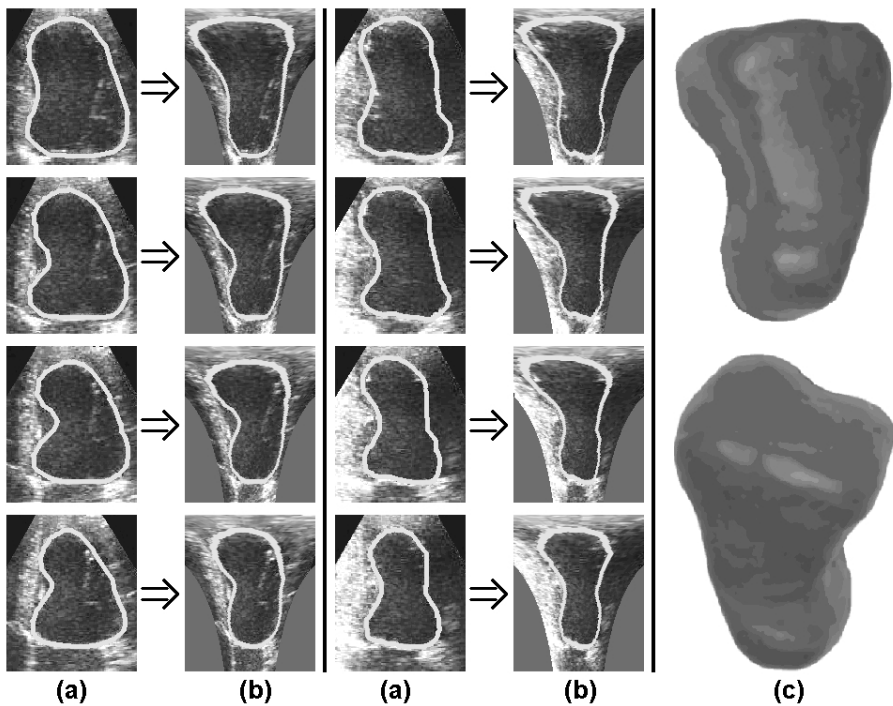
Fig. 4. Results of shape reconstruction: (a) and (b) time varying 2-D contour of the left ventricle before and after normalization, (c) reconstructed 3-D structure of the left ventricle

4 Discussion

The recognition of the relation between echocardiography images and simultaneously recorded ECG signal is a key element in efficient image sequence
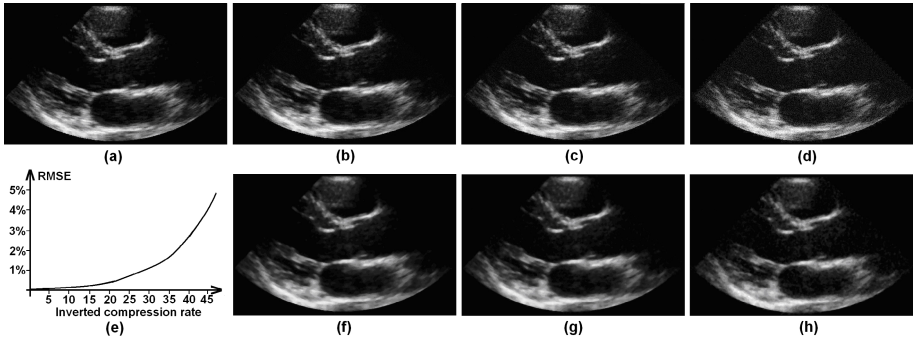
Fig. 5. Results of image reconstruction: (a) original image, (b) decoded image at 1/22 compression rate, (c) decoded image at 1/39 compression rate, (d) decoded image at 1/54 compression rate, (e) representation of root mean square error (RMSE) vs. inverted compression rate, (f) feature-base corrected image at 1/22 compression rate, (g) feature-base corrected image at 1/39 compression rate, (h) feature-base corrected image at 1/54 compression rate

compression (see Table 1). However, various events like aspiration and expiration may influence the measured data. During a whole cardiac cycle, the shape and volume of the left ventricle changes considerably. It is difficult to determine the performance of the reconstruction method for the sporadically occurred ventricular extra-systolic beats. Even for patients that produce at least five extra beats with similar shapes in each minute the reconstruction performance remains well below the normal QRS cluster's accuracy, due to the sparse distribution of the processable slices.

From Fig. 5 we can observe that even a well-working WDD correction method cannot handle a compression rate better than 1/60 without a serious image distortion that can lead to wrong medical diagnosis. Table 1 demonstrates the higher performance of the proposed image compression method, that exists due

Table 1. The obtained inverted compression rates obtained for normal beats, at various RMSE levels, using the following methods: Wavelet-based compression, Image comparison-based estimation, ECG and echocardiography image compression using QRS long-term prediction (LTP), JPEG 2000, Matching Pursuits, proposed AAM-based compression

Compression Method vs. RMSE	1 %	2 %	3 %	4 %	5 %
Wavelet-based compression [8]	10.2	15.4	17.3	18.8	19.9
Image comparison [22]	14.2	21.2	24.0	26.1	27.8
QRS and LTP image comparison [26]	17.4	26.6	29.6	31.8	33.7
JPEG 2000	13.7	20.5	23.2	25.1	26.6
Matching pursuits [12]	15.7	22.9	27.1	29.5	31.4
Proposed AAM-based	22.7	36.3	40.2	44.1	47.7

to the advanced QRS beat analysis and spatial AAM-based organ reconstruction. Such an analysis can lead to a much better 'estimated image' quality that reduces the amplitude of the residual signal. The improvement brought by the proposed method is more relevant in case of normal beats, because the AAM can better adapt itself to their characterization due to their higher incidence.

5 Conclusions

The investigation of simultaneously recorded ECG and echocardiography images enables us to study the relations between the electrical and mechanical phenomena concerning the heart. The signal and image estimation is made by using various priori medical information, and the algorithm yields lower amplitude residual signal and better compression ratio at given distortion level.

The compression method presented in this paper performs well in case of normal and quite well for ventricular beats. The presence of pathological image and signal samples may lower the performance difference among the proposed method and the tested algorithms. This kind of approach of the problem may result in deeper understanding of electrical and mechanical properties of the heart, that provides a much efficient compression than other algorithms using less a priori information.

References

1. Bosch, J.G., Mitchell, S.C., Lelieveldt, B.P.F., Nijland, F., Kamp, O., Sonka, M., Reiber, J.H.C.: Automatic segmentation of echocardiographic sequences by active appearance motion models. IEEE Trans. Med. Imag. 21, 1374–1383 (2002)
2. Chiu, E., Vaisey, J., Atkins, M.S.: Wavelet-Based Space-Frequency Compression of Ultrasound Images. IEEE Trans. Inf. Tech. Biomed. Eng. 5, 300–310 (2001)
3. Cootes, T.F., Edwards, G.J., Taylor, C.J.: Active appearance models. IEEE Trans. Patt. Anal. Mach. Intell. 23, 681–685 (2001)
4. Erickson, B.J., Manduca, A., Palisson, P., Persons, K.R., Earnest, D., Savcenko, V.: Wavelet compression of medical images. Radiology 206, 599–607 (1998)
5. Erickson, B.J.: Irreversible Compression of Medical Images. J. Digit. Imag. 15, 5–14 (2002)
6. Evans, A.N., Nixon, M.S.: Biased motion-adaptive temporal filtering for speckle reduction in echocardiography. IEEE Trans. Med. Imag. 15, 39–50 (1996)
7. Fidler, A., Skaleric, U.: The impact of image information on compressibility and degradation in medical image compression. Med. Phys. 33, 2832–2838 (2006)
8. Hang, X., Greenberg, N.L., Zheng, Y.F., Thomas, J.D.: Compression of 3-D echocardiographic images using a modified 3-D set-partitioning-in-hierarchical-trees algorithm based on a 3-D wavelet packet transform. J. Electr. Imag. 15, 1–13 (2006) art. no. 023016
9. Joshi, D., Li, J., Wang, J.Z: A Computationally Efficient Approach to the Estimation of Two- and Three-Dimensional Hidden Markov Models. IEEE Trans. Imag. Proc. 15, 1871–1886 (2006)

10. Lagerholm, M., Peterson, C., Braccini, G., Edenbrandt, L., Sörnmo, L.: Clustering ECG complexes using Hermite functions and self-organizing maps. IEEE Trans. Biomed. Eng. 47, 838–848 (2000)
11. Lelieveldt, B.P.F., van der Geest, R.J., Mitchell, S.C., Bosch, J.G., Sonka, M., Reiber, J.H.C.: 3-D active appearance models: fully automatic detection of endoand epicardial contours in short-axis cardiac MR data. Proc. Int. Soc. Magn. Res. Med (ISMRM) 2, 1668 (2002)
12. Mallat, S., Zhang, Z.: Matching pursuits with time-frequency dictionaries. IEEE Trans. Signal Proc. 41, 3397–3415 (1993)
13. Mitchell, S.C., Bosch, J.G., Lelieveldt, B.P.F., van der Geest, R.J., Reiber, J.H.C., Sonka, M.: 3-D active appearance models: segmentation of cardiac MR and ultrasound images. IEEE Trans. Med. Imag. 21, 1167–1178 (2002)
14. Neff, R., Zakhor, A.: Very low bit rate video coding based on matching pursuits. IEEE Trans. Circ. Syst. Video Techn. 7, 158–171 (1997)
15. Said, A., Pearlman, W.A.: A new, fast, and efficient image codec based on set partitioning in hierarchical trees. IEEE Trans. Circ. Syst. Video Techn. 6, 243–250 (1996)
16. Shapiro, J.: Embedded image coding using zerotrees of wavelet coefficients. IEEE Trans. Sign. Proc. 41, 3445–3462 (1993)
17. Shiao, Y.H., Chen, T.J., Chuang, K.S., Lin, C.H., Chuang, C.C.: Quality of Compressed Medical Images. J. Digit. Imag. 20, 149–159 (2007)
18. Stegmann, M., Pedersen, D.: Bi-temporal 3D active appearance models with applications to unsupervised ejection fraction estimation. Progr. Biomed. Opt. Imag. Proc. SPIE 5746, 336–350 (2005)
19. Szilágyi, S.M., Szilágyi, L., Benyó, Z.: Support Vector Machine-Based ECG Compression. Ser. Adv. Soft Comput (IFSA 2007) 41, 737–745 (2007)
20. Szilágyi, S.M., Szilágyi, L., Benyó, Z.: Volumetric Analysis of the Heart Using Echocardiography. In: FIMH 2007. LNCS, vol. 4466, pp. 81–90 (2007)
21. Winslow, R.L., Hinch, R., Greenstein, J.L.: Mechanisms and models of cardiac excitation-contraction coupling. Lect. Notes Math. vol. 1867, pp. 97–131 (2005)
22. Wu, X., Memon, N.: Context-based adaptive lossless image coding. IEEE Trans. Comm. 45, 437–444 (1997)
23. Wu, X., Bao, P.: L-infinity constrained high-fidelity image compression via adaptive context modeling. IEEE Trans. Imag. Proc. 9, 536–542 (2000)
24. Yuan, Y., Evans, A.N., Monro, D.M.: Low Complexity Separable Matching Pursuits. In: Proc. IEEE Int. Conf. Acoust. Speech Sign. Proc. III, pp. 725–728. IEEE Computer Society Press, Los Alamitos (2004)
25. Zhenga, Z., Yang, J.: Supervised locality pursuit embedding for pattern classification. Imag. Vis. Comp. 24, 819–826 (2006)
26. Zigel, Y., Cohen, A., Katz, A.: ECG Signal Compression Using Analysis by Synthesis Coding. IEEE Trans. Biomed. Eng. 47, 1308–1316 (2000)

Unified Neural Network Based Pathologic Event Reconstruction Using Spatial Heart Model

Sándor M. Szilágyi[1], László Szilágyi[1,2], Attila Frigy[3], Levente K. Görög[1], and Zoltán Benyó[2]

[1] Sapientia - Hungarian Science University of Transylvania,
Faculty of Technical and Human Science, Târgu-Mureş, Romania
szs@ms.sapientia.ro
[2] Budapest University of Technology and Economics,
Dept. of Control Engineering and Information Technology, Budapest, Hungary
[3] County Medical Clinic No. 4, Târgu-Mureş, Romania

Abstract. This paper presents a new way to solve the inverse problem of electrocardiography in terms of heart model parameters. The developed event estimation and recognition method uses a unified neural network (UNN)-based optimization system to determine the most relevant heart model parameters. A UNN-based preliminary ECG analyzer system has been created to reduce the searching space of the optimization algorithm. The optimal model parameters were determined by a relation between objective function minimization and robustness of the solution. The final evaluation results, validated by physicians, were about 96% correct. Starting from the fact that input ECGs contained various malfunction cases, such as Wolff-Parkinson-White (WPW) syndrome, atrial and ventricular fibrillation, these results suggest this approach provides a robust inverse solution, circumventing most of the difficulties of the ECG inverse problem.

Keywords: Heart model, unified neural network, inverse ECG problem.

1 Introduction

Nowadays the health problems related to the malfunction of the heart affects large groups of people and have become the most important mortality factor [3]. These malfunctions are usually caused by heart attack, rhythm disturbances and pathological degenerations. Modern health study is focusing on predicting these kinds of tragic events, and identifying the endangered patients, to make it possible to apply a preventing therapy.

Traditional computerized electrocardiogram (ECG) analyzer systems used the collected signal as an input to suggest an empiric-information-based evaluation of the ECG [10]. These systems may recognize various waveforms, but the leakage of information about the inner functioning of the heart inhibits to understand the producing phenomena [13].

The construction of a heart model [20] may allow computers to recognize the origin and the evolvement process of the ECG signal [5]. These systems may

unify the vast empiric information applied in traditional systems with model-based-recognition, creating hybrid processing structures [17]. These hybrid systems may activate the model-based-approach at any moment to handle correctly almost all unrecognizable waveform. The strange waveforms may appear in case of unknown patients or uncommon states, such as ventricular fibrillation [19]. In these cases the model-based approach estimates the causes of the encountered phenomenon.

A dynamic organ such as the heart places special demands on modeling techniques. To understand its physiology and patho-physiology, not only the electrical activity and spatial distribution of its structures is important, but also their movement during cardiac cycles [10]. The shape of the measured ECG signal is influenced during repolarization by the mechanical contraction of the heart [9].

The main problem of inverse ECG processing consists in reconstruction of cardiac electrical events from measurements [14]. In contrast to the forward problem of electrocardiography, the inverse problem does not possess a mathematically unique solution [6] and in order to improve stability, it needs to adopt regularization techniques [4,15].

The problem of multiple solutions of the inverse models enforced the development of several approaches such as equivalent cardiac generators (such as equivalent dipole and multi-pole) [9], heart surface isochrones [1], or epicardial potential [2]. These methods led to a significant progress, but the different uncertainty elements of the processing method hinder the potentially beneficial ECG inverse solutions from becoming a routine clinical tool.

An almost complete ECG data acquisition from the human torso is accomplished by the body surface potential mapping (BSPM) technique [8]. BSPM may have a great advantage over the standard 12-lead system in different situations due to deeper accessible information. Mirvis has shown some cases of BSPM recordings that clearly demonstrate the inadequacies of the standard ECG lead sets in a variety of pathologies [8]. The better understanding of the depolarization-repolarization mechanism may enlighten the origin of diverse pathological events.

In the area of data processing, numerous interesting biomedical applications of artificial neural networks are included [7]. The best known neural solutions involve multilayer perceptrons [20], Kohonen self-organizing networks [17], fuzzy or neuro-fuzzy systems [16], genetic algorithms [19] and the combination of various solutions within a hybrid system [11].

Earlier heart modeling systems applied many neural networks and chose the best one, while the others were discarded. After a deep investigation of the obtained results, it was recognized that the most efficient approaches should rely on the combination of many classifiers utilizing either different classifier network structures or different data preprocessing methods [11].

The conventional artificial neural networks (ANNs) suffer from diverse drawbacks that can be handled by the support vector machines (SVMs) pioneered by Vapnik [21], which had to face to following problems:

- Modern biological problems are high-dimensional, and if the underlying mapping is not very smooth, the linear paradigm needs an exponentially increasing number of terms with an increasing dimensionality of the input space, that implies an increase in the number of independent variables. This is known as 'the curse of dimensionality';
- The real-life data generation laws may typically be far from the normal distribution and a model-builder must handle any kind of distribution in order to construct an efficient learning algorithm;
- The maximum likelihood estimator (consequently the sum-of-error-squares cost function, too) should be replaced by a new induction paradigm that is uniformly better. This indicator may accomplish the properly modeling of non-Gaussian distributions.

SVM classifiers have become quite popular due to their robustness and stability [12]. A SVM used in a heart modeling system is rigorously based on statistical learning theory and simultaneously minimizes the training and test errors. Apart from that, they produce a unique globally optimal solution and hence are extensively used in diverse applications including medical diagnosis [16].

This paper presents an event recognition study performed with ECG signal analysis and 3D heart model using unified neural networks (UNNs). These UNNs are based both on conventional ANNs and SVMs. The main purpose is to evaluate the strength and weakness of the method, and to analyze the cooperation efficiency in malfunction diagnosis.

2 Materials and Methods

2.1 Unified Neural Networks

In case of two-class classification using linear discriminant functions, the respective decision hypersurface in the n-dimensional feature space is a hyperplane that can be described as:

$$g(x) = w^T \cdot x + w_0 = 0, \tag{1}$$

where $w = [w_1, \ldots, w_n]^T$ is known as the weight vector and w_0 as the threshold value. A given vector x_d is situated on the decision hyperplane if only if $g(x_d) = 0$. The distance z between a vector x and the decision hyperplane is computed as: $z = |g(x)|/||w||$, where $||w|| = \sqrt{\sum_{i=1}^{n} w_i^2}$.

The purpose in a classification problem consists in the optimization of a vector w in such a way, that the criteria function $J(w)$ is minimized. Let ω_1 and ω_2 be the two classes that we need to separate. We assume this task can be performed using a linear relation, meaning that there exists at least one such hyperplane $\bar{w}$ that fulfils the following relations:

$$\bar{w}^T \cdot x > 0 \text{ for } \forall x \in \omega_1, \text{ and } \bar{w}^T \cdot x < 0 \text{ for } \forall x \in \omega_2. \tag{2}$$

If we design a classifier with a desired output $y = 1$ for $\forall x \in \omega_1$ and $y = -1$ for $\forall x \in \omega_2$, and try to modify weights in vector w in such a way that the

criteria function $J(w) = \sum_{i=1}^{N}(y_i - f_s(w^T \cdot x_i))^2$ is minimized, then we have constructed a root mean square (RMS) error based separation method. In the previous formula, f_s denotes a sigmoid function.

The SVM-s based classifier algorithms are very popular due their robustness. The main concept incorporates the search for the 'most robust solution' vector w that gives the maximum possible margin. The margin is represented by the minimal distance $z = |g(x)|/||w||$, which requires the minimization of $||w||$.

Although both these methods, the traditional RMSE approximation and SVM-based classification, deliver good results in a certain noise-free environment, in biomedical simulation such sterile conditions never occur, mainly because of measurement errors and the improper estimation of unmeasurable biological parameters.

Root mean square classifiers have the following drawbacks:

- Improper solution in case of asymmetric transfer functions;
- Large estimation error of the criteria function in case of border-close high dispersion (uncertain) inputs;
- In a noisy environment, the criteria function may possess multiple local minimal solutions that may cause low quality results;
- The white noise is 'non-learnable', so the function $J(w)$ will saturate at an uncontrollable error level.

The SVM produces a considerably superior result in hostile environment, and can avoid the above mentioned problems, but fails to take into consideration the topology of the input vectors, as presented in Fig. 1(a). This topology becomes more important is case of multi-dimensional spaces and non-linear separation borders, than in case of linear separation in a two dimensional space.

To overcome the above mentioned problems for both presented classification metods, we propose for classification a UNN. The main difference between UNN and the described classifiers consists in the equation of its criteria function:

$$J(w) = \lambda_d \cdot \sum_{i=1}^{N}(y_i - f_s(w^T \cdot x_i))^2 + \lambda_m \cdot f_m(z) + \lambda_u \cdot \sum_{i=1}^{N} f_u(w^T \cdot x_i), \quad (3)$$

that is composed by three additive terms responsible for the difference error, margin and smoothness, respectively. The function $f_u(\alpha) = \alpha^{-2}$ represents a repelling force that doesn't let the boundary be close to any of the vectors x_i. Coefficients $\lambda_d, \lambda_m, \lambda_u$ adjust the tradeoff among these three terms. The margin value is represented by z.

The presented UNN can work in non-linear environment, too. In this case the distance of a point from the separation hyperstructure is considered the closest distance from any point of it. The SVM formulation can work in the same manner, the structure tries to have a shape that keeps maximal distance from the clusters elements. The third term forces the separation structure to places that suffer from minimal repelling force.

The non-linear form of the criteria function takes into consideration the topology of the separation hyperstructure as presented in Figure 1(b). For example,
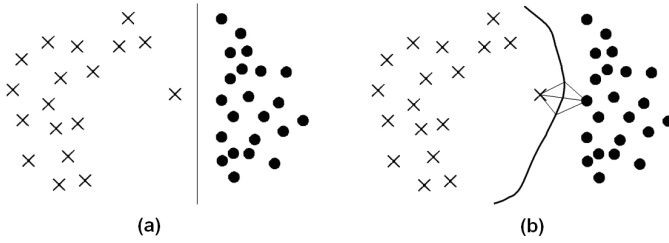
Fig. 1. A two-class separation problem is presented: (a) linear separation performed by SVM-based classifier cannot yield optimal solution in all cases; (b) distance of an object from the non-linear separation barrier should depend on the topology of the classes

the two closest $\times$ and $\bullet$ have the same distance from the non-linear separation barrier, but the $\times$ has better topology (the adjacent calculated distances are shorter for $\times$ than for the $\bullet$ point) so is considered closer than the $\bullet$ point.

2.2 Study Records

The BSPM signal resource contains 192-channels sampled at 1000 Hz with 12-bit resolution, obtained from the Research Institute for Technical Physics and Materials Science (MTA-MFA) of Budapest. These registrations, which were separated in two independent series, hold various malfunction cases, such as WPW syndrome, atrial and ventricular fibrillation, flutter. Our 12-lead ECG registrations were recorded at the County Medical Clinic Nr. 4 of Târgu Mureş. These signals were sampled at 500-1000 Hz with 12-bit resolution.

The coarse calibration of the implemented models, such as cell model, tissue model, torso model and spatial heart model was realized using the Series 1 BSPM measurements. The preliminary ECG analyzer system (PAS) uses both the Series 2 of the BSPM recods and our 12-lead registrations.

2.3 The Approach of ECG Inverse Problem

Most fundamental problems in theoretical ECG can be described by an inverse solution. Their goal is to describe bioelectric cardiac sources based on knowledge of the ECG and the volume conductor properties that surrounds the sources.

As mentioned earlier, the most cumbersome point of the inverse solutions consist in its stability. In order to decrease the sensibility of our solution, in our approach the heart model parameters are obtained indirectly. This approximation of the inverse problem is in contrast to methods that directly solve the matrix equation linking electrical sources with electrical potential fields to estimate the inverse ECG solution.

We constructed the PAS based on detailed, a priori knowledge of human anatomy and physiology. It was developed using an ANN, tested and validated by physicians in clinical environment (see Fig. 2).

The most important parameter that describes a whole cardiac cycle is related to the site of origin of cardiac activation. This information was obtained using the PAS module, where the output of the ANN provides the initial heart model parameters.

The ECG generator unit uses the cell, tissue and torso model to simulate a BSPM or 12-lead ECG. The objective functions that assess the similarity between the measured and simulated signals were also determined. As the structure of the used models was determined by the anticipative general model creation unit (AGMCU), only the proper parameter values has to be established. These heart model parameters were determined and adjusted with the aid of optimization algorithms or in certain cases by physicians. The simulation procedure is performed until the objective functions satisfy the a priori given convergence criteria. Finally the parameters are validated by physicians.

2.4   ANN-Based Preliminary ECG Analyzer System

The high number of heart model parameters implies a high dimensional searching problem. The a priori biological knowledge must be used to drastically reduce the number of necessary dimensions of the parameter space of heart model. The role of PAS unit consists in a rough determination of the cardiac status and state, that is used to initialize the model parameters and to simplify the searching problem for the optimization system.

In the present study, the PAS was developed using a three-layer UNN. This network is capable of mapping the non-linear input-output relationship, with the desired degree of accuracy. An adaptively weighted coefficient calculation method was used to train the ANN. The input layer incorporates 192 neurons, corresponding to the number of body surface electrodes used in the present simulation study. In case of 12-lead records, the unused channels' signals were estimated. From heuristical considerations, the number of hidden layer neurons was selected to 125. The output layer had 512 neurons, which corresponded to 32 ventricular myocardial segments of computer heart model. Sixteen cardiac cellular units were selected for each of the 32 myocardial segments in the ventricles, and each of these $16 \times 32 = 512$ sites was then paced in the forward simulation using the computer heart-torso model, generating the data set for training the ANN.

3   Results

A parameter classification algorithm was applied to distinguish normal QRS complexes from abnormal ones, in order to determine the specific differences between the normal and abnormal parameter values. For normal cases the detection ratio is practically 100%. The signals presented in Fig. 3 were obtained via simulation using the initial parameter set for a normal and abnormal (bypass tract) situation.

Figure 4 presents a series of cell activation simulations. In Fig. 4(a) and (b) the simulation of the cell depolarization mechanism is presented. The excitation rises
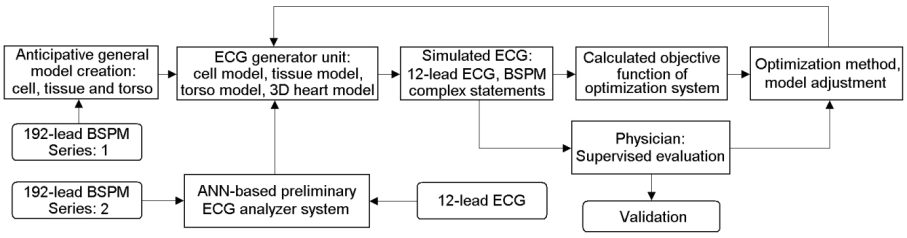
Fig. 2. The schematic diagram of the heart analyzer and modeling method
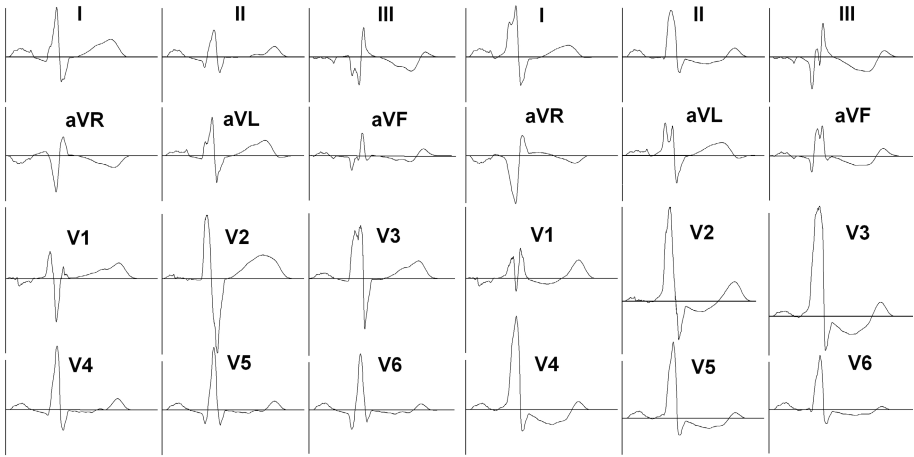
Fig. 3. The simulated ECG signal in normal and abnormal case (bypass tract)
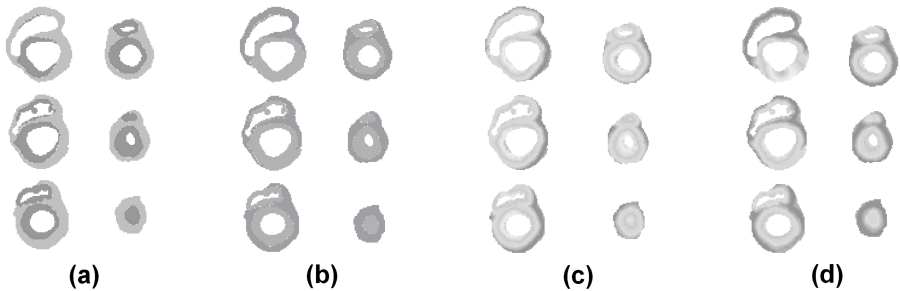
Fig. 4. The simulated depolarization in normal and abnormal case (bypass tract): (a) activated cells in normal case after 200ms (b) activated cells in case of WPW syndrome after 200ms (c) activation time of cells in normal case (d) activation time of cells in case of WPW syndrome

at the sino-atrial node. The state of the cells is illustrated with a 200ms delay from the excitation moment. Figures 4(c) and (d) show the activation moment of the cardiac cells. The neighbor slices have 10mm distance from each other, so a totally 5 centimeter wide ventricular tissue is visualized. The position of the slices is considered at a repolarized moment. Table 1 shows the efficiency of simulation for different cases. The evaluation of the simulated results was made by physicians. The performance was determined as the ratio of correct and total decisions.

Table 1. Simulation performance for normal and pathological cases

Pathological case	Correct decisions	Failed decisions	Performance
Normal	49	0	100.00 %
Ectopic beat	24	0	100.00 %
WPW syndrome	15	1	93.75 %
Atrial flutter	43	2	95.55 %
Atrial fibrillation	20	1	95.23 %
Ventricular fibrillation	21	1	95.45 %
Re-entry mechanisms	29	3	90.62 %
Triggered activity	41	2	95.34 %
Aberrant ventricular conduction	21	1	95.45 %
Total cases	263	11	95.98 %

4   Discussion and Conclusion

Table 1 reveals that the 3D heart simulation [17,18] succeeds in most cases, such as WPW (Wolf Parkinson White) syndrome, pre-excitations, and tissue activation modeling. The performance in case of re-entry mechanisms and triggered events is slightly decreased due to the hazard nature of the events. The application in practice of the model has several obstacles, which can be classified into the following groups:

- Effects of internal and external perturbations (such as environment, sympathetic and parasympathetic despondence);
- Lack of information on different elements of the model;
- Lack of technical background.

Several problems could be found, but the most important limitations are:

- The processes performed inside the cells are not well known, the behavior of the studied components cannot be determined with an acceptable precision;
- In critical cases, if a group of cells does not get the necessary food, it changes its behavior. A model created to simulate the normal behavior of the cell will not simulate it correctly in abnormal case;

- Because the structure of the heart differs from patient to patient, this structure is not known a priori, it has to be determined in real-time, based on the available information;
- The structure of the torso introduces the same problem. It is hard to determine the electrical conductivity and precise position of its elements.

In case of human system identification the most important disturbing phenomena are:

- It is known, that respiration makes the heart change its shape and position. Although the motion of the heart can be tracked, it is not possible to determine from the ECG the amplitude of the motion;
- The continuous motion and displacement involves very hard problems. Because the motion has an effect on the behavior of all internal elements, the behavior of the heart will also be modified. The model has to follow the changes of the cell properties. For example: a resting man suddenly jumps out of the bed. The controlling mechanisms start their adjustment, the values of model parameters will change;
- Fever and respiration frequency can also cause alterations.

External events (the patient senses something annoying or pleasant) change the dependence between the previously measured signals, and the determined parameters. This is one of the causes why the perfect simulation of a human body is impossible.

At present, the performance of personal computers does not make possible the real-time determination of parameter values. The practical application is possible only in case of strongly parallel systems. The simplified model can be applied in real-time, but its efficiency is reduced because of the neglected parameters. The waveform of the simulated ECG in normal cases can be considered acceptable. The shape and duration of basic waves have realistic values. In case of abnormal cases the obtained waveform is not acceptable and more simulations are needed.

References

1. Cuppen, J.J.M., van Oosterom, A.: Model studies with inversely calculated isochrones of ventricular depolarization. IEEE Trans. Biomed. Eng. 31, 652–659 (1984)
2. Guanglin, L., Bin, H.: Localization of the site of origin of cardiac activation by means of a Heart-Model-Based electrocardiographic imaging approach. IEEE Trans. Biomed. Eng. 48, 660–669 (2001)
3. Haider, A.W., Larson, M.G., Benjamin, E.J., Levy, D.: Increased left ventricular mass and hypertrophy are associated with increased risk for sudden death. J. Am. Coll. Cardiol. 32, 1454–1459 (1998)
4. Johnson, C.R., MacLeod, R.S.: Adaptive local regularization methds for the inverse ECG problem. Progr. Biophys. Mol. Biol. 69, 405–423 (1998)

5. Lagerholm, M., Peterson, C., Braccini, G., Edenbrandt, L., Sörnmo, L.: Clustering ECG complexes using Hermite functions and self-organizing maps. IEEE Trans. Biomed. Eng. 47, 838–848 (2000)
6. MacLeod, R.S., Brooks, D.H.: Recent progress in inverse problems in electrocardiology. IEEE EMBS Mag. 17(1), 73–83 (1998)
7. Minami, K., Nakajima, H., Yoyoshima, T.: Real time discrimination of the ventricular tachyarrhythmia with Fourier-transform neural network. IEEE Trans. Biomed. Eng. 46, 179–185 (1999)
8. Mirvis, D.M.: Validation of body surface electrocardiographic mapping. In: Mirvis, D.M. (ed.) Body surface electrocardiographic mapping, pp. 63–74. Kluwer, Boston-Dordrecht-London (1988)
9. Moreau-Villéger, V., Delingette, H., Sermesant, M., Ashikaga, H., McVeigh, E., Ayache, N.: Building maps of local apparent conductivity of the epicardium with a 2-D electrophysiological model of the heart. IEEE Trans. Biomed. Eng. 53, 1457–1466 (2006)
10. Noble, D.: Modeling the heart. Phys. 19, 191–197 (2004)
11. Osowski, S., Hoai, L.T.: ECG beat recognition using fuzzy hybrid neural network. IEEE Trans. Biomed. Eng. 48, 1265–1271 (2001)
12. Osowski, S., Hoai, L.T., Markiewicz, T.: Support vector machine-based expert system for reliable heartbeat recognition. IEEE Trans. Biomed. Eng. 51, 582–589 (2004)
13. Sermesant, M., Delingette, H., Ayache, N.: An electromechanical model of the heart for image analysis and simulation. IEEE Trans. Med. Imag. 25, 612–625 (2006)
14. Sermesant, M., Moireau, P., Camara, O., Sainte-Marie, J., Andriantsimiavona, R., Cimrman, R., Hill, D.L.G., Chapelle, D., Razavi, R.: Cardiac function estimation from MRI using a heart model and data assimilation: advances and difficulties. Med. Imag. Anal. 10, 642–656 (2006)
15. Shahidi, A.V., Savard, P., Nadeau, R.: Forward and inverse problems of electrocardiography: modeling and recovery of epicardial potentials in humans. IEEE Trans. Biomed. Eng. 41, 249–256 (1994)
16. Smola, A., Scholkopf, B.: A tutorial on support vector regression. Royal Holloway College, Univ. London, NeuroColt Tech. Rep. NV2-TR-1998-030
17. Szilágyi, S.M., Benyó, Z., Dávid, L.: Heart model based ECG signal processing. In: Proc. 5th IFAC Symp. Modell. Contr. Biomed. Syst. pp. 213–217 (2003)
18. Szilágyi, S.M., Benyó, Z., Dávid, L.: WPW syndrome identification and classification using ECG analysis. Proc. World Congr. Med. Phys. Biomed. Eng. 4423.pdf (2003)
19. Szilágyi, S.M.: Event recognition, separation and classification from ECG recordings. In: Proc. 20th Ann. Int. Conf. IEEE EMBS, pp. 236–239 (1998)
20. Thaker, N.V., Ferrero, J.M.: Electrophysiologic models of heart cells and cell networks. IEEE EMBS Mag. 17(5), 73–83 (1998)
21. Vapnik, V.: Statistical learning theory. Wiley, New York (1998)

Fuzzy Spatial Growing for Glioblastoma Multiforme Segmentation on Brain Magnetic Resonance Imaging⋆

Alejandro Veloz[1], Steren Chabert[1], Rodrigo Salas[1], Antonio Orellana[2], and Juan Vielma[3]

[1] Departamento de Ingeniería Biomédica, Universidad de Valparaíso, Chile
alejandro.veloz@yahoo.es, steren.chabert@uv.cl, rodrigo.salas@uv.cl
[2] Servicio de Neurocirugía, Hospital Carlos Van Buren, Valparaíso, Chile
[3] Servicio de Imagenología Compleja, Hospital Carlos Van Buren, Valparaíso, Chile

Abstract. Image segmentation is a fundamental technique in medical applications. For example, the extraction of biometrical parameter of tumors is of paramount importance both for clinical practice and for clinical studies that evaluate new brain tumor therapies.

Tumor segmentation from brain Magnetic Resonance Images (MRI) is a difficult task due to strong signal heterogeneities and weak contrast at the boundary delimitation. In this work we propose a new framework to segment the Glioblastoma Multiforme (GBM) from brain MRI. The proposed algorithm was constructed based on two well known techniques: Region Growing and Fuzzy C-Means. Furthermore, it considers the intricate nature of the GBM in MRI and incorporates a fuzzy formulation of Region Growing with an automatic initialization of the seed points.

We report the performance results of our segmentation framework on brain MRI obtained from patients of the chilean Carlos Van Buren Hospital and we compare the results with Region Growing and the classic Fuzzy C-Means approaches.

Keywords: Fuzzy Spatial Growing (FSG), Magnetic Resonance Imaging (MRI), Glioblastoma Multiforme, Fuzzy C-Means, Region Growing, Anisotropic Diffusion Filter, Image Segmentation.

1 Introduction

The high definition, contrast and resolution of soft tissues obtained with Magnetic Resonance Imaging (MRI), makes this image modality very useful in the characterization of many pathological diseases located at the Central Nervous System (CNS) (see [8], [9] and [10]). Image processing techniques, such as segmentation, have motivated the development of many quantitative analysis methods to improve diagnostic and therapeutical outcomes (see [1], [9] and [15]).

In the present work, our interest is advocated to Glioblastoma Multiforme (GBM) segmentation from MRI. This class of glial tumor (also called glioma grade IV) has the highest mortality and morbidity ratio between all known brain tumors, due primarily to its very aggressive pathological behavior. This aggressive behavior causes uncertainty in the pathological border definition and constitutes the main inconvenient to obtain a precise anatomical diagnosis (see [4] and [10]).

In the context of medical images many different segmentation methods exist, but there is no universally applicable segmentation technique for all kind of image characteristics even for the same acquisition modality (see [6]). To develop or to apply a segmentation method, the specific pathology characteristics must be considered before analyzing the image (see [11] and [13]).

An improved framework to segment the Glioblastoma Multiforme is proposed. This method considers the fuzzy nature of the pathological appreciation made by radiologist. This new algorithm incorporates the fuzziness definition of the GBM boundaries in MRI. The formulation of our method is based on the classical Region Growing and Fuzzy C-Means algorithms to perform tumor segmentation, and considers the pathological nature of the GBM. We call our algorithm *Fuzzy Spatial Growing (FSG)* for GBM segmentation.

We report the performance results of our segmentation framework on brain MRI obtained from patients of the chilean Carlos Van Buren Hospital and a comparative study with the classical Region Growing and Fuzzy C-Means algorithms is made.

This work is organized as follows. In section 2 the proposed segmentation framework is stated. Section 3 shows the results obtained by applying the segmentation framework to the dataset. Discussion of the results are given in section 4. Finally concluding remarks are given in the last section.

2   Methodology

In this section we propose a framework for the GBM segmentation on MRI. We begin the explanation with the description of the available images and then the segmentation algorithms.

2.1   Magnetic Resonance Images Dataset

The images available for this study were obtained from two patients of the Carlos Van Buren chilean Hospital. The patients were histopathologically confirmed to be affected with Glioblastoma Multiforme. The images were acquired in a 1.5T General Electric (GEMS, Milwaukee, USA) MRI System[1]. Each slice consists of the following featured images: in the axial plane, T1-weighted (*Fluid Attenuated Inversion Recovery* (FLAIR) sequence, with TE/TR/TI of 24/1875/750 ms),

---

[1] This study has the corresponding agreement and authorization of the Carlos Van Buren Hospital.

T1-weighted + C (with *gadolinium* contrast enhancement, *Spin Echo* (SE) sequence, with TE/TR of 100/4375 ms and 80° flip angle) and T2-weighted (*Fast Spin Echo* (FSE) sequence, with TE/TR of 100/4375 ms). In the coronal plane, T1-weighted + C and T2-weighted with the same acquisition parameters as described above. Lastly, in the sagittal plane, T1-weighted + C and T1-weighted were acquired. From the two patients we obtained 77 images from a total of 32 anatomical slices, with spatial resolution of 4 mm^3 and a slice gap of 1.5 mm.

2.2 Anisotropic Diffusion Filter

A fundamental step in medical image processing is the application of filters to minimize effect of noise. Classical techniques for noise reduction, such as gaussian filter or isotropic linear diffusion filter, shift the edges localization and blur the images. This situation is undesirable due to the mismatching between the original and resulting localization of the boundaries between regions (i.e. Glioblastoma Multiforme).

In this work, the anisotropic diffusion filter (see [2] and [7]) was employed to minimize noise contamination as well as to avoid boundary localization problems (i.e. blurring) by reduction of the diffusivity in the edges that have high gradient magnitudes. Their nonlinear process behaves as a feedback system that preserves the edges in the different regions by adapting a diffusivity function to the image gradient. The filter is given by:

$$\frac{\partial f}{\partial t} = div(g(f,t) \cdot |\nabla f|) \tag{1}$$

where $|\nabla f|$ is the gradient magnitude of the image f, and $g(f,t)$ is the diffusivity function given by

$$g(f,t) = \exp\left(-\frac{|\nabla f|^2}{\kappa^2}\right) \tag{2}$$

where κ is the diffusivity parameter and determines the gradients magnitudes where the diffusion will begin to decrease, and therefore the edges that will be preserved. The performance of anisotropic diffusion filter is strongly dependent on the diffusivity function $g(f,t)$ and on the time interval t (or the number of iterations in the discrete domain). This function modulates the gradient magnitude in each iteration to decrease diffusion along the image prominent edges.

2.3 Region Growing

The Region Growing algorithm is a classical region-based approach for medical image segmentation (see [3] and [16]). The basic approach is to start with a set n of seed points $v_i, i = 1..n$, of voxels interactively selected. From these seed points regions grow by adding to each seed those neighboring voxels that have similar properties based on predefined criteria. In this successive growing process n regions $R_i, i = 1..n$, will be formed.

The similarity criteria to consider a voxel as member of the region R_i is established according to the image properties, for example texture, topology,

etc. In our implementation, let x be a neighbor voxel to some voxel belonging to the region R_i. If the euclidean distance between the voxel x and the seed point v_i is less than a threshold θ then the voxel x is included to the region R_i. Finally, the region of interest is obtained by merging each grown region $\bigcup_{i=1..n} R_i$.

Unfortunately, the performance of this algorithm will strongly depend on the correct selection of seed points and this selection depends directly on the histopathological behavior of the Glioblastoma Multiforme in MRI. The capability of the user (radiologist) to identify the several tumor domains will be of paramount importance for the appropriate growing process. Such domains will be, for example, necrosis, i.e., high cellularity activity, and other biological features proper to this tumor class.

2.4   Fuzzy C-Means

Other common approach to segment MR images is Fuzzy C-Means (FCM). This technique is an unsupervised clustering algorithm that has been extensively used in Pattern Recognition (see [14]). The fuzzy set obtained from classification of the intensity distribution is especially interesting in MRI of Glioblastoma Multiforme, due to the fuzzy definition between the tumor boundary and its surrounding brain tissue.

This unsupervised method is an iterative procedure of fuzzy partition of the p-dimensional feature space in C clusters. The algorithm starts from C randomly selected vectors $\{v_1, ..., v_C\}$ called centroids or clusters centers. The membership of each data $x_j, j = 1..N$, to the class $i, i = 1..C$, is computed with the membership function given by

$$\mu(v_i, x_j) = \mu_{ij} = \frac{1}{\sum_{k=1}^{C} \left(\frac{d(x_j, v_i)}{d(x_j, v_k)} \right)^{\frac{2}{m-1}}} \tag{3}$$

where m is the fuzziness exponent and $d(x_j, v_i)$ is the euclidean distance measure between the x_j feature vector and the v_i centroid. The membership function (3) satisfies the properties that $0 \leq \mu_{ij} \leq 1$ and $\sum_{i=1}^{C} \mu_{ij} = 1$. The centroids of each cluster are computed in each iteration as:

$$v_i = \frac{\sum_{j=1}^{N} \mu_{ij}^m x_j}{\sum_{j=1}^{N} \mu_{ij}^m} \quad i = 1..C \tag{4}$$

The cost function, that should be minimized, is given by

$$J_m = \sum_{j=1}^{N} \sum_{i=1}^{C} \mu_{ij}^m d^2(x_j, v_i) \tag{5}$$

The centroids and the membership degrees of all features vectors are updated until there is no meaningful change in the cost function, or equivalently, in the centroid location in the feature space.

In our application, we selected four clusters: fat/tumor, white matter, gray matter and cerebral spinal fluid (CSF)/background. Additionally, to improve the tumor classification with this method, a preprocessing (simply thresholding) step is applied in order to eliminate fat in the images.

After applying FCM a defuzzification stage is performed in order to convert the fuzzy membership of the feature vectors into a crisp set. This stage consists in the specification of a certain threshold for decoding the membership degrees into a crisp set to obtain the tumor voxels.

2.5 Fuzzy Spatial Growing for Glioblastoma Multiforme Segmentation

A new segmentation framework is introduced in this section to avoid the drawbacks of the above mentioned algorithms for Glioblastoma Multiforme segmentation. Our method is based on the classical Fuzzy C-Means and Seeded Region Growing approaches described above. We call our proposed framework *Fuzzy Spatial Growing (FSG)* for Glioblastoma Multiforme segmentation.

The FSG method incorporates an automatic procedure to obtain seed points. The method starts by applying first the anisotropic diffusion filter and then the Fuzzy C-Means (FCM) algorithm. The clusters are defuzzified and the tumor cluster is obtained. The tumor intensity features is obtained according to the skeleton of the tumor region obtained with FCM.

The skeleton is a mathematical morphology technique described in [5]. The skeleton determines the closest boundary points for each point in an object and allows to extract a region-based features representing the tumor of interest. With this approach, we obtain a vector composed by the histopathological intensity patterns across the tumor region represented by all tumor intensities in the skeleton (i.e., low to high contrast enhancement). The automatic seed points initialization is done on points located at the skeleton of the tumor (see figure 1).

The membership function of the tumor voxels is constructed from the information of the skeleton intensity pattern and the filtered image is considered as a fuzzy set F. The membership values $\mu_F(x)$ are computed for each voxel x of the image and depends on the information of the global gray-level image histogram. The membership function is a trapezoidal linguistic variable constructed as

$$\mu_F(x) = \begin{cases} 0 & 0 \leq x < \alpha \\ \frac{x-\alpha}{\beta-\alpha} & \alpha \leq x \leq \beta \\ 1 & \beta < x \leq \gamma \\ \frac{x-1}{\gamma-1} & \gamma < x \leq 1 \end{cases} \quad (6)$$

where the parameters α, β and γ are computed from the histogram. α is the mode of the histogram and correspond to the most frequent intensities values of the intracraneal cavity. The parameters β and γ are the minimum and maximum of the tumor skeleton intensities respectively, and the parameters correspond to the range of intensities where the membership to the tumor is 1, because we know for certain that the tumor has this intensities. The intrinsic heterogeneity signal of

the GBM in MRI and the variable degree of GBM neighboring tissue infiltration determines that some intensities of poor contrast enhancement are between the histogram mode and β, that are formed mostly by the gray and white matter. Figure 1 shows how the gold standard has similar intensities than the gray and white matter. For this reason we define α as the mode of the histogram. On the other hand, some high cellularity tumor domains, blood vessels or fat have similar high intensities bigger than γ, then the voxels are considered to have some membership degree (less than one) at high intensity levels. The left side of figure 1 shows the membership function.

After the image fuzzy set F is obtained, the spatial growing process begins from a seed extracted from the skeleton. All the skeleton voxels are included to the fuzzy tumor region R. The algorithm picks a voxel x from R and will add to the fuzzy tumor region R all the neighboring voxels $v \in N_8(x)$ that satisfy the following similarity criteria:

$$T\{\mu_F(x), S^*\{v_1, v_2, ..., v_8\}\} \geq \lambda \tag{7}$$

where

$$S^*\{v_1, v_2, ..., v_8\} = S\{S\{S\{\mu_F(v_1), \mu_F(v_2)\}, S\{\mu_F(v_3), \mu_F(v_4)\}\},$$
$$S\{S\{\mu_F(v_5), \mu_F(v_6)\}, S\{\mu_F(v_7), \mu_F(v_8)\}\}\}$$

λ is an inclusion threshold, and, T and S are the T-norm and T-conorm respectively, examples of this triangular norms are the Zadeh and Lukasiewicz approaches (see [12]).
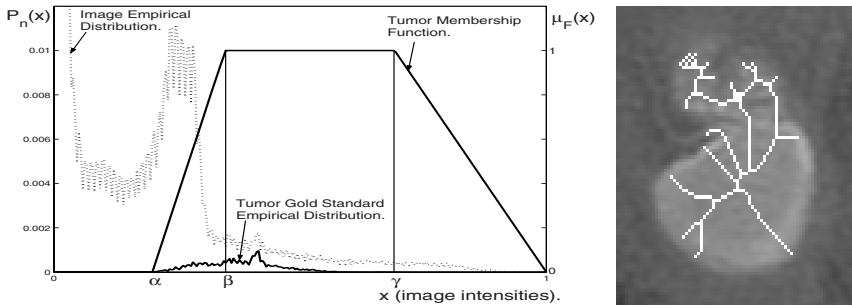
Fig. 1. (left) Histogram of the GBM MR image intensities, shows the empirical distribution of the intensities of the overall image and the tumor gold standard, furthermore it shows the tumor membership function used in the *FSG* algorithm. **(right)** Skeleton used to estimate the parameters of the tumor membership function.

2.6   Evaluation Criteria

To evaluate the quality of segmentation of the algorithms, GBM were manually segmented on MRI with the assistance of a neuroradiologist of the Carlos Van

Buren Hospital. This manually segmented image will be our *gold standard*, or also called ground truth (see [9]).

The quality was evaluated with the accuracy index. The accuracy index is expressed as the percentage of tumor area present in both the segmented image and in the *gold standard*.

The false positive error (FP) is expressed as the percentage of tumor area segmented that does not belong to the *gold standard*, i.e., region that was erroneously segmented as tumor region with the algorithm. The false negative error (FN) is the percentage area of the tumor region of the *gold standard* that were not segmented with the algorithm.

3   Results

In this section, we compare the quality of segmentation of the Fuzzy Spatial Growing algorithm with the classical region growing and Fuzzy C-Means approaches. The Region Growing, FCM monospectral (1-dimensional) and FSG algorithms were applied to T1-weighted + C images. The FCM multispectral (2 and 3-dimensional) was applied to T1-weighted, T1-weighted + C and T2-weighted images in the axial plane, T1-weighted, T1-weighted + C in coronal plane, and in T2-weighted and T1-weighted + C in sagittal plane. Additionally, for the FCM multispectral algorithm we present the results obtained with a preprocessing stage to eliminate the fat available in all the images.

The anisotropic diffusion filter was used with parameter $\kappa = 10$ and with 10 iterations. In fuzzy clustering techniques a value of $m = 2$ was employed for fuzziness exponent and four clusters were considered (gray matter, white matter, CSF-background and fat-tumor). Furthermore, all thresholds were applied interactively.

During the experiments, the FSG algorithm outperforms the Region Growing and FCM algorithms when the pathological condition of the tumor have an insufficient contrast enhancement and high fuzziness in the boundary between the tumor and the white matter. This phenomenon is due to the low cellular metabolism or high infiltration to the neighboring tissue. Figure 2 shows two cases, a typical segmented image and the worst GBM segmentation case.

The accuracy, false positive error and false negative error results of the three algorithms are shown in table 1. Note that our FSG algorithm outperforms in the three criteria to the other algorithms. This results will be discussed in the next section.

Table 1. Outcomes obtained with each segmentation method

Technique.	Accuracy (std. desv.).	FP (std. desv.).	FN (std. desv.).
Fuzzy Spatial Growing	96.38 % (7.16)	9.18 % (9.84)	3.63 % (7.16)
Region Growing	95.54 % (7.35)	7.65 % (9.55)	4.87 % (7.64)
FCM monospectral	93.75 % (12.63)	5.51 % (7.19)	6.24 % (12.62)
FCM multispectral	93.93 % (12.36)	5.78 % (7.79)	6.08 % (12.35)
FCM multispectral (fat eliminated)	94.79 % (9.25)	5.63 % (7.16)	5.21 % (9.25)
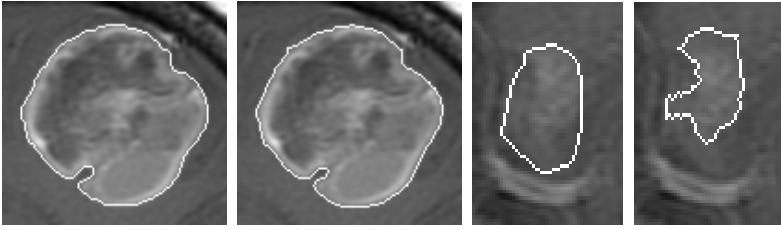
Fig. 2. Segmented T1-weighted + C Magnetic Resonance images of GBM with Fuzzy Spatial Growing algorithm: (left) Gold Standard of a segmented GBM. **(middle-left)** GBM segmented with FSG. **(middle-right)** Gold Standard of a segmented GBM, worst case. **(right)** Worst segmented case of the GBM with the FSG.

4   Discussion

We have described a flexible method for Glioblastoma Multiforme Segmentation in MRI that allows us to deal with the difficult properties of this tumor class. The difficulty is due to the aggressive infiltration of cancerous cells into neighboring tissue. This situation is the main disadvantage of the segmentation of this tumor and is the focus of our formulation.

The possible guidance of the user expert knowledge gives Fuzzy Spatial Growing approach an additional suitability and flexibility in the segmentation process and allows a continuous refinement of the outcomes.

The tumor segmentation result will depend on both the histopathological properties of the Glioblastoma Multiforme and the characteristics revealed in the MR image. After processing of all the images by Fuzzy Spatial Growing, Region Growing and FCM, these results were compared with the *gold standard*. We found both false positives and false negatives errors in the comparison between the segmented image and the gold standard. The false negative errors corresponds to areas with weak or intermediate contrast enhancement in the tumor boundary. In this sense, Fuzzy Spatial Growing was better to include these areas, but yet it could be further optimized.

In those GBM boundary areas between the tumor and neighboring tissue where the tumor presents high cellular activity pattern, the performance of the FCM (monospectral and multispectral), and Region Growing algorihtms were higher than 95%. Instead, in situations where the tumor has low contrast enhancement areas the performance of these algorithms was poor in terms of accuracy, with respect to the tumor areas that have more angiogenesis ratio (formation of blood vessels, resulting in high intensities and better definition of the tumor). For this reason, the possibility to obtain a good performance of the segmentation algorithms resides in the detection of these tumor areas that exhibit low contrast enhancement.

Fuzzy Spatial Growing has the advantage that it does not require seed points initialization, i.e., the parameters selection by the users are minimized, although

the FSG requires at least one seed point, automatically selected. On the other hand, the drawback of the Region Growing approach in this work is that the seed points should be selected manually by the users, and the performance of the algorithm will depend on the expert knowledge to identify the several tumor areas like necrosis, low and high contrast enhancement domains.

The FCM approach is intrinsically an automated method and we used it as automatic initialization of the seed points for the FSG. Furthermore, the intensity patterns obtained for both fuzzification stage and automatic seed points initialization take into account more information content along the tumor that the classical method of manually select seed points.

The assumptions that we made about the parameter values to obtain the fuzzy set of the tumor and to initialize a single seed point work well in all of our images. Furthermore, in the different stages of our method, the user can modify parameter values in order to consider certain biological situations of the GBM, that allows to refine and to grant flexibility of the segmentation process.

The only necessary user interaction consists in selecting a region of interest to specify the tumor location and the threshold λ that controls the spatial growing of the obtained tumor border.

5   Conclusion

In this work, we introduced and applied a suitable algorithm to segment Glioblastoma Multiforme on Magnetic Resonance Images. Furthermore, our reliable method combines the expert knowledge and fuzzy properties of Glioblastoma Multiforme to segment the brain tumor slices separately.

Our developed algorithm is based on classical approaches for image segmentation, such as Fuzzy C-Means and Mathematical Morphology to extract pattern of intensities of the Glioblastoma Multiforme and to select seed points automatically to perform the Fuzzy Spatial Growing. Additionally, a Fuzzy similarity criteria is considered to measure the voxels memberships to the tumor.

Further work is needed to incorporate the bias field estimation to correct or compensate the intensity inhomogeneities introduced during the acquisition process in MRI. The FSG algorithm can be applied to other types of brain tumors, such as low grade gliomas. Last but not least, other types of membership functions to obtain the fuzzy sets can be explored in the algorithm.

In conclusion, Fuzzy Spatial Growing approach constitutes an applicable method to the daily clinical practice for Computer Assisted Techniques that have an enormous potential to increase the safety in surgical intervention of Glioblastoma Multiforme, improving the surgical outcome and the prognosis of the patients.

Acknowledgements

References

1. Gering, D., Nabavi, A., Kikinis, R., Hata, N., O'Donnell, L., Grimson, W., Jolesz, F., Black, P., Wells, W.: An integrated visualization system for surgical planning and guidance using image fusion and an open MR. Journal of Magnetic Resonance Imaging 13, 967–975 (2001)
2. Bloch, I., Gousseau, Y., Matre, H., Matignon, D., Pesquet-Popescu, B., Schmitt, F., Sigelle, M., Tupin, F.: Le traitement des images, Polycopié du cours ANIM, Département TSI - Télécom-París (2004)
3. Feng, D.: Segmentation of soft tissues in medical images, Ph.D. thesis, National University of Singapore (2005)
4. Gaensler, E.H.: Neurorradiología fundamental, Marban (1998)
5. González, R., Woods, R.: Digital image processing, 2nd edn. Prentice Hall, Englewood Cliffs (2001)
6. Bonnie, N.J., Melanie, B.F., Carolyn, C.M., Qing-shou, H., Roger, S.D., Phil, J.G., Michael, E.B.: Brain tumor volume measurement: Comparison of manual and semi-automated methods. Radiology 212, 811–816 (1999)
7. Jahne, B., Haubecker, H.: Computer vision and applications. Academic Press, London (2000)
8. Kalousek, M., Birbamer, G., Kampfl, A., Aichner, F., Felber, S.: Principal advantages of CNS diagnostics by magnetic resonance imaging. Neurolog/'ia cro/'atica 40(2), 73–84 (1991)
9. Kaus, M.: Contributions to the automated segmentation of brain tumors in magnetic resonance images, Ph.D. thesis, Der Technischen Fakultat der Universitat Erlangen-Nurnberg (1999)
10. Kaye, A.H., Laws, E.R.: Brain tumors, Churchill Livingstone Edition (1995)
11. Moon, N., Bullitt, E., Van Leemput, K., Gerig, G.: Model-based brain and tumor segmentation. In: IEEE International Conference on Pattern Recognition, pp. 528–531. IEEE Press, Los Alamitos (2002)
12. Moraga, C., Salas, R.: A new aspect for the optimization of fuzzy if-then rules. In: Proceedings. 35th International Symposium on Multiple-Valued Logic, pp. 160–165. IEEE Press, Los Alamitos (2005)
13. Oppelt, A.: Imaging systems for medical diagnostics. Wiley, Chichester (2006)
14. Shen, S., Sandham, W., Granat, M., Sterr, A.: MRI fuzzy segmentation of brain tissue using neighborhood attraction with neural-network optimization. IEEE Transaction on Information Technology in Biomedicine 9(3), 459–467 (2005)
15. Veloz, A.: Esquema de trabajo para segmentar glioblastomas multiformes en MRI mediante técnicas de crecimiento de regiones y fuzzy c-means, Tesis de Grado de Ingeniería Biomédica, Universidad de Valparaíso (2007)
16. Xuan, J., Adah, T., Wang, Y.: Segmentation of magnetic resonance brain image: Integrating region growing and edge detection. In: IEEE Conference on Image Processing, pp. 544–547. IEEE Press, Los Alamitos (1995)

Conformal Geometric Algebra for Endoscope-Traking System Calibration in Neurosurgery

Silena Herold-García[1], Jorge Rivera-Rovelo[2], and Eduardo Bayro-Corrochano[2]

[1] Universidad de Oriente, Santiago de Cuba
`silena@csd.uo.edu.cu`
[2] CINVESTAV del IPN, Unidad Guadalajara,
Department of Electric Engineering and Computer Sciences,
Av. Científica 1145, El Bajío, Zapopan, Jalisco, México
`{rivera,edb}@gdl.cinvestav.mx`

Abstract. One necessary task in the operating room is to establish a common reference frame, in order to relate the information obtained from different sensors, and to combine both the preoperative with the intraoperative information. To estimate the transformations between different data, fiducial markers are typically used. In this paper we present a formulation of the known hand-eye calibration problem, to estimate the transformation between an endoscopic camera and the set of spherical markers placed on it, using the conformal geometric algebra framework. Such markers are tracked by an optical stereo tracking system, which help to relate the real world with the virtual model created before surgery. Experimental results shows that our method is reliable and useful for medical applications in real time like neurosurgery.

Keywords: Hand-Eye Calibration, Geometric Algebra, Neurosurgery, Endoscope Calibration.

1 Introduction

In general, the *registration* process consists in the estimation of a common geometric reference frame between two or more data sets. These data sets can be data taken using different modalities, or the same modality but in different times. In surgery, the registration is made with the purpose of having more preoperative and intraoperative information for diagnostic and navigation. That is, registration helps to relate the positions of surgical instruments tracked in real time by an optical tracking system, with the virtual model created with preoperative images. In the operating room, there are multiple local coordinates systems that must be related in order to show to the surgeon a virtual model of what is happening in the real world. The figure 1 illustrates the scenario. When using information obtained from endoscopy or neuro-sonography, we must relate what is been observed by the endoscopic camera (or ultrasound system), with
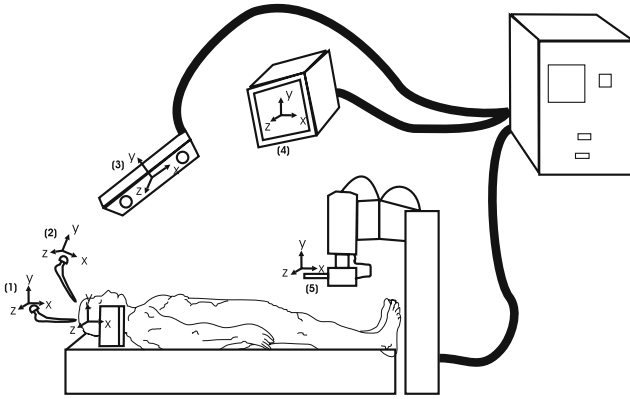
Fig. 1. Some of the different coordinates systems present in the operating room: surgical instruments (1,2), optical tracking system (3), virtual model(4), endoscopy (5)

the virtual model. Therefore, calibration techniques are needed to register all the equipment needed in surgery.

In this paper we are proposing a formulation of the hand-eye calibration problem, which is known in robotics community [3,4,5,6], but in terms of the Conformal Geometric Algebra in order to calculate the transformation (rotation and translation) between the coordinate system of the endoscopic camera, and the coordinate system of the spherical markers placed to the endoscope. We call this task the *endoscope-tracking* calibration. The proposed method in this paper in contrast to [3], computes both rotation and translation, at the same time; in addition to, our formulation avoids to take care of certain particularities which we need to take into account in other methods [4,5,6], making simpler to understand and to compute them.

2 Geometric Algebra

The Geometric Algebra $G_{p,q,r}$ is constructed over the vector space $\mathcal{V}^{p,q,r}$, where p, q, r denote the signature of the algebra; if $p \neq 0$ and $q = r = 0$, the metric is Euclidean; if only $r = 0$, the metric is pseudo euclidean; if $p \neq 0, q \neq 0, r \neq 0$, the metric is degenerate. In this algebra, we have the *geometric product* which is defined as in (1) for two vectors a, b, and have two parts: the inner product $a \cdot b$ is the symmetric part, while the wedge product $a \wedge b$ is the antisymmetric part.

$$ab = a \cdot b + a \wedge b. \tag{1}$$

The dimension of $G_{n=p,q,r}$ is 2^n, and G_n is constructed by the application of the geometric product over the vector basis e_i. This results in a basis for G_n containing elements of different grade called *blades* (e.g. scalars, vectors, bivectors, trivectors, etc): $1, e_1...e_{12}...e_{123}...I$, which is called *basis blade*; where the element of maximum grade is the pseudoscalar $I = e_1 \wedge e_2... \wedge e_n$. Given a multivector M

(linear combination of blades), if we are interested in extracting only the blades of a given grade, we write $\langle M \rangle_r$ where r is the grade of the blades we want to extract (obtaining an homogeneous multivector M' or a r-vector).

2.1   Conformal Geometric Algebra

To work in Conformal Geometric Algebra (CGA) $G_{4,1,0}$ means to embed the Euclidean space in a higher dimensional space with two extra basis vectors which have particular meaning; in this way, we represent particular objects of the Euclidean space with subspaces of the conformal space. The vectors we add are e_+ and e_-, which square to $1, -1$, respectively. With these two vectors, we define the null vectors

$$e_0 = \frac{1}{2}(e_- - e_+); \quad e_\infty = (e_- + e_+), \tag{2}$$

interpreted as the origin and the point at infinity, respectively. From now and in the rest of the paper, points in the 3D-Euclidean space are represented in lowercase letters, while conformal points in uppercase letters. To map a point $x \in \mathcal{V}^3$ to the conformal space in $G_{4,1}$, we use

$$X = x + \frac{1}{2}x^2 e_\infty + e_0. \tag{3}$$

The table 1 shows the representation some the entities in CGA. All these entities and their transformations can be managed easily using the rigid motion operators described later.

Table 1. Standard representation of different entities in conformal geometric algebra

Entity	Standard representation	Entity	Standard representation
Sphere	$S = c + \frac{1}{2}(c^2 - \rho^2)e_\infty + e_0$	Point pair	$PP = S_1 \wedge S_2 \wedge S_3$
Point	$X = x + \frac{1}{2}x^2 e_\infty + e_0$	Circle	$Z = S_1 \wedge S_2$
Line	$L = rI_E + e_\infty m I_E$	Plane	$P = nI_E - de_\infty$
	$r = a - b$		$n = (a - b) \wedge (a - c)$
	$m = a \wedge b$		$d = (a \wedge b \wedge c)I_E$

In CGA, rotations are represented by the *rotors*, which are defined as

$$R = e^{\frac{1}{2}\mathbf{b}\theta} = \cos\frac{\theta}{2} + \mathbf{b}\sin\frac{\theta}{2} \tag{4}$$

where $\mathbf{b}$ is the bivector dual to the rotation axis, and θ is the rotation angle. Rotation of an entity is carried out by multiplying it by the left with the rotor R, and by the right for the reversion of the rotor $\tilde{R}$: $X' = RX\tilde{R}$. Translation is carried out by the so called *translator*

$$T = e^{\frac{e_\infty t}{2}} = 1 + \frac{e_\infty t}{2} \tag{5}$$

where $t \in \langle G_3 \rangle_1$ is the translation vector. Note that this operator can be inter-preted as a special rotor, expressed in a null space because $e_{infty}^2 = 0$. Transla-tions are applied in a similar way to rotations: $X' = TX\tilde{T}$.

To express rigid body transformations, rotors and translators are applied con-secutively. The result is called *motor*:

$$M = TR \tag{6}$$

Such operator is applied to any entity of any dimension by multiplying the entity by the operator from the left, and by the reverse of the operator from the right: $X' = MX\hat{M}$. The motor M is a special multivector of even grade. To see its components, let us carry out the multiplication of R and T

$$
\begin{aligned}
M &= TR \\
&= (1 + \frac{1}{2}e_\infty t)(\cos(\frac{\theta}{2}) + \mathbf{b}\sin(\frac{\theta}{2})) \\
&= \cos(\frac{\theta}{2}) + \mathbf{b}\sin(\frac{\theta}{2}) + \frac{1}{2}e_\infty(t(\cos(\frac{\theta}{2}) + \mathbf{b}\sin(\frac{\theta}{2}))) \\
&= R + R' \tag{7}
\end{aligned}
$$

Since the multiplication of a vector $t \in \langle G_3 \rangle_1$ by a bivector $\mathbf{b} \in \langle G_3 \rangle_2$ results in a multivector of the form $\lambda_1 e_1 + \lambda_2 e_2 + \lambda_3 e_3 + \lambda_4 e_{123}$, and since $t\cos(\frac{\theta}{2}) \in \langle G_3 \rangle_1$, we can rewrite (7) as

$$
\begin{aligned}
M &= \cos(\frac{\theta}{2}) + \mathbf{b}\sin(\frac{\theta}{2}) + \frac{1}{2}e_\infty(t\cos(\frac{\theta}{2}) + t\mathbf{b}\sin(\frac{\theta}{2})) \\
&= \cos(\frac{\theta}{2}) + \mathbf{b}\sin(\frac{\theta}{2}) + \frac{1}{2}e_\infty(t\cos(\frac{\theta}{2}) + \lambda_1 e_1 + \lambda_2 e_2 + \lambda_3 e_3 + \lambda_4 e_{123} \\
&= \cos(\frac{\theta}{2}) + \mathbf{b}\sin(\frac{\theta}{2}) + e_\infty(t' + \lambda e_{123}) \\
&= \cos(\frac{\theta}{2}) + \mathbf{b}\sin(\frac{\theta}{2}) + e_\infty t' + \lambda e_{\infty 123}) \tag{8}
\end{aligned}
$$

where $t' \in \langle G_3 \rangle_1$ and $\lambda = \frac{1}{2}\lambda_4$. Note that $e_\infty t'$ is a bivector with components $e_{\infty 1}, e_{\infty 2}, e_{\infty 3}$. If we take only the bivectorial parts of the motor M, we obtain

$$
\begin{aligned}
\langle M \rangle_2 &= \langle R \rangle_2 + \langle R' \rangle_2 \\
&= \mathbf{m} + \mathbf{m}' \\
&= \sin(\frac{\theta}{2})\mathbf{b} + e_\infty t' \tag{9}
\end{aligned}
$$

Therefore, if we express the vector t' in terms of their dual bivector $t' = t''I_E$, we can rewrite (9) as

$$\langle M \rangle_2 = b'I_E + e_\infty t''I_E \tag{10}$$

If we see the representation of the lines in the table 1, we observe that the bivectorial part of the motor M is in fact a line and it corresponds to the screw axis in which is carried out the rotation and translation of the object.

3   The Endoscope-Polaris Calibration in CGA

The hand-eye calibration is the calculation of the relative pose (position and orientation) between a robotic hand (arm) and a rigid camera mounted on it. Using this camera, we can determine the position in its coordinate system of an objective to catch or to reach; however, the commands of movements are in the coordinate system of the robotic hand (arm); therefore, to know the hand-eye transformation can be of great utility in this kind of tasks.

The usual way to describe the hand-eye calibration is by means of homogeneous transformation matrices [3,4]. In order to solve this problem, at least two movements are required with non parallel rotation axes, and several methods have been proposed to find the solution: some people estimate the rotation at first and later the translation [3], while others make it simultaneously [4]. Daniilidis [5] presents a solution based on dual quaternions, while [6] proposes the use of the motor algebra $G_{3,0,1}$. This work formulates the problem in terms of motors of the conformal geometric algebra framework. Since motor algebra is a subalgebra of conformal algebra, we can also formulate in conformal geometric algebra the hand-eye problem making use of the motors in CGA. Following the formulation of [6] for the hand-eye calibration problem, it will be expressed as

$$M_A M_X = M_X M_B \tag{11}$$

where $M_A = A + A'$, $M_B = B + B'$ and $M_X = R + R'$ (Sect. 2.1). In [6], it is shown that the problem is solved using the lines defined by the motors

$$
\begin{aligned}
L_A &= \mathbf{a} + \mathbf{a}' \\
&= M_X L_B \tilde{M}_X \\
&= (R + R')(\mathbf{b} + \mathbf{b}')(\widetilde{R + R'}) \\
&= R\mathbf{b}\tilde{R} + e_\infty (R\mathbf{b}\tilde{R}' + R\mathbf{b}'\tilde{R} + R'\mathbf{b}\tilde{R})
\end{aligned} \tag{12}
$$

where $\mathbf{a}$, $\mathbf{a}'$, $\mathbf{b}$, $\mathbf{b}'$ are bivectors (like in (9)). By separating the real part and the part multiplied by e_∞, we have

$$\mathbf{a} = R\mathbf{b}\tilde{R} \tag{13}$$
$$\mathbf{a}' = R\mathbf{b}\tilde{R}' + R\mathbf{b}'\tilde{R} + R'\mathbf{b}\tilde{R} \tag{14}$$

Multiplying from the right by R and using the relationship $\tilde{R}R' + \tilde{R}'R = 0$, the following relationships are obtained

$$\mathbf{a}R - R\mathbf{b} = 0 \tag{15}$$
$$(\mathbf{a}'R - R\mathbf{b}') + (\mathbf{a}R' - R'\mathbf{b}) = 0 \tag{16}$$

which can be expressed in matrix form as

$$
\begin{bmatrix}
\mathbf{a} - \mathbf{b} & [\mathbf{a} + \mathbf{b}]_\times & \mathbf{0}_{3\times 1} & \mathbf{0}_{3\times 3} \\
\mathbf{a}' - \mathbf{b}' & [\mathbf{a}' + \mathbf{b}']_\times & \mathbf{a} - \mathbf{b} & [\mathbf{a} + \mathbf{b}]_\times
\end{bmatrix}
\begin{bmatrix}
R \\
R'
\end{bmatrix} = 0 \tag{17}
$$

We call D to this 6×8 matrix; the unknown vector $[R, R']^T$ is 8-dimensional. The notation $[u]_\times$ represents the skew-symmetric matrix formed with the vector u. The matrix D is composed only by bivectors (blades of any other grade are not included), therefore we can use the SVD method to find $[R \; R']^T$ as the kernel of D.

Considering that we have $n \geq 2$ movements, the following matrix is built

$$C = \begin{bmatrix} D_1^T \; D_2^T \; D_3^T \; D_4^T \; ... \end{bmatrix}^T \tag{18}$$

in order to apply the SVD method and to find the solution for $[R, R']^T$. Since the range of the matrix C is at most 6, the last right two singular vectors, v_7 and v_8 correspond to the two singular values whose value is zero or near to zero, and such vectors expand the null space of C. Therefore, as $[R, R']^T$ is a null vector of C, we can express it as a linear combination of v_7 and v_8. If we express these vectors in terms of two vectors of 4D $v_7 = (u_1, v_1)^T$ and $v_8 = (u_2, v_2)^T$, this linear combination can be expressed as

$$\begin{bmatrix} R \\ R' \end{bmatrix} = \alpha \begin{bmatrix} u_1 \\ v_1' \end{bmatrix} + \beta \begin{bmatrix} u_2 \\ v_2' \end{bmatrix} \tag{19}$$

Taking into account the geometric constraints

$$R\tilde{R} = 1 \quad \text{y} \quad \tilde{R}R' + \tilde{R}'R = 0 \tag{20}$$

we obtain the following quadratic equations in terms of α and β

$$\alpha^2 u_1^T u_1 + 2\alpha\beta u_1^T u_2 + \beta^2 u_2^T u_2 = 1 \tag{21}$$
$$\alpha^2 u_1^T v_1 + \alpha\beta(u_1^T v_2 + u_2^T v_1) + \beta^2 u_2^T v_2 = 0 \tag{22}$$

In order to solve these equations, we make a change of variable, substituting in (22) $\mu = \alpha/\beta$ and we obtain two solutions for μ. Going back to (21) and replacing the relationship $\alpha = \mu\beta$, we obtain

$$\beta^2(\mu^2 u_1^T u_1 + \mu(2u_1^T u_2) + u_2^T u_2 = 1 \tag{23}$$

which takes two solutions for β.

The optical tracking system used is the *Enhanced Hybrid Polaris System*, which is labeled as (3) in the scenario shown in figure 1. This system emits infrared light that is reflected by markers placed to the object we are interested to track; the reflected light is detected by the sensors of the Polaris system, and then it estimates the 3D position of the different markers. We attach the local coordinate system of the markers to one of them. By this way, we know the transformation between the markers reference frame and the Polaris reference frame.

When using information obtained from endoscopy or neuro-sonography, we must relate what is been observed by the endoscopic camera (or ultrasound system), with the virtual model. To solve this problem, we propose the formulation

of the hand-eye calibration problem in terms of the Conformal Geometric Algebra, to calculate the transformation between the coordinate system of the endoscopic camera, and the coordinate system of the spherical markers placed to the endoscope. We call this task the *endoscope-Polaris* calibration. The scenario is shown in figure 2, where the reader can see that there is a (rigid) transformation between the calibration grid, and the Polaris System, $\mathbf{M_{Bg}}$. Such transformation will be used to validate the results of the endoscope-Polaris calibration method. The transformations involved in the problem are expressed as motors of the
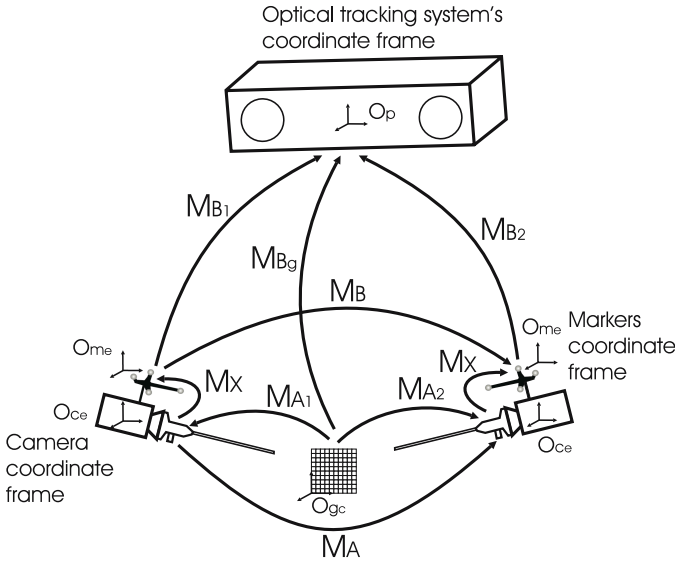
Fig. 2. The problem of the calibration between the endoscopic camera and the optical tracking system (Polaris)

CGA: $M = TR$.

The procedure is summarized as follows

1. Given n movements of the endoscopic camera (we move it freely by hand to arbitrary positions), M_{B_i}, and their corresponding movements M_{A_i}, verify if their scalar parts are equal.
2. For the movements that fulfill the previous requirement, extract the directions and moments of the lines L_{A_i} and L_{B_i} defined by the motors. Build the matrix C as in (18).
3. Apply SVD to matrix C. Take the right singular vectors v_7 and v_8 corresponding to the two singular values nearest to zero (a threshold is applied by the noise).
4. Compute the coefficients for (22) and find the two solutions of μ.

5. For both values of μ, compute the value of $\mu^2 u_1^T u_1 + 2\mu u_1^T u_2 + u_2^T u_2$ and choose the one that gives the biggest value. Then, compute α and β.
6. The final solution is $\alpha v_7 + \beta v_8$

4   Experimental Results

In order to validate the accuracy of the estimated transformation $\mathbf{M_X}$, we use the calibration grid used to calibrate the endoscopic camera by Zhang's method [7], and shown in Fig. 3.a. Let be X_g the set of points corresponding to the corners of the calibration grid, referred to $\mathbf{O_{g_c}}$. These coordinates are expressed in millimeters, according to the size of each square in the calibration grid, which in our case has 1.25 mm by side.

1. Taking the points X_g in the grid reference frame, apply the transformation $\mathbf{M_{A_i}}$ to express them in the camera's reference frame. Let be X_{A_i} the resulting points.
2. Project the points X_{A_i} to the image plane using

$$x_{A_i} = K\ [R_{M_A}\ \ t_{M_A}]\ X_{A_i} \tag{24}$$

These points should be projected on the corners of the squares in the calibration grid on the image (Fig. 3).
3. Taking the points X_g, apply the transformations $\mathbf{M_{B_g}}$, $\mathbf{M_{B_i}}$ and $\mathbf{M_X}$. Let be $X_{M_{B_i}X}$ the resulting points.
4. Project the points $X_{M_{B_i}X}$ onto the image plane using

$$x_{B_i} = K\ [R_{M_{B_i}X}\ \ t_{M_{B_i}X}]\ X_{M_{B_i}X} \tag{25}$$

In the ideal case (without noise), the projected points x_{A_i} should match with the projected points x_{B_i}. However, as a result of noise in the Polaris readings or noise in the estimation of transformations, takes place a small linear displacement between x_{A_i} and x_{B_i} (see Fig. 4.a). We can measure the error ϵ between the two projections as

$$\epsilon = \frac{\sum_{i=1}^{n}(x_{A_i} - x_{B_i})}{n} \tag{26}$$
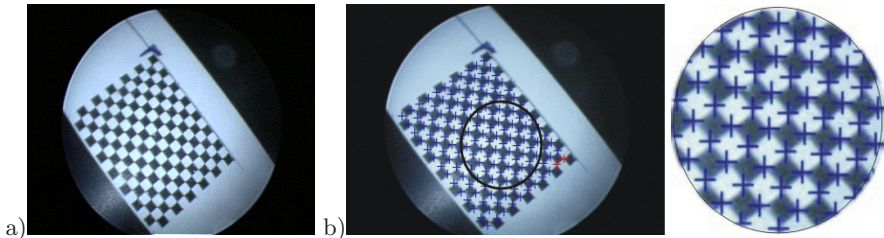
Fig. 3. a) Original image; b) Result of the projection using (24); it is included a zoom of the marked region for better visualization
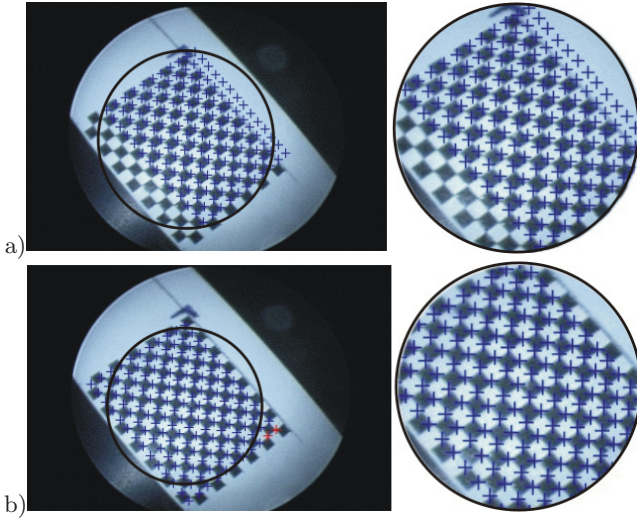
Fig. 4. a) Result of the projection using (25); b) Result applying (27)

5. In order to correct the displacement, the centroid of each point set is calculated: c_{A_i} and c_{B_i}. Then, the points x_{B_i} are displaced in such a way that the centroids match.

$$x'_{B_i} = x_{B_i} + (c_{A_i} - c_{B_i}) \tag{27}$$

After the displacement, the average error is calculated as

$$\epsilon' = \frac{\sum_{i=1}^{n} (x_{A_i} - x'_{B_i})}{n} \tag{28}$$

The figure 4.b shows the result after doing such correction to the points showed in figure 4.a.

The table 2 shows the errors measured for 9 different images without the telescope, while the table 3 shows the measured errors with 16 images with the telescope attached to the camera. Remember that the telescope is attached to the camera, then it is introduced to the patient's head in order to see and navigate inside the head.

Table 2. Average errors according to (27) and (28), measured in millimeters when projecting to the image plane the points X_g, according to (24) and (25) without the telescope attached to the camera

Image	ϵ (26)	ϵ' (28)	Image	ϵ (26)	ϵ' (28)	Image	ϵ (26)	ϵ' (28)
1	0.029	0.246	4	0.038	0.254	7	0.036	0.242
2	0.029	0.291	5	0.054	0.273854	8	0.030	0.290
3	0.029	0.327	6	0.026	0.285	9	0.030	0.263

Table 3. Average errors according to (27) and (28), measured in millimeters when projecting to the image plane the points X_g according to (24) and (25) attaching the telescope to the camera

Image	ϵ (26)	ϵ' (28)	Image	ϵ (26)	ϵ' (28)	Image	ϵ (26)	ϵ' (28)	Image	ϵ (26)	ϵ' (28)
1	0.068	0.111	5	0.125	0.149	9	0.039	0.041	13	0.048	0.051
2	0.067	0.222	6	0.057	0.146	10	0.244	0.258	14	0.031	0.103
3	0.048	0.150	7	0.163	0.204	11	0.063	0.462	15	0.057	0.082
4	0.076	0.162	8	0.075	0.090	12	0.048	0.142	16	0.033	0.1022

5   Conclusions

In this work we have presented a method to estimate the transformation relating an endoscopic camera used in surgical procedures, with the set of spherical markers placed on it, which are tracked by an optical tracking system. By this way, we have all the transformations needed to appropriately compute a composed transformation relating the preoperative data (virtual model) with the intraoperative data obtained from the endoscopic camera.

The presented approach take advantage of the representation of rigid transformations (rotation and translation) in the conformal geometric algebra, which are expressed as versors called *motors*. The composition of such motors was analyzed, showing that they contain the line representing the screw axis in which is carried out the rotation and translation of the object. Then the transformation is estimated based on the lines defined by the motors in different movements of the endoscopic camera. We think that numerical results prove that the method is accurate enough and it is suitable to be used in real surgeries.

References

1. Bayro-Corrochano, E.: Robot perception and action using conformal geometry. In: Handbook of Geometric Computing. Applications in Pattern Recognition, Computer Vision, Neurocomputing and Robotics. ch. 13, Springer Verlag, Heidelberg (2005)
2. Rosenhahn, B., Sommer, G.: Pose Estimation in Conformal Geometric Algebra. Christian-Albrechts-University of Kiel, Technical Report No. 0206, pp. 13–36 (2002)
3. Tsai, R.Y., Lenz, R.K.: A New Technique for Fully Autonomous and Efficient 3D Robotics Hand/Eye Calibration. IEEE Transactions on Robotics and Automation 5(3), 345–358 (1989)
4. Horaud, R., Dornaika, F.: Hand-Eye Calibration. International Journal on Robotics Research 14(3), 195–210 (1995)
5. Daniilidis, K.: Hand-Eye Calibration Using Dual Quaternions. The International Journal of Robotics Research 18(3), 286–298 (1999)
6. Bayro-Corrochano, E., Sommer, G., Dannilidis, K.: Motor Algebra for 3D Kinematics: The Case of the Hand-Eye Calibration. Journal of Mathematical Imaging and Vision 13, 79–100 (2000)
7. Zhang, Z.: A Flexible New Technique for Camera Calibration. Microsoft Research 1–21 (1999)

Quality Controlled Multimodal Fusion of Biometric Experts

Omolara Fatukasi, Josef Kittler, and Norman Poh

Centre for Vision, Speech and Signal Processing,
University of Surrey Guildford, GU2 7XH Surrey, UK
{O.Fatukasi,J.Kittler,N.Poh}@surrey.ac.uk

Abstract. The quality of biometric samples used by multimodal biometric experts to produce matching scores has a significant impact on their fusion. We address the problem of quality controlled fusion of multiple biometric experts and focus on the fusion problem in a scenario where biometric trait quality expressed in terms of quality measures can be coarsely quantised. We develop a fusion methodology based on fixed rules that exploit the respective advantages of the sum and product rules and can be easily trained. We show in experimental studies on the XM2VTS database that the proposed method is very promising.

Keywords: Biometric authentication, fixed rules, multiple classifiers system, multimodal fusion, quality dependent fusion.

1 Introduction

Biometric authentication is the verification of a user's identity by means of his/her physical and behavioural characteristics. Studies, e.g. [1] have shown that the fusion of experts improves the system performance when compared with individual experts. However poor quality biometric data may have the opposite effect [2,3]. This finding motivated the investigation of quality based fusion. It has been shown in [4,5,6,7,8,9,10] that quality based fusion improves significantly the performance, as compared to conventional fusion methods (fusion without the use of quality information).

The recent research into quality based score fusion shows that it is beneficial to include quality information as input to the fusion process. In confidence based decision fusion, quality information is also used as a control parameter to select which modality's decision to follow. Most of the quality based multimodal fusion techniques deploy training for the fusion stage design [4,5,6,10]. The exception is [7], where the product rule is used, after adapting the scores by computing the likelihood ratio of estimated densities.

In this paper we address the problem of quality controlled fusion of multiple biometric experts. We focus on the fusion problem in a scenario where biometric trait quality expressed in terms of quality measures can be coarsely quantised. We develop a fusion methodology based on fixed rules that can be easily trained. The methodology involves a two stage process whereby in the first stage expert

scores are grouped according to the quality of the underlying biometric sample. In each quality group the scores are combined by averaging. The resulting group scores are finally combined by product. We argue that the proposed scheme exploits the properties of fixed fusion rules in the best possible way and provide experimental evidence to support this argument. The proposed scheme is experimentally evaluated on the XM2VTS database. The results show that significant performance gains can be achieved. The performance is comparable to the state of the art method reported in [10] but the proposed fusion system is much easier to design and requires less data for training.

The rest of the paper is organised as follows. In Section 2 we introduce the proposed methodology. The database used in the study is described in Section 3. An overview of the biometric experts used for experiments is presented in Section 4. Section 5 discusses the quality measures used to characterise biometric sample quality. We also report in this section the coefficients of correlation between expert scores in different quality categories. The fusion experiments carried out are described in Section 6 where the results of experiments are also discussed. Section 7 draws the paper to conclusion.

2   Proposed Methodology

The study of fixed fusion rules in [1] demonstrates that the sum rule outperforms all other fixed rules. Alkoot *et al.* showed in [11] that the product rule may outperform even the sum rule, provided the veto effect of conflicting low valued scores is suppressed. The product rule and the sum rule have been compared by Kittler *et al.* in [1] and Tax *et al.* in [12]. These studies demonstrate that the sum rule is robust to noise. The sensitivity of the product rule to noise is due to the veto effect. Tax *et al.* also show that the product rule outperforms the sum rule when the correlation between data is low and noise is low. However if the noise is high, the product rule becomes unreliable even when correlation is low. These studies lead to the following conclusion:

- if a high level of noise is present, the sum rule is preferable.
- for low noise and low correlation, the product rule should be favoured as it outperforms the sum rule in these conditions.
- when experts are highly correlated, even when the noise level is low the sum rule should be chosen, as it outperforms the product rule under these conditions.

[1] shows theoretically that the product rule is more sensitive to noise than the sum rule, hence why it deteriorates on noisy data.

In this paper we consider the problem of fusing multiple experts providing scores on biometric data of varying quality. The scores are assumed to be normalised, so that any fixed rule, including the product rule can be used for fusion. Thus the score values are confined to the interval $[0, 1]$. Without loss of generality, we assume that a score is high (close to 1) for a good match, i.e. when comparing a probe of a genuine claimant against a template of the true client

identity. Impostor score values, of course, would be lower. Clearly for biometric samples of low quality, both the client scores and impostor scores would shift towards the lower end of the score range. It is evident, that when the quality of the biometrics trait varies, a single threshold would not be adequate, as the scores generated by high quality traits of imposters are likely to exceed the scores of true clients derived from low quality biometric data. This problem can be solved by considering the threshold to be a function of the set of quality measures characterising the biometric data. However learning the regression function requires a large amount of data which is not always available.

A similar problem, but greatly amplified, arises in multiple expert fusion. The additional complexity derives from the fact the threshold for the fused score becomes a function of the quality measures of all biometric modality traits jointly. The reason for this is that the fusion potentially involves expert scores associated with different qualities and this will impact on the optimal threshold to be applied to the fused score. The regression function defining the optimal threshold is much more difficult to learn, as the number of variables involved in regression increases without the commensurate increase in the number of training samples. This problem was investigated in detail in [10] where it was demonstrated that significant gains in performance can be obtained by quality dependent fusion where the fusion was realised as a Support Vector machine using both component expert scores and biometric trait qualities as features.

It would appear, therefore, that the key advantage of fixed fusion rules, namely their simplicity and ease of training, is seriously compromised when the experts to be fused use data of different quality. However, in many situations the biometric data quality will not necessarily be uniformly distributed with respect to the various quality measures. Instead, it is likely to be clustered. For instance, if the biometric data is collected in a small set of distinct environments, or using a small set of devices supplied by different manufacturers or involving sensor technology for a particular biometric trait designed on different principles, the data acquired will tend to cluster into a number of quality states corresponding to the distinct conditions of data acquisition. In such situation it would be feasible to group the experts according to the quality state of the biometric data used for computing their score. In each group, it should then be possible to use a fixed fusion rule and subsequently, combine the group scores to produce the final fused result.

We shall develop the above ideas into a practical fusion methodology applicable under the assumption that the biometric data can sensibly be divided into two quality states. We shall see in Section 5 that this assumption is valid for the biometric database, XM2VTS, used for our experiments. In order to be more specific, we shall introduce the necessary mathematical notation.

Let $i = 1 : n$ samples, $j = 1 : R$ experts, and $m = 1 : M$ modalities. The decision whether to assign the quality of a biometric sample $x_{j,i}$ to high or low quality, is dependent on the quality measure, $q_{i,m}$, of the sample, its mean $\overline{q_m}$ and the standard deviation σ_{q_m} and biometric modality in the evaluation data set. A sample $x_{j,i}$ is marked as high quality if $q_{i,m} \geq \overline{q_m} - \sigma_{q_m}$, else it is of

low quality. Let $r_{z,i}$ be the number of experts working with samples of quality $z\epsilon\{high,low\}$. Based on this decision rule we can identify three situations: i) all-high $r_{low,i} = 0$, ii) all-low $r_{high,i} = 0$, and iii) mixed where both $r_{high,i}$ and $r_{low,i}$ are nonzero.

We shall see in Section 5 that experts tend to be correlated. Thus for every sample, within each group, the preferable fixed fusion rule is the sum rule. The fused score for the ith sample in group with quality z is thus given as

$$S_z(i) = \begin{cases} \frac{1}{r_{z,i}} \sum_{p=1}^{r_{z,i}} x_{p,i} & if \quad r_{z,i} \geq 1 \\ 1 & if \quad r_{z,i} = 0 \end{cases} \tag{1}$$

Setting the sum to 1 when a group contains no expert is for a later convenience.

Now, in each group we will end up with two averaged scores $S_{high}(i)$ and $S_{low}(i)$. Especially in the mixed group these two scores can further be combined by a fixed rule. We shall see later that the score averaging process in each group results in fused scores $S_z(i), z\epsilon\{high,low\}$ which are much less noisy, and surprisingly, also less correlated. This suggests that the optimal fixed fusion rule for this second fusion stage should be the product rule. Accordingly, the final fused score $S(i)$ for sample i will be given as

$$S(i) = S_{high}(i) \times S_{low}(i) \tag{2}$$

The resulting score $S(i)$ is then compared against the threshold D_θ where $\theta\epsilon\{high,low,mixed\}$. These thresholds are estimated from the training data but it is a relatively simple task.

3   Database

In the current study, we used the original XM2VTS database[13] and its degraded version [14] in both the training and the test phase of the fusion methods. The original database contains mugshot images with well controlled illumination. The low quality section contains images taken under strong side illumination, which has been shown to degrade significantly face verification performance [14]. This database contains 295 individuals, divided into 200 clients, 25 impostors for the algorithm development (training), and 70 impostors for algorithm evaluation (testing). For each subject, face and speech biometric modalities are acquired in four sessions; the first three are used for training the classifiers and the last one for testing. For the face modality we consider the dark data set with left illumination as the "fifth session" and the one with right illumination as the "sixth" session. There is unfortunately no equivalent of degraded speech data that can be paired with the degraded face images. We created degraded biometric data by first introducing additive white noise with a uniform random distribution between 0 and 20dB signal-to-noise ratio on the clean speech database, hence resulting in a degraded speech database with exactly the same size as the clean database. We then paired the degraded face images with the degraded speech data according to Table 1. For instance, the first row shows that the first shot

Table 1. Matching of degraded face and speech data

Degraded face		Degraded speech	
session	shot	session	shot
5	1	1	2
5	2	2	2
6	1	3	2
6	2	4	2

of degraded face image in the fifth session is matched with the second shot of the degraded speech recorded in session one, and so on.

Experimentation with good and degraded data set is important as it reflects a more realistic scenario than the use of only good data. During the data capture of the development data set the environment can be controlled, however in operation the quality is likely to be more varied. Having a good biometric data for the development set and mixed quality biometric data for the operational phase can lead to bad system performance as degraded data is not taken into account in the development stage. It is therefore essential to have representative examples of degradation also for the development.

Unfortunately, the way the experimental data set has been constructed does not allow us to test systematically the merit of fusion when one modality is of good quality and the other one is degraded. Although this is more realistic, there is no obvious solution to introducing this scenario.

The original experimental protocols known as the Lausanne Protocols, did not envisage that for the XM2VTS database the degraded data sets would be used for algorithm development. However, in order to make degraded data avaliable for training, we used the 25-impostor data set in which good and degraded quality data is available. For clients, we divided these 200 subjects into 20- and 180-client data sets such that the 20-client data set is set aside uniquely for algorithm development and the 180-client for both algorithm development and evaluation. The resulting protocol for mixed quality scenario is summarised in Table 2.

Table 2. The XM2VTS clean and degraded protocol

Sessions	Shots	180 Clients	20 Clients	25 Imposter	70 Imposter
S1	1	Training	Training	Evaluation	Test
	2	Evaluation	Evaluation		
S2	1	Training	Training		
	2	Evaluation	Evaluation		
S3	1	Training	Training		
	2	Evaluation	Evalaution		
S4	1	Test	Test		
	2				
Degraded	L1,R1	Test	Evalaution	Evaluation	Test
	L2,R2	degraded	degarded	degraded	degraded

4   Experts

The classifiers used for the face experts in this paper can be found in [15]. There are two classifiers with three types of pre-processing, hence resulting in a matrix of six classifiers. The two classifiers used are Linear Discriminant Analysis (LDA) with correlation as a measure of similarity [16] and Gaussian Mixture Model (GMM) with maximum a posteriori adaptation, described in [17]. The use of the GMM in face authentication was proposed in [18]. The face pre-processing algorithms used include the photometric normalisation as proposed by Gross and Brajovic [19], histogram equalisation and local binary pattern (LBP) as reported in [15]. The feature extraction and classification algorithms are implemented in the open-source Torch Vision Library[1].

The speech system used is implemented with the ALIZE toolkit [20].

5   Quality Measures

In this paper, we used a set of proprietary quality measures developed by Omniperception Ltd for the face image quality assessment. These measures are: "frontal quality", measuring the deviation from the frontal face; and "illumination quality", quantifying the uniformity of illumination of the face.

Two quality measures are used for the speech system: signal-to-noise ratio (SNR) and "entropy quality". Both measures are used for voice activity detection, i.e., to separate speech from non-speech.

These measures can be found in [21]. Thus each modality has two quality measures; "frontal quality" and "illumination quality" for face, signal-to-noise ratio (SNR) and "entropy quality" for speech. These are averaged for each modality.

Table 3. Coefficient of correlation between the six face and one speech experts computed on the development set for the **client** (in bold) and *imposter* (in italic). f1 to f6 are the six face experts and v1 is the speech expert. (a), (b) and (c) shows the correlation coefficient for claims where the quality measure for the biometric data is mixed, low, or high for all experts repectively.

	f1	f2	f3	f4	f5	f6	v1
			(a) Mixed quality dataset				
f1	**1.00**/*1.00*	**0.82**/*0.51*	**0.76**/*0.39*	**0.74**/*0.20*	**0.71**/*0.06*	**0.70**/*0.08*	**0.32**/*0.00*
f2	**0.82**/*0.51*	**1.00**/*1.00*	**0.85**/*0.47*	**0.84**/*0.17*	**0.84**/*0.07*	**0.79**/*0.03*	**0.42**/*-0.02*
f3	**0.76**/*0.39*	**0.85**/*0.47*	**1.00**/*1.00*	**0.78**/*0.16*	**0.73**/*0.08*	**0.80**/*0.11*	**0.20**/*-0.01*
f4	**0.74**/*0.20*	**0.84**/*0.17*	**0.78**/*0.16*	**1.00**/*1.00*	**0.93**/*0.39*	**0.02**/*0.31*	**0.38**/*0.05*
f5	**0.71**/*0.06*	**0.84**/*0.07*	**0.73**/*0.08*	**0.93**/*0.39*	**1.00**/*1.00*	**0.91**/*0.37*	**0.49**/*0.09*
f6	**0.70**/*0.08*	**0.79**/*0.03*	**0.80**/*0.11*	**0.92**/*0.31*	**0.91**/*0.37*	**1.00**/*1.00*	**0.29**/*0.07*
v1	**0.32**/*0.00*	**0.42**/*-0.02*	**0.20**/*-0.01*	**0.38**/*0.05*	**0.49**/*0.09*	**0.29**/*0.07*	**1.00**/*1.00*

---

[1] Available at "http://torch3vision.idiap.ch". See also a tutorial at "http://www.idiap.ch/marcel/labs/faceverif.php".

It is interesting to note the correlation between the experts using low and high quality data. Table 3 shows the correlation coefficient between all the experts for clients (in bold) and imposters (in italic) in the development data set. It can be noted that all the face experts are correlated, but the speech expert is not correlated to any of the face experts.

Most importantly, for the mixed quality scenario the resulting two fused scores have low correlation. In fact the correlation coefficient of the combined scores obtained by averaging in each group is **0.3684**/*-0.2888* client/imposter for the development set and **0.2946**/*-0.3235* client/imposter for the evaluation set. This confirms that these group scores are better suited for fusion by the product rule, as proposed in Section 2.

6   Experiments and Results

We have designed experiments to compare the following:

- fixed rule fusion with trained fusion.
- fixed rule fusion with quality and conventional fixed rule fusion
- using quality as a feature in the fusion process and using quality controlled fusion.

The performance of the six face and one speech experts is shown in Table 4. The overall performance is not high due to the influence of low quality biometric data. We consider the set of all $2^6 - 1$ possible combinations of the face experts to be fused with the speech expert for multimodal authentication.

Table 4. Baseline systems, *a priori* half total error rate (HTER) (%) of good + degraded test data, with the *a priori* HTER (%) of the good and degraded data sets recorded separately. The separate good and degraded data results were obtain by using the threshold (Δ) set on the good + degraded training data.

modality	no.	good + degraded HTER (%)	good HTER (%)	degraded HTER (%)
face	1	11.06	6.66	13.50
face	2	7.67	3.48	9.78
face	3	8.29	5.86	9.57
face	4	10.39	2.13	17.17
face	5	24.56	2.97	39.28
face	6	16.96	5.51	23.42
speech	1	11.40	1.15	17.48

Figure 1(a) shows the result of the sum rule vs the proposed quality controlled fusion. It can be seen that the quality controlled fusion outperforms the sum rule in all fusion tasks. Another interesting point to note is that the best performance was not obtained when all the face experts were used jointly, but when two, three, or at most four experts are fused together.
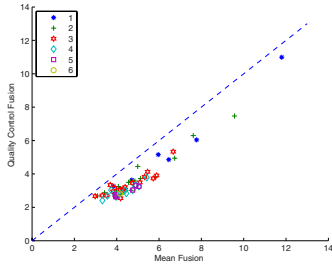
(a) Sum Fusion vs Quality Controlled Fusion
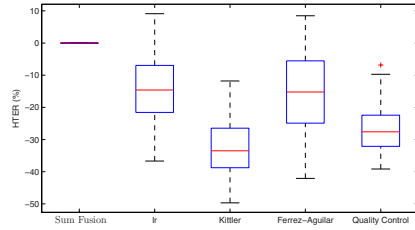
(b) Relative *A priori* HTER(%)

Fig. 1. (a) *A priori* HTER (%) of good + degraded test data, with Mean Fusion vs Proposed Quality Controlled Fusion. Each point in the figure represents one of the possible 63 multimodal fusion tasks. The numeric labels in the legend indicate the number of face experts fused with the only speech expert. (b) Relative *a priori* HTER(%) of the sum fusion, logistic regression without quality measure, logistic regression with quality (Kittler *et al.* [10]), SVM with quality measure (Fierrez-Aguilar *et al.* [4]), and the proposed quality controlled fusion.

Figure 1(b) shows the relative *a priori* HTER (%) of conventional sum fusion, a logistic regression with just the expert score as the input to the fusion process, logistic regression with quality measure added as an input feature, proposed in [10], SVM with quality measure used to normalised the score proposed by Fierrez-Aguilar *et al.* in [4], and the proposed quality controlled fusion method. It is interesting to note the following:

1. For logistic regression the average observed relative improvement is 14% with the best improvement realising 39%. This is expected as a trained rule is likely to outperform a fixed rule when the performance of expert varies, as shown in Table 4. However for certain sets of experts, the logistic regression can degrade the performance by as much as 9%.
2. For the method proposed in [10], there is an improvement in all fusion tasks with an average of 33% but as much as 49% can be achieved.
3. For the method proposed by Fierrez-Aguilar *et al.* in [4] an average improvement of 15% with a peak gain of 42% and the worst loss of 8%.
4. For our proposed quality controlled fusion method, there is an improvement in all the fusion tasks with an average improvement of 27%, but up to 39% can be achieved.

These observations highlight the following:

1. Fusion using quality information outperforms conventional fusion.
2. In score level fusion, quality measures can be used in two ways; as input to the fusion process, or as a control parameter.
3. When using quality measures as part of the input to the score level fusion, the method proposed in [10] provides the best average performance and clear improvement in all the fusion experiments. This is evident from Figure 1(b).

4. The score level fusion with the proposed quality control offers very good average performance, and it also provides improvement in performance in all fusion tasks in the experimental comparison with the sum rule. In fact the proposed quality control with a fixed rule performs better than the logistic regression, as shown in Figure 1(b).

7   Discussion and Conclusion

We addressed the problem of quality controlled fusion of multiple biometric experts. We focused on the fusion problem in a scenario where biometric trait quality expressed in terms of quality measures can be coarsely quantised. We developed a fusion methodology based on fixed rules that can be easily trained. The methodology involves a two stage process whereby in the first stage expert scores are grouped according to the quality of the underlying biometric sample. In each quality group the scores are combined by averaging. The resulting group scores are finally combined by product. We argued that the proposed scheme exploits the properties of fixed fusion rules in the best possible way and provided experimental evidence in support of this argument. The proposed scheme was experimentally evaluated on the XM2VTS database. The results showed significant performance gains over conventional fusion. The performance is comparable to the state of the art method reported in [10] but the proposed fusion system is much easier to design and requires less data for training. The proposed method can be used not only for multimodal fusion, but also for intramodal fusion, provided the quality measures of the biometric sample is different for each expert [9].

References

1. Kittler, J., Hatef, M., Duin, R.P.W., Matas, J.: On combining classifiers. IEEE Transactions on Pattern Analysis and Machine Intelligence 20, 226–239 (1998)
2. Poh, N., Bengio, S.: A score-level fusion benchmark database for biometric authentication. In: Kanade, T., Jain, A., Ratha, N.K. (eds.) AVBPA 2005. LNCS, vol. 3546, pp. 1059–1070. Springer, Heidelberg (2005)
3. Tabassi, E., Wilson, C., Watson, C.: Fingerprint image quality: Nistir 7151. Technical report, NIST (2004)
4. Fierrez-Aguilar, J., Ortega-Garcia, J., Gonzalez-Rodriguez, J., Bigun, J.: Kernel-Based Multimodal Biometric Verification Using Quality Signals. In: Defense and Security Symposium, Workshop on Biometric Technology for Human Identification, Proc. of SPIE. vol. 5404, pp. 544–554 (2004)
5. Bigun, J., Fierrez-Aguilar, J., Ortega-Garcia, J., Gonzalez-Rodriguez, J.: Multimodal Biometric Authentication using Quality Signals in Mobile Communnications. In: 12th Int'l Conf. on Image Analysis and Processing, Mantova, pp. 2–11 (2003)
6. Kryszczuk, K., Richiardi, J., Prodanov, P., Drygajlo, A.: Error Handling in Multimodal Biometric Systems using Reliability Measures. In: Proc. 12th European Conference on Signal Processing, Antalya, Turkey (September 2005)
7. Nandakumar, K., Chen, Y., Dass, S., Jain, A.: Quality-based score level fusion in multibiometric systems. In: ICPR, Hong Kong, pp. 473–476 (2006)

8. Kryszczuk, K., Drygajlo, A.: On combining evidence for reliability estimation in face verification. In: Proc. 13th European Conference on Signal Processing, Florence, Italy (2006)

9. Fierrez-Aguilar, J., Chen, Y., Ortega-Garcia, J., Jain, A.K.: Incorporating image quality in multi-algorithm fingerprint verification. In: ICB (2006)

10. Kittler, J., Poh, N., Fatukasi, O., Messer, K., Kryszczuk, K., Richiardi, J., Drygajlo, A.: Quality dependent fusion of intramodal and multimodal biometric experts. In: Proceedings of SPIE. vol. 6539 Orlando (2007)

11. Alkoot, F.M., Kittler, J.: Improving the performance of the product fusion strategy. In: ICPR, vol. 02, pp. 164–167. IEEE Computer Society, Los Alamitos, CA, USA (2000)

12. Tax, D., van Breukelen, M., Duin, R.: Combining multiple classifiers by averaging or by multiplying? Pattern Recognition 33, 1475–1485 (2000)

13. Matas, J., Hamouz, M.: K.Jonsson, Kittler, J., Li, Y., Kotropoulos, C.,Tefas, A., Pitas, I., Tan, T., Yan, H., Smeraldi, F., Begun, J., Capdevielle, N., Gerstner, W., Ben-Yacoub, S., Abdeljaoued, Y., Mayoraz, E.: Comparison of face verification results on xm2vts database. In: Proceedings of SPIE. Pattern Recognition. vol. 6539 Orlando (2007)

14. Messer, K., Kittler, J., Short, J., Heusch, G., Cardinaux, F., Marcel, S., Rodriguez, Y., Shan, S., Su, Y., Gao, W.: Performance characterisation of face recognition algorithms and their sensitivity to severe illumination changes. In: Zhang, D., Jain, A.K. (eds.) Advances in Biometrics. LNCS, vol. 3832, pp. 1–11. Springer, Heidelberg (2005)

15. Heusch, G., Rodriguez, Y., Marcel, S.: Local binary pattern as an image preprocessing face authentication. In: Proc. FGR 2006, Washington, DC, 9–14 (2006)

16. Kittler, J., Li, Y., Matas, J.: On matching score for lda-based face verification. In: BMVC (2000)

17. Reynolds, D.A., Quatieri, T., Dunn, T.: Speaker verification using adapted guassian mixture models. In: Digital Signal Processing, pp. 19–41 (2000)

18. Cardinaux, F., Sanderson, C., Bengio, S.: User authentication via adapted statistical models of face images. In: IEEE Trans. on Signal Processing, pp. 361–373 (January 2006)

19. Gross, R., Brajovic, V.: An image preprocessing algorithm for illumination invariant face recognition. In: AVBPA 2003, 10–18 (2003)

20. Bonastre, J.F., Wils, F., Meignier, S.: ALIZE, a free toolkit for speaker recognition. In: Proc. IEEE International Conference on Speech, Acoustics and Signal Processing, Philadelphia pp. 73–740 (2005)

21. Richiardi, J., Prodanov, P., Drygajlo, A.: Speaker verification with confidence and reliability measures. In: Proc. 2006 IEEE International Conference on Speech, Acoustics and Signal Processing, Toulouse, France (May 2006)

Fully Automatic and Robust Approach for Remote Sensing Image Registration

Chi-Farn Chen, Min-Hsin Chen, and Hsiang-Tsu Li

Center for Space and Remote Sensing Research
National Central University
Jhongli, Taiwan
`cfchen@csrsr.ncu.edu.tw`

Abstract. Image registration is an important preprocessing procedure for remote sensing image applications, such as geometric correction, change detection, and image fusion. Since it is a time-consuming and labor-intensive task to correctly register the remote sensing image, this paper proposes a fully automatic and robust approach for the remote sensing image registration. First, the image pyramid of working and reference images are constructed for coarse to fine matching processing. Second, the feature points can be automatically extracted from the reference image, and the matching point can be searched on the working image. Third, in order to improve the accuracy of registration, the robust estimation serves as an important tool in preserving the correctly matched points. Three sets of satellite images, which include multi-sensor, multi-temporal and multi-spectrum images, are used to test the proposed approach. Results show that the approach is capable of automatically registering the working image to the reference image with great precision.

Keywords: Image Registration, Remote Sensing Image, Automatic and Robust.

1 Introduction

The use of satellite images has become an increasingly important tool in environmental monitoring in recent years, as they own a large swath width, a high spatial resolution and a high receive frequency. In order to efficiently and accurately use the remote sensing images, image registration is a necessary preprocessing procedure for remote sensing image applications, such as image geo-correction, land change detection, and image fusion [1][2]. Image registration is a process that involves the establishment of a geometric mapping function between two images, which can be adopted in multi-temporal, multi-sensor, multi-spectrum and multi-resolution images. Conventionally, after the remote sensing images are acquired, the images will be corrected systematically by colinear condition models [3]. However, due to limitations in the digital terrain model accuracy and number of ground control points, various systematic geometric errors (sometimes more than 1 pixel) will exist in the satellite image products, which could result in problems when applied further. Hence, in order to improve the results of remote sensing applications, image registration is a necessary process in eliminating the geometric distortions within two images. Over

the past years, a considerable amount of studies have been made on image registration techniques and applications. The image registration method can be divided into two major categories [4], the geometric image feature based method and voxel similarity measure based method. The geometric image feature based algorithm uses the point, line or surface features to register two images via least squares fitting [5][6]. As the algorithm is a scale, offset and rotation invariant transformation, it is widely used in computer vision applications. The voxel similarity measure based algorithm maximizes the similarity between the target and search window, the most accurate registration position can be determined [7][8]. The image registration of remote sensing images is quite different to the registration on medical and computer vision images. In general, the radiometric responses of the same feature on the satellite images may very with the viewing angles, atmospheric conditions, cloud, haze and land cover changes. Therefore, in order to perform the automatic and accurate registration of the remote sensing images, the algorithm has to take into account the radiometric variation of the features, when applied to multi-temporal, multi-sensor and multi-spectrum remote sensing images.

A fully automatic approach for accurate and robust remote sensing image registration is proposed in this paper. In light of the high efficiency advantages in the geometric image feature based method, and high accuracy in the voxel similarity measure based method; proposed approach not only uses the normalized cross correlation to accurately match the conjugate points, but also constrains the geometric relations of matching points in finding out the correctly matching ones. By repeatedly removing the points with the largest geometric errors, the incorrect matching point will be eliminated point by point. Moreover, the accuracy of the image registration can be further improved to the sub-pixel level. In order to make the image registration task more efficient and accurate, the concept of the coarse to fine matching is also applied in this research [9]. The proposed approach consists of three major steps: (1) the construction of image pyramids, (2) the detection and matching of feature points, and (3) the robust estimation and image registration. A detailed explanation of the three procedures will be presented in the following segments. The organization of this paper is as follows. Section 2 delineates the methodologies used in this research. The three different experiments that were conducted to test the proposed approach are introduced in section 3. The experimental results are shown in section 4, and the conclusions will be addressed in section 5.

2   Methodologies

Image registration can be regarded as a precision correction procedure, which provides the relative orientation of two images. Conventionally, the relative orientation of two images can be described by a mapping function, and the parameters of the mapping function can be calculated via finding the conjugate points on both images. In this study, an automatic feature point operator is applied to detect the feature points on the reference image and an area based matching is used to find the most similar point on the working image. By using the least squares adjustment and the coordinates of conjugate points, the parameters of the mapping function can be calculated. However, the area based matching can only provide the matched point

with the highest similarity instead of the highest correctness. Accordingly, in order to increase the accuracy of the image registration, the incorrect matched points will be continuously detected and eliminated by the robust estimation, until the registration accuracy reaches the sub-pixel level.

One of the critical processes of the proposed approach is the feature point matching. Needless to say, the efficiency and correctness of the matching process are highly dependent on the size of the search area. A larger search area will increase the computation time and decrease the correctness of the matching results. Hence, based on the coarse to fine matching concept, during the first step of the proposed method, an image pyramid is constructed on both the reference and working images. Afterwards, each image pyramid level will be registered respectively from a coarse to fine and level-by-level basis. A systematic flowchart of the proposed approach is illustrated in Fig 1. The following sections will describe the physical mechanisms of each step in greater detail.
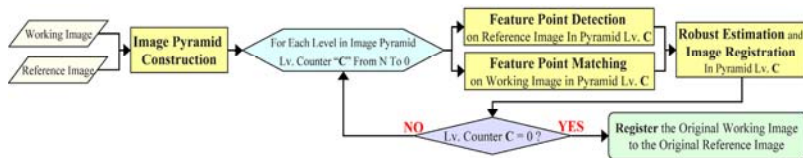
Fig. 1. Flowchart of the proposed approach

2.1   The Construction of Image Pyramid

The purpose of this paper is to register the working image by finding the correct matched feature points in both the working and reference images. However, due to influences from the viewing angle, atmospheric conditions and land cover changes, it is impossible for two temporal images to be exactly the same. Accordingly, the image pyramid concept is employed in the first step. The image pyramid is a hierarchical structure and the original image is the Lv.0 of pyramid. Lv.0 is low-pass filtered and sub-sampled by a factor of two to construct the next pyramid level. Further repetitions of the filter/sub-sample steps generate the remaining pyramid levels. The low-pass-filter properties of the image pyramid not only can reduce the differences between the two images but also increase the efficiency and accuracy of the matching task. Fig. 2 is a simple example in illustrating the advantages of the image pyramid construction procedure. A QuickBird image with a higher spatial resolution (2.4m) is regarded as the reference image, while a FORMOSAT2 image with a lower spatial resolution (8m) is adopted as the working image. Results of the image pyramids of both the QuickBird and FORMOSAT2 images are presented respectively in Fig. 2. Fig. 2(a) and (b) are the original images at the first level of the image pyramid; (c) and (d) are both the images at the second level, (e) and (f) are the images at the third level. Since the image pyramid can improve the accuracy of the matching results, and also shrink the boundary of the search area, its construction is a necessary pre-processing step for the following procedures.
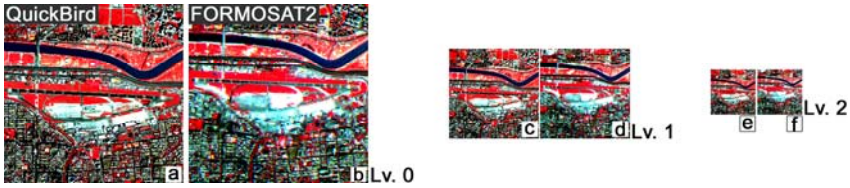
Fig. 2. Illustration of image pyramids. (a) and (b) are original images of QuickBird and FORMOSAT2 at the first level (Lv. 0). (c) and (d) are both images at the second level (Lv.1). (e) and (f) are both images at the third level (Lv.2).

2.2 Detection and Matching of Feature Points

In order to establish the mapping function between the reference and working images in each image pyramid, it is required to find the conjugate points on both images. Hence, the proposed method detects the feature points on the reference image, and searches the matching points on the working image. It is clear that the large amount of well-distributed conjugate points can improve the accuracy of the image registration. The Target Defined Ground Operator (TDGO) is employed in this approach to automatically and uniformly detect a significant number of feature points from the reference image [11]. A bit pattern table is used in TDGO to detect the points with the right-angle features. The bit patterns of feature points are illustrated in Fig. 3(a). In order to quantitatively measure the pattern of a 3 x 3 window, a bit value (BV) calculated from the grey value differences in a 3 x 3 window is defined in Eq. (1) and (2). Therefore, the points that have exactly the same BV's as the patterns of feature points (Fig. 3(a)) will be regarded as the feature points. The advantage of TDGO is the ability of identifying the points with right-angle features, which is critical for image matching. Accordingly, an area-based matching algorithm for each feature point is subsequently applied to find the matching points on the working image. This study selects the Normalized Cross Correlation (NCC) as the objective function for the area-based matching. The NCC measures the correlation via a two blocks' comparison. A higher value of the NCC means a higher probability of the two blocks being similar. Since the NCC is a normalized operation, the matching results will not be influenced by illumination conditions. Thus, the NCC is more suitable for the application of satellite image matching.

$$if \ (\left| G_x - G_i \right| \geq Threshold) \ \ B_i = 2^{i-1} \ \ else \ \ B_i = 0 \qquad i = 1,2,\cdots 8 \qquad (1)$$

$$BV_x = \sum_{i=1}^{8} B_i \qquad\qquad (2)$$

Where G_x is the grey value at pixel x; G_i are the grey value of 8 neighbouring pixels; B_i is the binary code transformed from the grey level differences; the TDGO *Threshold* used in this study is 70 and the BV_x is the Bit Value at pixel *x*.

After the NCC matching procedure, each feature point, which is detected by TDGO on the reference image, can find a matching point with the highest correlation coefficient on the working image. The value of the correlation coefficient is between −1 to 1, where a higher correlation coefficient value signals a higher similarity of two matching blocks. In this study, 0.75 is used as a threshold to evaluate

the matching results. It is deemed successful when the correlation coefficient value is higher than the threshold, and vice versa when it is lower. Fig.3 indicates the results of the feature point detection and matching procedure. The green crosses in Fig. 3(b) denote the feature points, which are detected automatically by TDGO on the reference image pyramid Lv. 1(QuickBird), while the yellow crosses in Fig. 3(c) represent the success matching points on the working image pyramid Lv. 1(FORMOSAT2). The area-based matching technique is a viable tool for finding success matching points. However, if there are several similar features on the searching area (e.g. the corner of building or the central line of the runway), it may lead to incorrect matching results. Consequently, the next logical step is to preserve the correct matching points from the success matching points, and register the working image via the construction of a mapping function.
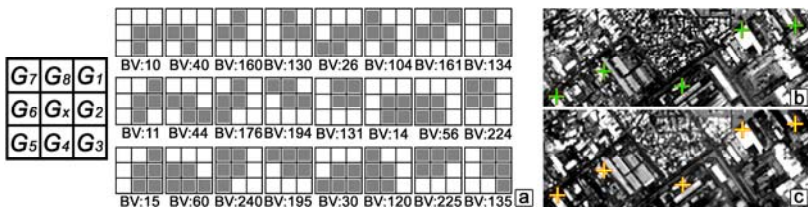
Fig. 3. Results of the feature points detection and matching. (a) Patterns of feature points used in TDGO. (b) Feature points (green crosses) detected on the reference image. (b) Success matching points (yellow crosses) on the working image.

2.3 Robust Estimation and Image Registration

The detection and feature points matching can automatically extract the success matching points on the working image. However, it is difficult to guarantee that the point with the highest similarity will be the correctly matched one. Hence, it is necessary to remove the incorrect matching points, as they decrease the accuracy of the image registration. Therefore, based on the assumption that all of the conjugate points have common transformation parameters, the robust estimation is a powerful criterion in preserving the correct matching points. Since both the working and reference images have been systematically corrected, the assumption used in this step is reasonable. The geometric relation between the working and reference image can be described by the Affine-Transformation in Eq. (3). By using the least squares adjustment, the variation of the observation equation is an important index that notably figures out which point has the largest bias relative to the others. The equations are shown in Eq. (4).

$$X = ax + by + c \qquad Y = dx + ey + f \tag{3}$$

$$
\begin{bmatrix} v_{1_x} \\ v_{1_y} \\ v_{2_x} \\ v_{2_y} \\ \vdots \\ v_{n_x} \\ v_{n_y} \end{bmatrix}_{[2n][1]}
=
\begin{bmatrix}
x_1 & y_1 & 1 & 0 & 0 & 0 \\
0 & 0 & 0 & x_1 & y_1 & 1 \\
x_2 & y_2 & 1 & 0 & 0 & 0 \\
0 & 0 & 0 & x_2 & y_2 & 1 \\
\vdots & \vdots & \vdots & \vdots & \vdots & \vdots \\
x_n & y_n & 1 & 0 & 0 & 0 \\
0 & 0 & 0 & x_n & y_n & 1
\end{bmatrix}_{[2n][6]}
\bullet
\begin{bmatrix} a \\ b \\ c \\ d \\ e \\ f \end{bmatrix}_{[6][1]}
-
\begin{bmatrix} X_1 \\ Y_1 \\ X_2 \\ Y_2 \\ \vdots \\ X_n \\ Y_n \end{bmatrix}_{[2n][1]}
\tag{4}
$$

Where:

n	: Number of success matching points
(X_i, Y_i)	: Coordinates of feature point i in reference image
(x_i, y_i)	: Coordinates of matching point i in working image
(v_{i_x}, v_{i_y})	: Transformation variations of point i in x and y axis
$[a \quad b \quad c \quad d \quad e \quad f]^T$	: Parameters of Affine Transformation

By calculating the variation of each success matching point, the point P_L with the largest variation can be found. If the variation of P_L is larger than the given threshold, it denotes that the accuracy of the matching point P_L is not good enough, where it will be eliminated from the success matching points. The removal of the P_L and the recalculation of the preserved point variations will proceed repeatedly until the largest variation is smaller than the threshold. However, when the working image is totally different with the reference ones, and the number of success matching points is less than 10 points, the robust estimation procedure will stop, resulting in the image registration task to fail. If the procedure of the robust estimation is completed, the working image can be correctly registered to the reference image via the parameters of the Affine Transform. The flowchart of the robust estimation and image registration is illustrated in Fig 4.
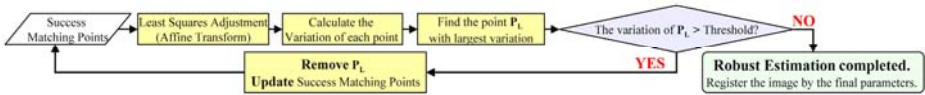
Fig. 4. Flowchart of robust estimation and image registration

As mentioned above, the proposed method is a coarse to fine matching approach, and the image registration task is processed by a level-by-level and coarse-to-fine procedure. Hence, the highest level of the working image pyramid will be registered to the referenced ones during the beginning. Since the working image has already been refined in the previous level, the size of the searching area used in the feature points detection and matching step can be decreased. Moreover, the efficiency and accuracy of the image registration can be improved level-by-level.

3   Experiments

Three different experiments containing the "Multi-sensor", "Multi-temporal" and "Multi-spectrum" images are used to test the practicability and robustness of the proposed approach. The purpose of the "Multi-Sensor" experiment is to test the ability of the proposed approach in robustly correcting the satellite image. A roughly corrected satellite image can register to a well-corrected one by the image registration technique. Therefore, in the "Multi-sensor" experiment, the reference image is a well geometric corrected QuickBird satellite image, where the accuracy of the image is less than 2 meters. The working images used in this experiment are two poor quality corrected FORMOSAT2 images, which are corrected only by the satellite orbit parameters. The error in the image can reach up to 300 meters. Moreover, in order to

perform the robustness test of the proposed method, two images containing clouds and featuring a distinctive black border are selected as the working images. In order to distinguish the reference image from the working one, it is shown in true color in Fig. 5(a), while the two working images are depicted by a false color in Fig. 5(b) and 5(c). The ground coverage of the reference and working images are 3km by 3km and 4km by 4km, respectively. The geometric difference between the reference and working images can be observed clearly in Fig. 5(d) and 5(e) after they are overlapped.
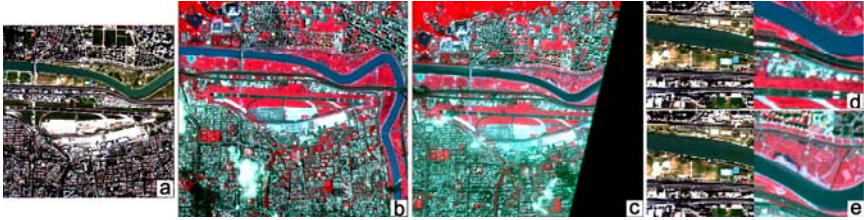
Fig. 5. Test images used in the "Multi-sensor" experiment. (a) Reference image. (b) Working image 1. (c) Working image 2. (d) and (e) are image enlargements of the overlapping reference and working images.

Land change detections are an important application of remote sensing images. However, to ensure a successful change detection, there should be no relative distortion between the temporal images. Since it is difficult to satisfy the condition merely through a systematic geometric correction, the image registration technique serves as a powerful tool in eliminating the relative distortion of the temporal images. Two different sets of images are tested in the "Multi-temporal" experiment. Both the reference and working images are well geo-corrected FORMOSAT2 images and taken respectively on 02/06/2007 and 02/27/2007. The reference images are shown in false color in the left of Fig. 6(a) and 6(c), and the working images are illustrated by a true color in the right. Since both test images are well geo-corrected, there appears to be no obvious geometric gap when the two images are overlapped. However, the small geometric gaps (about 10 meters) can still be observed in both two sets from the border between the two images in Fig. 6(b) and 6(d).
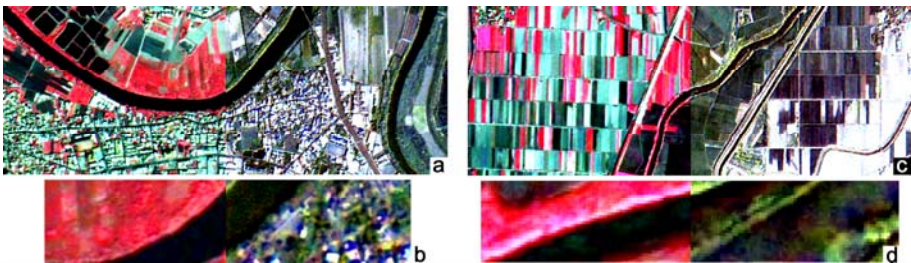
Fig. 6. Test images used in the "Multi-temporal" experiment. (a) The overlapping of the reference and working image 1. (c) The overlapping of the reference and working image 2. (b) and (d) are image enlargements of the overlapping reference and working images.

The "Multi-Spectrum" experiment is designed for image fusion applications. Caused by the different spatial resolution in the multi-spectrum (8m in FORMOSAT2) and panchromatic (2m in FORMOSAT2) images, they undergo the systematic geometric correction by their own respectively. Accordingly, even though the multi-spectrum and panchromatic images were taken within the same time frame, small geometric displacements may still occur. In this experiment, the FORMOSAT2 panchromatic image, which owns a higher accuracy of the image ground position, serves as the reference image. The FORMOSAT2 multi-spectrum image, on the other hand, functions as the working image. The overlapping of the two different images is shown in Fig. 7(a), where an image enlargement is shown in Fig. 7(b). Some displacements are seen to exist between the reference and working image. (Marked by the green circle in the image enlargement).
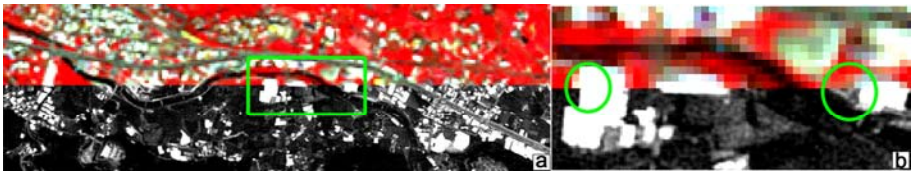
Fig. 7. Test images used in the "Multi-spectrum" experiment. (a) The overlapping of the reference (Panchromatic 2m resolution in bottom) and working (Multi-spectrum 8m resolution in top) images. (b) Image enlargements of the overlapping reference and working images.

4   Results and Discussions

The experimental results in this research were evaluated by overlapping the reference and registered images for visual comparisons, along with calculations of the Root Mean Square Error (RMSE) of the check points in the registration accuracy evaluation. The visual comparison results of the three experiments (Multi-sensor, Multi-temporal and Multi-spectrum) are shown respectively in Fig. 8, Fig. 9 and Fig. 10; the RMSE of the check points are presented in Table 1. Two working images were tested in "Multi-sensor" experiment via the overlapping of the reference and working images. Fig. 8(a) and Fig. 8(b) both demonstrate that the proposed approach can correctly register the Working Image 1 and 2 to the reference ones. Table 1 also indicates that the RMSE of the check points have been substantially decreased to a level less than 2 pixels. Even though the black border and clouds cover resulted in differences between the working and reference images, the proposed approach can still correctly register them. As that the working images used in the "Multi-sensor" experiment were geo-corrected only by the orbit parameters, it is impossible to correct the geometric distortion without the terrain model. Consequently, the roughly geo-corrected working images in the "Multi-sensor" case led to a higher RMSE in the check points.

In the "Multi-temporal" experiment, since both the reference and working image are systematically geo-corrected, the geometric displacement between the temporal images is relatively small (Fig. 9(a)(c)(e) and (g)). However, the proposed approach can still improve the accuracy of the working image to the sub-pixel level (Fig. 9(b)

(d)(f) and (h)). Fig.10 indicates the difference of the fusion results between, before, and after the image registration process in the "Multi-spectrum" experiment. The color-mismatch phenomenon can be clearly observed in the fusion results without the image registration preprocessing (Fig. 10(a) (c) and (e)). The fusion results with the image registration preprocessing are shown in Fig. 10 (b) (d) and (f). As both the figures and the table indicate, the proposed approach can successfully and accurately be applied to the multi-spectrum applications.

Fig. 8. Overlapping of the reference and registered working images in the "Multi-sensor" case. (a) The registration results of Image 1. (b) The registration results of Image 2.
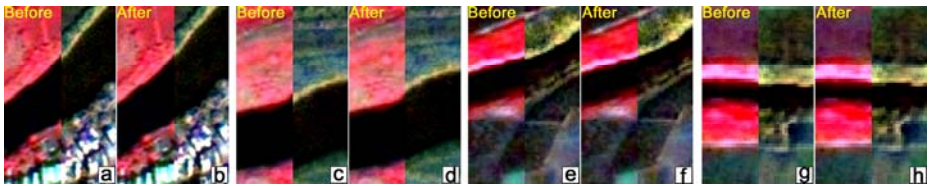
Fig. 9. Overlapping of the reference and working image before and after registration in the "Multi-temporal" case. The image enlargements of the overlapping before the registration are shown in (a) (c) (e) and (g); the results after the registration are shown in (b) (d) (f) and (h).
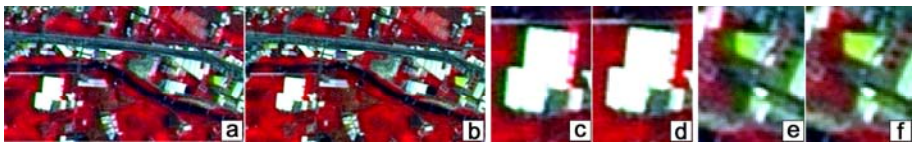
Fig. 10. The fusion results before and after the image registration process in the "Multi-spectrum" case. The fusion results without the image registration are shown in (a), (c) and (e); the fusion result with the image registration preprocessing are shown in (b), (d) and (f).

Table 1. The Root Mean Square Error of the check points before and after the registration

Case	RMSE of Check points (Pixels) *Before* Registration	RMSE of Check points (Pixels) *After* Registration
Multi-Sensor (Image 1/2)	38.9 / 7.1	1.7 / 1.9
Multi-Temporal (Image 1/2)	3.2 / 1.9	0.9 / 0.5
Multi-Spectrum	1.1	0.6

5   Conclusions

This paper introduces a fully automatic approach for an accurate and robust remote sensing image registration. The proposed approach consists of three major steps – Step1: Construction of the image pyramids of both the reference and working image. Step2: In order to establish the geometric relation between the two images, the feature point detection and matching techniques are applied to find the conjugate points. Step3: The working image can be accurately registered to the reference image by the robust estimation. Three different sets of satellite image were designed to test the reliability of the proposed approach. The experimental results indicate it can indeed successfully and accurately register the working image to the reference image. This hold true even if the two images were taken by different sensors or varying time frames and spectrums. These results prove that the proposed approach can successfully be applied as a preprocessing procedure to the remote sensing image application, such as geometric correction, land change detection and image fusion.

References

1. Li, W., Leung, H.: A Maximum Likelihood Approach for Image Registration Using Control Point And Intensity. IEEE Transactions on image processing 13(8), 1115–1127 (2004)
2. Mao, Z., Pan, D., Huang, H., Huang, W.: Automatic registration of SeaWiFS and AVHRR imagery. Int. J. Remote Sensing 22(9), 1725–1735 (2001)
3. Chen, L.C., Teo, T.A., Rau, J.Y.: Optimized patch back-projection in ortho-rectification for high resolution satellite images. In: IAPRS, pp. 586–591 (2004)
4. Mäkelä, T., Clarysse, P., Sipilä, O., Pauna, N., Pham, Q.C., Katila, T., Magnin, I.E.: A Review of Cardiac Image Registration Methods. IEEE Transactions on medical image 21, 1011–1021 (2002)
5. Arun, K.S., Huang, T.S., Blostein, S.D.: Least-squares fitting of two 3-D point sets. IEEE Transactions on Pattern Anal. Machine Intell. PAMI-9, 698–700 (1987)
6. Umeyama, S.: Least-squares estimation of transformation parameters between two point patterns. IEEE Transactions on Pattern Anal. Machine Intell. 13, 376–380 (1991)
7. Van Den Elsen, P.A., Pol, E.D., Sumanaweera, T.S., Her, P.F., Napel, S., Adler, J.R.: Grey value correlation techniques used for automatic matching of CT and MR brain and spine images. In: Proc. SPIE Visualization in Biomedical Computing, vol. 2357 pp. 227–237 (1994)
8. Netanyahu, N., Le Moigne, J., Masek, J.: Geo-Registration of Landsat Data by Robust Matching of Wavelet Features. IEEE Transactions on Geoscience and Remote Sensing 42(7), 1586–1600 (2004)
9. Stone, H.S., Le Moigne, J., McGuire, M.: Image Registration Using Wavelet Techniques. In: Proceedings of SPIE, vol. 3240, pp. 116–125 (1998)
10. Thevenaz, P., Ruttimann, U.E., Unser, M.: A pyramid approach to sub-pixel registration based on intensity. IEEE Transactions on image processing 7, 27–41 (1998)
11. Chen, L.C., Lee, L.H.: Progressive Generation of Control Frameworks for Image Registration. Photogrammetric Engineering and Remote Sensing 58(9), 1321–1328 (1992)

Robust Local Localization of a Mobile Robot in Indoor Environments Using Virtual Corners

Carlos Lara and Leonardo Romero

Universidad Michoacana, Morelia Mich. Mexico

Abstract. This paper deals with the problem of finding the movement of a mobile robot given two consecutive laser scans. The proposed method extracts a line map from the sequence of points in each laser scan, using a probabilistic approach, and then computes *virtual corners* between two lines in the same line map. The movement of the robot is estimated from correspondences of virtual corners between the two line maps. The combination of the probabilistic approach to find lines and the reduced number of virtual corners are the key ideas to get a simple, fast, robust to outliers, and reliable method to solve the local localization problem.

Keywords: Mobile Robotics, Local Localization, Line Based Map.

1 Introduction

A large number of today's mobile robots use a 2D laser range finder as a proximity sensor because it is fast and accurate. The range images given by a laser range finder can be used directly to perform simple tasks. However, most autonomous mobile robot tasks require that a map be built from the environment.

Normally a laser range finder takes measurements on a plane parallel to the floor and each laser scan provides n points from the environment, with each point expressed in polar format (α_i, r_i), $i = 1 \ldots n$, where r_i is the distance from the sensor to the detected object at direction α_i.

The local localization problem consists of finding the relative pose of the robot. One way to solve the localization problem is to register two consecutive range images while the robot is moving, such as those shown in figure 1. In other words, we want to find the best parameters: translation and rotation of the robot $[\Delta x, \Delta y, \Delta \theta]$ that match sensed image (figure 1b) and the reference image (figure 1a). The problem of matching two images is known as *image registration*. An overview of techniques to solve image registration in computer vision is presented in [18].

There are two general methods to solve the registration problem: *area–based methods* and *feature–based methods*[18]. The feature–based methods are recommended if the images to be matched contain enough distinctive and easily detectable objects. The main idea relative to feature based–methods is to find invariant features in both images, find their correspondences, and then estimate the optimal transformation.

It is possible to apply the simple *Iterative Closest Point* (ICP) algorithm [2] directly to the raw points of the two consecutive range images. The ICP can

(a)   (b)

Fig. 1. Two consecutive Range Images

be considered as an area–based method because it uses raw data and does not extract any features from the data.

The ICP algorithm is specially effective when the robot has a good initial estimate of the post–move position. Unfortunately, without a good post–move position estimate, excessive processing time is required to achieve a good estimation. To solve the excessive processing time as well as including some information related to the environment, feature–based methods have been proposed. The kind of feature selected to resolve the image registration problem depends on the application. Many applications use lines, such as in [7]. For indoor mobile robots lines are useful because man–made environments are rich in planar objects. Lines also have a simple model and they are easy to detect.

Several features based on lines have been proposed to solve the laser scan matching problem in indoor environments: complete line segments [17], angles between consecutive or random lines [1], parallel or orthogonal lines [13], corners [9] or statistical information from the original raw data of the lines [6]. Other authors such as [11] [16] [15] select polylines instead of lines because polylines integrate information from several adjacent lines into a single feature. Polylines can be viewed as a generalization of lines or as an approximation of other types of curves.

This paper proposes a feature–based method to find the parameters of the rigid transformation $[\Delta x, \Delta y, \Delta \theta]$ between two range images provided by a laser scan mounted on a mobile robot. In order to do this, the method takes advantage of the angle invariance of any two lines along the point intersection of the lines, these information is merged in a single feature called *virtual corner*. It is important to note that a virtual corner can be produced by two adjacent lines or by any two lines. The method consists in two steps:

1. **Feature detection.** This step first learns a set of lines, called the line map, from both range images. This is done by using a probabilistic search to manage outliers. Then, from each line map a set of virtual corners are calculated, one per each line map.

2. **Feature matching.** In this step every virtual corner of the first image is matched with one or more virtual corners of the second image. Every pair of virtual corners gives a set of parameters for the rigid transformation. To select the best set of parameters, an evaluation function measures the similarity between line maps using only the geometric parameters of their lines and the number of points associated with each line.

This approach has many advantages: it is simple, robust to noise, fast and reliable. In addition, feature detection is based on a probabilistic method to manage outliers. It also avoids the problem of estimate real corners (like [9]), specially when data are noisy, and it takes advantage of the intersection of any two lines. The proposed similarity measure is fast to compute and includes line comparisons and the number of points of each line.

The rest of the paper is organized as follows: section 2 describes the feature detection step and the section 3 describes the feature matching step. Section 4 shows some experimental results, and section 5 presents the advantages and drawbacks of the method and future work.

2   Feature Detection

Given a rigid transformation (translation and rotation only), the angle between any two lines, denoted by $\widehat{l_1 l_2}$, is an invariant. See for instance lines in polar representation $l_1 : (\alpha_1, \rho_1)$ and $l_2 : (\alpha_2, \rho_2)$ shown in figure 2a. If lines l_1' and l_2' in figure 2b correspond to l_1 and l_2 then $\widehat{l_1 l_2} = \widehat{l_1' l_2'}$ or $\widehat{l_1 l_2} \simeq \widehat{l_1' l_2'}$ for real situations where measurements are noisy. While other methods can use length ratios as an invariant, in the case of range images taken by a mobile robot some lines can be detected partially and the length ratio can differ drastically (specially when the robot approaches a door).

Virtual corners are based on the angle invariance of two lines, but also includes the intersection point of the lines. A virtual corner can correspond to a real corner of two adjacent line segments or an imaginary corner if the actual line segments are replaced by their lines. Even two parallel lines have a virtual corner located in the ideal or infinite point where parallel lines meet, see [8] for more information about infinite points. For further processing, a virtual corner of two lines l_1 and l_2 is represented by the intersection point p_{12}, the minor angle $\widehat{l_1 l_2}$ between the lines, and their line's inclinations α_1 and α_2.

This section describes the process of finding *virtual corners* from a range image, this process is comprised of two steps: line map computation and virtual corner detection.

2.1   Computing Line Maps

There are several methods to calculate a set of lines, called line map, $\mathcal{M} = \{l_1 \ldots l_m\}$ from a sequence of points $\mathcal{P} = (p_1 \ldots p_n)$, for an overview see [14]. To manage problems associated with outliers (atypical data) it is preferable to use
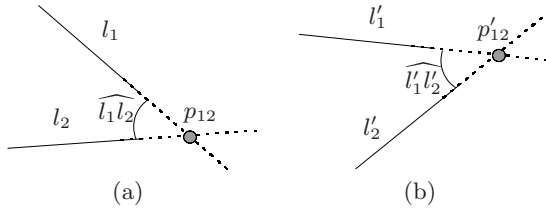
Fig. 2. Angle invariance between two range images

a robust method. We use the *Window Sampled Consensus* (WSAC) algorithm [12] because it is fast and gives good quality line maps. To extract a line the WSAC algorithm is divided in two stages:

Local Search. The local search stage looks for a line l inside a set of t_l consecutive points. As an example figure 3a shows a window with $t_l = 25$ consecutive points. To find the best local line l this stage is based on the well–known RANSAC algorithm [5] and the M–Estimators [10]. If the algorithm successfully finds a local line l then the global fit is performed.

Global Fit. This step looks for other points that fit with the line l, as shown in figure 3b. The global search is comprised by three steps: First the algorithm determines the set of points that support line l by searching into the whole laser scan $\mathcal{P}$. Second, the points that belong to small length segments are removed. This step finds the segments by applying a *Breakpoint Detector* algorithm similar to the one presented in [3]. Finally the line parameters are recomputed using the set of inliers and the line is added to the map $\mathcal{M}$. Figure 3b shows the line l after the global fit, it has three segments: s_1, s_2 and s_3.

An important consideration is that after the global fit the points that belong to l are removed from the laser scan $\mathcal{P}$. The WSAC algorithm tries iteratively the local search step and global fit step to find the line map $\mathcal{M}$.

2.2   Detecting Virtual Corners

Given the line map $\mathcal{M} = \{l_1 \ldots l_n\}$, a set of virtual corners is calculated by intersecting any two lines $l_i, l_j \in \mathcal{M}$. Virtual corners that have point intersection at infinity or at some point far away are removed from the map. The number of possible virtual corners is $O(n^2)$.

3   Feature Matching

In this step, the correspondence between the virtual corners detected in the sensed image and those detected in the reference image is established. For this purpose, every virtual corner in the sensed image is compared against virtual corners in the reference image. Only pairs of virtual corners having similar angles
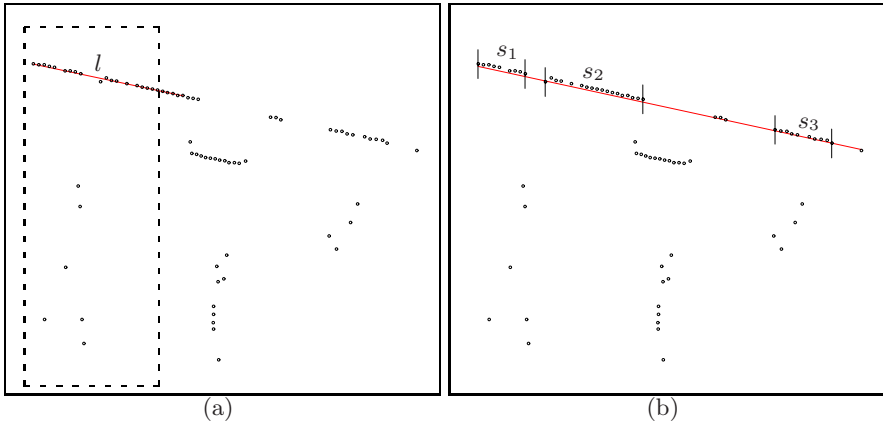
Fig. 3. WSAC Algorithm

are selected. Every pair of virtual corners give a putative set of parameters $[\Delta\theta, \Delta x, \Delta y]$. Given two virtual corners from the reference and the sensed images as the shown in 4a and 4b, the parameter $\Delta\theta$ is calculated from two lines (for instance l_2 and l'_2 in figure 4c), then parameters Δx and Δy are also calculated by aligning virtual corners as shown in figure 4d. Other putative parameters can be calculated by aligning two different lines, for instance l_1 and l'_2. For reducing the complexity and avoiding incorrect estimations the set of parameters must fulfil some requirements, as an example, $|\Delta\theta| < t_\theta$ and $\sqrt{(\Delta x)^2 + (\Delta y)^2} < t_t$, where t_θ and t_t are thresholds that depends on the maximum rotation and translation expected of the robot.

To select the best set of parameters, line maps $\mathcal{M}$ and $\mathcal{M}'$ associated to reference and sensed image respectively, must be compared. To compare them the first step is to transform the line map $\mathcal{M}'$ into $\mathcal{M}'_T$, that is, for each line $l' \in \mathcal{M}'$ new parameters (α'_T, ρ'_T) are calculated considering the putative transformation $T : [\Delta\theta, \Delta x, \Delta y]$. This is done by using:

$$\alpha'_T = \alpha' + \Delta\theta$$
$$\rho'_T = \rho' + \Delta x \cos\alpha' + \Delta y \sin\alpha'$$

To evaluate the similarity S between $\mathcal{M}$ and $\mathcal{M}_T$, we propose the following function;

$$S(\mathcal{M}, \mathcal{M}_T) = \sum_{\substack{l \in \mathcal{M} \\ l'_T \in \mathcal{M}'_T}} s(l, l'_T) \cdot \min(\mathrm{w}, \mathrm{w}') \left(1 - \frac{|\mathrm{w} - \mathrm{w}'|}{\max(\mathrm{w}, \mathrm{w}')} \right) \qquad (1)$$

where w and w' are the number of inliers of l and l'_T respectively and $s(l, l'_T)$ is a similarity value between any two lines $l \in \mathcal{M}, l'_T \in \mathcal{M}'_T$. The measure of similarity between lines was taken from [4]:

$$s(l, l'_T) = \frac{1}{1 + (\Delta\alpha)^2 * \alpha_0 + (\Delta\rho)^2 * \rho_0}$$

where $\Delta\alpha = \alpha - \alpha'$, $\Delta\rho = \rho - \rho'$, and α_0, ρ_0 are constants. The optimal transformation T^* is retrieved as the transformation T which gives the highest value $S(\mathcal{M}, \mathcal{M}'_T)$.
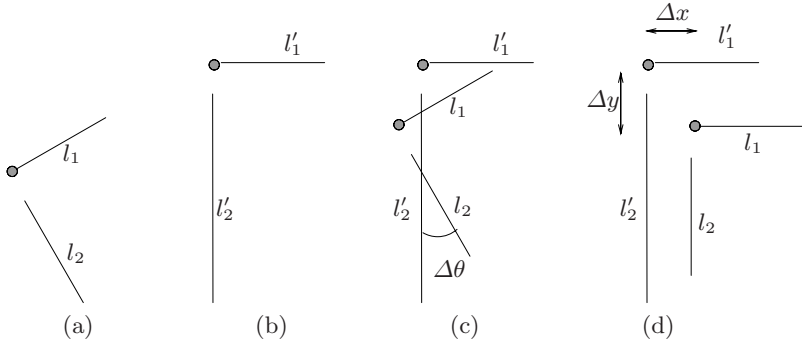
Fig. 4. Aligning two virtual corners. a) A corner in the reference image, b) on the sensed image, c) finding $\Delta\theta$, d) finding Δx, Δy.

4   Experimental Results

The algorithm described above was tested in a set of range images taken by our real mobile robot equipped with a LMS209–S02 SICK Laser Measurement System. Each laser scan covers $180°$ with a lateral resolution of $0.5°$, a total of 361 points per laser scan. The values used for t_θ and t_t were $\frac{\pi}{2}$ and $1m$ respectively.

Figure 5 shows an example of the proposed method using range image 1 and range image 2. The final match achieves the desired result and so the translation of the robot was accurately estimated.

Figure 6 shows a more complex example where the robot rotates and so each laser scan see different parts of the environment. In other words, there are some points in one laser scan which do not correspond to any points in the other laser scan. The final match achieves the desired result and so the rotation of the robot was accurately estimated.

Table 1 shows a summary of the test performed considering 50 movements of the robot, translations ($50cm$) and rotations ($\pm25°$). This table shows the average number of lines detected per laser scan, the average number of virtual points, the total number of virtual corner correspondences, and finally the actual number of correspondences which were evaluated using the similarity measure. As the reader can see, there is a significant amount of correspondences that are not evaluated, because they do not have a similar angle (first filter) or they give translations or rotations greater than t_t or t_θ (second filter).
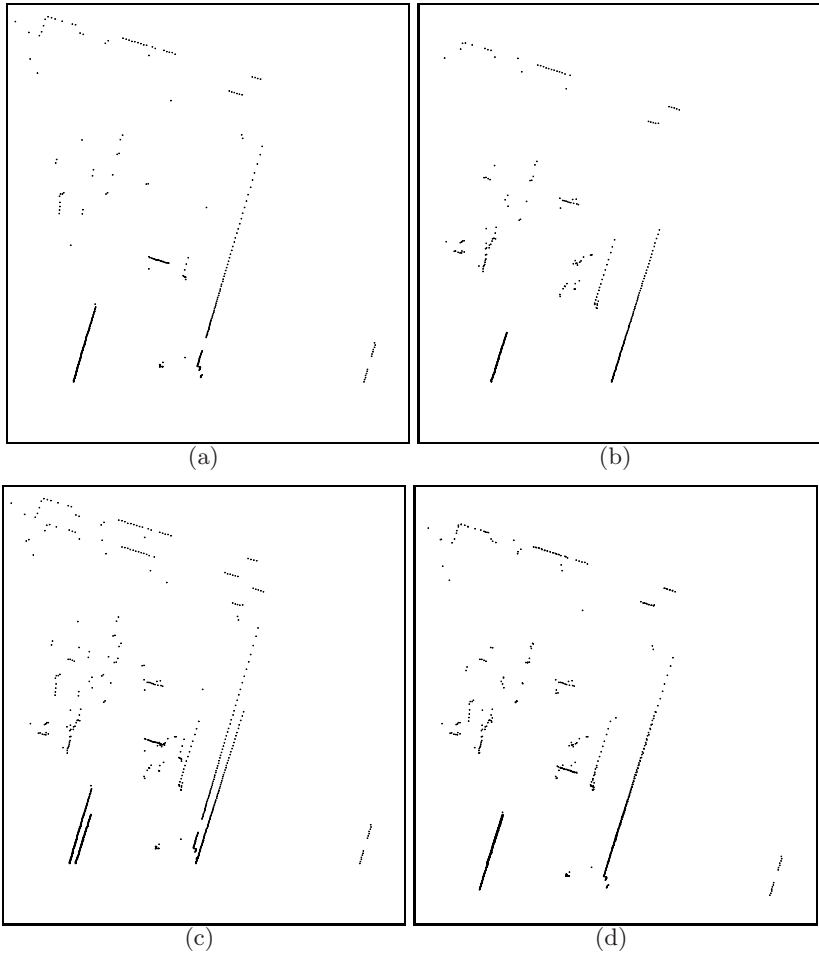
Fig. 5. The robot moves forward: (a) Range image 1, (b) Range image 2, (c) overlapped images with no robot movement and (d) Final match

5   Conclusions and Future Work

Local localization is one of the most important tasks for mobile robots. One way to solve the local localization problem is the registration of consecutive range images provided by a laser range finder. This paper proposes a method that uses virtual corners to solve the localization problem and it does not require an odometric estimation. A virtual corner is a feature that includes geometric information of any two lines discovered in range images. The results show that the method is fast and reliable but requires that almost two reliable virtual corners being discovered: one from the reference image and their equivalent from the sensed image.
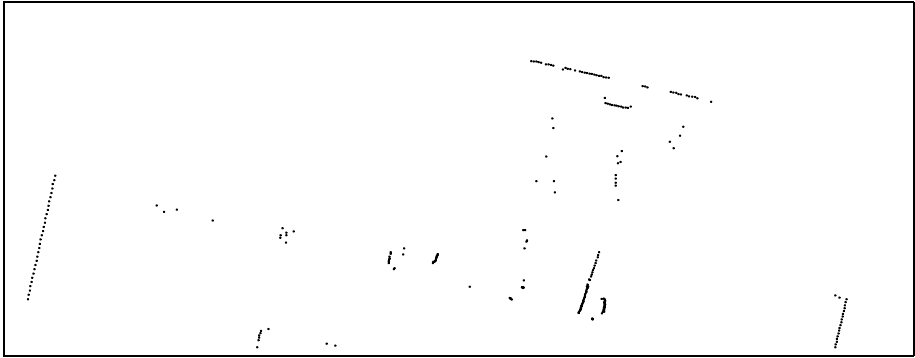
(a) Range image 1
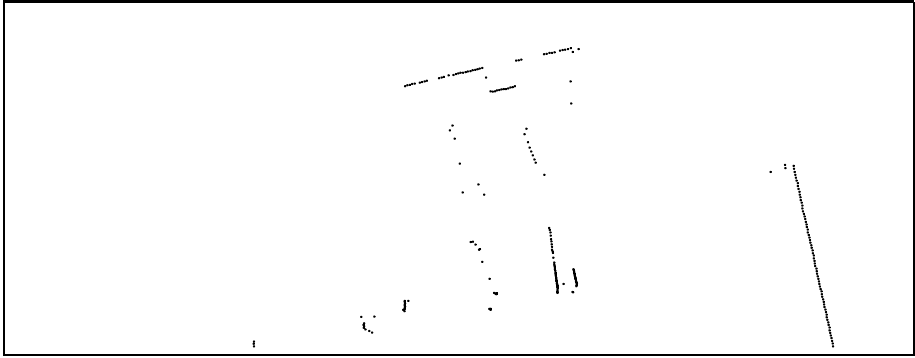
(b) Range image 2
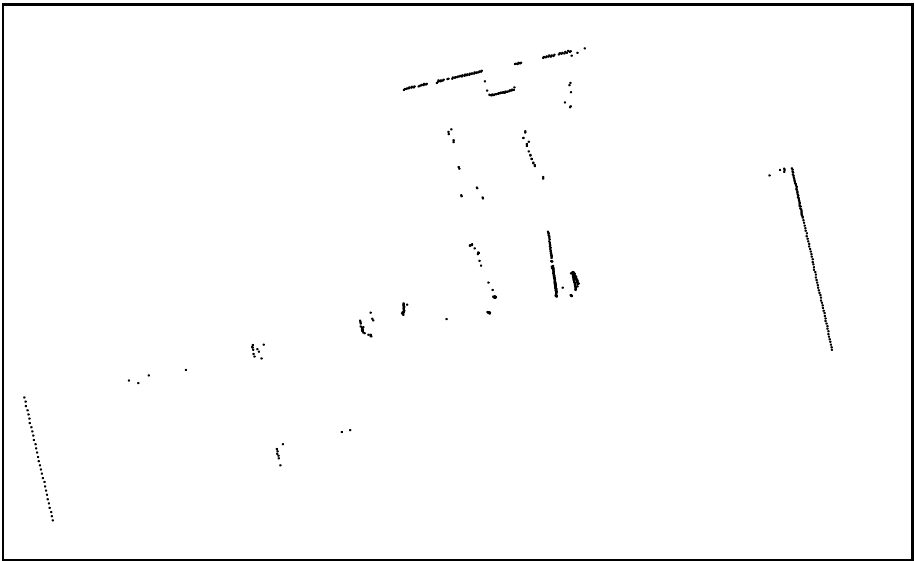
(c) Final match

Fig. 6. Local localization when the robot rotates

Table 1. Results considering 50 movements (translations and rotations) of a mobile robot

Parameter	Average
Lines detected	10.92
Virtual Points	118.36
Correspondences	15148.96
Evaluated Correspondences	160.10

In the near future we are going to include: i) a robust line estimator in the global fit stage, ii) a new filter to reduce the number of correspondence evaluations, for instance clustering results, iii) a new probabilistic similarity measure based on the points supporting lines, and iv) more features such as single points. The goal is to improve the accuracy of the results and the method could be applied to solve the global localization and mapping problems.

References

1. Amigoni, F., Gasparini, S., Gini, M.: Building segment-based maps without pose information. Proceedings of the IEEE 94(7), 1340–1359 (2006)
2. Besl, P.J., Mckay, N.D.: A method for registration of 3-d shapes. IEEE Transactions on Pattern Analysis and Machine Intelligence 14(2), 239–256 (1992)
3. Borges, G.A., Aldon, M.-J.: Line extraction in 2d range images for mobile robotics. J. Intell. Robotics Syst. 40(3), 267–297 (2004)
4. Einsele, T.: Localization in indoor environments using a panoramic laser range finder. PhD thesis, Technische Universit at Munchen (2001)
5. Fischler, M.A., Bolles, R.C.: Random sample consensus: a paradigm for model fitting with applications to image analysis and automated cartography. Commun. ACM 24(6), 381–395 (1981)
6. Garulli, A., Giannitrapani, A., Rossi, A., Vicino, A.: Simultaneous localization and map building using linear features. In: Proceedings of the 2nd European Conference on Mobile Robots (2005)
7. Gros, P., Bournez, O., Boyer, E.: Using local planar geometric invariants to match and model images of line segments. Comput. Vis. Image Underst. 69(2), 135–155 (1998)
8. Hartley, R.I., Zisserman, A.: Multiple View Geometry in Computer Vision, 2nd edn. Cambridge University Press, Cambridge (2004)
9. Hernandez-Alamilla, S., Morales, E.: Global localization of mobile robots for indoor environments using natural landmarks. In: IEEE Conference on Robotics Robotics, Automation and Mechatronics, pp. 1–6 (2006)
10. Huber, P.: Robust Statistics. Wiley, New York (1981)
11. Lakmper, R., Latecki, L.J., Sun, X., Wolter, D.: Geometric robot mapping. In: DGCI, pp. 11–22 (2005)
12. Lara, C., Romero, L.: A robust approach to build 2d line maps from laser scans. Advances in Computer Science and Engineering. Research in Computing Science 19, 197–208 (2006)

13. Nguyen, V., Harati, A., Tomatis, N., Martinelli, A., Siegwart, R.: Orthogonal slam: a step toward lightweight indoor autonomous navigation. In: Proc. of the IEEE-RSJ Int. Conf. on Intelligent Robots and Systems (2006)
14. Sack, D., Burgard, W.: A comparison of methods for line extraction from range data. In: IAV (2003)
15. Veeck, M., Burgard, W.: Learning polyline maps from range scan data acquired with mobile robots. In: IROS (2004)
16. Wolter, D., Latecki, L.J.: Shape matching for robot mapping. In: Zhang, C., W. Guesgen, H., Yeap, W.-K. (eds.) PRICAI 2004. LNCS (LNAI), vol. 3157, pp. 693–702. Springer, Heidelberg (2004)
17. Zezhong, X., Jilin, L., Zhiyu, X.: Map building and localization using 2d range scanner. In: Proceedings 2003 IEEE International Symposium on Computational Intelligence in Mobile Robotics and Automation, pp. 848–853 (2003)
18. Zitova, B., Flusser, J.: Image registration methods: a survey. Image and Vision Computing 21(11), 977–1000 (2003)

An Algorithm for Foreground-Background Separation in Low Quality Patrimonial Document Images

Carlos A.B. Mello

Department of Computing Systems, University of Pernambuco
Recife, Brazil, 50720-001
`carlos@dsc.upe.br`

Abstract. In this article, we present a new algorithm to deal with foreground-background separation in very degraded documents. In particular, our work is applied to patrimonial document images which suffer from several types of degradation as aging effects, noise, back-to-front ink interference, etc. Our main objective is to correctly classify ink and paper to allow an efficient segmentation of the image creating high quality monochromatic images. This makes easier the broadcast of these images through the Internet. The new algorithm is based on the classical Shannon definition of entropy and a generalization defined as Tsallis Entropy and it is compared to 19 well-known classical algorithms, including DjVu algorithm. It achieved the best results by analyzing precision, recall, accuracy, specificity, PSNR and MSE.

Keywords: Document processing, Image thresholding, Entropy.

1 Introduction

This research is part of the DocHist Project [8][9][10] for image processing of historical documents which aims the preservation and broadcast of a file of thousands of patrimonial documents. Even more, it is important to improve the readability of the digital documents. The archive used in this paper is composed of more than 6,500 letters and documents which amounts more than 30,000 pages from the end of the nineteenth century onwards.

For preservation purposes, the documents are digitized in 200 dpi resolution in true color and stored in JPEG file format with 1% loss for better quality/space storage rate. Even in this format each image of a document reaches, in average, 400 KB. In spite of the common use of broadband Internet access nowadays, the visualization of a bequest of thousand of files is not easy. Even in JPEG all the archive consumes Giga Bytes of space. The conversion of the digital images to bi-level comes as a possible solution to this problem.

There are several research efforts in the development of image thresholding or binarization techniques [11]. This is the first step in some image processing applications as optical character recognition (OCR). Threshold algorithms search for a cut-off value that separates object and background in an image. This value defines which colors belong to one or another class. In the case of images of documents these two

classes are the paper (the background) and the ink (the foreground). A good threshold value for this application is one that preserves in the final bi-level image all the information content of the document. This is quite a simple task when one deals with recent documents where, in general, the paper is almost completely clear which is not the case of ancient documents. This type of documents is degraded by the presence of background artifacts. For these cases, image enhancement techniques could be used first to improve the visual appearance of the image for further thresholding.

Images of historical documents present some unique features that make a binarization process very difficult 1) some documents are written on both sides of the paper and the ink from one side passes to the other side, creating a back-to-front interference (also known as bleed-through effect); 2) some paper sheets are very consumed and the paper has darkened over the time (the show-through effect); 3) the last case presents the documents where the ink has faded so much that it has almost the same color as the paper. Examples of these classes of documents can be seen in Fig. 1.
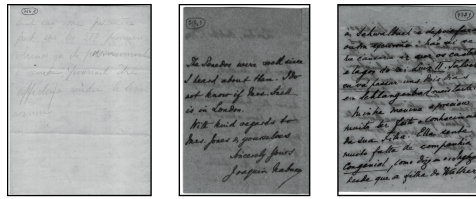
Fig. 1. Sample documents: (left) a very faded document; (center) a document with darkened paper and (right) a document with back-to-front interference

Next Section discusses some of the researches being developed for processing images of historical documents. The new proposed method is fully described in Section 3 and its results are disposed in Section 5, followed by the Conclusions of the paper.

2   Image Thresholding of Patrimonial Documents

Thresholding [11] is a classical problem for image processing. There is a great variety of algorithms defined for this purpose. Most of them are for general use, but there are specific algorithms for historical documents.

Previous works related to image processing of patrimonial documents can be found in literature. The problem of bleed-through interference is dealt in [16] where a canny edge detector is used to detect and to suppress undesired background patterns considering that the writing angle in the foreground opposes the writing angle in the background. This approach, however, does not deal with horizontal and vertical lines as can be found in a handwritten letter "T" for example. The same authors also propose a new method to deal with ink bleeding through the matching of the images from both sides of the paper which is a very difficult task [17].

The authors in [7] propose the use of multi-stage thresholding, *i.e.*, different algorithms are used in different stages of the complete process in order to create the best image possible. The authors propose this and they also claim that global thresholding algorithms must not be used in this kind of images which is not validated in our work.

It is proposed in [3] the use of quadtree decomposition to break down the image into sub-regions and to apply different thresholding algorithms in each of these regions. Background removal is also treated in [6] and [1].

An algorithm for background normalization is proposed in [15] to decrease the background influence and for further binarization. Unfortunately, the method is adjusted only for documents written on just one side of the paper.

A combination of global and local thresholding algorithms is presented in [5] using Iterative Global Thresholding (IGT). Sub-areas *n by n* of the image are analyzed to verify if they have more black pixels than they should have. The authors, however, do not explain how the size of the sub-areas must be defined.

Several well-known thresholding algorithms were tested in the images of our archive. None of them achieved satisfactory results. The tested algorithms are: Brink, C-Means, Fisher, Huang, Iterative Selection, Kapur, Kittler, Li-Lee, Mean Grey Level, Otsu, Percentage of Black, Pun, Renyi, Two Peaks, Wu-Lu, Yager and Ye-Danielsson.. A review of these methods can be found in [13] and the results of the application of some of them are presented in Fig. 2.
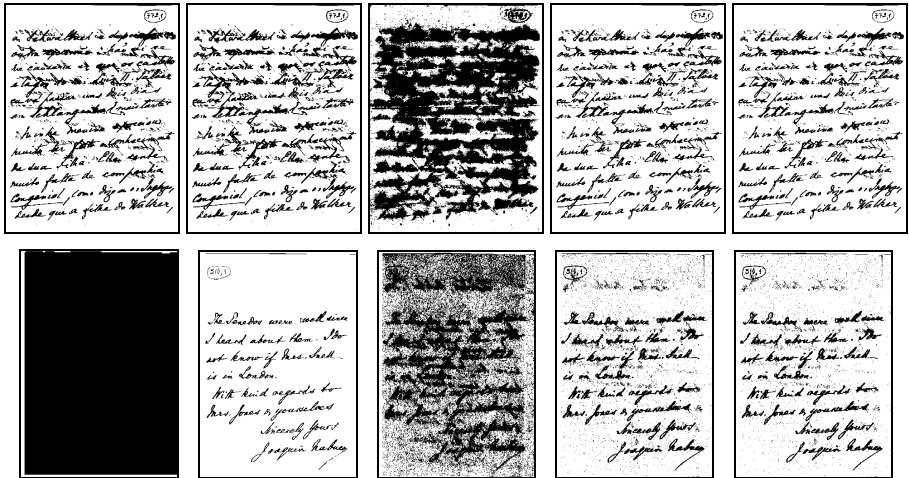
Fig. 2. Application of Brink, Huang, Pun, Percentage of Black and Otsu thresholding algorithms in (top) document of Figure 1-right and (bottom) document of Figure 1-center

3   A New Tsallis-Entropy Based Thresholding Algorithm

Tsallis entropy [18] has been considered a new information measure. It has been used in several image processing applications as Content Based Image Retrieval (CBIR) [12] and even thresholding [19][20] (however both papers present just the possibilities of the use of Tsallis entropy; certain parameters are not clearly specified in them). According to Tsallis, an universal definition of entropy is given by:

$$H_\alpha(S) = \frac{1 - \sum_i p(i)^\alpha}{\alpha - 1} \qquad (1)$$

where $p(i)$ is a probability as in the classical definition of entropy and α is a real parameter. When α tends to 1, Tsallis entropy reduces to Boltzmann-Gibbs entropy:

$$H(S) = -\sum_i p(i)\ln(p(i))$$

Shannon's definition of entropy (H) [14] defines that:

$$H(S) = -\sum_{i=0}^{n} p[s_i]\log(p[s_i]) \tag{2}$$

Eq. 2 settles that if a system can be decomposed into two statistical independent subsystems, say A and B, then H has the extensive or additivity property. This means that $H(A+B) = H(A) + H(B)$. This fact is used in Pun's thresholding algorithm, for example. Tsallis entropy has a nonextensive property for statistical independent subsystems, defined by the following pseudo addivity entropic rule:

$$H_\alpha(A + B) = H_\alpha(A) + H_\alpha(B) + (1 - \alpha)\, H_\alpha(A)\, H_\alpha(B)$$

However, mathematically, Tsallis entropy (Eq. 1) can be broken into two parts:

$$H_\alpha(S) = \frac{1 - \sum_i p(i)^\alpha}{\alpha - 1} = \frac{1}{\alpha - 1} - \frac{1}{\alpha - 1}\sum_i p(i)^\alpha$$

$$H_\alpha(S) = \frac{X_b}{\alpha - 1} + \frac{X_w}{\alpha - 1} - \frac{1}{\alpha - 1}\sum_{i=0}^{t} p(i)^\alpha - \frac{1}{\alpha - 1}\sum_{i=t+1}^{255} p(i)^\alpha$$

$$H_\alpha(S) = \left(\frac{X_b}{\alpha - 1} - \frac{1}{\alpha - 1}\sum_{i=0}^{t} p(i)^\alpha\right) + \left(\frac{X_w}{\alpha - 1} - \frac{1}{\alpha - 1}\sum_{i=t+1}^{255} p(i)^\alpha\right)$$

where $X_b + X_w = 1$. It can be defined then that:

$$H_\alpha(S) = H_{b\alpha}(A) + H_{w\alpha}(B) \tag{3}$$

with

$$H_{b\alpha}(A) = \frac{X_b}{\alpha - 1} - \frac{1}{\alpha - 1}\sum_{i=0}^{t} p(i)^\alpha \tag{4}$$

and

$$H_{w\alpha}(B) = \frac{X_w}{\alpha - 1} - \frac{1}{\alpha - 1}\sum_{i=t+1}^{255} p(i)^\alpha \tag{5}$$

In the equations above, t is the threshold value. In our case, t is the most frequent color in the image. It is reasonable to consider that this most frequent color is part of the background. $H_{b\alpha}$ is the entropy of the pixels below the color t and $H_{w\alpha}$ is the entropy of the colors above the threshold t. The variable t is also used to define the values of X_b and X_w, as X_b is the percentage of colors below t and X_w is the percentage of colors above t.

The α parameter is a real number and it characterizes the degree of nonextensivity. Its value is not fixed in Tsallis definition. For thresholding purposes, variations in this value can modify the cut-off value. For our project, α is equal to 0.3 for the most part of the images, changing in just one case as further explained.

At first, the document images are separated into classes. There are three main classes of documents:

- Class 1: documents with few parts of text or documents where the ink has faded;
- Class 2: common documents with around 10% of text elements;
- Class 3: documents with more black elements than it should have; this includes documents with a black border or documents with bleed-through effect.

In order to classify an image as one of these classes, we evaluate Shannon entropy (*H*) using Equation 2 but with the logarithmic basis taken as the product of the dimensions of the image. As defined in [4], changes in the logarithmic basis do not alter the definition of the entropy. The previous three classes of documents are defined by:

- *H ≤0.26*: Class 1 documents;
- *0.26 < H < 0.30*: Class 2 documents;
- *H ≥0.30*: Class 3 documents.

These boundaries were defined in previous works [9][10] and they were adjusted in our new proposal. For example, the sample documents of Fig. 1 belong, from left to right, to classes 1 (*H = 0.23*), 2 (*H = 0.29*) and 3 (*H = 0.32*).

The entropy value can be broken into the entropy of black pixels, *Hb*, and the entropy of the white pixels, *Hw*, bounded by a threshold *t*:

$$Hb = -\sum_{i=0}^{t} p[s_i]\log(p[s_i])$$

$$Hw = -\sum_{i=t+1}^{255} p[s_i]\log(p[s_i])$$

(6)

In our case, *t* is the most frequent color of the image.

For each of these classes, an analysis must be made to process the images that belong to them as can be seen next. The final threshold value, *th*, is defined by:

$$th = mb * H_{b\alpha} + mw * H_{w\alpha}$$

where *mb* and *mw* are multiplicative constants that are going to be defined for each class. $H_{b\alpha}$ and $H_{w\alpha}$ can be seen as projections of the $H\alpha$ value; changes in those values (generated by the product by *mw* or *mb*) produces changes in $H\alpha$ itself.

Class 1 Documents:
As said before, this class involves documents with few ink elements or few text parts. This can happens in cases where the letter has just few words or the ink has faded. In this class, we can also find most part of the typewritten documents as, in general, the typewriter ink is not so strong as handwritten characters making them more susceptible to degradation of their colors.

Although the images of this class have similar features in some way, they differ in basic aspects as, for example, typewritten documents must occupy a complete sheet of paper (opposing the fact that this class groups documents with few text parts). Because of this, another aspect must be considered within this class. We must consider the distribution of the pixels of the original image using the values of *Hw* or *Hb*. We choose *Hw* with no loss of generality. For these kind of images, we have:

- If ($Hw \geq 0.1$), then $mb=2.5$ and $mw=4.5$ (typewritten documents with dark ink and bright paper);
- If ($0.08 < Hw < 0.1$), then $mb=mw=6$ and $\alpha=0.35$ (documents with the ink faded);
- If ($Hw \leq 0.8$), then $mb=mw=4$ (documents with dark ink and paper).

Class 2 Documents:

The most common documents just need a boost in $H_{b\alpha}$ and $H_{w\alpha}$ to achieve the best threshold value. So, in general, the algorithm defines $mb = 2.2$ and $mw = 3$. Some darkened documents need another treatment. If a document belongs to class 2 and $Hw > 0.1$, then the value of mw decreases by half (i.e., $mw = 1.5$), unless the most frequent color is greater than 200 (brighten documents) for which $mw = 9$. Fig. 6 shows sample documents from class 2 darkened or not and their bi-level images.

Class 3 Documents:

These are the documents with more black pixels than expected in a normal document. In this class, we have documents with a black border or documents with back-to-front interference. As the ink from one side transposes to the other side, it creates an intermediary element in the image: there is no more just paper or background; the transposed ink is an element between them. In these cases, there is no need to increase the dark measures. The system must deal just with the paper and the transposed ink turning them to white. Because of this, the mb parameter is fixed as 1. In most documents, we have $mw = 2$. Some cases, however, must be considered when the documents have brightened paper again. In this class, brighten paper documents are the ones with most frequent color (t) greater than 185:

- If ($t >= 185$) then
    - If ($0.071 < hw < 0.096$) then $mw = 9$;
    - If ($0.096 <= hw < 0.2$) then $mw = 6$;

4   Results

The proposed algorithm was tested in a set of 200 images that are considered representative of the complete file. The results were considered very satisfactory by visual inspection. However a most objective measure is also necessary. In this set, 18% of the documents belong to the class 1, 40% are from class 2 and 42% from class 3.

To make a quantitative evaluation of the performance of the new algorithm, its results are compared against the ground truth knowledge (an ideal image with the background removed manually). This comparison is made using the concepts of: precision, recall, accuracy and specificity. In order to use a more automatic process, our analysis is based on the number of pixels correctly classified as paper or ink. For this purpose the ideal image is considered as what should be the final target of the algorithm. With this in mind, we can have the number of ink pixels correctly classified as ink (TP - True Positives), the number of pixels correctly classified as paper (TN - True Negatives), the number of pixels misclassified as ink (FP - False Positive) and number of ink elements misclassified as paper (FN - False Negative), defining:

Precision = TP/(TP + FP)   Recall = TP/(TP + FN)
Accuracy = (TP + TN)/(TP + TN + FP + FN)   Specificity = TN/(FP + TN)

Based on these measures, a good algorithm must have:

- Precision=1: there were no misclassification of the paper elements (FP = 0);
- Recall=1: there were few mistakes in the classification of the ink elements (FN=0);

- Accuracy=1: there was no misclassification at all (FP + FN=0);
- Specificity=1: every pixel that belongs to the paper were classified as that (FP=0).

Table 1 presents the average result for these four measures applied to a set of 200 documents binarized by the new proposed algorithm and classical algorithms in comparison with their ideal versions. Our algorithm achieved very good values for the four measures. We also analyzed the values of PSNR (*Peak Signal-to-Noise Ratio*) and MSE (*Mean Square Error*). Their average values are also presented in Table 1.

Table 1. Average values of precision, recall, accuracy, specificity, PSNR and MSE in a set of 200 bi-level documents generated by the new proposal and classical methods compared with their ideal version generated manually

Algorithm	Precision	Recall	Accuracy	Specificity	PSNR	MSE
New Algorithm	**0.82**	**0.88**	**0.97**	**0.98**	**21.65**	**0.03**
Brink	0.91	0.69	0.95	0.98	20,91	0.06
C-Means	0.88	0.79	0.93	0.99	15.61	0.27
Fisher	0.95	0.51	0.73	0.99	20.97	0.06
Huang	0.88	0.80	0.94	0.99	20.63	0.07
Iterative Selection	0.38	0.48	0.94	0.94	20.27	0.06
Kapur	0.88	0.79	0.93	0.98	20.30	0.05
Kittler	0.94	0.73	0.96	0.99	16.33	0.11
Li-Lee	0.00	0.57	0.89	0.89	20.13	0.04
Mean Grey Level	0.95	0.71	0.96	0.99	20.21	0.07
Otsu	0.81	0.81	0.97	0.98	21.18	0.03
Percentage of Black	0.99	0.23	0.63	0.99	19.20	0.05
Pun	0.94	0.69	0.93	0.99	10.41	0.37
Renyi	0.88	0.77	0.93	0.99	19.54	0.07
Two Peaks	0.87	0.82	0.95	0.98	8.49	0.62
Wu-Lu	0.94	0.71	0.95	0.99	18.89	0.06
Yager	0.99	0.17	0.39	0.91	21.37	0.05
Ye-Denielsson	0.87	0.77	0.93	0.99	19.86	0.05

We should expect that the perfect algorithm must have the four measures next to 1, high PSNR value and low MSE value. So a good algorithm must have all these features at the same time. Our new proposal has the higher PSNR and lower MSE. For precision, recall, accuracy and specificity, other algorithms achieved satisfactory results (as Otsu, Brink, Mean Grey Level, Huang) but our algorithm has a better performance in average.

Table 2 presents a second test as our algorithm is compared to images generated by DjVu technology [2] which is defined specifically for document image thresholding and compression. Table 2 shows the average and standard deviation values of the

same measures as before, comparing the images generated by our algorithm and the ones created by DjVu and the ideal images.

Fig. 3 presents some very difficult images and the results of the application of the algorithm. In particular, Fig. 3–left presents the same document of Fig. 1-left. This is the best response ever achieved by an automatic algorithm for this image without any pre-processing technique for contrast enhancement.

Table 2. Average and standard deviation values of precision, recall, accuracy, specificity, PSNR and MSE in a set of 200 bi-level documents generated by the new proposal and DjVu technique in comparison with their ideal versions

Measure		DjVu	New Algorithm
Precision	Average	0.90	0.82
	Standard Deviation	0.12	0.12
Recall	Average	0.72	0.88
	Standard Deviation	0.24	0.09
Accuracy	Average	0.90	0.97
	Standard Deviation	0.20	0.01
Specificity	Average	0.99	0.98
	Standard Deviation	0.01	0.02
PSNR	Average	19.60	21.65
	Standard Deviation	0.10	2.03
MSE	Average	0.90	0.03
	Standard Deviation	0.12	0.01

Fig. 4 presents a document with differences of illumination along it. Even with this problem, our algorithm reached the best global threshold value possible as it can be seen in the comparison with classical well-known algorithms as Otsu and DjVu, which results are presented in the center part of this figure.
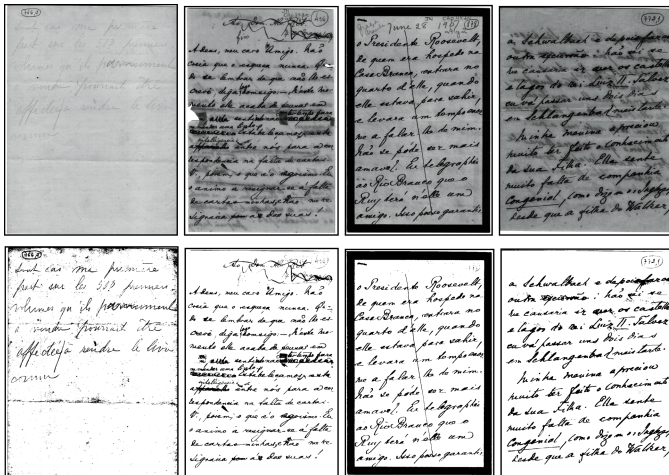
Fig. 3. (top) Sample documents and (bottom) their bi-level images produced by the new algorithm

Other sample document from another database is shown in Fig. 5. This document is available at http://www.site.uottawa.ca/~edubois/documents. Fig. 5 presents a zooming into one of these documents and the binary versions generated by Otsu and our new algorithm. Again, our method achieved higher values of precision, recall, accuracy, specificity, PSNR and lower value of MSE. This shows that our method can be applied to other databases of similar features.
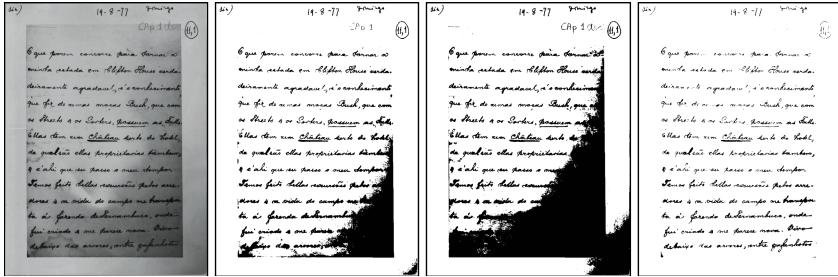
Fig. 4. (left) A document with different illumination along it, (right) the binarization produced by our new algorithm and at the center the results of the application of Otsu and DjVu algorithms
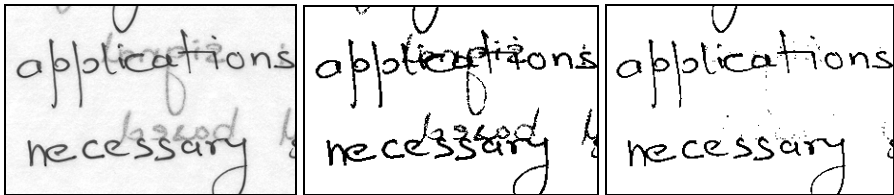
Fig. 5. (left) Zooming into another sample document from a different database; (center) bi-level image generated by Otsu algorithm and (right) the one produced by our new algorithm

5 Conclusions

This paper presents a new entropy-based thresholding algorithm for images of historical documents. The algorithm uses both Shannon and Tsallis definition of entropy to find the best cut-off value. The algorithm was applied in a set of 200 representative images of a file from the 19th century and beginning of the 20th century. The use of the algorithm was analyzed by visual inspection and by comparison with perfect bi-level images. The values of precision, recall, accuracy and specificity were evaluated for the complete set and the algorithm achieved satisfactory results.

Three classes of documents are identified using the classical Shannon entropy definition. After this, a set of rules is used to define the best threshold value. For this, Tsallis entropy is separated into two components which are boosted in order to define the cut-off value. The method proved to be very effective as could be analyzed using precision, recall, accuracy, specificity, PSNR and MSE metrics in comparison with several well-known thresholding algorithms, including the DjVu technique.

References

1. Antonacopoulos, A., Castilla, C.C.: Flexible Text Recovery from Degraded Typewritten Historical Documents. In: Int. Conf. on Pattern Recognition, pp. 1062–1065, Japan (2006)
2. Bottou, L., Haffner, P., Howard, P.G.: High Quality Document Image Compression with DjVu. Journal of Electronic Imaging, 410–425 (1998), http://www.djvu.org
3. Chen, Y., Leedham, G.: Decompose algorithm for thresholding degraded. Historical document images, Vision, Image and Signal Processing 152(6), 702–714 (2005)
4. Kapur, J.N.: Measures of Information and their Applications. J.Wiley & Sons, Chichester (1994)
5. Kavallieratou, E., Stamatatos, E.: Improving the Quality of Degraded Document Images, Int. Conf. on Document Image Analysis for Libraries, pp. 340–349, France (2006)
6. Kennard, D.J., Barrett, W.A.: Separating Lines of Text in Free-Form Handwritten Historical Documents. In: Int. Conf. on Document Image Analysis for Libraries, pp. 12–23, France (2006)
7. Leedham, G., et al.: Separating Text and Background in Degraded Document Images - A Comparison of Global Thresholding Techniques for Multi-Stage Thresholding. In: International Workshop on Frontiers in Handwriting Recognition, pp. 244–249, Canada (2002)
8. Mello, C.A.B., et al.: Image Thresholding of Historical Documents: Application to the Joaquim Nabuco's File. In: Digital Cultural Heritage Conference - Eva Vienna, pp. 115–122, Vienna, Austria (2006)
9. Mello, C.A.B.: Image Segmentation of Historical Documents: Using a Quality Index. In: International Conference on Image Analysis and Recognition, pp. 209–216, Portugal (2004)
10. Mello, C.A.B., et al.: Image Segmentation of Historical Documents. Visual (2000), Mexico (2000)
11. Parker, J.R.: Algorithms for Image Processing and Computer Vision. John Wiley & Sons, Chichester (1997)
12. Rodrigues, P.S., et al.: Using Tsallis Entropy into a Bayesian Network for CBIR. In: Int. Conf. on Image Processing, pp. 1028–1031, Genova (2005)
13. Sezgin, M., et al.: Survey over image thresholding techniques and quantitative performance evaluation. Journal of Electronic Imaging, vol. 13(1) (2004)
14. Shannon, C.: A Mathematical Theory of Communication. Bell System Technology Journal 27, 370–423 (1948)
15. Shi, Z., Govindaraju, V.: Historical Document Image Enhancement Using Background Light Intensity Normalization. In: International Conference on Pattern Recognition, pp. 473–476, UK (2004)
16. Tan, C.L., et al.: Removal of Interfering Strokes in Double-Sided Document Images. In: Workshop on Applications of Computer Vision, pp. 16–21, USA (2000)
17. Tan, C.L., et al.: Restoration of Archival Documents Using a Wavelet Technique. IEEE Trans.on Pattern Analysis and Machine Intelligence 24(10), 1399–1404 (2002)
18. Tsallis, C.: Possible Generalization of Boltzmann-Gibbs statistics. Journal of Statistical Physics 52(1-2), 479–487 (1988)
19. Yan, L., et al.: An Application of Tsallis Entropy Minimum Difference on Image Segmentation, World Congress on Intelligent Control and Automation, pp. 9557–9561, China (2006)
20. Yan, L., et al.: Image Segmentation based on Tsallis-entropy and Renyi entropy and Their Comparison. In: Int. Conf. on Industrial Informatics, pp. 943–948, Singapore (2006)

Information Extraction and Classification from Free Text Using a Neural Approach

Ignazio Gallo and Elisabetta Binaghi

Department of Computer Science and Communication
Universitá degli Studi dell'Insubria
via Mazzini 5, Varese, Italy
ignazio.gallo@uninsubria.it
http://www.uninsubria.eu/

Abstract. Many approaches to Information Extraction (IE) have been proposed in literature capable of finding and extract specific facts in relatively unstructured documents. Their application in a large information space makes data ready for post-processing which is crucial to many context such as Web mining and searching tools. This paper proposes a new IE strategy, based on symbolic and neural techniques, and tests it experimentally within the price comparison service domain. In particular the strategy seeks to locate a set of atomic elements in free text which is preliminarily extracted from web documents and subsequently classify them assigning a class label representing a specific product.

Keywords: Information Extraction, Neural Network, Text Classification.

1 Introduction

With the Internet becoming increasingly popular, more and more information is available in a relatively free text format. This situation creates the premise for efficient on line services and Web mining application in several domains. The on line availability of ever larger amounts of commercial information, for example, creates the premise for profitable *price comparison services* allowing individual to see lists of prices for specific products.

However critical aspects such as information overload, heterogeneity and ambiguity due to vocabulary differences limit the diffusion and usefulness of these advanced tools requiring expensive maintenance and frustrating users instead of empowering them.

To address these problems, efficient *Information Extraction* (IE) techniques must be provided capable of finding and extract specific facts in relatively unstructured documents. Their application in a large information space makes data ready for post-processing which is crucial to many context such as Web mining and searching tools.

Information extraction programs analyze a small subset of any given text, e.g., those parts that contain certain trigger words, and then attempt to fill out a fairly simple form that represents the objects or events of interest. An IE task is defined by its input and its extraction target. The input can be unstructured documents like free text that are written in natural language (e.g., Fig. 1) or the semi-structured documents that abound on the Web such as tables or itemized and enumerated lists (e.g., Fig. 2). The extraction target

> The Motorola RAZR V3i is fully loaded* - delivering the ultimate combination of design and technology. Beneath this sculpted metal exterior is a lean mean, globe-hopping machine. Modelled after the Motorola RAZR V3, the RAZR V3i has an updated and streamlined design, offering consumers a large internal color screen, . . .

Fig. 1. An unstructured document written in natural language that describes the product 'Motorola RAZR V3i'

Fig. 2. Semi-structured documents written in natural language that describes a set of products

of an IE task can be a relation of k-tuple (where k is the number of attributes in a record) or it can be a complex object with hierarchically organized data.

Many approaches to IE have been proposed in literature and classified from different points of view such as the degree of automation [1], type of input document and structure/constraint of the extraction pattern [2].

This paper proposes a new IE strategy and tests it experimentally within the price comparison service domain. Most price comparison services do not sell products themselves, but show prices of the retailers from whom users can buy. Since the stores are heterogeneous and each one describes products in different ways (see example in Fig. 3), a generic procedure must be devised to extract the content of a particular
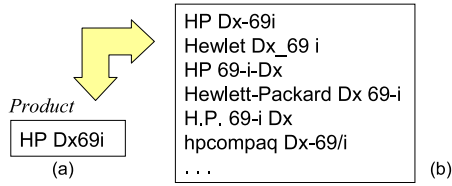
Fig. 3. List of potential descriptions in (b) that may be used to describe product (a)

information source. In particular our IE strategy seeks to locate a set of atomic elements in free text preliminarily extracted from web documents and subsequently classify them accordingly. In this context, our principal interest is to extract, from a textual description, information that identify a commercial product with an unambiguous label in order to be able to compare prices. In our experiments product price was associated to the description, therefore its extraction is not necessary.

Following the terminology used by Chang et. al[3] the salient aspects are

– an hybrid solution for building thesaurus based on manual and supervised neural technics
– a tree structured matcher for identifying meaningful sequences of atomic elements (tokens);
– a set of logical rules which interpret and evaluate distance measures in order to assign the correct class to documents.

2   System Overview

The IE system developed is composed of two main parts, *matcher* and *classifier*, and acts on free text documents obtained from original web documents. It specifically addresses the following problems typical of the price comparison service information space: an attribute may have zero (missing) or multiple instantiations in a document; various permutations of attributes or typographical errors may occur in the input documents (see an example in Fig. 3).

Prior to both matching and classification phases the *tokenizer* divides the text into simple tokens having the following nature:

– **word:** a word is defined as any set of contiguous upper or lowercase letters;
– **number:** a number is defined as any combination of consecutive digits.

2.1   Matcher

In our context the matcher has to operate on specific annotations that can be matched to brands (B) and models (M) of products enlisted in the price comparison service. The matcher is then constructed starting from a set $KB = \{(b, m) | b \in B, m \in M_b\}$ that contains the couples formed by a brand b and a model m. b belongs to the set of brands B of a given category of products, while m belongs to the set of models M_b that have b as brand.

A thesaurus that collects all the synonyms commonly used to describe a particular category of products is used to extend the *KB*. In particular if there are one or more synonyms in the thesaurus for a couple (b, m) then we add a new couple $(\bar{b}, \bar{m})$ to the *KB* for each synonym.

The tokenizer associates with every couple in the KB a sequence of tokens $T_{b,m} = (t_1^b, t_2^b, \ldots, t_1^m, t_2^m, \ldots)$ where t_i^b and t_j^m are all the tokens obtained from the brand b and the model m respectively. Every sequence $T_{b,m}$ is used to construct a path within the matcher tree structure: it starts from the first node associated with token t_1^b and arrives at a leaf node associated with the label derived from (b, m) (see example in Fig. 4).
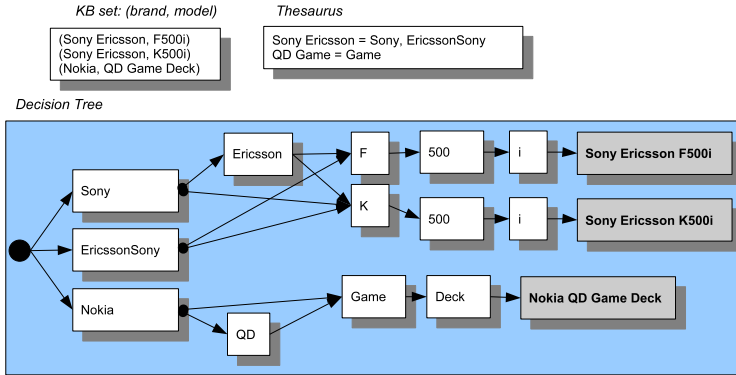
Fig. 4. An example of KB set and thesaurus used to build the matcher
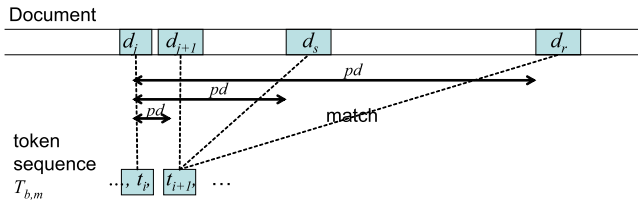
Fig. 5. Role of edit distance and position distance during the matching process. In case of tokens having equal ed measure ($ed(t_{i+1}, d_{j+1}) = ed(t_{i+1}, d_s) = ed(t_{i+1}, d_r)$) the token d_{j+1} with minimum pd is selected

Based on these solutions, the IE task is accomplished splitting an input document into a tokens sequence $(d_1, d_2, \ldots)$. Starting from the root node the search for the subsequent node (better match in the subsequent layer) is performed using the concept of *edit distance* (ed) between input tokens and every token of a tree's layer and the *position distance* (pd) between two matched input tokens. The *edit distance* between two tokens measures the minimum number of unit editing operations of *insertion, deletion, replacement of a symbol*, and *transposition of adjacent symbols* [4] necessary to convert one token into another. The *position distance* measures the number of tokens d_i found between two matched d_j d_k tokens that would have to be consecutive

The system first searches a sequence of perfect match ($\sum ed = 0$) that leads to recognition of all the tokens t_i^b associated with one brand. In this way we obtain a list of possible brands associated with the input document. Starting from the last node (with token t_i^b) of a matched brand, the algorithm begins the search for the most probable model. The system searches all the paths that lead to a leaf node with the sum of ed equal to zero. If this is not possible the system returns the path with minimum ed.

In case of a token t_i with multiple match $(d_j, d_k, \ldots)$, with identical minimum ed, the input token with minimum pd (compared to the parent token in the tree) will be selected (see example in Fig. 5).

2.2 Classifier

A rule based classifier was designed with the aim of assigning a class label representing a specific product to each document using the information extracted from the matching phase.

The classifier receives in input the output of the matcher i.e. the set of matched sequence $T_{b,m}$ of tokens weighted as a function of the ed. These input values are used to construct a sub-tree of the Matcher starting from which the classifier computes the class of the given document.

The set of predefined classes is constituted by all the products (b, m) inserted in the KB. The classifier selects a class from a subset obtained by the input set of matched sequence $T_{b,m}$ (there is one class for each matched sequence).

Position and edit distances are evaluated to decide class assignment: the classifier start from the leaves of the sub-tree and at each step compares each node t_{ij} with its parent t_{i-1} using the following rules:

- select the node t_{ij} having minimum $pd(t_{ij}, t_{i-1})$ for each j or with minimum average pd computed through all the seen tree nodes;
- in case of a node t_{ij} with multiple match associated with its parent t_{i-1}, with identical minimum ed, the input token t_{i-1} with minimum pd will be selected (see example in Fig. 6);
- between two nodes t_{ij} with identical weight $(ed + pd)$ in the same layer i, select that with a greater path starting from the leaf node;
- if all the previous rules find no differences between two nodes t_{ij} and its parent t_{i-1} then selects that with minimum pd computed by the matcher.
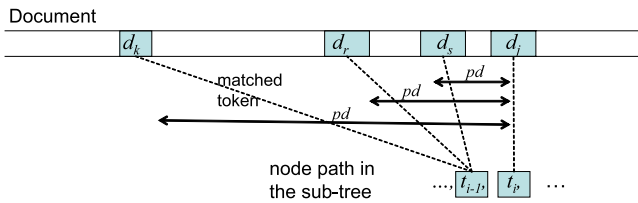
Fig. 6. Role of edit distance and position distance during the classification process. In case of tokens having equal ed measure ($ed(t_{i-1}, d_k) = ed(t_{i-1}, d_r) = ed(t_{i-1}, d_s)$) the token d_s with minimum pd is selected.

3   Automatic Thesaurus Building

The accuracy strongly depends on the completeness of the thesaurus. Unfortunately, thesaurus maintenance is an expensive process. The present work proposed a neural adaptive tool able to support thesaurus updating.

The main idea of our solution is to automatically induce from examples general rules able to identify the presence of synonyms within sequences of tokens produced by the matcher. These rules, difficult to hand-craft and define explicitly, are obtained adaptively using neural learning. In particular, a Multilayer Perceptron (MLP) [5] is trained to receive in input the following types of features from the sequence of matched tokens:

- edit distance between the tokens
  $(t_1^b, t_2^b, \ldots, t_1^m, t_2^m, \ldots)$ of the *KB* and tokens found in the document;
- number of characters between two consecutive tokens found in the document;
- typology of found tokens (word or number);
- bits that identify the presence of each token.

As illustrated in Fig. 7, each pattern is divided into four groups of P features, where P represents the maximum number of tokens obtainable from a product (b, m).
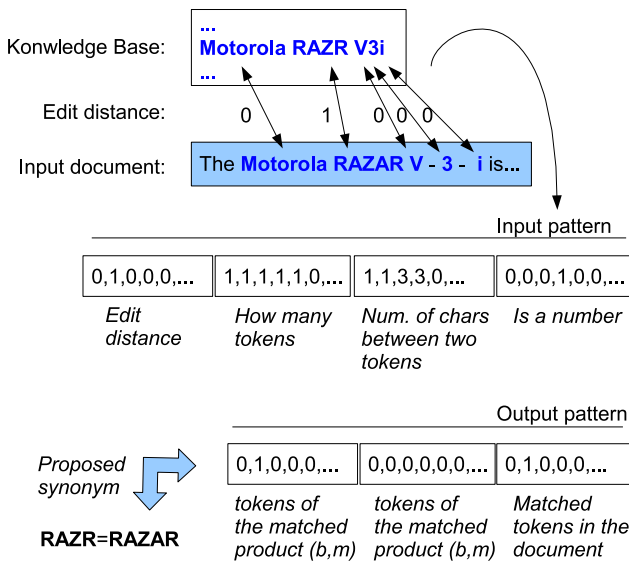
Fig. 7. An example of input pattern/output construction for the MLP model

The output pattern identifies a synonym $\bar{S}$ of S, where S is a particular sequence of tokens extracted from $T_{b,m}$, and $\bar{S}$ is a different sequence of tokens extracted from $T_{b,m}$ or from the sequence of matched token of the document. Each output pattern has a dimension equal to $3P$. The output of the trained neural network is used to add a new item $S = \bar{S}$ to the thesaurus: when an output neuron has a value greater than a threshold, the corresponding token will be considered part of a synonym.

4   Experiments

The aim of these experiments was to measure the classification effectiveness in terms of precision and recall, and to measure the contribution of neural thesaurus updating within the overall strategy.

4.1   Text Collection

Document collection is taken from the price comparison service Shoppydoo (http://uk.shoppydoo.com and http://www.shoppydoo.it), a price comparison service that allows users to compare prices and models of commercial products.

Two experiments were conceived and conducted in the field of price comparison services. Two product categories were identified, *cell-phones* and *digital-cameras*. Three specific brands were considered in our set of couples (b, m) KB for each category (Nokia, Motorola, Sony for cell phones and Canon, Nikon Samsung for digital-camera). The total number of documents collected for the cell-phone category was 1315 of which 866 associated with one of the three identified brands. The number of documents belonging to the digital-camera category were 2712 of which 1054 associated with one of the three identified brands. Remaining documents belonging to brands different from those considered in the experiment, must be classified *not relevant*.

4.2   Evaluation Metrics

Performance is measured by recall, precision and F-measure. Let us assume a collection of N documents. Suppose that in this collection there are $n < N$ documents relevant to the specific information we want to extract (brand and model of a product). The IE system recognizes m documents, a of which are actually relevant. Then the *recall, R*, of the IE system on that information is given by

$$R = a/n \qquad (1)$$

and the *precision, P*, is given by

$$P = a/m \qquad (2)$$

One way of looking at recall and precision is in terms of a 2×2 contingency table (see Table 1).

Table 1. A contingency table analysis of precision and recall

	Relevant	Not-relevant	Total
Matched	a	b	$a + b = m$
Not-matched	c	d	$c + d = N - m$
Total	$a + c = n$	$b + d$	$a + b + c + d = N$

Overall accuracy   (OA): $(a + b)/N$

Another measure used to evaluate information extraction that combines recall and precision into a single measure is the F-measure F_α defined as follows:

$$F_\alpha = \frac{1}{\alpha\frac{1}{P} + (1-\alpha)\frac{1}{R}} \tag{3}$$

where α is a weight for calibrating the relative importance of recall versus precision [6].

4.3 Results

The results of the two experiments are summarized in Tables 2 and 3. We started with an empty thesaurus that was then populated with the support of the neural network. For both datasets we obtained *Precision* and *Recall* equal to 100% after adding new synonyms to the thesaurus to resolve all the cases not perfectly matched.

Table 2. Evaluation metrics for the problem 'cell-phone' with thesaurus (a) and without the-saurus(b)

	Relevant	Not-relevant	Total
Matched	866	0	866
Not-matched	0	449	770
Total	866	449	1315

Recall 100%
Precision 100%
$F_{\alpha=0.5}$ 100%
OA 100%

(a)

	Relevant	Not-relevant	Total
Matched	755	0	755
Not-matched	111	449	560
Total	866	449	1315

Recall 87.18%
Precision 100%
$F_{\alpha=0.5}$ 93.15%
OA 91.56%

(b)

Table 3. Evaluation metrics for the problem 'digital-camera' with a thesaurus (a) and without thesaurus(b)

	Relevant	Not-relevant	Total
Matched	1054	0	1054
Not-matched	0	1658	1659
Total	1054	1658	2712

Recall 100%
Precision 100%
$F_{\alpha=0.5}$ 100%
OA 100%

(a)

	Relevant	Not-relevant	Total
Matched	963	0	963
Not-matched	91	1658	1749
Total	1054	1658	2712

Recall 91.37%
Precision 100%
$F_{\alpha=0.5}$ 95.49%
OA 96.64%

(b)

5 Conclusions and Future Works

The present work tested a system that make use of IE and classification in the context of a price comparison service. The approach proved highly accurate but it requires the assis-tance of an expert during the construction of the KB and the corresponding thesaurus.

Future work will extend the present solution including a tool for building the KB by automatically extracting unknown models of a product from a document.

References

1. Chang, C.H., Hsu, C.N., Lui, S.C.: Automatic information extraction from semi-structured web pages by pattern discovery. Decis. Support Syst. 35(1), 129–147 (2003)
2. Muslea, I.: Extraction patterns for information extraction tasks: A survey. In: Califf, M.E. (ed.) Papers from the Sixteenth National Conference on Artificial Intelligence (AAAI-99) Workshop on Machine Learning for Information Extraction, Orlando, FL, AAAI Press (1999)
3. Chang, C.H., Kayed, M., Girgis, M.R., Shaalan, K.F.: A survey of web information extraction systems. IEEE Transactions on Knowledge and Data Engineering 18(10), 1411–1428 (2006)
4. Damerau, F.J.: A technique for computer detection and correction of spelling errors. Communications of the Association for Computing Machinery 7(3), 171–176 (1964)
5. Rumelhart, D.E., Hinton, G.E., Williams, R.J.: Learning internal representations by error propagation, 318–362 (1986)
6. Jackson, P., Moulinier, I.: Natural Language Processing for Online Applications: Text Retrieval, Extraction, and Categorization. Natural Language Processing, 5. John Benjamins Publishing Co. (2002)

Formal Distance vs. Association Strength in Text Processing

José Medina Pagola, Ansel Y. Rodríguez González,
and Abdel Hechavarría Díaz

Advanced Technologies Application Center (CENATAV), 7th Avenue # 21812
% 218 and 222, Siboney, Playa, Havana City, Cuba
{jmedina,arodriguez,ahechavarria}@cenatav.co.cu

Abstract. Text information processing depends critically on the proper document representation. Traditional models, like vector space model, have significant limitations because they do not consider semantic relations amongst terms. In this paper we analyze a document representation that uses an association graph scheme model called Global Association Distance Model or GADM, the significance of the formal distance for the association strength, and the application of several distance-strength functions in this model. We evaluate this significance for topic classification tasks.

Keywords: Document modelling, Document processing, Document re-presentation.

1 Introduction

Nowadays, due to the rapid scientific and technological advances, there are great creation, storage and data distribution capacities. This situation has boosted the necessity of new tools to transform this big amount of data into useful information or knowledge for decision makers. This transformation process is known as Knowledge Discovery in Databases (KDD).

Recent studies and analyses have concluded that complex data require a high number of components to be completely described. This data has to be embedded in high-dimensional spaces (from tens to thousands dimensions). Examples are spectrophotometer data, gene expression data, pictures and texts. In this paper, we focus our analysis on textual data and their representation.

The representation model that is used affects critically almost any text processing task; like information retrieval, classification, clustering, summarization, question-answering, etc. The vector space model is the classic one and by far the most widely used model. Nevertheless, some studies have shown that the weakness of this model is to leave out semantic complexity of the textual data.

As terms appear related to other terms in any document, their meanings strongly depend on the meanings of the surrounding terms; even more, term meanings emerge from mutual sense reinforcement. If we assume that sentences

are the main semantic unit in texts, then mutual sense reinforcements or associations amongst their terms should be as strong as possible. Nevertheless, it is well known that these reinforcements or associations are feasible in other contexts, such as paragraphs or groups of them. The Global Association Distance Model (GADM) is an association graph scheme that includes this consideration for document representation.

In this paper we analyze the significance of the formal distance for the association strength in GADM, especially in classification tasks using a K-NN classifier. Besides, we evaluate the characteristics of the distance-strength function proposed for this model and propose other functions with better performance.

The basic outline of this paper is as follows. Section 2 is dedicated to related work. In section 3 we describe GADM. Section 4 analyzes several considerations related to formal distance, the association strength, the characteristics of the original distance-strength function and other better functions proposed for GADM, as well as the experimental results obtained.

2   Related Work

Document categorization, clustering and information retrieval tasks are often based on good data representation. At a high level, the manipulation of textual data can be described as a series of processing steps that transform the original document representation into another one, simpler and easier to be processed automatically by computers.

This usually involves enriching the document content by adding information, using background knowledge, normalizing terms, etc. At the start of the process, the textual data may exist as a paper, for instance, and the final representation of the preprocessing could be a straight ASCII text enriched with some additional information. This preprocessing final representation is used to represent data in a useful way for computer calculation.

These terms could be organized in different forms but, in general, they are considered as groups or bags of words, usually structured using a vector space model [1]. In this model, term sequences, or their syntactical relations, are not analyzed; therefore, they are considered as unigrams supposing an independence of their occurrences.

In the vector space model, each document is a vector of terms. The values of these vectors could be assumed as weights according the term occurrences in the document or in the document collection, and considering different interpretations [2]: Boolean, Term Frequency and Term Frequency - Inverse Document Frequency.

These vectors of terms are used in a second stage, among other tasks, to analyze the similarities among documents, or groups of them, using different measures as the cosine, applied to the angle between the vectors, defined as [2]:

$$sim(d_i, d_j) = cos(d_i, d_j) = \frac{(d_i \bullet d_j)}{||d_i|| * ||d_j||} = \frac{\sum w_{ir} * w_{jr}}{\sqrt{\sum w_{ir}^2 * \sum w_{jr}^2}} \ , \qquad (1)$$

where d_i, d_j are the vectors of documents i, j, $||di||$, $||dj||$ the norms of the vectors, and w_{ir}, w_{jr} are the term weights in the vectors di, dj, respectively. Other common measures are Dice and Jaccard coefficients.

Alternative approaches to the vector space model are the language models. These consider the probabilities of occurrence of a phrase S in a language M, indicated by $P(S/M)$. However, the phrases are usually reduced to one term, assuming again unigrams and independence among them. An example of this model is the Kullback-Leibler Divergence (a variation of the cross-entropy), defined as:

$$D(d_i||d_j) = \sum P(t/d_i) log \frac{P(t/d_i)}{P(t/d_j)} \ . \tag{2}$$

This expression could be combined in both directions to obtain a similarity measure, as was pointed out by *Feldman and Dagan* [3].

Other implementation is the proposal of Kou and Gardarin [4]. This proposal is a kind of language model, considering the similarities between two documents as:

$$sim(d_i, d_j) = d_i \bullet d_j = \sum_r w_{ir}w_{jr} + \sum_r \sum_{s \neq r} w_{ir}w_{js}(t_r \bullet t_s) \ , \tag{3}$$

where w_{ir} and w_{js}, using Kou-Gardarin terminology, are the term weights in document vectors d_i, d_j, respectively, and $(t_r \bullet t_s)$ is the a priori correlation between terms t_r and t_s. Actually, the authors included in the first part of the expression the self-correlation in t_r, considering that $(t_r \bullet t_r) = 1$. The authors propose the estimation of the correlation through a training process. As can be noticed, those correlations express the probabilities $P(t_r, t_s/M)$ of phrases containing the terms t_r, t_s in a language M. Besides, that expression could be reduced to the cosine measure (normalized by the length of the vectors) if the term independence is considered and, for that reason, the correlation $(t_r \bullet t_s)$ is zero.

Another vector space model is the Topic-based Vector Space Model (TVSM) [5]. The basic premise of the TVSM is the existence of a space R which only has positive axis intercepts. Each dimension of R represents a fundamental topic. It is assumed that all fundamental topics are independent from the others. In this model, each document is represented as a vector of term-vectors; each term-vector is a set of weights between the term and the fundamental topics.

The approaches mentioned above are variants of the Generalized Vector Space Model proposed by *S.K.M Wong et al.* [6]. In their work, they expressed that there is no satisfactory way of computing term correlations based on automatic indexing scheme.

We believe that up to the present time that limitation has not been solved yet. Although several authors have proposed different methods of recognizing term correlations in the retrieval process, those methods try to model the semantic dimension by a global distribution of terms, but not with a local evaluation of documents.

In general, it could be assumed that the better the semantic representation of the information retrieved and discriminated, the better this information is mined.

3   Global Association Distance Model

The Association Graph Model assumes that the same term in two documents could designate different concepts [7]. Besides, two terms could have different relations, according to the subject of each document, and those relations could exist only in the context of some documents, forming a specific group, and regardless of the relations in a global dimension or language.

In order to model the relation between two terms in a document, the shortest formal (or physical) distance between those terms has been considered. The basic premise of this model can be expressed as follows: *Two documents should be closer if the number of common terms is greater and the shortest formal distances among them in each document are similar.*

Considering the distance by paragraph, without ignoring the natural co-occurrence when appearing in the same sentence, and considering: (p_r, n_r), (p_s, n_s), the paragraph and sentence numbers of terms t_r and t_s respectively, the formal distance between these terms (D_{rs}) is defined as follows.

$$D_{rs} = \begin{cases} 1 & (r = s) \vee [(p_r = p_s) \wedge (n_r = n_s)] \\ |p_r - p_s| + 2 & otherwise \end{cases} . \tag{4}$$

Observe that the minimum value of D_{rs}, as could be expected, is not zero, but one. This consideration is only a convenient assumption to expressions defined further on.

According to this, a document is modeled by a graph, where the vertices are the distinguished terms and the edges are their relations, weighted by their distances. Notice that this is a fully connected graph, where any term has some relation (stronger or not according to the distance) with the others.

As an improvement to this model, the Global Association Distance Model (GADM) has been proposed [8]. This model uses the preliminary ideas of the classical vector space model proposed by Salton, i.e. to consider "*a document space consisting of documents ..., each identified by one or more index terms ... weighted according to their importance*" [1]. In GADM, the importance of a term t_r in a document d is related to its Global Association Strength (g_{t_r}) and can be calculated as follows.

$$g_{t_r} = \sum_{t_s \in d} \frac{1}{\sqrt{D_{rs}}} . \tag{5}$$

Therefore, the Global Association Distance Model can be defined as a vector space model (VSM) where each term is weighted by their global association strength. Nevertheless, in contradistinction to the original VSM that considers the term relevance by the number of its occurrences in a document, GADM considers the co-occurrences (actually, the association strengths) amongst terms in sentences, paragraphs and so on.

So, a document d can be modelled by a vector of association strengths (6).

$$\vec{d} = (g_{t_1}, ..., g_{t_n}) . \tag{6}$$

It is not difficult to understand that the similarity measure between two documents in this model can be calculated by any of the measures defined for the classic vector space model. In that proposal, and also in this work, the cosine measure (1) has only been considered.

4   Relevance of Formal Distance for the Association Strength

In order to better understand GADM, consider - as a very simplified example-the following four terms that appear in the introduction of this proper paper: *data*, *model*, *classification*, and *distance*. The association strengths amongst these terms are shown in Table 1.

Table 1. Formal distances in the introduction

D_{rs}	t_1	t_2	t_3	t_4
t_1 - data	1	1	2	3
t_2 - model	1	1	1	1
t_3 - classification	2	1	1	1
t_4 - distance	3	1	1	1

Notice that $D_{12} = 1$, because *data* and *model* appear together in the third sentence of the third paragraph; $D_{13} = 2$, because *data* and *classification* appear together on the third paragraph but in different sentences; and $D_{14} = 3$, because the third paragraph is the last where *data* appeared and the fourth paragraph is the first where *distance* appeared. Also, it can be noticed that the term *model* has the highest association strength and the term *data* has the lowest.

Although, in the original work, the formal distance amongst terms was explicitly considered and the authors showed that this single feature can improve the classical VSM with a primary proposal, the relevance of this feature has not been evaluated in all the possible approaches. In the following subsections we will analyze other characteristics of this feature, its significance for this model, and other proposals with better performance.

4.1   The Distance-Strength Assumption

The basic assumption of the Global Association Distance Model is that two documents should be closer if the shortest formal distances amongst terms in each document are similar. But also, it indirectly considers the following assumption: *The association strength between two terms decreases (increases) as their shortest formal distance increases (decreases)*. Nevertheless, in the original work, the experimentation was made with two repositories: TREC-5 and Reuters-21758, both with short documents. So, a question is open: Is that assumption true for any distance? Can an upper limit for the distance be considered without losing accuracy?

In order to find the correct answer, we evaluated one of the short corpora: TREC-5 in Spanish [1]. TREC-5 is an AFP news corpus with 695 items published during 1994-1995 and classified in 22 topics. Besides, we prepared a new one with the proceedings of the 18th International Conference on Pattern Recognition (ICPR 2006), held in Hong Kong in 2006. The proceedings have 1130 papers explicitly split into four classes.

All documents were preprocessed and lemmatized with TreeTager [9]. In all the evaluations, we have used a k-NN classifier with $k = 5$. The experimental evaluation was done using s-fold cross-validation with $s = 10$.

Precision, Recall and F-measure are three evaluation measures of performance commonly used. For a single category or topic, these measures can be defined as [10]. Precision is the quotient of the correctly assigned and the ones assigned to the category, Recall is the quotient of the correctly assigned and the ones belonging to the category, and F-measure is a ponderable representation of both above.

For evaluating the performance average across categories, there are two conventional methods: Macro-averaging and Micro-averaging performance. Macro-averaged performance scores are computed by a simple average of the performance measures for each category. Macro-averaged performance score gives equal weights to every category or topic, regardless of its frequency. Micro-averaged performance scores are computed by first accumulating the corresponding variables in the per-category expressions, and then using those global quantities to compute the scores. Micro-averaged performance score gives equal weights to every document.

Fig. 1 a) and b) show the experimental results for Micro-average with TREC-5 and ICPR-2006 respectively. In this experimentation, we have considered different upper limits of the formal distance, from 1 to 8, and 10 and 50. So, those terms t_s, whose distances D_{rs} are greater than each limit, are not considered in formula (5) for term t_r.
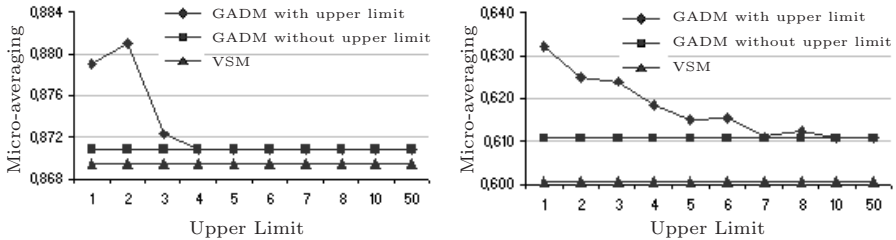
Fig. 1. Results for different upper limits a) TREC-5 b) ICPR-2006

As can be noticed in TREC-5, the best performance is obtained when the formal distance is limited to the same paragraph (upper limit = 2). However, in ICPR-2006 unexpectedly, the best performance is obtained when the upper

---

[1] http://trec.nist.gov/pubs/trec5

limit is one, although the results for almost all the upper limits are better than the original results. Nevertheless, as we will show afterwards, it is partially true for GADM.

As a preliminary conclusion, apparently we can obtain better results limiting the formal distance and considering not fully connected graphs, but thresholded graphs with a very small upper limit.

4.2   The Distance-Strength Function Shape

In the original work, the global association strength is calculated using formula (5). Nevertheless, other formulae could be used. So, this expression can be generalized in the following way:

$$g_{t_r} = \sum_{t_s \in d} ds(D_{rs}) \ , \tag{7}$$

where $ds(D)$ is a distance-strength function applied over a formal distance between two terms. In (5) this formula is the function $1/\sqrt{D}$. However, it has not been proved that this function is the best choice for this model.

The shape of the function is one aspect that should be evaluated first. In this work we have considered three types of functions: convex, linear and concave types.

$$ds(D) = M^a - D^a \ . \tag{8}$$

The function (8) can be used to model those three types of functions, where M is a superior value of D and a is a parameter that generates the three shapes in the following way:

- If $a < 1$, it is a convex function; that is, firstly the strength quickly decreases and at the end it decelerates the decrease with the distance increase.
- If $a > 1$, it is a concave function; that is, firstly the strength slowly decreases and then it accelerates the decrease with the distance increase.
- If $a = 1$, it is a linear function.

Fig. 2 shows examples of this function with $a = 0.5$, 1, and 2.

Fig. 3 a) and b) show the behavior of (8) for Micro-average with TREC-5 and ICPR-2006 respectively, taking M as the maximum of paragraph number of each data set. In both figures, the behavior of (8) is compared to the VSM and the
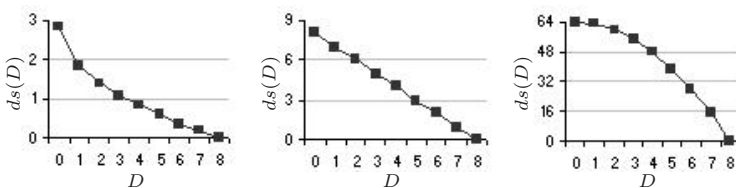
Fig. 2. Example of a convex (left), a linear (center) and a concave (right) function
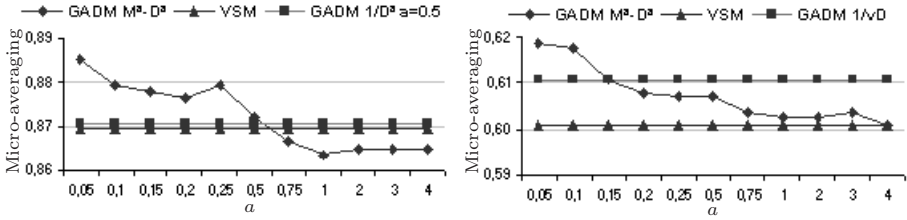
Fig. 3. Behavior of the function with different shapes a) TREC-5 b) ICPR-2006

original GADM formula (5). As can be noticed in both figures, the best results are obtained with convex shapes. It means that, although the formal distance could have a relevant effect, its strength decreases relatively quickly for shortest distances (or nearest paragraphs).

4.3 The Optimum Distance-Strength Function

Although the function (8) with a convex shape achieves the best results, it has, as a constraint, to define a constant M which completely depends on document sizes. As an alternative, we can use another family of convex functions, defined in (9), easier to be applied with any document size. Observe that the formula used in (5) is the same as (9) with $a = 0.5$.

$$ds(D) = \frac{1}{D^a} \quad . \tag{9}$$

Fig. 4 a) and b) show the behaviors of this new formula for Micro-average with TREC-5 and ICPR-2006 respectively. In both, the behavior of (9) is compared with the VSM and the original GADM formula (5). From this experimentation, we can observe that the original formula (5) is not amongst the best results; moreover, the best results are achieved with formula (9) for values of a in the interval $[4, 5]$ in both data sets.

Considering, as a result of the first experimentation made in subsection 4.1 that using an upper limit over the formal distance could improve the behavior, we decided to evaluate formula (9) with different values of a and different upper limits.

Fig. 5 a) and b) show the behaviors of these combinations for Micro-average with TREC-5 and ICPR-2006 respectively. In both, the behavior of (9) is compared with the VSM. Analyzing these results, we can observe that the preliminary conclusion made in subsection 4.1 is partially valid; that is, we can consider not fully connected graphs, or thresholded graphs, with a reasonable upper limit, simplifying the processes associated to GADM. Besides, we can notice that, in TREC-5, the best upper limits are 2 or 3 and in ICPR-2006 could be from 2 to 5.

As a conclusion, at least in classification tasks with the Global Association Distance Model, we recommend to use the formula (10) as a distance-strength function, considering thresholded graphs with upper limits according to the size
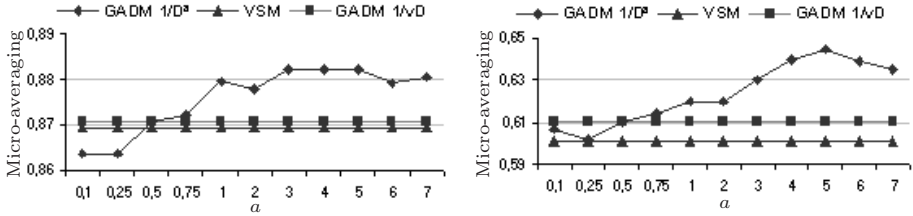
Fig. 4. Behavior of formula (9) a) TREC-5 b) ICPR-2006
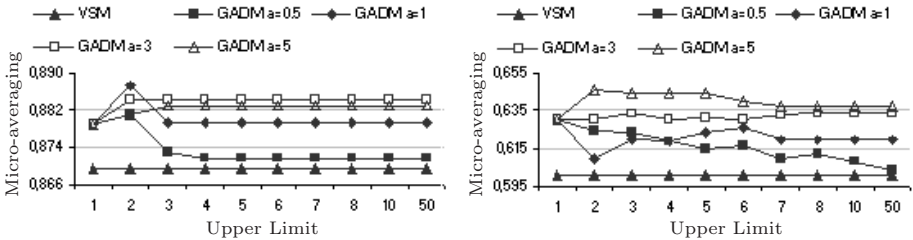
Fig. 5. Behavior of formula (9) and different upper limits a) TREC-5 b) ICPR-2006

of documents to be processed. Also, we can conclude that, although the distances limited to sentences and paragraphs produce the biggest association strengths, and so it is modeled by the best functions, we should take into account the distances to nearest paragraphs because these also contribute, to a lesser extent, to the global improvement.

$$ds(D) = \frac{1}{D^5} \ . \tag{10}$$

With this new formula and a thresholded graph we obtain the results shown in Table 2 for Micro-average.

Table 2. Results for Micro-average

Collection	VSM	GADM,$1/\sqrt{D}$	GADM,$1/D^5$
TREC-5	0.869401	0.870809	0.882238
ICPR-2006	0.600885	0.610619	0.645133

Notice that formula (10) represents a 1.48% improvement in performance compared to VSM and a 1.31% to the primary proposal in TREC-5, and 7.36% to VSM and 5.65% to the primary proposal in ICPR-2006.

5   Conclusion

In this paper we have analyzed the significance of the formal distance for the association strength in GADM, especially in classification tasks using a k-NN classifier.

In our experimentation, we showed that GADM not only achieves better results than the classic vector space model in the original formulation, but also in a family of functions with significant improvements.

Besides, we evaluated the characteristics of the distance-strength assumption with different functions and distance thresholds. Also, we proposed a new function with a better performance.

As a future work, it can be analyzed the performance of these considerations with other similarity measures or other forms for modelling the association strength.

References

1. Salton, G.: The SMART Retrieval System - Experiments in Automatic Document Processing. Prentice-Hall, Englewood Cliffs, New Jersey (1971)
2. Berry, M.: Survey of Text Mining, Clustering, Classification and Retrieval. Springer, Heidelberg (2004)
3. Feldman, R., Dagan, I.: Knowledge Discovery in Textual Databases (KDT). In: KDD 1995, Montreal, pp. 112–117 (1995)
4. Kou, H., Gardarin, G.: Similarity Model and Term Association for Document Categorization. In: Andersson, B., Bergholtz, M., Johannesson, P. (eds.) NLDB 2002. LNCS, vol. 2553, pp. 223–229. Springer, Heidelberg (2002)
5. Becker, J., Kuropka, D.: Topic-based Vector Space Model. In: BIS 2003 (2003)
6. Wong, S.K.M, Ziarko, W., Wong, P.C.N.: Generalized Vector Space Model in Information Retrieval. In: Proc. of the 8th Int. ACM SIGIR Conference on Research and Development in Information Retrieval, p. 11. ACM, New York (1985)
7. Medina-Pagola, J.E., Guevara-Martinez, E., Hernández-Palancar, J., Hechavarría-Díaz, A., Hernández-León, R.: Similarity Measures in Documents using Association Graphs. In: Sanfeliu, A., Cortés, M.L. (eds.) CIARP 2005. LNCS, vol. 3773, pp. 741–751. Springer, Heidelberg (2005)
8. Medina-Pagola, J.E., Rodríguez, A.Y., Hechavarría, A., Hernández-Palancar, J.: Document Representation using Global Association Distance Model. In: Amati, G., Carpineto, C., Romano, G. (eds.) ECIR 2007. LNCS, vol. 4425, pp. 565–572. Springer, Heidelberg (2007)
9. Schmid, H.: Probabilistic Part-Of-Speech Tagging Using Decision Tree. In: Proc. of International Conference on New Methods in Language Processing, Manchester, UK (1994)
10. Yang, Y.: An evaluation of statistical approaches to text categorization. Journal of Information Retrieval 1(1/2), 67–88 (1999)

Restoration of Double-Sided Ancient Music Documents with Bleed-Through

Pedro Castro, R.J. Almeida, and J.R. Caldas Pinto

IDMEC/IST, Technical University of Lisbon
Av. Rovisco Pais, 1049-001 Lisboa, Portugal
pedro.melo.castro@ist.utl.pt,
rjalmeida@ist.utl.pt,
jcpinto@dem.ist.utl.pt

Abstract. Access to collections of cultural heritage is increasingly becoming a topic of interest for institutions like libraries. With the easy access to information provided by technologies such as the Internet, new ways exist for consulting ancient documents without exposing them to more dangers of degradation. One of those types of documents is written ancient music. These documents suffer from multiple kinds of degradation, where bleed-through outstands as the most damaging. This paper proposes a new method based on the Takagi Sugeno fuzzy classification algorithm to classify the pixels as bleed-through, after performing a general background restoration. This method is applied to a set of double-sided ancient music documents, and the obtained results compared with methods present in the literature.

Keywords: Ancient Music Restoration, Image Processing, Document Degradation, Bleed-through Removal, Registration, Adaptive Thresholding, Fuzzy Classification, Clustering.

1 Introduction

One of the main current goals for institutions like libraries is to give access to its rich collections of cultural heritage, written documents in particular. However, much of those documents suffer from different kinds of degradations that are not corrected in the digitization process. As such, there is an active research on automatic methods to restore these kinds of documents.

Restoration can be seen as a transformation that gives the original aspect to documents showing a certain state of degradation. Degradation, on the other hand, can be described as "every sort of less-than-ideal properties of real document images, e.g. coarsening due to low digitizing resolution, ink/toner drop-outs and smears, thinning and thickening, geometric deformations, etc" [1]. Restoration is necessary not only to enhance the visual appearance of a document, but also to improve the results of further segmentation and recognition operations.

Degradation can be divided into three types [2], according to the parts of a document that are subject to interference: 1) background degradation;

2) foreground degradation; and 3) global degradation. We are concerned with background degradation, which accounts for the majority of defects found in documents of ancient music. It includes blotches due to humidity, marks resulting from ink that traverses the paper (bleed-through) or resulting from the scanning process (show-through), underlines, strokes of pen, annotations, and the superimposition of other symbols. Examples of these degradations are depicted in Fig. 1.

(a)   (b)
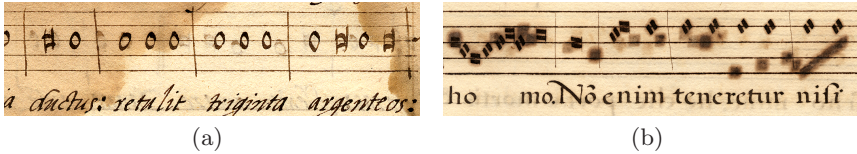
Fig. 1. Images of ancient music showing background degradation

Current approaches for bleed-through removal are split between blind and non-blind methods. Blind methods process a single side of a leaf of paper – the recto – while non-blind methods use both sides – the recto and the verso. Blind methods have the immediate advantage of not requiring the verso image to be present. Non-blind methods, however, dispose of additional features that can be extracted by processing both sides simultaneously, which can lead to a better segmentation.

A previous work by Castro and Pinto [3] has analyzed and compared different recto-based approaches to restore images of ancient music, including global and adaptive thresholding, color clustering, and edge detection. One of the work's conclusions was that none of the methods was able to successfully remove the defect that resulted from sipped ink, i.e., bleed-through. This therefore demands for a specialized treatment, which is the main focus of this paper.

Non-blind methods are typically comprised of: 1) matching of the recto and verso images; 2) heuristics to distinguish bleed-through from the valid foreground; 3) bleed-through removal; 4) inpainting [4], to fill in the removed bleed-through regions; and 5) pre and/or post-processing algorithms. Sharma [5] developed a simple model of the show-through effects, assuming that the distortion in the documents is due to show-through and that the impairment when scanning such documents can be modeled by the properties of the physical scanning process. However, this method does not apply to the case of bleed-through due to its nature in the derivation of a physical model that describes the show-through phenomenon. Wang and Tan [6] proposed a method that matches pixels on the two sides to remove interference and corrects the result using a Canny edge detector [7]. However, this correction is favored by the orientation of the characters, which cannot be applied to the case of written ancient music as these are typically written in a nearly vertical orientation. Dubois and Dano [8] segment a document into four regions: foreground only, bleed-through only, background, and foreground and bleed-through overlap. Bright areas are considered to be background, whereas areas that are dark on the side of interest and not on

the reverse are considered to be foreground. Areas that are dark on both sides, but more so on the reverse side, are considered to be bleed-through, while if they are dark on both sides but similar they are considered regions of overlap. Thresholds are used to determine if one side is sufficiently darker than the other, and correlations are used to determine whether they are similar. They state that their segmentation scheme is empirical and could therefore be improved.

The rest of this paper is organized as follows. Section 2 details our proposed method. Section 3 presents and analyzes the results, comparing them to an existing method. Section 4 concludes the paper and indicates future work directions.

2   Method

The method we propose processes the images corresponding to the two sides of a leaf of paper in order to restore them. General deterioration, like water blotches and inhomogeneous backgrounds, is removed, but the main focus is on eliminating bleed-through.

The images are converted to gray scale before processing. Besides this conversion, the verso image is flipped horizontally in order for its coordinate system to match that of the recto.

The method is comprised of multiple steps. First, the recto and the verso images are registered. Background homogenization is then performed using adaptive thresholding. Following thresholding, the staff lines are detected. Finally, features are extracted and classification is performed, after which the method proceeds with a final post-processing step.

The result of the method is a binary image that distinguishes from the foreground and the background. All the detected deterioration, including bleed-through, is incorporated into the background. Throughout the exposition of the method, the recto image will stand as the target for restoration, with the verso image being used, in addition, to restore it. The restoration of the verso image follows the exact same approach and therefore will not be covered here.

Problem Formulation. We formulate the problem using a notation that is similar, in part, to that found in the work of Dubois and Dano [8]. Let $f_r^O(x, y)$ and $f_v^O(x, y)$ denote the original recto and verso digital images, respectively, after being converted to gray scale and flipping the verso. The points (x, y) lie on a two-dimensional rectangular space and the range of the functions is the interval $[0, 1]$, with 0 and 1 corresponding to white and black, respectively. Each of the two images is comprised of foreground, background and bleed-through areas. The foreground area contains the writing that was intentionally applied to the paper. The bleed-through area contains part of the verso's writing that has bled through the page. The remainder of the recto corresponds to the background. The original recto image can therefore be represented as

$$f_r^O(x, y) = f_{rfg}^O(x, y) + f_{rbt}^O(x, y) + f_{rbg}^O(x, y) \ , \tag{1}$$

where $f_{rfg}^O(x, y)$, $f_{rbt}^O(x, y)$ and $f_{rbg}^O(x, y)$ correspond to the original recto foreground, bleed-through and background areas, respectively.

This allows us to model the relationship between the two sides:

$$f_r^O(x, y) = C(f_{rfg}^O(x, y), f_{rbg}^O(x, y), f_{vfg}^O(x, y)) \ , \tag{2}$$

where $f_{vfg}^O(x, y)$ denotes the original verso foreground and C is a function that combines its arguments in some way. Possible models for this combining function were presented by Dubois and Pathak [9]. A simple additive model defines it as

$$C(\mu, \rho, \tau) = \mu + \rho + \alpha \cdot \tau \ , \tag{3}$$

where α represents the attenuation of the verso foreground sipping to the recto.

Still, our method does not highly depend on a specific model of the bleed-through effect. Its ideal purpose is to create a restored recto image, which we denote as $f_r(x, y)$, that nullifies both the background and the bleed-through areas, maintaining only the valid writing:

$$f_r(x, y) = C(f_{rfg}^O(x, y), 0, 0) = f_{rfg}^O(x, y) \ . \tag{4}$$

Conceptually, we wish to determine the parts of an image that correspond to the valid intentional writing. To this accomplishment, the background and bleed-through areas need to be removed. As the bleed-through areas depend on the verso's writing, information from the verso needs to be incorporated and combined with the recto. In practice, however, it is not possible to establish a perfect relation between the two sides. On one hand, the sipping of ink is irregular, as only part of the verso writing does sip to the recto and the bleed-through area may be somewhat diffuse, thus occupying a larger area in the recto than it originally occupied in the verso. On the other hand, ink may have sipped to areas of the recto that already contained valid writing, thereby making it extremely difficult, even for human readers, to distinguish the foreground from bleed-through. Therefore, the main purpose of our method is to restore as much deterioration as possible, recognizing the problem's difficulties beforehand.

Registration. The necessity for using registration comes from the variability in the way the recto and the verso images are captured. When scanning the recto and the verso using typical machines, differences may arise in the resulting images, when compared to each other. This includes mostly shifting, rotation, and some skewing. These properties can be modeled by an affine transformation A_t, of parameter vector $t = [t_{11} \ t_{12} \ t_{13} \ t_{21} \ t_{22} \ t_{23}]$ [10], defined as [8]

$$(A_t f)(x, y) = f(t_{11}x + t_{12}y + t_{13}, t_{21}x + t_{22}y + t_{23}) \ . \tag{5}$$

The parameter vector is estimated by solving the optimization problem:

$$\hat{t} = \arg\min_t \sum_x \sum_y \left[f_r^O(x, y) - (A_t f_v^O)(x, y) \right]^2 \ . \tag{6}$$

The registered verso image, i.e., the image that results after applying the affine transformation to the original verso, can then be calculated with

$$f_v^R(x, y) = (A_{\hat{t}} f_v^O)(x, y) \ , \tag{7}$$

while the recto image remains unchanged, thereby having its registered version represented as

$$f_r^R(x, y) = f_r^O(x, y) \ . \tag{8}$$

Background Homogenization. After registering the images, the registered recto background f_{rbg}^R is estimated and removed, along with the degradation it contains. Sauvola's adaptive thresholding method [11] was chosen, as it not only aims at dealing with cases in which the background contains light texture, big intensity variations and uneven illumination, but also has been shown to perform well with written ancient music [3]. This algorithm calculates a threshold value for each pixel based on the mean and standard deviation of all the pixels in a local neighborhood. A window of size $W \times W$ is moved over the image and the threshold value, for a pixel (x, y), is calculated as

$$t(x, y) = m(x, y) \cdot \left[1 + K \cdot \left(\frac{s(x, y)}{R} - 1 \right) \right] \ , \tag{9}$$

where $m(x, y)$ and $s(x, y)$ are the mean and standard deviation values, respectively, in a local neighborhood of size $W \times W$ of pixel (x, y), and R is the dynamic range of standard deviation. The values of $W = 15$, $K = 0.2$ and $R = 128$ were used, as they provided the best results in previous experiments [3].

We denote f_r^B as the binary image that results after applying Sauvola's thresholding to f_r^R. This image contains all background pixels set to 0 and the remaining pixels set to 1. It will be the task of the classification step to distinguish from the registered recto foreground and bleed-through, now that the background has been detected.

Staff Line Detection. Staff lines are detected because line pixels may become incorrectly classified as bleed-through in the classification step, leading to broken lines. This allows to restore those lines as a post-processing step.

We used a method that has been shown to perform well with written ancient music [12]. This method uses horizontal projections and small rotations of f_r^B, finding peak areas of the projections and classifying them as staff lines.

Features. The extraction of features was accomplished by taking both the recto f_r^R and the verso f_v^R into account. All the pixel positions (x, y) were selected as possible candidates according to the following criteria:

$$\forall_{x,y} \left[((f_r^B(x, y) = 1) \wedge (f_r^R(x, y) < f_v^R(x, y))) \rightarrow ((x, y) \in \text{Candidates}) \right] \ .$$

From these candidates, 4 features were extracted: 1) correlation coefficients; 2) differences; 3) recto values; and 4) verso values. The correlation coefficients relate to information about whether the verso is similar to the recto, near a certain candidate pixel. For each candidate position, a window of size 9×9 is centered on the recto and the verso, forming two matrices A and B, respectively. The correlation coefficient for a given candidate is then calculated as

$$r = \frac{\sum_m \sum_n (A_{mn} - \overline{A})(B_{mn} - \overline{B})}{\sqrt{(\sum_m \sum_n (A_{mn} - \overline{A})^2)(\sum_m \sum_n (B_{mn} - \overline{B})^2)}} \ , \tag{10}$$

where A_{mn} and B_{mn} are pixels with coordinates (m, n) within the windows A and B, respectively, and $\overline{A}$ and $\overline{B}$ are the means of the pixels within A and B, respectively.

The differences correspond to the distances between the pixel values on the two sides. They relate to the subtraction of the recto from the verso, i.e., $f_v^R - f_r^R$. The last two features correspond to the pixel values in the recto and the verso.

Classification. In a classification problem the aim is to learn the behavior between the input and output of the training data. The use of fuzzy models in classification problems has been adopted in many domains [13,14,15], because they are able to solve difficult problems, exhibit robust behavior and present linguistic representations, which are easy to interpret.

The fuzzy models used in this paper are an extension of the Takagi-Sugeno fuzzy models [16] in the affine form. This fuzzy classification rule is a fuzzy if-then rule whose consequent part is a class label [14,15]. It can be described by

$$R^k : \text{ If } x \text{ is } A^k \text{ then } x \ \in \text{class}_\kappa \text{ with confident value } CV^k \ , \qquad (11)$$

where $k = 1, 2, \ldots, K$, $i = 1, \ldots, K$, K denotes the number of rules in the rule base, R_i is the ith rule, n is the number of features, $A_{i1}, \ldots, A_{in}$ are fuzzy sets defined in the antecedent space, y_i is the output feature for rule i, a_i is a parameter vector and b_i is a scalar offset, κ is the number of classes, and CV^k is the confident value of the rule R^k. The confident value of the if-then rule represents the rule weight interpreted as its confident strength. This type of model is used because it focuses on the precision of the obtained model.

To form the fuzzy system model from the data set with N data samples, given by $X = [x_1, x_2, \ldots, x_N]^T$, $Y = [y_1, y_2, \ldots, y_N]^T$ where each data sample has a dimension of n $(N >> n)$, first the structure is determined and afterwards the parameters of the structure are identified. The number of rules characterizes the structure of a fuzzy system. Fuzzy clustering in the Cartesian product-space $X \times Y$ is applied to partition the training data. The partitions correspond to the characteristic regions where the system's behavior is approximated by local linear models in the multidimensional space. Given the training data X_T and the number of clusters K, a suitable clustering algorithm is applied. In this paper we used the fuzzy c-means [17], one of the most widely used clustering algorithms.

As result of the clustering process a fuzzy partition matrix $U = [\mu_{ik}]$ is obtained. The fuzzy sets in the antecedent of the rules are identified by means of the partition matrix U which has dimensions $[N \times K]$. One-dimensional fuzzy sets A_{ij} are obtained from the multidimensional fuzzy sets by projections onto the space of the input variables x_j. This is expressed by the point-wise projection operator of the form $\mu_{A_{ij}}(x_{jk}) = \text{proj}_j(\mu_{ik})$. The point-wise defined fuzzy sets A_{ij} are then approximated by appropriate parametric functions. The consequent parameters for each rule are obtained by means of linear least square estimation, which concludes the identification of the classification system.

Post-processing. Having classified all pixels as bleed-through or foreground, we now have f_{rfg}^R and f_{rbt}^R, where the first corresponds to the registered image

without bleed-through. As a final step, two operations need to be performed. First, the initially detected staff lines are restored. Second, bleed-through diffusion, visible as a set of pixels surrounding bleed-through, is suppressed. To this intent, a window of size 5×5 is centered on each bleed-through pixel and all the pixels connected to it, inside that window, showing intensity levels at most 0.04 darker or lighter than the center pixel value, are marked as bleed-through.

We now have the final restored image f_r, containing the detected valid writing, which is derived from the detected foreground f_{rfg}^R, according to (4) and (8), as

$$f_r(x, y) = f_{rfg}^O(x, y) = f_{rfg}^R(x, y) \ . \tag{12}$$

3   Results

Experiments were conducted in order to determine whether our method achieves a good segmentation. The method of Dubois and Dano [8] was also tested, and the results of the two methods compared. The quality of the restoration, as observed in the resultant images, was the main emphasis of our tests. Computational issues were therefore not considered.

Methodology. Images of written ancient music were provided by the Portuguese National Library and the Biblioteca Geral da Universidade de Coimbra, Portugal. A total of 14 images, i.e., 7 pairs of recto-verso images, scanned at a resolution of 150 *dpi*, were used throughout the experiments. These images contain diverse degradation types, as well as different musical notations and illumination characteristics. They are representative of the majority of images present in the studied collections from the two referred libraries. All images were first manually restored, using graphics editing software, in order to be used as a standpoint for comparison. From the 14 images, one side of each pair was used for training and the other for validation.

It must be noted that the method of Dubois and Dano [8] does not perform binarization. Its purpose is to detect and remove bleed-through areas, preserving the remaining parts of the image. Therefore, for it to be comparable to our method, Sauvola's thresholding was applied to it. The image is thresholded after registration, but the algorithm proceeds as normal, ignoring the thresholded image. Only in the end, when bleed-through pixels have been detected, thresholds are combined to form the resulting image, which constitutes of the thresholded image with the detected bleed-through pixels removed.

The test images were processed by the chosen methods and compared to the manually restored images. The comparison was evaluated by the standard measures of *precision* and *recall* [18], with a slight modification. To evaluate text segmentation, these measures are typically used with the precision of a character or word. In the context of ancient music, this does not apply so well as the musical notation is varied, including notes, clefs, key and time signatures, rests, bar and staff lines, as well as text, among other symbols. All of these symbols could be treated as characters, but that would ignore the great differences in shapes and

sizes among them. Therefore, we opted to perform a bitwise comparison and, as such, the *precision* (P) and *recall* (R) measures were used as

$$P = \frac{\text{Correctly Detected BT}}{\text{Total Detected BT}} \text{ and } R = \frac{\text{Correctly Detected BT}}{\text{Total BT}} \; , \qquad (13)$$

where "Correctly Detected BT" refers to the bleed-through pixels that were correctly binarized (i.e., that are equal to those of the manually restored images), "Total Detected BT" refers to the total bleed-through pixels that were binarized, and "Total BT" refers to the total bleed-through pixels that are present in the manually restored images.

Precision and *recall* reflect the performance of removing interfering strokes and restoring valid strokes, respectively. To relate the two measures, the geometric mean (g-mean) was used, being defined as

$$g\text{-mean} = \sqrt{P * R} \; . \qquad (14)$$

This measure was used because it does not depend on the distribution of examples between classes [19]. This is convenient as the number of bleed-through pixels is typically a minority, when compared to the entire set of pixels within an image.

Results. The results of evaluating our method, which we denote as CAP, and that of Dubois and Dano, denoted as DD, on the 7 selected images, are presented in Table 1. Our method achieved a good overall segmentation, with a better performance in almost all images. It should be noted that there is an inherent degree of error in these results, as they are based on a pixel-wise comparison with manually restored images. When restoring those images by hand, it is hard to determine the exact class for each pixel, as the value of some pixels is not visually distinct.

Table 1. Detailed *precision (P)*, recall (R) and g-mean (G) results obtained by applying the methods to 7 images of ancient music

Image		1	2	3	4	5	6	7	Average
CAP	P	0.249	0.719	0.487	0.713	0.514	0.400	0.025	0.444
	R	0.921	0.814	0.718	0.770	0.795	0.833	0.788	0.806
	G	0.479	0.765	0.591	0.741	0.639	0.577	0.139	0.562
DD	P	0.135	0.423	0.254	0.667	0.230	0.241	0.032	0.283
	R	0.832	0.737	0.509	0.807	0.859	0.845	0.894	0.783
	G	0.335	0.558	0.360	0.734	0.444	0.452	0.169	0.436

Parts of two images used throughout the tests are presented in Fig. 2. It can be noted that the readability is greatly improved with the removal of bleed-through areas. It can also be observed that the removal is naturally not perfect, as some bits of diffusion still remain. However, these bits are dispersed, therefore not creating a serious visual impact to the reader.

(a)   (b)

(c)   (d)

Fig. 2. Results of processing two of the original images with the proposed method. The first column presents the original images, while the second shows the restoration results.

4   Conclusion

Written ancient music images often present multiple types of degradation. Typical cases of degradation were presented and analyzed, including the specialized case of bleed-through. A restoration method for images of ancient music suffering from bleed-through has been proposed. A methodology for method evaluation was established and the method compared to an existing one. The results demonstrate that the proposed method performs well and greatly improves the visual appearance of the documents.

Some work is still necessary to fine-tune the proposed method. This includes the difusion removal in the post-processing step, as well as a general performance optimization that should be considered. Furthermore, some research is still necessary to fully automate the application of this method to the mass restoration of written ancient music. This will be the concern of future work.

References

1. Baird, H.: The state of the art of document image degradation modeling (2000)
2. Drira, F.: Towards restoring historic documents degraded over time. In: Document Image Analysis for Libraries, pp. 350–357 (2006)
3. Castro, P., Pinto, J.R.C.: Methods for written ancient music restoration. Image Analysis and Recognition. In: Forth International Conference ICIAR (to be published, 2007)

4. Bertalmio, M., Sapiro, G., Caselles, V., Ballester, C.: Image inpainting. In: SIGGraph- 2000 pp. 417–424 (2000)
5. Sharma, G.: Show-through cancellation in scans of duplex printed documents. IEEE Transactions on Image Processing 10(5), 736–754 (2001)
6. Wang, Q., Tan, C.L.: Matching of double-sided document images to remove interference. In: CVPR, pp. 1084–1089. IEEE Computer Society, Los Alamitos (2001)
7. Canny, J.: A computational approach to edge detection. In: RCV 1987, 184–203 (1987)
8. Dubois, E., Dano, P.: Joint compression and restoration of documents with bleed-through. In: IS&T Archiving, pp. 170–174 (2005)
9. Dubois, E., Pathak, A.: Reduction of bleed-through in scanned manuscript documents. In: PICS, pp. 177–180 (2001)
10. Brown: A survey of image registration techniques. CSURV: Computing Surveys 24 (1992)
11. Sauvola, J., Pietikainen, M.: Adaptive document image binarization. Pattern Recognition 33(2), 225–236 (2000)
12. Pinto, J.R.C., Vieira, P., da Costa Sousa, J.M.: A new graph-like classification method applied to ancient handwritten musical symbols. IJDAR 6(1), 10–22 (2003)
13. Setnes, M., Roubos, H.: GA fuzzy modeling and classification: Complexity and performance. IEEE Transactions on Fuzzy Systems 8(5), 509–522 (2000)
14. Hirota, K., Pedrycz, W.: Fuzzy computing for data mining. Proceedings of the IEEE 87(9), 1575–1600 (1999)
15. Thawonmas, R., Abe, S.: Function approximation based on fuzzy rules extracted from partioned numerical data. IEEE Transactions on Systems, Man and Cybernetics, Part B 29(4), 525–534 (1999)
16. Takagi, T., Sugeno, M.: Fuzzy identification of systems and its aplication to modeling and control. IEEE Transactions on Systems, Man and Cybernetics 15(1), 116–132 (1985)
17. Bezdek, J.C.: Pattern Recognition with Fuzzy Objective Function Algorithms. Plenum Press, New York (1981)
18. Junker, M., Dengel, A., Hoch, R.: On the evaluation of document analysis components by recall, precision, and accuracy. In: ICDAR, pp. 713–716 (1999)
19. Kubat, M., Holte, R., Matwin, S.: Machine learning for the detection of oil spills in satellite radar images. Machine Learning 30, 195–215 (1998)

Multiple Assessment for Multiple Users in Virtual Reality Training Environments

Ronei M. Moraes[1] and Liliane S. Machado[2]

[1] Department of Statistics
[2] Department of Informatics
Universidade Federal da Paraíba
Cidade Universitária s/n – João Pessoa/PB - Brazil
ronei@de.ufpb.br, liliane@di.ufpb.br

Abstract. With recent computational advances, several interaction devices can be used by different users who share the same virtual world, allowing the simulation of realistic environments, such as surgical rooms. In order to deal with this feature, assessment systems must be generalized to evaluate, individually, all users of the simulation and to make the aspects of their interactions known. In this paper we propose a new assessment system for training based on virtual reality which can evaluate more than one user at a time. The methodology proposed uses data collected from user interaction and group interactions during training to create user profile and group profile. The main advantages of that approach are: both of reports can be used to increase group performance and the interactions among users, during training, can be monitored to correct and improve group tasks in procedure such as sequential, simultaneous or collaborative tasks.

Keywords: Multiple Assessment System, Training Based on Virtual Reality, Fuzzy Expert System, Statistical Measures, Statistical Models.

1 Introduction

The features found in training systems based on virtual reality can be the 3D environments composed of objects with topologies and behaviours similar to real objects, the interaction ways to deal with this world, the possibility of performing the training as much as necessary without risk or damage, among others [4]. Systems for different modalities in medicine have been developed as training in laparoscopy [23], bone marrow harvest [9], gynaecological exam [10] and bone surgery [17]. The goal of most of these systems is to provide a training environment similar to a real procedure environment by the use of devices and techniques which explore the human senses. All these systems can provide training for only one user at a time. However, some procedures need to be performed by more than one person.

Training systems based on VR for simultaneous use in complex training environments are being planned, as virtual surgery rooms for several purposes of training. The advances of cluster machines, improvements of video cards, processors and networks will provide training system for multiple users simultaneously in a few

years at a low cost. Other important advance is the speed of input/output devices for virtual reality systems such as haptic devices. Nowadays, it is possible to connect more than one interaction device on a single computer.

Although the possibilities of training which can be simulated in VR systems, any kind of training has little value if the trainee does not have any feedback about his/her performance. Then, the existence of an on-line assessment tool attached to a simulation system based on VR is important to allow the learning improvement and the users assessment. This paper presents a brief overview of assessment in VR training systems for single users and proposes a method for assessment in collaborative training environments for simulators based on VR.

2   Assessment in Virtual Reality Simulators

The first methodologies for automatic assessment of training were proposed only a few years ago. This section presents a brief overview of assessment methodologies for training based on virtual reality. It can be noticed that several of them may also be potentially applied to other research areas. Basically, assessment methods can be divided in off-line and on-line. Off-line methods can be defined as methods not coupled to VR systems, whose assessment results are provided some time (which can be minutes, hours or days) after the end of the VR-based training. On the other hand, on-line assessment methods are coupled to the training system and collect user data to provide a result of his/her performance at the end of the simulation.

In medicine, some models for off-line or on-line assessment of training have been proposed. Some of them use Hidden Markov Models (HMM) [12, 19], fuzzy rule-based system [8], Fuzzy Gaussian Mixture Models [13], Evolving Fuzzy Neural Networks [14] and, recently, Fuzzy Bayes Rule [15]. An evaluation tool must continuously monitor all user interactions and compare his performance with pre-defined expert's classes of performance to recognize user's level of training. In spite of the methodologies proposed in literature, they are concerned with the assessment of only one user at a time. Up to the time being, methodologies which monitor multiple users in complex training environments based on virtual reality have not been found in literature.

3   Multiple Assessment for Multiple Users in Virtual Reality Simulators

Computational systems for multiple users have been developed since the 1990's, as RB2 [3], DIVE [5], MR Toolkit [20], some of them support haptic devices. Systems to provide interaction among multiple-user have been proposed too. Baier et al. [2] proposed a system for telepresence using haptic and visual interactions. Recently, systems for multi-user collaboration were developed [7, 16, 24]. The main differences of training systems based on virtual reality for multiple users are: increase of complexity of the virtual reality system – use of clusters of computers or a computer capable to generate realistic multiple views, support changes in virtual environments for multiple users and support assessment system; high speed peer-to-peer network

for communication among computers without compromising the simulation. Eventually, more than one haptic device were installed in a computer and/or tracking systems for each user in training.

The most common problem in distributed systems based on network or Web, for multi-user interactions, is the latency [18]: users may have different views in the shared workspace which damages the users' performance involved in the simulation. For user assessment, the main problems related are the computational complexity and the accuracy, even when only one user is been trained. An on-line assessment system must have low complexity to does not compromise VR simulations performance, but it must have high accuracy to does not compromise the assessment.

Due to several specific necessities for multi-user training, a different approach for the assessment system is required. The requirements are: to monitor all users in training according to relevant variables to the training; in multi-user environment some tasks must be completed by specific users and according to a specific schedule; take measures of specific interactions among users during the time of simulation; take into account the length of assessment; to create a user profile and a group profile; to present low complexity not to compromise VR simulations performance, but present high accuracy level.

In the literature, some kinds of assessment have been proposed. Gande and Devarajan [6] have used an Instructor/Operator Station to monitor user movements and to increase or decrease the degree of difficulty in a simulation. Their Instructor Station is able to evaluate and monitor the resident's performance, based on the specifications mentioned, to generate training effectiveness reports. The GeRTiSS system [1] can provide the user an assessment report at the end of simulation. That report contains the total time of intervention, number of cuts and cauterisations, among other information. The surgeon can use these pieces of information to perform an assessment of his/her intervention.

4   A Proposal for Multiple Assessment

A tool for multiple assessment must be interconnected with all users and must receive from them synchronized information about all variables of interest. An assessment system works coupled to a virtual reality simulator, as showed in the Figure 1 [13]. As an on-line assessment system, which should be capable to monitor user interactions while he/she operates the simulation system, a multiple assessment must be capable to monitor, simultaneously, the interactions of each user. In order to reach that, it is necessary to collect information about position in the space, forces, torque, resistance, speeds, accelerations, temperatures, visualization and/or visualization angle, sounds, smells, etc. To collect some information as force, force feedback, angles and torques, it is necessary to use specific devices to provide them. This information will be collected for each user in training system, as well as for all groups, to be used to feed the assessment system. Additionally, synchronization in time and space is necessary for all users to measure interactions among them, to determine the ordering of tasks and to provide details of user's performance.

User's interactions with the system are monitored and the information are sent to the assessment system which analyses the data and emits, at the end of the training, an

assessment report about the user's performance according pre-defined classes of performance. Therefore, a multiple assessment tool must be capable to monitor each user individually, as well as, all group. Then, at the end of simulation, another assessment report will be emitted about the group performance.
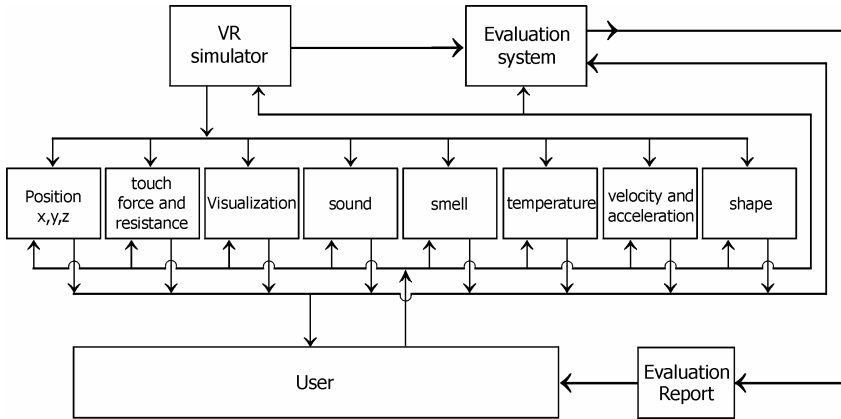
Fig. 1. Diagram of a VR simulator with an assessment system for a single user

As mentioned above, several methods were proposed to assess single user in training based on virtual reality. Most of them were based on classical classifiers. However, besides the fact that several of them could be used in multiple assessment tasks, there are calibration problems for multiple users. To minimize those problems, a multiple assessment system based on a fuzzy expert system [3, 11, 22] is proposed in this paper. This way, a set of fuzzy rules of an expert system time dependent defines each one of the possible performance classes. This set is designed, for single users and for group, from specialists knowledge. Additionally, interaction variables will be monitored according to their relevance to the training. Then, each application will have their own set of relevant variables which will be monitored [13]. The same happens with relevant variables which measure interactions among users in the group.

The methodology proposed for multiple assessment uses data collected from user interaction and group interactions during training to create user profile and group profile. That information is used to evaluate trainee and allows the improvement [21] of his performance in real tasks. That methodology makes a union of statistical tools and fuzzy rule based expert systems to construct an individual profile for trainee and for group. Statistical tools are programmed to make an automatic analysis of the database and construct statistical measures, tables, graphics and time dependent statistical models. From this information (statistical measures and parameters), the fuzzy expert system will create an individual user and group profiles and two kinds of report. These assessment reports present individual and group profiles and shows the performance of specific tasks with statistical measures, tables, graphics, models and some phrases in pseudo-natural language.

Figure 2 shows the new methodology presented. It can be observed that the Assessment System from Figure 1 has been changed and now it is called Individual

Assessment System. To construct the Multiple Assessment System, the Group Assessment Tool, the Users and Group Profiles were also added. The N users perform their training using a VR Simulator and interacting with a Interactive System, which is responsible by management of the virtual environment. The Interactive System must provide visual and haptic simulations for all users according their point of view and their haptic devices. From these information, statistical measures and parameters are taking and they are used as input for a fuzzy expert system, which analyse that information to recognize user's and group levels of training.

At the end of training, the new Multiple Assessment System creates two kinds of report: individual assessment report, for each user, and group assessment report. The first report is about the individual user performance on the training and the second assessment report is about group performance and the interactions among users during training. That kind of interactions are monitored to correct and improve details in specific procedures, as sequential tasks, simultaneous tasks or collaborative tasks. These kind of tasks are common in surgical rooms and the group's performance in some tasks can be essentials for the life and the patient's recovery.
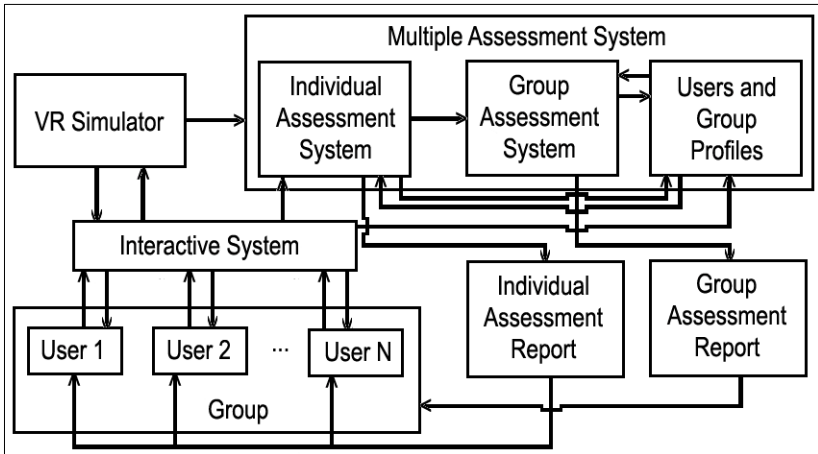
Fig. 2. Diagram of new Assessment System with approach of Continuous Assessment

This methodology for Multiple Assessment System can be used for several kind of training in medicine, as procedures in surgical rooms, training paramedics groups in emergency situations, etc. However, it is a generic methodology and can be used in training systems for other areas, as aeronautical simulators, maintenance group, managing of nuclear, thermoelectric, hydroelectric power plant, etc.

However, this Multiple Assessment System cannot be classified as on-line or off-line as in single user assessment systems. As mentioned before, an on-line assessment system must generate reports immediately after of the end of training session. Sometimes, the Multiple Assessment System will be capable to do that, but in another cases it will be not. The main reasons for that involve: computers configuration, possible delay in networks, number of statistical time dependent models necessary to measure some variables, complexity of simulation and number of interactions.

5 Conclusions

This paper presents a review for assessment systems for training based on virtual reality for single user. It was presented also the future of training based on virtual reality for multiple users with interactions among them. For this, are necessary new methodologies to allow the assessment of training for each user as well as for the group. In order to do that, was introduced a new methodology for multiple assessment for multiple users in training. This methodology is based on time-dependent fuzzy based rules expert system which uses input variables from training, statistical measures and time dependent statistical models in order to create measures of assessment for trainees and group performance.

The Multiple Assessment System can create two kinds of report: an assessment report for individual user, about his/her performance on the training, and an assessment report about group performance and interactions among users during the training. The Multiple Assessment System can be used in training situations when a group of trainees performs a task together, as in surgical rooms.

The methodology is generic and can be used in training systems for other areas, as aeronautical simulators, maintenance group, managing of nuclear, thermoelectric, hydroelectric power plant, etc. The main advantages of that approach are: a) individuals and group reports can be used to increase group performance and b) the interactions among users during training can be monitored to correct and improve specific details in procedure such as sequential tasks, simultaneous tasks or collaborative tasks.

References

1. Alcañiz, M., et al.: GeRTiSS: Generic Real Time Surgery Simulation. Studies in Health Technology and Informatics 94, 16–18 (2003)
2. Baier, H.: Distributed PC-based haptic, visual and acoustic telepresence system - experiments in virtual and remote environments. In: Proc. of IEEE VR, USA, pp. 118–125 (1999)
3. Blanchard, C., et al.: Reality built for two: a virtual reality tool. ACM CG 24(2), 35–36 (1992)
4. Burdea, G., Coiffet, P.: Virtual Reality Technology, 2nd edn. Wiley, Chichester (2003)
5. Carlsson, C., Hagsand, O.: DIVE: a platform for multi-user virtual environments. Computers & Graphics 17(6), 663–669 (1993)
6. Gande, A., Devarajan, V.: Instructor station for virtual laparoscopic surgery: requirements and design. In: Proc. of Computer Graphics and Imaging, USA, pp. 85–90 (2003)
7. Low, K-L., et al.: Combining head-mounted and projector-based displays for surgical training. In: Proc. of the IEEE VR, USA, pp. 110–117 (2003)
8. Machado, L.S., et al.: Fuzzy Rule-Based Evaluation for a Haptic and Stereo Simulator for Bone Marrow Harvest for Transplant. In: 5th PUG Workshop Proc. USA (2000)
9. Machado, L.S., et al.: A Virtual Reality Simulator for Bone Marrow Harvest for Pediatric Transplant. Studies in Health Technology and Informatics 81, 293–297 (2001)
10. Machado, L.S., Moraes, R.M.: Online Training Evaluation in Virtual Reality Simulators Using Evolving Fuzzy Neural Networks. In: Proc. 6th FLINS Conference. Belgium, pp. 314–317 (2004)

11. Machado, L.S., Valdek, M.C.O., Moraes, R.M.: Assessement of Gynecological Procedures in a Simulator Based on Virtual Reality. In: Proc. of the 7th FLINS Conference. Italy, pp. 799–804 (2006)
12. Moraes, R.M., Machado, L.S.: Using Fuzzy Hidden Markov Models for Online Training Evaluation and Classification in Virtual Reality Simulators. International Journal of General Systems 33(2-3), 281–288 (2004)
13. Moraes, R.M., Machado, L.S.: Fuzzy Gaussian Mixture Models for On-line Training Evaluation in Virtual Reality Simulators. In: FIP 2003, China, vol. 2, pp. 733–740 (2003)
14. Moraes, R.M., Machado, L.S.: Evaluation System Based on EFuNN for On-line Training Evaluation in Virtual Reality. In: Sanfeliu, A., Cortés, M.L. (eds.) CIARP 2005. LNCS, vol. 3773, pp. 778–785. Springer, Heidelberg (2005)
15. Moraes, R.M., Machado, L.S.: On-line Training Evaluation in Virtual Reality Simulators using Fuzzy Bayes Rule. In: Proc. 7th FLINS Conference, Italy, pp. 791–798 (2006)
16. Morris, et al.: A Collaborative Virtual Environment for the Simulation of Temporal Bone Surgery. In: Proc. MICCAI, France, pp. 319–327 (2004)
17. Morris, et al.: Visuohaptic simulation of bone surgery for training and evaluation. IEEE Computer Graphics and Applications 26(6), 48–57 (2006)
18. Park, K-S., Kenyon, R.V.: Effects of network characteristics on human performance in a collaborative virtual environment. In: Proc. of IEEE Virtual Reality, USA, pp. 104–111 (1999)
19. Rosen, J., Solazzo, M., Hannaford, B., Sinanan, M.: Objective Laparoscopic Skills Assessments of Surgical Residents Using Hidden Markov Models Based on Haptic Information and Tool/Tissue Interactions. Studies in Health Technology and Informatics 8, 417–423 (2001)
20. Shaw, C., Green, M.M.: Toolkit peers package and experiment. Proc. IEEE VRAIS, USA, pp. 463–469 (1993)
21. Sternberg, R.J., Grigorenko, E.: Dynamic Testing: The Nature and Measurement of Learning Potential. Cambridge University Press, Cambridge (2001)
22. Terano, T., Asai, K., Sugeno, M.: Fuzzy systems theory and it's applications. Academic Press Inc. San Diego (1987)
23. Voss, G., et al.: Intelligent Training System for Laparoscopy and Hysteroscopy. Studies in Health Technology and Informatics (70), 359–364 (2000)
24. Yoshida, S., Noma, H., Hosaka, K., Proactive Desk, I.I.: Development of a New Multi-object Haptic Display Using a Linear Induction Motor. In: Proc. IEEE VR Conference, USA, pp. 269–272 (2006)

Dynamic Penalty Based GA for Inducing Fuzzy Inference Systems

Tomás Arredondo V.[1], Félix Vásquez M.[2], Diego Candel C.[2],
Lioubov Dombrovskaia[2], Loreine Agulló[3], Macarena Córdova H.[3],
Valeria Latorre-Reyes[3,4], Felipe Calderón B.[2], and Michael Seeger P.[3]

[1] Departamento de Electrónica
tarredondo@elo.utfsm.cl
[2] Departamento de Informática
[3] Millennium Nucleus EMBA, Departamento de Química
Universidad Técnica Federico Santa María
Av. España 1680, Valparaíso, Chile
[4] Universidad de Magallanes, Punta Arenas, Chile

Abstract. Fuzzy based models have been used in many areas of research. One issue with these models is that rule bases have the potential for indiscriminant growth. Inference systems with large number of rules can be overspecified, have model comprehension issues and suffer from bad performance. In this research we investigate the use of a genetic algorithm towards the generation of a fuzzy inference system (FIS). We propose using a GA with a dynamic penalty function to manage the rule size of the fuzzy inference system (FIS) while maintaining the exploration of good rules. We apply this method towards the generation of a fuzzy classifier for the search of metabolic pathways. The GA based FIS includes novel mutation and a penalty based fitness scheme which enables the generation of an efficient and compact set of fuzzy rules. Encouraging implementation results are presented for this method as compared with other classification methods. This method should be applicable to a variety of other modelling and classification problems.

Keywords: Fuzzy logic, inference system, genetic algorithm, system modelling.

1 Introduction

A common task in bioinformatics research consists in the search and identification of genes encoding the enzymes of metabolic pathways of interest in recently sequenced genomes. Towards this purpose there exists a diverse set of tools, databases (e.g. KEGG, NCBI) and applications (e.g. BLAST, Artemis, Vector NTI). The integration of these resources is a current area of interest given the complexity and skill required to manually utilize all these means efficiently. One of these initiatives is GeXpert [1,2], an implementation of an integration framework that involves a systematic search scheme for the identification of genes encoding enzymes of metabolic pathways.

One of the tools that GeXpert includes is a gene evaluator based on a set of fuzzy rules [3] that attempts to estimate how good a candidate DNA coding sequence is for a given enzyme in a metabolic path. Until now, the rules used by this classifier were created manually from the knowledge provided by a group of bioinformatics researchers. Our current proposal is to use a penalty based GA to data-mine the classification rules from the set of previously analyzed genes for the organism under investigation. To the best of our knowledge, a GA based agent for fuzzy inference system (FIS) rule data-mining and training in bioinformatics is a novel application that has not been attempted before. We have also introduced new mutation and fitness schemes in this GA which attempt to emulate how a researcher would operate. Finally we have introduced a dynamic penalty function in order to constrain the number of fuzzy rules generated without affecting the initial exploration of the system. Initial results have shown that this algorithm is capable of synthesizing an efficient and compact fuzzy rule set when compared to other methods.

In section 2, we briefly explain the integration architecture and the implementation of GeXpert. Section 3 describes the FIS used in GeXpert. Section 4 describes the fuzzy trainer module that was implemented. In section 5, we describe the experiments performed to validate our work. In section 6, we explain our test results. Finally, in section 7 some conclusions are drawn and future research directions are presented.

2   Integration Framework Architecture

Towards metabolic reconstruction based on sequenced genomes, GeXpert implements an efficient research methodology as has been proposed in [4]. This methodology considers the following integrated workflow:

1. Create or import (e.g. KEGG) the metabolic pathway of interest in the organism under study.
2. Download the sequence of the enzyme (or subunits) being searched from a database (e.g. GenBank).
3. Perform alignments using tblastn between the selected proteins and the genome under investigation.
4. Using the fuzzy classifier, classify the sequences found according to their alignment scores: Identity, E-value, Gaps, Bit-Score.
5. Verify (e.g. using ARTEMIS) if there is an coding sequence (CDS) containing the sequence of the best alignments that were found.
6. If a CDS is found, the sequence is tested with a blastp alignment versus the proteins in a public database (e.g. GenBank).
7. If the proteins found that are aligned with the CDS sequence correspond with the enzyme that was searched for initially and there are documentation references (e.g. PUBMED) that validate its existence as a non putative protein then this enzyme or subunit is considered to have been found in the organism.
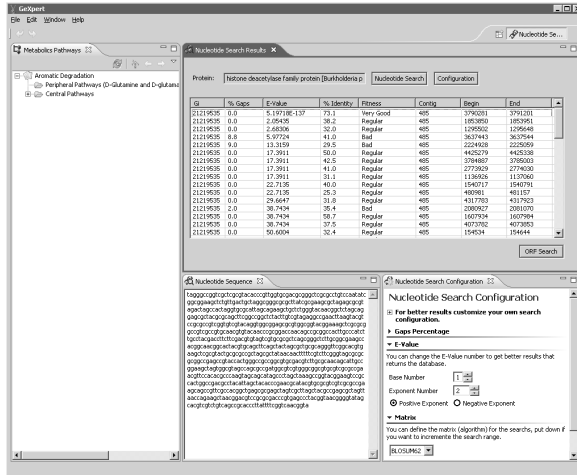
Fig. 1. GeXpert FIS graphical interface

The integration architecture includes three layers: the presentation layer, the logical layer and the data layer [2]. In our implementation of the presentation layer several graphical interfaces (e.g. as seen in Fig. 1) have been developed (e.g. to edit metabolic pathways, protein searches, visualizing CDS results and blast alignments). The logical layer contains the business logic relating with the different objects that encapsulate the applications and utilities used in the research process (e.g. relating with alignments, fuzzy classification, and CDS searches). The data layer manages all the interfaces (e.g. App Call, JDBC, SOAP) with various internal and external data sources (e.g. KEGG, GenBank, NCBI) and applications (e.g. BLAST, CN3D, Artemis). In this implementation, the training agent initiates interfaces with the core engine which is where the fuzzy system resides.

3 Fuzzy Inference System Workflow

The fuzzy inference system workflow is shown in Fig. 2. After a protein that forms part of a metabolic pathway that is being reconstructed has been identified, the researcher will perform a GenBank search using tblastn (Fig. 2(a)). This is to verify that the gene encoding the protein in question is found in another organism. Next, a list of possible candidates (each including four BLAST output values) will be transmitted to the fuzzy engine (Fig. 2(b)). The fuzzy engine will analyze the parameters and will make a recommendation to the user with respect to the quality of each of the candidates (Fig. 2(c)). Once the expert concludes (True of False) whether the gene encodes or not an enzyme or subunit of the metabolic pathway then the parameters, fuzzy recommendation and the expert conclusion are stored in the database as a training case (Fig. 2(d)).

If sufficient database entries are available, the scheduling agent or a user can initiate the fuzzy engine training process with the goal of tuning the recommendations
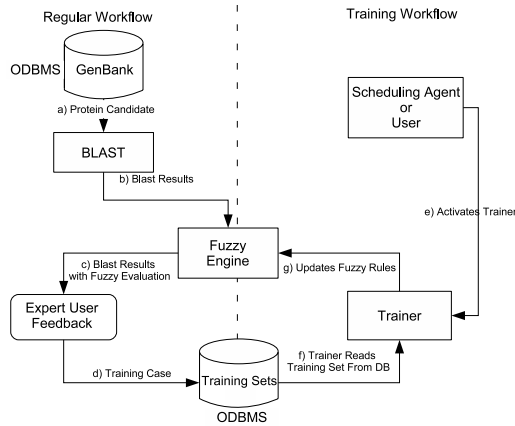
Fig. 2. FIS workflow

generated by the fuzzy inference engine (Fig. 2(e)-2(g)). This tuning can be periodically performed as the size of the training set increases.

4   Fuzzy Trainer Module Design

Fuzzy inference systems (FIS) are generally composed of: fuzzy rules, membership functions and a form of fuzzyfication/deffuzyfication. Any of these elements could be updated or modified towards tuning the FIS. In [5] the simultaneous modification of the membership functions and the rule base is proposed to optimize an FIS. The approach taken in our work follows [6,7] in which only the rule base is actualized during training.

4.1   Fuzzy Engine Structure

Fuzzy Rules. The rule base of the system follows the Mamdani method and has the following structure:

IF *E-value* is INVALUE **AND** *Bit-Score* is INVALUE **AND** *Identity* is INVALUE **AND** *Gaps* is INVALUE **THEN** *Output* is OUTVALUE.

Where INVALUE is a membership values with one of the following possible values { Very Low, Low, Medium, High, Very High }. OUTVALUE is the expected result for said combination of fuzzy inputs. OUTVALUE can take the following values { Very Bad, Bad, Regular, Good, Very Good }.

Membership Functions. Fuzzy membership functions take input parameters from $[0, 1]$. Input parameters that have different ranges are normalized before they are introduced into the FIS. Membership functions are triangular as is seen in Fig.3. The defuzzifier uses the centroid method using the maximum of all activated functions.
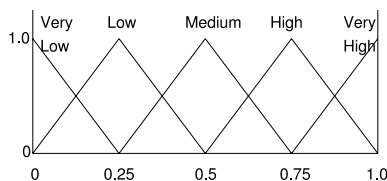
Fig. 3. Membership functions

4.2 GA Trainer Structure

As mentioned previously, the FIS is trained using a genetic algorithm. In this algorithm, each individual is composed of n genes, where each gene corresponds to a fuzzy rule.

GA Individuals. In our encoding, each fuzzy rule is defined by a set of 5 values that identify the different fuzzy sets for each of the four BLAST output values (E: E-value, B: Bit Score, I: Identity, G: Gaps) and the result (O: Output). These four output values are scored according to the alignment between sequences. Their relationship to whether a CDS truly encodes a given enzyme is not trivial to determine. As seen by the example in Fig. 4, the fuzzy values {Very Low, ..., Very High} and {Very Bad, ..., Very Good} are represented by {1, 2, 3, 4, 5} respectively.
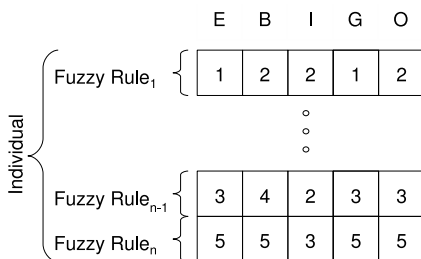
Fig. 4. GA codification

Genetic Operators. In our scheme, we have used one crossover operator and three different mutation operators. The mutation operators used generate a variable number of rules used which is essential to explore the problem search space given that we are using fixed membership functions. Using fixed membership functions and a variable number of rules is in our opinion more intuitive than other methods and better emulates how a human expert would update the FIS.

Crossover. In our system we are using a simple one point crossover that selects two individuals, ind_1 and ind_2, from the current population. Randomly selecting a value e, that is found in the interval $[0, a]$, with $a = \min(\text{size}(\text{ind}_1), \text{size}(\text{ind}_2))$. After this, the first e number of rules are exchanged between the individuals.

Mutation. The three mutation operators implemented are the following:

1. Adding Rules. This operator increases the rules of an individual by adding new random rules (genes) up to a specified factor μ of the original number of rules.
2. Removing Rules. This operator reduces the number of rules of an individual by removing up to a certain percentage factor ν of number of rules (genes). The rules are selected at random for removal.
3. Changing rules. This operator selects a random number of genes for modification in each individual. This operator selects the first b rules of an individual and mutates them, where b is a whole number chosen at random in the interval $[0, \text{size(ind)}]$. The mutation consists in choosing and changing at random one of the parameters that compose it.

The values for μ and ν were empirically chosen to be 0.33 as to not be too destructive but at the same time to allow for significant changes in the individuals.

Fitness Function. The fitness function used consists of two parts, the first is the sum of the hits (sh) obtained using the FIS. The value of sh is calculated based on the training cases tc_i that are stored in the database where $tc = [tc_1, tc_2, \ldots, tc_n]^T$ are generated as shown in Fig. 2. The second part consists of a penalty value that is applied to individuals which have a large number of rules (rp). To obtain the value of sh we sum the points obtained by the individual when we apply the values from each training example tc_i. The value of $sh(tc_i, O_i)$ is calculated using the values from scoring Table 1, where tc_i will have the values True or False and where O_i is the output expected for the i-th training example. Hence, $sh(tc)$ is calculated according to

$$sh(tc) = \sum_{i=1}^{n} sh(tc_i, O_i). \tag{1}$$

A bivariate sigmoid function is used for penalizing individuals with an excess number of rules depending on the current iteration number of the GA. This equation is defined as

$$rp(x, y) = \left(\frac{\alpha(y - \beta)}{1 + e^{(x-\gamma)\delta}} \right), \tag{2}$$

where x indicates the number of rules that compose the individual, y is the iteration number and $\alpha, \beta, \gamma, \delta$ are parameters. The parameter β indicates up to which iteration exploration should be favored (thus rewarding new rule creation and exploration). Past this iteration, the penalty for the number or rules begins to be effective. The other parameters are for sigmoid scaling. Finally, the fitness of an individual can be expressed as

$$F = sh(tc) - rp(x, y) \tag{3}$$

The parameters used in our experiments were empirically determined. Six tests were performed with various GA parameter values (e.g. crossover and mutation

probability) and in all situations only marginal fitness differences were seen (e.g. $1 - 5\%$). The number of elite individuals was chosen as to not cause too much premature convergence. In the case of α (penalty scaling) and β (beginning iteration for penalization) another six combinations were investigated. All resulted in minor differences in final results (e.g. considering true positives and negatives). Finally these were set to: $\alpha = 0.08, \beta = 80, \gamma = 100, \delta = -0.06$. γ and δ were set such that the penalty curve have an impact within a range of $0 - 225$ iterations.

Table 1. Scoring table for truth value assignment

	Very Bad	Bad	Medium	Good	Very Good	No Rule Fired
True	3	4	5	6	7	0
False	7	6	5	4	3	0

GA Parameters. The GA parameters were set as follows:

- Crossover probability=0.6.
- Mutation probability=0.26.
- Maximum generations=225.
- Population size=30.
- Number of elite individuals=4.
- Roulette selection method.

(a)   (b)
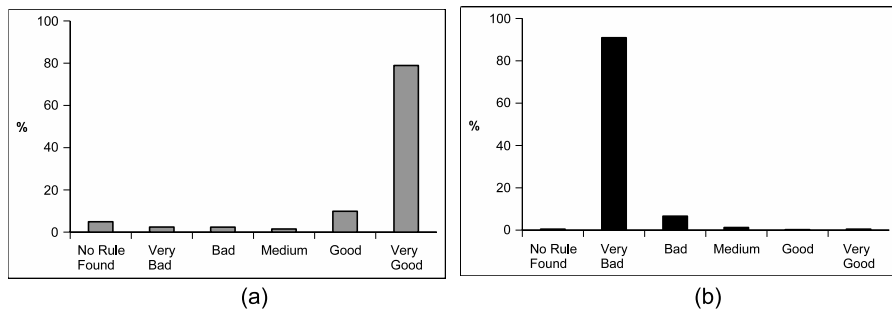
Fig. 5. Results obtained for the best set of rules (GA-2). In (a) we show true positives (Good, Very Good) and false negatives (Very Bad, Bad, Medium). In (b) we show true negatives (Very Bad, Bad, Medium) and false positives (Good, Very Good).

5   Experiments

Two experiments were performed in order to test our approach. The first was to compare the efficiency of using the current GeXpert system versus the previous manual research method. Results considered compared timings for 6 different metabolic pathways which genes are were organized in operon(2), distributed (2) and non existent(2). These results were taken from seven users of varying

competence. Three pathways were researched using the manual method and the other three were researched using GeXpert.

The other experiment was done in order to examine the training system developed. For this experiment, we used 248 sample genes. Out of these, 124 genes (true positives or TP) are encoding proteins of metabolic pathways of the bacteria *Burkholderia xenovorans* strain LB400 [8]. The other 124 genes were determined not be part of its genome (true negatives or TN). Out of this sample space, the system was trained with 62 true positive (TP) genes chosen at random and 62 true negatives that were also chosen at random. The other 124 genes (50% TN and 50% TP) were used as test cases to validate the method.

6 Results Obtained

In this section we present the results for the two experiments previously described. We present pathway search times and compare classifier performance.

The efficiency experiment showed that for our six researchers using GeXpert provides an average 400% faster search time than when using the previous manual research method. This vast improvement in time was tempered by a small average increase in enzyme error recognition (about 15%) which could be explained due to a lack of system familiarity or the reduced amount of spare time (e.g. idle time waiting) when using GeXpert. This error is reduced or even non existent in those researchers who were most familiar with GeXpert.

Table 2. FIS result comparison

Classifier	# Rules	SD Rules	TP%	FN%	TN%	FP%	Total True%	Total False%
SVM	NA	NA	86.0	14.0	100.0	0	92.7	7.3
H-Naive	400	0	86.0	14.0	30.0	70.0	58.0	42.0
H-Expert	163	0	70.0	30.0	100.0	0.0	85.0	15.0
GA-1	93	31	89.8	10.2	98.5	1.5	94.1	5.9
GA-2	60	15	89.9	10.1	98.9	1.1	94.4	5.6

In the fuzzy rule performance experiment, we compare five different classifiers: two sets of fuzzy rules (GA-1 and GA-2) that were generated by the GA training method, two human generated rules (H-Naive and H-Expert) and a standard SVM classifier implementation (Weka SMO [9]). GA-1 uses the method described previously but the fitness value (F) does not include the penalty function (rp) while GA-2 does. The H-Naive rules were constructed by analyzing in a short timespan (about 3 hours) the training data with the aim of covering the entire spectrum of possibilities. For the H-Expert rules a more detailed analysis was performed (about 6 hours) of the training data. For this analysis, fuzzy rules were created based on the input given by expert biochemists that work in the field of gene searching. Table 2 shows the results that were obtained including true positives (TP), true negatives (TN), false positives (FP), false negatives

(FN) as well as the total percentage true values obtained. For each test case of GA-1 and GA-2 an average of 40 test experiments are shown.

7   Conclusions

As seen by the test results, using the integrated search environment provides for much faster metabolic pathway search times than previous manual methods without much penalty in terms of additional error. The small error introduced was found in users who had less experience with the application and should be reduced as they gain more experience with it.

From these initial results it can be observed that using our training best algorithm (GA-2) we have obtained an overall improvement of 9% over the results obtained from the human expert rule sets. When compared with the other classifiers, GA-2 also provided good results with the lowest FN and FP values. GA-2 and its included penalty also produced smaller rule sets that had a lower standard deviation with respect to the number of rules generated (e.g. more predictable and smaller execution times). Otherwise results between GA-1 and GA-2 generated rule sets seem equivalent. GA-2 has a somewhat better overall performance than SVM given that its results are comparable when classifying true negatives but are better in the classification of true positives.

In our observations, in the case of GA-2 the number of rules is significantly lower than the rules that would be generated by other methods. The resulting reduction in FP and FN in GA-2 could be due to a reduction in the overspecification of the model regarding the training data or due to a reduction in rule contradictions. Other GA based fuzzy optimization methods [6,7] (without such a penalty function) could possibly benefit from such an approach. Also a reduction in the number of rules makes the FIS much more intuitive and easier to understand. Another benefit of the system is the flexibility provided by having multiple sets of parameter values (e.g. scoring table values, F function parameters) in order to penalize FP and FN in a differentiated manner.

Reducing rule bloat is an objective that seems to have been accomplished without any real damage to classification capability. In the future, we will focus on implementing our penalty based method on other fuzzy based classification applications (e.g. robotics [10]) to validate whether this approach is applicable to a variety of other problems. In general the system was robust to parameter variations which leads us to believe that they should work in a variety of situations. Function penalty is calculated in each generation and for each individual during training, but being a simple evaluation should not greatly increase the total execution time. Also, run time savings obtained through rule reductions should more than compensate for the training time increase.

Acknowledgements

References

1. GeXpert: Gexpert project website, http://sourceforge.net/projects/gexpert
2. Arredondo, T., Seeger, M., Dombrovskaia, L., Avarias, J., Calderón, F., Candel, D., Muñoz, F., Latorre, V., Agulló, L., Cordova, M., Gomez, L.: Bioinformatics integration framework for metabolic pathway data-mining. In: Ali, M., Dapoigny, R. (eds.) IEA/AIE 2006. LNCS (LNAI), vol. 4031, pp. 917–926. Springer, Heidelberg (2006)
3. Zadeh, L.: Fuzzy sets. Information and Control 8, 338–353 (1965)
4. Sun, J., Zeng, A.P.: Identics - identification of coding sequence and in silico reconstruction of the metabolic network directly from unannotated low-coverage bacterial genome sequence. BMC Bioinformatics 5, 112 (2004)
5. Peña-Reyes, C.A., Sipper, M.: Designing breast cancer diagnostic systems via a hybrid fuzzy-genetic methodology. In: FUZZ-IEEE 1999, vol. I, pp. 135–139. IEEE Press, Piscataway, NJ (1999)
6. Herrera, F., Lozano, M., Verdegay, J.L.: Generating fuzzy rules from examples using genetic algorithms. In: IPMU 1994, pp. 675–680 (1994)
7. Wang, W.J., Yen, T.G., Sun, C.H.: A method of self-generating fuzzy rule base via genetic algorithm. Control Conference, 2004. 5th Asian 3, 1608–1615 (2004)
8. Chain, P.S.G., Denef, V.J., Konstantinidis, K.T., Vergez, L.M., Agulló, L., Reyes, V.L., Hauser, L., Córdova, M., Gómez, L., González, M., Land, M., Lao, V., Larimer, F., LiPuma, J.J., Mahenthiralingam, E., Malfatti, S.A., Marx, C.J., Parnell, J.J., Ramette, A., Richardson, P., Seeger, M., Smith, D., Spilker, T., Sul, W.J., Tsoi, T.V., Ulrich, L.E., Zhulin, I.B., Tiedje, J.M.: Burkholderia xenovorans LB400 harbors a multi-replicon, 9.73-mbp genome shaped for versatility. Proc. Natl. Acad. Sci. USA 103, 15280–15287 (2006)
9. Weka: Waikato environment for knowledge analysis, http://sourceforge.net/projects/weka/
10. Arredondo, T., Freund, W., Muñoz, C., Navarro, N., Quirós, F.: Fuzzy motivations for evolutionary behavior learning by a mobile robot. In: Ali, M., Dapoigny, R. (eds.) IEA/AIE 2006. LNCS (LNAI), vol. 4031, pp. 462–471. Springer, Heidelberg (2006)

Author Index